Proceeding

ASRAM2025

Asian Symposium on Risk Assessment and Management

27-29 August 2025, Pattaya, Thailand

Preface

This volume is the Proceedings of the Asian Symposium on Risk Assessment and Management 2025 (ASRAM2025).

It compiles all peer-reviewed full papers and extended abstracts presented during the conference, organized according to the official program sessions. The purpose of these proceedings is to provide an internal academic record and a reliable reference for participants and organizers, as well as to support future collaboration among the community.

The editors gratefully acknowledge the contributions of all authors, reviewers, and session chairs who made this conference a success.

Local organizing committee

Content

Technical Session No.	Program	Page
Technical Session 1	Risk Assessment for Internal Event, Hazard and Safety Function Survivability, and Risk and Consequence Assessment Tool Development	1
Technical Session 2	Dynamic PSA, Accident Modelling and Uncertainty Analysis	42
Technical Session 3	Accident Modelling and Uncertainty Analysis	71
Technical Session 4	Human Reliability Analysis and Human and Organizational Factors I	103
Technical Session 5	Risk and Resilience Engineering and AI-based Risk Assessment, Decision Analysis, Security Analysis, Risk Communication and Policy	133
Technical Session 6	Source Term Analysis, Offsite Consequence Analysis and Emergency Preparedness and Response	163
Technical Session 7	Risk and Resilience Management and Risk-informed Decision Making, and AI based Tools	203
Technical Session 8	Safety, Security and Risk Analysis of Nuclear and Non-nuclear Facilities and Applications (Fuel and Equipment, Waste Facility, Tokamak Fusion, Radiation, Ship, Vehicle, Chemical Plants)	244
Technical Session 9	Risk Management and Risk-informed Decision Making and Severe Accident Modelling	274
Technical Session 10	Severe Accidents and Thermal Hydraulic Analyses and Accident Modelling	319
Technical Session 11	Advanced PSA technologies, Multi-unit PSA, and SMR PSA I	357
Technical Session 12	Risk Assessment for External Event and Hazard (Earthquake and Tsunami)	381
Technical Session 13	Advanced PSA technologies, Multi-unit PSA, and SMR PSA II	425
Technical Session 14	Offsite Consequence Analysis, Emergency Preparedness and Response	454
Technical Session 15	Risk Management and Risk-informed Decision Making, Operational Risk Analysis	495
Technical Session 16	Human Reliability Analysis and Human and Organizational Factors II	516
Poster Session 1	Severe Accidents and Thermal Hydraulic Analyses, External Events, Risk Communication and Policy	559
Poster Session 2	Safety and Risk Analysis of Nuclear Facilities and Radiation Application (Research Reactor, Tokamak Plasma Fusion, Nuclear Fuel Cycle, Cyclotron, Agricultural and Medical Industries) I	584
Poster Session 3	Safety and Risk Analysis of Nuclear Facilities and Radiation Application (Research Reactor, Tokamak Plasma Fusion, Nuclear Fuel Cycle, Cyclotron, Agricultural and Medical Industries) II	604

Technical Session No.	Program	Page
Poster Session 4	Safety and Risk Analysis of Nuclear Facilities and Radiation Application (Research Reactor, Tokamak Plasma Fusion, Nuclear Fuel Cycle, Cyclotron, Agricultural and Medical Industries) III	619
Special Workshop 2	ASEAN dialogue partner collaboration on safety and risk assessment (Closed Workshop)	650

Technical Session 1 (13:40 - 15:40)	The Port 1, C Floor	Risk Assessment for Internal Event, Hazard and Safety Function Survivability, and Risk and Consequence Assessment Tool Development
		Chair/Facilitator 1: Dr. Mazleha Maskin (Malaysian Nuclear Agency (NMA))
		Chair/Facilitator 2: Dr. Sung-Min Shin (Korea Atomic Energy Research Institute (KAERI))
13:40 - 14:00		ID 86: Development of the Internal Flooding PRA Guide for Use by the Japanese Nuclear Industry Speaker: Koji SHIRAI (Central Research Institute of Electric Power Industry (CRIEPI)) Contributors: Koji SHIRAI (Central Research Institute of Electric Power Industry (CRIEPI))
14:00 - 14:20		ID 38: Consideration on the Applicability of Mobile Equipment in Nuclear Power Plants Speaker: CHANGJU LEE (KINS) Contributors: CHANGJU LEE (KINS)
14:20 - 14:40		ID 131: Study on Influence of CCF Modeling in IE Fault Trees in Risk Monitor PSA Model of Nuclear Power Plants Speaker: Yuehua Hu (Shanghai Nuclear Engineering Research and Design Institute, 29 Hongcao Road, Xuhui District, Shanghai) Contributors: Yuehua Hu (Shanghai Nuclear Engineering Research and Design Institute, 29 Hongcao Road, Xuhui District, Shanghai)
14:40 - 15:00		ID 85: Failure Mode and Effect Analysis of PUSPATI TRIGA Systems: A Preliminary Step Towards PSA Level 1 Speaker: Mazleha Maskin (Malaysian Nuclear Agency) Contributors: Mazleha Maskin (Malaysian Nuclear Agency), Fedrick Charlie Matthew Brayon (Atom Malaysia), Phongsakorn Prak Tom (Malaysian Nuclear Agency), Mohd Zulfadli Ramli (Atom Malaysia), Ahmad Hassan Sallehudin Mohd Sarif (Universiti Tun Hussein Onn Malaysia)
15:00 - 15:20		ID 23: Enhancing Accuracy in Level 2 PSA Application of Partial BDD Method for High-Failure Rate Portable Equipment Speaker: Hyun-bin CHANG (Department of Nuclear Engineering, Kyung Hee University) Contributors: Hyun-bin CHANG (Department of Nuclear Engineering, Kyung Hee University), Gyunyoung Heo (Department of Nuclear Engineering, Kyung Hee University), Gyeongyeol KIM (FNC technology Co., Ltd.), Jaebeol Hong (FNC technology Co., Ltd), Junghyun Ryu (FNC technology Co., Ltd), Gunhyo JUNG (FNC technology Co., Ltd.)
15:20 - 15:40		ID 65: Investigating the Validity of Weather Bin Sampling in Level 3 PSA Speaker: Sung-yeop Kim (Korea Atomic Energy Research Institute) Contributors: Sung-yeop Kim (Korea Atomic Energy Research Institute)

ASRAM2025
www.asram2025.org
Asian Symposium on Risk Assessment and Management 2025
Pattaya, Thailand, 27 – 29 August 2025

DEVELOPMENT OF THE INTERNAL FLOODING PRA GUIDE FOR USE BY THE JAPANESE NUCLEAR INDUSTRY

Koji Shirai[1], Tsuyoshi Uchida[2], Motomu Suzuki[3], Kohei Nonose[4], Daichi Nagai[5]

[1] *1646 Abiko, Abiko-shi, Chiba, 270-1194, Japan, shirai@criepi.denken.or.jp*
[2] *2-11-1 Iwadokita, Komae-shi, Tokyo 201-8511, Japan, t-uchida@criepi.denken.or.jp*
[3] *2-6-1 Nagasaka, Yokosuka-shi, Kanagawa 240-0196, Japan, s-motomu@criepi.denken.or.jp*
[4] *2-6-1 Nagasaka, Yokosuka-shi, Kanagawa 240-0196, Japan, nonose@criepi.denken.or.jp*
[5] *1646 Abiko, Abiko-shi, Chiba, 270-1194, Japan, nagai41245@criepi.denken.or.jp*

ABSTRACT

The Nuclear Risk Research Center (NRRC) is promoting R&D activities on risk assessment to contribute to the implementation of Risk-Informed Decision-Making (RIDM) processes for safety control and improvement in Japanese nuclear power plants. Regarding internal hazard events (e.g., internal fire and flooding), although the utilities have deterministically evaluated and managed the impact of these events for the business licensing activities to restart the NPPs in Japan, the NRRC has been working on the R&D activities to promote the development of technologies for assessing the risks due to internal hazard events.

The NRRC expects to ensure the scientific rationality and transparency of newly developed techniques through discussion in academic societies or associations, to quantify the uncertainties associated with such risks and with their assessment, and to achieve realistic (i.e., free from excessive conservatism) assessment by applying PRA and other developed methodologies to use them in daily activities, such as responding to regulatory inspections, revising procedural documents and improving training programs. This paper will focus on key issues related to recent innovative research results obtained from NRRC risk assessment activities, particularly the development of the internal flooding PRA guide. The guide is expected to be published by the end of 2025.

Keywords: Internal hazard, Internal Flooding, Risk-Informed Decision-Making, Flooding Propagation Event Tree, Internal Flooding Damage State

I. BASIS FOR DEVELOPING NUCLEAR RISK RESEARCH CENTER INTERNAL FLOODING PRA GUIDE

I.A. Introduction

Internal Flooding Probabilistic Risk Assessment (IF-PRA) serves as an effective systematic assessment tool for evaluating the baseline risk contribution from internal flooding (IF). It is also an important consideration during plant operations, including corrective and predictive maintenance on both safety and non-safety-related systems. Additionally, insights gained from IF-PRA can help enhance various plant programs, such as piping aging management and in-service inspection.

Japanese nuclear power plant owner-operators, along with the Japanese regulator, are highly interested and motivated to conduct high-quality IF-PRA to better understand baseline risk, identify potential vulnerabilities, and integrate these models into a comprehensive strategy for transitioning to risk-informed programs, including the Significance Determination Process (SDP) and On-Line Maintenance (OLM) [1].

I.B. Objectives for Developing the NRRC's IF-PRA Guide

To address the nuclear industry's need for developing high-quality IF-PRAs, the NRRC evaluated existing IF-PRA guidance documents (IF-PRAG), such as those from the Electric Power Research Institute (EPRI), as well as publicly available IF-PRA reports, including that for the Surry Power Plant. Based on this evaluation, the NRRC initiated the development of a

comprehensive IF-PRAG with the following objectives and with the aim of completing the establishment of the IF-PRAG by the end of 2025:

- Improve the ease of application in Japan, taking into account the current state of practice and expertise in the country [2]
- Incorporate NRRC's research in specific areas, such as the narrative base human reliability analysis (HRA) methodology [3], impingement direction [4] and the potential failure of flood doors [5]
- Fully leverage publicly available information, especially the data and specific methodologies outlined in the EPRI reports, through referencing these valuable sources of information [6], [7]

Conducting the IF-PRA analysis in Japan using this guide will facilitate the systematic collection, integration and evaluation of operational experience that is unique to nuclear power plants in Japan. This includes site-specific maintenance practices, localized equipment failure data, and historical records of piping degradation and structural failures. Incorporating these insights enables the analysis to more accurately reflect actual plant conditions and the operational environment. In addition, the approach outlined in the guide enables the identification of high-priority research areas where further investigation could yield significant safety and reliability improvements. At the same time, the methodology supports the use of relevant international data and best practices, ensuring consistency with global standards and enabling benchmarking and continuous improvement. This dual benefit of leveraging both domestic and international experience enhances the robustness and applicability of the IF-PRA results for regulatory, operational and research purposes.

I.C. An Example of Differences Between NRRC IF-PRA Guide and EPRI Guides

The two EPRI IF-PRA related reports that are extensively leveraged in the NRRC IF-PRAG are:

- "Guidelines for Performance of Internal Flooding Probabilistic Risk Assessment", EPRI 1019194, Final Report, December 2009
- "Pipe Rupture Frequencies for Internal Flooding Probabilistic Risk Assessments", Revision 5, EPRI 3002024904 Final Report, August 2023

The first listed EPRI document is directly equivalent to the NRRC's IF-PRA guide. This EPRI document is over 190 pages and contains highly valuable and insightful information. This valuable information include:

- Material which forms the basis for the latest version of the EPRI guide (e.g., section 1.31., "Lessons Learned from Ft. Calhoun IFPRA" and section 1.3.2, "Results of 2009 Survey on IFPRA"),
- Use of specific example to provide a methodology. For example, in Section 5.5, "Flood From HELB-Induced Fire Protection System Actuation" (from page 5-10 to page 5-26), an example for a specific plant SDP is used " to show how to address several technical issues and associated requirements in the ASME/ANS PRA Standard."

The NRRC's IF-PRAG values and leverages this insightful information while streamlining the assessment steps to enhance ease of application. It eliminates historical background and unnecessary direct information for performing an analysis step while incorporating other publicly available resources and NRRC's research findings to complement the information in the EPRI report and the significant publicly available IF-PRA report [8] that the NRRC's guide leverages.

II. Overall Task Flows

A task flow chart of the overall IF-PRA is divided into two major phases:

- ***Qualitative phase (Phase A)***, consisting of Tasks 1 through 4.
- ***Quantitative phase (Phase B)***, consisting of Tasks 5 through 14.

II.A. Qualitative Phase A

II.A.1. Task flow of Phase A

Fig.1 shows the task flow of Phase A. This phase pertains to acquiring the information that forms the foundation for the IF PRA and performing the qualitative phase of the project.

- ***Task 1 - Plant Boundary Definition, Flood Areas and SSCs***: The purpose of this task is to clearly delineate the areas

within a facility that are to be included in the scope of the internal flooding PRA analysis and to identify flood characteristics of the locations.

- ***Task 2 - IF Scenarios***: The IF scenarios are first developed in this task using conservative assumptions. The output of this task is a list of the IF scenarios that start at a specific source and end with either exhaustion of the source or reaching a steady state (i.e., no further failures and no increase in flood depth).
- ***Task 3 - Walkdown***: Walkdown is a critical element of IF-PRA. The key issues of plant walkdowns are as follows:
  - Verification of Information
  - Identification of Vulnerabilities
  - Assessing Consequences
  - Gathering Accuracy and Completeness
- ***Task 4 - Qualitative Screening***: Those flood areas that their pertinent flooding scenarios do not impact any PRA SSCs or operator actions are screened out at this step.

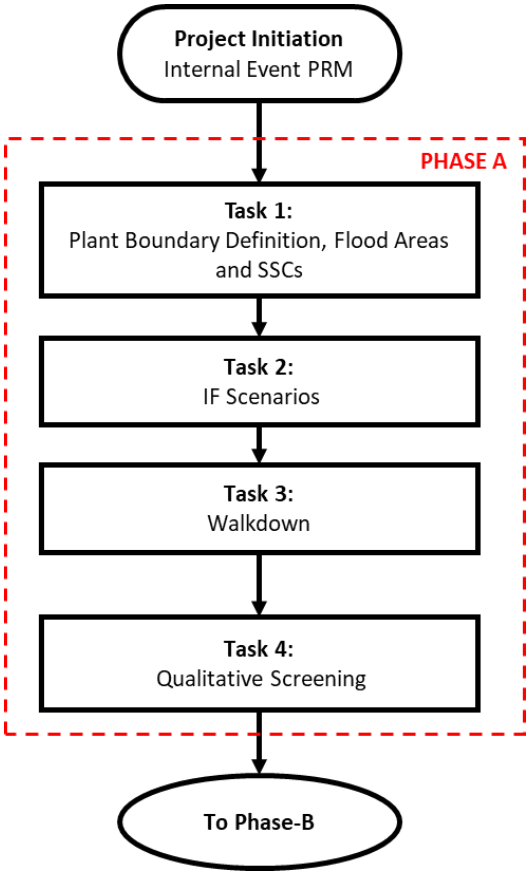

FIGURE 1. QUALITATIVE PHASE (PHASE A) OF AN IF-PRA

II.A.2. Discussion: Importance of Plant Walkdowns

In the NRRC's IF-PRAG, the importance of plant walkdown is emphasized. Plant walkdowns are a critical element of the IF-PRA process. They play a vital role in defining flood areas and identifying potential flood sources, affected components, propagation paths, and features for damage prevention and mitigation. The most significant contributions of walkdowns include:

- ***Verification of Flood Protection Systems:*** Walkdowns can verify that flood barriers (e.g., walls and doors), and protection measures are or are not capable and reliable under various flooding conditions.
- ***Verification of Information Accuracy:*** Walkdowns can verify the accuracy of the information used in the PRA (e.g., flood sources, flood propagation pathways, etc.)

- ***Gathering Supplemental Information:*** Walkdowns can provide additional information that may not be available in plant drawings and documents.

Walkdowns are typically conducted multiple times throughout the completion of an IF-PRA, including the following phases:

- ***Plant Familiarization Walkdown***: Conducted before the analysis phase of the project (e.g., prior to developing scenarios as outlined in Task 2). This walkdown allows team members to become fully acquainted with the plant layout and flood area configuration. This early familiarity is especially critical if the analytical work is performed by an internal flooding expert who may not be fully knowledgeable about the plant.
- ***Verification Walkdown***: Typically performed prior to the screening phase to ensure that the scenarios identified in Task 2 are reasonable and that no potential scenarios have been overlooked.
- ***Detailed Analysis Walkdown***: Typically conducted to gather additional information needed for the detailed analysis. This may include measuring the height of components or verifying the spray zone of influence.

The IF-PRAG presents the procedures for performing all three types of walkdowns in Task3 as described later, aiming to streamline the structure of guidance. However, it is crucial for IF analysts to be fully aware of all three walkdown types and to ensure that thorough walkdowns are conducted.

II.B. Quantitative Phase B

II.B.1. Task flow of Phase B

Fig.2 shows the task flow of Phase B. The quantitative analysis is conducted using IF scenarios that have passed Phase A. Phase B may involve several iterations in which risk-significant scenarios are further detailed. The process concludes when either the scenarios can no longer be refined or when the risk reduction becomes negligible.

- ***Task 5- Flood Propagation Event Tree (FPET) Preparation***: The purpose of this task is to initiate an event tree that represents flood propagation through different stages for each flooding source. For each flood source a FPET is developed based on the applicable failure mechanisms (e.g., equipment failure vs. maintenance-induced), applicable failure mode (e.g., spray or pipe breaks), and any mitigating features or operator actions that are credited to terminate flooding to limit the damage. This may result in a flooding scenario to be sub-divided into a number of sub-scenarios.
- ***Task 6 - IF Scenario Frequencies and Flooding Rates***: The IF scenarios are first developed in this task using conservative assumptions. The output of this task is a list of the IF scenarios that start at a specific source and end with either exhaustion of the source or reaching a steady state (i.e., no further failures and no increase in flood depth).
- ***Task 7- Equipment Damage Probability***: The scope of this task is to provide guidance on estimating probability of equipment damage, in a particular flooding area, based on the scenario and area specific flooding scenario characterization derived from performing Tasks 5 and 6.
- ***Task 8 - Internal Flooding Damage State (IFDS) Characterization***: The purpose of this task is to establish a comprehensive process for characterizing IFDS based on the end states derived from flood propagation event trees for each area within the facility.
- ***Task 9 - PRM for IF-PRA***: The purpose of this task is to review and modify the internal-events PRM to reflect the postulated IFDSs.
- ***Task 10 - Analysis of Operator Action***: The purpose of this task is to review and modify the human failure events (HFEs) included in the PRM to account for the impact of IFs, conduct a HRA of the HFEs added to the PRM that address IF specific conditions, identify process parameters that should be added to the PRM to properly model human actions and update the human error probabilities (HEPs) and dependency matrix.
- ***Task 11 - Risk Quantification***: The purpose of this task is to quantify the risk for each postulated IFDS, summation of which will provide an estimate of the IF risk. The main objectives of the risk quantification task are quantifying risk levels and identification of key contributors.
- ***Task 12 - Reduction in Conservatism***: The purpose of this task is to provide a list of items (e.g., event timing, refinements in HEP Evaluation, spray direction, location and range and so on) that can be utilized to reduce conservatism in the characterization and risk quantification of IFDSs.
- ***Task 13 - Uncertainty Analysis and Sensitivity Analysis***: A set of sensitivity analyses cases are defined in this task to examine the effect of certain assumptions incorporated in the analysis on the final results.

- ***Task 14 – IF-PRA Final Report***: IF-PRA includes a wide range of documents and computer files that should be organized in a fashion amenable to quality control and updates at a later time when plant or other changes are considered. It should be noted that the detailed documentation for each task is included in each task and this task provides guidance for a summary report for the IF-PRA.

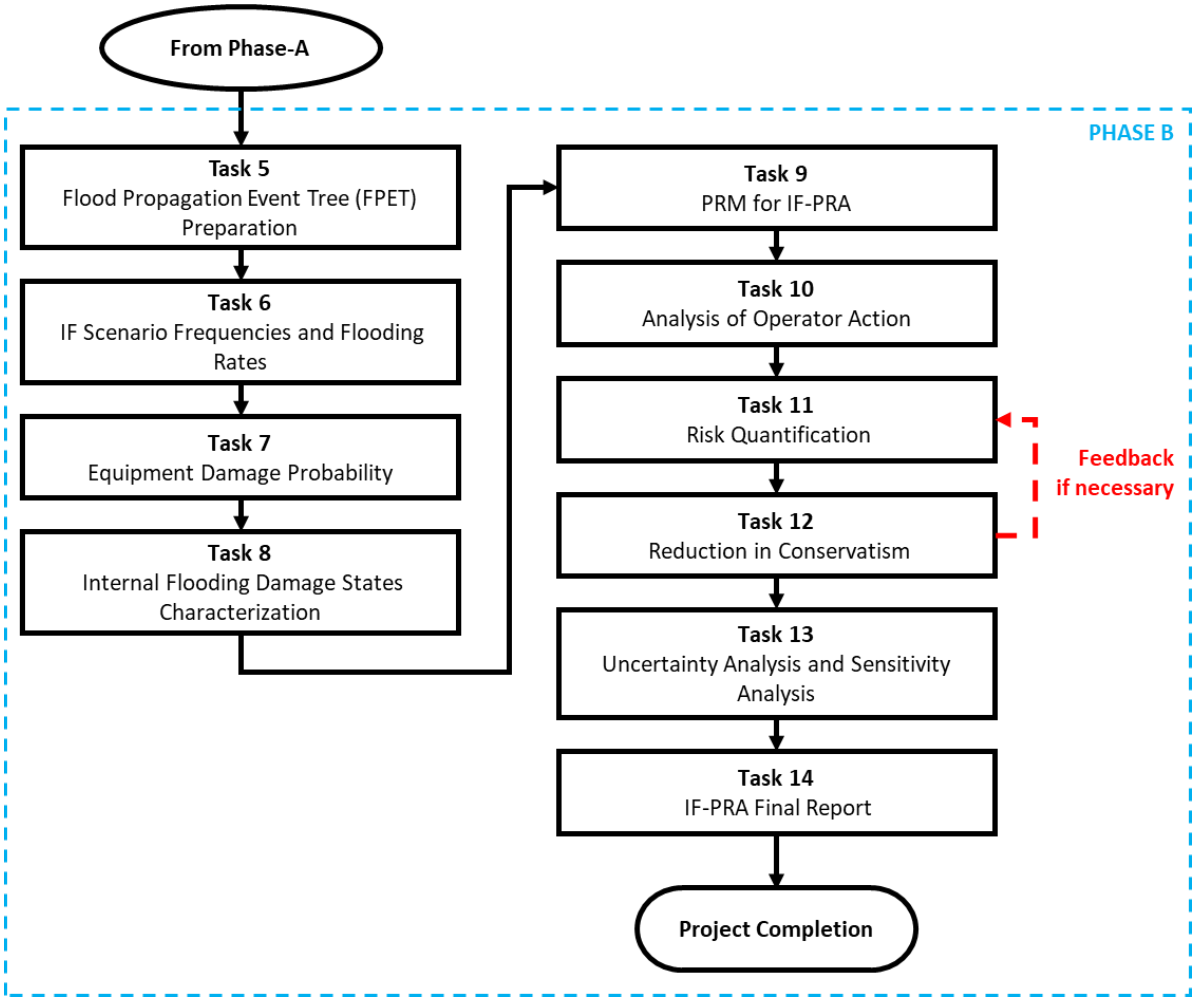

Figure 2 QUANTITATIVE PHASE (PHASE B) OF AN IF-PRA

II.B.2. Discussion: Practical Implementation of Uncertainty Analysis

When performing IF analysis, several key parameters should be assessed for uncertainty. These parameters include flood initiation frequency, flood volume and rate, flood propagation Modeling, SSC failure criteria and fragility, HRA, and success criteria and logic modelling. This guide discusses the following recommendations for practical implementation.

- Begin with a qualitative uncertainty evaluation to ensure reasonable assurance that important scenarios are not missed
- Focus detailed uncertainty quantification on risk-significant scenarios or sequences
- Revisit uncertainty treatment as plant configuration, data, or methods evolve
- Coordinate IF uncertainty analysis with the broader PRA uncertainty framework to ensure consistency

An important consideration is the strategic use of NUREG-1855 [9] and the concept of 'consensus models'. This strategy plays a critical role in establishing the credibility and regulatory acceptability of the technical models used in PRA. Its benefits are summarized below.

- Reduced burden of justification
- Increased regulatory confidence

- Alignment with NUREG-1855's risk-informed framework
- Facilitates consistency across PRA applications

In summary, due to the modeling complexity, lack of reliable input data, dominance of epistemic uncertainties, and complexity of the analysis, full-scale uncertainty analysis for IF PRA may provide limited value. Instead, a qualitative uncertainty screening, supported by targeted sensitivity analyses and justified conservative modeling assumptions, is likely to offer a more efficient and technically defensible approach for addressing uncertainty in internal flooding analyses.

III. FLOOD PROPAGATION EVENT TREE (FPET) EXAMPLE

In this guide, an example of a flood propagation event tree is introduced, which illustrates the potential scenarios that may occur during flooding incidents within the designated areas of an assumed facility. For this illustration, we are focusing on two specific assumed flood areas as shown Fig.3, which are:

- Flood Area 01 (FA-01): High Head Injection Pump 1A Room
- Flood Area 02 (FA-02): High Head Injection Pump 1B Room

Each of these two postulated flood areas house a high head charging pump. These rooms are physically separated by a fire door, which has a two-inches gap at the bottom. This design element is critical as it slows down the propagation of floodwater between the two rooms. Additionally, both FA-01 and FA-02 incorporate the following critical flood protection measures designed to reduce the impact of a potential flooding event:

- Elevated Installation of Charging Pumps- Each charging pump in FA-01 and FA-02 is mounted on a 30 cm (approximately one-foot) high base. This elevation serves a dual purpose: it raises the pump above potential floodwaters and provides additional time to isolate a faulted header should there be a loss of structural integrity within the piping system. By allowing personnel a brief window to respond to the situation, this measure helps limit water damage.
- Construction of Berms- A 60 cm (approximately two feet) high berm has been strategically constructed around the door that connects FA-01 and FA-02. This berm acts as a vital containment feature, specifically engineered to mitigate the impact of flooding by effectively blocking water from entering or exiting the designated areas. The berm is designed to withstand potential floodwater, providing a physical barrier that helps protect the sensitive infrastructure and equipment within both flood zones.
- An alarm in the sump in each flood area, which alarms in the control room, to notify operators of a flooding event in each flood area.
- Abnormal operating procedure to respond to the sump alarm in each room.

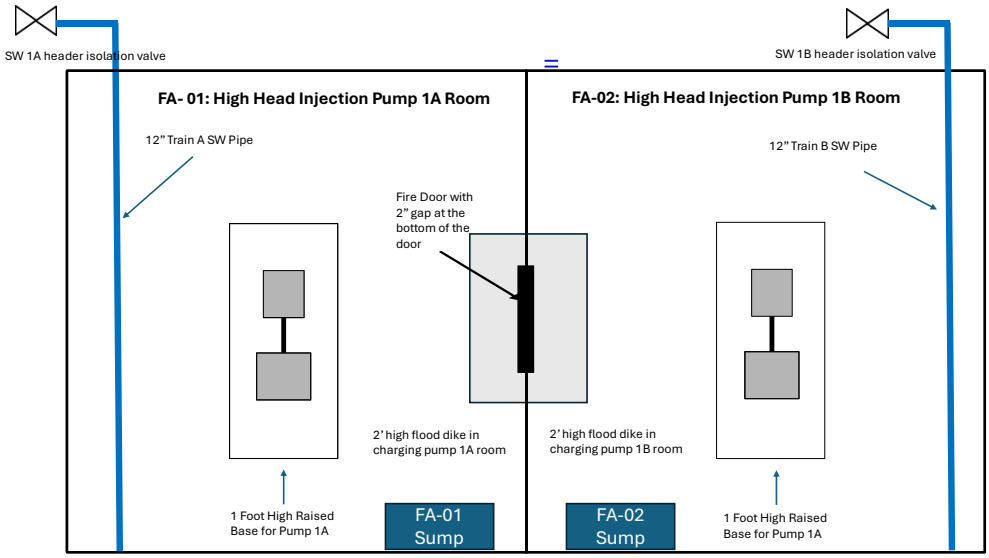

Figure 3 EXAMPLE OF FLOOD PROPAGATION SCENARIO

To simplify the example, the primary flooding source in each of these example flood areas is attributed to the pressurized Service Water (SW) headers. Specifically, within FA-01, the relevant header is identified as the SW 1A, while the header serving FA-02 is designated as the SW 1B. These pressurized headers transport service water throughout the facility for operational purposes, and their maintenance and integrity are crucial for mitigating flooding risks.

Each SW header is equipped with a manual isolation valve, which is a critical component for controlling the flow of service water. In the event of a leak or rupture in one of the headers, the appropriate isolation valve can be closed to quickly isolate the affected section, thereby minimizing the potential for flooding in the adjacent areas. It is essential to note that these isolation valves are strategically located in the corridor that lies adjacent to the two flood areas, providing easy access for personnel during emergencies.

In the case of a flooding incident, prompt action is required to operate the manual valves, as any delay could result in significant water intrusion into FA-01 or FA-02. Therefore, it is imperative for staff to be well-trained in the procedures for swiftly accessing and operating these isolation valves. Regular drills and maintenance checks on both the headers and their associated valves should be conducted to ensure they remain functional and responsive in case of an emergency.

The above information is typically gathered during execution of Tasks 1-3. Additionally, neither of these areas are screened out in Task 4. Finally, step by step execution of Tasks 5 through 10 should be executed to develop a flood propagation event tree as well as quantifying the resulting internal flooding damage states.

In Task5, FPET preparation will be executed to establish a comprehensive and well-defined set of flooding scenarios based on the flooding sources in the area. This will facilitate analysis of the unique impacts of resulting scenarios on plant operations. This identification process serves as a crucial foundation for subsequent steps, such as grouping and screening the scenarios, as well as estimating the frequencies of flood-initiating events. This Task5 includes the following steps.

- Identify Flooding Initiator for Each Flood Propagation Event Tree
- Assign Flooding Mechanisms for Each Flooding Initiator
- Assign Flooding Modes (e.g., Spray, Small Breaks, Lage Breaks) to the Flooding Mechanisms
- Credit Each Flood Mitigating and Flood Damage Prevention Feature

Finally, after execution of Tasks 6-8. IFDS can be characterized based on the end states derived from FPETs for each area within the facility. Fig.4. shows the example of the FPET. As a result, the contributions of the aforementioned IFDSs to the plant internal flooding risk are calculated by quantifying the modified event trees. The total internal flooding risk contribution from FA-01 is estimated by summing up the risk estimates for the three IFDSs. The total internal flooding risk contribution from FA-02 is judged to be the same as FA-01 due to both FAs been identical from the flooding risk perspective.

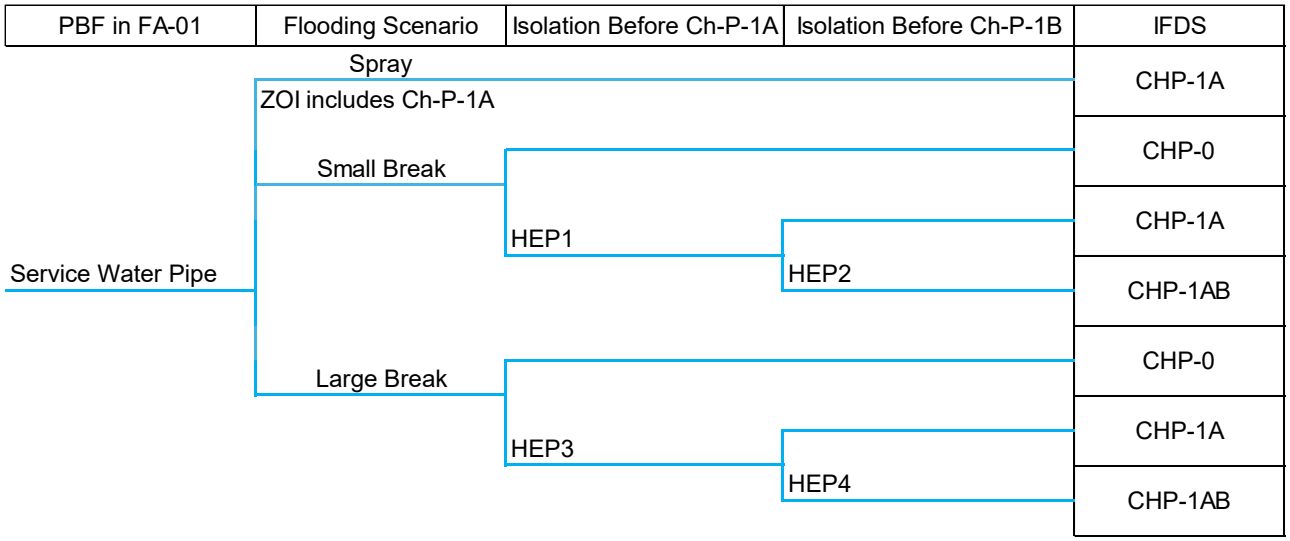

Note PBF: Pressure Boundary Failure

FIGURE 4 EXAMPLE OF FPET

IV. CONCLUSIONS

The utility and regulator's desire for developing IF-PRAs for various purposes, ranging from understanding potential baseline vulnerabilities to applications in risk-informed programs, has necessitated the rapid development of high-quality IF-PRAs. Considering the current state of expertise and practice in Japan, along with a review of available guidelines, the NRRC concluded that the best option is to produce a high-quality, streamlined guide focusing primarily on the steps to be performed and the methodologies for executing them.

To this end, the NRRC's IF-PRAG is being developed to:

a. Concentrate on the essential steps that need to be performed, and
b. Utilize the most relevant references - primarily the EPRI guide, supplemented by the results of the NRRC's research - to clarify how to perform those steps. The importance of plant walkdowns is also emphasized extensively.

Additionally, a slightly different approach is suggested in certain areas, such as when addressing the potential consequences of spray flooding mode. Finally, the NRRC's IF-PRAG aims to be consistent in its usage of IF-related terms by distinguishing between flooding sources, mechanisms, and modes. The guide is expected to be published by the end of 2025.

ACKNOWLEDGMENTS

Members of the working group on internal flooding and fire PRA who come from Japanese utilities have discussed the NRRC's IF-PRAG with NRRC analysts and provided helpful comments. Dr. Mardy Kazarians, a PRA expert in the U.S., provided valuable input during the development of the IF-PRAG. Mr. Amir Afzari, an IF-PRA expert in the U.S., provided valuable suggestions and recommendations when reviewing this guide. Dr. Apostolakis, Director of the NRRC, offered valuable feedback and encouragement to the authors regarding their progress and technical issues. We, the authors of this paper, would like to express our sincere gratitude.

REFERENCES

[1] Hokkaido Electric Power Co., Inc., Tohoku Electric Power Co., Inc., Tokyo Electric Power Co., Inc., Chubu Electric Power Co., Inc., Hokuriku Electric Power Co., Inc., The Kansai Electric Power Co., Inc., The Chugoku Electric Power Co., Inc., Shikoku Electric Power Co., Inc., Kyusyu Electric Power Co., Inc, The Japan Atomic Power Co. Inc., Electric Power Development Co., Inc., "Strategic and Action Plans for the Establishment of a Risk-Informed Decision-Making Process at Nuclear Power Plants (updated in 2023)", December 2023.
[2] T. Uchida, K. Shirai, K. Nonose, M. Suzuki and J. Ji, "LESSONS LEARNED FROM AN INTERNAL FLOODING PRA FOR A MODEL PLANT", ASRAM2022, Asian Symposium on Risk Assessment and Management 2022, 30 November – 2 December 2022
[3] Kirimoto et.al, "Guide for Qualitative Analysis in the Human Reliability Analysis (HRA) with Emphasis on Narratives (FY 2020 Edition)," O20003, Central Research Institute of Electrical Power Industry (CRIEPI), May 2021.
[4] Shun WATANABE et.al, "Evaluation of dispersion behavior of horizontal water jet by using flow visualization method (in Japanese)," Transaction of the JSME (DOI:10.1299/transjsme.20-00109), August 2020.
[5] D. Nagai et.al, "Internal flooding fragility experiments using full-scale fire doors to evaluate door failure water height and leakage flow rate under hydrostatic pressure loads", Probabilistic safety assessment and management PSAM16, 2022.
[6] Electric Power Research Institute (EPRI), "Guidelines for Performance of Internal Flooding Probabilistic Risk Assessment", EPRI-1019194, Final Report, December 2009.
[7] ANS/ASME RA-S-1.1-2022, "Standard for Level 1/Large Early Release Frequency Probabilistic Risk Assessment for Nuclear Power Plant Applications", May 2022.
[8] Virginia Electric and Power Company, "Surry Power Station Units 1 and 2, Individual Plant Examination - Internal Flooding Reanalysis", 1991.
[9] United States of Nuclear Regulatory Commission (U.S. NRC), "Guidance on the Treatment of Uncertainties Associated with PRAs in Risk-Informed Decision making", NUREG-1855 Revision 1, Final Report, March 2017.

ASRAM2025
www.asram2025.org
Asian Symposium on Risk Assessment and Management 2025
Pattaya, Thailand, 27 – 29 August 2025

Consideration on the Applicability of Mobile Equipment in Nuclear Power Plants

Chang-Ju Lee

Korea Institute of Nuclear Safety (KINS): 62 Kwahak-ro, Yuseong-gu, Deajeon, Rep. of Korea, 34142, cjlee@kins.re.kr

ABSTRACT

The experience of the Fukushima accident in Japan, where the stationary safety equipment at the power plant was not available, highlighted the usefulness of mobile equipment. In Korea, the implementation of an Accident Management Program (AMP) was mandated by law in 2015, and one of the requirements is to meet nuclear safety goals. Currently, the Korean utility recognizes that the use of mobile equipment is essential to meet the safety goals, which means that it has become important to introduce new mobile equipment at domestic nuclear power plants to reduce nuclear risk. However, in the initial application process to achieve the original purpose, there have been many trial-and-errors in terms of the type of equipment, the variety of specifications and accident management strategies used, and the adequacy of functional tests.

This paper discusses the basic safety strategy concepts for the introduction of mobile equipment in terms of a time-based approach and a safety function-based approach, and examines whether it is possible to establish specific acceptance criteria for risk reduction based on safety objectives when these concepts are considered. In addition, it will be examined whether it is possible to specify the currently proposed role of mobile equipment through this process.

Keywords: Mobile Equipment, Accident Management Program, PSA, Safety Goals, CDF, LERF, Nuclear Risk

I. Introduction

The Fukushima accident in Japan showed that stationary safety equipment at the nuclear power plants (NPPs), such as emergency diesel generators, could not be used under the adverse conditions of a combined natural disaster such as earthquake and tsunami, highlighting the utility of mobile equipment.

In Korea, the implementation of an Accident Management Program (AMP) became a legal requirement in 2015 [1]. The Korean utility was required to implement AMP for all their plants, which included operating guidelines for relevant equipment, including severe accident management, so the establishment of an accident management strategy for the effective operation of this equipment became an issue.

AMP-related requirements need compliance with nuclear safety goals and safety assessments for natural hazards. Nuclear safety goals, which respond to various internal and external events, include the core damage frequency (CDF), the frequency of large and early release (LERF) and, in particular, the CS-137 release requirement. At present, the domestic utility recognizes that safety systems with enhanced safety capabilities are needed to meet nuclear safety goals, and for this purpose it is essential to strengthen the in-depth defense of NPPs not only by strengthening existing stationary facilities but also by adding mobile equipment, i.e. MACST (Multiple-barrier Accident Coping Strategy) facilities. In other words, it has become important to reduce NPP's risks by introducing new mobile equipment at domestic NPPs.

However, there has been much trial-and-errors in the initial application to achieve the original purpose, including the variety of equipment types, specifications and accident management strategies used, as well as the adequacy of functional demonstration tests. There are two main approaches to assessing the safety of mobile installations. The first is to improve response capabilities through the design and strengthening of facilities, and the second is to establish accident mitigation strategies for the use of mobile equipment, taking into account the failure of stationary facilities. At this stage, deterministic or probabilistic methods are used to determine the level of accidents to be assessed. For example, the deterministic method is a method that increases the magnitude determined by the design criteria by a certain ratio (e.g. 1.5 times), and the probabilistic

method is a magnitude determined based on a conventional cycle of 10,000 years as an example. Once the magnitude of the disaster has been determined, the impact of the NPP's facilities is assessed.

In a general concept, mobile equipment should be stored in a location that minimizes the possibility of damage from an extreme disaster, and the optimal transport route should be secured so that the equipment can be transported to the connection site of the reactor facility with minimal impact from the extreme disaster. There are two ways to verify the safety of mobile equipment: cyclic test and demonstration test. A cycle test is a test in which the mobile equipment is manually started at the storage site and connected to a simulated load to verify the possibility of continuous operation for a specified period of time. A demonstration test, as an example of power generator, is a way to verify the ability to supply power by moving and connecting the mobile equipment from the storage site to the electric bus connection point, manually starting it and applying loads to the bus in a specified sequence. These tests shall meet the evaluation criteria of the relevant test procedure. In addition, new operating guidelines and procedures must be prepared for the actual use of the mobile equipment in a NPP after safety verification.

Strategies for MACST facilities are currently being developed and there has been little research on the utilization or effectiveness of these facilities. Yoon [2] conducted a Probabilistic Safety Assessment (PSA) model-based sensitivity analysis to develop an optimization strategy for the effective use of limited MACST facilities in a multi-units site.

Chapter 2 of this paper describes the current accident management strategies for the use of mobile equipment, and Chapter 3 presents the evaluation results for each case based on the PSA analysis. Chapter 4 presents the available acceptance criteria and measures, and describes the application cases of the analyzed application results.

II. Accident Management Strategy for the Use of Mobile Equipment

An accident management strategy using mobile equipment in a NPP is to have equipment that can respond to simultaneous or sequential loss of essential safety functions. This is based on lessons learned from the Fukushima accident in Japan and focuses on the use of mobile equipment to restore essential safety functions in response to external events that exceed design criteria. For example, individual US NPPs have implemented FLEX (Diverse and Flexible coping strategy) strategies in accordance with NEI 12-06 guidance [3] to reduce the risk of core damage and release of radioactive material in the event of an extended loss of all AC power (ELAP) event and a loss of ultimate heat sink (LUHS) event.

The Korean AMP PSA model focuses on risk reduction by reflecting improvements to existing facilities and the addition of mobile equipment, taking into account their practical use. The types of accidents that require PSA to meet nuclear safety goals include not only internal events but also external events such as earthquakes, internal fires and internal floods. Therefore, it is not enough to get insights in the consequences of external events when assessing risks only based on internal event model.

A practical challenge is to ensure that the guidance required for the use of mobile equipment is properly aligned with existing plant procedures and/or guidelines. The accident management guidelines describe the specific actions to be taken by the personnel of the plant emergency organization to implement the accident management strategy in the event of an accident and are prepared taking into account the necessary information, wording and structure, terminology and units of measurement to enable efficient implementation of accident management. Examples of annexes to AMP and its guidance documents are given in Table 1.

In the event of a design basis accident or multiple failure incident, an applicable abnormal procedure is clearly defined and will be implemented through alarms and key parameter checks. Alternatively, if a reactor is shutdown, the applicable emergency operating procedures (EOPs) will be applied based on clear symptoms determined through diagnosis of the accident. A natural disaster that exceeds the design basis will always result in an initial response that is similar. If we need to respond to an accident using mobile equipment, such as in the event of an extreme disaster during the execution of the EOP, follow the multi-defense operation guidelines (MOGs). When the accident worsens during recovery and mobile equipment are required, this guideline is used. If the condition for entering any severe accident becomes during mitigation, the accident is mitigated by switching to the severe accident management guideline (SAMG). The extensive damage mitigation guideline implements a wide area damage mitigation strategy in case of man-made disasters that exceed the design criteria. The necessary measures can be linked to the EOP. It is essential that the impact assessment of these various accidents can be evaluated both deterministically and probabilistically.

Table 1. AMP Supplemental Reports/Guidelines

No.	Title of Guideline/Procedure	Remarks
1	Multi-Failure Incident Management Capability Assessment Report	Not related to PSA
2	Composite PSA Reports	
3	Emergency Operating Guidelines (EOGs)	
4	Multi-Defense Operation Guidelines (MOGs)	Related to MACST
5	Severe Accident Management Guidelines (SAMG)	Related to Level 2 PSA
6	Extensive Damage Mitigation Guidance (EDMG)	Not related to PSA

In this paper, we set out the fundamental safety strategy concepts for introducing mobile equipment. We can categorize the concepts as a mitigating time-oriented approach and a safety function-oriented approach, etc.

II.A. Mitigating Time-oriented Approach

The basic strategy for securing necessary functions to respond to accidents such as natural disasters that exceed design criteria is done by the MACST facilities, which consists of three phases depending on the time of utilization. Figure 1 shows the overall response strategy by phase.

* Phase 1: Response strategy using stationary equipment in a plant
* Phase 2: Response strategy using mobile equipment within a site boundary
* Phase 3: Response strategy using stationary-but-failed equipment restoration, mobile equipment within the site, and off-site resources.

The Phase 1 is to maintain the plant in a hot standby state with natural circulation using fixed stationary equipment until mobile equipment is available. The priority action in the Phase 1 is to quickly cool the reactor coolant system (RCS) within the maximum cooling rate using the atmosphere dump valves (ADVs) in accordance with the RCS early cooling/decompression strategy. In the ELAP event, non-essential loads are switched off to extend the life of the storage batteries as much as possible. In addition, plant walkdown is conducted to determine the damage to the plant caused by the accident, and mobile equipment is required to be appropriately deployed from the consolidated storage to a pre-planned area to prepare for the implementation of the second phase of the strategy.

The Phase 2 is to utilize mobile equipment as much as possible. This means that the mobile equipment that were moved and deployed from the consolidated storage in Phase 1 are operated according to the appropriate operating procedures for the plant conditions to continue maintaining the plant in a stable state. For power restoration, the 1 MW Mobile Power Generator (MPG) is connected to a 4.16 kV safety bus to provide alternating current power. After connecting the 1 MW MPG, the RCS inventory is maintained using charge pumps. If a charge pump is inoperable or the depressurization of RCS is delayed, a high-pressure mobile pump can be used to replenish the RCS inventory. If turbine-driven auxiliary feedwater (AFW) pump is inoperable, a low-pressure mobile pump is used to supply cooling water to the steam generator through the external injection line.

Finally, the third phase is basically to stabilize the plant by continuing to use stationary equipment and mobile equipment used before. This long-term recovery strategy also includes the use of resources within the site or at other nuclear sites in Korea. In particular, in the case of mobile equipment used in domestic NPPs, the MACST facilities can be effectively implemented because the equipment specifications and operation methods are the same for each mobile equipment at each NPP. The three-step strategy is to first connect a 3.2 MW MPG for the operation of component cooling water (CCW) system and essential service water (ESW) system. If the ESW pump is not operational, a high-flow mobile pump will be used to supply seawater to the CCW heat exchanger. Once the 4.16kV safety-rated power supply and the final heat removal source for the operation of the unit CCW system are secured, the shutdown cooling system is operated to maintain the plant in a safe shutdown state. Therefore, even in the event of a natural disaster that exceeds the design condition, such as ELAP or LUHS event, the RCS inventory is sufficiently maintained to ensure core cooling by responding to the accident according to these 3-phase strategies.

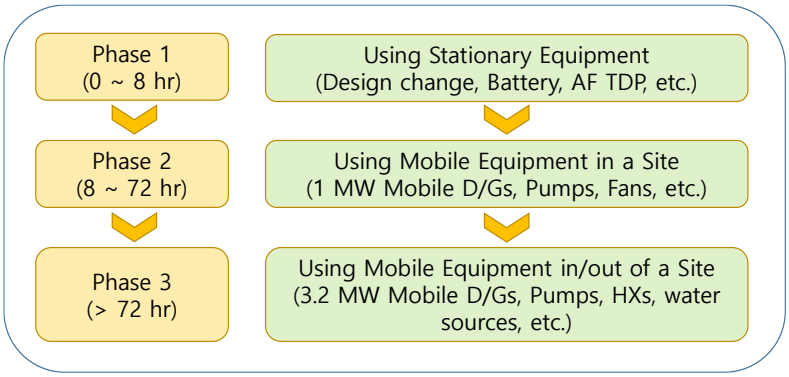

Figure 1. Strategy for utilizing Equipment (stationary and mobile) by 3 Phases

II.B. Safety Function-oriented Approach

MACST, like FLEX, is one of the critical accident prevention and mitigation strategies and facilities to maintain and restore essential safety functions under extreme natural disaster conditions, primarily through the provision of power and cooling water. Specific safety functions considered in the function-oriented approach are typically power supply, RCS inventory control, final heat removal source, containment overpressure protection, and spent fuel pool cooling, etc.

Depending on its safety function, mobile equipment is relevant to each of the initiating events covered by the PSA. For instance, MPGs supply power to essential loads by connecting to the local power grid within an acceptable timeframe if the alternate AC generator (AAC) installed to cope with a station blackout (SBO) is unavailable. Therefore, this equipment is closely related to the SBO mitigation function. At developing SBO event tree scenario in PSA, this equipment is modeled and evaluated in case of AAC failure, which is assigned as an additional mitigation function. This evaluation process is applied similarly to external events, though the evaluation modeling may change depending on the characteristics of an external event.

An ELAP event is a situation where both the emergency diesel generator and the alternate AC power source are unavailable due to a natural or man-made disaster that exceeds the external conditions considered in the multiple failure design criteria in the accident management scope. In such a case, a stationary AC power or mobile source shall be available to provide reliable power to the essential loads connected to the main electric safety bus. The utility has proposed a 3.2 MW MPG, a 1 MW MPG and a 10 kW MPG as means to fulfill the power supply function (Category A as shown in Table 2). A 1 MW MPG provides power to a series of safety-related AC bus, and a 10 kW MPG performs the function of supplying electricity to the control panel of AFW pump.

External water injection facilities for inventory control are used to inject alternative emergency cooling water into the reactor, steam generators, and spent fuel pool to prevent a severe accident when stationary means of cooling water in the plant, such as emergency core cooling system or AFW system, are not available. Low-pressure mobile pump are proposed as a means of accomplishing this function (Category B). In addition, a high-pressure mobile pump is proposed for the reactor coolant pump (RCP) leakage replenishment and RCS inventory control.

To secure the ultimate heat sink function (Category C), a high-flow mobile pump is deployed and operated to supply alternative CSW to the residual heat exchanger during low-pressure cold leg recirculation operation. Containment pressure control function (Category D) is used to protect the containment building from high temperature and/or overpressure conditions that could be caused by a severe accident. For certain NPPs, this control function is considered to be either an emergency containment spray backup system (ECSBS) or a containment filtered-vent system (CFVS). The ECSBS also uses mobile pumps.

In case of large area damage caused by man-made disasters such as aircraft crashes (Category E), a high-pressure mobile sprinkler truck or a 30 kW MPG is provided. High-pressure mobile sprinkler truck can spray directly from outside of the plant

building for cooling water supply. 30kW MPG performs the function of supplying electricity to the reactor cavity filling valve for cooling core melting materials in case of loss of core cooling function. In addition, a low-pressure mobile pump and a high-pressure mobile sprinkler truck are proposed as means for performing the cooling function in the spent fuel pool.

Table 2 lists the mobile equipment used for each of the above functions, classified by 5 categories. Auxiliary supporting equipment for each functions include fuel oil tankers, tow trucks, emergency lighting, communication equipment, mobile air compressors, and temporary fans and ducts, etc. The mobile equipment is primarily stored in the consolidated depot of plant headquarters. The mobile equipment stored in the consolidated depot is transported to the plant along the main or alternate transportation routes. In a natural disaster that exceeds the design criteria, for example, debris from the tornado causes road traffic obstructions, the consolidated depot is equipped with road restoration facilities. The road repair equipment removes debris from the traveled way to ensure the passage of towed or vehicle-mounted mobile equipment.

Table 2. List of Mobile equipment utilizations by Safety Function Categories

Category	Safety Function	Essential Equipment	Optional Equipment
A	Securing emergency power	Mobile Power Generators	
B	Obtaining/Refilling Coolant	Low Pressure Mobile Pump, High Pressure Mobile Pump	Mobile Water Purification
C	Secure ultimate heat sink	High-flow mobile pump	
D	Containment building overpressure protection	(ECSBS) Pumps	
E	Human-caused disaster response	High-pressure mobile sprinkler truck	

II.C. Operating mode-oriented Approach (Optional)

For some NPPs, a 3.2 MW MPG or a 1 MW MPG is being considered to be pre-positioned through the power cable installed at all times to solve the issue of power supplying time in the ELAP situation due to extreme disasters. Also, for some NPPs, pre-deploying mobile equipment nearby a NPP, such as low pressure mobile pump, during the shutdown operation is considered.

As such, selectively adopting different application situations such as the operation mode of mobile equipment may result in risk differences through the applicability assessment.

III. Results of Sensitivity Analysis

In order to understand the practical applicability of each proposed mobile equipment to currently operating NPPs, accident scenario analysis and system analysis, for example, are additionally performed. Also, ultimately, the following insights should be provided:

- The level of increased risk that would be affected by the exclusion of the mobile equipment
- The level of risk increase or decrease due to changes in the way the equipment is operated
- Determine the impact on key safety functions based on the level of risk change.

For the case of risk impact assessment, which includes accident scenario analysis, system analysis, and/or human reliability analysis, the level 1 PSA method is primarily used. However, if the mobile equipment affects the containment building integrity, Level 2 PSA method is used. The result is usually expressed as a delta CDF or LERF, which provides risk insight into the increase or decrease in risk with and without mobile equipment.

III.A. Assumptions

When performing the evaluation with the relevant mobile equipment, the followings are assumed in the accident scenario analysis or human reliability analysis, and the others.

a) If initial secondary heat removal operation by turbine-driven AFW pump is successful after an alternate diesel generator fails to start, and both the restoration of offsite power and the mobile MPG are unsuccessful, the external feedwater

supply is provided to at least one of the two steam generators using a mobile pump, and steam release is performed using at least one of the two ADVs installed on the steam generator to which the feedwater is supplied or one or more main steam safety valves.

b) In the accident of steam generator tube rupture, if the operator is unable to perform IRWST filling from the boric acid water storage tank and the supplementary water tank, the IRWST filling is performed using a low-pressure mobile pump.
c) In the event of a complete loss of CCW and a RCP seal failure, a high-pressure mobile pump shall be used to fill the RCS inventory.
d) If RCP seal is intact, the secondary side heat removal is maintained using the turbine drive AFW pump by supplying power to the battery charger using a MPG within the battery availability time extended by non-essential load shedding.
e) Maintaining containment heat removal by supplying external cooling water to the containment spray nozzles using the mobile pump of the ECSBS.
f) Assuming the establishment of a response organization to operate the mobile equipment, the operator arrives at the consolidated depot and operates and applies it in available time. The related human tasks are divided into cognition, execution, and recovery measures. So, available times are assumed for accident diagnosis, arrival at the depot, moving the equipment and taking the load, and additional allowances.
   - 3.5 hours to remove a mobile equipment from depot, connect it to the grid, and start it up.
   - 2 hours for pre-deployed mobile equipment during planned maintenance to be connected to the grid and operation.
   - 1.5 hours to connect to the grid and start operation of a pre-positioned MPG (with pre-laid power lines)

III.B. Evaluation Case #1 - Impact on the whole Exclusion of Mobile Equipment

The sensitivity analysis of Level 1 full power (FP), including low power and shutdown (LPSD) states, PSA for all initiating events (internal, earthquake, fire, and flooding) for recently operating NPPs (specific #1) is shown in Table 3, reflecting the exclusion situation of mobile equipment. The internal event has the largest increase in CDF when mobile equipment is excluded, while the flooding event has the smallest impact on CDF.

Table 3. Results of Level 1 PSA sensitivity analysis for Specific NPP #1

Initiating Events	Operating Mode	Increasing Rate of CDF w/o Mobile Equipment	Remark
Internal Events	Full Power (FP)	307.4 %	
Seismic	FP	56.4 %	
Fire	FP	96.1 %	
Flooding	FP	53.7 %	On-going Update
Internal Events	Low Power and Shutdown (LPSD)	264.6 %	
Seismic	LPSD	3.6 %	
Fire	LPSD	84.7 %	
Flooding	LPSD	2.8 %	
Total Value		200.4 %	

Table 4 also shows that the sensitivity analysis results of Level 1 PSA for all initiating events on the relatively-old NPP (specific #2). The initiating event with the largest increase in CDF, when mobile equipment is excluded, is internal events during LPSD operation, while the initiating event with the smallest impact in CDF is the FP flooding event.

As shown in the results of evaluation case above, we can identify that mobile equipment are more useful for internal events and relatively less useful for external events. The reason for these results is probably due to differences in analysis methodology or assumptions for using mobile equipment and different event response conditions. Also, in the LPSD internal event model, mobile equipment provide mitigation measures for scenarios where it is difficult to mitigate the accident with conventional stationary facilities, reducing the CDF of the corresponding accident scenarios in the base model. The details of sensitivity analysis show that some of changed accident scenarios without mobile equipment are located in the upper minimal cutset of CDF.

Table 4. Results of Level 1 PSA sensitivity analysis for Specific NPP #2

Initiating Events	Operating Mode	Increasing Rate of CDF w/o Mobile Equipment	Remark
Internal Events	FP	84.8 %	On-going Update
Seismic	FP	18.8 %	
Fire	FP	20.7 %	
Flooding	FP	0.0 %	
Internal Events	LPSD	1,257.0 %	
Seismic	LPSD	28.1 %	
Fire	LPSD	30.6 %	
Flooding	LPSD	362.6 %	
Total Value		336.8 %	

There is a difference between the results in Table 3 and Table 4 for each initiating event in terms of the percentage increase in CDF when whole mobile equipment are excluded. This may be due to the presence or absence of safety design enhancements between the new and old plants, differences in analytical modeling, and differences in the baseline CDF values themselves, and a detailed understanding of the causes would require a lot of effort from an expert perspective that encompasses the knowledge of both plants. However, there is an interesting point that the CDF change rate in terms of total CDF (for both full power and LPSD modes in all initiating event cases) has no significant difference between the specific NPPs, but it's hard to say for sure without more information. A comparison of the two reveals that specific NPP #2 is more likely to contribute to plant safety than specific NPP #1 with regard to the utilization of mobile equipment.

The results in Table 4 show that mobile equipment contributed significantly to the growth rate of internal events in SBO accidents. However, cases such as flooding events had little change in the CDF growth rate when mobile equipment were excluded because these events do not cause a loss of offsite power or SBO due to their event characteristic.

III.C. Evaluation Case #2 - Impact on the Fire Risk of Specific Plant Exclusion

The sensitivity analysis result of FP fire PSA for specific NPP #2 shows that the impact of mobile equipment (20.7%) is not significant. Also, the sensitivity analysis results for the LPSD fire PSA without mobile equipment show an increase by 29.0% compared to the original result. We can find that, in case of fire event, the increase is smaller than internal events, when excluding mobile equipment, because some mitigating features are not often available due to lack of supplying electric power or water from mobile equipment due to cable fire and/or equipment fire damage.

Table 5. Results of Sensitivity Analysis for Selected Fire Zones of Specific NPP #2

Fire Zones	Initiating Event	Mobile Equipment used in the Analysis	Increasing Rate of CDF (in a fire zone) w/o Mobile Equipment
Room A (given with safety-grade switchgear)	Loss of Offsite Power	3.2 MW MPG and 1 MW MPG	162 %
Room B (Ditto)			213 %
Room C (given with CCW pumps)	Loss of CCW	High-pressure Mobile Pump	256 %
Room D (given with ESW pumps)			256 %

In addition, the following results of Specific NPP #2 show in Table 5 that a significant increase of CDF without mobile equipment for each fire zone. Table 5 also provides the list of mobile equipment used in the analysis with representative

initiating event of the fire zone. For example, because it typically results in the loss of equipment and cables due to room C or room D fires, while the impact of high-pressure mobile pump, which can provide cooling water at loss of CCW event to replace stationary equipment failure due to fire, is identified as more significant. We believe that the currently proposed role of mobile equipment and its risk impact, depending on equipment-specific initiating event, could be identified.

III.D. Evaluation Case #3 – Impacts by Pre-positioning and/or Pre-deployment Strategy

Pre-positioning means that some of mobile equipment normally stored in the consolidated site depot is regarded as permanently-placed on a NPP. On the other hand, pre-deployment refers to the temporary deployment of some of mobile equipment stored in the consolidated site depot to a plant during preventive maintenance period.

The 1 MW MPG, which is considered as a representative pre-positioning equipment, has one for each unit in the NPP and spare one in the consolidated site depot. Therefore, human error probability estimation for 1 MW MPG excludes the task associated with moving to the site, unlike other mobile equipment. For other mobile equipment, the human action associated with moving to the site is added because they are stored in a consolidated site depot. This is the same for both FP and LPSD periods. The sensitivity analysis without pre-positioning of mobile equipment, reflected in the Level 1 LPSD PSA, shows that the CDF increases by approximately 3.9%.

III.E. Evaluation Case #4 - Impact on the Medium MPG Uninstallation

In the case of Specific NPP #2, a 500 kW medium-sized MPG was initially proposed to reduce the risk by using it as a direct power supply to the containment fan cooler (RCFC) to maintain the integrity of the containment building during severe accident. However, as a result of Level 2 PSA, it was found that there was little risk reduction from the operation of the RCFC with this mobile equipment, therefore, the installation of the equipment was ultimately canceled.

IV. Risk Metrics and Acceptance Criteria for the Application

One of consideration in the application of mobile equipment is checking the applicability by the choice of risk metrics. Depending on the selected metric, sound decisions can be made, such as prioritizing the adoption of the equipment. The most common metric can be selected is the delta CDF. Other metrics other than delta CDF may be considered, e.g., targets such as LERF. As you know, LERF and other endpoints can be determined by performing a Level 2 PSA or Level 3 PSA. Therefore, for mobile equipment (e.g., one for external containment spraying) that contribute to the results of the PSA, and also the relevant evaluation metrics, including calculated Cs-137 releases, should be applied.

We checked whether it is possible to establish acceptance criteria or specific selection categories for risk reduction based on the delta CDF when reflecting the basic safety strategy concept presented in Chapter 2. We also checked whether it is possible to prioritize the adoption of the currently proposed mobile equipment through this process.

For example, there is a regulatory document [4] that provides general requirements and procedures that are considered appropriate for checking relevant issues and assessing their impacts during the review process when risk information is utilized in an application for a license to modify a reactor facility submitted by the licensee. Since this regulatory guidance is intended to provide a general basis for decision-making in the safety review of risk-informed applications, we believe that it can be adopted as an acceptance criterion for the applicability of the problem in this paper.

The acceptance criteria in the relevant regulatory guidance, i.e., Reference [4], are applied to ensure that the increase in risk from the proposed modification is minimized and consistent with safety objectives. They also represent a judgment on the cumulative and synergistic effects of the proposed modification on the overall risk profile of the reactor facility, as well as the risk variation. Reference [4] establishes acceptable, unacceptable and detailed evaluation zones for risk changes representing specific adoption categories. An example of the results of applying the above Evaluation Case #1 for Specific NPP #2 is shown in Figure 2.

Referring to Figure 2, it can be seen that the sensitivity analysis of the total delta CDF of this NPP without mobile equipment is in the unacceptable zone, indicating that the proposed mobile equipment is essentially required for this NPP.

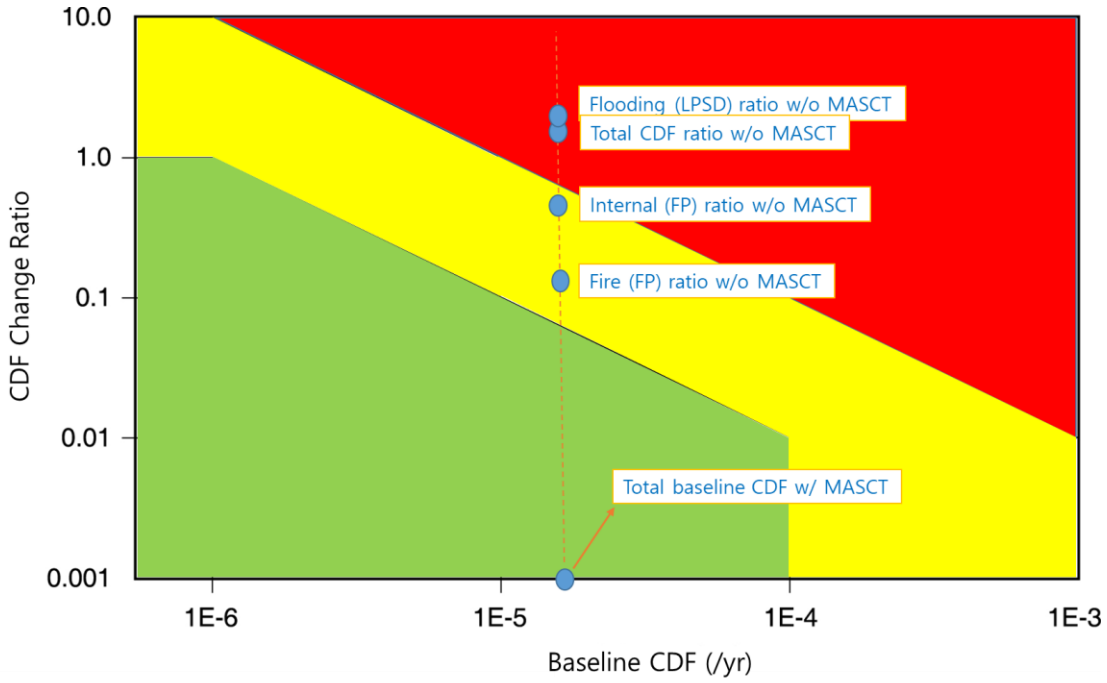

Figure 2. Results of Applying Acceptance Criteria from Reference [4] to Evaluation Case #1 (Specific NPP #2)

V. Conclusions

In this paper, we first discussed various concepts for implementing AMP strategies for extreme disasters in NPPs and the current application status of related mobile equipment. In addition, to determine the applicability of each proposed mobile equipment to currently operating NPPs, we evaluated the level of increased risk affected by excluding these equipment and the level of increased risk due to specific changes in the way the equipment is not utilized.

The risk matrices for the application of mobile equipment were considered and the results of the sensitivity analysis of the change of these risk measures to the exclusion of mobile equipment from certain NPP were presented, as well as the acceptance criteria. Finally, we can identify that this approach can support to confirm the applicability of each of the proposed mobile equipment.

References

[1] Nuclear Safety Act, Article 20(2), NSSC, June 22 2015, Rep. of Korea.
[2] J. Y. Yoon, H. Lim and J. Park, “Evaluating the Application of Portable Safety Equipment in Nuclear Power Plants using Multi-unit PSA”, J. of the Korean Society of Safety, Vol.38, pp.110-120, 2023.
[3] NEI 12-06, Diverse and Flexible Coping Strategies (FLEX) Implementation Guide, Rev. 4, NEI, Dec. 2016.
[4] KINS/RG-N16.09, "General Guidance in Use of Risk Information at Current Licensing Changes", Rev.2, Jan. 2021.

ASRAM2025
www.asram2025.org
Asian Symposium on Risk Assessment and Management 2025
Pattaya, Thailand, 27 – 29 August 2025

STUDY ON INFLUENCE OF CCF MODELING IN IE FAULT TREES IN RISK MONITOR PSA MODEL OF NUCLEAR POWER PLANTS

Hu Yuehua[1], Yi Yan[2], Xu Yiquan[1], Wang Jie[1], Zhang Qinfang[1], Zhang Wuhang[1], Qian Yalana[1]

[1] *Shanghai Nuclear Engineering Research & Design Institute CO.LTD, Shanghai, China*
[2] *Nuclear and Radiation Safety Center, Beijing, China*

ABSTRACT

Abstract: In the risk monitor PSA model of nuclear power plant, the initiating event frequency of loss of support system should be calculated by the fault tree method, with the initiating event fault tree linked to the risk monitor model to generate frequency-type results. There are two ways to model the IE fault trees, one is the single multiplier method and the other is the frequency-based basic event method. This paper makes a comparative study of the advantages and disadvantages of these two methods when applied in risk monitors and their influence on configuration risk management. The study shows that although the single multiplier method can reflect the influence of common cause factors on the frequency of initiating events when a certain equipment fails, the modeling of common cause is too conservative, and it may produce unreasonable cut sets and risk views that are not in accordance with the actual nuclear power plant conditions, and the frequency-type basic event method cannot reflect the influence of common cause factors on IE frequency. This paper presents a new modeling method combining the above two methods, which can reflect the influence of common cause factors on IE frequency when an important component fails, and avoid unreasonable risk views caused by excessive amplification of common cause contributions.

Keywords: PSA, Risk Monitor, Initiating Event Fault Tree, Common Cause Failure, Nuclear Power Plants

I. INTRODUCTION

According to the group standard of Nuclear Power Plant Configuration Risk Management Peer Review Guide (T/CNSCPA 011-2023) [1] in China, the risk monitor model should properly consider how nuclear power plant configuration changes affect the frequency of initiating events (IEs). Typically, for the loss of support system, the frequency of initiating events should be calculated by fault tree method, and the support system initiating event fault trees should be linked to the risk monitor model, simultaneously the calculation core damage frequency (CDF) result should be frequency type.

At present, there are two common cause failure (CCF) modeling methods in IE fault tree in the industry, one is single multiplier method, and the other is frequency-based basic event method. In the practice of peer review of configuration risk management in nuclear power plants, it is found that these two methods are prone to exaggerate or weaken the influence of component common cause failure on the risk of nuclear power plants, thus forming a risk opinion inconsistent with many years of operation experience of nuclear power plants. In this paper, a new modeling method is proposed. The analysis results show that this method can effectively solve the above problems.

II. EXISTING IE FAULT TREE CCF MODELING METHODS

II.A. Single Multiplier Method

In the initiating event frequency calculation model, the main models adopt a modeling method similar to the fault tree models of the mitigation system, which only contain probabilistic basic events whose names are consistent with those of the mitigation system, while only one time factor is set as a frequency-type event to convert the result to a frequency. (Figure 1.)

The fault tree model of the modeling method is relatively simplified. Because the basic event types and names are the same with mitigating systems' model, the common cause group can be established to calculate the common cause failure. The IE and mitigation fault trees of the same system use the same basic event coding to facilitate correlation analysis.

For the systems with the number of sub-trains greater than or equal to 3 and the number of normally operating trains greater than or equal to 2, it is impossible to distinguish the equipment with initial failure and the trains that play a mitigating role through the model. In order to ensure that the contribution of random failure to the frequency of the initiating event is reasonable, the multiplier should be multiplied by the number of combinations. At present, there are two practices in the industry, taking the multi-Greek Letter method (MGL) and two-stage CCF as examples:

1) One practice is that The multiplier is directly taken as 365 (days) ;

$$CCF\ frequency = \beta \times Q \times 365 \quad (/reactor\ year) \tag{1}$$

Among them:

β is a CCF MGL parameter, β factor in the MGL method is a conditional probability that the common cause of a component failure will be shared by one or more additional components;

Q is the failure probability of equipment demand failure or the operation failure probability within 24 hours.

2) Another practice is to increase the multiplier to consider the number of trains' combinations. For example, for the compressed air system with two trains operation and another two trains standby, the multiplier is 365 × 2 = 730.

$$CCF\ frequency = \beta \times Q \times 365 \times 2 \quad (/reactor\ year) \tag{2}$$

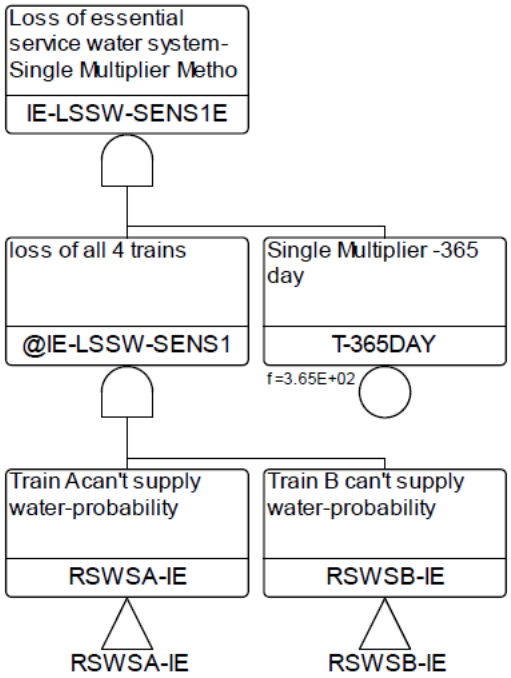

FIGURE 1. Example for Single Multiplier Method

These two practices consider the mission time of 1 year or several years for common cause failure, respectively. In particular, the second approach considers the mission time of several years, and overestimates the influence of common cause failure.

According to reference [2], in the risk monitor model, the common cause failure model may need to be improved so that it is able to take account of the reduction in redundancy when components are removed from service for maintenance and when failures have been identified.

In the risk monitor model, for two components considering the two-order common cause, when one component fails, Q = 1, according to the common cause processing method, the failure probability of another redundant component failure caused by the common cause will be replaced by the common cause parameter (such as β, which reflects the potential for a CCF to have occurred), and the quantitative results including CCF = β × 365 or CCF = β × 730 cutsets will appear. This kind of

cutsets further over-amplify the influence of common cause failure, and prone to inconsistent with the operation practice of nuclear power plants for many years.

Taking the component cooling water system and essential service water system of a nuclear power plant as an example, when the single multiplier method is used in the model, the risk monitor model results are shown in Table 1.

TABLE 1. Risk Assessment Example by Single Multiplier Method

Single Multiplier Method	CDF（/reactor year）	Risk Increase Factor	Risk Zone
If a component cooling water pump fails	3.42E-03	257	RED
If a service water pump fails	2.29E-03	172	RED

It can be seen from Table 1. that only one pump failure will cause the nuclear power plant to enter the risk unacceptable zone (RED zone) [3,4], which requires the measures such as shutdown the nuclear power plant being taken immediately. However, in this case, the technical specification of the nuclear power plant just requires that the faulty component should be restored to the operational state within 72 hours. The results of risk monitor are quite different with the requirements of technical specifications and nuclear power plant practice.

II.B. Frequency-type Basic Event Method

According to the industry standard 'ASME/ANS RA-Sb-2013' [5] HLR-IE-C10: If fault-tree modeling is used for initiating events, include all relevant event combinations in the IE fault tree models, such as the annual frequency of one component failure and the unavailability of other components (or failure during the repair time of the first component). In the IE fault tree model of this method, a frequency-based basic event is established for each component of the running train (the mission time is usually 1 year), while the remaining running trains or standby trains are probabilistic, and the mission time is 24 hours or the time required to repair the faulty train, i.e. the average maintenance time (MTTR), as shown in Fig. 2.

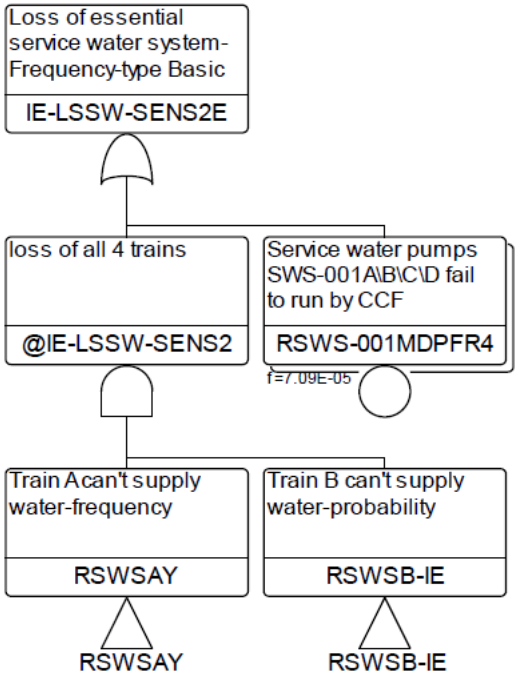

FIGURE 2. Example for Frequency-type Basic Event Method

The frequency of the IE fault tree top event is the sum of the frequencies of all frequency-type event groups, that is, only one frequency-type event is allowed in each cutset. Each cutset is composed of a frequency-type basic event and several probability-type basic events, and it is easy to distinguish the equipment with initial cause failure.

Because different types of basic events for different trains are used in this method, it is impossible to directly establish a common cause group, and additional CCF basic events need to be established. Taken the MGL method and two-order CCF as an example, the value of the common cause basic event $f_{CCF} = \beta \times \lambda \times T$ (where λ is the hourly running failure rate, T generally takes 8760 hours) is modeled as an independent frequency basic event. Therefore, in the application of risk monitor model, when a component is set to fail, the fault tree model cannot easily and intuitively reflect the change of the IE frequency caused by the common cause failure of the component.

Similarly, taking the component cooling water system and the essential service water system of a nuclear power plant as an example, the risk monitor model results are shown in Table 2 when the frequency-type basic event method is used in the model.

TABLE 2. Risk Assessment Example by Frequency-type Basic Event Method

Frequency-type Basic Event Method	CDF（/reactor year）	Risk Increase Factor	Risk Zone
If a component cooling water pump fails	1.57E-04	14.40	YELLOW
If a service water pump fails	4.81E-05	4.41	YELLOW

It can be seen from Table 2 that a pump failure will cause the nuclear power plant to enter the configuration risk management area (YELLOW area) [2, 3], which represent acceptable risk increases, provided that actions are taken to address non-quantifiable factors and establish risk-management actions that are appropriate to the configuration. Therefore, such configurations should not be treated as unsafe conditions to be avoided in all circumstances. The risk assessment results meet the requirements of the technical specifications and are in good agreement with the operation practice of the nuclear power plant. However, since the influence of CCF upon equipment failure only considers the increase in the failure probability of the mitigation system, without taking into account its impact on the CCF frequency of initiating events, the results tend to be overly optimistic

III. NEW INTEGRATION MODELING METHOD

According to the definition of common cause failure factor in NUREG/CR-5485[6], common cause failure factor is the conditional probability that a component failure will be shared by one or more additional components, indicating that the common cause parameter is a probabilistic parameter and has nothing to do with time duration.

Taking the common cause failure of two components of the same type in the IE fault tree as an example, if the MGL method is used to calculate the common cause failure probability, the common cause operation failure probability of the two components is:

$$\text{CCF frequency} = \beta \times Q = \beta \times \lambda \times T \text{ (/reactor year)} \quad (3)$$

Among them.

λ is the failure rate per hour.

β is a two-order common cause failure factor.

T = 8760h.

In the risk monitor model, the common cause failure probability after the failure of the operating equipment (i.e., Q = 1) should be :

$$CCF = \beta \times Q = \beta \quad (4)$$

It can be seen that in the risk monitor model, the failure of a component has a great influence on the frequency of initiating events, and it is easy to overestimate the influence of common cause failure on the risk of nuclear power plants.

In addition, according to the common cause failure data collection and statistical method given in Reference [7], in general, the common cause failure mainly refers to the failure of two or more similar components in the same system due to the same cause and failure mode within a selected period of time. In Reference [8], it is considered that the common cause failure should be considered when the standby or redundant equipment fails before the damaged equipment is repaired. Therefore, when calculating the IE frequency of the loss of the support system caused by the common cause, the time window is generally taken as the average maintenance time (MTTR) or 24 hours of the corresponding equipment. If the mission time of the common cause failure is taken as 1 year, it is too conservative and does not conform to the actual operation experience of the nuclear power plant. Only when the first failed component is repaired, the failure of the second same component due to the same cause and failure mode should be considered as the common cause of the initiating event. If the first failure component has been repaired before the second failure, even if the failure cause is a common cause factor, it does not cause the initiating event of loss of the support system.

The reference [8] also provides a recommended method for using the common cause parameters in the IE fault trees: one is to screen and remove the common cause events that do not cause the initiating event, and the other is to correct the common cause parameter. However, in the actual implementation process, both methods are difficult. The first method is limited to the difficulty of obtaining the details of the events collected in the CCF database, and the second method is limited to the difficulty of evaluating the selection method and rationality of the correction factor.

Reference [9] also suggests that it is necessary to correct the common cause parameters used in the initiating event fault tree. It is recommended to use the Bayesian updating method, but it is also necessary to correct the independent failure rate. The method proposed in this paper is also difficult in engineering application, especially when the IE fault trees need to interlink with the event trees and mitigation fault trees, because a basic event can't exist in different CCF groups simultaneously.

Therefore, according to the common cause failure analysis mechanism of IE fault tree in the above risk monitor model, a new integration modeling method is constructed. On the premise of using the existing common cause database, the above two methods in section 2 are combined, that is, one part adopts the single multiplier method, and the same basic events as those in the mitigation system fault trees are adopted in the IE fault trees, and the CCF groups are established to consider the common cause failure. The multiplier can be taken as the allowed maintenance time required by the technical specification, MTTR or mission time of level 1 PSA (usually 1 day). The other part adopts the frequency-based basic event method, in this part, the frequency-based basic events are established for the initial cause sub-train, and their frequencies are calculated by (365-the number of days corresponding to the multiplier)×failure rate per hour × 24. The same probability-based basic events as the mitigation system fault trees are established for the remaining sub-trains, without using additional CCF basic events but using the same CCF groups as those established in the mitigating system fault trees. The two parts are connected by OR gate to construct an IE fault tree, which can be interlinked with the corresponding event tree and mitigation fault trees, as shown in Figure 3.

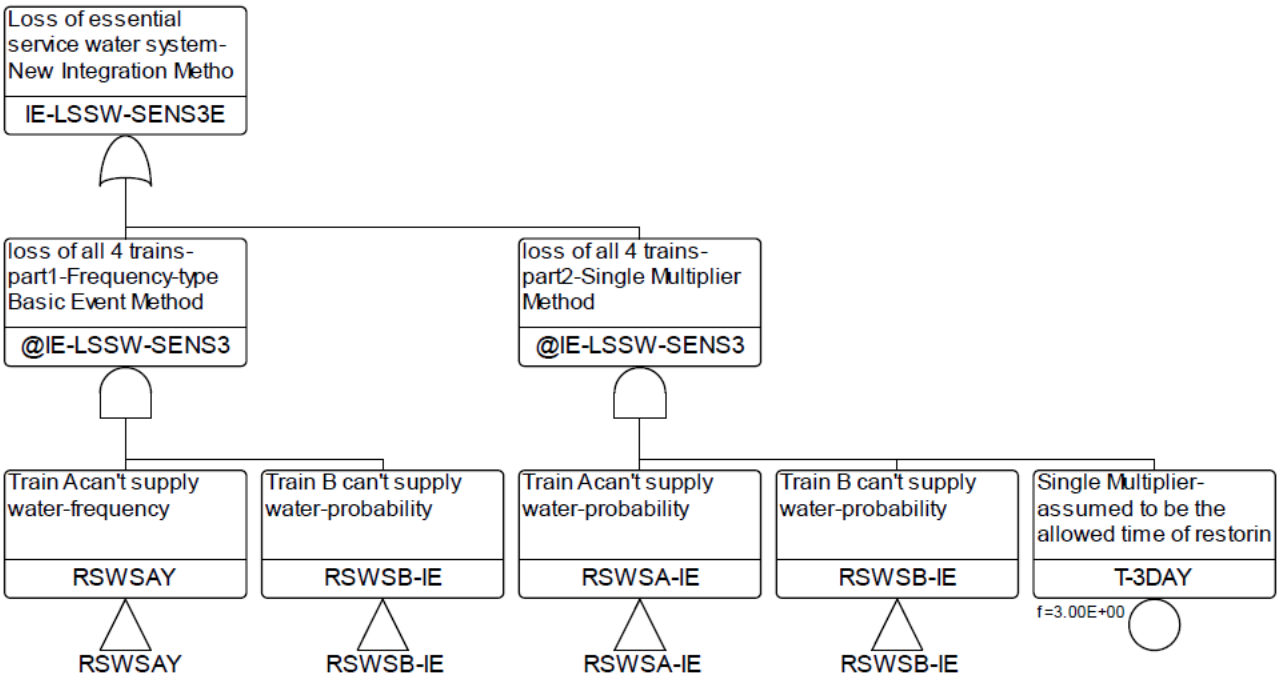

FIGURE 3. Example for New Integration Method

This modeling method matches the mechanism of common cause failure analysis, and can reflect the influence of common cause factors on the IE frequency change caused by the CCF in the IE fault tree after the failure of a component. It also avoids overestimating CCF influence and provides risk insights more consistent with nuclear power plant operational practices.

Similarly, taking the component cooling water system and the essential service water system of a nuclear power plant as examples, the risk monitor model results are shown in Table 3 when the new integration modeling method is used in the

model. Since it considers both the impact of equipment failure on the increased probability of mitigation system failure caused by CCF and the impact on the increased frequency of initiating events caused by CCF, the results show a slight increase compared with Table 2.

It can be seen from Table 3 that a pump failure will cause the nuclear power plant to enter the risk management zone (YELLOW zone) [3, 4], which requires the nuclear power plant to control risks, measures should be taken to minimize the duration of YELLOW work windows or compensatory actions are put in place to reduce plant risk (reduced, yet adequate defense-in-depth). The risk assessment results meet the requirements of the technical specifications and are in good agreement with the operation practice of the nuclear power plant.

Comparing with Table 2, it can be seen that the Risk Increase Factor of the new integration method is slightly larger, which more appropriately reflects the influence of common cause failure on the risk of nuclear power plants, while avoiding the excessive amplification of influence on the risk of nuclear power plants.

TABLE 3. Risk Assessment Example by New Integration Method

New Integration Method	CDF（/reactor year）	Risk Increase Factor	Risk Zone
If a component cooling water pump fails	1.84E-04	17.52	YELLOW
If a service water pump fails	6.71E-05	6.39	YELLOW

IV. CONCLUSIONS

To address the challenge of how the risk monitor model of nuclear power plant can better reflect the influence of common cause failure of components on the risk of nuclear power plant, two IE fault tree modeling methods in the current industry are summarized in this paper. A comparative analysis of advantages and disadvantages in the application of risk monitor model are made, and the advantages of the two methods are integrated to propose a new integration modeling method. The examples show that the new integration modeling method can properly reflect the influence of common cause failure on the risk of nuclear power plant and avoid the excessive amplification of CCF influence on the risk of nuclear power plant. The application of new integration modeling method can provide an important reference for the implementation of configuration risk management of nuclear power plants.

ACKNOWLEDGMENTS

During the process of writing this paper, assistance was received from several colleagues such as Zhan Wenhui and He Jiandong. Moreover, in the peer review of configuration risk management, its application was recognized by many peers including Chu Yongyue from the Nuclear and Radiation Safety Center. Here, I would like to express my special gratitude.

REFERENCES

[1] Nuclear power plant configuration risk management peer assessment, T / CNSCPA 011-2023 [S], Beijing, China Nuclear Safety and Environmental Culture Promotion Association, 2023 : 15-16.

[2] RISK MONITORS - The State of the Art in their Development and Use at Nuclear Power Plants, NEA/CSNI/R(2004)20 [M], France, NUCLEAR ENERGY AGENCY COMMITTEE ON THE SAFETY OF NUCLEAR INSTALLATIONS, 2004.

[3] Technical Policy for Configuration Risk Management of Nuclear Power Plants (Trial), *National Nuclear Safety Administration* [2019] No.262 [S], Beijing, National Nuclear Safety Administration (2019).

[4] T.Morgan, Applications of Colors as Risk Metrics – Background and Effective Practices, 2018 Configuration Risk Management Forum Research Task, 3002012995[M], California, Electrical Power Research Institute, Sep.2018.

[5] ASME/ANS RA- Sb-2013, Addenda to ASME/ANS Ra -S - 2008 Standard for Level 1/Large Early Release Frequency Probabilistic Risk Assessment for Nuclear Power Plant Applications [S], New York, The American Society of Mechanical Engineers, Sep. 2013.

[6] A.Mosleh, et al. Guidelines on modeling common-cause failures in probabilistic risk assessment, NUREG/CR-5485[M], Washington DC, United States Nuclear Regulatory Commission, June 1998.

[7] M.Marshall. et al. Common-Cause Failure Parameter Estimations， NUREG/CR-5497[M]， Washington DC, Idaho 1National Engineering and Environmental Laboratory， 1998: 1-2.

[8] K. Canavan, et al. Support System Initiating Events: Identification and Quantification Guideline, EPRI-1013490[M], California, Electrical Power Research Institute, 2006:5-8.
[9] J. Julius, et al. Support System Initiating Events Identification and Quantification Guideline, EPRI-1016741[M], California, Electrical Power Research Institute, 2008:2-14, 15.

ASRAM2025
www.asram2025.org
Asian Symposium on Risk Assessment and Management 2025
Pattaya, Thailand, 27 – 29 August 2025

FAILURE MODE AND EFFECT ANALYSIS OF PUSPATI TRIGA SYSTEMS: A PRELIMINARY STEP TOWARDS PSA LEVEL 1

Mazleha Maskin[1], Fedrick Charlie Matthew Brayon[2], Phongsakorn Prak Tom[3], Mohd Zulfadli Ramli[4], Ahmad Hassan Sallehudin Mohd Sarif[5]

[1,3] *Malaysian Nuclear Agency: Bangi, 43000 Kajang, City, Selangor, Malaysia, and mazleha@nm.gov.my*
[2,4] *Atom Malaysia: Bangi, 43000 Kajang, City, Selangor, Malaysia, and fedrick@atom.gov.my*
[5] *Universiti Tun Hussein Onn Malaysia: Pagoh Education Hub, 84600 Muar, Johor, and hassan@uthm.edu.my*

ABSTRACT

The PUSPATI TRIGA reactor (RTP), a vital component of Malaysia's nuclear research infrastructure, requires a robust safety assessment to ensure its reliable and secure operation. As a preliminary step towards conducting a comprehensive Level 1 Probabilistic Safety Assessment (PSA), this study focuses on the identification and analysis of failure modes and their effects across critical systems and components of the reactor. Failure Mode and Effect Analysis (FMEA) was utilized to systematically identify potential failure modes, assess their impact on reactor safety, and prioritize them based on severity, occurrence, and detectability. The findings highlight key vulnerabilities in reactor systems and provide insights into the relative risk contributions of each failure mode. This work lays the foundation for quantitative PSA Level 1 modeling, enabling the estimation of core damage frequency and guiding the development of targeted risk mitigation strategies. The results will support the enhancement of the reactor's safety framework and compliance with international nuclear safety standards.

Keywords: PUSPATI TRIGA, Failure Mode and Effect Analysis (FMEA), Probabilistic Safety Assessment (PSA), reactor safety, core damage frequency.

I. INTRODUCTION

In the Asia-Pacific region, growing nuclear research capacity brings a shared responsibility to ensure reactor safety is robust and well managed [1]. The devastating Fukushima disaster of 2011 reminded the world that even research reactors demand rigorous scrutiny – indeed, analysts observed that in its wake "the safety aspects of the one and only research reactor (31 years old) in Malaysia need be reviewed" [2]. This spirit of vigilance is especially important for Malaysia's sole nuclear facility: the PUSPATI TRIGA research reactor

Commissioned in 1982 as a 1-MW TRIGA Mark II reactor [3], the PUSPATI TRIGA (RTP) at Bangi has been a workhorse for Malaysian nuclear science and engineering. Over the decades it has supported neutron- beam experiments, neutron radiography, and the production of medical and industrial radioisotopes [3]. It also serves as a training and education platform for students and operators. As Malaysia's only research reactor, RTP occupies a strategic niche in the national nuclear landscape; its safe operation is therefore a matter of both technical and national importance.

Modern nuclear safety analysis employs both deterministic design rules and probabilistic methods. Probabilistic Safety Assessment (PSA) – sometimes called PRA – is now a standard tool used to quantify nuclear plant risk [4]. In a PSA model, a plant is systematically represented by its design and operating procedures, and a spectrum of possible "disturbances" (known as initiating events) is considered [4]. Each initiating event (for example, a pump failure or operator error) is then traced through the logic of the plant's safety systems and operator responses. The result is a comprehensive picture of accident sequences and their probabilities. In short, PSA asks "what can go wrong, how likely is it, and what is the end effect?" – yielding core-damage frequencies or radiological risk measures. Because PSA relies on having a complete set of initiating events, the accuracy of the risk picture depends critically on identifying all plausible beginnings of accident chains [4].

As according to the International Atomic Energy Agency (IAEA) [5], a powerful way to ensure completeness in initiating-event analysis is Failure Mode and Effects Analysis (FMEA). FMEA is a well-known bottom-up technique that examines each system component to ask "what can fail and what happens then" [6], [7]. In practice, engineers list each component or subsystem, enumerate its potential failure modes (e.g. "valve stuck closed"), and then trace the consequences of that failure on

larger subsystems and plant functions. By doing so, FMEA uncovers how individual hardware failures or human errors could serve as initiating events. As one authoritative source puts it, "FMEA can be used to determine the initiating events…which could lead to the hazard," by tracing individual failures forward to the final effect . In other words, FMEA complements PSA's top-down approach (often fault trees or event trees) by exhaustively finding bottom-up accident starters. For the RTP project, a systematic FMEA of its major systems reveal all potential component malfunctions and the hazards they could cause including human error [4], [8].

This paper's scope is a detailed FMEA of RTP's systems, covering relevant operational modes and core safety functions. Both full-power (steady-state) operation and shutdown/maintenance conditions are analyzed, as system dependencies and risks vary with reactor state. In each mode, we examine how failures would affect the reactor's fundamental safety functions, namely:

1. Reactivity Control: shutting down or controlling the chain reaction through control/safety rods and reactivity feedback.
2. Heat Removal: removing decay heat from the core via the primary cooling system and auxiliary cooling.
3. Radioactive Confinement: containing radioactive material through shielding and containment structures.

Each of these safety functions is supported by redundant components and protective systems (for example, multiple control rods and diverse cooling loops). Our FMEA traces how failures in pumps, valves, sensors, or operator actions in each system could disable these functions. By doing so, we enumerate the credible initiating events for RTP – the very inputs needed for a Level-1 PSA (core damage frequency calculation).

II. METHODOLOGY

The study utilizes existing documentation and system diagrams of the RTP to identify all critical components and functions. The systems and subsystems were carefully reviewed, with expert input from operators and engineers involved in the reactor's maintenance and operation. RTP has seven (7) safety systems, consisting of: (1) Reactor core and control system; (2) Primary cooling system; (3) Secondary cooling system; (4) Purification system; (5) Instrumental and control system; (6) Electric power supply; and (7) Auxiliary system.

II.A. Identification of Failure Modes

All RTP's safety related systems and components that can fail the system are identified. For each component, all possible ways of failure could happen then were identified next which is known as potential failure modes show a loss of that function. Failure mode is different for each component. TABLE 1 indicates an example of designator failure mode for each component.

TABLE 1. Failure Mode Designator

Component Type	Failure Mode
Pump and diesel generator (DG)	Fails to start [FS]; Fails to run [FR]
Valves	Fails to open [FO]; Fails to close [FC]
Equipment	Mechanical failure [MF]
Automatic signal	No signal [NS]
Operator action	Human error [HE]
Offsite power	No power supply [NP]

II.B. Identification of Consequences

For each failure mode, if the component fails, all the consequences on the system are identified. Eventually whether it is an IE or vice versa is then identified.

II.C. Human Reliability Analysis

In PSA, evaluation of the human factor contribution to the risk this is fulfilled under the framework of human reliability analysis (HRA) [9]. A Type A human errors (HE) happen before something goes wrong, during normal operations. These actions can cause important safety systems to be unavailable later when they are needed in an emergency. Type A HEs usually happen during tasks like repair, maintenance, testing, or calibration. If mistakes from these actions are not found and fixed,

they can cause system failure when needed. Type B HEs are mistakes that directly cause unwanted events, either on their own or along with equipment failure while Type C HEs are critical responses operators must take after an event has occurred. To support the current FMEA study, the focus is on the Type A and Type B HEs.

Routine (scheduled) human actions, done during normal conditions, can lead to Type A or B HEs. These actions are based on normal operating, testing, and maintenance procedures. Since the main purpose of a research reactor is to support research, procedures for research activities are also part of normal operations.

The written procedures at RTP for the following tasks are reviewed: i) Reactor startup, operation, and shutdown, ii) Loading, unloading, and moving fuel or irradiated materials, iii) Inspecting and testing safety-related items, iv) Setting up and running experiments. In addition, various technical documents - such as logbooks, maintenance/test reports, the Safety Analysis Report (SAR), system and component drawings, and vendor manuals for maintaining safety-related reactor systems are also reviewed. The procedures and documents are then checked by discussing and walking through them with the reactor operators. This helps confirm the information and gather more details, such as who does the task, the steps involved, how long it takes, any special tools needed, and the working environment. These details help in understanding the nature of the actions [10].

Following the identification of the routine human actions, qualitative screening is performed on these human actions. The purpose of qualitative screening is to select human actions with significant potential errors that could contribute to the system failure and initiating event (IEs).

III. RESULTS

TABLE 2 presents the lists of systems or components (SCs) with its failure mode and the consequences or effects to RTP if it fails to function properly. Each of the SCs was also noted as either to be a probable IE or not in the current scope of study. Of the seven systems with 98 related components involved, both failure mode and consequences were listed in this table.

Meanwhile, for HRA study, 88 tasks were identified, following the qualitative screening phase, two Type A HEs for the significant reactor systems during accident condition have been derived: i) area radiation monitor (ARM) system miscalibration during the maintenance (effect: ARM unavailable) and ii) erroneous dropping of foreign objects into the reactor pool (effect: degradation of SCRAM). Meanwhile, a HE which contributes to an accident initiation is identified: unintended insertion of sample with large positive reactivity influence is considered as the Type B HE (IE: reactivity insertion accident (RIA)).

TABLE 2. List of IEs and related systems and components in FMEA

No	System / Component	Failure Mode	Consequences / Effects	IE
A	Reactor Core and Control System			
1.	Motor Driven Safety Rod	Fail to Insert	Degradation of the System	Yes
		Spurious Withdraw	Reactivity Increase	Yes
2.	Motor Driven Shim Rod	Fail to Insert	Degradation of the System	Yes
		Spurious Withdraw	Reactivity Increase	Yes
3.	Motor Driven Regulator Rod	Fail to Insert	Degradation of the System	Yes
		Spurious Withdraw	Reactivity Increase	Yes
4.	Pneumatic Drive Transient Rod	Spurious Withdraw	Reactivity Increase	Yes
5.	Core Aluminum Tanks	Fail to Retain Integrity	Loss of Coolant	Yes
6.	Bottom Grid Plates	Fail to Provide Support	Reactivity Increase and Loss of Flow	Yes
7.	Neutron Chamber	Fail High	Spurious Automatic SCRAM	Yes
		Fail Low	Degradation of Reactor SCRAM System Reliability	No
8.	Fission Counter Detector	Fail High	Spurious Automatic SCRAM	Yes
		Fail Low	Degradation of Reactor SCRAM System Reliability	No
9.	Thermo-Couple 1	Fail High	Spurious Automatic SCRAM	Yes
		Fail Low	Degradation of Reactor SCRAM System Reliability	No

10.	Thermo-couple 2	Fail High	Spurious Automatic SCRAM	Yes
		Fail Low	Degradation of Reactor SCRAM System Reliability	No
B	Primary Cooling System			
1.	Main circulation pump1	Fail to Start	Loss of Flow	Yes
		Fail to Run	Loss of Flow	Yes
2.	Manual Butterfly Valve	Fail to Open	Loss of Flow	Yes
3.	Motor Operated Valve	Fail to Open	Loss of Flow	Yes
4.	Manual Butterfly Valve	Fail to Open	Loss of Flow	Yes
5.	Heat Exchanger	Fail to Function	Loss of Heat Removal	Yes
6.	Temperature Probe	Fail to Function	Unavailability of Safety Parameter	Yes
C	Secondary Cooling System			
1.	Secondary Circulation Pump	Fail to Start	Loss of Flow	Yes
		Fail to Run	Loss of Flow	Yes
		Fail to Run	Loss of Flow	Yes
2.	Manual Butterfly Valve	Fail to Open	Loss of Flow	Yes
3.	Motor Operated Valve	Fail to Open	Loss of Flow	Yes
D	Purification System			
1.	Demineralizer	Fail to Function	Loss of Flow	Yes
2.	Demineralizer Pump	Fail to Start	Loss of Flow	Yes
		Fail to Run	Loss of Flow	Yes
3.	Manual Butterfly Valve	Fail to Open	Loss of Flow	Yes
E	Instrumental and Control System			
1.	Magnet Power key	Fail to Function	Unavailability of Control System	Yes
2.	Power On Switch	Fail to Function	Unavailability of Control System	Yes
3.	Reactor Power Display	Fail to Function	Unavailability of Safety Indicator	Yes
4.	Safety Channel	Fail to Function	Unavailability of Safety Indicator	Yes
5.	Power Measuring Channel	Fail to Function	Unavailability of Safety Indicator	Yes
6.	Operation Mode Switch	Fail to Function	Unavailability of Control System	Yes
7.	Bistable Circuit	Fail to Function	Unavailability of Control System	Yes
8.	Shim Rod Initiation Circuit	Fail to Function	Unavailability of Control System	Yes
9.	Safety Rod Initiation Circuit	Fail to Function	Unavailability of Control System	Yes
10.	Regulating Rod Initiation Circuit	Fail to Function	Unavailability of Control System	Yes
11.	Transient Rod Initiation Circuit	Fail to Function	Unavailability of Control System	Yes
12.	Shim Rod Actuation Circuit	Fail to Function	Unavailability of Control System	Yes
13.	Safety Rod Actuation Circuit	Fail to Function	Unavailability of Control System	Yes
14.	Regulating Rod Actuation Circuit	Fail to Function	Unavailability of Control System	Yes
15.	Transient Rod Actuation Circuit	Fail to Function	Unavailability of Control System	Yes
16.	Control Rod Switch Up / Down	Fail to Function	Unavailability of Control System	Yes
17.	Control Rod Position Indicator	Fail to Function	Unavailability of Safety Indicator	Yes
18.	Period / Second Indicator Log	Fail to Function	Unavailability of Safety Indicator	Yes
19.	Safety Channel Indicator	Fail to Function	Unavailability of Safety Indicator	Yes
20.	Water temperature indicator	Fail to Function	Unavailability of Safety Indicator	Yes

21.	Fuel Temperature Indicator	Fail to Function	Unavailability of Safety Indicator	Yes
F	Electric Power Supply			
1.	11kV Bus1	Fail to Function	Reactor Blackout	Yes
2.	Substation Transformer 1	Fail to Function	Reactor Blackout	Yes
3.	Substation Transformer 2	Fail to Function	Reactor Blackout	Yes
4.	Substation Transformer 3	Fail to Function	Reactor Blackout	Yes
5.	Substation Transformer 4	Fail to Function	Reactor Blackout	Yes
6.	500kV Genset1	Fail to Start	Reactor Blackout	Yes
		Fail to Run	Reactor Blackout	Yes
		Failure on Demand	Reactor Blackout	Yes
7.	Uninterruptable Power Supply (UPS)	Fail to Function	Station Blackout	Yes
G	Auxiliary System			
1.	Compressed Air Supply System	Fail to Function	Unavailability of Transient Rod	Yes
2.	Ventilation And Air-Conditioner System	Fail to Function	Negative Pressure Loss in Reactor Hall	Yes

IV. DISCUSSION

The preliminary findings from the FMEA highlight several key vulnerabilities in the PUSPATI TRIGA reactor's systems. While the reactor has multiple safeguards in place, the analysis underscores the importance of regular maintenance, system updates, and training to mitigate the identified risks. The next step will involve using these findings as a foundation for a Level 1 PSA, which will estimate the probability of core damage and guide the development of safety enhancements.

V. CONCLUSIONS

In summary, this narrative-driven introduction has highlighted the centrality of the RTP to Malaysia's nuclear mission, the global imperative of stringent safety, and the complementary roles of PSA and FMEA in risk assessment. Conducting this FMEA is a preliminary step: it ensures that the upcoming Level-1 PSA for the RTP rests on a solid foundation of well-identified failure modes. In turn, this work will strengthen Malaysia's reactor safety framework and support informed safety improvements for the TRIGA reactor.

ACKNOWLEDGMENTS

The authors wish to thank the team at the Malaysian Nuclear Agency, Atom Malaysia, Universiti Kebangsaan Malaysia and Universiti Tun Hussein Onn Malaysia for their support in conducting this study. Special thanks are also extended to the reactor operators for their invaluable input.

REFERENCES

[1] G. J. Storr and K. Kwong, "Initiatives supporting research reactor safety in the Asia-Pacific region," in *Research Reactors: Safe Management and Effective Utilization*, 2011

[2] M. Maskin *et al.*, "Development and methodology of level 1 probability safety assessment at PUSPATI TRIGA reactor," in *Proceedings of the International Nuclear Science, Technology & Engineering Conference 2013 (iNuSTEC2013)*, Feb. 2014 pp. 240–244 doi: 10.1063/1.4866138.

[3] M. S. Minhat *et al.*, "Instrumentation and control system at reaktor TRIGA PUSPATI (RTP)," in *Reaktor TRIGA PUSPATI Colloquium RTP 39 years*, 2021
[4] IAEA, *Defining initiating events for purposes of probabilistic safety assessment (TECDOC Series) No. 719*. International Atomic Energy Agency, Vienna, Austria (1993).
[5] IAEA, *Development and application of level 1 probabilistic safety assessment for nuclear power plants specific safety guide (Safety Series) No. SSG-3*. International Atomic Energy Agency, Vienna, Austria (2010).
[6] S. Authén, J. E. Holmberg, T. Tyrväinen, and L. Zaman1, "Guidelines for reliability analysis of digital systems in PSA context - Final report," Nordic Nuclear Safety Research, NKS-330, 2015.
[7] R. R. Fullwood, *Probabilistic safety assessment in the chemical and nuclear industries*. Butterworth-Heinemann Publications, Boston, MA (1998). doi: 10.1016/B978-075067208-5/50010-X.
[8] C. A. Ericson, "Failure mode and effect analysis," *Hazard analysis techniques for system safety*, pp. 235–455, John Wiley & Sons, Inc., Hoboken, NJ (2005).
[9] IAEA, *Human reliability analysis in probabilistic safety assessment for nuclear power plants (Safety Series No. 50-P-10)*. International Atomic Energy Agency, Vienna, Austria (1996).
[10] A. Kolaczkowski, "Good practices for implementing human reliability analysis (HRA)," US Nuclear Regulatory Commission, Office of Nuclear Regulatory Research, Division of Risk Analysis and Applications, Washington, DC, 2005.

Enhancing Accuracy in Level 2 PSA: Application of Partial BDD Method for High-Failure Probability Portable Equipment

Hyun-bin, CHANG[1*], Kyeongyeol KIM[2], Junghyun RYU[3], Gyunyoung Heo[4]

[1] *Department of Nuclear Engineering, Kyung Hee Univ: Deogyeong-daero, Giheung-gu, Yongin-si,Gyeonggi-do, 17104, Republic of Korea, and jhangkr@khu.ac.kr*
[2] *FNC technology Co., Ltd.: 10fl, 13, Heungdeok 1-ro, Giheung-gu, Yongin-si, Gyeonggi-do, 16954, Republic of Korea, and gykim@fnctech.com*
[3] *FNC technology Co., Ltd.: 10fl, 13, Heungdeok 1-ro, Giheung-gu, Yongin-si, Gyeonggi-do, 16954, Republic of Korea, and jhryu@fnctech.com*
[4] *Department of Nuclear Engineering, Kyung Hee Univ: Deogyeong-daero, Giheung-gu, Yongin-si,Gyeonggi-do, 17104, Republic of Korea, and gheo@khu.ac.kr*

ABSTRACT

This study addresses a critical issue in Level 2 Probabilistic Safety Assessment (PSA) models that include high-failure probability portable equipment. When using the Rare Event Approximation technique for quantification, these models often result in plant damage state frequencies that are disproportionately higher than core damage frequencies. To mitigate this discrepancy, we propose and evaluate the application of the Partial Binary Decision Diagram (BDD) method. The primary objective of this research is to verify that implementing the Partial BDD method in Level 2 PSA models with high-failure probability events reduces the gap between core damage frequency and plant damage state frequency. Our methodology involves applying the Partial BDD method to high-failure probability branches within a Level 2 PSA model that incorporates portable equipment, and subsequently analyzing the differences in frequencies. Key findings demonstrate that appropriate utilization of Partial BDD in quantifying Level 2 PSA models with portable equipment significantly narrows the disparity between core damage and plant damage state frequencies. Importantly, this is achieved without substantially increasing overall computation time. In conclusion, for PSA models of plants where high-failure probability portable equipment plays a significant role, the judicious application of Partial BDD in quantification effectively prevents the excessive divergence between core damage and plant damage state frequencies typically caused by Rare Event Approximation. This approach offers a valuable solution for enhancing the accuracy of Level 2 PSA models without compromising computational efficiency.

Keywords:

Level 2 PSA, PSA Quantification, Partial BDD, Portable Equipment, PDS Frequency

I. Introduction

Since the Fukushima accident in Japan, many countries operating nuclear power plants have established strategies to cope with severe accident scenarios caused by extreme hazard such as loss of ultimate heat sink (LUHS) and extended loss of AC power (ELAP). In the United States, accident mitigation strategies using portable equipment, represented by FLEX, have been introduced to many power plants. In Korea, a similar accident mitigation strategy using portable equipment, represented by MACST, has also been introduced.

In Korea, MACST was introduced after the Nuclear Safety Act Article 20 (Operation License) was fully legislated in June 2016, requiring the submission of accident management plans and the preparation of new portable equipment for extreme hazard preparedness in all nuclear power plants. Consequently, there was a growing need to conduct PSAs that include portable equipment to assess how much nuclear power plant safety is improved when accident mitigation strategies such as MACST are applied.

An investigation of FLEX in the U.S. and MACST in Korea, it was revealed that strategies using portable equipment are effective in maintaining containment integrity after core damage. Particularly, in LUHS or ELAP situations, where containment

damage occurs later than core damage, containment heat remove through external water injection or power restoration using portable equipment can be very effective in preventing containment failure. However, since portable equipment requires implementation and installation at the time of an accident, compared to installed equipment that is always maintained under optimal operating conditions, portable equipment can have a higher unavailability.

In Level 2 Probabilistic Safety Assessment (PSA), the Plant Damage State Event Tree (PDSET) serves as an interface between Level 1 and Level 2 analysis. It classifies accident sequences into Plant Damage States, which represent the plant's condition from the time of core damage to containment failure. In theory, the sum of the frequencies of all accident sequences developed by expanding core damage scenarios in the PDSET should be equal to the Core Damage Frequency (CDF). However, due to limitations in current computer calculation capabilities for PSA, approximate solutions are used for quantification. When PSA models are expanded or include many non-rare events, the difference between the approximate solution and the accurate value increases. Therefore, when developing PDSETs for Level 2 PSA models that include many portable equipment with high failure probability, the PDS frequency can differ significantly from the CDF, which can lead to errors in interpreting Level 2 PSA results.

In this study, we confirmed the results of applying accident mitigation strategies using portable equipment with very high failure probabilities to maintain containment integrity in Level 2 PSA, and performed quantification using the Partial BDD method. We also compared how much the error was reduced compared to cases where the Partial BDD method was not used.

II. Method

PSA models have recently developed using hundreds to thousands of basic events and logic gates to develop fault trees for internal events at full power. When analyzing such large fault trees, it is impossible to solve exact Boolean algebra even with current advanced computer performance. Therefore, the Delete Term Approximation (DTA) method is generally used to process success branches and obtain minimal cut sets.

In conventional accident management plans that consider only installed equipment, the unavailability of single components is generally very low, with most having failure probabilities below 0.01. These events are defined as rare events. To overcome the limited computational capabilities, Rare Event Approximation (REA) or Minimal Cut Upper Bound (MCUB) methods are used for minimal cut set-based quantification. This process is illustrated in Figure 1.

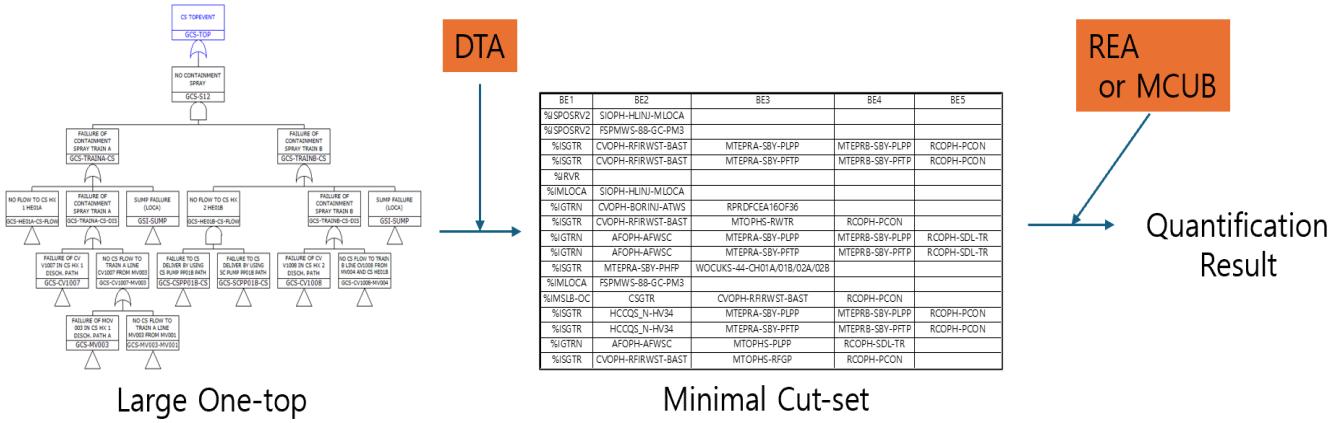

BE1	BE2	BE3	BE4	BE5
%ISPOSRV2	SIOPH-HLINJ-MLOCA			
%ISPOSRV2	FSPMWS-88-GC-PM3			
%ISGTR	CVOPH-RFIRWST-BAST	MTEPRA-SBY-PLPP	MTEPRB-SBY-PLPP	RCOPH-PCON
%ISGTR	CVOPH-RFIRWST-BAST	MTEPRA-SBY-PFTP	MTEPRB-SBY-PFTP	RCOPH-PCON
%IRVR				
%IMLOCA	SIOPH-HLINJ-MLOCA			
%IGTRN	CVOPH-BORINJ-ATWS	RPRDFCEA16OF36		
%ISGTR	CVOPH-RFIRWST-BAST	MTOPHS-RWTR	RCOPH-PCON	
%IGTRN	AFOPH-AFWSC	MTEPRA-SBY-PLPP	MTEPRB-SBY-PLPP	RCOPH-SDL-TR
%IGTRN	AFOPH-AFWSC	MTEPRA-SBY-PFTP	MTEPRB-SBY-PFTP	RCOPH-SDL-TR
%ISGTR	MTEPRA-SBY-PHFP	WOCUKS-44-CH01A/01B/02A/02B		
%IMLOCA	FSPMWS-88-GC-PM3			
%IMSLB-OC	CSGTR	CVOPH-RRRWST-BAST	RCOPH-PCON	
%ISGTR	HCCQS_N-HV34	MTEPRA-SBY-PLPP	MTEPRB-SBY-PLPP	RCOPH-PCON
%ISGTR	HCCQS_N-HV34	MTEPRA-SBY-PFTP	MTEPRB-SBY-PFTP	RCOPH-PCON
%IGTRN	AFOPH-AFWSC	MTOPHS-PLPP	RCOPH-SDL-TR	
%ISGTR	CVOPH-RFIRWST-BAST	MTOPHS-RFGP	RCOPH-PCON	

FIGURE 1. General Quantification Method

However, when there are many non-rare events with high failure probabilities, using the REA method can result in significant overestimation errors. Although the MCUB method can compensate for this, it can conversely cause underestimation.

In Korea, NUREG/CR-6928 is generally used as the data source for deciding equipment failure probabilities in PSA. NUREG/CR-6928 provides equipment failure probability for various equipment used in nuclear power plants based on empirical data. However, since accident mitigation strategies using portable equipment have been established relatively recently, data on equipment failure probability for portable equipment used in accident mitigation are limited. PWROG-18042-NP, which collected operational experience data related to portable equipment, provides the following generic failure probabilities for FLEX components:

TABLE I. Generic Failures Rates for FLEX Equipment

FLEX Component	Failure Mode	Mean
Portable Diesel Generator	Fail to Run	1.03E-02/hour
	Fail to Start	4.35E-02/demand
Portable Combustion Turbine Generator	Fail to Run	1.86E-02/hour
	Fail to Start	3.30E-02/demand
Portable Diesel-Driven Pump	Fail to Run	1.55E-02/hour
	Fail to Start	3.38E-02/demand

By applying the mission time of 24 hours, which is commonly used in PSA, to the values in Table I, the failure rate for each equipment type and failure mode can be calculated. For example, for a portable diesel generator, the probability of running failure is about 0.2472 (1.03E-02/h × 24 hours), and the probability of starting failure is 0.0435. Similarly, the running failure probabilities for portable combustion turbine generators and portable diesel-driven pumps are 0.4464 and 0.372, respectively. This shows that most basic events for portable equipment are non-rare events.

It is well known that accurate quantification results are difficult to obtain when quantifying fault trees that include many non-rare events using conventional methods. Therefore, the Partial BDD method, which was developed for quantifying seismic event models with many non-rare events, was applied to quantify Level 2 PSA models that include many portable equipment related events.

II.A. Application of Partial BDD

To obtain exact solutions for Boolean expressions that include non-rare events, methods such as Binary Decision Diagram (BDD) and Monte Carlo are available. When quantifying fault trees using the Monte Carlo method, relatively accurate results can be obtained in a short time, but only simple quantification results are provided, and it is not possible to evaluate the importance of basic events or perform cut set-based follow-up actions through post-processing, which limits its usefulness. Applying the BDD method to the entire fault tree to obtain an exact solution is possible only for small fault trees, as described above, and is difficult to apply to current nuclear power plant PSA models.

Suppose that many non-rare events are included in a single gate A, and there are few or no transfer gates shared with other gates. In this case, instead of applying the BDD method to the entire fault tree, the Partial BDD method introduced in reference 2 can be applied to gate A for conversion, reducing errors due to non-rare events in the overall quantification results without significantly slowing down the quantification speed.

The AIMS-PSA code developed by the Korea Atomic Energy Research Institute (KAERI) provides a function that allows the user to convert a specified gate to a BDD. Using this function, a one-top model can be created by partially converting a heading that includes many non-rare events to a BDD.

II.B. Development of Level 2 PSA Model with Partial BDD Applied

To apply the Partial BDD method, as described above, it is advantageous for many non-rare events to be included in a single gate and for there to be few transfer gates shared with other equipment. Otherwise, if BDD conversion is performed for many events including shared gates, the overall size of the fault tree can become too large, making quantification impossible or very time-consuming.

II.B.1. Separate Model for Accident Mitigation Strategies Using Portable Equipment

Accident management strategies using portable equipment are highly likely to satisfy the above two conditions. In particular, since portable equipment can be used for accident mitigation even when existing installed equipment is completely unavailable, such as in ELAP or LUHS, there are few shared equipment with installed equipment. Also, when reflecting accident management strategies using portable equipment in the event tree, strategies using installed equipment for the same purpose can be considered simultaneously in the same heading, but they can also be separated according to the developer's judgment. As shown in Figure 2, an alternative containment spray strategy using a high-capacity portable pump can be reflected in the containment spray heading using the containment spray pump with AND logic, or, as shown in Figure 3, the headings can be separated so that failure of the containment spray heading using the containment spray pump is considered in different headings.

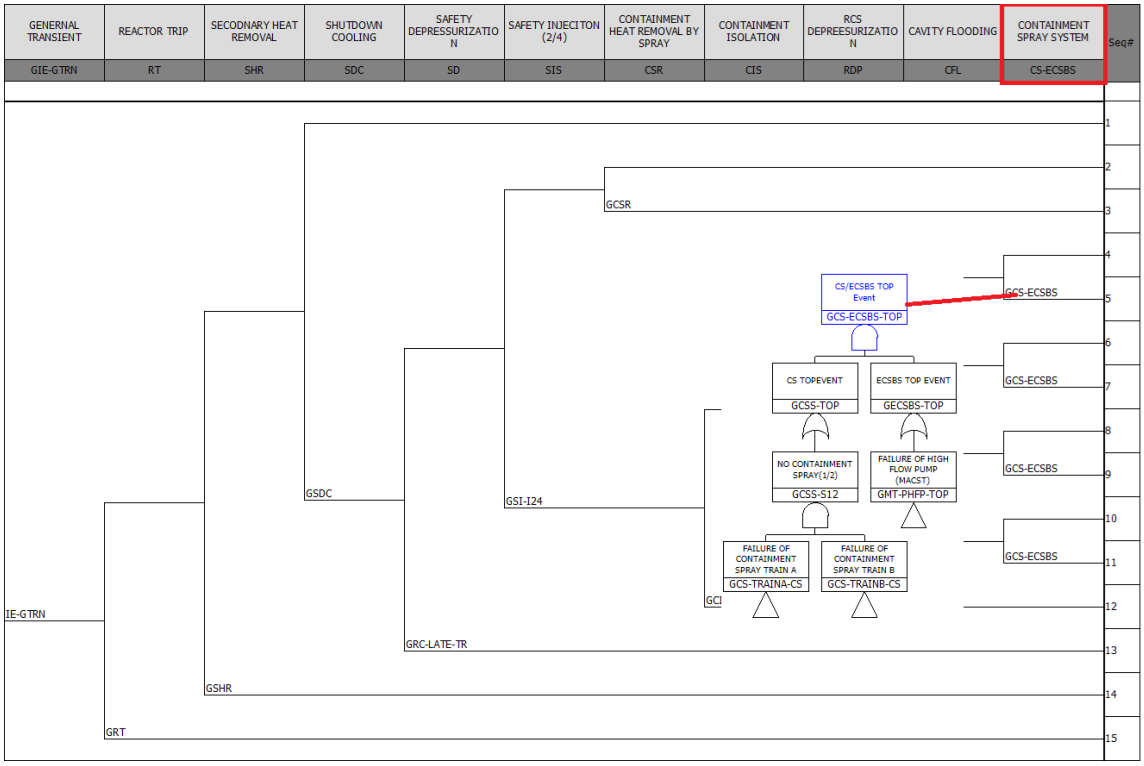

FIGURE 2. Portable Equipment Strategy Merged Event Tree

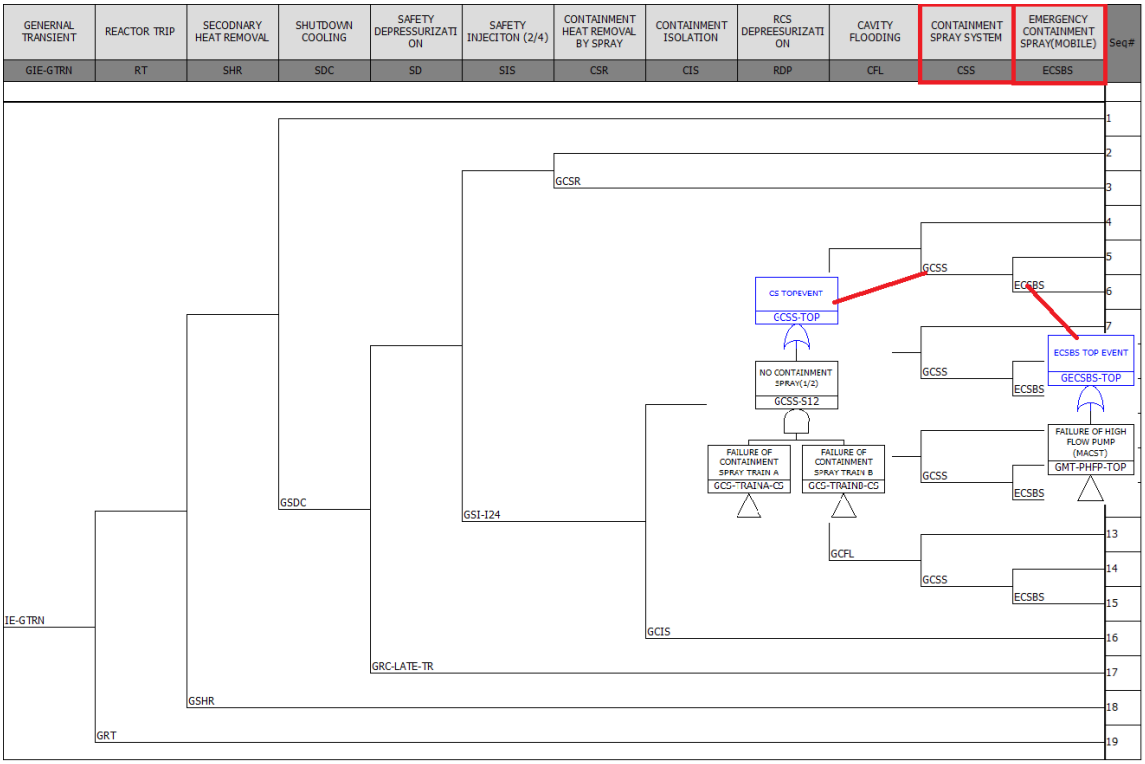

FIGURE 3. Portable Equipment Strategy Separated Event Tree

Generally, as the number of headings increases, the number of branches increases, making it difficult for model developers or reviewers to understand the structure. Therefore, analysts prefer the method shown in Figure 2. However, to perform the Partial BDD method, it is advantageous to separate gates that include many non-rare events for quantification speed and results. Therefore, as shown in Figure 3, accident management strategies using portable equipment were developed as separate headings.

II.B.2. Development of Fault Tree for Partial BDD Application

To consider long-term containment heat removal strategies using portable equipment, an LTHR fault tree was developed. In the LTHR fault tree, when containment heat removal using installed equipment fails, strategies to restore containment heat removal function using a portable high-flow pump (diesel-driven pump) and portable generator (portable combustion turbine generator) were simulated. In addition, since the portable pump uses diesel fuel, two portable fuel transfer pumps (diesel-driven pumps) for fuel replenishment were considered in the fault tree. The developed LTHR fault tree is shown in Figure 4. Reliability data for the portable diesel-driven pump and portable combustion turbine generator were taken from the data in Table I from PWROG-18042-NP.

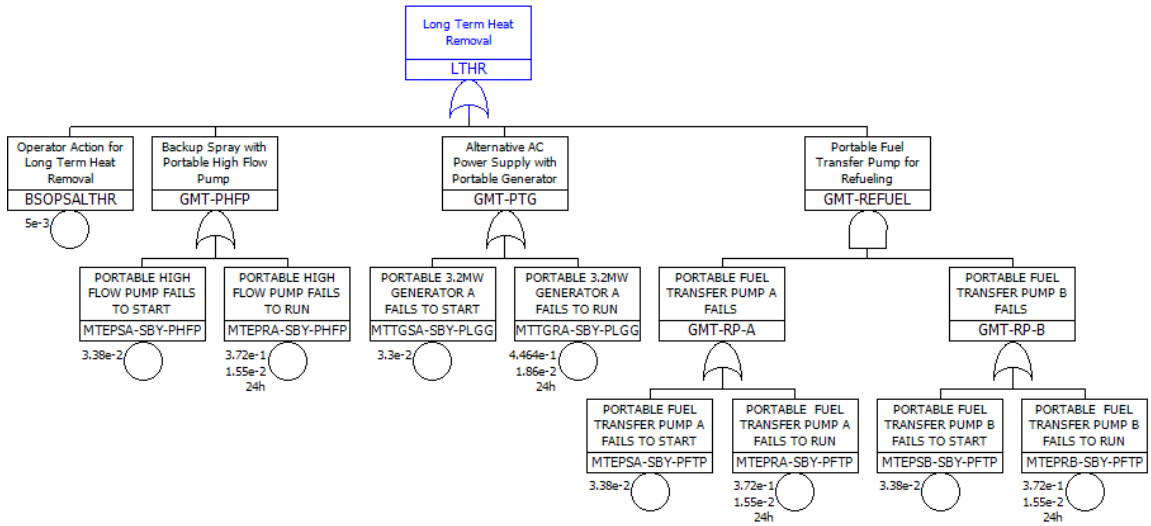

FIGURE 4. LTHR Fault Tree

II.C. Application of Partial BDD Using AIMS

The AIMS-PSA code provides an option that allows the user to convert a specified gate to BDD logic according to user settings. Using this function, some of the gates connected to the failure branch of the LTHR heading were changed, as shown in Figure 5.

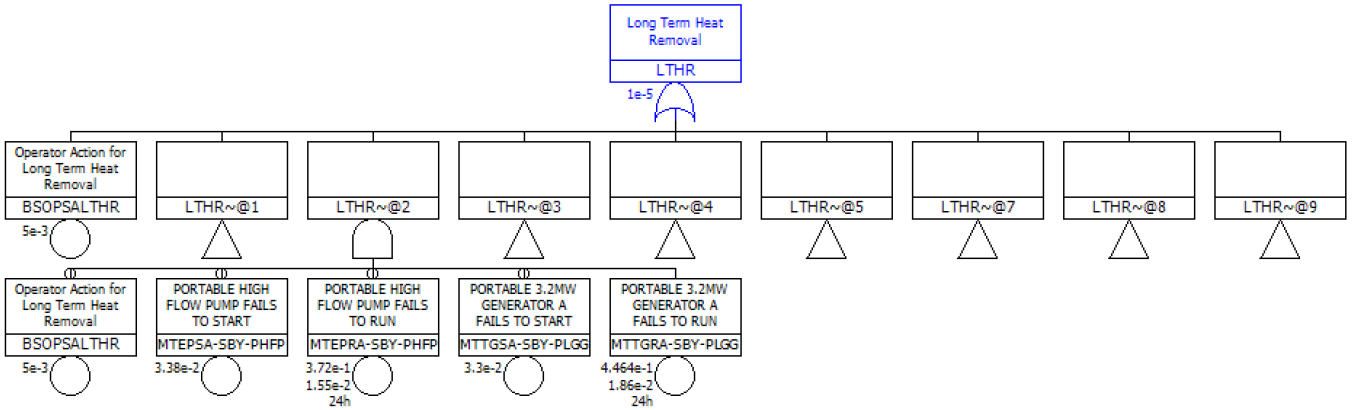

FIGURE 5. Converted LTHR Fault Tree(Failure Branch)

On the other hand, the fault tree connected to the success branch of the LTHR heading is shown in Figure 6.

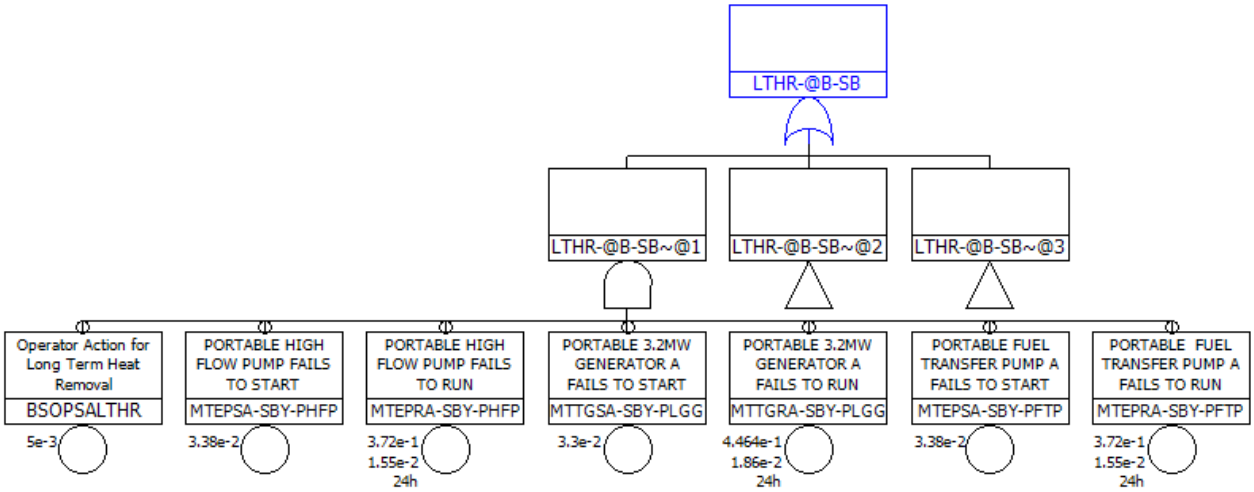

FIGURE 6. Converted LTHR Fault Tree(Success Branch)

III. Quantification Results

The results of quantifying the PDS event tree of a Level 2 PSA model that reflects accident coping strategy using portable equipment with high failure probability, with the Partial BDD method applied, were compared with the core damage frequency from Level 1 PSA. The results of quantification without applying the Partial BDD method were also compared. The computer used for quantification had the following specifications, typical for office laptops:

- CPU : Intel(R) Core(TM) Ultra 7 258V
- RAM : 32.0GB
- VGA : Intel(R) Arc(TM) 140V 16GB

III.A. Quantification Results with Partial BDD Applied

The results of quantification with the Partial BDD method applied to the LTHR heading are shown in Table II.

TABLE II. Quantification Result with Partial BDD

Cut-off Value	CDF (/ry)	PDS Frequency (/ry)	No. of Cutset (#)	Quant. Time (sec)	Difference (%)
1.00E-11	1.70E-06	1.66E-06	9205	6.9	(2.4)
1.00E-12	1.78E-06	1.78E-06	49553	12.2	0.0
1.00E-13	1.82E-06	1.84E-06	231215	33.1	1.1
1.00E-14	1.83E-06	1.86E-06	975924	128.0	1.6

Table II shows that when quantification is performed with the Partial BDD method applied, the core damage frequency calculated by quantifying Level 1 PSA event trees and the result calculated by quantifying PDSETs developed by expanding core damage scenarios are similar. When a high cut-off value is used for quantification, there are cases where the PDS frequency is lower than the CDF, but this problem does not occur when a sufficiently low cut-off value is selected for convergence. Even when a sufficiently low cut-off value is selected to ensure enough cut sets and convergence, the time required for quantification remains at an acceptable level.

III.B. Quantification Results without Partial BDD Applied

To check how much the PDS frequency differs from the core damage frequency when the Partial BDD method is not applied, the results of quantification without applying the Partial BDD method to the LTHR gate are shown in Table III.

TABLE III. Quantification Result without Partial BDD

Cut-off Value	CDF (/ry)	PDS Frequency (/ry)	No. of Cutset (#)	Quant. Time (sec)	Difference (%)
1.00E-11	1.70E-06	2.03E-06	11663	6.9	19.4
1.00E-12	1.78E-06	2.17E-06	61129	12.8	21.9
1.00E-13	1.82E-06	2.24E-06	277622	33.9	23.1
1.00E-14	1.83E-06	2.26E-06	1141833	111.3	23.5

The results in Table III show that when quantification is performed without the Partial BDD method, the core damage frequency and PDS frequency differ significantly. The current quantification model considered only one accident management strategy using portable equipment, but if multiple strategies using portable equipment are considered, this error is expected to increase.

III.C. Quantification Results with Partial BDD Applied to Multiple Gates

To check how the results change when the Partial BDD method is applied to multiple gates, quantification was performed by changing the model so that other mitigation strategies are performed using portable equipment, and the results are shown in Table IV.

TABLE IV. Quantification Result with Partial BDD

Cut-off Value	CDF (/ry)	PDS Frequency (/ry)	No. of Cutset (#)	Quant. Time (sec)	Difference (%)
1.00E-11	1.70E-06	1.52E-06	12379	7.3	(10.6)
1.00E-12	1.78E-06	1.68E-06	49553	15.1	(5.6)
1.00E-13	1.82E-06	1.76E-06	331839	43.6	(3.3)
1.00E-14	1.83E-06	1.79E-06	1446739	225.2	(2.2)
1.00E-15	1.84E-06	1.81E-06	5933891	610.1	(1.6)

The results in Table IV show that when the Partial BDD method is applied to multiple gates, the PDS frequency can be underestimated compared to the core damage frequency from Level 1 PSA. When quantification is performed using Partial BDD, the success event probability is multiplied for accident sequences corresponding to the success branch to calculate the exact value. In this process, minimal cut sets with frequencies that are not cut off are multiplied by success event probability and truncated. As described above, when a sufficiently low cut-off value is selected for convergence, the error gradually decreases, but the time required for quantification increases significantly.

IV. CONCLUSIONS

This study analyzed the effect of applying the Partial BDD method in Level 2 PSA models that include portable equipment with high failure probability. The results showed that when the Partial BDD method is applied, the discrepancy between core damage frequency (CDF) and plant damage state (PDS) frequency is significantly reduced. According to PWROG-18042-NP data, many portable equipment has failure probabilities exceeding 0.1, which causes significant errors in conventional quantification methods.

The Partial BDD method has the advantage of improving accuracy without significantly increasing computational burden. Even when a sufficiently low cut-off value is used, the quantification time remains at an acceptable level. However, when the Partial BDD method is applied to multiple gates, even if a sufficiently low cut-off value is used for convergence, the PDS frequency can be somewhat underestimated compared to the CDF.

In conclusion, in nuclear power plants where portable equipment with high failure probability plays an important role in accident mitigation strategies, the application of the Partial BDD quantification method effectively prevents excessive differences between core damage frequency and plant damage state frequency. When the Partial BDD method is applied to multiple gates, the PDS frequency may be somewhat underestimated compared to the CDF, but if a sufficiently low cut-off value is used for convergence, the error is at an acceptable level.

REFERENCES

[1] S. H. Han, "Comparison of Various Quantification Approaches for Seismic PSA," Trans. Korean Nucl. Soc. Spring Meeting, Jeju, Korea, May 18-19 (2023).
[2] S. H. Han, "A hybrid approach of partially applying BDD for seismic PSA quantification," Nucl. Eng. Technol., 56, 10, pp. 4289–4295 (2024).
[3] Wei Wang, O. Bäckström, and P. Krcal, "The RiskSpectrum MCS BDD Algorithm," Proceedings of the 12th International Conference on Probabilistic Safety Assessment and Management (PSAM12), Honolulu, Hawaii, June (2014).
[4] Risk Management Committee, "FLEX Equipment Data Collection and Analysis," PWROG-18042-NP rev. 1, Westinghouse Electric Company LLC (2022).
[5] KAERI, "AIMS-PSA Release 3," KAERI-ISA-MEMO-AIMS-03-KOR, Korea Atomic Energy Research Institute (2024).
[6] EPRI, "FTREX 2.0 Software Manual," EPRI 3002018234 (2020).

ASRAM2025
www.asram2025.org
Asian Symposium on Risk Assessment and Management 2025
Pattaya, Thailand, 27 – 29 August 2025

INVESTIGATING THE VALIDITY OF WEATHER BIN SAMPLING IN LEVEL 3 PSA

Sung-yeop Kim*

Korea Atomic Energy Research Institute: 111, Daedeok-daero 989beon-gil, Yuseong-gu, Daejeon, 34057, Republic of Korea

sungyeop@kaeri.re.kr

EXTENDED ABSTRACT

Level 3 probabilistic safety assessment (Level 3 PSA) requires statistical consideration of weather because of the presence of uncertainty in the risk assessment, as it involves postulating an accident that has not happened. One year of meteorological data consisting of 8,760 hours of data is typically utilized. A set of weather data considered in one offsite consequence analysis is defined as a weather sequence or weather trial. Traditionally, a weather sequence includes a series of meteorological data of one hour or a few hours, but more recently, it includes data for several days, such as 72 hours. The best-estimate statistical analysis is to perform 8,760 offsite consequence analyses using all 8,760 starting points of weather sequences and find statistical values such as mean, peak, and percentile values. However, the computing time or burden increases proportionally to the number of calculations. To overcome this limitation, sampling methods such as bin sampling and stratified random sampling have been employed in MACCS code [1, 2].

Stratified random sampling randomly samples a user-specified number of calculation starting points during each 24-hour day. This method is independent of the length of the weather sequence because it randomizes the calculation starting points. This approach does not employ weather binning. Instead, a user-defined number of weather trials is randomly selected from each individual weather day [3].

Bin sampling groups similar weather sequences into a bin and only performs computations representing each bin. However, it is questionable whether it is possible to find commonalities in weather sequences containing tens of hours of changing meteorological data and assign them to a bin. This study investigated whether bin sampling is still a valid method in the recent research trend of considering long weather sequences. The bin structure is designed to characterize precipitation conditions across varying downwind distance intervals from the accident site, in conjunction with 16 predefined bins representing initial meteorological conditions categorized by atmospheric stability class and wind speed. The rain bins are defined by user-specified values for rain intensity and distance intervals, which are entered via the Rain Distances and Rain Intensities configuration forms. The total number of weather bins is determined by the number of rain intensities (NRINTN) and the number of rain distance intervals (NRNINT), which are specified in the respective configuration forms. The aggregate number of weather bins is calculated as NRNINT × (NRINTN + 1) + 16. Consequently, depending on user input, the total number of bins may range from 28 to 40.

In the uniform bin sampling approach, the parameter NSMPLS specifies the number of weather sequences to be selected from each individual weather bin. Increasing the number of samples enhances the statistical robustness of the simulation outcomes. The actual number of sequences extracted from a given weather bin corresponds to the lesser of either the total number of time periods available within that bin or the value specified by NSMPLS. Nonuniform bin sampling operates similarly to uniform bin sampling, with the key distinction that the user separately specifies the number of weather trials (INWGHT) to be sampled from each bin. As with the uniform method, 1200 hours of weather data are retrieved per trial to characterize temporal variation.

For the analysis, two site data sets, the Korean reference site and the NRC Sample provided by MACCS, were used. Since the NRC sample problem uses nonuniform bin sampling, the nonuniform bin sampling method is adopted as a representative method of bin sampling. Stratified random sampling was analyzed by increasing the number of samples (NSMPLS) from 1 to 24. This study focused on a one-week emergency phase and cases with or without emergency responses such as evacuation and relocation were analyzed. As results, population-weighted risks for early fatality and cancer fatality were considered.

TABLE I. Relative error of the mean value for each sampling method compared to the mean value considering all weather data (NSMPLS = 24)

		Pop-weighted Risk	Nonuniform Bin Sampling	Stratified Random Sampling (Number of Samples per Day)						
				1	2	4	8	12	18	24 (Best-estimate)
With Emergency Response	NRC Point Estimate LNT	Early Fatality	18.75%	2.08%	1.46%	-4.48%	2.92%	0.42%	-3.12%	0.00%
		Cancer Fatality	-2.69%	8.52%	-4.93%	-0.45%	0.90%	-0.45%	-17.49%	0.00%
	Reference Site	Early Fatality	N/A	N/A	N/A	N/A	N/A	N/A	N/A	N/A
		Cancer Fatality	2.02%	-1.01%	1.35%	1.68%	0.67%	-0.67%	-10.44%	0.00%
Without Emergency Response	NRC Point Estimate LNT	Early Fatality	4.39%	-1.88%	-13.79%	-2.35%	0.63%	0.16%	-7.84%	0.00%
		Cancer Fatality	-4.12%	8.82%	-4.41%	-0.88%	1.18%	-0.44%	-17.35%	0.00%
	Reference Site	Early Fatality	N/A	N/A	N/A	N/A	N/A	N/A	N/A	N/A
		Cancer Fatality	2.02%	-1.18%	1.18%	1.68%	0.34%	-0.84%	-10.59%	0.00%

Table I shows the results of the analysis, the average value derived from considering all weather data and the average value derived from each sampling. In Stratified random sampling, when the number of samples to be extracted per day is set to 24, the results can be calculated considering all weather data and this becomes the best-estimate case. For stratified random sampling, the results tend to be closer to the best-estimate case as the number of samples increases. However, it can be observed that there is an unusually high difference when the number of samples is 18. This is because the number of samples can introduce bias into the sampling algorithm if the number of samples is not a factor of 24, which is the number of days in a year. Users should be careful not to enter a number of samples that is not a factor of 24. It can also be seen that nonuniform bin sampling has a relatively large difference in results. This is due to the MACCS sample problem entering a nonuniform number of samples for the 36 weather bins and over-sampling from some bins. Therefore, when utilizing nonuniform bin sampling, it is necessary to carefully consider the number of weather trials to be sampled from each bin.

In conclusion, the results of this study show that the error of stratified random sampling is less than 5%, 3%, and 1% when the number of weather trials to be sampled per day is set to 4, 8, and 12, respectively. While, when nonuniform bin sampling is utilized, the results can be skewed toward some weather bins and show a large error from the best-estimate. The results of this study may not be representative of all cases, so it is necessary to consider more years of weather data, different numbers of plumes, and other factors. It is also worth extending the study to the long-term phase, not just the emergency phase, to evaluate the impact of the sampling method.

ACKNOWLEDGMENTS

This work was supported by the Nuclear Safety Research Program through the Korea Foundation of Nuclear Safety (KoFONS) using financial resources granted by the Nuclear Safety and Security Commission (NSSC) of the Republic of Korea (No. RS-2023-00240452).

REFERENCES

[1] Sandia National Laboratories, *MACCS User Guide – Version 4.2*, SAND2023-01315, Sandia National Laboratories (2023).
[2] Sandia National Laboratories, *MACCS Model Description*, NUREG/CR-4691, SAND86-1562 Vol. 2, Sandia National Laboratories (1990).
[3] J.C. Helton, J.D. Johnson, C.J. Sallaberry, C.B. Storlie, Survey of sampling-based methods for uncertainty and sensitivity analysis, *Reliability Engineering and System Safety*, **91**, 1175–1209 (2006).

Technical Session 2 (13:40 - 15:40)	The Port 2, C Floor	Dynamic PSA, Accident Modelling and Uncertainty Analysis
		Chair/Facilitator 1: Prof. Topan SETIADIPURA, Research Center for Nuclear Reactor Technology (BRIN)
		Chair/Facilitator 2: Asst. Prof. Takafumi NARUKAWA (The University of Tokyo (UTokyo))
13:40 - 14:00		ID 123: Decomposing Event-Timing Randomness and Epistemic Uncertainty in Dynamic PRA Speaker: Takafumi NARUKAWA (The University of Tokyo (UTokyo)) Contributors: Takafumi NARUKAWA (The University of Tokyo (UTokyo)), Takashi Takata (The University of Tokyo)
14:00 - 14:20		ID 34: Development of Clustering Method for Accident Scenarios Using UMAP and Dynamic Time Warping Technique Speaker: Hyeonho Byun (KAERI) Contributors: Hyeonho Byun (KAERI), Hyeonmin Kim (KAERI)
14:20 - 14:40		ID 46: Research on the Automatic Generation Method of Dynamic Event Tree Scene Based on SBLOCA Speaker: He Wang (Harbin Engineering University) Contributors: Chongxiao Xie (Harbin Engineering University), Haoyin Chen (Harbin Engineering University), He Wang (Harbin Engineering University)
14:40 - 15:00		ID 121: Application of Time-Dependent Dynamic Accident Sequence Generation Method to MACST Equipment using Optimized Simulations Speaker: Wooseok Jo (Ulsan National Institute of Science and Technology) Contributors: Wooseok Jo (Ulsan National Institute of Science and Technology), Junyong Bae (Ulsan National Institute of Science and Technology), Seung Jun Lee (Ulsan National Institute of Science and Technology)
15:00 - 15:20		ID 111: Effect of Including Motor-Driven Auxiliary Feed Water Pump and Operators' Load-Shedding Action Time in SBO's CCDP Calculation Speaker: Younghak Lee (Chung-Ang University) Contributors: Man Cheol Kim (Chung-Ang University), Younghak Lee (Chung-Ang University)

ASRAM2025
www.asram2025.org
Asian Symposium on Risk Assessment and Management 2025
Pattaya, Thailand, 27 – 29 August 2025

DECOMPOSING EVENT-TIMING RANDOMNESS AND EPISTEMIC UNCERTAINTY IN DYNAMIC PRA

Takafumi Narukawa[1], Takashi Takata[1]

[1] *Department of Nuclear Engineering and Management, Graduate School of Engineering, the University of Tokyo, 7-3-1 Hongo, Bunkyo-ku, Tokyo 113-8656, Japan, narukawa@nse.t.u-tokyo.ac.jp, takata_t@nse.t.u-tokyo.ac.jp*

EXTENDED ABSTRACT

Dynamic probabilistic risk assessment (PRA) methods are being developed to explicitly simulate time-dependent system behaviors and stochastic event sequences. These features enable the direct modeling of system dynamics and temporal interactions that are difficult to capture using conventional static PRA methods with event and fault trees. One key advantage of dynamic PRA is its capacity to represent both aleatory and epistemic uncertainties [1] within a unified computational framework. The aleatory uncertainty is stemming from inherent randomness and generally irreducible and the epistemic uncertainty arises from incomplete knowledge and potentially reducible through data collection or model refinement. Therefore, decomposing these two types of uncertainty is essential for risk-informed decision making, as it allows analysts to identify which sources of uncertainty dominate and which can be reduced through additional data or model refinement. This insight, in turn, supports more rational and efficient allocation of resources for risk management actions. This study presents a generalizable framework based on a continuous Markov chain Monte Carlo (CMMC) method [2], a class of dynamic PRA, to quantify and distinguish between epistemic and aleatory uncertainties. A novel metric, the Epistemic-to-Aleatory Ratio (EAR), is proposed to evaluate the relative contribution of epistemic uncertainty to the overall variance in system-level outcomes. The EAR is conceptually adapted from the Gelman–Rubin convergence statistic [3], which compares between-chain and within-chain variances for Markov chain Monte Carlo samplings. To demonstrate the effectiveness of the framework, we conduct a numerical analysis using a holdup tank model [4], which is a simplified reliability model.

Fig. 1 illustrates a generalized simulation workflow for the CMMC method. The core structure consists of a double-loop Monte Carlo sampling procedure. The outermost loop, indexed by $i = 1,...,N$, corresponds to epistemic uncertainty. In this loop, a set of model parameters—such as demand failure probabilities and operational (time-dependent) failure rates—is sampled from their respective probability distributions. These sampled parameters remain fixed throughout the corresponding inner loop. For each outermost-loop sample, the inner loop, indexed by $j = 1,...,M$, represents aleatory uncertainty by generating stochastic realization of the system's behaviors. Each realization simulates the system evolution over time steps ($t = 0, \Delta t, ..., T$). At each time step t , system transitions—including component demands, operator actions, or external disturbances—are determined based on the current system state and operational logic. Component failures or state changes are then evaluated probabilistically, using the fixed epistemic parameters. The system state is updated accordingly, and system dynamics are re-evaluated. This process continues until the simulation reaches the final time T or a termination condition is satisfied. After repeating this process for all combinations of N epistemic samples and M aleatory realizations, we obtain a total of $N \times M$ system-level outcomes ψ_{ij} . From these outcomes, we can compute epistemic variance v_{epi} (between-sequence variance) and aleatory variance v_{alea} (within-sequence variance) as:

$$v_{epi} = \frac{1}{N-1}\sum_{i=1}^{N}\left(\overline{\psi}_{i\cdot} - \overline{\psi}_{\cdot\cdot}\right)^2, \text{ where } \overline{\psi}_{i\cdot} = \frac{1}{M}\sum_{j=1}^{M}\psi_{ij},\ \overline{\psi}_{\cdot\cdot} = \frac{1}{N}\sum_{i=1}^{N}\overline{\psi}_{i\cdot}, \tag{1}$$

$$v_{alea} = \frac{1}{N}\sum_{i=1}^{N}s_i^2, \text{ where } s_i^2 = \frac{1}{M-1}\sum_{j=1}^{M}\left(\psi_{ij} - \overline{\psi}_{i\cdot}\right)^2. \tag{2}$$

Then, EAR is defined as:

$$EAR = \frac{v_{epi}}{\widehat{var}}, \text{ where } \widehat{var} = v_{epi} + \left(1 - \frac{1}{M}\right)v_{alea}. \tag{3}$$

This metric represents the ratio of epistemic variance to the total variance. $EAR > 0.5$ implies that epistemic uncertainty dominates, guiding the need for data acquisition or model refinement. Conversely, an $EAR < 0.5$ suggests that aleatory uncertainty is more influential, and additional resource investment for data acquisition or model refinement should be considered with caution.

To demonstrate the utility of the proposed EAR metric, we apply the framework to the holdup tank model, which simulates water inflow and outflow with probabilistic failures of components (a valve and two pumps) as illustrated in Fig. 2. The simulation procedure follows the CMMC workflow in Fig. 1, and the analytical setup is consistent with our previous study [5], assuming Pump 1 failed-off as the initiating event and dryout—defined as the tank water level dropping to zero—as the endpoint. Epistemic uncertainty is introduced in both demand failure probabilities and time-dependent failure rates. Two cases are analyzed: Case A (base case with a unimodal distribution) and Case B (amplified epistemic uncertainty, represented by a bimodal distribution). Uncertainty propagation to EAR is performed via the CMMC method (Fig. 1). The computed EAR values for Case A and Case B were 0.19 and 0.52, respectively. These results demonstrate that EAR is sensitive to the relative magnitude of epistemic uncertainty and can support resource allocation decisions in data refinement.

In conclusion, this study presents a generalized framework for decomposing two types of uncertainty, epistemic and aleatory uncertainties, in a dynamic PRA using the CMMC method. To quantify the relative contribution of epistemic uncertainty to overall system uncertainty, we propose a novel metric, EAR. The application to a holdup tank model demonstrates how EAR can support the prioritization of epistemic uncertainty reduction in risk-informed decision making. Future work includes extending the proposed metric toward uncertainty importance evaluations.

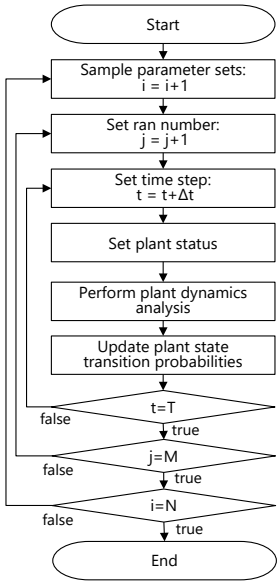

FIGURE 1. CMMC Simulation Workflow

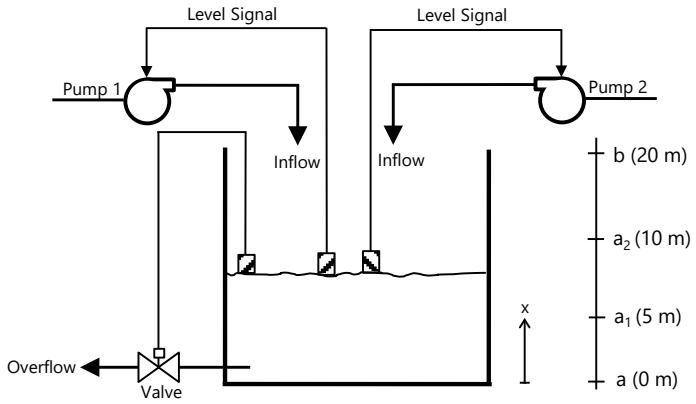

FIGURE 2. Schematic of Holdup Tank Model

REFERENCES

[1] J. C. HELTON and D. E. BURMASTER, "Guest Editorial: Treatment of Aleatory and Epistemic Uncertainty in Performance Assessments for Complex Systems," *Reliability Engineering & System Safety*, **54**, 91 (1996).
[2] T. TAKATA and E. AZUMA, "Event sequence assessment of deep snow in sodium-cooled fast reactor based on continuous Markov chain Monte Carlo method with plant dynamics analysis," *Journal of Nuclear Science and Technology*, **53**, 11, 1749 (2016).
[3] A. GELMAN et al., Bayesian Data Analysis, pp. 284–285, CRC Press, Boca Raton, FL (2013).
[4] N. SIU, "Risk assessment for dynamic systems: an overview," *Reliability Engineering & System Safety*, **43**, 1, 43 (1994).
[5] T. NARUKAWA et al., "Development of Risk Importance Measures for Dynamic PRA Based on Risk Triplet (1) The Concept and Measures of Risk Importance," Proc. PSAM17 & ASRAM2024, Sendai, Japan, October 2024, PSAM17&ASRAM2024-1026 (2024).

ASRAM2025
www.asram2025.org
Asian Symposium on Risk Assessment and Management 2025
Pattaya, Thailand, 27 – 29 August 2025

Development of Clustering Method for Accident Scenarios Using UMAP and Dynamic Time Warping Technique

Hyeon Ho Byun[1], Hyeon Min Kim[2]

[1] *111, Daedeok-daero 989beon-gil, Yuseong-gu, Daejeon, Republic of Korea, and byunhh@kaeri.re.kr*
[2] *111, Daedeok-daero 989beon-gil, Yuseong-gu, Daejeon, Republic of Korea, and hyeonmin@kaeri.re.kr*

ABSTRACT

The enhancement of reactor safety is crucial for the widespread adoption of nuclear energy. In particular, Small Modular Reactors (SMRs), due to their multi-reactor nature and relatively fewer personnel per module, may present more complex accident response procedures compared to large-scale reactors. Therefore, the Korea Atomic Energy Research Institute (KAERI) is developing a system to detect accidents and provide optimal response strategies to operators, with plans for its application to virtual reactors. In this study, we propose a methodology for extracting representative accident scenarios by analyzing various accident progressions and identifying scenarios with similar peak cladding temperature profiles. Although Uniform Manifold Approximation and Projection (UMAP) has been reported to perform excellently in data classification tasks such as image recognition, its effectiveness in time-series data classification remains unverified. Given that UMAP's performance depends on the similarity measure (i.e., metric) used between data points, we applied the dynamic time warping (DTW) method, which is capable of detecting trends and patterns in time-series data, as a metric for UMAP. We then compared the result of accident scenario classification using UMAP with its default metric to evaluate the performance of the DTW-based approach.

Keywords: Severe accident, UMAP, dimensionality reduction, dynamic time warping, machine learning

I. Introduction

To develop new reactor types such as Small Modular Reactor (SMRs), it is essential to conduct probabilistic safety assessment (PSA) to verify the safety of the reactor. In Level 1 PSA, representative accident scenarios are classified for each initial event (IE), and comprehensive risk assessment is performed up to the pre-core damage phase. PSA results are also utilized as reference data to improve the safety system design. Traditional PSA approaches have evaluated safety systems by applying several conservative assumptions that negatively affect reactor states. However, such conservative assessment methods may lead to the design of excessively redundant safety systems, which can increase the levelized cost of electricity for SMRs.

To address this issue, dynamic PSA (DPSA), which assesses risk more progressively and realistically, has been proposed in recent years [1]. DPSA diversifies event timing and branches resulting from events (i.e., branch points) and comprehensively evaluates the risks of scenarios corresponding to all branches [2]. Therefore, DPSA theoretically allows for an infinite number of scenarios to unfold beyond an IE. However, performing safety analysis for all possible scenario is highly inefficient. Thus, it is necessary to identify representative scenarios with similar accident progression and establish safety measures based on theses representative scenarios. This study aims to propose a methodology for deriving representative accident scenarios by applying clustering algorithms to identify the structural relationships among accident scenario data and assigning similar scenarios to the same cluster.

Since risk assessment of nuclear reactors cannot be directly experimented with using real-scaled reactors, severe accident (SA) codes (e.g., MARS, MAAP, MELCORE) are employed to simulate such events. The SA code used in this study is MAAP. MAAP terminates calculations beyond the core damage (CD), a critical event that occurs when the temperature of the nuclear fuel exceeds its melting point. Thus, peak cladding temperature (PCT) is a key thermohydraulic variable that determines whether CD has occurred and provides insight into accident scenarios based on the shape of its curve. Therefore, this study assumes that PCT is the primary thermohydraulic variable that defines accident scenarios and utilizes PCT for accident clustering and deriving representative scenarios. This study developed a methodology for generating random accident scenarios

based on the Monte Carlo method. Using this approach, 6,400 random scenarios were produced, followed by the application of dimensionality reduction and clustering algorithms to derive representative scenarios.

In general, previous studies have used uniform manifold approximation and projection (UMAP), a dimensionality reduction algorithm, to compute differences between data points in image datasets [3]. Data points with smaller calculated differences are densely distributed within the latent space. Subsequently, clustering algorithms (e.g., DBSCAN) are applied to the latent space to group nearby data points into the same cluster, completing the clustering process. For image data, two-dimensional data are typically flattened into one-dimensional vectors, and their similarities are calculated using Euclidean distance (ED) for dimensionality reduction. However, due to the characteristics of time-series data, when the graphical representation of data on the x-y plane shifts horizontally along the x-axis (time direction), ED evaluates such data as having low similarity (i.e., large data distance). This indicates a limitation of traditional image-based similarity evaluation methods in assessing the similarity of time-series data, even when the overall shape of the graphs is similar.

In this study, UMAP was employed for dimensionality reduction of time-series data, while soft dynamic time warping (soft-DTW) was used as a substitute for ED [4]. Soft-DTW, an improved algorithm derived from dynamic time warping (DTW) for gradient computation, is a specialized metric for evaluating structural similarities in time-series data. The mathematical details of this approach are discussed in Section 2. Additionally, clustering performance was validated by comparing results obtained using the traditional ED metric. It was observed that the embedding results using the soft-DTW metric made it easier to derive representative accident scenarios specifically for time-series data.

The target reactor type for the methodology developed in this study is the OPR-1000, which is internationally widespread and has undergone numerous safety validation studies. According to the Level 1 PSA report on the OPR-1000 conducted by Korean Atomic Energy Research Institute (KAERI), there are 14 IEs, each with dozens of sub-scenarios [5]. While this study focused on a case study for the loss of offsite power (LOOP), the methodology could technically be applied to derive representative accident scenarios for other ISs as well. In summary, the academic contribution of this study are as follows:

1. Enhanced clustering performance for time-series data using an improved metric
2. Diversification of reactor accident scenarios based on the Monte Carlo method
3. Derivation of representative accident scenarios based on thermohydraulic data calculation

II. Methodology

This study is organized by two research materials: the generation of accident simulation results from MAAP based on random sampling in Monte Carlo simulations, and the clustering of the derived accident scenarios using UMAP with soft-DTW for dimensionality reduction and DBSCAN for scenario clustering. All research materials were implemented in Python. The UMAP algorithm was applied using the umap-learn library, DBSCAN was utilized via the sklearn libaray, and soft-DTW, as it is an unsupported custom metric, was implemented manually.

II.A. Random scenario sampling

Random Scenario Sampling (RSS) refers to the process of stochastically determining the states of key systems and components of a reactor over time to define accident scenarios. Using the Monte Carlo method, RSS stochastically decides whether each component operates successfully, fails, or the timing of failure if it occurs. However, given that MAAP involves hundreds of components, RSS is applied only to key Structures, Systems, and Components (SSCs) to reduce the computational calculation cost.

When performing random sampling for SSCs, the success or failure of each SSC is sampled based on failure data from conventional PSA. For instance, if an SSC is in standby mode and is activated or fails to be activated, the probability of failure on demand is used to make probabilistic determinations. Secondly, for components already in operation, the time to failure is determined using operational failure rate data. If operator intervention is required, it becomes part of RSS, where the action time required for task execution and the success probability of the task are stochastically calculated. Lastly, as reactors involve interconnected systems, the operation of specific components may depend on the proper functioning of other components, which are designed as combinations of AND/OR gates.

This study conducted a case study by assuming LOOP as a representative IE. Instead of performing RSS for all reactor components, only SSCs related to LOOP were considered. SSCs associated with LOOP can be categorized into power-related components and safety systems. The power-related components include key equipment and human actions that are activated when external power is lost, or additional power supply is required. Major components associated with failures such as fail-to-start or fail-to-run include the emergency diesel generator (EDG) and the alternative alternating current diesel generator (AAC-DG). The power supply from these components is used for HVAC (heating, ventilation, air conditioning) systems and to support the high-pressure safety injection system (HPSIS), which is critical for system recovery during a loss of coolant accident

(LOCA). The HPSIS is a critical safety system in nuclear reactors designed to inject coolant into the reactor pressure vessel during LOCA. The system operates at high pressure, typically capable of injecting borated water even when the reactor is at or near operating pressure (15 – 16MPa). HPSIS consists of high-pressure pumps, borated water storage tanks, injection piping, and associated valves that automatically activate upon detection of accident signals such as low reactor pressure or high containment pressure. The OPR-1000 reactor is equipped with two EDGs connected in parallel, ensuring successful operation as long as at least one of them functions (Figure 1).

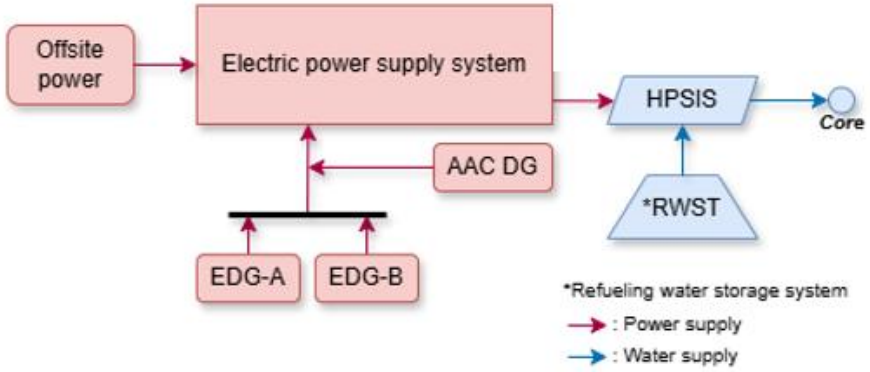

FIGURE 1. Simplified diagram of power-related SSCs in OPR-1000 [5]

Human actions related to the power systems come into play when EDGs fail following a LOOP, and offsite power is not restored, leading to the declaration of a Station Blackout (SBO). After the SBO is triggered, the operator activates the AAC-DG. Similarly, if the AAC-DG fails before offsite power is restored, the Technical Support Center (TSC) attempts to recover power using a mobile diesel generator (MDG). The safety systems are activated following SBO to circulate feedwater and cool down the reactor core, necessitating the operation of the auxiliary feedwater system (AFWS) pumps. The turbine-driven pump (TDP) of the AFWS must be activated proactively, and if the AFWS fails, the motor-driven pump (MDP) is engaged. The operation of the TDP and AAC-DG determines the feasibility of sealing coolant leakage caused by the reactor coolant pump (RCP). If sealing the coolant leakage fails, a LOCA will occur.
If both the TDP and MDP fail, the operator initiates feed and bleed (F&B) operations, which involve a deliberate LOCA by the operator. Additionally, during the initial stage of an SBO, the pressure safety valve (PSV) may become stuck open, which can also trigger a LOCA. Following a LOCA, cooling is attempted through the insertion of control and safety rods (CSR) and by employing the safety injection system (SIS), such as the HPSIS and low-pressure safety injection system (LPSIS). The operational status, failure timing, and other parameters of all the mentioned equipment are randomly sampled using the Monte Carlo method based on the given failure data. Similarly, human actions, including action time and mission success probability, are also stochastically sampled.

II.B. Scenario labeling method

This study aims to cluster scenarios and extract representative scenarios solely based on PCT data. Although the proposed methodology follows an unsupervised approach, assigning labels to each scenario enables an effective evaluation of the clustering results by comparison with the labeled data. Therefore, this section explains the labeling methodology for accident scenarios that occur in OPR-1000 reactor following a LOOP event. The possible accident scenarios after an IE, under the system conditions described in Section 2.1, are summarized in Figure 2. In Figure 2, each branch point represents a decision point, with the lower branch indicating the failure of the corresponding component or action. For example, after a LOOP occurs, if the emergency diesel generator (EDG, referred to as DG in Figure 2) operates successfully and the pressure safety valve (PSV) re-closes, core damage (CD) does not occur, regardless of whether the AFWS operates or fails but is mitigated by a successful F&B operation. These scenarios are labeled as LOOP-1 and LOOP-2, respectively.
Similarly, if the AFW fails and F&B also fails, CD occurs, and this scenario is labeled as LOOP-3. The labeling process systematically assigns labels to all possible scenarios based on the sequence of events and outcomes shown in Figure 2. If the EDG operates but the PSV becomes stuck open, a small-loss-of-coolant accident (SLOCA) scenario unfolds (Figure 3). When a LOOP occurs, the EDG may either fail to start or fail during operation, and these two cases are categorized as separate events due to their significantly different occurrence frequencies. However, once the EDG fails, the subsequent safety measures do not vary significantly. Therefore, scenarios following an EDG failure are collectively categorized as SBO scenarios (Figure 4).

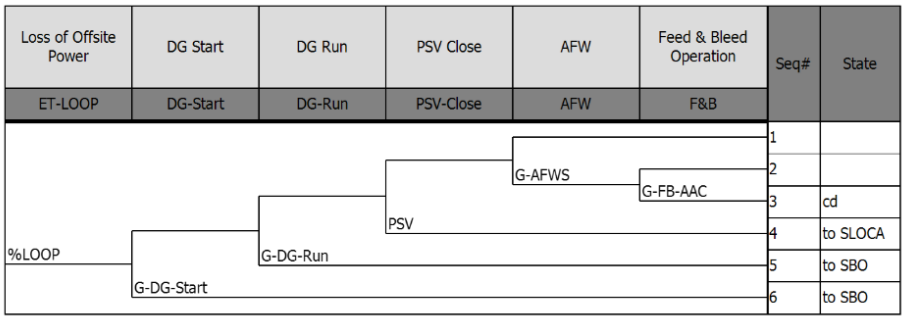

FIGURE 2. Event tree summary beyond LOOP [5]

In Figure 2, when the fourth sequence occurs, it is assumed that detailed scenarios, as depicted in Figure 3, exist. Even if the PSV becomes stuck open, no CD occurs if the SIS and AFW (i.e., AFWS in Figure 8) operate successfully. Furthermore, even if the AFW fails, successful execution of F&B ensures that CD does not occur. In all other cases, CD is inevitable. If both the SIS and AFW succeed (Seq#1 in Figure 3), the scenario is labeled as LOOP-SLOCA-1. Similarly, scenarios for Seq#2 to Seq#4 are named LOOP-SLOCA-2, LOOP-SLOCA-3, and LOOP-SLOCA-4, respectively.

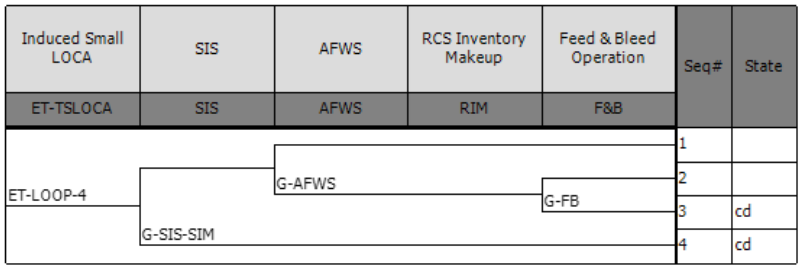

FIGURE 3. Event tree summary of SLOCA [5]

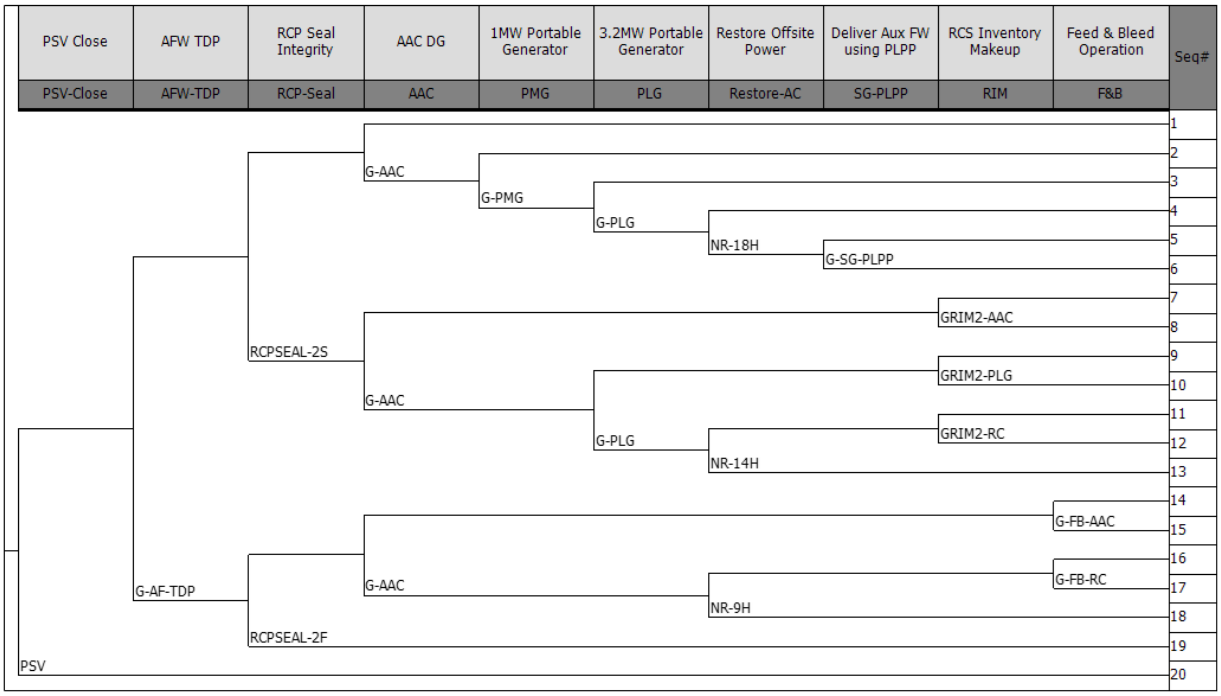

FIGURE 4. Event tree summary of SBO [5]

In Figure 2, Seq#5 and Seq#6 represent scenarios leading to SBO (Station Blackout). The potential accident scenarios stemming from these sequences are depicted in the event tree format shown in Figure 4.
If power recovery using EDG fails, the scenario evaluates the presence or absence of a PSV stuck condition, AFW (i.e., AFW TDP in Figure 4), and RCP seal integrity, proceeding through four stages of power recovery attempts. Subsequently, strategies such as utilizing PLPP for secondary-side cooling of the SG or performing F&B are employed to remove the heat generated in the reactor core. After EDG failure, 20 possible SBO accident scenarios are considered. Each scenario is assigned a sequence number (i.e., Seq# in Figure 4) and is labeled as LOOP-SBO-1 through LOOP-SBO-20.

II.C. Soft-DTW method

Soft-DTW builds upon DTW by introducing a mathematical trick to make DTW differentiable. This section first outlines the general features of the DTW algorithm and then provides a detailed explanation of soft-DTW. While UMAP supports various custom metrics, the custom metric must calculate both the distance and the gradient between two time-series datasets. Hence, this study adopted soft-DTW instead of DTW. The soft-DTW can be applied for two vectors which has different length of series. P and Q are defined as time-series data and their lengths are m and n. First, the two time-series are arranged to form a matrix E (with shape $m \times n$). The (i, j)-th element of E represents the squared Euclidean distance between the points p_i and q_j. The warping path (W) represents the set of mappings between P and Q and can be expressed as follows:

$$W = [w_1, w_2, \dots, w_K] \\ \max(m, n) \le K < m + n - 1 \tag{1}$$

At this point, every element of W corresponds one-to-one with the elements of the matrix E. The k-th element of W, denoted as w_k, represents the warping distance. The objective is to find the path among all possible warping paths that minimizes the total sum of the warping distances. This is referred to as the minimum warping path cost (WPC_{min}) and is mathematically expressed as follows:

$$WPC_{min}(P, Q) = \min\left(\frac{1}{\mathrm{K}}\sqrt{\sum_{k=1}^{K} w_k}\right) \tag{2}$$

Starting from i=0, j=0, the cumulative warping distance D for the k-th warping distance is defined as follows:

$$D(i, j) = E(i, j) + \min\begin{pmatrix} D(i-1, j-1) \\ D(i-1, j) \\ D(i, j-1) \end{pmatrix} \tag{3}$$

where the initialization $D(0, 0)$=0.
However, due to the second term in Equation (3), which involves selecting the minimum among three elements, DTW suffers from being non-differentiable. To address this limitation, soft-DTW replaces the non-differentiable operation in Equation (3) with a differentiable alternative. In soft-DTW, the minimum function used in Equation (3) to choose the smallest value among three terms is replaced with a differentiable approximation called the softmin. The softmin function is defined as:

$$\mathrm{softmin}_{\gamma}(a_1, a_2, \dots, a_n) = -\gamma \log \sum_i e^{-\frac{a_i}{\gamma}} \tag{4}$$

where γ>0 is a smoothing parameter that controls the trade-off between strict minimum selection and a softer, differentiable approximation. This replacement ensures that the resulting cumulative distance is differentiable, enabling the computation of gradients and facilitating the use of soft-DTW in optimization problems.
In this study, to calculate the distance between two time series data, features are extracted from all elements of the two data sets (P, Q). This is because the number of scenarios is relatively small and the sequence length is not particularly long, so clustering takes only one to two days to compute. However, if additional scenarios are added for the further works, it could take several weeks or more corresponding to the number of scenarios. In such cases, time could be saved by applying a warping window that restrictively searches only the neighboring indices of each time series data element.

III. Results

This section presents the results of clustering 6,400 accident scenarios using soft-DTW as the metric for UMAP-based dimensionality reduction and DBSCAN for clustering. Typically, clustering large-capacity data requires two primary steps. First, it is necessary to reduce the dimensionality of the data and project it into points. Previous studies have utilized convolution methods for feature extraction from deep learning or t-distributed stochastic neighborhood embedding (t-SNE), which has been conventionally used as a dimensionality reduction algorithm. However, UMAP was employed in this study because it is implemented as a library in Python and offers advantages of being faster and more accurate than existing methods, while requiring fewer hyperparameters. Second, an algorithm is needed to form clusters among adjacent points. DBSCAN is commonly utilized due to its advantage of requiring fewer hyperparameters. DBSCAN is an algorithm that explores the neighborhood of embedded points and forms clusters when the number of points exceeds a minimum threshold within the search radius. Therefore, the hyperparameters of DBSCAN are the point search radius and the minimum number of points required within the radius for cluster formation. This study used default sets of hyperparameters of UMAP and DBSCAN.
The results obtained with the soft-DTW metric were compared and analyzed against those obtained using the Euclidean metric. To generate the dataset, 6,400 accident scenarios were randomly sampled based on the Monte Carlo method. The input data for these scenarios was simulated using MAAP, and the corresponding PCT data was extracted. PCT was calculated for a duration of 72 hours following the IE and recorded at 50-second intervals. In this study, the sampling time (i.e., 50-second intervals) was determined intuitively. If the sampling time were shorter than 50 seconds, the sequence length for each scenario would become excessively long, thereby requiring an impractically long time to perform clustering. Furthermore, since the soft-DTW utilized in this study has a clustering time that increases proportionally to the square of the sequence length, an appropriate sequence length was determined empirically. Figure 5 illustrates the scaled PCT results for all scenarios. The scaling ensures that the average value of the entire PCT curve for each scenario is normalized to 1, providing a consistent basis for comparison. This figure represents the scaled PCTs of all 6,400 accident scenarios.

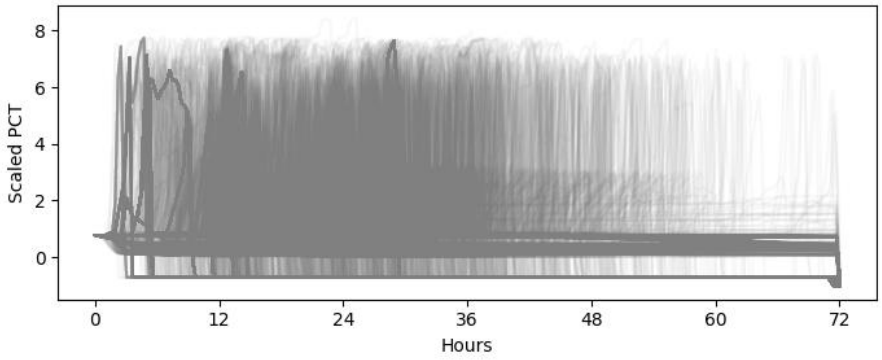

FIGURE 5. Scaled PCTs corresponding to every LOOP scenario

The fact that PCT results repeat across multiple scenarios indicates that, regardless of the random actions, component failures, or timing of events following the reactor IE, the thermohydraulic progression of the reactor eventually converges into a limited set of outcomes. To quantitatively analyze this, UMAP and DBSCAN algorithms were used to cluster scenarios exhibiting similar PCT trends, and the results were compared.
UMAP was employed to embed the PCTs of the 6,400 accident scenarios into a 3-dimensional space (i.e., latent space). Instead of using traditional metrics from UMAP, soft-DTW was applied to measure the similarity between time series data. The embedded data scattered in the 3D space are shown in Figure 6. The left graph in Figure 6 represents the embedding results using the traditional Euclidean metric in UMAP, while right graph shows the embedding results with the soft-DTW metric applied in this study.

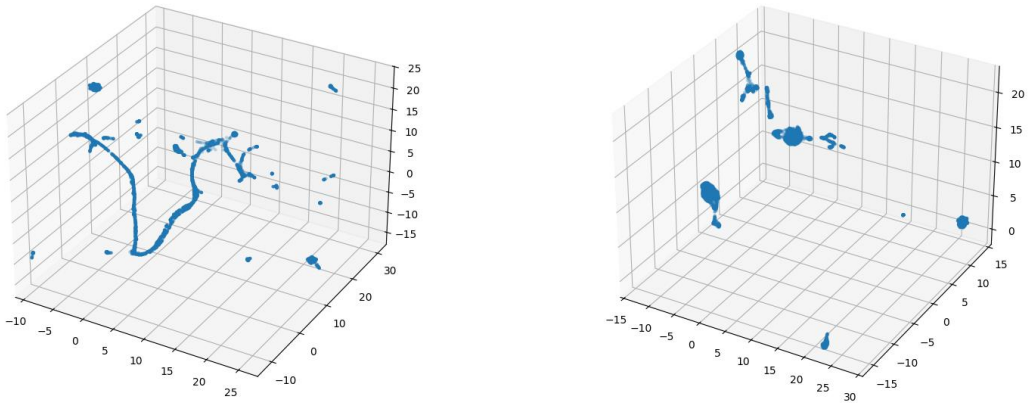

FIGURE 6. Embedded results (ED: left, soft-DTW: right)

Visually, it can be observed that the ED embedding has more scattered points that spread wider, with some forming clusters in the shape of a curved line. In contrast, the soft-DTW embedding generally shows a cloud-like shape where the data points are clustered. However, assessing the performance of the metric solely based on the visual appearance of the scattered data is challenging. To gain further insight, DBSCAN was used to cluster the scattered embedded data, and a more detailed analysis was conducted to identify which data points belong to each cluster. The results from DBSCAN are shown in Figure 7. Data points identified as noise in DBSCAN were labeled as -1, so the minimum value on the color bar in the figure is -1.

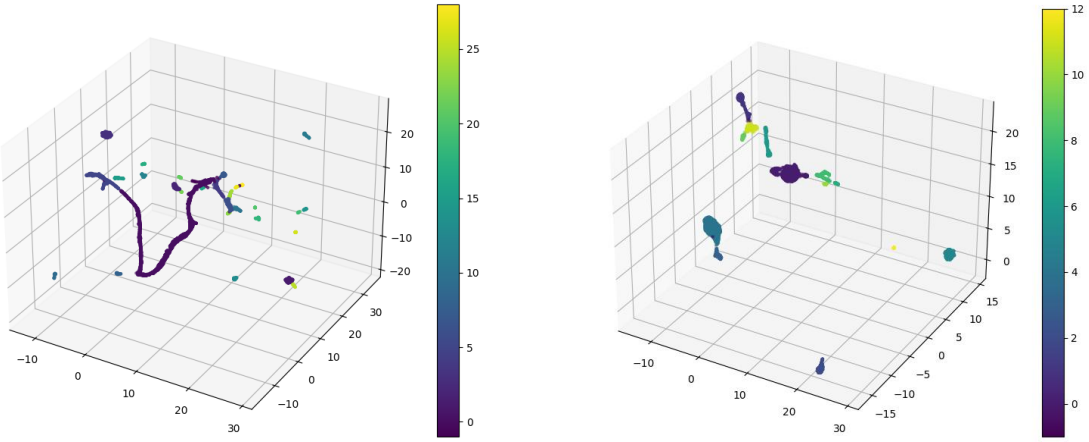

FIGURE 7. Clustered results (ED: left, soft-DTW: right)

To derive representative accident scenarios for each cluster, the most effective method is to identify data points near the centroid of the cluster. However, if the cluster shape is skewed (e.g., a curved line), the centroid may lie outside the cluster structure, leading to the potential for selecting an inappropriate representative scenario. In Figure 7, the cluster with the most data points takes the form of a twisted curve. In fact, the centroid of this cluster lies outside its structure, meaning that the samples close to the centroid cannot be considered representative of the cluster. In contrast, using the soft-DTW metric, it was confirmed that the centroids of all clusters lie within their respective structures. However, in the case of the ED metric, it was found that for 7 out of 29 clusters, the centroid lies outside the cluster structure. Consequently, the ED metric demonstrates limitations when used for deriving representative scenarios in time series data analysis. As a result, the total number of clusters classified by DBSCAN, excluding noise, is 13. The PCT results representing each cluster are shown in Figure 8.

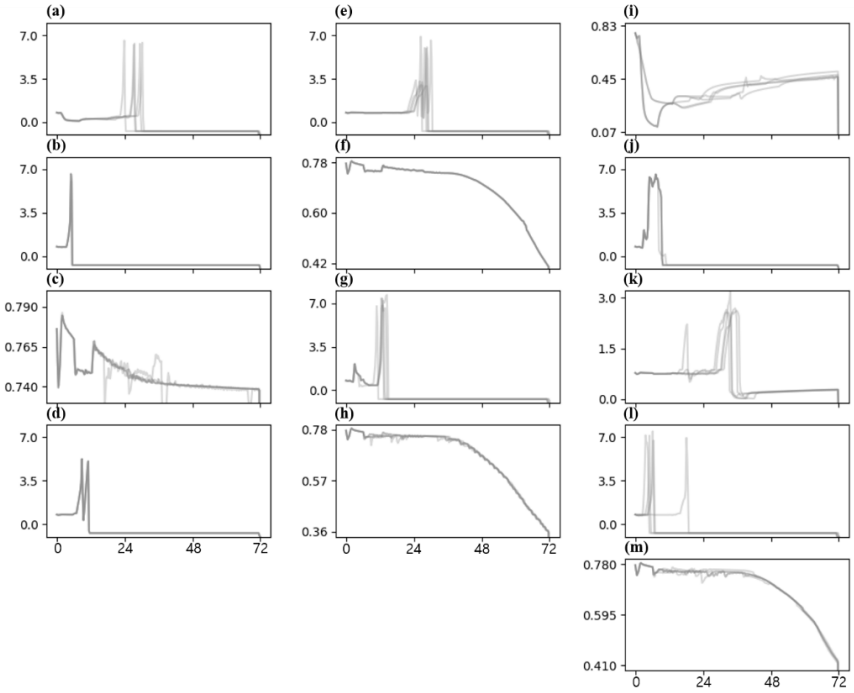

FIGURE 8. Extracted representative scenarios

However, as previously analyzed in the LOOP event tree, it was confirmed that there are total of 27 possible scenarios. Some scenarios, such as LOOP-1 and LOOP-SBO-1, involve the activation of AFW and the restoration of power after an IE, meaning they can be categorized as the same type of scenario. Therefore, the actual number of accident scenarios will be fewer than the 27 possible outcomes. By excluding identical accident scenarios in the event tree, the total number of fundamentally different accident scenarios is identified as 19. However, this number is still greater than the number of clusters derived in this study. There are two possible reasons for this.

First, the scenarios classified as noise in DBSCAN. Since the hyperparameters of DBSCAN (e.g., epsilon, minimum number of samples) and UMAP's parameters have not been fine-tuned, it is possible that the samples classified as noise could be reclassified into a few additional clusters. To achieve this, fine-tuning of DBSCAN and UMAP parameters may be required. The second reason could be due to missing data during the preprocessing step. In this study, clustering was performed after excluding approximately 1,100 data points from the MAAP simulation results with unusually short sequence lengths. Including those data points and performing follow-up research could yield more clusters.

IV. Discussion and Conclusion

This study derived representative accident scenarios from 6,400 randomly sampled LOOP scenarios. The number of scenarios used in this study was determined intuitively. However, since fewer clusters were found compared to the number of scenarios derived using conventional PSA methods, it is considered that the accuracy of clustering performance verification would improve if additional scenarios were supplemented to address the shortfall. Among the various IEs that can occur in nuclear power plants, LOOP is the most complex and has the largest number of possible scenarios, so more than 6,400 samples would be required for accurate verification. However, other IEs (e.g., large break LOCA, steam generator tube rupture) have relatively simple accident sequences, so it is considered that representative accident scenarios can be derived with fewer samples. In other words, the complexity of safety system is determined by the type of IE, and the appropriate number of samples is determined by the complexity of the safety system. The correlation between these two factors can be mathematically analyzed or empirically derived in the future works.

If accident scenarios can be analyzed based on time-series data in this manner, it becomes easier to numerically present the failure limits of safety functions. For example, the results in Figure 8 (m) show that the PCT curve does not exhibit any sharp peak but follows a downward-sloping curve. This indicates that CD did not occur during 72 hours. Therefore, we can analyze

the minimum power recovery time to avoid CD in case of IE. Likewise, safety equipment operation start time, and average operation time can be analyzed to avoid CD.

In this study, MAAP simulation results with excessively short sequence lengths were excluded from clustering target. The ratio shows that 1,100 out of 7,500 scenarios were excluded, representing approximately 14.67% of the total. In comparison, the proportion of missing scenarios among the 19 possible scenarios is approximately 31.57%, suggesting that some of the excluded 1,100 scenarios may correspond to the missing scenarios. The reason for excessively short sequence lengths in MAAP simulations could be due to computational instability, as the MAAP code simulates reactor accidents with the nature of high uncertainty. Alternatively, the input scenarios may represent impossible reactor conditions, causing the MAAP calculation to terminate prematurely. Finally, there is a possibility that these are very short scenarios that terminated normally. However, since the underlying cause of short sequence lengths in MAAP simulations has not yet been identified, future research that elucidates this issue could contribute to the validation of representative accident scenario studies.

Furthermore, scenarios generated based on the existing DPSA concept are theoretically infinite in variety, which has limitations in calculating total risk. However, if representative accident scenarios can be derived for each IE, the number of scenarios used in risk calculation becomes finite. Consequently, if this study is supplemented, it will become possible to calculate total risk targeting representative accident scenarios derived using DPSA. This is expected to contribute to realistic risk calculation by making fewer conservative assumptions compared to the conservatively calculated and highly evaluated risks in existing PSA.

ACKNOWLEDGMENTS

This research was supported by the National Research Council of Science & Technology (NST) grant by the Korea government (MSIT) (No. GTL24031-000).

REFERENCES

[1] Devooght, Jacques, and Carol Smidts. "Probabilistic dynamics as a tool for dynamic PSA." *Reliability Engineering & System Safety* 52.3 (1996): 185-196.
[2] Verma, Ajit Kumar, et al. "Dynamic PSA." *Reliability and safety engineering* (2016): 373-392.
[3] McInnes, Leland, John Healy, and James Melville. "Umap: Uniform manifold approximation and projection for dimension reduction." *arXiv preprint arXiv:1802.03426* (2018).
[4] Keogh, Eamonn, and Chotirat Ann Ratanamahatana. "Exact indexing of dynamic time warping." *Knowledge and information systems* 7 (2005): 358-386.
[5] KAERI, Probabilistic Safety Assessment for Ulchin Units 3&4 [Level 1 PSA for Internal Events : Main Report]

Research on the Automatic Generation Method of Dynamic Event Tree Scene Based on SBLOCA

Chongxiao Xie[1], Longcong Wang[2], Haoyin Chen[3], He Wang[4]

1 College of Nuclear Science and Technology, Harbin Engineering University, Heilongjiang, 150000, xcx1@hrbeu.edu.cn

2 College of Nuclear Science and Technology, Harbin Engineering University, Heilongjiang, 150000, longcongwang@hrbeu.edu.cn

3 College of Nuclear Science and Technology, Harbin Engineering University, Heilongjiang, 150000, chenhaoyin@yeah.net

4 College of Nuclear Science and Technology, Harbin Engineering University, Heilongjiang, 150000, wanghe@hrbeu.edu.cn

ABSTRACT

Dynamic Event Trees are used in the safety analysis of Nuclear Power Plants for the effective modeling of complex accident scenario evolutions. However, traditional Dynamic Event Trees analysis is challenged by the significant dependence on expert knowledge for branch node selection, leading to reduced modeling efficiency. This study introduces an automatic Dynamic Event Trees generation method for Nuclear Power Plants accident scenario modeling. The method utilizes system code input deck of the accident and integrates logical algorithms (logical algorithms written according to the writing rules of accident card) to automate the construction of accident Dynamic Event Trees models. The efficacy of this approach was demonstrated through the automatic generation of small break loss of coolant accident scenarios, using the Chinese double-loop pressurized water reactor as a case study. The results show that this method can automate the generation of accident scenarios and identify safety characteristics of accidents. This support for operational optimization and safety decision-making in Nuclear Power Plants.

Keywords: Dynamic event tree; Sma‖ break loss of coolant accident; Accident scenario modeling; Automatic generation metho; Nuclear safety assessment

Ⅰ. Introduction

The dynamic event tree (DET) method enhances the traditional event tree by considering time and comprehensively simulates the possible consequences of an accident through the coupling of system codes and random response model of nuclear power plants. At present, this field has attracted widespread attention and is being actively investigated[1-2]. The DET method has been successfully applied to analyze different types of nuclear accidents[3-4]. Amirsortani[5] analyzed the station blackout (SBO) accident and established a DET model using RAVEN coupling RELAP5. By considering the number of available safety systems, operator action time, and AC power recovery time, the core damage frequency (CDF) of SBO was obtained. Jang[6] analyzed the steam generator tube rupture (SGTR) accident and developed a DET generation program DPRA-SGTR using PASCAL language. CDF was estimated by analyzing operator behaviors and safety system failures. Sun [7] analyzed the small break loss of coolant accident (SBLOCA) using the DET method and found that the safety of the core cannot be guaranteed by relying only on the normal input of a column of medium pressure injection. Using the DET method to establish time-dependent branches for branch nodes such as the steam assisted feedwater system and AC power restoration, Chen [8] analyzed the SBO accident and found that an increase in the operating time of the steam assisted feedwater system can extend the time window for power restoration. Moreover, there exist an upper limit to the power restoration time. If the upper limit is exceeded, core damage is inevitable.

However, in most applications, the DETs are manually branched based on expert knowledge and judgment. This often leads to inconsistency in the selection of branch nodes among different DET analysts for the same accident scenario, this results in incomplete DET modeling and analysis. Therefore, an automatic DET generation method is proposed in this paper and demonstrates it using a case study of the SBLOCA analysis for the typical double loop pressurized water reactor in China (CNP300).

In this paper, Section 1 provides a brief literature review of DET method and identifies the current problems. Section 2 introduces the DET method and represent the automatic DET-based analysis method. In Section 3 the model CNP300 used for case study is introduced. Section 4 analyzes the model developed using the DET-based automatic analysis method to obtain the core damage probability and compared with the results calculated in Literature 7. Section 5 summarizes this paper and provides directions for future work.

II. DET-based automated analysis method

DET generates a series of event sequences containing time-dependent changes based on certain branching rules, and determines the evolution path of the system or component by determining the branching conditions. When the branching conditions are met, it will cause the system or component to evolve on different branching paths, thereby obtaining a set of event sequences to generate a DET branching model. DET branch types are divided into demand type failure branch and operation type failure branch. Demand type failure branch refers to the branch where the function of the system or component has not been successfully achieved, as shown in Root1 in Figure 1. The probability of successful action is p_1, and the probability of unsuccessful action is $1 - p_1$. Operational failure branch refers to the branch where a system or component is successfully deployed, but operational failure occurs, i.e. the system or component fails to complete its corresponding action within the specified task time period. The branch shown as Root2 in Figure 1, assuming that the operating time of the system or component satisfies the probability density function $F(x)$, the probability of operational failure occurring at t_1 is $F(t_1)$, the probability of operational failure occurring at t_2 is $F(t_2) - F(t_1)$, and so on. If no operational failure occurs, the probability is $1 - F(t_1)$.

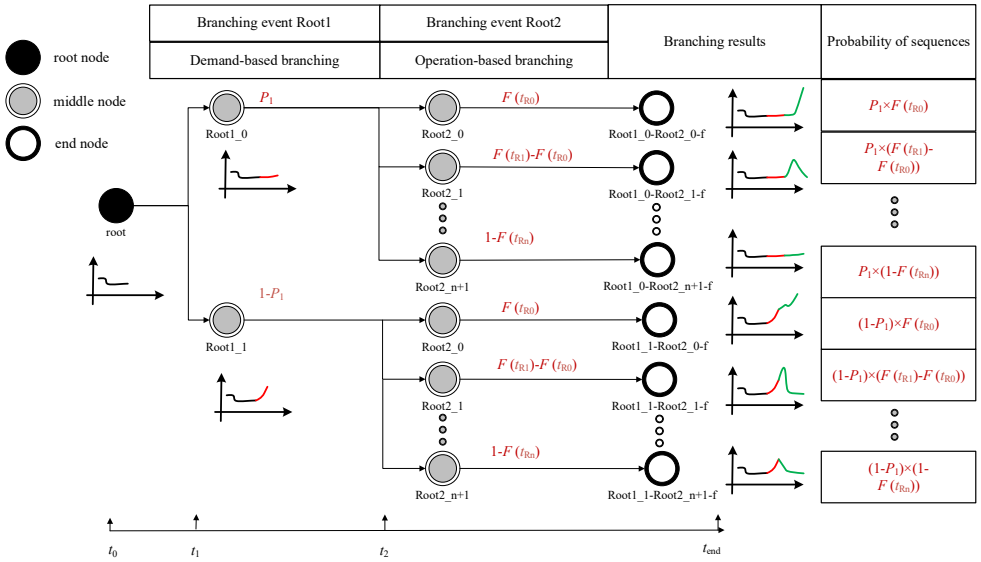

Figure 1. Schematic diagram of DET structure for state evolution of nuclear power plant [8]

When conducting DET analysis on nuclear power plant accidents, the accident card is important because it is an important carrier for accident simulation, and the writing of the accident card follows the rules on the thermal software manual. The content of the card includes time information, control signals, and systems or components. Since the control signals in the accident card directly provide action signals for the system or components, finding the control signals on the card is equivalent to finding the branch nodes in the DET. However, in the actual analysis process, due to the presence of some intermediate signals in the control signal, which do not directly affect the actions of the system or components, but assist in the transmission of control signals, it is necessary to isolate these intermediate signals and retain those that directly affect the system or components during modeling. Based on the above analysis, a method for automatic analysis based on DET is proposed, and the specific flowchart is shown in Figure 2:

1. Read all control signals: Extract all control signals from the corresponding accident card according to the rules in the thermal software manual used.

2.Classification of control signals into valid control signals and intermediate signals: Scan each line of the accident card, screen the read control signals one by one, and determine whether they are directly used by the system or components. If yes, it is determined to be a valid control signal and retained; No, it is judged as intermediate signal and isolated.

3.Create branching objects based on the type of part being controlled and its failure mode: Targeted modeling is conducted based on the identified different component types and their failure modes, as shown in Table 1.

4. Conduct DET analysis based on the modeling object.

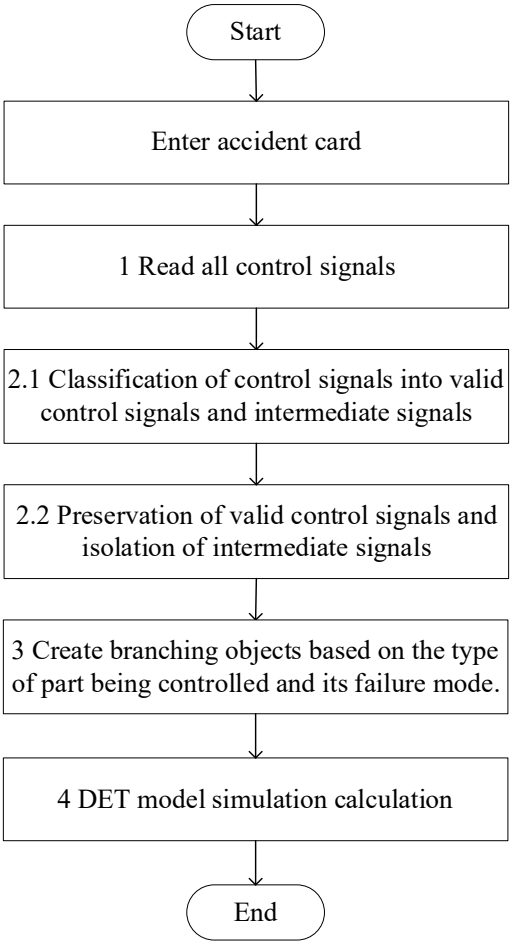

Figure 2. Flow chart of automatic analysis method

TABLE I. Modeling Object

Component Type	PFMEA	Demand Failure/Operational Failure
tmdpvol	No failure mode	simulate according to users' needs
tmdpjun	No failure mode	
valve	refuse to open/close	demand Failure
pump	start failure/operation failure	operational Failure
accum	refuse to open/close	demand Failure

As the DET module of advanced Coupling Platform for Advanced Risk Simulation (CARS) is used for DET analysis [9], the DET module principle of CARS software is shown in Figure 3. When the module monitors the action of the system or components, two branches will be generated, one is to maintain the original action, and the other is the opposite action. Therefore, based on the DET module of advanced CARS software and combined with the above methods, this paper develops an automatic analysis software.

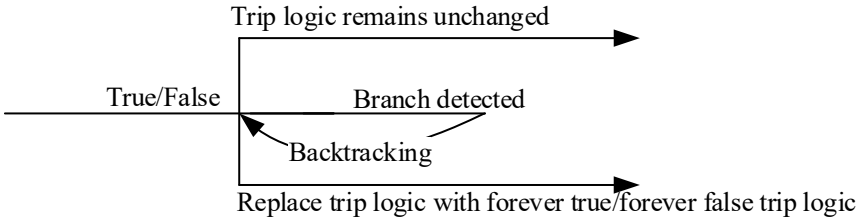

Figure 3. Schematic diagram of DET module of CARS software [9]

Ⅲ. Modeling of SBLOCA

In this paper, the double loop pressurized water reactor (CNP300) is selected as the modeling object, and the model node diagram is shown in Figure 4. The model is mainly divided into two parts: primary and secondary circuit. The main system equipment includes pressure vessel, reactor coolant pump, steam generator, pressurizer, safety injection system and other dedicated safety systems. The primary loop is mainly composed of two complete loops and reactor core. Each loop includes cold pipe section, hot pipe section, main coolant pump, SG primary side and other components and equipment. The break is set in the cold pipe section with an area of $43cm^2$.

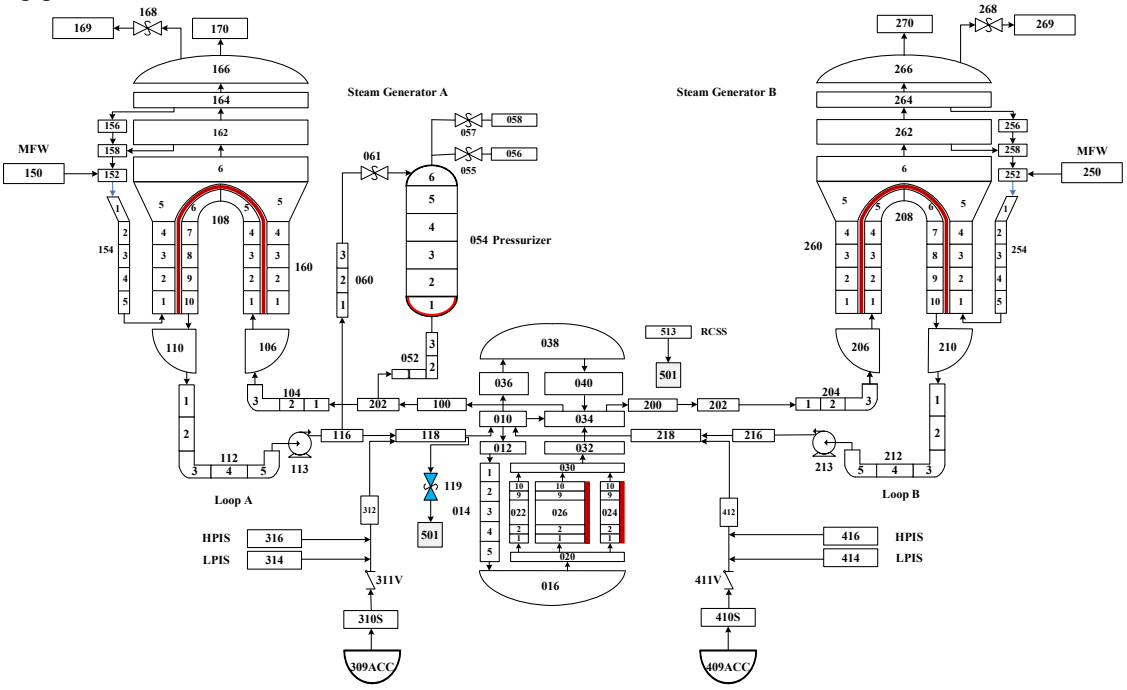

Figure 4. CNP300 model modulization

Ⅳ. Result analysis

Ⅳ.A DET sequence analysis

The SBLOCA established in Section 3 is analyzed using the DET-based automatic analysis method proposed in Section 2, and a total of 35 control signals are identified, 14 valid control signals are retained according to the rules and compared with the manual identification to conclude that there is no error in the identification. Then the model is built according to the component type and failure mode. The modeling object is shown in Table 2, and the modeling results are shown in Figure 5. The total core damage probability is calculated based on the modeling results and the equipment reliability data report of China nuclear power plant [8].

TABLE 2. Modeling Object of SBLOCA

System/Component	Component Type	Trip	Demand Failure/Operational Failure
Reactor Coolant Pump(RCP)	pump	501	operational failure
Main Steam Isolation Valve(MSIV)	valve	615	demand failure
Main Steam Relief Valve(MSRV)	valve	618	demand failure
Pressurizer Spray Valve(PSV)	valve	603	demand failure
Pressurizer Relief Valve(PRV)	valve	606	demand failure
Pressurizer Safety Relief Valve(PSRV)	valve	609	demand failure
First Column of High Pressure Injection System(HPIS)	tmdpjun	612	demand failure
Second Column of High Pressure Injection System(HPIS)	tmdpjun	614	demand failure
First Column of Medium Pressure Injection System(MPIS)	accum	403	demand failure

Second Column of Medium Pressure Injection System(MPIS)	accum	411	demand failure
First Column of Low Pressure Injection System(LPIS)	tmdpjun	402	demand failure
Second Column of Low Pressure Injection System(LPIS)	tmdpjun	410	demand failure
Containment Spray System(CSS)	tmdpjun	401	demand failure
Rupture Valve(RV)	valve	404	demand failure

(Note: The failure time of the reactor coolant pump during operation is 1 hour and 1.6 hours)

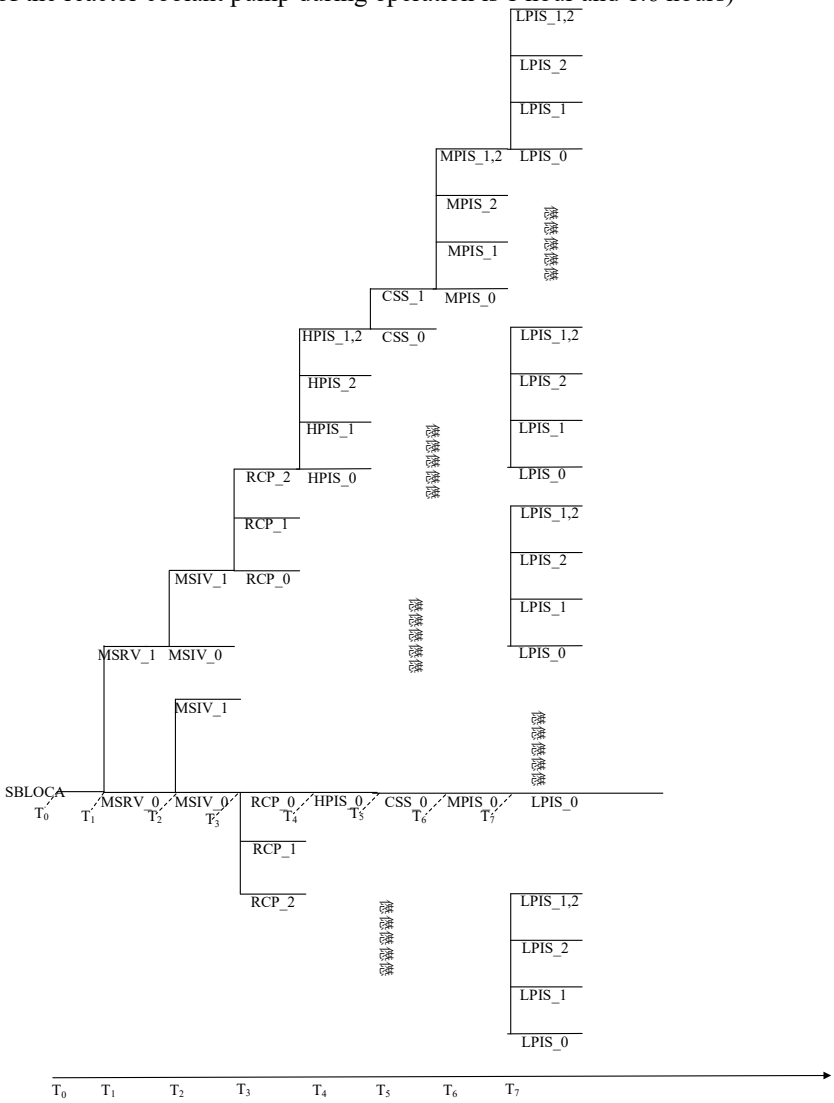

Figure 5 SBLOCA DET Model

In Figure 5, HPIS is explained as an example, HPIS_0 represents that two columns of high pressure injection system are available and can be put into operation normally, HPIS_1 represents that only the second column of high pressure injection system is available and can be put into operation normally, HPIS_2 represents that only the first column of high pressure injection system is available and can be put into operation normally, and HPIS_1,2 represents that columns of high pressure injection system are not available.

In this paper, Peak Cladding Temperature (PCT) is chosen as the key safety parameter. Therefore, comparing the maximum PCT during the accident process with the safety limit of 1477K can clearly reflect whether the core remains intact during the overall development of the accident.

The DET automatic analysis method was used to analyze SBLOCA, generating a total of 739 sequences. This paper used the coupled CARS software, and the branch calculation taken about 14 hours in total. Among them, 98 sequences failed to complete the whole process calculation due to insufficient transient stability of the model. For these 98 sequences, a two-step

approach is taken. The first step is to reasonably infer incomplete sequences based on the already calculated sequences. The second step is to treat all sequences that cannot be reasonably inferred based on the already calculated sequences as invalid sequences. The probabilities of each branch node are shown in Table 3 [10].

TABLE 3 Demand Type Branch Node Probability

Branch Node	main steam isolation valve has failed to close	main steam release valve has failed to open	safety shell spray system has failed to operate
Node Probability	7.51E-04	4.35E-05	2.126E-03
Branch Node	High pressure injection system failure	medium pressure injection system failure	low pressure injection system failure
Node Probability	2.585E-03	5.26E-08	2.635E-03

The cumulative probability density distribution function for the operating time of the operating type branch reactor coolant pump is

$$F(t) = 1 - e^{-\lambda t_n} \quad (1)$$

In the equation (1), λ is an exponential distribution constant, and the λ of the reactor coolant pump is $\lambda = 4.25E-6$[10].

Among the 641 fully calculated sequences, 45 sequences have a maximum PCT exceeding the safety limit; Among the 98 sequences that could not be fully calculated, 42 were deemed invalid, resulting in a total of 87 invalid sequences. Therefore, the core damage probability is $6.84E-18$. The sequence with the greatest impact on failure is shown in Table 4.

TABLE 4 Maximum Impact Sequence

Sequence	PCTMAX	Failure Probability
root-614_1-612_1-403_1-402_1-410_1	1869.5	2.43E-18
root-614_1-612_1-411_1-410_1-402_1	3317.3	2.43E-18

(Note: root-614_1-612_1-403_1-402_1-410_1 represents two columns of high pressure injection system failure, the first column of medium pressure injection system failure, and two columns of low pressure injection system failure; Root-614_1-612_1-411_1-410_1-402_1 represents two columns of high pressure injection system failure, second column of medium pressure injection system failure, and two columns of low pressure injection system failure)

According to the automatic DET analysis method, an SBLOCA study identified two sequences with the highest core damage probability. These two sequences differ only in the number of loops where the medium pressure injection system fails; consequently, their physical parameter evolution is identical. As they were identical, the first sequence was selected for analysis in this paper. Figures 6, 7, 8 and 9 give the graphs of key security parameters of this sequence over time.

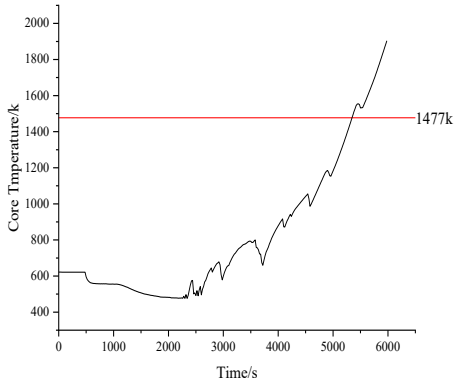

Figure 6 Core Temperature

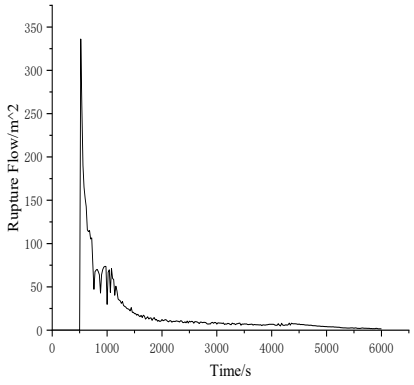

Figure 7 Rupture Flow

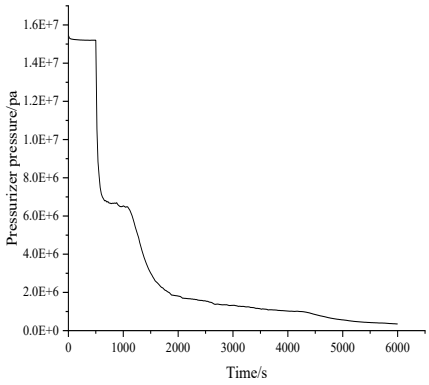

Figure 8 Pressurizer Pressure

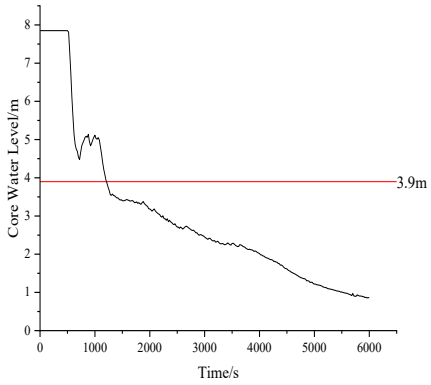

Figure 9 Core Water Level

When the small breach in the cold tube section appeared, as shown in Figures 7 and 8, the core coolant was continuously ejected from the breach into the containment, which resulted in a continuous drop in pressurizer pressure. As the coolant kept spraying out of the breach and there was no coolant replenishment to the core. As shown in Figure 9, the core level will continue to drop. When the pressurizer pressure is less than 4.9 MPa, there will be a column of medium pressure injection, but the coolant injected into the core is difficult to make the core submerged, so although the injection of medium pressure injection has a mitigating effect on the accident, it is difficult to maintain the decreasing level of the core, which leads to further exposure of the core, and then leads to the increasing temperature of the core, as shown in Figure 6. The result was that the core temperature exceeded the safety limit and the core melted down. In summary, the case of only one column of medium pressure annealing input will result in a prolonged core exposure during the accident process, with the PCT rising all the way up and eventually exceeding the safety limit.

Ⅳ.B Comparative analysis

As shown in Table 5, Literature 7[7] used DET to analyze SBLOCA, mainly studying the impact of different injection system inputs on accident mitigation. The calculation results generated a total of 64 branches, among which the maximum PCT of 3 branches exceeded the safety limit, namely, only the first column of medium pressure injection can be put into operation normally, only the second column of medium pressure injection can be put into operation normally, and all injection systems fail, all of which will cause core meltdown.

This paper uses the developed automatic analysis method based on DET to analyze SBLOCA. It not only studies the impact of different safety injection system inputs on accident mitigation, but also investigates the impact of other equipment failures on accident mitigation. The calculation results generated a total of 739 branches, of which 87 branches had a maximum PCT exceeding the safety limit, 3 failed branches were the same as those calculated in Literature 7 and the remaining 84 failure branches are composite failure scenarios not covered by traditional methods. For example, if the main steam relief valve fails to open and two columns of high pressure and medium pressure injections cannot be put into operation normally, it will cause the maximum PCT of the core to exceed the safety limit, resulting in core meltdown.

The above differences primarily stem from variations in the application of dynamic event trees in nuclear accident analysis. When using DET, users must manually specify branch nodes to construct the accident DET model. The authors of Literature 7 focused their research on the impact of different operational states of high-, medium-, and low-pressure injection systems on accident mitigation. Given this research direction, other equipment failure factors were not considered. In contrast, the accident scenario automatic generation method based on DET employed in this paper uses the accident system code input file as a basis and leverages integrated logical algorithms to comprehensively identify all simulable equipment in the input file, thereby achieving the automatic construction of the accident DET model. As a result, this paper can not only study the role of different operational conditions of high-, medium-, and low-pressure injection systems in accident mitigation but also fully consider the impact of failures in other equipment, Deeply analyze possible accident scenarios with low probability of occurrence but serious consequences, leading to differences between the two methods.

Table 5 Comparison of Literature 7

Method	Literature 7	automated analysis method based on DET
Number of simulated devices	6	14

Types of simulation equipment	2	4
Number of Branches	64	739
Number of Failure Sequences	3	84

Ⅴ. Conclusion

This work developed an automatic DET analysis method and applied it to SBLOCA of CNP300. The proposed method can automatically generate accident scenarios and reduce the requirement of expert knowledge. In addition, it can provide a more comprehensive analysis of the dynamic responses of NPPs during accidents.

In the case of SBLOCA with a rupture area of $43cm^2$ in the cold pipe section, if the failure of the main steam relief valve opening is combined with the failure of the two high-pressure injections and the failure of the medium pressure injections, it is not sufficient to ensure the safety of the reactor core only by the normal operation of the two low pressure injections; therefore, it is necessary to pay attention to the situation that only the two low pressure injections can be put into operation normally after the occurrence of the SBLOCA.

There are still some deficiencies in this paper. For example, in the discrete method of running failure branches, this paper chooses 1 hour and task time to discrete. In fact, for the running failure branch, its discrete time is at any time of the task time, so this problem will be studied later.

REFERENCES

[1] Glingler T, Alfonsi A, Mandelli D, et al. Dynamic event tree analysis of a severe accident sequence in a boiling water reactor experiencing a cyberattack scenario[J]. Annals of Nuclear Energy, 2023, 192: 109994.

[2] Alfonsi A, Rabiti C, Mandelli D, et al. Dynamic Event Tree analysis through RAVEN[R]. Idaho National Lab.(INL), Idaho Falls, ID (United States), 2013.

[3] Yan C, Chaojun L, Pan Z, et al. Research on Safety Margin Analysis Method Based on Discrete Dynamic Event Tree for Risk Guidance [J]. Atomic Energy Science and Technology, 2022, 56 (09): 1944-1951

[4] Dan L. Risk analysis of small break loss of coolant accident based on dynamic event tree [D]. Harbin Engineering University, 2017

[5] Amirsoltani, M.E., Pirouzmand, A, Nematollahi, M.R. Development of a dynamic event tree (DET) to analyze SBO accident in VVER-1000/V446 nuclear reactor[J]. Annals of Nuclear Energy, 2022, 165: 108786.

[6] Chao Chun-Chang, Chin-Jang Chang. Development of a dynamic event tree for a pressurized water reactor steam generator tube rupture event [J]. Nuclear technology, 2000, 130(1): 27-38.

[7] Dabin S. Optimization Study on Probability Safety Margin Analysis Method for Pressurized Water Reactor Nuclear Power Plants [D]. Harbin Engineering University, 2023

[8] Haoyin C, He W, Qiang Z, et al. Analysis of station black out accident in nuclear power plants based on dynamic event trees [J]. Nuclear Power Engineering, 2024, 45 (05): 192-198

[9] Liangjun W. Development of a Prototype Software for Coupling Determinism and Probability Theory Based on RELAP5 [D]. Harbin Engineering University, 2021

[10] National Nuclear Safety Administration. Reliability Data Report on Equipment of Chinese Nuclear Power Plants [R]. Beijing: National Nuclear Safety Administration. 2022

ASRAM2025
www.asram2025.org
Asian Symposium on Risk Assessment and Management 2025
Pattaya, Thailand, 27 – 29 August 2025

APPLICATION OF TIME-DEPENDENT DYNAMIC ACCIDENT SEQUENCE GENERATION METHOD TO MACST EQUIPMENT USING OPTIMIZED SIMULATIONS

Wooseok Jo, Junyong Bae, Seung Jun Lee*

[1] *Ulsan National Institute of Science and Technology: UNIST-gil 50, Ulsan, Republic of Korea, 44919, and*
cws5528@unist.ac.kr
Corresponding author: sjlee420@unist.ac.kr

EXTENDED ABSTRACT

Probabilistic Safety Assessment (PSA) is a critical methodology for evaluating nuclear power plant (NPP) safety by modeling accident sequences and estimated associated risks. Traditional event tree (ET)-based PSA methods employ binary success/failure criteria to model accident scenarios, but they struggle to account for the time-dependent progression of dynamic variables, system interactions, and operator actions [1]. Although dynamic event tree (DET) methods have been introduced to overcome these limitations by allowing accident sequences to develop based on time-dependent system and operator responses, DET-based analyses often result in a massive number of branches, making it difficult to interpret accident sequences and requiring significant computational resources.

To address these challenges, a time-dependent accident sequence generation method was proposed with optimized simulations to reduce the high computational cost and accident sequence generation method to automatically generate dynamic accident sequences to facilitate the analysis for dynamic scenarios. The proposed method employs a limit surface searching algorithm coupled with a thermal-hydraulic system code to optimize a massive number of simulations for dynamic PSA [2]. This algorithm efficiently identifies the boundary (i.e., limit surface, LS) between success and failure scenarios through intensive simulations of scenarios proximate to the LS with iterative process.

However, comprehending the LS with more than three-dimensional space can be intricate. Therefore, the predicted scenarios with LS from above algorithm should be converted into more understandable form such as DET or other comprehensible forms. To settle this issue, automatic accident sequence generation method is applied [3]. In this method, the alpha shape method is adopted to analyze the optimized simulation data. The automatic generation algorithm analyzes success scenario data from optimized simulations and identifies the branching points that froms multiple boxes containing only success scenarios. Before applying alpha shape to success scenario data, conservative data preprocessing was applied, whereby if scenarios with better performance were estimated as failures while scenarios with poorer performance were estimated as successes, such cases were conservatively processed as failures. These boxes are optimally determined the number of the branching points specified by the user, and the regions partitioned by determined boxes can be converted into DETs. But, DETs have limitations to represent the time-dependent accident sequences since there are some mismatched dynamic scenarios over event headings in DETs, and the mismatched scenarios may be included in one region to construct the DET. So, the other comprehensible forms are needed to visualize the time-dependent accident scenarios.

For this, this study proposes a new method to generate the time-dependent accident sequences using branching points determined above automatic generation algorithm. The branching point means specific scenario when each simulation variable occur over time. So, dynamic scenario domains are splitted based on each value relevant to factors in branching points, and the branching points are subdivided. Then, subdivided branching points are depicted based on the each value relevant to simulation variables in time series.

To demonstrate the applicability of the the proposed method, the case study was conducted to a station blackout scenraio involving the multi-barrier accident coping strategy (MACST) equipment. The possible dynamic scenarios are predefined with generating a total of 14,400 scenarios through three dynamic variables; Running time for alternate AC−diesel generator (AAC-DG), delay time for atomspheric dump valve (ADV) open and potable low−pressure pump (PLPP) deployment. From the optimized simulations, a LS can be identified only 1,096 simulations among 14,400 scenarios. From the LS, the 4,087 and 10,313 scenarios are predicted as success and failure scenarios, respectively. Then, automatic generation algorithm

analyzed 13 branching points, which covers about 80.188% out of a total success scenarios. To visualize the time-dependent accident sequences using these points, 3 branching points were selected: (17, 24, 6), (11, 18, 5), and (16, 11, 12), corresponding to the (AAC-DG running time, Delay time for ADV open, Delay time for PLPP deployment). There points were optimally determined by considering all possible combinations of three out of a total of 13 branching points and identifying the combination that yielded the highest coverage. The resulting coverage corresponds to 59.46% of the total success scenarios. Among these variables, the PLPP variable is dependent for AAC-DG variable, whereas the ADV variable is independent for other variables. These points are further subdivded based on the specific values of the associated simulation variables.

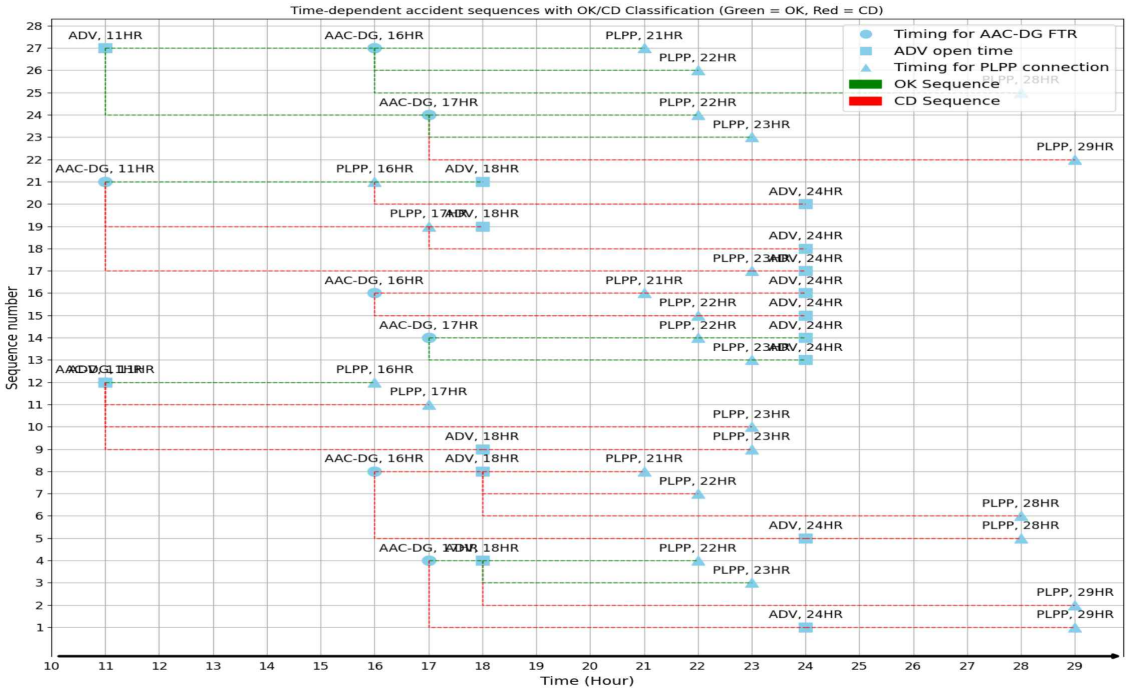

FIGURE 1. Time-Dependent Accident Sequences for AAC-DG Running Time, ADV Open Time, PLPP Deployment Time

Fig. 1 shows the visualized results of the time-dependent accident sequences for subdivided branching points with AAC-DG running time, ADV open time, PLPP deployment time. The circle, rectangle, and triangle shapes represent AAC-DG running time, ADV open time, and PLPP delay time, respectively. The green and red lines indicate success and failure (i.e., core damage in this case study), respectively. From this result, three event ordering sequences can be identified. From 1 to 12 sequences, the events are ordered as AAC-DG running time, ADV open time, PLPP delay time while, from 13 to 21 sequences, the events are ordered as AAD-DG running time, PLPP delay time, ADV open time. In addition, from 22 to 27 sequences, the events are ordered as ADV open time, AAC-DG running time, PLPP delay time. In case of first event order, it can be known that the success criterias for delay time of PLPP deployment are in 16 hours when AAC-DG running time and ADV open time are 11 hours from sequence 12 or in 23 hours when AAC-DG running time is 17 hours and ADV open time is 18 hours from sequence 4.

We believe this novel method can serve to analyze the time-dependent scenarios for dynamic PSA. Further study will be conducted to validate the proposed method for more realistic accident scenarios

ACKNOWLEDGMENTS

This work was supported by National Research Foundation of Korea(NRF) grant funded by the Korea government(MSIT) (No. RS-2022-00144328) and Korea Institute of Energy Technology Evaluation and Planning(KETEP) grant funded by the Korea government(MOTIE)(RS-2024-00403194, Next-Generation Nuclear Technology Creation IP-R&D Talent (Human Resources) Development Project)

REFERENCES

[1] S. HOGENBOOM, T. PARHIZKAR, JE VINNEM, "Temporal decision-making factors in risk analyses of dy namic positioning operations," *Reliability Engineering & System Safety,* **207**. 107347 (2021).
[2] J. BAE, J.W. PARK, and S.J. LEE, "Limit surface/states searching algorithm with a deep neural network and Monte Carlo dropout for nuclear power plant safety assessment," *Applied Soft Computing*, **124**, 109007 (2022).
[3] W.S. JO, et al, "Optimized Simulation-Driven Automatic Generation of Dynamic Accident Sequences for LOCA Scenarios," *Transactions of the Korean Nuclear Society Autumn Meeting*, Changwon, Korea, October 24-25 (2024).

ASRAM2025
www.asram2025.org
Asian Symposium on Risk Assessment and Management 2025
Pattaya, Thailand, 27 – 29 August 2025

Effect of Including Motor-Driven Auxiliary Feed Water Pump and Operators' Load-Shedding Action Time in SBO's CCDP Calculation

Younghak Lee[1], Man Cheol Kim[2]

[1] *Department of Energy Systems Engineering, Chung-Ang University: 84 Heukseokro, Dongjak-gu, Seoul, Korea, 06974, bill0501@cau.ac.kr*
[2] *Department of Energy Systems Engineering, Chung-Ang University: 84 Heukseokro, Dongjak-gu, Seoul, Korea, 06974, charleskim@cau.ac.kr*

ABSTRACT

Station blackout (SBO) is one of the most significant initiating events that can lead to core damage in a nuclear power plant. Therefore, accurately assessing the risk of SBO is a critical task. Since the outcome of an SBO scenario is highly affected by the time required for the recovery of off-site power, it is essential to precisely evaluate the available time margin for power recovery. In previous studies, the convolution approach was introduced to improve the accuracy of conditional core damage probability (CCDP) by addressing the excessive conservatism inherent in the conventional event tree/fault tree (ET/FT) approach. This paper enhances the consistency of the computational methodology used in prior convolution-based analyses and further improves accuracy by incorporating a motor-driven auxiliary feedwater pump (MDAFWP) that is powered by the Alternative AC diesel generator (AAC DG). In addition, the battery depletion time, previously assumed to be constant without considering operator action, is modeled as a function of the operators' load-shedding action time. The revised convolution model is validated through Monte Carlo simulations. Furthermore, the results obtained from the revised convolution model are compared with those from the previous convolution model, and key differences are discussed.

Keywords: Station Black Out, Convolution, Load-Shedding, Motor Driven Auxiliary Feed Water Pump

I. INTRODUCTION

Station blackout (SBO), a representative initiating event in nuclear power plants, refers to the loss of all alternating current (AC) power following a loss of offsite power (LOOP) and the subsequent failure of emergency diesel generators (EDGs). In such scenarios, critical safety systems responsible for decay heat removal lose their AC power supply, making the availability of the auxiliary feedwater pumps (AFWPs) a crucial safety issue. Under SBO conditions, an alternative AC diesel generator (AAC DG) is expected to power the motor-driven auxiliary feed water pump (MDAFWP) to maintain core cooling. If the AAC DG fails, a turbine-driven auxiliary feed water pump (TDAFWP), temporarily operable via Class-1E DC batteries, can be still used. Thus, both MDAFWP and TDAFWP perform secondary-side cooling roles, and the operable time of TDAFWP is determined by the depletion time of the DC battery in the absence of AC power. SBO has been recognized as one of the most significant contributors to core damage in many probabilistic safety assessment (PSA) reports.

Conventionally, event tree/fault tree (ET/FT)-based analysis methods have been widely used for assessing SBO risk. Convolution-based methods have been proposed to overcome the limitations of these approaches in addressing time-dependent phenomena. In the previous study [1], the convolution approach integrates the non-recovery probability of AC power with the failure timing distributions of AAC DG and TDAFWP to calculate the conditional core damage probability (CCDP) of each accident sequence. However, previous convolution models did not explicitly consider the contribution of the MDAFWP powered by the AAC DG, nor did they incorporate the dependency of battery depletion time on operators' load-shedding action time.

To reflect the time-dependent characteristics, this study proposes an extended convolution-based CCDP evaluation model that includes two key improvements. First, the model explicitly incorporates the MDAFWP powered by the AAC DG. Second, the TDAFWP's battery depletion time is modeled as a function of operators' load-shedding action time rather than being treated as a fixed parameter, allowing for a more realistic representation of time-dependent behavior. The updated convolution formulation integrates the failure probability density functions of AAC DG, MDAFWP, and TDAFWP, along with the non-

recovery probability of AC power, and introduces a logical condition that activates MDAFWP operation only when the AAC DG has successfully started.

The validity of the proposed model is verified through the Monte-Carlo simulation, and the results are quantitatively compared with those from a previous convolution model.

This study enables a more realistic assessment of SBO risk by incorporating operator actions and system configurations, potentially reducing the conservatism inherent in traditional PSA models. The results can serve as a basis for improving plant design and developing more effective accident management strategies.

II. COMPARISON OF SBO SEQUENCES IN THE PREVIOUS AND UPDATED CONVOLUTION APPROACH

In the previous convolution model, the failure modes of the AAC DG and the TDAFWP were divided into fail-to-start (FTS) and fail-to-run (FTR), allowing for more detailed modeling than the conventional ET/FT approach, where these modes were combined into a single branch.

In this study, the convolution model is updated by incorporating the MDAFWP, adding new sequences. The modification of battery depletion time from a constant to a variable did not require the introduction of new sequences. Figure 1 presents the updated convolution approach.

In the updated model, the FTS and FTR of the MDAFWP are considered under the following conditions: “When the AAC DG experiences an FTS, the MDAFWP cannot receive power, and therefore, its failure modes (FTS and FTR) are not modeled. Similarly, if the AAC DG fails to run after being successfully started, the MDAFWP also loses power, and its FTR is not modeled.” As such, no branch is created for the MDAFWP failure in sequences where the AAC DG fails to start.

III. MATHEMATICAL FORMULA FOR SEQUENCE PROBABILITY

In this study, we consider SBO scenarios in which EDGs fail to start following a loss of offsite power (LOOP). Before presenting the mathematical formulas, we define the parameters and subscripts used throughout the equations. Sequence probabilities are denoted by P, component failure probabilities by p, and failure rates by λ. The probability density function and cumulative distribution function are represented as $f(t)$ and $F(t)$ respectively, while the reliability function is represented as $R(t)$. The subscripts $A, O,$ and T refer to the AAC DG, MDAFWP, and TDAFWP, respectively. The subscripts S and R indicate FTS and FTR. Additionally, the subscripts op and bd denote the operators’ load-shedding action time and battery depletion time.

For example, the subscript AS refers to the FTS of the AAC DG and the probability $P_{AS,BD}$ denotes the sequence probability in which the FTS of AAC DG and the TDAFWP operates successfully until the battery depletion time, at which point it fails. p_{OS} and $f_{TR}(t)$ denote the FTS probability of the MDAFWP and the FTR probability density function of the TDAFWP. $T_{bd}(t_{op})$ represents the battery depletion time as a function of the operators’ load-shedding action time, and $f_{op}(t_{op})$ is the probability distribution of the operators’ load-shedding action time.

The operators’ load-shedding action time is assumed to follow a lognormal distribution, based on empirical evaluations in human reliability analysis (HRA). The non-recovery time of offsite power is also assumed to follow a lognormal distribution, based on NUREG/CR-6890 and its update report[2,3].

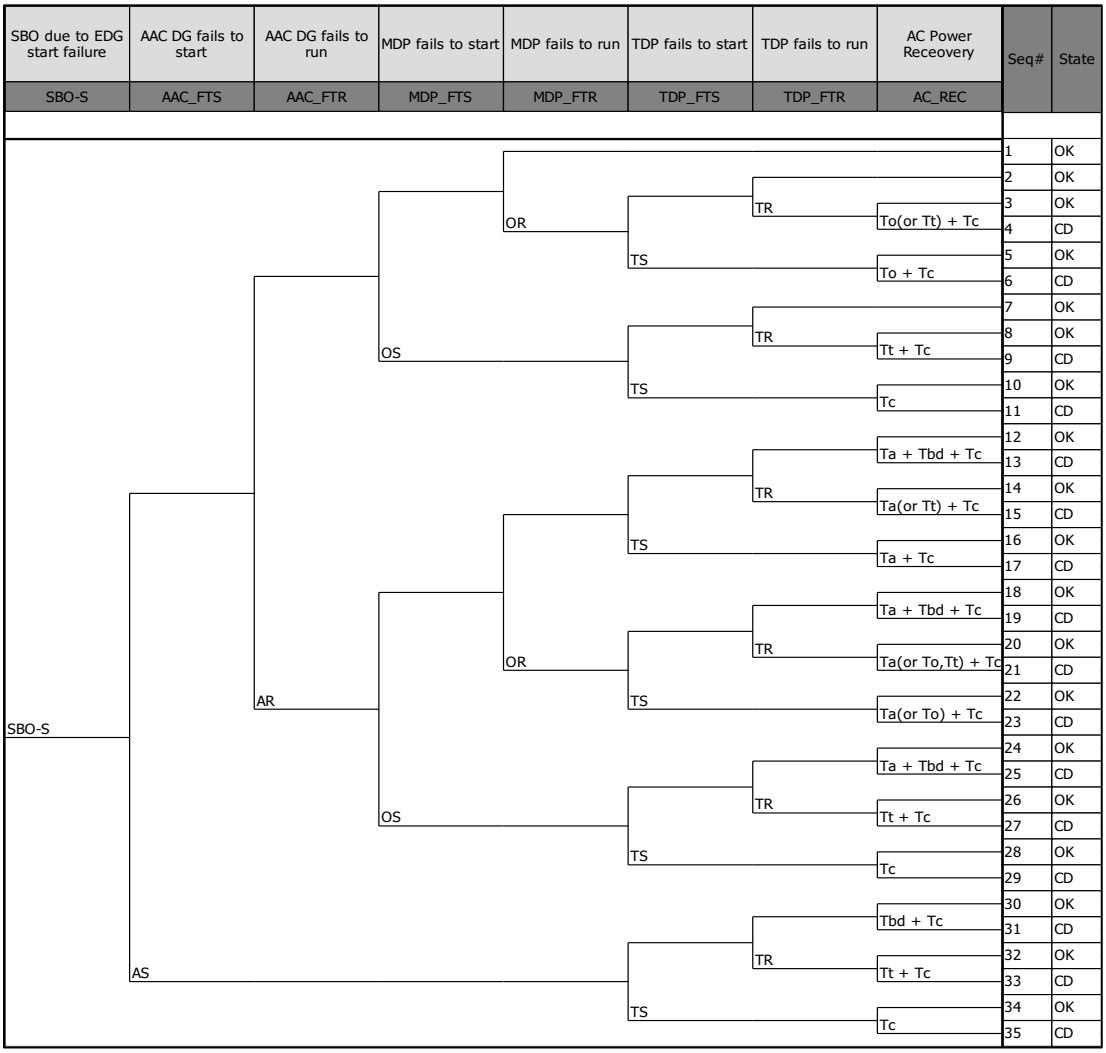

FIGURE 1. Updated Convolution Approach

Using interpolation, the battery depletion time, expressed as a function of the operators' load-shedding action time, is assumed by the following equation:

$$T_{bd}(t_{op}) = \begin{cases} 12 - 8t_{op} & (t_{op} \le 1)\ [\text{h}] \\ 4 & (t_{op} > 1)\ [\text{h}] \end{cases} \tag{6}$$

For comparing with previous convolution model, minimum of $T_{bd}(t_{op})$ was set to 4 hours, since the previous model assumed a fixed battery depletion time of 4 hours without considering the operators' load-shedding action time.

III.A. Updated Convolution Approach

In this section, mathematical formulas are presented for calculating the sequence probabilities based on the updated convolution approach, which incorporates the MDAFWP and the variable battery depletion time. As shown in Figure 3, a total of 16 equations are developed. One representative equation, corresponding to sequence 4, is presented as an example. This formula corresponds to a sequence in which the AAC DG successfully operates and the TDAFWP fails to run, but core damage occurs due to the failure of the MDAFWP. This sequence had not been considered as leading to core damage in the previous

convolution model but is newly identified as a core damage sequence in the updated model by incorporating MDAFWP failure. The example illustrates how previously non-consequential sequences can newly contribute to the core damage probability when additional failure modes and system dependencies are considered. The example formula is given as:

$$P_{OR,TR} = (1 - p_{AS})R_{AR}(T_m)(1 - p_{OS})(1 - p_{TS})$$
$$[\int_0^{T_m}\int_{t_O}^{T_m} f_{TR}(t_T)f(t_O)p_{NRAC}(t_T + T_c)dt_T dt_O + \int_0^{T_m}\int_{t_T}^{T_m} f_{OR}(t_O)\, f_{TR}(t_T)\, p_{NRAC}(t_O + T_c)dt_O dt_T] \quad (7)$$

IV. VALIDATION AND RESULTS

In this section, the formulas for sequence probabilities are validated through Monte Carlo simulation, and the results are compared with those from a previous study. Monte Carlo simulations were performed with 10^9 trials for each sequence. This trial count ensures each dominant sequence ($P \geq 10^{-6}$) is sampled thousands of times, yielding ≤1 % uncertainty per sequence. The numerical data used for the calculations and the simulations are presented in Table I. Failure probability, failure rate, and μ_2, σ_2 are taken from NUREG/CR-6928, NUREG/CR-6890, and their updated reports[4,5].

Lognormal distribution parameters, μ_1 and σ_1, for the operators' load-shedding action time are assumed values. The time to core damage T_c-when the failure of secondary side heat removal using the AAC DG, MDAFWP and TDAFWP- and the mission time T_m are assumed to be typical values. The calculation results and Monte Carlo simulation results can be found in Table II. In Table III, the CCDP values obtained from the previous convolution model, the updated convolution model, and the Monte Carlo simulation are presented.

Table I. Numerical data for calculation

Symbol	Description	Numerical data
p_{AS}	The probability of the AAC DG fail-to-start	2.94E-2
p_{OS}	The probability of the MDAFWP fail-to-start	5.88E-4
p_{TS}	The probability of the TDAFWP fail-to-start	5.32E-3
λ_{AR}	The failure rate of the AAC DG	1.13E-3 [h^{-1}]
λ_{OR}	The failure rate of the MDAFWP	8.12E-6 [h^{-1}]
λ_{TR}	The failure rate of the TDAFWP	6.35E-3 [h^{-1}]
μ_1	Mean of the natural logarithm of the operators' load-shedding action time	-0.77
μ_2	Mean of the natural logarithm of the AC power recovery time distribution	0.44
σ_1	Standard deviation of the natural logarithm of the operators' load-shedding action time	0.37
σ_2	Standard deviation of the natural logarithm of the AC power recovery time distribution	1.66
T_c	The time to core damage after the failure of secondary-side heat removal using the AAC DG, MDAFWP, and TDAFWP	1 [h]
T_m	The mission time	24 [h]

Table II. Sequence probability of calculations and Monte Carlo simulation

Sequence number	Sequence probability	Updated convolution	Monte Carlo simulation	Relative error (%)
4	$P_{OR,TR}$	2.34E-06	2.37E-06	1.27
6	$P_{OR,TS}$	1.43E-07	1.57E-07	8.92
9	$P_{OS,TR}$	1.18E-05	1.19E-05	0.84
11	$P_{OS,TS}$	1.79E-06	1.75E-06	2.29
13	$P_{AR,BD}$	1.29E-03	1.29E-03	0.00
15	$P_{AR,TR}$	2.79E-04	2.79E-04	0.00
17	$P_{AR,TS}$	2.03E-05	2.04E-05	0.49
19	$P_{AR,OR,BD}$	6.71E-08	7.00E-08	4.14
21	$P_{AR,OR,TR}$	3.56E-08	3.00E-08	18.67
23	$P_{AR,OR,TS}$	2.74E-09	3.00E-09	8.67
25	$P_{AR,OS,BD}$	7.61E-07	7.05E-07	7.94

27	$P_{AR,OS,TR}$	1.61E-07	3.07E-07	47.56
29	$P_{AR,OS,TS}$	4.91E-08	4.00E-08	22.75
31	$P_{AS,BD}$	4.10E-03	4.10E-03	0.00
33	$P_{AS,TR}$	4.02E-04	4.02E-04	0.00
35	$P_{AS,TS}$	9.46E-05	9.42E-05	0.42
	CCDP	6.21E-03	6.20E-03	0.16

Table III. CCDP of previous convolution, updated convolution

	Previous convolution	Updated convolution	$\Delta CCDP$ (%)
CCDP	9.54E-03	6.21E-03	34.9

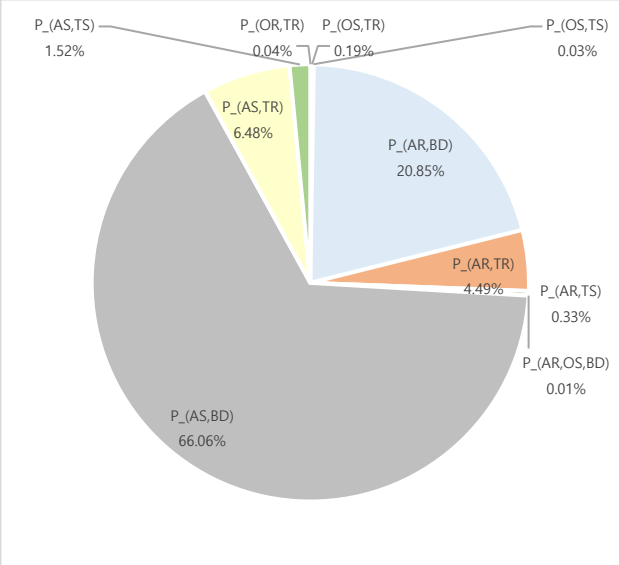

Figure 2. Contribution of top 10 sequences to CCDP (updated convolution model)

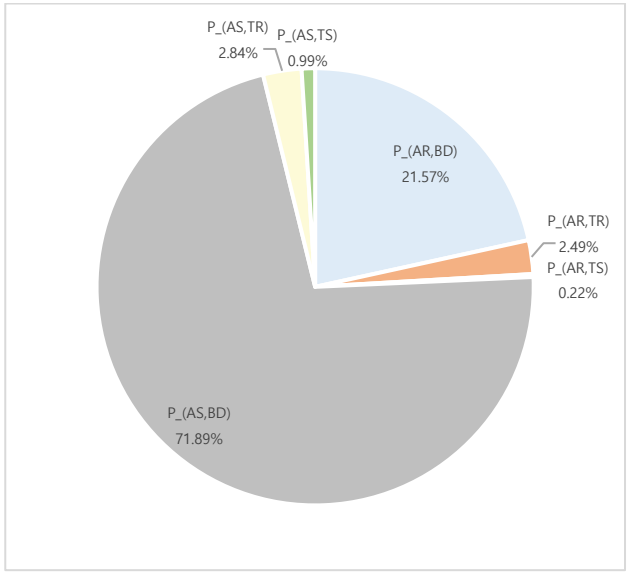

Figure 3. Contribution of each sequence to CCDP (previous convolution model)

To assess the validity of the proposed convolution formula, the results were compared with those obtained from Monte Carlo simulation. The calculated results (6.21E-03) and the simulation results (6.20E-03) show a relative difference of approximately 0.16%. Based on this comparison, the proposed formulas can be considered valid for evaluating CCDP under the given modeling conditions.

As shown in Table 3, the updated convolution model resulted in a 34.9% reduction in CCDP compared to the previous convolution model. Figure 4 illustrates the p_{NRAC}. When the battery depletion time is modeled as a function of operator action time, the updated model incorporates lower values of p_{NRAC}, up to approximately 66% smaller than those in the previous model. The sequences that contributed most significantly to the reduction in CCDP were $P_{AS,BD}$ and $P_{AR,BD}$, which decreased by 2.76E-03 and 7.7E-04, respectively. In relative terms, these correspond to reductions of 40.2% and 37.4%.

Incorporating the failure of the MDAFWP makes the evaluation more conservative, whereas reflecting battery depletion time as a function of operators' load-shedding action time reduces the conservatism of the previous model. The significant decrease in CCDP suggests that the impact of modeling battery depletion time based on the operators' load-shedding action time is greater than the impact of considering MDAFWP failure. As shown in Table 1, the failure probabilities of the MDAFWP are approximately 2% and 11% of those of the AAC DG and TDAFWP, respectively, and the failure rates are approximately 0.7% and 0.1%, respectively. This supports the conclusion that the inclusion of MDAFWP failure (FTS & FTR) has a limited impact on the overall CCDP.

A closer examination reveals two contributing factors. First, in the updated model, sequences that include the failure of all components, including TDAFWP battery depletion, have extremely low probabilities and therefore negligible contributions to the CCDP. This is evident in sequences 13, 15, and 17 compared to sequences 19 through 29, as shown in Table II. Second, sequences such as 4, 6, 9, and 11 reflect scenarios where core damage occurs despite AAC DG success, due to subsequent MDAFWP failure. However, the combined contribution of these additional sequences to the CCDP is only about 0.26%.

By incorporating the variable battery depletion time, the probability contribution profile of the CCDP across sequences was slightly altered. In sequences involving TDAFWP BD, T_{bd} used in $p_{NRAC}(t)$ in the previous model was replaced by $T_{bd}(t_{op})$, which has a minimum value equal to $T_{bd} = 4$ hours. As a result, the sequence probabilities decreased. Conversely, in sequences involving TDAFWP FTR, the extended battery depletion time allows the TDAFWP to operate for a longer time, thereby increasing the chance of failure within that extended period, leading to higher probabilities for those sequences.

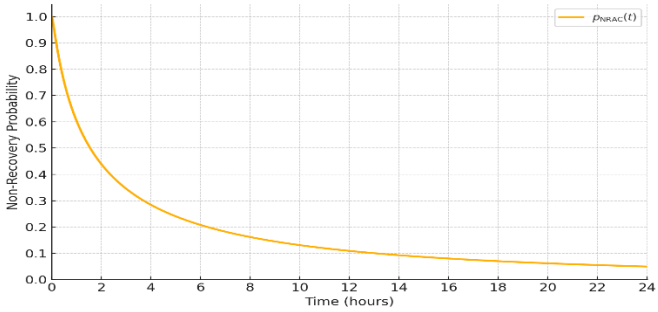

Figure 4. Probability of non-recovery of AC power (p_{NRAC})

V. CONCLUSION

This study proposes an updated convolution model for evaluating the CCDP under SBO by incorporating two key elements that were not explicitly considered in previous models: the MDAFWP and the operators' load-shedding action time. The updated model logically enables MDAFWP operation only when the AAC DG successfully starts and models the battery depletion time as a function of the operators' load-shedding action time rather than assuming a constant value.

The updated convolution formulas were validated through Monte Carlo simulations and the results showed good agreement, with a relative error of 0.16%. The CCDP calculated by the updated model was 6.21E-03, representing a 34.9% reduction compared to the previous model. In addition to the CCDP reduction, the sequence probability profile was also affected. $P_{AS,BD}, P_{AR,BD}$ which had been dominant in the previous model became less significant due to changes in the battery depletion time modeling, while $P_{AS,TR}, P_{AR,TR}$ which previously constituted the second most contributing group, gained more importance. This is because of the longer availability of the TDAFWP, resulting from time-dependent battery modeling, and thus becoming more dominant in the updated profile. Despite this change, the overall ranking of dominant sequences concerning contribution remained consistent.

This study showed that while the modeling of MDAFWP failure had a limited effect on CCDP, the introduction of a variable battery depletion time significantly reduced conservatism in the previous model. The proposed approach enables a more realistic and less conservative evaluation of SBO risk. Therefore, it may contribute to better-informed decisions in plant design and accident management planning.

ACKNOWLEDGMENTS

This work was supported by the Korea Institute of Energy Technology Evaluation and Planning (KETEP) grant funded by the Ministry of Trade, Industry and Energy (MOTIE) of Republic of Korea [grant number RS-2024-00398867].

REFERENCES

[1] M.C. Kim, "Comparison of Event Tree/Fault Tree and Convolution Approaches in Calculating Station Blackout Risk in a Nuclear Power Plant," *Nuclear Engineering and Technology,* **56**, 141-146, 2024.
[2] S. A. Eide, et al., Industry-average performance for components and initiating events at U.S. commercial nuclear power plants, NUREG/CR-6928, U.S. NRC, 2007
[3] Z. Ma, et al., Industry-average performance for components and initiating events at U.S. commercial nuclear power plants: 2020 update, INL/EXT-21-65055, Idaho National Laboratory, 2021.
[4] S. A. Eide, et al., Analysis of loss-of-offsite-power events: 1986–2004, NUREG/CR-6890, U.S. NRC, 2005.
[5] Johnson, N. & Ma, Z., Analysis of loss-of-offsite-power events: 2020 update, INL/EXT-21-64151, Idaho National Laboratory, 2021.

Technical Session 3 (13:40 - 15:40)	The Port 3, C Floor	Accident Modelling and Uncertainty Analysis
		Chair/Facilitator 1: Prof. Yu YU (North China Electric Power University) Chair/Facilitator 2: Dr. Adolphus
		Lye (Singapore Nuclear Research and Safety Institute, National University of Singapore)
13:40 - 14:00		ID 11: Robust Probabilistic Risk Assessment with Fault-Trees via an Entropy-based Affine-invariant Stochastic Model updating Framework with Probability Bounds Analysis FRAMEWORK WITH PROBABILITY BOUNDS ANALYSIS Speaker: Adolphus Lye (Singapore Nuclear Research and Safety Institute, National University of Singapore) Contributors: Adolphus Lye (Singapore Nuclear Research and Safety Institute, National University of Singapore), Wasin Vechgama (Thailand Institute of Nuclear Technology), Scott Ferson (Institute for Risk and Uncertainty, Department of Civil and Environmental Engineering, University of Liverpool), Sicong Xiao (Singapore Nuclear Research and Safety Institute, National University of Singapore)
14:00 - 14:20		ID 18: Study on Best Estimate of Fuel Rod Fracture during LOCA including Uncertainty in Stress-Strength Model Speaker: Hiroki Tanaka (Department of Nuclear Engineering and Management, Graduate School of Engineering, the University of Tokyo) Contributors: Hiroki Tanaka (Department of Nuclear Engineering and Management, Graduate School of Engineering, the University of Tokyo), Takafumi Narukawa (Department of Nuclear Engineering and Management, Graduate School of Engineering, the University of Tokyo), Takashi Takata (Department of Nuclear Engineering and Management, Graduate School of Engineering, the University of Tokyo)
14:20 - 14:40		ID 27: Research on Sensitivity Analysis and Evaluation of cosCONT Software Speaker: Yichun Wang (North China Electric Power University) Contributors: Yichun Wang (North China Electric Power University), Jiulong Yang (North China Electric Power University), Yu Yu (North China Electric Power University)
14:40 - 15:00		ID 70: Effect of Model Uncertainty on the System Physical Process Failure Probability Speaker: Yu YU (North China Electric Power University) Contributors: Yu YU (North China Electric Power University), Guanyu LIU (North China Electric Power University), Cheng YANG (North China Electric Power University)
15:00 - 15:20		ID 100: The Performance and Safety Analysis of Passive Safety Features in APR1000 Speaker: Jiyong Oh (Korea Hydro and Nuclear Power) Contributors: Jiyong Oh (Korea Hydro and Nuclear Power), Yongsoo Kim (Korea Hydro and Nuclear Power), Wookcheol Seol (Korea Hydro and Nuclear Power)
15:20 - 15:40		ID 99: Analysis of Operational Effects of External Water Injection During Extended Loss of Ac Power under Hazard Conditions Speaker: Wookcheol Seol (Korea Hydro and Nuclear Power) Contributors: Wookcheol Seol (Korea Hydro and Nuclear Power), Yongsoo Kim (Korea Hydro and Nuclear Power), Jiyong Oh (Korea Hydro and Nuclear Power)

ASRAM2025
www.asram2025.org
Asian Symposium on Risk Assessment and Management 2025
Pattaya, Thailand, 27 – 29 August 2025

ROBUST PROBABILISTIC RISK ASSESSMENT WITH FAULT-TREES VIA AN ENTROPY-BASED AFFINE-INVARIANT STOCHASTIC MODEL UPDATING FRAMEWORK WITH PROBABILITY BOUNDS ANALYSIS

Adolphus Lye[1], Wasin Vechgama[2], Scott Ferson[3], Sicong Xiao[4]

[1] *Singapore Nuclear Research and Safety Institute, National University of Singapore: 16 Prince George's Park, #05-01 SNRSI Building, Singapore 118415, Singapore, Singapore. Email: snrltsa@nus.edu.sg*
[2] *Thailand Institute of Nuclear Technology: 9/9 Village no.7 Saimoon Sub-district, Ongkarak District, Nakhon Nayok Province 26120, Bangkok, Thailand. Email: wasin@tint.or.th*
[3] *Institute for Risk and Uncertainty, Department of Civil and Environmental Engineering, University of Liverpool, Chadwick Building, Liverpool L697ZF, Liverpool, United Kingdom. Email: ferson@liverpool.ac.uk*
[4] *Singapore Nuclear Research and Safety Institute, National University of Singapore: 16 Prince George's Park, #05-01 SNRSI Building, Singapore 118415, Singapore, Singapore. Email: snrxs@nus.edu.sg*

ABSTRACT

Fault-tree analysis is a widely adopted method for performing probabilistic risk assessment within the nuclear industry. However, its effectiveness is often constrained by the availability and quality of reliability data, especially concerning basic events. This limitation introduces significant uncertainty in the probability distributions used to model failure events. Furthermore, the assumption of independence among fault-tree events can result in an underestimation of the overall system risk. The paper proposes a two-step probabilistic framework aimed at improving fault-tree analysis under such uncertainties. The first step applies an entropy-based affine-invariant stochastic model updating scheme to construct probability-boxes over limited data. The second step propagates these probability-boxes through the fault-tree logic using probability bounds analysis, which explicitly incorporates dependency uncertainties. The result provides a more robust and conservative estimate of the top-event failure probability, enhancing the probabilistic risk assessment towards nuclear safety.

Keywords: Fault-tree, Probability-box, Bayesian model updating, Probability bounds analysis, Uncertainty analysis

I. INTRODUCTION

In recent years, nuclear energy has become an increasingly promising option on a global scale considering climate change and the need for de-carbonisation. Such an option, however, comes with significant risks as seen from the past severe nuclear accidents such as the Three Mile Island accident in 1979, the Chernobyl accident in 1986, and the Fukushima-Daiichi accident in 2011 [1]. This brings about the importance of nuclear safety, and therefore the need for probabilistic risk assessment. A standard tool for probabilistic risk assessment is fault-tree analysis. However, its effectiveness is often limited by two practical issues: 1) the polymorphic uncertainty associated with the limited availability of reliability data to characterise the failure probability distribution associated with a given basic event; and 2) the epistemic uncertainty over the dependency between the basic and the intermediate events of the fault-tree.

Hence, the research objectives and contributions of the paper are two-fold: 1) the proposal of a two-step approach towards performing a fault-tree analysis under limited data and uncertain event dependencies, which involves the entropy-based affine-invariant stochastic model updating framework along with probability bounds analysis. Such approach is yet to be presented within the existing literature; and 2) to implement and validate the proposed approach on a fault-tree model of a "reversed flow of the water inlet system" accident within the Thai Research Reactor-1/Modification 1 (TRR-1/M1) research reactor [2].

To realize the research objectives, the paper is structured as follows: Section II presents an overview of the proposed methodology. This includes a review of the Bayesian model updating theory, and the Boolean algebra under the independence assumption and uncertain dependencies between multiple events; Section III presents the application case study which

introduces the TRR-1/M1 research reactor, the problem set-up, and the results and discussions; and Section IV provides a summary of the key findings and concludes the paper.

II. PROPOSED METHODLOGY

II.A. Stochastic Model Updating

II.A.1. Approximate Bayesian Computation

Bayesian model updating is a stochastic approach towards model updating to which the mathematical formalism follows:

$$P(\boldsymbol{\theta}|\boldsymbol{D},M) = \frac{P(\boldsymbol{\theta}|M)\cdot P(\boldsymbol{D}|\boldsymbol{\theta},M)}{P(\boldsymbol{D}|M)} \tag{1}$$

where $P(\boldsymbol{\theta}|M)$ is the prior distribution characterising the prior knowledge on the inferred parameter(s) $\boldsymbol{\theta}$ before collecting data $\boldsymbol{D}$, $P(\boldsymbol{D}|\boldsymbol{\theta},M)$ is the likelihood function reflecting the degree of agreement between the observed data $\boldsymbol{D}$ and the model prediction from M given $\boldsymbol{\theta}$, and $P(\boldsymbol{D}|M)$ is the evidence which ensures that the posterior integrates to one. Details on the terms in Eq. (1) are found in [3] and [4]. As $P(\boldsymbol{D}|M)$ is a numerical constant, it can be neglected, and the posterior is re-expressed as:

$$P(\boldsymbol{\theta}|\boldsymbol{D},M) \propto P(\boldsymbol{\theta}|M)\cdot P(\boldsymbol{D}|\boldsymbol{\theta},M) \tag{2}$$

An important aspect in Bayesian model updating is the definition of the likelihood function $P(\boldsymbol{D}|\boldsymbol{\theta},M)$, which at times may not be possible. In such case, the Approximate Bayesian Computation (ABC) approach is implemented as it provides a likelihood-free approach. For the work, the approximate Gaussian likelihood function is implemented [5]:

$$P(\boldsymbol{D}|\boldsymbol{\theta},M) = \exp\left[-\frac{d^2}{\varepsilon^2}\right] \tag{3}$$

where d is the distance function, while ε is the width-factor acting as the pre-defined parameter controlling the centralisation degree of the posterior. It is proposed in [5] that the width-factor should lie within the interval of $[10^{-3}, 10^{-1}]$. For the work presented in the paper, the Jensen-Shannon divergence d_{JS} is implemented as the distance function which is defined as:

$$d_{\mathrm{JS}}(p_1,p_2) = \frac{1}{2}\cdot\left(d_{\mathrm{KL}}(p_1\,||\,T) + d_{\mathrm{KL}}(p_2\,||\,T)\right), \quad \text{for T} = \frac{1}{2}\cdot(p_1+p_2) \tag{4}$$

where:

$$d_{\mathrm{KL}}(p_1||p_2) = \sum_{x_d=1}^{N_{\mathrm{bin}}}\ldots\sum_{x_1=1}^{N_{\mathrm{bin}}} p_1\left(b_{x_1,\ldots,x_d}\right)\cdot\log\left[\frac{p_1\left(b_{x_1,\ldots,x_d}\right)}{p_2\left(b_{x_1,\ldots,x_d}\right)}\right] \tag{5}$$

for which N_{bin} denotes the total bin number used to approximate the distributions p_1 and p_2, and log is the natural logarithm (to the base e).
In the context of ABC, the interest would be to compute $d_{\mathrm{JS}}(p_M, p_{\boldsymbol{D}})$ where p_M is the distribution of the model prediction while $p_{\boldsymbol{D}}$ is the distribution of the observed data. Such distance function was first implemented for ABC in [7], and recently in [8] and [9].

An important aspect of the Jenson-Shannon divergence is the computation of the parameter N_{bin}. An approach to do so would be via the adaptive-binning algorithm, details on which the readers may refer to [10].

II.A.2. Transitional Ensemble Markov Chain Monte Carlo

An approach to sample from the posterior defined by Eq. (2) would be the Transitional Ensemble Markov Chain Monte Carlo (TEMCMC) method [11]. It is a variant of the Transitional Markov Chain Monte Carlo sampling technique proposed in

[12] which allows for the generation of samples from complex-shaped posteriors (e.g., very peaked or having multiple peaks) in an iterative manner. This is done using a series of intermediate functions known as transitional distributions P^j defined as:

$$P^j \propto P(\theta|M) \cdot P(D|\theta, M)^{\beta_j} \tag{11}$$

where $j \geq 0$ is the sampling iteration number, β_j is the tempering parameter such that $0 = \beta_0 < \beta_1 < \cdots < \beta_{m-1} < \beta_m = 1$, and m is the final iteration number. Readers may refer to [11] for further details on the algorithm and implementation of the TEMCMC sampler.

II.B. Probability Bounds Analysis With Uncertain Boolean Logic

For the research work, only the Boolean "AND" and "OR" logical operations of the fault-tree are of interest and, hence, discussed in the section. Consider n distinct events of the fault-tree denoted as x_i with an associated probability $P(x_i) = p_i$, for $i = 1, \dots, n$. In the interest of the research undertaken here, the probabilities p_i are characterised by a probability-box (p-box) [13] to express its associated polymorphic uncertainty such that: $p_i \sim [p_i^L, p_i^R]$, where p_i^L and p_i^R are the left and right-bounding distributional envelope of the p-box respectively.

Under the independence assumption, the resulting associated probability of the event defined by the Boolean "AND" logical operation between the events x_i follows [14]:

$$P(\wedge_{i=1}^n x_i) = \prod_{i=1}^n p_i = \left[\prod_{i=1}^n p_i^L, \prod_{i=1}^n p_i^R\right] \tag{12}$$

while the resulting associated probability of the event by the Boolean "OR" logical operation between the events x_i follows [14]:

$$P(\vee_{i=1}^n x_i) = 1 - \prod_{i=1}^n (1 - p_i) = \left[1 - \prod_{i=1}^n \left(1 - p_i^L\right), 1 - \prod_{i=1}^n (1 - p_i^R)\right] \tag{13}$$

In general, the individual events x_i may not be independent from one another. Instead, some form of dependency may exist between them. To provide for a relatively conservative yet robust risk analysis, the element of event dependency can be treated as an epistemic entity. Under the uncertain dependency between the n input p-boxes $P_i(x) \sim [P_i^L(x), P_i^R(x)]$ for $i = 1, \dots, n$, the output imprecise distribution is defined as:

$$P(x) = [P^L(x), P^R(x)] \tag{14}$$

Such that in the case of the Boolean "AND" logical operation between the events x_i, the bounds are [15]:

$$P^L(x) = \sup_{x = \wedge_{i=1}^n z_i} \left[\max\left(0, \sum_{i=1}^n P_i^L(z_i) - (n-1)\right)\right] \tag{15a}$$

$$P^R(x) = \inf_{x = \wedge_{i=1}^n z_i} \left[\sum_{i=1}^n P_i^R(z_i) - \max\left(0, \sum_{i=1}^n P_i^R(z_i) - (n-1)\right)\right] \tag{15b}$$

whereas in the case of the Boolean "OR" logical operation between the events x_i, the bounds follow [15]:

$$P^L(x) = \sup_{x = \vee_{i=1}^n z_i} \left[\sum_{i=1}^n P_i^L(z_i) - \min\left(1, \sum_{i=1}^n P_i^L(z_i)\right)\right] \tag{16a}$$

$$P^R(x) = \inf_{x = \vee_{i=1}^n z_i} \left[\min\left(1, \sum_{i=1}^n P_i^R(z_i)\right)\right] \tag{16b}$$

It is to be highlighted that the proposed conservative risk analysis under uncertain event dependencies is currently applicable when there are no repeated variables (i.e., repeated basic events of a fault-tree). Such challenge is discussed in [14] and remains an open research question.

The proposed methodology is outlined as follows: The entropy-based affine-invariant stochastic model updating framework is implemented to probabilistically update a given distribution model over an Empirical Cumulative Distribution

Function (ECDF) of p_i based on the limited experimental data. This yields a p-box over p_i to account for the epistemic uncertainty over the distribution shape parameters. This is done for each root event. From there, the resulting p-boxes across all the root events are propagated through the Boolean logic, while accounting for the uncertain event dependencies, to yield the output p-box for the Top event. In summary, a flow-chart is presented in Fig. 1.

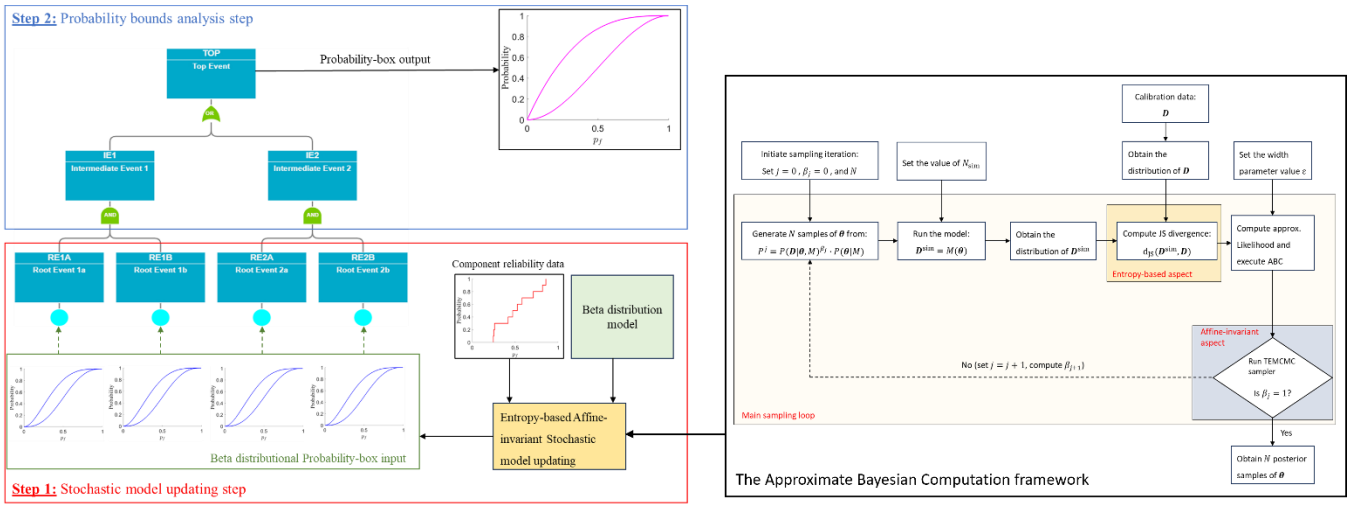

FIGURE 1. Flow-chart Of The Proposed Methodology

III. CASE STUDY - THAI RESEARCH REACTOR-1/MODIFICATION 1

The case study is based on the TRR-1/M1, which is a Training, Research, Isotopes, General Atomics nuclear research reactor located within Thailand, and is operated by the Thailand Institute of Nuclear Technology [2]. Since reaching criticality on 7-NOV-1977, the TRR-1/M1 nuclear research reactor operates at a normal operating power of 1MW with a maximum licensed power at 1.3 MW [2]. During normal operations, the research reactor generates radioisotopes for industrial, medical, and agricultural purposes. On top of that, these radioisotopes have also been used to conduct various beam experiments, neutron radiography, and the prompt-gamma neutron activation analysis. The schematic diagram of the research reactor is provided in Fig. 2.

III.A. Problem Set-up

The Top event of interest for the fault-tree analysis is the "reversed flow of the water within the inlet system", for which the imprecise probability distribution is to be obtained via the proposed methodology. The corresponding fault-tree is illustrated in Fig. 3, and details on the respective intermediate and basic events are presented in Table 1. The failure probability data for the associated basic events of the fault-tree is obtained from Vechgama et al. (2021) [2], and presented in Table 2.

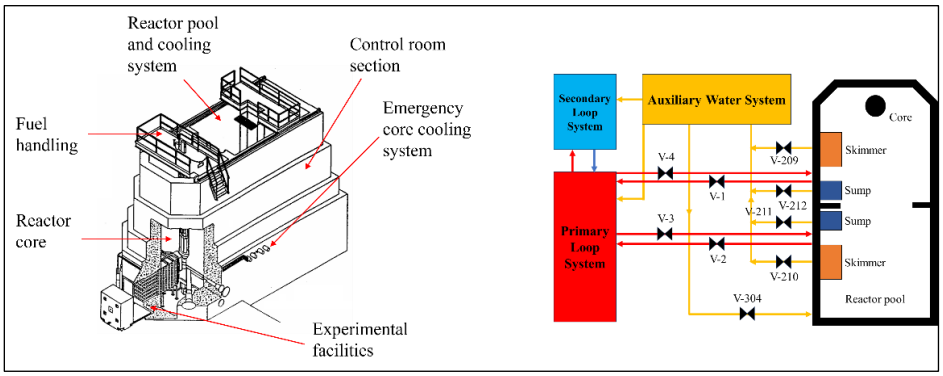

FIGURE 2. Schematic Diagram Of The TRR-1/M1 Research Reactor Adopted From Vechgama et al. (2021) [2].

In the case of the basic events 1, 3, 5, and 6, the distribution on the failure probability p_f refers to the stochastic variability (i.e., aleatory uncertainty) of the component's reliability [14]. To simulate the case where there is limited component reliability data due to the limited reliability/life tests, the work shall consider $N_{\text{obs}} = 20$ observations on the p_f for the aforementioned basic events. The resulting ECDF on the p_f for the corresponding basic events are presented in Fig. 5.

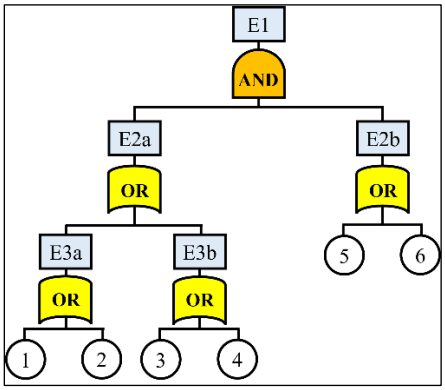

FIGURE 3. Fault-tree Diagram For The Top Event – Reversed Flow Of The Water Inlet System

TABLE 1. Details On The Respective Events Of The Fault-Tree Presented In Fig. 3

Intermediate events		Basic events	
Symbol	**Description**	**Symbol**	**Description**
E1	Reversed flow of the water within the inlet system.	1	Valve V-3 failed to open.
E2a	Inlet valve failed to open.	2	Operator failed to open valve V-3.
E2b	Inlet pipe breaks.	3	Valve V-4 failed to open.
E3a	Valve V-3 failed.	4	Operator failed to open valve V-4.
E3b	Valve V-4 failed.	5	Inlet pipe of V-3 breaks.
		6	Inlet pipe of V-4 breaks.

To calibrate a probability distribution over the component reliability data ECDF for basic events 1, 3, 5, and 6, a Beta distribution is chosen due to such distribution having defined bounds between 0 and 1, and having sufficient degrees of freedom in characterising different distributional shapes. Next, the entropy-based affine-invariant stochastic model updating framework is implemented to update the Beta distribution over the respective ECDF where the inferred parameters are as follows: $\boldsymbol{\theta} = \{\alpha_i, \beta_i\}$, for $i = 1, 3, 5, 6$. For each inferred parameter, the prior is defined by a Uniform distribution with the corresponding bounds defined in Table 3. The likelihood is defined by Eq. (3) with the corresponding width parameter ε defined in Table 3. The choice of ε is to ensure that the TEMCMC sampler samples from the posterior over 7 sampling iterations to achieve convergence over the posterior sample distribution.

TABLE 2. Failure Probability Data For The Associated Basic Events Of The Fault-tree Presented In Fig. 3

Symbol	Description	Distribution	Shape parameters
1	Valve V-3 failed to open.	Beta	$\alpha_1 = 1.5,\ \beta_1 = 43.00$
2	Operator failed to open valve V-3.	Fixed value	3.45×10^{-5} per reactor year
3	Valve V-4 failed to open.	Beta	$\alpha_3 = 1.5,\ \beta_3 = 43.00$
4	Operator failed to open valve V-4.	Fixed value	3.45×10^{-5} per reactor year
5	Inlet pipe of V-3 breaks.	Beta	$\alpha_5 = 1.5,\ \beta_5 = 62.40$
6	Inlet pipe of V-4 breaks.	Beta	$\alpha_6 = 1.5,\ \beta_6 = 62.40$

TABLE 3. Parametric Settings Implemented For The Stochastic Model Updating Step

Basic event	1	3	5	6
Prior bounds α	$[0.01, 100]$	$[0.01, 100]$	$[0.01, 100]$	$[0.01, 100]$
Prior bounds β	$[0.01, 100]$	$[0.01, 100]$	$[0.01, 100]$	$[0.01, 100]$

Width parameter, ε	0.015	0.015	0.015	0.010

III.B. Results And Discussions

The resulting posterior distribution for the respective inferred parameter is illustrated in Fig. 4, which is also interpreted as a fuzzy set [17]. From each fuzzy set, the resulting updated epistemic bound over the inferred parameter is obtained at an alpha-cut level of 0.8 to ensure a non-conservative coverage which encloses the true value. The resulting updated epistemic bound for the respective inferred parameter is presented in Table 4.

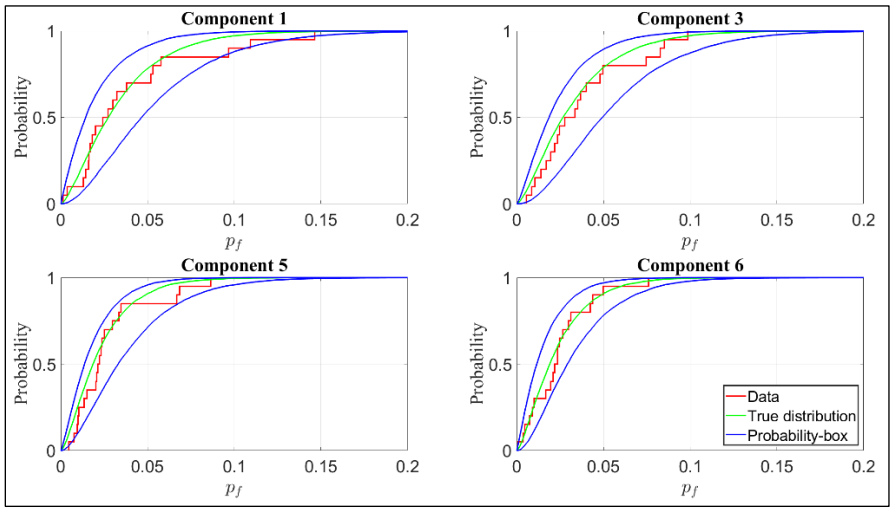

FIGURE 4. Resulting Beta Distribution P-box Over The ECDF Of The Component Reliability Data

TABLE 4. Results From The Stochastic Model Updating Step

Basic event	1	3	5	6
Updated bounds α	$[0.992, 1.950]$	$[1.326, 2.228]$	$[1.283, 1.843]$	$[1.129, 1.960]$
Updated bounds β	$[32.764, 49.039]$	$[36.713, 54.261]$	$[43.715, 72.931]$	$[54.029, 72.905]$

Based on the results in Table 4, a p-box is constructed over the failure probability p_f for the basic events 1, 3, 5, and 6. This is done via a Double-loop Monte Carlo approach where the outer loop generates $N_e = 1000$ samples from the epistemic bounds, while the inner loop generates $N_a = 10000$ samples from the resulting Beta distribution given the input realization from the outer loop. The creates a family of Beta distributions from which the distributional bounds are obtained and presented in Fig. 5. From there, the resulting p-box is propagated through the fault-tree in Fig. 3 under: 1) the independence assumption between the events (i.e., see Eq. (12) to (13)); and 2) under uncertain event dependency (i.e., see Eq. (15a) to (16b)). The results are illustrated in Fig. 6 which shows that under the independence assumption between events, the risk estimates of the Top event could be significantly underestimated, whereas that under the uncertain event dependency provides a conservative imprecise risk estimates but one that accounts for the worst-case scenario and the true risk of the Top event. Both resulting p-boxes enclose the true distribution (in black) as seen in Fig. 6 which verifies the applicability of the proposed methodology. The latter is obtained by propagating the true probability distribution and probability values (i.e., presented in Table 2) through the fault-tree under the independence assumption.

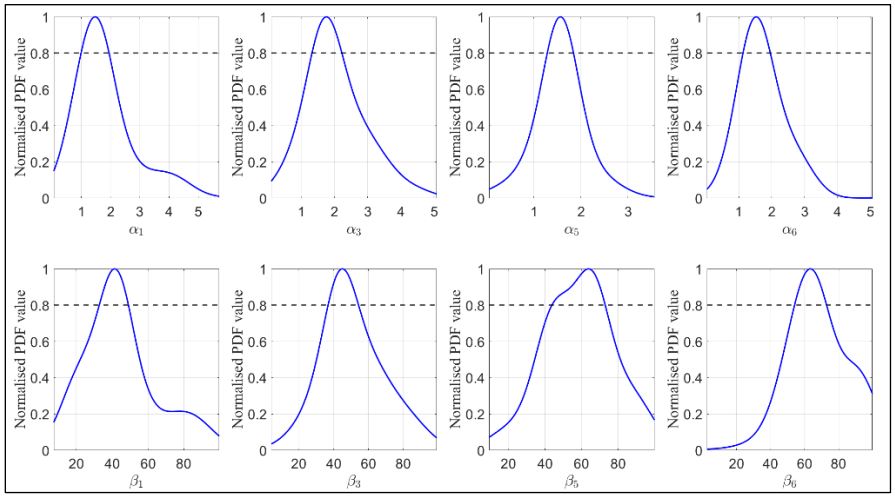

FIGURE 5. Resulting Posterior Distributions Over The Inferred Parameters

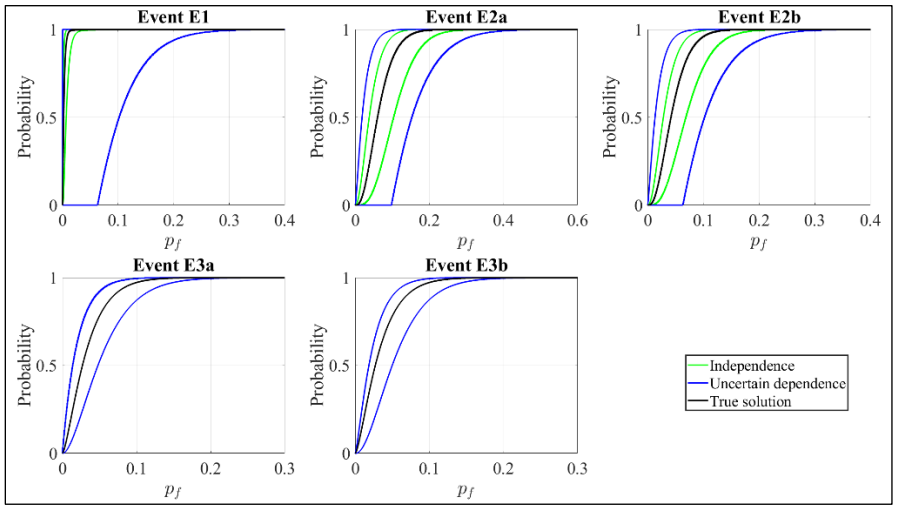

FIGURE 6. Resulting P-box Over The Top Event Under The Different Event Dependency Assumptions

IV. CONCLUSIONS

The paper proposed a two-step approach towards performing a robust fault-tree analysis under limited data and uncertain event dependence. The validity and feasibility of the proposed framework is demonstrated in computing the probability distribution for the reversed flow of the water within the inlet system within the TRIGA nuclear research reactor. The results support the hypothesis, and is shown to be consistent with what is expected in reality. A key selling point of the proposed methodology is that it is not reactor specific and can be applied towards any reactor design of interest. In fact, large conventional reactors such as pressurized water reactors can benefit from the proposed methodology given its relative system configuration complexity which presents significant epistemic uncertainty over the failure dependencies between its components. Future research efforts can be invested towards investigating the following: 1) a distribution-free approach towards performing such analysis with distribution-free probability boxes, aimed at eliminating the element of model form uncertainty; and 2) to investigate the simultaneous use of both confidence box and probability box to perform a fault-tree analysis, and provide a statistical interpretation over the resulting statistical structure associated with the Top event probability.

The MATLAB and R codes used to perform the analysis in the paper are made publicly available on GitHub via: https://github.com/Adolphus8/stochastic-model-updating.git

ACKNOWLEDGMENTS

The authors of the work would like to express their utmost gratitude to the University of Liverpool, the Thailand Institute of Nuclear Technology, and the Singapore Nuclear Research and Safety Institute for the support required to perform the necessary studies presented in the paper. In addition, the authors are grateful to the National Research Foundation Singapore (Funding no.: A-0001360-06-00) for their gracious funding, without which the research would not have been possible.

REFERENCES

[1] A. LYE, J. CHANG, S. XIAO, and K. Y. CHUNG, "An Overview of Probabilistic Safety Assessment for Nuclear Safety: What Has Been Done, and Where Do We Go from Here?", *Journal of Nuclear Engineering*, **5**, 456-485 (2024).
[2] W. VECHGAMA, K. SILVA, A. PECHRAK, and S. WETCHAGARUN, "Application of Hazard and Operability Technique to Level 1 Probabilistic Safety Assessment of Thai Research Reactor-1/Modification 1: Internal Events and Human Errors", *Progress in Nuclear Energy*, **138**, 103838 (2021).
[3] A. LYE, "Robust and Efficient Probabilistic Approaches towards Parameter Identification and Model Updating", *University of Liverpool Ph.D. Thesis Repository* (2023).
[4] A. LYE, S. FERSON, and S. XIAO, "Comparison between distance functions for Approximate Bayesian Computation towards Stochastic model updating and Model validation under limited data", *ASCE-ASME Journal of Risk and Uncertainty in Engineering Systems Part A: Civil Engineering*, **10**, 03124001 (2024).
[5] S. BI, M. BROGGI, and M. BEER, "The role of the Bhattacharyya distance in stochastic model updating", *Mechanical Systems and Signal Processing*, **117**, 437-452 (2019).
[6] F. NIELSEN, "On the Jensen–Shannon Symmetrization of Distances Relying on Abstract Means", *Entropy*, **21**, 485 (2019).
[7] L. YANG, S. BI, M. G. R. FAES, M. BROGGI, and M. BEER, "Bayesian inversion for imprecise probabilistic models using a novel entropy-based uncertainty quantification metric", *Mechanical Systems and Signal Processing*, **162**, 107954 (2022).
[8] A. LYE, S. FERSON, and S. XIAO, "Stochastic Model Updating Using The Jenson-Shannon Divergence For Calibration and Validation Under Limited Data", *34th European Safety and Reliability Conference: Advances in Reliability, Safety and Security*, Krakow, 23-27 June 2024, 1, 173-182 (2024).
[9] A. LYE, S. FERSON, and S. XIAO, "Distribution-free stochastic model updating for the Physics-guided reliability analysis of a material thermal property under limited data", *17th International Conference on Probabilistic Safety Assessment and Management & Asian Symposium on Risk Assessment and Management*, Sendai, 7-11 October 2024, 1 (2024).
[10] W. ZHAO, L. YANG, C. DANG, R. ROCCHETTA, M. VALDEBENITO, and D. MOENS, "Enriching stochastic model updating metrics: An efficient bayesian approach using Bray-curtis distance and an adaptive binning algorithm", *Mechanical Systems and Signal Processing*, **171**, 108889 (2022).
[11] A. LYE, A. CICIRELLO, and E. PATELLI, "An efficient and robust sampler for Bayesian inference: Transitional Ensemble Markov Chain Monte Carlo", *Mechanical Systems and Signal Processing*, **167**, 108471 (2022).
[12] J. CHING, and Y. C. CHEN, "Transitional Markov Chain Monte Carlo Method for Bayesian Model Updating, Model Class Selection, and Model Averaging", *Journal of Engineering Mechanics*, **133**, 816-832 (2007).
[13] S. FERSON, V. KREINOVICH, L. GRINZBURG, D. MYERS, and K. SENTZ, "Constructing probability boxes and Dempster-Shafer structures", *U.S. Department of Energy Office of Scientific and Technical Information*, 1 (2003).
[14] A. LYE, W. VECHGAMA, M. SALLAK, S. DESTERCKE, S. FERSON, and S. XIAO, "Advances in the Reliability Analysis of Coherent Systems under Limited Data with Confidence Boxes", *ASCE-ASME Journal of Risk and Uncertainty in Engineering Systems Part A: Civil Engineering*, **11**, 04024074 (2025).
[15] M. FRECHET, "Généralisation du théorème des probabilités totals", *Fundamenta Mathematicae*, **25**, 379-387 (1935).
[16] A. GRAY, A. WIMBUSH, M. DE-ANGELIS, P. O. HRISTOV, D. CALLEJA, E. MIRALLES-DOLZ, and R. ROCCHETTA, "From inference to design: A comprehensive framework for uncertainty quantification in engineering with limited information", *Mechanical Systems and Signal Processing*, **165**, 108210 (2022).
[17] A. LYE, M. KITAHARA, M. BROGGI, and E. PATELLI, "Robust optimization of a dynamic Black-box system under severe uncertainty: A distribution-free framework", *Mechanical Systems and Signal Processing*, **167**, 108522 (2022).

ASRAM2025
www.asram2025.org
Asian Symposium on Risk Assessment and Management 2025
Pattaya, Thailand, 27 – 29 August 2025

STUDY ON BEST ESTIMATE OF FUEL ROD FRACTURE DURING LOCA INCLUDING UNCERTAINTY IN STRESS-STRENGTH MODEL

Hiroki Tanaka[1], Takafumi Narukawa[1], Takashi Takata[1]

[1] *Department of Nuclear Engineering and Management, Graduate School of Engineering, the University of Tokyo, 7-3-1 Hongo, Bunkyo-ku, Tokyo 113-8656, Japan, tanaka@nse.t.u-tokyo.ac.jp*

ABSTRACT

Probabilistic risk assessments of nuclear power plants have relied on conservative deterministic criteria for core damage determination, despite advancements in plant response and system analyses, including the best-estimate plus uncertainty (BEPU) methodology. To achieve more rational and realistic assessments, we previously proposed a probabilistic approach for estimating fuel rod fracture during loss-of-coolant accidents (LOCAs) in light-water reactors by developing a fracture probability estimation model that integrates BEPU analysis. In this framework, fracture probabilities are estimated using a stress-strength model, in which stress and strength are represented as probability distributions modeled as functions of the equivalent cladding reacted (ECR)—a key indicator of fuel cladding oxidation under LOCA conditions. The stress distribution is represented by a log-normal model derived through Bayesian inference of BEPU analysis results, while the strength distribution is modeled with a log-probit model based on Bayesian inference applied to LOCA-simulated test data. A Monte Carlo simulation samples and compares random values from these distributions to calculate probabilities. However, this approach requires substantial computational resources. To address this, we explored a numerical integration method that replaces the full propagation of uncertainty with representative curves constructed from posterior distributions, aiming to approximate the fracture probabilities calculated by Monte Carlo simulation with reduced cost. This study investigates how representative curves—based on pointwise means or medians computed from sampled distributions at each ECR value—affect the accuracy of the numerical integration results compared to full Monte Carlo simulations. By analyzing four combinations of normal and log-normal distributions for stress and strength, we found that using the pointwise mean curve yields highly accurate results, with relative errors below 1%, while the use of the pointwise median curve causes larger discrepancies. This approach improves computational efficiency in rare fracture probability estimation while retaining compatibility with uncertainty-aware modeling.

Keywords: Fuel rod fracture, LOCA, BEPU, Stress-strength model, Bayesian inference, Monte Carlo simulation, Numerical integration

I. INTRODUCTION

In the field of nuclear power plant safety assessment, recent advancements have been made toward more realistic and rational evaluation methods, including best-estimate plus uncertainty (BEPU) [1] and probabilistic risk assessment (PRA). These methods have been primarily applied to estimate stress-side parameters, such as peak cladding temperature (PCT) and equivalent cladding reacted (ECR), which indicate the degree of oxidation in fuel cladding tubes. On the other hand, strength-side criteria used for core damage determination, such as regulatory ECR limits, remain highly conservative and deterministic, as they are based on conditions that ensure fuel rods (fuel cladding tubes) do not fracture during loss-of-coolant accidents (LOCAs) [2]. Importantly, fuel rod fracture itself does not directly lead to core damage; rather, core damage arises when fractured rods reduce the core's cooling capability. This imbalance—where stress is estimated using best-estimated methods with uncertainty consideration, while strength is estimated deterministically—can result in excessive conservatism in safety evaluation, as shown in Figure 1 [3].

To resolve this inconsistency, a previous study proposed a probabilistic model for estimating the fracture probability of fuel rods under LOCA conditions of light-water reactors (LWRs), incorporating uncertainties and using ECR [4]. This model serves as a best-estimate representation of the strength-side characteristics. Building on this model, we have previously developed a probabilistic framework for determining fuel rod fracture under LOCA conditions by integrating BEPU-based plant response analysis with the probabilistic fracture model [3].

Our proposed approach has provided a probabilistic fuel rod fracture determination method using the stress-strength model and Monte Carlo simulations. Furthermore, we have explored numerical integration to enhance the accuracy of the estimation for rare fracture probabilities, offering an alternative to Monte Carlo simulations, which might not effectively handle these events.

However, this issue remains, as numerical integration cannot directly handle uncertainties in their distributions. To address this limitation, we consider an approach in which uncertainty in the distribution parameters is replaced with representative curves—such as those based on pointwise means or medians, computed from sampled distributions at each ECR value—thereby enabling integration without repeated stochastic sampling. This study aims to explore how representative curves can be used effectively to ensure the reliability and accuracy of fracture probability estimation using numerical integration.

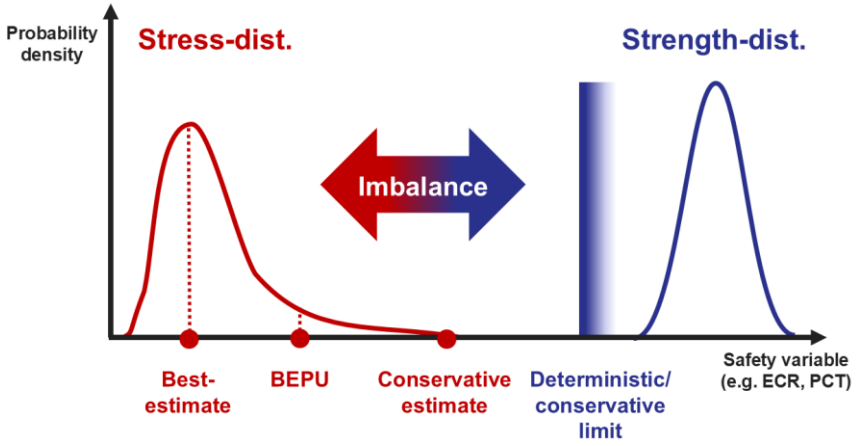

FIGURE 1. Imbalance Between Stress-side and Strength-side Estimations in Safety Assessments [3]

II. PROBABILISTIC FRACTURE DETERMINATION METHOD

II.A. Fracture Determination Using the Stress-Strength Model

In our previous study [3], we have proposed a fracture determination method utilizing the stress–strength model and Monte Carlo simulations. In this chapter, we present a detailed explanation of the method. The model employs probability distributions on both the stress side (representing plant response) and the strength side (representing the fracture threshold of fuel rods). These distributions are constructed using the ECR as the explanatory variable under LOCA conditions. The use of ECR is supported by previous studies indicating that it is a dominant factor in the fracture of fuel cladding tubes during LOCAs [4].

We present herein the complete methodology of the probabilistic fracture determination approach. First, distributions for ECR on both the strength and stress sides are estimated, including uncertainty. Then, values are randomly sampled from both distributions and compared. If the ECR value drawn from the stress distribution exceeds the corresponding value from the strength distribution, a fracture is considered to have occurred. Otherwise, no fracture is assumed. This process is repeated multiple times, and the fracture probability is calculated as the proportion of trials resulting in fracture.

II.B. Estimation of Stress Distribution

To estimate the stress distribution, we use ECR data obtained under specific accident conditions. In the study, we employ the BEPU analysis results for a pressurized water reactor (PWR) large break LOCA scenario conducted by Zugazagoitia et al. [5]. The analysis, performed using the TRACE5 code (Patch 4) [6], assumes a guillotine break at both ends of a reactor coolant system pipe. A total of 1021 simulations are performed to estimate parameters such as peak cladding temperature (PCT) and local maximum oxidation (LMO), where LMO is defined identically to ECR. This number of simulations is adopted directly from the dataset provided by Zugazagoitia et al. [5], as it is designed to ensure sufficient coverage of parameter variability while maintaining computational feasibility. We adopt the ECR values from this analysis because our estimation focuses on the relationship between ECR and fuel rod fracture.

Using this dataset, we estimate the stress distribution while incorporating uncertainty. For this purpose, we assume that the ECR follows a log-normal distribution. This choice reflects the distribution's ability to capture rare but high ECR values due to its long right tail and the fact that it is defined only for positive values. These features make the log-normal distribution well-suited for representing the probabilistic characteristics of the stress side ECR data. For the parametric estimation of the

distribution using the log-normal distribution, we use Bayesian inference with Markov chain Monte Carlo (MCMC) methods as follows:

$$X_{stress} \sim LogNormal(\mu, \sigma) \tag{1}$$

where X_{stress} represents the literature value of ECR (-), and μ and σ represent the mean and standard deviation of the log-normal distribution.

Using the posterior distribution of the parameters estimated from Eq. (1), the posterior predictive distribution of the stress side's ECR can be expressed as follows:

$$p_{pred}(x \mid X_{stress}) = \int \frac{1}{x\sigma\sqrt{2\pi}} \exp\left(-\frac{(\log x - \mu)^2}{2\sigma^2}\right) p_{post}(\mu, \sigma \mid X_{stress}) d\mu d\sigma \tag{2}$$

where $p_{pred}(x \mid X_{stress})$ represents the posterior predictive distribution of the stress side's ECR, x represents ECR, and $p_{post}(\mu, \sigma \mid X_{stress})$ represents the joint posterior distribution of the parameters.

The estimation involved running four chains with 2,000 iterations each, discarding the first 1,000 iterations in each chain as warm-up, resulting in 4,000 posterior samples in total. For the marginal prior distributions of the parameters, non-informative distributions are used, employing a normal distribution with a mean of 0 and a variance of 10^4 [7]. The convergence of MCMC sampling is confirmed by examining the $\hat{R}$ statistics [8] for all parameters, which are found to be sufficiently close to 1.0, indicating good mixing across chains. In addition, trace plots of all four chains are visually inspected to confirm that the samples have reached stationary distributions after the warm-up. These non-informative priors are selected to avoid imposing prior bias, allowing the data to drive the inferences while minimizing potential bias from weakly supported prior beliefs. The sampling is performed using the No-U-Turn Sampler (NUTS), an adaptive variant of Hamiltonian Monte Carlo (HMC), as implemented in the rstan package. NUTS is chosen over traditional because it adaptively tunes step sizes and trajectory lengths, offering faster convergence and more efficient exploration of the posterior distribution in low-dimensional models without requiring manual tuning of proposal distributions.

The results are shown in Figure 2 [3], where the blue histogram represents the ECR dataset from the simulation results of the previous study. The black line and shaded regions correspond to the median, 50% interval, and 95% interval of the posterior predictive distribution, respectively.

II.C. Estimation of Strength Distribution

The strength distribution is estimated based on a fracture probability model developed in a previous study [4]. In that study, LOCA-simulated tests were carried out under conditions designed to eliminate conservatism. The resulting data, including both fractured and unfractured outcomes of Zircaloy-4 cladding tubes, were used to construct a probabilistic model of the relationship between ECR and fracture probability using Bayesian inference. Assuming the binary fracture outcomes follow a Bernoulli distribution [8], a log-probit model was adopted to estimate the fracture probability curve [9]. In this model, ECR is calculated using the Baker–Just equation [10]. However, because the ECR values on the stress side are obtained using the Cathcart–Pawel equation [11], we recalculate the strength-side ECR values using the same equation to ensure consistency across both sides. The fracture probability estimation model is expressed as:

$$Y \sim Bernoulli(P(Y = 1 \mid X_{strength})) \tag{3}$$

$$P(Y = 1 \mid X_{strength}) = \Phi\left[\alpha + \beta \log X_{strength}\right] \tag{4}$$

$$p_{pred}(y = 1 \mid X_{strength}, Y) = \int \Phi\left[\alpha + \beta \log X_{strength}\right] p_{post}(\alpha, \beta \mid Y) d\alpha d\beta \tag{5}$$

where Y represents binary coded LOCA-simulated test data, where 1 indicates a fracture and 0 indicates no fracture. $X_{strength}$ is the ECR (-). $P(Y = 1 \mid X_{strength})$ is a fracture probability given $X_{strength}$. $p_{pred}(y = 1 \mid X_{strength}, Y)$ represents the posterior predictive distribution of the fracture probability, the link function Φ employs the cumulative distribution function (CDF) of

the standard normal distribution, α and β represent the scalars of unknown parameters to be estimated, and $p_{post}(\alpha, \beta \mid Y)$ represents the joint posterior distribution of the parameters.

While the stress distribution is represented by a probability density function (PDF), the strength distribution is initially given as a CDF. Therefore, we apply the inverse function method to derive the corresponding ECR probability density function from the CDF.

In this model, the parameters α and β are estimated using Bayesian inference with the MCMC method. The Bayesian estimation conditions are set identically to those used for the stress side. The convergence of MCMC sampling was confirmed in the same manner as for the stress side, through the examination of $\hat{R}$ statistics [8] and trace plots.

The results are shown in Figure 3 [3], where the red points represent the binary data concerning fracture and non-fracture of the test rods obtained from the LOCA-simulated test. The black line and shaded regions indicate the median, 50% interval, and 95% interval of the posterior predictive distribution of the fracture probability, respectively.

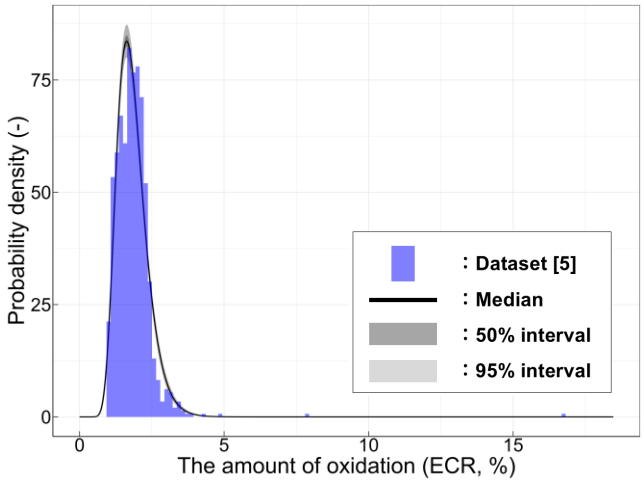

FIGURE 2. Probability Density Distribution of ECR Estimated Using Log-normal Distribution [3]

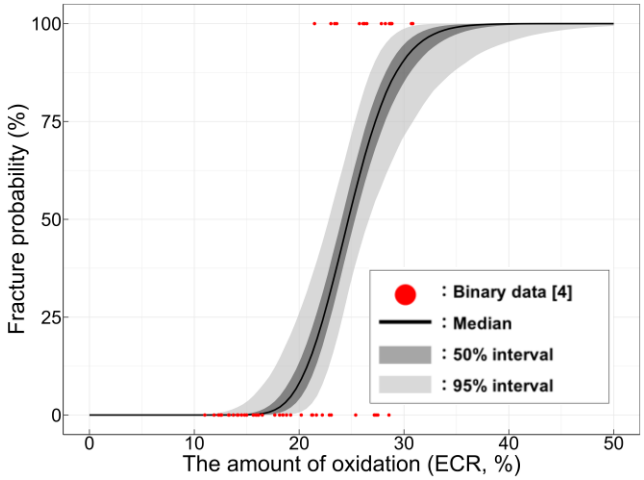

FIGURE 3. Fracture Probability Curve Estimated Using the Log-probit Model [3]

III. IMPROVING COMPUTATIONAL EFFICIENCY OF RARE FRACTURE PROBABILITIES

III.A. Fracture Probability Calculation Using Numerical Integration

According to Zugazagoitia et al. [5] and Nissley et al. [12], actual ECR values from BEPU analysis of large break LOCA scenarios are typically only a few percent. For such low ECR values, the corresponding fracture probabilities become extremely small, presenting challenges for Monte Carlo simulation-based estimation. This is because Monte Carlo methods require sample sizes proportional to the inverse of the target probability to achieve reasonable accuracy, meaning extremely large numbers of

trials are needed for rare events with very low probabilities. To address this issue, we have introduced a numerical integration approach as an alternative to Monte Carlo simulations for estimating rare fracture probabilities [3]. In this section, we outline the numerical integration approach introduced in our previous study [3].

This approach involves integrating the overlapping areas of the stress and strength distributions. Due to the complexity of deriving an analytical solution, the ECR domain from 0 to 1 is divided into sufficiently small intervals, and numerical integration using the trapezoidal rule is applied to find an approximate solution.

This method could estimate rare fracture probabilities with lower computational loads than the Monte Carlo simulation. However, using numerical integration, it is not possible to directly handle distributions that include uncertainties. Therefore, representative curves corresponding to specific credible levels are used, effectively removing the uncertainty in advance. The calculation of fracture probability using numerical integration is expressed as follows:

$$P_{\text{int}} = \int_0^1 [f_{stress}(x|\mu,\sigma) \times F_{strength}(x|\alpha,\beta)]dx \tag{6}$$

where $f_{stress}(x|\mu,\sigma)$ represents the probability density function of ECR for the stress side, $F_{strength}(x|\alpha,\beta)$ represents the cumulative probability distribution function of ECR for the strength side, x represents ECR, and other parameters represent those estimated via Bayesian inference, set to a specific credible level.

III.B. Consideration of Uncertainty in Numerical Integration

As mentioned in Section III.A, numerical integration offers a computationally efficient alternative to Monte Carlo simulation for estimating rare fracture probabilities. However, because numerical integration cannot directly incorporate parameter uncertainty, it requires the use of representative distributions or curves in which uncertainty is removed, which presents a methodological challenge.

As one approach to addressing this challenge, we have investigated whether using representative curves corresponding to specific credible levels could produce results comparable to Monte Carlo methods [3]. To conduct this investigation, we have created a virtual dataset by increasing the ECR values from a BEPU analysis [5] for a PWR large break LOCA scenario tenfold, resulting in 1020 data points after excluding one entry where ECR exceeded 100%. This modification was necessary as the original ECR values were too low to demonstrate significant fracture phenomena.

We then have examined how fracture probability estimates from numerical integration using curves corresponding to various credible levels compared to those from a Monte Carlo simulation. Our analysis has revealed that when curves corresponding to approximately a 55% credible level, the numerical integration produced fracture probability estimates (15.1%) that matched those from the Monte Carlo simulation. This finding suggests that by appropriately replacing parameter uncertainty with representative curves, it is possible to calculate fracture probabilities that consider uncertainties using numerical integration. This approach allows for estimating rare fracture probabilities with high computational accuracy and low computational load while considering uncertainties.

IV. EVALUATING THE APPLICABILITY OF NUMERICAL INTEGRATION UNDER VARIOUS UNCERTAINTY CONDITIONS

IV.A. Analytical Conditions

As described in the previous section, our previous study demonstrated that numerical integration using a representative curve corresponding to approximately the 55% credible level produces results comparable to a Monte Carlo simulation that evaluates overall uncertainties. However, this result was specific to the dataset used in our previous study [3], and may not necessarily generalize to other distribution types or uncertainty structures. Therefore, we investigate how representative curves—constructed by removing parameter uncertainty—can be used in numerical integration to ensure broad applicability under various combinations of stress and strength distributions and their associated uncertainties.

Considering how Monte Carlo simulation handles uncertainties, each trial involves fixing distribution parameters through random sampling, with the fracture probability calculated by repeating these trials sufficiently. Consequently, a Monte Carlo simulation with adequate trials should converge to numerical integration results using curves representing the mean of uncertainty distributions. To verify this approach, we prepared stress and strength distributions with uncertainties and performed numerical integration using pointwise mean curves, validating accuracy by calculating errors against true values. The pointwise mean curve refers to a line connecting mean probability density values calculated for each small interval across the ECR range. For comparison, we also computed errors for pointwise median curves derived through the same methods. The verification included all combinations of normal and log-normal distributions for both stress and strength distributions. When

both the stress and strength distributions are assumed to follow normal distributions, the fracture probability can be calculated analytically. The fracture probability under this assumption is given by the following expression:

$$P_f = \int_0^{\infty} \left\{ \int_0^{x} f_R(x)\,dx \right\} f_S(x)dx = 1 - \Phi\left(\frac{\mu_R - \mu_S}{\sqrt{\sigma_R^2 + \sigma_S^2}} \right) \tag{7}$$

where P_f represents the fracture probability, $f_R(x)$ and $f_S(x)$ represent the PDFs of the strength and stress distributions, respectively, x represents the ECR, μ_R and μ_S represent the mean values of strength and stress distributions, respectively, σ_R and σ_S represent the standard deviations of strength and stress distributions, respectively.

For the log-normal×log-normal case, logarithmic transformation of stress and strength values enables derivation of analytical solutions as same to the normal distribution case. For cases with different distribution types (normal×log-normal, log-normal×normal), Monte Carlo simulation results with 10^8 trials were used as true values. For numerical integration, the integration range was set to cover at least 99.99% of the total cumulative probability, with 10^3 divisions.

For each case, we assigned prior distributions to the parameters (mean μ, standard deviation σ), and used prior predictive distributions created from 4,000 extracted samples as stress and strength distributions. To ensure uniform parameter variation, normal distributions were used for μ priors, while log-normal distributions with small standard deviations were used for σ priors, since these parameter settings assume a symmetric uncertainty structure where the mean and median of the distributions are nearly equal. The specific prior settings for all four cases (Normal × Normal, Lognormal × Lognormal, Normal × Lognormal, and Lognormal × Normal) are summarized in Table I. The prior predictive distributions $p(x)$ can be expressed by the following equations:

$$p(x) = \iint p(x \mid \mu, \sigma) p(\mu) p(\sigma) d\mu d\sigma \tag{8}$$

The parameters were adjusted to ensure final fracture probabilities fell within a 0.1%–2.0% range, allowing meaningful comparison with Monte Carlo simulations. This range was selected because it corresponds to a level at which the true values can be accurately estimated using 10^8 Monte Carlo simulation trials, which were used in cases where analytical solutions were not available. Figure 4 shows an example of the predictive distributions for the normal×normal case, where the red dotted line represents the pointwise mean curve, the black solid line indicates the median curve, and the shaded regions show the 50% interval and 95% interval of the distribution.

IV.B. Results and Discussion

Table II summarizes the relative errors obtained using pointwise mean and median curves for each stress–strength distribution pairing. Numerical integration with the pointwise mean curve resulted in relative errors of 0.29%, 0.08%, 0.04%, and 0.06% across the four distributional combinations. In contrast, using the pointwise median curve yielded higher errors of 19%, 11%, 9.2%, and 8.6%, respectively. These findings indicate that numerical integration using the pointwise mean curve yields fracture probabilities that closely match analytical solutions and Monte Carlo simulation results, with relative errors below 1%. This approach outperforms the use of pointwise median curves, which leads to noticeably larger deviations.

While this chapter has focused on evaluating the applicability of numerical integration across different distributional combinations of stress and strength, it does not consider variations in the shape of the parameter uncertainty distributions. Addressing this limitation by incorporating a wider range of uncertainty characteristics remains an important direction for future research.

TABLE I. Prior Distribution Settings for Stress and Strength Parameters Across All Cases

		Normal × Normal	Lognormal × Lognormal	Normal × Lognormal	Lognormal × Normal
Stress Distribution	μ	Normal (1, 0.05^2)	Normal (0, 0.05^2)	Normal (1, 0.05^2)	Normal(0, 0.05^2)
	σ	LogNormal(log0.5, 0.1^2)	LogNormal(log0.5, 0.1^2)	LogNormal(log0.5, 0.1^2)	LogNormal(log0.5, 0.1^2)
Strength Distribution	μ	Normal(3, 0.05^2)	Normal(1.6, 0.05^2)	N(1.4, 0.05^2)	N(3, 0.05^2)
	σ	LogNormal(log0.5, 0.1^2)	LogNormal(log0.5, 0.1^2)	LogNormal(log0.5, 0.1^2)	LogNormal(log0.5, 0.1^2)

TABLE II. Relative Errors in Fracture Probability Estimation Accuracy for Each Distribution Combination

	Relative errors (%)			
	Normal × Normal	Lognormal × Lognormal	Normal × Lognormal	Lognormal × Normal
Mean Curve	0.29	0.08	0.04	0.06
Median Curve	19	11	9.2	8.6

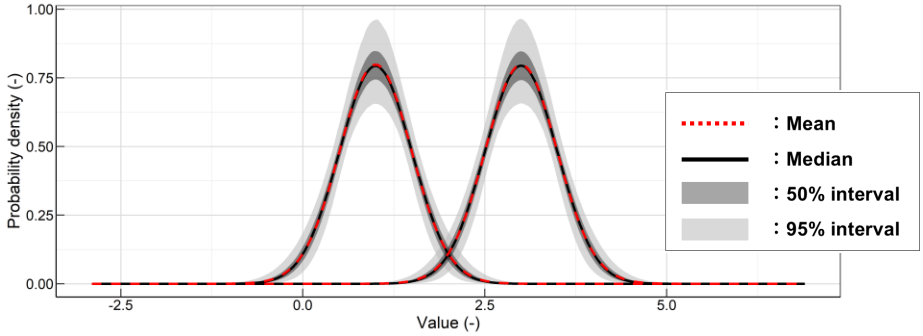

FIGURE 4. Prior Predictive Distributions for the Normal×Normal Case

V. CONCLUSIONS

In our previous study, we have proposed a probabilistic fracture determination method based on a stress–strength framework and Bayesian inference, aiming to efficiently estimate fuel rod fracture probabilities under LOCA conditions while accounting for parameter uncertainties. In this method, both stress and strength distributions are modeled as functions of ECR. As part of this method, we introduced numerical integration as an alternative to Monte Carlo simulation to estimate rare fracture probabilities with reduced computational cost. However, since numerical integration cannot be directly applied to distributions that retain parameter uncertainty, representative curves—constructed by summarizing the uncertainty (e.g., via pointwise means or medians computed from sampled distributions at each ECR value)—are required. Building on this framework, the present study investigated how representative curves derived from stress and strength distributions can be used in the numerical integration process to reproduce fracture probabilities consistent with those obtained from Monte Carlo simulations with full uncertainty propagation.

We evaluated the effect of different distributional combinations (normal and log-normal) and compared the accuracy of two approaches—using pointwise mean curves and pointwise median curves. The results showed that using the pointwise mean curve consistently achieved high accuracy, with relative errors below 1% in all cases, whereas using pointwise median curves resulted in larger errors ranging from 8% to 20%. These findings indicate that the performance of numerical integration is highly sensitive to the choice of statistical summary, and that using pointwise mean curves is robust across typical distribution types.

While the current study focused on symmetric uncertainty structures in which the mean and median are approximately aligned, future work should extend the applicability of the method to more general cases involving skewed or heavy-tailed uncertainty distributions.

Furthermore, generalizing our findings into a mathematical model that includes margins could be considered. Our current approach represents a best estimate method aimed at accurately understanding phenomena. By generalizing this into a mathematical model that incorporates margins, the method could produce outputs corresponding to required credible levels, making it more suitable for engineering applications.

While this study modeled fuel fracture, future efforts could model the entire process from fuel fracture to core damage. This would shift from the conservative evaluation of "fuel fracture equals core damage" to a more realistic evaluation. Potential applications could include using the integrity of the reactor pressure vessel to determine core damage.

ACKNOWLEDGMENTS

This work was supported by JSPS KAKENHI Grant Number JP23K13685. The authors thank Human Resources Training Center Japan for the financial support to attend the conference.

REFERENCES

[1] G.E. WILSON, "Historical insights in the development of Best Estimate Plus Uncertainty safety analysis," *Ann. Nucl. Energy*, **52**, 2 (2013).
[2] F. NAGASE, T. NARUKAWA, and M. AMAYA, “Technical basis of ECCS acceptance criteria for light-water reactors and applicability to high burnup fuel,” Japan Atomic Energy Agency, JAEA-Review 2020-076, Japan (2020).
[3] H. TANAKA, T. NARUKAWA, and T. TAKATA, "Probabilistic approach for best estimate of fuel rod fracture during loss-of-coolant accident," *J. Nucl. Eng.*, **6**, 6 (2025).
[4] T. NARUKAWA et al., "Experimental and statistical study on fracture boundary of non-irradiated Zircaloy-4 cladding tube under LOCA conditions," *J. Nucl. Mater.*, **499**, 528 (2018).
[5] E. ZUGAZAGOITIA et al., "Uncertainty and sensitivity analysis of a PWR LOCA sequence using parametric and non-parametric methods," *Reliab. Eng. Syst. Saf.*, **193**, 106607 (2020).
[6] Nuclear Regulatory Commission, TRACE V5.840, user's manual: input specification, NRC, USA (2014).
[7] K. MATSUURA, *Wonderful R 2, Bayesian Statistical Modeling Using Stan and R*, Kyoritsu Shuppan Co., Ltd., Tokyo, Japan (2016).
[8] A. GELMAN et al., *Bayesian Data Analysis*, 3rd ed., CRC Press, Boca Raton, USA (2013).
[9] S. SAND, K. VICTORIN, and A.F. FILIPSSON, "The current state of knowledge on the use of the benchmark dose concept in risk assessment," *J. Appl. Toxicol.*, **28**, 405 (2008).
[10] L. BAKER and L.C. JUST, Studies of Metal-Water Reaction at High Temperatures. III. Experimental and Theoretical Studies of the Zirconium-Water Reaction, Argonne National Laboratory, ANL-6548, USA (1962).
[11] J.V. CATHCART et al., “Zirconium metal-water oxidation kinetics. IV. Reaction rate studies,” Oak Ridge National Laboratory, ORNL/NUREG-17, USA (1977).
[12] M.E. NISSLEY, C. FREPOLI, and K. OHKAWA, "Realistic assessment of fuel rod behavior under large-break LOCA conditions," Proc. *Nuclear Fuels Sessions of the 2004 Nuclear Safety Research Conference*, Washington, DC, USA, 25–27 October 2004, 258 (2004).

Research on Sensitivity Analysis and Evaluation of cosCONT Software

Yichun Wang[1], Jiulong Yang[1], Yu Yu[1]

[1] *North China Electric Power University: No. 2 Beinong Road, Changping District, Beijing, 102206, and* wangyc@ncepu.edu.cn, 120242212034@ncepu.edu.cn, *yuyu2011@ncepu.edu.cn*

ABSTRACT

Thermal-hydraulic analysis of reactors serves as a critical technical foundation for the safety analysis and evaluation of nuclear power plants. Currently, the use of simulation modeling software, coupled with partial experimental validation, has become an essential method for scientific research and engineering training. The cosCONT software, developed by the Nuclear and Nuclear Technology Research Institute of the National Electric Power Group's State Nuclear Power Research Institute, is a module within the COSINE software package dedicated to thermal response analysis of containment structures. This software is capable of simulating various thermodynamic conditions within the containment. Given the inherent uncertainties associated with computer simulation modeling and input parameters, conducting uncertainty analysis on the software's simulation results is imperative. As changes in containment pressure to a certain level can lead to failure behaviors under accident conditions, this paper focuses on containment pressure variations as the primary output. A ranking of parameter importance is established by employing variance analysis methods to screen significant input parameters and conducting sensitivity analysis of the software. This approach aims to assess the reliability of the software in predicting pressure and to analyze the key influencing factors, thereby providing recommendations for the rational application of the software.

Keywords: cosCONT; Sensitivity analysis; Containment pressure

I. Introduction

Nuclear power plant safety is paramount for the sustainable development of nuclear energy. Reactor thermal-hydraulic analysis provides essential technical support for safety assessments, primarily achieved through simulation modeling software for research and engineering training.

This study focuses on cosCONT, the containment thermal response analysis module within the COSINE software package developed by the State Power Investment Group. Using the Main Steam Line Break (MSLB) accident scenario in the CAP1400 reactor as a case study, an integrated platform was designed and large-volume case calculations were optimized. Variance decomposition was employed to achieve technical optimization for sensitivity analysis, enabling the filtering and ranking of key parameters that influence containment pressure predictions.

II. Sensitivity analysis methods

II.A. Latin hypercube sampling (LHS)

Key input parameters were sampled using the Latin Hypercube Sampling (LHS) method. LHS is a statistical technique for generating stratified random samples from multidimensional distributions [1]. It partitions the distribution range of each variable into equiprobable strata, ensuring exactly one sample is drawn from each stratum. This stratification enhances sample homogeneity and improves accuracy compared to simple random sampling. Consider a unit hypercube in p-dimensional space, $C^p = [0,1]^p$, divided evenly into n intervals along each axis (n is the sample size), the LHS can be represented as a $n \times p$ array$[x_{i,j}]$ $(i = 1, \dots, n;\ j = 1, \dots, p)$, where $x_{i,j} \in [0,1]$, such that $x_{i,j}$ in column j belongs to only one interval, we denote this matrix as $LHS(n,p)$[2].

The sampling procedure is as follows:

- Generate a random permutation π_j for each dimension j, where $\pi_j(i)$ denotes the interval number of the i^{th} sample in dimension j;
- For each sample in dimension j, calculate the sampling point:

$$x_j^i = \frac{\pi_j(i) - u_{ij}}{N} \quad (1)$$

Where u_{ij} is the random number obtained by sampling in U(0,1).

II.B. Parallel computing enables efficiency gains

A single simulation of the CAP1400 containment thermal-hydraulic response under the MSLB accident scenario using the cosCONT platform requires approximately 10 hours. This computational burden severely limits the efficiency of iterative analyses required for large-scale sensitivity studies involving numerous design basis accidents. To address this challenge, a computational acceleration strategy was implemented: a parallel-serial hybrid model was constructed leveraging multi-core CPUs to achieve efficient resource allocation.

Parallel computing, a branch of high-performance computing, aims to maximize resource utilization, accelerate computation, and enhance processing power [3]. For engineering computing scenarios lacking dedicated supercomputing resources, this study proposes a hybrid acceleration scheme based on multi-core processors, illustrated in Fig. 1. The scheme employs a parallel-serial thread scheduling strategy. Computational resources are fully utilized by enabling parallel processing of multiple threads within the core simulation code. This approach facilitates parallel scheduling of multiple threads while maintaining simulation functionality [4], effectively minimizing the overhead associated with thread context switching.

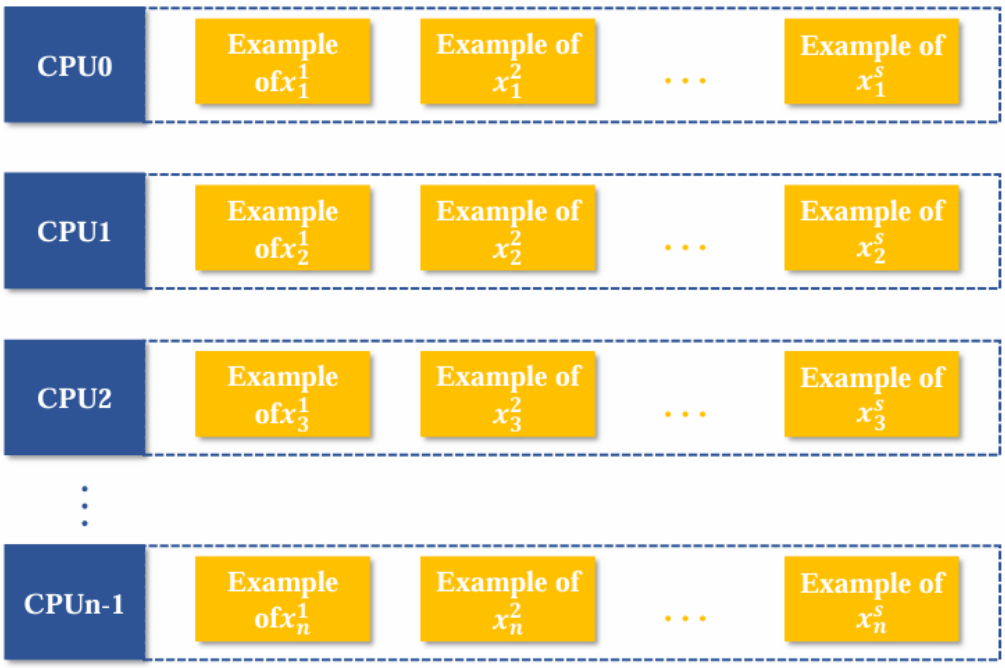

FIGURE 1. Multi-threaded parallel-serial architecture of a multi-core computer

II.C. variance decomposition

Following the execution of the T-H model hundreds of times via the parallel strategy, the variance decomposition method was applied to rank the importance of key input parameters based on the model outputs. Variance decomposition is an effective method for screening key inputs, yielding the significance factor ($\eta 2$) for each parameter. This method requires running the T-H model with inputs randomly sampled according to their probability distributions. The procedure is summarized as follows [5]:

First, assume a T-H model with n input parameters:

$$Y = f(X_1, X_2, \dots, X_n) \quad (1)$$

- X_1 of s samples, denoted as $\{x_1^1, x_1^2, \dots, x_1^s\}$;

- For each specific value x_1^j, sample r values for each of the remaining parameters $X_2,\ldots,X_n$ from their conditional distribution $f_{(x_2,\ldots,x_n|x_1^j)}$, yielding sets $\{x_2^1, x_2^2, \ldots, x_2^s\}$, …, $\{x_n^1, x_n^2, \ldots, x_n^s\}$;
- This forms an input parameter matrix of size $s \times r$ for the conditional runs;
- For each row j of the matrix(j=1,2,,...,s), calculate the conditional mean output:

$$\bar{y}(x_1^j) = \frac{1}{r}\sum_{k=1}^{r} y^{ik} = E_{X_{2,\ldots,}X_n}[Y|x_1^j] \tag{2}$$

- Calculate the mean value of Y:

$$\bar{y} = \frac{1}{s}\sum_{j=1}^{s} \bar{y}(x_1^j) = E[Y] \tag{3}$$

- Calculate the variance:

$$\overline{V_{X_1}}[E_{X_{2,\ldots,}X_n}(Y|x_1^j)] = \frac{1}{s-1}\sum_{j=1}^{s}\left[\bar{y}(x_1^j) - \bar{y}\right] \tag{4}$$

$$\bar{V}[Y] = \frac{1}{sr-1}\sum_{j=1}^{s}\sum_{k=1}^{r}(y^{ik} - \bar{y})^2 \tag{5}$$

Equation (4) represents within-group variance, and equation (5) represents between-group variance.

- Calculation of important factors:

$$\eta^2 = \frac{\overline{V_{X_1}}[E_{X_{2,\ldots,}X_n}(Y|x_1^j)]}{\bar{V}[Y]} \tag{6}$$

By the above calculation, the important factors of parameter X1 can be obtained, and the calculation of the important factors of other parameters is the same as above.

III. Objects of analysis

III.A. Introduction to the software

The sensitivity analysis was performed on cosCONT, the containment thermal response analysis module within the COSINE software package for thermal-hydraulic analysis, developed by the State Nuclear Power Research Institute. The functional architecture of the COSINE program is depicted in Fig. 2. cosCONT primarily comprises three components: control inputs, hydrodynamic parameters, and output settings [6]. It is suitable for thermal-hydraulic analyses of containment structures in passive safety nuclear power plants. The software calculates key parameters such as pressure, temperature, and flow within the containment, simulates internal phenomena during accidents, and models the behavior of various nuclear power plant system components [6].

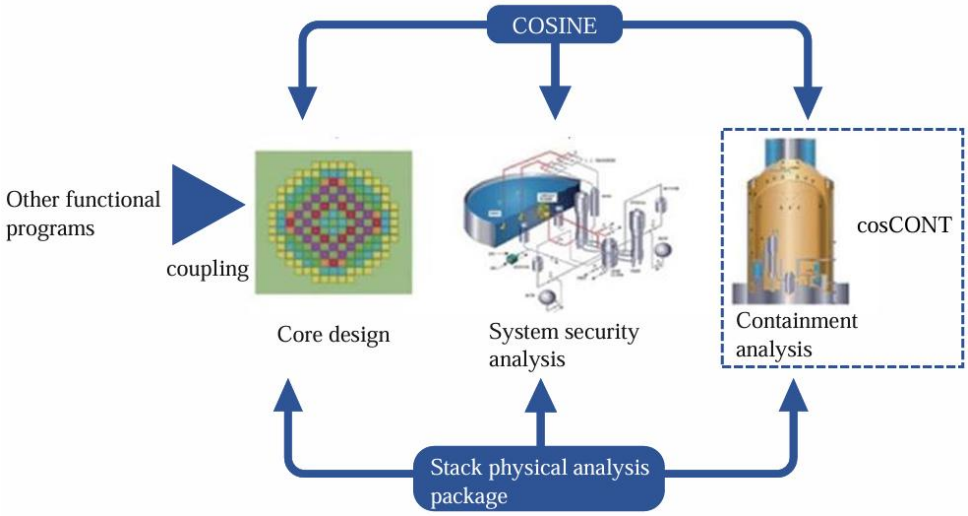

FIGURE 2. Functional block diagram of the COSINE software package system[7]

III.B. Modelling and working conditions

The CAP1400 containment design, shown schematically in Fig. 3, retains the Steel Containment Vessel (SCV) structure of the AP1000 design, which is based on passive containment cooling. The CAP1400 design features increased size and capacity compared to its predecessor.

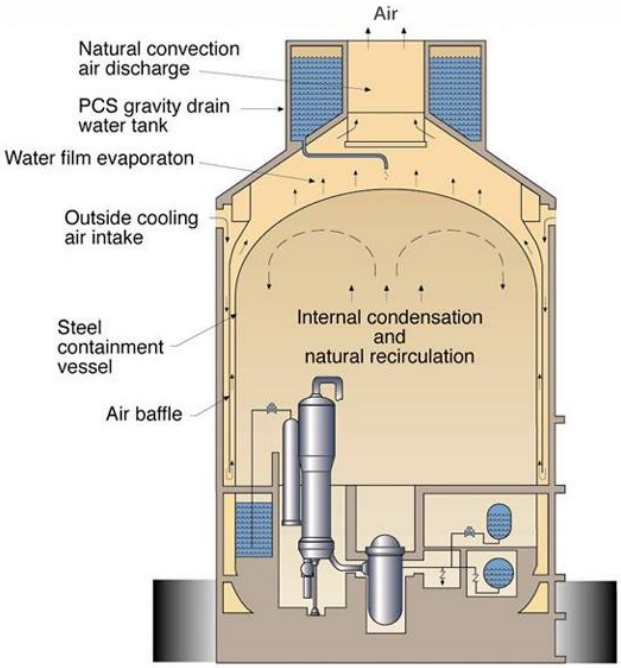

FIGURE 3. Overall schematic diagram of the CAP1400 containment vessel [8]

This study employs the self-developed cosCONT software to simulate the Main Steam Line Break (MSLB) accident for the CAP1400 reactor. This scenario serves as the basis for the software sensitivity analysis and the assessment of its applicability. In the hypothetical MSLB scenario, the pressure transient within the steel containment is illustrated in Fig. 4. Following the accident initiation (t=0), a large mass of steam is released into the containment, causing a rapid pressure rise. Pressure begins to decrease once the external Passive Containment Cooling System (PCS) water film is fully established, resulting in a distinct pressure peak. Maintaining containment pressure below its design value is critical for the success of the passive containment cooling system in preventing significant radioactive releases to the environment. Consequently, containment pressure is the primary focus of safety analyses related to containment integrity [8]

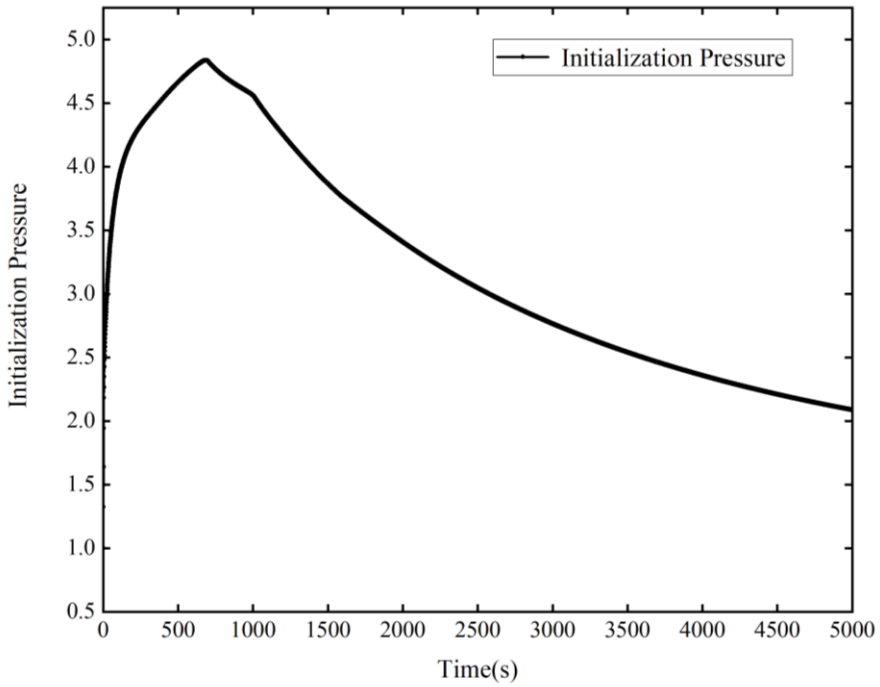

FIGURE 4. MSLB Process Pressure Change Curve (Since the model raw pressures are not publicly available, all raw data sections are initialised in this paper.)

IV. Analysis and discussion of results

IV.A Key Parameter Screening and Sampling

Seven key input parameters were identified, in order: atmospheric ambient temperature, condensation conservatism factor, evaporation conservatism factor, internal initial temperature, PCS water film initial temperature, internal initial pressure, and internal initial humidity, and the distribution ranges and characteristics of the parameters are demonstrated in Table 1.

TABLE I. Probability distribution of input parameters

Code	Parameter	Interval	Column Header Goes Here
X_1	Atmospheric environmental temperature	(30.4,8.44) (℃)	Normal
X_2	Condensation conservation factor	[0.5,1]	Uniform
X_3	Evaporation conservation factor	[0.6,1]	Uniform
X_4	Initial internal temperature	[283.15,323.15] (K)	Uniform
X_5	Initial temperature of PCS water film	[283.15,322.04] (K)	Uniform
X_6	Internal initial pressure	[0.09,0.11] MPa	Uniform
X_7	Internal initial humidity	[0,100%]	Uniform

Determining the appropriate sample size for variance decomposition is complex, and a trial algorithm is often employed based on a combination of computational accuracy and efficiency. We analysed seven input parameters. We took 100 samples (s = 10, r = 10) for each input parameter in the trial.

IV.B Analysis of variance decomposition

The importance factors ($\eta 2$) obtained from the variance decomposition for each parameter are listed in Table II and visualized in Fig. 5. The resulting parameter importance ranking is: X7 (Initial internal humidity) > X3 (Evaporation conservative factor) > X5 (Initial PCS water film temperature) > X6 (Initial internal pressure) > X2 (Condensation conservative factor) > X4 (Initial internal temperature) > X1 (Atmospheric environmental temperature).

TABLE II Importance factors for each parameter

Code	Parameter	Materiality factor η^2
X_1	Atmospheric environmental temperature	0.0047
X_2	Condensation conservation factor	0.0518
X_3	Evaporation conservation factor	0.0810
X_4	Initial internal temperature	0.0268
X_5	Initial temperature of PCS water film	0.0676
X_6	Internal initial pressure	0.0554
X_7	Internal initial humidity	0.5117

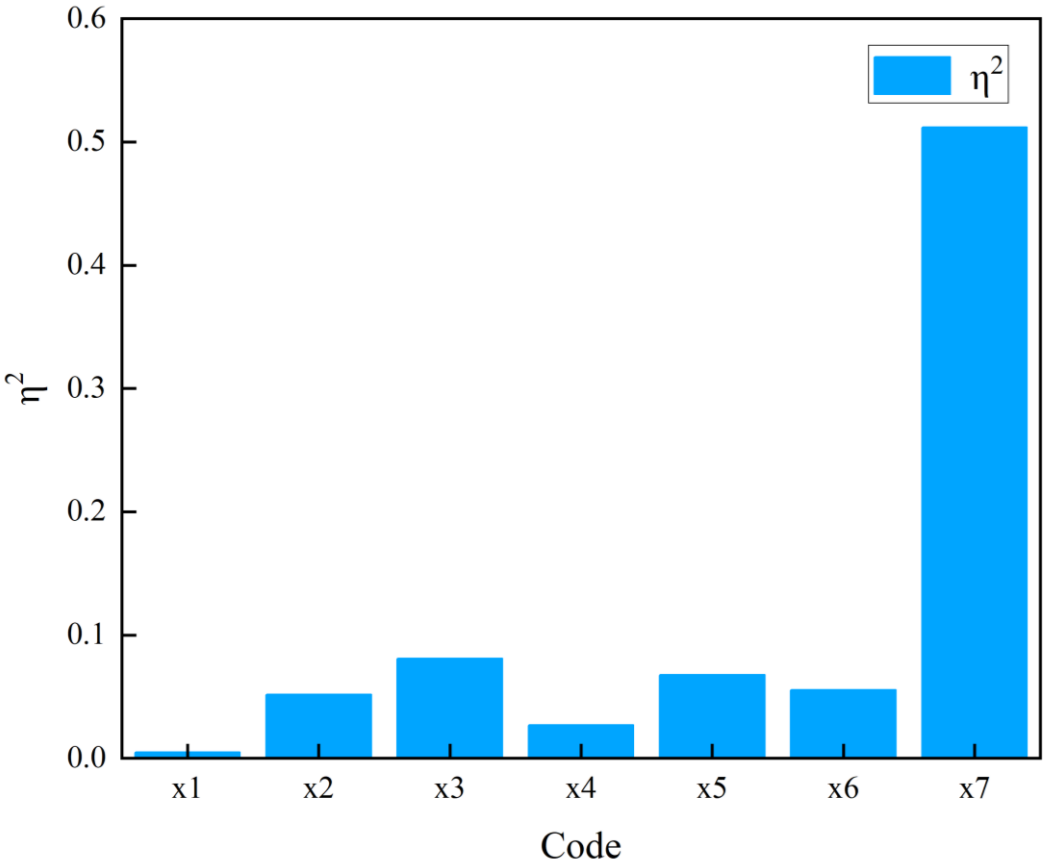

FIGURE 5. Graphical representation of the importance factor of each parameter

The initial internal humidity (X_7) exhibits a dominant influence ($\eta 2$=0.5117), consistent with its direct impact on the partial pressure of non-condensable gases (NCGs) within the containment. Furthermore, studies indicate that NCGs accumulate near condensing surfaces, forming a gas boundary layer that impedes steam contact with the cold wall, thereby reducing the heat transfer coefficient [9]. This underscores the criticality of initial humidity.

The evaporation conservative factor (X_3) and initial PCS water film temperature (X_5) also show significant influence. The PCS water film is the primary heat transfer pathway from the containment shell. The evaporation factor directly relates to the heat transfer coefficient governing evaporation from the water film surface, while its initial temperature sets the initial driving temperature difference for heat removal.

Initial internal pressure (X_6) and the condensation conservative factor (X_2) demonstrate moderate importance. Pressure influences the saturation temperature and condensation rates, while the condensation factor scales the heat transfer coefficient for condensation on internal surfaces. Initial internal temperature (X_4) has a lesser, though non-negligible, effect, primarily setting the initial thermodynamic state. Atmospheric environmental temperature (X_1) exhibits the smallest impact, likely because it primarily affects the natural convection heat transfer on the outer containment surface, which may be less dominant compared to the internal PCS-driven heat removal in this specific scenario.

The observed ranking aligns with physical understanding: parameters directly governing the dominant heat transfer mechanisms (humidity affecting NCG resistance, evaporation factor and water film temperature affecting PCS performance) and initial state conditions significantly influencing the transient evolution (pressure, humidity) rank highest.

V. Summary and analysis

In this study, a global sensitivity analysis is conducted for the MSLB condition of a CAP1400 nuclear power plant, simulated using the containment thermal response software cosCONT, to assess the variance decomposition method. In the analysis process, due to the complexity of the T-H model, the long computation time leads to low analysis efficiency. In this study, the parallel computing method is employed to facilitate the simultaneous operation of the thermal model, thereby reducing the overall running time and enhancing analysis efficiency.

Through this study, we obtained the important ordering of key parameters under the MSLB condition of the cosCONT simulation of CAP1400, and provided an efficient and reliable analysis case for the sensitivity analysis of the thermal model through parallel computing. In the future, we will conduct further sensitivity analysis from x_1 to x_6, do a more detailed sequencing job.

ACKNOWLEDGMENTS

The authors gratefully acknowledge the State Nuclear Power Research Institute for providing technical support and access to the cosCONT software platform. Special thanks to Prof. Yu from North China Electric Power University for valuable discussions on sensitivity analysis methodology, and to Kaixin Wu for the discussion of methods. The authors declare no conflict of interest.

REFERENCES

[1] Francesco Di Maio, Giancarlo Nicola, Enrico Zio, et al, Ensemble-based sensitivity analysis of a Best Estimate Thermal Hydraulics model: Application to a Passive Containment Cooling System of an AP1000 Nuclear Power Plant[J]. Annals of Nuclear Energy,73(2014).

[2] Curtis B. Storlie, Brian J. Reich, Jon C. Helton, et al. Analysis of Computationally Demanding Models with Continuous and Categorical Inputs.[J] Reliability Engineering & System Safety, 113(2013).

[3] Razi Sheikholeslami, Saman Razavi. Progressive Latin Hypercube Sampling: An Efficient Approach for Robust Sampling-based Analysis of Environmental Models[J].Environmental Modelling & Software, 93(2017).

[4] Xin Zhou, Xiaohan Shen, Zhaoru Liu, ET AL. A novel shadow calculation approach based on multithreaded parallel computing[J]. Energy and Buildings, 312(2024).

[5] Yu Yu , Shengfei Wang , Zhangpeng Guo ,et al. An Efficient Method of Key Parameter Screening for PCCS under SLB Accident in AP1000[J]. Progress in Nuclear Energy, 122(2020).

[6] Yi Yao, Dongxue Yang, Yu Yang. Containment Thermal Response Analysis Software cosCONT V2.0 User Manual[K]. Beijing: State Power Investment Group Science and Technology Research Institute Co., Ltd(2024).

[7] Xunyu Zhou. Validation of COSINE Containment Analysis Program and Parameter Sensitivity Study[D]. Harbin Engineering University(2015).

[8] Li, Dong, Penghao Jiang, Chen Hu, et al. Comparison of Local and Global Sensitivity Analysis Methods and Application to Thermal Hydraulic Phenomena[J]. Progress in Nuclear Energy 11,58(2023).

[9] Yu Yu , Shengfei Wang, Guanyu Liu, et al. Analysis of climatic conditions' effect on passive containment cooling system reliability in AP1000 for multi-unit nuclear power plant site[J]. Progress in Nuclear Energy, 170(2024).

[10] Zhao H, Peterson PF. An overview of modeling methods for thermal mixing and stratification in large enclosures for reactor safety analysis[R]. Idaho National Laboratory (INL) (2010).

ASRAM2025
www.asram2025.org
Asian Symposium on Risk Assessment and Management 2025
Pattaya, Thailand, 27 – 29 August 2025

EFFECT OF MODEL UNCERTAINTY ON THE SYSTEM PHYSICAL PROCESS FAILURE PROBABILITY

Yu YU, Cheng YANG, Guanyu LIU

School of Nuclear Science and Engineering, Beijing Key Laboratory of Passive Safety Technology
Nuclear Energy North China Electric Power University, Beijing, China,102206
Email Address: yuyu2011@ncepu.edu.cn

ABSTRACT

Passive safety system is widely used in new generation reactor design, and physical process failure due to the uncertainties of input parameters and Thermal-Hydraulic(T-H) model is one of the important contributors to system failure. Some methods are developed for input parameters' uncertainties analysis, in this paper, the effect of T-H model uncertainty on the system physical process failure probability is studied. Passive Containment Cooling System (PCCS) in AP1000 nuclear power plant is a typical safety system, which is analyzed as an example in the work, and Monte Carlo (MC) simulation is used to evaluate the system physical process failure probability, and the contributions of T-H model uncertainty is estimated.

Keywords: Passive safety system, Thermal-Hydraulic model uncertainty, physical process failure, MC simulation

I. INTRODUCTION

Passive system is widely used in new generation reactor design to improve the safety of nuclear power plant, and functional failure of passive system (i.e., the system fails to implement its safety function since the system operational condition deviates from the design condition.) should be considered in Probabilistic Safety Analysis (PSA) [1,2] since the system operates based on natural circulation. The system behavior is always described by the Thermal-Hydraulic (T-H) model in the system design and safety analysis, so the uncertainties of input parameters and the T-H model itself can induce system functional failure in some extreme conditions.

Passive Containment Cooling System (PCCS) in AP1000 nuclear power plant [3,4] is a typical passive safety system, the heat produced in the containment after accident is transferred to the atmosphere by natural circulations inside and outside the steel vessel, a T-H model is established based on lumped-parameter method to verify whether the system can complete the safety function in accident condition. The input parameters of such T-H model have uncertainties and the key parameters are screened, also the T-H model has uncertainty itself, since the heat transfer correlation is gained by fitting from the experimental data. And the uncertainty of the correlation can be described by the ratio between theoretical value and experimental value,[5] such uncertainty can have important effect on the hear transfer process, then influence the system physical process failure probability.

In this paper, a method based on Monte-Carlo (MC) simulation is proposed to evaluate the system functional failure probability considering uncertainties of both input parameters and T-H model, and the PCCS in AP1000 is analyzed as an example.

II. SYSTEM DESCRIPTION

Passive Containment Cooling System (PCCS) in AP1000 nuclear power plant is a typical passive safety system, the heat produced in the containment is transferred to the atmosphere through the natural circulations inside and outside the steel vessel, as shown in FIGURE 1[3].

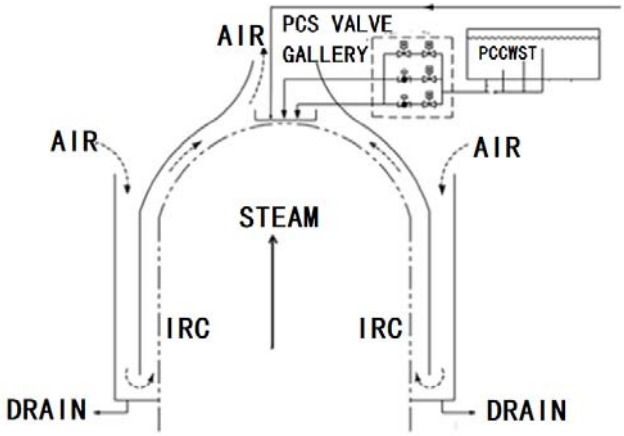

FIGURE 1: PCCS SYSTEM

The Thermal-Hydraulic (T-H) model is established based on lumped parameter method to describe the T-H behavior of the system, including the natural circulation and steam condensation inside the steel vessel, heat conduction through the steel wall and the natural circulation outside the steel vessel. The T-H model has dozens of input parameters including enviromental parameters, operation parameters and construction parameters, and the output is the curve of pressure in the containment varying with the time. The system failure can be judged if the peak value of pressure in the containment exceed 0.5 MPa, that is,

$$\text{Pcontainment} > 0.5 \text{ MPa} \tag{1}$$

Based on the sensitivity analysis, air temperature, air pressure and uncertainty of the steam mass flow are screened as the key inputs affecting the peak value of pressure in the containment.

III. METHOD

For the passive containment cooling system, the system behavior is described by T-H model in section II, and in the model, the heat transfer process inside and outside the steel vessel is expressed by formula:

$$\boldsymbol{\alpha = N_u \frac{\lambda}{L}} \tag{2}$$

Here, α is the heat transfer coefficient, λ is the thermal conductivity which can be gotten by the physical properties of the fluid, and L is characteristic length. The Nusselt number (Nu) is gained by the correlation which is fitted based on the experimental data, so the uncertainty of such correlation can have effect on the system reliability evaluation.

In order to describe the uncertainty of the correlation, we use the ratio $Nu_{(e)}$ / $Nu_{(c)}$ as the variable, $Nu_{(e)}$ is the Nusselt number value of the experiment, and $Nu_{(e)}$ is the Nusselt number value of calculation based on the correlation. The probabilistic distribution of such variable is shown in FIGURE 2 [5].

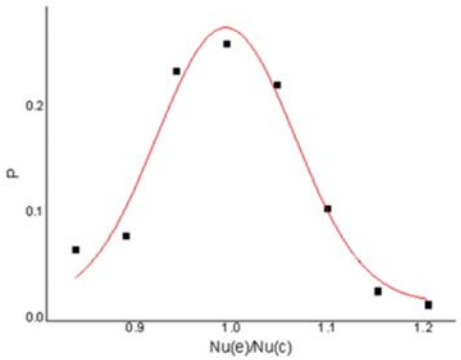

FIGURE 2 [5]. Distribution of ratio $Nu_{(e)} / Nu_{(c)}$

IV. RESULTS

The air temperature, air pressure and uncertainty of the steam flow are the key input parameters of the T-H model after Main Steam Line Break (SLB) accident, and the uncertainty distributions of the above parameters is shown in TABLE I:

TABLE I. Distributions of T-H model input parameters

Input Parameter	Uncertainty Distribution	Description
Air pressure /MPa	[0.09,0.11]	Fitting based on the historical data
Air temperature / ℃	Bi – Normal (FIGURE 3)	Fitting based on the historical data
Steam mass flow uncertainty	[0.98,1.02]	Design specification

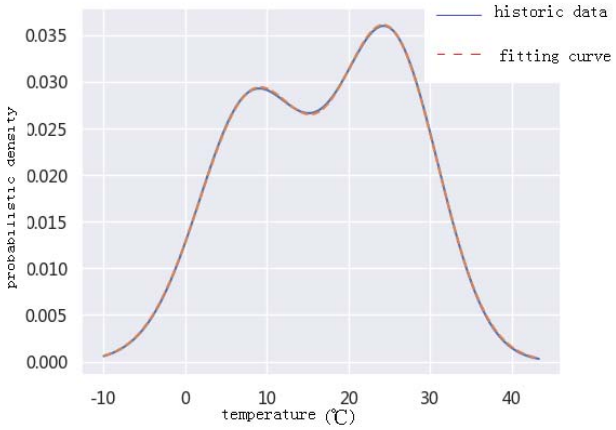

FIGURE 3. Distribution of air temperature

The Monte Carlo (MC) method is used to calculation the system reliability, in the simulation, uncertainties of both parameters and T-H model are considered, and the heat transfer correlation uncertainty is sampled based on FIGURE 2. And the 4.7×10^{-3} is gained for system failure probability, while 2.1×10^{-5} is gotten for without the effect of T-H model uncertainty.

V. CONCLUSIONS

From the results, it can be seen that the ratio $Nu_{(e)} / Nu_{(c)}$ can be used to describe the uncertainty of the heat transfer correlation, and such uncertainty can have important effect on the system physical process failure probability evaluation, based on the result, the failure probability may have increased about two orders.

REFERENCES

[1] IAEA, "Development and Application of Level 1 Probabilistic Safety Assessment for Nuclear Power Plants", DRAFT SPECIFIC SAFETY GUIDE (DS523), 2020.
[2] F.DI Maio, N. Pedroni, B.Toth, et al. "Reliability Assessment of Passive Safety Systems for Nuclear Energy Application State-of-the-Art and Open Issues", energies, Vol.14, 2021, 4688.
[3] L. T. Schulz, "Westinghouse AP1000 advanced passive plant", Nuclear Engineering and Design, vol.236, pp1547 – 1557, 2006.
[4] Y. Yu, F. Niu, SH. Wang, "One-dimensional model for containment in AP1000 nuclear power plant based on thermal stratification, Applied Thermal Engineering, Vol.70, pp25-32, 2014.
[5] Y. Yu, SH. Wang, F. Niu,etc. "Effect of Nu correlation uncertainty on safety margin for passive containment cooling system in AP1000", Progress in Nuclear Energy, Vol. 79, pp1-7, 2015,

ASRAM2025
www.asram2025.org
Asian Symposium on Risk Assessment and Management 2025
Pattaya, Thailand, 27 – 29 August 2025

THE PERFORMANCE AND SAFETY ANALYSIS OF PASSIVE SAFETY FEATURES IN APR1000

Ji-yong Oh[1], Wook-cheol Seol[2*], Yong-soo Kim[3]

[1,2,3] *Central Research Institute of Korea Hydro & Nuclear Power, Ltd. Yuseong-Gu, Daejeon, Korea, 305-343*
[*] *Corresponding author: wookcheol.seol@khnp.co.kr*

EXTENDED ABSTRACT

APR1000 is a Generation III+ reactor with thermal output of 2,825 MWt, electrical output of 1,000 MWe, and two steam generators. The design life of APR1000 is 60 years and its safety and economics have been significantly improved based on experience and proven technologies of the OPR1000 and APR1400. Safety systems used for Design Basis Accident (DBA) are designed to have N+2 redundancy, in which mechanical, electrical and I&C systems are comprised of fully independent four trains as shown in figure 1. The Passive Auxiliary Feedwater System (PAFS), which does not use electrical power supply, enhances plant safety considerably. APR1000 provides Diverse Safety Features that are used to reach and maintain safe shutdown state in the event of Design Extension Conditions (DEC) without core melt, where the DBA safety systems are not available. They include the Emergency Boration System (EBS), diverse residual heat removal function of Diverse Containment Spray System (DCSS), Diverse Spent Fuel Pool Cooling System (DSFPCS) and Alternate AC Diesel Generator (AAC DG). The Passive Auxiliary Feedwater System (PAFS) has been designed to replace the active auxiliary feedwater system enabling residual heat removal without external power supply. This paper presents the safety and performance analysis results of the PAFS using the SPACE code.

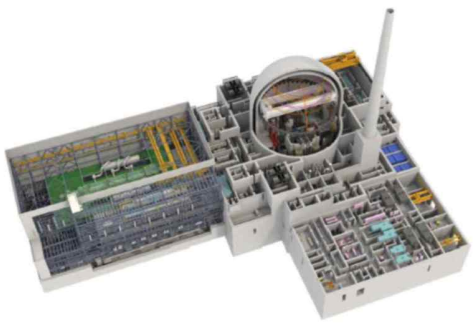

APR1000 Major Parameters

GENERAL PLANT DATA	Gross Power Output	1,050 MWe
	Thermal Power	2,825 MWth
	Design Lifetime	60 years
	Seismic Design Basis	DBE 0.3g
REACTOR CORE	Active Core Length	3.81 m
	Core Diameter	3.124 m
	Average Heat Flux at 100% Power	589.1 kW/m2
	Number of Fuel Assemblies	177, 16×16
	Fuel Cycle Length	12 to 24 months
REACTOR COOLANT SYSTEM	Number of Loops	2
	Operating Pressure	15.5 Mpa
	Inlet Temperature	295.8℃
	Outlet Temperature	327.3℃

FIGURE 1. APR1000 Overview and Major Parameters

The Passive Auxiliary Feedwater System (PAFS) of the APR1000 is an engineered safety system designed to perform critical safety functions by ensuring adequate condensate supply to the steam generators (SGs) under all accident conditions that require cooling of the Reactor Coolant System (RCS). Utilizing the SGs, the PAFS safely cools down the plant to conditions where shutdown cooling is achievable, thereby preventing core damage. The PAFS is composed of two independent trains per SG, with each train incorporating a Passive Condensation Heat Exchanger (PCHX) capable of removing 50% of the required decay heat [1] as shown in figure 2.

Each train consists of the following components: 1) A steam supply line branching off from the main steam line upstream of the Main Steam Isolation Valve (MSIV), which delivers steam to the PCHX, The PCHX, which condenses the supplied steam, 2) A Passive Condensation Cooling Tank (PCCT), which condenses steam through the PCHX tubes, A passive auxiliary feedwater supply line that returns the recovered condensate from the PCHX to the SG economizer nozzles, 3) Isolation and check valves, which isolate the system under normal conditions and actuate during accident conditions.

During an accident, the PAFS operates automatically upon receiving the Passive Auxiliary Feedwater Actuation Signal (PAFAS), which opens the system's isolation valves. The system is designed to passively supply sufficient condensate to the SGs to achieve a safe plant cooldown to shutdown conditions. The PAFS operates entirely through natural driving forces such as gravity, steam condensation, and fluid density differences.

The safety analysis of the APR1000, equipped with PAFS replacing the active auxiliary feedwater system, is performed using the SPACE code (version 3.22). To ensure the credibility of safety analysis results related to auxiliary feedwater injection, it is essential to understand both the PAFS input model and the associated analysis outcomes. The key aspects of the performance and safety analysis of PAFS consists of: 1) Description of the PAFS, 2) Assessment of the SPACE code's prediction capabilities for key thermal-hydraulic phenomena associated with the PAFS, 3) Development of the PAFS input model, 4) Performance analysis results of the PAFS.

The results of the SPACE code evaluation for major thermal-hydraulic phenomena in the PAFS are summarized as follows: 1) SPACE can simulate major PAFS phenomena such as single-phase and two-phase flow pressure drops, natural circulation, and phase-change heat transfer, 2) SPACE shows good predictive capability for single-phase pressure drops and natural circulation flow, 3) For two-phase flow regions, SPACE tends to underestimate pressure drop, which may lead to an overprediction of natural circulation flow rate, 4) The default heat transfer model in SPACE tends to underpredict heat transfer within the PCHX tubes, 5) SPACE successfully replicates the key thermal-hydraulic behaviors observed in the ATLAS integral effect tests related to PAFS [2].

Based on the understanding of key thermal-hydraulic phenomena and SPACE modeling methods, the PAFS input model for APR1000 was developed and performance analysis was conducted. The results confirmed that SPACE can physically and plausibly predict the key behaviors expected in PAFS operation and that the calculation results are stable [3]. Therefore, the developed PAFS input model is deemed suitable for safety analysis and is expected to provide physically reasonable results.

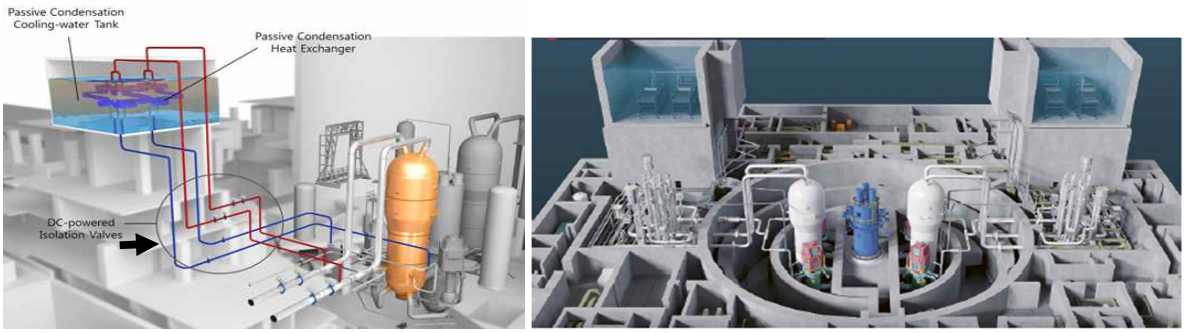

FIGURE 2. APR1000 Passive Auxiliary Feedwater System

REFERENCES

[1] Bae, B. B., Yun, B. J., Kim, S., and Kang, K. H., Design of condensation heat exchanger for the PAFS (Passive Auxiliary Feedwater System) of APR+ (Advanced Power Reactor Plus), Annals of Nuclear Energy, Vol. 46, pp. 134-143, 2012.
[2] KAERI/TR-4051/2010, Models and Correlations of flow regime maps for the SPACE code, 2010.
[3] Kang, K. H., Kim, S., Bae, B. B., Cho, Y. J., Park, Y. S., and Yun, B. J., SEPARATE AND INTEGRAL EFFECT TESTS FOR VALIDATION OF COOLING AND OPERATIONAL PERFORMANCE OF THE APR+ PASSIVE AUXILIARY FEEDWATER SYSTEM, Nuclear Engineering and Technology, Vol. 44, pp. 597-610, 2012.

ASRAM2025
www.asram2025.org
Asian Symposium on Risk Assessment and Management 2025
Pattaya, Thailand, 27 – 29 August 2025

ANALYSIS OF OPERATIONAL EFFECTS OF EXTERNAL WATER INJECTION DURING EXTENDED LOSS OF AC POWER UNDER HAZARD CONDITIONS

Wook-Cheol, Seol[1], Ji-yong Oh[2*], Yong-soo Kim[3]

[1,2,3] *Central Research Institute of Korea Hydro & Nuclear Power, Ltd. Yuseong-Gu, Daejeon, Korea, 305-343,*
[*] *Corresponding author: jiyong.oh@khnp.co.kr*

EXTENDED ABSTRACT

The Fukushima accident demonstrated that the flexible and diverse mitigation strategies are needed to cope with a variety of unforeseen accident conditions. These mitigation strategies will be typically implemented in Phase 2 or 3 when the evolving accident cannot be properly coped with by the use of fixed equipment alone [1]. There has been world-wide effort to implement the accident mitigation strategies at nuclear power plants to further strengthen defense in depth [2]. In the USA, the portable equipment that will be used to implement the mitigation strategies is called FLEX (Diverse and Flexible Coping Strategies) equipment. In Korea, the accident mitigation strategies will be carried out by so-called MACST (Multi-barrier Accident Coping Strategy) equipment, consisting of mobile diesel generators, mobile pumps, and so on. MACST is the strategy and equipment that KHNP (Korea Hydro & Nuclear Power) developed to cope with severe accident such as Fukushima Daiichi nuclear accident [3]. Since sufficient water sources are required to use these strategies, various water sources are currently being considered for nuclear power plants. However, these water sources cannot provide an infinite supply of coolant, and non-seismically designed water sources cannot be used during seismic-induced accidents. Therefore, in such limited situations, it will be difficult to expect proper cooling if an accident proceeds for days or more. In order to address this issue, it is necessary to develop response strategies that can utilize limited water sources effectively.

This analysis was therefore performed in consideration of operational parameters so that limited water sources and mobile pumps could be used during long-term accidents such as Fukushima. To analyze the effect of operational parameters on accident progression, the behaviors of the reactor coolant system, steam generator, and containment were considered. The present study is carried out for a nuclear power plant featuring a pressurized light water reactor with a thermal power rating of 3,000 MW. The base accident scenario is an extended loss of AC power (ELAP), which is a long-term loss of internal and external power in nuclear power plants. For evaluating the effectiveness of mobile pump operation in a severe accident after core damage, the applied accident scenario assumes that the core is damaged due to the absence of any safety actions. In the case of external power recovery after core damage, it is assumed that power is recovered by a mobile diesel generator before reactor vessel failure.

TABLE I. SCENARIO CASES

Case ID	Bleed	Feed	Injection Type	Set Points
Base Case	-	-	-	-
Case 1-1	ADV	Mobile Pump	Continuous	S/G water level
Case 1-2			Intermittent	

The base case is a scenario in which core damage occurs due to the loss of AC power without any safety measures such as depressurization or safety injection. Case 1 considers steam generator (S/G) depressurization through opening the ADV and on-site water(such as water tank or pond) injection into the secondary side using a mobile pump. Specifically, a comparative analysis was performed by dividing the cases into continuous injection using the mobile pump (Case 1-1) and injection operation adjusted according to the water level of the steam generator (Case 1-2).

The steam generator dries out in about 1.5 hours after station blackout occurs in the base case. Subsequently, it was analyzed that the core becomes uncovered at 2 hours due to the loss of all coolant in the primary system, and that the maximum core temperature exceeds 1,255 K (1,800°F) at 2.6 hours, resulting in core damage. After that, since no action is taken to cool

the core, the core melts and relocates to the reactor vessel lower head. The reactor vessel is continuously heated by the corium and eventually ruptures (FIGURE 1).

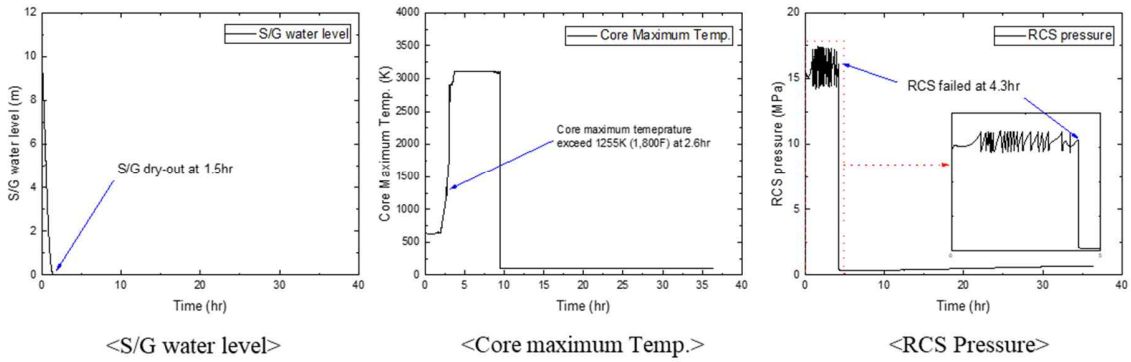

<S/G water level> <Core maximum Temp.> <RCS Pressure>

FIGURE 1. RESULTS OF BASE CASE

In Case 1-1, as shown in FIGURE 2, the water level is recovered due to external water injection starting at 2.6 hours after the accident occurs. The core exit temperature of the primary system decreases due to secondary heat removal. However, the temperature rises sharply again after the external water source is depleted. The core is heated up to melting temperature again, resulting in core melt and relocation to the lower head. The reactor vessel is continuously heated by the corium and eventually ruptures. In Case 1-2, when the timing of external water source depletion is delayed, corium relocation and reactor vessel failure timing are also delayed by approximately 3 hours each. As the external water depletion progresses, the time to vessel failure is delayed because the mobile pump is operated according to the secondary water level.

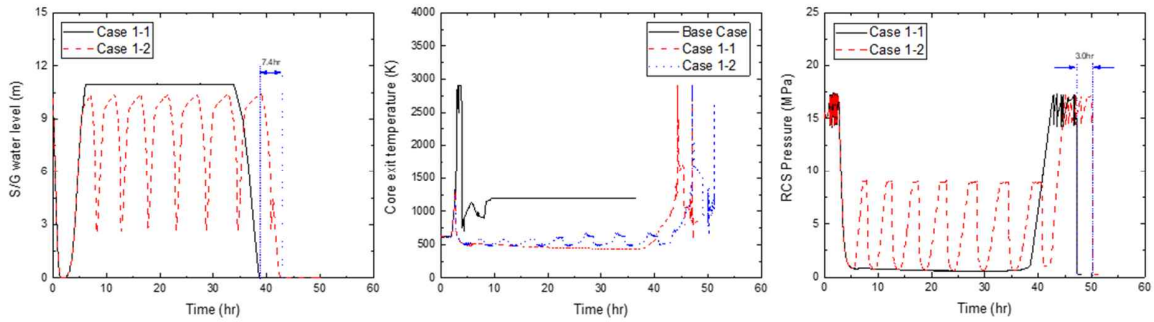

<S/G water level> <Core Exit Temp.> <RCS Pressure>

FIGURE 2. RESULTS OF CASE 1-1 AND 1-2

It was analyzed that performing secondary system heat removal through external water injection provides a time margin of approximately 40 hours before reactor vessel failure occurs. Furthermore, if the external water injection operation is appropriately adjusted based on the secondary system water level, an additional time margin of about 3 hours can be secured.

REFERENCES

[1] Nuclear Energy Institute, “Diverse and Flexible Coping Strategies (FLEX) Implementation Guide,” NEI-12-06 (2012).
[2] KAERI, “Uncertainty Analysis of SAM Strategy – 1000MWe PWR, TLOCCW, Emergency Excternal Water Injection Strategy,” KAERI/TR-7962(2019)
[3] Young A Suh, Jaewhan Kim, “Sensitivity Analysis via Modelling FLEX/MACST Equipment into a PSA Model,” KNS (2020).

Technical Session 4 (13:40 - 15:40)	The Port 4, C Floor	Human Reliability Analysis and Human and Organizational Factors
		Chair/Facilitator 1: Dr. Yochan Kim (Korea Atomic Energy Research Institute)
		Chair/Facilitator 2: Dr. Phongsakorn PRAK TOM (Malaysian Nuclear Agency (ANM))
13:40 - 14:00		ID 16: Characteristics of Parameter Uncertainty of the Embrace Method Based on Monte Carlo Simulations Speaker: Yochan Kim (Korea Atomic Energy Research Institute) Contributors: Yochan Kim (Korea Atomic Energy Research Institute), Jaewhan Kim (Korea Atomic Energy Research Institute)
14:00 - 14:20		ID 42: Comparison of Methodological Characteristics between EMBRACE and the EPRI HRA Methodology: Case Study on Critical Operator Actions in an Advanced Control Room Speaker: Jaewhan Kim (KAERI) Contributors: Jaewhan Kim (KAERI), Yochan Kim (KAERI)
14:20 - 14:40		ID 137: Study on Human Reliability Assessment for MCR and RSS Switching Switch Configuration Scheme Speaker: Zhihui Xu (State Key Laboratory of Nuclear Power Safety Technology and Equipment) Contributors: Zhihui Xu (State Key Laboratory of Nuclear Power Safety Technology and Equipment)
14:40 - 15:00		ID 105: Handbook on Training Observation for Qualitative Analysis of The Human Reliability Analysis with Emphasis on Narratives Speaker: Kenichi Hayase (Central Research Institute of Electric Power Industry) Contributors: Kenichi Hayase (Central Research Institute of Electric Power Industry), Daisuke Takeda (Central Research Institute of Electric Power Industry)
15:00 - 15:20		ID 20: Review of Measurement Properties for the Use of Integrated System Validations Speaker: Jinkyun Park (Korea Atomic Energy Research Institute) Contributors: Jung Hwan Kim (Korea Atomic Energy Research Institute), Jinkyun Park (Korea Atomic Energy Research Institute)
15:20 - 15:40		ID 36: Proposals to Reduce Human Error Probability regarding the Use of Portable Equipment during Multi-Unit Accident Responses Speaker: Seong Woo Kang (Korea Atomic Energy Research Institute) Contributors: Seong Woo Kang (Korea Atomic Energy Research Institute), Jaewhan Kim (Korea Atomic Energy Research Institute), Ho-Gon Lim (Korea Atomic Energy Research Institute), Jae Young Yoon (Korea Atomic Energy Research Institute), Jong Woo Park (Korea Atomic Energy Research Institute)

ASRAM2025
www.asram2025.org
Asian Symposium on Risk Assessment and Management 2025
Pattaya, Thailand, 27 – 29 August 2025

CHARACTERISTICS OF PARAMETER UNCERTAINTY OF THE EMBRACE METHOD BASED ON MONTE CARLO SIMULATIONS

Yochan Kim[1], Jaewhan Kim[1]

[1] *Risk Assessment Research Division, Korea Atomic Energy Research Institute, Yuseong-gu, Daejeon 34057, Republic of Korea, yochankim@kaeri.re.kr*

ABSTRACT

Characterizing and understanding the uncertainties of human reliability is a critical aspect of the risk-related decision-making process. Among various kinds of uncertainties, parametric uncertainty of human error probability (HEP) reflects variabilities in the method-dependent parameters, such as nominal HEP, effects of performance shaping factors on HEPs, and recovery factors. Because of a lack of data supporting these kinds of parametric bounds, the rules for bound determination in human reliability analysis (HRA) methods have not been grounded on sufficient evidence. This study attempts to estimate uncertainty bounds for parametric uncertainty using Monte Carlo simulations. Extending the authors' study, here uncertainties residing in the error rates of local manipulations and recovery behaviors were additionally involved in the simulations. Based on the results of this empirical estimation, we derived the characteristics of parametric uncertainties based on the failures and elements with the highest contribution. We expect that these characteristics will be useful in understanding the uncertainty of human reliability.

Keywords: Human error probability, Human reliability analysis, Monte Carlo simulation, Parameter uncertainty, Uncertainty analysis

I. INTRODUCTION

Human reliability analysis (HRA) is a key part of probabilistic safety assessment (PSA) that looks at how people interact with systems during specific events, examines how these interactions can fail, and calculates the chance of human errors occurring (known as human error probability or HEP) in these events [1]. However, in order to facilitate the application of HRA, HRA models simply represent the complex processes of human–system interactions and cognitive behaviors and rely on estimates from expert opinions or data extracted from similar contexts due to insufficient empirical data [2]. Therefore, a clear understanding and utilization of the uncertainty in HRA is necessary for risk-based decision making. Many uncertainty guidelines generally classify uncertainties into three categories: parameter, model, and completeness [3,4]. Among them, parameter uncertainty is associated with the values of the component parameters in the HRA model, such as the nominal HEPs, performance shaping factor (PSF) multipliers, and recovery multipliers. Current HRA methods employ beta or lognormal distributions to anticipate the parameter bounds [2]. In the case of lognormal distributions, the error factor, which is the ratio between the median and the 5th percentile or between the median and the 95th percentile, is often calculated to represent the bounds. When a random variable X is lognormally distributed, $\ln(X) \sim N(mu, sigma^2)$, $sigma$ is equivalent with ln(error factor)/1.645.

The authors' previous study attempted to estimate the bounds of HEP values that an HRA method can inherently produce [2]. To this end, we categorized the component parameters into method-dependent parameters and scenario-specific parameters and conducted random sampling according to the distribution of the method-dependent parameters within several scenario-specific parameter values found during current application examples of HRA. As a result, we showed that the HEP variable most closely matches the lognormal distribution and suggested that the error factor value according to the range of HEP can be used as a rule for estimating the parameter uncertainty of HEP. However, the paper also alluded to the fact that parameter uncertainties can be determined by factors other than simply the HEP magnitude. Therefore, the present study revisits the simulation data for understanding the root causes of the uncertainty variabilities of the EMBRACE (Empirical Data-Based Crew Reliability Assessment and Cognitive Error Analysis) method, following previous studies. Prior to this, in order to overcome the limitations of the previous Monte Carlo simulation, the simulation data are regenerated by (1) adding component

parameters regarding local operation and (2) considering the uncertainty in recovery multipliers. We then compare the statistical models that best explain the samples generated by Monte Carlo simulation using statistical measures and discuss the causes that explain the dispersion of the samples, focusing on the failure probabilities and the component parameters.

II. UNCERTAINTY PROPAGATION OF EMBRACE PARAMETERS

II.A. Monte Carlo Analysis

In this study, HEP values derived from the EMBRACE method [5,6] are generated by the Monte Carlo method [7]. The EMBRACE method is based on the nominal HEPs estimated from HuREX data and the PSF multipliers elicited from a formal expert evaluation process, which provides concrete evidence for the distribution of the component parameters. The method-dependent parameters and scenario-specific parameters of the EMBRACE method can be distinguished as shown in Fig. 1.

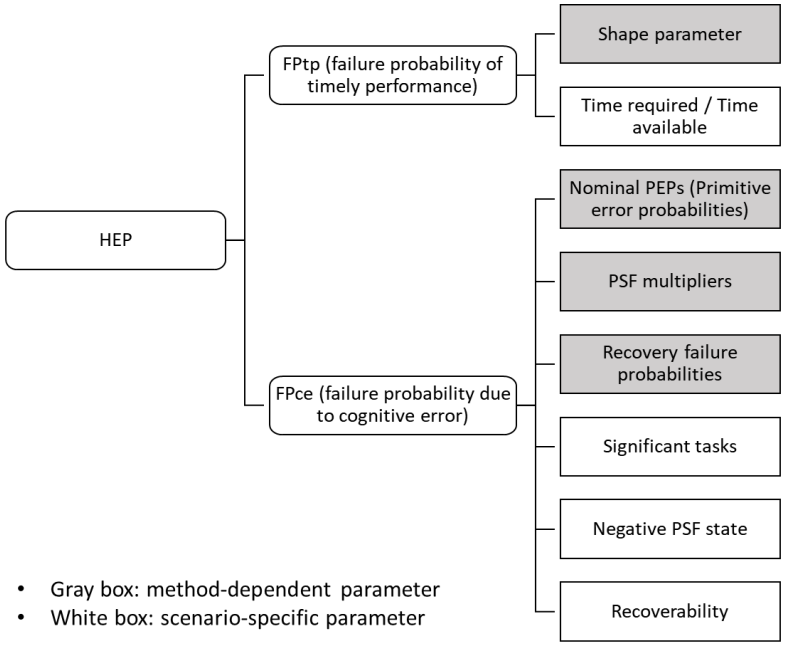

FIGURE 1. Method-dependent parameters and scenario-specific parameters of the EMBRACE method.

In the EMBRACE method, an HEP is calculated using Eqs. (1), (2), and (3):

$$HEP = FPtp + FPce\,, \tag{1}$$

where *FPtp* is the failure probability of timely performance and *FPce* is the failure probability due to cognitive error,

$$FPtp = 1 - \Phi\left[\frac{\ln(TR)}{\sigma}\right], \tag{2}$$

where Φ is the cumulative probability function of the standard normal distribution, *TR* is the time required divided by the time available, and σ is the standard deviation of the log of the distribution, and

$$FPce = \prod_{L} RM_L \sum_{j}\left[\prod_{M_j} PSFM_{M_j} \sum_{N_{ij}} NPEP_{N_{ij}}\right], \tag{3}$$

where $NPEP_{Nij}$ is the *N*th type of nominal primitive error probability (PEP) for the *i*th task in the *j*th step, $PSFM_{Mj}$ is the *M*th type of PSF multiplier in the *j*th step, and RM_L is the *L*th type of recovery multiplier.

II.A.1. Scenario-Specific Parameters

The scenario-specific parameters were determined by randomly selecting examples from APR1400 application cases [6]. For instance, 28 primitive task combinations were extracted from the APR1400 procedure steps. For each HEP simulation run, one, two, or three task combinations were randomly selected. At this time, one or zero PSFs for each combination could have negative values so that PSFM could be multiplied by each combination. In addition, assuming that one, two, or three recoveries were applicable, the recovery sources to be applied were randomly selected. The TR value was then randomly selected from one of the 22 values in the time analysis cases for the APR1400. Through this process, a total of 40 scenario-specific parameter combinations were generated. Table I shows a summary of the 40 scenario-specific cases.

TABLE I. Summary of scenario-specific parameter values for Monte Carlo simulation

Scenario ID	Step number	Task number for each step	Negative PSF	Recovery attempt number	TR
1	2	(1) 11 (2) 13	(1) Independent reviewer (Execution) (2) Complexity of required task (Execution)	1	0.31
2	3	(1) 5 (2) 8 (3) 11	(1) (All positive) (2) Training level (Execution) (3) (All positive)	1	0.11
3	3	(1) 6 (2) 3 (3) 5	(1) Subjective stress (Transition) (2) Support function of computer-based procedure (Execution) (3) (All positive)	1	0.30
4	2	(1) 8 (2) 11	(1) (All positive) (2) Independent reviewer (Execution)	3	0.40
5	1	(1) 8	(1) (All positive)	0	0.30
6	3	(1) 5 (2) 7 (3) 10	(1) (All positive) (2) (All positive) (3) (All positive)	0	0.47
7	3	(1) 9 (2) 5 (3) 5	(1) Career-experience level (Transition) (2) Complexity of human–machine interface (Transition) (3) Support function of computer-based procedure (Transition)	0	0.73
8	2	(1) 3 (2) 6	(1) Complexity of required task (Transition) (2) Complexity of human–machine interface (Transition)	0	0.11
9	3	(1) 10 (2) 11 (3) 6	(1) (All positive) (2) Support function of computer-based procedure (Transition) (3) (All positive)	2	0.14
10	3	(1) 11 (2) 10 (3) 7	(1) (All positive) (2) (All positive) (3) (All positive)	0	0.31
11	1	(1) 13	(1) Career-experience level (Transition)	0	0.80
12	2	(1) 11	(1) Career-experience level (Transition) (2) Subjective stress (Transition)	0	0.30
13	2	(1) 5 (2) 6	(1) (All positive) (2) (All positive)	0	0.73
14	2	(1) 5 (2) 6	(1) (All positive) (2) Independent reviewer (Transition)	3	0.73
15	1	(1) 10	(1) Communication level (Execution)	3	0.50
16	3	(1) 8 (2) 7 (3) 10	(1) Procedure quality (Execution) (2) (All positive) (3) (All positive)	3	0.10

17	3	(1) 8 (2) 3 (3) 10	(1) Procedure quality (Transition) (2) Procedure quality (Execution) (3) Independent reviewer (Transition)	3	0.11
18	2	(1) 6 (2) 5	(1) (All positive) (2) Crew dynamics (Transition)	3	0.40
19	2	(1) 12 (2) 6	(1) Subjective stress (Transition) (2) Training level (Transition)	2	0.08
20	1	(1) 9	(1) (All positive)	1	0.30
21	1	(1) 9	(1) (All positive)	3	1.00
22	2	(1) 5 (2) 6	(1) Career-experience level (Transition) (2) (All positive)	2	0.08
23	3	(1) 10 (2) 6 (3) 5	(1) (All positive) (2) Complexity of human–machine interface (Transition) (3) (All positive)	1	0.77
24	3	(1) 9 (2) 7 (3) 12	(1) Career-experience level (Execution) (2) (All positive) (3) (All positive)	2	0.35
25	2	(1) 9 (2) 11	(1) (All positive) (2) (All positive)	3	0.30
26	3	(1) 5 (2) 10 (3) 12	(1) Career-experience level (Execution) (2) Training level (Execution) (3) (All positive)	1	0.80
27	2	(1) 7 (2) 5	(1) (All positive) (2) (All positive)	0	0.23
28	1	(1) 3	(1) (All positive)	0	0.18
29	3	(1) 6 (2) 7 (3) 12	(1) Career-experience level (Execution) (2) (All positive) (3) (All positive)	0	0.73
30	3	(1) 5 (2) 7 (3) 5	(1) (All positive) (2) (All positive) (3) Procedure quality (Execution)	2	0.10
31	1	(1) 9	(1) (All positive)	3	0.40
32	3	(1) 5 (2) 6 (3) 9	(1) (All positive) (2) Procedure quality (Transition) (3) Communication level (Transition)	3	0.13
33	1	(1) 12	(1) Subjective stress (Execution)	0	0.13
34	2	(1) 7 (2) 3	(1) Training level (Transition) (2) Independent reviewer (Execution)	1	0.50
35	3	(1) 11 (2) 9 (3) 5	(1) Communication level (Transition) (2) Communication level (Transition) (3) Training level (Execution)	1	0.03
36	2	(1) 7 (2) 5	(1) (All positive) (2) (All positive)	2	0.18
37	1	(1) 5	(1) Training level (Transition)	0	0.47
38	2	(1) 5 (2) 11	(1) (All positive) 2) Procedure quality (Transition)	1	0.77
39	2	(1) 5 (2) 10	(1) Complexity of human–machine interface (Transition) (2) Career-experience level (Transition)	0	0.77
40	2	(1) 7 (2) 3	(1) (All positive) (2) (All positive)	3	0.50

II.A.2. Method-Dependent Parameters

Table II shows the median, 5th percentile, and 95th percentile of four types of method-dependent parameters. Most parameters are known to be most closely described by the lognormal distribution [5,6,8,9,10], while in the case of the PEP for situation understanding tasks, the beta distribution was used to estimate the PEP values [6]. For the parameters following a lognormal distribution, the median value and error factor value were used to estimate the parameter. In the case of FPtp, the median value was set when the shape parameter was 0.3403, and the error factor was calculated by regarding the values when the shape parameter was 0.4248 and 0.2766 as the 95th and 5th percentiles [5]. For the parameters following a beta distribution, the alpha and beta parameters derived from Bayesian inference were employed directly. A total of 10,000 random samples were generated from the lognormal or beta distribution of each component, and HEPs were calculated by combining them with scenario-specific parameters.

TABLE II. Distribution of the method-dependent parameters

Category	Parameter name	Median	5th percentile	95th percentile	Ref.
NPEP	Detection–trend	3.08E-04	1.02E-04	9.27E-04	[6,8]
	Detection–synthesis	1.51E-03	4.71E-04	4.80E-03	[6,8]
	Detection–others	1.10E-04	4.31E-05	2.81E-04	[6,8]
	Situation understanding (Beta distribution)	2.16E-03	3.22E-04	7.09E-03	[6,8]
	Decision–sequential step entry or Decision–external communication	1.85E-04	1.01E-04	3.39E-04	[6,8]
	Decision–procedure transfer or Decision–step transfer	5.62E-03	4.13E-03	7.47E-03	[6,8]
	Decision–detection	6.22E-05	3.28E-05	1.18E-04	[6,8]
	Decision–manipulation	1.96E-03	1.12E-03	3.38E-03	[6,8]
	Execution–single discrete manipulation or Execution–external communication	1.84E-03	1.20E-03	2.79E-03	[6,8]
	Execution–single continuous manipulation	1.53E-02	6.47E-03	3.19E-02	[6,8]
	Execution–dynamic manipulation	1.49E-02	7.51E-03	2.82E-02	[6,8]
	Execution-local discrete manipulation	5.00E-03	1.00E-03	2.50E-02	[10]
	Execution-local dynamic manipulation	1.00E-02	2.00E-03	5.00E-02	[10]
PSFM for transition	Complexity of required task	3	2	10	[6,8]
	Subjective stress	5	2	10	[6,8]
	Complexity of human–machine interface	3	1	5	[6,8]
	Procedure quality	5	3	20	[6,8]
	Support function of computer-based procedure	2	1	3	[6,8]
	Independent reviewer	3	1	5	[6,8]
	Crew dynamics	1	1	2	[6,8]
	Communication level	2	1	3	[6,8]
	Training level	5	3	20	[6,8]
	Career-experience level	5	3	20	[6,8]
PSFM for execution	Complexity of required task	3	2	10	[6,8]
	Subjective stress	5	2	10	[6,8]
	Complexity of human–machine interface	5	2	20	[6,8]
	Procedure quality	5	3	20	[6,8]
	Support function of computer-based procedure	3	1	5	[6,8]
	Independent reviewer	3	1	10	[6,8]
	Crew dynamics	1	1	2	[6,8]
	Communication level	2	1	5	[6,8]
	Training level	3	2	5	[6,8]
RM	Review after shift change	0.0164	0.0082	0.0328	[10]
	Review after procedure completion	0.05	0.018	0.14	[10]
	Advisor's monitoring–first check	0.5	0.25	1	[10]
	Advisor's monitoring–second check	0.14	0.04	0.5	[10]

	Step reviewing result	0.5	0.25	1	[10]
FPtp	FPtp	$1-\Phi[\ln(TR)/0.3403]$	$1-\Phi[\ln(TR)/0.2766]$	$1-\Phi[\ln(TR)/0.4248]$	[5]

II.B. Statistical Distribution Fitting

Table III shows the means of HEP, FPtp, and FPce calculated from 10,000 Monte Carlo samples. Among the 40 scenario cases, FPtp was calculated higher in 18 cases, and FPce was superior in the remaining 22 cases. We compared which statistical model best explained the distributions of HEP values among Weibull, normal, lognormal, exponential, and beta distributions. The results of comparing the goodness-of-fit using the Bayesian information criterion (BIC) and Akaike information criterion (AIC) measures revealed that the lognormal distribution provided models that best explained the HEPs in all cases. This is because most of the method-dependent parameters of EMBRACE follow the lognormal distribution.

TABLE III. Mean values of the simulation samples and estimates for lognormal distributions

Scenario ID	HEP mean	FPtp mean	FPce mean	*mu*	*sigma*	exp (*mu*)	Error factor
1	3.12E-02	1.36E-03	2.98E-02	−3.7969	0.807401	0.02244	3.77415
2	3.34E-03	1.00E-06	3.34E-03	−5.80472	0.45193	0.003013	2.10313
3	5.10E-03	1.04E-03	4.06E-03	−5.61288	0.796492	0.003651	3.70702
4	6.43E-03	6.43E-03	1.00E-06	−5.64835	1.09252	0.003523	6.0327
5	5.70E-03	1.13E-03	4.58E-03	−5.25482	0.34077	0.005222	1.75166
6	4.13E-02	1.72E-02	2.41E-02	−3.25275	0.346237	0.038668	1.76749
7	2.24E-01	1.84E-01	3.99E-02	−1.51491	0.189006	0.219827	1.36467
8	2.06E-02	1.00E-06	2.06E-02	−4.04016	0.557961	0.017595	2.50389
9	5.40E-05	1.00E-06	5.30E-05	−10.1841	0.84808	3.78E-05	4.03535
10	1.22E-02	1.43E-03	1.07E-02	−4.45038	0.233364	0.011674	1.46797
11	4.36E-01	2.57E-01	1.80E-01	−0.86441	0.257481	0.4213	1.52738
12	8.84E-02	1.15E-03	8.73E-02	−2.63458	0.644101	0.071749	2.88506
13	1.90E-01	1.84E-01	6.10E-03	−1.67613	0.16998	0.187097	1.32262
14	1.84E-01	1.84E-01	3.30E-05	−1.70744	0.174115	0.181329	1.33165
15	2.56E-02	2.56E-02	2.00E-06	−3.87966	0.653845	0.020658	2.93168
16	1.70E-05	1.00E-06	1.60E-05	−11.4394	0.942451	1.08E-05	4.71304
17	1.86E-03	1.00E-06	1.86E-03	−7.14578	1.306375	0.000788	8.57617
18	6.42E-03	6.30E-03	1.19E-04	−5.59127	1.038492	0.00373	5.51968
19	3.84E-04	1.00E-06	3.83E-04	−8.75841	1.324959	0.000157	8.84239
20	4.64E-03	1.11E-03	3.54E-03	−5.5471	0.528738	0.003899	2.38637
21	5.00E-01	5.00E-01	4.20E-05	−0.69306	0.000108	0.500042	1.00018
22	1.25E-03	1.00E-06	1.25E-03	−7.19002	1.001934	0.000754	5.19752
23	2.27E-01	2.26E-01	9.71E-04	−1.48954	0.13208	0.225477	1.24268
24	3.48E-03	2.80E-03	6.73E-04	−6.25344	0.988996	0.001924	5.08807
25	1.15E-03	1.15E-03	7.00E-06	−8.41806	1.74344	0.000221	17.6011
26	2.62E-01	2.57E-01	4.59E-03	−1.34527	0.108128	0.26047	1.19467
27	2.49E-02	2.43E-04	2.46E-02	−3.73083	0.26744	0.023973	1.55261
28	6.07E-03	1.60E-04	5.91E-03	−5.13759	0.189119	0.005872	1.36493
29	2.42E-01	1.84E-01	5.82E-02	−1.43336	0.173711	0.238506	1.33077
30	2.18E-03	1.00E-06	2.18E-03	−6.49762	0.861451	0.001507	4.12508
31	6.49E-03	6.48E-03	1.20E-05	−5.64347	1.089725	0.003541	6.00503
32	1.12E-04	1.00E-06	1.11E-04	−9.47932	0.869753	7.64E-05	4.18181
33	6.94E-02	1.00E-06	6.94E-02	−2.79994	0.513144	0.060814	2.32593
34	5.30E-02	2.55E-02	2.74E-02	−3.14204	0.619842	0.043194	2.7722
35	5.77E-03	1.00E-06	5.77E-03	−5.52182	0.845858	0.003999	4.02062
36	1.09E-04	8.30E-05	2.70E-05	−10.5947	1.0199	2.5E-05	5.35342
37	5.43E-02	1.68E-02	3.75E-02	−3.05301	0.522682	0.047217	2.36272
38	2.30E-01	2.27E-01	3.35E-03	−1.47787	0.131956	0.228123	1.24243

39	2.47E-01	2.26E-01	2.10E-02	−1.40508	0.130892	0.245347	1.24026
40	2.60E-02	2.59E-02	7.20E-05	−3.86554	0.657314	0.020952	2.94845

The parameters when fitting the HEP distribution to the lognormal distribution are thus shown in the fifth and sixth columns of Table III. The exponentiated *mu* shown in the seventh column indicates the median of the HEP estimated by the fitted lognormal distribution. The last column presents the error factor values according to the lognormal distribution.

III. DISCUSSION ON THE CHARACTERISTICS OF UNCERTAINTY BOUNDS

The characteristics of the parameter uncertainty bounds of HEPs can be discussed based on the relationship between exponentiated *mu* and error factor. A scatter plot of the exponentiated *mu* and error factor can be depicted as in Fig. 2. Here, the blue diamonds indicate cases where FPtp is higher than FPce, and the green triangles indicate cases where FPce is higher than FPtp. By examining Table III and Fig. 2, the uncertainty bounds of HEP can be said to have the following characteristics. First, when FPtp exceeds FPce, a typical trend of the uncertainty bounds of FPtp is observed. Table IV shows the relationship between FPtp values and their error factors presented in the previous report. Most blue diamonds in Fig. 2 are coincident with Table IV. For example, scenario ID 25 has an error factor of HEP higher than 17, which is consistent with the third row in Table IV. On the other hand, for ID 36, the error factor is not high even though the HEP is low. This can be attributed to the fact that FPce also affects the error factor because FPtp and FPce have similar values.

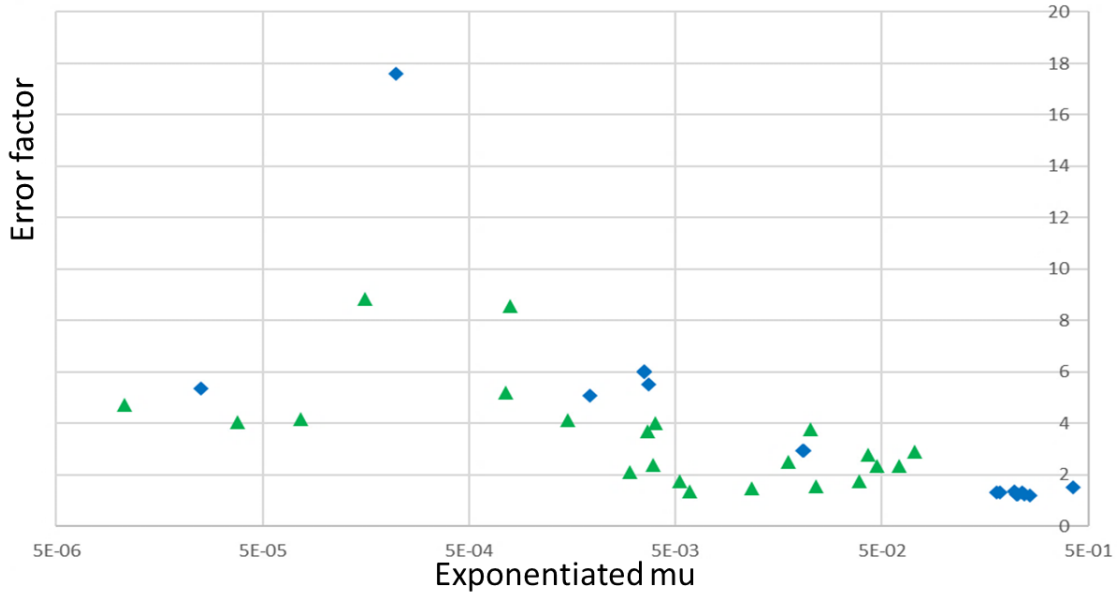

FIGURE 2. Scatter plot between exponentiated *mu* (x-axis) and error factor (y-axis).

TABLE IV. Uncertainty bound rule for FPtp in [5]

FPtp range	Error factor
0.5 <= FPtp	1
0.05 <= FPtp < 0.5	2
0.01 <= FPtp < 0.05	3
0.006 <= FPtp < 0.01	4
0.003 <= FPtp < 0.006	5
0.001 <= FPtp < 0.003	7.5
1.0E-4 <= FPtp < 0.001	17
1.0E-5 <= FPtp < 1.0E-4	40
FPtp < 1.0E-5	90

Second, when FPce is superior to FPtp, the error factor is found to have a value between 2 and 10. It is observed that the magnitude of the error factor is influenced not only by the dimensions of the HEP or FPce but also by the quantity of primitive tasks evaluated, the PSF multipliers applied, or the recovery multipliers considered. When the number of primitive tasks, the number of negative PSF states, and the number of recovery factors are noted as *a*, *b*, and *c*, respectively, $a*(b+1)*(c+1)-2$ could be a measure for the number of the component variables included (note that this scale adds 1 to *b* and *c* to avoid cases where the formula produces 0 when *b* and *c* are 0). Figure 3 shows the correlation between the variable number measure and the magnitude of the error factor. In general, it is understood that as the number of component variables increases or the HEP diminishes, the error factor escalates.

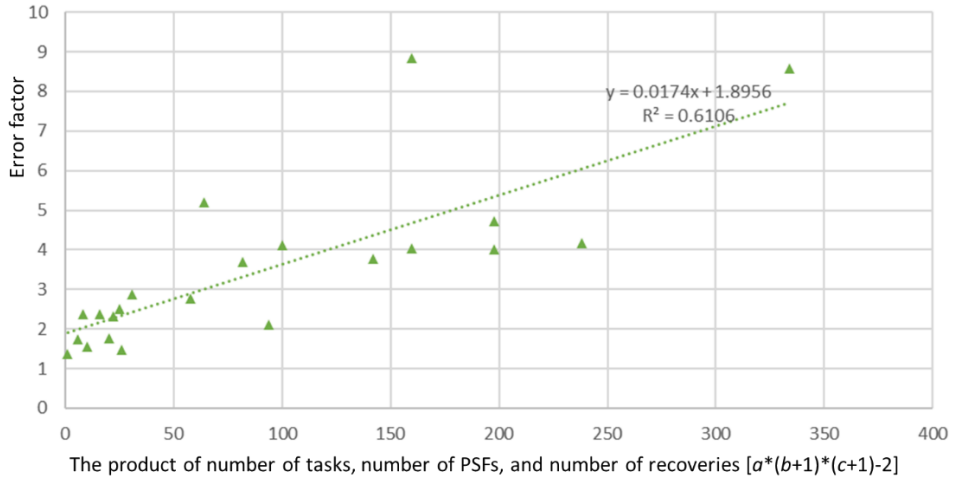

FIGURE 3. Scatter plot between the product of number of tasks included, number of PSFs having a negative state, and number of recoveries applied (x-axis), and error factor (y-axis).

Considering the trend of the error factor presented in Fig. 2, it is interpreted that the error factor determination rule according to the HEP range proposed in [2] (refer to Table V) conservatively explains the parameter uncertainty bound of HEP overall. However, it is difficult to estimate the parameter uncertainty of HEPs smaller than 1.0E-03. In particular, additional research is needed regarding the fact that an FPtp lower than 1.E-03 has a high error factor.

In addition, this study suggests that the determination rule in Table V can be modified to predict the uncertainty bounds more accurately. Since the trend of error factors varies slightly depending on whether FPtp or FPce is more dominant within HEP, different rules can be applied depending on their dominance. For example, the error factor of FPce can be anticipated based on the FPce range, as seen in Table VI. Therefore, after identifying the factor that has a greater impact on HEP between FPtp and FPce, HRA practitioners can employ either Table IV or VI as the rule for determining the error factor.

TABLE V. Uncertainty bound rule for HEP proposed in [2]

HEP range	Error factor
0.5 <= HEP	1
0.03 <= HEP < 0.5	3
0.01 <= HEP < 0.03	4
0.006 <= HEP < 0.01	5
0.001 <= HEP < 0.006	7
HEP < 0.001	10

TABLE VI. Uncertainty bound rule for FPce proposed based on Fig. 2

FPce range	Error factor
0.5 <= FPce	1
0.07 <= FPce < 0.5	2
0.03 <= FPce < 0.07	3
0.001 <= FPce < 0.03	4
FPce < 0.001	10

IV. CONCLUSION AND FUTURE WORKS

This study extended the Monte Carlo analysis developed in [2] to generate samples additionally considering the distributions of component parameters related to local manipulations and recovery behaviors and discussed parameter uncertainty rules that can apply to the results of HRA. Since many component parameters are mostly represented by lognormal distributions [2,5,6,11], it seems statistically appropriate to interpret HEP uncertainties with lognormal models. Therefore, the results of this paper reverified that the determination rule proposed in [2] conservatively describes the distribution of error factors with the assumption that simulated HEPs follow lognormal distributions. That is, it is judged that the results of Table V provide a reasonable approximation according to the parameter uncertainty rule of the EMBRACE method. For a more precise estimation, combining Table IV and Table VI can be a beneficial alternative by identifying which factor more significantly contributes to HEP among FPtp and FPce. These suggestions are believed to be realistic and pragmatic because a lot of human performance times are described with lognormal distributions [11] and because HEPs in existing PSA models are often assumed to be lognormally distributed with their uncertainties expressed using error factors. However, it should also be noted that HRA methods can have different distributions for uncertainty assessments depending on the purpose of the HRA application or the combination with a PSA model. In addition, more evidence should be generated to gain a clearer understanding of parameter uncertainty calculations through additional data collection and collaboration with HRA/PSA practitioners.

It is noted that this study used exponentiated *mu* to scrutinize the tendency of the error factor. The exponentiated *mu* implies the median value of HEP, which may differ from the mean value. In particular, low HEP values are expected to have a large difference between the median and the mean. We believe that additional research is needed on the accuracy of parameter uncertainty estimation in such cases.

ACKNOWLEDGMENTS

This work was supported by the Nuclear Safety Research Program through the Korea Foundation of Nuclear Safety (KoFONS) using a financial resource granted by the Nuclear Safety and Security Commission (NSSC) of the Republic of Korea (No. 2106054).

REFERENCES

[1] R. L. BORING, “Fifty years of THERP and human reliability analysis,” *INL report,* No. INL/CON-12-25623. Idaho National Lab.(INL), Idaho Falls, ID (United States), (2012).
[2] Y. KIM, J. KIM, and D. S. KIM, "Estimating parameter uncertainty bounds of human error probability using Monte Carlo simulation," *Annals of Nuclear Energy*, 211, 111024, (2025).
[3] EPRI, “Practical guidance on the use of probabilistic risk assessment in risk-informed applications with a focus on the treatment of uncertainty”, *EPRI report,* 1026511, (2012).
[4] US NRC, “Guidance on the Treatment of Uncertainties Associated With PRAs in Risk-Informed Decisionmaking,” *NUREG-1855, Revision 1*. Office of Nuclear Regulatory Research, US Nuclear Regulatory Commission (2017).
[5] Y. KIM, J. KIM, J. PARK, S. Y. CHOI, S. KIM, W. JUNG, H.E. KIM, & S. K. SHIN, “An HRA Method for Digital Main Control Rooms—Part I: Estimating the Failure Probability of Timely Performance,” *KAERI technical report*, KAERI/TR-7607/2019, (2019).
[6] Y. KIM, J. KIM, J. PARK, S. Y. CHOI, & S. H. KIM, “An HRA Method for Digital Main Control Rooms-Part II: Estimating the Failure Probability Due to Cognitive Error,” *KAERI technical report*, KAERI/TR-8065/2020, (2020).
[7] E. Zio, *Monte carlo simulation: The method." The Monte Carlo simulation method for system reliability and risk analysis.* London: Springer London, (2012).
[8] Y. KIM, “Estimate Comparison of Human Reliability Regression Models in Differently Classified Human Errors,” *ASRAM2022 (Asian Symposium on Risk Assessment and Management 2022),* November, Daejeon, Korea, (2022).
[9] Y. KIM, “Expert elicitation for estimating PSF effects on HEPs in computer-based control rooms,” *29th European Safety and Reliability Conference.(ESREL 2019)* (2019).
[10] A.D. Swain and H.E. Guttmann, “Handbook of human-reliability analysis with emphasis on nuclear power plant applications,” *NUREG/CR-1278; SAND-80-0200*, Sandia National Lab. (SNL-NM), Albuquerque, NM (United States) (1983).
[11] Y. KIM and W. S. KIM. "Which distribution best describes human performance time." *In Transactions of the Korean Nuclear Society Autumn Meeting*. (2023).

ASRAM2025
www.asram2025.org
Asian Symposium on Risk Assessment and Management 2025
Pattaya, Thailand, 27 – 29 August 2025

COMPARISON OF METHODOLOGICAL CHARACTERISTICS BETWEEN EMBRACE AND THE EPRI HRA METHODOLOGY: CASE STUDY ON CRITICAL OPERATOR ACTIONS IN AN ADVANCED CONTROL ROOM

Jaewhan Kim[1], Yochan Kim[2]

[1] *KAERI: 111, Daedeok-daero 989Beon-gil, Yuseong-gu, Daejeon, Republic of Korea, 34057, jhkim4@kaeri.re.kr*
[2] *KAERI: 111, Daedeok-daero 989Beon-gil, Yuseong-gu, Daejeon, Republic of Korea, 34057, yochankim@kaeri.re.kr*

EXTENDED ABSTRACT

With the modernization of nuclear power plant control rooms, advanced digital interfaces significantly impact operator performance. Human reliability analysis (HRA) methodologies must account for these changes to accurately assess human error probabilities and the influence of computerized systems. Two HRA methodologies, EMBRACE (Empirical data-Based crew Reliability Assessment and Cognitive Error analysis) and the EPRI HRA approach, incorporate digital aspects into reliability assessment. EMBRACE integrates empirical operator performance data and a cognitive error model, while EPRI HRA applies three HRA methods such as the Cause-Based Decision Tree Method (CBDTM), Human Cognitive Reliability/Operator Reliability Experiments (HCR/ORE), and Technique for Human Error Rate Prediction (THERP) to quantify human reliability.

The selected human action for a case study, feed and bleed operation, is evaluated under two distinct event scenarios: (1) loss of all feedwater (LOAF) following loss of main feedwater (LOFW) and (2) LOAF following a small loss of coolant accident (SLOCA). Step-by-step analyses of human error probabilities (HEPs) and methodological evaluations are conducted, highlighting key differences in cognitive error modeling, task structuring, and time reliability estimation.

EMBRACE quantifies human reliability using two primary components: (1) Failure Probability due to Time Performance (FPtp) – Represents the likelihood of exceeding the time available for task completion. FPtp is calculated based on log-normal distribution modeling of operator performance time. (2) Failure Probability due to Cognitive Error (FPce) – Evaluates cognitive errors at each procedural step, integrating performance shaping factors (PSFs) such as task complexity, stress levels, and human-machine interface challenges. FPce derives primitive error probabilities (PEPs) using structured procedural analysis.

EPRI HRA methodology applies multiple techniques to estimate human error probability: (1) CBDTM – Evaluates cognitive errors by categorizing operator failures in plant information processing and procedural adherence. (2) HCR/ORE – Uses empirical data for time-reliability correlations, assessing probability based on response time constraints. (3) THERP – Quantifies execution errors using human error rate data under varying conditions of complexity and stress.

Table I shows the results of EMBRACE and the EPRI HRA approach for the feed and bleed operation at two different event scenarios. For the ‘Case 1: Feed and bleed operation at a LOFW sequence’, the HEP from EMBRACE is 1.45 times larger than the one from the EPRI approach. For the ‘Case 2: Feed and bleed operation at a SLOCA sequence’, the HEP from the EPRI approach is 25.8 times larger than the one from EMBRACE. Even though the underlying fundamentals of two methods are different from each other, the main contributions to each Case from each method can be identified as follows.

- In Case 1, the main contributions by the EMBRACE FPce are multiple procedure and step transitions required at the selection of an appropriate response procedure. The main contribution by the EPRI CBDTM is the decision logic misinterpretation that could be arising from the decision logic for judging an unsatisfied condition of the safety function. For time reliability estimation, the EMBRACE FPtp provides a somewhat significant level of HEP, but the EPRI HCR/ORE provides a negligible level of HEP. This difference between two methods comes from the difference in the time span that each method takes it into account in the lognormal time reliability equation. The EMBRACE FPtp considers the total time covering both cognition and execution explicitly in estimating failure probability due to time performance, but the EPRI HCR/ORE primarily focuses on cognition time in estimating the time available and time required parameter.

- In Case 2, the main contributions by the EMBRACE FPce include the application of the situation interpreting (SI) task type to the critical steps requiring a high level cognitive activity, in addition to multiple procedure transitions. The main contribution by the EPRI CBDTM is similar to the Case 1. For the part of time reliability estimation, two methods provide highly different results. The EMBRACE FPtp provides a relatively lower level of HEP compared to the one estimated by the EPRI HCR/ORE equation, which provides a very high level of HEP. The reason for this difference is that the scenario considered in the Case 2 shows a very peculiar characteristics in event progression. For this kind of a peculiar case of time response, the EMBRACE FPtp provides specific guidance on how to determine the actual cue to be used in the time reliability estimation, while the application of the EPRI HCR/ORE equation as is given in the original guidance for the CP2 cue-response type leads to take very long time required for cognition.

TABLE I. Comparison of HEPs between EMBRACE and the EPRI HRA approach

HFE and Event Scenario	HEP from EMBRACE	HEP from the EPRI HRA
Case 1: Feed and bleed operation at a LOFW sequence	1.09E-2	7.50E-3
Case 2: Feed and bleed operation at a SLOCA sequence	1.19E-2	3.07E-1

The comparative case study identifies methodological differences influencing human reliability estimation:

- Cognitive Modeling: EMBRACE integrates structured procedural analysis, mapping individual primitive error probabilities along the procedural path. EPRI CBDTM applies rule-based errors using predefined decision trees.

- Time Reliability Estimation: EMBRACE FPtp explicitly considers both cognitive and execution time within a log-normal framework, while EPRI HCR/ORE primarily models cognitive response time, potentially yielding high failure probabilities in a peculiar scenario case.

- Procedural Transition Complexity: EMBRACE accounts for transitions between procedures and steps explicitly, reflecting computer-based procedure interface design characteristics. EPRI CBDTM focuses on isolated procedural errors without explicitly modeling step transitions.

From the applicability point of view, two methods depend on the analysts' knowledge and expertise on the operators' cognitive activities as well as procedural contents. In order to facilitate the analysts' identification of critical procedure steps and primitive task types for EMBRACE, a computer software is being developed.

ACKNOWLEDGMENTS

This work was supported by the Nuclear Safety Research Program through the Korea Foundation Of Nuclear Safety (KoFONS) using a financial resource granted by the Nuclear Safety and Security Commission (NSSC) of the Republic of Korea (No. 2106054).

REFERENCES

[1] Y. Kim, et al., *An HRA method for digital main control rooms – Part I: estimating the failure probability of timely performance*, KAERI/TR-7607/2019, KAERI, Daejeon, Republic of Korea (2019).
[2] Y. Kim, et al., *An HRA method for digital main control rooms – Part II: estimating the failure probability due to cognitive error*, KAERI/TR-8065/2020, KAERI, Daejeon, Republic of Korea (2020).
[3] J. Kim and Y. Kim, *Application and review of regulatory-purposed human reliability analysis method for digitalized MCRs*. KAERI/TR-10419/2024. KAERI, 2024.
[4] G. W. Parry, et al., *An approach to the analysis of operator actions in probabilistic risk assessment*, EPRI TR-100259, Palo Alto, California (1992).
[5] J. Julius, et al., *Human reliability analysis for digital environments: Preliminary guidance on HRA data collection, qualitative analysis and quantification*, EPRI TR-3002029331, Palo Alto, California (2024).
[6] W. Jung, et al., "HuREX – A framework of HRA data collection from simulators in nuclear power plants," *Reliability Engineering and System Safety*, 194, 106235 (2020).
[7] A. Swain and H. Guttmann, Handbook of human reliability analysis with emphasis on nuclear power plant applications, NUREG/CR-1278, Sandia National Laboratories, Albuquerque, New Mexico (1983).

ASRAM2025
www.asram2025.org
Asian Symposium on Risk Assessment and Management 2025
Pattaya, Thailand, 27 – 29 August 2025

Study on Human Reliability Assessment for MCR and RSS Switching Switch Configuration Scheme

Zhihui Xu[1], Siqi Jin[1], Huaqing Peng[1], Peng Wang[2]

1.State Key Laboratory of Nuclear Power Safety Technology and Equipment, China Nuclear Power Engineering Co., Ltd., Shenzhen, Guangdong, 518172, China
2.Taishan nuclear power joint venture Co., Ltd., Taishan, Guangdong,529200, China

ABSTRACT

In order to avoid the failure of MCR/RSS switching function caused by the failure of single MCR/RSS switch, MCR/RSS switch usually adopts redundant design and multi-position arrangement. This paper presents a specific case of human reliability assessment of nuclear power plant task, and systematically evaluates whether the operator can quickly evacuate to RSS and complete the switching operation from the perspective of human engineering. This paper provides a beneficial attempt for the overall assessment of human risk of specific personnel tasks, and puts forward reasonable opinions on the improvement of design scheme, which is convenient for modeling and iterative consideration with PSA model.

Keywords: Main control room, Remote shutdown station, Human reliability analysis, Human Factor Engineer

I. INTRODUCTION

The Main Control Room (MCR) provides centralized and effective supervision of the nuclear power plant under all operational conditions. It ensures the safe operation of nuclear power plant and can take measures to maintain its safety or return it to a safe state after experiencing a design basis accident. The Remote Shutdown Station (RSS) is an auxiliary control point that is physically and electrically separated from the MCR. The RSS is equipped to offer sufficient monitoring signals and operational capabilities, allowing the nuclear power plant to achieve a safe shutdown state and monitor key parameters in case the MCR is unavailable, such as during a fire. Operations from the MCR and RSS cannot occur simultaneously; they are interlocked with each other. The control functions switch and interlock between the MCR and RSS are achieved through the MCR/RSS transfer switch.

II. MCR/RSS SWITCHING SWITCH CONFIGURATION SCHEME

II.A. MCR/RSS Switching Switch Configuration

The MCR/RSS switching switch adopts mutually independent multi-contact models, ensuring that a single MCR/RSS switching switch signal can be independently connected to instrumentation and control systems and remain consistent with their total number of columns. To prevent the failure of a single MCR/RSS switching switch from causing the MCR/RSS switching function to fail, the MCR/RSS switching switch adopts a redundant design. Configuration is designed with three MCR/RSS switching switches, using a 3-out-of-2 voting logic. The MCR/RSS control function switch can be completed as long as any two or all three MCR/RSS switching switches function properly, as shown in Figure 1. The nuclear power plant normally operates in MCR mode. If an operator completes the MCR/RSS switching operation, the system enters RSS mode, and personnel in both MCR and RSS are informed through specific alarm signals.

II.B. MCR/RSS Switching Switch Configuration

Three MCR/RSS switching switches are arranged at three different locations, both inside and outside the RSS. These switches are non-keyed toggles and can be operated directly. Switch 1 is positioned on the panel surface inside the RSS room, covered by a protective shield to prevent inadvertent operations.

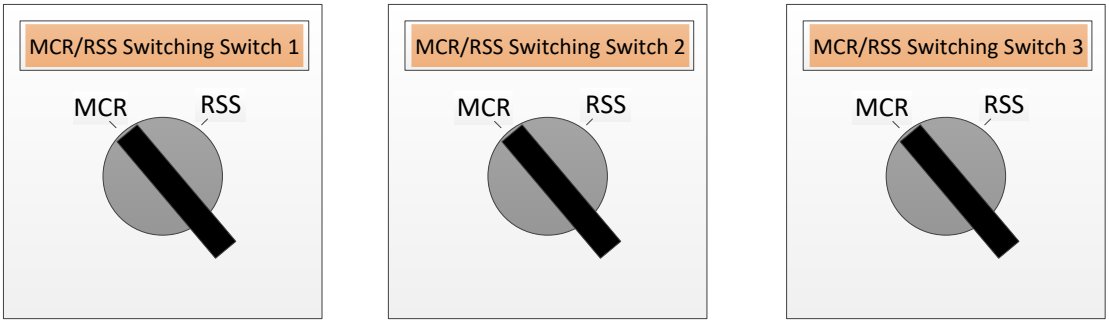

FIGURE 1. Schematic Diagram of MCR/RSS Switching Switch

II.C. MCR/RSS Switching Switch Environment

Adequate operating space is maintained around the three MCR/RSS switching switches, and the rooms they are situated in are ventilated by a ventilation system to provide suitable ventilation conditions, temperature, and humidity. Under normal circumstances, normal lighting is provided by the nuclear island lighting system. In special emergency situations, backup lighting is supplied by the nuclear island emergency lighting system.

III. ANALYSIS OF MCR/RSS SWITCHING OPERATION TASKS

If the environment in the main control room deteriorates for some reason, the operating shift decides to evacuate from the MCR to the RSS. The operator and coordinator simultaneously evacuate from the MCR to the RSS. The operator first switches the three MCR/RSS switchers at three different locations to the "RSS" position according to the guidance of the accident procedure. The coordinator confirms that the three MCR/RSS switchers at three different locations have been switched to the "RSS" position according to the guidance of their own accident procedure. After completing the operation and confirmation of the MCR/RSS switchers, the operator and coordinator also need to log in to the operator workstation in the RSS and activate its control function. The detailed task analysis is shown in Table 1.

Table 1. Main steps of the task and time consumption analysis

No.	Operation steps	Specific actions	Time required (minutes)	Possible failures	Failure consequences	Key steps	Recovery measures
1	Confirm RT	Use RPS0300TO1/0300TO2 (ECP panel)	0.8	1. Forgot to execute 2. Execution failure	RT failure	No	-
2	Carry materials	Take necessary materials and bring them to RSS	0.25	1. Forgot to take out 2. Took wrong materials	-	No	-
3	Decide to evacuate	Based on the deterioration of MCR, decide to evacuate MCR and go to RSS	1.6	1. Insufficient decision-making time	Failed to evacuate in time	No	-
4	Execute switch operation	Go to the chief's office to get the key of the switch protection box	2	1. Forgot to bring the key 2. Took the wrong key	Omitted carrying	Yes	Return to the chief's office to get the key
		Walking to the RSS room	3	-	-	Yes	-
		Open the protection box and put switch 1 in the "RSS" position	0.25	1. Forgot to take the switch	Switching fails	Yes	-

No.	Operation steps	Specific actions	Time required (minutes)	Possible failures	Failure consequences	Key steps	Recovery measures
		Open the protection box and put switch 2 in the "RSS" position	0.25	1. Switching is not in place 2. Forgot to bring the key	Switching fails	Yes	-
		Open the cover and put switch 3 in the "RSS" position	0.25	Switch is not turned on Forgot to take the switch	Switching fails	Yes	-
		OP logs in to the RSS workgroup and confirms activation	0.2	1. Forgot the login password and failed to log in	Failed login	No	Ask colleagues for help

Note: The time required was measured onsite.

IV. MCR/RSS Switching Switch Environment

IV.A. Failure analysis of switching operation

Based on the main task steps in Table 1, the key steps leading to failure in the MCR/RSS switchover are:
a) Taking the keys of the RSS small box (forgetting to take the keys or taking the wrong ones);
b) The switch was not turned in place (the operation was not carried out properly or the switch was missed).
Based on this, an event tree model as shown in Figure 2 and a fault tree model as shown in Figure 3 can be constructed.

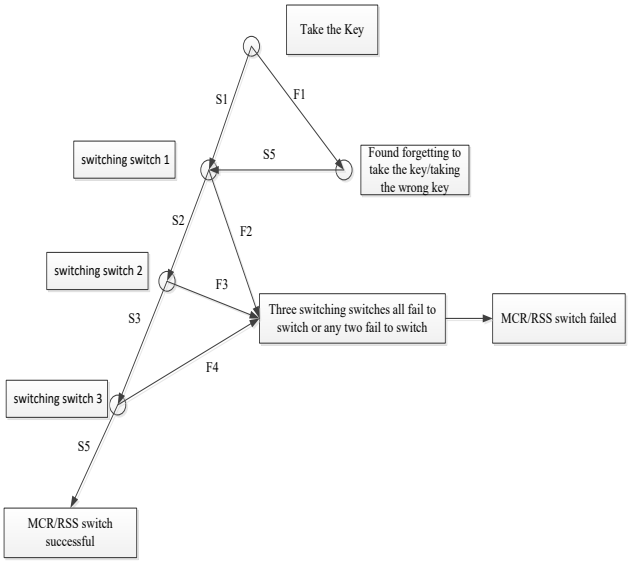

FIGURE 2.MCR/RSS Switching Event Tree

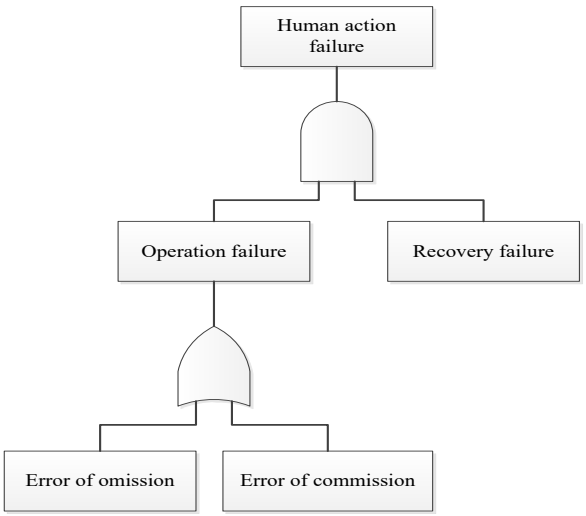

FIGURE 3.The Fault Tree

IV.B. Calculation of switching operation failure

This calculation is based on the failure data in the NUREG/CR 1278 Basic Failure Data Table, as shown in Table 2.

Table 2. Failure probability calculation of key steps

Human-induced events	Potential failures	Omission failures	Execution failures	Recovery failures	HEP
Step 1: Operator retrieves key	Key not retrieved or wrong key retrieved	Probability of key not retrieved: 0.001, according to NUREG/CR 1278, Table 20-8: Item 1	Probability of wrong key retrieved: 0.001, according to NUREG/CR 1278, Table 20-9, analogous to Item 2	Probability of recovery: 0.5 , according to NUREG/CR 1278, Table 20-22 (Item 8)	HEP1 = (0.001 + 0.001) * 0.5 = 1.0E-3
Step 1 recovery: Discovers forgotten key, returns to retrieve it	N/A	N/A	N/A	S5=1, recovery is successful	Opening of protective box reveals forgotten key; time analysis indicates sufficient time to return and retrieve it
Step 2: Executes switch operation 2201CC-	Switch operation fails	Probability of switch operation forgotten: 0.003 , according to NUREG/CR	Switch operation fails to reach target position: 0.003. According	Probability of recovery: 0.1, according to NUREG/CR 1278, Table 20-22 (Item 1)	HEP2 = (0.003 + 0.003) * 0.1 = 6.0E-4

		1278, Table 20-7, Item 1 (procedure with >10 steps)	to NUREG/CR 1278, Table 20-12 (Item 10)		
Step 3: Executes switch operation 3201CC-	Switch operation fails	Probability of switch operation forgotten: 0.003, according to NUREG/CR 1278, Table 20-7, Item 1 (procedure with >10 steps)	Switch operation fails to reach target position: 0.003, according to NUREG/CR 1278, Table 20-12 (Item 10)	Probability of recovery: 0.1 , according to NUREG/CR 1278, Table 20-22 (Item 1)	HEP3 = (0.003 + 0.003) * 0.1 = 6.0E-4
Step 4: Executes switch operation 1201CC-	Switch operation fails	Probability of switch operation forgotten: 0.003, according to NUREG/CR 1278, Table 20-7, Item 1 (procedure with >10 steps)	Switch operation fails to reach target position: 0.003, according to NUREG/CR 1278, Table 20-12 (Item 10)	Probability of recovery: 0.1, according to NUREG/CR 1278, Table 20-22 (Item 1)	HEP4 = (0.003 + 0.003) * 0.1 =6.0E-4

Note: The HEP maintains its original value in table 2, and will be transformed into a median by PSA analysts when introduced into the PSA model.

In the calculation process, NUREG/CR 6883 is referred to, and 1.0E-5 is adopted as the lower limit of human failure probability. Based on the relatively severe fire scenario in the main control room, from the time of discovering fire in the main control room, a total time window of 30 minutes without intervention is taken for the entire evacuation and switch task. The experienced time of about 12 minutes for the temperature or smoke in the main control room to exceed the environmental conditions for people to continue residing due to fire combustion is deducted, i.e., the effective time window from MCR evacuation to RSS is about 30-12=18 minutes. According to the evaluation in Table 1, the whole evacuation task takes about 9 minutes, so the surplus time is 18-9=9 minutes, while the time for returning to take the keys again due to forgetting is 3+2+3=8 minutes. Therefore, after forgetting to take keys, it is allowed to return and take keys again before continuing to perform switch operation.

IV.C. Calculation of switching operation failure

Since the failure of step 1 can be completely recovered, the correlation between steps 2, 3, and 4 is considered for the failure of switching from MCR to RSS. Since the operations of steps 2, 3, and 4 are performed sequentially, the correlation factors and analysis results are shown in Table 3.

Table 3. Correlation analysis between steps

Correlation	Personnel	Time	Location	Clues	Relevance
Step 2 and Step 3	Same	Similar	Different	Different	High
Step 3 and Step 4	Same	Similar	Different	Different	High

Note: In order to quickly interface the HRA calculation results with the PSA model, this table conducted correlation analysis based on the commonly used SPAR-H method's correlation calculation formula, aiming to further examine the HRA calculation results that are more in line with reality.

The criteria for correlation judgment based on NUREG/CR 6883 are considered. After correlation consideration, the failure probabilities of steps 2, 3, and 4 can be corrected as follows:

$$F_2=HEP_2=6.0E\text{-}4 \quad (1)$$

$$F_3=(1+6.04E\text{-}4)/2=0.5 \quad (2)$$

$$F_4=F_3=0.5 \quad (3)$$

The switch failure from MCR to RSS includes the failure of all three buttons to switch, or the failure of any pair of two buttons to switch. The failure probabilities for each sub-scenario are as follows:

a) The probability of all three buttons failing to switch is:

$$HEP_f=F_2*F_3*F_4=6.0E\text{-}4*0.5*0.5=1.5E\text{-}4 \quad (2)$$

b) The probability of steps 2 and 3 failing to switch, while step 4 switches successfully is:

$$HEP_{(2/3)}=F_2*F_3*(1-F_4)=1.5E\text{-}4 \quad (3)$$

c) The probability of steps 2 and 4 failing to switch, while step 3 switches successfully is:

$$HEP_{(3/4)}=(1-HEP_2)*HEP_3*F_4=6.0E\text{-}4*0.5=3.0E\text{-}4 \quad (4)$$

d) The probability of steps 3 and 4 failing to switch, while step 2 switches successfully is:

$$HEP_{(2/4)}=F_2*(1-F_3)*HEP_4=6.0E\text{-}4*0.5*6E\text{-}4=1.8E\text{-}8 \quad (5)$$

Which adopts the human factor failure probability value of HPLV=1.0E-5.
Therefore, the overall mission failure probability is:

$$HEP_t=HEP_f+HEP_{(2/3)}+HE_{P(3/4)}+HEP_{(2/4)}=1.5E\text{-}4+1.5E\text{-}4+3E\text{-}4+1.0E\text{-}5=6.1E\text{-}4 \quad (6)$$

V. CONCLUSIONS

According to the task analysis of the MCR/RSS switching scheme, it can be found that the configuration and layout of the MCR/RSS switch are reasonable. The operation team can refer to the procedures to check important operation steps, the operator evacuation path is clear and accessible, and the implementation location of the switching operation has good ventilation and lighting. The verbal communication between the operator and coordinator is not hindered, and the communication requirements of the operator and coordinator are met. Through the calculation of the probability of task error in switch switching, it can be found that the probability of task error is low, and the operator can reliably evacuate to RSS and complete the switching operation, which will not have an unacceptable impact on the overall safety of the nuclear power plant. At the same time, the improvement suggestions proposed in this article are as follows: it is necessary to add guidance in the operation rules that can clarify the evacuation rules and criteria under fire scenarios.

ACKNOWLEDGMENTS

This paper is supported by State Key Laboratory of Nuclear Power Safety Technology and Equipment.

REFERENCES

[1] Boring R., Boring L. and Gertman, D.I. Atomistic and Holistic Approaches to Human Reliability Analysis in the US Nuclear Power Industry[J]. Safety and Reliability, 2005, 25(2): 21 – 37.
[2] Lee S.W., Kim A.R., Ha J.S. and Seong, P.H. Development of a Qualitative Evaluation Framework for Performance Shaping Factors (PSFs) in Advanced MCR HRA[J]. Annals of Nuclear Energy, 2011, 38:1751-1759.
[3] Ma Zhanguo, Yoshikawa Hidekazu, Nawaz Amjad, Yang Ming. A human–machine interaction design and evaluation method by combination of scenario simulation and knowledge base. Journal of Nuclear Science and Technology, v 55, n 5, p 516-529, May 4, 2018.
[4] Gertman D., Blackman H., Marble J., Byers and Smith C. The SPAR-H Human Reliability Analysis Method, NUREG/CR-6883[R]. Idaho National Laboratory, Washington D.C.:USNRC, 2004.
[5] U.S Nuclear Regulatory Commission. Human Factors Engineering Program Review Model [R]. NUREG-0711, Rev 3, 2012.
[6] Zhihui Xu, Jiemei Zhang, Xuegang Zhang. Study for Reliability Analysis of Operator Response Process under IBLOCA Accident in Nuclear Power Plant [C]// International Symposium on Software Reliability, Industrial Safety, Cyber Security and Physical Protection for Nuclear Power Plant. Springer, Singapore, 2020: 599-609.
[7] Swain A.D. Accident Sequence Evaluation Program Human Reliability Analysis Procedure, NUREG/CR-4772 [R]. Washington D.C.: USNRC,1987.
[8] International Electrotechnical Commission (IEC). Nuclear power plants - Design of control rooms - Functional analysis and assignment[S]. IEC 61839. Geneva: International Electrotechnical Commission, 2000.
[9] International Electrotechnical Commission (IEC). Design for control rooms of nuclear power plants[S]. IEC 60964. Geneva: International Electrotechnical Commission, 1989.
[10] Denham L. Phipps, George H. Meakin, Paul C.W. Beatty. Extending hierarchical task analysis to identify cognitive demands and information design requirements[J], Applied Ergonomics, 2011, 42(5): 741-748.
[11] Ormerod T.C., Shepherd, A. Using task analysis for information requirements specification: the sub-goal template (SGT) method[J]. Diaper, D., Stanton, N.A. (Eds.), The Handbook of Task Analysis for Human- Computer Interaction. Lawrence Erlbaum Associates, 2004, 16: 347-365.

ASRAM2025
www.asram2025.org
Asian Symposium on Risk Assessment and Management 2025
Pattaya, Thailand, 27 – 29 August 2025

Handbook on Training Observation for Qualitative Analysis of The Human Reliability Analysis with Emphasis on Narratives

Kenichi Hayase[1], Daisuke Takeda[2]

[1] *Central Research Institute of Electric Power Industry: 2-6-1 Nagasaka, Yokosuka-shi, Kanagawa 240-0196 JAPAN, hayase@criepi.denken.or.jp*
[2] *Central Research Institute of Electric Power Industry: 2-6-1 Nagasaka, Yokosuka-shi, Kanagawa 240-0196 JAPAN, d-takeda@criepi.denken.or.jp*

ABSTRACT

As a part of the technological improvement of probabilistic risk assessment (PRA) methods, it is necessary to improve human reliability analysis (HRA) that quantitatively assesses the probability of human errors. As a HRA methodology reflecting reality more appropriately, the Nuclear Risk Research Center (NRRC) published "Guide for Qualitative Analysis in The Human Reliability Analysis (HRA) with Emphasis on Narratives" in FY2018 and revised it in FY2020 and FY2023. Of the techniques for collecting information described in the Guide, observations of training and interviews with personnel relevant to tasks to be analyzed are both ways of collecting information from people, which require tips and know-how to efficiently obtain quality sources of information that are necessary for appropriately reflecting realities when performing HRA.

This Handbook covering observation of training systematically compiles tips and know-how for obtaining correct information relevant to the actual situation in a plant, which HRA practitioners can refer to when observing training of the tasks. The tips and know-how are incorporated from knowledge on observing methods obtained from HRA-related literature such as the reports of the Halden Reactor Project and from literature on observing methods in fields such as ergonomics, as well as from hearing survey for experts in observing operator's behavior in simulator experimental studies.

Keywords: Human Reliability Analysis, Narrative, Training, Observation

I. INTRODUCTION

Probabilistic risk assessments (PRAs) need to take into account not only facility and equipment failures but also human failure events (HFEs) which are events happening in situations where operators/other personnel are executing certain tasks and unable to achieve the task objective or fail to accomplish the task, thereby significantly impacting an accident. The probability of failing at such tasks is known as a human error probability (HEP), the assessment of which is required to be made through a human reliability analysis (HRA).

Various HRA techniques have been proposed thus far, but whichever the employed technique may be, the key to HRA that appropriately reflects realities is having a good understanding of actual field conditions for task execution. To this end, it is important to perform a qualitative analysis to develop "Narratives," with regard to plant-specific and accident scenario-specific conditions that affect human performance. As such, the Nuclear Risk Research Center (NRRC) of the Central Research Institute of Electric Power Industry (CRIEPI) developed a guide on HRA qualitative analyses (HRA Guide) [1].

The HRA Guide defines the following three elements comprising narratives for tasks required to respond to the PRA accident scenario:

(1) Task structure information: information regarding plant conditions concerning task structure such as subtasks ("cognitive task" and "execution task") that comprise a task and their relationships to each other, and error recoveries of each subtask.

(2) Time progression information: information regarding plant conditions concerning time such as the time limit for task completion and the time required to perform each of the above subtask.
(3) Performance shaping factors (PSFs) information: information regarding factors that affect personnel in performing each of the above subtask.

The HRA Guide also presents the following three techniques for collecting information to develop narratives:

(a) Review of plant information and scenario consideration results
(b) Field investigation and observation of training
(c) Interviews with relevant personnel

From the aspect of understanding actual field conditions to perform HRA that appropriately reflects realities, the Guide considers items (b) and (c) as important information-collecting methods.

Of the three techniques for collecting information described in the HRA Guide, observations of training and interviews referred to in items (b) and (c) respectively are both ways of collecting information from people. Since time and opportunities for observations of training and interviews are limited, HRA practitioners need tips and know-how to efficiently obtain accurate information concerning actual field conditions.

And, so, NRRC compiled a handbook on interview methods that systematically organizes tips and know-how for conducting interviews with relevant personnel to efficiently obtain accurate information on the actual situation in the field [2][3]. Then, NRRC compiled a handbook on observation of training as well and integrated it with the handbook on interview methods [4].

II. PURPOSE

The purpose of this paper is to present the contents of the handbook on observation of training (hereinafter the "Handbook") systematically compiles tips and know-how for obtaining correct information relevant to the actual situation in a plant, which HRA practitioners can refer to when observing training of the tasks. The tips and know-how of training observation are based on the literature on HRA qualitative analysis of the MTO (Man-Technology-Organisation) program of the Halden Reactor Project[1)] [5][6], which contains many relevant findings, and incorporate findings from training observation methods obtained by reviewing other HRA-related literature as well as literature on ergonomics methods of behavioral observations. In addition, findings about behavior observation interviewed from researchers of Norway's Institute for Energy Technology (interview date: September 2, 2022), who are experienced in observing operator behavior in simulator experiments for operators[2)], will be incorporated.

III. TRAINING OBSERVATION METHODS

Training observation targets operator training using training simulators and worker training for field operations. HRA practitioners visit the training center or plant to attend the training of the task to be assessed and observe operator and worker behavior such as cooperation, communication methods and use of procedure manuals. If necessary and possible, questions are asked after the training. This Q&A session helps verify PSF (Performance Shaping Factors) which affect behavior and decision making behind the behavior.

IV. Preparation of Training Observation

IV.A. Preparing resources and other materials used in interviews

(1) Prepare resources to explain an accident scenario and task

[1)] The project has been carried out under the auspices of the Organisation for Economic Co-operation and Development's Nuclear Energy Agency (OECD/NEA). It is an international joint research project for the purpose of safely and reliably operating nuclear power plants and administered by Norway's Institute for Energy Technology.
[2)] Conducted in the MTO program (until 2020) of the Halden Reactor Project and the succeeding Halden HTO (Human-Technology-Organisation) Project (after 2021).

If necessary and possible, ask questions after observing training. If accident scenarios and tasks need to be explained with such questions, prepare resources to explain the following content about the accident scenarios and tasks to relevant personnel [1][6].

- Initiating events, initial conditions for systems and personnel (the status and condition of systems and personnel that have implications for accident scenario progression)
- Task situations (e.g. various constraints in settings where the task is executed)
- Time information (e.g. time limit for tasks)

(2) Prepare resources to be used during training observation and questions to be asked after training observation

Prepare resources that organize the tasks in chronological order (in a format where unclear points can be marked and questions can be noted) so that the training scenario can be followed during the observation.

List up items to be observed and prepare questions to be asked after the training observation by referencing examples of items and content of collected information presented in Chapter 4 of the HRA Guide (examples of items and survey contents pertaining to task structure information, time progression information, PSF information) and examples of evaluations provided in appendices to the HRA Guide [1]. In doing so, it is desirable to cooperate with people with good operation knowledge such as training personnel.

(3) Prepare supplementary resources for the Q&A session after training observation

Based on the documents collected in the "consideration of accident scenario and identification of tasks" phase, prepare materials that may be used as supplemental material to be presented to relevant personnel during the Q&A session after the training observation, such as procedures, relevant photos (e.g. facilities and tools used while tasks are underway), facility layout drawings, and event reports [7][8][9].

If necessary, also create figures and tables that would be helpful for the Q&A session after the training observation [7].

(4) Verify prepared resources and other materials

Verify that the resources and other materials prepared in items (1) to (3) for the Q&A session after the training observation use proper expressions (e.g. accuracy as to equipment name of facility, use of terms that relevant personnel can understand).

When buffer time is not enough for the Q&A session after the training observation, pick essential items that must be asked in the Q&A session [10].

If an HRA practitioner prepared resources and other materials alone, ask individuals such as other members of the HRA team to verify the materials.

(5) Other pre-training observation preparation

Re-verify documents on such topics as design and operation/maintenance management [5][6][11].

From the PRA perspective, re-verify the importance of the tasks that are to be assessed [12]. Understand the content of previous events, if relevant event reports are available [5][6][7].

When holding a Q&A session after the training, understand the terms used in accident scenarios and tasks, and get used to talking about the scenarios and tasks in those terms before the Q&A session [11][13].

IV.B. Arranging training observation

(1) Select observation targets and coordinate the date, time and location of the visit

Request the plant contact to coordinate the date and time to visit the plant or training center so that HRA practitioners can visit according to the schedule of the training that includes the task to be assessed.

Even if the training schedule that includes the task to be observed conflicts with availability, general information can be obtained about operator behavior at the plant to be assessed, use of procedure manuals and interface of the control room by observing other trainings [6][7]. Thus, request coordination of training observation of a different task, as needed, if such information collection is beneficial even if it is training of a different task.

(2) Prepare observation methods

To observe behavior in detail and collect information, prepare videotaping and recording equipment. However, it is necessary to gain consent for videotaping and recording the observation in advance. It is very difficult to observe behavior in detail and take notes during the training without videotaping or recording the observation.

Many HRA practitioners are required as observers if the observation cannot be videotaped or recorded despite observation targets and information to be collected being a wide range. For example, assign an observer dedicated to recording time when focusing on information on the time required for a task, or assign an observer for each operator to be followed when observing multiple operators.

If there is narrative information (e.g. data of time until operators notice signs such as alarms) that is collectable with the training simulator system on the day of the training, request the plant contact to provide such information.

(3) Prepare knowledge on the plant

The more familiar HRA practitioners conducting the observation are with tasks to be assessed, control room, interface and the plant, the more reliable information can be collected through the observation. It is desirable for HRA practitioners with such knowledge to conduct the observation.

It is also beneficial to have training instructors knowledgeable about such information to be present at the training observation and Q&A session after the training observation, so request the plant contact to have training instructors attend the observation if possible.

V. OBSERVING TRAINING

In order to obtain necessary information within the allotted time and in step with the training observation objective, observe trainings while thoroughly bearing in mind the precautions of training observation (see VII. PRECAUTIONS OF TRAINING OBSERVATION). Note that trainings may not necessarily be observed according to the flow described in this Handbook due to conflicts with the training schedule, but in this case, observe trainings according to said flow as much as possible.

(1) Exchange greetings and explain the objective of training observation

Exchange greetings and self-introductions. Also, thank the observed personnel for setting aside time and cooperating with the training observation.

Explain that training observation is very important as a way to understand the actual conditions for HRA appropriately reflecting reality. Also, explain how information obtained through it will be utilized [5][7][14].

(2) Explain the recording methods

Explain how the training observation will be recorded (e.g. videotaped and notes taken) and how the recorded information will be handled.

Before videotaping or recording the observation, gain consent of the relevant personnel subject to training observation [7].

(3) Training observation

Even when videotaping and recording the observation, immediately take notes so that uncertainties and questions that arise during the observation are not forgotten [5][7].

When videotaping and recording the observation, record the time of important events instead of taking notes of everything, so that details can be confirmed with footage and audio later.

Also, it is beneficial to have training personnel accompany the training observation. They may help interpret what is going on in the training or point out operator behavior that might not be noticed by HRA practitioners [5].

(4) Participate in post-training debriefing

By attending the post-training debriefing between the operators and training personnel, HRA practitioners can gain insight on what the operators were thinking when they executed the task [5].

(5) Q&A after training observation

If it is possible to hold a Q&A session after the training observation, agree on the observed content among the observers (HRA practitioners, accompanying training personnel, etc.) beforehand to determine the focus of the questions.

Ask questions that were prepared in advance, and resolve the unclear points and questions that were noted during the observation. It is necessary to resolve the unclear points and questions as much as possible especially if the HRA practitioners cannot meet with the operators again or when the observation is not videotaped or recorded.

PSF (Performance Shaping Factors), which is considered to affect performance, can be confirmed by talking with operators in addition to observing training [5].

If there is interest in decision making, ask in the post-training Q&A session, "What were you thinking in this step?" Also have the operators explain what was happening during the training and how they responded to it, and later ask questions about decision making behind the response to extract the decision-making process.

(6) End training observation

Check with the operators and training personnel if they can be contacted via email or other means in case any clarification or additional information becomes necessary when compiling the results, or in case confirmation of any results is needed [5][7][15].

Thank the personnel for offering their time, and end the training observation.

VI. ORGANIZING TRAINING OBSERVATION RESULTS

Organize the collected information using figures and tables as appropriate [10], and check for any shortcomings or inconsistencies. When verifying information, endeavor to eliminate cognitive biases (see VII.(7) Eliminate cognitive biases) [8].

(1) Consolidate information using figures, tables, etc.

Consolidate the collected information. If the obtained information is complex, organize it using figures and tables [10]. This makes it easier to notice missing information and inconsistencies.

(2) Check for missing information

After the training observation ends, review the obtained information in further detail to check for information that might be missing or needs to be ascertained further [7][15]. If any information is missing, ask the relevant personnel to cooperate in an additional interview, cooperate in an additional training observation or provide information by email or other means.

If the HRA practitioners are not familiar with the tasks to be assessed, it is difficult to record everything that happened during the training observation, If possible, receive a copy of the timeline recording key actions and responses from the training personnel and match it to your own records (e.g. what was happen when a specific PSF was observed) [5].

(3) Check for contradictions in information

Check also for contradictions in the obtained information (e.g. inconsistencies among information obtained from multiple training observations). In the event contradictions are found, work to eliminate them by, for instance, collecting additional information from other relevant personnel for cross-checking [6][10][11][15][16]. As for how the contradictions are eventually addressed, document and record in a clear-cut and objective manner the content of decisions that were made [6][16].

VII. PRECAUTIONS OF TRAINING OBSERVATION

(1) Consider the impact of the observation on the observed personnel

The HRA practitioners conducting the observation may affect the observed personnel such as operators conducting the training [27]. When people become conscious of being observed, they are known to stop behaving normally (e.g. observed personnel try to behave in a way expected by the observer) [14][17].

Observed personnel may also be affected even through indirect observation with videotaping and recording and not just through direct observation by the HRA practitioners [14].

During the observation, HRA practitioners should place themselves where they would not attract attention from the observed personnel as much as possible [18]. When using videotaping and recording equipment, also place them where they would not attract attention from the observed personnel as much as possible.

(2) Pay attention to the impact of fatigue of the observer

Information collected toward the end of the observation tends to be less reliable than information collected early on [18]. Since the HRA practitioners conducting the observation are affected by reduced attention caused by fatigue [14], conduct observation paying close attention to such impact. Pay special attention if the observation takes a long time.

(3) Be careful of observer drift

If the definition of the behavior to be observed is vague, the observer may unintentionally change the observation and recording methods. This is known as observer drift [29].

HRA practitioners should clearly define the behavior to be confirmed (e.g. whether it is 3-way communication when referring to communication) of operators to be observed to confirm their behavior.

(4) Bear in mind the characteristics of indirect observation methods such as taping and recording

Recordings with a video camera are limited to the camera range and recordings with an audio recorder are limited to the microphone recording range, so events that are not videotaped or recorded cannot be analyzed [18][20].

Additionally, selection of the targets to be videotaped or recorded may be affected by cognitive bias as there is room for the subjectivity of the HRA practitioner who will be setting the equipment for such [14].

While indirect observation methods using videotaping and recording lets you repeatedly re-examine the records and transcribe what was spoken, it requires time and cost for such analysis [13][14][17][20]. Use indirect observation methods keeping in mind such time and cost.

(5) Bear in mind that the training objective and HRA objective are not aligned

HRA tries to understand potential errors in the task and their contributing PSF, but training is conducted to acquire necessary skills to succeed in the task [1][6]. HRA practitioners should collect narrative information from training observations bearing in mind such differences. For example, in the post-training Q&A session, training participants may feel discomfort, in some cases, when asked in detail questions that highlight human errors. In such cases, questions need to be asked bearing in mind to create a relaxed atmosphere conducive to conversation [2][3][4].

(6) Use tips and know-how for interviews in the post-training Q&A

In the post-training Q&A session, use tips and know-how for interviews organized in the handbook on interviews [2][3][4].

(7) Eliminate cognitive biases

Similarly to interviews, cognitive bias may occur during a training observation among the HRA practitioners who are the observers. Table I shows specific examples of cognitive bias in training observations.

TABLE I. Examples of cognitive bias that could occur during a training observation

Types of cognitive bias	Description
Confirmation bias	If HRA practitioners have their own hypotheses, thoughts and inferences before an observation, their desire to obtain information that supports them affect information collection during the observation. [14]. [Example] HRA practitioners have their own hypotheses before an observation, so they only focus on behavior that supports such hypotheses and overlook other behavior.
Excessive generalization	It is assumed that there is a common narrative, without considering the differences of the accident scenario and the plant from the previous assessment. It is important to assess in a way that allows for incorporating the current state subject to the current assessment each time [6][16]. [Example] If there are training observations results by HRA practitioners of a previous task similar to the task to be observed this time, differences in operator behavior may be overlooked during the observation even if there are any, because HRA practitioners do not pay attention to them thinking that it is the same as before.

XIII. CONCLUSIONS

The key to conducting HRA is to understand, through qualitative analysis, situations where tasks that appropriately reflect realities are executed. The NRRC of the CRIEPI has compiled qualitative analysis methods into an HRA Guide to collect plant-specific and accident scenario-specific conditions that affect human performance as “narratives.” Interviews and training observation are regarded as important techniques for collecting information to develop a narrative. As an attachment to the HRA Guide, this Handbook provides tips and know-how for methods of training observation employed when conducting HRAs.

ACKNOWLEDGMENTS

The members participating in the Level 1 PRA Sub-Working Group and Risk Assessment Working Group of the NRRC of the CRIEPI discussed and offered advice and provided a broad range of other considerations.

Researchers of Norway's Institute for Energy Technology cooperated in interviews.

Also, Yuko Hirotsu, former staff of the NRRC, greatly contributed to creating this Handbook.

We would like to express our gratitude to all of them.

REFERENCES

[1] Kirimoto, Y; Nonose, K; Hirotsu, Y; Sasou, K.; Guide for Qualitative Analysis in The Human Reliability Analysis (HRA) with Emphasis on Narratives (FY 2023 Edition). CRIEPI REPORT(NR23005). 2024.
[2] Hayase, K; Hirotsu, Y; Takeda, D. Handbook on Interviews for Qualitative Analysis of The Human Reliability Analysis (HRA) with Emphasis on Narratives. CRIEPI REPORT (NR22011). 2023.
[3] Hayase, K; Takeda, D. Handbook on Interviews for Qualitative Analysis in The Human Reliability Analysis with Emphasis on Narratives. 17th International Conference on Probabilistic Safety Assessment and Management &Asian Symposium on Risk Assessment and Management (PSAM17&ASRAM2024). 2024.
[4] Hayase, K; Takeda, D. Handbook on Interviews and training observation for Qualitative Analysis of The Human Reliability Analysis (HRA) with Emphasis on Narratives. CRIEPI REPORT NR23009. 2024.
[5] Taylor, C. Improving Scenario Analysis for HRA: Handbook of Good Practices. Organisation for Economic Co-operation and Development. Halden Reactor Project, HWR-1145. 2015. (Available on request)
[6] Taylor, C. Improving Scenario Analysis for Human Reliability Analysis. Organisation for Economic Co-operation and Development, Halden Reactor Project, HWR-1120. 2015. (Available on request)
[7] Bye, A., et. al. The Petro-HRA Guideline, Revision 1, Vol.1&2. Institute for Energy Technology, IFE/E-2022/001&2. 2022.
[8] Turner III, D. Qualitative interview design: A practical guide for novice investigators. The Qualitative Report 15 (3). 2010. 754–760.
[9] Wilson, J.R.; Sharples, S. Evaluation of human work fourth edition. CRC Press. 2015.
[10] Motozawa, T.; Takeda, Y.; Nomura, A.; Aonuma, S. Methods of Interviewing the people involved in an accident triggered by Human Error. JR EAST Technical Review No.29. 2009. (In Japanese)
[11] Electric Power Research Institute (EPRI) and US Nuclear Regulatory Commission Office of Nuclear Regulatory Research (USNRC-RES). NUREG-1921 Supplement 1, Final Report, "EPRI/NRC-RES Fire Human Reliability Analysis Guidelines – Qualitative Analysis for Main Control Room Abandonment Scenarios". 2020.
[12] US Nuclear Regulatory Commission (NRC). NUREG-2156, "The U.S. HRA Empirical Study- Assessment of HRA: Method Predictions against Operating Crew Performance on a U.S. Nuclear Power Plant Simulator ". June 2016.
[13] Kirwan, B.; Ainsworth, L.K. A guide to task analysis. Taylor & Francis.1992.
[14] Sharples, S. and Cobb, S. Methods for Collecting and Observing Participant Responses. Evaluation of human work fourth edition. CRC Press. 2015.
[15] Boeing, Maintenance Error Decision Aid (MEDA) User's Guide. 2016.
[16] USNRC. NUREG-2198, "The General Methodology of an Integrated Human Event Analysis System (IDHEAS-G)". May 2021.
[17] Stanton,N. A. Human Factors Methods: A Practical Guide for Engineering and Design 2nd Edition. CRC Press. 2013.
[18] Pershing, J.A., et. al. Observation methods for human performance technology. Handbook of human performance technology: third edition. Pfeiffer. 2006.
[19] Dojo, Y. Chapter 6 Reliability and Validity of Observation Data. Miura, A (Supervisor); Sato, H (Ed.) I see! Psychological Observation Methods. Kitaohji Shobo. 2018. p.74-p.90.
[20] Bisantz, A., et. al. Study and Analysis of Complex Cognitive Work. Evaluation of human work fourth edition. CRC Press. 2015.

ASRAM2025
www.asram2025.org
Asian Symposium on Risk Assessment and Management 2025
Pattaya, Thailand, 27 – 29 August 2025

REVIEW OF MEASUREMENT PROPERTIES FOR THE USE OF INTEGRATED SYSTEM VALIDATIONS

Jinkyun Park[1], Jung Hwan Kim[2]

[1] 989-111 Daedeok-daero, Yuseong-gu, Daejeon, 34057, Republic of Korea, kshpjk@kaeri.re.kr
[2] 989-111 Daedeok-daero, Yuseong-gu, Daejeon, 34057, Republic of Korea, jhkim21@kaeri.re.kr

EXTENDED ABSTRACT

One of the important approaches ensuring the safety of a nuclear power plant (NPP) is to carry out diverse verification and validation activities including integrated system validation (ISV). The underlying idea of the ISV is to make sure that the performance of human operators who have to accomplish safety-critical tasks can be maintained without any degradation during the operation of NPPs. This implies that the development of ISV scenarios that contain representative safety-critical tasks is very important. In addition, it is also crucial to select appropriate measurements that can properly capture the change of human performance observed from ISV scenarios. In this regard, regulatory guidelines of the ISV suggest several dimensions that should be used as criteria for the selection of human performance measurements (i.e., performance measurement criteria). Typical dimensions include (1) Diagnosticity, (2) Sensitivity, (3) Construct validity, (4) Intrusiveness, (5) Reliability, (6) Objectivity, (7) Simplicity, (8) Impartiality, and (9) Resolution [1-3]. Table 1 shows the definition of each property available from existing literature.

TABLE I. Definitions of Nine Properties

ID	Property	Definition
1	Diagnosticity	Measurement should be able to identify the cause of unacceptable human performance.
2	Sensitivity	Measurement should detect the changes in the concept it measures
3	Construct Validity	Measurement should represent what it claims in terms of human performance.
4	Intrusiveness	Measurement should not intervene participants in terms of physical and psychological aspects.
5	Reliability	Human performance should be similar when it is repeatedly measured in an identical condition.
6	Objectivity	Measurement should provide objective information instead of subjective information.
7	Simplicity	Straightforward measurement should be used to make sure of its applicability.
8	Impartiality	Measurement should be equally capable of reflecting good as well as bad performance.
9	Resolution	Measurement should reflect an appropriate level of detail to permit meaningful analysis.

From Table I, it should be noted that the eighth and ninth property (‘Impartiality’ and ‘Resolution’) seem to largely overlap with those of other dimensions. For example, the definition of ‘Impartiality’ is that “Measurement should be equally capable of reflecting good as well as bad performance.” With this definition, it is reasonable to expect that a specific human performance measurement will satisfy impartiality if it can provide a reliable, diagnostic and objective value that is straightforward to understand without any additional knowledge and/or information. Similarly, since ‘Resolution’ mainly focuses on a sufficient level of details, it is possible to say that the ninth property of Table I can be satisfied if its captured value provides diagnostic and sensitive information with a firm technical basis. With these definitions, it is possible to specify detailed explanations that provide practical use cases. In this regard, Table II summarizes practical examples of selective properties. It should be noted that, as the meanings of both ‘Validity’ and ‘Intrusiveness’ seem to be self-explainable, practical examples for these two properties were not explicitly given in Table II.

TABLE II. Practical examples to clarify the characteristics of each property

Property	Practical example
Diagnosticity	C1. Satisfied when the value is obtained through direct observation or expert survey. C2. Satisfied when a human performance measure provides specific standards.
Sensitivity	Time does not satisfy this property since it is difficult to define the exact range (0 to infinity). In contrast, a measure that specifies its range (e.g., 0 to 100) could provide the upper limit for visualizing the change rate of human performance with respect to the change of its value.

Reliability	Satisfied if its value has repeatability.
Objectivity	C1. Satisfied if a human performance measure is based on facts, phenomena, and behavior. C2. Not satisfied if an additional statistical analysis is required to understand the meaning of its value.
Simplicity	C1. Not satisfied when a human performance measure requires further knowledge of nuclear science, ergonomics, or psychology, or special data acquisition methods. C2. Not satisfied when a human performance measure requires special knowledge to understand the measurement results

Based on Tables I and II, it is possible to distinguish the characteristics of a human performance measurement. However, it seems that the definitions of the available dimensions are somewhat controversial because of a lack of detailed information clarifying the performance measurement criteria. Therefore, securing such detailed information would be helpful for practitioners who are responsible for the selection of human performance measurements. For this reason, in this paper, literature available from safety-critical industries such as the nuclear, aviation, and railway sectors were revisited in order to suggest the catalog of common properties with respect to the performance measurement criteria. In order to investigate the appropriateness of Tables I and II, Table III shows classification results for representative workload measurements: (1) Modified Cooper-Harper (MCH) scale, (2) NASA Task Load Index (TLX) and (3) Subjective Workload Assessment Technique (SWAT). From Table III, several insights can be obtained. For example, the characteristics of all measurements are very similar while 'Objectivity' seems to be the common limitation to be resolved. In other words, if the workload of human operators was measured by these three measurements, it is necessary to collect additional information to make up missing property (Objectivity). Accordingly, Tables I and II would be a good starting point to secure relevant human performance data to address diverse human factors issues. It is to be noted that, although many kinds of measurements are available, it is hard to specify a specific measurement that is preferable to a dedicated industrial sector. Indeed, this could be a goof rationale supporting the necessity of Table III that allows us to capture the pros and cons of individual measurement.

TABLE III. Property comparisons for representative workload measurements

Measurement	Diagnosticity		Sensitivity	Reliability	Objectivity		Simplicity	
	C1	C2			C1	C2	C1	C2
Modified Cooper-Harper scale [4]	Yes	N/A	Yes	Yes	No	No	Yes	Yes
NASA Task Load Index [5]	Yes	Yes	Yes	Yes	No	No	Yes	Yes
Subjective Workload Assessment Technique [6]	Yes	N/A	Yes	Yes	No	No	Yes	Yes

ACKNOWLEDGMENTS

This work was supported by Nuclear Safety Research Program grant from the Korea Foundation of Nuclear Safety (KOFONS), funded by the Nuclear Safety and Security Commission of the Republic of Korea (No. RS-2021-KN052610).

REFERENCES

[1] L. Reinerman-Jones, S. Guznov, J. Tyson, A. D'Agostino, N. Hughes, *Workload, situation awareness, and teamwork*, NUREG/CR-7190, United States Nuclear Regulatory Commission, Washington D.C. (2015).

[2] J. M. O'Hara, W. F. Stubler, J. C. Higgins, W. S. Brown, *Integrated system validation: Methodology and review criteria*, NUREG/CR-6393, United States Nuclear Regulatory Commission, Washington, D.C.(1997).

[3] J. M. O'Hara, J. C. Higgins, S. Fleger, P. Pieringer, *Human factors engineering program review model*, NUREG - 0711, Rev. 3, United States Nuclear Regulatory Commission, Washington, D.C. (2012).

[4] M. L. Cummings, K. Myers, S. D. Scott, "Modified Cooper Harper evaluation tool for unmanned vehicle displays," *Proceedings of Conference on Unmanned Vehicle Systems Canada* (2006).

[5] S. G. Hart, "NASA-task load index (NASA-TLX); 20 years later," *Proceedings of the Human Factors and Ergonomics Society Annual Meeting*, Sage CA: Los Angeles, CA, Vol. 50, p. 904-908, SAGE Publications (2006).

[6] G. B. Reid, T. E. Nygren, "The subjective workload assessment technique: A scaling procedure for measuring mental workload," *Advances in Psychology*, Vol. 52, p. 185-218 (1998).

PROPOSALS TO REDUCE HUMAN ERROR PROBABILITY REGARDING THE USE OF PORTABLE EQUIPMENT DURING MULTI-UNIT ACCIDENT RESPONSES

Seong Woo Kang[1*], Jaewhan Kim[1], Ho-Gon Lim[1], Jae Young Yoon[1], Jong Woo Park[1]

[1] *Korea Atomic Energy Research Institute, (34057) 111, Daedeok-daero 989beon-gil, Yuseong-gu, Daejeon, Korea*
** Corresponding author: swkang@kaeri.re.kr*

EXTENDED ABSTRACT

The objective of this study is to make several proposals to reduce human errors on utilizing portable equipment during multi-unit accident responses, ultimately in order to reduce the multi-unit core damage frequency (CDF). For this purpose, several suggestions are made in order to reduce the human error probabilities (HEPs) on using the portable equipment during accidents such as multi-unit accidents and beyond design basis external events (BDBEEs).

To assess the improvement in nuclear power plant (NPP) safety, multi-unit human/organizational reliability analysis (MU-HRA) methodology developed in Korea Atomic Energy Research Institute (KAERI) was used. The developed MU-HRA methodology 1) performs the target human failure event (HFE) sub-task identification using System Theoretic Process Analysis (STPA), 2) simulate off-site workers arrival time estimation using agent-based modeling (ABM), and 3) estimates the HEPs of portable equipment human failure by grouping the HFE sub-tasks into three categories for the HEP estimation: a) diagnostic errors (DEP) in situation assessment, b) communication errors (CEP) during information transfer and response-related instruction activities between organizations and personnel, and c) execution errors (EEP) arising from various individual measures for applying the portable equipment during the BDBEE accident responses. These are shown in Fig. 1 and Eqn. 1, and details of these methodologies are included in [1]-[3].

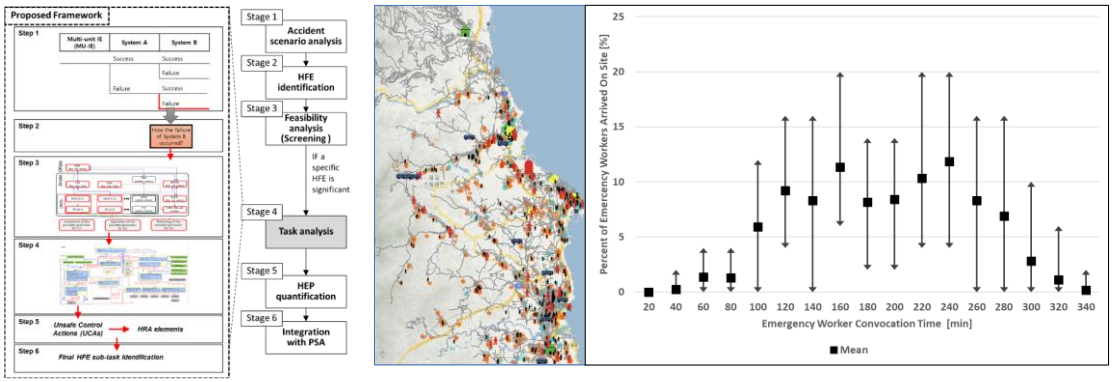

FIGURE 1. Examples of HFE Sub-Task Analysis Framework using STPA and Off-Site Workers Arrival Time Estimation using ABM

$$HEP_{total} = DEP + CEP + EEP \quad (1)$$

The proposals/suggestions to improve accident responses were assessed in a case study based on the east coast nuclear power plant site in Korea. Note that the Korean emergency response guidelines/procedures are not set in stone yet, so the initial condition assumed current state-of-knowledge in Korean portable equipment emergency responses. On behalf of those assumptions, there are five proposals to reduce the HEP regarding the use of portable equipment during multi-unit accident responses.

1) Let the minimum staffing level required to transfer, move, install, and operate the portable equipment during the multi-unit accident response be on site at all times (i.e., no requirement for mobilization of the off-site workers)
2) Operate the arrived off-site workers/personnel at a site-level, not at a twin-unit level (i.e., share the workers at a site-level for the operation of portable equipment).

3) Improve the DC battery capacity and mandatorily set in the procedure the non-essential load shedding to enable the required AC recovery time of 8 hours or more
4) Install fixed and seismic-resistant pipes to more easily connect the portable pumps
5) Minimize the number of portable equipment vehicles for transfer (e.g., reduce from 2~3 trucks/cars into 1)

Preliminary results on the maximum reduction in HEPs for different level of NPP accident (one unit, twin-unit, and site-level) and different earthquake categories (G1, G2, G3, and G4, where higher category means stronger external hazard i.e., earthquake and less means for emergency response) are shown in Fig. 2. Maximum reduction means reduction in HEPs for the units which may not be able to perform full portable equipment emergency response since offsite workers may arrive on time (i.e., no credit for off-site workers). The reason why there is a noticeable drop in HEP reduction between categories G1-G3 versus G4, because G4 is the most extreme external hazard case and thus has highest HEP values regardless of applying the proposed strategies (e.g., having workers on time and doing all those improved strategies may still not have as great of impact for the worst cases of external hazards).

The results and insights from this study can be utilized for other NPP sites to improve their accident responses using portable equipment, by assessing the organizational/human errors required in the multi-unit risk model.

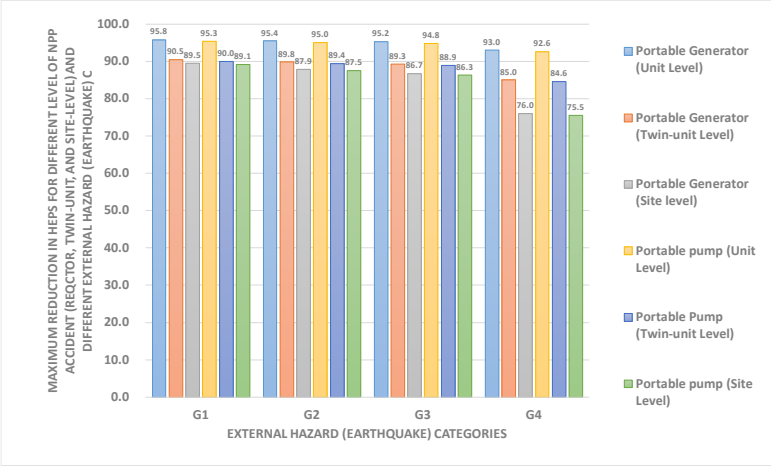

FIGURE 2. Preliminary Results on the Maximum Reduction in HEPs for Different Level of NPP Accident (One Unit, Twin-Unit, and Site-Level) and Different Earthquake Categories (G1, G2, G3, And G4)

ACKNOWLEDGMENTS

This work was supported by the Korea Institute of Energy Technology Evaluation and Planning (KETEP) and the Ministry of Trade, Industry & Energy (MOTIE) of the Republic of Korea (No. 20224B10200050). This research was also supported by the National Research Council of Science & Technology (NST) grant by the Korea government (MSIT) (No. GTL24031-000).

REFERENCES

[1] S.W. Kang, J. Kim, J. Park, J.W. Park, and S.M. Shin, "A Framework to Identify the Catalog of Important Tasks Reflecting Interorganizational Characteristics Regarding the Deployment of Portable Equipment," IEEE Access, **13**, 65690-65703 (2025).
[2] S. W. Kang and J. Park, G. Kim, G. Heo, and S. Jang, "Proposal to Estimate the Mobile Equipment Installation Time during a Multi-unit Accident Management using an Agent-Based Model," 2023 Korean Nuclear Society Autumn Meeting, Gyeongju, Korea, Oct. 26-27 (2023).
[3] J. Kim, S.W. Kang, Y. C. Kim, J. Park, and H.G. Lim, "Multi-unit Human and Organizational Reliability Analysis Method under Various Emergency Organization Structures assuming Staffing Availability," KAERI/TR-10991/2025, Technical Report in Korean (2025).

Technical Session 5 (16:00 - 18:00)	The Port 1, C Floor	Risk and Resilience Engineering and AI-based Risk Assessment, Decision Analysis, Security Analysis, Risk Communication and Policy
		Chair/Facilitator 1: Dr. Kanokrat TIYAPUN, Manager of Research Reactor Center, Thailand Institute of Nuclear Technology (TINT)
		Chair/Facilitator 1: Dr. Kampanart Silva (National Energy Technology Center (ENTEC))
16:00 - 16:20		ID 108: Quantum-Inspired Reinforcement Learning for Binary Decision Diagram Optimization Speaker: Young Ho Chae (KAERI) Contributors: Young Ho Chae (KAERI), Seo Ryong Koo (KAERI)
16:20 - 16:40		ID 135: A Framework to Identify Factors Affecting SMR Acceptance in Thailand Speaker: Ornjira Promsorn (Department of Industrial Engineering, Kasetsart University) Contributors: Ornjira Promsorn (Department of Industrial Engineering, Kasetsart University), Naraphorn Paoprasert (Department of Industrial Engineering, Kasetsart University), Kampanart Silva (ENTEC), Pidpong Janta (ENTEC), Nuwong Chollacoop (ENTEC)
16:40 - 17:00		ID 52: A Study on Evacuation Time Estimation for Offsite Consequence Analysis using Agent-Based Modeling Speaker: Gibeom Kim (Korea Atomic Energy Research Institute (KAERI)) Contributors: Gibeom Kim (Korea Atomic Energy Research Institute (KAERI)), Sung-yeop Kim (Korea Atomic Energy Research Institute (KAERI))
17:00 - 17:20		ID 68: Effectiveness and Practicality of Severe Accident Mitigation Strategies with Uncertainty Considerations Speaker: Jemo Ryu (Chung-Ang University) Contributors: Jemo Ryu (Chung-Ang University), Jaehyun CHO (Chung-Ang University)
17:20 - 17:40		ID 79: Consideration of Levelized Cost of Electricity and Investment Risks of Small Modular Reactors in Emerging Countries Speaker: Kampanart Silva (National Energy Technology Center) Contributors: Kampanart Silva (National Energy Technology Center), Pidpong Janta, Nuwong Chollacoop (National Energy Technology Center)
17:40 - 18:00		ID 47: Evaluation of Kass-Steffey Adjustment for Component Reliability Uncertainty Analysis Speaker: Gyun Seob Song (Chung-Ang university) Contributors: Gyun Seob Song (Chung-Ang university), Man Cheol Kim (Chung-Ang university)

ASRAM2025
www.asram2025.org
Asian Symposium on Risk Assessment and Management 2025
Pattaya, Thailand, 27 – 29 August 2025

Quantum-Inspired Reinforcement Learning for Binary Decision Diagram Optimization

Young Ho Chae[1], Seo Ryong Koo[2]

[1,2] *A Korea Atomic Energy Research Institute, (34057) 111, Daedeok-daero 989Beon-gil, Yuseong-gu, Daejeon, Republic of Korea 34057, yhchae@kaeri.re.kr, srkoo@kaeri.re.kr*

ABSTRACT

Binary Decision Diagrams (BDDs) are fundamental data structures for Boolean function manipulation, but their size depends exponentially on variable ordering—an NP-complete optimization problem. We present a quantum-inspired reinforcement learning (QIRL) algorithm that combines quantum inspired principles with classical optimization to efficiently find near-optimal variable orderings. The algorithm employs four adaptive phases: quantum exploration using superposition states, classical exploitation via Q-learning, pattern-based optimization, and quantum tunneling for escaping local minima. Experimental results on hierarchical dependency and deceptive local minima benchmarks (sizes 32-128) demonstrate performance improvements over traditional sifting and simulated annealing algorithms. These results show the effectiveness of quantum-inspired approaches for combinatorial optimization problems.

Keywords: Binary Decision Diagrams, Quantum-inspired computing, Reinforcement learning, Variable ordering optimization

I. Introduction

Binary Decision Diagrams (BDDs) are widely used data structures for representing and manipulating Boolean functions in various domains including circuit design, formal verification, and reliability analysis [1]. The efficiency of BDD-based algorithms critically depends on the chosen variable ordering, as different orderings can result in exponentially different BDD sizes. Finding an optimal variable ordering that minimizes the BDD size is known to be NP-complete [2], making it a challenging combinatorial optimization problem.

Traditional approaches to BDD variable ordering include static heuristics based on structural analysis (depth-first search, top-down left-right) and dynamic optimization algorithms. The sifting algorithm [3] iteratively improves orderings through local variable repositioning, while simulated annealing applies stochastic optimization principles. While these methods work reasonably well for small to medium-sized problems, they often struggle with larger instances, particularly those with complex dependency structures or deceptive fitness landscapes containing numerous local optima. Jung et al. [4] demonstrated that even specialized algorithms for coherent fault trees face scalability challenges, with BDD size being drastically dependent on variable ordering choices.

Recent advances in quantum computing have inspired new classical algorithms that borrow quantum mechanical principles such as superposition and entanglement [9, 10]. These quantum-inspired algorithms have shown promise in various optimization domains by enabling more effective exploration of solution spaces. Similarly, reinforcement learning has emerged as a powerful paradigm for sequential decision-making problems, learning optimal policies through interaction with the environment [8].

Quantum-inspired reinforcement learning (QIRL) represents a promising direction that combines these two paradigms. Beloborodov et al. [13] recently applied QIRL to the Ising energy minimization problem using a Rescaled Ranked Reward method, achieving strong performance on Max-Cut instances. However, their approach maintains a single quantum state and relies on ranked rewards for escaping local optima. In contrast, our method employs dynamic phase rotations and entanglement groups that continuously learn variable relationships, providing more nuanced control specifically designed for permutation-based problems like BDD ordering.

Other QIRL approaches have focused on different aspects of combinatorial optimization. Khairy et al. [14] optimized QAOA parameters using RL agents, demonstrating generalization from small to large instances. While effective for continuous parameter optimization, BDD ordering requires handling discrete permutation spaces with structural constraints—a challenge we address through our four-phase adaptive framework rather than single-mode optimization. SimCIM by Tiunov et al. [15]

excels at Ising problems through continuous relaxation but lacks the structural awareness needed for maintaining variable relationships throughout BDD optimization.

This paper introduces a novel quantum-inspired reinforcement learning algorithm that specifically addresses the unique challenges of BDD variable ordering optimization. The key innovation lies in maintaining a superposition of multiple variable orderings that evolve through quantum-inspired operations, while using reinforcement learning to guide local optimization decisions. Our approach introduces several novel mechanisms: (1) dynamic phase rotations that encode learned position preferences for each variable, (2) continuously updated entanglement groups that capture and preserve variable relationships, and (3) an adaptive four-phase framework that balances quantum exploration, classical exploitation, pattern recognition, and quantum tunneling based on optimization progress.

II. Problem Formulation and Proposed Method

II.A. BDD Variable Ordering Problem

Given a Boolean function $f:\{0,1\}^n \to \{0,1\}$ over variables $\{x_1, x_2, \ldots, x_n\}$, a BDD is a directed acyclic graph representation where each non-terminal node is labeled with a variable and has two outgoing edges (0-edge and 1-edge), and terminal nodes represent Boolean values [1]. The size of a BDD, measured by the number of non-terminal nodes, depends on the variable ordering $\pi:\{1,2,\ldots,n\} \to \{1,2,\ldots,n\}$, where $\pi(i)$ denotes the position of variable x_i.

The optimization problem seeks to find (1):

$$\pi^* = \arg\min_{\pi \in \Pi_n} |BDD(f,\pi)| \tag{1}$$

where Π_n is the set of all $n!$ possible permutations and $|BDD(f,\pi)|$ denotes the BDD size under ordering π. The exponential size of the search space and the lack of obvious gradient information make this a challenging discrete optimization problem [5].

II.B. Quantum-Inspired State Representation with Phase and Entanglement

Our algorithm maintains a quantum-inspired state representing a superposition of K variable orderings, borrowing concepts from quantum computing (2) [11]:

$$\left|\Psi\right\rangle = \sum_{k=1}^{K} \alpha_k \, e^{i\phi_k} \left|\pi_k\right\rangle \tag{2}$$

where $|\pi_k\rangle$ represents the k-th ordering, α_k is the amplitude with $\sum_{k=1}^{K} |\alpha_k|^2 = 1$, and ϕ_k is the phase factor. When measuring the state, the probability of obtaining ordering π_k is $P(\pi_k) = |\alpha_k|^2$.

Beyond the basic superposition, QIRL maintains two critical quantum-inspired structures:

Phase Rotations: Each variable x_i has an associated phase rotation $\theta_i \in [0, 2\pi]$ that encodes its preferred position in the ordering. These phases are learned from successful orderings using (3):

$$\theta_i^{(t+1)} = \lambda \theta_i^{(t)} + (1-\lambda) \cdot \frac{2\pi \cdot \text{pos}(x_i)}{\text{ordering_length}} \tag{3}$$

where λ is a decay factor (typically 0.8) and $\text{pos}(x_i)$ is the average position of variable x_i in recent successful orderings. This phase information guides the generation of new orderings by suggesting optimal positions for each variable.

Entanglement Groups: The algorithm maintains entanglement sets $\mathcal{E} = \{E_1, E_2, \ldots, E_m\}$, where each E_i contains variables that exhibit strong correlations in high-quality orderings. Variables x_i and x_j are considered entangled if their average proximity in good orderings is below a threshold (4):

$$\text{entangled}(x_i, x_j) = \text{True} \Leftrightarrow \frac{1}{|S|} \sum_{\pi \in S} \left|\text{pos}_\pi(x_i) - \text{pos}_\pi(x_j)\right| < \frac{n}{5} \tag{4}$$

where S is the set of successful orderings. These entanglement groups capture structural relationships and guide both the generation of new orderings and quantum tunneling operations.

II.C. Four-Phase Optimization Framework

Phase 1: Quantum Exploration generates diverse candidate orderings by measuring the quantum state and applying quantum-inspired transformations. The state initialization creates orderings using various patterns, with phase information guiding variable placement. When applying transformations, the algorithm uses learned phase rotations to determine rotation amounts and consulting entanglement groups to preserve learned relationships.

Phase 2: Classical Exploitation employs Q-learning [8] for local optimization. The state space encoding incorporates phase-based position features, using the difference between current and preferred positions (from phase rotations) as part of the state representation. Actions are biased toward moves that align with learned phase preferences.

Phase 3: Pattern-Based Optimization learns and exploits structural patterns from the evaluation history. This phase directly utilizes variable position preferences derived from phase rotations, variable groupings from entanglement relationships, and adjacency strengths between entangled variable pairs. New orderings are constructed by placing variables according to their phase-encoded positions while maintaining entanglement group cohesion.

Phase 4: Quantum Tunneling enables escape from local minima through non-local transformations. The tunneling operations are guided by phase shift transformations that use accumulated phase information to determine optimal rotation amounts, and entanglement-based rearrangements that restructure orderings while preserving learned variable relationships. The intensity of tunneling increases with stagnation duration, but learned relationships are always respected.

II.D. Learning Variable Positions and Relationships

The algorithm continuously updates its understanding of optimal variable positions and relationships:

```
// Update phase rotations for position learning
for each variable xi:
    positions = [position of xi in each good ordering]
    avg_position = mean(positions)
    scaled_position = (avg_position / n) * 2π
    θi = 0.8 * θi + 0.2 * scaled_position

// Update entanglement groups for relationship learning
for each pair (xi, xj):
    proximities = [|pos(xi) - pos(xj)| in each good ordering]
    avg_proximity = mean(proximities)
    if avg_proximity < n/5:
        add_to_entanglement_group(xi, xj)
```

These learned structures directly influence optimization by: - Biasing new ordering generation toward learned positions - Preserving variable relationships during transformations - Guiding escape from local minima while maintaining structural insights

II.E. Adaptive Phase Selection

The algorithm dynamically selects phases based on their historical success rates (5):

$$w_i^{(t+1)} = 0.1 + 0.9 \cdot \frac{S_i}{\sum_{j=1}^{4} S_j} \tag{5}$$

where S_i tracks the cumulative success count for phase i. Additional heuristics ensure adequate exploration in early iterations and increased tunneling during extended plateaus. This adaptive mechanism allows the algorithm to respond to the optimization landscape characteristics.

.

II.F. Algorithm Structure

Input: Boolean function f, time limit T
Output: Best ordering π*, BDD size s*

1: Initialize quantum state Ψ with K superpositions
2: Initialize Q-table, phase rotations θ, entanglement groups E
3: π* ← random ordering, s* ← BDD_size(f, π*)
4: while elapsed_time < T do
5: phase ← SelectPhase(weights, history, E)
6: π_new ← ExecutePhase(phase, current_best, θ, E)
7: s_new ← BDD_size(f, π_new)
8: if s_new < s* then
9: π* ← π_new, s* ← s_new
10: UpdatePhaseSuccess(phase)
11: UpdatePhaseRotations(θ, recent_good_orderings)
12: UpdateEntanglementGroups(E, recent_good_orderings)
13: UpdateQuantumState(Ψ, recent_evaluations, θ, E)
14: return π*, s*

III. Experimental Evaluation

III.A. Benchmark Test Design

We designed two benchmark classes that create challenging optimization landscapes:

Hierarchical Dependency Benchmark models systems with layered structures common in many applications [4, 7]. Variables are distributed across levels with exponentially growing sizes (1, 2, 4, 8, …). The Boolean function implements different operations at each level: level $\ell \bmod 3 = 0$ uses XOR operations, level $\ell \bmod 3 = 1$ uses AND operations, and level $\ell \bmod 3 = 2$ uses OR operations. Cross-level dependencies are created using combinations of if-then-else (ITE), AND, OR, and XOR operations based on level indices. The optimal ordering places all variables from level i before level $i + 1$.

Deceptive Local Minima Benchmark creates a landscape with multiple local optima that challenge traditional optimization methods. Variables are grouped using modulo-4 partitioning, with the optimal ordering following the non-intuitive sequence where variables are ordered by $i \bmod 4$ values in the pattern [0, 2, 1, 3]. The Boolean function applies different operations (XOR, AND, OR, ITE) to each modulo group and includes higher-order interactions between groups. This structure creates deceptive gradients that mislead greedy optimization methods.

III.B. Experimental Setup

Experiments evaluated three algorithms: QIRL (our proposed method), Sifting [3] (classical iterative improvement), and Simulated Annealing (stochastic optimization). Problem sizes of 32, 64, and 128 variables were tested, representing increasing complexity levels. Each algorithm was run with a 600-second time limit, with 5 independent runs per configuration. QIRL parameters included $K = 32$ superposition states, learning rate $\alpha = 0.2$, and discount factor $\gamma = 0.95$.

Performance metrics focused on the relative BDD size compared to the best known solution (normalized to 1.0) and convergence characteristics in terms of both evaluation count and time. All algorithms were implemented in Python using the dd library for BDD operations.

IV. Results and Discussion

The experiment results are shown in FIGURE 1, 2, 3, 4, and 5. The discussion about the results are in following sections.

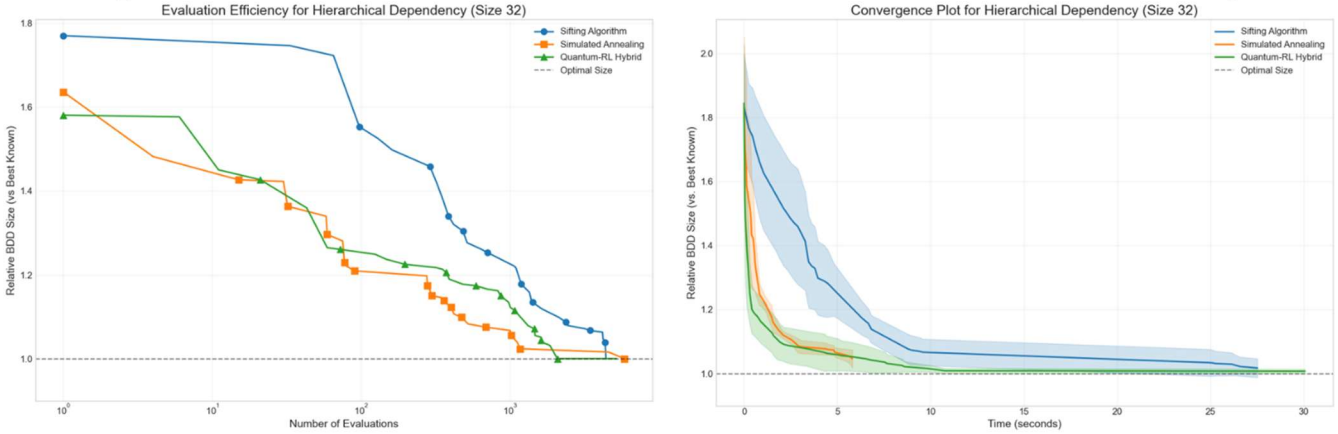

FIGURE 1. Hierarchical Dependency – Size 32

.

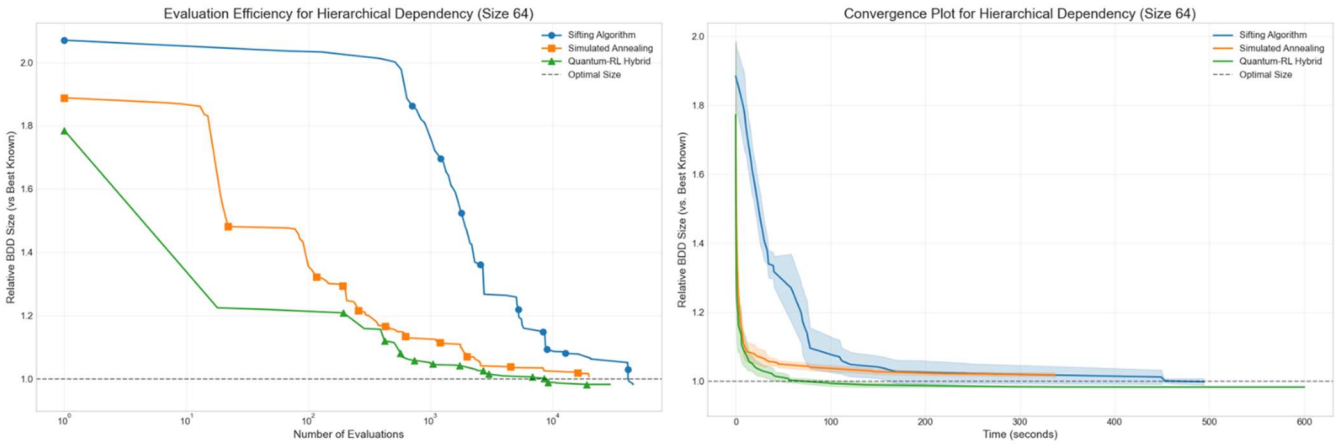

FIGURE 2. Hierarchical Dependency – Size 64

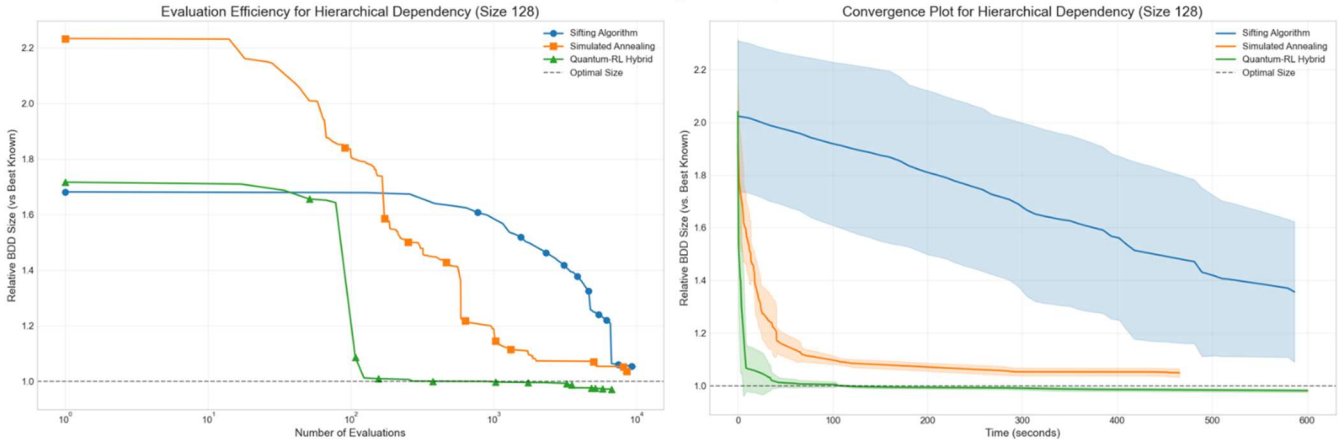

FIGURE 3. Hierarchical Dependency – Size 128

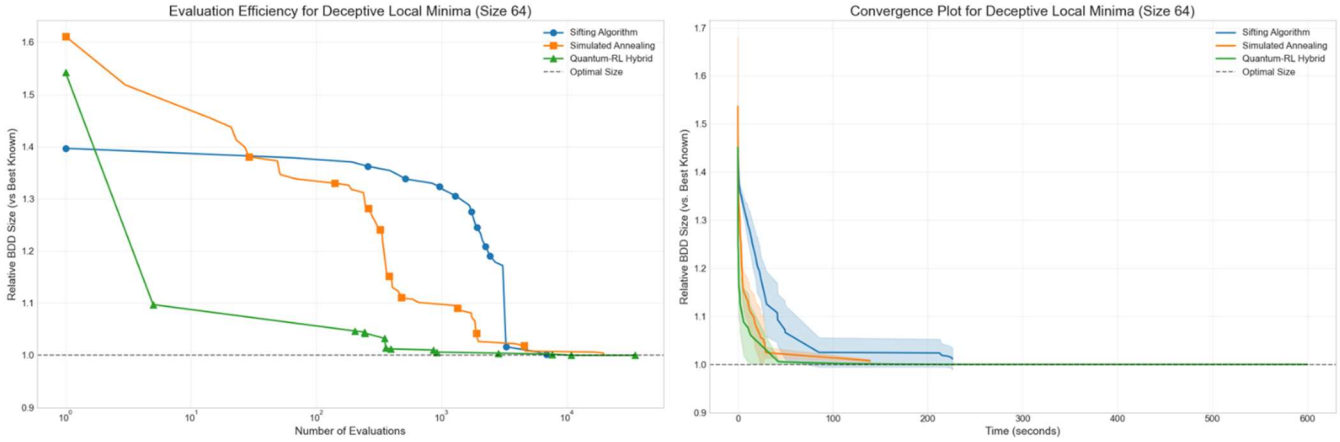

FIGURE 4. Deceptive Local Minima – Size 64

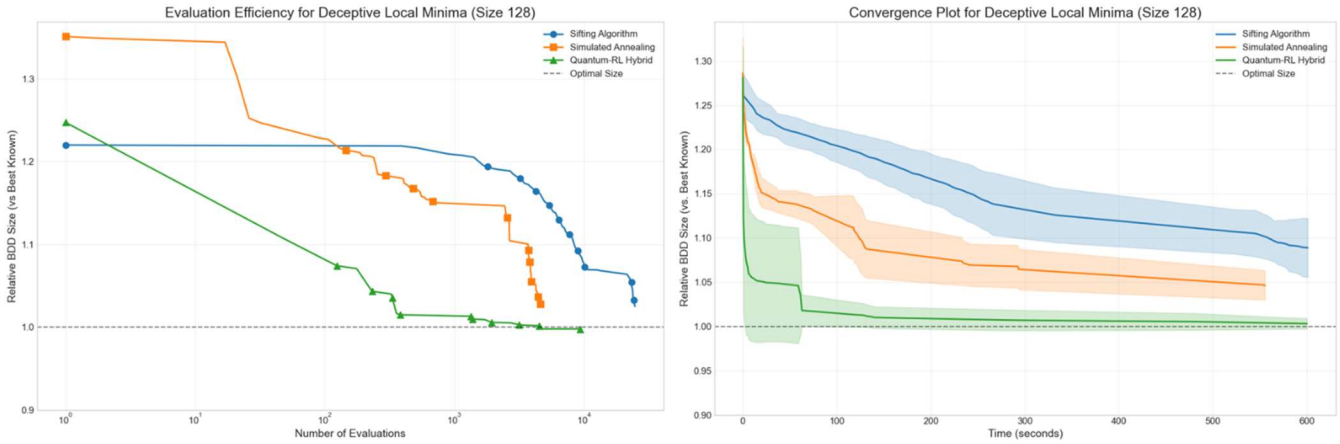

FIGURE 5. Deceptive Local Minima – Size 128

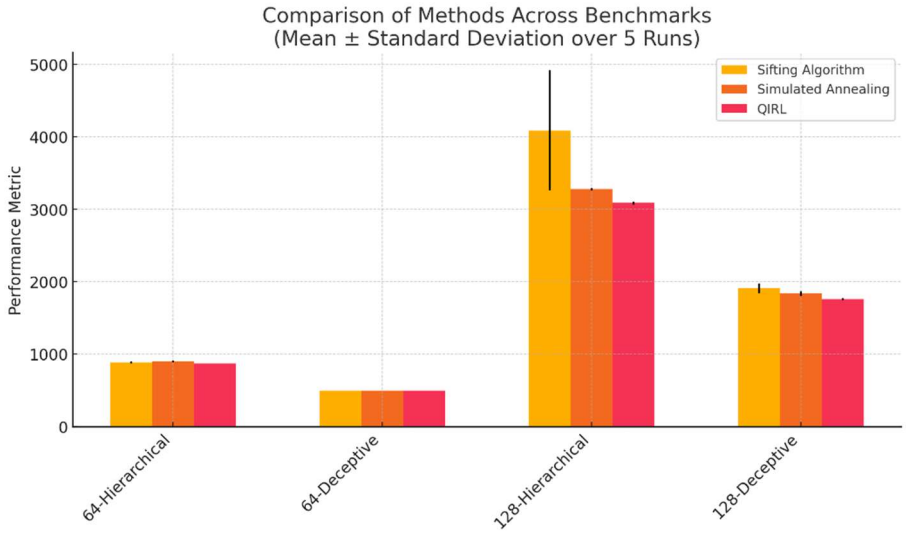

FIGURE 6. Performance Comparison Results

IV.A. Evaluation Efficiency

The evaluation efficiency plots reveal substantial performance differences between algorithms. For the Hierarchical Dependency benchmark, QIRL demonstrates rapid convergence to optimal solutions across all problem sizes. At size 32 (FIGURE. 1), QIRL reaches the optimal ordering within the first 15 seconds, while Simulated Annealing becomes stuck in local optima. This rapid convergence stems from QIRL's quantum exploration phase, which evaluates multiple diverse orderings simultaneously through superposition states. While classical methods test orderings sequentially, QIRL's parallel exploration quickly identifies promising regions of the search space. As problem size increases to 64 and 128 variables (FIGURE. 2, 3), this performance gap widens further. QIRL maintains its efficiency because learned phase rotations guide the search toward optimal variable positions, preventing wasteful exploration of poor orderings. The entanglement groups ensure that variables with strong dependencies are kept together during optimization, reducing the effective search space from n! to manageable subspaces that respect learned relationships.

The Deceptive Local Minima benchmark highlights QIRL's ability to escape suboptimal regions. For size 64 (FIGURE. 4), both Sifting and Simulated Annealing become trapped in local minima at approximately 1.4× the optimal size. These classical methods lack mechanisms to escape once all local improvements are exhausted. In contrast, QIRL successfully navigates the deceptive landscape through quantum tunneling operations that make intelligent non-local transformations while preserving learned variable relationships. At size 128 (FIGURE. 5), the logarithmic evaluation scale shows QIRL achieving near-optimal performance with 100× fewer evaluations than Sifting. This efficiency gain occurs because QIRL learns the deceptive modulo-4 pattern through its entanglement mechanism, allowing it to make coordinated moves that classical single-variable methods cannot discover.

The FIGURE. 6 reveals substantial performance differences between algorithms. Table 1 presents the detailed performance metrics with standard deviations across five independent runs, addressing the stochastic nature of the optimization algorithms. A key finding from our statistical analysis is the remarkable stability of QIRL compared to classical methods. The coefficient of variation (CV) provides insight into the relative variability of each algorithm:

- **QIRL**: Average CV = 0.27% (Range: 0.00% - 0.72%)
- **Sifting**: Average CV = 6.48% (Range: 0.00% - 19.11%)
- **Simulated Annealing**: Average CV = 1.39% (Range: 0.29% - 1.83%)

Table 1: Performance Summary: BDD Sizes (Mean ± Standard Deviation over 5 runs)

Benchmark	Size	QIRL	Sifting	Simulated Annealing
Hierarchical	64	870.2 ± 0.4	882.2 ± 10.4	898.2 ± 7.9
Hierarchical	128	3083.2 ± 22.2	4085.8 ± 780.8	3273.8 ± 15.6
Deceptive	64	494.0 ± 0.0	494.0 ± 0.0	496.0 ± 1.4
Deceptive	128	1759.4 ± 11.9	1909.8 ± 70.5	1834.8 ± 33.5

IV.B. Time-Based Convergence Analysis

Time-based convergence plots provide complementary insights into algorithm dynamics. QIRL exhibits characteristic behavior with rapid initial improvement (0-50 seconds) followed by periodic breakthroughs. The initial steep descent reflects the quantum exploration phase effectively surveying the solution landscape through superposition states. The subsequent breakthroughs correspond to successful quantum tunneling operations that escape local optima—these are not random restarts but intelligent transformations guided by accumulated phase and entanglement information. The narrow confidence bands indicate consistent performance across runs, demonstrating that the learned structural information makes QIRL's optimization process more deterministic and reliable than stochastic methods.

Simulated Annealing shows gradual improvement with occasional jumps during temperature reheating. However, these jumps become increasingly rare and smaller in magnitude over time, indicating the algorithm's inability to learn from past exploration. Without mechanisms to remember good variable relationships, each temperature cycle essentially starts fresh, explaining why progress stagnates at suboptimal solutions. The wider variance bands reflect this lack of learning—different runs may discover different local optima without any way to share or accumulate knowledge.

Sifting demonstrates predictable but slow convergence through systematic variable repositioning. The extended plateaus in FIGURES 2-5 indicate exhaustion of local improvements, where no single variable move can improve the BDD size. This fundamental limitation arises because Sifting lacks both the parallel exploration of QIRL's quantum states and the relationship

learning of entanglement groups. For larger problem sizes, Sifting's linear search through variable positions becomes increasingly inefficient, explaining why it requires 100-1000× more time than QIRL to achieve comparable results.

V. Conclusion and Future Works

This paper presented a quantum-inspired reinforcement learning algorithm for BDD variable ordering optimization. By combining quantum superposition principles with reinforcement learning, the algorithm achieves 2-10× performance improvements over classical methods on challenging benchmarks. The four-phase adaptive framework successfully balances exploration and exploitation, with quantum-inspired mechanisms proving particularly effective for escaping local optima.

The results demonstrate that quantum-inspired approaches offer significant potential for combinatorial optimization problems, even when implemented on classical hardware. As BDD applications continue to grow in complexity across various domains including circuit verification, reliability analysis, and formal methods, such advanced optimization techniques become increasingly valuable for practical deployment.

While QIRL demonstrates significant advantages, several areas warrant further investigation. Current experiments limited problem sizes to 128 variables; behavior on larger instances requires study. The algorithm's performance on different Boolean function classes beyond the tested benchmarks needs evaluation. Integration with domain-specific heuristics could potentially improve performance further.

ACKNOWLEDGMENTS

This work was supported by the National Research Foundation of Korea (NRF) grant funded by the Korea government (Ministry of Science and ICT) (No. RS-2022-00144150)

REFERENCES

[1] Bryant, R.E. (1986). Graph-based algorithms for Boolean function manipulation. IEEE Transactions on Computers, 35(8), 677-691.
[2] Bollig, B., Wegener, I. (1996). Improving the variable ordering of OBDDs is NP-complete. IEEE Transactions on Computers, 45(9), 993-1002.
[3] Rudell, R. (1993). Dynamic variable ordering for ordered binary decision diagrams. Proceedings of IEEE/ACM International Conference on Computer-Aided Design, 42-47.
[4] Jung, W.S., Han, S.H., Ha, J. (2004). A fast BDD algorithm for large coherent fault trees analysis. Reliability Engineering & System Safety, 83(3), 369-374.
[5] Somenzi, F. (1999). Binary decision diagrams. In Calculational System Design, NATO Science Series, 303-366.
[6] Meinel, C., Theobald, T. (1998). Algorithms and Data Structures in VLSI Design. Springer-Verlag.
[7] Rauzy, A. (1993). New algorithms for fault trees analysis. Reliability Engineering & System Safety, 40(3), 203-211.
[8] Sutton, R.S., Barto, A.G. (2018). Reinforcement Learning: An Introduction (2nd ed.). MIT Press.
[9] Kadowaki, T., Nishimori, H. (1998). Quantum annealing in the transverse Ising model. Physical Review E, 58(5), 5355.
[10] Grover, L.K. (1996). A fast quantum mechanical algorithm for database search. Proceedings of ACM Symposium on Theory of Computing, 212-219.
[11] Nielsen, M.A., Chuang, I.L. (2010). Quantum Computation and Quantum Information. Cambridge University Press.
[12] Farhi, E., Goldstone, J., Gutmann, S. (2014). A quantum approximate optimization algorithm. arXiv:1411.4028.
[13] Beloborodov, D., Ulanov, A.E., Foerster, J.N., Whiteson, S., Lvovsky, A.I., 2020. Reinforcement Learning Enhanced Quantum-inspired Algorithm for Combinatorial Optimization. https://doi.org/10.48550/arXiv.2002.04676
[14] Khairy, S., Shaydulin, R., Cincio, L., Alexeev, Y., Balaprakash, P., 2019. Reinforcement-Learning-Based Variational Quantum Circuits Optimization for Combinatorial Problems. https://doi.org/10.48550/arXiv.1911.04574
[15] Tiunov, E.S., Ulanov, A.E., Lvovsky, A.I., 2019. Annealing by simulating the coherent Ising machine. Opt. Express 27, 10288. https://doi.org/10.1364/OE.27.010288

A Framework to Identify Factors Affecting SMR Acceptance in Thailand

Ornjira Promsorn[1], Naraphorn Paoprasert[1], Kampanart Silva[2], Pidpong Janta[2], Nuwong Chollacoop[2], Wasin Vechgama[3]

[1]*Department of Industrial Engineering, Kasetsart University, Bangkok, 10900, Thailand.*

[2]*National Energy Technology Center, National Science and Technology Development Agency, 114 Thailand Science Park, Phahonyothin Road, Khlong Nueng, Khlong Luang, Pathum Thani, 12120, Thailand.*

[3]*Thailand Institute of Nuclear Technology (Public Organization),16 Vibhavadi Rangsit Road, Chatuchak, Bangkok, 10900, Thailand.*

EXTENDED ABSTRACT

In an era marked by the global energy crisis, climate change, and mounting pressure to reduce carbon emissions, Small Modular Nuclear Reactors (SMRs) have gained increasing attention as a stable, flexible, and low-carbon energy alternative. These advancements highlight the potential of SMRs for application in Thailand, both in electricity generation and industrial cogeneration, such as in oil refineries, petrochemical plants, seawater desalination, and clean hydrogen production. Thus, SMRs present a promising option for Thailand's energy future.

At the policy level, Thailand's 2024 Power Development Plan identifies SMRs as a future energy source of national importance. However, nuclear technology is often perceived as riskier than its actual risk, especially after the Fukushima event. Hence, this study proposed a framework to identify factors affecting the acceptance of SMRs in Thailand, drawing upon established theoretical models of technology acceptance and public perception, including insights from previous research on nuclear technology acceptance in Thailand (Tantitaechochart et al., 2020), as shown in Figure 1. In this figure, we hypothesized that risk and benefit perceptions and trust were influenced by information perception. Information perception was hypothesized to be influenced by socioeconomic status. Finally, the SMR acceptance was hypothesized to be influenced by risk attitude, trust, information perception, and socio-economic status.

The proposed framework is grounded in well-established theories. The extended Technology Acceptance Model (TAM) provides a basis for understanding how individual beliefs, such as perceived trust and perceived information quality, influence the intention to adopt new technologies. In this context, technology acceptance is conceptualized as a multidimensional outcome influenced by cognitive, affective, and informational factors, rather than solely by perceived usefulness and ease of use. The concept of risk-benefit perception suggests that individuals often evaluate technologies through an intuitive, affect-driven process, in which higher perceived benefits tend to reduce perceived risks, and vice versa. This inverse relationship reflects the influence of emotional responses known as the affect heuristic on how people interpret the desirability and safety of unfamiliar technologies. Social trust theory emphasizes the importance of public confidence in institutions and stakeholders responsible for developing or regulating technologies. When these entities are perceived as transparent, benevolent, and competent, trust increases, thereby reducing perceived risk and enhancing perceived benefits. These perceptions are further shaped by the quality and clarity of information individuals receive, aligning with risk communication theory, which posits that accessible and credible information fosters informed evaluations. Socioeconomic status (SES) is integrated as a background factor influencing how individuals access, process, and interpret such information. This perspective draws conceptually from the knowledge gap hypothesis, information-processing capacity theory, and broader insights from social stratification research, which collectively suggest that individuals with higher socioeconomic status (SES) often possess greater informational access and cognitive resources, thereby shaping their trust, perceptions, and ultimately, their acceptance of new technologies. Structural Equation Modeling (SEM) is employed to test these theoretical relationships and quantify their influence on SMR acceptance, as illustrated in Figure 1

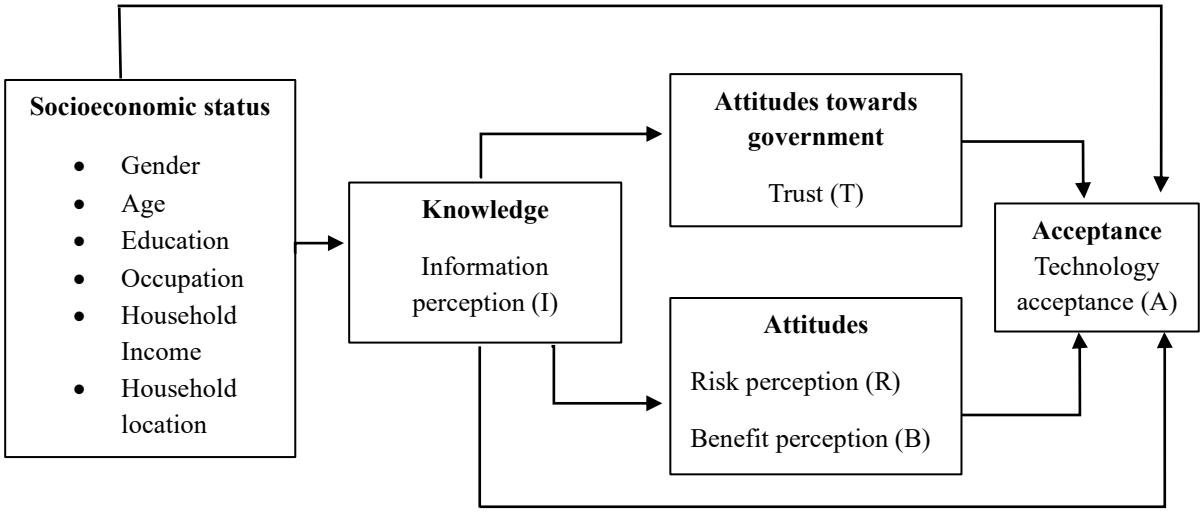

Figure 1: The framework to measure public perceptions toward SMR acceptance in Thailand

A questionnaire carefully designed to contain potential exogenous variables in the SEM model in Figure 1 is presented below. This questionnaire was developed based on established literature and theory, with its questions specifically formulated to operationalize the constructs and gather data for empirically testing the hypothesized relationships within the framework.

Information perception (I):

I1: I receive sufficient and continuous information about Small Modular Reactor (SMR) power plants.
I2: I have a basic understanding of how Small Modular Reactor (SMR) power plants operate.
I3: Small modular reactors (SMR) power plants use less fuel than fossil fuel power plants.
I4: Small modular reactors (SMR) power plants require cooling towers to dissipate heat.

Trust (T):

T1: If a Small Modular Reactor (SMR) power plant is constructed, the public will have access to information about it.
T2: The government will implement strict and thorough security policies for SMR power plants.
T3: In the event of an accident at an SMR power plant, the government is well-equipped to manage the emergency.
T4: Thailand has knowledgeable and capable personnel necessary to ensure the safety of SMR power plants, which meet international standards.
T5: Thailand has the knowledgeable and capable personnel necessary to manage radioactive waste from SMR power plants following international standards.

Risk perception (R):

R1: The risk of an accident at an SMR power plant is higher than that of a traffic accident.
R2: An accident at an SMR power plant could have impacts comparable to a large nuclear power plant.
R3: The prospect of living near an SMR power plant is frightening.
R4: I have extreme concern about the potential impact of radiation from radioactive waste on my family if our home were near an SMR power plant.

Benefit perception (B)

B1: Constructing an SMR power plant can create jobs for the communities around the site, which is a significant economic development opportunity.
B2: I would be willing to have an SMR power plant in my community if the residents received appropriate compensation.
B3: SMR power plants could lower electricity prices in Thailand.

B4: SMR power plants are crucial to ensuring the nation's energy security.
B5: Nuclear energy can help reduce greenhouse gas emissions, essential for transitioning to a low-carbon society.

Technology acceptance (A):

A1: I support the construction of an SMR power plant in my community.
A2: I support the construction of an SMR power plant in my province.
A3: I support the construction of an SMR power plant in Thailand.
A4: Thailand should increase the number of SMR power plants instead of relying on fossil fuels.

We developed this framework to measure SMR acceptance, with the questionnaire designed based on established literature and theory. Our data collection aimed to capture responses from diverse citizens across different socioeconomic backgrounds to reflect varied perspectives. Structural Equation Modeling (SEM) was then employed to validate the model and identify significant predictors of public acceptance. The findings are expected to provide actionable insights for policymakers and stakeholders to enhance public engagement and foster informed decision-making in the implementation of SMR technologies.

Keywords: Small Modular Nuclear Reactors (SMRs), Questionnaire, Public Perception, Risk Communication, Structural Equation Modeling (SEM), Technology Acceptance

ASRAM2025
www.asram2025.org
Asian Symposium on Risk Assessment and Management 2025
Pattaya, Thailand, 27 – 29 August 2025

A Study on Evacuation Time Estimation for Offsite Consequence Analysis Using Agent-Based Modeling

Gibeom Kim[1], Sung-yeop Kim[2]

[1] *Korea Atomic Energy Research Institute, 111, DAEDEOK-DAERO 989BEON-GIL, YUSEONG-GU, DAEJEON, KOREA, 34057, gbkim@kaeri.re.kr*
[2] *Korea Atomic Energy Research Institute, 111, DAEDEOK-DAERO 989BEON-GIL, YUSEONG-GU, DAEJEON, KOREA, 34057, sungyeop@kaeri.re.kr*

EXTENDED ABSTRACT

The offsite consequence analysis of nuclear power plants represents a critical component of Probabilistic Safety Assessment (PSA), evaluating both early and long-term impacts on residents following accidents involving radioactive material release. The MACCS (MELCOR Accident Consequence Code System), developed by Sandia National Laboratories (SNL), serves as the representative computational tool for conducting comprehensive offsite consequence analysis within the Level 3 PSA framework.

The current MACCS protective action modeling approach maintains safety margins through conservative assumptions while achieving computational efficiency through simplified models. However, this approach has inherent limitations due to highly simplified evacuation scenarios and static timetables that highly depend on expert judgment for determining resident accident awareness time (alarm time), sheltering duration, and evacuation timing. Although detailed configurations are possible, such as subdividing cohorts to establish cohort-specific scenarios or setting evacuation speeds for individual sections within the Emergency Planning Zone (EPZ), establishing scientific basis for these detailed parameter values remains challenging.

This study presents a methodology to address these limitations through Agent-Based Modeling (ABM) approach for protective action modeling and simulation, along with the development of a comprehensive software tool. ABM provides a computational approach for predicting macroscopic system behavior through microscopic agent interactions, enabling more realistic protective action modeling by incorporating spatial heterogeneity, individual behavioral variations, and dynamic interaction effects.

The ultimate goal of this study is to integrate the ABM into the existing Level 3 PSA framework by utilizing the results of agent-based protective action simulation as inputs for MACCS. In other words, while maintaining the well-established Level 3 PSA framework, this study aims to provide more detailed and realistic inputs for the protective action modeling stage, thereby enhancing the scientific basis and validity of offsite consequence analysis results.

The key input variables constituting MACCS protective action modeling are structured as follows:

TABLE I. Key variables of MACCS protective action modeling

Variable Name	Data Type	Data Dimension	Description
Population	integer	[nCohort][nDirection][nRadius]*	Population distribution for each section (grid)
DURBEG & DURMID	integer	[nCohort]	Duration of Evacuation 1 (DURBEG) and Evacuation 2 (DURMID) for each cohort
ESPEED	float	[nCohort]	Evacuation speeds for each cohort in Evacuation 1, 2, and 3 sections (in m/s)
Network evacuation direction	integer	[nCohort][nDirection][nRadius]	Network evacuation direction for each section (1: outward, 2: rightward, 3: backward, 4: leftward)
Network evacuation speed	float	[nCohort][nDirection][nRadius]	(Optional) Speed multiplier for each section
DLTSHL	float	[nCohort][nRadius]	Delay time to sheltering for each cohort and each radius
DLTEVA	float	[nCohort][nRadius]	Delay time to evacuation for each cohort and each radius

(* nCohort: number of cohorts, nDirection: number of directions, nRadius: number of radii)

The developed agent-based protective action simulation tool basically incorporates Geographic Information System (GIS) data to represent realistic spatial configurations and consists of numerous agents simulating resident evacuation behavior. GIS data primarily requires road network information, while residential, commercial, and tourist area distributions, along with population distributions, can be effectively utilized. Resident agents implement pathfinding models for predicting routes to evacuation destinations and traffic models for predicting evacuation speeds considering traffic congestion and interactions with other agents. Real-time data such as evacuation speeds and routes generated from ABM simulations are reprocessed and clustered to provide inputs for MACCS protective action models. For the clustering, K-Means is used. However, Given the complex, multi-dimensional nature of evacuation data, non-linear, multi-dimensional clustering methods such as OPTICS are also being considered for future refinement.

To accomplish this, a prototype program has been developed as shown in the figures. The program's main functions include GIS data processing, agent-based evacuation simulation incorporating pathfinding and traffic models, simulation visualization, simulation result processing and conversion to MACCS input data, and graphical user interface capabilities. Figure 1 (a) presents portions of the program's key inputs. The left panel shows evacuation simulation settings that enable more realistic simulations by utilizing GIS data to configure population distributions and evacuation destinations. The right panel displays settings related to MACCS input conversion. Figure 1 (b) presents the GIS data-based simulation visualization window, which provides intuitive understanding of evacuation route and speed behaviors through visualization.

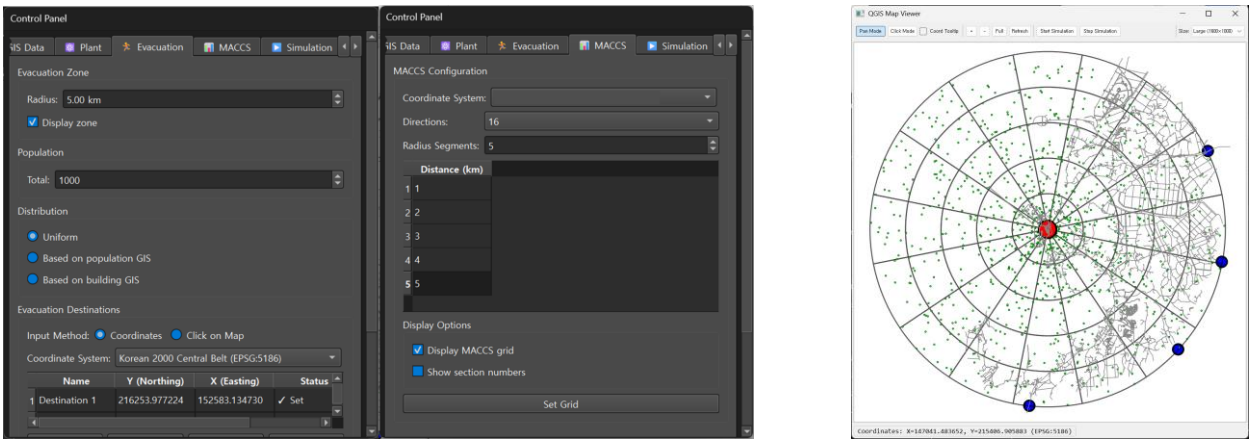

(a) (b)

FIGURE 1. Developed prototype program

The developed methodology can provide a more reasonable foundation for protective action model inputs in Level 3 PSA applications. Fine-tuning of MACCS inputs through ABM simulation results enables more realistic and valid analysis outcomes. Future work will focus on conducting MACCS sensitivity analyses using various ABM simulation-based inputs to improve MACCS input conversion methodologies. Additionally, the methodology will be expanded to incorporate additional behavioral factors, weather conditions, and infrastructure variations that influence evacuation effectiveness under diverse emergency conditions. This comprehensive approach will enhance the scientific basis for nuclear emergency preparedness and risk assessment activities.

ACKNOWLEDGMENTS

This work was supported by a National Research Foundation of Korea (NRF) grant funded by the Korean government (MSIT: Ministry of Science and ICT) (No. RS-2022-00143695).

REFERENCES

[1] Bixler, N., & Nosek, A. (2021). MACCS Theory Manual (SAND2021-11535, 1820907, 699454; pp SAND2021-11535, 1820907, 699454). https://doi.org/10.2172/1820907

[2] Salgado, M., & Gilbert, N. (2013). Agent based modelling. In Handbook of quantitative methods for educational research (pp. 247-265). Brill.

[3] Kim, G., & Heo, G. (2023). Agent-based radiological emergency evacuation simulation modeling considering mitigation infrastructures. *Reliability Engineering & System Safety*, *233*, 109098.

ASRAM2025
www.asram2025.org
Asian Symposium on Risk Assessment and Management 2025
Pattaya, Thailand, 27 – 29 August 2025

Effectiveness and Practicality of Severe Accident Mitigation Strategies with Uncertainty Considerations

Jemo Ryu[1], Jaehyun Cho[2]

[1]*Chung-Ang University, Heukseok-ro 84, Dongjak-gu, Seoul, 06974, Republic of Korea, jemo2000@cau.ac.kr*
[2] *Chung-Ang University, Heukseok-ro 84, Dongjak-gu, Seoul, 06974, Republic of Korea, jcho@cau.ac.kr*

ABSTRACT

Following the Fukushima Daiichi nuclear accident, nuclear power plants (NPPs) in Korea have undergone significant changes in their severe accident management plan. The updated Accident Management Plans (AMP) systematically integrates the specific procedures for Korean NPPs, such as emergency operation procedure, multi-barrier accident coping strategy, and severe accident management guidelines, to effectively respond to design basis accident scenarios. As NPPs deviate from normal operational conditions, the level of uncertainty in our predictions increases. In particular, severe accidents are characterized by limited experimental and empirical data, leading to greater predictive uncertainty. During the accident progression, diagnosing the NPP's state and applying mitigation strategies rely on human judgment, inevitably leading to time delays. This study proposes an evaluation framework that incorporates human reliability analysis (HRA) and the uncertainties associated with severe accident phenomena. Parametric uncertainty analyses were conducted using MAAP5, a severe accident analysis code, and the proposed framework was applied to the OPR1000, a domestic NPP in Korea. The framework, demonstrated through the external steam generator injection strategy in an extended loss of AC power accident, produced visual profiles by evaluating uncertainty, mitigation strategy time delays, and equipment performance. These profiles serve as decision-making indicators for the technical support center in diagnosing NPP status and determining appropriate mitigation strategies during severe accidents. By evaluating the effectiveness of MACST while considering uncertainties and reflecting these uncertainties in the AMP, this study is expected to improve the Severe Accident Management Guideline (SAMG) and thereby enhance the safety of nuclear power plants (NPPs) against severe accident scenarios.

Keywords: severe accident, MAAP5, accident management plan, accident management plans, OPR1000

I. Severe Accident and Multi-barrier Coping Strategy

After the Fukushima Daiichi incident, the OPR-1000 nuclear power plants in Korea have adopted a range of new systems and protocols to both prevent and mitigate accidents, even under extreme circumstances such as severe natural disasters or intentional human actions. Among these enhancements, an external injection line was established to facilitate the supply of water to the steam generator(SG) from outside the plant, and mobile pumps were procured to enable flexible water injection capabilities. Should the Alternative AC(AAC) Diesel Generator fail to restore power after an initial station blackout(SBO), the plant is anticipated to remain in a prolonged power loss condition. Under such circumstances, the plant formally declares an Extended Loss of AC Power(ELAP) and proceeds to implement measures aimed at restoring AC power and removing residual heat. The initial response to ELAP involves attempting to reestablish AC power using a portable generator. If these strategies are unsuccessful, reliance on internal plant equipment is no longer viable for prevention and mitigation, necessitating the deployment of mobile pumps. When restoration of AC power using the mobile generator is not achieved, the next step is to depressurize the SG via the atmospheric dump valve, after which a mobile pump is connected to the external injection line to supply water and sustain secondary side heat removal. The criterion for determining a severe accident is continuously monitoring whether the CET(Core Exit Temperature) exceeds 650°C, and repeatedly performing SG (Steam Generator) depressurization and injection as necessary. Depending on the evolving status of the plant, additional actions such as depressurizing the reactor coolant system(RCS) and injecting water into the RCS using a mobile pump may also be implemented. Figure 1 shows a simplified Plant Damage State Event Tree(PDS-ET) that incorporates accident mitigation strategies utilizing mobile equipment during an initial SBO scenario. Extended loss of all AC power refers to a situation where all alternating current (AC) power sources are lost, making rapid recovery of AC power and the use of on-site fixed equipment malfunctioned. In this scenario, as indicated by all headings up to the AAC heading in Figure 1 being marked as Fail, mobile equipment is used to ensure the safety of the power plant. Figure 2 outlines the sequence for executing external injection strategies following the declaration of ELAP.

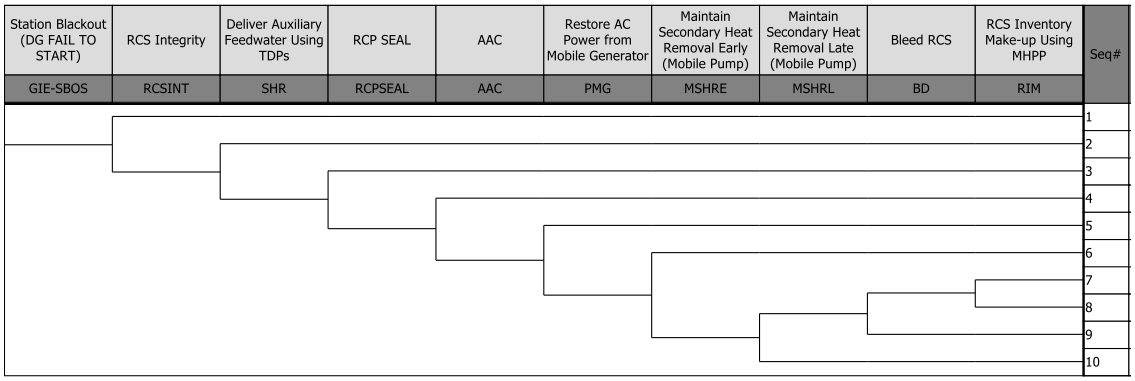

Figure 1. Simplified PDS-ET with Multi-barrier Accident Coping Strategy

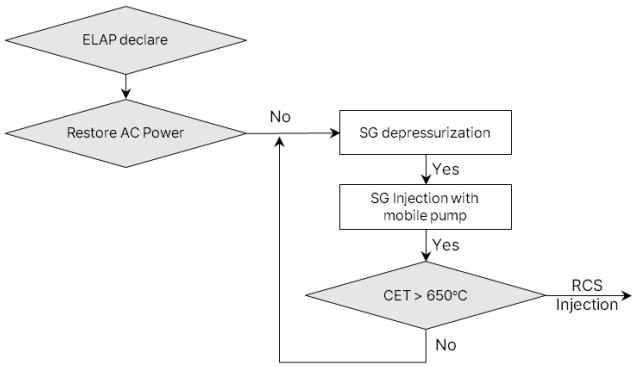

Figure 2. SG External injection strategies in Extended SBO scenario

I.A. SG Injection with Multi-barrier Coping Strategy

To quantify the efficacy of portable pump deployment strategies, three accident sequences were evaluated under sustained failure conditions of both secondary heat removal by turbine-driven auxiliary feedwater and AC power restoration:

1. Timely SG Injection: Mobile pump implementation for steam generator water injection within optimal response windows, absent RCS inventory replenishment measures.
2. Delayed SG Injection: SG injection strategy execution postponed due to operational time lags, without supplementary countermeasures.
3. Combined SG/RCS Make-up: Concurrent SG injection and RCS inventory restoration when SG injection initiation is delayed.

   Notably, Scenario 3 (integrated SG/RCS strategy) falls outside the analytical scope of this study.

II. Time delay of accident management with MACST strategies

After the initiating event occurs, there is inevitably a time delay before the accident diagnosis and the implementation of the preventive/mitigation strategies determined by the operators. When a severe accident such as significant fuel damage or core meltdown occurs, the SAMG(Severe Accident Management Guideline) systematically presents measures to suppress the progression of the accident and minimize the release of radioactive materials to the outside. SAMG is applied in severe accident situations where response is not possible even with Emergency Operating Procedure. From an accident management perspective, there are time delay factors in diagnosing the accident and deciding on the application of preventive/mitigation strategies by the Main Control Room(MCR) or the Technical Support Center(TSC). From the Emergency Plan(EP) perspective, there is a time delay from the radiation emergency declaration to the response of the Emergency Response Organization(ERO) to the plant, and the deployment of personnel and equipment to the site for mission execution. In this study, the major time delay factors were identified as SG injection strategy diagnostic/decision, RCS depressurization, RCS injection strategies diagnostic/decision, ERO ready, and MACST(portable equipment) moving/installation was considered. To consider realistic severe accident scenarios, research on time delay phenomena was conducted[1], and each time delay factors were based on

Table-top Exercise(TTX) data[2], based on experimental data from former MCR and TSC personnel considering portable equipment scenarios. The time delay factors and with each delay time based on the TTX data are as follows:

1. SG injection strategy diagnostic/decision: 30 min(from Initiating Event)
2. mobile pump moving/installation for SG injection: 20 min(from decision)
3. ERO call-up/ready: 90 min(from Initiating Event)
4. RCS depressurization: 25min(after SG injection or CET > 650°C)
5. RCS injection strategy diagnostic/decision and mobile pump moving/installation: 15 min (after RCS depressurization)

Severe accident progression modeling fundamentally diverges from design basis accident assessments through its explicit integration of operational realism. This investigation establishes three temporally distinct implementation pathways for the steam generator (SG) injection protocol, preserving conservative safety margins while reflecting plausible emergency response conditions. The schematic representation of these temporal frameworks is provided in Figure 3.

Case 1: Optimized Response Sequence

Characterizes an ideal emergency protocol execution where:

- ELAP declaration occurs immediately upon incident initiation
- First-responder emergency team deploys mobile pumping systems without delay
- SG injection strategy implementation completes within 50 minutes of ELAP

Case 2: Delayed Organizational Activation

Represents suboptimal organizational response where:

- Initial emergency crew fails to declare ELAP promptly
- Full emergency response organization (ERO) mobilization precedes action
- Mobile pump deployment and SG injection commence 140 minutes of ELAP

Case 3: SAMG-Triggered Intervention

Depicts worst case procedural delay:

- ELAP remains undeclared despite full ERO mobilization
- Strategy initiation requires meeting SAMG entry criteria (CET > 650°C)
- Implementation follows diagnostic confirmation and procedural validation

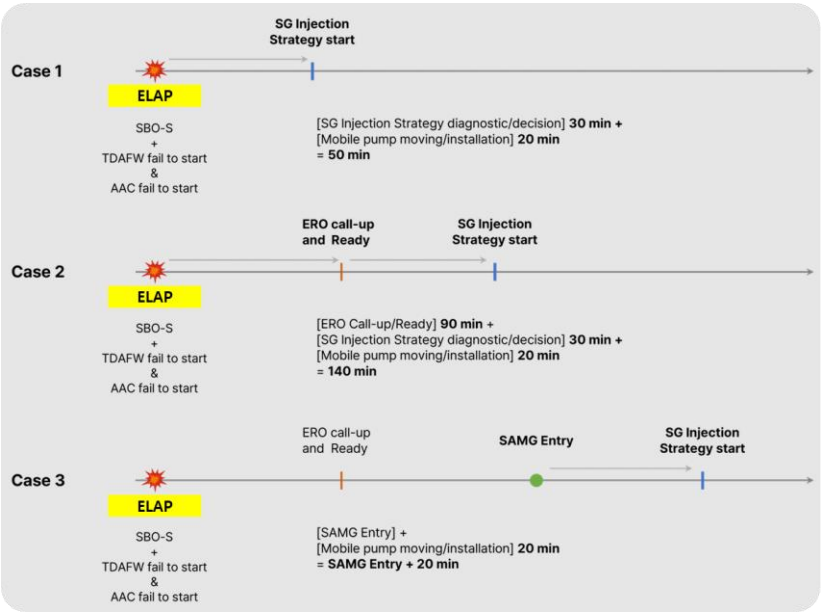

Figure 3. MAAP Simulation for Effectiveness Evaluation of ELAP Cases

III. Effectiveness Assessment of MACST strategies

As nuclear power plants transition from normal operating states to accident conditions, the degree of uncertainty in predicting accident progression increases significantly. This heightened uncertainty is largely attributable to the scarcity of empirical data and limited precedent for severe accident scenarios. Recognizing these challenges, the 2020 revision of the accident management plan in Korea incorporated the latest scientific findings to better address knowledge gaps and improve the reliability of severe accident response strategies.[3]

In the present study, the primary focus was placed on uncertainties arising from model parameters, which are known to exert a substantial influence on accident outcome predictions. The analysis was structured in accordance with the accident management strategy outlined by Korea Hydro & Nuclear Power Co. (KHNP), with the overarching objective of minimizing core damage and ensuring that molten core materials remain confined within the reactor vessel. To systematically explore the impact of parameter uncertainty on reactor vessel failure, a probabilistic approach was adopted.

A set of 27 distinct input parameter combinations was generated for each scenario using Monte Carlo sampling, with each set representing a plausible variation in the key variables that govern RV failure in the MAAP code.[4] Alongside the uncertainty assessment, a sensitivity analysis was performed to determine how variations in mobile pump performance could affect the overall effectiveness of accident mitigation strategies. In this analysis, the feedwater injection rate, a key parameter for maintaining adequate secondary cooling, was systematically adjusted from 0kg/s to 35 kg/s, increasing in steps of 5 kg/s. This approach enabled a detailed evaluation of how changes in injection capacity directly influence the probability of preventing reactor vessel failure.

By integrating the outcomes of both the uncertainty and sensitivity analyses, a comprehensive picture of the MACST strategy's robustness was developed. The study mapped the relationships among parameter variability, equipment performance, and accident progression, thereby highlighting the strengths and limitations of current severe accident management protocols under realistic operational challenges. Furthermore, the results for each time-delay scenario, underscore that both prompt implementation and maintaining injection rates above critical thresholds are essential for the successful mitigation of severe accident consequences.

IV. Result and Discussion

To determine how uncertainty in severe accident phenomena affects the performance of accident management strategies, a comparative analysis was performed. This involved contrasting the results of probabilistic simulations, where key model parameters were treated as distributions, with those from deterministic calculations that held all parameters at their default values. The primary criterion for evaluating each strategy was the likelihood of RV failure, which serves as a central indicator of severe accident management effectiveness. For each scenario, the RV failure probability was quantified and visualized using the results of the uncertainty and sensitivity analyses, as illustrated by Equation 1 in Figure 4.

$$P_{RV\ Fail} = \frac{(\#\ of\ total\ RV\ Fail\ case)}{(\#\ of\ Total\ case)} \times 100(\%) \qquad (1)$$

The inclusion of uncertainty consistently led to more conservative estimates, with higher projected probabilities of RV failure compared to the deterministic baseline. This effect was particularly pronounced in the scenario where the SG injection strategy was delayed by approximately 90 minutes(Case 2), highlighting how time delays can amplify the impact of RV Failure. In the scenario where mitigation measures were initiated after the SAMG entry threshold(CET > 650°C) was reached(Case 3), the probability of RV failure remained high, even when the SG injection rate exceeded 15 kg/s. In the deterministic results shown in Figure 4(a), the RV Fail Probability is simply divided into fail/intact. However, in Figure 4(b), which reflects code and HRA uncertainties, there is high uncertainty observed in the portions evaluated as intact in the dichotomized results of Figure 4(a). In particular, for Case 3 where the injection time is significantly delayed high probability uncertainty occurs even though a sufficient injection flow rate is achieved. These findings underscore that accounting for uncertainty is essential for realistic and robust assessment of accident management strategies, especially in situations where response actions are not implemented promptly. The purpose of quantification and visualization is to clearly understand the effectiveness of accident management strategies and the impact of uncertainties, and to intuitively provide this information to decision-makers and stakeholders. By presenting how changes in variables affect accident outcomes through numerical data and graphical representations, it enables operators to intuitively recognize critical information during an accident.

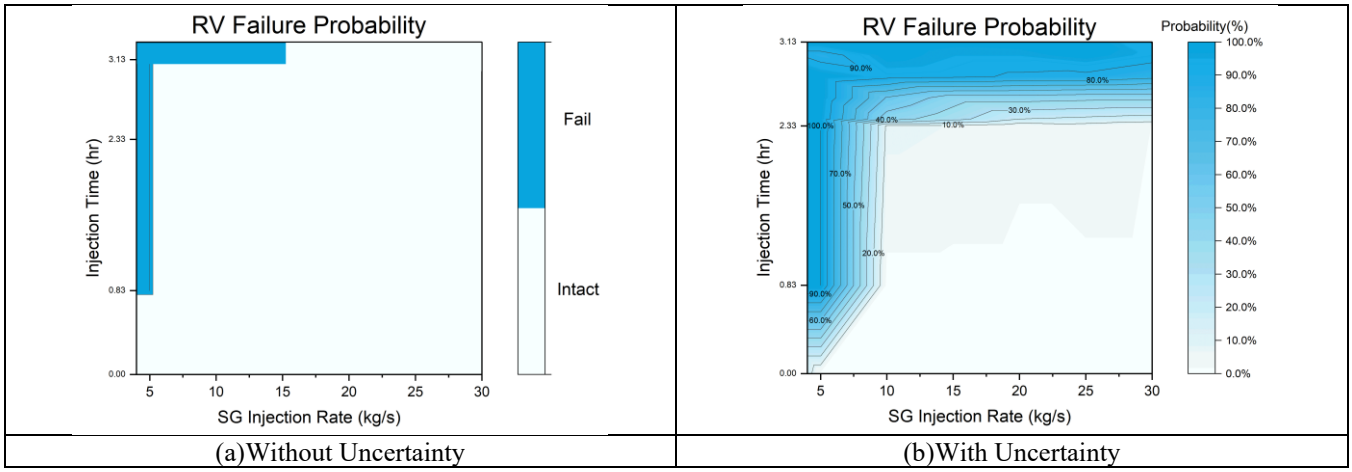

(a)Without Uncertainty (b)With Uncertainty

Figure 4. Effectiveness of the SG Injection strategy

V. CONCLUSIONS

A thorough evaluation of accident management strategies must explicitly address the inherent unpredictability of severe accident phenomena. In this research, the focus was placed on extended loss of AC power scenarios, examining how different mitigation actions, especially those involving external water delivery to the steam generator via mobile pumps, influence overall plant safety. The findings indicate that prompt deployment of mobile injection equipment, coupled with adequate flow rates, is highly effective in safeguarding the reactor vessel from failure. The analysis demonstrated that, while the use of portable equipment for steam generator injection can help prevent reactor vessel failure under optimal conditions, there remains significant uncertainty in the outcome when the injection rates are near the threshold values required for effective mitigation. The results of this study offer valuable insights that can directly inform the revision and enhancement of both the SAMG and the AMP for nuclear power plants in Korea. By systematically analyzing the uncertainties inherent in severe accident phenomena and quantifying the impact of human response delays and equipment performance, the proposed evaluation framework identifies critical factors that influence the effectiveness of accident mitigation strategies. These findings can be leveraged to refine the structure and content of the SAMG, particularly by improving its clarity and visibility for plant operators and emergency response teams. Enhanced clarity in the SAMG will enable more rapid and accurate diagnosis of plant conditions and selection of appropriate mitigation actions during severe accidents. Furthermore, the integration of uncertainty analysis into the AMP ensures that accident management procedures are robust and adaptable to a wide range of unpredictable scenarios. Ultimately, the application of this research will support the continuous improvement of accident management strategies, contributing to the overall safety and resilience of nuclear power plants in the face of severe accident risks.

ACKNOWLEDGMENTS

This work was supported by Korea Institute of Energy Technology Evaluation and Planning (KETEP) grant funded by the Korea government (MOTIE) (RS-2024-00401705, Convergent and practical human resource development program specialized in nuclear power plant export).

REFERENCES

[1] Young A Suh and Jaewhan Kim, Soo Yong Park, “Time uncertainty analysis method for level 2 human reliability analysis of severe accident management strategies”, Nuclear Engineering and Technology, Nucl. Eng. Tech. 53(2), pp. 484-497 (2021)
[2] Jaewhan Kim and Jaehyun Cho, Sooyong Park, Jinkyun Park, “SAMG-based human reliability analysis method in support of Level 2 PSA. Part I: Table-top eXercise experiments”, Nuclear Engineering and Technology, Nucl. Eng. Tech. In Press, Corrected Proof, (2024)
[3] Korea Institute of Nuclear Safety, “Status of review of accident management plan and future plan”, (2020)
[4] Fauske & Associates LLC (FAI), Modular Accident Analysis Program 5.05 (MAAP5.05), Electric Power Research Institute, Washington DC, USA (2019)

ASRAM2025
www.asram2025.org
Asian Symposium on Risk Assessment and Management 2025
Pattaya, Thailand, 27 – 29 August 2025

CONSIDERATION OF LEVELIZED COST OF ELECTRICITY AND INVESTMENT RISKS OF SMALL MODULAR REACTORS IN EMERGING COUNTRIES

Kampanart Silva, Pidpong Janta, Nuwong Chollacoop

[1] *National Energy Technology Center (ENTEC), National Science and Technology Development Agency (NSTDA) 114 Thailand Science Park Phaholyothin Road, Klong Nueng, Klong Luang, Pathumthani 12120 Thailand,*
kampanart.sil@entec.or.th, pidpong.jan@entec.or.th, nuwong.cho@entec.or.th

ABSTRACT

Global commitment towards net-zero emissions led to increasing interests of newcomers in nuclear power. Southeast Asian countries are particularly interested in small modular reactor (SMR) due to its claims for better safety, better flexibility, better economic performance, and lower financial risks. The levelized cost of electricity (LCOE) for nuclear power is lower than many alternative sources in some countries, though it is much higher in other countries. This study aims to identify crucial factors affecting LCOE of SMR and understand their tendencies in emerging countries, in order to gain accurate perception of investment risks of SMR. Insights on factors affecting LCOE are gathered from historical records of LCOE of nuclear power and cost projections in energy outlooks and preceding studies. LCOE of nuclear power in developing countries is typically low due to lower material and labor costs. Countries with multiple types of reactors and more stringent regulations tend to have higher LCOE. While large reactors benefit from economy of scale, SMRs are expected to benefit from economy of multiples. LCOE of SMR will be much higher in the beginning and gradually decrease with multiplication over time. SMR will also have lower financial risk since it has smaller capital cost per unit. Additionally, LCOE in emerging countries may vary according to markup from exporting countries and options for backend management. Strategies for emerging countries to reduce LCOE and minimize investment risk include wait-and-see approach, gradual localization, and negotiation at regional scale.

Keywords: levelized cost of electricity (LCOE), small modular reactor (SMR), financial risk, economy of scale, economy of multiples

I. INTRODUCTION

Global commitment towards net-zero emissions led to increasing interest in nuclear power, and the number of newcomer countries expressing the eagerness to go nuclear is the largest in history. 25 countries from four continents, including newcomer countries, jointly launch declaration to triple nuclear energy capacity by 2050 at COP28 in United Arab Emirates in 2023 [1], and six more nations endorsed the declaration at COP29 in Azerbaijan in 2024 [2]. The International Energy Agency (IEA) [3] noted that nuclear generation is set to hit an all-time high in 2025. Around 420 reactors are in operation and an additional 63 with total capacity of roughly 70 GW are under construction. SMR is said to be the catalyst for the world's transition towards nuclear power.

Southeast Asian countries are particularly interested in deploying SMR, including Indonesia, Malaysia, the Philippines, Thailand, and Vietnam. Many of these have already included SMR in their national energy plan, including Thailand that included two 300 MWe SMRs at the end of the latest draft national energy plan. SMR is claimed to have enhanced safety through the adoption of the latest technology, better flexibility due to its modularity, better economic performance from economy of serial production, and lower financial risk due to lower upfront capital cost [4].

The lower levelized cost of electricity (LCOE) of nuclear and the lower financial risk of SMR have been the two crucial selling points of SMR in emerging countries. For example, a representative of Federation of Thai Industries expressed support for the inclusion of SMRs in the national energy plan as they can cut the electricity unit price by half [5]. As there are only two operating SMRs to date, the narratives on LCOE of SMRs have been built upon the LCOE of conventional nuclear power plants. The LCOE for nuclear power is lower than many alternative sources in some countries while statistics also show that it

can be much higher than other sources in other countries. To create a fair ground for discussion of LCOE of SMRs, this study aims to identify crucial factors affecting LCOE of an SMR and understand their tendencies in emerging countries.

II. METHODOLOGY

This study employs exploratory research to clarify factors that affect levelized cost of electricity (LCOE) generated from a small modular reactor (SMR) project in a newcomer country and factors that affect investment plan of the project. Information is gathered from historical records of project investment cost (overnight cost), fuel cost, operation and maintenance cost (O&M cost), decommissioning cost, and any other costs that may occur throughout the project from energy outlooks, international reports, news, and preceding academic studies. Note that the majority of the information is still based on large nuclear power plants as there are still only two SMRs in operation to date. Factors are then synthesized from the pool of information considering two aspects: (1) effects on any elements of LCOE, and (2) effects on investment model, capacity, and schedule of SMR projects.

III. RESULTS AND DISCUSSION

III.A. Overnight cost remains the largest component of LCOE, but it might not be as large as expected in some countries.

Fig. 1 shows the components of LCOE of existing nuclear power plants projected by the International Energy Agency (IEA) in 2020 [6]. The discount rate is set at 7%. Information for IEA's LCOE projection are shown in Table I. As commonly recognized, the largest component of LCOE of nuclear power is the investment cost (also known as overnight cost) in all countries, unlike a fossil fuel plant where fuel price plays a crucial role. It is also noteworthy that in many Asian countries, the projected O&M cost occupies a significant share of LCOE in many Asian countries which might be due to the expenses for safety enhancement based on lessons learned from the accident at Fukushima Daiichi Nuclear Power Plant in March 2011. The projected fuel cost is generally low and is similar across the board, except for Russia. Finally, the decommissioning cost is projected to be very low as it arises at the end of the long life of a nuclear power plant. It is yet to be noted that decommissioning cost will be the largest portion of a nuclear power plant around the end of its life.

III.B. A single type of reactor helps streamline construction, operation, maintenance, and regulatory processes, leading to lower LCOE.

Taking a closer look at the two nuclear power leading countries, Japan and Korea, in Fig. 1. The proportions of each component of the projected LCOE of a similar advanced light water reactor (generation III+) are very similar (5:2:3:0). However, the total projected LCOE of Korea is significantly lower. The tighten regulatory requirements following the Fukushima accident, which could have been more consequential in Japan, may not be the only reason to this difference. While Korea has been focusing on APR-1400, which is an updated version of OPR-1000 in all its recent newbuilds, Japan has continued its programs on different types of advanced light water reactors. Focusing on a single type of reactor helps leverage efforts in technological advancement, optimization of operation and maintenance, and streamlining the regulatory process, potentially resulting in lower LCOE.

TABLE I. Information on nuclear power plants used for IEA's LCOE projection [6]

Country	Technology	Net capacity [MWe]	Efficiency [%]
France	EPR	1650	33%
Japan	ALWR	1152	33%
Korea	ALWR	1377	36%
Russia	VVER	1122	38%
Slovak Republic	Other	1004	32%
United States	LWR	1100	33%
China	LWR	950	33%
India	LWR	950	33%

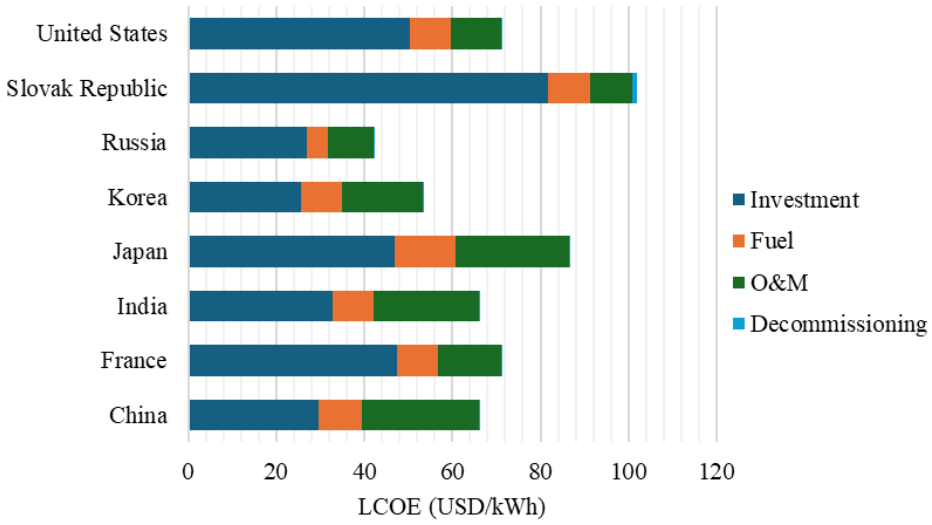

FIGURE 1. LCOE of existing nuclear power plants [6]

III.C. While material and labor costs are generally lower in developing nations, the LCOE is not necessarily always low depending on other circumstances.

Lower income countries tend to have lower material and labor costs compared to others. Russia is an exceptional case of a country with highly advanced nuclear power technology, but it still benefits from relatively low material and labor costs. As a result, the projected investment cost is low, and the projected fuel and O&M costs are exceptionally low. With a similar reason, the projected investment cost is also low for China and India. While there was a question on the correctness of the O&M cost data of China and India [7], the adjusted variable O&M cost of China at 15 cents per kWh is still higher than average. There might be other reasons for the high O&M cost which cannot be compensated for by the low labor cost.

III.D. A first-of-a-kind (FOAK) reactor tends to have a longer construction period and undergo longer inspections, resulting in a significantly higher LCOE.

Next is the case of France. While the Flamanville 3 EPR is theoretically not a first-of-a-kind (FOAK) reactor since its construction started after Olkiluoto 3 EPR, it can be practically considered as a FOAK plant as the two projects have only around two years' time lag. As it took nearly two decades (from December 2007 to September 2024) from the first concrete until the first criticality, the investment cost ballooned to nearly 70% of the projected LCOE. Note that the numbers in Figure 1 are the projected values based on the expectation in 2020 when the reactor was not yet in operation. It is highly likely that FOAK SMRs will follow a similar path with longer construction and inspection periods. It can be observed from the announced budget of Ontario Power's BWRX-300 where the first SMR is expected to be 7.7 billion CAD, and the total four units will cost up to 21 billion CAD [8].

III.E. Political stability is an important prerequisite for a lower LCOE while its impact is difficult to quantify.

The case of Slovak Republic also provides a good lesson to a newcomer regarding the influence of political situation. Czechoslovakia was separated into Czech Republic (currently Czechia) and Slovak Republic in 1992, and the construction of the nuclear power reactors was temporarily halted. The country also faces protests from the anti-nuclear neighboring country. While the impact from political instability can be observed from the projected overnight cost which becomes extremely high, it can only be quantified after the construction. While political risks are expected to be large, they are highly uncertain and will likely result in higher markups by vendors to compensate for the risks.

III.F. SMR in a newcomer country will always be more expensive, as it requires setting up legislative and regulatory frameworks and vendors will likely add markups to absorb their risks.

As SMR design requires multiple installations to maximize the economy of multiples, it is highly likely that many designs will involve export, with newcomer countries as their promising targets. For example, apart from its effort to promote VOYGR domestically, NuScale approaches foreign countries, including Romania which plans to deploy VOYGR-6 at Doicesti to replace a coal power plant [9]. However, statistics show that the same type of reactor will likely cost much more in the exported destination than in the original location. For example, the projected capital cost of an APR-1400 unit in Barakah Power Station is more than twice that in Saeul Power Station [3]. Apart from the costs for setting up the infrastructure based on the IAEA Milestones Approach [10], it is undeniable that the vendors should have added markups to cover the very large export risks. This may also be applicable to the case of BWRX-300 in Ontario [8] even if Canada is not a newcomer country as BWRX-300 will requires modification in regulatory requirements and additional infrastructure preparation.

III.G. While backend expenses are not typically included in LCOE, it may pose significant cost to the operator depending on the backend model employed.

Backend expense is not included in many LCOE calculations as there is no comparable component in other power sources. However, the cost to construct a final repository for spent nuclear fuel can be extremely high, and it will definitely affect the overall cost of an SMR project. There are also some other models for backend management, including spent fuel reprocessing and/or recycling abroad, a shared disposal facility, or a fuel leasing program [11]. All models require a significant amount of investment, and the country and the operator should be aware of it before making a commitment to a nuclear power program.

III.H. Initial estimates of LCOE are always much lower than the actual LCOEs.

Like other megaprojects, a nuclear power project is typically overbudget and delayed [12]. This is because it involves a high level of innovation and complexity, resulting in unexpected stumbling. IEA reported the statistics showing that the overnight cost of nuclear power projects can increase from 30% to three times of the initial estimation, and the construction period can be extended by 0.5 to three times. Emerging countries will need to be aware of the possibility of budget inflation and be prepared to deal with it.

III.I. While large reactors benefit from economy of scale, SMRs are expected to benefit from economy of multiples.

Economy of scale has been the very reason to continue enlarging the size of a nuclear reactor in the 90s and 2000s to reduce the unit cost [13]. On the other hand, despite the small size of SMRs which becomes a disadvantage in terms of scale, the economy of multiples with more opportunities to optimize, learn from the lessons, and shorten the construction time and regulatory process, multiple SMRs can be competitive to a single large reactor [14]. There is a high chance that a FOAK SMR will have a much higher LCOE than a typical large reactor, but the cost will likely reduce significantly for the second SMR and gradually decrease until it becomes relatively stable around the fifth SMR [15]. Therefore, it is advisable for a newcomer country to plan for a series of SMR construction of more than five reactors to sufficiently benefit from the economy of multiplication.

III.J. Good strategies are needed to enable the economy of multiples without losing SMR's benefit on financial risk.

With a significantly smaller capital cost per unit, an SMR is likely to have lower financial risk than a large reactor. It will be more affordable and have a shorter payback period. The modularity will allow the operator to benefit from scalability and design suitable portfolio strategy [16]. However, newcomer countries must note that the multi-module SMR may add up the total investment to be equivalent to that of a large reactor. While some SMR models allow gradual addition of SMRs, other models suggest deploying all modules at the same time. On one hand, multiple SMRs need to be installed to gain economy of multiples. On the other hand, deployment of SMRs needs to be carefully scheduled to distribute the investment in order to ensure low financial risk.

IV. CONCLUSIONS

Factors affecting the levelized cost of electricity (LCOE) of a small modular reactor (SMR) were identified and their tendencies when the SMR is deployed in a newcomer country are investigated and summarized below.

- The overnight cost is still generally the largest portion of the LCOE.
- Selecting a single model of SMR will lead to a lower LCOE when compared to multiple models.
- Developing nations may have lower LCOE as material and labor costs are lower, though it still depends on other circumstances.
- A first-of-a-kind (FOAK) SMR will yield a significantly higher LCOE.
- Political stability is an important factor affecting LCOE, though it is very difficult to quantify.
- Preparation of infrastructure and institutional frameworks, along with the high markups by the vendors will largely increase the LCOE of the first SMR in a newcomer country.
- All backend models require a significant budget, and its cost should be carefully considered before a newcomer country makes a commitment to an SMR program.
- Initial estimates of LCOE are always much lower than the actual LCOEs.
- The economy of multiples will compensate for the lack of economy of scale in SMRs, though it requires at least five SMRs for the impact to be significant.
- Strategies to distribute SMR investment are needed to benefit from economy of multiples through the deployment of multiple SMRs.

The findings show that there are many factors that will make the LCOE of an SMR higher than a conventional large reactor. A newcomer should plan for the deployment of a number of same type of SMRs with a carefully designed schedule. Rather than pushing forward with a FOAK SMR or an SMR model that has not been constructed elsewhere, a wait-and-see approach might be a wiser choice for a newcomer country with limited experience. For a developing nation, gradual localization will allow the country to benefit from lower material and labor costs and will also contribute to the advancement of domestic industry. To allow simultaneous deployment of multiple SMRs and enable regional approach to backend management, newcomer countries in an emerging region may consider negotiating SMR projects at a subregional scale.

REFERENCES

[1] "At COP28, Countries Launch Declaration to Triple Nuclear Energy Capacity by 2050, Recognizing the Key Role of Nuclear Energy in Reaching Net Zero," https://www.energy.gov/articles/cop28-countries-launch-declaration-triple-nuclear-energy-capacity-2050-recognizing-key (2023).
[2] "Six More Countries Endorse the Declaration to Triple Nuclear Energy by 2050 at COP29," https://world-nuclear.org/news-and-media/press-statements/six-more-countries-endorse-the-declaration-to-triple-nuclear-energy-by-2050-at-cop29 (2024).
[3] IEA, *The Path to a New Era for Nuclear Energy*, IEA, Paris (2025).
[4] M. H. SUBKI, "Advances in Technology Developments of Small Modular Reactors – including Microreactors," 21st INPRO Dialogue Forum on the Deployment of SMR Projects and Technologies to Support the Sustainable Development Goals, Saint Petersburg, 28 August – 1 September 2023, IAEA (2023).
[5] "Counting One for a Nuclear Power Plant, Defining the Framework in November 2024, Significantly Reducing Electricity Price by 50% (in Thai)," https://www.prachachat.net/economy/news-1693729 (2024).
[6] IEA, *Projected Costs of Generating Electricity 2020*, IEA, Paris (2020).
[7] G. ROTHWELL, "Projected Electricity Costs in International Nuclear Power Markets," *Energy Policy*, **64**, 112905 (2022)
[8] "Ontario's Darlington SMR Project to Cost Nearly $21-Billion, Significantly Higher Than Expected," https://www.worldnuclearreport.org/Ontario-s-Darlington-SMR-project-to-cost-nearly-21-billion-significantly-higher (2025).
[9] "NuScale Power and RoPower Announce Signing of the Contract for Phase 1 of Front-End Engineering and Design Work for First SMR Power Plant in Romania," https://www.nuscalepower.com/press-releases/2023/nuscale-and-ropower-announce-signing-of-the-contract-for-phase-1-engineering-and-design-work (2023).
[10] IAEA, *Milestones in the Development of a National Infrastructure for Nuclear Power*, *IAEA Nuclear Energy Series No. NG-G-3.1 (Rev. 2)*, IAEA, Vienna (2024).

[11] IAEA, Options for Management of Spent Nuclear Fuel and Radioactive Waste for Countries Developing New Nuclear Power Programmes, *IAEA Nuclear Energy Series No. NW-T-1.24*, IAEA, Vienna (2018).
[12] G. LOCATELLI, *Why Are Megaprojects, Including Nuclear Power Plants, Delivered Overbudget and Late? Reasons and Remedies*, MIT, Massachusetts (2018).
[13] B. MIGNACCA, G. LOCATELLI, "Economics and Finance of Small Modular Reactors: A Systematic Review and Research Agenda," *Renewable and Sustainable Energy Reviews*, **118**, 109519 (2020).
[14] D. T. INGERSOLL, "Deliberately Small Reactors and the Second Nuclear Era," *Progress in Nuclear Energy*, **51(4-5)**, 589-603 (2009).
[15] F. M. MITENKOV, B. A. AVERBAKH, I. N. ANTYUFEEVA, "Economic Effect of the Development and Operation of Serially Produced Propulsion Nuclear Power Systems," *Atomic Energy*, **102**, 42-47 (2007).
[16] OECD NEA, *Small Modular Reactors: Challenges and Opportunities*, OECD, Paris (2021).

ASRAM2025
www.asram2025.org
Asian Symposium on Risk Assessment and Management 2025
Pattaya, Thailand, 27 – 29 August 2025

Evaluation of Kass-Steffey adjustment for component reliability uncertainty analysis

Gyun Seob Song[1], Man Cheol Kim[2]

[1] *Department of Energy Systems Engineering, Chung-Ang University: 84 Heukseok-ro, Dongjak-gu, Seoul, 06974, Korea, dyrnfmxm678@cau.ac.kr*
[2] *Department of Energy Systems Engineering, Chung-Ang University: 84 Heukseok-ro, Dongjak-gu, Seoul, 06974, Korea, charleskim@cau.ac.kr*

ABSTRACT

Reliability data in the probabilistic safety assessment is analyzed by Bayesian inference with empirical data. In the analysis, prior knowledge distribution is updated using empirical data collected from specific data group of interest. When there is a variability in the data groups, such as plant-to-plant variability, the variability distribution is used for prior knowledge distribution. The variability is represented by hyperparameters, and there are uncertainties not only the reliability parameters but also their hyperparameters. Thus, in the context of Bayesian approach, uncertainties in the reliability parameters and their hyperparameters should be analyzed simultaneously. Hierarchical Bayes assigns uncertainty distributions for both the reliability parameters and their hyperparameters and can derive analytic uncertainty distribution for specific data groups. However, due to its mathematical complexity, the hyperparameters are estimated as point values using the empirical Bayes method. Although the empirical Bayes method has been implemented to estimate the variability distribution, there is an uncertainty in the estimate because it varies with the collected data set. Therefore, a Kass-Steffey adjustment also has been implemented to take account the additional uncertainty in the estimate. However, due to several approximations in the Kass-Steffey adjustment, there exists approximation errors in the estimate compared to analytic solution.
This paper presents the mathematical formula of posterior distribution of hierarchical Bayes for fail-to-run events and evaluates the approximation errors in the empirical Bayes method with Kass-Steffey adjustment. In the mathematical formula, it is shown that the support of hyperparameters should be restricted to make proper distribution. Thus, the empirical Bayes method with Kass-Steffey adjustment is compared to three different restriction conditions.

Keywords: Uncertainty analysis, Empirical Bayes, Kass-Steffey adjustment, Hierarchical Bayes, Reliability data

I. INTRODUCTION

In the probabilistic safety assessment (PSA) for nuclear power plants, risk is quantified as a function of input parameters, such as component failure probabilities and failure rates. These parameters are typically estimated using empirical data and statistical inference because the parameters are not directly observable. Thus, state-of-knowledge uncertainties exist in the estimated parameters, and Bayesian inference is adopted to derive the uncertainty distributions for the parameters. A characteristic of Bayesian inference is using prior knowledge distribution to derive current knowledge distribution. When the number of observed data is sufficient, prior knowledge distribution does not significantly affect current knowledge distribution. However, the effect of prior knowledge distribution is increased when the number of observed data is not sufficient, and therefore, it is important to determine appropriate prior knowledge distributions. When there is plant-to-plant variability in the parameters, empirical Bayes method has been widely applied to estimate prior distributions using maximum likelihood estimation. However, an additional source of uncertainties arises in the estimation because empirical data is used to estimate hyperparameters of prior distribution. To handle these uncertainties, Kass and Steffey proposed an adjustment method that approximate posterior expected values and variances and uses the values to approximate current knowledge distribution with defined uncertainty distribution model [1]. The Kass-Steffey adjustment method has been presented to parameter estimation in the PSA when the empirical Bayes is used to estimate prior distributions [2] and implemented for component reliability analysis [3].

Although the Kass-Steffey adjustment reflects additional uncertainties in the estimated hyperparameters by extending variances of current knowledge distribution, there is a limitation corresponding to approximations of the moments and the uncertainty distribution model. Another approach to take account of uncertainties in the hyperparameters is hierarchical Bayes

that assigns uncertainty distributions for the hyperparameters, referred to as hyperprior. In the hierarchical Bayes, both prior distribution for parameters and hyperprior are updated to current knowledge distribution and therefore, analytic current knowledge distribution for parameters given hyperprior can be derived. Since the empirical Bayes method including Kass-Steffey adjustment is an approximation for the hierarchical Bayes when diffuse hyperprior is used, their approximation error should be analyzed to identify uncertainties in the quantification method.

This paper presents current knowledge distribution for component independent failure rates in the context of hierarchical Bayes using diffuse hyperpriors with respect to bounds of hyperparameters and evaluate the empirical Bayes and Kass-Steffey adjustment. A brief description of the empirical Bayes and Kass-Steffey adjustment is described in Section II. In Section III, mathematical formula of current knowledge distribution with the hierarchical Bayes is derived. Section IV compares the resultant distributions using a case study and evaluates the approximation error. A conclusion of this paper is presented in Section V.

II. EMPIRICAL BAYES AND KASS-STEFFEY ADJUSTMENT

In the PSA, a basic assumption is that reliability of components varies among the plants to reflect plant-specific characteristics. Thus, plant-specific estimate for PSA input parameters is performed by Bayesian update of prior distribution using plant-specific empirical data. An additional assumption is that component reliability resembles each other even though they are not identical. In this context, population variability distribution is adopted to represent plant-to-plant variability in the parameters, and it is used for the prior distribution. To derive the population variability distribution, empirical Bayes has been implemented using maximum likelihood estimation. The empirical Bayes is based on two-stage hierarchical model, determining model parameters for the specific plant and the following data generation. In the case of fail-to-run events, the data generation is a Poisson process with constant failure rate as a model parameter, and the failure rate comes from the population variability distribution. Due to mathematical characteristics, conjugate prior is typically used for the population variability distribution model.

Empirical Bayes uses maximum likelihood estimation to estimate the hyperparameters, and the likelihood function is a marginal likelihood function that marginalizes model parameters. Since gamma distribution is a conjugate prior for the Poisson likelihood function, posterior distribution for plant-specific failure rate follows another gamma distribution.

The Empirical Bayes method determines the prior empirically and therefore, there is a source of uncertainty in the estimated hyperparameters depending on the empirical data set. Thus, Kass-Steffey adjustment has been implemented to account for the uncertainty when there are few plants of observation. Kass-Steffey adjustment accounts for the uncertainty using first order approximation for expected value and variance of posterior distribution with mode of hyperparameters. When the hyperprior is a uniform distribution, the mode can be substituted by maximum likelihood estimator, which is the results of the empirical Bayes method. Consequently, variance of posterior distribution is extended, while expected value is equal to the result of simple Bayesian update with the prior distribution derived by the empirical Bayes method. Based on the approximated posterior expected value and variance, the posterior distribution for failure rate is approximated as another gamma distribution using moment matching.

Even though Kass-Steffey adjustment can reflect the additional variance that comes from the uncertainties in the hyperparameters, there are approximation errors not only the moments but also the distribution model. The error should be analyzed to provide appropriate information to decision makers.

III. HIERARCHICAL BAYES

Empirical Bayes is typically considered as a half-Bayesian approach because some parameters of interest are estimated as point values empirically. In contrast, hierarchical Bayes is a fully Bayesian approach that uncertainty distributions are assigned to parameter of interest. In the two-stage hierarchical model, hyperparameters present uncertainties in the population variability and there is typically no prior knowledge for the variability. Thus, diffuse prior is applied for the hyperprior, such as uniform prior distribution. Since the Kass-Steffey adjustment assumes a uniform prior for using the result of empirical Bayes method, uniform hyperprior is assumed in this paper. According to Bayes theorem, posterior distribution for the failure rate and hyperparameters is proportional to the product of likelihood function, prior distribution given hyperparameters, and hyperprior. When the hyperprior follows a uniform distribution, the posterior distribution for the failure rate accounting for hyperparameters can be derived by marginalizing the hyperparameters out.

$$f(\lambda_i|k_i,t_i) \propto \int_0^A \int_0^B \frac{\beta^\alpha}{\Gamma(\alpha)} \lambda_i^{\alpha+k_i-1} e^{-\lambda(\beta+t_i)}\, d\alpha d\beta = \lambda_i^{k_i-2} e^{-\lambda_i t_i} \int_0^A \frac{\gamma(\alpha+1,\lambda_i B)}{\Gamma(\alpha)}\, d\alpha \quad (1)$$

where A and B are upper bounds of the hyperparameters, and γ is a lower incomplete gamma function.

The posterior distribution for the failure rate in Eq. (1) is proper except for a condition that supports of all the hyperparameters are positive real values. Since the posterior distribution depends on the support of the hyperparameters, the double bound condition and two single bound conditions are used to evaluate the empirical Bayes method and Kass-Steffey adjustment. Although the posterior distribution for failure rate follows gamma distribution in the case of infinite upper bound of β, the posterior distributions for the other cases do not follow gamma distribution. Furthermore, the parameters of posterior distribution have differences compared to the result of Kass-Steffey adjustment even when the upper bound of β is infinite and the posterior distribution for failure rate follows gamma distribution.

IV. CASE STUDY

A case study is applied to evaluate approximation error in the empirical Bayes and Kass-Steffey adjustment method. INL/RPT-23-73954 provides performances of emergency diesel generators (EDGs) collected from 1998-2022 [4]. The empirical Bayes method and Kass-Steffey adjustment are implemented when there is a variability in the collected data group, such as plant-to-plant variability. Since INL/RPT-23-73954 provides yearly failure data for fail-to-run events of EDGs, year-to-year variability is analyzed in this study. Table I shows the failure data for EDG fail-to-run and point estimated failure rate for each year.

TABLE I. EDG fail-to-run data from 1998 to 2022

Year	Failures	Operation time (hour)	Failure rate (/hour)
1998	4	11,285	3.544E-04
1999	1	11,694	8.551E-05
2000	7	13,607	5.144E-04
2001	2	14,162	1.412E-04
2002	7	13,233	5.289E-04
2003	10	11,931	8.381E-04
2004	13	11,733	1.107E-03
2005	14	12,293	1.138E-03
2006	4	11,365	3.519E-04
2007	17	11,458	1.483E-02
2008	20	11,615	1.721E-03
2009	8	11,637	6.874E-04
2010	13	11,299	1.150E-03
2011	21	12,332	1.702E-03
2012	11	7,352	1.496E-03
2013	17	7,913	2.148E-03
2014	17	7,228	2.351E-03
2015	12	7,788	1.540E-03
2016	10	7,584	1.318E-03
2017	22	7,390	2.976E-03
2018	10	7,875	1.269E-03
2019	8	7,389	1.082E-03
2020	6	7,405	8.102E-04
2021	4	7.186	5.566E-04
2022	5	7.321	6.829E-04

Based on the failure data, prior distribution and its hyperparameters can be derived using the empirical Bayes method, maximum likelihood estimation with marginal likelihood function.

When the estimated distribution is used as prior distribution, current knowledge distribution for year-specific EDG failure rate can be derived using Bayesian inference and its variance is adjusted using Kass-Steffey adjustment method to account for uncertainties in the estimated hyperparameters depending on the collected data set. Table II shows uncertainty distributions for year-specific EDG failure rates and their variances with respect to implementation of Kass-Steffey adjustment. Due to the

uncertainties of the hyperparameters in the empirical Bayes method, it can be shown that there is an additional variance when Kass-Steffey adjustment is implemented.

TABLE II. Posterior distributions and variances for EDG failure rates

Year	Hyperparameters		Variance	
	Simple EB	EB-KS	Simple EB	EB-KS
1998	(6.874, 13885.9)	(6.749, 13633.5)	3.565E-08	3.631E-08
1999	(3.874, 14294.9)	(3.751, 13839.5)	1.896E-08	1.958E-08
2000	(9.874, 16207.9)	(9.749, 16001.8)	3.759E-08	3.807E-08
2001	(4.874, 16762.9)	(4.750, 16335.7)	1.735E-08	1.780E-08
2002	(9.874, 15833.9)	(9.749, 15632.6)	3.938E-08	3.989E-08
2003	(12.874, 14531.9)	(12.748, 14389.9)	6.096E-08	6.157E-08
2004	(15.874, 14333.9)	(15.748, 14220.1)	7.726E-08	7.788E-08
2005	(16.874, 14893.9)	(16.748, 14782.6)	7.607E-08	7.664E-08
2006	(6.874, 13965.9)	(6.749, 13712.0)	3.524E-08	3.590E-08
2007	(19.874, 14058.9)	(19.748, 13969.5)	1.006E-07	1.012E-07
2008	(22.874, 14215.9)	(22.748, 14137.1)	1.132E-07	1.138E-07
2009	(10.874, 14237.9)	(10.749, 14073.4)	5.364E-08	5.427E-08
2010	(15.874, 13899.9)	(15.748, 13789.5)	8.216E-08	8.282E-08
2011	(23.874, 14932.9)	(23.748, 14853.6)	1.071E-07	1.076E-07
2012	(13.874, 9952.9)	(13.748, 9862.5)	1.401E-07	1.413E-07
2013	(19.874, 10513.9)	(19.747, 10446.7)	1.798E-07	1.809E-07
2014	(19.874, 9828.9)	(19.747, 9766.0)	2.057E-07	2.070E-07
2015	(14.874, 10388.9)	(14.748, 10300.8)	1.378E-07	1.390E-07
2016	(12.874, 10184.9)	(12.748, 10085.3)	1.241E-07	1.253E-07
2017	(24.874, 9990.9)	(24.746, 9939.3)	2.492E-07	2.505E-07
2018	(12.874, 10475.9)	(12.748, 10373.5)	1.173E-07	1.185E-07
2019	(10.874, 9989.9)	(10.749, 9874.5)	1.090E-07	1.102E-07
2020	(8.874, 10005.9)	(8.749, 9864.6)	8.864E-08	8.991E-08
2021	(6.874, 9786.9)	(6.749, 9609.2)	7.177E-08	7.310E-08
2022	(7.874, 9921.9)	(7.749, 9764.3)	7.999E-08	8.128E-08

To evaluate the empirical Bayes method and Kass-Steffey adjustment, hierarchical Bayes is applied for failure rate of each year. When the upper bound of α is finite, the upper bound is assumed to be 10 times of α of average performance distribution to make a sufficient upper bound. Figure 1 shows the posterior distribution for failure rate with respect to the analysis method and support of hyperparameters. Three specific year failure rates are presented as representative cases, the minimum failure rate (2001), the median failure rate (2004), and the maximum failure rate (2018). Even though the actual minimum failure rate occurs in case 1999, the representative minimum failure rate case is designated as 2001, the second lowest, because the posterior distribution becomes an improper distribution when the upper bound of β goes to infinite. It can be shown that the distributions of β infinite support are more conservative compared to those of α infinite support. In the case of 2001, the result distribution of double bounded support is very similar to the result of α infinite support. Consequently, the central tendencies of distributions derived from the double bounded support and the empirical Bayes with Kass-Steffey adjustment decrease, compared to those of the single bound conditions, as the point estimated failure rate increases. The increment and decrement of central tendency are larger when the empirical Bayes with Kass-Steffey adjustment compared to the double bounded support case. The reason for these results is associated with a characteristic of the empirical Bayes method. In the empirical Bayes method, prior distribution is determined based on the empirical data collected from all the data set. Therefore, information of other data groups affects the results of group-specific distribution, year-specific in this case. Due to the information, there is a central tendency in the year-to-year variability, and it attracts failure rates to average performance of pooled data. On the other hand, in this case study, the upper bounds of the hyperparameters are assumed to be 10 times the average performance. It is expected that the central tendency of β infinite distribution will shift in the same direction as increases and decreases in the upper bound of α, while the central tendency of α infinite distribution will shift in the opposite direction as increases and decreases in the upper bound of β.

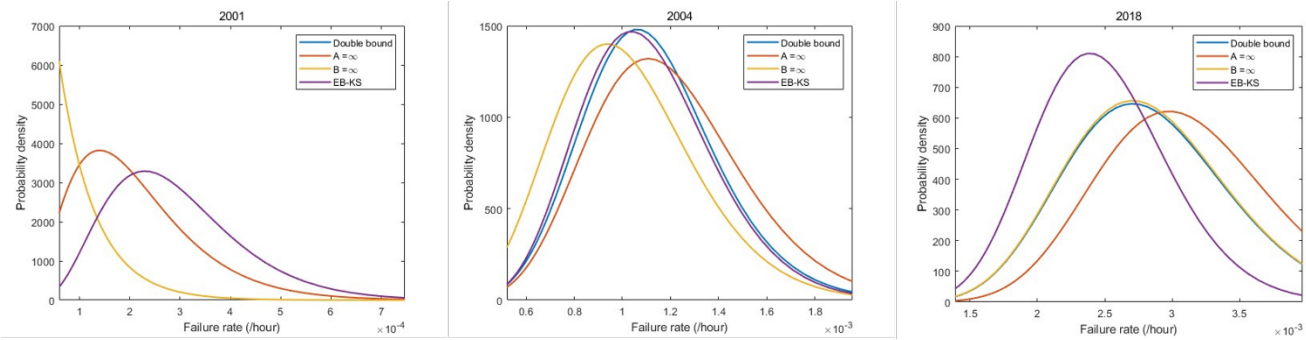

FIGURE 1. Posterior distribution for EDG failure rates

V. CONCLUSIONS

This paper evaluates empirical Bayes and Kass-Steffey adjustment, conventionally implemented in reliability analysis for nuclear power plants using hierarchical Bayes. If the hyperprior is assumed as a uniform distribution, the posterior distribution becomes an improper distribution when the upper bound of support is not restricted. Thus, at least one of the hyperparameters should have a finite upper bound. Two single bound cases and a double bound case are examined, and the results are compared using emergency diesel generator fail-to-run data. It is shown that the double bound case is located between the results of single bound cases. On the other hand, central tendencies of empirical Bayes and Kass-Steffey adjustment decreases compared to the other results from conservative to optimistic as point estimated failure rate of the specific group of interest increases because empirical Bayes contains information from all the data groups and the central tendency of population variability attract the results of empirical Bayes with Kass-Steffey adjustment. Therefore, the empirical Bayes with Kass-Steffey adjustment presents conservative result for low failure rate group and optimistic result for high failure rate group, and the difference is increased as the population variability increases. Thus, approximation error becomes significant when the group of interest has relatively higher failure rate compared to the average performance because the failure rate can be underestimated in this case. In practice, empirical Bayes and Kass-Steffey adjustment remain valuable due to their mathematical simplicity, even though they introduce the approximation errors. However, analysts should account for these errors when there is high population variability in data groups.

ACKNOWLEDGMENTS

This work was supported by the Korea Institute of Energy Technology Evaluation and Planning (KETEP) grant funded by the Ministry of Trade, Industry and Energy (MOTIE) of Republic of Korea [grant number RS-2024-00398867].

REFERENCES

[1] R. E. Kass and D. Steffey, Approximate Bayesian inference in conditionally independent hierarchical models (Parametric empirical Bayes models), Journal of the American Statistical Association, 84 (407), 717-726 (1989).
[2] C. L. Atwood, J. L. Lachance, H. F. Martz, D. J. Anderson, M. Englehardt, D. Whitehead, T. Wheeler, Handbook of parameter estimation for probabilistic risk assessment, NUREG/CR-6823, Nuclear Regulatory Commission, Washington D.C., United State (2003).
[3] Z. Ma, T. E. Wierman, K. J. Kvarfordt, Industry-average performance for components and initiating events at U.S. commercial nuclear power plants: 2020 update, INL/EXT-21-65055, Idaho National Laboratory, Idaho Falls, Idaho, United State (2021).
[4] Z. Ma, Enhanced component performance study: Emergency diesel generators 1998-2022, INL/EXT-23-73954, Idaho National Laboratory, Idaho Falls, Idaho, United State (2023).

Technical Session 6 (16:00 - 18:00)	The Port 2, C Floor	Source Term Analysis, Offsite Consequence Analysis and Emergency Preparedness and Response
		Chair/Facilitator 1: Dr. Wasin VECHGAMA (Thailand Institute of Nuclear Technology (TINT))
		Chair/Facilitator 2: Mr. Jia Hao TANG (Singapore Nuclear Research and Safety Initiative (SNRSI))
16:00 - 16:20		ID 33: Implementation of New Methodology for Determination of Iodine Thyroid blocking Efficacy around KORI Nuclear Power Plant to Perform Offsite Consequence Analysis Speaker: Jia Hao TANG (Korea Atomic Energy Research Institute, University of Science and Technology, Singapore Nuclear Research and Safety Initiative) Contributors: Jia Hao TANG (Korea Atomic Energy Research Institute, University of Science and Technology, Singapore Nuclear Research and Safety Initiative), Sung-yeop KIM (Korea Atomic Energy Research Institute, University of Science and Technology)
16:20 - 16:40		ID 40: Probabilistic Assessment of Radiation Exposure Risk Considering Shadow Evacuation Near a Nuclear Facility: Application of Evacuation Simulation and Level 3 PRA Speaker: Kazumasa Shimada (JAPAN NUS Co., LTD) Contributors: Ryosuke Kakuya (JAPAN NUS Co., LTD), Masahiko Kozuka (JAPAN NUS Co., LTD), Kazumasa Shimada (JAPAN NUS Co., LTD)
16:40 - 17:00		ID 78: Development of Risk Profile for Accident Sequences with Source Term Analysis Speaker: Yunho Kim (Chung-Ang University) Contributors: Yunho Kim (Chung-Ang University), Jaehyun Cho (Chung-Ang University)
17:00 - 17:20		ID 91: Analysis of On-site Impact and Feasibility of Outdoor Work under a Fission Product Release at a Nuclear Power Plant Speaker: Riku Iwata (Hokkaido University) Contributors: Riku Iwata (Hokkaido University), Sunghyon Jang (Hokkaido University), Eishiro Higo (Central Research Institute of Electric Power Industry)
17:20 - 17:40		ID 102: Release Time-based Source Term Grouping Method for Level 3 Multi-unit Probabilistic Safety Assessment of Cascading Accidents Speaker: Hee Young Lee (Sejong University) Contributors: Hee Young Lee (Sejong University), Gee Man Lee (Sejong University), Woo Sik Jung (Sejong University), Seong Kyu Park (Nuclear Engineering Services & Solutions)
17:40 - 18:00		ID 130: Development of a Source Term Assessment Framework Integrating Uncertainty Analysis Speaker: Seunghyeon Hwang (Chung-Ang University (CAU)) Contributors: Seunghyeon Hwang (Chung-Ang University (CAU)), Jaehyun CHO (Chung-Ang University)

ASRAM2025
www.asram2025.org
Asian Symposium on Risk Assessment and Management 2025
Pattaya, Thailand, 27 – 29 August 2025

IMPLEMENTATION OF METHODOLOGY FOR DETERMINATION OF IODINE THYROID BLOCKING EFFICACY AROUND KORI NUCLEAR POWER PLANT VIA LEVEL 3 PSA

Jia Hao Tang[1,2,3], Sung-yeop Kim[1,2*]

[1] *Korea Atomic Energy Research Institute (KAERI): 111, Daedeok-daero 989beon-gil, Daejeon, 34057, Republic of Korea*
[2] *University of Science and Technology (UST): 217, Gajeong-ro, Yuseong-gu, Daejeon, 34113, Republic of Korea*
[3] *Singapore Nuclear Research and Safety Initiative (SNRSI): 16, Prince George's Pk, Singapore, 118415, Republic of Singapore*

[*] *sungyeop@kaeri.re.kr*

ABSTRACT

Iodine thyroid blocking (ITB) is an important protective action in the radiological emergency action plan. However, the efficacy of such protective action is highly dependent on the accident scenario and site-specific factors. It is important to be able to assess ITB with site specific factors to support decision-making over implementation of ITB. In this work, a new methodology for determination of the efficacy of ITB will be applied for the Kori nuclear power plant located in South Korea. In previous Level 3 PSA assessment, ITB has been applied as a general protection factor that is dependent on expert judgement and does not incorporate scenario specific nature of ITB. The new methodology will produce an ITB protection factor that is based on specific scenario and iodine biokinetic model. The methodology estimates ITB protection factors by utilizing scenarios of Level 3 PSA to obtain the timepoint of exposure to radioactive plume and coupling it with the user defined ingestion time of iodine tablet. This will allow for an assessment of radiological impact that is grounded on technical results, rather than relying on expert judgement, while providing insights for the implementation of ITB. Utilizing publicly available information for weather conditions and source terms, offsite consequence analysis was performed alongside the methodology to assess the impact of ITB. This work would hopefully provide insight to further enhance the implementation of ITB in the emergency protection zone of Kori nuclear power plant.

Keywords: Iodine thyroid blocking, Emergency protective action, Emergency planning, Level 3 PSA, MACCS

I. INTRODUCTION

Iodine thyroid blocking (ITB) plays an important role in limiting the impact on thyroid in the event of an accident. It is one of the protective actions in the radiological emergency plan and the implementation of ITB is particularly important for younger population groups [1]. ITB involves the ingestion of stable iodine tablets that saturate the thyroid organ and would lead to a reduction in the amount of radioiodine absorbed by the thyroid organ when exposed to radioiodine. While the implementation of ITB has been widely recognized and general recommendations have been provided such as provision of stable iodine tablets 24 hours prior to and 2 hours after exposure to radioiodine, implementation of ITB in practice is difficult due to inability to accurately pinpoint the timepoint of exposure. Coupled with limited research in the optimal implementation of ITB in emergency scenario, practical application of ITB has been proven to be difficult [2]. This could be due to the complexity surrounding the efficacy of ITB which are dependent on factors such as time of exposure to radioiodine and time of ingestion of stable iodine tablets that are hard to ascertain and predict in an emergency scenario. As a result, estimation of the impact of ITB has conventionally been dependent on expert judgement which has clear limitations.

Hence, this study demonstrates the use of an alternative methodology to quantify efficacy of ITB via Level 3 PSA [3] in the context of Kori nuclear power plant in South Korea. The study will estimate efficacy of ITB based on offsite consequence analysis and provide some insight to better support ITB implementation around Kori nuclear power plant. The applied methodology combines insights from an iodine biokinetic model [4] and results from Level 3 PSA to determine the efficacy and dose reduction factor for a hypothetical accident at Kori nuclear power plant. The distribution strategy of ITB was also considered by incorporating time delays attributed to the distribution of iodine tablets. With these results, the study will provide some recommendations to the implementation of ITB for Kori Nuclear power plant to enhance emergency planning around the vicinity of the nuclear power plant. The rest of this study is organized as follows. Section II presents a summarized methodology applied in this case study, and section III presents the simulation results with the illustration of the efficacy curve and dose reduction factor of ITB. Finally, section IV provides the conclusion to this study

II. METHODOLOGY

The study estimates the impact of ITB particularly around the Kori nuclear power plant with publicly available data. The methodology used combines iodine biokinetic model and Level 3 PSA. It consists of three steps which are atmospheric dispersion analysis, efficacy calculation and dose analysis.

II.A. Atmospheric Dispersion Analysis

In the first step, the atmospheric dispersion analysis will be conducted with MELCOR Accident Consequence Code System (MACCS) code [5] was utilized. MACCS is widely used in the nuclear industry and provides a good estimate of the offsite consequences. The analysis will be centered around Kori Nuclear power plant, a facility located in Busan, South Korea. This nuclear power plant is of interest as it has a significant population density around the plant and could benefit from the analysis of ITB implementation. For this study, the accident scenario will be limited to a hypothetical accident occurring in one of the pressurized water reactor of APR1400 design which result in release of radionuclides. Due to the limitations of publicly available data on the source term, a hypothetical accident source term would be used. The source term was assumed to be iodine-131 with 4.43E18 Bq and a release fraction of 0.1 [6], released over an hour. For this assessment, only iodine-131 was simulated as ITB only affects iodine radionuclide and significant amount in an accident release. Weather data over three years from 2021-2023 was extracted from the Korean meteorological agency website [7]. MACCS simulates the consequences by repeating the simulations with a series of weather sequences extracted from the weather data. In this instance, the results are an average of the 8760 scenarios in which weather sequences are created with each hour in the year as a starting point and the average results over three years are recorded for a conservative analysis. This allows for a probabilistic representation of the average consequences from a hypothetical accident.

The distances of interest were set to represent conventional distances in emergency planning such as 3.22 (2 mi) and 16.1 km (10 mi) [8, 9]. In addition, a range of distances provides an overall view of the impact of ITB for population at different distances. For each of this distance, an estimate for the average timepoint of radioiodine exposure for the population residing at that distance was obtained. Table 1 shows the timepoint of exposure for different population groups at the respective distance.

TABLE I. Timepoint of exposure for different population groups

Distance (km)	Timepoint of exposure (h)
2.5	0.35
3.22	0.45
5	0.71
7.5	1.08
10	1.48
12.5	1.90
15	2.32
16.1	2.51

II.B. Efficacy Calculation

Subsequently, ITB efficacy will be calculated based on the exposure timepoint from the previous step with insight from an iodine biokinetic model. The biokinetic model simulates the transport of iodine within the human organs as compartments which exchange radionuclides with each other. One output of iodine biokinetic model is the relationship of efficacy and administration time. Administration time, T_{Admin} has been conventionally defined as the timepoint of iodine tablet ingestion relative to the timepoint of radioiodine exposure and it can be related to the results from step 1. Administration time was divided into two parts which are the timepoint of ingestion of iodine tablets and the timepoint of radionuclide exposure both relative to the start of radionuclide release as shown in Eq. (1).

$$T_{Admin} = T_{Ingest} - T_{Expose} \quad (1)$$

The time of ingestion, T_{Ingest} is the timepoint in which a population group ingests the iodine tablet relative to the start of radionuclide release and is dependent on the user definition. Timepoint of exposure, T_{Expose} is the timepoint in which a population group is exposed to radioiodine relative to the start of radionuclide release and this is directly obtained from the prior step. With the calculated administration time, an estimate of the efficacy of ITB can be obtained based on technical analysis via Level 3 PSA. In addition, A variation of the formula was also introduced to address potential administrative delays associated with the implementation of ITB. The equation for administration time will then take the following form as shown in Eq. (2).

$$T_{Admin} = T_{Announce} + T_{Delay} - T_{Expose} \quad (2)$$

The timepoint of announcement, $T_{Announce}$ will be user defined and is based on the activation timepoint of the protective action by the governing authority. Timepoint of exposure remains the same and will be obtained from step 1. The time delay, T_{Delay} was used to represent the associated delays due to the distribution policy of iodine tablets. Two distribution strategies were considered which are pre-distribution and stockpile distribution. The pre-distribution strategy distributes the iodine tablets preemptively and the time delay is assumed to be zero. In the stockpile distribution strategy, the iodine tablets are stored in a central location and distributed in the event of an accident thus resulting in a time delay. The analysis for this part will focus on distance 3.22, 5, 10 and 16.1 km to provide an overall perspective of the corresponding strategies. The time delay will be set to 20, 40, 60 and 80 minutes as evacuation is expected to be completed within around 90 minutes [10]. This analysis allows policy makers to have a deeper insight of ITB and how the distribution strategies could potentially affect the effectiveness of ITB. These estimated timepoints will be used to calculate efficacies of ITB which will be used in the next step of the methodology.

II.C. Dose Analysis

The estimated ITB efficacies from step 2 will be applied in MACCS code to estimate the impact of ITB. The MACCS simulation will focus on inhalation exposure for the thyroid organ over a period of seven days. This will simulate ITB impact in the early phase of the emergency. The key output from this step would be dose reduction factors which are defined as the ratio of the resulting impact with the protective measure against a scenario without protective measure in place. A dose reduction factor of 1 would imply that the protective action has no effect. The more effective the protective action is, the lower the dose reduction factor would be. The dose reduction factor for the WHO recommendation [1] would be approximately equal to less than 0.3 based on a standard iodine biokinetic model [4] and this would be used as a benchmark for the subsequent analysis. Through consideration of the different scenarios mentioned in the prior steps, different aspects of ITB can be analyzed and optimized in emergency planning.[11] In this study, the main objective would be to obtain the dose reduction factors for each of the population groups and provide recommendations for distribution strategy of ITB around the Kori nuclear power plant.

III. RESULTS AND DISCUSSION

III.A. Efficacy Curve and Dose Reduction Factors

ITB efficacy curves for each population group located at each distance were obtained and shown in Fig. 1. This provides an illustration of the efficacy of ITB against the time of ingestion of iodine tablet for population at different distances from the nuclear power plant. The origin point of this illustration also represents the timepoint where radioiodine is first released from the site. Hence a timepoint of ingestion at the origin point would indicate that the population consumes the stable iodine tablet at the same time as when radioiodine was first released from the site. The efficacy of ITB is expected to be high if it can be preemptively administered and the efficacy values diminish quickly after the timepoint of radionuclide exposure. Fig. 1 illustrates that each of the efficacy curve follows the typical ITB efficacy curve shape but the population at further distance experience shift of the curve according to the timepoint of exposure shown in Table 1. This is to be expected as a population located further from the release point would have more buffer time for the ingestion of stable iodine pills to obtain a high level of ITB efficacy.

This characteristic of ITB efficacy would results have critical impact to the implementation as delayed ingestion of iodine tablet would result in significantly diminishing impact. From this efficacy curve, the critical period for the change in efficacy falls within the 4 hours timeframe after the release of radionuclide. Coupled with the evacuation and emergency planning

timeline, a reduced timeframe would provide more details on the key period for ITB implementation. Hence, subsequent analysis will focus on the time frame between 4 hours prior to the radionuclide release to 4 hours after the radionuclide release.

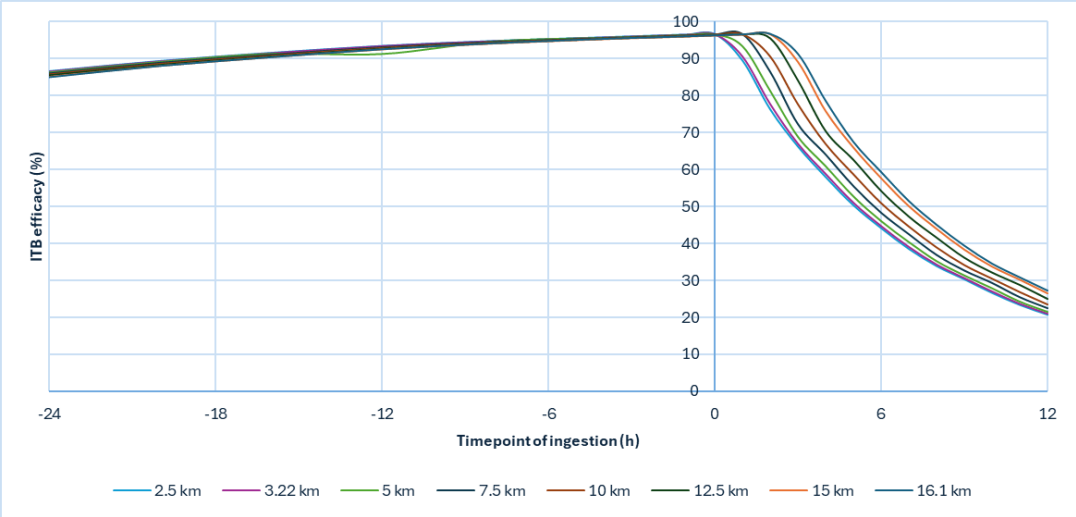

FIGURE 1. Efficacy curve for different population groups

Following the methodology, dose reduction factors were estimated from the offsite consequence analysis. The dose reduction factors for each group with respect to the time of ingestion of stable iodine tablets are shown in Fig. 2. The dose reduction factors were displayed in two categories which are divided based on the maximum distance of precautionary action zone. Radiological emergency planning typically consists of precautionary action zone (PAZ) and urgent protective action zone (UPZ). PAZ populations are required to evacuate immediately when prompted by the alert while UPZ population are required to take suitable protective action dependent on the results of detected radiation counts or predicted simulation result. The maximum boundary of the PAZ at the Kori nuclear power plant site is 5 km and the dose reduction factor will be characterized by being within PAZ and outside of PAZ.

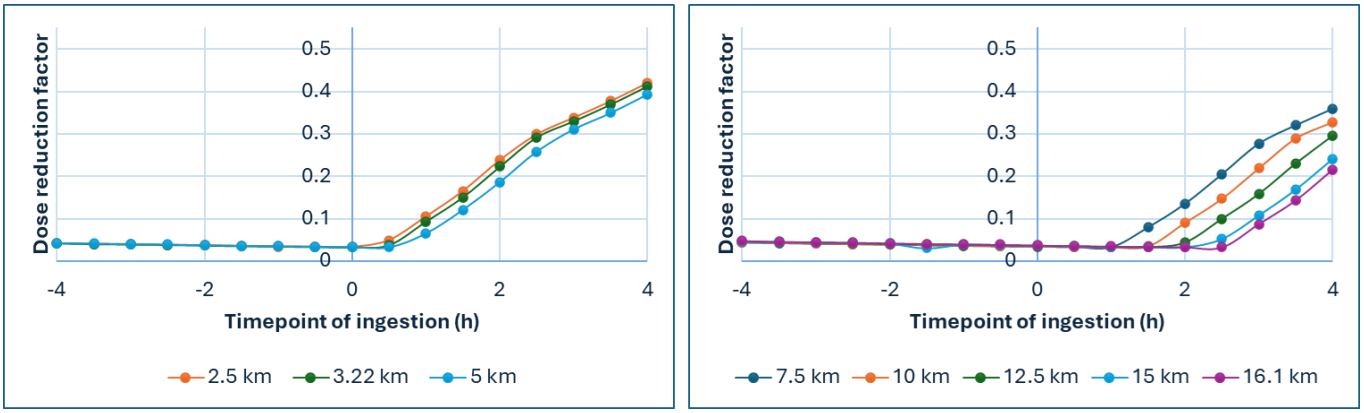

FIGURE 2. Dose reduction factor for different population groups within PAZ (left) and outside of PAZ (right)

Based on Fig. 2, population groups within the PAZ must ingest stable iodine tablet 30 minutes after release of radioiodine in order to obtain the highest level of protection from radioiodine. However, dose reduction factor would still be within the recommended range of less than 0.3, if iodine tablet is ingested within 2.5 hours from the release of radioiodine based on Level 3 PSA analysis of the average timepoint of plume exposure. Especially for the population at 3.22 km where thyroid dose can be reduced by 90%, if ITB is ingested within an hour of radionuclide release. For population groups outside of the PAZ till 16.1 km, Fig. 2 shows that best period of ingestion varies from 1 hour to 2.5 hours from release. For the population at 7.5 km and 10 km, optimal period of ingestion of stable iodine tablet for adherence to general recommendations is before 3.25 and 3.5

hours timepoint after release. For population groups at further distance that the one mentioned before, the recommended protective effect can be met as long as the tablet are ingested 4 hours after the release of radioiodine. This could indicate the merit of preemptive administration of iodine tablets and the incorporation of ITB into evacuation plans. With ITB optimal effectiveness heavily overlapping with emergency evacuation timeline and the possibility of accidental exposure during evacuation, it may be worthwhile considering the early administration of ITB, especially for vulnerable population groups.

III.B. Distribution Strategies

For practical application of ITB, the implementation of ITB was analyzed based on the distribution strategy. This is crucial as ITB effectiveness is time dependent. The time delay due to the distribution strategy would result in the delayed ingestion of iodine tablets and reduced effectiveness of ITB. The dose reduction factors for the distribution strategies were estimated with different delay time for different populations at 3.22 km, 5 km, 10 km and 16.1 km. The results are shown in Fig. 3.

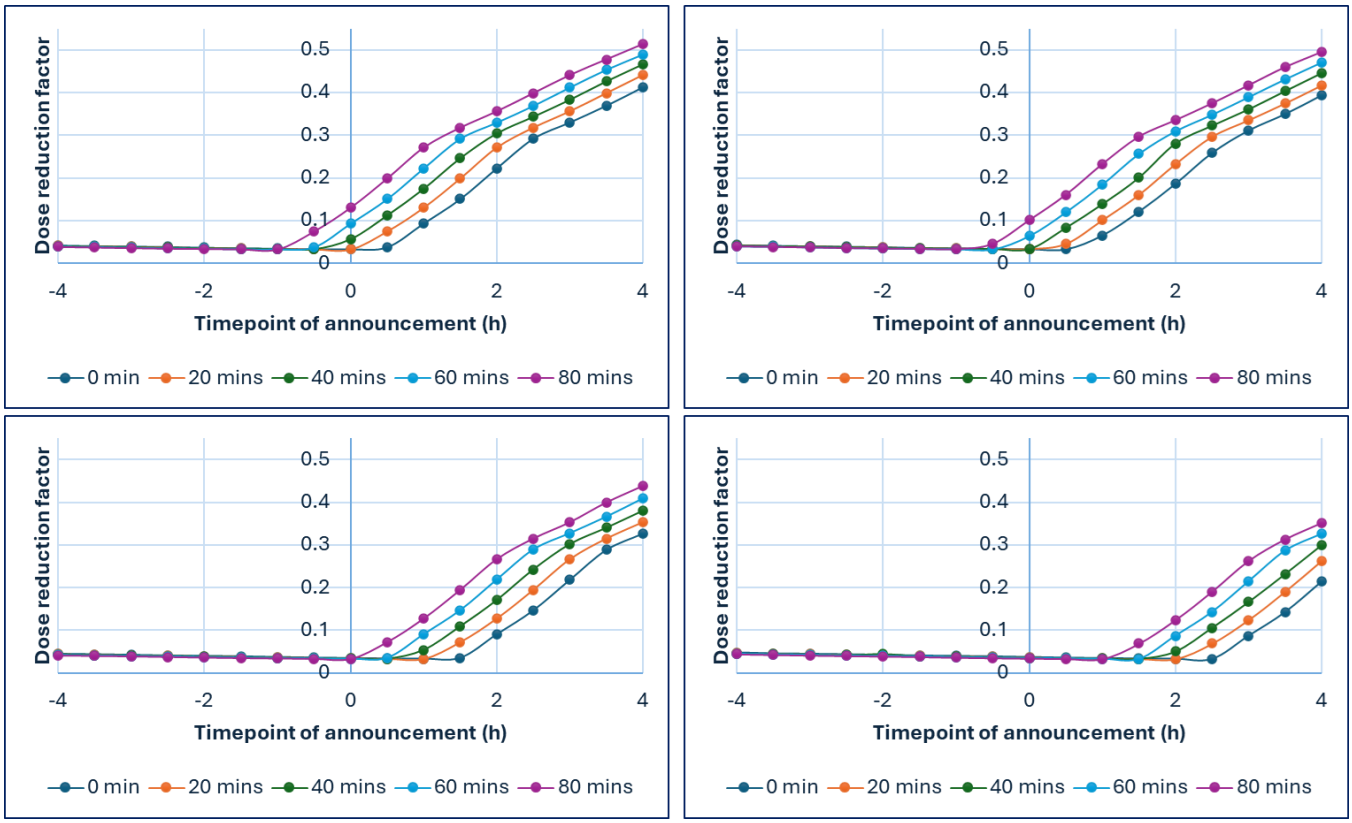

FIGURE 3. Dose reduction factor for different distribution strategies at different distance 3.22 km (top left), 5 km (top right), 10 km (bottom left), 16.1 km (bottom right)

As observed from Fig. 3, the time delay generally results in reduction in the effectiveness of ITB as can be seen by the increasing dose reduction factor with higher delay duration. Announcement of ITB must be implemented progressively earlier to achieve the same level of dose reduction compared to a scenario with lower time delay. Population closer to the Kori nuclear power plant will be more susceptible to the potential delays from the distribution strategy as optimal effectiveness of ITB involve implementation of ITB before the release of radioiodine. For the population group at 3.22 km to achieve 90% reduction in thyroid dose, announcement of ITB must be before the release of radioiodine for any time delays more than 60 minutes. Recommended effectiveness of ITB can be achieved by ensuring activation of ITB before 1.5 hour timepoint and 2.5 hour timepoint for 80 minutes and 0 minute time delay respectively.

For the 5 km population group, only the 80 minutes time delay scenario require the announcement of ITB to be coincident with the release of radioiodine to achieve 90% reduction in thyroid dose. Activation of ITB within the 1.5 hour timepoint would ensure the effectiveness of ITB falls within the recommended values. With evacuation of population around 5 km vicinity of Kori nuclear power plant expected to be completed within 1.5 hours, the preferred distribution strategy would likely be pre-

distribution which would ensure that the effectiveness of ITB be maximized. ITB can potentially be coupled with evacuation to ensure that ITB will be activated in an accident scenario. In order to ensure the effectiveness of ITB for the population within the PAZ, ITB should be activated before the start of emergency evacuation. In the case of population group at 10 km, the additional distance provides sufficient buffer time for the implementation of ITB. Even with a time delay of 80 minutes, ITB can reduce thyroid dose by 80% when announced 1.5 hours after the release of radionuclides. For population at 16.1 km, dose reduction of 80% can be achieved if ITB is announced before 2.5 hours after release. Thus, this could suggest that both distribution strategies are viable at these distances if the time delay for stockpile distribution is kept at a minimum.

The above summarized the analysis of ITB implementation in Kori nuclear power plant based on the assumed source term. It should be noted that the analysis is based on a conservative source term and there may be variance in a potential accident. While the general recommendations of early implementation of ITB would still be valid for most scenario, there are certain limitations that should be considered. When considering the results, scenarios with significant time delay for the radionuclide release would result in a later exposure time. This tends to result in a greater time window for the implementation of ITB compared to the results shown in which release was expected to begin at the zero timepoint. In extreme scenarios where release of radionuclides was delayed by 24 hours would result in early implementation of ITB being ineffective as the efficacy is expected to only last for 24 hours.

IV. CONCLUSIONS

In conclusion this study assessed the impact of iodine thyroid blocking around Kori nuclear power plant via a methodology that utilized Level 3 PSA and insights from iodine biokinetic model. From the results, it is ideal for ITB to be activated as early as possible, especially for population in the vicinity of the nuclear power within PAZ. In order to ensure recommended effectiveness of ITB with dose reduction factor equal to less than 0.3, population residing within the PAZ must consume iodine tablets before the timepoint of 2.5 hours after the radionuclide release. However, to ensure dose reduction of 90 %, population groups within the PAZ should ingest stable iodine tablet within 30 minutes after release of radionuclides. Thus, it will be beneficial to consider the early administration of ITB, especially for vulnerable population groups. For population groups outside of the PAZ, the recommended dose reduction factor can be met, if the tablets are ingested 3 hours after the release of radioiodine.

In addition, analysis of the distribution strategies illustrates that pre-distribution strategy would be preferred scenario especially with the evacuating population at less than 5 km within PAZ. This is due to the time delays of stockpile distribution significantly affecting effectiveness of ITB. For a population at 3.22 km and stockpile distribution time delay of 60 minutes to attain 90% reduction in thyroid dose, the activation of ITB must be before the release of radionuclide. As such, it may be ideal to implement pre-distribution strategy and couple ITB with evacuation to ensure maximum effectiveness of ITB for the population within PAZ. For population at greater distance, stockpile distribution can be considered as the dose reduction factors can still be at an acceptable level, if tablets can be provided in a timely manner at least 1.5 to 2.5 hours after release for populations at 10 and 16.1 km.

This study showcases the analysis of ITB effectiveness which could be incorporated into emergency planning around Kori nuclear power plant. This is especially crucial for the PAZ population that are closest to the nuclear power plant and will be instructed to evacuate during the emergency. By considering the dose reduction factor with the evacuation timeline, it would be possible to minimize the dose exposure for the population in the PAZ. In order to maintain a 90% thyroid dose reduction, ITB should be implemented before the start of emergency evacuation. With more clarity of the implementation of ITB would also help to ensure that ITB will be activated in a timely manner during an emergency. This could potentially be used to support and enhance future emergency planning around the Kori nuclear power plant.

ACKNOWLEDGMENTS

This work was supported by the Nuclear Safety Research Program through the Korea Foundation of Nuclear Safety (KoFONS) using financial resources granted by the Nuclear Safety and Security Commission (NSSC) of Korea (No. RS-2023-00240452).

REFERENCES

[1] World Health Organization, *Iodine Thyroid Blocking: Guidelines for Use in Planning for and Responding to Radiological and Nuclear Emergencies*, PMID: 29630192 (2017).

[2] International Atomic Energy Agency, *The Fukushima Daiichi Accident*, **Technical Volume 3**, ISBN 978-92-0-107015-9 (2015).
[3] J.H. TANG, S-Y. Kim, "Methodology to Quantify the Efficacy of Iodine Thyroid Blocking via Level 3 PSA to Support Emergency Planning," *Nucl. Eng. Technol.*, **53**, 1738-5733 (2025).
[4] TE. Kwon, Y. Chung, WH. Ha, YW. Jin, "Application of the New ICRP Iodine Biokinetic Model for Internal Dosimetry in Case of Thyroid Blocking," *Nucl. Eng. Technol.*, **52 (8)**, 1826-1833 (2020).
[5] Sandia National Laboratories, *MELCOR Accident Consequence Code System (MACCS) Users Guide (V.4.2)*, Sandia National Laboratories, SAND2023-01315 (2024).
[6] Korea Electric Power Corporation and Korea Hydro & Nuclear Power Co. Ltd, *APR1400 Design Control Document and Environmental Report*, Chapter 15, APR1400-K-X-FS-14002-NP (2018).
[7] "Korea Meteorological Administration," https://data.kma.go.kr/data/ (2025).
[8] U.S. Environment Protection Agency (US EPA), *PAG Manual: Protective Action Guides and Planning Guidance for Radiological Incidents*, EPA-400/R-16/001 (2016).
[9] International Atomic Energy Agency, *Arrangements for Preparedness for a Nuclear or Radiological Emergency*, IAEA Safety Standards Series No. GS-G-2.1 (2007).
[10] GB. Kim and GY. Heo, "Agent-based Radiological Emergency Evacuation Simulation Modeling Considering Mitigation Infrastructures," *Reliab. Eng. Syst. Safety*, **233**, 0951-8320 (2023).
[11] K. Oh et al., Study on Multi-unit Level 3 PSA to Understand a Characteristics of Risk in a Multi-unit Context, *Nucl. Eng. Technol.*, **52 (5)**, 975-983 (2020).

ASRAM2025
www.asram2025.org
Asian Symposium on Risk Assessment and Management 2025
Pattaya, Thailand, 27 – 29 August 2025

Probabilistic Assessment of Radiation Exposure Risk Considering Shadow Evacuation Near a Nuclear Facility: Application of Evacuation Simulation and Level 3 PRA

Kazumasa Shimada[1], Masahiko Kozuka[1], Ryosuke Kakuya[1],

[1]*JAPAN NUS CO., LTD , Shinjuku-ku, Tokyo, 160-0023, shimada-kzms@janus.co.jp*

ABSTRACT

This study presents a novel probabilistic risk assessment of radiation exposure that incorporates the impact of "shadow evacuations" — voluntary evacuations by residents in the Urgent Protective Action Planning Zone (UPZ) — on prioritized evacuations from the Precautionary Action Zone (PAZ) during a nuclear emergency. In Japan, PAZ residents are expected to evacuate promptly before the release of radioactive material, while UPZ residents are generally advised to shelter indoors initially. However, uncoordinated UPZ evacuations can cause severe traffic congestion, potentially delaying PAZ evacuations and increasing radiation exposure. To quantify these effects, we combined evacuation simulations using PTV VISUM-SBA with radiological consequence assessments using the MACCS2 (v1.13) code. A densely populated area surrounding a representative Japanese nuclear facility was modeled, and Evacuation Time Estimation (ETE) were derived under varying UPZ shadow evacuation rates. As MACCS2 does not natively support detailed traffic flow modeling, we developed a method to translate simulation-based delays into phase-specific evacuation speeds, enabling realistic integration of congestion effects into Level 3 PRA. We also introduced a new risk metric, the Relative Population Dose (RPD), to capture changes in collective dose under different evacuation scenarios. The results indicate that increasing levels of UPZ shadow evacuation substantially delay PAZ evacuations, leading to elevated radiation risk depending on the timing of protective actions. Conversely, UPZ residents themselves experience lower exposure if evacuation occurs after the release has concluded, reinforcing the rationale behind Japan's current phased evacuation policies. These findings emphasize the critical need for real-time, risk-informed decision-making in emergency response planning.

Keywords: Level 3 PRA, Evacuation Simulation, Shadow evacuations, Emergency Preparedness and Response, ETE

I. INTRODUCTION

In the field of nuclear safety assessment, it is essential not only to evaluate system reliability and hardware integrity but also the effectiveness of protective actions for surrounding residents[1]. One critical behavioral phenomenon during nuclear emergencies is "shadow evacuation," where residents outside designated evacuation zones voluntarily evacuate, potentially causing severe traffic congestion and delaying priority evacuations[2].

In Japan, nuclear emergency planning zones are divided into the Precautionary Action Zone (PAZ, approximately 5 km radius), where residents must evacuate immediately before radioactive release, and the Urgent Protective Action Planning Zone (UPZ, approximately 30 km radius), where residents are initially instructed to shelter indoors[3]. However, spontaneous evacuation by UPZ residents can interfere with PAZ evacuations, creating a policy dilemma.

Level 3 Probabilistic Risk Assessment (PRA) is widely used to quantitatively assess risks to the public during nuclear accidents[4, 5]. While Level 3 PRA considers dispersion of radioactive materials and resulting health effects, conventional models simplify evacuation behavior with fixed parameters, failing to reflect real-world evacuation dynamics[6].

This study aims to evaluate how shadow evacuations by UPZ residents influence the evacuation performance and radiation exposure risk for PAZ residents. We integrate a traffic simulation model (PTV VISUM with Simulation-Based Assignment (SBA)[7]) with a Level 3 PRA tool (MACCS2[8]), allowing us to probabilistically assess the impact of evacuation behavior on radiation exposure. Compared to prior studies, this research:

- Develops a high-resolution method to reflect evacuation delay caused by shadow evacuations;
- Applies the analysis to a Japanese nuclear site with realistic demographic and infrastructural data;
- Provides policy-relevant insights into managing shadow evacuations under uncertainty.

This study builds on prior U.S.-based research[9, 10] but represents the first application of this integrated framework to a Japanese context, contributing to both methodological advancement and policy formulation.

II. METHODOLOGY

This study integrates traffic simulation with Level 3 PRA to evaluate radiation risk under different shadow evacuation scenarios. The methodology consists of three main components: evacuation simulation using VISUM-SBA, risk calculation using MACCS2, and definition of risk indicators.

II.1. Evacuation Simulation using VISUM-SBA

For ethical and security reasons, the name of the study area is not disclosed. This study does not aim to evaluate site-specific radiological risk, but to generalize how evacuation behavior influences radiation exposure risk. Accordingly, the analysis emphasizes causal mechanisms and structural patterns over region-dependent numerical values.

A hybrid traffic model, VISUM-SBA, was selected to simulate evacuation from areas near a Japanese nuclear power plant. VISUM-SBA combines a macroscopic road network model (VISUM) with a simplified behavioral algorithm (SBA) to estimate Evacuation Time Estimations (ETE) under varying population and traffic conditions. The macroscopic model calculates traffic flow based on road capacities and demand, while SBA distributes departure times and route choices based on probabilistic rules. This hybrid approach enables efficient simulation of large-scale evacuations without requiring full microsimulation. The model estimates ETE for residents in both PAZ and UPZ zones. The population distribution was based on Japanese census data, mapped to concentric mesh zones. While the specific location is not disclosed, the characteristics of the study area are broadly consistent with those of a mid-sized Japanese municipality in a semi-urban region. The population density in the PAZ (0–5 km) and UPZ (5–30 km) zones ranges from approximately 500 to 2,000 persons per square kilometer. The local road network includes both arterial roads and residential streets, with daily traffic volumes on main evacuation routes ranging from a few thousand to over ten thousand vehicles per day. These conditions provide a representative context for testing the effects of evacuation behavior on radiation risk without relying on site-specific identifiers. Shadow evacuation rates for UPZ residents under various shadow evacuation rates (0% to 90%). Road network data were extracted from OpenStreetMap[11] and processed to represent realistic evacuation routes, considering road type, lane count, and signal locations.

Vehicle counts were estimated assuming a Vehicle Occupancy Rate (VOR) of 2. The simulation output includes time-dependent vehicle passage across the 30 km zone boundary. The departure time for both PAZ residents and shadow evacuees in the UPZ was assumed to be within 0 to 1 hour after the initiation of the evacuation order.

Figure 1 shows the cumulative evacuation rates for PAZ and UPZ residents under different shadow evacuation scenarios.

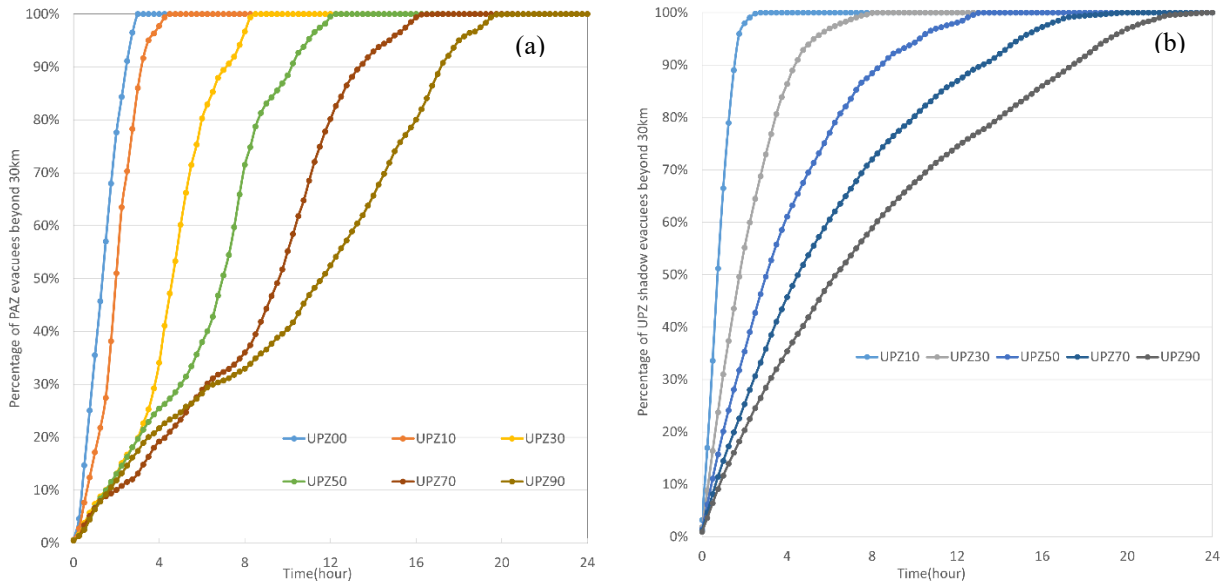

FIGURE 1. Cumulative evacuation rates of residents are beyond the 30 km zone under different shadow evacuation scenarios: (a) PAZ residents and (b) UPZ residents.
Each curve represents a scenario with a different percentage of shadow evacuation in the UPZ, ranging from 0% to 90%. The data reflects traffic simulation results using VISUM-SBA.

II.2. Development of a New Method for Integrating ETE into MACCS2

In MACCS2, the analysis domain is divided into multiple spatial meshes to represent evacuation behavior. Each mesh is assigned a population, and since the size of the meshes is not uniform—outer meshes tend to have larger areas than central ones—meshes on the periphery generally contain more people, even when population density per unit area is assumed to be constant. Due to this spatial structure, evacuation tends to be completed earlier in the outer regions with larger populations, while the inner meshes, which contain fewer people, tend to remain until later in the process. As a result, the rate of increase in the evacuation completion ratio (ECR) tends to slow down over time.

In this study, significant inflection points in the ECR curve—approximately 28% for PAZ residents and 17% for UPZ residents—were used to define the timing of the first change in ESPEED1 (DURBEG). In addition, following the U.S. NRC's ETE guidelines[12], where the 90% Evacuation Completion Time (ECT) is considered a key benchmark, the midpoint of the evacuation period (DURMID) in ESPEED2 was set accordingly. The final evacuation speed (ESPEED3) was adjusted to align with the time when ECR reaches 100%. Meanwhile, the values of ESPEED1 and ESPEED2 were also modified based on the results of the evacuation simulation to ensure consistency with the traffic conditions observed in VISUM-SBA.

These parameter settings were determined approximately based on the results of traffic simulations and applied to MACCS2. Since these settings involve a degree of analyst discretion, future work should aim to develop more objective and automated methods for parameter estimation.

To bridge the gap between traffic simulation results and MACCS2 inputs, we developed a new approximation method that quantitatively relates ECT and ECR. Specifically, ECT_i for each concentric mesh cell i is computed using the following piecewise function based on its evacuation distance d_i, which represents the distance from mesh cell i to the designated evacuation destination:

(1) $if\ d_i \le ESPEED1 \times DURBEG$

$$ECT_i = \frac{d_i}{ESPEED1} \tag{1}$$

(2) $if\ ESPEED1 \times DURBEG < d_i \le ESPEED1 \times DURBEG + ESPEED2 \times DURMID$

$$ECT_i = DURBEG + \frac{d_i - ESPEED1 \times DURBEG}{ESPEED2} \tag{2}$$

(3) if $d_i > ESPEED1 \times DURBEG + ESPEED2 \times DURMID$

$$ECT_i = DURBEG + DURMID + \frac{d_i - (ESPEED1 \times DURBEG + ESPEED2 \times DURMID)}{ESPEED3} \tag{3}$$

Here, ESPEED1–3 represent evacuation speeds (km/h) for each phase, and DURBEG and DURMID are their respective duration periods (hours). To calibrate ECR_i in MACCS2 based on VISUM-SBA results, the following steps were performed: The ECR_i in MACCS2 is defined as a cumulative value representing the proportion of the population in mesh i that has relocated to the designated evacuation mesh over time.

(1) Data Acquisition： The d_i for each mesh and the corresponding ECR_i are extracted from the MACCS2 output, assuming a constant-speed NETWORK evacuation scenario.
(2) Calculation of ECT_i: Using the previously obtained distance d_i, ECT_i for each location is calculated by applying a predefined piecewise function.
(3) Data Structuring: The calculated ECT_i are paired with their corresponding ECR_i values to construct the ECT_i–ECR_i correspondence dataset for MACCS2.
(4) Graph Generation: To compare the results with the ETE obtained from VISUM, both the MACCS2-derived ECT_i and ECR_i values and the VISUM ETE results are plotted on the same graph.
(5) Adjustment of ESPEED3: The evacuation speed parameter for the third period in MACCS2 (ESPEED3) is iteratively adjusted to align the ECR_i curve with the *ECR* curve obtained from the VISUM ETE results.

Figure 2 compares the ETE results from VISUM-SBA and MACCS2. Under the 0% shadow evacuation scenario, VISUM-SBA produced a smooth *ECR* curve for PAZ residents, reflecting continuous vehicle flow. In contrast, MACCS2's curve exhibited stepwise increases due to mesh-based movement assumptions. While both models yielded similar 90% ETE values, MACCS2 showed more abrupt changes, particularly between 1.5 and 2.5 hours, highlighting the limitations of discrete spatial modeling. For the 90% shadow evacuation scenario, UPZ residents' *ECR* curves revealed greater discrepancy in the early phase (0–8 hours), with MACCS2 lagging VISUM-SBA. From 8 to 24 hours, the models aligned more closely, ultimately converging in final ETE. These results underscore the impact of initial evacuation speed settings and spatial granularity in MACCS2. While the developed parameter adjustment approach improved overall alignment, deviations in the mid-phase suggest areas for future refinement in evacuation modeling.

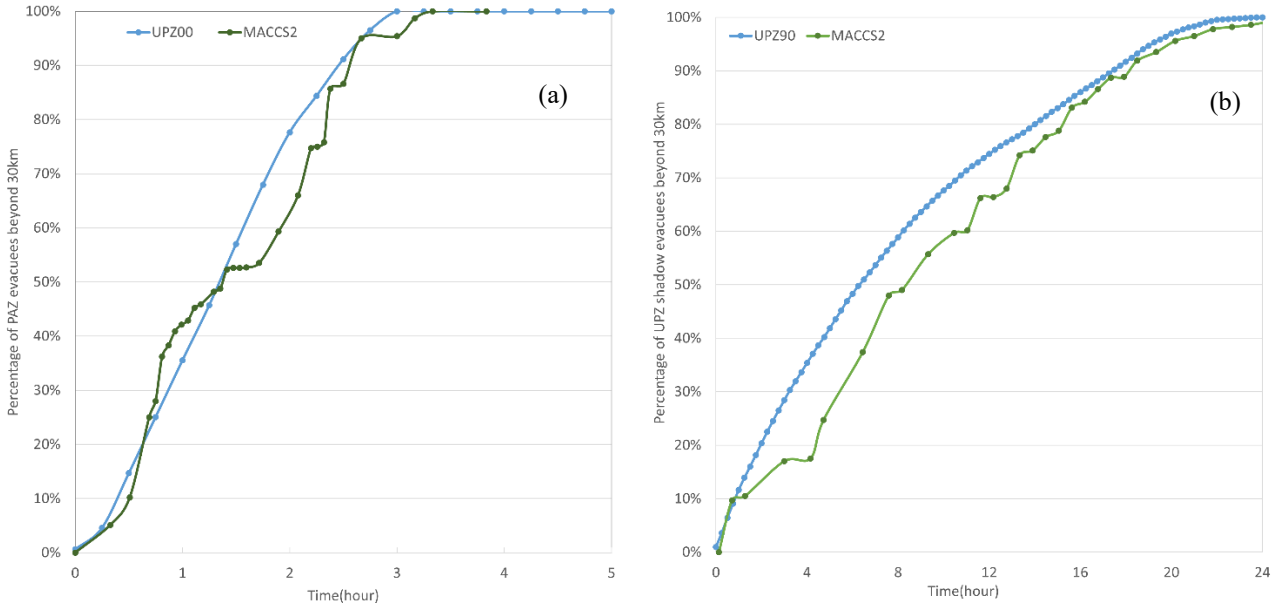

FIGURE 2. Comparison of evacuation completion rates between PAZ and UPZ residents using VISUM-SBA and MACCS2 simulations:(a) PAZ evacuation under 0% shadow evacuation scenario, and(b) UPZ evacuation under 90% shadow evacuation scenario.

II.3. MACCS2 inputs Configuration

The MACCS2 (v1.13) input configuration in this study followed the default settings from Sample Problem A as described in NUREG/CR-6613, except where it was modified for this analysis. Spatial mesh boundaries were adjusted to clearly delineate the PAZ (0–5 km) and UPZ (5–30 km) zones, following Japan's nuclear emergency response guidelines.

Meteorological sampling was configured using the "Stratified Random Samples for Each Day of the Year" option with 1,460 samples. The weather dataset from the Surry site, included in MACCS2's default input, was used without modification.

Radiation dose assessments were conducted using the EARLY module for the following four cohorts: PAZ evacuees, UPZ evacuees, UPZ shelterers, and non-evacuating residents outside 30 km. The proportions of Cohorts 2 and 3 were varied to simulate different shadow evacuation scenarios.

Evacuation modeling in MACCS2 used dynamic speed settings derived from VISUM-SBA results. While the definitions of ESPEED1–3 and DURBEG/DURMID are provided in the previous section, we note here that these parameters were carefully calibrated based on traffic patterns observed in the VISUM-SBA simulation. Specifically, DURBEG and DURMID were determined so that their combination with corresponding speeds reproduces realistic evacuation distances and timings. Although in several scenarios the product of ESPEED1 and DURBEG is approximately 30 km, this reflects the intended evacuation distance for PAZ residents and is not arbitrary. Phase-specific congestion effects are then captured through adjustments to ESPEED2, ESPEED3, and the respective durations. The evacuation speeds and durations were scenario-specific and are summarized in Tables 1 and 2. In the MACCS2 configuration, the evacuation start time for the PAZ cohort (Cohort 1) and the shadow evacuee cohort from the UPZ (Cohort 2) was also set to be the same.

To reflect realistic evacuation delays under varying traffic conditions, this study did not use the MACCS2 default evacuation speed of 1.8 m/s (6.48 km/h), which is uniformly applied across all time periods in the Surry site sample input. Instead, speeds were adjusted based on VISUM-SBA simulation results. As shown in Table 1, the initial speed (ESPEED1) for PAZ residents was set as high as 40.4 km/h in the baseline scenario (UPZ00), reflecting the assumption that they can evacuate promptly before plume release when no shadow evacuation occurs.

As the shadow evacuation rate in the UPZ increases, traffic congestion worsens, leading to a general decline in ESPEED1, ESPEED2, and ESPEED3 for both PAZ and UPZ residents. This trend is evident across the scenarios in Tables 1 and 2. Additionally, longer travel times in congested conditions necessitate extended phase durations (DURBEG and DURMID), resulting in increased total evacuation time. These speed and duration parameters were systematically varied for shadow evacuation rates of 0%, 10%, 30%, 50%, 70%, and 90%, and used in MACCS2 to evaluate radiation risk for both PAZ and UPZ populations. |

In the evacuation simulation, the endpoint of evacuation was defined as the central area of a real city located more than 50 km from the release point, based on actual designated evacuation destinations.

In contrast, for the MACCS2 network evacuation modeling, the evacuation destination was defined as a point beyond 100 km from the release point. This is because in MACCS2, once evacuees reach the destination, further dose calculation ceases, potentially underestimating the actual exposure if the destination is too close to the source. Therefore, a more distant endpoint was used to capture a more conservative dose estimate.

Table 1. Evacuation Speeds and Durations for PAZ Residents

Scenario	ESPEED1 (km/h)	ESPEED2 (km/h)	ESPEED3 (km/h)	DURBEG (h)	DURMID (h)
UPZ00	40.4	5.5	2.0	0.75	1.75
UPZ10	20.2	6.4	1.0	1.5	1.5
UPZ30	8.1	3.2	1.0	3.8	3.0
UPZ50	6.7	1.8	0.5	4.5	5.3
UPZ70	5.1	1.4	0.5	6.0	6.8
UPZ90	5.1	0.9	0.5	6.0	10.8

Table 2. Evacuation Speeds and Durations for UPZ Residents

Scenario	ESPEED1 (km/h)	ESPEED2 (km/h)	ESPEED3 (km/h)	DURBEG (h)	DURMID (h)
UPZ10	25.0	20.0	5.0	0.5	1.0
UPZ30	18.3	5.3	2.0	0.5	4.3
UPZ50	9.2	2.8	1.0	1.0	8.0
UPZ70	6.1	1.8	1.0	1.5	12.5
UPZ90	3.1	1.5	1.0	3.0	15.5

II.4. Radiation Risk Metrics

Radiation risk was quantified using the Population Dose (PD), defined as the product of average effective dose and population size (person-Sv). A new normalized indicator, Relative Population Dose (RPD), was introduced to evaluate the risk reduction effect of evacuation. RPD is defined as the ratio of PD under evacuation to PD under 7-days indoor sheltering. RPD > 1 indicates evacuation increased exposure; RPD < 1 indicates risk reduction.

This modeling framework enables probabilistic assessment of evacuation behavior's impact on radiation exposure, considering both traffic congestion and meteorological variability.

III. RESULTS AND DISCUSSION

III.A. Results of PAZ residents

Using MACCS2 simulations, this study evaluated radiation risk for PAZ residents under varying shadow evacuation rates by UPZ residents. The RPD was used to compare evacuation scenarios against a baseline of 7-days indoor sheltering. Figure 3 illustrates the RPD of PAZ residents under both average (Mean) and worst-case (Max) meteorological conditions. In this study, the "worst-case meteorological condition" refers to the condition under which the collective dose to the population becomes the highest among the meteorological scenarios considered. It does not necessarily correspond to extreme values of individual weather variables such as wind speed or precipitation but rather reflects the atmospheric conditions most conducive to maximizing radiological exposure.

III.A 1. Pre-Release Evacuation

When evacuation began before the release of radioactive plumes (i.e., in the negative X-axis region), a general reduction in radiation exposure risk for PAZ residents was observed. Under scenarios where the shadow evacuation rate of UPZ residents was 10% or lower, PAZ residents could evacuate without encountering the plume, resulting in an RPD of 0. This was due to minimal traffic congestion, allowing timely evacuation.

However, when the shadow evacuation rate exceeded 30%, delays in PAZ evacuation occurred, preventing completion before plume arrival and making it difficult to avoid exposure.

In the Max case (Figure 3(b)), the RPD values were higher compared to the Mean case (Figure 3(a)), indicating that shadow evacuations by UPZ residents significantly affect the effectiveness of pre-emptive evacuation of PAZ residents. This result highlights the critical role of UPZ shadow evacuation behavior in determining the evacuation success and radiation risk for PAZ residents.

III.A 2. Evacuation During Release (0–1 Hour)

When evacuation was initiated during plume release (0–1 hour), RPD values for PAZ residents exceeded 1 in both Mean and Max cases once the shadow evacuation rate reached approximately 30%. This implies that exposure doses during evacuation could surpass those from 7 days of sheltering in place.

A sharp increase in radiation dose was observed for PAZ residents under scenarios with shadow evacuation rates above 30%, due to evacuation congestion delaying PAZ movement and increasing exposure during plume passage. These results highlight the critical importance of evacuation timing, as well as the influence of UPZ residents' unplanned evacuation on PAZ evacuation strategy.

Although the RPD values did not show significant differences between the Mean and Max meteorological conditions, this should not be interpreted as an indication that the radiation dose received during evacuation is insensitive to weather conditions. Here, RPD is defined as the ratio of the collective dose under the evacuation scenario to that under the full indoor sheltering scenario. Since the denominator—the collective dose from indoor sheltering—varies between meteorological conditions, the apparent similarity in RPD values reflects the relative relationship between two distinct group dose estimates rather than absolute insensitivity. Therefore, the results should be interpreted with caution. Nevertheless, these findings reinforce the importance of initiating evacuation prior to plume release under any meteorological condition.

III.A 3. Post-Release Evacuation (After 1 Hour)

When evacuation began after the plume release (>1 hour), RPD values for PAZ residents remained relatively constant, regardless of the UPZ shadow evacuation rate. Since exposure occurred primarily during indoor sheltering before evacuation, the act of post-plume evacuation had limited additional impact.

Differences in ECT had only minor effects on additional exposure from surface-deposited radionuclides. Notably, there was little difference between the Mean and Max cases, suggesting that post-release weather variations had limited influence. Therefore, route selection and destination planning are more critical than speed in reducing radiation exposure in this phase.

III.A 4. Evacuation Time and Radiation Risk Correlation

Even under a high shadow evacuation rate of 90% among UPZ residents, the *ECT* for PAZ residents remained around 20 hours (see Figure 1(a)). Since RPD = 1 corresponds to the dose from 7 days of indoor sheltering, post-plume evacuation can still reduce exposure.

The results show that increased shadow evacuation significantly affects PAZ residents' risk, mainly by delaying their evacuation. Thus, emergency planning must account for the impact of UPZ residents' spontaneous evacuation on PAZ evacuation efficiency and radiation exposure.

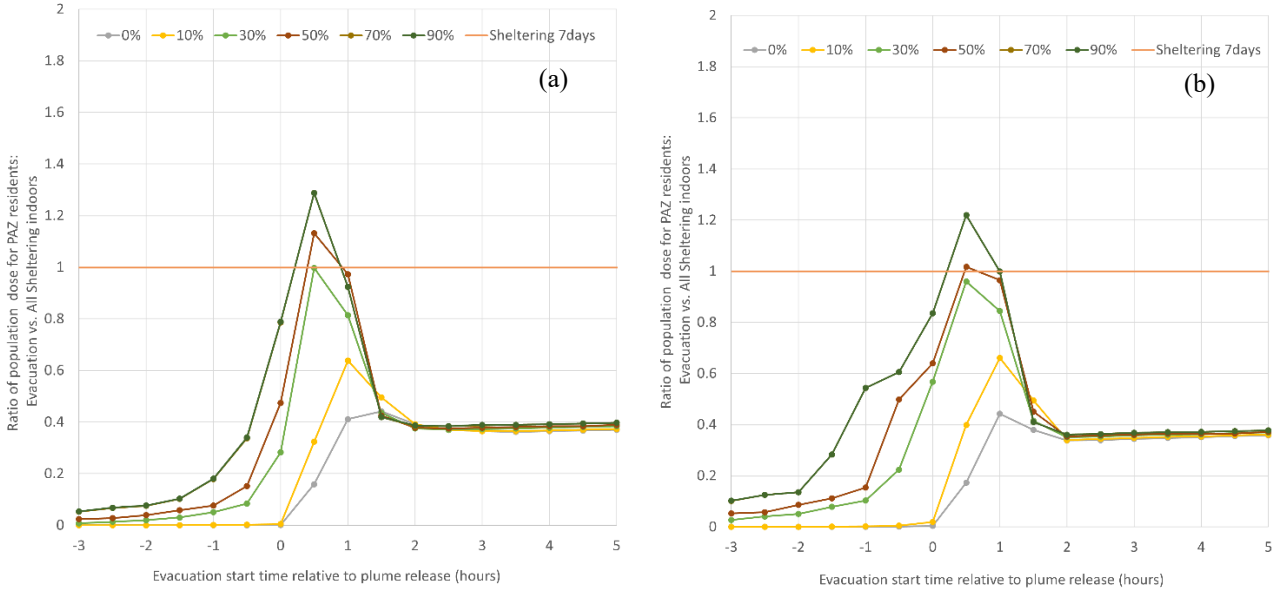

FIGURE 3. Relative Population Dose (RPD) for PAZ residents under two meteorological conditions based on MACCS2 output: (a) average condition (Mean), and (b) worst-case condition (Max). Each line represents a different shadow evacuation rate in the UPZ, showing the relative radiation dose from evacuation compared to a baseline of 7-days indoor sheltering (RPD = 1).

III.B. Results of UPZ residents

Under Japan's nuclear emergency guidelines, UPZ residents are advised to shelter indoors before plume release and evacuate based on post-release ambient dose rates. In this study, the remaining population in the UPZ—those who do not evacuate under each scenario—is assumed to shelter in place indoors for 7 days. The RPD in this section is calculated based on the collective dose of the entire UPZ population, and not on individual exposure levels. As shown in Figures 4(a) (Mean) and 4(b) (Max), the RPD remains at 1 when all residents shelter indoors. However, when evacuation is implemented, the RPD varies depending on the evacuation timing and the shadow evacuation rate. These variations are especially pronounced in the Max case, where meteorological conditions tend to amplify exposure differences. This highlights the importance of evacuation timing and the effect of traffic-induced delays on the overall population dose.

III.B.1. Pre-Release Evacuation

In the Mean case (Figure 4(a)), when UPZ residents began shadow evacuation before plume release (i.e., negative X-axis), the RPD generally decreased compared to the shelter-in-place scenario. Notably, evacuating more than 3 hours prior to release led to lower RPDs, especially with higher shadow evacuation rates.

However, one hour before release, scenarios with a 90% shadow evacuation rate resulted in higher RPDs than those with 30%, due to severe congestion delaying evacuation. This inversion indicates that excessive shadow evacuation can increase risk by preventing timely evacuation.

Figure 4(b) (Max case) further reveals that even when evacuation began three hours prior, high shadow evacuation rates (≥70%) could still lead to RPD >1, highlighting the dominant influence of adverse weather. The Max results consistently show higher RPDs than Mean, stressing the impact of meteorological variability and plume behavior under congested conditions.

III.B.2. Evacuation During Release (0–1 Hour)

Evacuation during plume release led to a rapid increase in exposure, especially with higher shadow evacuation rates. In the Mean case, RPDs exceeded 1 at 50% shadow evacuation and reached over 1.4 at 90%. The Max case showed even more severe outcomes, with RPDs reaching up to 3 under a 90% shadow evacuation rate.

The highest risk scenario occurred under specific winter morning meteorological conditions: wind speed of 2.5 m/s, Pasquill–Gifford stability class F, and wind direction directly impacting densely populated areas. These stable atmospheric conditions promoted ground-level plume retention and high localized radiation concentrations.

Thus, evacuating during plume release, particularly under high congestion and unfavorable weather, significantly increases UPZ residents' radiation risks. This finding underscores the need for cautious evacuation timing in emergency plans.

III.B.3. Post-Release Evacuation (After 1 Hour)

Post-release evacuation generally led to decreasing RPDs over time, regardless of shadow evacuation rate. This was attributed to accumulated exposure during sheltering, which was then mitigated by evacuation. Higher shadow evacuation rates further reduced collective doses by shifting more residents from sheltering to evacuation.

However, practical challenges such as shelter capacity and route congestion must be considered; maximizing evacuation participation does not automatically minimize risk.

In the Max case, trends diverged from the Mean case: RPDs remained above 1 at three hours post-release across all evacuation rates, indicating potential risk from premature evacuation before plume clearance. These results highlight the importance of verifying plume passage using real-time dose rate monitoring before initiating evacuation.

Given that current guidelines recommend evacuation only in high-contamination zones, more realistic modeling reflecting heterogeneous behavior and localized contamination is essential for future Level 3 PRA applications.

It should be noted that while RPD is used as a common metric in both PAZ and UPZ analyses, the underlying assumptions and cohort compositions differ between the two zones. Specifically, the population size, evacuation behavior, and sheltering assumptions are distinct. Therefore, direct comparison of RPD values across Figure 3 (PAZ) and Figure 4 (UPZ) should be made with caution, as they do not represent equivalent baseline conditions. Additional context is necessary for meaningful interpretation of relative values between the zones.

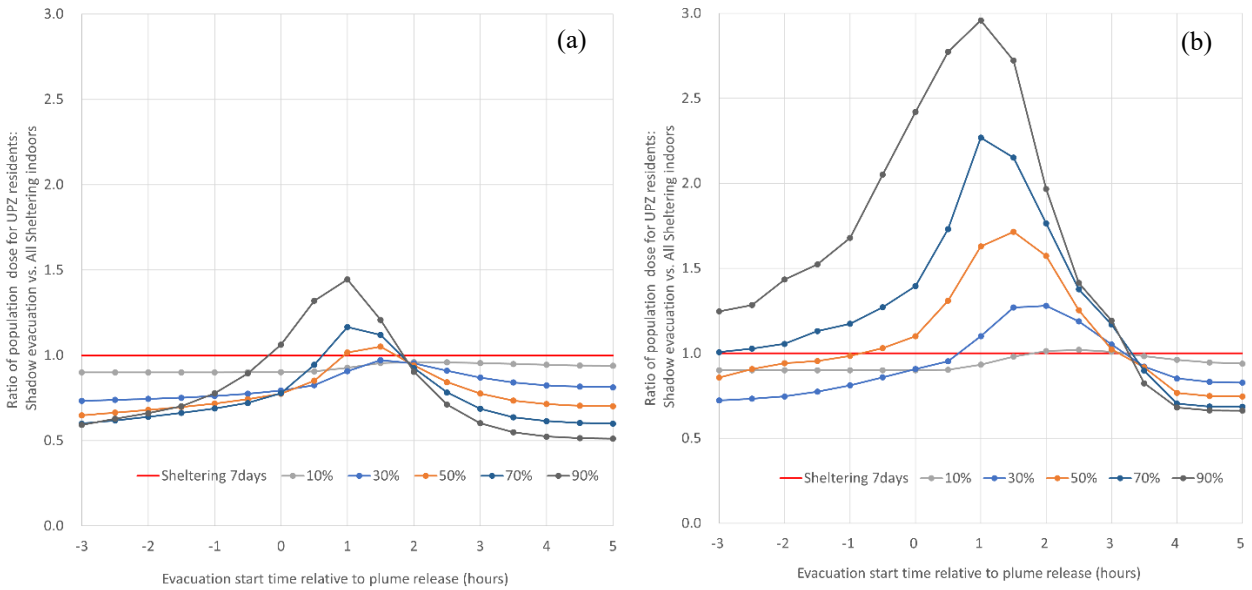

FIGURE 4. Relative Population Dose (RPD) for UPZ residents under two meteorological conditions based on MACCS2 output: (a) average condition (Mean), and (b) worst-case condition (Max). Each line represents a different shadow evacuation rate in the UPZ, showing the relative radiation dose from evacuation compared to a baseline of 7-days indoor sheltering (RPD = 1).

IV. CONCLUSION AND FUTURE WORK

This study integrated a traffic simulation model (PTV VISUM-SBA) with a Level 3 Probabilistic Risk Assessment tool (MACCS2) to evaluate how shadow evacuations by UPZ residents affect the radiation exposure risk of both PAZ and UPZ populations during a nuclear emergency in Japan. A new risk indicator, the Relative Population Dose (RPD), was introduced to quantify the relative effectiveness of evacuation versus sheltering.

The results demonstrate that shadow evacuation rates exceeding 30% significantly delay PAZ evacuation, leading to increased exposure risk, especially if evacuation occurs before or during the radioactive release. For UPZ residents, early evacuation can be effective under favorable conditions, but under adverse weather scenarios—such as stable atmospheric conditions and low wind speeds - high shadow evacuation rates can lead to elevated radiation doses, with RPD values exceeding 3 in extreme cases.

These findings highlight the complex, nonlinear relationship between evacuation timing, traffic congestion, and plume dynamics. They support Japan's current emergency response guidelines, which recommend pre-release evacuation for PAZ residents and indoor sheltering for UPZ residents until environmental radiation dose rates justify relocation. Managing shadow evacuation is critical not only for protecting PAZ residents but also for ensuring UPZ residents do not inadvertently increase their own exposure.

This study contributes to nuclear emergency planning by providing a quantitative framework to assess behavioral impacts on evacuation efficiency and public radiation risk. It underscores the importance of incorporating dynamic traffic modeling, and behavioral uncertainty into future Level 3 PRA applications.

Future work will focus on enhancing the realism and robustness of evacuation and risk modeling.

First, sensitivity analyses will be conducted on key traffic simulation parameters, including the distribution of evacuation start times, the vehicle occupancy rate (VOR), and the number of iterations for route assignment in VISUM-SBA. These factors could significantly influence Evacuation Time Estimation (ETE) and evacuation completion dynamics. This task is considered to have the greatest immediate impact on the calculated radiation risk, particularly through changes in evacuation delay and congestion. While sensitivity analysis in VISUM-SBA is technically feasible, performing it within MACCS2 presents a challenge due to its limited support for parameter uncertainty.

Second, future improvements will include integrating road hazard data such as blocked roads, reduced speed zones, and malfunctioning traffic signals, using disaster hazard maps. This task is technically feasible in principle and has been applied by

the authors in prior U.S.-based studies using tools such as FEMA's HAZUS. However, the lack of equivalent geospatial hazard evaluation tools in Japan currently limits the ability to apply this method to domestic nuclear sites.

Third, more realistic behavioral rules for UPZ residents will be incorporated. Rather than assuming uniform shadow evacuation rates, future models will introduce Operational Intervention Levels (OILs) to trigger evacuation decisions based on real-time spatial dose rate measurements. Although MACCS2 supports protective action decisions based on cumulative dose (e.g., 7-day exposure), it does not natively support dose-rate-based evacuation logic. Implementing this capability would require model adaptation, such as estimating dose rates from integrated dose thresholds.

These developments aim to improve the generalizability and practical value of Level 3 PRA by more accurately capturing the dynamic and uncertain nature of evacuation behavior under nuclear emergency scenarios.

ACKNOWLEDGMENTS

We would like to express our gratitude to Mr. Sidney Schreiner and Mr. Yoshihiko Hashino of PTV Japan for their invaluable assistance in conducting the evacuation simulation using VISUM-SBA.

REFERENCES

[1] IAEA, Preparedness and Response for a Nuclear or Radiological Emergency, 2015.
[2] P.B. Kevin Weinisch, The impact of shadow evacuation on evacuation time estimates for nuclear power plants, Journal of Emergency Management 13(2) (2015) 145-158.
[3] Nuclear Regulation Authority, Nuclear Emergency Response Guideline, 2019.
[4] J. Hirouchi, M. Watanabe, N. Hayashi, A. Nagakubo, S. Takahara, Effects of different accident scenarios and sites on the reduction factor used for expressing sheltering effectiveness, Journal of radiological protection : official journal of the Society for Radiological Protection (2025). https://doi.org/10.1088/1361-6498/adba6e.
[5] N.E. Bixler, S.-y. Kim, Performing a multi-unit level-3 PSA with MACCS, Nuclear Engineering and Technology 53(2) (2021) 386-392. https://doi.org/https://doi.org/10.1016/j.net.2020.07.034.
[6] JAEA, User's manual for the OSCAAR code package, 2020.
[7] PTV Group, PTV Visum. https://www.ptvgroup.com/en/products/ptv-visum, 2025.
[8] U.S.NRC, Code Manual for MACCS2, Users Guide 1998.
[9] K. Shimada, T. Sakurahara, S. Reihani, Z. Mohaghegh, Integration of transportation simulation with a level 3 PRA code for nuclear power plants, in: Proceedings of Asian Symposium on Risk Assessment and Management 2020 (ASRAM 2020)
[10] K. Shimada, T. Sakurahara, P. Farshadmanesh, S. Reihani, Z. Mohaghegh, Integration of Level 3 probabilistic risk assessment for nuclear power plants with transportation simulation considering earthquake hazards, Annals of Nuclear Energy 197 (2024) 110243. https://doi.org/https://doi.org/10.1016/j.anucene.2023.110243.
[11] Open Street Map Fundation, Java Open Street Map. https://josm.openstreetmap.de/, 2025.
[12] U.S.NRC, Criteria for Development of Evacuation Time Estimate Studies, NUREG/CR-7002 (2011).

ASRAM2025
www.asram2025.org
Asian Symposium on Risk Assessment and Management 2025
Pattaya, Thailand, 27 – 29 August 2025

Development of Risk Profile for Accident Sequences with Source Term Analysis

Yunho Kim[1], Jeahyun Cho[2]

[1] Energy Systems Engineering, Chung-Ang University, 84 Heukseok-ro, Dongjak-gu, Seoul, Republic of Korea

EXTENDED ABSTRACT

As nuclear energy systems evolve toward advanced designs such as Small Modular Reactors (SMRs) and Generation IV reactors, the need for risk assessment methodologies that are both efficient and universally applicable becomes increasingly urgent. Traditional Probabilistic Safety Assessment (PSA) frameworks divided into Level 1, 2, and 3 remain fundamental for evaluating reactor safety, although they face certain challenges in broader applicability, efficiency and presence of uncertainty due to lack of data. These include high computational cost, inflexibility for early design-phase applications, and difficulty in encompassing diverse accident scenarios or new reactor configurations. Risk is generally quantified as a function of accident frequency and consequence. While frequency estimation is well-established within PSA, the quantification of accident consequences tends to receive comparatively less emphasis. The MELCOR Accident Consequence Code System (MACCS), developed by the U.S. NRC, is a widely used tool for Level 3 PSA consequence analysis. Level 3 PSA typically involves detailed modeling of site-specific parameters such as meteorology, emergency response, and population distribution, which can make its application resource-intensive in early-stage design assessments or generic reactor comparisons [1]. To address these challenges, this study proposes a novel methodology that develops risk profiles by correlating source term characteristics (e.g., fission product release amount and timing) directly with accident consequences. This correlation-based approach enables efficient risk quantification without requiring full Level 3 PSA. By bypassing detailed consequence modeling, the method enhances general applicability, reduces computational overhead, and offers intuitive insight into the relative risk of accident sequences. In this study, for simplification, only Cs-137, which is the most representative radionuclide among many fission products, was considered. A correlation-based equation model, as shown in Eq. (1), was developed, assuming that the accident consequence is proportional to the release amount and inversely proportional to the release start time.

$$C = k_{env} \cdot \left(k_q \cdot Q + \frac{k_t}{{t_{release}}^a} \right) \quad (1)$$

where C is the accident consequence, n is the number of analyzed fission products (FPs), Q is the Cs-137 release amount [TBq], $t_{release}$ is the start time of Cs-137 release [hr], and k_{env} is an environmental adjustment coefficient [hr/TBq]. As for the other variables, k_q is the relative influence of Q the accident consequence C, k_t is the relative influence of t on C, and a is an exponent adjusting the effect of time t.

Eq. (2) was derived through regression analysis using data from the State-of-the-Art Reactor Consequence Analyses (SOARCA) report published by U.S. Nuclear Regulatory Commission (NRC). In this equation, denotes the scenario-specific individual latent cancer fatality (LCF) probability at 10 miles reported in NUREG/CR-7110 [2,3]. Table 1 shows absolute and relative errors between simulation value of consequence in SOARCA and predicted C.

$$C = k_{env} \cdot \left(0.79 \times 10^{-8} \cdot Q + \frac{3.55 \times 10^{-4}}{{t_{release}}^{0.655}} \right) \quad (2)$$

Table I. Absolute and relative errors between simulation value and predicted value of the consequences

Nuclear power plant	Severe accident Scenario	Observed C	Predicted C	Absolute error	Relative error (%)
Surry	1	4.7e-05	5.307e-05	6.070e-06	12.91

	2	9.4e-05	8.222e-05	1.178e-05	12.53
	3	3.2e-04	3.003e-04	1.970e-05	6.16
	4	3.0e-04	3.016e-04	1.600e-06	0.53
	5	2.8e-04	3.003e-04	2.030e-05	7.25
Peach Bottom	6	8.9e-05	8.346e-05	5.540e-06	6.22
	7	7.1e-05	8.928e-05	1.828e-05	25.75
	8	2.1e-04	2.043e-04	5.700e-06	2.71

The study proposes a methodology for developing reactor risk profiles based on the above correlation model. As a case study, the framework was applied to the Korean OPR-1000 nuclear power plant, focusing on two initiating events: Loss of Feedwater (LOFW) and Small Break Loss of Coolant Accident (SLOCA). Each accident sequence was identified from the Level 1 PSA model, and corresponding source terms were generated using the MAAP 5.05 code [4]. The uncertainty in source term release was evaluated through Latin Hypercube Sampling of 46 parameters, generating 124 cases per sequence. To estimate accident consequences, a simplified correlation model derived from regression on SOARCA data was developed using the release amount and start time of Cs-137 as predictors of latent cancer fatality probability. Risk profiles were then visualized as Frequency-Consequence (F-C) curves, allowing for intuitive comparison of accident scenarios as shown in Fig 1. The results showed that SLOCA has a substantially higher risk approximately 50 times greater than LOFW at the 95th percentile.

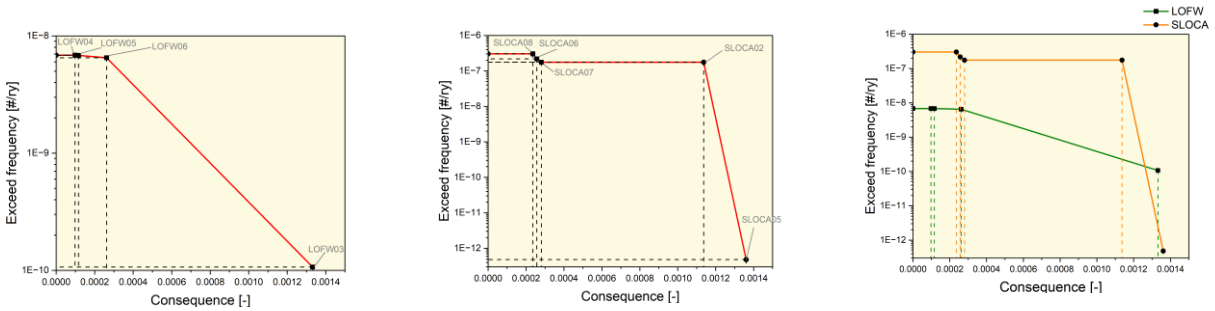

FIGURE 1. Comparison of the 95th percentile F-C curves for LOFW and SLOCA

This study highlights the potential of a source term-based consequence estimation model in enabling faster, more scalable, and broadly applicable risk assessments. The proposed methodology supports risk informed decision-making across design, licensing, and emergency planning stages, especially in the context of emerging reactor technologies [5].

ACKNOWLEDGMENTS

This work was supported by Korea Institute of Energy Technology Evaluation and Planning (KETEP) grant funded by the Korean government (MOTIE) (RS-2024- 00401705, Convergent and practical human resource development program specialized in nuclear power plant export).

REFERENCES

[1] Chanin, David I., et al. "Code manual for MACCS2: volume 1, user's guide." SAND97-0594, Sandia National Laboratories, Albuquerque, USA (1997).
[2] NRC, U. (2013). State-of-the-art reactor consequence analyses project volume 2: surry integrated analysis. SOARCA report, NUREG/CR, 7110.
[3] NRC, U. (2013). State-of-the-Art Reactor Consequence Analyses Project Volume 1: Peach Bottom Integrated Analysis (NUREG/CR-7110). Washington: Office of Nuclear Regulatory Research, 1, 329.
[4] Kindred, T. (2017). "Modular Accident Analysis Program 5 (MAAP5) Applications Guidance: Desktop Reference for Using MAAP5 Software–Phase 3 Report." Electric Power Research Institute.
[5] Yang, Joon-Eon, et al. "The role of risk-informed approaches for advanced reactors in Korea." *Nuclear Engineering and Design* 417 (2024): 112805.).

Analysis of on-site impact and feasibility of outdoor work under a fission product release at a nuclear power plant.

Riku Iwata[1], Sunghyon Jang[1], Munemichi Kawaguchi[1], Kazuhiro Sawa[1], Eishiro Higo[2]

[1] *Hokkaido University: Kita-13jo, Nishi-5chome, Kita-ku, Sapporo, Hokkaido, Japan, 060-8628,* iwata.riku.q1@elms.hokudai.ac.jp, jang@eng.hokudai.ac.jp, kawaguchi.munemichi@eng.hokudai.ac.jp, *and* sawa@eng.hokudai.ac.jp

[2] *Central Research Institute of Electric Power Industry: 2-6-1 Nagasaka, Yokosuka-shi, Kanagawa, Japan,* higo3791@criepi.denken.or.jp

ABSTRACT

Studies of multi-unit probabilistic risk assessment (PRA) have conservatively assumed that outdoor work is not feasible after the release of fission products. However, the Fukushima Daiichi Nuclear Power Plant (1F) accident showed that mitigation measures could be implemented during the removal of contaminated debris and the establishment of detours. This study proposes a simple method for evaluating the feasibility of outdoor work during a multi-unit accident. We develop and clarify outdoor work feasibility scenarios by comparing individual and team exposure doses with their respective dose limits. If the expected exposure dose by the completion time—either individual or team—is below the applicable dose limit, outdoor work is considered feasible. Conversely, outdoor work is not feasible if the expected exposure exceeds the dose limit. Since the exposure dose is calculated as the product of the ambient dose rate and the exposure time, we define the feasible work time as the exposure dose limit divided by the ambient dose rate. Work is considered feasible if the required completion time is shorter than the feasible work time. In the case of team-based work, it is assumed that all workers within a team receive the same exposure dose. Based on this assumption, the number of teams required to complete the work can be determined. This study confirms that the feasibility of outdoor work can be evaluated using five parameters: the time required to complete the work, the ambient dose rate, the number of teams, the individual dose limit, and the outdoor work distance. Furthermore, this study demonstrates the preliminary assessment of the feasibility of work after the release of fission products in the 1F accident in terms of the number of teams that could be deemed able to work through a review of available information on the 1F accident.

Keywords: Fukushima Daiichi Nuclear Power Plant accident, individual and team dose limits, Multi-unit PRA, Site risk, Ambient dose rate

Ⅰ.Introduction

Following the Fukushima Daiichi Nuclear Power Plant accident (hereafter referred to as the “1F accident”), increasing attention has been directed toward Multi-Unit Probabilistic Risk Assessment (MUPRA). The accident highlighted critical limitations of traditional Single-Unit Probabilistic Risk Assessment (SUPRA), which is not sufficient to address scenarios involving concurrent damage to multiple reactor units. MUPRA overcomes these limitations by incorporating factors such as inter-unit dependencies, shared systems and resources, and concurrent initiating events—elements that are typically outside the scope of SUPRA [1].

In previous studies, it has often been conservatively assumed that outdoor work is infeasible under conditions involving fission products releases or elevated ambient dose rates [2]. However, during the actual 1F accident, various mitigation efforts—such as the removal or detouring of contaminated debris, the use of personal protective equipment, and continuous dose rate monitoring—were carried out in outdoor environments.

Nevertheless, only limited research has quantitatively assessed the feasibility of conducting outdoor work under realistic radiation conditions. To address this gap, the present study proposes a method to evaluate the feasibility of outdoor work during fission products releases. Based on a literature review of the 1F accident, actual mitigation actions were selected, and the feasibility of work was assessed using the developed method.

II.A Scenario Analysis of Working Conditions during Fission Products Release

Under conditions where fission products have been released, the feasibility of work is determined based on the individual dose limit. If the estimated dose by the end of the work does not exceed the limit, the work is feasible; otherwise, it is not.

Work is assumed to be conducted in teams. Even if an individual's dose exceeds the limit, the work can continue if replacement personnel are available. Conversely, if no substitutes are available and the dose exceeds the individual limit, the work becomes infeasible. Therefore, feasibility is determined by both the individual dose limit and the team dose limit (i.e., the cumulative dose capacity of the teams). Figure 1 illustrates the decision-making scenario for work feasibility. For single-person work, feasibility is governed solely by the individual dose limit. In contrast, team-conducted work may still be feasible even if the individual limit is exceeded, as long as the team dose limit is not. If both the individual and team dose limits are exceeded, work is deemed infeasible.

This study considers both single-person and multi-team work. It is assumed that all team members perform nearly identical work in approximately the same location and therefore receive the same radiation dose regardless of team size. Furthermore, any increase in total working time due to team rotation is not considered.

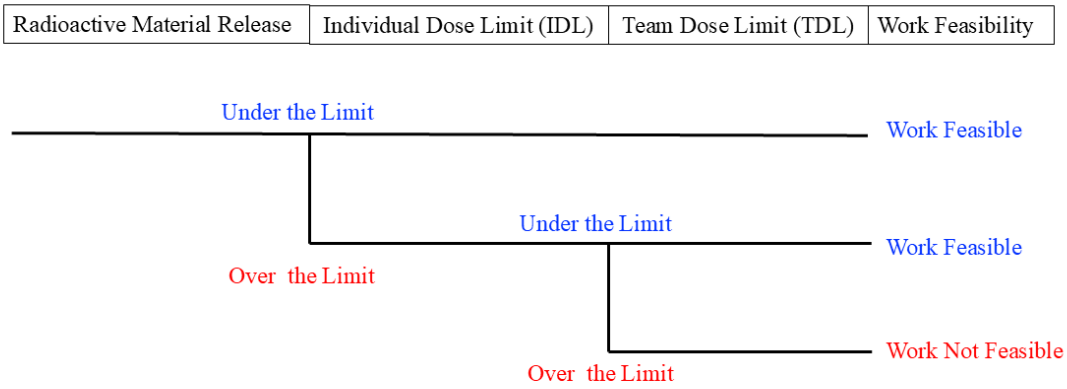

Figure 1 Scenario Definition for Operations during Fission Products Release

II.B Setting of Individual Dose Limits

In Japan, regulations regarding occupational exposure to radiation are governed by the Ordinance on Prevention of Ionizing Radiation Hazards (OPIRH). This ordinance stipulates that, in the event of an accident involving a large-scale release of fission products, the exposure dose limit for workers engaged in emergency operations is set at 100 mSv.

However, a special emergency provision allows the dose limit to be immediately raised to 250 mSv, but only for tasks essential to prevent catastrophic consequences at a nuclear facility [3].

Although 250 mSv is permitted in emergencies, once workers reach this threshold—illustrated in Figure 1—they are no longer allowed to continue working. Since workers typically perform multiple tasks rather than just one, allowing some margin within the individual dose limit is necessary. Furthermore, setting the dose limit to 50 mSv would not provide sufficient time to complete necessary tasks. Therefore, in this study, the individual dose limit is treated as a variable parameter ranging from 100 to 250 mSv.

II.C Evaluation Formula

The radiation dose received by a worker can be calculated by integrating the dose rate (DR) over the working time. Letting T_{fin} represent the time required to complete the work, the individual exposure dose (ID) is given by:

$$ID = \int_0^{T_{\mathrm{fin}}} DR(t)dt \qquad (1)$$

If the dose rate is constant, the exposure dose can be calculated by multiplying the dose rate by the duration of exposure:

$$ID = (T_{\text{fin}} - 0) \times DR \quad \textbf{(2)}$$

Since ambient dose rates at the work site can fluctuate significantly due to meteorological conditions (e.g., wind direction), this study simplifies the evaluation by using a time-averaged ambient dose rate($\overline{DR}$) over the duration of the work, treating it as a constant.

By dividing the individual dose limit (IDL) by the dose rate, the maximum allowable working time (T) for a single worker can be calculated as:

$$T = {}^{IDL}/_{DR} \quad \textbf{(3)}$$

The feasibility of work for an individual worker is then evaluated by comparing this allowable working time (T) with the work completion time T_{fin} :

$$Feasible : T \leq T_{\text{fin}}$$
$$Not\ feasible : T > T_{\text{fin}}$$

Assuming that each worker in a team receives the same radiation dose regardless of the number of team members, the total working time for all teams (T_{N_T}) can be expressed as the product of the allowable working time per team and the number of teams (N_T):

$$T_{N_T} = N_T \times {}^{IDL}/_{DR} \quad \textbf{(4)}$$

By assuming uniform dose exposure among team members, it is possible to calculate the number of teams required to complete the work within the given dose constraints.

II.D Selection of Work Environment and Derivation of Ambient Dose Rates

In realistic outdoor work scenarios, it is possible to anticipate a sharp increase in ambient dose rates due to venting; however, such an increase is difficult to predict in the case of containment vessel damage. Therefore, this study focuses on two specific scenarios: one assuming containment vessel damage, and the other assuming venting. For each scenario, the ambient dose rate is time-averaged over a selected period and treated as a constant value.

First, based on the measurement data from 1F provided by TEPCO [4], a graph showing the ambient dose rate transition at monitoring post MP4 from March 12 to March 14 was derived as shown in Figure 2. The period from 8:00 to 19:00 on March 13 at MP4 was chosen as the scenario assuming containment vessel damage, and the period from 21:00 on March 12 to 8:00 on March 13 was selected as the scenario assuming venting. The time-averaged ambient dose rates for both cases are shown in Table 1.

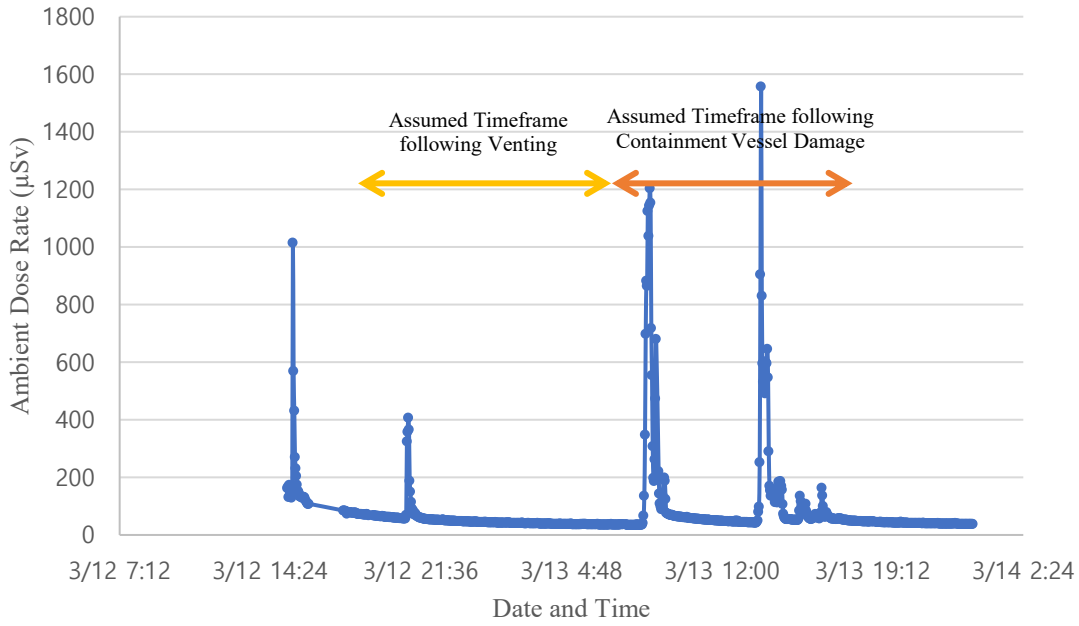

Figure 2 Transition of Ambient Dose Rate and Selected Timeframes at MP4

Table 1 Time-Averaged Ambient Dose Rate under Assumed Conditions of Containment Vessel Damage and Venting

Timeframe	Time-Averaged Ambient Dose Rate (mSv/h)
Assumed Timeframe following Containment Vessel Damage	1.23E-01
Assumed Timeframe following Venting	4.59E-02

II.E Selection of Outdoor Work

As an example of outdoor work, we selected the procedure titled "Natural Convection Cooling of the Containment Vessel Using Mobile High-Capacity Pump Vehicles with A and B Containment Recirculation Units," which is intended to prevent over pressurization and failure of the reactor containment vessel [5].

This procedure consists of five tasks. Two of them can be completed quickly, so the remaining three are selected for evaluation. The task is carried out by six workers over a period of 11 hours, and thus Tfin is set to 11 hours.

II.F Distance from MP4 and Locations of Monitoring Posts

Since the monitoring posts used to observe ambient dose rates are located away from the actual work site, it is necessary to estimate the dose rate at the real work location. As shown in Figure 3, the distance from MP4 to the reactor is approximately 1300 meters [6].

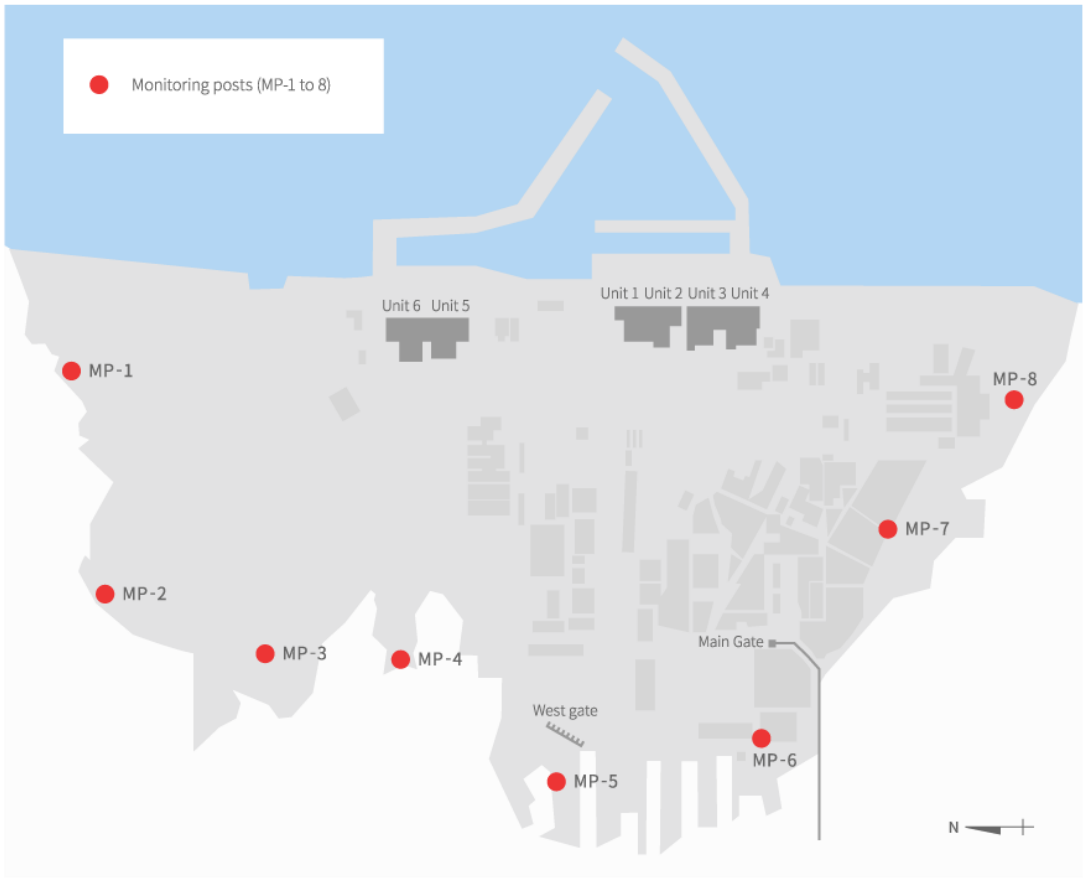

Figure 3 Monitoring points
(Source: Tokyo Electric Power Company, 2020 [4])

II.G Calculation of Dose Rate Based on Distance

Assuming the radiation source is a point source, the dose rate is inversely proportional to the square of the distance. This is expressed in the following formula [7]:

$$I = \frac{k}{r^2} \quad \textbf{(5)}$$

I: dose rate [mSv/h]
r: distance [m]
k: constant [mSv·m²/h]

II.H Outdoor Work Distance and Ambient Dose Rates Within the Range

Since the monitoring posts that observed ambient dose rates were located far from the actual work site, it is necessary to convert the dose rates to reflect the actual work location. In this study, the outdoor work distance is set to range from 30 m to 100 m, based on the area where outdoor work was conducted during the 1F accident. Using Equation (5), the ambient dose rates under the assumptions of containment vessel damage and venting were converted to distances of 30 m, 50 m, and 100 m. The converted values are shown in Tables 2 and 3.

Table 2 Ambient Dose Rates Converted for Each Distance under the Assumption of Containment Vessel Damage

Distance (m)	Ambient Dose Rate (mSv/h)
30	2.30E+02
50	8.29E+01
100	2.07E+01

Table 3 Ambient Dose Rates Converted for Each Distance under the Assumption of Venting

Distance (m)	Ambient Dose Rate (mSv/h)
30	8.62E+01
50	3.10E+01
100	7.76E+00

III. Results

Based on the converted ambient dose rates for each distance under the assumptions of containment vessel damage and venting, the number of teams required to make work feasible was calculated for individual dose limits of 100 mSv and 250 mSv. As shown in Tables 4 and 5, the maximum number of teams required decreased from 26 to 10 when comparing the scenarios of containment vessel damage and venting. As expected, the number of required teams is smaller when the individual dose limit is increased from 100 mSv to 250 mSv. Furthermore, the greater the distance from the radiation source, the fewer teams are required to complete the work.

Table 4 Number of Teams Required to Make Work Feasible under the Assumption of Containment Vessel Damage, for Individual Dose Limits of 100 mSv and 250 mSv

Distance (m)	Ambient Dose Rate (mSv/h)	Number of Teams Required	
		For 100 mSv limit	For 250 mSv limit
30	2.30E+02	26	11
50	8.29E+01	10	4
100	2.07E+01	3	1

Table 5 Number of Teams Required to Make Work Feasible under the Assumption of Venting, for Individual Dose Limits of 100 mSv and 250 mSv

Distance (m)	Ambient Dose Rate (mSv/h)	Number of Teams Required	
		For 100 mSv limit	For 250 mSv limit
30	8.62E+01	10	4
50	3.10E+01	4	2
100	7.76E+00	1	1

The above results represent only the number of teams required for limited values of individual dose limits and outdoor working distances; therefore, response surfaces were developed to evaluate the number of teams required to make work feasible under broader conditions. Based on the ambient dose rates under the two assumed scenarios—containment vessel damage and venting (as shown in Table 1)—response surfaces were generated with the individual dose limit and the outdoor working distance from the radiation source as parameters. The range for the individual dose limit was set from 100 mSv to 250 mSv, and the outdoor working distances were set from 30 m to 100 m.

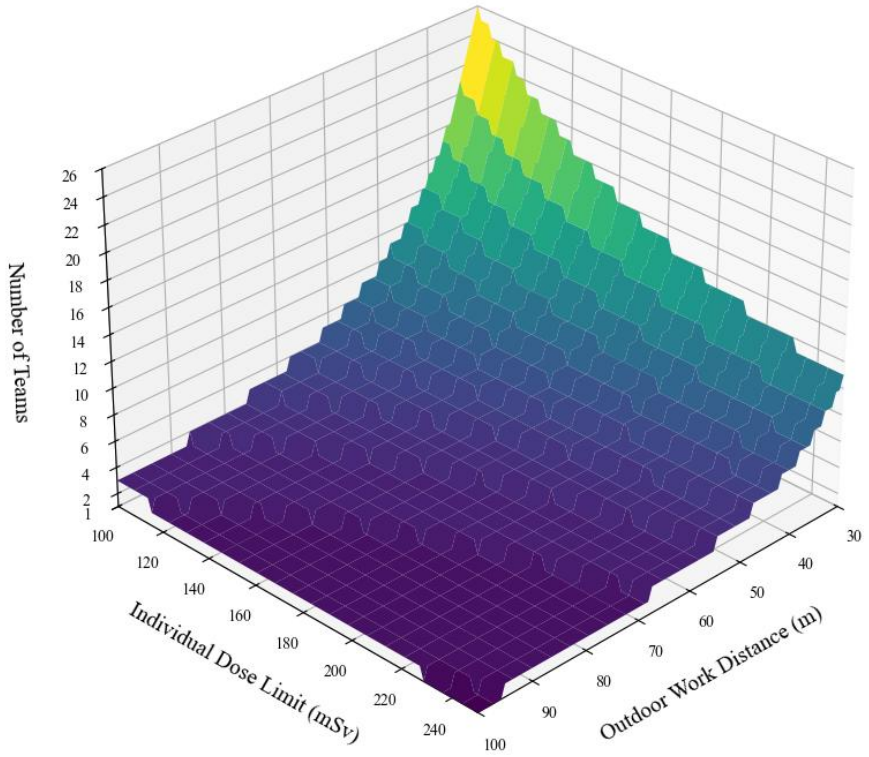

Figure 4 Response Surface of the Number of Teams under the Assumption of Containment Vessel Damage

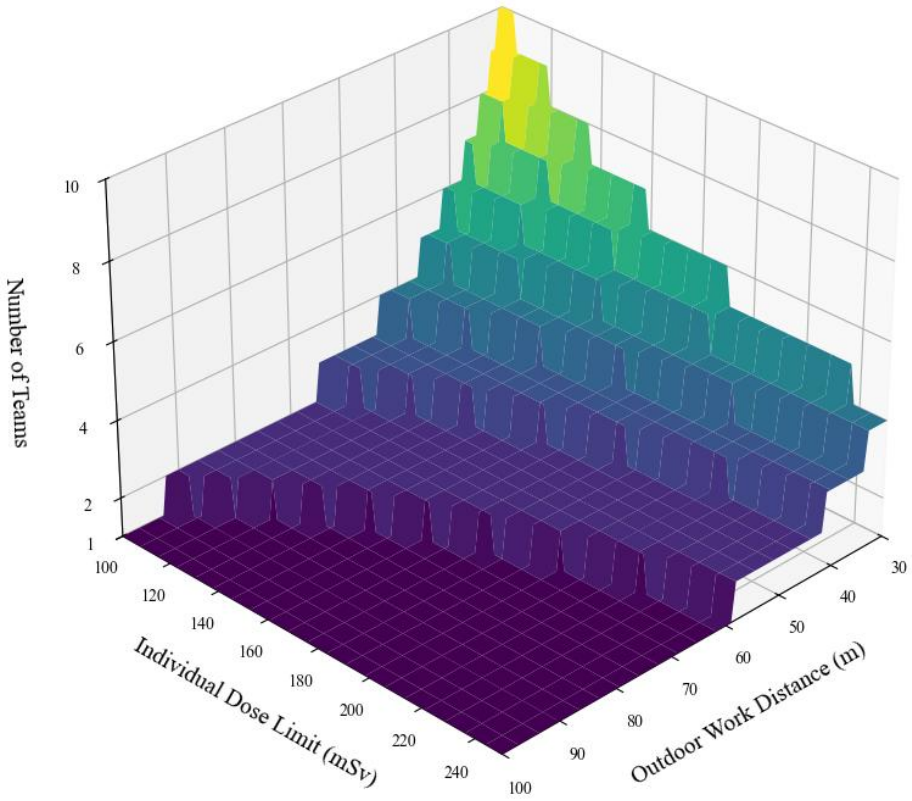

Figure 5 Response Surface of the Number of Teams under the Assumption of Venting

In the scenario assuming containment vessel damage, the number of teams required ranged from a minimum of 1 to a maximum of 26. In the scenario assuming venting, the number of teams required ranged from a minimum of 1 to a maximum of 10 in all cases.

IV. CONCLUSIONS

This study proposed a methodology for evaluating the feasibility of outdoor work during multi-unit nuclear accidents, taking into account realistic impact areas.

Feasibility was evaluated from the perspective of the number of required teams, using the Fukushima Daiichi Nuclear Power Plant accident as a case study. The evaluation demonstrated that the feasibility of conducting outdoor work can be assessed using five parameters: required work completion time (T_{fin}), ambient dose rate (DR), number of teams (N_T), individual dose limit (IDL:100-250 mSv), and outdoor working distance (r:30-100 m).

As a result, it was found that under the assumption of containment vessel damage, between 1 and 26 teams would be required to complete the work, while under the assumption of venting, between 1 and 10 teams would be sufficient.

REFERENCES

[1] International Atomic Energy Agency, “Multi-unit Probabilistic Safety Assessment”, Safety Reports Series No. 110, (2023).
[2] International Atomic Energy Agency, “Development and Application of Level 1 Probabilistic Safety Assessment for Nuclear Power Plants”, IAEA Safety Standards Series No. SSG-3 (Rev. 1), (2023).
[3] Ministry of Health, Labour and Welfare of Japan, “Overview of the Amendment to the Ordinance on Prevention of Ionizing Radiation Hazards,” (2015).
[4] Tokyo Electric Power Company, “Measurement Data on the Premises of the Fukushima Daiichi Nuclear Power Station, 2011.”(2011).
[5] Tokyo Electric Power Company Holdings, Inc., “Procedures for Preventing Overpressure Failure of the Reactor Containment Vessel,” (2017).
[6] Tokyo Electric Power Company, “Radiation Dose measured at Monitoring Post of Fukushima Daiichi Nuclear Power Station”(2011)
[7] Ministry of the Environment of Japan, “Chapter 2: Radiation Exposure,” (2019).

ASRAM2025
www.asram2025.org
Asian Symposium on Risk Assessment and Management 2025
Pattaya, Thailand, 27 – 29 August 2025

Release time-based source term grouping method for level 3 multi-unit probabilistic safety assessment of cascading accidents

Hee Young Lee [1], Gee Man Lee [1], Woo Sik Jung [1], Seong Kyu Park[2]

[1] *Department of Nuclear Engineering, Sejong University, 209 Neungdong-ro, Gwangjin-gu, Seoul, 05006; sym25@sju.ac.kr, narak@sejong.ac.kr, woosjung@sejong.ac.kr*
[2] *Nuclear Engineering Services & Solutions, 1305 U-Tower, Dongcheon-dong, Yongin-si, Gyeonggi-do, 16827; sparkpsa@ness.re.kr*

ABSTRACT

Following the Fukushima Daiichi nuclear accident, research into multi-unit probabilistic safety assessment (MUPSA) has increased significantly. Currently, level 3 MUPSA (L3 MUPSA) is typically conducted using results from Level 2 single-unit PSA (L2 SUPSA), with source terms grouped based on their release scale. Consequently, the release timing of each source term remains unspecified. MUPSA is generally modeled under the assumption of simultaneous releases. However, since most multi-unit accidents occur as cascading accidents, L3 MUPSA must be performed specifically for cascading accident scenarios. To perform L3 MUPSA for cascading accident scenarios, two elements are required: (1) a release time-based source term grouping method to facilitate the determination of release timing in L2 SUPSA; and (2) a post-processing code that integrates unit-specific MELCOR Accident Consequence Code System (MACCS) calculation results while accounting for inter-unit release timing differences. Therefore, this study aims to: (1) develop a release time-based source term grouping methodology for L3 MUPSA of cascading accident scenarios; (2) establish a method for integrating unit-specific MACCS calculations that accounts for inter-unit release timing; and (3) implement a method for integrating unit-specific MACCS calculations in a MACCS post-processing code, MURCC.

Keywords: Level 3 multi-unit probabilistic safety assessment, Level 2 single-unit probabilistic safety assessment, source term grouping, Source term category (STC)

I. Introduction

Current research on level 3 multi-unit probabilistic safety assessment (L3 MUPSA) is primarily based on single-unit probabilistic safety assessment (SUPSA) frameworks [1]. While L3 MUPSA remains in its early developmental phase, studies have been conducted in several countries, including the United States [2–10], the United Kingdom [11], Japan [12], China [13], and South Korea [14–18]. However, these studies show variations in source term selection, release timing, and release location, often relying on simplified or constrained assumptions. In L3 MUPSA, a commonly adopted method, involves aggregating source terms from multiple units into a single multi-unit source term, based on the assumption that all releases originate from a common location. This simplification allows the scenario to be modeled as a single-unit accident [1,11,14]. In this study, this approach is referred to as the center of mass (COM) method. The primary advantage of the COM method is its compatibility with conventional L3 SUPSA methodologies. However, this approach may introduce distortions in the results, depending on the spatial configuration of reactor units and prevailing wind direction. To address this limitation, multi-unit accidents have been analyzed in several studies [12,13,17] by modeling each reactor unit at its actual geographic location. In this study, this modeling approach is termed the Multiple location (ML) method, with the implementation developed in a previous study [17] adopted.

In L3 MUPSA, source term categories (STCs) are derived from level 2 SUPSA (L2 SUPSA) using release scale-based grouping. However, since this grouping does not uniquely specify the release timing for each STC, the simplifying assumption that all STCs are released simultaneously in L3 MUPSA analyses have been adopted in most studies [11,12,14]. In practice, even identical initiating events can yield different release timings due to variations in accident progression and safety system responses across reactor units. Therefore, modeling multi-unit cascading accidents as concurrent accidents may lead to distorted risk estimates. While temporal offsets have been introduced in some studies [12,13], these were based on arbitrary intervals rather than actual release timings. Consequently, the outcomes of such analyses remain susceptible to potential inaccuracies.

A realistic cascading accident-based L3 MUPSA requires both a methodology and a computational framework for

integrating unit-specific radionuclide concentrations based on their respective release timings. However, the MELCOR accident consequence code system (MACCS) [19-21] does not support aggregating radionuclide concentrations from multiple units with non-simultaneous releases, and scale-based STCs inherently lack the temporal resolution necessary for such analysis. Consequently, the conventional MUPSA framework is fundamentally limited in its ability to accurately model cascading accident-based L3 MUPSA scenarios.

This study aims to develop a release time-based source term grouping method that facilitates the determination of release timing, and to implement a post-processing code that integrates unit-specific MACCS calculation results while accounting for inter-unit release timing differences. These developments are motivated by the need to enable more realistic L3 MUPSA for cascading accident scenarios. Section II outlines a release time-based source term grouping method. Section III presents a methodology for integrating unit-specific MACCS simulations with temporal release data, incorporating modifications to the multi-unit radiological consequence calculator (MURCC) code. Section IV outlines the framework validation through a two-unit cascading accident scenario.

II. Release time-based source term grouping method

Fig. 1 illustrates the procedure for determining source terms in L2 SUPSA. Following core damage, the progression of the accident, from the status of key safety systems in the nuclear power plant (NPP) to potential containment failure, was analyzed using event trees and logical diagrams. Subsequently, representative accident sequences were selected for each resulting STC, with the associated radionuclide releases quantified.

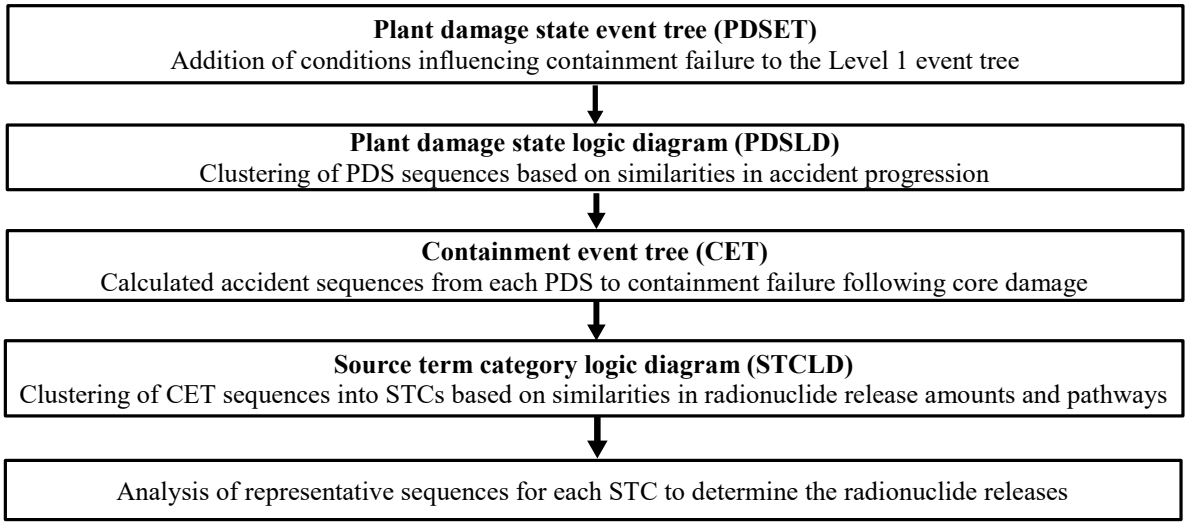

FIGURE 1. Procedure for level 2 single-unit probabilistic safety assessment
Abbreviations: PDSET, Plant Damage State Event Tree; PDSLD, Plant Damage State Logic Diagram; CET, Containment Event Tree; STCLD, Source Term Category Logic Diagram; PDS, Plant Damage State; STC, Source Term Category.

Table 1 presents a comparison of the conventional release scale-based source term grouping method [22] and the release time-based source term grouping approach developed in this study. In the release scale-based source term grouping method, only the interval between core damage and containment failure was considered, followed by the release of radioactive materials. However, in realistic multi-unit cascading accident scenarios, the timing of core damage can vary across reactor units. Therefore, defining a reference time and distinguishing between the time from the initiating event to core damage and the interval from core damage to containment failure are essential. In the release time-based source term grouping method, the source term release timing was classified into three groups (Table 2). Table 1 summarizes the methods used for assessing the time from the initiating event to core damage (T1) and from core damage to containment failure (T2).

TABLE I. Comparison of release scale-based and release time-based source term grouping methods

Category		Release scale-based source term grouping method [22]	Release time-based source term grouping method
Advantages		Utilizes established methodologies, eliminating the need to develop new analytical frameworks.	Enables more precise L3 MUPSA by incorporating source term release timing interval across multiple reactor units.
Disadvantages		Cannot identify the release timing of the source term for each unit, limiting the accuracy of multi-unit analysis.	Requires the development of new event tree headings and logic diagram classification rules to incorporate release timing.
PDSET	Time Information	Difficult to estimate the time from the initiating event to core damage.	Time from initiating event to core damage can be approximately estimated.
	Method	The Level 1 event tree does not account for systems affecting building performance post-core damage. → Develop a PDSET incorporating critical systems for analyzing accident progression.	1) Supplement time information by refining the release scale-based method. 2) Use specific event tree headings indicating event initiation timing. 3) When timing is unclear (e.g., due to operational malfunctions), group minimal cut sets by occurrence time to estimate timing.
PDSLD	Time Information	Time from the initiating event to core damage is not used as a classification criterion for PDS.	Time from initiating event to core damage is used as a classification criterion.
	Method	Clustering variables include system status, system-dependent parameters, initiating event types, and key event timings (e.g., power recovery).	PDS classification incorporates time as an additional clustering variable alongside existing ones.
CET	Time Information	Time from core damage to source term release can be approximately estimated.	Time from core damage to source term release can be approximately estimated.
	Method	1) Analyze reactor building behaviors, including building conditions and failure types. → Reflect severe accident phenomena, accident progression paths, and operator actions affecting containment failure and source term evaluation. 2) Incorporate complex and detailed elements in decomposition event trees, supplementing the CET.	1) Incorporate time-related information into the conditions used in the scale-based method. 2) Account for variations in release timing based on the containment failure mechanism, necessitating more detailed event tree headings. 3) Classify source terms released after a delay as delayed releases, while applying a single release timing if timing differences are insignificant for assessment.
STCLD	Time Information	Time from core damage to source term release is not used as a primary classification criterion for PDS.	Time from core damage to source term release is used as a primary classification criterion for PDS.
	Method	1) In the CET, accident sequences with similar containment degradation and fission product release characteristics are grouped into STCs. 2) For a multi-unit analysis, single-unit STC characteristics such as population-weighted early fatality risk, collective dose, release scale, and containment failure mode are stored in a database. STC data for each unit are retrieved and integrated to estimate the characteristics of STC combinations, which are then used as headings in a logic diagram.	Further classifies STCs by incorporating release timing into the clustering variables used in the scale-based method.
Selection and Analysis of Representative STC Sequences		For each STC, the sequence with the highest frequency or most severe release characteristics is selected as the representative case, while severe accident analysis is performed.	The same selection and analysis procedure is applied as in the scale-based method.

Abbreviations: PDSET, Plant Damage State Event Tree; PDS, Plant Damage State; PDSLD, Plant Damage State Logic Diagram; CET, Containment Event Tree; STC, Source Term Category; STCLD, Source Term Category Logic Diagram; L3 MUPSA, Level 3 Multi-Unit Probabilistic Safety Assessment.

TABLE II. Definitions and calculations method for T1, T2, and T

Variable	Definition	Calculation method
T1	Time interval from the initiating event to core damage	Determined using the PDSET
T2	Time interval from core damage to containment failure	Determined using the CET
T	Total time from the initiating event to the release of radioactive materials	Calculated as the sum of T1 and T2

Abbreviations: PDSET, Plant Damage State Event Tree; CET, Containment Event Tree.

III. Calculation method for cascading accidents in Level 3 multi-unit probabilistic safety assessment

In this study, L3 MUPSA for cascading accidents was performed using the MACCS code and its post-processing tool, MURCC. Fig. 2 illustrates the computational procedure used for conducting L3 MUPSA in a cascading accident scenario involving two reactor units. Source terms for each unit were derived from L2 PSA tools, yielding M source terms for Unit 1 and N for Unit 2. The MACCS code was used to conduct $M + N$ atmospheric dispersion simulations, while MURCC was used to generate $M \times N$ combinations of source terms. MACCS outputs time-integrated air concentrations and atmospheric dispersion parameters (sigma-y, sigma-z) along the plume centerline at specified distances from the release point, based on user-defined input. Using these 1D outputs, 2D time-integrated air concentrations at ground level can be calculated [17].

The total amount of radioactive material released and the duration of the release are provided as inputs to MACCS, and the release rate is derived from these input values. MURCC applies the proportional relationship between the release amount and the time-integrated radionuclide concentration to calculate 2D time-resolved ground-level radionuclide concentrations at specified intervals. This calculation derives 2D time-resolved ground-level radionuclide concentrations at specified intervals based on the previously calculated 2D time-integrated air concentrations and the time-dependent release rate or release amount. Subsequently, MURCC evaluates radiation doses using the equations presented in Table 3 [23], while risk calculations are performed using the same equations [19] as those employed in MACCS.

Under weather sampling conditions, 8,760 hourly meteorological samples were incorporated in L3 MUPSA. MACCS was used to perform dispersion calculations for each sample, and MURCC was used to calculate radionuclide concentrations, radiation doses, and corresponding risks. The final results are expressed as the mean and percentile values of the estimated risk.

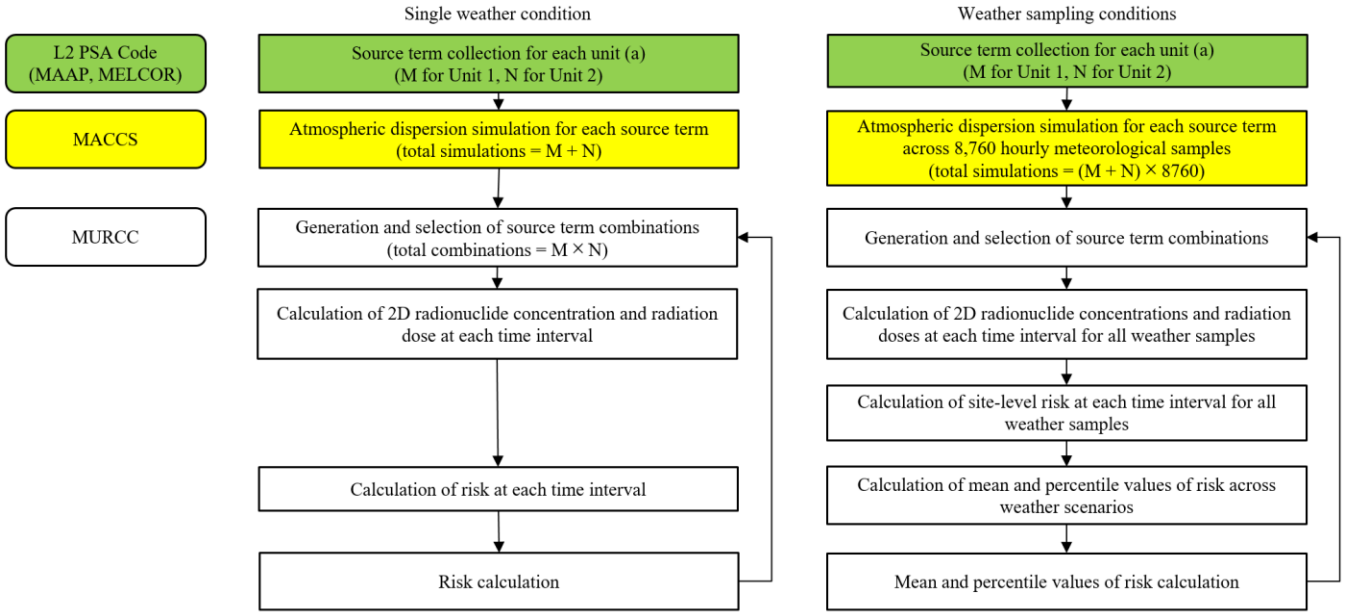

(a) If the release amount by time is available, Level 2 PSA information is used as input to MURCC; otherwise, only the MACCS results are used under a constant release rate assumption.

FIGURE 2. Computational procedure for conducting L3 MUPSA for a cascading accident involving two reactor units.

TABLE III. Equations used in MURCC for radiation dose calculation [23]

Cloudshine	$D(x,y) = \sum_{n=1}^{N} \chi_n(x,0,H) \times DC_{cs,n} \times FCDCF(x,y)$	D [Sv], χ [Bq·s/m^3], DC [(Sv/Bq) / (s/m^3)], FCDCF [dimensionless],
Groundshine	$D(x,y) = \sum_{n=1}^{N} C_n(x,y,0) \times DC_{gs,n} \times Time$	D [Sv], C [Bq/m^2], DC [(Sv/Bq) / (s/m^2)], Time [s]
Cloud Inhalation	$D(x,y) = \sum_{n=1}^{N} \chi_n(x,y,0) \times DC_{ih,n} \times BR$	D [Sv], χ [Bq·s/m^3], DC [Sv/Bq], BR [m^3/s]

In contrast to the conventional L3 MUPSA approaches that rely solely on time-integrated calculations of radionuclide concentrations and radiation doses, both time-integrated and time-resolved concentrations were computed in this study. In a cascading accident scenario involving two reactor units (Fig. 3), radioactive materials were released from Unit 1 and Unit 2 at different times. Subsequently, these materials were transported downwind, sequentially passing through Receptor 1 and Receptor 2. The two graphs on the right side of Fig. 3 show the time-integrated radionuclide concentration for the cascading accident involving two reactor units and, for comparison, the time-integrated radionuclide concentration calculated by assuming that the cascading accident occurs concurrently. These time-integrated concentrations are identical in both graphs because the time-integrated values are determined by integrating the radionuclide concentration over time, i.e., by calculating the area under the concentration–time curve. Therefore, if the measurement is taken after both source terms have been fully released, the time-integrated radionuclide concentration remains the same regardless of the release timing from the two units. However, in practice, the radiation dose received at each time interval varies depending on the timing of the radioactive releases. To accurately assess multi-unit cascading accidents, particularly when considering evacuation of the public, time-resolved dose information is essential. This approach requires time-dependent release rates from each unit and the corresponding time-resolved radionuclide concentrations and radiation doses at each receptor calculated.

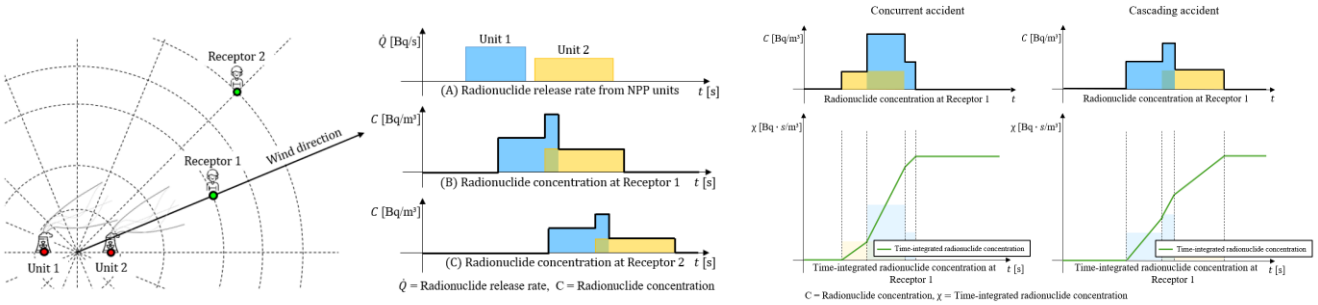

FIGURE 3. Time-resolved and time-integrated radionuclide concentrations for a two-unit cascading accident scenario

IV. Application of the proposed L3 MUPSA methodology to a multi-unit cascading accident scenario

IV.A. Multi-unit cascading accident scenario on the East Coast of Korea

To demonstrate the proposed L3 MUPSA methodology, a hypothetical multi-unit accident scenario was developed for the Hanul and Shin-Hanul NPPs on the East Coast of Korea. Reactor-specific information (Table 4) was obtained from Korea Hydro & Nuclear Power (KHNP), while Fig. 4 illustrates the corresponding site layout. In this study, the maximum fission product inventory of the APR1400 reactor type was used as the reference source term. Given that the site comprises different reactor types, the source terms were scaled accordingly: the inventories for the FRA900 and OPR1000 reactor types were assumed to be 0.64 and 0.71 times that of the APR1400, respectively.

To simplify the analysis, a multi-unit accident scenario involving two reactor units was assumed. Based on the plant damage state event tree (PDSET) and containment event tree (CET) from the L2 SUPSA for a single-unit APR1400 accident, 20 STCs were identified. Among these, STC 6 and STC 20 were selected as representative source terms for the large early release (LER) and large late release (LLR) models, respectively, using the PSA for Shin-Hanul Units 1 and 2 as the basis. Table 5 and 6 summarize the details of each STC and their associated release fractions following the initiation of off-site release, respectively. Owing to the lack of detailed time-dependent release fractions data, a constant release fraction was assumed to occur at a constant rate within two defined intervals: from 0 h to 24 h and from 24 h to 72 h after the initiation of release.

Table 7 presents the combinations of accident units and source terms selected for the analysis to examine the differences based on the key parameters for multi-unit accidents, which will be further discussed in Sections IV.B and IV.C under the given conditions. To enable a clear comparison, the combinations were determined so that in each case, only one parameter (reactor type, inter-unit distance, or source term type) varies, while the others remain constant. Although all cases listed in Table 7 were evaluated, only representative cases that best illustrate the differences for each key parameter are presented in this paper.

To evaluate the release characteristics of radioactive materials, an accident impact analysis was conducted for the selected source terms (STC 6 and STC 20). For each source term, the calculation was performed from the onset of the accident up to 120 hours, considering the release timing and the transport time for radionuclides from the release point to the emergency planning zone (EPZ) boundary. It was assumed that the source term is released in two phases: a predetermined fraction is released uniformly during the first 24 hours following the initiation of the release, and the remaining fraction is released uniformly over the subsequent 48 hours. A wind speed of 3 m/s was assumed, and the receptor was assumed to be located 10 km downwind from the release point along the centerline at ground level. The analysis results showed that, for STC 6, the cumulative effective dose during the first 24 hours following the initiation of the release was 5.464 mSv, while the cumulative effective dose during the subsequent 48 hours was 0.1244 mSv. For STC 20, the cumulative effective dose during the first 24 hours after the release was 0.1382 mSv, and 9.153 μSv during the following 48-hour period. These results confirm that the total release from STC 20 is approximately 1/38 of that from STC 6.

TABLE IV. Reactor unit specifications for the Hanul and Shin-Hanul NPPs

Unit number	Unit	Commercial Operation Date	Reactor Type	Capacity(MW)
1	Hanul Unit 1	1988.09.10	FRA900	950
2	Hanul Unit 2	1989.09.30	FRA900	950
3	Hanul Unit 3	1998.08.11	OPR1000	1000
4	Hanul Unit 4	1999.12.31	OPR1000	1000
5	Hanul Unit 5	2004.07.29	OPR1000	1000
6	Hanul Unit 6	2005.04.22	OPR1000	1000
7	Shin-Hanul Unit 1	2022.12.07	APR1400	1400
8	Shin-Hanul Unit 2	2024.04.05	APR1400	1400

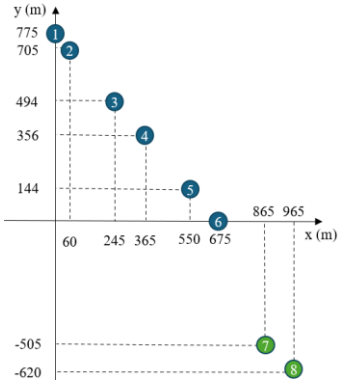

FIGURE 4. Site layout of Hanul and Shin-Hanul NPPs

TABLE V. Selection of representative STCs

CF model	Representative STC	Remark	Source Term Release Timing	Remark
LER	STC-06	Failure of CIS in SBO scenario; failure of Containment Spray	2 h after accident initiation	Core damage (assumed TDP failure)
LLR	STC-20	CIS integrity maintained in SBO scenario; failure of Containment Spray	38 h after accident initiation	Damage caused by RPV over-pressurization (conservative assumption)

Abbreviations: CF, Containment Failure; STC, Source Term Category; LER, Large Early Release; LLR, Large Late Release; CIS, Containment Isolation System; SBO, Station Black Out; TDP, Turbine-Driven Pump; RPV, Reactor Pressure Vessel.

TABLE VI. Release fractions by STC (Following the initiation of off-site release)

STC	Release Time (h)		Noble Gas	I	Cs	Te	Sr	Ru	Ba	La	Ce
	Start	End									
6	1.8	25.8	9.53E-01	1.25E-02	2.02E-02	2.25E-02	2.91E-03	1.39E-03	7.25E-03	1.99E-04	4.23E-03
	1.8	73.8	9.98E-01	1.28E-02	2.02E-02	2.37E-02	2.91E-03	1.39E-03	7.25E-03	1.41E-04	4.26E-03
20	37.9	61.9	5.24E-01	2.18E-03	3.45E-04	1.18E-03	2.04E-05	1.93E-06	1.64E-05	2.30E-07	2.66E-05
	37.9	109.9	5.91E-01	2.48E-03	3.96E-04	1.74E-03	2.05E-05	1.93E-06	1.65E-05	2.41E-07	3.51E-05

TABLE VII. Analyzed STC combinations

Case ID	Unit 1	Unit 2	Unit 1 Source Term	Unit 2 Source Term	Case ID	Unit 1	Unit 2	Unit 1 Source Term	Unit 2 Source Term
U12-LL	U1	U2	LLR	LLR	U78-LL	U7	U8	LLR	LLR
U36-LL	U3	U6	LLR	LLR	U12-EE	U1	U2	LER	LER
U34-LL	U3	U4	LLR	LLR	U36-EE	U3	U6	LER	LER
U12-EL	U1	U2	LER	LLR	U34-EE	U3	U4	LER	LER

U36-EL	U3	U6	LER	LLR	U78-EL	U7	U8	LER	LLR
U34-EL	U3	U4	LER	LLR	U78-EE	U7	U8	LER	LER

IV.B. Comparison of time-integrated calculation results for multi-unit accident scenarios

IV.B.1. Multi-unit layout and wind direction

In Case U12-LL, the wind direction producing the greatest radiological impact was identified. The computational domain was defined as a square region extending from –2000 m to 2000 m along both the x-axis and y-axis. A uniform wind speed of 2 m/s was assumed. The radiation dose was evaluated as the cumulative effective dose over a 120-hour period following initiation, based on the ICRP-60 dose coefficients.

The lowest cumulative effective doses were observed under southwesterly and northeasterly wind conditions, while the highest occurred under northwesterly and southeasterly winds. The two units are located along a line with a negative slope, forming an angle of approximately 49° with the x-axis. When the wind direction aligns with this axis, the contributions from both units are assumed to overlap significantly, resulting in higher cumulative effective dose. Therefore, the closer the wind direction is to the line connecting the two units, the higher the resulting radionuclide concentration.

TABLE VIII. Cumulative effective dose by wind direction for Case U12-LL

Northeasterly (Max: 6.47E-02 Sv)	Southeasterly (Max: 7.19E-02 Sv)
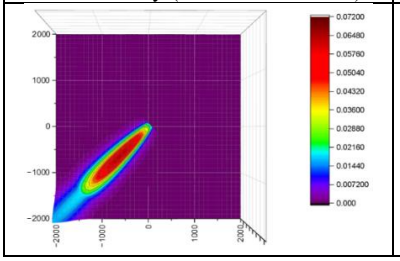	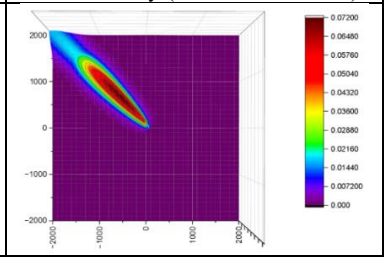

IV.B.2. Inter-unit distance

To analyze the relationship between inter-unit distance and the cumulative effective dose, simulations were performed for Cases U36-LL and U34-LL under southeasterly and northeasterly wind directions. The simulation conditions were consistent with those outlined in Section IV.B.1.

Table 9 shows that Case U36-LL, which has a greater inter-unit distance, results in a lower cumulative effective dose compared to Case U34-LL, where the units are more closely spaced. This suggests that, under identical accident scenarios and wind directions, a greater inter-unit distance leads to a lower cumulative effective dose. As mentioned in the introduction, placing all source terms at a common location for compatibility with conventional L3 SUPSA methodologies may lead to overestimation of results, particularly when the inter-unit distance is large. Therefore, modeling multiple units as co-located at a single point using the conventional COM method can overestimate radionuclide concentrations. To address this issue, multi-unit accidents should be assessed using the ML method [17], which accounts for the actual spatial configuration of reactor units.

TABLE IX. Cumulative effective dose by wind direction for Cases U36-LL and U34-LL

U36-LL		U34-LL	
Northeasterly (Max: 4.02E-02 Sv)	Southeasterly (Max: 7.13E-02 Sv)	Northeasterly (Max: 5.64E-02 Sv)	Southeasterly (Max: 7.84E-02 Sv)
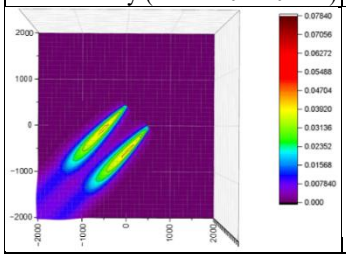	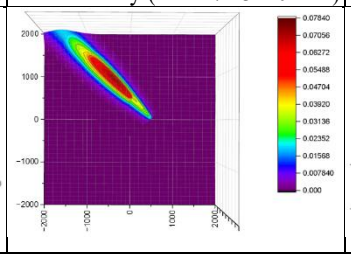	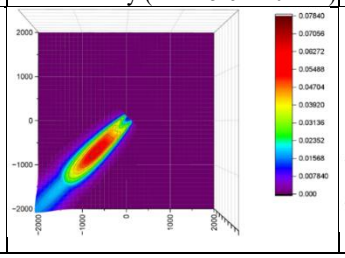	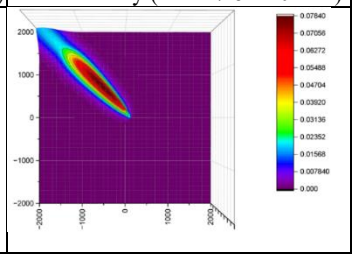

IV.B.3. Effect of source term differences

To examine the effect of source term differences between LLR and LER, cumulative effective doses for Cases U12-LL and U12-EE were calculated. In both cases, all conditions were kept identical except for the applied source term. A comparison of the cumulative effective doses from Table 8 (U12-LL) and Table 10 (U12-EE) indicates that the LER source term yields a significantly higher cumulative effective dose than the LLR source term.

The cumulative effective dose for Case U12-EL, involving both LLR and LER source terms, was calculated. All other conditions were identical to those for Case U12-LL and U12-EE, except for the source terms. Table 11 presents the results. In U12-EL, the difference in cumulative effective doses between southeasterly and northeasterly wind directions was smaller than in U12-EE, primarily due to the significantly lower scale of the LLR source term than that of the LER source term.

TABLE X. Cumulative effective dose by wind direction for Case U12-EE

Northeasterly (Max: 2.84E+00 Sv)	Southeasterly (Max: 3.15E+00 Sv)
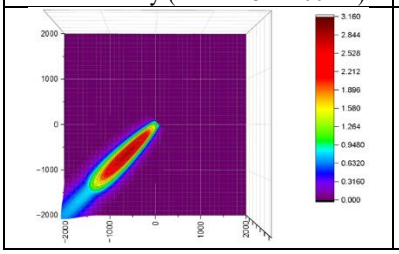	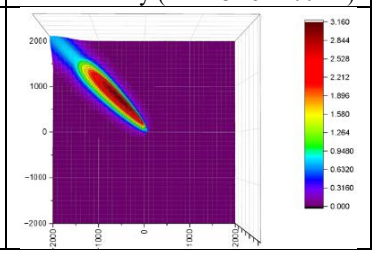

TABLE XI. Cumulative effective dose by wind direction for Case U12-EL

Northeasterly (Max: 1.60E+00 Sv)	Southeasterly (Max: 1.61E+00 Sv)
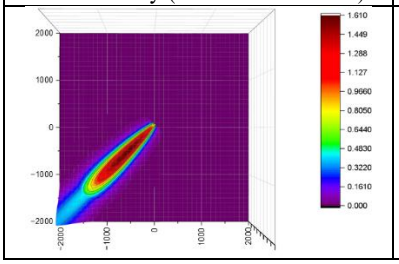	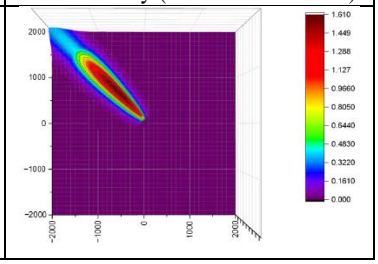

IV.C. Comparison of time-resolved calculation results for multi-unit accident scenarios

As previously discussed (Section IV.B.3), when different source terms are released in a scenario such as U12-EL, a time lag occurs between the releases. Once both source terms have been fully released, the time-integrated radionuclide concentrations and cumulative doses become similar for both concurrent and cascading accident scenarios. Therefore, distinguishing between these scenarios requires calculating radionuclide concentrations and radiation doses at specific time intervals.

Under southeasterly wind conditions at 2 m/s, radionuclide concentration was calculated for Case U36-EL. The computational domain was defined as a square region extending from –2000 m to 2000 m along both the x-axis and y-axis. The receptor was assumed to be located at (–500 m, 500 m). Considering the assumption that the release fraction is constant within two release periods (from 0 to 24 hours and from 24 to 72 hours after the initiation of release) radionuclide concentrations were calculated at 2-h intervals to balance temporal resolution with computational efficiency. Fig. 5 illustrates the radionuclide concentrations at 2-h intervals and the time-integrated radionuclide concentration results. The time-integrated radionuclide concentration previously discussed (Section III) represent the cumulative levels of radionuclides released from all multi-unit source terms up to the calculation time. Therefore, if both source terms are released within the evaluation period, the time-integrated concentration remains similar regardless of the release timing. Consequently, when the scales of the two source terms are identical, the time-integrated radionuclide concentrations will be equivalent for both concurrent and cascading accident scenarios.

However, Fig. 5 illustrates that the radionuclide concentrations at each time interval vary depending on the release timing of each source term. Based on these data, to assess the effective dose corresponding to the timing of each source term release,

radiation doses for Case U36-EL were calculated for the 4–6 h and 40–42 h intervals under southeasterly and northeasterly wind conditions. The results are presented in Table 12.

Owing to the significant difference in scale between the LER and LLR source terms, the effect of the LLR source term is relatively small. In multi-unit accident scenarios, when the release scales differ significantly between units, the contribution from the unit with the smaller source term is relatively minor in the results. However, for off-site consequence assessments at specific time intervals or when incorporating evacuation modeling, accurately evaluating even relatively minor contributions is essential.

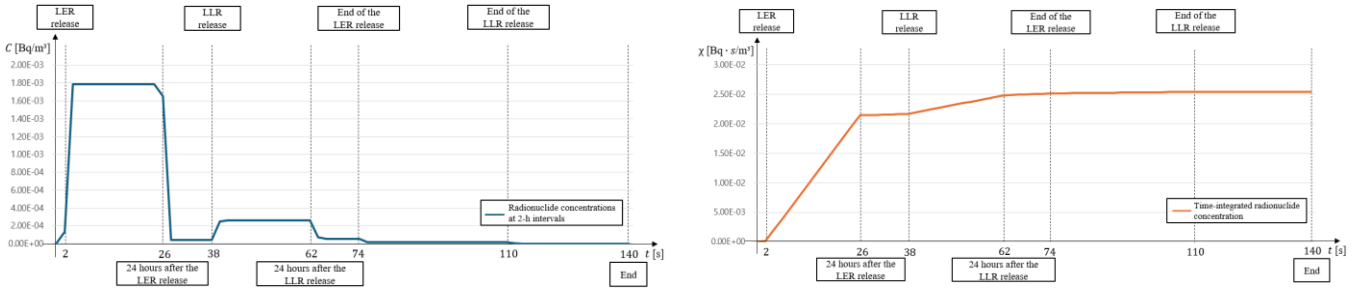

FIGURE 5. Radionuclide concentrations at 2-h intervals and time-integrated radionuclide concentration at the receptor location (–500 m, 500 m) for Case U36-EL

TABLE XII. Effective dose at each time interval by wind direction for Case U36-EL

Northeasterly		Southeasterly	
4–6 h	40–42 h	4–6 h	40–42 h
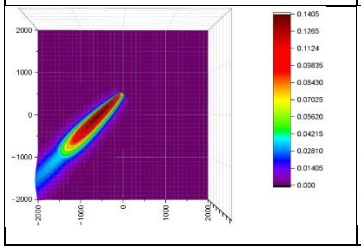	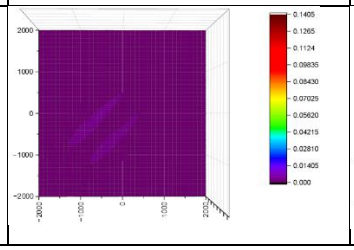	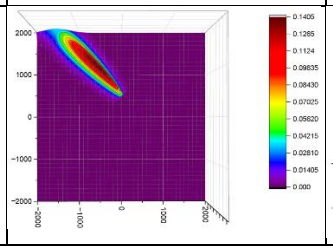	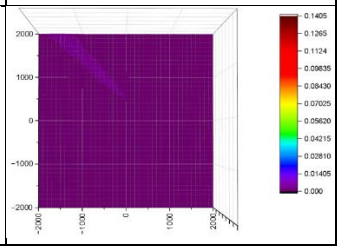

V. Conclusions

In this study, a release time-based source term grouping method is proposed, and MURCC is enhanced to integrate unit-specific calculations by accounting for inter-unit release timing differences in the MUPSA of cascading accidents. The methodology was applied to a hypothetical two-unit accident scenario on the East Coast of Korea.

In time-integrated calculations of released radionuclides, cascading and concurrent accident scenarios yield similar results once all source terms are fully released. In contrast, time-resolved calculations consistently reveal differences between the two scenarios, as the staggered release in cascading accidents distributes radionuclide concentrations and radiation doses over time. In a multi-unit cascading accident scenario, evacuation of the public may begin after the release of a single source term. Under these conditions, radiation exposure to the population remains lower in the cascading accident than in the concurrent accident. To ensure accurate L3 MUPSA results, the analysis should incorporate the actual release timing of each unit, rather than assuming concurrent releases. In multi-unit accident scenarios with significant differences in release scale between units, the effects of the smaller source term may not be observable. However, when off-site consequence assessments are conducted at specific time intervals or when evacuation modeling is incorporated, even minor contributions require precise evaluation.

Table 13 summarizes the additional research required to support the implementation of the release time-based source term grouping method. The proposed methodology requires further refinement before application to real-world multi-unit cascading accident scenarios. These limitations are identified for future investigation.

TABLE XIII. Additional research needs for the release time-based source term grouping method

Procedure in L2 PSA	Additional research needs for the release time-based source term grouping method
PDSET	1) Revise event tree headings to reflect the timing of key events more accurately.

	2) Develop a method to determine the time from the initiating event to core damage with greater precision.
PDSLD	1) Establish classification rules that more clearly distinguish timing differences. 2) Since incorporating time from the initiating event to core damage as a classification criterion may significantly increase the number of PDSs, develop a logic-based approach to reduce this complexity, such as grouping PDSs that result in similar off-site consequences.
CET	Revise event tree headings to reflect the timing related to source term release more accurately.
STCLD	1) Establish classification rules that differentiate source term release timing. 2) Since incorporating release timing as a classification criterion may significantly increase the number of STCs, develop a logic-based approach to reduce complexity, such as grouping STCs with similar off-site consequences.

ACKNOWLEDGMENTS

This work was supported by the Nuclear Safety Research Program through the Korea Foundation Of Nuclear Safety(KoFONS) using the financial resource granted by the Nuclear Safety and Security Commission(NSSC) of the Republic of Korea. (Nos. RS-2022-KN067010 and RS 2021-KN050610)

REFERENCES

[1] International Atomic Energy Agency, Multi-unit probabilistic safety assessment, (2023).
[2] STUTZKE. M., “Scoping estimates of multiunit accident risk”. In Proc. 12th Int. Probabilistic Safety Assessment and Management Conf. (PSAM12), Honolulu, HI, 22–27 Jun 2014, (2014).
[3] U.S. Nuclear Regulatory Commission, Chapter 19.0: Probabilistic risk assessment and severe accident evaluation for new reactors, Revision 3, NUREG-0800, US NRC, Washington, DC, (2015).
[4] Nuclear Energy Institute, Modernization of technical requirements for licensing of advanced non-light water reactors: Risk-informed performance-based guidance for non-light water reactor licensing basis development, NEI 18-04, Draft N, ADAMS Accession No. ML18242A469, NEI, Washington, DC (2019).
[5] American Society of Mechanical Engineers & American Nuclear Society, Probabilistic risk assessment standard for advanced non-LWR nuclear power plants, ASME/ANS RA-S-1.4–2021, Trial Use and Pilot Application, ASME/ANS, La Grange Park, IL (2021).
[6] U.S. Nuclear Regulatory Commission, Update on staff plans to apply the full-scope site Level 3 PRA project results to the NRC’s regulatory framework, SECY-12-0123. US NRC, Washington, DC, http://www.nrc.gov/reading-rm/doc-collections/commission/secys/2012/ 2012-0123scy.pdf (2012).
[7] U.S. Nuclear Regulatory Commission, Technical analysis approach plan for Level 3 PRA project. Rev. 0B — Working Draft, US NRC, Washington, DC, https://www.nrc.gov/docs/ML1329/ML13296A064.pdf (2013).
[8] Electric Power Research Institute, Framework for assessing multi-unit risk to support risk-informed decision-making: Phase 1: Initial framework development, 3002015991, EPRI, Palo Alto, CA (2019).
[9] HIROKAWA, N., et al., “Multi-unit probabilistic safety analysis for Wylfa Newydd site”, In Proc. OECD/NEA Int. Workshop on Status of Site Level PSA (including Multi-Unit PSA) Developments, Munich, 18–20 Jul, (2018).
[10] HENNEKE, D., Li, J., “Simplified methodology for multi-unit probabilistic safety assessment (PSA) modelling”, In Proc. Int. Topical Mtg on Probabilistic Safety Assessment and Analysis (PSA 2019), Charleston, SC, American Nuclear Society, La Grange Park, IL (2019).
[11] Office for Nuclear Regulation, Research report on multi-unit Level 3 PSA — Executive summary, ONR-1908/ONR-RRR-084, Bootle, UK, http://www.onr.org.uk/documents/2019/onr-rrr-084.pdf (2019).
[12] Japan Nuclear Energy Safety Organization, Development of Level 3 PSA methodology, JNES/SAE06-005, (2006).
[13] Ding, H., Tong, J., Raskob, W., Zhang, L., An approach for radiological consequence assessment under unified temporal and spatial coordinates considering multi-reactor accidents, Ann. Nucl. Energy 127, 450–458, (2019)
[14] Kim, S., Jung, Y. H., Han, S. H., Han, S., Lim, H., Multi-unit Level 3 probabilistic safety assessment: Approaches and their application to a six-unit nuclear power plant site. Nuclear Eng. Technol. 50(8):1246–54, (2018).
[15] Song, W., Park, S., Seo, Y., Jae, M., A source term binning methodology for multi-unit consequence analyses, Reliab. Eng. Syst. Saf., 202(C), (2020).

[16] Oh, K., Kim, S. Y., Jeon, H., Park, J. S., Study on multi-unit level 3 PSA to understand a characteristics of risk in a multi-unit contex, Nucl. Eng. Technol. 52(5), 975–983, (2020).
[17] Jung, W. S., Lee, H. R., Kim, J. R., Lee, G. M., Development of MURCC code for the efficient multi-unit level 3 probabilistic safety assessment, Nucl. Eng. Technol. 52(10) 2221–2229, (2020).
[18] Lee, G. M., Jung, W. S., A new method to calculate a standard set of finite cloud dose correction factors for the level 3 probabilistic safety assessment of nuclear power plants, Nucl. Eng. Technol. 56(4), 1225–1233, (2024).
[19] Chanin, D., Young, M. L., Randall, J., Jamali, K., Code manual for MACCS2: Volume 1, User's guide, NUREG/CR-6613, SAND97-0594, U.S. NRC, (1998).
[20] McFadden, K., Bixler, N. E., Lee Eubanks, Haaker R., WinMACCS, a MACCS2 interface for calculating health and economic consequences from accidental release of radioactive materials into the atmosphere: User's guide and reference manual for WinMACCS version 3, U.S. NRC, (2009).
[21] Sandia National Laboratories, MACCS, https://maccs.sandia.gov/maccs.aspx.
[22] Korea Foundation of Nuclear Safety, Nuclear Safety and Security Commission, Development of multi-unit PSA regulatory verification technology, TRKO202200007854, National R&D Report (2022).
[23] Slade, D. H., Meteorology and atomic energy, 1968, TID-24190, U.S. AEC, (1968).

ASRAM2025
www.asram2025.org
Asian Symposium on Risk Assessment and Management 2025
Pattaya, Thailand, 27 – 29 August 2025

Development of a Source Term Assessment Framework Integrating Uncertainty Analysis

Seunghyeon Hwang, Jaehyun Cho*

Chung-Ang University: 84, Heukseok-ro, Dongjak-gu, Seoul, Republic of Korea, 06974, univiewers@cau.ac.kr
** Chung-Ang University: 84, Heukseok-ro, Dongjak-gu, Seoul, Republic of Korea, 06974, jcho@cau.ac.kr*

EXTENDED ABSTRACT

When assessing source terms in various nuclear power plants accident scenarios, the importance of risk-informed approaches has been increasingly emphasized. Although current probabilistic safety assessment (PSA) systems have been systematically developed and advanced, there is a growing recognition of the need for a framework that can quantify uncertainties, systematically manage risks, and effectively support decision-making processes. In response, this study aims to extend conventional PSA by proposing an integrated framework that incorporates uncertainty quantification into the assessment of safety goals. A case study on Cs-137 is conducted to demonstrate the application of the proposed framework.

The developed framework consists of three major parts. First, the release amount or mass distribution of the source term is quantified using the MAAP5 code combined with sampling techniques. Second, the uncertainty in accident frequency is derived by applying PSA results along with a predefined error factor. Finally, the integrated risk information is visualized as a Risk Density Map, disaggregated by source term categories (STCs).

The case study focuses on the OPR-1000, a pressurized water reactor (PWR) design developed in Korea. The table below shows source term category results from the Level 2 PSA for Hanul Units 3 and 4. Based on these results, two representative STCs were selected for analysis: STC-02, which has the highest release frequency, and STC-20, which shows the highest release magnitude. Specifically, STC-02 corresponds to a scenario within a station blackout (SBO) accident, while STC-20 represents an interfacing system loss-of-coolant accident (ISLOCA).

TABLE I. OPR-1000 STCs Level 2 PSA data

STCs of OPR-1000 and Containment failure mode			Cs-137 Release (TBq)	Frequency (/RY)
STC-01	NOCF	MBLOCA	1.05E+01	5.19E-07
STC-02	NOCF	SBO	5.33E+01	1.20E-06
STC-03	ECF	LEAK, CS-YES	4.29E+00	1.09E-08
... (omitted for brevity)				
STC-19	NOISO	CS-NO	1.16E+04	1.08E-09
STC-20	BYPASS	ISLOCA	2.19E+05	1.01E-08
STC-21	BYPASS	SGTR	1.13E+05	2.37E-07

In the second part of the framework, which addresses the uncertainty of frequency, the parameters of the frequency distribution are generally determined based on expert judgment. However, in some cases, detailed statistical data required for precise analysis may not be available. To address this limitation, frequency distributions were constructed using error factor values referenced from U.S.NRC and Korea Hydro & Nuclear Power Co. (KHNP) design certification documents, applying the following formula.

$$Error\ Factor\ (EF) = \frac{P_{95}}{Median} = \frac{Median}{P_5} = 207.3 = \frac{2.09E-6}{1.01E-8} = \frac{1.01E-8}{4.87E-11} \quad (1)$$

To integrate the two distributions, release mass and frequency distributions, a Kernel Density Estimation (KDE) method was applied. The release amount of Cs-137 corresponds to the consequence metric, and together with frequency, it constitutes the primary components of risk. The resulting Risk Density Map, derived from the combined uncertainty distributions of each STC, is visualized as shown in the following figure.

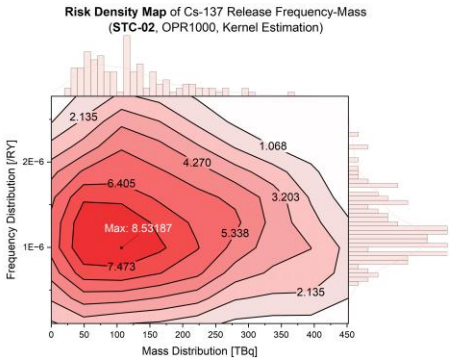

FIGURE 1. Cs-137 Release Risk Distribution (STC-2)

This type of risk visualization helps identify which scenarios or risk contributors require closer attention by explicitly reflecting the range of uncertainties. It ultimately contributes to enhancing the technical basis for data-driven safety management.

A key advantage of the risk density map, a primary output of this framework, is its ability to overcome the limitations of deterministic point estimate assessments. For instance, conventional Level 2 PSA data present the risk of the STC-02 scenario as a single point: a release of 53.3 TBq with a frequency of 1.20E-06 /RY. However, the Risk Density Map, which incorporates uncertainties, provides a much richer set of information.

The map reveals that the highest risk density (Max: 8.53187) occurs at a release of approximately 100 TBq, a value different from the original point estimate. More importantly, the contour lines effectively classify the level of risk. The dense inner contours (value > 6.405) delineate the most critical risk region, while the outer contours (value > 2.135) identify potential risk areas that, despite having lower probability, cannot be ignored. This allows for the quantitative understanding that even scenarios with releases as high as 250 TBq, far from the initial point estimate, fall within a significant risk boundary that warrants consideration.

Such analysis offers more powerful insights when comparing different risk profiles, such as the high-frequency STC-02 and the low-frequency, high-consequence STC-20. Ultimately, the proposed framework provides the technical basis for establishing safety management priorities and developing more robust response strategies by considering the entire spectrum of plausible risk scenarios, rather than focusing on a single accident outcome.

ACKNOWLEDGMENTS

This work was supported by the Nuclear Safety Research Program through the Regulatory Research Management Agency for SMRS (RMAS) and the Nuclear Safety and Security Commission (NSSC) of the Republic of Korea (No. 1500-1501-409).

REFERENCES

[1] J. Cho, S. H. Lee, Y. Bang, S. W. Lee and S. Park, “Exhaustive simulation approach for severe accident risk in nuclear power plants: OPR-1000 full-power internal events,” *Reliability Engineering and System Safety*, Vol. 225 (2022).

[2] International Atomic Energy Agency (IAEA), *Experience in the Development and Application of Level 2 Probabilistic Safety Assessment for Nuclear Power Plants*, IAEA-TECDOC-2081, IAEA, Vienna (2025).

[3] J. Yang, “Development of an integrated framework to implement the nuclear safety goals with various safety criteria,” *Nuclear Engineering and Technology*, Vol. 57 (2025).

[4] W. Vechgama, J. Cho, “Realistic estimation framework of radioactive release distributions into the environment during nuclear power plant accidents,” *Nuclear Engineering and Technology*, Vol. 56, p. 3097-3111 (2024).

Technical Session 7 (16:00 - 18:00)	The Port 3, C Floor	Risk and Resilience Management and Risk-informed Decision Making, and AI based Tools
		Chair/Facilitator 1: Assoc. Prof. Naraphorn Paoprasert (Department of Industrial Engineering, Faculty of Engineering, Kasetsart University)
		Chair/Facilitator 2: Asst.Prof. Piyatida Trinuruk KAEWCHINDA (King Mongkut's University of Technology Thonburi (KMUTT))
16:00 - 16:20		ID 107: The Risk of AI chatbots in Engineering Students' Critical Thinking, Analytical, Logical Skills, and Self-learning Determination Attitude Speaker: Cherlita Jantimaporn (Department of Industrial Engineering, Faculty of Engineering, Kasetsart University) Contributors: Sasarose Jaijit (Department of Industrial Engineering, Faculty of Engineering at Kamphaeng Saen, Kasetsart University), Cherlita Jantimaporn (Department of Industrial Engineering, Faculty of Engineering, Kasetsart University), Naraphorn Paoprasert (Department of Industrial Engineering, Faculty of Engineering, Kasetsart University), Pongthorn Ruksorn (Department of Industrial Engineering, Faculty of Engineering, Kasetsart University)
16:20 - 16:40		ID 72: Study on Methods for Assessing Risk Importance considering the Effects of Radiation Exposure at the ROKKASHO Reprocessing Plant Speaker: Masahiro Yamamoto (Japan Nuclear Fuel Limited) Contributors: Masahiro Yamamoto (Japan Nuclear Fuel Limited), Kazumi Takebe (Japan Nuclear Fuel Limited), Takashi Kodama (Japan Nuclear Fuel Limited), Futoshi Tanaka (Mitsubishi Heavy Industries, Ltd.), Asei Kawasaki (MHI NS Engineering Co.,Ltd.), Hidetaka Nagata (Mitsubishi Heavy Industries, Ltd.), Isao Hongo (Mitsubishi Heavy Industries, Ltd.), Makoto Takahashi (Tohoku University)
16:40 - 17:00		ID 109: Optimization of Fuzzy Membership Function-based Abnormal Event Diagnosis Model in Nuclear Power Plants Speaker: Seung Gyu Cho (Ulsan National Institute of Science and Technology) Contributors: Seung Gyu Cho (Ulsan National Institute of Science and Technology), Seung Jun Lee (Ulsan National Institute of Science and Technology)
17:00 - 17:20		ID 119: Operator-Centric Visualization of Explainable Diagnosis for Abnormal Situations Using Multilevel Flow Modeling Speaker: Ji Hyeon Shin (Korea Atomic Energy Research Institute) Contributors: Ji Hyeon Shin (Korea Atomic Energy Research Institute), Seo Ryong Koo (Korea Atomic Energy Research Institute), Seung Jun Lee (Ulsan National Institute of Science and Technology)
17:20 - 17:40		ID 77: Standard Operating Procedure for Development of Adaptive Resilience Curve to Assess Resilience of Clean Energy Systems Speaker: Pidpong Janta (ENTEC) Contributors: Kampanart Silva (ENTEC), Takashi Takata (UTokyo), Takafumi Narukawa (UTokyo), Nuwong Chollacoop (ENTEC)
17:40 - 18:00		ID 50: Development and Evaluation of Automatic Tools of Fault Tree Creation Using Artificial Intelligence Technology with the Ability to Integrate Fault Tree Created from Multiple Design Documents to assist Probabilistic Risk Assessment Engineers Speaker: Yuki Kondo (Japan Atomic Energy Agency) Contributors: Yuki Kondo (Japan Atomic Energy Agency), Satosh Futagami (Japan Atomic Energy Agency), Kenichi Kurisaka (Japan Atomic Energy Agency), Hidemasa Yamano (Japan Atomic Energy Agency)

The risk of AI chatbots in engineering students' critical thinking, analytical, logical skills, and self-learning motivation attitude

Naraphorn Paoprasert, Pongthorn Ruksorn, Sasarose Jaijit, Chaerlita Jantimaporn

Department of Industrial Engineering, Kasetsart University, Bangkok, 10900, Thailand. and Chaerlita.j@ku.th

EXTENDED ABSTRACT

Large Language Models (LLMs), such as ChatGPT, Gemini, and DeepSeek, can help students solve their homework, summarize learning content, and write academic work. Because of their convenience and speed, LLMs are widely used in education. However, using LLMs too much can affect students' thinking skill development. This study focuses on how LLMs might reduce students' development of critical, analytical, and logical thinking skills. And these three thinking skills might affect students' self-learning motivation.

In this study, critical thinking skill is defined as a careful and self-regulatory judgment that includes evaluation, analysis, interpretation, and inference, as well as a clear explanation of what evidence, concepts, or conditions the judgment is based on (Facione 1990, 2015). Analytical thinking skill refers to the ability to break down the complex components of information, arguments, or problems into smaller parts, identify the relationship among the parts in order to understand or solve problems (Halpern, 1998). Logical thinking skill is the ability to apply systematic reasoning, both deductive and inductive, to draw conclusions from evidence or assumptions in order to understand problems, make decisions, and find effective solutions, while being aware of cognitive biases that can distort decisions away from true reasoning (Davidson & Sternberg, 2003). The term self-learning motivation is internal drive and confidence that students have in their ability to study independently and with eagerness, without relying on external support, particularly the tools that provide solutions and answers for them, such as LLMs.

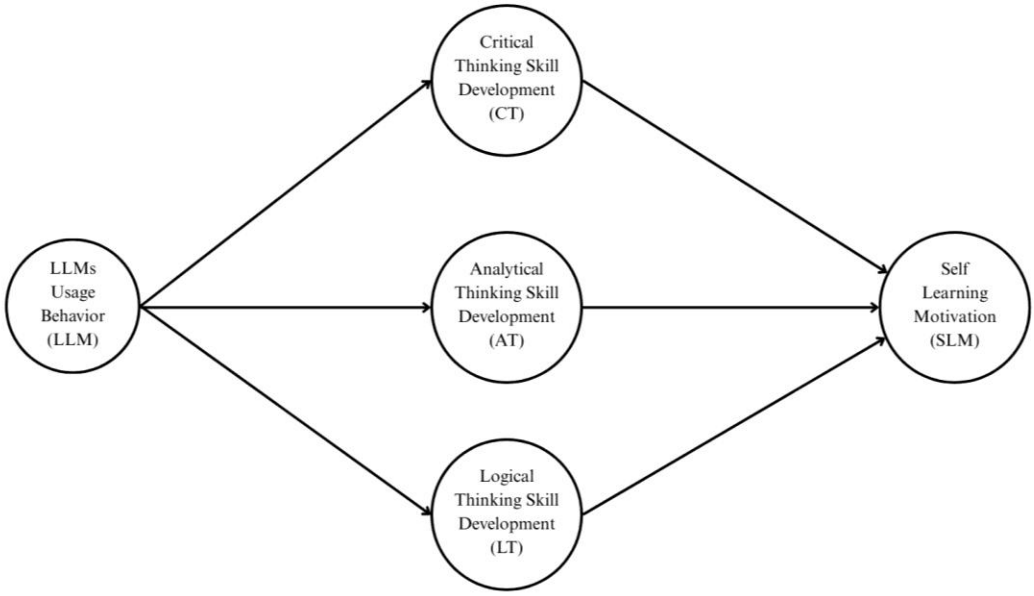

Figure 1: Conceptual Framework for Analyzing the Impact of LLM Usage on Cognitive Skill Development and Self-Learning Motivation

The conceptual framework was developed by reviewing the previous studies on the effects of AI tools on students' cognitive development. Overreliance on LLMs has been found to negatively affect cognitive ability (decision-making, critical thinking, and analytical thinking) because students tend to accept AI-generated answers without verification, which reduces their ability to think on their own and leads to cognitive offloading (Zhai et al., 2024). Frequent LLMs use may also decrease deep thinking activity, resulting in reduced cognitive development (Gerlich, 2025). Similarly, increased use of LLMs has been associated with lower problem-solving skills among students (Çela et al., 2024).

The core structure of the model was influenced by Facione's definition of critical thinking, as well as many existing research studies, which found that overreliance on LLMs can lead to cognitive offloading and a decline in thinking performance (Zhang et al., 2024; Zhong et al., 2024). When students rely on LLMs to generate answers, analyze content, or solve problems, they may avoid the necessary thinking process without realizing it, such as evaluating evidence, comparing alternatives, or constructing logical arguments. They may weaken their critical, analytical, and logical thinking abilities. Furthermore, the decline in these skills may negatively impact students' self-learning motivation. As students lose confidence in their ability to think and learn independently, they may become more passive learners, increasingly relying on external assistance.

The conceptual framework shows the relationship among the five latent variables. In this model, LLM usage behavior functions (LLM) as the independent variable, while self-learning motivation (SLM) is the dependent variable. The three types of thinking skills serve as the mediating variable, connecting the relationship between LLM usage and self-learning motivation. LLM usage has direct effects on three core cognitive skills: critical thinking (CT), analytical thinking (AT), and logical thinking (LT). These skills influence students' self-learning motivation. Each latent variable is measured by survey items developed from the literature review.

The questionnaire was developed based on the conceptual framework and academic research. It contains 25 questions, representing the indicators. These indicators (Observed Variables) are used to measure Latent Variables, which cannot be measured directly. Each question uses a 7-point Likert scale (1 = Strongly Disagree, 7 = Strongly Agree). The form was completed via Google Forms, and 128 responses were collected from engineering students at Kasetsart University.

The questionnaire is divided into six sections, each aiming to assess how LLMs may influence student learning and cognitive development. The sections and their focus areas are as follows:

1. Users's General Information
   1.1. Please select your department.
   1.2. Please select your current year of study.
   1.3. Which program are you enrolled in?
   1.4. Are you Thai? If not, please specify your nationality.
2. Basic Information on AI Usage in Learning
   2.1 Which AI do you usually use to assist with your studies?
   2.2 You use AI to do your homework or assignment FIRST every time, before thinking for yourself.
   2.3 You use AI more than listening to lectures in class.
3. Usage Related to Critical Thinking Skills
   3.1 You feel that using AI-Assisted Learning Tools makes you overly dependent on them, rather than analyzing information on your own.
   3.2 Using AI-Assisted Learning Tools makes you neglect verifying the accuracy of the information provided.
   3.3 You mostly use AI responses from AI-Assisted Learning Tools without any modification.
   3.4 AI discourages you from weighing the pros and cons of different solutions since it selects the best response for you.
4. Usage Related to Analytical Thinking Skills
   4.1 Using AI-Assisted Learning Tools eliminates the need to break down problems yourself, as AI structures the information for you.
   4.2 AI reduces your ability to identify connections between pieces of information since it provides conclusions instantly.

4.3 Using AI-Assisted Learning Tools reduces your effort in analyzing solutions since AI provides the "correct" answers immediately.

5. Usage Related to Logical Thinking Skills
   5.1 You tend to trust AI-Assisted Learning Tools' responses without verifying if they follow correct logic.
   5.2 After frequent AI usage, you put less effort into solving problems using your logical reasoning.
   5.3 AI usage reduces your need to analyze the reasoning and logic behind answers since AI has already done it for you.
   5.4 You have used AI-generated information without verifying whether the assumptions and logic behind it are reasonable.
   5.5 After frequent AI usage, you feel less capable of constructing clear reasoning and logic on your own.
6. Usage Related to Self-Learning Motivation
   6.1 When trying to solve problems without AI, you find it more complicated than before.
   6.2 AI discourages you from testing different ideas yourself since it provides an instant conclusion.
   6.3 AI-Assisted Learning Tools make learning more convenient, but they also reduce your analytical thinking ability.
   6.4 Using AI-Assisted Learning Tools has diminished your confidence in your thinking abilities.
   6.5 Using AI-Assisted Learning tools diminishes your creativity because the tools provide answers instead of encouraging independent thinking.

The structural relationship between the latent variables was analyzed by Partial Least Squares Structural Equation Modeling (PLS-SEM) via the SmartPLS 4.0 program. This method evaluates the influence of LLMs usage behavior on the development of critical thinking skills, analytical thinking skills, logical thinking skills, and self-learning motivation.

The results showed that all constructs had composite reliability values ranging from 0.812 to 0.876 and average variance extracted (AVE) values above 0.50, indicating good convergent validity. Additionally, the model passed the criterion for discriminant validity, as evaluated by the Fornell-Lacker Criterion and HTMT ratio.

Table 1: Hypothesis Testing Results

Relationship	Path Coefficient (β)	t-statistics	p-values	Results
LLM → CT	0.321	2.969	0.003	Supported
LLM → AT	0.387	4.290	0.000	Supported
LLM → LT	0.425	5.356	0.000	Supported
CT → SLM	0.101	1.127	0.260	Non-supported
AT → SLM	0.236	2.529	0.011	Supported
LT → SLM	0.522	5.974	0.000	Supported

Moreover, the results show that LLMs usage significantly positively affects all three types of thinking skills. However, only logical and analytical thinking skill development affects self-learning motivation, while critical thinking skill development does not significantly affect self-learning motivation ($p > 0.05$). This could be because analytical and logical thinking skills often lead to immediate, visible problem-solving success (e.g., solving math problems, coding, logical puzzles), which creates a positive feedback loop. Hence, skill improvement could eventually result in motivation to learn more. However, critical thinking skills are often viewed as abstract reasoning, argument evaluation, and nuanced judgment, which may not yield immediate or clear-cut success. Students may not easily see or feel the results of improved critical thinking. Without this visible feedback, self-efficacy and motivation may not increase. This result is not surprising, especially with a group of engineering students, since engineering students are often trained to analyze or use logic to find an answer rather than to debate, discuss, and provide multiple perspectives.

REFERENCES

[1] Facione, P. A. (2015). *Critical Thinking: What It Is and Why It Counts*. Insight Assessment. https://www.insightassessment.com/wp-content/uploads/Critical-Thinking-What-It-Is-and-Why-It-Counts-2015-Update.pdf

[2] Facione, P. A. (1990). *Critical Thinking: A Statement of Expert Consensus for Purposes of Educational Assessment and Instruction. Research Findings and Recommendations*. American Philosophical Association. (ERIC Document Reproduction Service No. ED315423)
[3] Halpern, D. F. (1998). Teaching critical thinking for transfer across domains: Dispositions, skills, structure training, and metacognitive monitoring. *American Psychologist*, *53*(4), 449–455.
[4] Davidson, J. E., & Sternberg, R. J. (Eds.). (2003). *The psychology of problem solving*. Cambridge University Press.
[5] Zhai, C., Wibowo, S., & Li, L. D. (2024). The effects of over-reliance on AI dialogue systems on students' cognitive abilities: a systematic review. *Smart Learning Environments*, *11*(28). https://doi.org/10.1186/s40561-024-00316-7
[6] Gerlich, M. (2025). AI Tools in Society: Impacts on Cognitive Offloading and the Future of Critical Thinking. *Societies*, *15*(1), 6. https://doi.org/10.3390/soc15010006
[7] Çela, E., Fonkam, M. M., & Potluri, R. M. (2024). Risks of AI-assisted learning on student critical thinking: A case study of Albania. *International Journal of Risk and Contingency Management*, *12*(1), 1–19. https://doi.org/10.4018/IJRCM.350185
[8] Zhong, T., Niu, Y., Zhang, W., Han, Y., Li, Y., Wang, J., & Li, J. (2024). *Generative AI as a Tool or Leader? Exploring AI-Augmented Thinking in Student Programming Tasks*. arXiv. https://doi.org/10.48550/arXiv.2411.19490
[9] Zhang, S., Zhao, X., Zhou, T., & Kim, J. H. (2024). Do you have AI dependency? The roles of academic self-efficacy, academic stress, and performance expectations on problematic AI usage behavior. *International Journal of Educational Technology in Higher Education*, *21*(1), 1–14. https://doi.org/10.1186/s41239-024-00467-0
[10] Pitts, G., Marcus, V., & Motamedi, S. (2025). *Student Perspectives on the Benefits and Risks of AI in Education*. arXiv. https://arxiv.org/abs/2505.02198
[11] Cotton, W. D., & Gribble, G. D. (2023). *AI, Critical Thinking, and Education: A Review of the Literature*. arXiv. https://arxiv.org/abs/2312.02422
[12] Lepik, K. (2024). *Trust, but Verify: Students' Reflections on Using Artificial Intelligence in Written Assignments*. ResearchGate. https://www.researchgate.net/publication/377857351_Trust_but_Verify_Students%27_Reflections_on_Using_Artificial_Intelligence_in_Written_Assignments
[13] Lepik, K. (2024). *Trust, but Verify: Students' Reflections on Using Artificial Intelligence in Written Assignments*. ResearchGate. https://www.researchgate.net/publication/377857351_Trust_but_Verify_Students%27_Reflections_on_Using_Artificial_Intelligence_in_Written_Assignments
[14] Fan, Y., Tang, L., Le, H., & Shen, K. (2024). Beware of metacognitive laziness: Effects of generative artificial intelligence on learning motivation, processes, and performance. *British Journal of Educational Technology*. https://doi.org/10.1111/bjet.13544

ASRAM2025
www.asram2025.org
Asian Symposium on Risk Assessment and Management 2025
Pattaya, Thailand, 27 – 29 August 2025

Study on methods for assessing risk importance considering the effects of radiation exposure at the Rokkasho Reprocessing Plant

Masahiro Yamamoto[1, 4], Kazumi Takebe[1], Takashi Kodama[1], Futoshi Tanaka[2], Asei Kawasaki[3], Hidetaka Nagata[2], Isao Hongo[2], Makoto Takahashi[4],

[1] *Japan Nuclear Fuel Limited: 4-108, Okizuke Obuchi, Rokkasho-Mura, Aomori-Ken, 039-3212, masahiro.yamamoto@jnfl.co.jp, kazumi.takebe@jnfl.co.jp, takashi.kodama@jnfl.co.jp*
[2] *Mitsubishi Heavy Industries, Ltd: 1-1,Wadasaki-cho 1-chome, Hyogo-ku Kobe, Hyogo-Ken, 652-8585 futoshi.tanaka.j2@nu.mhi.com, hidetaka.nagata.w7@nu.mhi.com, isao.hongo.h5@nu.mhi.com*
[3] *MHI NS Engineering Co.,Ltd.: 1-1-1,Wadasaki-cho, Hyogo-ku Kobe, Hyogo-Ken, 652-8585 asei.kawasaki.ar@nu.mhi.com*
[4] *Tohoku University: 6-6-11-907, Aoba Aramaki Aoba-ku Sendai, Miyagi-Ken, 980-8579 yamamoto.masahiro.r1@dc.tohoku.ac.jp, makoto.td@tohoku.ac.jp*

ABSTRACT

In the Rokkasho Reprocessing Plant (RRP), it is required by regulation to implement accident measures against specific severe accidents, such as “Loss of cooling function (LOCF)” and “Loss of Hydrogen Scavenging Function (LOHSF)”. The LOCF event may involve about 50 tanks that share common safety system equipment. In addition, some tanks require both cooling and hydrogen scavenging. Therefore, there is a possibility of severe accidents occurring simultaneously in multiple storage tanks and different types of severe accidents. We are conducting a PRA study to identify vulnerabilities associated with equipment and operations to prevent and mitigate severe accidents at reprocessing plants. In this study, we selected the “Multi-unit Event Combinations Approach (MECA)” as an evaluation method. In the reprocessing plant, the impact of radiation exposure in a severe accident varies depending on the risk source (e.g., storage tanks). In addition, some equipment failure affects multiple tanks and/or scenarios (multi-unit events), while some affect a single tank (individual events). For the risk assessment, it is important to use a methodology capable of evaluating the important measures that consider the impacts of radiation exposure. In this study, we referred to the concept of importance based on point estimate of risk and exceedance frequency of consequence described in the ASME/ANS PRA standards for non-light water reactors. In this study, we used Fussell-Vesely (FV) importance as a measure of importance and examined methods for evaluating the importance of both multi-unit events and individual events, considering the impact of radiation exposure.

Keywords: Multi-Unit, Multi-Event, Reprocessing, Risk Importance

I. INTRODUCTION

Probabilistic risk assessment (PRA) is an effective measure to quantitatively understand the risks associated with nuclear facilities. There are a number of PRA evaluation reports and utilization reports covering nuclear power plants.

On the other hand, there are very few PRA evaluation reports targeting reprocessing plants. The reason is thought that the limited number of reprocessing plants and the differences in facility characteristics between nuclear power plants and reprocessing plants. Reprocessing plants handle various types, quantities, and forms of nuclear fuel materials, which are widely distributed across multiple processes. Consequently, as shown in Figure 1, a wide variety of severe accidents are anticipated.

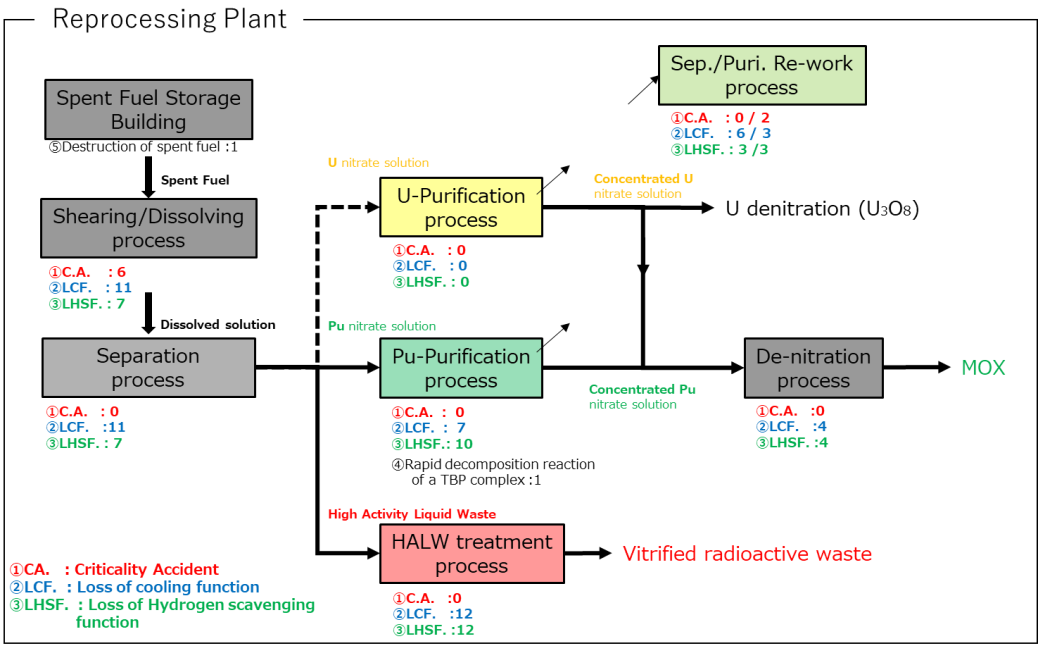

FIGURE 1. The reprocessing process outline and the number of equipment which severe accidents expected to occur

We have implemented various safety measures to prevent severe accidents in compliance with regulatory requirements. To investigate further safety improvements, we are advancing the development of PRA to identify vulnerabilities related to severe accident counter measures. Currently, we are developing internal event PRA models for severe accidents, focusing on ”The Loss of cooling function (LOCF)” and “The Loss of Hydrogen Scavenging Function(LOHSF)”. In this development, we are developing PRA models for each individual tank. However, since safety equipment related to design basis accidents and severe accidents is shared among multiple tanks, it is necessary to study for PRA methods that can evaluate the simultaneous occurrence of multiple severe accidents (multiple events) across multiple tanks. Therefore, in order to evaluate the simultaneous occurrence of multiple storage tanks and multiple events accidents, the preceding case in which nuclear power plants were targeted was confirmed in the previous studies by the authors[1]. As a result, we selected Multi-unit Event Combination Approach (Hereinafter referred to as “MECA”.) as the evaluation method suitable for the application to reprocessing plants. This method does not require the creation or recalculation of event trees and fault trees, and the calculation load is reduced compared with other methods.

In the authors previous study [1], in order to sort out the technical challenge related to the first two items among the following challenges in the application of MECA to actual machines, we studied the case of two tanks, which is the most basic system configuration among multiple storage tanks and multiple events.

Challenge (1): The existence of a large number of multi-unit events in reprocessing plants compared to nuclear power plants

Challenge (2): Large Number of Radioactive Sources (Tanks) have to be evaluated

Challenge (3): Establishment of a Method to Calculate Importance Considering Radiation Exposure Impact

As a result of the examination, we were able to confirm the applicability of MECA in the case of two tanks. Therefore, we were able to organize the issues for further examination of Challenge (1) and (2).

In this study, a method to evaluate the " risk importance of basic events considering the effects of radiation exposure " was studied in order to summarize the technical challenge mentioned above in Challenge (3). The applicability of the proposed method is verified by case studies using the evaluation results of the authors previous study.

II. Evaluation method of importance based on characteristics of reprocessing plants and investigation of precedent cases

II.A. Necessity of importance assessment considering the effects of radiation exposure

In risk-informed decision making for nuclear power plants, importance relative to the occurrence frequency of accidents such as core damage frequency (CDF) and containment failure frequency (CFF) is used as general measures[2] [3].

On the other hand, reprocessing plants have the following features.
(1) There are large number of radioactive sources (storage tanks etc.) that may cause severe accidents, and the type and quantity of radioactive materials contained in these storage tanks differ from tank to tank.
(2) In addition to LOCF and LOHSF, a wide variety of severe accidents, such as Explosion of chemical substances and Criticality, may occur.

The above characteristics affect the "exposure impact on the public" in the event of an accident. For example, assume an accident at two storage tanks (independent of each other) with the same accident frequency. If the effect of radiation exposure from a single storage tank accident is large in either one of the two tanks, the risk, which is the product of the frequency of the accident and the effect at the time of the accident, is different among the tanks even if the accident frequencies are the same. Therefore, in order to advance the study on the identification of vulnerability in the facilities and operations of reprocessing plants using PRA, it is necessary to carry out Challenge (3) "Establishment of a method to calculate importance considering radiation exposure impact" mentioned in the previous chapter.

II.B. Investigation of precedent cases of significance considering radiological consequence.

The ASME/ANS "PRA Standard for advanced Non-light water reactor nuclear power plants" [4] of the United States provides the following two examples of relative significance considering radiological consequence.

(1) Point estimate of risk method

This method evaluates the importance of accident sequences by weighting the occurrence frequency of accident sequences by the exposure effect.

The importance evaluated by this method has the following features.
a. The importance tends to be higher for equipment of those involved in sequences with greater frequency.
b. The importance tends to be higher for equipment of those involved in sequences that has a greater effect on exposure.
c. Equipment involved in frequent but low-impact sequences may result in high importance. For this reason, depending on the magnitude of the exposure effects of interest, equipment of high importance may not necessarily be important in terms of the exposure effects.

(2) Exceedance frequency of consequence method

In this method, the threshold value of the exposure effect (Hereinafter referred to as "reference point".) is determined, and the exceedance frequency of "the sequence in which the exposure effect exceeds the reference point" in the accident sequence is focused. Then, the degree to which the occurrence frequency of each accident sequence group contributes to the excess frequency is calculated as the importance.

The importance evaluated by this method has the following features.
a. The significance for the exposure effect of interest is evaluated.
b. The effects of equipment that only affects sequences with small exposure effects can be eliminated.
c. The reference point for calculating the excess frequency should be set appropriately according to the purpose.

In the ASME/ANS "PRA Standard for advanced Non-light water reactor nuclear power plants", technology neutral PRA methods for reactor types such as molten salt reactors and gas-cooled reactors, where there is no clear definition of core damage, are proposed by using the Level 3PRA evaluation method for existing LWRs. In addition, as mentioned above, examples of importance evaluation considering the effects of exposure are also mentioned. As described in the previous chapter, in PRA for reprocessing plants, it is important to evaluate the radiation exposure impact. Therefore, this standard is a very useful reference. In the previous studies[5], "multi-module interaction" was considered for SMRs. However, it is expected that the number of multiple storage tanks and multiple events corresponding to multi-module interaction will increase in reprocessing plants.

The ASME/ANS evaluation example focus on event sequences occurring in a single reactor core. In contrast, in a reprocessing plant, simultaneous releases from multiple tanks are anticipated, necessitating information on the frequency of event sequences occurring at multiple storage tanks, their aggregated release effects, and importance measures within the event sequences. Therefore, in this study, we established a method to evaluate occurrence frequency of release from multiple tanks, and expanded it to a method to evaluate basic event level risk importance with consideration of exposure effects.

III. Definition of importance analysis for reprocessing plants

Referring to evaluation methods of the significance of the accident sequence exemplified in the ASME/ANS standard in order to simplify the evaluation described in Chapter 2, evaluation methods of the significance of basic events were examined

considering the exposure effects in reprocessing plants. It should be noted that the two evaluation methods exemplified in the ASME/ANS standard can achieve a high level of analysis by using the appropriate methods according to the purpose of evaluation. The "(1) Point estimate of risk method" has the advantage of being straightforward, but does not distinguish the importance of SSC that contribute to high frequency but small consequence accidents between those that contribute to low frequency but large consequence accidents. On the other hand, "(2) Exceedance frequency of consequence method" has the advantage that it provides importance with consideration of the magnitude of the consequence or exposure effects of interest. Therefore, a study was made so that both methods can be used as evaluation methods for multiple storage tanks and accident events in RRP.

Method (1): Importance for exposure effect risk (corresponds to (1) Point estimate of risk method of the ASME/ANS standard)

As an importance measure showing the extent to how significantly a specific basic event (Equipment failure, human error, etc.) contributes to the exposure risk from the entire reprocessing plant, the " Fussell-Vesely importance(FV) " of basic events with regards to the exposure risk from the entire reprocessing plant was defined.

The formula for defining the importance of basic event "A" to the exposure effect risk is as follows.

$$I_{Risk}(A) \equiv \frac{R_{total} - R_{total_{QA=0}}}{R_{total}} \quad (1)$$

where

$I_{Risk}(A)$: Risk importance of basic event "A" considering the effects of radiation exposure (-)

Q_A : Probability of occurrence of basic event "A"

R_{total} : The risk of the radiation exposure impact from the entire Reprocessing Plant (mSv/y etc.)

$R_{total_{QA=0}}$: The risk of the radiation exposure impact from the entire Reprocessing Plant when the probability of occurrence of a basic event "A" is set to zero (mSv/y etc.)

Method (2): Importance for the exceedance frequency of reference point (corresponds to ASME standard (2) Exceedance frequency of consequence method)

For accident events that result in exposure effects exceeding a reference point, as an importance measure to show the degree of contribution of a specific basic event, the FV of the basic event with regards to "the exceedance frequency of exposure effects" in the entire reprocessing plant was defined.

We defined "the excess frequency of exposure effects" as follows

The exceedance frequency of exposure effects: Frequency of accident events involving the release of radioactive material that exceed the reference point

The formula for defining the importance of basic event "A" relative to the exceedance frequency of exposure effect "X" is as follows.

$$I_{DC}(A, X) \equiv \frac{F_{total}(X) - F_{total}(X)_{QA=0}}{F_{total}(X)} \quad (2)$$

where

$I_{DC}(A, X)$: Importance of basic event "A" relative to the exceedance frequency of exposure effect "X" (-)

X : Magnitude of the radiation exposure impact(mSv etc.)

Q_A : probability of occurrence of the basic event "A" (-)

$F_{total}(X)$: The exceedance frequency of exposure effect "X" in the entire reprocessing plants (/ year)

$F_{total}(X)_{QA=0}$: The exceedance frequency of exposure effect "X" in the entire reprocessing plants when the probability of occurrence of a basic event "A" is set to zero(/ year)

IV. Study of calculation method for risk importance considering the effects of radiation exposure

IV.A. Assumptions applied in this study

On the premise of using the analysis results by MECA, we examined the method to evaluate the accident frequencies of the system described chapter I, and the method to evaluate risk importance with consideration of radiation exposure. Methodologies are respectively described in IV.B and IV.C,.

In this study, as the simplest case, we focused on two Storage tanks and considered scenarios where release sequence of radioactive materials in each Storage tank (storage Tank and the release of Radioactive Materials (T/R.M.) Sequence) occurs simultaneously or independently.

In addition to the above, the following assumptions were also applied in this study to simplify the evaluation.

a. The probability of occurrence of each T/R.M. Sequence is assumed not to be affected by the occurrence of the other T/R.M. Sequence (There is no causal influence between T/R.M. Sequences).
b. Multi-unit events are assumed to be independent of each other.
c. It is assumed that the occurrence probability of the multi-unit event is not affected by the occurrence of a particular T/R.M. Sequence.
d. The radiation exposure impact of "a combination of T/R.M. Sequences (Hereinafter referred to as Multiple T/R.M. patterns.) " are assumed to be the simple sum of the exposure effects when each T/R.M. Sequences included in Multiple T/R.M. patterns occurs.

IV.B. Evaluation scheme of MECA and evaluation method of occurrence frequency

Figure 2 shows the concept of calculating the frequency of occurrence by MECA, the frequency of occurrence of each Multiple T/R.M. patterns for each multi-unit event scenarios, and the relationship between the radiation exposure impacts when each Multiple T/R.M. patterns occurs.

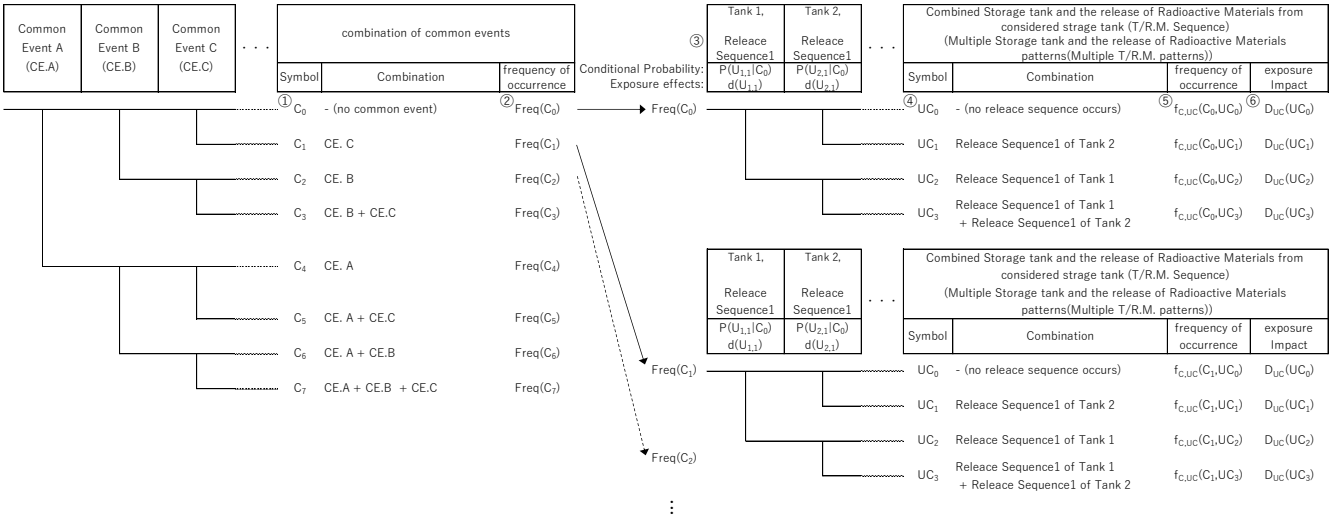

Locat	Symbol	Description	Supplement
①	i	Sequence number for the combination of common events	-
	C_i	Symbol representing the i-th common event scenarios	-
②	Freq(C_i)	Frequency of ommon event scenarios Ci (/year)	Values calculated by the MECA
③	j	Serial number for the storage tank	-
	k	Serial number for the releace sequence	-
	$U_{j,k}$	Symbol representing the k-th release sequence in the j-th reservoir	-
	$P(U_{j,k}\|C_i)$	Conditional probability of Uj,k occurring when Ci occurs (-)	Values calculated by the MECA
	$d(U_{j,k})$	Radiation exposure impact when Uj,k occur (mSv, etc.)	Value set based on the results of the radiation exposure impact
④	n	Sequence numbers for Multiple T/R.M. patterns	-
	UC_n	Symbol representing the n-th Multiple Storage tank and the release of Radioactive Materials patterns(Multiple T/R.M. patterns))	-
⑤	$f_{C,UC}(C_i,UC_n)$	Frequency of Multiple T/R.M. patterns UCn with occurrence of common event events Ci (/year)	-
⑥	$D_{UC}(UC_n)$	Exposure effects when Multiple T/R.M. patterns UCn occur (mSv, etc.)	Values calculated according to the following $D_{UC}(UC_n) = \sum_{U_{j,k} \in UC_n} d(U_{j,k})$

FIGURE 2. Relationship between analysis results from MECA, frequency of Multiple T/R.M. patterns, and radiation exposure impact

As shown in Figure 2, for each multi-unit event scenario "Ci", several Multiple T/R.M. patterns may occur. In the absence of causal dependency between T/R.M. Sequence, the frequency of occurrence of Multiple T/R.M. patterns with the occurrence of any T/R.M. Sequence can be calculated by the following equation:

$$f_{C,UC}(C_i, UC_n) = Freq(C_i) \times \prod_{U_{j,k} \in UC_n} P(U_{j,k}|C_i) \times \prod_{U_{j,k} \notin UC_n} \{1 - P(U_{j,k}|C_i)\} \quad (3)$$

where

n : identification number for Multiple T/R.M. patterns

UC_n: n-th Multiple T/R.M. pattern

$f_{C,UC}(C_i, UC_n)$: Frequency of Multiple T/R.M. patterns with occurrence of multi-unit event scenario "Ci"

$Freq(C_i)$: Frequency of multi-unit event scenario "Ci"

$\prod_{U_{j,k} \in UC_n} U_{j,k}$: Symbol representing the multiplication of all T/R.M. Sequence "Uj,k"s in Multiple T/R.M. pattern "UCn"

$\prod_{U_{j,k} \notin UC_n} U_{j,k}$: Symbol representing the multiplication of all T/R.M. Sequence "Uj,k"s in "Uj,k" that are not in Multiple T/R.M. pattern "UCn"

IV.C. Assessing the Exposure effect risk and Importance of exposure effect risk

(1) Consideration of exposure effect risk

Since exposure effect risk is the product of "frequency of occurrence of the accident" and "the radiation exposure impact", exposure effect risk for the occurrence of Multiple T/R.M. pattern "UCn" accompanied by the occurrence of any multi-unit event scenarios(Ci) is as shown in Eq. (4).

The occurrence probability of Multiple T/R.M. patterns differs depending on multi-unit event scenarios. Also, the radiation exposure impact differs according to Multiple T/R.M. patterns. Therefore, it is necessary to calculate the frequency, the radiation exposure impact and exposure effect risk for each multi-unit event scenarios and Multiple T/R.M. patterns.

$$r_{C,UC}(C_i, UC_n) = f_{C,UC}(C_i, UC_n) \times \sum_{U_{j,k} \in UC_n} d(U_{j,k}) \quad (4)$$

where

$r_{C,UC}(C_i, UC_n)$: The exposure effect risk of Multiple T/R.M. patterns""UCn with development of multi-unit event scenario""Ci(mSv/y etc)

$f_{C,UC}(C_i, UC_n)$: Frequency of Multiple T/R.M. patterns with occurrence of multi-unit event scenarios " Ci"(/y)

$d(U_{j,k})$: The radiation exposure impact when T/R.M. Sequence "Uj,k" occurs

$\sum_{U_{j,k} \in UC_n} U_{j,k}$: Symbol representing the sum of all T/R.M. Sequence "Uj,K"s in Multiple T/R.M. patterns

In addition, when exposure effect risk calculated by equation (4) is summed for all Multiple T/R.M. patterns and all multi-unit event scenarios, the overall exposure effect risk is obtained.

$$R_{total} = \sum_i \sum_n r_{C,UC}(C_i, UC_n) \quad (5)$$

where

R_{total} : Overall exposure effect risk of reprocessing plant

(2) Consideration of the exceedance frequency of exposure effects

In evaluating the exceedance frequency of exposure effects, the examination proceeded as follows,

a. Set the magnitude of the radiation exposure impact X as criteria for evaluating the exceedance frequency according to the radiation exposure impact when Multiple T/R.M. patterns "UCn" occurs.

b. Sum all frequencies of Multiple T/R.M. patterns "UCn" that exceed the magnitude of the radiation exposure impact X.

c. When the frequency of occurrence in equation (3) is summed for all multi-unit event scenarios "Ci" and the radiation exposure impact "X", the frequency of exceedance exposure effects for the entire reprocessing plant can be obtained using the equation below.

$$F_{total}(X) = \sum_i \sum_{\substack{n \\ D_{UC}(UC_n)>X}} f_{C,UC}(C_i, UC_n) \quad (6)$$

where
$F_{total}(X)$: Exceedance frequency of the radiation exposure impact X in the entire reprocessing plant (/ year)
X : Magnitude of the radiation exposure impact
$\sum_{\substack{n \\ D_{UC}(UC_n)>X}}$: Symbol representing the summation of the series number n for which the exposure effect due to Multiple T/R.M. patterns"UCn" exceeds the radiation exposure impact "X"
$f_{C,UC}(C_i, UC_n)$: Frequency of Multiple T/R.M. patterns with occurrence of multi-unit event scenarios" Ci"(/y)
$D_{UC}(UC_n)$: Exposure effects in the event of Multiple T/R.M. patterns "UCn"

In order to calculate the importance based on equations (1) and (2), $R_{total_{QA=0}}$ and $F_{total}(X)_{QA=0}$ is required in addition to $R_{total}$and$F_{total}(X)$. $R_{total_{QA=0}}$ and $F_{total}(X)_{QA=0}$ is obtained by recalculating Equations (3) to (6) in the same manner as in previous section a. and section b, setting the probability of occurrence of the basic event to zero.

In the PRA model of a reprocessing plant, multi-unit event(basic events associated with multiple tanks/events) and individual event(basic events associated only with a single tank/event) exist. Since the multi-unit event is included in the multi-unit event scenario, $R_{total_{QA=0}}$ and $F_{total}(X)_{QA=0}$ can be calculated only by recalculating $Freq(C_i)$ with the probability of occurrence of the basic event set to zero.

On the other hand, since individual events are not included in the multi-unit event scenario, they cannot be calculated in the same way as multi-unit events. At present, if the assumption which referred to in 4.(1) "There is no causal influence between T/R.M. Sequences" is applied, the importance for exposure effect risk of individual events with T/R.M. Sequence can be calculated by the following equation.

$$I_{Risk}(A) = \frac{d(U_{J,K}) \times f_{SU}(U_{J,K}) \times FV_{SU}(A,U_{J,K})}{R_{total}} \quad (7)$$

where
$d(U_{J,K})$: Exposure effects in the event of Multiple T/R.M. Sequence "Uj,k" (mSv etc.)
$f_{SU}(U_{J,K})$: Analysis result of frequency of T/R.M. Sequence "Uj,k" using the single-unit PRA model (/ year)
$FV_{SU}(A, U_{J,K})$: Analysis result of FV for individual events "A" of T/R.M. Sequence "Uj,k" using the single-unit PRA model

V. The case study of risk importance considering the effects of radiation exposure

(1) Explanation of evaluation system for trial evaluation

Using the evaluation system set for the calculation of the frequency of simultaneous accidents (as reported in the authors previous study [1]), we conducted the analysis of the risk importance discussed in the previous chapter. Outline of the event and evaluation case used for the methodology verification is shown below.

a. Target Events for Verification

(a) Loss of Cooling Function in the Safety Cooling Water System

The safety cooling function prevents radioactive solution in the tank from boiling due to decay heat. If the cooling function is lost, the temperature of the solution increases and lead to boiling. When the solution boils, radioactive materials will be transferred along with vapor and release into the atmosphere. The safety cooling water system consists of an internal loop (including the internal loop pump, intermediate heat exchanger, and connecting pipes) and an external loop (including the external loop pump, cooling tower, and connecting pipes). From the perspective of accidents in multiple tanks, it has the characteristic of sharing an external loop among all tanks. The system configuration is illustrated in Figure 3.

(b) Loss of Hydrogen scavenging Function in the Safety Compressed Air System

The hydrogen generated by the radiolytic decomposition of the radioactive solution in the tank is scavenged to the ventilation system by compressed air. If the scavenging function is lost, the hydrogen concentration increases and lead to hydrogen explosion. When hydrogen explosion occurs, radioactive materials are released into the atmosphere. The safety compressed air system consists of hydrogen scavenging pipes and valves, and an air compressor that produces compressed

air. The air compressor is cooled by the safety cooling water system. The related system configuration is illustrated in Figure 3.

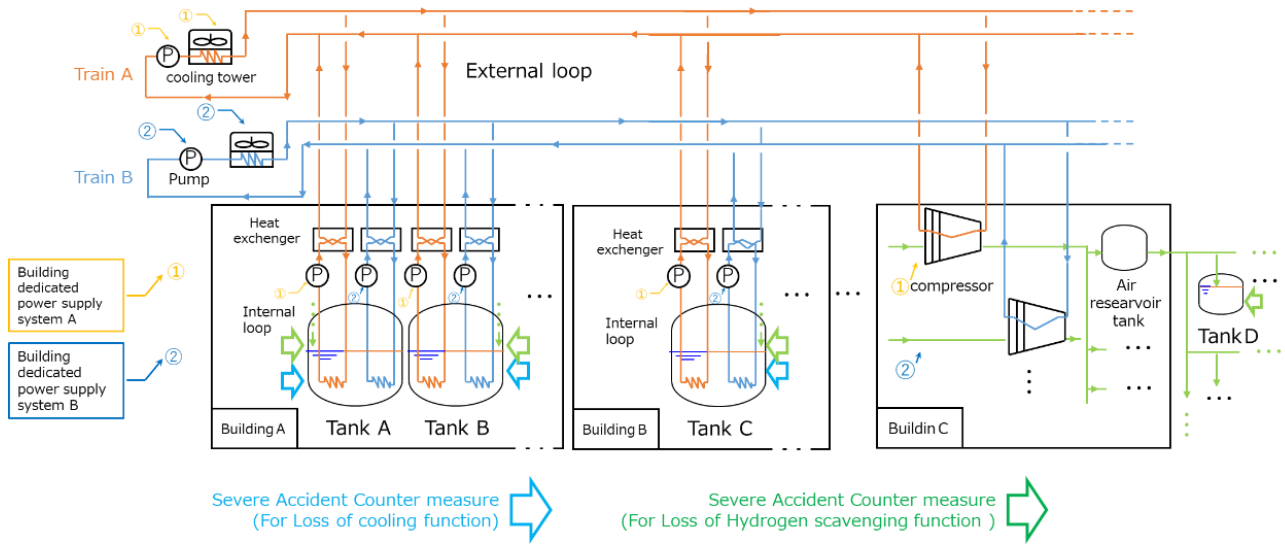

FIGURE 3. Illustration of systems related to Loss of Cooling Function and Loss of Hydrogen scavenging Function

b. Evaluation Case

Evaluation Case 1:Loss of cooling function events in the same building.

We focused on the event of loss of cooling function in Tank A and Tank B, both located in Building A, as illustrated in Figure 3. In this case, the fraction of accidents occurring in individual tank is very small, and the fraction of accidents occurring simultaneously in two tanks is more than 99% [1].

Evaluation Case 2: Loss of cooling function event and loss of hydrogen scavenging function event

We focused on the events of loss of cooling function in Tank A located in Building A, and loss of hydrogen scavenging function in Tank C in Building B, as illustrated in Figure 3. In this case, the fraction of accidents occurring in each individual tank is relatively large, and the percentage of accidents occurring simultaneously in two tanks is approximately 1% [1].

(2) The case study analysis results of risk importance

a. Results of importance for exposure effect risk

The top 10 basic events(Equipment failure, human error, etc.) with the highest risk importance for each evaluation case are shown below.

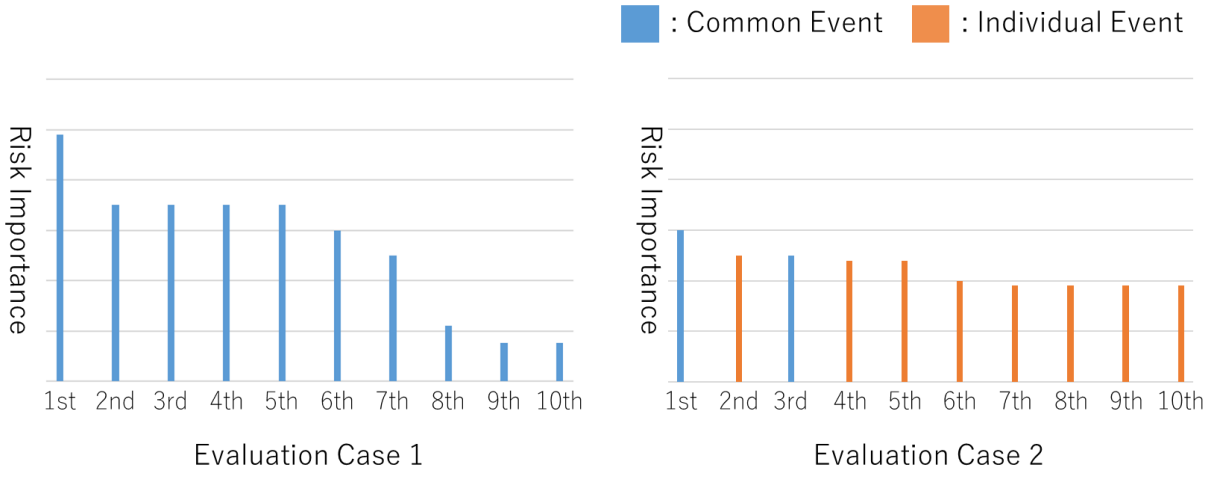

FIGURE 4. The importance for exposure effect risk of each evaluation case (top 10 basic events)

In evaluation case (1), the top 10 events were all multi-unit events (mitigation measures commonly used in the two storage tanks). The two storage tanks in evaluation case (1) share many equipment, and the scenario in which the two set of T/R.M. Sequence occur simultaneously due to the occurrence of a multi-unit event was dominant. Therefore, the risk importance of multi-unit events tended to be high.

On the other hand, in the evaluation case(2), the top events were individual events (mitigation measures used separately for each storage tank) except for the first and third. The two storage tanks in evaluation case (2) share relatively little number of equipment, and the contribution of the scenario in which two T/R.M. Sequences occur separately is larger than that in Case (1). Therefore, the risk importance of individual events was also high. As mentioned in (1), the fraction of simultaneous occurrence in two T/R.M. Sequences is high in the evaluation case (1), and the fraction of simultaneous occurrence in two T/R.M. Sequences is low in the evaluation case (2). Therefore, the trend of the case study results in this study is consistent with the trend expected.

b. Results of importance for the exceedance frequency of reference point

Fig. 5 shows the result of the importance for the exceedance frequency of reference point when the reference points are set as shown in Table 1 for the evaluation case (1). Table 1 shows correspondence between reference points and T/R.M patterns categorized by whether an accident occurred in storage tank A or B, or both. Here, the “reference points” indicates the threshold value of the exposure effect depending on the occurrence of the accident. The results of evaluation case (2) is not shown in this paper because most of the basic events with high risk importance are individual events, and the evaluation method examined in this study cannot calculate the risk importance of individual events.

TABLE I. Reference Points to evaluate exceedance frequency

Reference Points	Multiple T/R.M. patterns (1: occur, 0 : no-occur)	
	Tank A (LOCF)	Tank B(LOCF)
1	0	0
2	1	0
	0	1
3	1	1

As shown in Fig. 5, the importance for the exceedance frequency of reference point was calculated. In evaluation case (1), there was no difference in the exceedance frequency at each reference point because the fraction of simultaneous occurrence of accidents in two storage tanks within the total accident frequency was high, majority of the probable accident scenarios in case (1) involves release from two tanks.

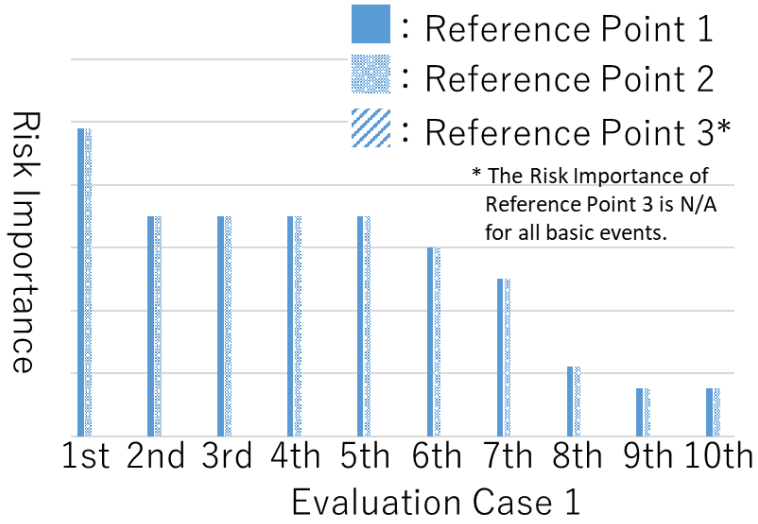

FIGURE 5. The Importance for the exceedance frequency of reference point (top 10 basic events) for the Evaluation Case 1.

VI. CONCLUSION

In this paper, calculation method of risk importance considering the effects of radiation exposure was examined using the evaluation result of MECA, to promote the utilization of risk informed decision making based on the characteristics of reprocessing plant.

As a result of the examination, we developed methods to evaluate "importance for exposure effect risk" and "importance for exceedance frequency by exposure effect category" for reprocessing plants, referring to the ASME/ANS PRA standards for non-light water reactors which is a precedent case. In addition, it was confirmed that the importance in the case of two T/R.M. Sequences could be calculated by case study evaluation using the developed evaluation method. Using the risk importance evaluated by the two methods, system and component important not only in terms of accident frequency but also from the viewpoint of exposure effect from multi-sources can be assessed. This will contribute to a higher level of risk-informed decision making for future reprocessing plants.

On the other hand, in order to simplify the evaluation, the number of storage tanks were limited to two, and consequential effects of release that can impact accident progression or system reliability were omitted. In the future, we will streamline these limitations. Furthermore, we will further explore to expand this methodology to evaluate risk importance considering the effects of radiation exposure when the evaluation target is expanded to three or more T/R.M. Sequence, and also to evaluate importance of individual events.

REFERENCES

[1] Masahiro Yamamoto, Kazumi Takebe, Takashi Kodama, Futoshi Tanaka, Isao Hongo, Asei Kawasaki, Makoto Takahashi, “Development of methods for evaluating the frequency of accidents related to multiple storage tanks and multiple events at the Rokkasho Reprocessing Plant” Proceedings of PSAM17&ASRAM2024, Sendai, Miyagi, Japan (2024).
[2] OECD/NEA, USE AND DEVELOPMENT OF PROBABILISTIC SAFETY ASSESSMENT NEA/CSNI/R(2007)12
[3] OECD/NEA, Probabilistic Risk Criteria and Safety Goals, NEA/CSNI/R(2009)16
[4] ASME/ANS RA-S-1.4 - Probabilistic Risk Assessment Standard for Advanced Non-Light Water Reactor Nuclear Power Plants
[5] Ola Bäckström, Pavel Krcal, Xuhong He, “Use of PSA for Small Modular Reactors” Proceedings of PSAM16, Honolulu, Hawaii, USA (2022).

ASRAM2025
www.asram2025.org
Asian Symposium on Risk Assessment and Management 2025
Pattaya, Thailand, 27 – 29 August 2025

OPTIMIZATION OF FUZZY MEMBERSHIP FUNCTION-BASED ABNORMAL EVENT DIAGNOSIS MODEL IN NUCLEAR POWER PLANTS

Seung Gyu Cho[1], Seung Jun Lee[2*]

[1] *Ulsan National Institute of Science and Technology, 50, UNIST-gil, Eonyang-eup, Ulju-gun, Ulsan, Republic of Korea, and sgcho@unist.ac.kr*
[*2] *Ulsan National Institute of Science and Technology, 50, UNIST-gil, Eonyang-eup, Ulju-gun, Ulsan, Republic of Korea, and sjlee420@unist.ac.kr*

ABSTRACT

Abnormal event diagnosis models for nuclear power plants have been extensively studied using plant simulators. However, discrepancies exist between real plant data and simulator-generated data due to factors such as the simplification of thermal-hydraulic codes in simulators and sensor noise in actual plants. These discrepancies can reduce the effectiveness of artificial intelligence-based diagnosis models and limit real-plant applicability. To solve this problem, we propose an abnormal event diagnosis model incorporating an optimized fuzzy membership function-based feature extraction method to represent trend features from simulator-generated data. By optimizing fuzzy membership functions, the model improves the extracting performance of trend features and this method can make abnormal event diagnosis model more representative of actual plant behavior. A membership function optimization algorithm is employed to systematically adjust membership function parameters and ensures more effective trend extraction from the data. This approach enhances the diagnostic performance of the deep neural network-based diagnosis model by providing optimally extracted data trends that adjust more robust for real plant conditions. Experimental results demonstrate that the optimized fuzzy membership function-based feature extraction method effectively captures data trends while mitigating discrepancies between simulated and synthetic data designed to mimic real plant characteristics. The findings suggest that the proposed method can improve the robustness and reliability of abnormal event diagnosis models by facilitating applicability in real plant environments. This study contributes to developing a more robust and reliable artificial intelligence-based abnormal event diagnosis model and ultimately supporting safer and more efficient plant operations.

Keywords: Nuclear power plant, Deep neural network, Abnormal event, Diagnosis, Fuzzy membership function

I. INTRODUCTION

An abnormal event diagnosis in nuclear power plants remains a crucial safety task because operators must recognize changes in plant behavior quickly and decide on corrective actions under severe time pressure. Most artificial-intelligence diagnosis models are trained almost exclusively on data generated by high-fidelity plant simulators, because such simulators can reproduce a wide range of events without endangering actual equipment. Unfortunately, when these same models are deployed in actual control rooms, we cannot expect the same level of performance they demonstrated in the simulator. One root cause is that the thermal-hydraulic codes embedded in simulators, although detailed, still simplify or omit secondary phenomena, for example three-dimensional mixing, sub-cooled boiling in complex geometries. At the same time, real instruments in an operating plant introduce additional uncertainties: sensor drift accumulates over months, calibration bias shifts set-points, electromagnetic interference injects random noise, and control-system delays distort time stamps. The combined effect is a systematic distribution shift: statistical properties such as mean, variance, and cross-correlation of simulator signals differ from those of real-plant signals, as shown in Fig. 1 [1]. Models that learned fine-grained decision boundaries in the simulator domain therefore encounter unfamiliar patterns in real plants, leading to reduced diagnostic accuracy in the transient [1].

To solve the discrepancies between simulator data and real-plant data, we propose an abnormal event diagnosis framework that converts each plant variable into fuzzy membership functions capturing long-term trends—decrease, stay equal, or increase—through a fuzzy-based feature extraction method (FFEM) [2]. In addition, the membership functions for

key variables are optimized via gradient descent to maximize inter-class separation, and the resulting optimized membership functions are fed into a neural classifier, enabling the extracted features to reproduce real-plant behavior with much higher fidelity. Supplying these optimized fuzzy features to a simple one-dimensional convolutional neural network (CNN) greatly improves robustness: accuracy stays above 95 percent even when synthetic plant data emulates harsh plant conditions, whereas a conventional CNN model without FFEM degrades sharply. The remainder of this paper details the data preparation pipeline, the FFEM design, the membership-function optimization algorithm, and the diagnosis network architecture.

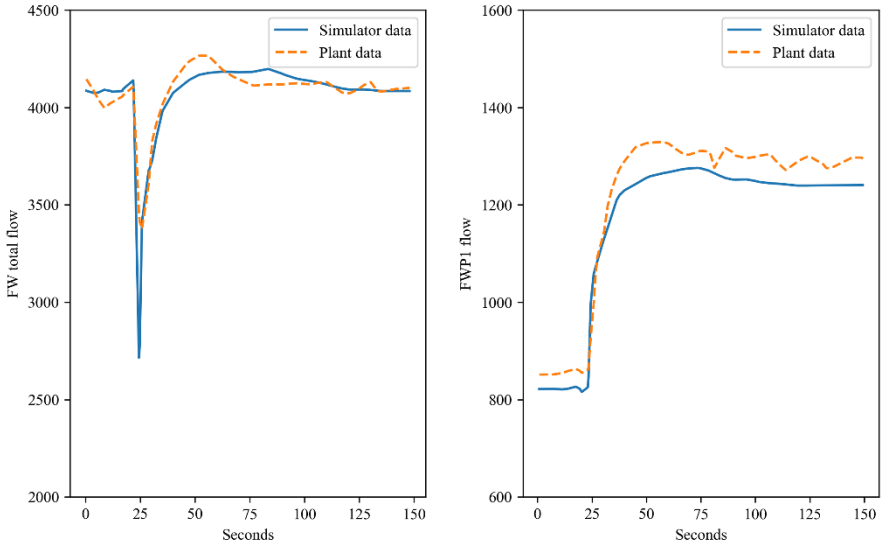

FIGURE 1. Data discrepancies between simulator and plant data for feedwater total flow (left) and feedwater pump 1 flow (right).

II. METHOD

I.A. Fuzzy-based Feature Extraction Method

Fuzzy logic was proposed to describe ambiguous or uncertain situations that ordinary binary logic cannot handle. Instead of assigning a crisp "true" or "false" value, fuzzy logic expresses how strongly a numerical input belongs to intuitive linguistic concepts such as low, normal, or high. This graded approach helps machines interpret real-world sensor signals that include noise and drift [3]. Our abnormal event diagnosis framework applies fuzzy logic at the feature level and a neural network at the decision level. Every process variable is first converted to a long-term trend value that compares the current reading with two earlier points. The trend enters a set of membership functions that assign fuzzy grades for decrease, stay equal, and increase, as shown as Fig. 2. The resulting fuzzification represents plant behavior in a form that is less sensitive to short-term fluctuations than raw data. A simple one-dimensional convolutional classifier then maps the fuzzy features to an event label.

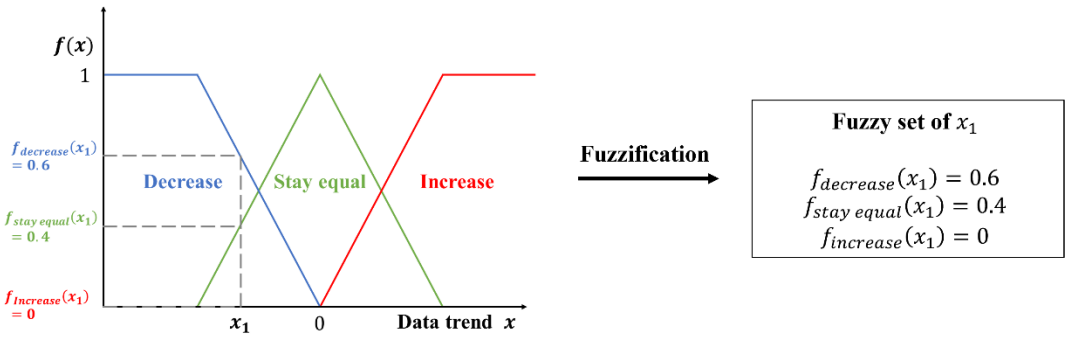

FIGURE 2. Fuzzification process of a data trend.

Fig 3. Overall architecture that connects a conventional fuzzy-inference system (top) with the proposed abnormal event diagnosis framework (bottom). In the classical scheme, crisp sensor measurements are first fuzzified, evaluated against rules stored in the knowledge base by the inference engine, and finally defuzzified into crisp control actions. The lower panel shows how the same three-step logic is embedded in our pipeline: simulator variables pass through the optimized FFEM to create fuzzy inputs; a neural-network classifier learns an abnormal event diagnosis model during the training phase (black arrows); and, during deployment (orange arrows), real-plant measurements flow through the optimized FFEM and the trained model to support operator judgment.

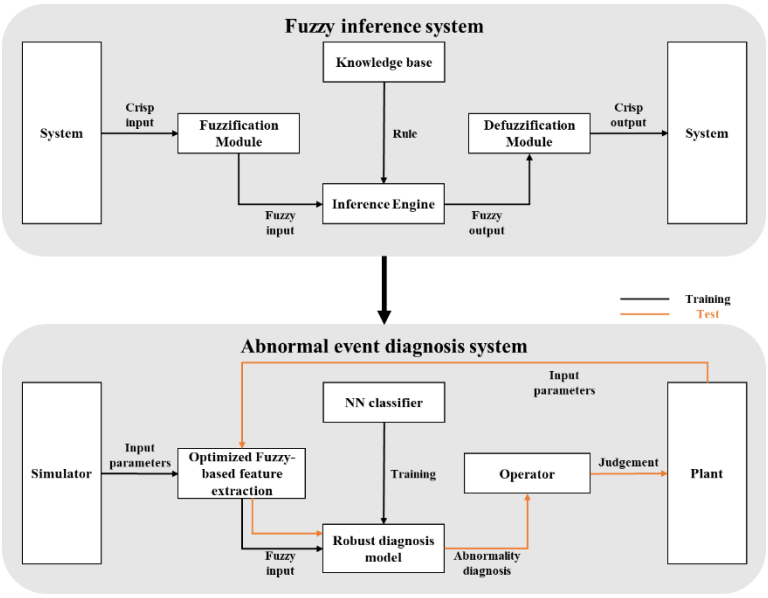

FIGURE 3. Schematic frameworks of a fuzzy inference system and the abnormal event diagnosis system

Fig. 4 illustrates the two-step Fuzzy-based Feature Extraction Method (FFEM) described. For each selected time-series variable $x(t)$, the long-term trend is computed. The three black traces show typical sensor histories; the red markers denote the start and end points used to evaluate Δx. A positive Δx (red arrow) indicates a sustained increase, a negative value (blue arrow) indicates a sustained decrease, and values near zero (green arrow) correspond to a steady condition.

$$\Delta x = x(t) - x(t - 120s) \tag{1}$$

First, the long-term trend Δx is obtained from the time series by Eq. (1). The normalized trend is then evaluated by seven triangular membership functions, μ_1 through μ_7, displayed in the center of Fig. 4 and labeled “high decrease,” “intermediate decrease,” “low decrease,” “stay equal,” “low increase,” “intermediate increase,” and “high increase.” Each function returns a grade between 0 and 1, and the seven grades collectively form the fuzzy-value vector defined in Eq. (2),

$$f(\Delta x) = [\mu_1(\Delta x), \mu_2(\Delta x), \dots, \mu_7(\Delta x)] \tag{1}$$

The right-hand bar charts in Figure 4 visualize this fuzzy set: for a moderate decrease (green path), the “low decrease” and “intermediate decrease” grades dominate; for a pronounced drop (blue path), only “high decrease” is active; and for a sharp rise (red path), “intermediate increase” dominates with a smaller contribution from “high increase.”

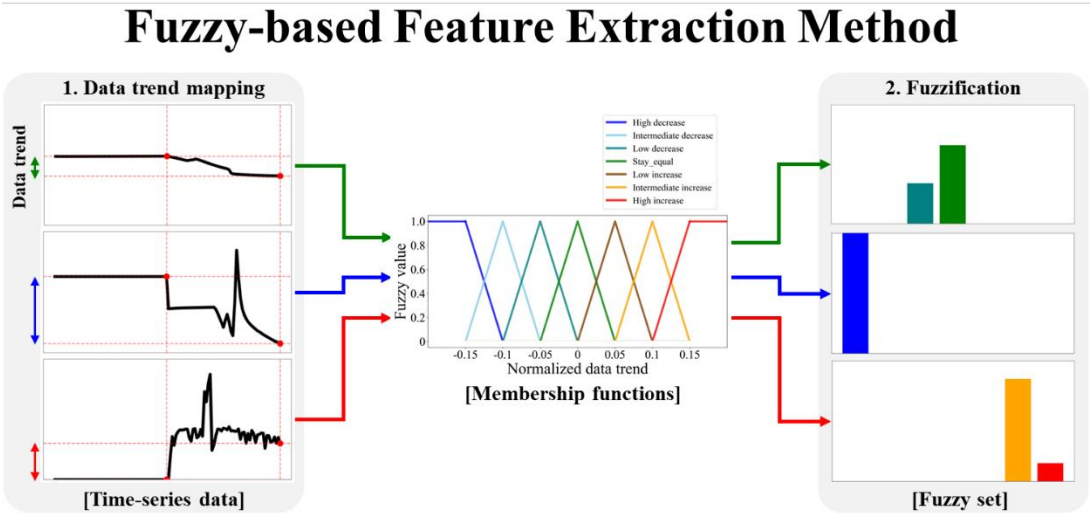

FIGURE 4. Fuzzy-based feature extraction method (FFEM)

I.B. Optimized Fuzzy-based Feature Extraction Method

Before launching the gradient-descent procedure, we compute gain-based feature-importance scores for the entire set of process variables using light gradient boosting machine (LGBM). The scores are sorted in descending order, and we keep only those variables whose cumulative importance exceeds 95 percent of the total. Membership functions associated with this 95 percent subset are updated by gradient descent, while the remaining variables retain their default membership functions and are excluded from tuning. This filter ensures that optimization targets the most diagnostically relevant variables without being distracted by low-information channels.

To sharpen the discriminative power of the seven membership functions $\mu_1, \ldots, \mu_7$, we adjust their break-point parameters θ by gradient descent. The update is driven by a inter-class separation loss that enlarges the distance between every in-class sample and every out-of-class sample in fuzzy space. where C is the number of classes, D_c and $D_{\bar{c}}$ denote the index sets of samples with label c and "not c", and n_c and $n_{\bar{c}}$ are their sizes. The loss is negative because we maximize inter-class separation; minimizing $\mathcal{L}_{separ}$ therefore pushes the squared distance term upward. In practice we implement Eq. (5).

$$\mathcal{L}_{separ}(\theta) = -\sum_{c=0}^{C-1} \frac{1}{n_c n_{\bar{c}}} \sum_{k \in D_c} \sum_{l \in D_{\bar{c}}} \left| \left| f_\theta(x_k) - f_\theta(x_l) \right| \right|_2^2 \tag{5}$$

III. EXPERIMENTAL SETTINGS

The complete workflow for data generation, feature selection, fuzzy feature extraction, and model evaluation is shown in Fig. 5. A simulator is used as the common data source, but the datasets for the training environment (left, green) and the test environment (right, blue) are generated independently. For training, baseline runs are collected, passed through feature selection, the Optimized Fuzzy-based Feature Extraction Method (FFEM), and a CNN classifier that is trained on the resulting fuzzy features. For testing, the simulator is re-run under diversified operating conditions and sensor-noise injection to create synthetic plant data. The same feature-selection rules and the optimized FFEM are applied, and the pretrained CNN classifier is copied into the test pipeline to produce abnormal-event diagnoses. Dashed arrows highlight the noise-injection step (upper right) and the internal operation of FFEM (lower right).

We created the entire data set with a 1 400 MWe two-loop Barakah pressurized-water-reactor simulator. One "normal" condition and 52 distinct abnormal events were simulated. Each record spans 240 s; the abnormal event is injected exactly at $t = 120\,s$. The raw log contains about 14,000 variables. We trained an LGBM model on the changeable variable set and ranked the gain-based feature-importance scores. Only the 785 variables whose importance is positive were retained. Among those 785 variables, we applied membership-function optimization only to the 99 variables whose cumulative importance accounted for 95 percent of the total. The remaining variables retained the default membership functions shown in Fig. 4.

Normalization relies on physical units: Boolean or categorical variables are left unchanged; level signals expressed in percent are divided by 120 % of the design span; all other variables are divided by 120 % of their maximum observed value. This unit-aware scaling keeps numeric inputs in a consistent range without distorting engineering meaning.

We adopted a simple one-dimensional CNN consisting of a single Conv1D layer (128 filters, kernel size = 3) followed by ReLU activation, max-pooling, 20 % dropout, flattening, and a soft-max output layer. The model is optimized with Adam (learning rate = 0.001); training uses a batch size of 64 and early stopping with a patience of 30 epochs. The same architecture is applied to both the baseline FFEM and the optimized FFEM so that performance improvements can be attributed solely to membership-function optimization.

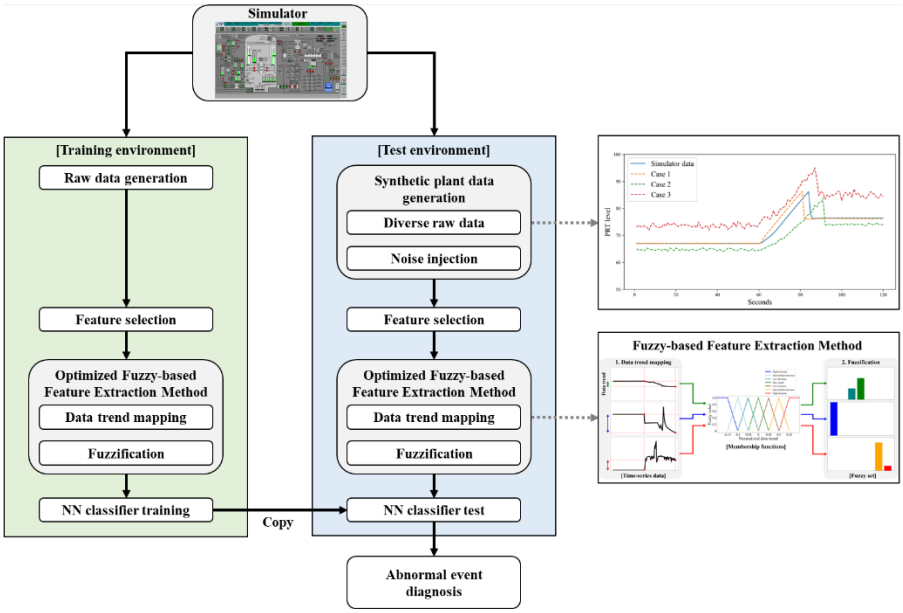

FIGURE 5. Abnormal event diagnosis training and test process.

IV. RESULTS

Table 1 compares the diagnostic accuracy of the baseline model ("Not optimized") and the proposed model with optimized FFEM under four test conditions. When no synthetic noise is added ("None"), the accuracy increases from 97.0 % to 97.9 %, which is a modest yet measurable improvement. Under progressively harsher noise (Case 1 to Case 3), the optimized model consistently outperforms the baseline by 1.0 to 1.4 percentage points and never drops below 95 %. Averaged over the four test sets, membership-function optimization delivers a mean improvement of 1.2 percent point.

These findings follow the trend reported by Cho et al. [2]. In their study, removing the FFEM stage caused a clear accuracy collapse whenever sensor noise was present, whereas including fuzzy-trend features kept accuracy in the mid-90 % range. Our results show the same pattern: the optimized FFEM preserves high accuracy under all three noise cases, confirming that (i) fuzzy features shield the classifier from distribution shift and (ii) further tuning of membership functions adds an extra margin of robustness.

Fig. 6 shows the seven optimized membership functions for pressurizer pressure control system variable. After gradient descent, the triangles are evenly spaced and symmetric, fully covering the observed trend range while maximizing separation between adjacent grades. This reshaping explains the systematic accuracy gains observed in Table 1.

TABLE I. Abnormal event diagnosis results.

		Diagnostic accuracy (%)	
		Not optimized model	Optimized model
Test dataset	None	97	97.9
	Case 1	96.4	97.4
	Case 2	95.9	97
	Case 3	94.5	95.9

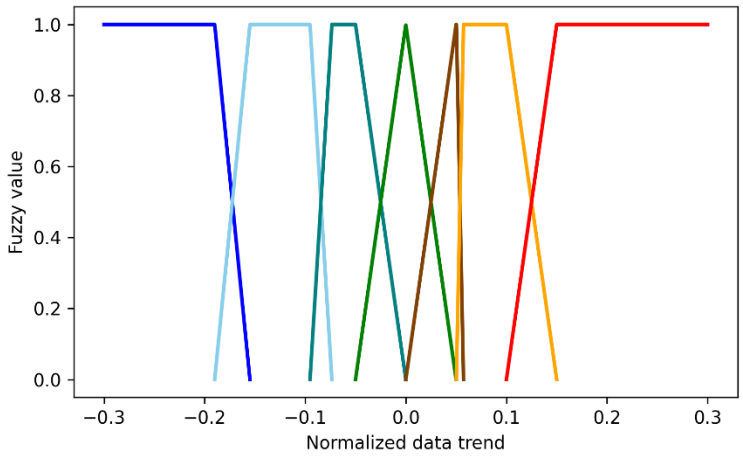

FIGURE 6. Optimized membership function of pressurizer pressure control system.

V. CONCLUSIONS

This work proposed an abnormal event diagnosis framework that combines (i) LightGBM-based feature selection, (ii) the Fuzzy-based Feature Extraction Method (FFEM), and (iii) gradient-descent optimization of membership functions. Only variables whose cumulative importance exceeds 95 % are tuned, focusing computational effort on diagnostically relevant channels. Experiments with a Barakah 1 400 MWe two-loop PWR simulator demonstrate that the optimized FFEM raises average accuracy by 1.2 percent points and maintains over 95 % accuracy even under severe synthetic noise. These outcomes confirm that optimizing membership functions to maximize inter-class separation is an effective strategy for bridging the simulator-to-plant distribution discrepancies.

Future research will (a) validate the method against actual plant variables, (b) extend the optimizer to Gaussian membership shapes, and (c) integrate uncertainty quantification to provide confidence levels alongside diagnostic decisions.

ACKNOWLEDGMENTS

This work was supported by Korea Institute of Energy Technology Evaluation and Planning(KETEP) grant funded by the Korea government(MOTIE)(RS-2024-00403194, Next-Generation Nuclear Technology Creation IP-R&D Talent (Human Resources) Development Project)

This work was supported by the National Research Foundation of Korea(NRF) grant funded by the Korea government(MSIT) (No. RS-2022-00144042)

REFERENCES

[1] J. H. Shin, J. M. Kim, and S. J. Lee, "Abnormal state diagnosis model tolerant to noise in plant data," *Nuclear Engineering and Technology,* vol. 53, no. 4, pp. 1181-1188, 2021.

[2] S. G. Cho, J. H. Shin, and S. J. Lee, "Robust diagnosis of abnormal events using fuzzy-based feature extraction in nuclear power plants," *Progress in Nuclear Energy,* vol. 185, p. 105765, 2025.
[3] N. Sabri, S. Aljunid, M. Salim, R. Badlishah, R. Kamaruddin, and M. Malek, "Fuzzy inference system: Short review and design," *Int. Rev. Autom. Control,* vol. 6, no. 4, pp. 441-449, 2013.

ASRAM2025
www.asram2025.org
Asian Symposium on Risk Assessment and Management 2025
Pattaya, Thailand, 27 – 29 August 2025

Operator-Centric Visualization of Explainable Diagnosis for Abnormal Situations Using Multilevel Flow Modeling

Ji Hyeon Shin[1,*], Seo Ryong Koo[1], Seung Jun Lee[2]

[1] *Korea Atomic Energy Research Institute, 111, Daedeok-daero 989 beon-gil, Yuseong-gu, Daejeon, Republic of Korea*
[2] *Ulsan National Institute of Science and Technology, 50, UNIST-gil, Ulsan 44919, Republic of Korea*
[*] *jhshin0127@kaeri.re.kr*

ABSTRACT

In nuclear power plants, the rapid and accurate diagnosis of abnormal states is crucial to ensure safe operations and mitigate the risk of accidents. This study introduces an operator-centered approach for explainable diagnostics that emphasizes human understandability, making complex information accessible to operators when it matters most. By utilizing Multilevel Flow Modeling (MFM), this method significantly enhances the interpretability of diagnostic results, enabling operators to grasp underlying system behaviors and causal relationships during abnormal states. By integrating explainable artificial intelligence (XAI) techniques with MFM, this approach provides visual, intuitive explanations that bridge the gap between advanced AI outputs and operator decision-making needs. Through this, operators are better equipped to understand diagnostic insights, fostering a sense of trust and confidence in the model's conclusions, even in challenging situations.
The proposed approach was tested using simulation data from various abnormal scenarios in nuclear power plants, validating model performance with a primary focus on usability and operator comprehension. This operator-centric design is expected to lead to improved clarity in understanding diagnostic results, which in turn should increase operator confidence when responding to critical situations. By prioritizing human-centered explainable AI applications, this work seeks to support safer, more effective nuclear plant operations. Ultimately, it aims to create diagnostic systems that operators can rely on fully during high-stakes decision-making, thus promoting more resilient plant management in the face of potential risks.

Keywords: Nuclear power plant, Abnormal state diagnosis, Explainable artificial intelligence, Multilevel flow modeling, Visualization

I. INTRODUCTION

In nuclear power plants (NPPs), abnormal conditions occurring in individual components can influence surrounding monitoring parameters such as flow rate, temperature, and pressure. Operators play an important role in diagnosing such situations as specific abnormal events based on alarms and symptoms triggered by changes in these parameters. To support operators in this diagnostic task, various classification models based on artificial neural networks (ANNs) have been developed. These models also perform diagnoses by learning the patterns of parameter changes associated with abnormal events in the input data. However, due to the inherent black-box nature of neural networks, it is difficult to understand how these models make their decisions. For operators to trust and effectively utilize the model outputs, it is required that the diagnostic results be clearly explained in terms of which parameter changes, which symptoms, led to a specific diagnosis.

ANNs can address part of their black-box problem by using appropriate explanation methods, enabling them to provide users with explanations for their outputs. However, the explanations generated by advanced artificial intelligence (AI) models do not necessarily align with the reasoning processes traditionally used by human operators. This mismatch can lead to a gap in understanding, thereby limiting the practical usability of such models in operational contexts. Accordingly, an effective approach is needed to enhance operator understandability. To address this challenge, the present study aims to explain neural network–based abnormal state diagnosis models using explainable AI (XAI) techniques and to present the resulting explanations in a manner that is meaningful to human operators. Specifically, the study compares and analyzes explanations for an abnormal event: (1) explanations derived from the diagnostic model via XAI, (2) symptom-based explanations traditionally used by operators, and (3) causal explanations based on system structure and physical flow using Multilevel Flow Modeling (MFM). Through this comparison, we identify parameters that are commonly emphasized across the different

explanations as well as those that are not, gaining insight into which aspects are most understandable from the operator's perspective. Based on this comparison, we propose strategies for bridging the gap between AI-generated diagnostic reasoning and operator understandability. To clarify the objective of this study, we pose the research question and insight that how operators can make use of the explanations provided by XAI techniques. Ultimately, this research aims to support the development of diagnostic systems that operators can trust and use effectively, even under abnormal conditions in NPPs.

II. EXPLAINABLE DIAGNOSIS MODEL FOR ABNORMAL EVENT

In this study, we purpose to identify the symptoms associated with specific abnormal events by leveraging both XAI techniques and MFM. The contributed symptoms corresponding to the abnormal events diagnosed by the neural network model can be analyzed using appropriate XAI methods. Meanwhile, MFM allows for the understanding of physically connected flow resulting from abnormalities in specific components or functions. The following sections describe these two methodologies as applied in this study.

II.A. Explainable Artificial Intelligence

XAI refers to techniques that provide human-understandable explanations for the decisions made by AI models. In other words, XAI helps users understand why a model produced a certain output and which input features contributed most significantly to that result. By providing this interpretability, XAI enhances users' ability to understand and trust the model's decisions, which is particularly important in safety-prioritized domains such as NPP operation. Among them, post-hoc explanation methods are commonly used to explain the outputs of already-trained models when given specific input data. These methods aim to explain model behavior without altering the internal structure of the model. Among the various post-hoc approaches, the XAI technique introduced below has been employed in previous studies to explain the outputs of neural network-based diagnostic models in the context of NPP condition monitoring.

II.A.1. Deep Explainer SHAP

Shapley Additive exPlanations (SHAP) is a method that explains model predictions by decomposing them into the contributions of individual features [1]. A Shapley value, originally derived from cooperative game theory, represents the average marginal contribution of a feature across all possible combinations of features, offering a fair way to quantify each feature's importance in a prediction. Among its variants, Deep Explainer SHAP is specifically designed for application to neural networks. It approximates Shapley values by leveraging the structural characteristics of deep learning models. Specifically, it extends the principles of the Deep Learning Important FeaTures (DeepLIFT) algorithm, calculating feature contributions through activation differences between input data and a baseline across the model's layers [2]. This integration allows it to produce explanations more efficiently than sampling-based SHAP methods.

II.B. Multilevel Flow Modeling

Multilevel Flow Modeling (MFM) is a framework utilized to represent the structure and behavior of complex industrial systems—such as NPPs—by capturing their functional objectives, means-end relationships, and causal dependencies within mass flow systems and energy flow systems [3, 4]. It facilitates qualitative assessment of system performance by reflecting the underlying physical flow mechanisms. In this study, the modeling and analysis of MFM were conducted using MFMSuite, a software platform originally developed by the Technical University of Denmark, in conjunction with a graphical editor provided by IFE Harden.

III. CASE STUDY

III.A. Experimental Setup

This study provides diagnostic information that is understandable and trustworthy to human operators by integrating the previously introduced methods. The experimental procedure consists of the following sequential steps, through which the analysis and discussion are conducted based on the resulting observations:

(1) The abnormal event diagnosis model training and application to a scenario for case study: A neural network-based classification model is trained to diagnose various abnormal conditions in NPPs. The trained model is then applied to case scenarios to generate diagnostic outputs.

(2) Application of the XAI method to the model's diagnostic results: To enhance interpretability, the XAI technique are applied to the output of the trained model. This step aims to identify which input features most significantly influenced the diagnosis of the case abnormal scenario.
(3) Comparison with actual alarms and symptoms: The diagnostic outcomes and their explanations are compared against actual alarm signals and symptoms from the scenario, enabling assessment of how well the AI model's reasoning aligns with human-understandable indicators.
(4) Analysis of MFM-based consequent trees for the diagnosed event: For the event diagnosed by the model, MFM is used to generate and examine the corresponding consequent tree, which captures the causal propagation of functional disruptions throughout the system.
(5) Visualization of diagnostic explanations: The results of the XAI analysis are visualized with highlighting the key system by considering physical flow in step (4) [5].

III.A.1. Abnormal Event Diagnosis Model

In this case study, the diagnosis model was trained using abnormal scenario data obtained from the 3KEYMASTER NPP simulator [6, 7]. The model was trained on 23,375 data to classify 15 kinds of abnormal events. The Deep Explainer SHAP technique is model-agnostic and can be applied regardless of the model structure. Therefore, the choice of model does not affect the applicability of this explanation method. The simple convolutional neural network (CNN) was adopted in this study. The structure of the abnormal event diagnosis model used in this case study is as follows.

TABLE I. The Abnormal Event Diagnosis Model Structure

Layer name	Layer type	Output shape
Conv1d	Conv1D	(None, 391, 16)
Conv1d_1	Conv1D	(None, 391, 32)
Max_pooling1d	MaxPooling1D	(None, 195, 32)
Conv1d_2	Conv1D	(None, 195, 64)
Max_pooling1d_1	MaxPooling1D	(None, 97, 64)
Flatten	Flatten	(None, 6208)
Dense	Dense	(None, 16)
activation	Activation	(None, 16)

III.A.2. Multilevel Flow Modeling for Abnormal Events

In this case study, we aim to understand the physical flow associated with each abnormal event by analyzing the corresponding consequent trees. To facilitate this, an MFM representation was developed based on the system structure of the 3KEYMASTER NPP simulator and 15 abnormal events that were used to training data for the diagnostic model. As summarized in the table below, the constructed MFM includes a total of six systems, comprising three mass flow systems and three energy flow systems.

TABLE II. Systems and Functions including in the MFM Model

Type	System	Included components about each function
Mass flow system	Reactor coolant system and chemical volume control system	Cold-leg, reactor pressure vessel, hot-leg, reactor heat remover, pressurizer, pressurizer relief tank, steam generator U-tube, letdown heat exchanger, letdown demineralizer, volume control tank, charging pump, regenerator, reactor coolant pump
	Steam generator and secondary system	Steam generator, main steam system, turbine bypass valve, condensate storage tank, turbine, condenser, condensate pump, low-pressure feedwater heater, main feedwater pump, high-pressure feedwater heater, moisture separator reheater, steam generator blowdown
	Containment spray system	Refueling water storage tank, containment pump, containment spray
Energy flow system	Reactor coolant system heat remover	Fuel, reactor pressure vessel, pressurizer, pressurizer relief tank, steam generator U-tube, steam generator, main steam system, turbine, turbine bypass valve, condenser, circulating water system

	Primary component cooling system	Reactor heat removal, letdown heat exchanger, component cooling water system, essential service water system
	Electrical system	Turbine, main generator protection, switchyard, high-voltage 13.8kV, 1E medium voltage 4.16kV, diesel generators control, medium voltage 4.16kV

III.B. Case Study with Pressurizer Spray Valve Positioner Failure

In Section III.A, we compare the explanations derived from the CNN model by Deep Explainer SHAP and the MFM-based model in the context of abnormal event occurrences. We then discuss whether the explanations generated by the neural network are comprehensible to plant operators. The consistency between the AI-derived interpretation and the physically grounded reasoning provided by the MFM model is examined. Based on this comparison, we identify which information should be conveyed to operators and which can be excluded, and propose a visualization method to effectively present the finalized diagnostic information.

III.B.1. Explanation Results

In this case study, the abnormal scenario for case study is a Pressurizer Spray Valve Position Failure. This event was selected as the case study because, although the event itself is relatively simple, it affects several key parameters such as pressurizer pressure and water level. These changes can propagate to other components, making it useful for analyzing system-wide behavior. While not one of frequent failures, it is representative of control component malfunctions that can lead to cascading effects. When this event occurs, the primary symptom is a noticeable decrease in pressurizer pressure. In addition, secondary symptoms such as the temperature of the pressurizer spray line and the operation of the pressurizer heaters are also affected. Based on these peripheral symptoms and corresponding alarms, plant operators are expected to identify the abnormal condition and follow appropriate tasks as prescribed in the operating procedure. The table below presents the explanation results from the abnormal event diagnosis model trained in this study by Deep Explainer SHAP, illustrating how the model recognizes and explains the pressurizer spray valve failure scenario.

TABLE III. The Explanation Result of Deep Explainer SHAP

Monitoring parameter	Location	Description	Feature importance
hmi_RCSLT459A_VALUE	Pressurizer	Pressurizer level	1
hmi_RCSLT459_VALUE	Pressurizer	Pressurizer level	0.7738
hmi_RCSTT463A_VALUE	Cold-leg	RCL-2B delta temperature	0.5072
hmi_NBXIT6_VALUE	Medium voltage 4.16kV	LC feeder breaker NBX209 current	0.4248
movBBHV8000B.avpVlvPos	Reactor coolant system	HV8000B valve position	0.3779
movBBHV8000A.avpVlvPos	Reactor coolant system	HV8000A valve position	0.3614
vmodEGTV0030.avpVpos	Component cooling water system	TV30 valve position	0.3536
hmi_NBXWT15_VALUE	Medium voltage 4.16kV	Engineered safety features transformer XNB02 power	0.3431
hmi_CVCTT130A_VALUE	Letdown heat exchanger	Letdown heat exchanger outlet temperature	0.3362
hmi_RCSLT502_VALUE	Steam generator	Steam generator 2 wide-range level	0.3354

The model diagnosed the event as a Pressurizer Spray Valve Position Failure with a high predicted value, and the Deep Explainer SHAP analysis identified pressurizer level as the most important parameter in the diagnosis. In addition, the model also utilized other key parameters such as the opening of surrounding valves near the pressurizer spray valve and the cold-leg temperature, indicating that it considered a range of contributed parameters in reaching its conclusion. It is worth noting that the NPP simulator used in this study is designed to simulate a generic pressurized water reactor, and thus may not fully capture the precise symptom progression observed in an actual plant. Nevertheless, the results reveal that the model relies on a set of parameters that differ from those typically used by human operators, highlighting a potential gap in understandability and trust.

We analyze the possible end consequence from the constructed MFM model's consequence tree that most closely aligns with the feature importance identified by the abnormal event diagnosis model. Figure 1 below illustrates the branch of this

possible end consequence, which includes the pressurizer, reactor coolant system, and charging system. While the MFM consequence tree does not capture all potential symptoms resulting from the pressurizer spray valve malfunction, it effectively represents the surrounding flow relationships involving the pressurizer. In this way, the MFM model conveys a flow-based understanding that aligns with the operator's understandable model and supports human-centered interpretability.

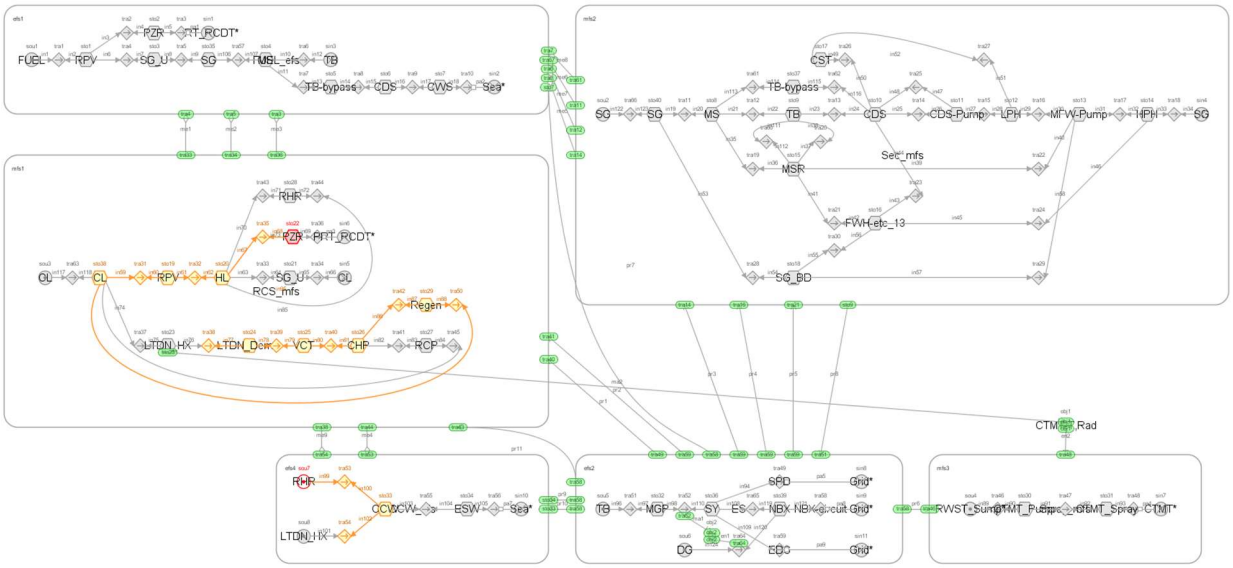

FIGURE 1. The Consequence Tree Result of the MFM Model

III.B.2. Explanation Visualization

In this study, only the explanation results from the Deep Explainer SHAP results that correspond to operator-understandable flow paths are visualized. Specifically, parameters that are not represented in the MFM model or do not align with the most relevant consequence tree branch were excluded from the visualization. The resulting explanation visualization, shown below, highlights components such as the pressurizer, reactor coolant system, and chemical and volume control system, while excluding parameter such as the LC feed breaker current, which are less relevant from a flow-based understandability perspective.

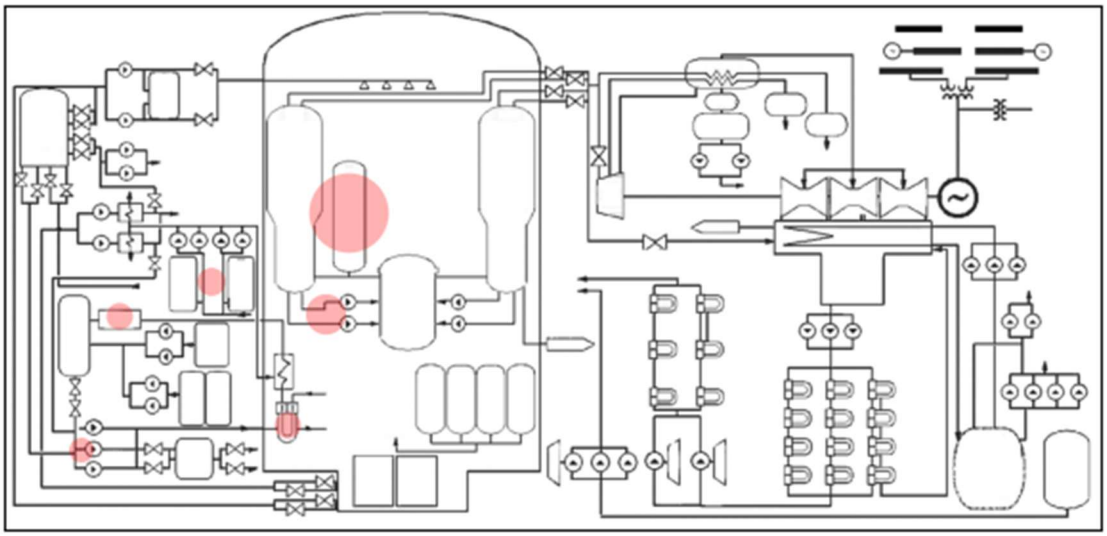

FIGURE 2. Explanation Visualization with Selected Information

IV. CONCLUSIONS

AI models have been recently researched to support operator tasks in NPP main control rooms. However, to ensure operator acceptance of AI-based diagnostic information, it is need to provide not only the results but also the reasoning in a form that is understandable to human operators. XAI techniques offer a way to explain model outputs by identifying key input features that influence the model's predictions. In the context of abnormal event diagnosis, several previous studies have sought to apply XAI to provide explainability alongside neural network-based decisions. Nevertheless, the parameters identified by XAI as contributing to a diagnosis may not always align with operators' understanding. Presenting such mismatched information can lead to confusion rather than clarity. To address this problem, this study examined the diagnostic reasoning of an CNN model through the perspective of operator understanding. Using Deep Explainer SHAP, we explained the model's decisions and analyzed the understandability of the resulting feature importance from an operator's perspective. Additionally, we applied MFM to derive the consequence branch for a specific abnormal event scenario, allowing us to cross-check the relevance of Deep Explainer SHAP-identified parameters with physical flow-based reasoning. By filtering out provided information that did not conform to operator-acceptable flow logic, we visualized a refined set of diagnostic information that better aligns with human understandability. This study contributes to propose the human-centered XAI by demonstrating how XAI-based explanations can be adapted to the operator understanding in the context of abnormal event diagnosis. While this study qualitatively explores explanation understandability, no user study has yet been conducted to quantitatively assess improvements in operator understanding and trust. Therefore, future work will involve user-centered experiments to assess how the proposed visualization method influences understandability, trust, and usability in practice. Furthermore, it is necessary to test various abnormal event cases, not just a single one, to examine the potential for generalization.

ACKNOWLEDGMENTS

This research was supported by the National Research Council of Science & Technology(NST) grant by the Korea government (MSIT) (No. GTL24031-000).

REFERENCES

[1] Lundberg, Scott M., and Su-In Lee. "A unified approach to interpreting model predictions." Advances in neural information processing systems 30 (2017).
[2] Shrikumar, Avanti, Peyton Greenside, and Anshul Kundaje. "Learning important features through propagating activation differences." In International conference on machine learning, (2017): 3145-3153. PMlR.
[3] Lind, Morten. "An introduction to multilevel flow modeling." Nuclear safety and simulation 2, no. 1 (2011): 22-32.
[4] Kang, Jung Sung, and Seung Jun Lee. "Concept of an intelligent operator support system for initial emergency responses in nuclear power plants." Nuclear Engineering and Technology 54, no. 7 (2022): 2453-2466.
[5] Shin, Ji Hyeon, Jung Sung Kang, Jae Min Kim, and Seung Jun Lee. "Concept of understandable diagnostic cause visualization with explainable AI and multilevel flow modeling." Nuclear Engineering and Technology 57, no. 8 (2025): 103589.
[6] F. Western Service Corporation, MD, USA, 3KEYMASTER Simulator (2013)
[7] Lee, Gyumin, Seung Jun Lee, and Changyong Lee. "A convolutional neural network model for abnormality diagnosis in a nuclear power plant." Applied Soft Computing 99 (2021): 106874.

ASRAM2025
www.asram2025.org
Asian Symposium on Risk Assessment and Management 2025
Pattaya, Thailand, 27 – 29 August 2025

STANDARD OPERATING PROCEDURE FOR DEVELOPMENT OF ADAPTIVE RESILIENCE CURVE TO ASSESS RESILIENCE OF CLEAN ENERGY SYSTEMS

Pidpong Janta[1], Kampanart Silva[2], Takashi Takata[2], Takafumi Narukawa[2], Nuwong Chollacoop[1]

[1] National Energy Technology Center (ENTEC), National Science and Technology Development Agency (NSTDA) 111 Thailand Science Park, Phaholyothin Road, Khlong Nueng, Khlong Luang, Pathum Thani, 12120, Thailand, pidpong.jan@entec.or.th, kampanart.sil@entec.or.th, nuwong.cho@entec.or.th
[2] Department of Nuclear Engineering and Management, School of Engineering, the University of Tokyo, 7-3-1 Hongo, Bunkyo-ku, Tokyo 113-8656 Japan, takata_t@n.t.u-tokyo.ac.jp, narukawa@n.t.u-tokyo.ac.jp

ABSTRACT

Quantification of resilience is crucial for monitoring evaluating performance of energy systems. Several past studies attempted to quantify adaptability and resilience while findings do not yet lead to mathematical quantification and practical application. Our previous study conceptualized adaptive resilience curve for this purpose, though its applicability has not been demonstrated. Therefore, this study aims to review adaptive resilience curve proposed in the previous study to extract key elements which used to build the adaptive resilience curve, and to develop a standard operating procedure based on the key elements. Since the curve adopted adaptive attributes from three concepts, including global catastrophic risk, beyond design basis accident, and foresight, the standard operating procedure consists of step-by-step instructions corresponding to each concept. The procedures for global catastrophic risk emphasized identifying a target disruptive event based on historical record and determining figures-of-merit to cover variety of transition functions. The procedures for beyond design basis accident involved determining actions to address the disruptive event by mitigating the disruption or quicken the recovery, and comparing the function with and without the actions to understand their effectiveness. The procedures for foresight aimed at investigating possible scenarios for function variations. The developed standing operating procedure resulted in four line graphs to visualize transitions of functions throughout a period of time. This study shows that the standard operating procedure can guide practitioners to construct case-specific adaptive resilience curves based on the local context of systems. The adaptive resilience curve offers a clear picture of how a disruptive event affects the operation of clean energy systems and how a measure alleviates the impacts of system disruption.

Keywords: Adaptability, Standard operating procedure, Global catastrophic risk, Beyond basis design, Foresight

I. INTRODUCTION

Climate adaptation has grown rapidly in response to climate change impact. Globally, progress in the pursuit of climate adaptation draws attention among high-risk countries in which it is believed to enhance adaptive capacity, strengthen resilience, and reduce vulnerability [1]. Quantification of adaptability and resilience becomes crucial for monitoring and evaluating the performance of energy systems. Several past studies attempted to address the question yet found to rely on investigating a set of characteristics needed for resilience [2], measuring delivery function for transition [3], exploring adaptation options [4], and engaging decision making to provide climate change responses [5]. In order to quantify adaptability and resilience in energy systems, there is a need for methodological frameworks to measure time dependent characteristics of events and capture changes which occurred after the events and actions applied to address the impact. The previous study [6] proposed a concept on adaptive resilience curve which was theoretically conceptualized to quantify adaptability of systems. The adaptive resilience curve is an event-based and time dependent metric for resilience. The adaptive resilience curve attempted to capture adaptability in which it was constructed of a delivery function for transitions in resilience proposed by Henry and Ramirez-Marquez [3] and introduced contributions of global catastrophic risk, beyond design basis accident, and foresight in order to capture the adaptability. Originally, the delivery function for transitions in resilience quantifies resilience of systems in a time dependent metric. By integrating the contributions, the adaptive resilience curve quantifies adaptability of systems in an event-based basis. Yet, the concept of adaptive resilience curve was developed and proposed, applicability of the adaptive resilience curve was not demonstrated.

To demonstrate the applicability of adaptive resilience curve with a system, there is a need for a procedure organized to maintain consistency, efficiency, and quality across the practice. A standard operating procedure, referred to as a set of step-by-step instructions organized to guide practitioners carrying out complex routine tasks [7], can be utilized to assist in conducting the adaptive resilience curve. According to the previous study, the adaptive resilience curve is not only difficult to conceptualize but also difficult to conduct in rigorous and mathematical manners. Since the adaptive resilience curve has a delivery function for transitions in resilience as its foundational principle and is integrated with global catastrophic risk, beyond design basis accident, and foresight, the standard operating procedure should be developed to guide practitioners throughout each key elements of the theories. The adaptive resilience curve should be reviewed to extract the key elements in order to systematically design the standard operating procedure. Thus, the objective of study is to review adaptive resilience curve proposed in the previous study to extract key elements which used to build the adaptive resilience curve, and to develop a standard operating procedure based on the key elements.

II. METHODOLOGY

This study employs a methodology to review adaptive resilience curve proposed in the previous study [6] to extract key elements which are used to build the adaptive resilience curve, and to develop a standard operating procedure based on the key elements.

In order to review the adaptive resilience curve to extract key elements, a fundamental idea of conceptualizing the adaptive resilience curve needs to be investigated. The fundamental idea of adaptive resilience curve consists of contributions of global catastrophic risk, beyond design basis accident, and foresight. Mentioned in scholarly works [8], information extracted from the contributions can be utilized to structure the standard operating procedure. The scopes of the contributions are included: contribution of global catastrophic risk involves identifying target disruptive events and determining proper figures-of-merit to exhibit the disruptive events based on historical record. Contribution of beyond design basis accident involves determining actions (measure) to address the target disruptive events and comparing function with and without the actions. Contribution of foresight involves investigating possible scenarios for function variations.

In order to develop the standard operating procedure for conducting the adaptive resilience curve, it is important to provide a set of written instructions that outline steps for performing tasks to produce the contributions. Each contribution has its own set of instructions to ensure consistency.

III. RESULT

This section presents results from review of adaptive resilience curve and its key elements, and standard operating procedure for conducting adaptive resilience curve. The review of adaptive resilience introduced contributions of global catastrophic risk, beyond design basis accident, and foresight, respectively to extract key elements. The standard operating procedure is developed based on the contributions introduced in the previous section. The set of instructions outlines steps for performing tasks to produce each contribution.

III.A. Review of adaptive resilience curve and its key elements

The adaptive resilience curve was built upon the delivery function for transitions in resilience, which is a time dependent metric for resilience. The metric is mathematically quantified to assist in computation of resilience in systems, time for resilience, and total cost in resilience improvement. The adaptive resilience curve was conceptualized by integrating the contributions of theories including global catastrophic risk, beyond design basis accident, and foresight. The essence of ideas to integrate the theories is to improve the delivery function for transitions in resilience in order to mathematically quantify adaptability of systems in a time dependent basis. To quantify adaptability of systems, variety of functions, function transitions, alternative scenarios of a function transition are needed to access. The sub sections below discuss how variety of functions, function transitions, alternative scenarios of a function transition are derived from the contributions of global catastrophic risk, beyond design basis accident, and foresight, respectively

III.A.1. Contribution of global catastrophic risk

Global catastrophic risk in general characterizes severity of risks into scales and dimensions using variables including scope, intensity, and probability. To assess the variety of functions, the variable of scope was utilized to investigate scope of risks perceived by systems. The scope of risks determines a function ($F(t)$), transition on a time dependent basis is assessed and translated into a level of resilience. In this sense, the scope of risks is utilized to explore risks and reflects resilience of systems in different aspects. Thus, the key element for the contribution of global catastrophic risk is function variation derived from scopes of risk.

III.A.2. Contribution of beyond design basis accident

Beyond design basis accident emphasizes a set of actions: preventing the escalation of an event into a severe accident, mitigating consequences of a severe accident, and achieving a long-term safe stable state, to address impacts on systems. System functionality is transitioned when an event occurs, and an action applies. Transitions derived from an event are assessed by the scope of risks, transitions derived from an action are assessed by action effectiveness. In this sense, it is important to know how an action contributes to function transitions. Thus, adaptability of systems is perceived as differences between the transition derived from an event and the transition derived from an action. The key element for the contribution of beyond design basis accident is function transitions derived from a set of actions.

III.A.3. Contribution of foresight

Foresight is known as a systematic approach to translate and interpret information for alternative scenarios and futures. In a function transition, there is a possibility of a variety of scenarios derived from an event. Foresight plays a key role in depicting alternative scenarios of a function transition using available information to translate and interpret. In adaptive resilience curve, transitions derived from an event and transition derived from an action can be foresee for alternative scenarios. Thus, the key element for the contribution of foresight is alternative scenarios of a function transition depicted by foresight.

III.B. Standard operating procedure for conducting adaptive resilience curve

The standard operating procedure is developed based on the abovementioned key elements including scope of risks, a set of action, and alternative scenarios. In order to produce the contributions, the following sub sections outline steps for performing necessary tasks.

III.B.1. Instructions for function variation derived from scopes of risk

1. Select an event to investigate function variation
2. Determine time window for the event
3. Set up a function ($F_0(t_x)$) to be assessed as a baseline function
    a. Determine $F_0(t_0)$: status at the beginning of the time window
    b. Determine $F_0(t_e)$: status at the initiation of the disruption
    c. Determine $F_0(t_d)$: status at the initiation of the disruptive state
    d. Determine $F_0(t_s)$: status at the end of the disruptive state
    e. Determine $F_0(t_f)$: status at the beginning of the stable recovered state, and
    f. Determine $F_0(t_a)$: status at the beginning of the adaptive state, if any.
4. Create a line graph of the determined function ($F_n(t_x)$) using available data.
    a. The determined function ($F_n(t_x)$) is represented as Y-axis, and the time window is represented as X-axis.

III.B.2. Instructions for function transitions derived from a set of actions

It is important to note that this set of instructions is only performed when an action is applied and instructions for III.B.1. is completed.

1. Determine time window for the action implementation
2. Determine one function ($F_{n,r}(t_x)$) to be assessed as an action function
    a. The function ($F_{n,r}(t_x)$) must have an identical nature to the function ($F_0(t_x)$)
3. Create a line graph of the determined function ($F_{n,r}(t_x)$) using available data.

   a. The determined function ($F_{n,r}(t_x)$) is represented as another Y-axis, and the time window for action implementation is represented as X-axis.
4. Integrate the determined function ($F_n(t_x)$) and function ($F_{n,r}(t_x)$) into a line graph and use time window for action implementation
5. Compare differences between the determined function ($F_n(t_x)$) and function ($F_{n,r}(t_x)$)

III.B.3. Instructions for alternative scenarios of a function transition depicted by foresight

It is important to note that this set of instructions is only performed when instructions for III.B.2. is performed.

1. Study the selected event from external sources of information
   a. Gather information for possible function transitions including a range of small to large severity of impacts, cascading impact, a range of short to long time of disruptions
2. Integrate outputs from the gathered information into the determined function ($F_n(t_x)$), and determine as an alternative scenario of determined function ($F_n(t_x)$)
3. Study the implemented action from external sources of information
   a. Gather information for possible function transitions including varying speed and target of transition.
6. Integrate outputs from the gathered information into the determined function ($F_{n,r}(t_x)$), and determine as an alternative scenario of determined function ($F_{n,r}(t_x)$)
7. Create a line graph for the alternative scenario of determined function ($F_n(t_x)$) and the alternative scenario of determined function ($F_{n,r}(t_x)$)

When completed III.B.1, III.B.2, and III.B.3, a total of four line graphs, as shown in Fig.1, are generated including:
1. Determined function ($F_n(t_x)$) represents function transition when the selected event occurred.
2. Determined function ($F_{n,r}(t_x)$) represents function transition when the selected event occurred and the implemented action applies.
3. Alternative scenario of determined function ($F_n(t_x)$) represents possible transition when the selected event occurred.
4. Alternative scenario of determined function ($F_{n,r}(t_x)$) represents possible transition when the implemented action applies.

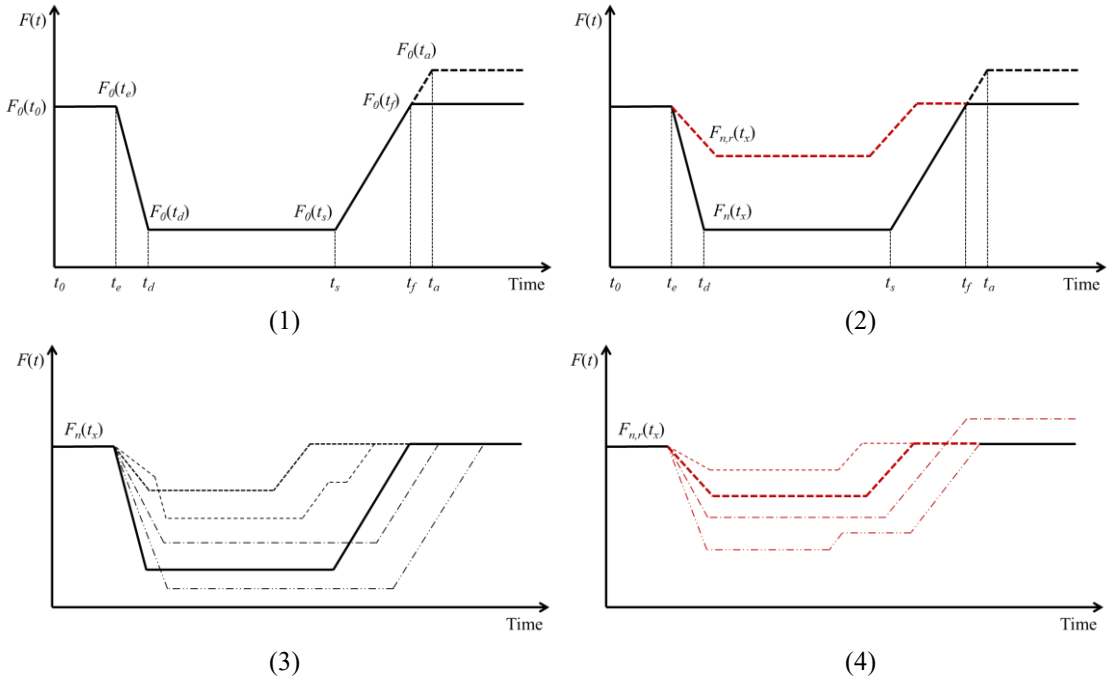

FIGURE 1. graph representations as outputs of standard operating procedure

The adaptive resilience curve is a mathematical approach assisting users in computation and quantification of the adaptability of systems. The outputs can also visualize transitions of a function under various conditions of systems. The standard operating procedure provides flexible use to practitioners in response to specific needs. Conducting adaptive resilience curve is an iterative process in which practitioners decide which insight or interpretation is necessary to fulfill the specific needs and sets of instructions can be performed iteratively. In order to investigate further variation of transition and time window, instructions for function variation derived from scopes of risk can be repeated. To compare differences in the implemented actions, practitioners follow instructions for function variation derived from scopes of risk and instructions for function transitions derived from a set of actions. To foresee other alternative scenarios, repetitive completion of instructions for alternative scenarios of a function transition depicted by foresight alone is an option.

IV. DISCUSSION

The adaptive resilience curve is developed to quantify the adaptability of systems through investigating function transitions after an occurrence of events and implementation of actions. In a certain sense of resilience improvement, the adaptive resilience curve acts as a tool to visualize function transitions and quantify effectiveness of actions, which are interpreted as resilience improvement. The investigation of function transitions does not only visualize impact on systems and effectiveness of actions but also indicates how exposed systems are against events. This implicit finding reflects current conditions of a system and creates awareness for stakeholders to make decisions. It signifies urgency to improve resilience in systems. It is important to note that actions implemented to address impact on systems should be central to reduction of severity, occurrence, and time of impact. Since severity, occurrence, and time of impact are the primary aspects which resilience is central on, actions to pursue the aspects are expected to contribute to the adaptability of systems. Suitability of an action is determined based on current conditions of a system and how urgent the actions need to be.

The standard operating procedure for conducting adaptive resilience curve is developed based on the key elements extracted from the contributions of global catastrophic risk, beyond design basis accident, and foresight. Three sets of instructions are developed and contribute to a total of four line graphs for further discussion. It is important to note that instructions for function variation derived from scopes of risk and instructions for function transitions derived from a set of actions require extensive data generated or gathered from the system. Availability of data before an event occurs until an action applies is crucial to the instructions. Further research and study on alternative scenarios of the selected event and implemented action depicted by foresight require sufficiently detailed data. Thus, this can imply that success of adaptive resilience curve is based on availability of data.

V. CONCLUSION

This study has objectives to review adaptive resilience curve proposed in the previous study to extract key elements which used to build the adaptive resilience curve, and to develop a standard operating procedure based on the key elements. The finding on review of adaptive resilience curve indicates that the delivery function for transitions in resilience is the fundamental principle of the adaptive resilience curve, which is a time dependent quantifiable metric. In order to equip with an ability to quantify adaptability of systems, contributions of theories including global catastrophic risk, beyond design basis accident, and foresight were integrated. The key elements adopted from the contributions consist of variety of functions, function transitions, alternative scenarios of a function transition, respectively. The key elements play a crucial role in investigating adaptability of systems through considerations of scope of risks, a set of actions, and alternative scenarios of event and action.

The study develops the standard operating procedure for conducting adaptive resilience curve by utilizing the key elements of contributions. The standing operating procedure consists of three sets of instructions including instructions for function variation derived from scopes of risk, instructions for function transitions derived from a set of actions, and instructions for alternative scenarios of a function transition depicted by foresight. Each set of instructions is developed to produce identical contributions to global catastrophic risk, beyond design basis accident, and foresight. As a result, the standard operating procedure guides to four line graphs: function transition when the selected event occurred, function transition when the selected event occurred and when the implemented action applies, possible transition when the selected event occurred, and possible transition when the implemented action applied. When the line graphs are interpreted implicitly, the finding contributes to current conditions of a system against an event, effectiveness of actions applied to the system, and possible transitions of the event and action. Thus, the standard operating procedure can lead to quantification of adaptability of systems which can be perceived by numeric differences between function transition when the selected event occurred and when the implemented action applies.

ACKNOWLEDGMENTS

Not applicable.

REFERENCES

[1] UN, "Global Goal on Adaptation," https://unfccc.int/topics/adaptation-and-resilience/workstreams/gga (2025)
[2] P.E. ROEGE, Z.A. COLLIER, J. MANCILLAS, et al, "Metrics for energy resilience," Energy Policy 72:249–256 (2014)
[3] D. HENRY, J.E. RAMIREZ-MARQUEZ, "Generic metrics and quantitative approaches for system resilience as a function of time," Reliability Engineering & System Safety 99:114–122 (2012)
[4] INL, "Infrastructure Climate Adaptation and Resilience (ICAR) Framework," https://resilience.inl.gov/icar (2025)
[5] UNDP, "Adaptation Policy Frameworks for Climate Change: Developing Strategies, Policies and Measures," Cambridge University Press (2004)
[6] P. JANTA, K. SILVA, T. TAKASHI, et al, "Development of Conceptual Framework for Adaptive State for Energy Resilience Assessment of Clean Energy Systems," PSAM2024, Japan (2024)
[7] S. ESKANDARZADEH, B. FAHIMNIA, K. HOBERG, "Adherence to standard operating procedures for improving data quality: An empirical analysis in the postal service industry," Transportation Research Part E: Logistics and Transportation Review: 103178 (2023)
[8] K. TAKAAKI, W. JIEH-JIUH, T. NING-YU, "Elements of standard operating procedures and flexibility issues in emergency management: A Japan-Taiwan comparison," International Journal of Disaster Risk Reduction: 102813 (2022)

ASRAM2025
www.asram2025.org
Asian Symposium on Risk Assessment and Management 2025
Pattaya, Thailand, 27 – 29 August 2025

Development and Evaluation of Automatic Tools of Fault Tree Creation Using Artificial Intelligence Technology with the Ability to Integrate Fault Tree Created from Multiple Design Documents to assist Probabilistic Risk Assessment Engineers

Yuki KONDO [1], Satoshi FUTAGAMI [1], Kenichi KURISAKA [1], Hidemasa YAMANO [1]

[1] *Japan Atomic Energy Agency: 4002 Narita-cho, O-arai-machi, Higashi-ibaraki-gun, Ibaraki 311-1393, Japan,*

ABSTRACT

In recent years, utilization field of probabilistic risk assessment (PRA) has been widened. On the other hand, PRA engineers have been needing to endure the laborious task to read and understand a huge amount of design documents and utilize the information obtained. One of key methods for solving these issues is to use AI technology. Therefore, the authors have been developing an automatic fault tree (FT) creation tool using AI technology for the aim of enabling any engineer to easily perform PRA with the same quality as a conventional approach. This paper describes the updates of the automatic FT creation method as the progress of the final step under our three-year program. There are two updates. One is that AI technologies such as image recognition can be used to extract information necessary to create FT not only from design documents for piping and power supply systems but also from design documents for signal systems. And the function has been expanded so that a signal FT can be generated from a multi-page design document. The other one is the newly added function to integrate FT, considering the functional dependencies between the frontline system and the support system. The effectiveness of the AI tool was evaluated by comparison between the time required to create an FT using the tool and the time required to create an FT without using the tool, confirming that the enhanced automatic FT creation tool significantly reduced work time for PRA engineers.

Keywords: Artificial Intelligence, AI, Probabilistic Risk Assessment, PRA, Fault Tree

1. INTRODUCTION

In recent years, power plants have been implementing risk informed decision making (RIDM) for improved safety, and PRA is used to quantify those risks [1]. To implement PRA, engineers have been needing to endure the laborious tasks to read and understand a huge amount of design documents. One of key methods to reduce the laborious tasks is to automate FT creation [2, 3]. However, this method had room for improvement such as the information extraction process from design documents. The authors have been trying to assist PRA engineers using AI and developing an automatic FT creation tool using AI technology [4]. The AI tools are intended to enable any users to easily perform PRA with the same quality less depending on user's PRA skill. From this background, the authors have conducted a three-year program. In the first step, the prototype tool with a FT creation function of component level piping systems was developed [5]. In the second step, the tool was updated to create more detailed failure mode level FT. And, the image recognition process in the FT creation from the design documents was improved to consider power supply systems [6]. Automatic FT creation tool using AI technology is basically designed to include two key functions. One is the information extraction function from paper design documents. And, the other is FT data creation function form extracted design information. In the information extraction process, template matching and object detection are used for image-based information such as component and piping. And, optical character recognition is used for character-based information such as name of component and piping. Because of the errors come from low resolution of design document and AI technology origin, some of extracted information are practically needed to check and correct by PRA engineers. Automatic FT creation tool is also designed to include annotation function. Because of the less annotation work is the better for PRA engineers, automatic FT creation tool can easily switch future AI technology updates such as improvement of AI technology origin errors.

In this paper, the updates of the automatic FT creation method are described, as the final step progress.

2. UPDATES OF AUTOMATIC FT CREATION METHOD

Automatic FT creation process from the design documents was improved to expand two functions. One is that AI technologies such as image recognition can be used to extract information necessary to create FT not only from design documents for piping and power supply systems but also from design documents for signal systems. This function expansion also enables to generate signal system FT from a multi-page design document. The other one is the logical data construction function to integrate FT, considering the functional dependencies between the frontline system and the support system.

2.1. Function expansion for FT creation of signal system

Figure 1 shows an example of signal system components and signal paths identified from multiple design documents of the experimental fast reactor "Joyo". This is the temperature control system of the secondary sodium system by using air cooler inlet vane/damper. To create an FT from design documents of the signal system, PRA engineers will manually conduct several tasks as follows.

① Select the target component and determine its failure mode from the design document.

② Identify the signal system components and signal path that constitute to the failure mode analyzed from multiple design documents such as interlock circuit diagram, control circuit diagram and sequence diagram.

③ Identify the basic events of each component or failure mode.

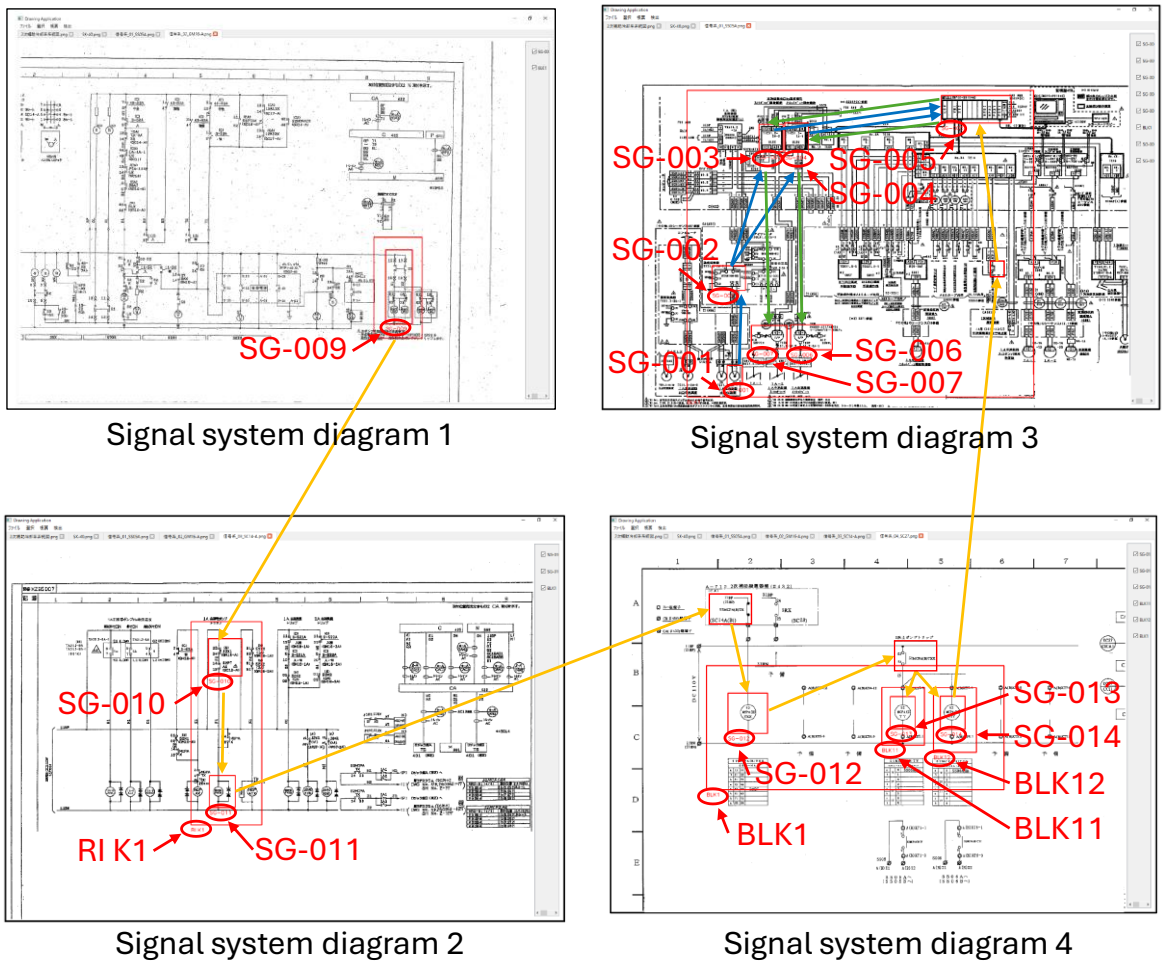

FIGURE 1. Example of signal system components and signal paths identified from multiple design documents

Based on the understanding of manual FT creation tasks mentioned above, function expansion of automatic FT creation method was designed to conduct 4 steps.

Step 1: Extraction of signal system components from design documents

In this process, the signal components of the design documents are extracted by the AI tool. The AI tool can assist human work, such as Graphical User Interface (GUI) function that displays design data on the screen and a function that makes it easy to detect and specify the target with a mouse. Extraction of signal system components from design documents was assisted by AI technology such as template matching and object detection. In this process, extracted components are specified as shown in the red frame of Figure 1, and are recorded in the list file (Excel format).

Step 2: Setting basic events IDs of component level and failure mode level

Signal system component names and images cropped from design documents are included in the list file. In this process, basic events of component level and failure mode level are set to list files based on component names and images.

Step 3: FT data creation

In this process, FT data is created from the list file by the AI tool. The FT data is generated to be a textual input to PRA analysis software such as SAPHIRE [7].

Step 4: FT drawing

In this process, FT diagram can be drawn using FT drawing function provided in the PRA analysis software SAPHIRE etc.

The authors demonstrated to confirm the function of the AI Tool for FT creation with comparing conventional manual FT creation method. Figure 2 shows the example of signal system FT created using the AI Tool combined with the FT drawing software provided in SAPHIRE in step 4. From the demonstration results, the authors confirmed that the expanded function of the AI tool is consistent with conventional manual method.

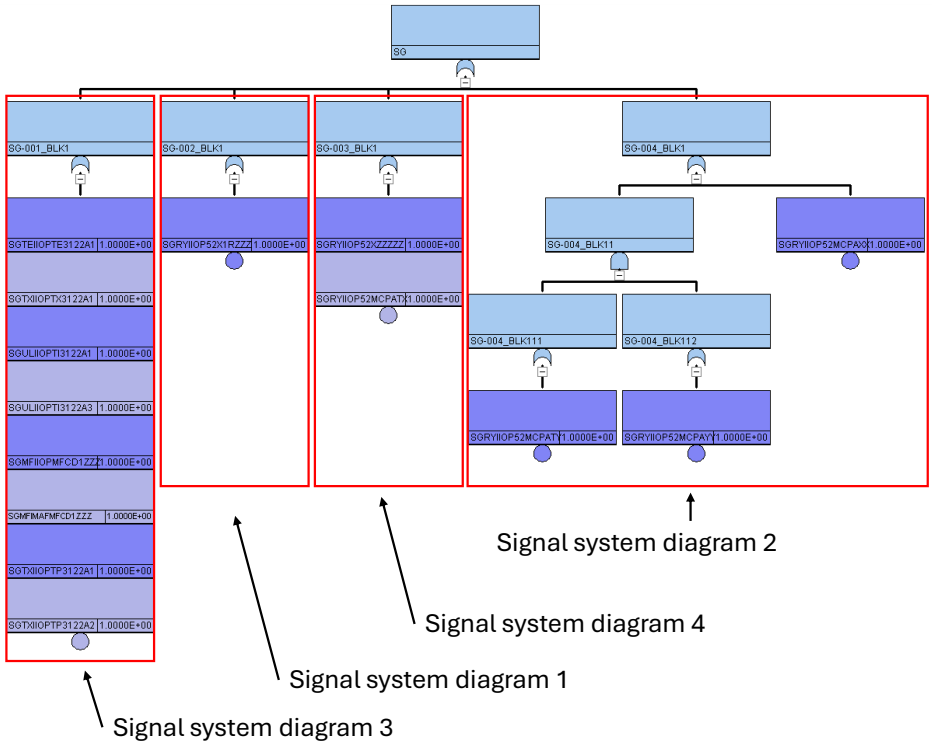

FIGURE 2. Example of the signal system FT

2.2. Function expansion for FT creation considering the functional dependencies between a frontline system and its support systems.

To consider the functional dependencies between a frontline system and its support systems, function was expanded to link support systems to the frontline system via the transfer gates. For the topical example of linking these systems, experimental fast reactor “Joyo” was considered to demonstrate how to link the secondary cooling system, which is a frontline system for decay heat removal, with its support systems, i.e., the secondary sodium purification system, the power supply system, and the signal system. The secondary cooling system is connected to the secondary sodium purification system for sodium purification through piping. Active components in the secondary cooling system are also connected to the power supply system and the signal system through electrical wiring. Based on these connections, linking points in the secondary cooling system is indicated on the display of the AI tool by the PRA engineer as shown in Figure 3. In this example, an FT top event of the secondary sodium purification system was named “SP”, a top event of the signal system was determined to “SG”, and a top event of the power supply system was determined to “EPS_6C”, and then the support system FTs are automatically created using the AI tool. The AI tool identifies these top events in the support system FTs as linking points with the frontline components or area and the tool connects the frontline system FT and its support system FTs via the transfer gates. The transfer gates linking to the support system FTs mentioned above were named “SP”, “SG”, and “EPS_6C” by the AI tool, respectively.

The authors demonstrated to confirm the function of the AI Tool for FT creation with comparing conventional manual FT creation method. An example of the frontline system FT including the transfer gates is shown in Figure 4, and examples of the support system FTs are shown in Figure 5. From the demonstration results, the authors confirmed that the expanded function of the AI tool is consistent with conventional manual method.

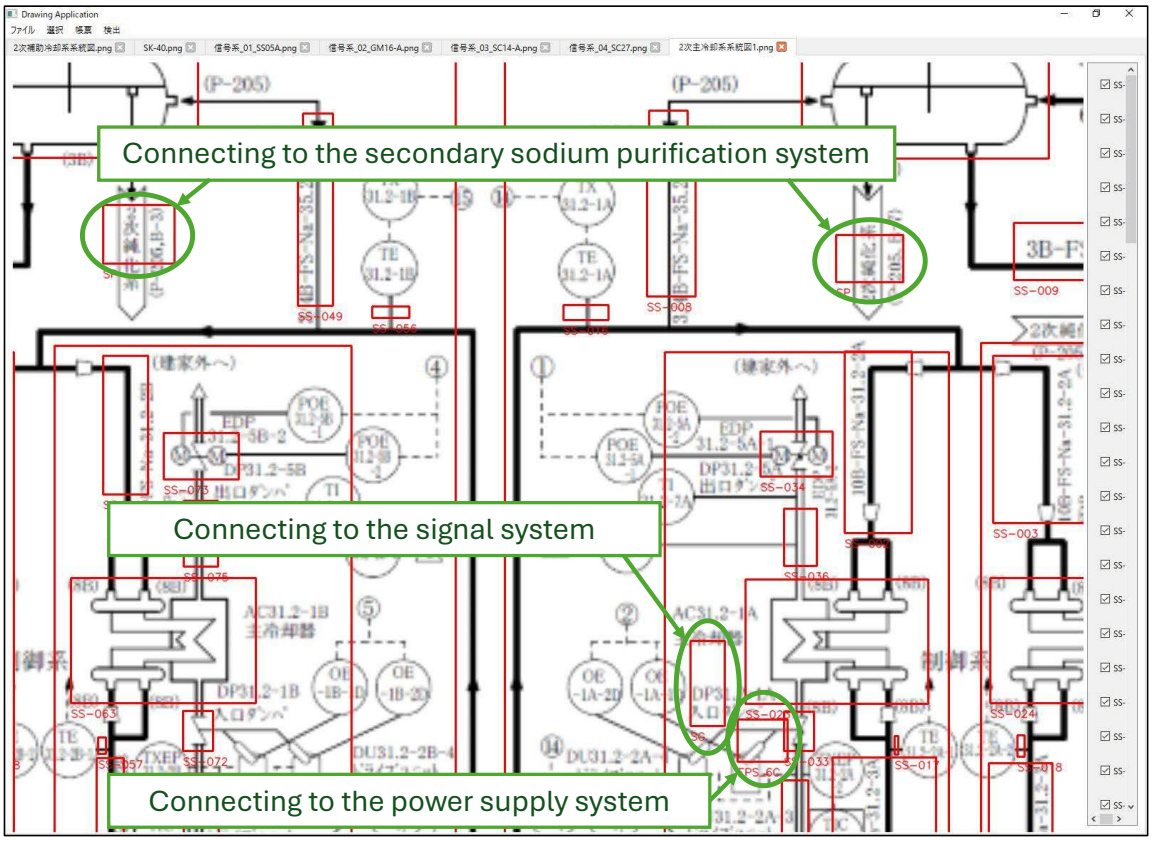

FIGURE 3. Linking points in the secondary cooling system

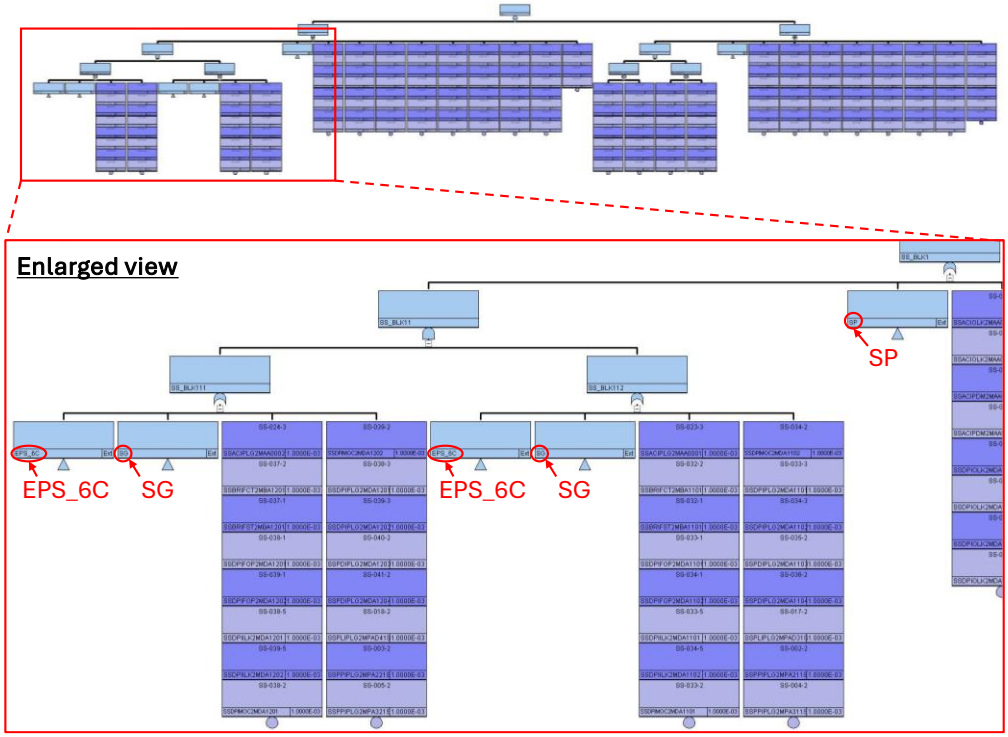

FIGURE 4. Example of the frontline system FT including the transfer gates

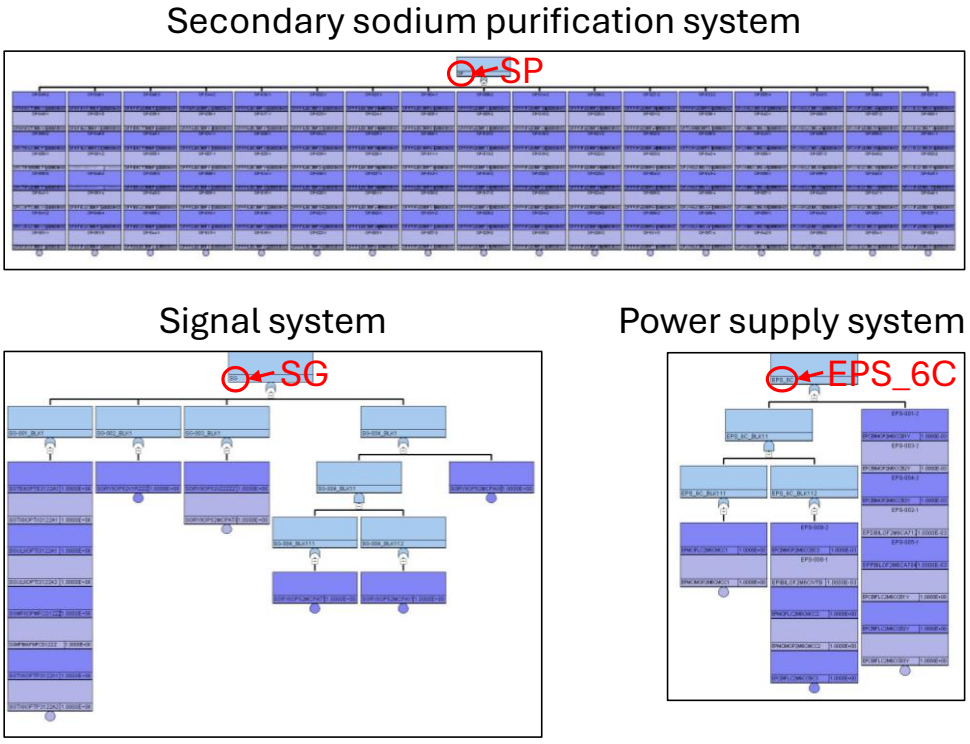

FIGURE 5. Examples of the support system FTs

3. QUANTITATIVE EVALUATION OF FT CREATION TIME THROUGH TRIAL HUMAN WORK

In order to confirm the effectiveness of the AI tool, comparisons were made between the time required to create an FT using the tool and the time required to create an FT without using the tool. In these comparison, 2 cases of FT creation time were measured. One case is a case for signal system FT creation. The other case is a case for FT creation considering support systems. These comparison results are shown in Figure 6. For the signal system creation, the work time was reduced to 29%. In the other case, the work time was reduced to 22%. The AI tool contributed to reduce the work time in both cases.

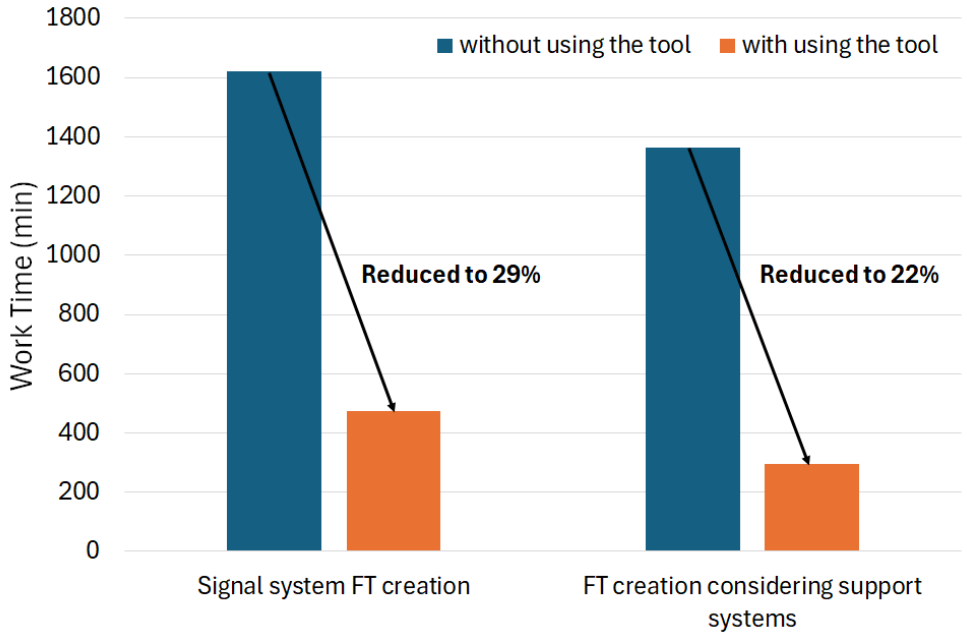

FIGURE 6. Comparison results of work time

4. CONCLUSIONS

The authors have been conducting a three-year program including development of the AI tool for automatic FT creation. The AI tool is intended to enable any users to easily perform PRA with the same quality without user effect. As the final step of the three-year program, the AI tool was expanded the functions to create FT of signal system and to create FT considering support systems. The demonstration results showed that the expanded functions of the AI tool are consistent with conventional manual method. The quantitative evaluation of work time indicated that the AI tool contributed to reduce work time. This three-year program was finished for now. Demonstration results of the three-year program provide a basic outlook for social implementation as an early stage of development. The authors will prepare to download this tool to applicant users.

ACKNOWLEDGMENTS

This work was supported by MEXT Innovative Nuclear Research and Development Program Grant Number JPMXD0222682583.

REFERENCES

[1] NEI, "Risk-Informed Performance-Based Technology Inclusive Guidance for Non-Light Water Reactor Licensing Basis Development Report Revision 1", 18-04 (2019).
[2] H. UJITA, "Development of SUPKIT-II: Computer Aided Fault Tree Analysis System", Journal of Nuclear Science and Technology, 21[8], 625-633 (1984).
[3] M. Roth, M. Wolf, U. Lindemann, "Integrated Matrix-Based Fault Tree Generation and Evaluation", Procedia Computer Science, 44, 599 – 608 (2015).
[4] S. FUTAGAMI, H. YAMANO, K. KURISAKA, H. UJITA, "Development of Probabilistic Risk Assessment Methodology Using Artificial Intelligence Technology, 1; Automatic fault tree creation", PSAM 2023 Topical Conference AI & Risk Analysis for Probabilistic Safety/Security Assessment & Management, 2023.
[5] S. FUTAGAMI, H. YAMANO, K. KURISAKA, H. UJITA, "Development of probabilistic risk assessment methodology using artificial intelligence technology, 2; Application of automatic tools to component level fault tree creation", Atomic Energy Society Japan 2024 Annual Meeting, 2024.
[6] S. FUTAGAMI, Y. KONDO, H. YAMANO, K. KURISAKA, "Development of Probabilistic Risk Assessment Methodology Using Artificial Intelligence Technology, 3; Automatic Fault Tree Creation Tools for Failure Mode Level Fault Tree", Probabilistic Safety Assessment and Management & Asian Symposium on Risk Assessment and Management (PSAM17 & ASRAM2024), 2024.
[7] USNRC, *Systems Analysis Programs for Hands-on Integrated Reliability Evaluations (SAPHIRE) Version 8*, 2011, NUREG/CR-7039 Vol.1-Vol.7
(https://www.nrc.gov/reading-rm/doc-collections/nuregs/contract/cr7039/index.html)

Technical Session 8 (16:00 - 18:00)	The Port 4, C Floor	Safety, Security and Risk Analysis of Nuclear and Non-nuclear Facilities and Applications (Fuel and Equipment, Waste Facility, Tokamak Fusion, Radiation, Ship, Vehicle, Chemical Plants)
		Chair/Facilitator 1: Asst.Prof. Apiwat WISITSORASAK (Department of Physics, King Mongkut's University of Technology Thonburi (KMUTT))
		Chair/Facilitator 2: Dr. Nart Noodee (Thailand Institute of Nuclear Technology (TINT))
16:00 - 16:20		ID 60: Discussion on the Possibility of BLEVE occurring in Liquefied Natural Gas StorageTanks Speaker: Yu-Ting Chiu (National Atomic Research Institute (NARI)) Contributors: Yu-Ting Chiu (National Atomic Research Institute (NARI)), Hao-Ti Hsu (National Atomic Research Institute (NARI)), Tsu-Mu Kao (National Atomic Research Institute (NARI))
16:20 - 16:40		ID 140: Risk Assessment of Leakage Failure of Key Facilities at Oil and Gas Gathering and Transportation Stations Speaker: Qingqing Xu (College of Safety and Ocean Engineering, China University of Petroleum (Beijing)) Contributors: Qingqing Xu (College of Safety and Ocean Engineering, China University of Petroleum (Beijing)), Yichen Huang (Xi'an Jiaotong University), Xuan Zhang (College of Safety and Ocean Engineering, China University of Petroleum (Beijing)), Ge Chen (Hubei Yiwei Power Co., LTD, Hubei, China), Shaohua Dong (College of Safety and Ocean Engineering, China University of Petroleum (Beijing)), Yi Shuai (College of Safety and Ocean Engineering, China University of Petroleum (Beijing))
16:40 - 17:00		ID 142: Monte Carlo Simulation for Evaluating the Efficiency of an HPGe Detector Speaker: Jamiyansuren Terbish (Nuclear Research Center, National University of Mongolia) Contributors: Munkhsaikhan Jargalsaikhan (Nuclear Research Center, National University of Mongolia), Jamiyansuren Terbish (Nuclear Research Center, National University of Mongolia)
17:00 - 17:20		ID 125: Preliminary Risk Assessment of Nuclear Security Considering the Potential for Future SMR Developments in Thailand Speaker: Piyawan Krisanangkura (Office of Atoms for Peace) Contributors: Piyawan Krisanangkura (Office of Atoms for Peace)
17:20 - 17:40		ID 81: Neutronic Analysis of PeLUIt Reactor with Heavy Metal Loading and Power Variations in the OTTO Refueling Scheme Speaker: Ahmad Muzaki Mabruri (Bandung Insitute of Technology) Contributors: Ahmad Muzaki Mabruri (Bandung Insitute of Technology), Nuri Trianti (Indonesian National Research and Innovation Agency (BRIN)), Zaki su'ud (Bandung Insitute of Technology), Dwi Irwanto (Bandung Insitute of Technology), Topan Setiadipura (Indonesian National Research and Innovation Agency (BRIN))

ASRAM2025
www.asram2025.org
Asian Symposium on Risk Assessment and Management 2025
Pattaya, Thailand, 27 – 29 August 2025

Discussion on the Possibility of BLEVE occurring in Liquefied Natural Gas Storage Tanks

Yu-Ting Chiu* , Hao-Ti Hsu, Tsu-Mu Kao

National Atomic Research Institute (NARI)
No. 1000, Wenhua Rd., Longtan Dist., Taoyuan City 325207 , Taiwan (R.O.C.)
ytchiou@nari.org.tw; hthsu@nari.org.tw; tmkao@nari.org.tw

ABSTRACT

To safeguard workers and equipment at liquefied natural gas (LNG) terminals, the tanks are stored and operated under cryogenic conditions. However, fire accidents may affect the tanks' temperature and pressure, leading to a boiling liquid expanding vapor explosion (BLEVE). Thus, in order to evaluate the risks from BLEVEs of LNG storage tanks, this study first analyzes historical data (1920–2024) on BLEVEs involving any substance and identifies the key factors contributing to incidents. Then, we estimate the impact range of the overpressure generated specifically from vaporized LNG by utilizing the empirical formulas proposed by Prugh [1] and Hemmatian et al. [2], as well as the quantitative risk analysis (QRA) software Safeti/Phast developed by Det Norske Veritas (DNV). Our results indicate that, owing to the design of current storage tanks, the blast radius remains relatively small, limiting the extent of the damage.

Keywords: Liquefied Natural Gas (LNG), BLEVE, Overpressure

I. INTRODUCTION

A boiling liquid expanding vapor explosion (BLEVE) occurs when the liquid contents in a vessel reach or exceed their boiling point and rapidly vaporize and expand, causing the vessel to violently rupture [3]. Hence, fossil fuel facilities, including liquefied natural gas (LNG) terminals, must recognize the risk of BLEVEs arising during fire accidents, when the containers may be exposed to and consequently weakened by pool fires or jet flames. As these explosions are physical rather than chemical—i.e., caused by the release of mechanical energy—their hazards can be broadly categorized as overpressure shock waves, explosive fragments, or, when the event involves a persistent fire source and flammable materials, fireballs.

In this study, we primarily focused on the probability and magnitude of overpressure shock waves propagated by BLEVEs of LNG storage tanks. To accurately quantify the hazards in different scenarios, we compared and verified the results obtained with three methods:The equivalent-mass-of-trinitrotoluene (TNT) formula proposed by Prugh [1], the statistical model developed by Hemmatian et al. [2], and the quantitative risk assessment (QRA) and consequence analysis software Safeti/Phast, developed by Det Norske Veritas (DNV), are utilized in this study.

II. HISTORICAL BLEVES AND CAUSES

To identify the risk factors for BLEVEs, we examined 71 historical incidents inventoried in the Analysis, Research and Information on Accidents (ARIA) database, which is maintained by France's Bureau for Analysis of Industrial Risks and Pollutions within the Ministry of Ecology and has been recording incidents globally since 1950 [4]. To supplement these data and improve our analysis of the frequency of occurrence (Figure 1), the substances involved and the accompanying circumstances, we also consulted *The Handbook of Hazardous Materials Spills Technology* [5] and *Evaluation of the Effects and Consequences of Major Accidents in Industrial Plants* [6], which cover a period from 1920 to 2024 and include 65 incidents.

There were 136 accidents in total, of which 66 were BLEVEs during transportation, 64 were at fixed facilities, and 6 were other types, such as BLEVEs at road construction sites.

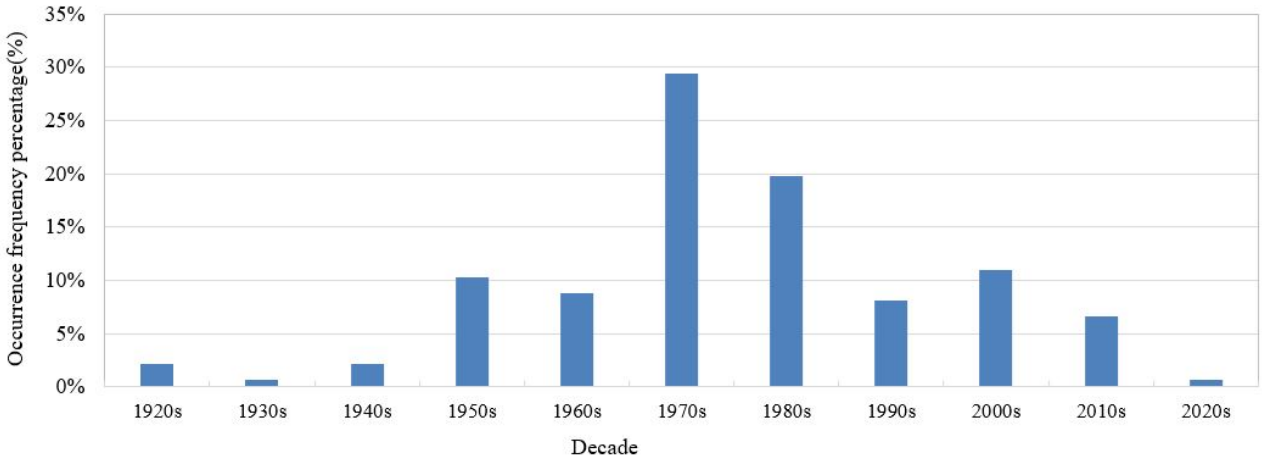

Figure 1. The distribution chart of BLEVE accident occurrence time and frequency

According to ARIA and the relevant literature, the causes of BLEVEs fall into five general categories, viz., impact failures, external events, human factors, mechanical failures, and severe reactions, which can be further divided into specific factors (Table 1). Impact failures, which comprise collisions, derailments, and road accidents, account for the largest proportion of incidents (~40%, or 51 incidents), followed by external events (~29%, or 39 incidents), which encompass earthquakes, explosions, and fires. However, external fires alone are responsible for more than a quarter of the total incidents (~27%, or 37 incidents), rendering them the most frequent cause among specific factors.

Table 1 Causes of BLEVE Accidents

General causes	Specific factors	Percentage of occurrences (%)
Impact Failure(39.71%)	Collision	8.1
	Derailing	16.2
	Road accident	15.4
External Event(28.68%)	Earthquake	0.7
	Explosion	0.7
	Fire	27.2
Human Factor(15.44%)	Overfilling	7.4
	Human error	8.1
Mechanical Failure(11.02%)	Overpressure	2.2
	Overheating	1.5
	Leak	2.9
	Corrosion	0.7
	Other	3.7
Violent Reaction (5.15%)	Runaway reaction	5.1

Additionally, we identified the 12 substances most likely to be involved in BLEVEs (Table 2), with liquefied petroleum gas (LPG) and propane appearing in half (or 68 incidents)) of the incidents. Gasoline and butane each contributed ~7% to the total occurrences (with 10 and 9 incidents, respectively), whereas LNG accounted for merely ~1% (with 2 incidents).

We also investigated the contributing factors in the disaster that unfolded on November 19, 1984, in San Juan Ixhuatepec, Mexico, when a ruptured pipeline at the Pemex LPG storage and transportation station released enough LPG to form a massive gas cloud, which eventually ignited, and, within minutes, triggered the first of multiple BLEVEs. Failed emergency isolation systems, nonfunctioning fire protection systems, and nonexistent gas detection systems in conjunction with poor facility location and traffic congestion exacerbated the severity of this industrial accident, which killed ~500, injured ~6,000, and destroyed almost all of the storage tanks at the station.

Although BLEVEs of LNG storage tanks seldom occur, mainly because these containers are generally constructed with thermal insulation and double walls (e.g., an outer shell of concrete and an inner shell of steel) as well as kept at a relatively low operating pressure, accidents involving LNG are still possible. For example, a road tanker transporting LNG in Spain during 2002 ignited after tipping over [7]. The heat of the fire caused the LNG to vaporize and, consequent to the high set pressure of the safety valve (nearly 8 bar), accumulate unchecked inside the trailer, resulting in a BLEVE [8].

Table 2 Substances Involved In BLEVE Accidents

substance	Percentage of occurrences (%)
LPG, Propane	50
Gasoline	7.35
Butane	6.62
Ethylene, ethylene oxide	5.15
Ammonia	5.15
Chlorine	5.15
Propylene	2.94
Vinyl chloride	2.94
Carbon dioxide	1.47
LNG	1.47
Water	0.74
Other chemical substances	11.02

III. ESTIMATING THE IMPACT FROM BLEVES OF LNG STORAGE TANKS

Using three methods and comparing their results, we assessed the impact range of a potential BLEVE if an LNG storage tank with a capacity of 160,000 m^3 (diameter = 76 m, length = 35.26 m) were filled to 80 %. The first method applied Prugh's equivalent-mass-of-TNT formula [1], which relies on the assumption that vapor expands isentropically; the second employed the statistical approach pioneered by Hemmatian et al. [2], which predicts the magnitude of the overpressure based on simple inputs; and the third utilized the Safeti 8.71/Phast software developed by DNV, which integrates QRA and consequence analysis. Based on typical storage conditions and the standard tank design, a rupture would ensue when the temperature of the LNG reached −157.8 °C (above the boiling point) and the pressure inside the tank equaled 0.26 bar—1.21 times the level that would trigger the tank's pressure safety valve (a general gauge pressure of 0.22 $kg \cdot cm^{-2}$, or ~0.216 bar) [9]. Furthermore, adopting Zipf 's scale of overpressure thresholds or effects on structures and human bodies (Table 3)[10], we estimated the distances at which minor injury (1 psi), severe injury (2 psi), and fatality (3 psi) would occur (Table 4).

Table 3 Damage Standards for Overpressure

Overpressure	Impact on Equipment	Impact on Personnel
1 psi	Window glass shatters	Minor injuries caused by flying glass shards
2 psi	Moderate house damage (doors/windows destroyed, severe roof damage)	Injuries caused by flying glass shards
3 psi	Collapse of residential structures	High likelihood of severe injuries or fatalities
5 psi	Most buildings collapse	Severe injuries and fatalities common
10 psi	Damage or collapse of reinforced concrete structures	Most people will die
20 psi	Heavily built concrete buildings are severely damaged or demolished	Fatality rate approaches 100%

Table 4 BLEVE Impact Radius (m) for LNG Storage Tanks Simulated by Different Methods

Consequence Analysis	Impact radius (m)		
	Prugh	Hemmatian et al.	Safeti/Phast
Minor injury radius (1 psi)	164.5	313	164.5
Severe injury radius (2 psi)	91.4	174	100
Fatality radius (3 psi)	73	139	79.2

III.A. Application of Prugh's TNT Equivalent Formula

As detailed by Planas-Cuchi et al.[11], the amount of energy released during a BLEVE, E_V (kJ), is the product of the vapor's mass and the vapor's change in internal energy:

$$E_V = m(U_1 - U_2) \tag{1}$$

where m is the mass of vapor already existing in the vessel at the moment of the failure(kg), U_1 is the internal energy of the vapor preceding the rupture (kJ·kg^{-1}), and U_2 is the internal energy of the vapor following the rupture once the vapor has expanded and achieved equilibrium with the atmospheric pressure (kJ·kg^{-1}).

Adopting Prugh's empirical approach, we assumed the vaporization and expansion of the LNG to be isentropic (i.e., adiabatic and reversible) and calculated the energy of the BLEVE as an equivalent mass of TNT, W_{TNT} (kg), by inputting values for methane, the primary component of LNG, as parameters:

$$W_{TNT} = 0.021 \times \left(\frac{P \times V^*}{\gamma - 1}\right) \times \left(1 - \left(\frac{P_a}{P}\right)^{\frac{\gamma-1}{\gamma}}\right) \tag{2}$$

where P is the vapor pressure (bar), P_a is the atmospheric pressure (bar), V^* is the total volume of the vapor (including that produced by instantaneous vaporization) inside the tank (m^3), and γ is the heat capacity ratio (1.31).

Obtaining $V^*$and its prerequisites required two additional formulas:

$$V^* = V + V_l \times f \times \left(\frac{\rho_l}{\rho_V}\right) \tag{3}$$

where V and V_l are the volumes of the vapor (m^3) and the liquid (m^3), respectively, inside the tank prior to the rupture; ρ_l and ρ_V are the densities of the liquid (443 kg·m^{-3}) and the vapor (2.44 kg·m^{-3}), respectively; and f is the vapor fraction of the liquid, i.e., the proportion of liquid that vaporizes during flash evaporation, and:

$$f = 1 - \exp(-2.63 \cdot (C_p/H_v) \cdot (T_c - T_b) \cdot (1 - ((T_c - T_o)/(T_c - T_b))^{0.38})) \tag{4}$$

where T_c, T_b, and T_0 are the critical temperature of the substance (190.56 K), the boiling temperature of the substance at atmospheric pressure (111.55 K), and the temperature of the substance at the time of rupture (−157.8 °C, or 115.35 K), respectively; C_p is the specific heat capacity at constant pressure (2.232 × 10^3 J·kg^{-1}·K^{-1}); and H_v is the enthalpy of vaporization for the substance (5.11 × 10^2 kJ·kg^{-1}).

Hence, f and V^* equal 0.0167 and 420,097 m^3, respectively, yielding a W_{TNT} of 1,908.4 kg. Since breaking the tank alone would require a significant amount of energy, we multiplied W_{TNT} by an adjustment factor, β, of 0.4 (which is suitable when the overpressure involves ductile materials)[12] to estimate the remaining available energy for the blast, $(W_{TNT})_{overpressure}$: 763.4 kg.

Lastly, we evaluated the scaled distance, d_n (m·kg$^{-⅓}$), to determine the impact radius of the BLEVE for different levels of harm:

$$d_n = \frac{d}{(\beta W_{TNT})^{⅓}} \tag{5}$$

where d is the actual distance (m). Calculating the pressure wave as a function of the scaled distance (Figure 2), we thereby found the impact radii for minor injuries, severe injuries, and fatalities to be ~164.5 m (d_n = 18), ~91.4 m (d_n = 10), and ~73 m (d_n = 8), respectively.

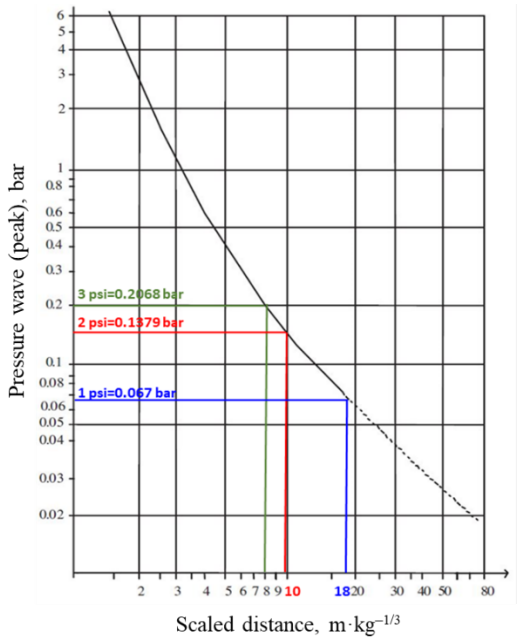

Figure 2. Pressure Wave as A Function of The Scaled Distance[13]

III.B. Statistical Overpressure Estimation Based on Hemmatian et al.'s Model

Hemmatian et al. used MATLAB's Curve Fitting Toolbox 3.4.1 and related statistical models to develop an easy-to-use formula that requires only the initial filling degree of the tank (FD) and the temperature at which rupture occurs (T, K). This approach assumes that the expansion of the vapor is irreversible and adiabatic (in contrast to Prugh's method) .The comparison of its predictions with the values corresponding to experimental data gives very positive results, this validating the reliability of the method.

To estimate the mechanical energy released per cubic meter by the BLEVE, e (MJ·m^{-3}), we simply input our values for FD and T (0.8 and 115.35 K, respectively) into the formula provided for methane (Table 5):

$$e = 6.13 - 42.71 \times FD - 0.06558 \times T + 0.5629 \times FD \times T - 0.0001499 \times T^2 - 0.001647 \times FD \times T^2 + 2.327 \times 10^{-6} \times T^3 \quad (6)$$

Obtaining an e of 0.387 MJ·m^{-3} enabled us to calculate the total amount of released energy, E (MJ):

$$E = e \times V_T \quad (7)$$

where V_T is the volume of the tank (160,000 m^3). E therefore equals 61,920 MJ.

Converting E to the equivalent mass of TNT (the energy released by 1 W_{TNT} = 4,680 kJ·kg^{-1}) yielded a W_{TNT} of 13,230 kg and consequently a (W_{TNT})overpressure of 5,292 kg (β = 0.4). We then solved Equation (5) with the latter value, obtaining ~313 m (d_n = 18), ~174 m (d_n = 10), and ~139 m (d_n = 8) as the impact radii for minor in as the impact radii for minor injuries, severe injuries, and fatalities, respectively.

Table 5. Mechanical Energy Released Per Cubic Meter of Vessel As A Function of Explosion Temperature and Initial Filling Degree (Expressed in Parts Per Unit Instead of Percentage) For Different Substances

Substance	Released mechanical energy ($MJ \cdot m^{-3}$)
Propane	$e = 43.97 - 213.9 \cdot FD - 0.152 \cdot T + 1.349 \cdot FD \cdot T - 0.0004361 \cdot T^2 - 0.002045 \cdot FD \cdot T^2 + 1.55 \cdot 10^{-6} \cdot T^3$
Butane	$e = 21.32 - 87.2 \cdot FD - 0.136 \cdot T + 0.4756 \cdot FD \cdot T + 0.0001885 \cdot T^2 - 0.0005805 \cdot FD \cdot T^2 + 9.693 \cdot 10^{-6} \cdot T^3$
Methane	$e = 6.13 - 42.71 \cdot FD - 0.06558 \cdot T + 0.5629 \cdot FD \cdot T - 0.0001499 \cdot T^2 - 0.001647 \cdot FD \cdot T^2 + 2.327 \cdot 10^{-6} \cdot T^3$
Water	$e = 56.36 - 275.6 \cdot FD - 0.2341 \cdot T + 1.076 \cdot FD \cdot T + 0.0001696 \cdot T^2 - 0.0009183 \cdot FD \cdot T^2 + 1.626 \cdot 10^{-6} \cdot T^3$
Vinyl chloride	$e = 20.71 - 92.48 \cdot FD - 0.1206 \cdot T + 0.5346 \cdot FD \cdot T + 9.836 \cdot 10^{-5} \cdot T^2 - 0.0006987 \cdot FD \cdot T^2 + 2.503 \cdot 10^{-7} \cdot T^3$
Ethylene oxide	$e = 23.61 - 119.4 \cdot FD - 0.1182 \cdot T + 0.6295 \cdot FD \cdot T + 4.505 \cdot 10^{-5} \cdot T^2 - 0.0007463 \cdot FD \cdot T^2 + 2.946 \cdot 10^{-7} \cdot T^3$
Propylene	$e = 104.9 - 86.15 \cdot FD - 1.035 \cdot T + 0.5013 \cdot FD \cdot T + 0.00329 \cdot T^2 - 0.0005726 \cdot FD \cdot T^2 - 3.321 \cdot 10^{-6} \cdot T^3$
Ammonia	$e = 28.34 - 168.4 \cdot FD - 0.1447 \cdot T + 1.048 \cdot FD \cdot T - 6.71 \cdot 10^{-5} \cdot T^2 - 0.001471 \cdot FD \cdot T^2 + 7.984 \cdot 10^{-7} \cdot T^3$
Chlorine	$e = -2.469 - 81.17 \cdot FD + 0.08234 \cdot T + 0.4975 \cdot FD \cdot T - 0.0005088 \cdot T^2 - 0.0006739 \cdot FD \cdot T^2 + 8.889 \cdot 10^{-7} \cdot T^3$
Ethylene	$e = 9.356 - 69.53 \cdot FD - 0.04289 \cdot T + 0.6194 \cdot FD \cdot T - 0.0003058 \cdot T^2 - 0.001262 \cdot FD \cdot T^2 + 1.454 \cdot 10^{-6} \cdot T^3$

III.C. Application of Safeti/Phast Software in QRA (by DNV)

We simulated the consequences of an LNG tank explosion by running the BLEVE blast model in Safeti 8.71/Phast.The impact range of BLEVE in LNG storage tanks causing minor injuries (1 psi), serious injuries (2 psi) and death (3 psi) is shown in Figure 3. The blue color represents the 1 psi contour map, and its influence radius is ~164.5 m; the green color represents the 2 psi contour map, and its influence radius is ~100 m; the red color represents the 3 psi contour map, and its influence radius is ~79.2 m.

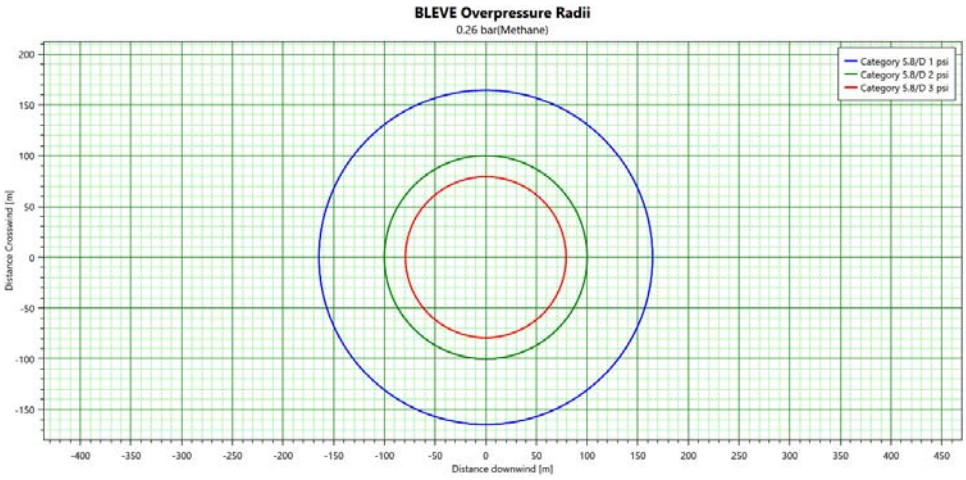

Figure 3. BLEVE Overpressure Contour

IV. DISCUSSION

Under the same initial conditions (temperature, pressure and the volume of tank), although the impact radii obtained using Prugh's empirical formula and Safeti/Phast show good agreement for all three damage levels, the method of Hemmatian et al. produces significantly higher values - up to ~148.5 m - which may be attributed to the differences in thermodynamic assumptions mentioned earlier. Among them, Prugh's empirical formula assumes ideal gas and isentropic expansion;

Hemmatian et al.'s method assumes real gas and adiabatic irreversible expansion; Safeti/Phast assumes real gas and isentropic expansion. The three different thermodynamic assumptions lead to slightly different results.

V.CONCLUSION

Historically, two BLEVEs involving LNG have been recorded, but both incidents occurred with trailers, which can transform into high-pressure vessels when exposed to heat. By contrast, LNG storage tanks maintain an extremely low internal pressure at all times (the standard set pressure of the safety valves is ~0.216 bar, or less than 3% of that for trailers), minimizing the fraction that flashes during a rupture (which is only ~0.03 times that of LPG). Furthermore, the multi-layered construction of these containers resists heat transfer, reducing the rate of vaporization. However, in spite of BLEVE being unlikely to occur—and being limited in magnitude when they do—storage tanks and related equipment should be regularly inspected to ensure safety at LNG terminals.

References

[1] Prugh, R. W. ‘‘Quantify BLEVE Hazards ’’, Chemical Engineering Progress, vol. 87, 66–72. , 1991.
[2] Hemmatian, B., Casal,J., Planas, E., ‘‘A new procedure to estimate BLEVE overpressure’’, Process Safety and Environmental Protection, vol.111, 320-325, 2017.
[3] Hemmatian, B., Planas, E., Casal, J. “On BLEVE definition, the significance of superheat limit temperature (Tsl) and LNG BLEVE's ”, Journal of Loss Prevention in the Process Industries, 40, 81., 2016.
[4] ARIA, “Analysis, Research and Information on Accidents,” from www.aria.developpement-durable.gouv.fr.
[5] Merv Fingas, “Handbook of Hazardous Materials Spills Technology,” McGraw-Hill Professional, 2001.
[6] Joaquim Gasal, “Evaluation of the Effects and Consequences of Major Accidents in Industrial Plants” , Elsevier, 2017.
[7] Planas Cuchi, E., Gasulla, N., Ventosa, A., Casal, J. ‘‘Explosion of a road tanker containing liquified natural gas”, Journal of Loss Prevention in the Process Industries, 17(4), 315-321., 2004.
[8] Venart, J. E. S. “Letter to the editor,” Process Safety Progress, 24(4), 226-226., 2005.
[9] The Netherlands Organization of Applied Scientific Research, “Guidelines for quantitative risk assessment Methods (Purple Book)”, 2005.
[10] R. Karl Zipf, Jr., Ph.D., P.E. Kenneth L. Cashdollar, “Explosions and Refuge Chambers”, 2015.
[11] Planas-Cuchi, E., J. Casal, A. Lancia, and L. Bordignon. 1996. ‘‘Protection of Equipment Engulfed in a Pool Fire,’’ Journal of Loss Prevention in the Process Industries, vol. 9, pp. 231–240.
[12] J. Casal, J. Arnaldos, H. Montiel, E. Planas-Cuchi, J.A. Vı´lchez, 22.1-22.27 in: M. Fingas (Ed.),Modelling and Understanding BLEVE. The Handbook of Hazardous Materials Spills Technology, McGraw-Hill, New York, 2001.
[13] Van den Berg, A. C., and A. Lannoy. ‘‘Methods for Vapor Cloud Explosion Blast Modelling’’, Journal of Hazardous Materials, vol. 34, 151–171., 1993.

ASRAM2025
www.asram2025.org
Asian Symposium on Risk Assessment and Management 2025
Pattaya, Thailand, 27 – 29 August 2025

RISK ASSESSMENT OF LEAKAGE FAILURE OF KEY FACILITIES AT OIL AND GAS GATHERING AND TRANSPORTATION STATIONS

Qingqing Xu [1], Yichen Huang [2], Xuan Zhang [3], Ge Chen [4], Shaohua Dong [5], Yi Shuai [6]

[1] *College of Safety and Ocean Engineering, China University of Petroleum (Beijing), Beijing, China, 102249; China Academy of Work Safety Sciences, Beijing, China, 100012. Email: xuqq@cup.edu.cn*
[2] *Xi'an Jiaotong University, Shanxi, China, 710049. Email: 2440735253@qq.com*
[3] *College of Safety and Ocean Engineering, China University of Petroleum (Beijing), Beijing, China, 102249. Email: 1617955165@qq.com*
[4] *Hubei Yiwei Power Co., LTD, Hubei, China, 448000. Email: 1244709682@qq.com*
[5] *College of Safety and Ocean Engineering, China University of Petroleum (Beijing), Beijing, China, 102249. Email: shdong@cup.edu.cn*
[6] *College of Safety and Ocean Engineering, China University of Petroleum (Beijing), Beijing, China, 102249. Email: yshuai@cup.edu.cn*

ABSTRACT

Leakage of key equipment in oil and gas gathering and transportation stations may trigger major accidents such as fires and explosions, making risk assessment crucial for ensuring safe production. This paper proposes an integrated risk assessment method based on event tree analysis and numerical simulation to quantify the probability and impact range of leakage accidents. First, an event tree analysis is used to establish a leakage failure mode model, identifying pool fires and vapor cloud explosions (VCEs) as the primary accident types and calculating their occurrence probabilities under different leakage scenarios. Next, PyroSim and ALOHA software are employed to simulate accident progression, quantitatively analyzing hazard parameters such as thermal radiation and overpressure to determine the affected zones. Finally, combining failure probability and severity of consequences, a risk assessment matrix for critical equipment leakage at oil and gas gathering and transportation stations was constructed to enable dynamic assessment of risk levels. The research results indicate that the proposed risk assessment method can quantify the probability of leakage accidents and their potential consequences, providing reliable decision support for risk prevention and control of critical equipment leakage at oil and gas gathering and transportation stations.

Keywords: Oil and gas gathering and transportation stations; Quantitative risk assessment; Key equipment leakage; Numerical simulation

I. INTRODUCTION

With the rapid development of oil and gas pipeline construction in China, oil and gas gathering and transportation stations, as critical nodes in energy transmission, face significant challenges in ensuring safe operation. These stations, characterized by the handling of flammable and explosive media, complex process flows, and densely arranged equipment, pose significant accident risks.

Currently, risk assessment of key equipment at oil and gas gathering and transportation facilities primarily relies on traditional methods such as fault tree analysis (FTA) [1], fuzzy comprehensive evaluation (FCE) [2], Layer of Protection Analysis (LOPA) [3], and Hazard and Operability Analysis (HAZOP) [4]. While these methods are effective for static risk assessment, they have significant limitations: they struggle to reflect the dynamic interactions between system elements and the real-time propagation of risks, and they cannot assess the cascading loss effects triggered by a single event.

To overcome these limitations, this study innovatively proposes an event tree-failure simulation model. By analyzing the leakage model, the leakage size and leakage rate can be determined, and the probabilities of various failure consequences can be calculated, enabling a quantitative analysis of the overall risk level. This assessment framework can accurately quantify the consequences of accidents and achieve a comprehensive assessment of risk levels.

II. LEAKAGE FAILURE ANALYSIS OF KEY FACILITIES AT OIL AND GAS GATHERING AND TRANSPORTATION STATIONS

II.A. Station Key Equipment Leakage Event Tree

Leaks in critical equipment at oil and gas gathering and transportation stations facilities are categorized into four types: process equipment leaks, pipeline connection leaks, pipeline rupture leaks, and pipeline perforation leaks. Oil and gas gathering and transportation facilities primarily include equipment such as oil-gas separators, heaters, crude oil electrostatic dehydrators, towers, pumps, valve assemblies, pipelines, temperature gauges, and pressure gauges. These devices and instruments are connected via flanges, threads, or welds. The most common locations for leaks are static seals, such as flanges and threaded joints.

Based on whether the critical equipment ignites after a leak, whether it ignites immediately, and the speed of the flame front, several different failure consequence patterns are obtained, and a failure consequence event tree model for critical equipment at the station is established, as shown in Fig. 1.

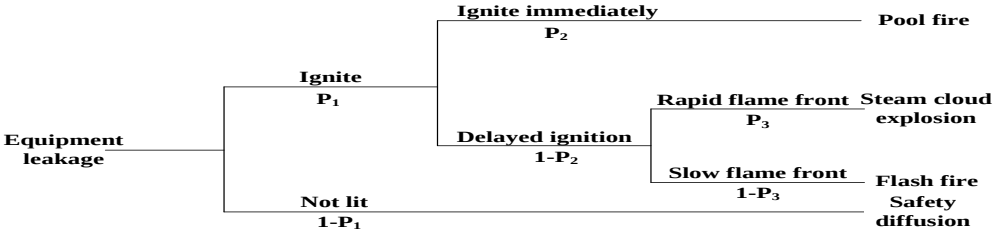

FIGURE 1. Event Tree Model for the Consequences of Failure of Key Station Equipment

II.B. Analysis of the Consequences of Leaks in Key Station Facilities

II.B.1 Leakage Model Analysis

(1) Determine leak size and leak rate

Leakage size is categorized into four types in API 581[5], the state of oil in the gathering station field is generally liquid, so the Bernoulli equation is utilized to obtain the formula for calculating the leakage rate of the liquid, as in Eq. (1).

$$Q = C_d A \rho_1 \sqrt{\frac{2(p_s - p_0)}{\rho_1}} \tag{1}$$

Where Q is the liquid leakage rate, kg / s; C_d is the aperture leakage coefficient, ranging from 0.61 to 0.65; A is the leakage aperture area, m^2; ρ_1 is the liquid density, kg/m^3; p_s is the medium pressure in the container, Pa; p_0 is the atmospheric pressure, Pa.

(2) Calculate the upper limit of total leakage

The upper limit of leakage of key equipment in the station needs to be determined by considering the total amount of media in the equipment subsystem and the amount of replenishment that the subsystem can obtain from other places when leakage occurs[6].

II.B.2 Probability of Failure Occurrence

(1) Probability of immediate versus delayed ignition

According to API581, the probability of ignition of a liquid at room temperature can be calculated according to Eq. (2).

$$P_{1,a} = \begin{pmatrix} 1.00982 - 0.70372 \cdot \ln \mathrm{M} - 0.013045 \cdot \ln(C_1 \cdot Q) + 0.18554 \cdot \ln(\mathrm{M}^2) - \\ 0.0014619 \cdot \ln(C_1 \cdot Q)^2 + 0.022131 \cdot \ln \mathrm{M} \cdot \ln(C_1 \cdot Q) - 0.016572 \cdot \ln \mathrm{M}^3 + \\ 0.00011281 \cdot \ln(C_1 \cdot Q)^3 + 0.00050697 \cdot \ln \mathrm{M} \cdot \ln(C_1 \cdot Q)^2 - \\ 0.0035535 \cdot \ln \mathrm{M}^2 \cdot \ln(C_1 \cdot Q) \end{pmatrix} \tag{2}$$

Where $P_{1,a}$ is the probability of ignition under specific temperature conditions; M is the relative molecular weight of the leaking liquid, g/mol; Q is the leakage rate, kg/s ; C_1 is the constant, generally taken as 2.205.

If the current ambient temperature reaches the automatic ignition of the leaking substance, the ignition probability at this time reaches the maximum value of 1. Therefore, the ignition probability of the leaking substance at this time is determined according to Eq. (3).

$$P_1 = P_{1,a} + (P_{1,b} - P_{1,a}) \left(\frac{T_s - C_2}{T_b - C_2} \right) \tag{3}$$

Where P_1 is the ignition probability of the leaking liquid under the current operating conditions; $P_{1,b}$ is the ignition probability when the leaking ambient temperature reaches the ignition point; Ts is the current operating temperature, K; T_b is the automatic ignition point, K; C_2 is the constant, generally taken as 303.89.

According to the time of ignition can be divided into immediate ignition and delayed ignition, according to API581 it can be seen that the time of ignition is related to the leakage state of the leaking substance, the temperature of the leaking environment and the type of leakage, the probability of immediate ignition occurring when the leakage state is a liquid, P_2can be obtained by calculating in Eq. (4).

$$P_2 = P_{2,a} + (P_{2,b} - P_{2,a}) \left(\frac{T_s - C_2}{T_b - C_2} \right) \tag{4}$$

Where $P_{2,a}$ is the probability of immediate ignition; $P_{2,b}$ is the probability of ignition when the temperature of the leaking environment reaches the ignition point.

Therefore, the probability of a pool fire $P_{pool} = P_1 \cdot P_2$.

(2) The probability of vapor cloud explosion

It can be seen that after delayed ignition, when the flame front is fast, a vapor cloud explosion will occur, the probability of P_{VCE}. Like the pool fire, the probability of a VCE incident depends on the type of leakage and the fluid phase state.

Therefore, the probability of a vapor cloud explosion is $P_{\mathrm{VCE}} = P_1 \cdot (1 - P_2) \cdot P_3$.

II.B.3 Accident Hazard Consequences

(1) Pool fire hazard model

① Determine the radius of the liquid pool

Assuming that the liquid pool is a circular pool with a radius of *r*, when the hazardous area for the tank, according to the area of the liquid pool surrounded by the fire breakwater to determine its radius as shown in Eq. (5).

$$r = \left(\frac{S}{3.14} \right)^2 \tag{5}$$

② Determine the flame height

Assuming that the site is a windless environment, the application of Thomas empirical formula to calculate the flame height *H* as shown in Eq. (6).

$$H = 84r \left[\frac{dm/dt}{\rho_0 \sqrt{gr}} \right]^{0.61} \tag{6}$$

Where *H* is the combustion flame height, m; *r* is the leakage area pool radius, m; ρ_0 is the air density, generally taken as 1.293kg/m^3; g is the free-fall acceleration, generally taken as 9.8s/m^2; *dm/dt* is the combustion rate, $kg/(m^2 \cdot s)$, crude oil taken as 0.022 $kg/(m^2 \cdot s)$.

③ Determine the heat radiation flux

The total thermal radiation flux generated during the combustion of the liquid pool is *Q*, which is calculated by Eq. (7).

$$Q = \left[\left(\pi r^2 + 2\pi rH \right) (dm/dt) \eta H_c \right] / \left[72 (dm/dt) + 1 \right] \tag{7}$$

Where *Q* is the thermal radiation flux generated during combustion [7], W; H_c is the heat of combustion of the liquid, J/kg, typically taken as 4.954× 10^{7}J/kg for crude oil; η is the efficiency factor, typically in the range of 0.13 to 0.35.

④ Calculate the incident intensity

For the convenience of calculation, it is set that all the thermal radiation caused by combustion comes from the center of the liquid pool, then the incident intensity received by a certain location *x* away from the center of the liquid pool is I, which is calculated by Eq. (8):

$$I = Qt_c / 4\pi x^2 \tag{8}$$

Where *I* is the incident intensity, KW/m^2; t_c is the thermal conductivity [8], generally taken as 1; *x* is the the distance from the target point to the center of the liquid pool, m .

⑥ Consequences of fire

The consequences of a pool fire are mainly transmitted outward by thermal radiation, and the effects of different thermal radiation intensities on the surrounding personnel and equipment are different.

(2) Cloud explosion hazard model

When the vapors generated by the crude oil spill after diffusion, encountered a fire source to form a vapor cloud, when the vapor cloud combustion rate is relatively low, its pressure will not exceed 5KPa, the personnel and equipment will not have an impact, but the station is often a compact layout, in the small space, the pressure value rises rapidly.

Using the TNT equivalent method for the shock wave pressure caused by the VCE accident, the overpressure equation at *r* from the explosion center is as follows:

$$P = 0.145 e^{9.097 - \sqrt{25.13 \ln\left(\frac{0.397r}{m_{TNT}^{1/3}} \right) - 5.267}} \tag{9}$$

Where *P* is the shock wave overpressure value, MPa; *r* is the target point to the explosion center distance, m; m_{TNT} is the equivalent TNT mass, kg. where m_{TNT} is calculated according to Eq. M_C is calculated using Eq.

$$m_{TNT} = 2.07\times10^{-7} Y_f M_c H_c \tag{10}$$

$$M_c = \frac{Q_c}{u_a} min\left(x_c, u_a t_a\right) \tag{11}$$

Where Y_f is the yield factor, taken as 0.03; M_C is the total mass of combustible gas in the cloud, kg; Hc is the heat of combustion of gas, J/kg; Q_c is the equivalent release rate, kg / s; x_c is the limit of combustible gas diffusion distance, m; u_a is the wind speed, m/s.

Vapor cloud explosion are generally in the form of shock waves affecting people and the surrounding environment, the impact of the shock wave range of influence according to the shock wave overpressure damage guidelines.

II.B.4 Accident Damage Area Size

According to the event tree analysis of the consequences of key equipment failure at the oil and gas gathering station site shown in Fig. 2, the integrated area of personnel casualties and the integrated area of equipment damage are S_p and S_s, respectively, which can be obtained by probability-weighted summation according to the occurrence of pool fires and the area of VCE hazards as shown in Eq. (12) and Eq. (13).

$$S_P = P_{pool} S_{pool,P} + P_{\mathrm{VCE}} S_{VCE,P} \tag{12}$$

$$S_s = P_{pool} S_{pool,S} + P_{\mathrm{VCE}} S_{VCE,S} \tag{13}$$

Where S_p is the total area of casualties, m ^{2}; $S_{pool,P}$ is the area of casualties caused by the pool fire area, m ^{2}; $S_{vce,P}$- is the area of casualty area due to VCE, m^2; S_s is the total area of equipment damage area; $S_{pool,S}$ is the area of equipment damage area due to pool fire, m^2; $S_{vce,S}$ is the area of equipment damage area due to VCE, m^2.

III. RISK ASSESSMENT OF LEAKAGE FAILURE OF KEY FACILITIES AT STATIONS

III.A. Quantification of Failure Consequences

Leaks, fires, or explosions involving critical equipment at oil and gas gathering and transportation stations will inevitably result in casualties and property damage. The losses incurred are as follows[9]:

$$t_s = 10^{1.242+0.585\cdot\lg\left[S_s/\left(6.21410^2\right)\right]} \tag{14}$$

Thus, the total economic loss is C , which is expressed in Eq. (15).

$$C = \rho_s \cdot S_s + t_s \cdot D \tag{15}$$

Where ρ_s is the equipment failure around the property density, million yuan / m ^{2}; D is the number of days of production interruption losses due to fire and explosion accidents, days.

III.B. Risk Matrix Establishment

A risk matrix is a tool used to assess and categorize risks. It usually consists of two axes, one representing the probability of failure and the other the severity of the consequences of failure. By cross-combining the probability of failure and the consequences of failure in a matrix, different levels of risk ratings are formed to better identify high-risk areas and prioritize issues.

Based on the failure assessment of a certain oil and gas gathering and transportation station, the maximum quantified failure value is 15 million yuan. Taking every 3 million yuan as one level, the failures are classified into five levels, as shown in Table I.

TABLE I. Classification of Failure Consequences

Classification of failure consequences	Quantitative value of consequences (million yuan)	Remarks
A	0 - 3	The loss is very small and the resulting impact is not serious
B	3 - 6	There is some equipment damage, minor casualties
C	6 - 9	There are casualties and more serious equipment damage
D	9 - 12	With more serious casualties and serious equipment damage
E	12 - 15	With serious personnel casualties and serious equipment losses

Combined with the probability of failure, the final risk matrix of oil and gas gathering and Transportation Stations are shown in Table II.

TABLE II. Risk Matrix of Oil and Gas Gathering and Transportation Stations

Risk evaluation matrix		Failure consequence level				
		A	B	C	D	E
Failure Probability	$0\text{-}10^{-5}$					
	$10^{-5}\text{-}10^{-4}$					
	$10^{-4}\text{-}10^{-3}$					
	$10^{-3}\text{-}10^{-2}$					
	$10^{-2}\text{-}1$					

In Table II, the green zone is classified as Risk Level I, indicating a low-risk condition under which the facility can operate normally. The blue zone corresponds to Risk Level II, representing a relatively low-risk state where normal operations are possible, but heightened vigilance and preventive measures are required. The yellow zone is designated as Risk Level III, reflecting a moderate risk level; the facility remains operational, though certain areas have already exhibited significant issues. The orange zone is categorized as Risk Level IV, indicating a relatively high-risk condition where most systems within the station are no longer functional. The red zone is assigned Risk Level V, denoting a high-risk state in which the Oil and gas gathering and transportation stations are largely inoperable and immediate control measures must be taken.

IV. CASE STUDY - RISK ANALYSIS OF LEAKAGE FAILURE OF KEY FACILITIES AT AN OIL AND GAS GATHERING AND TRANSPORTATION STATION

Given that the failure of critical equipment poses the most significant risk to the functioning of the oil and gas gathering and transportation station, this section presents an analysis of the leakage failure risk of such equipment.

IV.A. Calculation of Failure Consequences

(1) Determine the leakage rate and the total amount of leakage

When the aperture leakage is 5mm, the system pressure is 0.1MPa, the leakage rate Q = 0.74kg / s, the total amount of leakage W = 967.5kg, calculated by Eq. (1).

(2) Determine the probability of occurrence of various types of consequences

According to Section *II.B.2*, we can get P_{pool}= 0.016, P_{VCE}= 0.001.

IV.B. Calculation of Impact Scope

The PyroSim software was used to simulate the consequences of a pool fire caused by a crude oil leak from key equipment, and five thermocouples with a spacing of 0.5 were set up on the centerline of the simulation area. The basic parameters of the leakage medium used in the simulation are shown in Table III, combined with the previous calculations, are used to simulate the consequences of failure when the leakage aperture is 5mm. The simulation results are shown in Fig. 2.

TABLE III. Basic Parameter Table

Basic parameter	Numerical value	Basic parameter	Numerical value
Heat of combustion (KJ/kg)	49540	Density (Kg/m^3)	890
Burning rate ($kg/(m^2\text{-}s)$)	0.045	Hydrocarbon ratio	0.43
Boiling point (℃)	200	Relative Density (Kg/m^3)	0.75~0.95
Constant pressure specific heat (KJ/(kg-k))	2.4	Heat of vaporization (KJ/kg)	350
Molarity (g/mol)	290	Explosive limit (ppm)	41.24%-141.01
Amount of substance (m^3)	530		

From the analysis of Fig. 2, it is concluded that the maximum temperature at the center of the flame produced by the leakage combustion can reach 900°C, and the temperature radiated to the outside is around 300°C.

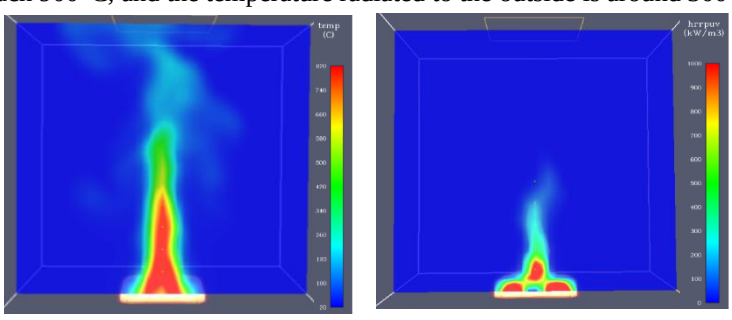

1) Temperature 2) Heat release rate per unit area

FIGURE 2. Simulated Pool Fire Aftermath Diagram

Fig. 3 shows the concentration of CO and O_2in the air during the simulated 10s.

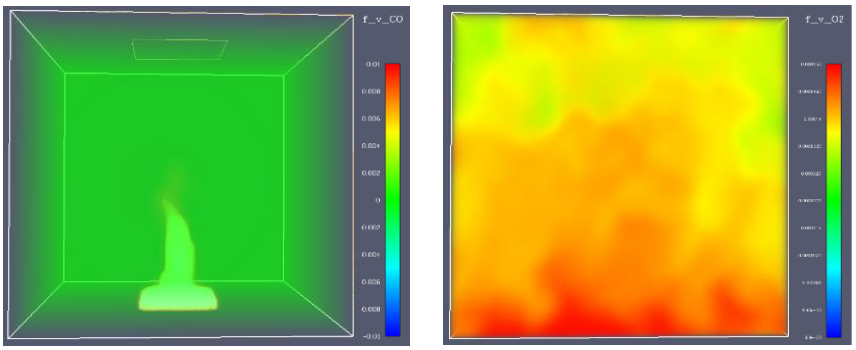

1) CO_2 concentration 2) CO concentration

FIGURE. 3 The Change of Gas Concentration After Pool Fire Combustion

Fig. 4 and 5 show the heat release rate per unit area and heat flux, respectively. It can be analyzed from the figure that the highest value of heat release rate per unit area of combustion reaches 1257KW/s, and the highest value of heat flux reaches 936KW.

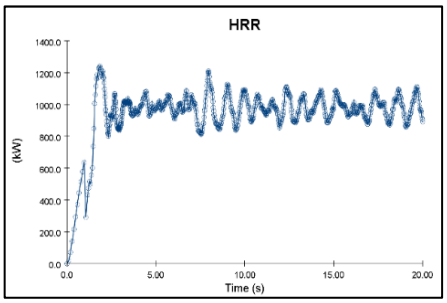

FIGURE. 4 Heat Release Rate per Unit Area

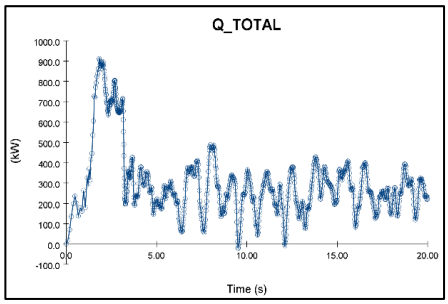

FIGURE. 5 Change in Heat Flux

The VCE accident is simulated using ALOHA software. The parameters of the simulation scenario are set as follows: southeast wind speed 5m/s, measurement height 3m, cloudiness 20%, humidity 25%, ambient temperature 15℃, tank diameter 16m, height 10m, tank capacity 70%, leakage hole diameter 5mm, leakage height 3m.

If crude oil leakage is not immediately ignited, it will form a vapor cloud. When the vapor cloud accumulates to a certain concentration in the air, it will explode upon encountering an ignition source, as shown in Figure 6. This is the flammable zone of the vapor cloud when the leakage diameter is 5 mm. The impact range of the vapor cloud explosion can reach 390 meters, and the dispersion range of toxic fumes is 2,655 meters.

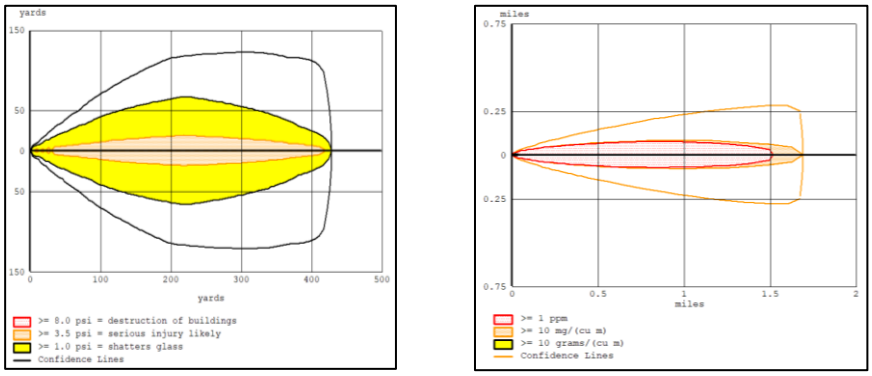

1) The explosive range of vapor cloud explosion 2) Toxic gas dispersion range

FIGURE. 6 Range of Vapor Cloud Explosion Consequences

The casualty and equipment damage areas from pool fire and VCE were obtained using Eq. (3) - Eq. (9) and simulations from PyroSim and ALOHA, as shown in Table IV.

TABLE IV. Area of Casualties and Equipment Damage

Pool fire hazard area/m^2		Vapor cloud explosion hazard area/m^2	
$S_{pool,P}$	$S_{pool,S}$	$S_{VCE,P}$	$S_{VCE,P}$
92.06	31.87	189.31	106.94

TABLE V. Different Leakage Aperture Damage Area

Leakage aperture size	Personnel casualty area S_P/m^2	Equipment damage area S_s/m^2
5mm	1.66	0.62
25mm	21.78	8.34
140mm	190.90	54.04

From Eq. (12) - Eq. (13), *the* S_P and S_s of the crude oil dewatering station can be obtained when the leakage aperture diameter is 5mm, and similarly, *the* S_P and S_s of the leakage aperture diameters of 25mm and 140mm can be obtained according to the above steps, as shown in Table V.

According to API581 failure database, it is known that the ratio of the occurrence of three kinds of leakage apertures is 4:10:1, so according to Eq. (10) and Eq. (11), it can be obtained that the leakage from critical equipment leads to casualty area S_P=27.68m^2, and the area of equipment damage Ss=9.32m^2.

IV.C. Quantification of Failure Consequences

Utilizing the same process and calculation method, the quantified values of the consequences of several other moments are calculated, but due to some changes in the influencing factors at different moments, the results need to be corrected, and according to the empirical method, the corrected results are shown in Table VI. According to the corrected results, the total economic loss of each moment is obtained as shown in Table VII.

TABLE VI. Consequence Value Correction Table

Correction factor	Moment	Before correction	After correction	Correction Factor	Moment	Before correction	After correction
Leakage rate (kg/s)	t_1	0.76	0.77	Casualty area (m^2)	t_1	28.34	29.65
	t_2	0.80	0.79		t_2	29.57	30.91
	t_3	0.79	0.80		t_3	30.48	30.36
	t_4	0.82	0.80		t_4	29.66	30.14
	t_5	0.84	0.79		t_5	30.76	29.95
	t_6	0.83	0.78		t_6	31.25	28.73
	t_7	0.82	0.78		t_7	29.68	26.64
	t_8	0.79	0.77		t_8	27.63	25.38
	t_9	0.78	0.76		t_9	26.47	24.87
Total amount of leakage (kg)	t_1	970.8	971.1	Equipment damage area (m^2)	t_1	10.24	11.24
	t_2	974.3	973.4		t_2	11.92	10.87
	t_3	972.6	972.6		t_3	10.34	10.51
	t_4	977.2	972.5		t_4	9.76	10.03
	t_5	973.4	971.8		t_5	9.14	9.44
	t_6	971.4	971.4		t_6	8.94	8.76
	t_7	970.5	969.3		t_7	8.39	8.23
	t_8	969.8	967.1		t_8	9.57	7.68
	t_9	965.7	965.4		t_9	9.05	7.14

TABLE VII. Table of Total Economic Losses at All Times

Table of total economic losses at all times	t_0	t_1	t_2	t_3	t_4
Total Economic Loss (million dollars)	452.59	498.64	512.76	501.95	494.71
Moment	t_5	t_6	t_7	t_8	t_9
Total Economic Loss (million dollars)	477.32	458.86	437.65	409.78	376.65

IV.D. Determination of Failure Consequence Levels

According to the risk consequence level in Table I, the economic loss of each moment in the table is represented in the risk radar diagram as shown in Fig.7.

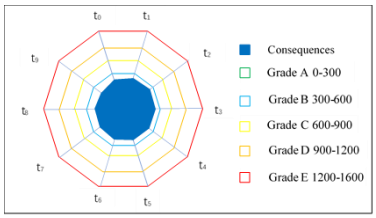

FIGURE. 7 Failure Consequence Level Diagram

V. COMPREHENSIVE RISK LEVEL

According to the risk matrix in Table. II, the comprehensive risk levels at various times for leaks from key equipment at a certain oil and gas station are shown below.

TABLE VIII. Comprehensive Risk Level at All Times

Moment	t_0	t_1	t_2	t_3	t_4
Risk level					
Moment	t_5	t_6	t_7	t_8	t_9
Risk level					

From Table VIII, it can be seen that the risk level of the first two moments is III, which is in medium risk, and the other moments are II, which is in lower risk, and with the change of time, the risk value is decreasing.

VI. CONCLUSION

(1) Establish an event tree model based on the ignition conditions following key equipment leakage, identifying failure modes such as pool fires and vapor cloud explosions. Analyze the leakage size and rate in accordance with API 581 standards, establish a quantitative calculation model, quantify the accident damage area and economic losses to personnel, and establish a risk evaluation matrix.

(2) Taking a 5mm leak diameter as an example, the leak rate W is calculated to be 967.5 kg/s, with a pool fire probability of 0.016 and a P_{VCE} probability of 0.001. Using PyroSim and ALOHA software to simulate the accident impact range, the comprehensive risk levels at each time point in the key facility leak are determined based on the probability and consequence quantification results, achieving dynamic risk level evaluation for the key facility.

ACKNOWLEDGMENTS

This paper is supported by the China National Petroleum Corporation (CNPC) Science and Technology Project (No. 2023DJ6508) and the China Petroleum Science and Technology Innovation Fund (No. 2021DQ02-0801).

REFERENCES

[1] X. Diao, J. Jiang, A. Mebarki, L. Ni, Y. Duo, S. Chen, Y. Wang, S. Zhang, Risk analysis of domino effect of leakage accident of petrochemical pipeline based on analytic hierarchy process and fuzzy fault tree analysis, Safety Science, 187 (2025) 106852-106852.
[2] A. Fetanat, M. Tayebi, Evaluation of carbon capture technologies in the oil and gas industry using a socio-technical systems perspective-based decision support system under interval type-2 trapezoidal fuzzy set, Digital Chemical Engineering, 12 (2024) 100164-.
[3] M. Ganaadhiban, J. Arunshankar, R. Venkataraman, K. Srinivasan, Hazard evaluation and safety assessment for subsea HIPPS, Process Safety Progress, 42 (2023) 772-781.
[4] L. Xinhong, M. Jie, P. Hans, Z. Renren, Dynamic risk investigation of urban natural gas pipeline accidents using Stochastic Petri net approach, Process Safety and Environmental Protection, 178 (2023) 933-946.
[5] G. He, P. Jiang, K. Liao, L. Sun, H. Qian, Y. Gu, B. Huang, A data-driven method for pipeline inhibition efficiency prediction and risk assessment based on MPF-GCA-FPT-FRA approach, Process Safety and Environmental Protection, 197 (2025).
[6] K. Zhou, Q. Zhou, X. Wang, W. Wang, Z. Rui, J. Yang, Hydrogen jet fire due to high-pressure pipeline leakages in pits, Process Safety and Environmental Protection, 200 (2025) 107362-107362.
[7] D.G.S. Prayoga, D. Priyanta, N. Siswantoro, Comparative Analysis of Probability of Failure Determination Using Weibull Distribution and Generic Failure Frequencies on Heat Exchanger Tube Bundles Based on API 581, International Journal of Marine Engineering Innovation and Research, 2 (2018).
[8] D.J. M., Z.H. M., D.Z. X., C. M., D.L. B., Simulation and Optimization for Oil and Gas Platform Placement in Mountainous Regions, International Journal of Simulation Modelling, 24 (2025) 297-308.
[9] C.S. Chun, C.J. Boong, H.I. Ju, Development of Risk-Based Inspection(RBI) Technology for LNG Plant Based on API RP581 Code, Corrosion Science and Technology, 11 (2012) 179-183.

Monte Carlo simulation for evaluating the efficiency of an HPGe detector

Munkhsaikhan Jargalsaikhan[1], Jamiyansuren Terbish[1]*
[1]*Nuclear Research Center, National University of Mongolia, Ulaanbaatar 13330, Mongolia*
Email: t.jamiyansuren@.num.edu.mn*

EXTENDED ABSTRACT

For research in radiation ecology, nuclear geochemistry, and radiation public health, it is essential to precisely determine the specific activity of natural and artificial radioactive isotopes/radionuclides in environmental samples (such as soil, water, air, and mountain rocks), mineral raw materials (including coal, uranium ore, and fertilizers), building materials, and food products. One of the most widely used techniques for measuring the amount and content of radioactivity is the gamma spectrometer, which determines radioactivity by detecting the photons emitted from a sample [1]. Its major advantages are being non-destructive, used for multi-element analysis, and simplified regarding sample preparation, i.e. mostly no need for any radiochemical separation processes [2,3]. In particular, precise detection and quantification of radionuclide activity are essential for reliable risk assessment and radiation safety management. Even small errors in determining radionuclide activity can lead to significant discrepancies in radiation dose estimates, affecting public health assessments and regulatory decisions. By ensuring accurate detector efficiency calculations, this work supports enhanced radiation protection strategies, enabling more reliable risk assessments and more effective public health protection measures.

In previous work [4], the absolute method of efficiency for determination of gamma-emitting radionuclides in the volume samples using gamma spectrometry was described. The chemical composition, gamma-ray attenuation coefficient, measurement geometry, density of the unknown sample and the standard sample need to be identical. Practically, the problem of preparing a standard sample that meets these conditions for each unknown sample is very complex. In particular, there are very limited food-based gamma standards available for purchase, and they are high in cost [5,6]. Therefore, an absolute method of gamma spectrometry has been developed to determine the detector efficiency for samples with a certain volume and density.

This study aims to accurately simulate the detector efficiency by modeling the actual experimental setup, with a particular focus on computational methodology. In the absence of calibration standards for varying geometries and densities, our approach offers an alternative for evaluating detector characteristics under real conditions. For the first time, detector efficiency was determined through a combination of simulations and experimental measurements. A standard Marinella beaker with a fixed volume was used in the experiment. By enclosing the detector over the entire surface, we increased the probability of detecting low-energy photons. Maintaining a constant sample position also improved the comparability between experimental and simulated results. We used the PHITS [7] code version 3.29 based on the Monte Carlo method developed by the Japan Atomic Energy Agency (JAEA), which simulates particle interactions randomly. The PHITS code demonstrates exceptional capabilities and is widely utilized across various fields. The research study on estimation of the detection efficiency of a gamma spectrometer equipped with a HPGe semiconductor detector was performed using a standard sample containing radioactive nuclides packed in a Marinelli beaker and calibration point source. Meanwhile, we determined values of energy resolution, a crucial part of the detector specifications. This research study is significantly important for further study to evaluate characteristics of the detector by computational analysis.

EXPERIMENTAL MEASUREMENT

Measurements were performed with a coaxial ORTEC GEM series HPGe coaxial detector system, DSpec-LF multichannel analyzer (up to 16384), lead shield and GammaVision program. The detector geometry is shown in Figure 1 provided by the manufacturer.

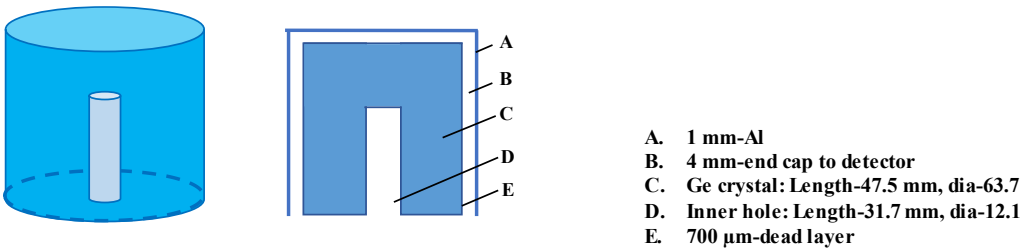

Figure 1. The geometric dimensions of the coaxial HPGe detector

The resolution is 0.85 keV at an energy of 122 keV (^{57}Co). The method of calculation included a Marinelli beaker standard and calibration point source. We utilized the 500 mL Marinelli beaker standard (No.1480-19-4) with multi-nuclide distributed in 0.65 g/cc epoxy matrix and the reference date was 01 Sep 2010.

The Particle and Heavy Ion Transport System (PHITS) calculates the interaction of all particles in the wide energy ranges based on the Monte Carlo method. The PHITS has been extensively applied in many fields including radiation protection, nuclear medicine, basic theoretical research, space science and environmental radiation research [8]. A T-deposit tally can be used to obtain accumulated energy in certain region and is suitable for estimating the detector responses. Specifically, this mode is capable for estimating the detector responses of semi-conductor devices, and it requires the setting of parameters to accurately represent the detector resolution.

RESULTS

We used PHITS version 3.29 to determine the detector efficiency. In the T-deposit tally, we have to set the width of the energy bin at 0.2 keV, the same as the HPGe detector used for experimental measurements. For the purpose of ensuring that the relative error would be less than one percent, the historical number 1 million and the batch number 500 were chosen. The calculation was performed in the three-dimensional coordination. Figure 4 depicts the process by which the PHITS was able to create a measurement configuration for a volume source. The results of the PHITS calculation for the Marinelli beaker standard, are the deposited gamma energies of ^{137}Cs and ^{60}Co isotopes. Figure 5 illustrates the comparison between the pulse height of the PHITS calculation and the measurement spectrum from the HPGe detector. We can indicate the values of efficiency for each position of the detector in Table 4 with the following high intensity gamma energies. The measured results at distances of 5, 10, and 15 cm in Figure 9 show that the efficiency decreases significantly as the distance increases.

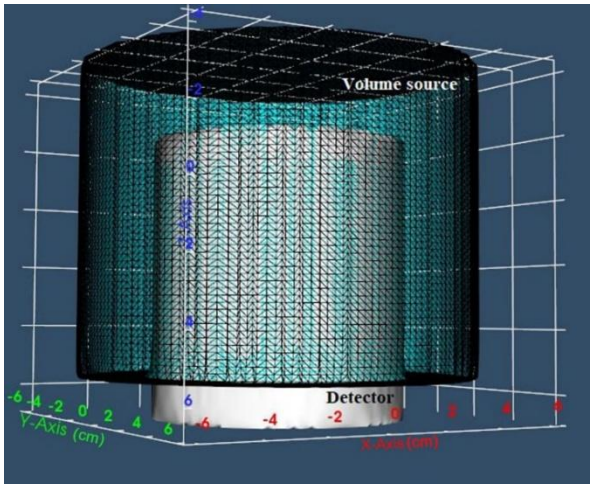

Figure 4. The three-dimensional geometry of the volume source and the detector was generated by PHITS.

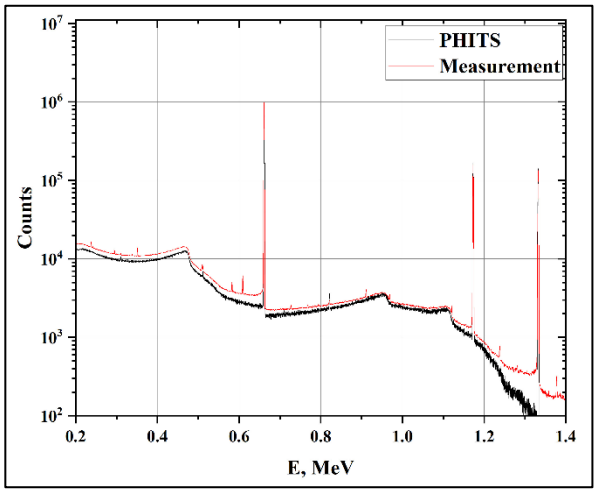

Figure 5. The gamma-ray spectrum from a certified standard volume source compared with the PHITS result

Table 4. Comparison of the detector efficiencies for a point source

E_γ (MeV)	Efficiency					
	(measured)			(calculated)		
	5cm	10cm	15cm	5cm	10cm	15cm
0.121	0.0311±0.0029	0.0116±0.0008	0.0057±0.0003	0.0320	0.0121	0.0061
0.245	0.0223±0.0021	0.0090±0.0006	0.0046±0.0002	0.0234	0.0092	0.0048
0.344	0.0154±0.0015	0.0062±0.0004	0.0031±0.0002	0.0163	0.0065	0.0034
0.778	0.0077±0.0007	0.0028±0.0002	0.0014±0.0001	0.0084	0.0033	0.0018
0.964	0.0063±0.0006	0.0025±0.0002	0.0012±0.0001	0.0069	0.0027	0.0014

0.1112	0.0057±0.0005	0.0022±0.0001	0.0011±0.0001	0.0061	0.0025	0.0013
0.1408	0.0045±0.0004	0.0018±0.0001	0.0009±0.0001	0.0047	0.0019	0.0010

CONCLUSION

In this work, the efficiency of a gamma spectrometer with a germanium detector was calculated by the PHITS code in a wide energy range. The T-deposit tally of the PHITS code was applied to obtain the accumulated energy in the detector region. The comparison of calculations and measurements was performed using the Marinelli beaker containing a homogeneous mixture of radioactive isotopes, and a ^{152}Eu point source. The results indicate that the PHITS code effectively simulates both source and detector responses, and quantifies the agreement between simulated and measured data. We aimed to validate the results by carrying out another measurement of the point source. It has been confirmed for detector response to photon energy ranges of 0.0–3.2 MeV compared to the measured one. Practically, we analyze a large volume of environmental samples, some factors were neglected for the point source. However, uncertainty of independent parameters was accounted for. Therefore, it can yield excellent results in terms of the detector efficiencies within that energy range. This work has significant implications for risk assessment, radiation safety, and management in environmental monitoring and nuclear industries. By providing insights into detector performance, it supports the enhancement of radiation protection strategies and the optimization of radiation safety protocols. Despite these advancements, limitations exist, such as the simplified modeling of point sources. Future research should address these limitations by including more detailed simulations of diverse radiation sources and energy ranges, along with exploring the application of this approach to real-world environmental monitoring and risk mitigation.

REFERENCES

[1] Encyclopedia of Analytical Science. 2nd edition. 2004
[2] A.E.M. Khater, Y.Y. Ebaid, A Simplified gamma-ray self-attenuation correction in bulk samples, Applied Radiation and Isotopes, vol.66, Issue 3, 2008, p.407-413
[3] M.J. Vargas, A.F. Timón, N.C. Díaz, D.P. Sánchez, Monte Carlo simulation of the self-absorption corrections for natural samples in gamma-ray spectrometry. Applied Radiation and Isotopes, vol.57, 2002, p.893-898.
[4] N. Norov et al., The absolute method for study of volume samples using Gamma Spectrometry, Scientific Transaction of the National University of Mongolia. Physics, 4(137), 62–67.
[5] C. Rolle, Z. Lin, S. Healey, Computational Approaches on Photon-Attenuation and Coincidence-summing Corrections for the detection of gamma-emitting radionuclides in foods. Applied Radiation and Isotopes, 126, 2017, p.134–137.
[6] A. Azbouche, M. Belgaid, H. Mazrou. Monte Carlo calculations of the HPGe detector efficiency for radioactivity measurement of large volume environmental samples, Journal of Environmental Radioactivity, vol.146, 2015, p.119-124.
[7] Tatsuhiko Sato, Features of Particle and Heavy Ion Transport Code System (PHITS) version 3.02, Journal of Nuclear Science and Technology, vol.55, Issue 6, p. 684-690
[8] T. Furuta, T.Sato, Medical Application of Particle and Heavy Ion Transport Code System PHITS, Radiological Physics and Technology, vol.14, 2021.

ASRAM2025
www.asram2025.org
Asian Symposium on Risk Assessment and Management 2025
Pattaya, Thailand, 27 – 29 August 2025

Preliminary Risk Assessment of Nuclear Security Considering the Potential for Future SMR Developments in Thailand

Piyawan Krisanangkura[1]

[1] *Office of Atoms for Peace: 16 Vibhavadi-Rangsit Rd., Ladyao, Chatuchak, Bangkok, 10900*
piyawan.k@oap.go.th

EXTENDED ABSTRACT

Thailand is exploring the development of Small Modular Reactors (SMRs) to diversify energy sources and meet growing sustainability demands. As part of this process, it is essential to assess and mitigate the security risks related to transportation, operation, and storage of nuclear materials, as well as the protection of reactor facilities. This report examines the current nuclear security landscape in Thailand, identifies key challenges, and offers practical recommendations to strengthen nuclear security for the potential deployment of SMRs. The two primary areas addressed are the policy and regulatory framework and personnel-related risks, both of which are crucial for ensuring a robust nuclear security system. The study concludes with recommendations aimed at addressing existing gaps and enhancing the sustainability of current security measures. Key proposals include aligning the regulatory framework with international standards, strengthening personnel training and risk management, and integrating advanced technologies to secure nuclear materials. Furthermore, strategies are outlined to improve and maintain long-term protection and resilience. Special attention is given to optimizing existing human resources and fostering institutional collaboration, alongside a training framework that supports technical competence across relevant stakeholder groups. The report aims to assess Thailand's readiness for nuclear security in the context of potential SMR development.

- **Key Risk Areas Identified**

The preliminary risk assessment highlights several nuclear security challenges associated with future SMR deployment. These include gaps in current policies and regulations—particularly the lack of SMR-specific provisions—along with a shortage of personnel trained in nuclear security. Additionally, coordination between safety and security authorities remains limited. Cybersecurity threats and the potential for insider actions, particularly with the adoption of digital systems, are also growing concerns. Transport vulnerabilities—such as the physical protection of nuclear and radioactive materials—further emphasize the need for targeted and systemic improvements.

- **Human Resource Risk & Competency Matrix**

TABLE I. Nuclear Security Competency Matrix

Role	Core	Safety	Security	Target Audience / Stakeholders	IAEA Ref.
Regulator	Legal, inspection	Licensing review	Physical-protection oversight	OAP, Energy regulators	NSS 20[1], GSR-Part 1[2]
Operator	Basic radiation protection, culture, communications	Reactor O&M, nuclear safety	Insider threat, awareness on computer-based system for operation	Power utility operators, Plant Managers	NSS 11[3],13[4] 17[5]
Security Officer	Access control, communication	Evac & safety interface	Physical protection system, detection and assessment, cyber security	Facility-security teams	NSS 11[3], 13[4], 17 [5], 18[6], 33-T[7]
First Responder	Coordination	Dose limits	Threat response	Police, firefighters, medical team	NSS 11[3], 13[4]
RPO	Monitoring	Radiation protection	MORC/Illicit material	Health physics staff, environmental labs	GSG-7[8], NSS 14[9]
Maintenance	Preventive plan, system diagnostics	Calibration	Tamper detection, secure config	Engineers and technicians	NSS 1[10]
Transport	Route, transport plan	Packaging	Secure convoy	Land transport Dept., couriers, Customs	NSS 9[11], 46-T[12]

A critical priority is developing and sustaining human resource capacity. Rather than establishing entirely new security teams, Thailand could enhance efficiency by expanding the roles of existing safety personnel through additional training in security functions. This cross-functional approach supports better integration between safety and security responsibilities. It is equally important to strengthen inter-agency cooperation among regulatory bodies, operators, emergency responders, and law enforcement. A role-specific competency matrix based on IAEA guidelines has been developed to support training efforts as summarized in Table I. Currently, Thailand has collaborated with the World Institute for Nuclear Security (WINS) on a train-the-trainer program for transport security. In partnership with the Land Transport Department, this initiative aims to develop the first pilot training course that focuses on the interface between safety and security in dangerous goods transport, including radioactive and nuclear material.

CONCLUSION

SMR deployment requires a proactive approach to nuclear security risk assessment and workforce development. The integration of a role-specific competency matrix—built upon the utilization of current safety personnel—supports cost-effective and sustainable readiness. Strengthening inter-agency collaboration and aligning with IAEA guidelines will be essential to securing Thailand's future in nuclear energy.

ACKNOWLEDGEMENTS

The author would like to thank the Office of Atoms for Peace (OAP), the World Institute for Nuclear Security (WINS), and the Thailand Institute of Nuclear Technology (TINT) for their support, collaboration, and the opportunity to participate in the scientific event.

REFERENCES

[1] IAEA Nuclear Security Series No. 20: Objective and Essential Elements of a State's Nuclear Security Regime, 2013.
[2] IAEA General Safety Requirements Part 1 (GSR Part 1): Governmental, Legal and Regulatory Framework for Safety, 2016.
[3] IAEA Nuclear Security Series No. 11: Security of Radioactive Sources, 2009.
[4] IAEA Nuclear Security Series No. 13: Nuclear Security Recommendations on Physical Protection of Nuclear Material and Nuclear Facilities (INFCIRC/225/Rev.5), 2011.
[5] IAEA Nuclear Security Series No. 17: Computer Security at Nuclear Facilities, 2011.
[6] IAEA Nuclear Security Series No. 18: Nuclear Security Systems and Measures for the Detection of Nuclear and Other Radioactive Material out of Regulatory Control, 2013.
[7] IAEA Nuclear Security Series No. 33-T: Computer Security of Instrumentation and Control Systems at Nuclear Facilities, 2018.
[8] IAEA Safety Guide GSG-7: Protection of the Public against Exposure Indoors due to Radon and Other Natural Sources of Radiation, 2020.
[9] IAEA Nuclear Security Series No. 14: Nuclear Security Recommendations on Radioactive Material and Associated Facilities, 2011.
[10] IAEA Nuclear Security Series No. 1: Technical and Functional Specifications for Border Monitoring Equipment, 2006.
[11] IAEA Nuclear Security Series No. 9: Recommendations on the Physical Protection of Nuclear Material during Transport, 2008.
[12] IAEA Nuclear Security Series No. 46-T: Security of Nuclear and Other Radioactive Material in Transport, 2024.

ASRAM2025
www.asram2025.org
Asian Symposium on Risk Assessment and Management 2025
Pattaya, Thailand, 27 – 29 August 2025

Neutronic Analysis of PeLUIt Reactor with Heavy Metal Loading and Power Variations in the OTTO Refueling Scheme

Ahmad Muzaki Mabruri[1]*, Nuri Trianti[2], Zaki Su'ud[1,3], Dwi Irwanto[1,3], Topan Setiadipura[2]

[1]*Department of Nuclear Science and Engineering. Bandung Institute of Technology, Bandung, Indonesia*
[2] *Nuclear Reactor Technology, National Research and Innovation Agency (BRIN), Bandung, Indonesia*
[3] *Department of Physics, Bandung Institute of Technology, Bandung, Indonesia*

ABSTRACT

The PeLUIt reactor is a high-temperature reactor (HTR) of the pebble-bed type that uses helium coolant and is being developed by Indonesia to support energy independence based on the Net-Zero Emission principle. The reactor design began in 2015 as part of the National Medium-Term Development Plan to meet the increasing national energy demands in the electricity generation and industrial sectors. The latest PeLUIt design features a flexible operational power range between 5 MWt and 30 MWt and adopts the OTTO fuel-loading scheme. The PeLUIt is planned to use U-235 enrichment reduced from 17 wo% to 8–11 wo% to improve economic feasibility; however, this reduction leads to a decrease in fuel criticality. Since PeLUIt fuel pebbles are typically undermoderated, criticality can be enhanced by adjusting the Heavy Metal Loading (HML) per pebble. This study analyzes the neutronic performance of the PeLUIt using UO_2 fuel in pebble-bed design based on the commercial HML values of HTR-10 and HTR-PM. Optimization results indicate that a minimum U-235 enrichment of 16 wo% is required for both fuel specifications to achieve operational conditions with a burn-up of 80 MWd/kgHM at power variations of 10, 20, and 30 MW. Under standard 10 MW operation, the required refueling rate is 25 pebbles/day for HTR-10 fuel and 15 pebbles/day for HTR-PM. Additionally, the fissile plutonium production rate under all three optimum power conditions reaches approximately 1.35 grams/day for HTR-10 fuel and 1.43 grams/day for HTR-PM. Based on these results, HTR-10 fuel, with its lower heavy metal loading, is considered more efficient and economical for use in the PeLUIt reactor.

Keywords: HTR, Indonesia, OpenMC, Pebble-bed, PeLUIt.

I. Introduction

PeLUIt (Industrial Power and Steam Generator or *Pembangkit Listrik dan Uap Industri*) is an advanced generation reactor of the High Temperature Reactor (HTR) type that has been developed by Indonesia since 2015 and continues to be improved to this day. It serves as part of the implementation of Indonesia's National Medium-Term Development Plan to meet the growing national energy demand in both the power generation and industrial sectors. The development of this reactor is part of the national energy transition strategy and aims to support industrial downstreaming schemes based on the principle of net-zero emission [1], [2]. With the capability to operate at high temperatures above 900°C, the PeLUIt reactor is highly suitable for industrial applications and hydrogen production as a form of co-generation.

PeLUIt is designed as a High Temperature Reactor (HTR) with a pebble-bed fuel type, in which uranium dioxide (UO_2) fuel is encapsulated in TRISO (tristructural-isotropic) particles and formed into fuel pebbles. These pebbles are then loaded into the reactor core and undergo circulation during operation. This system allows for continuous fuel reloading, supporting long-term reactor operation. PeLUIt is planned to operate using a One-Through-Then-Out (OTTO) scheme, in which the fuel pebbles undergo burnup until reaching a certain threshold before being discharged from the reactor core ([3], [4]

The use of two types of commercial pebble-bed fuels previously applied in HTR-10 and HTR-PM reactors should be considered in the development of PeLUIt to achieve operational efficiency and economic viability. The HTR-10 reactor uses fuel with a heavy metal loading (HML) of 5 grams per pebble and a U-235 enrichment of 17 wo%, while HTR-PM uses a higher HML of 7 grams per pebble and a U-235 enrichment of 8.5 wo%. Although both are pebble-bed HTRs, differences in design, operational power, and fuel quantity result in non-uniform fuel specifications [5], [6]. PeLUIt itself is designed with a flexible power output ranging from 5 MW to 30 MW, making the selection of an appropriate fuel type critical to both reactor

performance and cost-effectiveness [7]. In addition, the availability and affordability of commercially supplied fuel are also important factors in ensuring long-term operational sustainability.

Research related to PeLUIt reactor fuel has been conducted from various perspectives in previous studies. A study by [8] indicated the potential to reduce both heavy metal loading (HML) and uranium enrichment levels without altering the reactor's operational specifications. This potential arises due to the under-moderated condition of the current fuel system. However, the reduction in U-235 content results in increased production of fission products such as plutonium and minor actinides (MA), which require particular attention in terms of safety and radioactive waste management. In response to these findings, a study by [9], developed an optimization approach by enhancing graphite moderation effects within the pebble fuel to compensate for reactivity loss due to the decrease in fissile material. This approach successfully maintained reactor performance comparable to standard PeLUIt fuel conditions and demonstrated the potential for reduced plutonium production as a fission byproduct. Additionally, [10], [11] indicated that PeLUIt's fuel reloading scheme could still be optimized, either through the OTTO approach or a multi-pass scheme, to achieve optimal performance across various operational aspects.

The latest PeLUIt design plans to use pebble fuel with U-235 enrichment reduced to around 8–11 wo% to improve economic feasibility by lowering uranium fuel costs. The reduction of fissile U-235 enrichment plays a crucial role because it directly affects total fuel expenses and supports more competitive reactor operation. However, lowering enrichment may reduce fuel criticality and shorten the operational lifetime [8], [9]. This research takes two existing commercial pebble fuels as references: the HTR-10 fuel, which originally used about 17 wo% U-235, and the HTR-PM fuel, which uses about 8 wo% U-235. This study evaluates and optimizes both fuel types by adjusting their enrichment, while keeping the original Heavy Metal Loading (HML) unchanged to ensure their suitability for PeLUIt operation. Since PeLUIt fuel pebbles are typically under-moderated, criticality can be improved by adjusting the Heavy Metal Loading (HML) per pebble, but the suitability of existing HML specifications must be assessed for compatibility with the PeLUIt reactor. Therefore, this study aims to identify and optimize two types of commercial pebble fuels from HTR-10 and HTR-PM reactors for application in PeLUIt under various operational power schemes using the OTTO method. Once the optimal design is determined, a neutronic performance and plutonium production analysis is conducted to assess efficiency, safety, and proliferation risk. Through this approach, the study is expected to provide recommendations for the most suitable pebble fuel specifications for PeLUIt, supporting the development of a more competitive, safe, and sustainable national HTR design.

II. Method

This study was conducted using a Monte Carlo method approach, based on criticality, burn-up, and depletion calculations using the OpenMC code. This code is an open source neutronic analysis tool that employs a constructive solid geometry (CSG) modeling system and is capable of calculating material interaction characteristics with neutrons and photons [12]. OpenMC has been widely used and verified for modeling and analyzing reactor designs such as MSRs, GFRs, PWRs, and several other reactor types efficiently [13], [14], [15], [16], [17], [18]

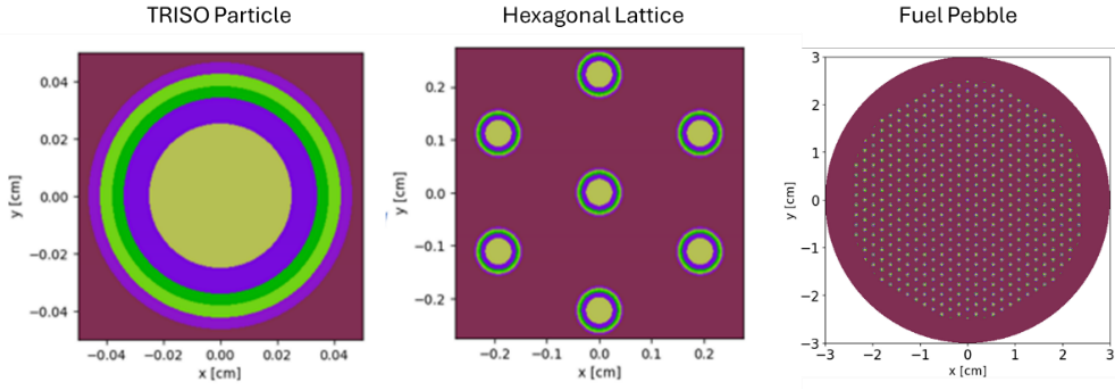

FIGURE 1. TRISO and Fuel Pebble Design

The reactor modeling in this study comprised three main levels: TRISO particle, pebble, and full core. The TRISO particle was modeled as a fuel element containing uranium dioxide (UO_2), placed at the center of the fuel kernel, and subsequently

coated in sequence with graphite (buffer), inner pyrolytic carbon (IPyC), silicon carbide (SiC), and outer pyrolytic carbon (OPyC), as shown in Fig. 1. These TRISO particles were then arranged within a graphite matrix and shaped into solid spherical fuel elements or pebbles. The arrangement of TRISO particles within the pebble, which is in reality randomly distributed during fabrication, was simplified in this study by using a hexagonal lattice pattern to improve computational efficiency. The spacing between TRISO particles in hexagonal lattice distribution was set to 0.20847315 cm to maintain the packing fraction and ensure the total number of TRISO particles per pebble remained around 8335, in accordance with the commercial fuel design of the HTR-10 [19]. As for the HTR-PM, since it contains more heavy metal (HM), the total number of TRISO particles per pebble was increased. Therefore, to represent a value of 7 g/pebble, the TRISO spacing for this fuel was set to 0.18604819 cm.

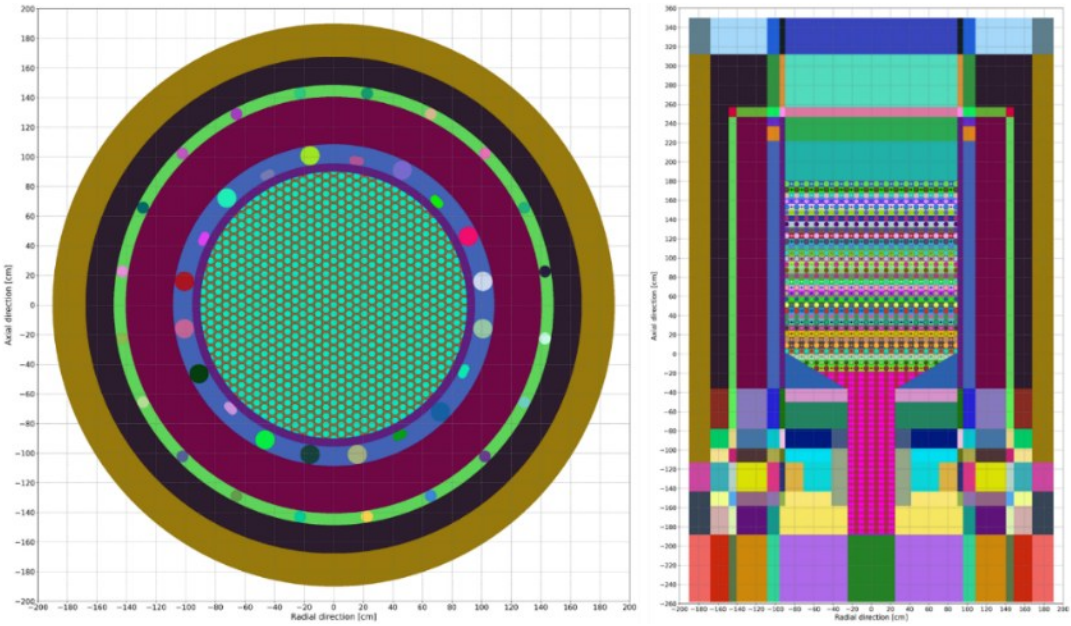

FIGURE 2. Reactor Design

The modeling of pebbles within the reactor core was simplified using a hexagonal lattice configuration, as illustrated in Fig. 1 and Fig. 2. This approach referred to a previously verified model by [19], which has been proven effective in representing fuel distribution efficiently within the geometry of a pebble-bed reactor. The hexagonal configuration was chosen due to its ability to closely approximate the actual arrangement of pebbles inside the reactor, as well as its ease of spatial representation in homogenized cell-based calculations. This simplification also aimed to enhance computational efficiency without compromising the accuracy of neutron and thermal distribution within the fuel.

TABLE I. Reactor Design Parameter [5], [6], [19]

Parameter	Specification
Pebble Diameter	6.00 cm
Fuel Zone Diameter	5.00 cm
Density of Graphite on Matrix and Outer	1.73 g/cm^3
Uranium Enrichments	17.0wt%
Fuel Kernel	
Fuel Kernel Radius	0.25 cm
UO_2 Density	10.4 g/cm^3
Coating	
Coating Material	Buffer/IPyC/SiC/PyC
Thickness (mm)	0.09/0.04/0.035/0.04
Density (g/cm^3)	1.1/1.9/3.18/1.9
Active Core Diameter / Height	180 cm / 180 cm
Picking Factor in Core	0.61
Number of Pebble	24720
Pebble in 1 layer	824
Total layer	30
Layer Height / Diameter	6 cm / 180 cm

TABLE II. Pebble Fuel Design Parameter

Pebble Type	HTR-10 (5SQ)	HTR-PM (7SQ)
Number of TRISO	8335	11669
Initial Enrichment	17%	8.50%
HML	5 gr	7 gr
TRISO Space	0.20847315 cm	0.18604819 cm
1 Layer Refueling Time (10MW/20MW/30MW)	33/22/11 days	46/23/15 days

The reactor design parameters, including the geometric dimensions of each element, material densities, and other detailed specifications, are comprehensively presented in Table 1. This study modeled two commercial fuel pebble types based on the data in Table 2. The HML values and the number of TRISO particles per pebble for both fuel pebble types were kept constant according to the values in Table 2 for all cases, with only the enrichment values varied to achieve fuel pebbles with optimal operating conditions. In this model, each layer was represented by 824 pebbles. Axially, the height of a single layer was set at 6 cm, meaning each layer consisted of a single, tightly packed row of pebbles in the vertical direction. To achieve the desired active core height of 180 cm, a total of 30 layers was required from the bottom to the top of the fuel zone. With this configuration, the packing fraction (pf) could be maintained at approximately 0.61, which remains within a reasonable range and is consistent with actual pebble filling conditions in pebble-bed reactors.

$$t = \frac{Burnup \times mHM}{Power \times CF} \tag{1}$$

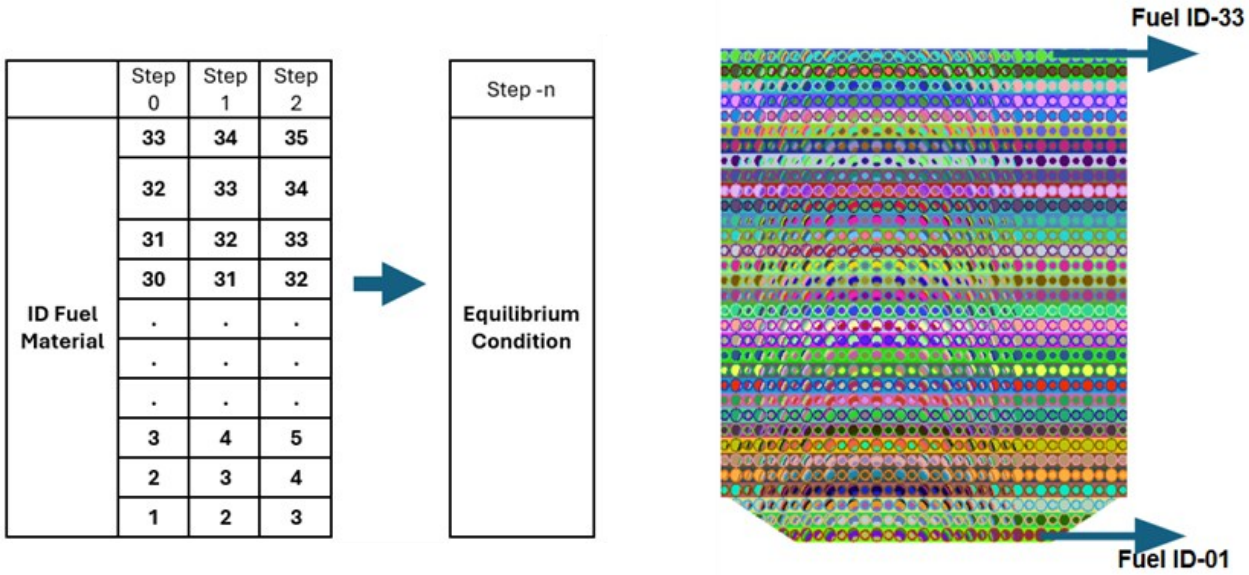

FIGURE 3. OTTO Scheme

The fuel operation scheme using the OTTO method was implemented based on the material ID shifting mechanism for pebble fuel, as illustrated in Fig. 3. As shown in the figure, the highest ID number always represented the position of a newly inserted pebble into the core, i.e., a pebble containing fresh fuel. At each simulation time step (n-step), the pebbles shifted axially downward, numerically represented by the shifting of material IDs for each fuel element. This process represented an open circulation, in which pebbles that reached the bottom of the core were discharged, and new pebbles were added from the top. The refueling time in this scheme was determined using a simplified burn-up equation, i.e., Eq. (1), under the assumption of a 100% capacity factor (CF). In all analyzed scenarios, the maximum burn-up value was set at 80 MWd/kgHM as the operational limit for the fuel. By calculating the heavy metal mass per layer (mHM), the refueling time for certain Power values (10, 20, and 30 MW) can be determined using Eq. (1) (see Table 2). Based on the calculations with these parameters, the operation and fuel reloading cycle can be carried out periodically, in which each fuel layer will continuously shift according to the scheme illustrated in Fig. 3.

III. Result and Discussion

The calculation began with the verification of the criticality value (k-eff), which serves as the main basis for determining the optimal operational conditions of the PeLUIt reactor in this study. The k-eff value was first verified at the point where the core was filled with fuel pebbles and moderator pebbles in a ratio of 53:47, following the initial operational reference of the HTR-10 reactor. Table 3 presents the verification results, showing that the hexagonal lattice distribution used for the pebble arrangement in the core in this study was able to calculate the k-eff value with a relative difference of less than 1.0% compared to the three reference calculation sources.

TABLE III. Code verification

Verivication Code	k-eff
OpenMC (Hexagonal lattice)	1.12214 ± 0.00033
OpenMC (Random lattice)	1.12125 ± 0.00054
MCNP6 (BCC lattice) [20]	1.12864 ± 0.00015
VSOP [6]	1.11956

III. A. U-235 enrichment optimization

Calculations using the OTTO method were performed on the commercial standard fuels of HTR-10 (5SQ) and HTR-PM (7SQ). These calculations optimized the U-235 enrichment in UO_2 and analyzed the results through the effective multiplication factor (k-eff), as shown in Fig. 4. The k-eff value represents the ratio of neutron production—dominated by the fission process—to neutron losses due to absorption and leakage, and serves as an indicator of criticality robustness, which must be greater than 1 for sustainable reactor operation. Fig. 4 shows the difference in timesteps for both cases, which reflects the different refueling time schemes applied in the OTTO refueling approach. The 7SQ pebble has a higher total heavy metal loading per pebble compared to the 5SQ pebble, resulting in a longer refueling duration according to Eq. (1). This indicates that, if the reactor operates at the same power level and burn-up limit (80 MWd/kgHM), the 7SQ pebble will reach its equilibrium point more slowly. Based on the calculated k-eff values, only the commercial fuel from HTR-10 with 17 wo% U-235 enrichment fully meets the criticality requirement for application in the PeLUIt reactor at a power level of 10 MWt and a burn-up of 80 MWd/kgHM, which shows that higher enrichment contributes significantly to maintaining stable fission reactions and achieving the desired operation cycle.

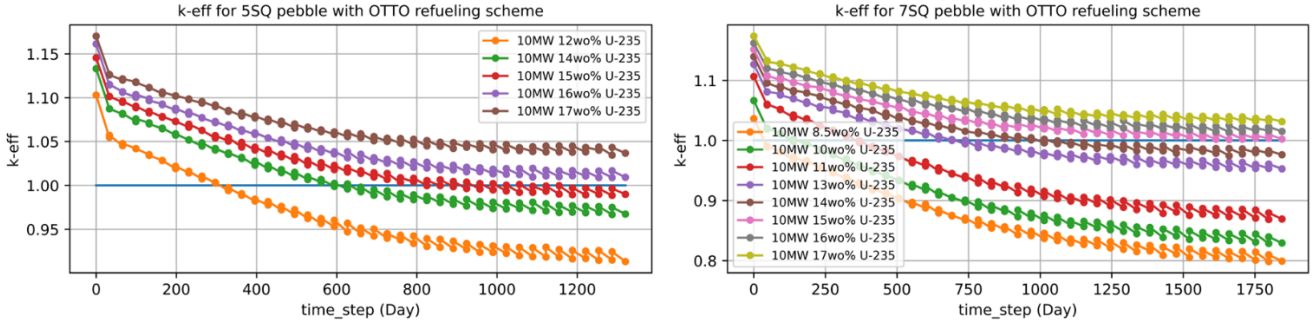

FIGURE 4. Effective multiplication factor values for pebble fuel 5SQ and 7SQ in the OTTO refueling method

Fig. 4 shows that the 7SQ fuel with 8.5 wo% U-235 enrichment, commonly used in the HTR-PM reactor, cannot be applied to the PeLUIt reactor under the assumption of 10 MWt power and 80 MWd/kgHM burn-up. This inability is caused by significant differences in core dimensions between HTR-10, HTR-PM, and PeLUIt. Although the 7SQ fuel has a better moderation ratio per pebble and higher heavy metal (HM) content, the total number of pebbles and fissile material available within the PeLUIt reactor core is insufficient to generate an optimal fission reaction. The k-eff data in Fig. 4 reinforces this finding, showing that for the 7SQ case, the desired operating conditions can only be met if the U-235 enrichment is increased to at least 16wo%. Conversely, the 5SQ fuel type, originally used in the HTR-10 reactor and having core dimensions more comparable to PeLUIt, can still operate stably even when the U-235 enrichment is reduced to 16wo%. The resulting k-eff values under these conditions remain above 1, thus supporting safe and sustainable reactor operation.

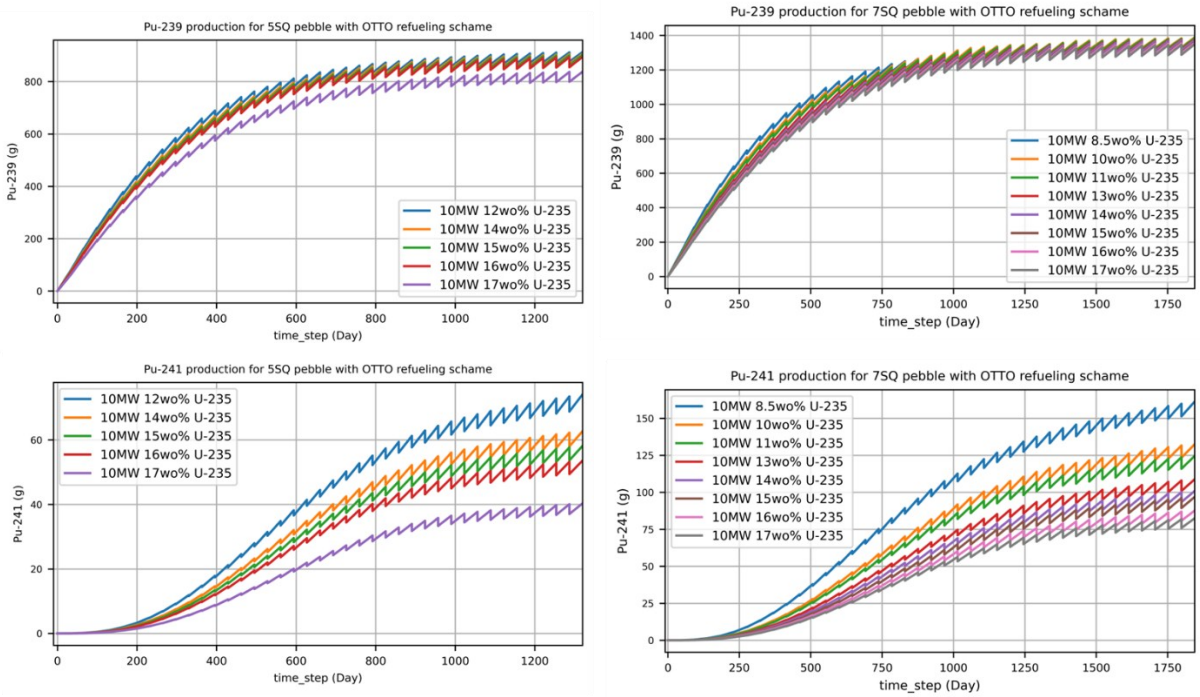

FIGURE 5. Fissile plutonium production for pebble fuel 5SQ and 7SQ in the OTTO refueling method

Equilibrium conditions, as shown in Fig. 4, were reached after the OTTO refueling scheme had been in operation for more than 1089 days for the 5SQ fuel and more than 1716 days for the 7SQ fuel. Based on Eq. 1 and the results presented in Fig. 4, the refueling time per layer was calculated to be 33 days for 5SQ and 46 days for 7SQ. Accordingly, the daily pebble insertion rate (pebbles per day) at 10 MWt power and 80 MWd/kgHM burn-up was 25 pebbles/day for 5SQ and 18 pebbles/day for 7SQ. The lower pebble per day value for 7SQ is due to the higher heavy metal loading (HML) per pebble. Nevertheless, to maintain k-eff above the critical limit, the 7SQ fuel still requires higher U-235 enrichment. Therefore, although fewer pebbles are needed, the economic effectiveness of this fuel requires further evaluation.

Fig. 5 shows the production of fissile plutonium material over the reactor operation period with the OTTO refueling scheme, which is also an important parameter in selecting effective fuel. According to Fig. 5, fissile plutonium production tends to increase as U-235 enrichment decreases. When comparing the two optimal conditions from Fig. 4 (i.e., at 16 wo% U-235 enrichment), during the same equilibrium period, fissile plutonium production (Pu-239 and Pu-241) in the 7SQ fuel tends to be higher than in 5SQ. This is likely due to the higher HML content in the 7SQ pebble, resulting in a larger fraction of U-238. However, when viewed on a daily average basis, the total fissile plutonium production amounts to 1.35 grams/day for 5SQ and 1.43 grams/day for 7SQ.

III. B. Power Variation at Optimal Enrichment

Variations in reactor operating power at 10 MW, 20 MW, and 30 MW were analyzed using the previously determined optimal enrichment values. The evaluation results are presented in Fig. 6, which shows that both fuel types (5SQ and 7SQ) were able to achieve the specified power targets, with the maximum burn-up remaining limited to 80 MWd/kgHM. As the power increased, the time required to reach equilibrium conditions shortened. This was due to the increased fuel burn rate, which directly accelerated the pebble refueling demand. This phenomenon demonstrates a linear relationship between reactor power, fuel consumption rate, and fuel reload frequency, which is a crucial factor in designing the refueling system for pebble-bed reactors.

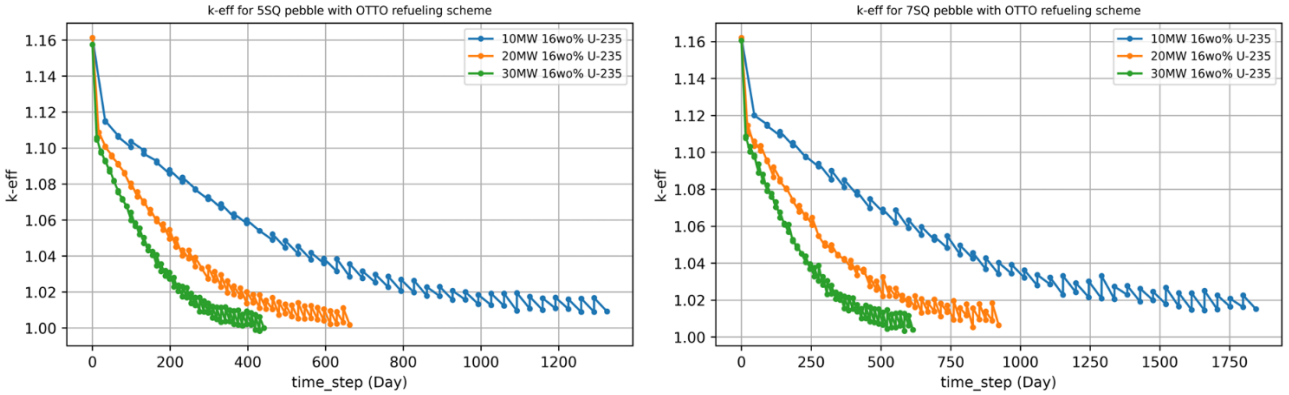

FIGURE 6. Effective multiplication factor value for optimal enrichment of 5SQ and 7SQ pebble fuel in OTTO refueling method with power variation.

For the 5SQ fuel, the number of pebbles required per day increased sequentially to 25, 51, and 75 pebbles per day for power levels of 10, 20, and 30 MW, respectively. Meanwhile, the 7SQ fuel required 18, 36, and 54 pebbles per day to achieve the same power levels. Although both fuel types were able to reach the target power, it was observed that at the operating powers of 20 MW and 30 MW, the k-eff value decreased significantly and approached the critical limit (k-eff ≈ 1). This condition indicates that at higher power levels, the criticality margin becomes narrower, potentially reducing the stability of reactor operation. Therefore, under higher power operating conditions, it is recommended that the refueling process be accelerated so that the burn-up per pebble can be reduced. By doing so, the availability of fissile material in the core is maintained, and the k-eff value can be kept above the critical threshold, thus supporting a more stable and safe reactor operation.

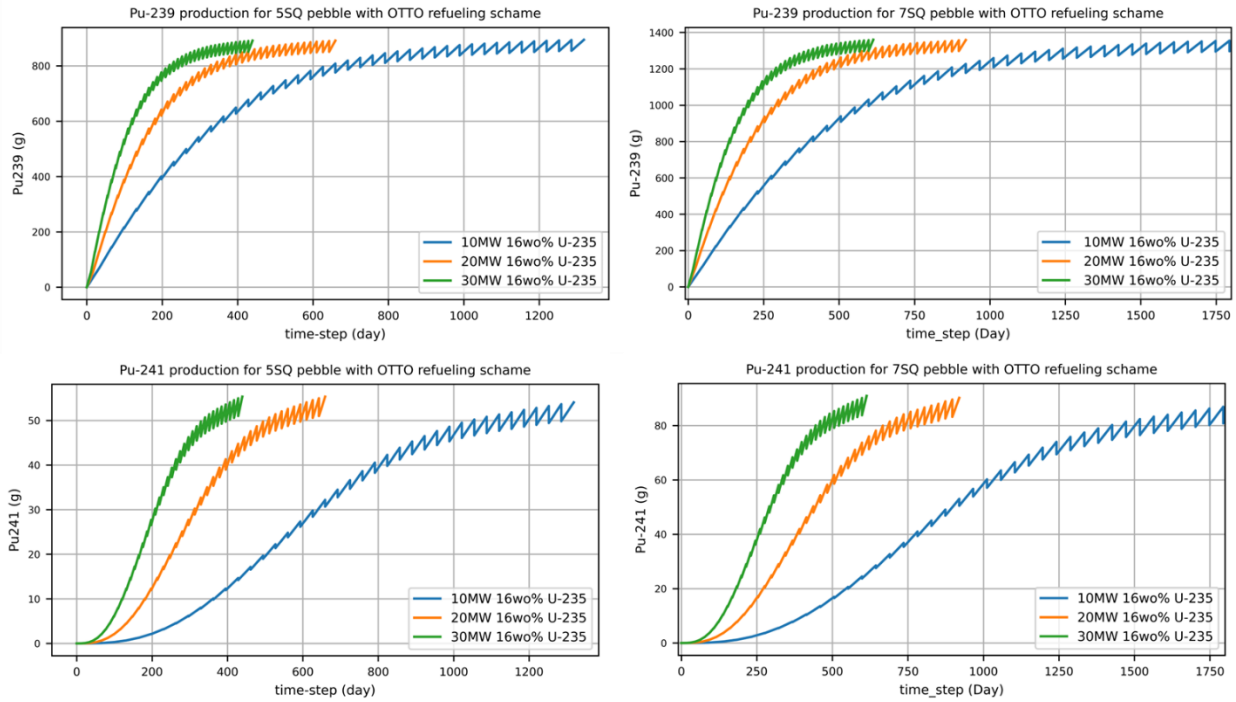

FIGURE 7. Fissile plutonium production for optimal enrichment of 5SQ and 7SQ pebble fuel in OTTO refueling method with power variation.

Fig. 7 illustrates the trend of fissile plutonium isotope production resulting from variations in reactor power using two types of pebble fuel (5SQ and 7SQ). Based on the graph, it can be concluded that increasing reactor power accelerates the

accumulation rate of plutonium until equilibrium is reached. The higher the operating power, the faster the fuel undergoes burnup, producing conversion of U-238 into Pu-239 and Pu-241. However, when observed during the equilibrium phase, the amount of plutonium produced per refueling cycle tends to remain constant across different power levels. This indicates that as long as the burnup per refueling cycle is maintained (in this case, 80 MWd/kgHM), the quantity of plutonium generated per cycle is not significantly affected by the reactor power level. In other words, despite variations in operating power, as long as neutron efficiency and burn-up level per cycles are consistently controlled, plutonium production per cycle remains within a comparable range.

IV. CONCLUSIONS

Pebble fuel with standard specification HTR-10, based on the method and results of this study, has been proven to be the most suitable for use in PeLUIt reactors at all three operating power levels: 10 MW, 20 MW, and 30 MW. Furthermore, the neutronic calculation results in this study indicate that, under the assumed maximum burn-up target of 80 MWd/kgHM, this fuel can still be optimized by reducing the enrichment from 17 wo% to 16 wo% while maintaining sufficient criticality. In terms of fissile plutonium isotope production, power variations only affect the speed at which equilibrium is reached but do not significantly influence the amount of plutonium produced per refueling cycle, provided the burn-up value is maintained. According to calculations, the 5SQ fuel type produces about 1.35 grams of fissile plutonium per day, while 7SQ produces approximately 1.43 grams per day. Additionally, both fuel types require the same enrichment level to exceed the specified operational targets. Therefore, due to its lower heavy metal loading (HML), 5SQ is considered superior in terms of design and economic efficiency compared to 7SQ pebble fuel.

ACKNOWLEDGMENTS

The authors would like to acknowledge the Bandung Institute of Technology and the National Research and Innovation Agency of the Republic of Indonesia for their support in this research and publication activity.

REFERENCES

[1] S. Permana, N. Trianti, and A. Rahmansyah, “Nuclear energy contribution potential to secure electricity demand with low carbon emission and low risk of power plant in Indonesia,” in IOP Conference Series: Earth and Environmental Science, IOP Publishing Ltd, Jun. 2021. doi: 10.1088/1755-1315/753/1/012048.
[2] S. Permana, N. Trianti, and A. Rahmansyah, “Nuclear Energy Contribution for Net Zero Emission and National Energy Mix 2060 in Indonesia,” in Journal of Physics: Conference Series, Institute of Physics, 2022. doi: 10.1088/1742-6596/2243/1/012066.
[3] F. Miftasani et al., “Investigating geometry adjustments for enhanced performance in a PeLUIt-10 MWt pebble bed HTGR with OTTO refueling scheme,” Nuclear Engineering and Design, vol. 422, Jun. 2024, doi: 10.1016/j.nucengdes.2024.113163.
[4] C. Wulandari et al., “Optimization of uranium and uranium-thorium fuel utilization in pebble bed for PeLUIt-10 reactor using PEBBED code,” Nuclear Engineering and Design, vol. 433, Mar. 2025, doi: 10.1016/j.nucengdes.2025.113873.
[5] D. She et al., “Prediction calculations for the first criticality of the HTR-PM using the PANGU code,” Nuclear Science and Techniques, vol. 32, no. 9, Sep. 2021, doi: 10.1007/s41365-021-00936-5.
[6] IAEA, Evaluation of high temperature gas cooled reactor performance : benchmark analysis related to initial testing of the HTTR and HTR-10. Vienna, Austria : International Atomic Energy Agency, 2003.
[7] N. Trianti et al., “Neutronic And Thermal-Hydraulic Analysis of HTGR-Based PELUIT-40 Reactor with PANGU-DAYU Code,” China, Oct. 2024.
[8] D. Mulyana, T. Setiadipura, and I. W. Ngarayana, “Heavy metal loading effects on special nuclear material and waste of an uprated Indonesian Reaktor Daya Eksperimental,” Nuclear Engineering and Technology, Jul. 2024, doi: 10.1016/j.net.2024.07.031.
[9] A. M. Mabruri, N. Trianti, Z. Su’ud, and R. D. Syarifah, “Optimizing Micro-PeLUIt reactor with UO2-ThO2 fuel mixtures and improved graphite moderation,” Nuclear Engineering and Design, vol. 438, Jul. 2025, doi: 10.1016/j.nucengdes.2025.114051.
[10] N. Trianti et al., “Optimum power determination and comparison of multi-pass and OTTO fuel management schemes of HTGR-based PeLUIt reactor,” Nuclear Engineering and Design, vol. 415, Dec. 2023, doi: 10.1016/j.nucengdes.2023.112696.

[11] D. Mulyana and S. S. Chirayath, "The impact of refueling schemes on the proliferation resistance of a pebble bed reactor," Ann Nucl Energy, vol. 170, Jun. 2022, doi: 10.1016/j.anucene.2022.109010.
[12] P. K. Romano and B. Forget, "The OpenMC Monte Carlo particle transport code," Ann Nucl Energy, vol. 51, pp. 274–281, Jan. 2013, doi: 10.1016/j.anucene.2012.06.040.
[13] R. D. Syarifah, F. Prasetya, A. M. Mabruri, A. Arkundato, and N. Trianti, "The Effect of Adding Minor Actinide Fuel Rods on GFR Reactor in Radiopharmaceutical Waste Production Using OpenMC Program," Science and Technology Indonesia, vol. 9, no. 4, pp. 857–865, Oct. 2024, doi: 10.26554/sti.2024.9.4.857-865.
[14] A. M. Mabruri, R. D. Syarifah, I. K. Aji, A. Arkundato, and N. Trianti, "Validation of OpenMC Code for Low-cycle and Low-particle Simulations in the Neutronic Calculation Criticality k-eff Low-cycle MSR FUJI-12 OpenMC Corresponding Author," Jurnal Ilmu Fisika, vol. 16, no. 2, pp. 107–117, 2024, doi: 10.25077/10.25077/jif.16.2.107-117.2024.
[15] A. M. Mabruri, R. D. Syarifah, I. K. Aji, Z. Hanifah, A. Arkundato, and G. Jatisukamto, "Neutronic analysis on molten salt reactor FUJI-12 using 235U as fissile material in LiF-BeF2-UF4 fuel," Eastern-European Journal of Enterprise Technologies, vol. 5, no. 8(119), pp. 6–12, 2022, doi: 10.15587/1729-4061.2022.265798.
[16] F. Prasetya, A. M. Mabruri, I. Karomah, R. D. Syarifah, I. K. Aji, and N. Trianti, "Validation of OpenMC Code Criticality Value Calculation for GFR Reactor with UN-PuN Fuel," in Journal of Physics: Conference Series, Institute of Physics, 2024. doi: 10.1088/1742-6596/2734/1/012065.
[17] R. D. Syarifah et al., "Analysis of variation minor actinide pin configurations Np-237, AM-241, AND Cm-244 IN UN-PuN fueled pressurized water reactor," EUREKA, Physics and Engineering, vol. 2024, no. 1, pp. 36–46, Jan. 2024, doi: 10.21303/2461-4262.2024.003048.
[18] R. D. Syarifah, B. A. Putri, I. K. Aji, and A. M. Mabruri, "Neutronic Analysis on Molten Salt Reactor (MSR) Using OpenMC Code With Variations of Geometry Core Fueled By LiF-BeF2-UF4," El-Cezeri Journal of Science and Engineering, vol. 11, no. 2, pp. 152–159, Jul. 2024, doi: 10.31202/ecjse.1364028.
[19] A. M. Mabruri, N. Trianti, Z. Su'ud, E. Umar, and R. D. Syarifah, "Comprehensive evaluation of nuclear data library variations and TRISO distribution methods on neutronic properties of HTR-10 pebble-bed fuel using OpenMC," Nuclear Engineering and Design, vol. 441, Sep. 2025, doi: 10.1016/j.nucengdes.2025.114168.
[20] O. Kabach, A. Chetaine, A. Benchrif, and H. Amsil, "The use of burnable absorbers integrated into TRISO/QUADRISO particles as a reactivity control method in a pebble-bed HTR reactor fuelled with (Th,233U)O2," Nuclear Engineering and Design, vol. 384, Dec. 2021, doi: 10.1016/j.nucengdes.2021.111476.

Technical Session 9 (13:40 - 15:40)	The Port 1, C Floor	Risk Management and Risk-informed Decision Making and Severe Accident Modelling
		Chair/Facilitator 1: Dr. Roppon PICHA (Thailand Institute of Nuclear Technology (TINT))
		Chair/Facilitator 2: Asst.Prof. Yanin SUKJAI Department of Physics, King Mongkut's University of Technology Thonburi (KMUTT))
13:40 - 14:00		ID 30: Implementation of Risk-Informed Performance-Based Regulation and Enhanced Inspection Programs in Korea Speaker: Jihan Lim (Korea Institute of Nuclear Safety) Contributors: Jihan Lim (Korea Institute of Nuclear Safety)
14:00 - 14:20		ID 41: Application of Dynamic Probabilistic Risk Assessment to Nuclear Power Plant Operation Support - Evaluation of Countermeasure in Multi-unit Operation Considering Operator State - Speaker: Nami Yamamoto (Mitsubishi Electric Corporation) Contributors: Nami Yamamoto (Mitsubishi Electric Corporation), Yuto Uchiyama (The University of Tokyo), Mami Kagimoto (Mitsubishi Electric Corporation), Yohei Ueno (Mitsubishi Electric Corporation), Takafumi Narukawa (The University of Tokyo), Takashi Takata (The University of Tokyo)
14:20 - 14:40		ID 128: System Availability Analysis: A Case Study on the Component Cooling Water System of Tsinghua High-Flux Reactor Speaker: Yi Wu (Tsinghua University) Contributors: Yi Wu (Tsinghua University), Wang Lin (Tsinghua University), Tao Liu (Tsinghua University), Jiejuan Tong (Tsinghua University), Zhuohan Wang (Tsinghua University)
14:40 - 15:00		ID 54: Development of an ABM-based Radiation Emergency Response Simulation Applying an Exposure Model Speaker: Minho Hwang (KyungHee University) Contributors: Minho Hwang (KyungHee University), Sungmin Han (KyungHee University), Geon Kim (KyungHee University), Joonseok Lim (KyungHee University), Gyunyoung Heo (KyungHee University)
15:00 - 15:20		ID 93: Comparative Analysis of Material Design and Performance Steam Generators for Nuclear Power Plants: Risk Assessment and Optimization Strategies Speaker: Muhammad Subhan (National Research and Innovation Agency of Indonesia) Contributors: Muhammad Subhan (National Research and Innovation Agency of Indonesia), Andini Efriyanto Putri (State Polytechnic of Jakarta), Muslimin Muslimin (State Polytechnic of Jakarta), Tresna Priyana Soemardi (University of Indonesia), Topan Setiadipura (National Research and Innovation Agency of Indonesia), Ario Sunar Baskoro (University of Indonesia)

ASRAM2025
www.asram2025.org
Asian Symposium on Risk Assessment and Management 2025
Pattaya, Thailand, 27 – 29 August 2025

IMPLEMENTATION OF RISK-INFORMED PERFORMANCE-BASED REGULATION AND ENHANCED INSPECTION PROGRAMS IN KOREA

Jihan LIM[1]

[1] *Korea Institute of Nuclear Safety, 62, Gwahak-ro, Yuseong-gu, Daejeon, 34142, Republic of Korea*
Email: jihan@kins.re.kr

ABSTRACT

This paper presents Korea's ongoing transition toward a Risk-Informed Reactor Oversight System (K-ROP), with the primary objective of enhancing regulatory effectiveness by integrating risk insights into inspection processes and decision-making. The legacy inspection system, which relied heavily on scheduled evaluations during overhaul (OH) periods, proved insufficient in detecting latent risks and systemic vulnerabilities. These limitations prompted the development of a revised approach that allows inspections to be conducted both during and outside OH periods, enabling more flexible, timely, and risk-sensitive oversight of nuclear power plants. A central component of this transformation is the Significance Determination Process (SDP), a structured methodology for assessing the safety significance of inspection findings. Utilizing quantitative indicators such as the change in Core Damage Frequency (ΔCDF), the SDP facilitates consistent classification of findings into minor or more-than-minor categories, thereby guiding the prioritization of enforcement actions. Through pilot applications and large-scale retrospective reviews, the SDP has demonstrated its effectiveness in supporting both targeted regulatory attention and efficient resource allocation. Case studies illustrate how SDP-based assessments contribute to identifying structural deficiencies and procedural gaps that may otherwise remain undetected under conventional inspection methods. The broader application of SDP has been accompanied by the establishment of a centralized data management system to monitor inspection outcomes and track risk trends. These developments reflect a more proactive, transparent, and evidence-based regulatory paradigm. While K-ROP remains under phased development, its implementation signals a significant departure from deterministic oversight practices, aligning Korea's nuclear regulatory strategy with global best practices and enhancing its capacity to ensure long-term operational safety.

Keywords: Nuclear Safety, Risk-Informed Regulation, Inspection Framework, Significance Determination Process, Regulatory Oversight

I. INTRODUCTION

Over the past two decades, the global nuclear industry has progressively transitioned toward risk-informed and performance-based regulatory frameworks to enhance safety and operational efficiency. A notable example is the United States, where the Nuclear Regulatory Commission (NRC) implemented the Reactor Oversight Process (ROP) in 2000. This approach integrates probabilistic risk assessments to prioritize regulatory focus on areas with the highest safety significance, thereby improving the objectivity and predictability of oversight activities. Following the U.S. lead, countries such as Mexico, Taiwan, Spain, and Japan have adopted similar frameworks, aligning their regulatory practices with international standards and emphasizing the importance of risk-informed decision-making in nuclear safety [1].

In Korea, the traditional inspection system has been characterized by rigid schedules and a deterministic approach, primarily focusing on compliance during overhaul (OH) periods. This methodology has shown limitations in effectively identifying and mitigating potential risks, particularly those that may arise during normal operations. The Fukushima Daiichi nuclear accident in 2011 served as a critical turning point, highlighting the need for a more proactive and comprehensive regulatory approach. In response, Korea's Nuclear Safety and Security Commission (NSSC) initiated a series of reforms aimed at strengthening the nation's nuclear safety framework. These efforts were encapsulated in the Comprehensive Plans for Nuclear Safety, with the second plan covering 2017–2021 and the third plan extending from 2022–2026, both emphasizing the adoption of risk-informed oversight strategies [2].

To address these challenges and align with international best practices, Korea embarked on the development of a Risk-Informed Reactor Oversight Process (K-ROP). This initiative aims to establish a regulatory framework that systematically monitors and manages the safety of operating nuclear power plants using risk information. Key components of K-ROP include

revising inspection methods to allow for evaluations during both OH periods and normal operations, integrating risk-based evaluation models such as the Significance Determination Process (SDP), and implementing pilot testing procedures tailored to domestic conditions. Through these measures, Korea seeks to enhance the effectiveness of its nuclear regulatory oversight, ensuring a higher level of safety and public trust in its nuclear energy program.

II. ONGOING DEVELOPMENT OF THE RISK-INFORMED OVERSIGHT SYSTEM IN KOREA

II.A. Project Initiation and Framework

In 2019, the Korea Institute of Nuclear Safety (KINS) launched the project titled “Establish Risk-Informed Reactor Oversight System”, aimed at developing both the technological basis and regulatory framework necessary for a system that can systematically monitor and manage the safe operation levels of nuclear power plants using risk information. This project consists of two major subprojects:

Subproject ①: Development of a Risk-Based Regulatory Framework

This subproject focused on establishing a domestic oversight system informed by international benchmarking. Drawing from the analysis of overseas case studies—particularly from countries that have implemented the ROP—the project developed a conceptual framework for Korea's own risk-informed oversight system. Key elements include a structured process comprising: monitoring, evaluation, and response, supported by improvements in inspection strategies and comprehensive safety assessments. Additionally, this subproject included the formulation of an improved regulatory inspection strategy and the design of a comprehensive evaluation process to assess the overall safety level of nuclear facilities more holistically and accurately.

Subproject ②: Development of MPAS Model and SDP Management System

In parallel, efforts were directed toward the development of the Multipurpose Probabilistic Analysis of Safety (MPAS) model and the Significance Determination Process (SDP) management system. The MPAS model supports structured planning and evaluation of maintenance activities, while the SDP management system enables risk-informed decision-making by quantifying the safety significance of inspection findings and supporting enforcement prioritization.

In terms of resource planning, the implementation of these two subprojects has been supported by a stable and consistent multi-year budget allocation. Between 2020 and 2026, Subproject ①, which focuses on the development of a risk-based regulatory framework, has been allocated an annual budget of $300,000, while Subproject ②, involving the development of the MPAS model and the SDP management system, has received $450,000 per year. The consistent funding structure reflects the long-term commitment of the KINS to systematically advance both the conceptual and operational dimensions of a risk-informed oversight system.

Together, these subprojects form the foundation for Korea’s transition toward a modern, risk-informed regulatory oversight structure tailored to its unique operational environment and safety culture.

II.B. Conceptual Overview of the Risk-Informed Oversight Process

The process integrates Monitoring, Assessment, and Response, and emphasizes public communication and transparency throughout.

(1) Monitoring

Monitoring involves both regular inspections and enhanced regulatory inspections, such as:

(i) Routine regulatory inspections including investigations of incidents and component failures
(ii) Supplementary or intensified inspections, triggered when potential safety concerns are suspected. The monitoring process provides the raw data and findings necessary to support further evaluation and decision-making.

(2) Assessment

The assessment phase consists of two key components:

(i) Performance Indicator Comparison: Actual safety performance data (Performance Indicators) are compared against predetermined threshold values to detect deviations or trends of concern.
(ii) SDP: Inspection findings and anomalies are evaluated based on their safety significance, determining the risk level associated with each issue.

Both assessment branches feed into a comprehensive evaluation, which synthesizes results from inspections and performance data.

(3) Response

When the assessment process identifies significant safety concerns, appropriate responses are initiated. These may include

(i) Strengthened inspections (targeted follow-up audits),
(ii) Administrative measures, such as enforcement actions,
(iii) Operational restrictions, including partial or full suspension of plant operations when safety margins are deemed insufficient. This response mechanism ensures that findings with higher risk implications are met with commensurate regulatory actions.

(4) Public Communication and Transparency

An essential supporting element of the oversight process is open communication with the public. This includes:

(i) Disclosure of information online,
(ii) Community outreach sessions to explain the regulatory framework and any identified risks to local residents. This aspect strengthens public trust in the regulatory system and reinforces accountability.

II.C. Revision of the Inspection System

The historical inspection system for nuclear power plants in Korea was originally designed to ensure that facilities operated in compliance with licensing standards and remained fit for continued operation. At its core, the system emphasized verification of plant performance through inspections conducted primarily during the licensee's Overhaul period (OH), which typically spanned two to three months. This timing limitation imposed constraints on the scope and depth of inspections. As a result, the regulatory activities were concentrated on performance checks of approximately 11 major facilities. From an initial list of about 57 inspection items in the early 2000s, the system expanded to cover around 100 items by 2012, reflecting increased regulatory expectations and complexity in plant operations.

However, over time, several limitations of the conventional inspection framework became apparent. Most significantly, the confined timing window during the OH period made it difficult to allocate sufficient time for thorough and balanced evaluations. This led to an excessive focus on whether systems met minimal technical standards, rather than on detecting latent vulnerabilities or degradation trends that could compromise long-term safety. Compounding the issue, document reviews and interviews with plant personnel also had to be conducted within this narrow timeframe, resulting in inefficiencies and logistical burdens for both regulators and operators.

Beyond temporal constraints, the system also struggled to adequately identify anomalies and vulnerabilities that may not yet manifest as technical noncompliance, but which could act as precursors to significant safety events. Despite institutional efforts - such as the establishment of regional regulatory offices and increases in inspection personnel - the existing system lacked a comprehensive mechanism to ensure consistent and risk-informed evaluations across all operational stages of nuclear power plants.

To address these shortcomings, a revised inspection approach has been proposed. The new strategy introduces comprehensive inspections that are no longer confined to the OH period but can also be performed during normal plant operation. This flexibility allows for more adaptive scheduling and timely response to evolving safety conditions. In addition, the revised model emphasizes in-depth inspections that enable systematic monitoring of plant conditions and identification of subtle indicators of risk or degradation. By incorporating such risk-informed strategies, the revised inspection system aims to enhance the overall effectiveness of regulatory oversight and better safeguard nuclear safety in a dynamic operating environment. Key distinctions between the traditional and revised systems are summarized in Table I.

TABLE I. Comparison Between the Past and Revised Inspection Systems

Category	Past Inspection System	Revised Inspection System
Purpose	Verify compliance with licensing standards and operational suitability	Monitor and manage safety levels using risk information
Scope of Items	Initially focused on 11 major facilities; expanded to ~100 items by 2012	Emphasis on both technical standards and potential vulnerabilities
Inspection Timing	Conducted during licensee's OH period (approx. 2–3 months)	Conducted during both OH and normal operation
Focus	Compliance with technical specifications	Identification of anomalies and precursors to safety degradation
Institutional Support	Expanded regional offices and staff, but limited integration of risk insights	Integrates risk-informed tools (e.g., SDP) and allows adaptation to real-time plant conditions

III. SDP IN THE ENHANCED INSPECTION FRAMEWORK

The introduction of the SDP plays a pivotal role in Korea's transition toward a Risk-Informed Reactor Oversight System, particularly as it directly supports and enhances the newly revised inspection regime. Under the former system, regulatory inspections lacked formalized procedures for identifying and prioritizing items for in-depth examination. This absence led to reactive or ad hoc inspection practices, often driven by routine cycles rather than meaningful safety signals.

In contrast, the enhanced inspection framework integrates the SDP as a foundational mechanism for risk-informed decision-making. It allows inspectors to assess the safety significance of findings, thereby guiding the selection of specific areas or components for focused evaluation. By introducing quantifiable thresholds and structured criteria, SDP enables regulators to identify issues that may not immediately violate technical standards but nevertheless warrant close attention due to their potential to contribute to future safety degradation.

This functionality is particularly crucial in the Korean context, where inspection time and resources are limited. The revised system, which permits inspections during both the outage and operational periods, requires a method to triage inspection efforts efficiently and effectively. SDP fills this need by filtering findings and channeling regulatory attention to areas of elevated risk.

Moreover, by explicitly linking safety evaluations to risk metrics, such as ΔCDF (Change in Core Damage Frequency), the SDP strengthens the logical and empirical basis of regulatory responses. This reinforces the credibility and transparency of regulatory actions, which is essential for building public confidence and fostering a proactive safety culture among plant operators.

In sum, the SDP does not function in isolation; it is tightly coupled with the broader structural reform of Korea's regulatory oversight system. It transforms the inspection process from a static checklist exercise into a dynamic, risk-informed safety assurance mechanism—one that supports targeted, evidence-based inspections and aligns with global best practices for reactor oversight.

III.A. Significance Determination Process

III.A.1. Definition and Identification of Performance Deficiency

The first step in the SDP is determining whether a Performance Deficiency (PD) exists. A PD is identified when an issue satisfies both of the following conditions:

(i) The issue involves a failure to meet a regulatory requirement or safety standard.
(ii) The issue was within the licensee's reasonable ability to foresee and correct, and therefore, it should have been prevented.

If both criteria are not met, the issue is categorized as a minor concern and does not proceed further in the SDP.

III.A.2. Screening for Safety Significance: "More-than-Minor" Evaluation

When a PD is confirmed, it is further evaluated to determine if it is "More-than-Minor", a classification that triggers detailed safety significance analysis. To be considered more-than-minor, the PD must meet at least one of the following conditions:

(i) It could reasonably be viewed as a precursor to a significant safety event.
(ii) If left uncorrected, it has the potential to lead to a more serious safety concern.
(iii) It is associated with a cornerstone objective (e.g., reactor safety, barrier integrity), and adversely affects that objective.

This screening step is essential to prioritize regulatory attention and resources on findings with potential safety consequences.

III.A.3. Application of the SDP Model

Once a finding is determined to be more-than-minor, it is subject to risk-informed evaluation through the SDP. This process uses metrics such as ΔCDF to quantify risk. The ΔCDF is calculated based on the increase in core damage probability due to a failure or deficiency, adjusted for the time duration the issue persisted during a year [3]. This quantitative approach allows regulators to consistently grade the severity of findings and determine the corresponding enforcement action or follow-up inspection intensity.

III.A.4. Cross-Cutting Aspects and Final Classification

The SDP also considers cross-cutting aspects such as human performance, safety culture, and organizational decision-making. By mapping findings to broader regulatory cornerstones and objectives, the process ensures a comprehensive understanding of systemic vulnerabilities. Final significance classifications are recorded in structured formats to inform corrective action planning, operator feedback, and performance trend analysis.

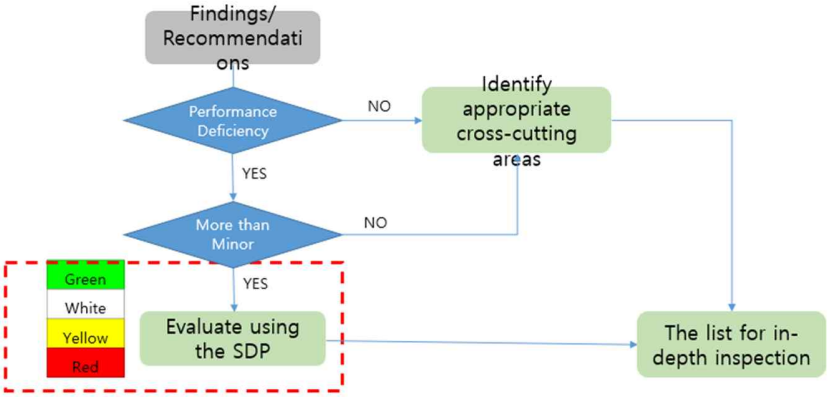

FIGURE 1. Process for Selecting In-Depth Inspection Items Using SDP

III.B. Case Studies

To illustrate the practical application of the SDP, this section presents two representative inspection cases. These examples highlight how SDP enables regulators to distinguish between issues requiring strong enforcement actions and those manageable with corrective measures, based on safety significance.

III.B. 1. Structural Deficiencies in Safety-Related Components

During an inspection of a nuclear power plant, several deficiencies were identified in structures critical to maintaining reactor safety. Specifically, corrosion was observed on the anchor bolts of a Seismic Category I condensate water storage tank, but no repair measures had been taken. In addition, loose or missing bolts were found on 24 structural brackets inside the containment building during the 14th outage inspection, and again, no corrective actions had been implemented. Lastly, cracks were discovered in the sealing material of a Component Cooling Water (CCW) penetration (PY3121), which had not been periodically maintained.

These findings met the criteria for a performance deficiency, as they involved failure to comply with established maintenance standards and were within the licensee's ability to prevent. Further evaluation revealed that, while these issues had not yet led to a significant incident, they posed a credible risk to barrier integrity, a key safety cornerstone. Additionally, if left unaddressed, the deficiencies could degrade the plant's defense-in-depth capabilities and potentially lead to more severe safety concerns.

Accordingly, the issue was classified as More-than-Minor, and the licensee was required to perform an integrity assessment of the affected components, implement targeted repairs, and establish preventive measures to avoid recurrence.

III.B. 2. Inadequate Qualification of Visual Examiner

In another instance, an inspection team identified that a visual examination of the secondary side of the steam generator had been carried out by a technician who lacked the proper certification. The areas examined included critical components such as the moisture separator, steam dryer, downcomer feedring, and recirculation feedring.

The inspection finding was indeed a performance deficiency, as it involved noncompliance with qualification standards. However, upon evaluation using the SDP, the issue did not meet any of the thresholds for classification as More-than-Minor. There was no evidence that the lack of certification contributed to inspection inaccuracies, nor did the finding affect a cornerstone objective or present a significant precursor to a safety event.

Consequently, the issue was deemed Minor, and the recommended corrective action was to re-conduct the inspection using a properly certified examiner and to implement internal checks to prevent future occurrences.

These case studies underscore the value of the SDP in ensuring that regulatory responses are proportionate to the actual risk posed. By providing a structured pathway from finding identification to enforcement decision, the SDP enhances both the efficiency and the integrity of Korea's evolving nuclear oversight system.

III.C. Scaling Up: Broad Application and Data Management of the SDP

In addition to individual inspection cases, the KINS has systematically applied the SDP across a broad set of historical and recent inspection data. In 2023, SDP evaluations were conducted for 27 issues identified at a specific nuclear power plant, marking one of the first extensive applications of the process in a real-world operational context.

Building on this experience, a large-scale retrospective review was initiated in 2024. This involved the examination of all inspection findings reported between 2013 and 2023 across Korea's operating NPPs. As part of this effort, SDP evaluations are being carried out at a pace of approximately 100 cases per month, demonstrating the scalability and practicality of the process.

To manage this growing body of data, KINS has maintained a dedicated database system, which serves as a centralized repository for tracking inspection findings, their associated risk significance levels, and follow-up actions. This structured

information management supports trend analysis, regulatory decision-making, and continuous improvement of the oversight system.

These ongoing efforts reflect a proactive and systematic approach to embedding SDP into the regulatory workflow, further aligning Korea's reactor oversight practices with international standards.

IV. CONCLUSIONS

This paper presented Korea's ongoing efforts to transition toward a Risk-Informed Reactor Oversight System, emphasizing the integration of risk insights into inspection processes and regulatory decision-making. Recognizing the limitations of the legacy inspection framework - such as its rigidity, limited timing, and insufficient ability to detect latent risks - KINS has launched a multi-faceted initiative to reform its oversight model.

At the core of this initiative lies the SDP, which provides a structured and risk-based method to evaluate inspection findings. Through carefully defined criteria and quantitative risk indicators such as ΔCDF, the SDP enables regulators to distinguish between minor and more-than-minor performance deficiencies [4], ensuring that enforcement actions are appropriately prioritized. Case studies have demonstrated how this process supports both safety assurance and regulatory efficiency by targeting high-risk conditions without overburdening operators.

Beyond individual case applications, the SDP is being systematically scaled up. Evaluations have been conducted not only for recent findings but also for inspection records spanning a decade, with results organized into a centralized data management system. This expansion underscores the practicality and scalability of the framework, reinforcing its role as a cornerstone of the future oversight model.

While the K-ROP has not yet been fully implemented, the foundational work completed to date - development of the regulatory framework, revision of inspection programs, establishment of evaluation tools, and pilot-scale data applications - represents a significant leap toward a modern, transparent, and risk-informed regulatory paradigm. Continued effort in refining the system, supported by international benchmarking and stakeholder engagement, - through international benchmarking, operator engagement, and policy alignment - will be critical to achieving a sustainable regulatory model for the future.

REFERENCES

[1] U.S. Nuclear Regulatory Commission (NRC), The Reactor Oversight Process, NUREG-1649, Revision 6, Washington D.C. (2016).
[2] Nuclear Safety and Security Commission (NSSC), The 3rd Comprehensive Plan for Nuclear Safety (2022–2026), Republic of Korea (2022).
[3] U.S. NRC, Significance Determination Process for Reactor Inspection Findings, Inspection Manual Chapter (IMC) 0609, Appendix A, Washington D.C. (2020).
[4] Canadian Nuclear Safety Commission (CNSC), Regulatory Framework for Risk-Informed Decision Making, RD-310, Ottawa, Canada (2012).

ASRAM2025
www.asram2025.org
Asian Symposium on Risk Assessment and Management 2025
Pattaya, Thailand, 27 – 29 August 2025

Application of Dynamic Probabilistic Risk Assessment to Nuclear Power Plant Operation Support - Evaluation of Countermeasure during Multi-unit Operation Considering Operator State -

Nami Yamamoto[1], Yuto Uchiyama[2*], Mami Kagimoto[1], Yohei Ueno[1], Takafumi Narukawa[2], Takashi Takata[2]

[1]*Mitsubishi Electric Corporation, 8-1-1 Tsukaguchi-Honmachi, Amagasaki-shi, Hyogo 661-0001, Japan, Yamamoto.Nami@bp.MitsubishiElectric.co.jp*
[2] *The University of Tokyo, 7-3-1 Hongo, Bunkyo-ku, Tokyo 113-8656, Japan, takata_t@n.t.u-tokyo.ac.jp*

ABSTRACT

Dynamic probabilistic risk assessment (PRA) coupled with plant-dynamics analysis is expected to be applied to the establishment of accident management programmes and operation support in addition to conventional safety assessments. In multi-unit operations, scenarios are expected to become complex during simultaneous disasters, making it increasingly difficult to determine the priorities of countermeasures such as response operation and personnel movement. It is possible to generate and evaluate complex scenarios efficiently and exhaustively with a dynamic PRA method, with which multiple scenarios are generated in accordance with changes in plant state. A previous study proposed using the continuous Markov chain Monte Carlo (CMMC) method, a dynamic PRA method, for determining countermeasure priorities to support nuclear-power-plant operations. Scenario generation and evaluation in a single unit using dynamic PRA, with which a uniform distribution was assumed, were carried out. This paper proposes a scenario-generation method for multi-unit operation using the CMMC method that takes into account plant and operator states, and reports preliminary-evaluation results. This method involves the following steps: 1) calculating the states of multi-unit plants on the basis of the water level of the reactor pressure vessel and state of response operations, 2) calculating the stress levels of operators on the basis of the plant states, 3) determining the occurrence of countermeasures such as personnel movement between units, considering the states from 1) and 2), and 4) alternately determining event occurrence and plant-dynamics analysis. The generated scenarios are evaluated on the basis of the plant states at the end of the analysis. The results suggest that it is possible to determine the priority of countermeasures such as personnel movement.

Keywords: Dynamic PRA, Plant Operation Support, Risk-informed Application, Multi-unit Operation, Operator Model

I. INTRODUCTION

Since the Great East Japan Earthquake, the importance of risk assessment and utilization of information has increased to ensure further safety in nuclear power plants. Dynamic probabilistic risk assessment (PRA) coupled with plant-dynamics analysis is expected to be applied to the establishment of accident management (AM) programmes and operation support in addition to conventional safety assessments. Regarding the establishment of AM programmes, it is difficult to determine the priority of countermeasures due to the diversity of accident scenarios, indeterminacy of the order in which events occur, and time dependence of the branching probability. The range of automation for efficiency improvement and precision during plant operation has been expanding in line with technological advances. It is thus considered possible to carry out multi-unit operations in which the scope of responsibility for monitoring and operation per operator is increased. However, it is difficult to rely entirely on automatic operation to respond to events, so intervention, including manual operation in accordance with the situation, using risk information is essential. In particular, in the event of simultaneous incidents during multi-unit operations, the scenario becomes more complicated than during single-unit operations, and the burden of determining the priority of countermeasures, including personnel movements between units, is expected to be higher.

The continuous Markov chain Monte Carlo (CMMC) method was developed as a dynamic PRA method [1–3]. It is possible to efficiently and exhaustively generate and evaluate complex scenarios by repeatedly executing event generation considering

[*] Current affiliation: Roland Berger Ltd.

the ever-changing situation and plant-dynamics analysis. In our previous study, a countermeasure-priority-determination function using the CMMC method was proposed as a support function for safer operation of nuclear power plants [4]. In that study, a simple single-unit plant-dynamics-analysis model was constructed, and the generation and evaluation of scenarios with corresponding operational events using uniform distributions were reported. The results indicated that the CMMC method can be used to evaluate the effectiveness of response operations on the basis of risk information considering uncertainty, and that it can be applied to determine countermeasure priority in complex scenarios.

The objective of this study is to extend that previous study and support the priority determination of countermeasures, including the movement of personnel between units, in a multi-unit-operation situation. As a first step, we propose a scenario-generation method that takes into account multi-unit plant and personnel states. We then report the results of evaluating the effectiveness of the countermeasures, such as personnel movement, by implementing the plant model constructed in the above previous study by extending it to a multi-unit model.

II. DEVELOPMENT OF MULTI-UNIT SIMULATION MODEL

II.A. Overview of Multi-unit Simulation Model

The multi-unit simulation model is constructed using the CMMC method. For the simulation of plant state, a simplified plant-dynamics-analysis model of the primary system of a pressurized water reactor with which a single phase is assumed, is used, which was developed in a previous study [4]. Multiple modules of this single-unit-plant model are operated in parallel, and necessary information is communicated to each other at each time step to represent multi-unit operation.

The scenario-generation procedure in each unit is shown in Fig. 1. At the beginning of each time step, a Monte Carlo state transition probability calculation and plant-dynamics analysis are conducted for a given sample. Next, the value of the evaluation index of the unit situation (unit score; details in II.B), calculated from the plant situation one time step before, is communicated between the units to determine whether personnel movement between units is necessary. The unit score is then updated according to the current situation. Finally, the AM state is analyzed to determine its state transition. This procedure is repeated until an arbitrary analysis end time, and then a unique scenario is created. When the analysis of one scenario is completed, the same procedure is repeated until all predetermined scenarios are generated. A large number of scenarios are thus created.

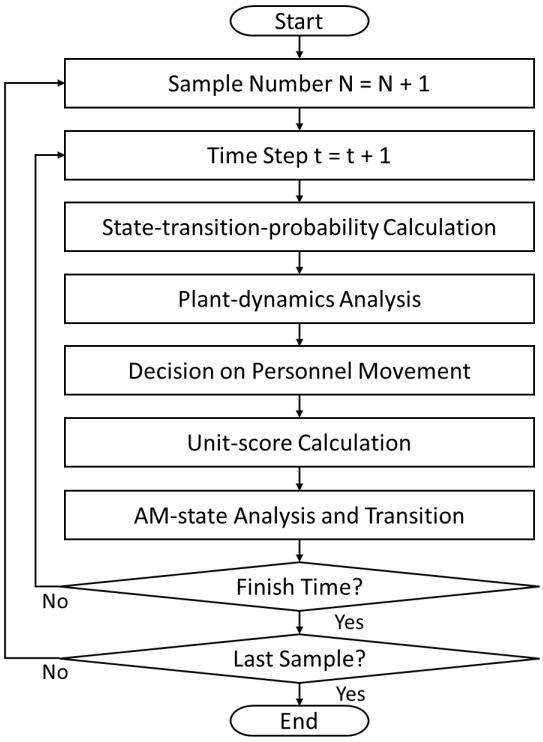

FIGURE 1. Scenario-generation procedure

Details of unit scores, AM states, and personnel movements are given in the following sections.

II.B. Index to Evaluate State of Units (Unit Score)

At nuclear power plants, various values, such as the water level and pressure of reactor pressure vessel (RPV), are monitored. When an event occurs, alarms are triggered in response to a drop in water level, etc. However, it is difficult for operators to determine which unit should be prioritized for response on the basis of numerical values, especially when the event progresses in a complex manner, such as when multiple units are simultaneously involved in an event. Therefore, we introduce a unit score that is based on the water level of the RPV and the prediction of future AM operation effects as an index to determine the implementation of AM operations by dynamically evaluating the state of each unit.

The calculation equation of the unit score $Score_{unit}$ is shown in Eq. (1), and the calculation equations of the base score $Score_{base}$ and the correction score $Score_{cor}$ constituting the $Score_{unit}$ are shown in Eqs. (2) and (3) respectively.

$$Score_{unit} = Score_{base} + Score_{cor} - Score_{fail} \quad (1)$$

$$Score_{base} = \frac{WH_t - WH_{CD}}{WH_{max} - WH_{CD}} \quad (2)$$

$$Score_{cor} = Score_{success} \times \frac{T_{AM_{left}}}{T_{AM_{total}}}. \quad (3)$$

The $Score_{unit}$ represents the unit state, the $Score_{base}$ indicates the margin of water level until core damage and is calculated from the RPV water level WH_t, the RPV water level corresponds to core damage WH_{CD}, and the maximum RPV water level WH_{max} at each time step. $The\ Score_{cor}$ is a correction score, which corrects the $Score_{base}$ by predicting how much the water level is expected to recover in the future according to the AM operation state. It is added to the highest value when the AM operation is successful, i.e., the success score $Score_{success}$, and decreased according to the remaining operating time $T_{AM_{left}}$ of the total operating time of AM $T_{AM_{total}}$. The $Score_{fail}$ is the failure score to reflect the disability of AM operation in the unit state. This value is constant only when AM operation fails and is set to 0 during other periods.

II.C. Construction of Accident-management Model Using Human Reliability Analysis

The number of personnel required for AM operation depends on the AM state. For example, more personnel are generally required when recovering AM from a failed condition than when AM is operating normally. To examine the allocation of personnel according to the AM state, the AM state is divided into seven states (waiting, starting, operating, stopping, cooling down, failed, and recovering). In practice, the probability of equipment failure is low. However, to evaluate the effectiveness of recovery through personnel movement, equipment failure that occurs with a certain probability is considered in addition to an operator's omission errors (e.g., forgetting to operate the equipment). The state transition of AM operation is shown in Fig. 2. AM is executed only during operation. However, a fixed number of operators are assigned from starting process to stopping process and during recovery, and they are not available for other tasks. On the basis of checking the possibility of optimizing AM operations during multi-unit operations by personnel movement, the recovery is designed to start only when the number of personnel required to recover failed AM and the number of personnel required to operate normal AM is secured.

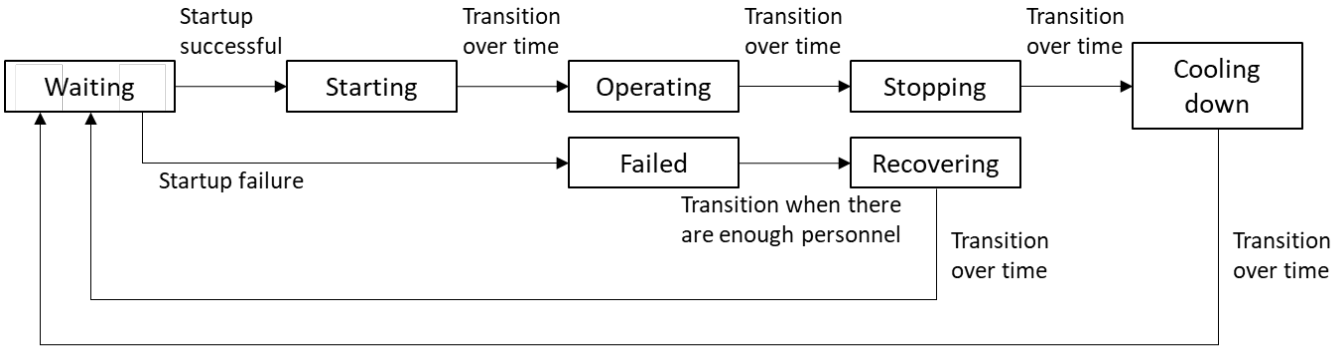

FIGURE 2. State transition of AM operation

To consider omission errors as operator human errors, we developed the following equation for calculating human error probability (HEP) on the basis of technique for human error rate prediction (THERP) [5], a first-generation human reliability analysis (HRA).

$$HEP = BHEP \times PSF \times MAX\left(0.5, \frac{HC_{AM}}{HC_{wait}}\right). \quad (4)$$

This model takes into account the performance-shaping factors (PSFs), which are factors that influence human behavior on the basis of the basic HEP (BHEP), and the impact of personnel margin, which is the ratio of the number of personnel waiting in a

unit HC_{wait} to the number of personnel required to execute each AM operation HC_{AM}. However, the decrease in HEP due to an increase in the number of waiting personnel is limited to a maximum of 50%.

There are various types of PSFs. For this study, the effect of stress due to plant conditions is reflected in the HEP as a PSF. In THERP, a PSF is determined for stress levels. We calculated the $Score_{stress}$ from the $Score_{unit}$ of calculation-target unit and other units, and the stress is categorized into four levels on the basis of the $Score_{stress}$ to determine the PSF. The $Score_{stress}$ is calculated as

$$Score_{stress} = SR_{tgt} \times Score_{unit} + \left(1 - SR_{tgt}\right) \times Score_{ave}, \tag{5}$$

where $Score_{ave}$ is the average of $Score_{unit}$ of the other units, and SR_{tgt} is the ratio of the $Score_{unit}$ of the unit to the $Score_{stress}$. Next, the correspondence between $Score_{stress}$, stress level, and PSF is shown in Table 1. The PSFs are determined so that the HEP would not exceed 1.0 when the BHEP is made larger than THERP to allow more simulation patterns to appear in the simulation while reflecting the tendency of THERP.

TABLE 1. Relationship between $Score_{stress}$, stress level, and PSF

$Score_{stress}$ [-]	Stress Level [-]	PSF [-]
More than 1.0	Extremely low	1.5
0.5 to 1.0	Optimal	1.0
0.25 to 0.5	Excessively high	2.0
Less than 0.25	Extremely high	3.0

To evaluate the impact of plant states that change from time to time on the HEP, we constructed an AM model to determine the success or failure of AM operation on the basis of the HEP calculated for each time step and referring to the concept of time-failure rate. The failure rate of a non-recovery system, which is a typical example of time failure, and the equation of variation of failure probability based on the Poisson process used in reliability engineering are used as references. The equation that replaces the failure rate with the success rate is shown in Eq. (6), and the success rate at time t obtained by separating and integrating the failure rate is calculated using Eq. (7). If AM operation is successful, the success probability is reset.

$$\Delta P_s = \left(1 - P_s(t)\right) \times \lambda \Delta t \tag{6}$$

$$P_s(t) = 1 - e^{-\lambda t}, \tag{7}$$

where $P_s(t)$ is the success probability of AM operation from time 0 to t, and λ is the success rate per time step. Since this AM model uses conditional branching by state, $\lambda \Delta t$ is the success probability per time step, and λ is obtained from the HEP in Eqs. (4) and (7). If the probability that AM is not executed from the possible AM start time to core damage is the HEP, then λ is derived from Eqs. (8) and (9).

$$1 - P_s\left(T_{CD} - T_{AM_{st}}\right) = e^{-\lambda\left(T_{CD} - T_{AM_{st}}\right)} = HEP \tag{8}$$

$$\lambda = -\frac{\log(HEP)}{T_{CD} - T_{AM_{st}}}, \tag{9}$$

where T_{CD} is the time at which core damage occurs if AM is not executed, and $T_{AM_{st}}$ is the possible starting time for each AM operation. Thus, AM success or failure is determined at each time step on the basis of the HEP, which varies depending on the situation while AM is in a waiting state.

II.D. Movement of Personnel Between Units

The necessity of personnel movement between units is determined on the basis of the $Score_{unit}$. For simplicity, we assumed personnel movement between two units. The equation for calculating the number of personnel HC_{NM} moved from unit N to unit M is as follows.

$$HC_{NM} = int\left(\frac{Score_{unitN} - Score_{unitM}}{Score_{move}} - \frac{HC_{unitN} - HC_{unitM}}{2}\right), \quad (10)$$

where $Score_{move}$ is the movement score, and HC_{unitN} and HC_{unitM} are the number of personnel in each unit. If the number of personnel in two units is the same, personnel movement is executed if the difference in $Score_{unit}$ is equal to or greater than $Score_{move}$. If the $Score_{unit}$ of the two units are the same, personnel are moved so that the number of personnel becomes equal. When HC_{NM} is negative, the number of personnel is moved from unit M to unit N by the absolute value of HC_{NM}. After HC_{NM} is calculated using Eq. (10), Eqs. (11) and (12) are used to put a limit on HC_{NM}.

$$HC_{NM} = min(HC_{waitN}, HC_{unitN} - HC_{\mathrm{minN}}, HC_{NM}) \quad (11)$$

$$HC_{NM} = max(-HC_{waitM}, -HC_{unitM} + HC_{\mathrm{minM}}, HC_{NM}). \quad (12)$$

These equations are control equations to ensure that the number of moving personnel does not exceed HC_{wait} of the unit from which the personnel are dispatched and the number of personnel in the current unit HC_{unit} minus the minimum number of personnel required of the unit HC_{min}. The minimum number of personnel required is established to avoid the potential risk of dispatching a large number of personnel to other units, i.e., a shortage of personnel when a countermeasure is required in the calculation-target unit. The above control alone may result in an instruction from unit M to unit N to move personnel while in the process of moving personnel from unit N to unit M. Since this would be inefficient, a restriction is added so that no personnel can be dispatched to other units when they are scheduled to receive personnel from other units.

III. ANALYSIS OF MULTI-UNIT SCENARIO

To confirm the effectiveness of the countermeasure of the movement of personnel in multi-unit operations, a preliminary evaluation was conducted using the models introduced in Section II.

III.A. Evaluation Scenario

As in a previous study [4], the failure scenario of steam-generator isolation during steam generator tube rupture (SGTR) was used as the evaluation scenario. It was assumed that the emergency core cooling system (ECCS) would always operate for 1350 s in the initial stage after an SGTR, but would fail to isolate the accident loop, leading to eventual core damage regardless of AM success or failure. Depressurization by opening the pressurizer relief valve (DP) and deheat by opening the main steam relief valve (DSG) were implemented as operator actions for AM. The progression of events and AM operations are shown in Fig. 3.

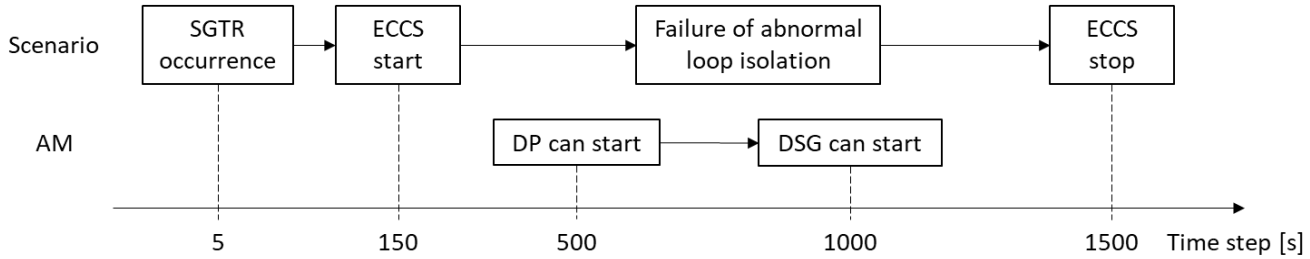

FIGURE 3. Progression of events and AM operations

III.B. Analysis Conditions

Scenarios were generated and evaluated for two cases, one with personnel movement between units and one without. Table 2 lists the analysis conditions.

TABLE 2. Analysis conditions

Item	Setting Value
Analysis period [s]	3600
Number of samples per unit [-]	100
Unit number [-]	3
Initial number of personnel in each unit [-]	3
Movement score [-]	0.2
Movement time between units [s]	0
Minimum number of personnel required for a unit [-]	2
BHEP of DP and DSG [-]	0.1
Number of personnel for DP and DSG implementation [-]	1
Number of personnel for DP and DSG recovery [-]	3
Probability of loss of function of DP and DSG [-]	0.1
Success score of DP and DSG [-]	0.3
Failure score of DP and DSG [-]	0.15
Start time of DP [s]	500
Start time of DSG [s]	1000
Time for starting of DP and DSG [s]	100
Time for operating of DP and DSG [s]	500
Time for stopping of DP and DSG [s]	100
Time for cooling down of DP and DSG [s]	200
Time for recovering of DP and DSG [s]	300

IV. RESULTS AND DISCUSSION

Table 3 lists the occurrences of successes, failures, and recoveries of AM operation for personnel movement based on the analysis conditions and without personnel movement. Without movement, if AM fails, the required number of personnel to meet the recovery start condition cannot be secured. Therefore, AM that has once failed remains in a failed state. With movement, the number of successful AM operations increased because the movement of personnel allowed the recovery of AM and AM become available again.

TABLE 3. Occurrences for each state

	Number of occurrences [-]					
	DP			DSG		
	Success	Failure	Recovery	Success	Failure	Recovery
Without movement	603	77	0	584	73	0
With movement	697	79	60	677	70	49

Tables 4 and 5 respectively list the time percentages for each state after the DP and DSG could be started. The time during failure decreased and that during standby and operation increased with movement compared to without movement.

TABLE 4. Time percentages for each state of DP

DP	Percentages [%]						
	Waiting	Starting	Operating	Stopping	Cooling down	Failed	Recovering
Without movement	57.01	3.25	15.76	3.08	6.09	14.80	0.00
With movement	64.76	3.76	18.36	3.56	6.96	1.61	0.98

TABLE 5. Time percentages for each state of DSG

DSG	Percentages [%]						
	Waiting	Starting	Operating	Stopping	Cooling down	Failed	Recovering
Without movement	52.25	3.75	17.99	3.49	6.89	15.63	0.00
With movement	58.25	4.35	21.00	4.02	7.89	3.54	0.94

The core-damage frequency for each unit is shown in Table 6. This frequency was lower with personnel movement than without personnel movement.

TABLE 6. Core-damage frequency for each unit

	Number of core-damage samples [-]			
	Unit 1	Unit 2	Unit 3	Total
Without movement	50	51	49	150
With movement	38	44	44	126

The average RPV water level for each unit at the end of the analysis is shown in Table 7. This RPV water level was higher with personnel movement than without personnel movement. The distribution of the RPV water level across all units is shown in Table 8. Since a total of 100 samples were generated per unit, the total number of samples for all units for each case was 300. With personnel movement, the number of samples below 5 m decreased and increased above 5 m. Therefore, it was found that the RPV water level, as well as the core-damage frequency, can be improved by personnel movement.

TABLE 7. Average RPV water level for each unit

	Average of RPV water level [m]			
	Unit 1	Unit 2	Unit 3	All units
Without movement	6.42	6.54	6.67	6.54
With movement	7.03	7.08	6.85	6.99

TABLE 8. Distribution of RPV water level across all units

	Number of samples for each RPV water level [-]			
	Below 3 [m]	3 to 5 [m]	5 to 7 [m]	Above 7 [m]
Without movement	21	47	82	150
With movement	10	23	93	174

By applying the CMMC method and creating scenarios that take into account the state-transition probabilities of AM and personnel movement based on plant conditions, it was found that the effectiveness of AM and the impact of personnel movement could be evaluated in complex scenarios involving simultaneous accidents in multiple units. The evaluation results indicate that personnel movement has the advantage of recovering AM operations, and that increasing the number of AM operations improves the core-damage frequency and RPV water level at the end of analysis.

V. CONCLUSION

We proposed a scenario-generation method that takes into account the plant state and operator state during multi-unit operation to support countermeasure determination such as personnel movement between units. The plant model developed in a previous study was extended to a multi-unit simulation model, and the state-transition probabilities of AM, considering the effect of the plant situation on the operator and movement of personnel between units according to the situation, were modeled. Scenario generation and evaluation were carried out for the failure scenario of steam-generator isolation during SGTR in multi-unit operation. The results indicate that the effectiveness of AM and that of personnel movement can be evaluated in complex scenarios considering the changing situation over time.

For future work, we will set various parameters to appropriate values and investigate indices for evaluating the priority of countermeasures during multi-unit operation.

REFERENCES

[1] S. Shinzaki, et al., "Quantification of Severe Accident Scenarios in Level 2 PSA of Nuclear Power Plant with Continuous Markov Chain Model and Monte Carlo Method," *10th International Probabilistic Safety Assessment & Management Conference*, PSAM10-132 (2010)
[2] T. Takata and E. Azuma, "Event Sequence Assessment of Deep Snow in Sodium-cooled Fast Reactor Based on Continuous Markov Chain Monte Carlo Method with Plant Dynamics Analysis," *Journal of Nuclear Science and Technology*, 53, 11, 1749-1757 (2016)
[3] S. Shinzaki, "Scenario Quantification of Dynamic Level 2 PSA Based on Continuous Markov Monte Carlo Method and Plant System Analysis Code," *Master thesis*, Osaka University (2012)
[4] N. Yamamoto, et al., "Application of Dynamic PRA to Nuclear Power Plant Operation Support - Evaluation of Plant Operation Support Using a Simple Plant Model -," *17th International Conference on Probabilistic Safety Assessment and Management & Asian Symposium on Risk Assessment and Management*, PSAM17&ASRAM2024-1123 (2024)
[5] A. D. Swain, H. E. Guttmann, "Handbook of Human Reliability Analysis with Emphasis on Nuclear Power Plant," *NUREG/CR-1278* (1983)

ASRAM2025
www.asram2025.org
Asian Symposium on Risk Assessment and Management 2025
Pattaya, Thailand, 27 – 29 August 2025

System Availability Analysis: A Case Study on the Component Cooling Water System of Tsinghua High-Flux Reactor

Yi Wu [1,2,3], Tao Liu [1,2,3], Wang Lin [1,2,3], Zhuohan Wang [1,2,3], Jiejuan Tong [1,2,3]

[1] *Institute of Nuclear and New Energy Technology, Tsinghua University, Beijing 100084, China*
[2] *Collaborative Innovation Center of Advanced Nuclear Energy Technology, Tsinghua University, Beijing 100084, China*
[3] *The Key Laboratory of Advanced Reactor Engineering and Safety of Ministry of Education, Beijing 100084, China*
wuyi23@mails.tsinghua.edu.cn, liu-tao@tsinghua.edu.cn, lw24@mails.tsinghua.edu.cn, wangzhuohan@tsinghua.edu.cn, tongjj@tsinghua.edu.cn

ABSTRACT

System availability analysis is essential for ensuring the reliability and safety of nuclear systems, particularly those characterized by complex configurations, diverse operational modes, and varying maintenance strategies. The Component Cooling Water System (CCWS) of the Tsinghua High-Flux Reactor (THFR) includes continuously operating, standby, and intermittently operated components, making the evaluation of its availability a complex challenge. This study proposes a structured workflow for system availability assessment and identifies critical input parameters such as system configuration, failure and repair rates, mission duration, logical dependencies, and maintenance policies. Traditional Fault Tree Analysis (FTA) provides a static view and fails to capture system state transitions, limiting its applicability under dynamic conditions. To overcome this limitation, a dynamic modeling approach using EMRALD is adopted, enabling the simulation of time-dependent behaviors including equipment failures and repairs over the mission period. Markov modeling is employed for cross-verification, offering a mathematical foundation for analyzing state transitions. The comparative analysis shows that EMRALD delivers a more accurate and adaptable representation of real-world system performance. This research highlights the necessity of dynamic modeling in system availability analysis and offers methodological insights into selecting appropriate tools for nuclear safety and reliability evaluations.

Keywords: system availability, EMRALD, component cooling water system (CCWS), Tsinghua High-Flux Reactor (THFR)

I. INTRODUCTION

To ensure system stability, availability analysis is vital in reliability assessment [1]. It evaluates the system's ability to sustain normal operation over time, reflecting effectiveness in accident prevention and mitigation, especially from failures or disturbances. Availability is the probability that the system is in a working state when needed [2].

Availability depends on functional equipment. In high-throughput reactors, the component cooling water system (CCWS) includes continuously, standby, and intermittently operating components [3]. As the main cooling for thermal equipment, it directly affects core heat removal and equipment operation [4]. Availability changes significantly impact plant reliability, especially during operation and accidents, thus influencing safety margins. Assessment focuses on events from total loss of CCWS [5].

Traditional methods like fault tree analysis (FTA) are still widely used. Yu Yu et al. used the Monte Carlo method to model a high-temperature gas-cooled reactor's CCWS and calculate failure frequency [6]. FTA uses Boolean logic for a clear, intuitive structure. However, as a static method, it struggles with maintenance, switching, recovery, and time-dependent interactions.

Thus, dynamic PSA models were developed. Zhang Binbin et al. applied a Markov model to dynamically evaluate a nuclear plant's CCWS and compared it to FTA [7]. The Markov model simulates random failures/repairs via state transitions. However, it suffers from state space explosion in large systems [8–10] and assumes exponential failure times. To address this, Qi Faqun et al. proposed a semi-Markov model for cold standby systems, allowing both exponential and Weibull distributions [11]. Distefano et al. used stage-type expansion and semi-Markov methods for non-Markovian models [10]. Temraz [12] used semi-Markov and regeneration point techniques for standby systems with general distributions. Wu et al. [13] also used semi-Markov models for repairable standby systems with perfect switching, though the semi-Markov property adds complexity.

With rising demand for dynamic risk assessment, tools like EMRALD, developed by INL, gained attention [14–15]. Combining finite state automata and temporal logic, EMRALD enables dynamic modeling and simulation of system behavior under failure, maintenance, and switching. Its flexibility and scalability provide advantages in availability modeling.

This paper analyzes availability of typical repairable systems (series, parallel, k/n, bypass) using both Markov and EMRALD methods, comparing their consistency. It evaluates availability considering equipment state transitions during

operation. EMRALD is used for dynamic modeling, incorporating fault behavior, maintenance, and time constraints; the Markov model verifies and mathematically explains state transitions. Key parameters include equipment structure, task time, failure rate, logical dependency, and maintenance time. A case study of the high-flux reactor's CCWS evaluates the frequency of the initiating event "loss of both trains of CCWS" during power operation.

THFR has high design and operation safety demands [16–17]. High-flux reactors are critical for testing fuels/materials, producing strategic nuclides and isotopes, and are key to national scientific strength. THFR will build a world-class water-cooled high-flux reactor and supporting systems to address the domestic gap in ultra-high-flux neutron sources.

This paper is organized as follows: Section II introduces the methodology for system availability analysis. Section III presents the EMRALD-based event modeling and risk assessment. Section IV explains the availability analysis methods for typical repairable systems. Section V provides a case study on the component cooling water system. Section VI compares the results of three analysis methods. Section VII concludes the paper.

II. METHODOLOGY FOR SYSTEM AVAILABILITY ANALYSIS

System availability analysis requires a structured methodology, especially for complex nuclear systems. This section outlines the evaluation process and modeling techniques, as shown in Fig.1. The first step defines system boundaries and functional requirements by identifying components, subsystems, interfaces, and their interactions, while specifying performance criteria under normal and degraded conditions. Next, essential parameters are collected, including component configuration (e.g., redundancy schemes), failure and repair rates (often exponential or other distributions), mission time, degraded operation duration, maintenance schedules, and logical constraints. Data sources include historical records, expert judgment, and databases. Modeling follows, with dynamic simulation in EMRALD capturing time-dependent behaviors like staggered failures and repairs, while the Markov model is used to verify results. Simulations are executed over a defined mission time (e.g., one year) using Monte Carlo runs to estimate system success probability and unavailability. Finally, results are analyzed and methods compared in terms of system-level availability, modeling complexity, and flexibility, providing guidance for method selection.

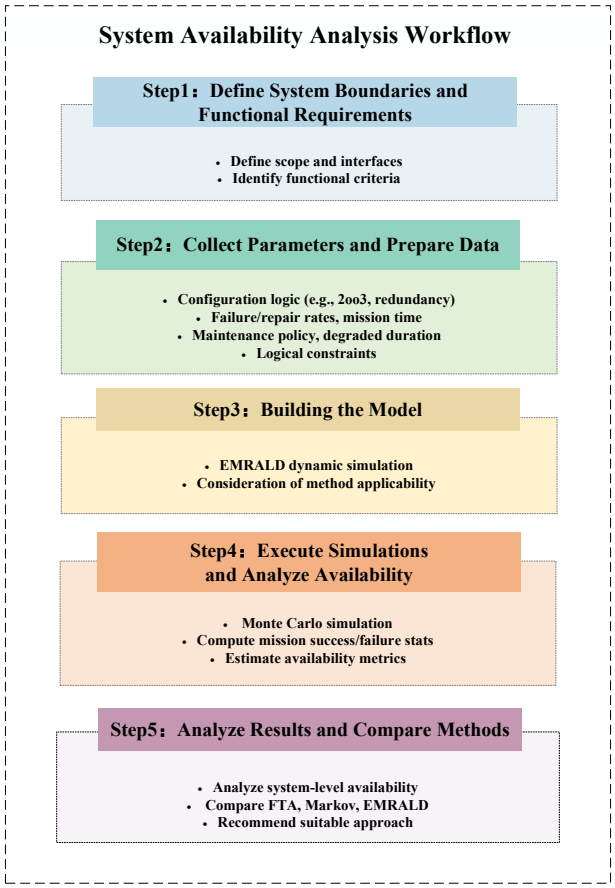

FIGURE 1. Workflow for System Availability Analysis Using EMRALD

III. EVENT MODELING RISK ASSESSMENT USING LINKED DIAGRAMS (EMRALD)

EMRALD, developed by INL, is a software tool for dynamic PRA (probabilistic risk assessment), considering time factors to more accurately assess operational risks. It has been updated to integrate with external physics-based simulation tools for external hazard PRA. Its goal is to provide modeling concepts for traditional PRA, a simple interface for complex interactions, and coupling functions for dynamic PRA challenges [18]. EMRALD uses three-stage discrete event analysis without fixed or variable time steps—simulation advances to the next event in time [19]. Results are derived statistically from Monte Carlo simulation runs. As shown in Fig. 2, its core elements are states, events, actions, and arrows.

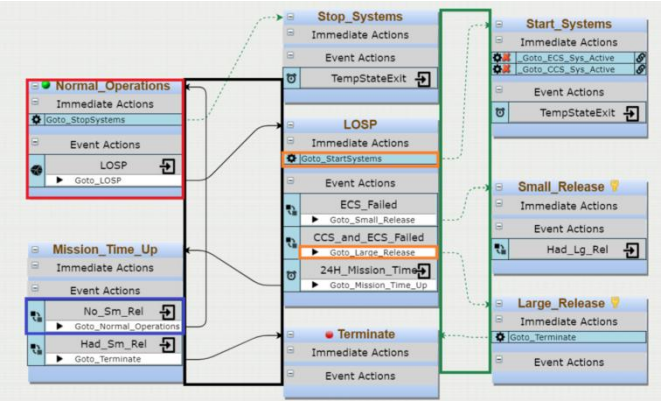

FIGURE 2. Elements of A Representative EMRALD Diagram. (Red) State S, (Orange) Actions A, (Blue) Events E, (Black) State Transition to Different State RB, (Green) State Transition to Current State RG.

This example illustrates the diagram's internal structure, including a state transition diagram with elements and set notation in Equation (1) [20]. The expected outputs are mean time to failure (MTTF) and fraction of key states.

$$\text{EMRALD} := < S, E, A, R_B, R_G, D > \quad (1)$$

IV. AVAILABILITY ANALYSIS METHOD of TYPICAL REPAIRABLE SYSTEM

For typical systems like series, parallel, k/n, and bypass systems [2], if the life and maintenance time of each unit follow an exponential distribution. This paper uses the Markov and EMRALD modeling methods to analyze the availability of these four systems and compare the consistency of the results, the Markov model can be applied for availability analysis..

IV.A. Availability of Repairable Series Systems

IV.A.1. Availability of 2-Unit Series System

Assume that the repairable series system consists of 2 units, whose failure rates are λ_1 and λ_2, and whose maintenance rates are μ_1 and μ_2. The maintenance strategy is one maintenance worker (or one group of maintenance workers), that is, the possible states of the system are: 0 state - both units work normally, the system is normal; 1 state - any one of the two units fails and is repaired, the other unit works normally, and the system fails; 2 state - both units fail, the system fails. EMRALD Modeling Diagram is shown in Fig. 3. The results are compared to the corresponding EMRALD model as shown in Table 1.

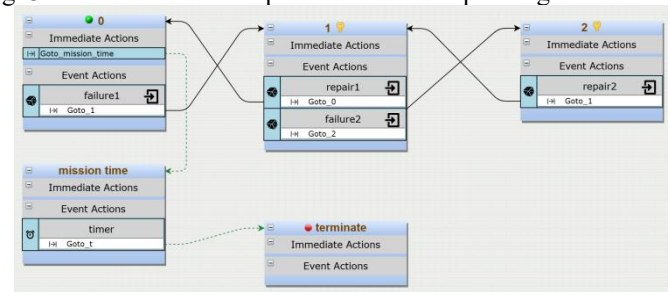

FIGURE 3. EMRALD Modeling Diagram of A Repairable Two-Unit Series System

TABLE Ⅰ. Availability of A Repairable Two-Unit Series System

Failure Rate	Repair Rate/time	Mission Time	Number of Runs	EMRALD Availability	Analytical Availability
1/10days	1/day	1000days	100000	0.81932	0.81967

IV.B. Availability of Repairable Parallel Systems

IV.B.1. Availability of A Parallel System of Identical Distribution Units

Assume that the system consists of two identical distributed units in parallel, with a failure rate of λ and a maintenance rate of μ. If one unit fails, a repairman will immediately repair it until it is repaired, and the system will still work normally. The possible states of the system are: State 0 - Both units work normally, and the system is normal; State 1 - Any one of the two units fails and is repaired, and the other unit works normally, and the system is normal; State 2 - Any one of the two units fails and is repaired, and the other unit fails and is waiting for repair, and the system fails. EMRALD Modeling Diagram is shown in Fig. 4. The results are compared to the corresponding EMRALD model as shown in Table 2.

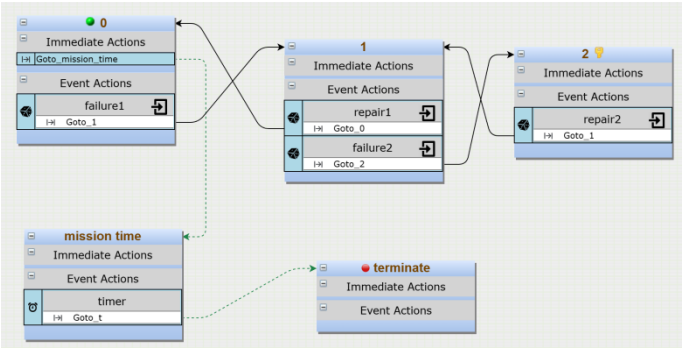

FIGURE 4. Repairable 2-Unit Parallel System EMRALD Modeling Diagram

TABLE Ⅱ. Availability of A Repairable 2-Unit Parallel System

Failure Rate	Repair Rate/time	Mission Time	Number of Runs	EMRALD Availability	Analytical Availability
1/10days	1/day	1000days	100000	0.9911	0.9836

IV.C. Availability of Repairable k/n Systems

IV.C.1. Availability of 2/3 Systems with the Same Distribution Unit

A 2/3 system composed of identically distributed units has a unit failure rate of λ and a maintenance rate of μ. With 1 repairman, the possible states of the system are: State 0 - All 3 units are working properly, and the system is normal; State 1 - Any one of the 3 units is repaired, and the system is normal; State 2 - Any one of the 3 units is repaired, and the other unit is waiting to be repaired, and the system is faulty. EMRALD Modeling Diagram is shown in Fig. 5. The results are compared to the corresponding EMRALD model as shown in Table 3.

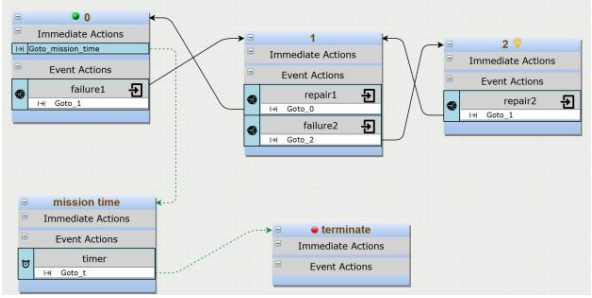

FIGURE 5. EMRALD Modeling Diagram of 2/3 System with 2 Identical Distributed Units

TABLE III. Availability of 2/3 Systems with Two Identical Distributed Units

Failure Rate	Repair Rate/time	Mission Time	Number of Runs	EMRALD Availability	Analytical Availability
1/10days	1/day	1000days	100000	0.95509	0.95588235

IV.D. Availability of Repairable Bypass Systems

IV.D.1. Availability of Repairable Bypass Systems

Only one of the n units in the system works. When the working unit fails, it is connected to another normal standby unit through the fault monitoring and conversion device to continue working. The system will not fail until all units fail. Such a system is called a bypass system. Suppose a bypass system composed of two different distributed units is maintained by a maintenance worker, with failure rates of λ_1 and λ_2, and maintenance rates of μ_1 and μ_2. According to the analysis of the system's working process, the possible states of the system are: State 0 - Unit 1 is working, Unit 2 is on standby, and the system is normal; State 1 - Unit 1 is repaired, Unit 2 is working, and the system is normal; State 2 - Unit 1 is on standby, Unit 2 is working, and the system is normal; State 3 - Unit 1 is working, Unit 2 is repaired, and the system is normal; State 4 - Unit 1 is repaired, Unit 2 is on standby, and the system is faulty; State 5 - Unit 1 is on standby, Unit 2 is repaired, and the system is faulty. EMRALD Modeling Diagram is shown in Fig. 6. The results are compared to the corresponding EMRALD model as shown in Table 4.

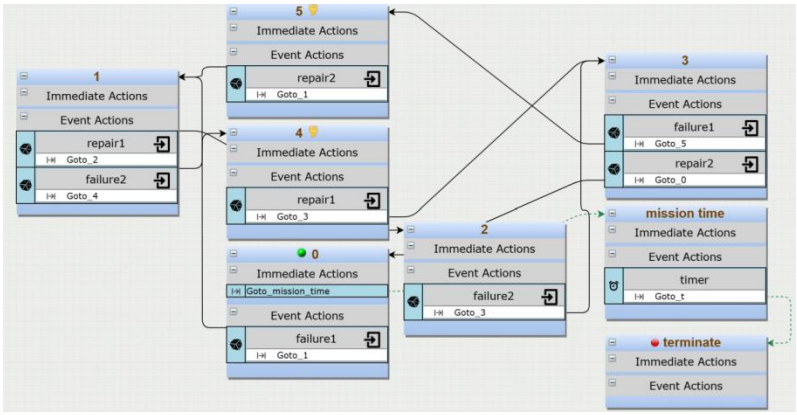

FIGURE 6. EMRALD Modeling Diagram of Two Different Distributed Unit Bypass Systems

TABLE IV. Availability of Two Different Distributed Unit Bypass Systems

Failure Rate	Repair Rate/time	Mission Time	Number of Runs	EMRALD Availability	Analytical Availability
1/10days	1/day	1000days	100000	0.9966	0.990991

The theoretical value here refers to the result calculated by the Markov model. Due to its random sampling characteristics, the result cannot be completely consistent with the theoretical calculation value. However, from the comparison results, the calculation results of EMRALD are highly consistent with the theoretical value, indicating the effectiveness and accuracy of its method in this problem.

V. A CASE STUDY on the COMPONENT COOLING WATER SYSTEM

V.A. EMRALD Model of Component Cooling Water System

This paper uses EMRALD software for dynamic modeling, and evaluates the frequency of the initiating event of "loss of both trains of the component cooling water system" during the power operation stage. The component cooling water system is a typical redundant backup system, and the failure of both trains is a typical support system initiating event. As shown in Fig. 7, it is a schematic diagram of typical component cooling water system in high flux reactor. The system consists of two independent series A and B. Each series includes two 100% capacity single-stage centrifugal pumps, one 100% capacity plate heat exchanger, and a water tank.

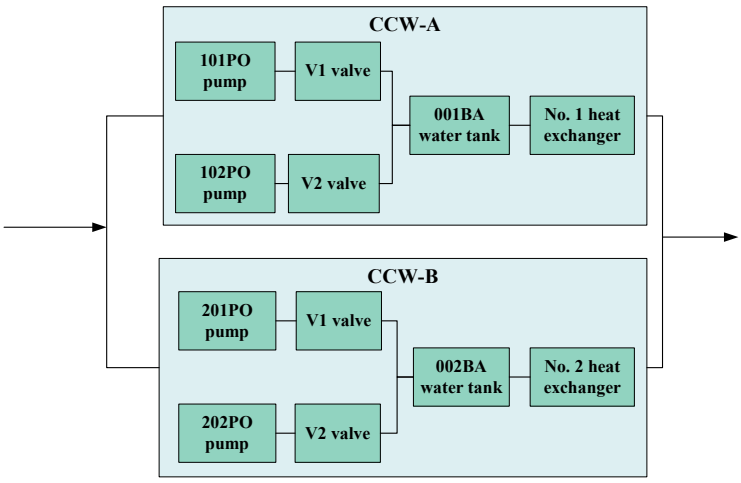

FIGURE 7. Component Cooling Water System Diagram

Assuming that the demand time of the chilled water system is 8760 hours, the operation procedures clearly stipulate the corresponding measures to be taken under different system configurations to ensure that the system availability meets the operation requirements. Under normal operation, the system is put into operation in one loop, and each loop must have at least 1 pump, 1 heat exchanger, and 1 water tank in an available state. The maintenance time after a single pump failure is assumed to be 36 hours. In this study, a fixed value was used for simplicity and consistency with the Markov model, which assumes constant rates.

The reliability data refers to the China Nuclear Power Plant Equipment Reliability Data Report [21], IAEA General Reliability Database [22], and NUREG/CR-5750 [23].

Based on the structure of the equipment component water system, the system operation procedures, and potential maintenance activities following equipment failure, the state transition diagram of the system is shown in Fig. 8. The system may be in 5 different states. If the system is in the P1 normal state, the standby train is activated when the running train fails completely. If two pumps in the running train fail, the standby train's heat exchanger and water tank are activated. When a pump or water tank/heat exchanger fails, the train is considered unavailable. From the normal state (P1), the system transitions to P2 due to a cooling pump failure. After the pump is successfully repaired, the system returns to P1. Similarly, P4 can transition to P3. When both pumps in a train fail, the train is considered failed, and maintenance of the pumps is not considered, so P3 cannot return to P2. The EMRALD modeling interface and calculation results are shown in Fig. 9.

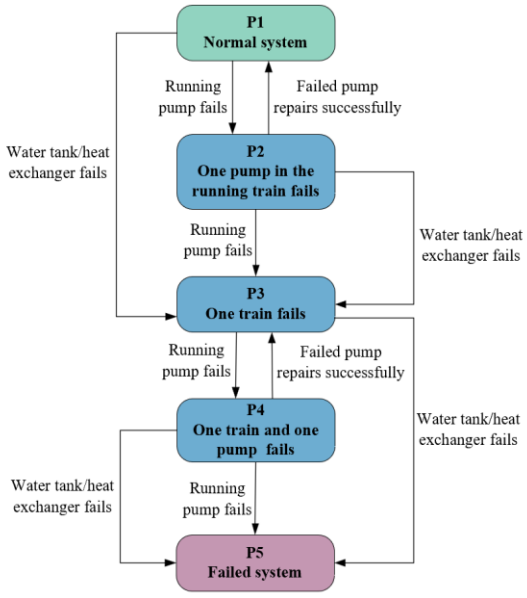

FIGURE 8. State Transition Diagram

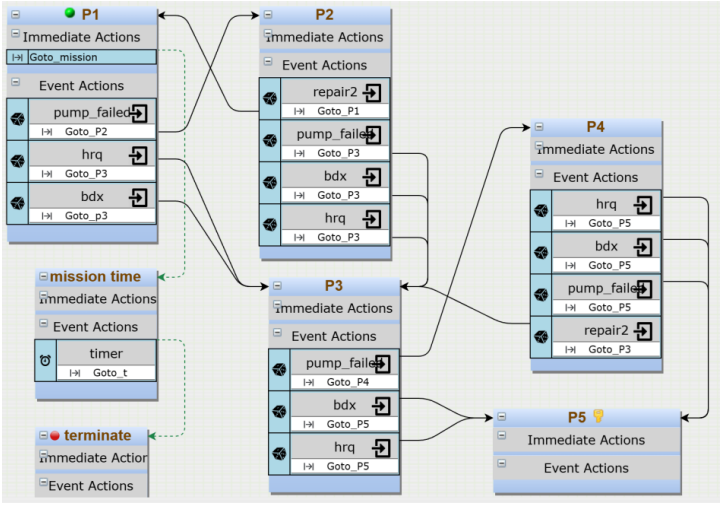

FIGURE 9. EMRALD Modeling Interface

V. B. Solution

Since the probability P of system failure within the required time can be approximately expressed by the Poisson distribution with its failure frequency F as parameter, the following formula can be obtained: f=-ln(1-P).

For 1,000,000 simulation runs with a mission time of 8760 hours, the key state "P5" occurred 355 times, resulting in a rate of 0.000355. The solution is that when the system is in the P1 state at the "current moment", the failure frequency of the system is 3.55E-04 times/reactor·year.

VI. COMPARISON of the RESULTS of THREE ANALYSIS METHODS

The EMRALD method yields a calculation result of 3.55E-04 times/ reactor·year, providing a more accurate description of the system's dynamic behavior compared to the fault tree analysis method (7.90E-04 times/ reactor·year) and the Markov method (3.64E-04 times/ reactor·year). Comparative analysis reveals that while the fault tree analysis method is computationally efficient, it struggles to dynamically model state changes due to the lack of maintenance consideration. Although the Markov method can account for maintenance, it faces challenges with state space explosion and high modeling complexity. The EMRALD method, with its event-driven approach, offers enhanced modeling flexibility and dynamic behavior simulation while maintaining calculation accuracy. Therefore, it demonstrates superior applicability for nuclear power system reliability and availability analysis, providing a more accurate and efficient modeling tool for related research. Future work can focus on expanding EMRALD's application and optimizing its computational performance to enhance its practical use in nuclear engineering safety analysis.

VII. CONCLUSIONS

In conclusion, this study presents a comprehensive system availability analysis of the component cooling water system (CCWS) in a high-flux reactor, highlighting the limitations of traditional fault tree analysis (FTA) in capturing dynamic behaviors such as maintenance, switching logic, and fault recovery. The EMRALD modeling approach, based on discrete event simulation and state transition logic, effectively represents complex system behaviors and allows integration of key factors such as mission time, failure and repair rates, and maintenance policies. The consistency between EMRALD and Markov model results for typical system configurations (series, parallel, k/n, bypass) confirms the reliability of the dynamic modeling approach. Applying these methods to the high-flux reactor's CCWS shows that EMRALD can effectively evaluate the frequency of critical initiating events, such as the loss of both cooling trains, thus offering valuable insights for risk-informed design and safety assessment. Overall, the research underlines the importance of adopting dynamic modeling techniques like EMRALD for availability analysis in nuclear systems and provides guidance for future applications in probabilistic safety assessments.

REFERENCES

[1] J. C. LEE and N. J. MCCORMICK, *Availability and Reliability of Systems with Repair*, pp. 109–139, Wiley, United States (2012).
[2] X. JIN, *System Reliability and Availability Analysis Methods*, National Defense Industry Press, Beijing, China (2007).
[3] L. W. BEI and J. Zhao, *Fault Tree Analysis of Initiating Events Due to Loss of Component Cooling Water System in CAP1400* [Dissertation], Tsinghua University, Beijing, China (2019).
[4] S. P. XING and Y. SUI, "Dynamic Reliability Assessment Method for Component Cooling Water System in Nuclear Power Plants," *Science Technology and Engineering*, 22(23), 10092–10101 (2022).
[5] B. GUO, *Research on the Estimation Method of Initiating Event Frequency in Online Risk Monitoring System* [Dissertation], Harbin Engineering University, Harbin, China (2016).
[6] Y. YU, J. J. TONG, J. ZHAO, et al. "Application of Monte Carlo Method to Simulate the Frequency of Initiating Events of Loss of Component Cooling Water System in Nuclear Power Plants," *Nuclear Power Engineering*, 31(4), 57-59 (2010).
[7] B. B. ZHANG and J. HE, "Research on the Calculation of the Frequency of Initiating Events Using Markov Model," *Proc. 2012 Nuclear Energy Probabilistic Safety Analysis Symposium*, Beijing, China, pp. 125–129, China Nuclear Energy Association (2012).
[8] L. XINGX, A. SHRESTHA, Y DAI, "Exact Combinatorial Reliability Analysis of Dynamic Systems with Sequence Dependent Failures," *Reliability Engineering & System Safety*, 96(10), 1375-1385 (2011).
[9] A. PEIRAVI, M. A. ARDAKAN, E. ZIO, "A New Markov-based Model for Reliability Optimization Problems with Mixed Redundancy Strategy," *Reliability Engineering & System Safety*, 201, 106987 (2020).
[10] S. DISTEFANO and K. S. TRIVEDI, "Non-Markovian State-Space Models in Dependability Evaluation," *Quality and Reliability Engineering International*, 29(2), 225-239 (2013).
[11] F. Q. QI, H. M. ZHONG, J. H. PANG, et al. "Optimization of Cold Standby System Maintenance Strategy Based on Semi-Markov Process," *China Mechanical Engineering*, 31(03), 336-343 (2020).
[12] N. S. Y. TEMRAZ, "Comparison of fuzzy semi-Markov models for one unit with mixed standby units with and without preventive maintenance using regenerative point method," *Heliyon*, 7(8) (2021).
[13] X. WU and J HILLSTON, "Mission reliability of semi-Markov systems under generalized operational time requirements," *Reliability Engineering & System Safety*, 140, 122-129 (2015).
[14] "git clone," https://github.com/inl-labtrack/EMRALD.git.
[15] "EMRALD - Overview," https://emrald.inl.gov/SitePages/Overview.aspx.
[16] M. CEPIN, Assessment of Power System Reliability: Methods and Applications, pp. 89–99, Springer, London, UK (2011).
[17] J. L. LIU, Probabilistic Safety Analysis of High Flux Engineering Test Reactor [Dissertation], University of Science and Technology of China, Hefei, China (2016).
[18] S. PRESCOTT, C. SMITH, L. VANG, "EMRALD, Dynamic PRA for the Traditional Modeler," *Proc. 14th International Probabilistic Safety Assessment and Management Conference,* Los Angeles, CA (2018).
[19] M. PIDD, "Object-orientation, Discrete Simulation and the Three-phase Approach," *Journal of the Operational Research Society*, 46(3), 362-374 (1995).
[20] A. EARTHPERSON, C. M. OTANI, D. NEVIUS, et al, "A combined strategy for dynamic probabilistic risk assessment of fission battery designs using EMRALD and DEPM," *Progress in nuclear energy (New series)*, 160(C), 104673 (2023).
[21] China Nuclear Energy Association, *Reliability Data Report of Equipment in Chinese Nuclear Power Plants (2022 Edition) [Technical Report]*, China Nuclear Energy Association, Beijing, China (2022).
[22] International Atomic Energy Agency (IAEA), *Generic Component Reliability Data for Research Reactor PSA* [Technical Report], IAEA-TECDOC-930, Vienna, Austria (1997).
[23] U.S. Nuclear Regulatory Commission (NRC), *Rates of Initiating Events at U.S. Nuclear Power Plants, 1987–1995* [Technical Report], NUREG/CR-5750, Washington, DC (1999).

ASRAM2025
www.asram2025.org
Asian Symposium on Risk Assessment and Management 2025
Pattaya, Thailand, 27 – 29 August 2025

Development of an ABM-based Radiation Emergency Response Simulation Applying an Exposure Model

Minho Hwang[1], Geon Kim[1], Joonseok Lim[1], Sungmin Han[1], Gyunyoung Heo[1]*

[1] *Department of Nuclear Engineering, Kyung Hee Univ., Deogyeong-daero, Giheung-gu, Yongin-si, Gyeonggi-do 17104, Republic of Korea*

ABSTRACT

Although radiological emergencies are extremely rare, their consequences can be widespread and devastating, demanding thorough preparedness. Existing evacuation simulation studies, however, have been limited by their reliance on static analysis, which fails to realistically reflect dynamic factors such as resident movement or changing traffic conditions. To overcome these limitations, this study develops and applies a real-time exposure dose evaluation model that considers the dynamic movements of residents, utilizing the agent-based radiological emergency simulation platform, PRISM (Platform for Radiological Emergency Integrated Simulation Model). The core of this research is the integration of time-varying data on radioactive material concentration and ground deposition, derived from the HYSPLIT atmospheric dispersion model, into the PRISM platform. Based on this, a methodology was implemented to dynamically track and precisely calculate the cumulative dose for each resident (agent) moving along an evacuation route, accounting for external exposure (from ground and cloud shine) and internal exposure (from inhalation of radioactive materials).

The simulations conducted in this study not only present specific analytical results but also demonstrate the broader applicability of the developed model. The true value of this platform lies in its ability to provide policy insights by exploring the potential effects and unforeseen outcomes of complex emergency response strategies through various 'what-if' scenarios. For instance, decision-makers can use PRISM to quantitatively evaluate the trade-offs of different strategies by adjusting variables such as mass transit utilization rates, evacuation routes, and assembly point logistics. Furthermore, it moves beyond conceptually emphasizing the importance of a 'golden time' for evacuation by scientifically demonstrating how delays numerically impact the average and maximum exposure doses within a population, thereby providing an evidentiary basis for designing the most effective response procedures. In conclusion, the dynamic exposure dose evaluation simulation developed in this study is significant as a powerful analytical tool capable of predicting potential problems and comparing the effectiveness of various strategies in a realistic evacuation scenario. This research can contribute to enhancing national radiological emergency preparedness by providing the key insights needed to formulate more effective and optimal response strategies.

Keywords: Radiological Emergency, Agent-Based Model, Evacuation Simulation

I. INTRODUCTION

Although radiological emergencies are extremely rare, their consequences can be widespread and devastating, demanding thorough preparedness. The Fukushima Daiichi nuclear power plant accident, triggered by the 2011 Great East Japan Earthquake, was a pivotal event that underscored this risk to the world. It vividly demonstrated how minimizing radiation exposure and systematically evacuating residents are essential for protecting lives and safety, and it highlighted the importance of simulations to verify the practical effectiveness of theoretical plans and identify unforeseen problems in complex and uncertain emergency situations [1].

In response, research on exposure dose calculation and dispersion models for radiological emergency scenarios has been actively conducted. For example, Srinivas used sophisticated atmospheric dispersion models based on initial data from the Fukushima accident to assess the dispersion of radioactive materials within a 40 km radius and the resulting public exposure [2]. Similarly, Marzo analyzed the extensive transport and deposition patterns of major radionuclides released into the atmosphere, supporting the scientific validity of the mandatory evacuation measures implemented at the time [3]. In fact, various investigations and studies after the Fukushima accident confirmed that, thanks to multi-layered protective measures

such as prompt public evacuation and restrictions on contaminated food, the exposure levels of the general public were managed within international safety standards [4]. To date, no statistically significant increase in cancer incidence due to radiation exposure has been observed [5]; however, psychological and social impacts, such as long-term anxiety and social stigma, have been identified as significant health risk factors [6].

These real-world accident experiences and research findings re-emphasize the importance of regulatory guidelines for radiation exposure. Domestic regulatory guidelines, based on recommendations from international organizations such as the ICRP and IAEA, strictly manage the annual effective dose limit for the general public at $1\ mSv$ under normal circumstances [7]. However, in large-scale emergencies like the Fukushima accident, the reference dose for judging public evacuation and sheltering can be flexibly applied up to $20 - 50\ mSv$, considering the realistic exposure risk [8].

However, existing simulation studies to support the effective implementation of these regulatory guidelines and the establishment of practical evacuation strategies have mostly been based on static analysis, such as calculating exposure doses at fixed points or assuming individuals remain in a particular location. This has resulted in a clear limitation in realistically reflecting dynamic factors such as resident movement during evacuation, changes in traffic conditions, and real-time variations in the dispersion of radioactive materials.

This study aims to overcome these limitations by utilizing PRISM (Platform for Radiological Emergency Integrated Simulation Model), an agent-based radiological emergency evacuation simulation platform developed at Kyung Hee University [9]. The core objective of this study is to develop and apply a methodology for more precisely and dynamically calculating the short-term exposure doses that residents receive while being exposed to a constantly changing environment during evacuation. This is achieved by integrating time-varying data on radioactive material concentration and deposition, derived from the HYSPLIT atmospheric dispersion model, into the simulation. Through this, the study aims to quantitatively analyze the impact of evacuation start time on cumulative exposure dose, evaluate how different evacuation methods (e.g., private vehicles, walking, assembly buses) affect exposure risk, and ultimately provide concrete insights for formulating optimal evacuation strategies that can minimize the total exposure dose for the entire population under specific conditions.

II. METHODOLOGY

II.A. PRISM (Platform for Radiological emergency Integrated Simulation Model)

PRISM (Platform for Radiological emergency Integrated Simulation Model) is an integrated modeling framework developed with the goal of establishing effective radiological emergency preparedness and response (EPR) plans to minimize damage in the event of an emergency, such as a radioactive leak [9]. The core technology of this system is agent-based modeling (ABM). This approach defines various individual elements related to a radiological emergency scenario (e.g., residents, vehicles, radioactive materials, relief supplies, etc.) as 'agents' and the 'environment'. These agents then act autonomously according to predefined rules and interact with each other, thereby reproducing and predicting the complex macroscopic phenomena that arise.

PRISM is built and simulated based on Netlogo, a free and accessible software with an easy-to-use programming language. The model focuses on illustrating the emergency modeling process by simulating the complex interactions that occur during an emergency. Additionally, it incorporates the concept of system resilience, which is defined as the probability that the degree of system recovery (resilience (RES)) returns to its original or a targeted level (targeted recovery (REC^*)) within a required time (t) following a radiological accident. This resilience is assumed to be determined by the interaction between risk factors, such as radiological concentration, and infrastructure elements, like relief supplies (for instance, exposure dose increases with the concentration of radioactive material and decreases with the availability of relief supplies).

The specific procedure for PRISM is as follows: first, it performs environmental modeling of the target area's road network, buildings, and infrastructure resources using Geographic Information System (GIS) data. Second, it identifies and selects components such as protected populations, risk factors, and mitigation infrastructure according to the scope of the simulation. Third, it selects models for pathfinding, traffic flow, and atmospheric dispersion to realistically reflect the interactions between these elements. Finally, it runs multiple simulations repeatedly to quantitatively estimate the system's degree of recovery (REC) and resilience ($RES(t)$) over time.

II.B. Application of the Dispersion Model using HYSPLIT

To improve the accuracy of the radiological emergency evacuation simulation, this study needed to precisely simulate the movement, atmospheric dispersion, and surface deposition of radioactive materials over time. For this purpose, the study used the HYSPLIT (HYbrid Single-Particle Lagrangian Integrated Trajectory) model, developed by the Air Resources Laboratory (ARL) of the U.S. National Oceanic and Atmospheric Administration (NOAA), to predict the spatiotemporal distribution of these materials [10]. The HYSPLIT model is a sophisticated atmospheric dispersion and trajectory prediction software designed to conduct detailed simulations of the transport, dispersion, and deposition of substances in the atmosphere across various time and space scales. Its key feature is the effective combination of a Lagrangian particle-tracking method and an Eulerian fixed-grid method to realistically simulate the behavior of air parcels and the pollutants they contain. It is widely used to predict how various atmospheric pollutants—like radionuclides, fine dust, hazardous chemicals, volcanic ash, and smoke—will travel, disperse, and deposit based on weather conditions after being released from a specific point. Running the model requires high-resolution gridded meteorological data (e.g., wind fields, temperature, precipitation) for the target area. Users can define the specific emission characteristics of the pollutant source (e.g., emission rate, time, and height) and can include a chemical transformation module to more accurately replicate changes in the real atmospheric environment.

The outputs of the HYSPLIT model include detailed analytical data that can be verified against actual environmental measurements, such as the pollutant's expected trajectory over time, its atmospheric concentration at specific locations and altitudes, and the amount of surface deposition per unit area. These results serve as a critical scientific foundation for various research and practical applications, including environmental impact assessments, backtracking of atmospheric pollution sources, support for developing rapid response strategies in emergencies, and related policymaking. In this research, the hourly data on the spatial distribution and deposition of radioactive materials calculated by HYSPLIT is used as input for the PRISM evacuation simulation model to enhance the accuracy of real-time exposure dose assessments along the evacuees' routes.

II.C. Exposure Dose Calculation

In this study, the exposure dose for evacuees is dynamically calculated within the PRISM simulation based on the location and time of each agent (evacuee). Based on the hourly atmospheric concentration and ground deposition data of radioactive materials derived from the HYSPLIT model, the dose assessment methodology for the primary exposure pathways considered in this study—external exposure and internal exposure (inhalation)—is as follows.

II.C.1. External Exposure Dose Calculation

The two primary external exposure pathways considered in this study are: (1) gamma radiation from radioactive materials deposited on the ground (ground-shine external exposure), and (2) gamma radiation from airborne radioactive materials (cloud-shine external exposure). The external exposure dose from these pathways is calculated by applying the Dose Conversion Factors (DCFs) provided in the U.S. Environmental Protection Agency's (EPA) "Federal Guidance Report No. 15." [11] Based on the hourly ground deposition and atmospheric concentration data derived from the HYSPLIT model, the hourly effective dose for each evacuee is calculated using the following formulas.

1. External Exposure Dose from Ground Deposition ($H_{ext,G}$)

$$H_{ext,G} = DCF_{ext,G} \times C_G \times t \quad (1)$$

2. External Exposure Dose from Airborne Concentration ($H_{ext,A}$)

$$H_{ext,A} = DCF_{ext,A} \times C_A \times t \quad (2)$$

In the formulas above, $H_{ext,G}$ and $H_{ext,A}$ represent the effective external exposure doses (in Sv) from the ground deposition and airborne pathways, respectively. The dose conversion factors used in the calculation, $DCF_{ext,G}$ and $DCF_{ext,A}$, are the external exposure dose coefficients for radionuclides deposited on the ground (in Sv/s per Bq/m^2) and for airborne radionuclides (in Sv/s per Bq/m^3), respectively. C_G, calculated from the HYSPLIT model, is the concentration of radioactive material deposited on the ground surface (in Bq/m^2), while C_A represents the atmospheric concentration near the ground at a height of 1 meter (in Bq/m^3). Finally, t denotes the exposure time in seconds.

II.C.2. Internal Exposure Dose Calculation

The internal exposure pathway considered in this study is the inhalation of airborne radioactive materials through the respiratory tract. The Committed Effective Dose Equivalent from inhalation is calculated using the Inhalation Dose Coefficients provided in the U.S. EPA's "Federal Guidance Report No. 11" [12].

The hourly effective dose from inhalation is calculated by multiplying the atmospheric concentration of the radioactive material, the individual's breathing rate, and the nuclide-specific dose coefficient, as shown in the following formula:

$$H_{int,inh} = DCF_{int,inh} \times C_A \times BR \times t \quad (3)$$

In this formula, $H_{int,inh}$ is the committed effective dose equivalent from inhalation (in Sv). The dose coefficient for the inhalation of a specific nuclide is represented by $DCF_{int,inh}$ (in Sv/Bq), and C_A is the atmospheric concentration of the radioactive material calculated by HYSPLIT (in Bq/m^3). Furthermore, BR is the breathing rate for a standard adult (for which this study applies a rate of $0.02\ m^3/s$), and t denotes the exposure time in seconds.

II.C.3. Total Effective Dose and Dynamic Accumulation

An evacuee's total effective dose is the sum of the doses from the previously defined external and internal exposure pathways. The total hourly effective dose rate (H_{total}), expressed in Sv/h, is calculated by summing the external dose from materials deposited on the ground ($H_{ext,G}$), the external dose from airborne materials ($H_{ext,A}$), and the internal dose from inhalation ($H_{int,inh}$):

$$H_{total} = H_{ext,G} + H_{ext,A} + H_{int,inh} \quad (4)$$

II.D. HYSPLIT Input Settings

To reproduce the release of radioactive materials into the environment and their atmospheric dispersion during the Fukushima Daiichi nuclear power plant accident, this study applied the 'Source Term 6 (JAEA-Katata-3h)' data, provided by NOAA (from the official HYSPLIT website), as the core source term (release scenario) for the HYSPLIT atmospheric dispersion model [13]. This source term, developed by Katata by compiling numerous field measurement data, accident progression analyses, and meteorological simulation results after the accident, provides highly detailed characteristics of the released radionuclides, including their form, the temporal variation of their release rates, and features corresponding to major physical events at different times during the accident (e.g., hydrogen explosions, pressure venting).

The most critical release information reflected in the 'Source Term 6 (JAEA-Katata-3h)' data is the distinction between I-131 and Cs-137, and the separate input for the 'gas' and 'particle' forms of each nuclide. Specifically, for I-131, both its gas and aerosol (particulate) forms were estimated and input at a rate of $3.4 \times 10^{12}\ Bq/h$ during the accident, while the particulate form of Cs-137 was applied with a release rate of $6.4 \times 10^{11}\ Bq/h$. This distinction in release forms is intended to reflect the actual differences in the behavior of radionuclides in the atmosphere—for example, gaseous iodine has much greater mobility and faster deposition characteristics, whereas particulate radioactive materials are more affected by their relatively heavier mass, slower dispersion, and surface deposition. Notably, I-131 is crucial for assessing initial atmospheric dispersion and rapid human exposure effects after the accident, while Cs-137 is a key factor in evaluating more long-term soil deposition and external exposure.

II.E. PRISM Exposure Calculation Implementation

To dynamically calculate the exposure dose for each agent within the PRISM simulation, the spatiotemporal concentration and deposition data from the HYSPLIT model are imported and processed. The detailed methodology is as follows:

First, the HYSPLIT simulation results are exported as .shp (shapefile) format using its built-in 'ESRI Generate' function. To capture the dynamic changes in the radioactive plume, data is extracted at one-minute intervals. This process generates separate datasets for ground surface deposition (C_G) and atmospheric concentration at a 1-meter height (C_A). This results in a total of six distinct data sets, accounting for the different nuclides and their forms:

- Cs-137 (Ground deposition)
- Cs-137 (Air concentration)
- I-131 particle (Ground deposition)
- I-131 particle (Air concentration)
- I-131 gas (Ground deposition)
- I-131 gas (Air concentration)

Each shapefile contains concentration data in a contour format, where the 'CONC' attribute field stores the value as a power of 10 (logarithmic scale). Within the PRISM environment, which is built on NetLogo, the gis extension is utilized to import this data. The 'gis:feature-list-of' function reads the contour features from each shapefile for each time step. The corresponding concentration values are then mapped onto the simulation's grid cells, known as 'patches'.

The simulation progresses in discrete time steps, where each 'tick' represents 10 seconds of real time. As an agent moves across the grid, the simulation identifies the patch the agent occupies at each tick. The exposure dose for that 10-second interval is then calculated using the concentration values stored in that specific patch. The total dose is computed by applying Equations (1), (2), and (3), where the time variable, t, is set to 10 seconds. This calculated dose is then added to the agent's individual cumulative dose variable. This process repeats every tick, allowing for a dynamic accumulation of the total effective dose based on the agent's unique trajectory through the evolving radiological environment. The Dose Conversion Factors used for the calculations are as follows:

- $DCF_{ext,G}$:
  - Cs-137: 7.85×10^{-18}
  - I-131: 2.44×10^{-16}

- $DCF_{ext,A}$:
  - Cs-137: 3.89×10^{-16}
  - I-131: 1.69×10^{-14}

- $DCF_{int,inh}$:
  - Cs-137: 8.63×10^{-9}
  - I-131: 8.89×10^{-9}

III. RESULTS

Utilizing the dynamic exposure dose evaluation simulation developed in this study, we quantitatively analyzed the effects of two primary research objectives on total exposure dose: the evacuation method and the evacuation start time. The simulation was conducted with a population of 5,000 agents, and to ensure the statistical reliability of the results, a total of 50 simulation runs were performed for each scenario.

A. Analysis of Exposure Dose by Designated Assembly Point Radius

The first simulation analyzed the impact of the designated walking distance to assembly points on residents' cumulative exposure dose and evacuation efficiency. In this simulation, it was assumed that residents not designated to walk to an assembly point would evacuate using their private vehicles. Two scenarios were compared, and the results are presented in Figure 1. In the figure, the solid and dashed lines represent the mean cumulative exposure dose from 50 simulation trials for each scenario, while the shaded areas represent the standard deviation. It is also important to note that the average cumulative exposure dose shown in the graph was calculated only for individuals who received a non-zero dose.

- Scenario 1: Only residents living within a 500m radius of an assembly point walk to it and then evacuate by bus.
- Scenario 2: Only residents living within a 300m radius of an assembly point walk to it and then evacuate by bus.

As shown in Figure 1, the '300m Scenario' (orange dashed line) tended to record a higher average cumulative exposure dose than the '500m Scenario' (blue line) throughout the simulation. However, an important additional finding is that despite the higher dose, the 300m scenario achieved a faster overall evacuation completion time.

This trade-off can be attributed to several complex factors. First, residents in the narrower 300m zone, covering a shorter distance, may have arrived at the assembly points almost simultaneously. This could have created a bottleneck, increasing the waiting time for buses and thereby raising the exposure dose for those individuals. Second, this outcome could also be influenced by the direction of the radioactive plume's dispersion. It is possible that, due to the specific simulated path of the plume, the 300m-radius assembly points were coincidentally located in areas with a relatively higher concentration of contamination.

In conclusion, this analysis clearly demonstrates that a potential trade-off can exist between the speed of evacuation completion and the minimization of individual exposure doses. This presents a critical policy dilemma when establishing radiological emergency response plans. Therefore, the value of an agent-based simulation platform like PRISM, as utilized in this study, is further highlighted. It allows decision-makers to run various 'what-if' scenarios—such as optimizing the utilization rates of buses and private cars or adjusting the catchment radius of assembly points—to gain key insights into optimal response strategies that can effectively minimize both total evacuation time and total exposure dose under given conditions.

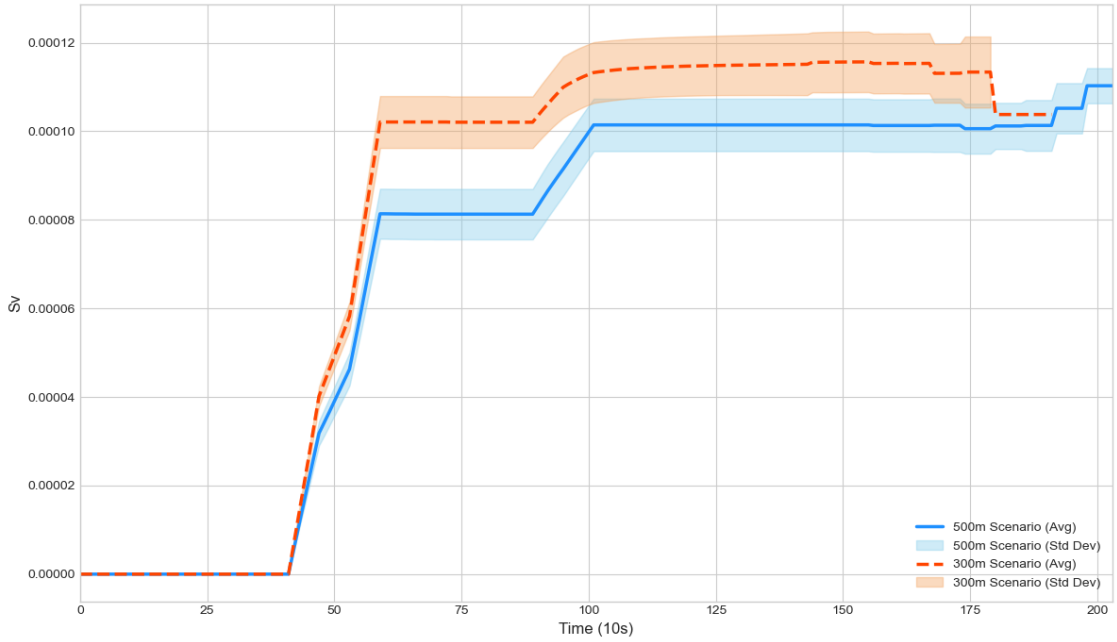

FIGURE 1. Comparison of cumulative exposure dose by assembly point radius scenario

B. Analysis of exposure dose by evacuation start time

The second simulation evaluated the impact of the delay between the disaster warning and the actual start of evacuation on exposure dose. The evacuation start time was varied from 10 to 30 minutes in two-minute intervals. Figure 2 shows the distribution of final cumulative exposure doses, with the results grouped according to each specific delay time. The mean, maximum, and minimum cumulative exposure doses for each scenario were analyzed, with the results shown in Figure 2.

The analysis shows a general trend of increasing average cumulative exposure dose (blue line) as the evacuation start time is delayed. The average dose, which was approximately $4.3 \times 10^{-5}\ Sv$ for a 10-minute delay, increased to about $6.0 \times 10^{-5}\ Sv$ with a 30-minute delay.

Particularly noteworthy is the change in the maximum dose (green line). The maximum exposure received by any single individual increased more sharply with delays. The maximum dose rose from approximately $7.0 \times 10^{-5}\ Sv$ at a 10-minute delay to a peak of nearly $1.2 \times 10^{-4}\ Sv$ at a 28-minute delay. This implies that delaying evacuation not only raises the average population dose but also significantly elevates the risk of severe exposure for certain individuals. Furthermore, the widening range between the minimum and maximum values indicates that longer delays lead to greater disparity in exposure outcomes

among the population. This result scientifically substantiates that securing a 'golden time' for evacuation through prompt decision-making and public action is critical to minimizing casualties in a radiological emergency.

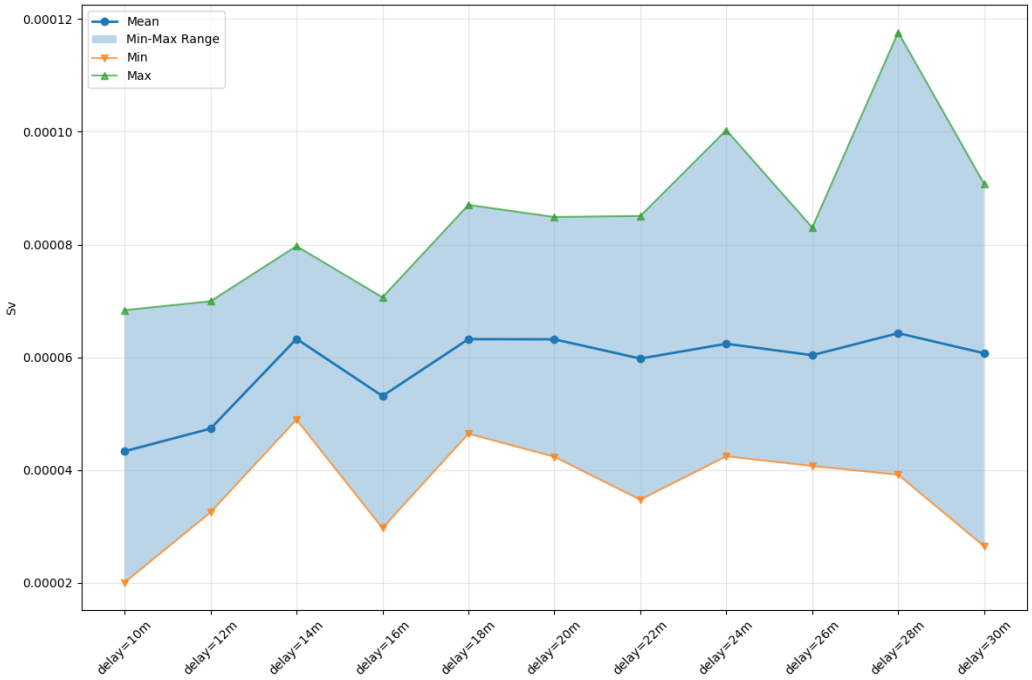

FIGURE 2. Distribution of final cumulative exposure dose by evacuation start delay

IV. CONCLUSIONS

This study developed and applied a real-time exposure dose evaluation model that considers the dynamic movements of residents during a radiological emergency, utilizing the agent-based radiological emergency evacuation simulation platform, PRISM. To overcome the limitations of existing static analysis models, this study integrated time-varying data on radioactive material concentration and ground deposition, derived from the HYSPLIT atmospheric dispersion model, into the simulation. Based on this, a methodology was implemented to dynamically track and precisely calculate the cumulative dose for each resident (agent) moving along an evacuation route, accounting for external exposure (from ground and cloud shine) and internal exposure (from inhalation of radioactive materials).

By using the developed simulation to quantitatively analyze the effects of evacuation method and start time on total exposure dose, significant policy implications were identified. First, the analysis of evacuation methods revealed that simply increasing the proportion of mass transit, such as buses, does not always guarantee an optimal outcome. A trade-off was observed where the scenario with a 500 m walking radius to assembly points resulted in a lower average cumulative exposure dose but a longer overall evacuation time compared to the 300 m radius scenario. This suggests that complex factors, including the assembly point radius, bottlenecks from bus waiting times, and the dispersion path of the radioactive plume, can create a policy dilemma between the goals of evacuation efficiency and exposure dose minimization.

Second, the analysis of evacuation start time delays clearly confirmed a trend of increasing average and maximum exposure doses as the time between the disaster warning and the actual start of evacuation grew longer. The average exposure dose increased from approximately $4.3 \times 10^{-5}\ Sv$ for a 10-minute delay to about $6.0 \times 10^{-5}\ Sv$ for a 30-minute delay, while the maximum individual exposure dose rose even more sharply. This result scientifically substantiates that securing a 'golden time' for evacuation through prompt decision-making and public action is the most critical factor in minimizing casualties during a radiological emergency.

However, this study has the following clear limitations. First, there is a temporal mismatch between the hourly data provided by the HYSPLIT atmospheric dispersion model and the 10-second timestep of the PRISM simulation. Calculations

were performed by interpolating the hourly data, which may limit the model's ability to precisely reflect rapid, real-time changes in concentration. Second, the current model assumes that residents immediately evacuate outdoors and does not consider an 'indoor sheltering' scenario, where individuals might wait inside before evacuating. As indoor sheltering provides significant radiation shielding, its omission may act as a factor that overestimates the actual exposure dose.

Despite these limitations, the dynamic exposure dose evaluation simulation developed in this study is significant as a powerful analytical tool that overcomes the shortcomings of static analysis, allowing for the quantitative comparison and assessment of various strategies in a realistic evacuation scenario. The findings of this research provide a scientific basis for determining optimal evacuation start times and transportation mode mixes. Furthermore, by laying the groundwork for incorporating more detailed protective actions like indoor sheltering, this study can contribute to formulating more effective emergency response strategies and enhancing national radiological emergency preparedness.

ACKNOWLEDGMENTS

This work was supported by the National Research Foundation of Korea(NRF) grant funded by the Korean government (MSIP:Ministry of Science, ICT and Future Planning) (No. NRF-2021M2D2A1A02044210).

REFERENCES

[1] Ten Hoeve, J. E., & Jacobson, M. Z. (2012). Worldwide health effects of the Fukushima Daiichi nuclear accident. Energy & Environmental Science, 5(9), 8743-8757.
[2] Srinivas, C. V., Rakesh, P. T., Hari Prasad, K. B. R. R., Venkatesan, R., Baskaran, R., & Venkatraman, B. (2014). Assessment of atmospheric dispersion and radiological impact from the Fukushima accident in a 40-km range using a simulation approach. Air Quality, Atmosphere & Health, 7, 209-227.
[3] Marzo, G. A. (2014). Atmospheric transport and deposition of radionuclides released after the Fukushima Dai-chi accident and resulting effective dose. Atmospheric Environment, 94, 709-722.
[4] Yamashita, S., Suzuki, S., Suzuki, S., Shimura, H., & Saenko, V. (2018). Lessons from Fukushima: latest findings of thyroid cancer after the Fukushima nuclear power plant accident. Thyroid, 28(1), 11-22.
[5] Sakai, A., Nakano, H., Hashimoto, K., Okazaki, K., Nagao, M., Shimabukuro, M., ... & Yasumura, S. (2025). Changes in peripheral blood test results among adults in the six years following the Great East Japan Earthquake: the Fukushima Health Management Survey. Fukushima journal of medical science, 24-00041.
[6] Harada, N., Shigemura, J., Tanichi, M., Kawaida, K., Takahashi, S., & Yasukata, F. (2015). Mental health and psychological impacts from the 2011 Great East Japan Earthquake Disaster: a systematic literature review. Disaster and military medicine, 1, 1-12.
[7] Protection, R. (2007). ICRP publication 103. Ann ICRP, 37(2.4), 2.
[8] Ishikawa, T. (2020). Individual doses to the public after the Fukushima nuclear accident. Journal of Radiation Protection and Research, 45(2), 53-68.
[9] Kim, G., & Heo, G. (2023). Agent-based radiological emergency evacuation simulation modeling considering mitigation infrastructures. Reliability Engineering & System Safety, 233, 109098.
[10] Stein, A. F., Draxler, R. R., Rolph, G. D., Stunder, B. J., Cohen, M. D., & Ngan, F. (2015). NOAA's HYSPLIT atmospheric transport and dispersion modeling system. Bulletin of the American Meteorological Society, 96(12), 2059-2077.
[11] Eckerman, K. F., & Ryman, J. C. (2019). External exposure to radionuclides in air, water, and soil (No. EPA 402-R-19-002). Oak Ridge National Lab., TN (United States).
[12] Eckerman, K. F., Wolbarst, A. B., & Richardson, A. C. (1988). Limiting values of radionuclide intake and air concentration and dose conversion factors for inhalation, submersion, and ingestion: Federal guidance report No. 11 (No. EPA-520/1-88-020). Environmental Protection Agency, Washington, DC (USA). Office of Radiation Programs; Oak Ridge National Lab.(ORNL), Oak Ridge, TN (United States).
[13] Katata, G., Chino, M., Kobayashi, T., Terada, H., Ota, M., Nagai, H., ... & Sanada, Y. (2015). Detailed source term estimation of the atmospheric release for the Fukushima Daiichi Nuclear Power Station accident by coupling simulations of an atmospheric dispersion model with an improved deposition scheme and oceanic dispersion model. Atmospheric chemistry and physics, 15(2), 1029-1070.

ASRAM2025
www.asram2025.org
Asian Symposium on Risk Assessment and Management 2025
Pattaya, Thailand, 27 – 29 August 2025

Comparative Analysis of Material Design and Performance Steam Generators for Nuclear Power Plants: Risk Assessment and Optimization Strategies

Muhammad Subhan[1,2], Tresna Priyana Soemardi[1], Ario Sunar Baskoro[1],
Topan Setiadipura[2], Dhandhang Purwadi[2], Andini Efriyanto Putri[3], Muslimin[3], Nafisah Amalia [3].
[1] *Department of Mechanical Engineering, Faculty of Engineering, Universitas Indonesia, Kampus UI Depok 16424, Indonesia.*
[2] *Research Center for Nuclear Reactor Technology, National Research and Innovation Agency of Indonesia (BRIN), PUSPIPTEK Serpong, 15314, Indonesia.*
[3]*Department of Mechanical Engineering, State Polytechnic of Jakarta, Kampus UI Depok 16425, Indonesia.*

ABSTRACT

Steam generators play a crucial role in nuclear power plants by converting thermal energy into steam to drive turbines. This study examines the material design and performance of steam generator configurations, through Failure Mode and Effect Analysis (FMEA) and Fishbone Diagram methodologies. The objective is to identify potential material failures, assess operational risks, and propose optimal strategies for the development of steam generators. The findings reveal that each model exhibits unique performance characteristics and failure risks. The helix model demonstrates superior heat transfer efficiency but is susceptible to structural degradation due to tensile stress introduced during fabrication. Conversely, the shell-and-tube model offers higher resilience against extreme pressure conditions, but it faces a greater risk of corrosion in the tube materials. These insights provide recommendations to enhance design robustness and optimize material selection, ensuring improved operational efficiency and safety. This research makes a significant contribution to the advancement of nuclear technology in Indonesia, particularly in optimizing steam generator configurations for improved reliability. The results serve as a valuable reference for strengthening nuclear power plant resilience and promoting the development of sustainable, environmentally friendly energy solutions.

Keywords: Steam Generator, Failure Mode and Effect Analysis (FMEA), Fishbone Diagram, Material, Performance.

I. INTRODUCTION

The operation of nuclear power plants relies heavily on steam generators, which are essential components of the heat transfer process that convert thermal energy into steam to power turbines. The dependability and efficiency of steam generators directly impact the longevity, safety, and general performance of a plant. Steam generator design and material selection optimization have gained a lot of attention as nuclear power remains a crucial source of low-carbon energy. Engineering and materials science developments present fresh chances to improve their effectiveness, robustness, and ability to withstand operating stresses. However, harsh operating circumstances, such as high temperatures, fluctuating pressures, and harsh chemical environments, can cause material deterioration and system failure in steam generators. Thus, a thorough comprehension.

Nuclear power facilities typically use one of two steam generator configurations: the shell-and-tube model or the helix model. Every design has intrinsic benefits and drawbacks regarding mechanical integrity, heat transfer efficiency, and susceptibility to failure mechanisms like fatigue, corrosion, and stress-induced cracking. Since the helix model has a larger surface area and better flow dynamics, it is well known for having higher heat transmission capabilities. On the other hand, tensile stress imposed during manufacture and operational cycling makes it more susceptible to structural failures. On the other hand, many nuclear reactor designs choose the shell-and-tube form because of its well-known strong structural stability and resistance to high-pressure conditions.

Using techniques like Failure Mode and Effect Analysis (FMEA) and Fishbone Diagram analysis, failure hazards in steam generators have been thoroughly investigated. These methods enable the systematic identification of potential failure modes, evaluation of their causes and effects, and development of mitigation plans. Specifically, FMEA offers a systematic framework for assessing risk priority numbers (RPN), which aid in ranking failure mechanisms according to their seriousness, frequency, and detectability. Analysis of fishbone diagrams also helps to identify contributory elements, including material selection, manufacturing flaws, operational stressors, and environmental impacts, that may result in failures. Applying these approaches together provides a comprehensive strategy for enhancing the safety and dependability of steam generators.

Numerous investigations have examined the performance of materials in nuclear steam generators, emphasizing important failure processes such as thermal fatigue, intergranular attack, pitting corrosion, and stress corrosion cracking (SCC). In particular, corrosion is still a major problem since it can weaken the integrity of tubes, resulting in leaks, decreased heat exchange efficiency, and even safety risks. Although the creation of sophisticated coatings and corrosion-resistant alloys has

demonstrated promise in addressing these problems, further experimental research and field data analysis are required to confirm their long-term efficacy.

This study aims to conduct a comparative analysis of the material design and performance of steam generators, employing FMEA and Fishbone Diagram methodologies to identify critical failure risks and propose optimization strategies. By systematically evaluating failure mechanisms, risk factors, and material properties, this research seeks to provide valuable insights into the selection and enhancement of steam generator designs for improved efficiency and reliability in nuclear power plants.

This research systematically investigates the operational vulnerabilities and performance dynamics of helical versus shell-and-tube steam generator (SG) configurations in nuclear power systems. By employing failure mode and effects analysis (FMEA) and fishbone diagram techniques, the study delineates critical failure pathways and proposes mitigation frameworks to enhance design robustness. A multidimensional assessment of degradation mechanisms—spanning material fatigue, thermal cycling, and mechanical stress interactions—serves to advance predictive models for SG reliability. The findings aim to establish actionable guidelines for optimizing safety margins and operational longevity in next-generation nuclear reactors.

II. METHODOLOGY

The objectives of this work are structured around three primary goals, the first is to perform a comparative analysis of design-specific failure probabilities, emphasizing geometric and material-driven risk factors. The Second is to evaluate how advanced alloy compositions and fabrication techniques impact long-term durability under extreme operational conditions; and the third is to propose targeted design modifications and maintenance protocols that mitigate identified risks while optimizing thermal and operational efficiency. By bridging empirical data with risk modeling, this research seeks to provide actionable insights for advancing SG technologies, supporting the development of resilient nuclear energy infrastructures aligned with global safety and sustainability imperatives. This research stands out due to its integrated comparative approach, which combines failure risk assessment, material performance evaluation, and design optimization. Additionally, the use of risk assessment techniques such as FMEA strengthens the systematic evaluation of failure probabilities and their impact on nuclear plant operations.

This study employs a qualitative research methodology, utilizing a literature review as the primary data collection method. Data is derived from diverse academic and technical sources, including books, scholarly journals, IAEA (International Atomic Energy Agency) documents, and publications from national seminars. The research aims to analyze specific conditions of the steam generator unit under investigation, particularly focusing on the mechanisms of damage formation in steam generator shell & tube structures and helical steam generator tubes. A comparative analysis is conducted to examine how variations in tube geometry contribute to distinct failure modes, which compromise component integrity and overall system performance. The descriptive approach is applied to systematically identify, categorize, and explain the nature of structural changes, degradation patterns, and operational impacts caused by these damages. By synthesizing theoretical insights and empirical findings from existing literature, the study seeks to provide a comprehensive understanding of the relationship between tube design variations and failure mechanisms in steam generator systems.

This research is particularly relevant in the context of Indonesia's emerging nuclear energy initiatives, where advancements in steam generator technology can significantly contribute to national energy security and environmental sustainability. The findings from this study can serve as a knowledge base for future innovations in nuclear reactor engineering and maintenance strategies. The following sections of this paper will elaborate on the research methodology for failure risk assessment, provide a comparative analysis of material performance and failure characteristics, and explore optimization strategies aimed at enhancing steam generator dependability. The conclusions derived from this study will offer actionable recommendations for industry professionals and policymakers, fostering ongoing improvements in nuclear power plant infrastructure and operations.

III. RESULTS AND DISCUSSION

In this discussion, the steam generator data comes from various sources, while the reactor types focusing on include CANDU, VVER (Russia), Siemens (Germany), Westinghouse (USA), and HTGR (China). We collected this data and analyzed it using two methods: Failure Mode and Effect Analysis (FMEA) and Fishbone Diagrams. Now, FMEA is a systematic approach used to spot potential failures in a process, product, or system before they happen. In this study, we applied FMEA specifically to examine steam generator failures that could impact the SG's materials or overall structural integrity. Meanwhile, the Fishbone Diagram is a visual tool that helps us dig into the root causes of a specific problem or effect. organizing and identifying all the different factors that might be contributing to an issue. For our steam generators, we used this method to group damage causes into categories like chemistry, operational issues, human factors, material problems, design flaws, and

maintenance practices and ultimately, the findings from both of these methods, analyze them together, and discuss them in more depth.

III. A. Analysis of Steam Generator Failure in CANDU Reactors

TABLE 1, Analysis Failure in CANDU Reactors

Failure Mode	Brief Description	Primary Controls	S	O	D	RPN
PH/SCC	Intergranular cracking due to residual stress, sensitized Alloy 600MA, and high temperatures.[1]	Alloy 800NG/690TT, routine eddy current inspections.	9	4	3	108
Fretting/Wear	Mechanical wear from fluid-induced vibrations or AVB contact.	Reinforced AVB design, debris removal, and inspections.	7	4	3	84
Pitting	Localized corrosion (chloride/sulfate) in the secondary system.[2]	Secondary water chemistry control (high pH, hydrazine).	6	3	2	36
High Cycle Fatigue	Cyclic cracking in U-bend regions due to flow-induced vibrations.	Vibration analysis, AVB reinforcement, and ultrasonic tests.	9	4	3	108
IGA/OD/SCC	Secondary-side cracking from impurities (Cl^-/sulfate) under deposits.[3]	Chemical cleaning, deposit control, Alloy 800NG/690TT.	9	4	3	108
Wastage	Generalized thinning due to chemical corrosion (phosphate/magnetite). [4]	Secondary chemistry conversion (AVT).	6	1	2	12

Based on the table above, the detailed explanation includes Severity (S) rated from 1 to 10 (with 1 indicating minimal impact and 10 indicating catastrophic failure, such as PWSCC with S=9 due to the high risk of primary-to-secondary leakage), Occurrence (O) rated from 1 to 10 (with 1 being very rare and 10 being almost certain, such as Fretting/Wear in older designs with O=4 due to frequent incidents before AVB modifications), Detection (D) rated from 1 to 10 (with 1 being easily detectable and 10 being hard to detect, such as Pitting with D=3 as it is easily identified via eddy current testing), and the Risk Priority Number (RPN) calculated as S × O × D, where high RPN values exceeding 100 indicate critical risks that necessitate priority action.[5]

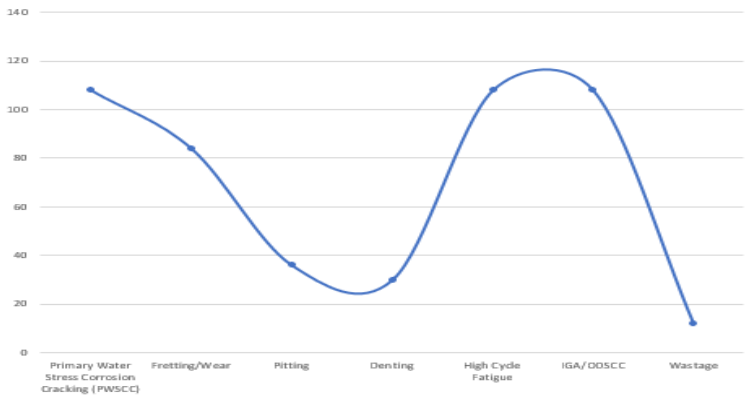

Figure 1. Damage/Failure Value Graph

Based on the graph, the highest damage values are found in High Cycle Fatigue and IGA/SCC. Therefore, this CANDU steam generator has several risks that need to be considered. The highest risks are found in Fretting/Wear and IGA/ODSCC, with an RPN value of 140 due to suboptimal AVB design and deposit accumulation. There is also a risk of High Cycle Fatigue with an RPN value of 108 in the U-bend area. To mitigate this, materials such as Alloy 690TT/800NG should be used to reduce PWSCC and ODSCC. The AVB design must be optimized to reduce fretting. Chemical control should maintain a high pH (>9.5) and reduce oxygen using hydrazine. Routine cleaning, including chemical cleaning, should be performed to remove deposits and impurities.[6]

Low-risk damages that should still be considered in the CANDU steam generator include wastage, with an RPN of 12, as it is already controlled through AVT, and denting, with an RPN of 30, due to the use of stainless steel supports. Furthermore, the damage factors in the CANDU steam generator are illustrated in the fishbone diagram as shown below.

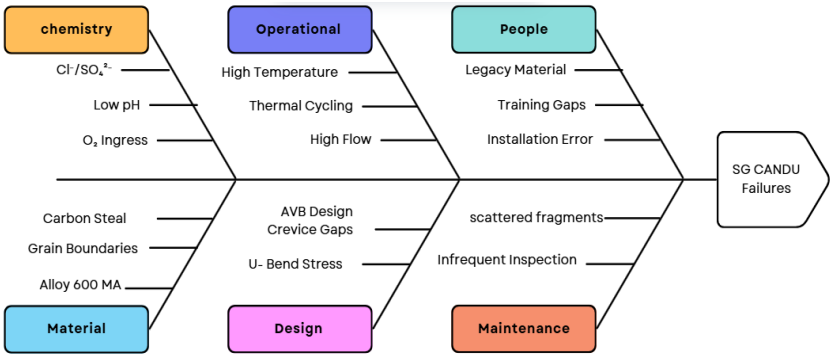

Figure 2. Fishbone CANDU Failure

The system issues are primarily due to the inherent weaknesses of the old material, Alloy 600MA, and carbon steel components, which lead to denting; design flaws, including suboptimal AVB and gaps between components, resulting in fretting and fatigue; chemical factors such as contamination and low pH, causing localized corrosion, including pitting and cracking such as ODSCC; inadequate maintenance practices, characterized by a lack of cleaning and inspection, allowing deposit buildup and undetected failures; operational conditions, involving temperature, flow, and thermal cycles, that exacerbate material degradation; and historical human factors, encompassing errors in material selection and installation, which contribute to ongoing risks.

III. B. Damage Analysis of Russian VVER Steam Generator

Table 2, Analysis Failure in Russian VVER

Failure Mode	Brief Description	Primary Controls	S	O	D	RPN
Tube Degradation	Stress corrosion cracking (SCC) or wear can cause leaks and contamination.[7]	Eddy current inspections, water chemistry control	8	5	3	120
Primary Secondary Leakage	Micro-cracks leading to secondary circuit contamination.[8]	Leak detection systems, isolation of damaged tubes	9	4	3	108
Thermal Fatigue	Cyclic cracking from operational temperature transients.[9], [10]	Operational design optimization, thermographic inspections	7	5	4	140
Flow-Accelerated Corrosion	Wall thinning due to high-velocity abrasive flow.[11]	Tube thickness monitoring, flow optimization	8	4	3	96
Uneven Feedwater Distribution	Hot spots and corrosion from damaged distributors.[12]	Feedwater distributor calibration and inspections	9	4	3	108

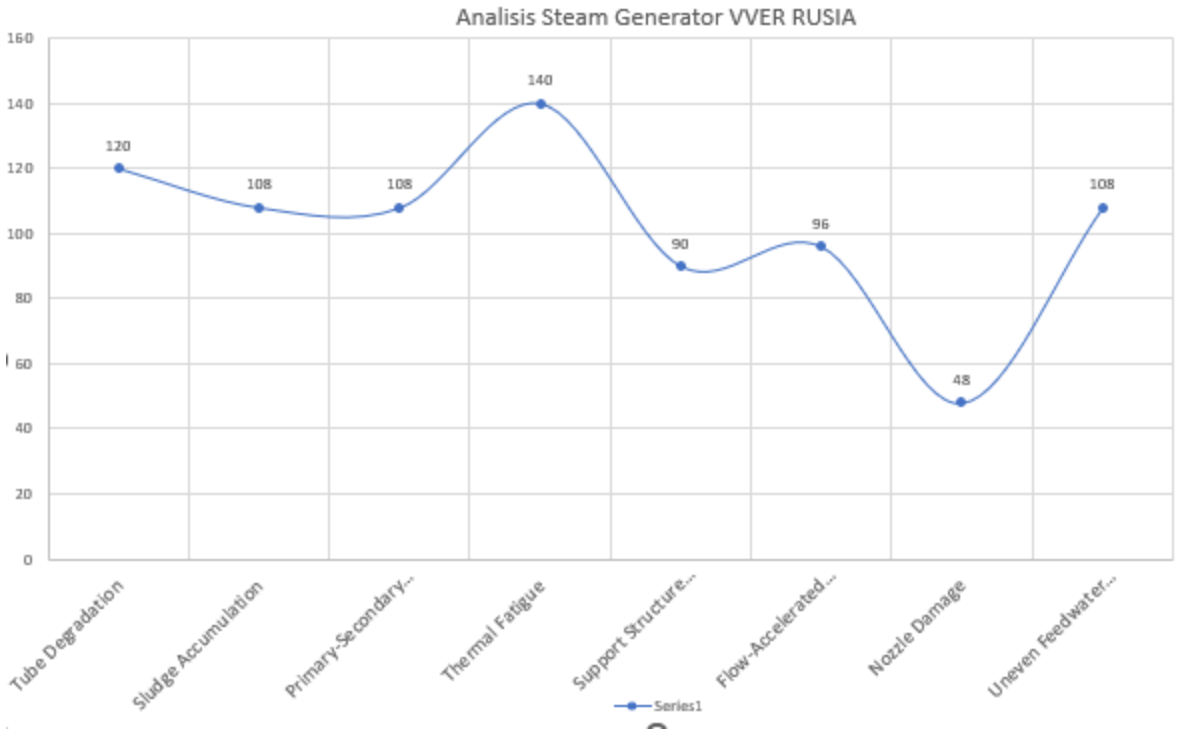

Figure 3. Damage/Failure Value Graph

Based on the graph, the damage case occurs due to thermal fatigue, which is caused by cyclic stress on tubes or components that can lead to structural failure though such failures are generally detected before reaching a critical leak. The issue originates from operational conditions, specifically sudden temperature changes due to operational transients. Additionally, design limitations, such as a lack of flexibility in the system to accommodate thermal expansion, contribute to the problem. The material used (Inconel 600/800) is also susceptible to cyclic cracking in high-temperature environments.

The lowest damage risk is associated with nozzle damage, with an RPN value of 48. This is because VVER nozzles are generally resistant to fatigue; however, cracking can occur due to fabrication defects, potentially leading to leaks.

If the causes of damage in the Russian VVER Steam Generator are mapped using a fishbone diagram, they are illustrated in the following image.[13]

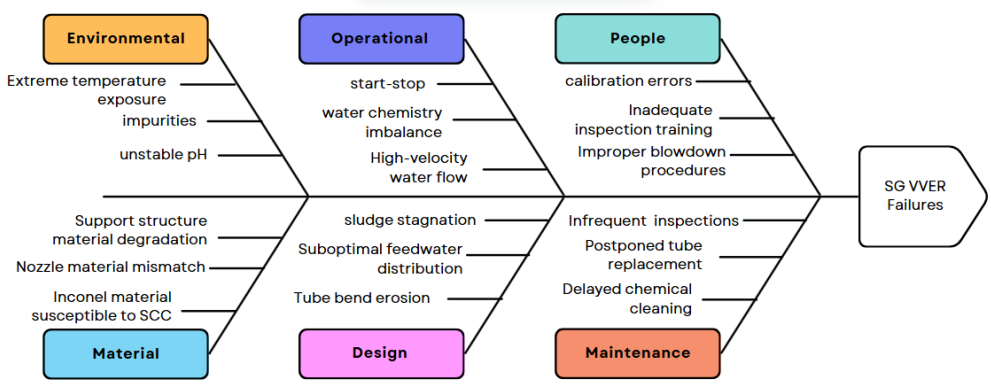

Figure 4. Fishbone Russian VVER Failure

Material failures, such as Stress Corrosion Cracking (SCC) in Inconel and wear of tube supports, are primary causes of tube degradation and structural deformation; the horizontal design of the VVER promotes sludge stagnation on the tube sheet, and uneven feedwater distribution leads to hot spots; operational transients, including sudden temperature changes, and chemical imbalance in water accelerate thermal fatigue and corrosion; contaminated feedwater, such as with chloride ions, and unstable

pH trigger corrosion and deposit buildup; human factors, like calibration errors or improper blowdown procedures, increase the risk of sludge accumulation and uneven water distribution; and irregular inspections and delayed cleaning worsen tube degradation and deposit accumulation.

III. C. **Damage Analysis of Siemens Steam Generator**

Table 3. Analysis Failure in Siemens

Failure Mode	Brief Description	Primary Controls	S	O	D	RPN
Tube Corrosion	Primary-secondary leakage and contamination due to water chemical imbalance or thermal/oxidation corrosion.[14]	Annual UT inspections, water chemistry monitoring	8	5	5	200
Tube Wear (Fretting)	Micro-cracks and leakage risk from fluid-induced vibrations or friction with supports.[15], [16]	Visual and eddy current testing (ECT)	6	5	5	180
Tube Denting	Flow restriction and crack risk from mechanical pressure or under-deposit corrosion.[17]	Eddy current testing (ECT) and profilometry	8	4	4	128
Primary Water Stress Corrosion Cracking	Leakage risk due to residual stress and corrosive environments.[18]	PWSCC-resistant materials (Alloy 690), ECT inspections	8	4	4	128
Flow-Induced Vibration	Accelerated wear from two-phase flow instability or suboptimal anti-vibration design.[19], [20], [21]	In-situ vibration analysis, support modifications	7	4	3	84
Tube Rupture	Catastrophic failure leading to LOCA and radioactive release.[22]	Automatic isolation systems, intensive ECT	9	4	7	252

Based on the table above, the assessment according to the highest SOD values reveals that Severity (S) is rated from 1, indicating minimal effect, to 10, indicating catastrophic failure such as a Loss of Coolant Accident (LOCA) and radioactive release; Occurrence (O) is rated from 1, indicating very rare, to 10, indicating almost certain, with corrosion due to secondary water chemical imbalance as a common example; and Detection (D) is rated from 1, indicating easily detected, to 10, indicating difficult to detect.

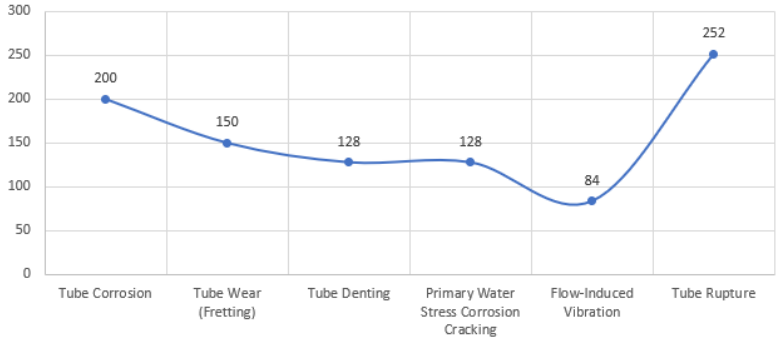

Figure 5. Damage/Failure Value Graph

Based on the graph, the highest risk condition is tube rupture, which leads to catastrophic failure (tube rupture) and can cause a Loss of Coolant Accident (LOCA), a massive loss of reactor coolant. This has the potential to trigger radioactive release into the environment and a severe nuclear accident. Tube rupture requires immediate action due to its extreme severity, presenting a direct threat to public safety, facility damage, and severe reputational impact. Detection delays in the case of cracks

or corrosion leading to rupture often go undetected until the final stages due to limitations in inspection technology (e.g., ECT cannot detect microcracks in hidden areas).

The lowest risk is tube plugging, which results in tube blockage that reduces thermal efficiency but does not pose an immediate safety threat. It can lead to decreased system performance and increased operational costs. However, tube plugging can be detected with strict plugging criteria and ECT inspection, which is very effective in identifying blocked tubes.

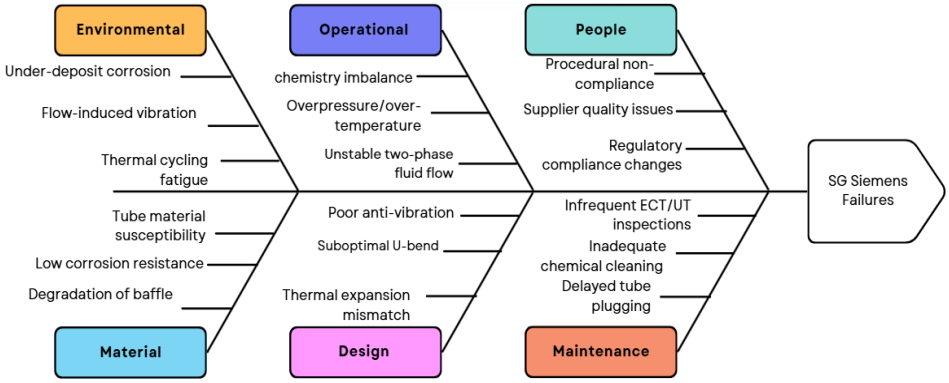

Figure 6. Fishbone Siemens Failure

The system issues are primarily due to the suboptimal design of the anti-vibration bar, leading to excessive vibrations; the use of Alloy 600, which is susceptible to Primary Water Stress Corrosion Cracking (PWSCC); operational factors such as water chemistry parameters, pressure/temperature, and fluid flow stability; failures in maintenance activities, including inspections, cleaning, and plugging criteria; environmental factors like corrosion, vibrations, and thermal fatigue; and a combination of human and external factors, such as training, procedures, supplier quality, and regulations.[13]

III. D. Damage Analysis of Westinghouse Steam Generator

Table 4. Analysis of Westinghouse Steam Generator

Failure Mode	Brief Description	Primary Controls	S	O	D	RPN
Stress Corrosion Cracking (SCC)	Primary-to-secondary leakage due to a corrosive environment, mechanical stress, or susceptible materials.[23], [24]	Eddy current inspections, corrosion-resistant alloys	9	4	3	108
Fouling (Deposits)	Reduced heat transfer and overheating from secondary water impurities (Fe, Cu, CaCO33).[25], [26]	Water chemistry control, periodic flushing	6	6	5	180
Crevice Corrosion	Structural damage from stagnant water and chloride/sulfate concentration in crevices.[27], [28]	Minimal crevice design, corrosion-resistant materials	7	5	4	140
Phosphate Wastage	Tube wall thinning due to erosion and high phosphate concentration.[29]	Chemistry monitoring, inspections	8	4	4	128
Primary Water Stress Corrosion Cracking (PWSCC)	Axial cracks in U-bends from low-pH water and residual stress.[30]	PWSCC-resistant Alloy 690, strict inspections	9	4	4	90

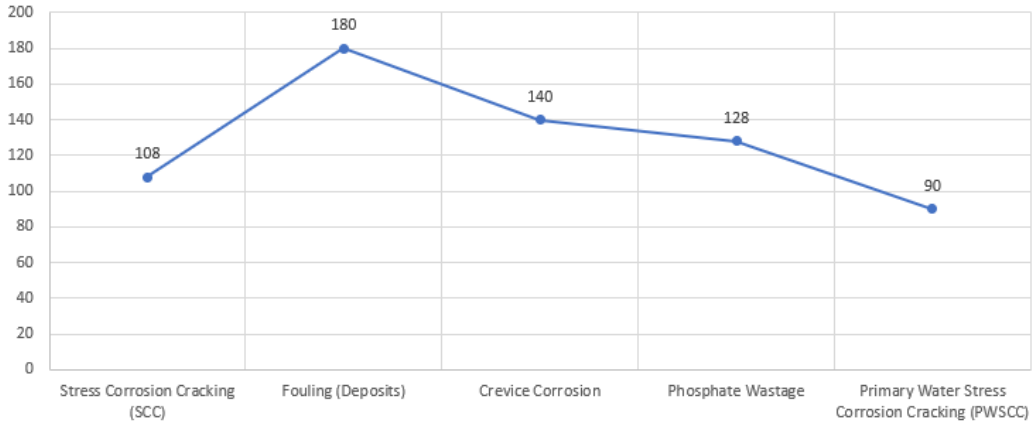

Figure 7. Damage/Failure Value Graph

The highest risk occurs in fouling, with an RPN value of 180. This is caused by Fe/Cu ion contamination in the secondary water and suboptimal filter design. The impact includes the accumulation of deposits, which then obstruct water flow, leading to secondary overheating. This event can result in a reduction in nuclear plant efficiency. If left unaddressed, extreme fouling could trigger an emergency shutdown for cleaning. The high RPN value is due to the difficulty in detecting fouling or the delays in detection.

The lowest risk is associated with PWSCC (Primary Water Stress Corrosion Cracking), with issues arising from Alloy 600's vulnerability in low pH environments and thermal stresses. As a result, microcracking can occur, leading to primary leakage, causing contamination of the secondary circuit. If this happens, a forced shutdown would be required. The RPN value for PWSCC is relatively low (90) because its detection is easier to carry out.

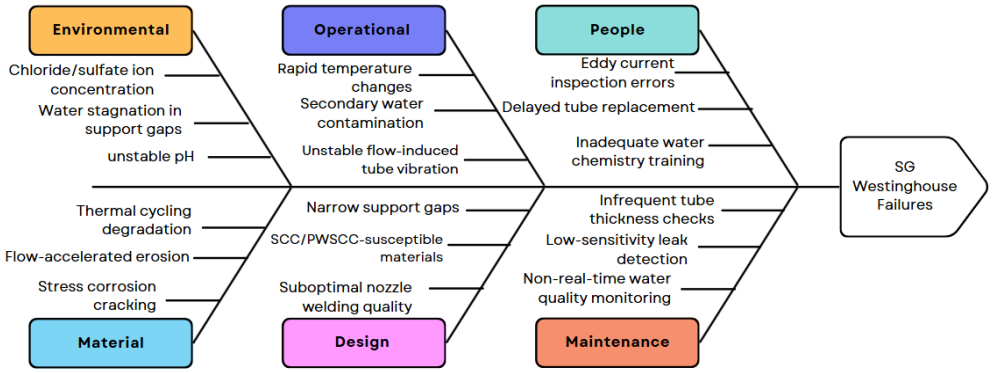

Figure 8. fishbone Westinghouse Failure

The system issues are due to several factors: design and manufacturing flaws, such as the use of Alloy 600, which is susceptible to SCC/PWSCC, and suboptimal nozzle welding quality; material degradation, including stress corrosion cracking in high pH environments and degradation caused by thermal cycling; operational factors, such as sudden temperature changes during startup and shutdown and secondary water contamination with elements like Fe, Cu, and $CaCO_3$, which exacerbate degradation; environmental conditions, including chloride and sulfate ion concentrations in water and uncontrolled pH levels in both primary and secondary circuits, that contribute to corrosion; human factors, such as inspection errors or procedural mistakes in performing eddy current inspections, which can lead to undetected issues; and inadequate inspection and monitoring, with a leak detection system that is not sensitive enough and water chemistry monitoring that is not real-time, delaying the detection of potential problems.

III. E. Damage Analysis of HTGR Steam Generator

Table 5. Analysis of HTGR Steam Generator

Failure Mode	Brief Description	Primary Controls	S	O	D	RPN
Creep Deformation	Pipe wall thinning and leakage risk due to sustained thermal/mechanical loads and inadequate creep-resistant materials.[31], [32], [33]	High-temperature alloys (Inconel 617), ultrasonic inspections	9	3	4	108
Thermal Fatigue	Cracking and fluid leakage from thermal cycling (startup/shutdown) and extreme gradients.[34]	Thermal expansion-compatible design, CFD analysis	8	4	5	160
Oxidation Corrosion	Material thinning and structural weakness caused by helium impurities (H22O, CO) at >800°C.[35], [36]	High-purity helium, anti-oxidation coatings (Al22O33)	8	4	4	128
Stress Corrosion Cracking	Secondary leakage due to residual stress and corrosive water (O22/Cl^-).[37], [38]	pH control (9–10), SCC-resistant alloys (Alloy 800H)	9	4	3	108

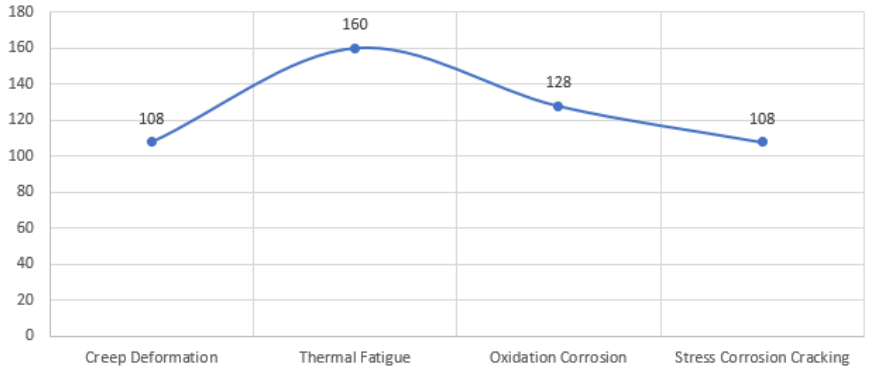

Figure 9. Damage/Failure Value Graph

The highest risk is Thermal Fatigue, which occurs due to repeated thermal cycles, such as those during startup/shutdown, causing material expansion/contraction. Extreme temperature gradients in the helical pipe area can lead to intergranular/circular cracks in the pipe, secondary or primary fluid leakage, and a reduction in heat transfer efficiency by up to 30%. The high RPN value is caused by high-pressure helium/water leakage, which poses a risk of reactor cooling loss. Thermal cycles are an inevitable part of reactor operation. Microcracks are difficult to detect without regular non-destructive testing (NDT). The lowest risk in this HTGR Steam Generator is Creep Deformation caused by long-term thermal/mechanical load at temperatures above 800°C. This is due to the material, Inconel 617/Alloy 800H, designed to withstand creep up to 950°C. Deformation can be detected via ultrasonic wall thickness measurement. The next lowest risk is Stress Corrosion Cracking (SCC) with an RPN value of 108, caused by a combination of residual stress and a corrosive environment (e.g., chloride-containing water). However, chemical control can be strictly maintained, ensuring the secondary water's pH stays between 9–10 and oxygen levels remain below 5 ppb. The material used, Alloy 800H, has high SCC resistance. When broken down in a fishbone diagram, HTGR damage can occur due to the following factors.

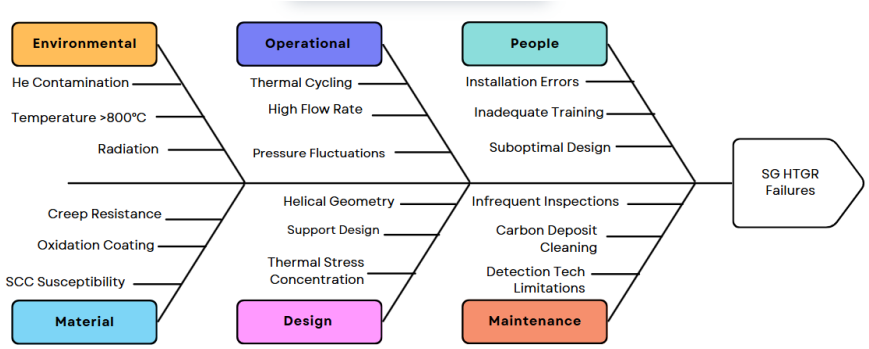

Figure 10. fishbone HTGR Failure

The system issues are primarily due to material problems, including plastic deformation caused by high temperatures, surface oxidation of the pipe from exposure to helium impurities, and cracking resulting from a combination of stress and a corrosive environment; design flaws, such as stress concentration at bend areas and uncontrolled helium flow vibration; operational challenges, like thermal cracking due to temperature gradients and turbulence and vibration caused by high flow velocity; environmental factors, including helium contamination from water or CO that triggers corrosion and material degradation due to neutron exposure; maintenance shortcomings, specifically the failure to detect microcracks early; and human factors, notably installation errors in the alignment of helical pipe sections.

III. F. Damage analysis of steam generator

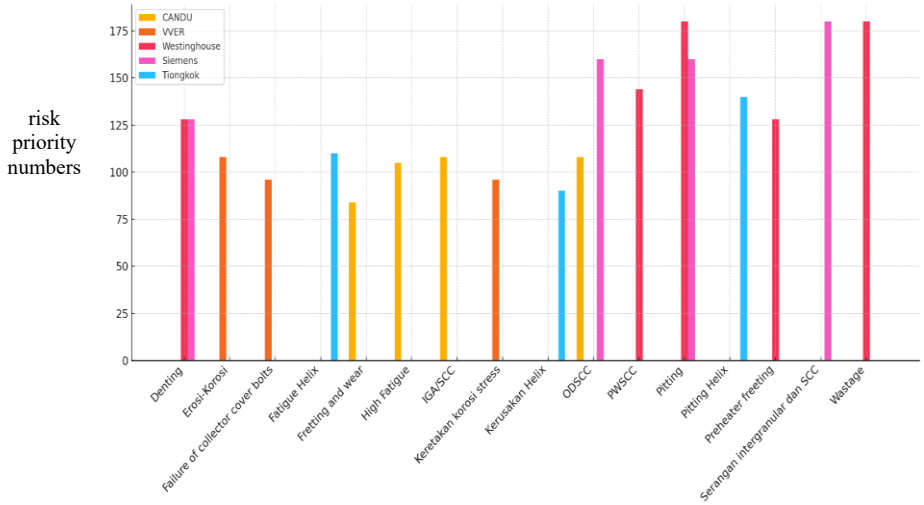

Figure 11. Diagram Of Damage Across Various Designs

The study diagram explains the distribution of damage across various designs in five plants (CANDU, VVER, Westinghouse, Siemens, and China). Based on the available data, it can be concluded that for the CANDU design, the most frequent damages are IGA/SCC and ODSC, with equal percentages, indicating that corrosion is the main challenge in this design. In the VVER design, the most common damage is erosion-corrosion, suggesting that the material and water handling must be given more attention. For the Westinghouse design, phosphate wastage and pitting are the dominant types of damage, signaling issues with water chemistry control and contamination. In the Siemens design, intergranular attack, SCC, and pitting are the most frequent types of damage, indicating challenges in managing corrosion stress and chemical environment control. In the Chinese design, the main damage is helix pitting, indicating that the helix tube design requires special attention to material fatigue and corrosion. Overall, pitting and corrosion occur frequently in various steam generator designs, requiring more attention in material development and water control methods.[13]

The chart serves as a visual tool for risk assessment, enabling stakeholders to identify and prioritize failure modes with the highest RPN values. The prominence of Siemens reactors with RPN values of 150 for multiple failure modes underscores the need for targeted interventions, such as enhanced maintenance, improved material selection, or design modifications, to mitigate these risks. Westinghouse and China, with RPN values of 125 for specific modes, also require attention, particularly for Dewetting, ODSCC, and PWSCC, which are critical in nuclear safety contexts.
The moderate RPN values for CANDU and VVER (around 100) suggest lower immediate risks, but these still warrant monitoring to prevent escalation. The absence of data for certain failure modes across some reactor types may indicate either low relevance (e.g., Helical Pretensioner not applicable to CANDU) or a lack of data, which could be an area for further research. This comparison facilitates informed decision-making in risk management, ensuring resources are allocated efficiently to address the most critical risks first, thereby enhancing the safety and reliability of nuclear reactor operations.

In the CANDU Steam Generator, High Cycle Fatigue and Intergranular Attack/Outside Diameter Stress Corrosion Cracking (IGA/ODSCC) exhibit the highest Risk Priority Number (RPN) of 108, indicating a significant failure risk due to cyclic stress and under-deposit corrosion. Fretting/Wear (RPN 84) arises from fluid-induced vibration and suboptimal design

of the Anti-Vibration Bar (AVB). This is further exacerbated by the use of older materials (Alloy 600MA), which are highly susceptible to Stress Corrosion Cracking (SCC). Inadequate AVB design and the accumulation of chemical deposits (chlorides/sulfates) aggravate corrosion processes. Therefore, it is recommended to replace the material with corrosion-resistant alloys such as Alloy 690TT or 800NG, optimize AVB design, and enhance routine chemical cleaning to reduce deposit buildup.

In the Russian VVER Steam Generator, Thermal Fatigue (RPN 140) is predominantly caused by extreme operational temperature transients, while Tube Degradation (RPN 120) is attributed to SCC and abrasive flow. The horizontal design leads to sludge stagnation and uneven feedwater distribution, and the use of Inconel 600/800 makes the tubes vulnerable to cyclic cracking. Thus, improvements are necessary in feedwater distribution, thermal flexibility of the design, the use of high-temperature-resistant materials, and the implementation of routine thermographic inspections.

In the Siemens Steam Generator, Tube Rupture (RPN 252) poses a high risk of Loss of Coolant Accident (LOCA), and Tube Corrosion (RPN 200) results from chemical imbalance in the water. These issues stem from ineffective AVB design, the vulnerability of Alloy 600 to Primary Water Stress Corrosion Cracking (PWSCC), and operational factors such as fluctuating water chemistry and flow-induced vibrations. Therefore, it is recommended to replace materials with Alloy 690, increase the frequency of Eddy Current Testing (ECT), optimize the AVB design, and implement real-time water chemistry control.

In the Westinghouse Steam Generator, Fouling (RPN 180) due to Fe/Cu ion contamination reduces thermal efficiency, while Crevice Corrosion (RPN 140) is triggered by water stagnation and chloride concentration. These issues are caused by suboptimal secondary filter design, the susceptibility of Alloy 600, and poor inspection procedures with non-real-time chemical monitoring. Therefore, there is a need to improve water chemistry control, implement regular deposit cleaning, use corrosion-resistant materials such as Alloy 800H, and optimize joint design.

Compared to these, in the HTGR Steam Generator, Thermal Fatigue (RPN 160) is caused by startup/shutdown cycles and extreme temperature gradients, while Oxidation Corrosion (RPN 128) results from helium impurities at temperatures above 800°C. This is likely due to the plastic deformation of Inconel 617/800H at elevated temperatures and the stress concentration in the helical tube design. To address these issues, it is recommended to apply anti-oxidation coatings (e.g., Al_2O_3), maintain helium purity, and conduct Computational Fluid Dynamics (CFD) analysis to optimize flow distribution and reduce vibration.

IV. CONCLUSIONS

In conclusion, the comparative analysis highlights the diverse performance and risk profiles of steam generator designs across nuclear reactor types. Helix models offer superior heat transfer but are prone to structural degradation, as seen in high RPN for helix-related failures in Westinghouse and Siemens, while shell-and-tube models, prevalent in these reactors, are pressure-resilient but face higher corrosion risks, evidenced by elevated RPN for SCC and wastage. Optimization strategies should focus on material selection, design enhancements, and tailored maintenance to mitigate these risks, ensuring improved safety and efficiency. This research underscores the importance of customized risk management for each reactor type, contributing to the advancement of nuclear technology in Indonesia and globally, promoting sustainable energy solutions.

ACKNOWLEDGMENTS

We would like to express our appreciation for the partial support received from the Research and Innovation Funding Program for Advanced Indonesia (RIIM) batch 3 Number B-848/II.7.5/FR.06/5/2023 and B-1031/III.2/FR.06.00/5/2023 as provided by LPDP and BRIN.

REFERENCES

[1] P. Liu *et al.*, "Quantitatively evaluating the contribution of intergranular carbides, Cr-depleted zone, and grain boundary to intergranular stress corrosion cracking of Alloy 600 in a simulated boiling water reactors environment with high oxygen concentrations," *Acta Mater*, vol. 269, 2024, doi: 10.1016/j.actamat.2024.119794.

[2] D. Lucan, "Behaviour of the steam generator tubing in water with different pH values," *Nuclear Engineering and Design*, vol. 241, no. 4, pp. 1172–1176, Apr. 2011, doi: 10.1016/j.nucengdes.2010.03.029.

[3] D. Lucan, "CANDU steam generator corrosion due to the impurities of concentration and deposition," in *Steam Generators: Design, Types and Applications*, 2017, pp. 197–225.

[4] C. W. Turner, M. Huang, and A. McKay, "Hideout, hideout return and crevice chemistry in nuclear steam generators," in *Steam Generators for Nuclear Power Plants*, Elsevier Inc., 2017, pp. 273–321. doi: 10.1016/B978-0-08-100894-2.00012-1.

[5] N. Fasya Fashihah Khalid, Z. Mohd Salleh, I. Amin Ishak, R. Hanizam Madon, I. Taib, and M. Fairuz Marian, "Advances in Fluid, Heat and Materials Engineering Analysis of the Performance of a Pressure Vessel Structure: A Numerical Method Approach," vol. 2, pp. 23–35, 2024, doi: 10.37934/afhme.2.1.2335.

[6] R. L. Tapping, J. Nickerson, P. Spekkens, and C. Maruska, "CANDU steam generator life management," 2000. [Online]. Available: www.elsevier.com/locate/nucengdes

[7] C. L. Verona and R. L. Higginson, "Stress corrosion cracking of CrNi martensitic stainless steels for steam turbine blades," *Materials at High Temperatures*, vol. 26, no. 1, pp. 79–83, 2009, doi: 10.3184/096034009X438202.

[8] O. Horner, E.-M. Pavageau, F. Vaillant, and O. De Bouvier, "Laboratory results of stress corrosion cracking of steam generator tubes in a 'Complex' environment - an update," in *EUROCORR 2004 - European Corrosion Conference: Long Term Prediction and Modelling of Corrosion*, 2004. [Online]. Available: https://www.scopus.com/inward/record.uri?eid=2-s2.0-84867263338&partnerID=40&md5=fbd37e50d3e7ebfbe10f008da44e8df3

[9] R. Adibi-Asl and R. Seshadri, "Thermal hot spot damage assessment in pressure vessels," in *American Society of Mechanical Engineers, Pressure Vessels and Piping Division (Publication) PVP*, 2016. doi: 10.1115/PVP2016-63903.

[10] R. Adibi-Asl, M. Rana, R. Seshadri, and C. Joshi, "Simplified procedure to assess hot spots in pressure vessels," in *American Society of Mechanical Engineers, Pressure Vessels and Piping Division (Publication) PVP*, 2020. doi: 10.1115/PVP2020-21825.

[11] IAEA, "Assessment and management of ageing of major nuclear power plant components important to safety: Steam generators," 1997.

[12] D. Féron and J.-M. Olive, *Corrosion issues in light water reactors: Stress corrosion cracking*. 2007. doi: 10.1533/9781845693466.

[13] Andini Efriyanto Putri, "ANALISIS PERBANDINGAN DESAIN, MATERIAL DAN KINERJA STEAM GENERATOR MODEL HELIX DAN MODEL SHELL&TUBE REAKTOR NUKLIR ," *https://repository.pnj.ac.id* , 2024.

[14] W. Tina, E. Donaldson, and T. E. Dickinson, "FAILURE ANALYSIS OF OTSG TUBE IN A COGENERATION POWER PLANT," in *American Society of Mechanical Engineers, Power Division (Publication) POWER*, 2023. doi: 10.1115/POWER2023-110584.

[15] S.-H. Jeong, B.-J. Lee, and Y.-Z. Lee, "Wear transitions of tube-support materials for a nuclear steam generator through sliding wear test and fretting wear test," in *Key Engineering Materials*, 2006, pp. 430–433. doi: 10.4028/0-87849-412-x.430.

[16] C. Y. Park and J. K. Lee, "Wear scar progression of impact-fretting at elevated temperature for steam generator tubes in nuclear power plants," in *Key Engineering Materials*, 2006, pp. 1251–1254. doi: 10.4028/0-87849-415-4.1251.

[17] S. S. Hwang, H. Pyo Kim, and J. Soo Kim, "Evaluation of the burst characteristics for axial notches on SG tubings," *Nuclear Engineering and Design*, vol. 232, no. 2, pp. 139–143, 2004, doi: 10.1016/j.nucengdes.2004.06.003.

[18] H. P. Kim, S. S. Hwang, D. J. Kim, J. S. Kim, Y. S. Lim, and M. K. Joung, "Stress corrosion cracking of a kori 1 retired steam generator tube," in *EUROCORR 2004 - European Corrosion Conference: Long Term Prediction and Modelling of Corrosion*, 2004. [Online]. Available: https://www.scopus.com/inward/record.uri?eid=2-s2.0-84867251478&partnerID=40&md5=236c0c98f1562647c939d005d45850fe

[19] E. Merzari *et al.*, "High-fidelity simulation of flow-induced vibrations in helical steam generators for small modular reactors," in *17th International Topical Meeting on Nuclear Reactor Thermal Hydraulics, NURETH 2017*, 2017. [Online]. Available: https://www.scopus.com/inward/record.uri?eid=2-s2.0-85052517479&partnerID=40&md5=78e05efd82aabb56498acf686842d478

[20] S. Khushnood, Z. M. Khan, M. A. Malik, Z. Koreshi, and M. A. Khan, "Modeling and simulation of cross-flow induced vibration in a multi-span tube bundle," in *Proceedings of the International Conference on Nuclear Engineering (ICONE12)*, 2004, pp. 253–264. doi: 10.1115/icone12-49161.

[21] L. Yang, X. Li, Y. Shi, and H. Chang, "Cfd simulated calculation of the test section of flow induced vibration for U-tubes in the two-phase flow," in *17th International Topical Meeting on Nuclear Reactor Thermal Hydraulics, NURETH 2017*, 2017. [Online]. Available: https://www.scopus.com/inward/record.uri?eid=2-s2.0-85052469457&partnerID=40&md5=0a2134dc39956a85f56de3e8cda0e45e

[22] C. W. Turner, M. Huang, and A. McKay, "Hideout, hideout return and crevice chemistry in nuclear steam generators," in *Steam Generators for Nuclear Power Plants*, 2017, pp. 273–321. doi: 10.1016/B978-0-08-100894-2.00012-1.

[23] C. L. Verona and R. L. Higginson, "Stress corrosion cracking of CrNi martensitic stainless steels for steam turbine blades," *Materials at High Temperatures*, vol. 26, no. 1, pp. 79–83, 2009, doi: 10.3184/096034009X438202.

[24] J. Wilson, "Controlling alloy 600 degradation," *Nuclear Plant Journal*, vol. 27, no. 2, pp. 36–37, 2009, [Online]. Available: https://www.scopus.com/inward/record.uri?eid=2-s2.0-67651096011&partnerID=40&md5=7ee084e80a493012b95f39765958fd35

[25] C. W. Turner, "Implications of steam generator fouling on the degradation of material and thermal performance," in *15th International Conference on Environmental Degradation of Materials in Nuclear Power Systems-Water Reactors 2011*, 2011, pp. 2162–2174. [Online]. Available: https://www.scopus.com/inward/record.uri?eid=2-s2.0-84867609048&partnerID=40&md5=96d24544168c9e4401ec680dceb6d175

[26] J. Mei, Y. Han, P. Chu, F. Xue, and Q. Peng, "Survey on fouling of steam generators in nuclear power plants," *Corrosion Science and Protection Technology*, vol. 30, no. 4, pp. 435–440, 2018, doi: 10.11903/1002.6495.2017.201.

[27] C. B. Bahn *et al.*, "Impurity concentration behaviors in a boiling tubesheet crevice: Part I. Open crevice," *Nuclear Engineering and Design*, vol. 225, no. 2–3, pp. 129–144, 2003, doi: 10.1016/S0029-5493(03)00179-1.

[28] C. B. Bahn, K. E. Kasza, J. Park, and W. J. Shack, "Experimental simulation of Na and Cl hideout in steam generator crevices," *Nuclear Engineering and Design*, vol. 250, pp. 156–166, 2012, doi: 10.1016/j.nucengdes.2012.05.019.

[29] L. Qiu, G. R. Burton, S. Rousseau, and J. Qian, "Kinetics and Thermodynamics of Sulfate Adsorption on Magnetite at Elevated Temperatures," *J Solution Chem*, vol. 48, no. 11–12, pp. 1488–1502, 2019, doi: 10.1007/s10953-019-00933-8.

[30] Y. Lu, "Effect of hazardous impurities on steam generator tube degradation," in *International Conference on Nuclear Engineering, Proceedings, ICONE*, 2010, pp. 283–291. doi: 10.1115/ICONE18-30120.

[31] R. I. Jetter, T.-L. Sham, and R. W. Swindeman, "The impact of material and design criteria on the assessment of negligible creep," in *American Society of Mechanical Engineers, Pressure Vessels and Piping Division (Publication) PVP*, 2010, pp. 717–726. doi: 10.1115/PVP2009-77953.

[32] R. I. Jetter, T.-L. Sham, and R. W. Swindeman, "Application of negligible creep criteria to candidate materials for HTGR pressure vessels," *Journal of Pressure Vessel Technology, Transactions of the ASME*, vol. 133, no. 2, 2011, doi: 10.1115/1.4001919.

[33] S. Wu, Y. Chen, Y. Yang, Y. Zhu, Y. Liu, and Y. Fan, "Validation analysis of high pressure turbine creep deformation for Ultra-supercritical steam turbine," in *Proceedings of the ASME Turbo Expo*, 2017. doi: 10.1115/GT2017-63059.

[34] T. Kokufuda and N. Kasahara, "Study on simplified prediction method of thermal ratchet deformation based on parallel bar model," in *American Society of Mechanical Engineers, Pressure Vessels and Piping Division (Publication) PVP*, 2014. doi: 10.1115/PVP2014-28631.

[35] W. Zheng *et al.*, "Oxidation behaviors of the high temperature alloys in the impure helium and argon," in *International Conference on Nuclear Engineering, Proceedings, ICONE*, 2021. doi: 10.1115/ICONE28-63659.

[36] H. Li *et al.*, "Study on Decarburization and Oxidation Corrosion Behavior of T-22 Alloy in Impure Helium of High-temperature Gas-cooled Reactor," *Hedongli Gongcheng/Nuclear Power Engineering*, vol. 43, no. 4, pp. 38–45, 2022, doi: 10.13832/j.jnpe.2022.04.0038.

[37] F. N. Smith, "DAMAGE CAUSED BY STRESS CORROSION CRACKING Stress corrosion cracking is an insidious form of damage that can occur when a susceptible metal is subjected to a tensile stress in a specific environment.," *Advanced Materials and Processes*, vol. 182, no. 7, pp. 27–29, 2024, doi: 10.31399/asm.amp.2024-07.p027.

[38] Q. Wang, W. Zheng, H. Yin, S. Li, X. He, and T. Ma, "Corrosion of high temperature alloys in the primary coolant of HTGR under very-high temperature operation," in *International Conference on Nuclear Engineering, Proceedings, ICONE*, 2020. doi: 10.1115/ICONE2020-16074.

Technical Session 10 (13:40 -15:40)	The Port 2, C Floor	Severe Accidents and Thermal Hydraulic Analyses and Accident Modelling
		Chair/Facilitator 1: Assoc.Prof. Somboon Rassame (Chulalongkorn University (CU))
		Chair/Facilitator 2: Mr. Zhe Chuan Tan (Singapore Nuclear Research and Safety Initiative)
13:40 - 14:00		ID 139: A Coupled ODR-DEM Method for Dispersion Fuel Analysis in RMC Code Speaker: Zhe Chuan Tan (Singapore Nuclear Research and Safety Initiative) Contributors: Zhe Chuan Tan (Singapore Nuclear Research and Safety Initiative), Zhiyuan Feng (China Nuclear Power Engineering Co., Ltd), Kok Yue Chan (Tsinghua University, Kan Wang (Tsinghua University)
14:00 - 14:20		ID 141: Parameter Trend Prediction Using Latent Space Forecasting for Operator Support in NPP Accidents Speaker: Donghee Jung (Ulsan National Institute of Science and Technology) Contributors: Donghee Jung (Ulsan National Institute of Science and Technology), Junyong Bae (Ulsan National Institute of Science and Technology), Seung Jun Lee (Ulsan National Institute of Science and Technology)
14:20 - 14:40		ID 21: Research on Hydrogen Risks in Large Advanced Passive Pressurized Water Reactor Speaker: Zining Hao (Beijing Key Laboratory of Passive Safety Technology for Nuclear Energy, North China Electric Power University) Contributors: Zining Hao (Beijing Key Laboratory of Passive Safety Technology for Nuclear Energy, North China Electric Power University), Zimeng Qin (Beijing Key Laboratory of Passive Safety Technology for Nuclear Energy, North China Electric Power University), Shaogang Du (Beijing Key Laboratory of Passive Safety Technology for Nuclear Energy, North China Electric Power University), Yongqi Huang (Huaneng Clean Energy Research Institute Co., Ltd), Xuefeng Lv (Beijing Key Laboratory of Passive Safety Technology for Nuclear Energy, North China Electric Power University), Yu Yu (Beijing Key Laboratory of Passive Safety Technology for Nuclear Energy, North China Electric Power University)
14:40 - 15:00		ID 51: Comparative Analysis of Experimental and Numerical Simulations of Two-Phase Flow in a Narrow Rectangular Duct Using OpenFOAM Speaker: Phakhinai Samor (Chulalongkorn University, Nuclear Engineering Department) Contributors: Phakhinai Samor (Chulalongkorn University, Nuclear Engineering Department), Autthasith Panyopas (Chulalongkorn University, Nuclear Engineering Department), Somboon Rassame (Chulalongkorn University, Nuclear Engineering Department), Narakhan khunsrimek (Chulalongkorn University, Nuclear Engineering Department)
15:00 - 15:20		ID 106: Sensitivity Analysis of Operator Actions in Bleeding Timing in OPR-1000 and APR-1400 Speaker: Gangmin KIM (CAU) Contributors: Gangmin Kim (CAU), Jaewhan Kim (KAERI), Jaehyun Cho (CAU), Changhyun Jang (CAU)
15:20 - 15:40		ID 87: Application of EMRALD for Simulation-Based Estimation of Station Blackout Sequence Frequencies in a Nuclear Power Plant Speaker: YOONSOO LEE (Chung-Ang university) Contributors: YOONSOO LEE (Chung-Ang university), Man Cheol Kim (Chung-Ang university)

ASRAM2025
www.asram2025.org
Asian Symposium on Risk Assessment and Management 2025
Pattaya, Thailand, 27 – 29 August 2025

A Coupled ODR-DEM Method for Dispersion Fuel Analysis in RMC Code

Zhe Chuan Tan[1,3], Zhi Yuan Feng[2], Kok Yue Chan[1], Kan Wang[1]

[1] *Department of Engineering Physics, Liu Qing Building, Tsinghua University, Beijing 100084, China;*
[2] *China Nuclear Power Engineering Co., Ltd, Beijing, 100840, China;*
[3] *Department of Safety Analysis, Singapore Nuclear Research and Safety Initiative, Singapore 138602, Singapore*

ABSTRACT

Dispersion fuels exhibit excellent fuel performance and thermal conductivity, coupled with exceptional safety characteristics, leading to their widespread use in research and next generation reactors such as High Temperature Gas-Cooled Reactors and Pebble-Bed Reactors. However, the arrangement of densely packed dispersion fuel such as Fully Ceramic Micro-Encapsulated (FCM) fuel is stochastic in nature, resulting in geometric complexity that challenges existing geometric modeling methods implemented in Monte Carlo codes. In this paper, we introduce a coupling method for the Optimized Dropping and Rolling (ODR) method and the Discrete Element Method (DEM), two explicit modeling methods known for the precise and efficient geometric modeling of stochastic media. The aim of this paper is two-fold; firstly, to reduce the high computational expense commonly associated with DEM, and secondly, to remove the packing fraction upper limit commonly associated with the ODR method. The coupled ODR-DEM method was then verified against particle distributions generated via existing explicit modeling methods, and the results showed that the methods are able to generate stochastic medium that exceed the particle packing fraction limit seen by the ODR method. The method also showed significant time savings over the original DEM, showing that the pre-arrangement of particles via ODR is able to reduce computational expense by DEM by a considerable margin.

Keywords: Discrete Element Method; Optimized Dropping and Rolling Method; Stochastic Media; Dispersion Fuel; RMC

I. INTRODUCTION

The spatial arrangement and modeling of fuel particles in stochastic media is fundamental in many nuclear reactor simulations, particularly for micro fuel particles such as TRISO particles, where these fuels comprise of stochastic mixtures of spherical fuel and/or poison particles embedded within a matrix. This study is motivated by the resurgence of interest in dispersion fuels, driven by recent advancements in research and industrial applications of Fully Ceramic Microencapsulated (FCM) Fuels [1] [2] [3] [4] [5], and secondly, the demand for high fidelity dispersion fuel models for use in RMC code, a continuous-energy Reactor Monte Carlo neutron and photon transport code currently being developed by the Department of Engineering Physics at Tsinghua University, Beijing [6].

The ODR method [7] [8] is a robust explicit modeling method, with previous research showing that ODR can generate particle distributions at much higher computational efficiencies compared to other explicit methods such as the Classical Dropping and Rolling (CDR) method [7] and DEM [9]. However, as the ODR method assumes that all dropped particles remain static and immovable, ODR-generated particle distributions are typically less dense than those produced by DEM [9]. On the other hand, DEM is a dynamic simulation approach that models the physical interactions between individual particles. While it is most suited for modelling high particle packing fraction stochastic media, DEM is inherently computationally intensive and time-consuming [9] [10] [11], making it highly unfeasible for the simulation of complex, memory-intensive dispersion fuel systems.

As such, given the motivations cited above, this paper proposes a coupled ODR-DEM Method for high-particle packing fraction dispersion fuel modelling, with the goal of generating high packing fraction particle distributions above the density constraints of the ODR method, whilst being computationally efficient compared to DEM. To ensure that the paper is self-contained, we describe the methodology behind the ODR and DEM methods in Sections II.A and II.B respectively, and the

coupling method in Section II.C. Section III elaborates on the results of the coupled ODR-DEM method, and in Section IV, we summarize and conclude the paper, as well as discuss limitations and future work.

II. METHODOLOGY

II.A. The Optimized Dropping-Rolling Method

The ODR Method is described below. Certain steps are described briefly as the reader is directed to previous studies [7] [8] [12] for further elaboration and pictorial descriptions.

1) Step 0 (Initiating): A spherical particle is newly generated above the top boundary of the stochastic media, with its initial position as $S_1^0 = S(c_1^0, r_1)$, where c_1^0 is the particle center with coordinates (x_1^0, y_1^0, z_1^0), and r_1 as the particle radius.
2) Step 1 (Dropping): Particles that may come into contact with the dropping particle are hence identified. The distance that the particle drops by just as it comes into first contact with either the bottom of the stochastic media, or other particles, is calculated. The particle position is then updated:

$$z_1^1 = z_2 + \sqrt{(r_1 + r_2)^2 - ((x_1^0 - x)^2 + (y_1^0 - y)^2)} \quad (1)$$

$$y_1^1 = y_1^0,\ x_1^1 = x_1^0 \quad (2)$$

$$S_1^1 = S(c_1^1(x_1^1, y_1^1, z_1^1), r_1) \quad (3)$$

3) Step 2 (Determining the Rolling Angle): The coordinates of c_1^1 are determined:

$$x_1^1 = x_2 + (r_1 + r_2)(cos\varphi)(cos\theta) \quad (4)$$

$$y_1^1 = y_2 + (r_1 + r_2)(cos\varphi)(cos\theta) \quad (5)$$

$$z_1^1 = z_2 + (r_1 + r_2)(sin\varphi) \quad (6)$$

where θ is the azimuthal angle, and φ is the polar angle. The unique pair of angles ($\theta \in [0, 2\pi], \varphi \in [0, \pi/2]$) is determined by the governing equations 4, 5, and 6. The new working basis $B_0 = (u_0, v_0, w_0)$ is established by applying a rotation defined by angle θ. The matrix that transforms coordinates from the canonical basis (*x, y, z*) to the rotated basis B_0 is denoted as M_0.
4) Step 3 (Rolling Phase 1): As described in Hitti and Bernacki [7], the initial step involves identifying the particles that intersect with the torus defined by the axis, a minor radius r_1, and a major radius of $(r_1 + r_2)$. If no particles intersect the torus, the updated coordinates of c_1^1 are computed by setting $\varphi = 0$ in Eq. 4, 5, and 6. In this case, the algorithm reverts to the initial dropping step, where $S_1^0 = S_1^2$. However, if particles are found to intersect the torus, the method proceeds to identify a particle S_3 for which the angle φ′ is maximized, with $\varphi' \in [0, \varphi]$. By setting $T = cos\varphi'$, the valid values of T correspond to the roots of the following:

$$(K_1^2 + K_2^2)T^2 - 2K_1K_3T + K_3^2 - K_2^2 = 0 \quad (7)$$

$$K_2(K_3 - K_1T_i) \geq 0 \quad (8)$$

where $K_1 = 2(W_x cos\theta + W_y sin\theta)$, $K_2 = 2W_z$, $K_3 = (W_x^2 + W_y^2 + W_z^2 + 1 - W^2)$, and the values of W correspond to $W_x = \frac{x - x_2}{r_1 + r_2}, W_y = \frac{y - y_2}{r_1 + r_2}, W_z = \frac{z - z_2}{r_1 + r_2}, W = \frac{r + r_1}{r_1 + r_2}$
5) Step 4 (Surface Intersection Check 1): The particle is then checked for intersection with the boundaries of the dispersion fuel, as per Hitti and Bernacki [7]. However, for a cylindrical annulus, the governing equations are slightly different, as per Feng et al [8]. If the particle drops below the lower surface, we compute φ'_{new} and reposition the particle so it touches the surface.
6) Step 5 (Local Coordinate System Transformation): Prior to the interaction of two colliding particles, a new coordinate system (Ω, B_1) must be established based on the rolling angle β. For more information on constructing this coordinate system, refer to Hitti and Bernacki [7] and Feng et al [8] [12]. In this local coordinate system, the position of c_1^2 is expressed as $(0;\ \Omega\, c_1^2 \cdot cos\,\beta;\ \Omega\, c_1^2 \cdot sin\,\beta)$
7) Step 6 (Rolling Phase 2): As per Step 3, we identify particles that intersect the torus defined by the axis c_2c_3, centered at $\Omega\, c_1^2$, with a small radius (r_1 and a large radius $\Omega\, c_1^2$. If no particle intersects the torus, we assign $\beta = \pi$, update the particle's position, and then check the new position of the dropping particle. If $z_1^3 \leq \min(z_2, z_3)$, we return to Step 1, setting $S_1^0 = S_1^3$. In other cases, we must consider a condition not accounted for in Hitti and Bernacki's study [7]: if $z_3 < z_1^3$ or $z_2 < z_1^3$, we revert to Step 2, replacing S_2 with S_3. If any particle does intersect the torus, we thus search for the particle associated with the smallest verified rolling angle β' in the (Ω, B_1) coordinate system, indicating that this particle is the first contacted particle along the dropping particle's rolling process, where β' is defined as:

$$\text{If } \beta < 0,\ \beta' \in [-\pi, \beta]; \quad (9)$$

$$\text{Else if } \beta \geq 0,\ \beta' \in [\beta, \pi]; \tag{10}$$

The coordinates of the particle in the transformed basis are also obtained per Eq. 11. By setting $T = cos\beta'$, the values of T that solve the system are thus the roots of the quadratic equation in Eq. 7 and 8.

$$\vec{x}_1^3 = 0,\ \vec{y}_1^3 = \Omega c_1^2 \cdot cos\ \beta',\ \vec{z}_1^3 = \Omega c_1^2 \cdot sin\ \beta' \tag{11}$$

8) Step 7 (Surface Intersection Check 2): The dropping particle is again checked for intersections with other particles and boundary surfaces, following the process in Step 4.
9) Step 8 (Stability Check): To check the stability of the dropped particle, we utilize the classical test, with the projection of the particle centers of the contacting particles onto the horizontal plane being considered. The reader is referred to previous work by Hitti and Bernacki [7] for the calculation process.

The ODR Method is highly efficient, working on the assumption that all other particles remain static during the dropping process, and neglecting particle dynamics. The utilization of a direct rolling system, although fast, results in the ODR method suffering from a lower saturation limit compared to other methods such as DEM, making the particle distributions produced by ODR much less realistic that these other methods.

II.B. The Discrete Element Method

The Discrete Element Method (DEM) simulates particle behavior in granular flows by explicitly modeling particle-particle interactions governed by Newtonian mechanics [13], where particle contacts and individual particle motions acting on each particle are considered. Newton's Second Law is used to determine the net displacement of each particle resulting from the cumulative contact forces acting on it, while a force-displacement law is applied to determine the contact forces arising from interactions with other particles or the boundaries of the stochastic medium. To determine the forces acting on the particle, normal overlap and tangential motion is considered during calculations. The dampened linear spring contact force model as discussed in Cundall and Strack [13] is utilized to derive the normal and tangential forces acting upon the particle:

$$F_{nij} = (-k_n \alpha^{3/2} - c_n \vec{v}_{ij}\, \vec{n}) \tag{12}$$

$$F_{tij} = (-k_t \vec{\delta} - c_t \vec{v}_{ct}) \tag{13}$$

Where F_{nij} and F_{tij} are the normal and tangential forces acting on the particle respectively; α represents the overlap distance between particles; δ is the tangential overlap displacement; k_n and k_t denote the linear spring stiffness in the normal and tangential directions; $\vec{v}_{ij}$ is the relative velocity of the interacting particles; and c_n and c_t are the dashpot coefficients in the normal and tangential directions, respectively.

As DEM considers particle dynamics, it is able to produce highly realistic and accurate particle distributions. However, DEM is highly computational expensive, especially in simulations involving large numbers of particles. Hence, there is motivation to reduce the high computational cost associated with DEM.

II.C. The Coupled ODR-DEM Method

The coupled ODR-DEM method is described in Fig. 1. ODR is used primarily to place particles within stochastic media in a "pre-arrangement" process. Afterwards, DEM is applied to simulate particle dynamics, while random forces are applied to the particles to simulate shaking processes, similar to that of existing manufacturing methods in FCM fuel. The post-DEM fuel is thus able to achieve packing fractions above the saturation limit of ODR, whilst having a reduced computational expense due to the application of ODR to place all particles prior to DEM.

III. RESULTS AND DISCUSSION

The algorithm was implemented as a function within RMC code, and was executed on an AMD Ryzen Threadripper 3990X 64-Core Processor, utilizing only a single thread for all computations. For each calculation set, 100 independent runs were performed, and the averaged result of these runs was used for comparison. In Section III.A, we discuss the performance of the coupled ODR-DEM method with respect to the saturation limit of the generated particle distributions. Section III.B discusses the effectiveness of the coupled ODR-DEM method with respect to computational expense and accuracy. In Section III.C, we discuss limitations and future work.

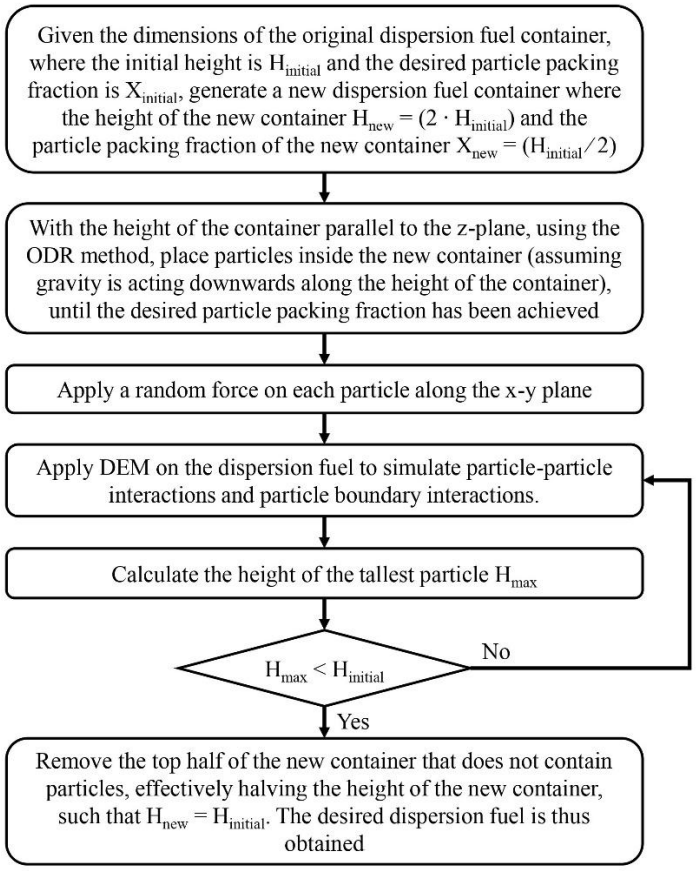

FIGURE 1. The Coupled ODR-DEM Method

III.A. Evaluation of Upper Particle Packing Fraction Limit of the Coupled ODR-DEM Method

In this Section, we utilized a cuboidal stochastic medium filled with mono-spheres as described in Hitti and Bernacki [7], and compared the results against the ODR and DEM methods respectively. Table I described the test parameters, whilst Table II displays the results for the saturation limit comparison.

TABLE I. Stochastic Medium Parameters

Parameter	Value (cm)
Length	30.0
Width	30.0
Height	35.0
Particle Radius	1.0

TABLE II. Saturation Limit Comparison between Different Geometry Modeling Methods in RMC

Method	Saturation Limit	Standard Deviation
Optimized Dropping and Rolling Method	0.576	0.0008
Discrete Element Method	0.638	0.0009
Coupled ODR-DEM Method	0.638	0.0011

The testing results from the ODR and DEM methods agree with those from current literature [7] [14]. Moreover, it can be observed that the coupled ODR-DEM Method is able to produce particle distributions that exceed the saturation limit of ODR, similar to those of DEM.

III.B. Evaluation of Upper Particle Packing Fraction Limit of the Coupled ODR-DEM Method

In this section, we compare the modelling methods in terms of stochastic media generation time and k_{inf} values between DEM and the coupled ODR-DEM Method. Tables III and IV describe the dispersion fuel parameters and fuel particle parameters respectively. In particular, in Table IV, **Layer** refers to the current layer of the particle, starting from the innermost layer of the fuel kernel, and **Rad** refers to the overall particle radius. **Rad** was varied between 0.150 and 0.350, and the particle packing fraction was set to 0.40. The results are shown in Tables V and VI, where the stochastic media generation time and k_{inf} values are compared respectively.

TABLE III. Dispersion Fuel Parameters

Parameter	Value
Boundary Condition	Full Reflection
Radius	9.00 (cm)
Height	40.00 (cm)
Matrix Material	Graphite

TABLE IV. Particle Parameters for k_{inf} Comparison

Layer	Radius/cm	Density/g/cm^3	Material
Fuel Kernel	(**Rad** - 0.085)	12.95	UC
Layer 1	(**Rad** - 0.035)	1.050	C
Layer 2	(**Rad** - 0.015)	1.900	C
Layer 3	(**Rad** - 0.005)	3.160	SiC
Layer 4	**Rad**	1.100	C

TABLE V. Stochastic Media Generation Time Comparison between Original DEM and Coupled ODR-DEM Method

Particle Radius (cm)	Stochastic Media Generation Time (seconds)		
	DEM	Coupled ODR-DEM	Factor
0.350	26.357	0.17017	154.88
0.300	69.782	0.50017	139.52
0.250	130.40	0.81112	160.77
0.200	345.32	2.30892	149.56
0.150	1443.8	9.58053	150.70

TABLE VI. k_{inf} Comparison between Original DEM and Coupled ODR-DEM Method

Particle Radius (cm)	Stochastic Media Generation Time (seconds)	
	DEM	Coupled ODR-DEM
0.350	1.000958 ± 0.000689	1.001195 ± 0.000648
0.300	1.001491 ± 0.000596	1.001733 ± 0.000718
0.250	1.002105 ± 0.000639	1.001638 ± 0.000597
0.200	1.001859 ± 0.000622	1.002295 ± 0.000712
0.150	1.000849 ± 0.000590	1.001501 ± 0.000691

As shown in Table V, the couple ODR-DEM Method generates particle distributions with a much reduced generation time, with the reduction in computational time by a factor of more than 100 across all particle radii. Furthermore, we can observe in Table VI that for all particle radii, the values of k_{inf} between the original DEM and coupled ODR-DEM methods are within three standard deviations of each other. It must be noted that as the particle distributions change, the k_{inf} will naturally change, hence the k_{inf} values cannot be directly compared with each other. However, this is a good gauge of how both processes are able to produce similar particle distributions with similar k_{inf} values. Hence, we can see that the coupled ODR-DEM method has achieved its objective of developing particle generations above the saturation limit of ODR, whilst being computationally effective against DEM.

III.C. Limitations and Future Work

There are inherent limitations to the results presented in this paper. Firstly, the computational time reported is solely the stochastic media generation time, which does not include processes that are typically considered in the total simulation time, such as inactive and active cycle calculations and burnup cycles. As the total simulation time is highly dependent on other factors, the proportion of the total simulation time that is spent on stochastic media generation may be much smaller than the time spent on other processes. Secondly, it can be observed that the ODR method is mainly used in simulating spherical particles, and as such, the coupled ODR-DEM method is limited only to spheres in this paper. This remains a potential area for improvement and research.

Regarding future work, there are a few improvements that we believe can be considered. The main mechanism within the coupled ODR-DEM method, where particles are placed via ODR and DEM is used to simulate particle shaking and settling, can be iterated for an even greater reduction in computational time. For instance, the configuration of the stochastic media may be maintained, and particles then added in via ODR. DEM is then applied to simulate particle dynamics, and the "settled" particles can then be "fixed" in space, so that future DEM processes will no longer consider particle dynamics for these "settled" portions of the stochastic media, hence reducing computational expense further. In the empty space that appears after the particles have been settled, ODR can then be used to place more particles, and this iterates until the required packing fraction is achieved. This method is algorithmically more complex, but it should promise even greater time savings.

IV. CONCLUSIONS

The ODR and DEM methods are well-established and extensively studied explicit modeling approaches, yet each comes with inherent limitations. Specifically, the ODR method does not account for particle dynamics and has a low saturation limit, while DEM is computationally intensive. To address these shortcomings, this work introduces the coupled ODR-DEM methods, designed to efficiently generate high packing fraction particle distributions that surpass the density limitations of ODR alone. The coupled ODR-DEM method successfully achieved packing densities beyond the ODR's upper threshold, comparable to those produced by DEM.

Moreover, when evaluated with variable particle radii, the coupled ODR-DEM method demonstrated significantly higher computational efficiency than DEM, while still producing particle arrangements with similar randomness and k_{inf} values—preserving both accuracy and reliability. As such, we consider this approach to be a valuable advancement in the modeling and simulation of dispersion fuel microstructures. Additionally, it holds potential for broader application in fields that rely on DEM, including granular flow and stochastic media containing non-spherical particles.

ACKNOWLEDGMENTS

This work is supported by the Department of Engineering Physics, Tsinghua University, where the use of High Performance Computing resources was supported.

REFERENCES

[1] Zaidabadi MZ, Ansarifa GR. Design of a small modular nuclear reactor with dual cooled annular fuel and investigation of the fuel inner radius effect on the power peaking factor and natural circulation parameters. Annals of Nuclear Energy. 2020 Apr;138:107185.

[2] Wang M, Zhou B, Bu S, Li Z, Chen D, Ma Z, Zhang L. A multi-annulus heat conductionmodel for predicting the peak temperature of nuclear fuels with randomly dispersed TRISO particles. Progress in Nuclear Energy. 2023 Apr;158:104602.

[3] Rabir MH, Ismail AF, Yahya MS. Neutronics calculation of the conceptual TRISO duplex fuel rod design. Nuclear Materials and Energy. 2021 Jun;27:101005.

[4] Ivanusa P, Jensen P, Condon CA, Bunn AL. Comparison of irradiated TRISO fuel radioactivity from multiple advanced reactor designs. Nuclear Technology. 2021 Sep;208:575–585.

[5] Choi JY, Hong SG, Kwon H. Conceptual design of a long cycle small modular reactor core with annular UO2 and FCM (TRU) fuels. International Journal of Energy Research. 2020 Sep; 45:11957–11975.

[6] Wang K, Li Z, She D, Liang J, Xu Q, Qiu Y, Yu J, Sun J, Fan X, Yu G. RMC - a Monte Carlo code for reactor core analysis. SNA + MC 2013 - Joint International Conference on Supercomputing in Nuclear Applications + Monte Carlo. 2014;06020.

[7] Hitti K, Bernacki M. Optimized dropping and rolling (ODR) method for packing of polydisperse spheres. Applied Mathematical Modelling. 2013 Apr;37:5715–5722.

[8] Feng Z, Liang J, Guo W, Wang K. Optimized dropping and rolling and virtual surface method for high packing fraction of dispersed fuel particles in annular container. Nuclear Science and Engineering. 2024 Sep;1–9.
[9] Feng Z, An N, Wang K. An improved distinct element method for high packing fraction stochastic media modeling. EPJ Web of Conferences. 2021;247:04026.
[10] Jajcevic D, Siegmann E, Radeke C, Khinast JG. Large-scale CFD–dem simulations of fluidized granular systems. Chemical Engineering Science. 2013 Jul;98:298–310.
[11] Berger KJ, Hrenya CM. Challenges of DEM: II. wide particle size distributions. PowderTechnology. 2014 Sep;264:627–633.
[12] Feng Z, An N, Liang J, Wang K. ODR-vs method for a high packing fraction of dispersed TRISO particles. Annals of Nuclear Energy. 2022 Feb;166:108821.
[13] Cundall PA, Strack OD. Discussion: A discrete numerical model for granular assemblies. G´eotechnique. 1980 Sep;30:331–336.
[14] Dai L, Sorkin V, Vastola G, Zhang YW. Dynamics calibration of particle sandpile packing characteristics via discrete element method. Powder Technology. 2019 Apr;347:220–226.

Parameter Trend Prediction Using Latent Space Forecasting for Operator Support in NPP Accidents

Donghee Jung, Junyong Bae, Seung Jun Lee

UNIST, Ulsan National Institute of Science and Technology, 50 UNIST-gil, Ulsan 44919, Republic of Korea
Joy00@unist.ac.kr

EXTENDED ABSTRACT

In emergency accident scenarios at nuclear power plants, operators must quickly assess the evolving plant status and determine appropriate mitigation actions. Real-time forecasting of key parameter trends can significantly enhance situational awareness and decision-making. While machine learning-based surrogate models have been developed for offline simulation analysis, their limited ability to process real-time signals restricts their use for operator support. To overcome this, we propose a latent space-based trend prediction framework using an LSTM Autoencoder and a decoder-assisted forecasting model. By optimizing predictions in the reconstructed signal space, the proposed approach improves the accuracy and interpretability of future trend forecasts during critical events.

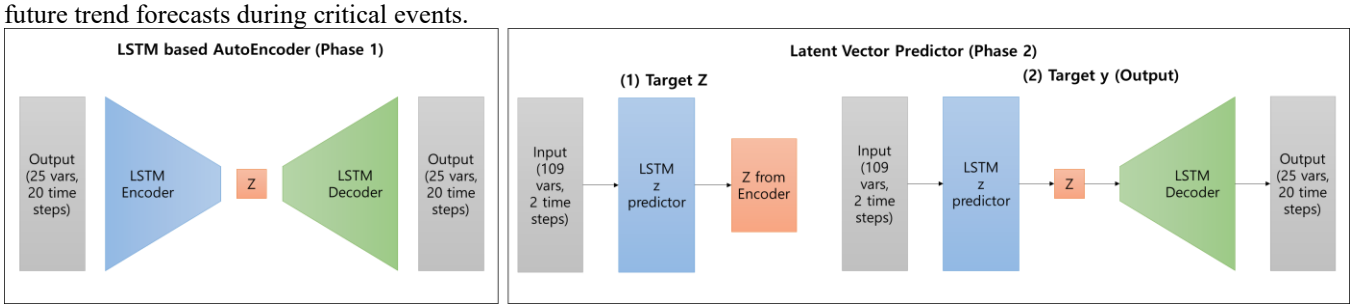

Figure 1 Overview of the proposed latent-space-based trend prediction framework. (1) latent vector prediction minimizing z error, and (2) minimizing y error.

The proposed prediction framework consists of two core components trained in two separate phases. An overview of this two-phase architecture is illustrated in **Figure 1**. In Phase 1, an LSTM-based Autoencoder (AE) compresses each 25-dimensional plant parameter sequence (20 time steps) into an 8-dimensional latent vector. The encoder is composed of seven stacked LSTM layers with decreasing units (512 → 8), each followed by batch normalization to improve convergence. The decoder mirrors this structure in reverse, expanding the latent representation back into full signal sequences. The AE is trained to minimize mean squared error between the input and reconstructed output, effectively learning a compact representation of plant dynamics. This latent space can be visualized using techniques like UMAP or t-SNE to assess the coverage of the training data and the generalizability of the model.

In Phase 2, a separate LSTM-based prediction model is trained to forecast the next latent vector using the recent plant state. This predictor receives a 2-step sequence of 743 input variables and consists of five LSTM layers (128 → 8) with dropout regularization. The predicted latent vector is then passed through the frozen decoder from Phase 1 to reconstruct the future signal trend. The entire model is optimized end-to-end using the true future sequence as ground truth. Compared to directly minimizing latent vector error (z-loss), this decoder-assisted training strategy (y-loss) encourages the predictor to capture more informative and interpretable trends in the plant behavior, leading to higher fidelity forecasting.

The framework is validated using data from the Compact Nuclear Simulator (CNS), covering scenarios such as LOCA (Loss of Coolant Accident), SGTR (Steam Generator Tube Rupture), and spurious trips. Each includes various operator mitigation actions. To determine the optimal configuration of the Autoencoder, we performed a sensitivity analysis by varying the number of LSTM layers, units, and latent dimensions. Among the tested configurations, the best result was achieved using a 14-layer structure with 512 units per layer and a latent space of 8 dimensions. This model achieved the lowest reconstruction error with a mean squared error (MSE) of 0.000235 and was used as the base for all subsequent experiments.

To evaluate model performance, both the latent-vector-based model and the full-trend model were trained on the same input data and evaluated using mean absolute error (MAE), MSE, root mean squared error (RMSE), and dynamic time warping (DTW). The results are summarized in **Table 1**. The full-trend prediction model consistently outperformed the latent-vector-based model across all evaluation metrics.

Table 1. Prediction Errors by Model Type

Model Type	MAE	MSE	RMSE	DTW
Latent Vector Predictor	0.0141	0.0014	0.0177	0.1778
Full-trend Predictor	0.0095	0.0005	0.0122	0.1101

The full-trend model achieved significantly lower DTW, indicating better alignment with the temporal dynamics of the plant parameters during transient events. This performance can be attributed to the use of the decoder during training, which enforces learning of the end-to-end mapping between latent space and observable signals. By optimizing prediction in signal space, the model learns to focus on patterns that matter most for accurate trajectory forecasting.

A qualitative analysis was performed on a LOCA scenario with a stuck-open pressurizer relief valve (PORV), focusing on three key variables: Cold Leg Temperatures (Loops 2 & 3) and Containment Pressure. **Figure 2** shows the prediction results compared to actual values, with a shaded band indicating a ±5% error range. The full-trend model's output closely follows the actual signal in all three variables, capturing both transient and steady-state behaviors more effectively than the latent-vector model.

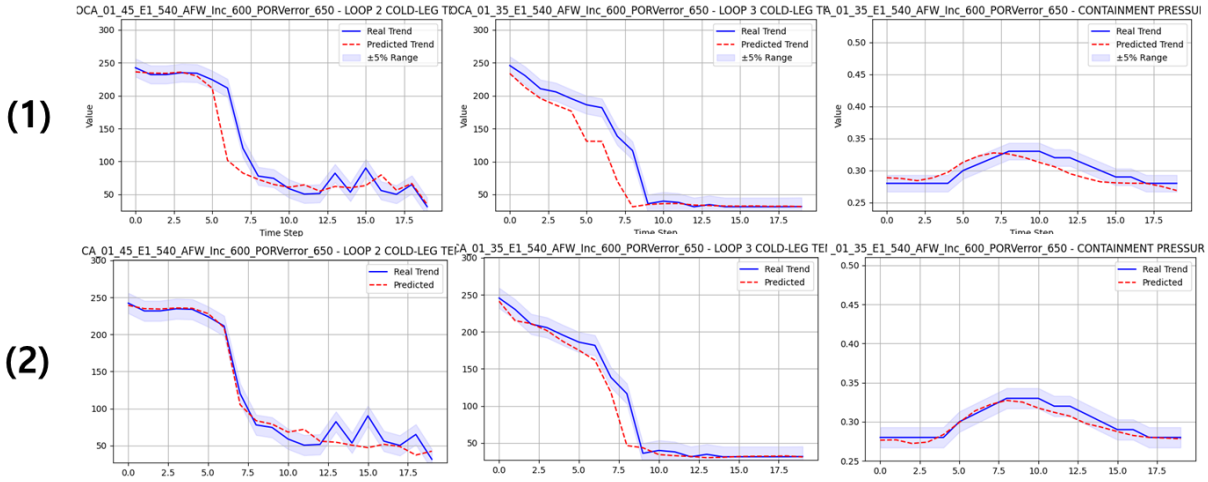

Figure 2 Trend prediction results for three key parameters: (1) shows the prediction results using latent vector loss, while (2) shows results using the full-trend loss strategy with a frozen decoder.

This study presents a latent-space-based trend prediction framework for real-time operator support in small modular reactors. The combination of a deep LSTM Autoencoder and a decoder-assisted predictor results in significantly improved accuracy and temporal alignment in accident scenarios. Future work will explore validation strategies for untrained scenarios, as well as integrate uncertainty quantification methods to improve the robustness and interpretability of predictions in digital control room environments.

ACKNOWLEDGMENTS

This work was supported by Korea Institute of Energy Technology Evaluation and Planning(KETEP) grant funded by the Korea government(MOTIE)(RS-2024-00403194, Next-Generation Nuclear Technology Creation IP-R&D Talent (Human Resources) Development Project)

This research was supported by the National Research Council of Science & Technology(NST) grant by the Korea government (MSIT) (No. GTL24031-400)

REFERENCES

[1] Bae, J., Kim, G., & Lee, S. J. (2021). Real-time prediction of nuclear power plant parameter trends following operator actions. *Expert Systems with Applications*, 186, 115848.

[2] Kim, H., & Kim, J. (2023). Long-term prediction of safety parameters with uncertainty estimation in emergency situations at nuclear power plants. *Nuclear Engineering and Technology*, 55(5), 1630–1643.

[3] Bae, J., Park, J.W., & Lee, S.J. (2022). Limit surface/states searching algorithm with a deep neural network and Monte Carlo dropout for nuclear power plant safety assessment. *Applied Soft Computing*, 124, 109007.

Research on Hydrogen Risks in Large Advanced Passive Pressurized Water Reactor

Zining Hao[1], Zimeng Qin[2], Shaogang Du[3], Yongqi Huang[4], Xuefeng Lyu[5], Yu Yu[6]

[1] *Affiliation Information: Beijing Key Laboratory of Passive Safety Technology for Nuclear Energy, North China Electric Power University, Beijing 102206, China, 120232212095@ncepu.edu.cn*
[2] *Affiliation Information: Beijing Key Laboratory of Passive Safety Technology for Nuclear Energy, North China Electric Power University, Beijing 102206, China, zmqin08@163.com*
[3] *Affiliation Information: Beijing Key Laboratory of Passive Safety Technology for Nuclear Energy, North China Electric Power University, Beijing 102206, China, 120232212137@ncepu.edu.cn*
[4] *Affiliation Information: Huaneng Clean Energy Research Institute Co., Ltd., Beijing, China, Beijing 102206, China, yq_huang@qny.chng.com.cn*
[5] *Affiliation Information: Beijing Key Laboratory of Passive Safety Technology for Nuclear Energy, North China Electric Power University, Beijing 102206, China, lxf01@ncepu.edu.cn*
[6] *Affiliation Information: Beijing Key Laboratory of Passive Safety Technology for Nuclear Energy, North China Electric Power University, Beijing 102206, China, yuyu2011@ncepu.edu.cn*

ABSTRACT

Severe accidents in nuclear power plants pose significant threats due to hydrogen generated by the zirconium-water reaction. This study focuses on the Large Advanced Passive Pressurized Water Reactor, evaluating hydrogen risks within various containment compartments under typical severe accident scenarios. The effectiveness and potential drawbacks of current hydrogen control strategies are also assessed. Simulation results indicate varying hydrogen risks across compartments. In confined spaces such as the In-Containment Refueling Water Storage Tank, hydrogen accumulation presents a heightened risk. Although the existing hydrogen control system effectively mitigates hydrogen-related risks, its failure necessitates alternative strategies, such as shutting down the Passive Containment Cooling System to promote steam accumulation and suppress hydrogen flammability. Nevertheless, this action may lead to elevated containment pressure and temperature, compromising containment integrity.

Keywords: Large Advanced Passive Pressurized Water Reactor, Severe accident, Hydrogen risk, Hydrogen control system, Containment pressure

I. Introduction

In the realm of nuclear power generation, ensuring the safety of nuclear power plants is of utmost importance. Among the various potential threats, hydrogen risk during severe accidents in nuclear power plants, especially in passive pressurized water reactor (PWR), has attracted significant attention in recent years.

Japan used the MAAP code to analyze hydrogen distribution in containment under severe accidents, showing that proper igniter placement minimizes pressure impacts from hydrogen combustion [1]. Dehjourian et al. simulated a LBLOCA at Beznau NPP and found combined use of spray systems and recombiners enhances hydrogen mitigation efficiency [2]. Joseph Amponsah employed ANSYS CFX to numerically investigate the substantial risks to containment and peripheral infrastructure integrity resulting from hydrogen release during severe accidents in light water reactors (LWRs) [3].However, most research focuses on Loss of Coolant Accidents (LOCA), with limited exploration of scenarios like Station Blackout (SBO) and Direct Vessel Injection (DVI) line breaks.

This paper establishes a passive PWR model and examines hydrogen risks under SBO and DVI accidents. The study also evaluates the implications of PCS shutdown as a mitigation measure.

II. Analysis method

Hydrogen risk analysis typically involves numerical simulations and experimental validation [4]. T Szabó coupled MELCOR with GASFLOW by developing an interface, enabling the function of receiving source terms from MELCOR during

operation and feeding back the containment pressure to MELCOR [5]. The Energy Institute of the Netherlands Joint Research Centre evaluated the hydrogen mitigation measures in the VVER - 440/213 containment using GASFLOW, CFX, and Fluent programs respectively [6].

This study utilizes a severe accident simulation code to model a typical passive PWR, emphasizing hydrogen release points and their effects on containment compartments. The role of the hydrogen control system and the consequences of shutting down the PCS are also analyzed.

II.A. Nuclear Power Plant System Model

This study employs an integrated accident analysis code to establish a nuclear power plant model, including the Reactor Coolant System (RCS), engineered safety features, and the containment. The RCS consists of the pressure vessel, reactor core, steam generators, pressurizer, and main coolant piping. The engineered safety facilities primarily include: a four-stage Automatic Depressurization System (ADS), two Core Makeup Tanks (CMTs), an In-Containment Refueling Water Storage Tank (IRWST), a Passive Residual Heat Removal System (PRHRS), two Accumulators (ACCs), and associated piping.

The containment interior is divided into nine compartments (numbered 1 – 9), sequentially as follows: two SG compartment, CMT compartment, reactor cavity, IRWST compartment, upper space of the containment, A - train PXS compartment, B - train PXS compartment, and CVS (Chemical and Volume Control System) compartment. Three control volumes outside the containment, numbered 10 - 12, simulate the Passive Containment Cooling System (PCS), representing the PCS upper compartment, PCS rising section, and PCS descending section respectively. Moreover, thirty containment flow passages are set up to simulate air - water circulation within the containment.

Hydrogen generation is modeled as a function of fuel temperature, initiating when zirconium-steam reactions occur at temperatures above 1300 K. The oxide layer growth follows a parabolic law, and the reaction rate constant κ is defined as [7]:

$$K = A\exp\left(-\frac{B}{RT}\right) \tag{1}$$

Where: A is pre - exponential factor, B is activation energy, R is universal gas constant, and T is absolute temperature.

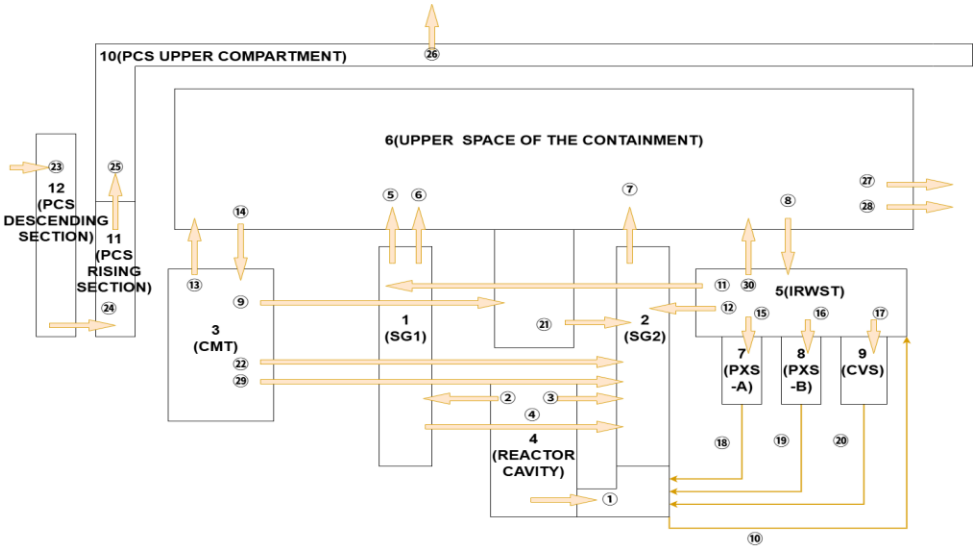

FIGURE 1 Containment Node Division

II.B. Hydrogen risk criteria

The Shapiro diagram is employed to evaluate hydrogen-air-steam mixture flammability [8]. Generally speaking, the formation conditions of a combustible gas mixture are as follows: when the water vapor content is less than 30%, the hydrogen concentration must exceed 4%; when the water vapor content is between 30% and 60%, the hydrogen concentration should be between 4% and 12%; and when the water vapor content exceeds 60%, the mixed gas is considered to be completely inert and cannot be ignited. The relationship is expressed as shown in Equation (2) and (3):

$$NF_{H_2O} < 60\% \quad (2)$$

$$NF_{H_2} \geqslant 4\% + \max\left[0, \frac{8}{30}\left(NF_{H_2O} - 30\%\right)\right] \quad (3)$$

Where: NF_{H20} is steam volume fraction, NF_{H2} is hydrogen volume fraction.

II.C. Severe accident sequences

This paper analyzes two typical severe accident scenarios in passive pressurized water reactors: Station Blackout Accident (SBO) and Direct Vessel Injection (DVI) Line Break Accident. To investigate the effects of different hydrogen release locations on combustion risks, comparative studies were conducted under SBO conditions with two configurations: failure of the fourth-stage ADS valves versus full opening of all ADS valves. The accident assumptions are as follows:

TABLE I. Severe Accident Sequences and Conditional Assumptions

Accident Sequence	SBO（ADS1-3）	SBO（ADS1-4）	DVI
Initiating Event	Loss of All Power Supplies	Loss of All Power Supplies	DVI Line Break
PRHR	N	N	N
ADS (1-3)	2/2	2/2	0/2
ADS4	0/4	4/4	0/4
CMT	2/2	2/2	1/2
ACC	2/2	2/2	1/2
Gravity Injection/Recirculation	0/2	0/2	0/2
PCS	Y	Y	Y
Hydrogen Control System	N	N	N

During SBO (ADS1-3) and DVI accidents, hydrogen is released into the IRWST compartment and the PXS compartment respectively. Since both compartments feature flow restrictions, they are ideal representatives for studying hydrogen - related risks in flow - restricted compartments during severe accidents.

III. Hydrogen risk analysis

III.A. Station Blackout Accident (SBO)

FIGURE 2 shows temporal hydrogen volume fraction changes in the IRWST and upper compartments. When only ADS1 - 3 valves are opened, core - generated hydrogen enters the IRWST. During the hydrogen release phase, a significant amount of hydrogen (82 %) initially accumulates in the IRWST compartment. Subsequently, the hydrogen diffuses into the containment atmosphere. Concurrently, the containment hydrogen concentration rises to 6.5 %, then gradually decreases and stabilizes at 5.3 % due to further diffusion to other compartments.

When ADS1 - 4 valves are opened, most hydrogen goes directly into the containment through the stage - 4 valve. The hydrogen volume fraction in the upper containment space peaks at 7.2% and ultimately stabilizes at 6.2%. Meanwhile, the IRWST peak concentration drops to 3.2%, much lower than the ADS1 - 3 scenario.

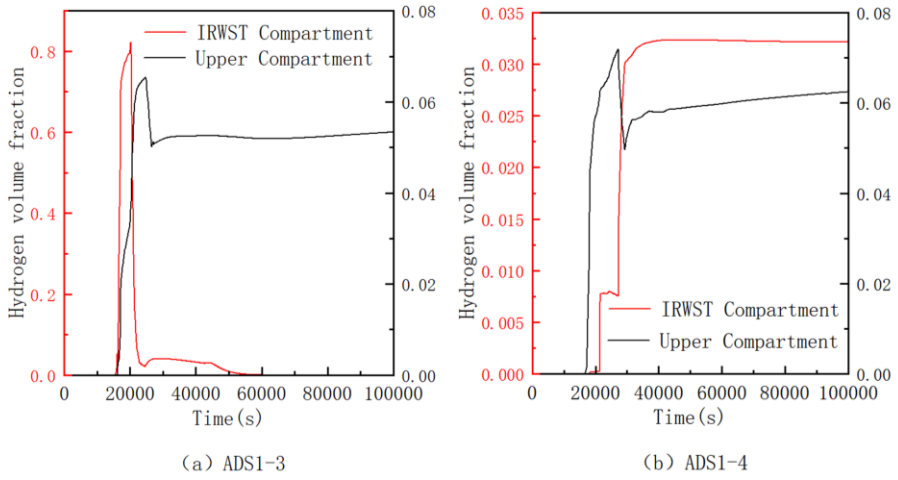

FIGURE 2. Hydrogen volume fraction in IRWST and Upper compartment under SBO scenarios

FIGURE 3 shows hydrogen combustion modes via the Shapiro diagram. The containment's upper space represents the well-mixed compartment, and the high - H_2 IRWST compartment represents the flow - restricted one.

For the 1 - 3 ADS valve scenario, the upper - containment H_2 concentration stabilizes at 5.3% later, slightly entering the combustion region. In the IRWST, H_2 stays in the combustion region for 700 s during the early rise and nears the deflagration region. In the 1 - 4 ADS valve case, the upper - containment H_2 stabilizes at 6.2%, also slightly entering the combustion region. As most H_2 releases directly into the containment, the IRWST H_2 concentration is low, keeping it out of the combustion region.

Comparative analysis reveals that during SBO accidents, the partial-opening configuration (ADS1-3) poses significantly higher hydrogen combustion risks in the IRWST compartment than the full-opening configuration (ADS1-4).

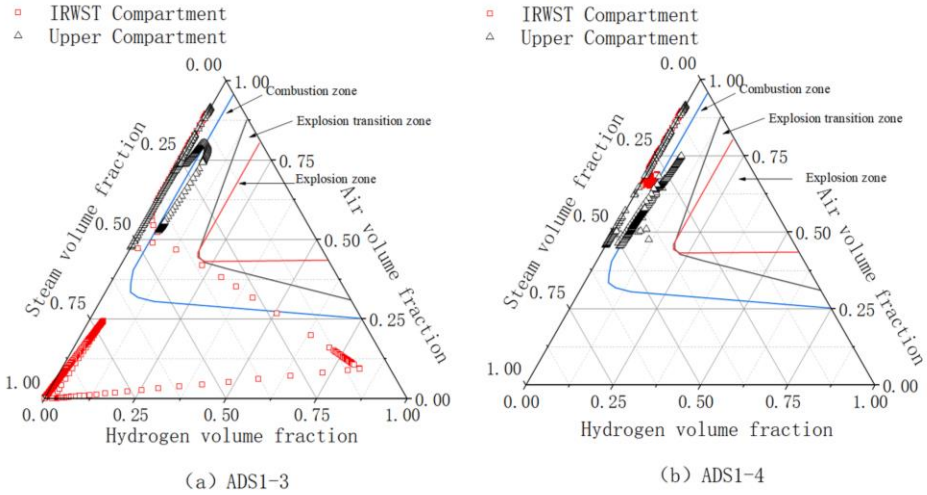

FIGURE 3. Hydrogen Combustion Modes under SBO scenarios

III.B. Direct Vessel Injection (DVI) Line Break Accident

FIGURE 4 (a) shows temporal hydrogen volume fraction changes in the IRWST and upper compartments. During this accident sequence, a DVI pipeline break and closed ADS1 - 4 valves force hydrogen release into the PXS compartment. Given its small size and flow restrictions, the PXS compartment sees a 92% concentration peak. As hydrogen diffuses into the containment, PXS concentration drops while the upper - containment concentration rises, stabilizing at 8.2%.

FIGURE 4 (b) shows hydrogen combustion modes via the Shapiro diagram. The upper - containment space represents the well - mixed compartment, and the PXS compartment represents the flow - restricted one. During the later accident stage, upper - containment H_2 stabilizes at 8.2%, entering the combustion region and nearing the deflagration - transition zone. In the PXS compartment, its small size, flow restrictions, and high initial water - vapor level prevent combustion at first. As H_2 concentration surges, there's insufficient air for combustion. Only later, as H_2 and water-vapor levels drop, does it enter the combustion region.

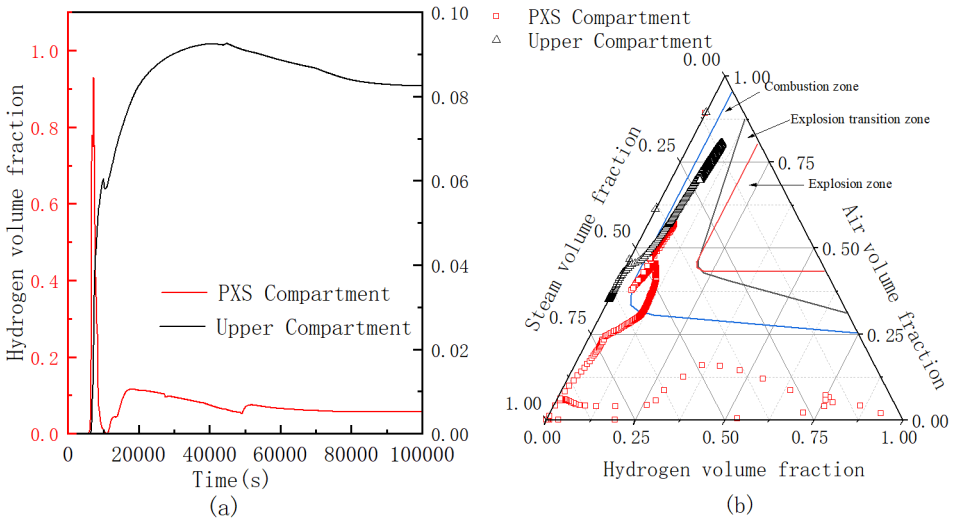

FIGURE 4. Hydrogen volume fraction and Combustion Modes under DVI scenarios

IV. Risk mitigation measures

Typical passive pressurized water reactors use a hydrogen control system to mitigate hydrogen risks. Each compartment is equipped with two hydrogen igniter subsystems, each consisting of 33 units and powered independently. Only one set runs during operation; the other serves as backup. The configuration of igniters is presented in TABLE II. To verify the system's effectiveness, we put it into operation. Below are the hydrogen concentrations in compartments and combustion modes under the aforementioned scenarios.

TABLE II. Igniter placement configuration

Compartment Name	Number of igniters
SG ROOM 1	4
SG ROOM 2	5
CMT Compartment	5
CAVITY	0
IRWST Compartment	4
UPPER Compartment	12
PXS-A Compartment	1
PXS-B Compartment	1
CVS Compartment	1
PCS upper compartment	0
PCS rising section	0
PCS descending section	0

IV.A. Research on the Effectiveness of Hydrogen Control System

Figures 5 and 6 illustrate that activation of the hydrogen igniter system reduces hydrogen concentrations in both SBO (ADS1-3) and DVI scenarios.

In the SBO (ADS1-3) accident, the peak hydrogen concentration in the IRWST compartment drops to 74%, and the hydrogen concentration in the upper space of the containment drops to 4.1%. The hydrogen combustion modes in both compartments are basically out of the combustion zone, and the hydrogen risk is mitigated.

In the DVI pipeline break accident, due to the action of the hydrogen igniters, the hydrogen concentration in the upper space of the containment decreases to 4.1%, and the risk is mitigated. However, as the number of igniters in the PXS compartment is small, there are no significant changes in the peak hydrogen concentration and combustion mode in the PXS compartment, which still remains in the combustion zone.

Therefore, the existing hydrogen control system of typical passive pressurized water reactors can basically mitigate the hydrogen risk under severe accidents, but the mitigation effect in the PXS compartment is not obvious due to limited ignition capacity and poor ventilation in the PXS compartment, increasing the number of igniters may enhance hydrogen removal efficiency.

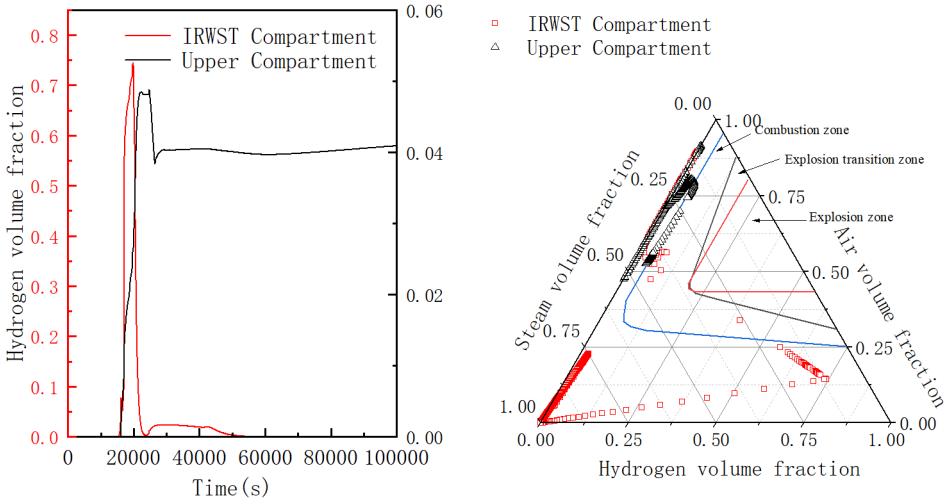

FIGURE 5. Hydrogen volume fraction and Combustion Modes under SBO(ADS1-3) scenarios (Hydrogen Control System)

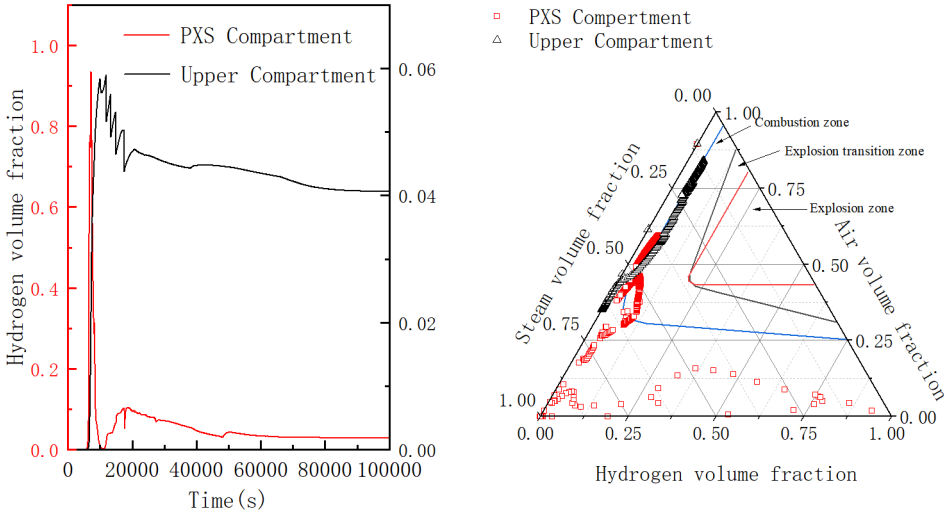

FIGURE 6. Hydrogen volume fraction and Combustion Modes under DVI scenarios (Hydrogen Control System)

IV.B. The Influence of PCS on Hydrogen Risk

When the igniters fail, steam volume fraction can be increased by closing the PCS to mitigate the hydrogen risk. This section conducts research on the aforementioned SBO (ADS1-3) condition. In this condition, hydrogen generation occurs mainly between 16,000 s and 17,000 s, and the igniters have already failed. After shutting off the PCS, the hydrogen volume fraction and combustion modes in both the IRWST compartment and the upper space of the containment are as follows:

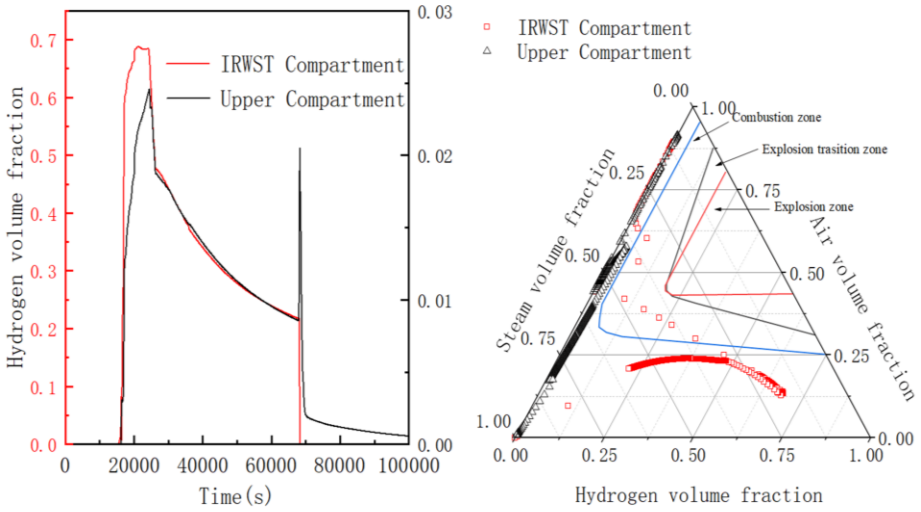

FIGURE 7. Hydrogen volume fraction and Combustion Modes under SBO(ADS1-3) scenarios (PCS Shut Down)

As can be observed, with the PCS shut down, water vapor entering the containment isn't condensed, leading to a large accumulation. This significantly reduces the hydrogen concentration, moving the combustion mode far from the combustion zone and easing the risk. High containment pressure slows hydrogen diffusion from the IRWST, causing its hydrogen concentration to drop slowly and remain in the combustion zone for a while.

While shutting down the PCS mitigates hydrogen risks in the containment, restricted compartments (e.g., IRWST) show limited improvement due to high pressure suppressing hydrogen diffusion, causing sustained high concentrations in the combustion zone. Additionally, this approach can cause overpressure in the containment, the containment pressure is as follows:

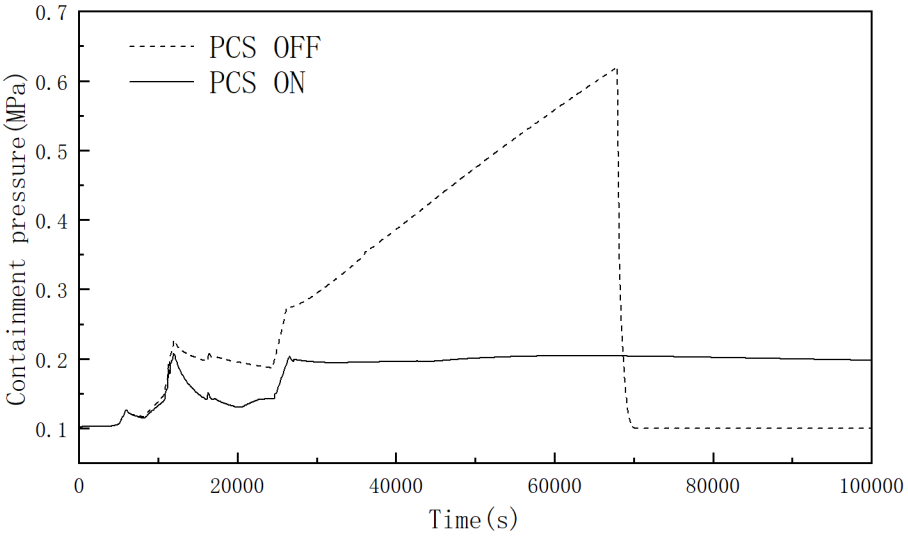

FIGURE 8. Containment Pressure under SBO(ADS1-3) scenarios

As can be seen, with the PCS closed, uncondensed water vapor accumulates in the containment, causing the pressure to rise. At around 68,000 s, the containment pressure hits 0.6 MPa, exceeding the design pressure, and then the pressure relief device activates, leading to a rapid pressure drop.

V. CONCLUSIONS

During severe accidents in large - scale advanced passive pressurized water reactors, hydrogen poses significant risks in flow - restricted compartments like the IRWST compartment and PXS compartment. Conversely, within the large - volume containment, good fluidity helps disperse hydrogen, resulting in relatively lower hydrogen - related risks.

During station blackout incidents, opening merely the ADS1-3 valves leads hydrogen to discharge into the IRWST compartment. This influx drives the IRWST compartment into the combustion regime. In contrast, when all four - stage ADS valves are opened, a substantial portion of hydrogen vents into the containment space via the fourth - stage valve. This effectively mitigates the hydrogen - related hazards in the IRWST compartment. During a DVI pipeline break accident, hydrogen is released into the PXS compartment, propelling it into the combustion region.

The hydrogen control system can effectively reduce hydrogen risks. However, due to the small number of igniters in the PXS compartment, its effect is not remarkable. When the igniters fail, closing the PCS to increase the steam volume fraction can reduce the hydrogen risk in the containment. Nevertheless, this measure has little effect on restricted compartments and meanwhile, it will pose a risk of over - pressurizing the containment.

In future research, more realistic boundary conditions and three-dimensional computational fluid dynamics (CFD) models will be incorporated to improve the accuracy of hydrogen risk assessment in confined compartments. Additionally, experimental validation of hydrogen distribution and mitigation strategies will be pursued, with particular focus on the optimization of hydrogen mitigation strategies under various accident scenarios.

REFERENCES

[1] Morfin F, Sabroux JC, Renouprez A. Catalytic combustion of hydrogen for mitigating hydrogen risk in case of a severe accident in a nuclear power plant: study of catalysts poisoning in a representative atmosphere. Applied Catalysis B Environmental. 2004;47(1):47-58.

[2] DEHJOURIAN M, SAYAREH R, RAHGOSHAY M, et al. Investigation of a Hydrogen Mitigation System During Large Break Loss-Of-Coolant Accident for a Two-Loop Pressurized Water Reactor[J]. Nuclear engineering and technology, 2016, 48(5): 1174-1183.

[3] Amponsah J, Archibong-Eso A. Mitigating Hydrogen Risks in Light-Water Nuclear Reactors: A CFD Simulation of the Distribution and Concentration[J]. Hydrogen, 2023, 4(4). DOI:10.3390/hydrogen4040045.

[4] Chen W, Xiong Q, Wu D,et al.Uncertainty analysis of HPR-1000 LOCA with probabilistic and deterministic methods[J].Progress in Nuclear Energy, 2022, 146:104174-.DOI:10.1016/j.pnucene.2022.104174.

[5] Szabó T, Kretzschmar F, Schulenberg T. Obtaining a more realistic hydrogen distribution in the containment by coupling MELCOR with GASFLOW. Nuclear Engineering and Design. 2014;269:330-339.

[6] Heitsch M, Huhtanen R, Téchy Z, et al. CFD evaluation of hydrogen risk mitigation measures in a VVER-440/213 containment. Nuclear Engineering & Design. 2010;240(2):385-396.

[7] Schanz G, Adroguer B, Volchek A. Advanced treatment of zircaloy cladding high-temperature oxidation in severe accident code calculations Part I. Experimental database and basic modeling[J]. Nuclear Engineering and Design, 2004.DOI:10.1016/j.neuroimage.2005.08.054

[8] Shapiro Z M, Moffette T R. Hydrogen flammability data and application to PWR loss-of-coolant accident[R]. Westinghouse Electric Corp., Pittsburgh, PA (United States). Bettis Plant, 1957.

ASRAM2025
www.asram2025.org
Asian Symposium on Risk Assessment and Management 2025
Pattaya, Thailand, 27 – 29 August 2025

COMPARATIVE ANALYSIS OF EXPERIMENTAL AND NUMERICAL SIMULATION OF TWO-PHASE FLOW IN A NARROW RECTANGULAR DUCT USING OPENFOAM

Phakhinai Samor, Narakhan Khunsrimek, Autthasith Panyopas, Somboon Rassame

Department of Nuclear Engineering, Faculty of Engineering Chulalongkorn University, Wangmai, Patumwan, Bangkok 10330, Thailand

ABSTRACT

Bubbly flow represents a fundamental two-phase flow regime characterized by the dispersion of gas bubbles within a continuous liquid phase. This regime plays a critical role in heat transfer and coolant performance, particularly within confined geometries such as narrow vertical channels commonly found in nuclear reactor systems. In this study, the open-source computational fluid dynamics (CFD) software, OpenFOAM version 12 is employed to simulate vertical air-water two-phase flow within a rectangular duct measuring 10 mm × 200 mm × 2.95 m. The simulation replicates two experimental cases reported by Liu (2008), which differ in gas injection rates while maintaining a constant liquid flow rate. The multiphaseEulerFoam solver is applied with interfacial force models that include drag, lift, wall lubrication, and virtual mass. Additionally, the two-group Interfacial Area Transport Equation (IATE) model is used to represent bubble coalescence and breakup mechanisms. Key flow parameters, including the Sauter mean diameter, void fraction, bubble velocity, and interfacial area concentration, are evaluated at six axial locations. The simulation results are validated against experimental data at z/D_{H} = 34.8, 88.2, and 141.7 through graphical trend comparisons and relative error analysis. The findings indicate that the model performs well in the low gas flow case, while greater discrepancies are observed in the high gas flow case, particularly in the Sauter mean diameter and interfacial area concentration. These differences highlight limitations in accurately predicting bubble coalescence and spatial distribution under more complex flow conditions.

Keywords: OpenFOAM, Two-phase flow, Bubbly flow, IATE model, Interfacial force

I. INTRODUCTION

Bubbly flow is one of the two fundamental flow regimes involving two phases, characterized by the dispersion of small gas bubbles within a continuous liquid phase without the bubbles coalescing to form larger clusters. It significantly affects shear stress, momentum exchange, and heat transfer and is commonly observed in thermal and energy systems such as nuclear reactor cooling, heat exchangers, and chemical processing units [1,2]. An accurate understanding of bubbly flow behavior is essential for ensuring system stability and improving performance, particularly in narrow channels where bubble distribution and interfacial interactions are greatly affected by confinement [1,3]. In marine engineering applications, where plate-type fuel elements are commonly used, narrow duct channels are often subjected to external ship motions such as rolling. Jin et al. [4] have shown that rolling motion can significantly influence two-phase flow characteristics, leading to oscillatory pressure drops and intensified interfacial interactions due to time-dependent inertial forces. Although the present work focuses on stationary vertical bubbly flow, these dynamic effects may be of interest for future investigations on flow stability in marine reactor systems.

Computational Fluid Dynamics (CFD) has become a powerful tool for analyzing complex flow phenomena such as bubbly flow [5]. However, commercial CFD software packages such as ANSYS Fluent and STAR-CCM+ often have high licensing costs and restricted access, which poses challenges for research groups and academic use, particularly at the student level [5]. OpenFOAM, an open-source CFD software package, is a popular alternative due to its free accessibility, high flexibility, and ability to simulate complex multiphase flows [6]. OpenFOAM supports a wide range of physical models, including multiphase flows, heat transfer, reacting flows, and turbulent phenomena [5]. It has been applied in a variety of academic and industrial contexts, including bubble columns, injectors, pipe flow, and narrow-duct simulations [2]. Furthermore, its use has been documented in the fields of power generation and nuclear engineering [6], demonstrating its relevance to high-stakes systems. In this study, OpenFOAM is used to simulate a case based on an experiment conducted by Liu et al. [1] in a vertical narrow

duct that mimics conditions in reactor cooling channels. This reinforces the relevance of this study to nuclear engineering applications. Although several studies have simulated bubbly flows using OpenFOAM, no prior work has been found that directly reproduces the experimental conditions of Liu while incorporating the two-group Interfacial Area Transport Equation (IATE) model. Liu's dataset provides high-quality benchmark data that is well-suited for validating CFD models. This study, therefore, aims to address this research gap by implementing a detailed Eulerian-Eulerian two-fluid CFD simulation in OpenFOAM. The simulation incorporates interfacial force models, including drag, lift, wall lubrication, and turbulent dispersion, in addition to the two-group IATE model.

This study aims to simulate bubbly two-phase flow under conditions similar to those in the experiment conducted by Liu (2008), using OpenFOAM version 12. The simulation replicates the air-water flow in a vertical narrow rectangular duct with dimensions of 10 mm × 200 mm × 2.95 m. While Liu's experiment collected data only at z/D_H = 34.8, 88.2, and 141.7, the present study extends the analysis to all six axial positions to enable a more detailed evaluation of bubble behavior along the vertical channel. Two gas injection cases are considered, and the simulation results are compared with Liu's experimental data. Key parameters analyzed include the Sauter mean diameter, void fraction, bubble velocity, and interfacial area concentration (IAC). The aim is to evaluate the accuracy of the CFD model based on the two-group Interfacial Area Transport Equation (IATE), and to demonstrate the applicability of OpenFOAM for detailed investigations of bubbly flow behavior.

II. THEORETICAL BACKGROUND

II.A. Two-Fluid Model

The two-fluid model is a mathematical framework employed to describe two-phase flow by treating each phase, such as gas and liquid, as a continuous medium governed by its own conservation equations for mass, momentum, and energy [7]. This facilitates the lucid modeling of interfacial phenomena, including drag, lift, wall lubrication, turbulent dispersion, virtual mass, and heat transfer [7]. To derive practical macroscopic field equations, Eulerian averaging methods are commonly applied, making the model suitable for engineering-scale problems such as transient flow and complex reactor geometries. In practice, the model can be formulated in two main approaches: the Euler-Lagrange method and the Euler-Euler method. The Euler-Lagrange approach is characterized by its ability to track dispersed-phase particles individually. In contrast, the Euler-Euler approach, which is the method employed in this study, treats both phases as interpenetrating continua. The volume fraction is employed to denote the proportion of each phase, and separate conservation equations are solved for each. Assuming negligible mass transfer between phases, the governing equations employed in this study consist of the continuity and momentum conservation equations, shown respectively in Equations (1) and (2) [6].

$$\frac{\partial(\alpha_k \rho_k)}{\partial t} + \nabla \cdot (\alpha_k \rho_k \vec{u}_k) = 0 \ , \tag{1}$$

$$\frac{\partial(\alpha_k \rho_k \vec{u}_k)}{\partial t} + \nabla \cdot (\alpha_k \rho_k \vec{u}_k \vec{u}_k) = -\alpha_k \nabla p + \alpha_k \rho_k \vec{g} + \nabla \cdot (\alpha_k \tau_k) + \overrightarrow{M}_{I \to k} \ , \tag{2}$$

where α_k is the volume fraction of the phase k [-], ρ_k is the density [kg/m^3], $\vec{u}_k$ is the velocity [m/s], p is the pressure [Pa], $\vec{g}$ is the gravitational acceleration [m/s^2], τ_k is the viscous stress tensor [Pa], and $\overrightarrow{M}_{I \to k}$ is the interfacial momentum transfer from phase I to phase k [N/m^3]. The two-fluid model serves as a fundamental approach for simulating multiphase flow, particularly in cases requiring high accuracy and clear phase separation.

II.B. Interfacial Force

Interfacial momentum transfer or interfacial forces exert a significant influence on the motion, distribution, and interaction of gas bubbles in two-phase flows. In vertical systems, the effects of these ions are of particular significance, as wall interactions influence the lateral migration and arrangement of bubbles. These forces have been shown to affect flow stability, phase distribution, and energy transport mechanisms [7]. In this study, five interfacial forces are considered, including drag, lift, wall lubrication, turbulent dispersion, and virtual mass forces. The total interfacial momentum exchange between phases is represented by Equation (3), which combines these individual components.

$$\overrightarrow{M}_{I \to k} = \overrightarrow{M}_{f \to g} = -\overrightarrow{M}_{g \to f} = \overrightarrow{F}_{D,f \to g} + \overrightarrow{F}_{L,f \to g} + \overrightarrow{F}_{TD,f \to g} + \overrightarrow{F}_{VM,f \to g} + \overrightarrow{F}_{WL,f \to g} \ , \tag{3}$$

Where $\vec{F}_{D,f\to g}$ is the drag force [N/m^3] resisting relative motion between phases, $\vec{F}_{L,f\to g}$ is the lift force [N/m^3] resulting from velocity gradients that cause lateral migration of bubbles, $\vec{F}_{TD,f\to g}$ is the turbulent dispersion force [N/m^3] that redistributes bubbles due to turbulence, $\vec{F}_{VM,f\to g}$ is the virtual mass force [N/m^3] arising from the acceleration of bubbles relative to the liquid phase, and $\vec{F}_{WL,f\to g}$ is the wall lubrication force [N/m^3] that repels bubbles from walls and reduces near-wall accumulation [7].

II.C. Interfacial Area Concentration and Transport Equation (IATE)

In gas-liquid two-phase flow, particularly under bubbly flow conditions, the dynamic behavior of the interfacial structure significantly affects the transport of mass, momentum, and energy. The interfacial area concentration a_i, defined as the total interfacial surface area per unit mixture volume, is a key parameter for characterizing gas-liquid interaction and predicting two-phase behavior [8]. The interfacial area is subject to continuous changes due to bubble coalescence and breakup, which must be considered for accurate modeling of the flow structure [8]. To account for these variations, the one-group Interfacial Area Transport Equation (IATE) is employed to describe the temporal and spatial evolution of a_i, incorporating source and sink terms representing physical bubble interactions [8]. Among these mechanisms, bubble breakup caused by turbulent eddies is dominant in bubbly flows, and the corresponding source term is given in Equation (4)

$$\frac{\partial a_i}{\partial t} + \nabla(a_i \vec{v}_i) \cong \frac{2}{3}\left(\frac{a_i}{\alpha}\right)\left(\frac{\partial \alpha}{\partial t} + \nabla \cdot \left(\alpha \vec{u}_g\right)\right) + \frac{1}{3\psi}\left(\frac{\alpha}{a_i}\right)^2 \sum_j R_j \tag{4}$$

Where a_i is the interfacial area concentration [m^{-1}], $\vec{v}_i$ is the interfacial velocity [m/s], α is the void fraction [-], $\vec{u}_g$ is the gas velocity [m/s], and R_j represents the source terms due to bubble interaction mechanisms such as coalescence and breakup. For spherical or near-spherical bubbles [m^{-3}/s^{-1}], the bubble shape factor ψ is taken as $1/(36\pi)$. Besides, $\vec{v}_i$ often approximated by the gas velocity $\vec{u}_g$

II.D. Turbulence Modeling

Turbulence plays a central role in the behavior of bubbly two-phase flows by influencing momentum exchange, phase dispersion, and interfacial interactions. In this study, turbulence in the continuous liquid phase is modeled using the Shear Stress Transport (SST) $k-\omega$ model [9], which combines the robustness of the $k-\varepsilon$ model in the freestream with the near-wall accuracy of the $k-\omega$ formulation through a blending function. The transport equation for the turbulent kinetic energy k is given in Equation (5), and the equation for the specific dissipation rate ω is given in Equation (6)

$$\frac{\partial(\alpha_f \rho_f k_f)}{\partial t} + \nabla \cdot (\alpha_f \rho_f \vec{u}_f k_f) = \nabla \cdot \left[\alpha_f \left(\mu_f{}^{mol} + \frac{\mu_f{}^{turb}}{\sigma_{k3}}\right)\nabla k_f\right] + \alpha_f \rho_f - \acute{\beta}\alpha_f \rho_f k_f \omega_f + S_k \tag{5}$$

$$\frac{\partial(\alpha_f \rho_f \omega_f)}{\partial t} + \nabla \cdot (\alpha_f \rho_f \vec{u}_f \omega_f) = \nabla \cdot \left[\alpha_f \left(\mu_f{}^{mol} + \frac{\mu_f{}^{turb}}{\sigma_{\omega 3}}\right)\nabla \omega_f\right] + (1-F_1)2\alpha_f \rho_f \frac{\nabla k_f \nabla \omega_f}{\sigma_{\omega 2}\omega_f} + a_3 \alpha_f \frac{\omega_f}{k_f} P_k - \beta_3 \alpha_f \rho_f k_f {\omega_f}^2 + S_\omega \tag{6}$$

In order to capture the additional turbulence generated by dispersed bubbles, the standard SST model is extended using a bubble-induced viscosity term based on Sato's formulation [10]. The modified turbulent viscosity is expressed in Equation (7).

$$\mu_L{}^{turb} = \frac{a_1 \rho_f k_f}{\max(a_1 \omega_f, F_2\sqrt{S^2})} + (1 - e^{-\frac{y^+}{16}})^2 \cdot C_{\mu b} \cdot d \cdot \alpha_f \cdot \left|\vec{u}_g - \vec{u}_f\right| \tag{7}$$

In these equations, α_f is the volume fraction [-] of the liquid phase, ρ_f is the liquid density [kg/m^3], $\vec{u}_f$ and $\vec{u}_g$ are the velocity [m/s^2] of the liquid and gas phases, respectively, k_f and ω_f are the turbulent kinetic energy [m^2/s^2] and specific dissipation rate [s^{-1}] of the liquid phase. $\mu_f{}^{mol}$ and $\mu_f{}^{turb}$ denote the molecular and turbulent viscosities $[Pa \cdot s]$ of the liquid phase. P_k is the turbulence production term due to shear, while S_k and S_ω represent additional source terms that account for bubble-induced turbulence. In the eddy viscosity expression, d is the bubble diameter [m], $C_{\mu b}$ is the empirical coefficient for bubble-induced turbulence, and y^+ is the dimensionless wall distance. The strain-rate magnitude is represented by S, and the

functions $F_1$and F_2 are first and second blending functions used in the SST formulation. The constants σ_{k3} ,$\sigma_{\omega 3}$, $\sigma_{\omega 2}$, $\acute{\beta}$, β_3, a_1, a_3 are model coefficients from the standard SST formulation. This set of equations provides a more accurate representation of near-wall turbulence in confined bubbly flows by including bubble-induced effects.

III. METHODOLOGY

III.A. Initial and Boundary Conditions

The computational domain was defined as a narrow rectangular channel with a width of 10 mm, a length of 200 mm, and a height of 2950 mm, consistent with the experimental setup of Liu et al. [1]. To capture spatially resolved data, surface probes were installed at six vertical positions along the z-axis (z/D_H) = 8.0, 34.8, 61.5, 88.2, 115.0, and 141.7) where D_H = 19.05 mm. These probes were used to monitor pressure, velocity, void fraction, interfacial area concentration, Sauter mean diameter (D_{sm}), and maximum bubble diameter. The results from these positions were later used for comparison with experimental data and model evaluation. These configurations are illustrated in Fig. 1.

In accordance with the study conducted by Liu et al. [1], which examined vertical two-phase air-water flow under conditions of non-uniform bubble distribution, the bubble structures were classified into two categories: bubbly flow and slug flow. The present study selected two cases that fall within the bubbly flow regime to investigate bubble behavior in water under high-turbulence conditions. As shown in Table I, the superficial liquid velocity (j_f) was fixed at 2.531 m/s for both cases, while the superficial gas velocity (j_g) was 0.090 m/s for Case A and 0.305 m/s for Case B. Since Liu et al. [1] did not report the void fraction at the inlet, the void fractions at z/D_H = 34.8 were adopted instead, with values of 0.029 for Case A and 0.086 for Case B. These were considered the most representative values for initializing the phase volume fraction (α) in the simulation. In addition, the fluid temperature was maintained at a constant 26.8°C throughout the entire simulation domain. The aforementioned values were then used to calculate the turbulent kinetic energy (k), specific dissipation rate (ω), and turbulent viscosity (μ). These turbulence quantities, along with the flow velocity (v) and the void fraction (α), were employed as the initial conditions for the numerical model.

The initial bubble diameters were set at 1.96 mm for Case A and 2.54 mm for Case B, based on calibration to match Liu's experimental results at z/D_H = 34.8. The definition of the boundary conditions was informed by the study conducted by Liao et al. [1], which also employed the OpenFOAM software to simulate bubbly flow. The two-phase system consisted of air and water. The air phase employed the two-group Interfacial Area Transport Equation (IATE) model from Ishii et al. (2001), with parameters selected specifically for bubbly flow. Water was designated as the continuous phase. The interfacial forces under consideration encompassed drag, lift, wall lubrication, turbulent dispersion, and virtual mass. The fluid properties were defined according to the same thermal conditions: water was defined with constant density and viscosity, while air was modelled with variable density. The turbulence model employed for the water phase was the k-omega SST Sato model, while the air phase was treated as laminar. The computational mesh used was a multigrading structured mesh consisting of 25 × 1 × 150 cells, as illustrated in Fig. 1. This configuration provided increased resolution near the channel walls, where shear and interfacial forces significantly influenced bubble behavior. The mesh type was selected to achieve a balance between computational efficiency, numerical stability, and solution accuracy. The simulation was performed for a total duration of 60 seconds.

III.B. OpenFOAM Software

OpenFOAM is a software solution for computational fluid dynamics (CFD) that is characterized by its open-source nature. It is utilized for the purpose of simulating complex fluid systems. The present study utilized the multiphaseEulerFoam solver, which is based on the Euler-Euler model, for the purpose of analyzing two-phase flows. The fundamental equations solved included the continuity and momentum equations. Moreover, supplementary models were incorporated to account for interfacial phenomena and turbulence characteristics: the Interfacial Area Transport Equation (IATE) for interfacial surface area prediction and the k-omega SST Sato model for modelling turbulence in the water phase.

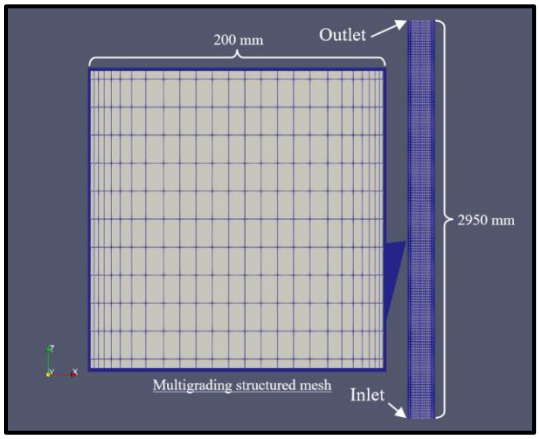

FIGURE 1. Computational domain geometry and multigrading mesh used in the OpenFOAM simulation.

TABLE I. Initial Conditions for Case A and Case B

Case	j_f [m/s]	j_g [m/s]
A	2.531	0.090
B	2.531	0.305

III.B. OpenFOAM Software

OpenFOAM is a software solution for computational fluid dynamics (CFD) that is characterized by its open-source nature. It is utilized for the purpose of simulating complex fluid systems. The present study utilized the multiphaseEulerFoam solver, which is based on the Euler-Euler model, for the purpose of analyzing two-phase flows. The fundamental equations solved included the continuity and momentum equations. Moreover, supplementary models were incorporated to account for interfacial phenomena and turbulence characteristics: the Interfacial Area Transport Equation (IATE) for interfacial surface area prediction and the k-omega SST Sato model for modelling turbulence in the water phase.

III.C. Calculation Process

With regard to the input part, the initial conditions were defined for the following parameters: velocity (v), phase volume fraction (α), turbulent kinetic energy (k), specific dissipation rate (ω), turbulent viscosity (μ), and temperature (T). The initial diameters of the bubbles, as well as the physical properties of both air and water, were assigned. Furthermore, parameter ranges were established for interfacial forces, turbulence models, and simulation controls (such as duration and output frequency). As for the pre-processing part, a multigrading structured mesh with 25 × 1 × 150 cells was created. This mesh increased the resolution near the wall region, where shear and interfacial forces have significant effects on the behavior of bubbles. The mesh configuration was influenced by the prior input values, and a validation process was conducted to confirm the accuracy of the mesh and input settings.

With regard to the calculation element, the solver performed numerical integration of the continuity and momentum equations at each time step. Additional calculations were carried out using the IATE model to estimate interfacial area and the k-omega SST Sato model to represent turbulence effects in the continuous phase. The simulation was executed over a total time period of 60 seconds. A comprehensive set of physical parameters was meticulously measured at six predetermined axial locations along the vertical channel. These parameters encompassed critical variables such as pressure, velocity, void fraction, interfacial area concentration, and bubble size. The measurements were obtained from surface probes, ensuring the collection of reliable and representative data. The void fraction, interfacial area concentration, and bubble size were processed using area averaging, whereas velocity was averaged using the area-weighted method. The mean values thus obtained were then utilized to calculate the relative error percentage (RE%) for model verification by comparing the simulation outcomes at three specific axial positions (z/D_H = 34.8, 88.2, and 141.7) against the experimental data in order to assess the model's accuracy and performance.

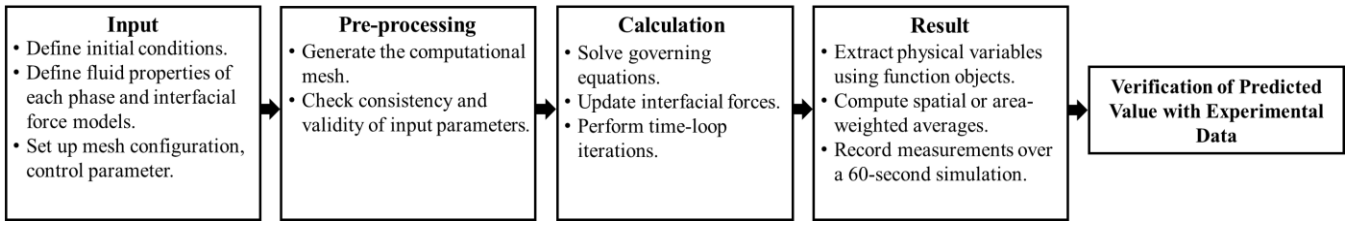

FIGURE 2. Workflow of the CFD Simulation Process in OpenFOAM

IV. RESULTS AND DISCUSSION

To assess the predictive performance of the computational fluid dynamics (CFD) model for vertical air–water two-phase flow, simulation results were benchmarked against experimental data obtained by Liu at three axial positions corresponding to dimensionless heights (z/D_H) of 34.8, 88.2, and 141.7. Four key parameters were evaluated, namely the Sauter mean diameter, void fraction, bubble velocity, and interfacial area concentration, which are presented in Figs. 3(a), 3(b), 3(c), and 3(d), respectively. Each plot illustrates the variation of the corresponding parameter along the dimensionless vertical axis (z/D_H). In the graphs, solid lines denote simulation results, while dashed lines represent experimental measurements. Case A is plotted in black, whereas Case B is represented in red to distinguish between the two test conditions.

IV.A. Sauter Diameter

As demonstrated in Fig. 3(a), the graph of Case A demonstrates a steadily increasing trend along the axial direction and remains closely aligned with the experimental data at all measurement points. Conversely, Case B demonstrates considerably elevated values in comparison to the experimental outcomes, particularly within the upper segment of the channel, where intensified bubble coalescence results in an overestimation of the mean bubble size. As illustrated in Table II, the simulation in Case A generates minimal relative errors of 0.30%, -0.83%, and -3.61% at z/D_H = 34.8, 88.2, and 141.7, respectively. Conversely, Case B exhibited substantially higher deviations, with relative errors reaching 38.57% and 44.51% at z/D_H = 88.2, and 141.7, respectively. These findings suggest that the current model is deficient in its capacity to adequately capture the phenomenon of bubble coalescence under conditions of elevated gas flow.

IV.B. Void Fraction

As shown in Fig. 3(b), both cases exhibit an increasing trend in void fraction along the vertical direction, which corresponds to the upward motion and accumulation of bubbles in the duct. In Case A, the simulation trend generally follows experimental data, but noticeable deviations remain at z/D_H = 34.8 and 141.7, with only z/D_H = 88.2 showing a relatively close match. In Case B, the void fraction is consistently overpredicted along the height, but the deviation appears to decrease with increasing axial length. As illustrated in Table II, the relative errors for Case A are 14.39%, 8.47%, and 17.57% at z/D_H = 34.8, 88.2, and 141.7, respectively, while for Case B, the errors decreased progressively from 22.28% to 17.89% and 11.60%. This finding indicates that the model's capacity to predict the void fraction in Case B is likely to undergo enhancement as the process progresses, a phenomenon that may be attributed to the escalating bubble dispersion over time.

IV.C. Velocity

As shown in Fig. 3(c), the graphs for both Case A and Case B remain relatively constant along the axial direction, reflecting the uniform upward motion of bubbles throughout the channel. In Case A, the simulated bubble velocity tends to exceed the experimental measurements at all positions to a minor extent. Table II shows relative errors of 17.11%, 15.26%, and 10.53% at z/D_H = 34.8, 88.2, and 141.7, respectively. A similar trend is observed in Case B, where the simulation also overpredicts the velocity with relative errors of 14.79%, 15.64%, and 13.37% at the corresponding positions. These results suggest that the model successfully captures the overall velocity trend, but moderate quantitative deviations remain, generally within the range of 10 - 17%.

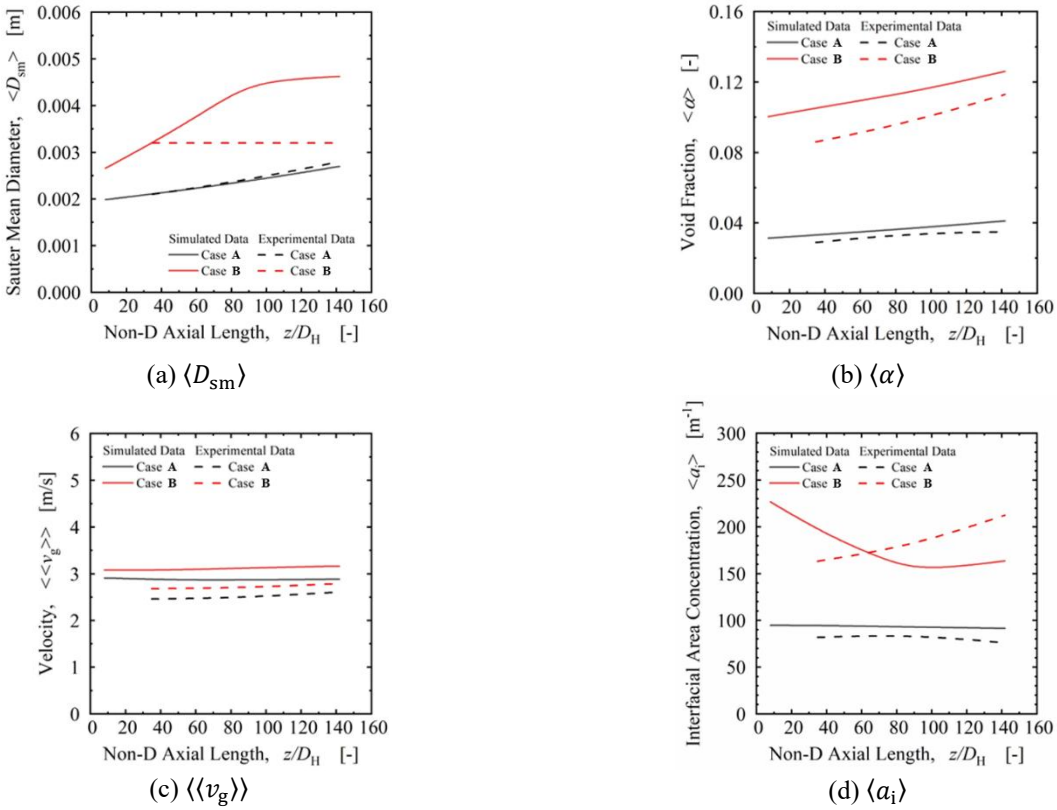

FIGURE 3. Comparison between Experimental data and Simulation data (a) $\langle D_{sm} \rangle$, (b) $\langle \alpha \rangle$, (c) $\langle \langle v_g \rangle \rangle$, and (d) $\langle a_i \rangle$

TABLE II. Relative Error Percentage

Cases	z/D_H	Percent of $\langle D_{sm} \rangle$ [%]	Percent of $\langle \alpha \rangle$ [%]	Percent of $\langle \langle v_g \rangle \rangle$ [%]	Percent of $\langle a_i \rangle$ [%]
A	34.8	0.30	14.39	17.11	15.52
	88.2	-0.83	8.47	15.26	9.51
	141.7	-3.61	17.57	10.53	20.37
B	34.8	0.04	22.28	14.79	20.70
	88.2	38.57	17.89	15.64	-13.70
	141.7	44.51	11.60	13.37	-23.00

IV.D. Interfacial Area Concentration (IAC)

As demonstrated in Fig. 3(d), both cases exhibit a decreasing trend in interfacial area concentration along the vertical axis, which reflects bubble coalescence leading to a reduction in total gas-liquid interface. In Case A, the simulation trend manifests as relatively flat, exhibiting reasonable congruence with the experimental data, though deviations emerge at z/D_H = 34.8 and 141.7. As illustrated in Table II., the relative errors for Case A are 15.52%, 9.51%, and 20.37% at z/D_H = 34.8, 88.2, and 141.7, respectively, indicating moderate agreement. In Case B, the simulation overpredicts the interfacial area at z/D_H = 34.8 with a relative error of 20.70%, but then increasingly underpredicts it at downstream locations, with errors of -13.70% and -23.00% at z/D_H = 88.2 and 141.7, respectively. This alteration in deviation direction indicates that, while the model does capture the decreasing trend caused by coalescence, it still lacks the necessary accuracy to adequately represent interfacial area dynamics under conditions of high gas flow, possibly due to intensified coalescence and vertical redistribution of bubbles.

V. CONCLUSIONS

The two-phase flow of bubbles in narrow vertical channels is of particular importance in determining heat transfer performance and system stability, particularly in the field of nuclear engineering. Although CFD is widely used to simulate such flows, commercial software packages present limitations in terms of cost and accessibility. OpenFOAM, an open-source and highly flexible CFD platform, offers an effective alternative for modelling complex multiphase systems. Although prior studies have employed OpenFOAM to simulate bubbly flow, only a limited number have focused specifically on turbulent bubbly flow in narrow rectangular channels. The present study aims to address this research gap by employing OpenFOAM with a two-group Interfacial Area Transport Equation (IATE) model and comprehensive interfacial force modelling to replicate Liu's experiment in a narrow rectangular duct. The key aspects of this study can be summarized as follows:

- The initial simulation parameters were defined according to the experimental setup of Cases A and B. The gas flow rates exhibited by these cases are subject to variation, with B demonstrating a higher rate in comparison to A. However, the liquid flow rate was maintained at a constant level throughout the experimentation. The simulations were conducted within a narrow vertical duct measuring 10 mm × 200 mm × 2.95 m. The OpenFOAM version 12 software was utilized for the execution of simulations, with the multiphaseEulerFoam solver employed to facilitate the computations. This solver incorporates interfacial force models, encompassing drag, lift, wall lubrication, and virtual mass. Furthermore, the two-group Interfacial Area Transport Equation (IATE) model was implemented in order to account for bubble coalescence and breakup.

- Six axial measurement positions were established along the duct's height. Surface probes were utilized to obtain area-averaged values of Sauter mean diameter $\langle D_{\mathrm{sm}} \rangle$, void fraction $\langle \alpha \rangle$, and interfacial area concentration $\langle a_{\mathrm{i}} \rangle$, while void-weighted averaging was applied to calculate the gas phase velocity $\langle \langle v_{\mathrm{g}} \rangle \rangle$. The simulation results were then compared with the experimental data set collected by Liu at z/D_{H} = 34.8, 88.2, and 141.7. The evaluation process entailed graphical comparisons of trends and quantitative assessments of relative errors (RE) for all four parameters: $\langle D_{\mathrm{sm}} \rangle$, $\langle \alpha \rangle$, $\langle \langle v_{\mathrm{g}} \rangle \rangle$, and $\langle a_{\mathrm{i}} \rangle$.

- Case A (low gas flow rate) demonstrated a strong correlation with the experimental data, particularly in $\langle D_{\mathrm{sm}} \rangle$ and $\langle \langle v_{\mathrm{g}} \rangle \rangle$, where the trends and relative errors remained within acceptable limits. Case B (high gas flow rate) exhibited greater deviation, especially in $\langle D_{\mathrm{sm}} \rangle$ and $\langle a_{\mathrm{i}} \rangle$, where the model failed to accurately capture the behavior of bubble coalescence. For $\langle a_{\mathrm{i}} \rangle$, the simulated values were higher than the experimental data in the lower region of the duct and lower toward the top, suggesting a shift in error direction along the vertical axis. This suggests a potential spatial inconsistency in the prediction of bubble distribution and interfacial area concentration. In conclusion, the model demonstrates reasonable predictive capability for bubbly flow behavior under low gas flow conditions. However, to improve accuracy under more complex flow regimes with higher gas injection rates, further refinement of the IATE model parameters such as the coalescence coefficient (C_{WE}), the breakup coefficient (C_{WE}), and the turbulent interaction coefficient (C_{WE}) as well as the interfacial force models is necessary.

REFERENCES

[1] Liu, Yang. "Three-dimensional interfacial area transport in gas-dispersed two-phase flow up to churn-annular flow transition." PhD diss., Purdue University, 2008.
[2] Liao, Yixiang, Kartik Upadhyay, and Fabian Schlegel. "Eulerian-Eulerian two-fluid model for laminar bubbly pipe flows: Validation of the baseline model." *Computers & Fluids* 202 (2020): 104496.
[3] Poullikkas, A. "Two phase flow performance of nuclear reactor cooling pumps." *Progress in Nuclear energy* 36, no. 2 (2000): 123-130.
[4] Jin, Guangyuan, et al. "Effect of rolling motion on transient flow resistance of two-phase flow in a narrow rectangular duct." *Annals of Nuclear Energy* 64 (2014): 135-143.
[5] Medina, Humberto, Abhinivesh Beechook, Jonathan Saul, Sophie Porter, Svetlana Aleksandrova, and Steve Benjamin. "Open source computational fluid dynamics using OpenFOAM." In *Royal Aeronautical Society, General Aviation Conference, London*. 2015.
[6] Jasak, Hrvoje. "OpenFOAM: Open source CFD in research and industry." *International journal of naval architecture and ocean engineering* 1, no. 2 (2009): 89-94.

[7] Ishii, Mamoru, and Kaichiro Mishima. "Two-fluid model and hydrodynamic constitutive relations." *Nuclear Engineering and design* 82, no. 2-3 (1984): 107-126.
[8] Wang, Xia, and Xiaodong Sun. "Three-dimensional simulations of air–water bubbly flows." *International journal of multiphase flow* 36, no. 11-12 (2010): 882-890.
[9] Menter, Florian R. "Elements of inductrial heat tranfer predictions." In *16th Brazilian Congress of Mechanical Engineering (COBEM), Uberlandia, Brazil, 2001*. 2001.
[10] Sato, Y., M. Sadatomi, and K. Sekoguchi. "Momentum and heat transfer in two-phase bubble flow—I. Theory." *International Journal of Multiphase Flow* 7, no. 2 (1981): 167-177.

Sensitivity Analysis of Operator Actions in Bleeding Timing in OPR-1000 and APR-1400

Gangmin Kim[1], Jaewhan Kim[2], Jaehyun Cho[3*], Changhyun Jang[4]

[1]*Chung-Ang University, Heukseok-ro 84, Dongjak-gu, Seoul, 06974, Republic of Korea, kkm371837@cau.ac.kr*
[2] *Korea Atomic Energy Research Institute, Daedeok-daero 989-111, Yuseong-gu, Daejeon, 34057, Republic of Korea, jhkim4@kaeri.re.kr*
[3] *Chung-Ang University, Heukseok-ro 84, Dongjak-gu, Seoul, 06974, Republic of Korea, jcho@cau.ac.kr*
[4]*Chung-Ang University, Heukseok-ro 84, Dongjak-gu, Seoul, 06974, Republic of Korea, ckdguso@cau.ac.kr*

ABSTRACT

This study presents a comprehensive sensitivity analysis of operator actions during feed-and-bleed operations in OPR-1000 and APR-1400 nuclear reactor types under Small Break Loss of Coolant Accident (SBLOCA) conditions. The SBLOCA event tree and the sequence leading to Feed-and-Bleed (F&B) operation for OPR-1000 and APR-1400 were constructed based on the probabilistic safety assessment (PSA) methodology and plant-specific accident analysis reports [1]. Using the MARS-KS thermal-hydraulic code, we analyzed the time margins available for operator intervention between Steam Generator (SG) Wide Range (WR) level reaching 2% and the necessity to initiate bleeding operations to prevent core damage. The analysis was conducted across various break sizes ranging from 0.5 to 2.0 inches. Results demonstrate significant differences in available response times between the two reactor designs, with OPR-1000 consistently providing longer time margins (9,100-16,000 seconds) compared to APR-1400 (5,500-15,200 seconds) for equivalent break sizes. For larger break sizes (>0.8 inches in OPR-1000 and >1.2 inches in APR-1400), the analysis revealed that bleeding operations become unnecessary as the break itself provides sufficient depressurization. These findings have important implications for Emergency Operating Procedures (EOPs) and operator training programs, suggesting that APR-1400 requires more stringent response protocols and potentially different decision-making criteria compared to OPR-1000. The study contributes valuable insights for enhancing nuclear safety by optimizing operator response strategies based on reactor-specific time constraints.

Keywords: feed and bleed, emergency operating procedure, SG wide range, SBLOCA

I. Introduction

I.A. Background

Small Break Loss of Coolant Accident (SBLOCA) in nuclear power plants occurs due to a break in the Reactor Coolant System (RCS), which can lead to core damage if not properly managed. The severity of a SBLOCA depends on the break size, location, and the effectiveness of emergency response systems. In Korean nuclear power plants, particularly OPR-1000 and APR-1400 designs. Figure 1 is a visualization of the SBLOCA event tree highlighting the sequence that leads to Feed and Bleed (F&B) operation, illustrating key decision points from Small Break LOCA initiation to successful primary depressurization and ECCS injection.

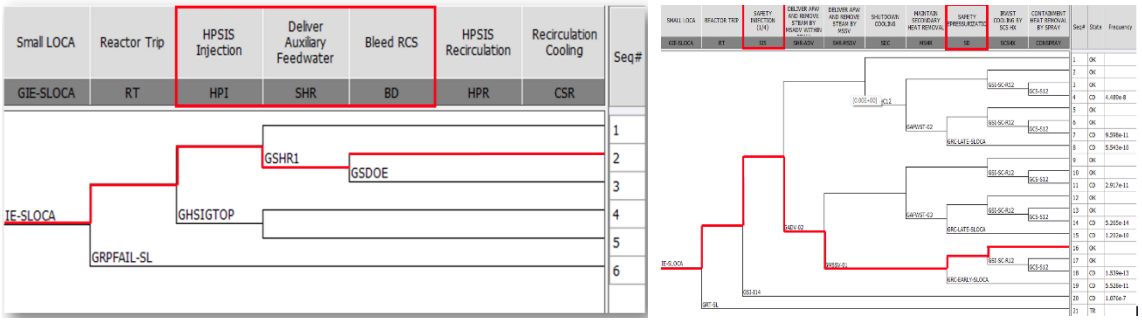

FIGURE 1. OPR-1000, APR-1400 SBLOCA Event Tree

I.B. Feed and Bleed Operation

F&B operation is a critical cooling strategy employed when normal heat removal pathways fail during accidents like SBLOCA. This operation involves depressurizing the reactor vessel by opening primary safety valves (SDS Valve in OPR-1000, POSRV in APR-1400) to release steam and injecting cooling water through the Emergency Core Cooling System (ECCS). When the primary system pressure decreases sufficiently, Safety Injection (SI) is activated to sustain core cooling, ensuring the removal of decay heat from the reactor core and preventing excessive temperature rise.

The successful implementation of F&B operations heavily depends on operator decision-making and response time. When the Steam Generator (SG) Wide Range (WR) level drops below 2%, operators must manually open the primary system safety valves to release steam. The SG WR level is a measurement signal that continuously monitors the water level over a broad span within the steam generator, taking into account the specific geometry and design of the SG. This parameter seves as a crucial indicator for assessing the available inventory of coolant, especially during emergency operations, since a drop below 2% WR level signals a significant depletion of water and necessitates prompt operator action. According to the Emergency Operating Procedures (EOP) for Shin-Kori 3 and 4, operator-initiated bleeding should be performed when the Steam Generator (SG) Wide Range level drops below 2% [2]. This study aims to analyze the impact of bleeding time and operator intervention on core damage prevention during SBLOCA in OPR-1000 and APR-1400 reactors, specifically focusing on determining the timing at which operators open the valves upon receiving the F&B signal and analyzing the effect of operator intervention delays on cooling performance and core integrity.

I.C. Research Objectives

This study aims to analyze the impact of bleeding time and operator intervention on core damage prevention during SBLOCA in OPR-1000 and APR-1400 reactors1. Specifically, the research focuses on:

1. Determining the timing at which operators open the valves upon receiving the F&B signal when the SG WR level falls below 2%
2. Analyzing the effect of operator intervention delays on cooling performance and core integrity
3. Comparing the time margins available for operator action between OPR-1000 and APR-1400 reactor designs
4. Developing recommendations for optimizing Emergency Operating Procedures based on reactor-specific time constraints

II. Methodology

The MARS-KS code was used for thermal-hydraulic system analysis of the SBLOCA scenarios. The accident scenario follows a specific sequence: Reactor Trip, Safety Injection, Auxiliary Feedwater (AFW) failure, and RCS Bleeding. In the OPR-1000 scenario, after Reactor Trip (RT), the High Pressure Safety Injection (HPSI) successfully operates, followed by the failure of the AFW. In the APR-1400 scenario, after RT, safety injection is successfully initiated, followed by AFW failure, successful opening of the Main Steam Safety Valve (MSSV), but ultimately, the secondary heat removal fails. Figure 3 is a schematic illustrating the key SBLOCA mitigation sequence from reactor coolant system breach and AFW failure to SG WR level dropping below 2%, Feed-and-Bleed valve actuation, and subsequent ECCS injection to maintain core cooling.

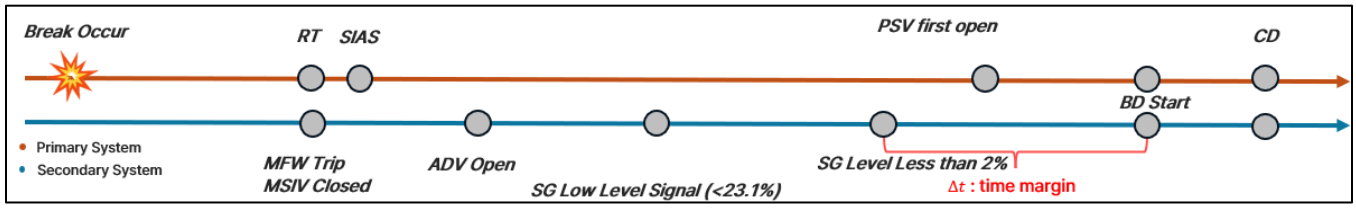

FIGURE 3. Emergency Operating Procedures (EOP) of APR-1400

II.A. Sensitivity Analysis Approach

This study analyzed break sizes ranging from 0.5 to 2.0 inches in 0.1-inch intervals to comprehensively evaluate the effect of break size on F&B operation performance. This range was selected based on the definition of SBLOCA in safety analysis reports and previous studies that identified these sizes as most critical for emergency responses evaluation. The incremental approach allowed for detailed analysis of the transition points where operator intervention becomes critical or unnecessary.

When the SG WR level reaches 2%, the valve open signal is generated, and sensitivity analysis was conducted by delaying the valve open time in 100-second intervals. The objective was to determine the maximum allowable time margin before core damage, defined as a peak cladding temperature (PCT) exceeding 1477K.

II.B. Time Margin Definition and Calculation

This approach enabled the identification of the critical time window available for operator action in each reactor type and for each break size. Time margin (Δt) is defined as the maximum allowable time between the SG WR level dropping below 2% and the initiation of bleeding, without leading to core damage. This margin represents the operator's available response time before the situation escalates to an irreversible state. The calculation involved determining the time at which the SG WR level reached 2% and then incrementally delaying the bleeding initiation until the PCT reached the critical threshold of 1477K. Figure 4 illustrates the operator time margin and core damage indicators during a OPR-1000 0.5-inch SBLOCA event: the left plot shows Steam Generator wide-range level decline and valve mass flow rate over time, highlighting the delay between SG level dropping below 2% and valve actuation; the right plot displays peak cladding temperature trends, indicating the point of core damage threshold (1477 K) when the time margin is exceeded.

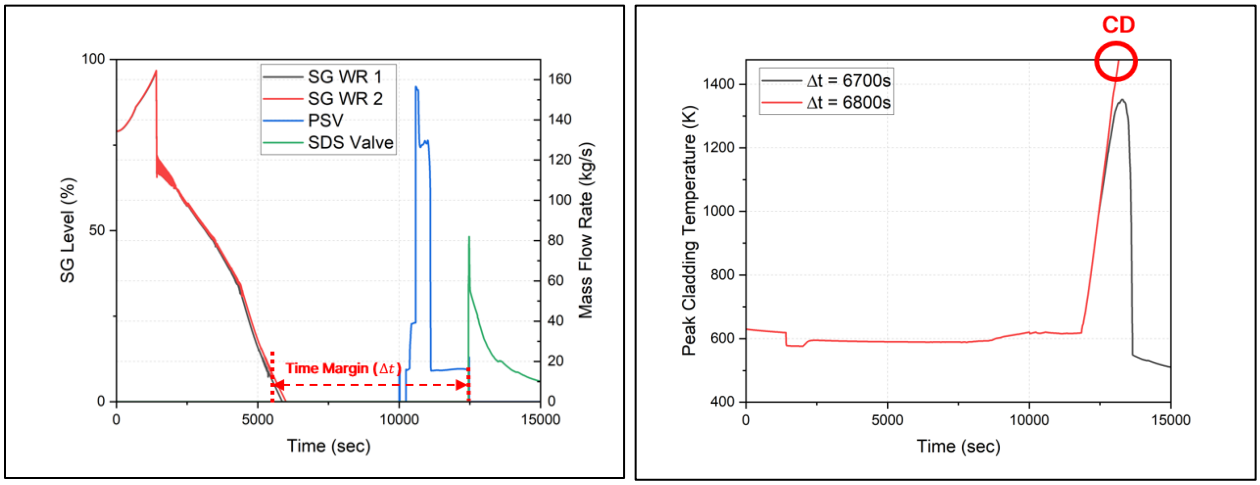

FIGURE 4. Major Operating Variables and Cladding Temperature Response in OPR-1000 SBLOCA Event

III. Results

III.A. OPR-1000 Time Margin Analysis

For OPR-1000, the analysis revealed significant time margins for operator intervention across various break sizes. The maximum allowable time margins were 9,100 seconds for a 0.5-inch break, 9,100 seconds for a 0.6-inch break, 11,000 seconds for a 0.7-inch break, and 16,000 seconds for a 0.8-inch break. For break sizes larger than 0.8 inches, the analysis showed that bleeding operations become unnecessary as the break itself provides sufficient depressurization to enable effective safety injection.

TABLE I. Results of OPR-1000 Analysis

Trip Signal	0.5[in]	0.6[in]	0.7[in]	0.8[in]
PZR low pressure signal	1,410s (24min)	925s (15min)	655s (11min)	492s (8min)
ADV open	2,310s (39min)	1,825s (30min)	1,555s (26min)	1,392s (23min)
SG low level signal	2,515s (42min)	2,194s (37min)	1,923s (32min)	1,760s (29min)
SG WR level 2[%]	2,789s (46min)	2,399s (40min)	1,948s (32min)	1,782s (30min)
PSV First Open	8,426s (140min)	8,773s (146min)	10,619s (177min)	15,443s (257min)
Bleeding Point	11,889s (198min)	11,499s (192min)	12,948s (216min)	17,782s (296min)
time margin (Δt)	**9,100s (152min)**	**9,100s (152min)**	**11,000s (183min)**	**16,000s (267min)**

III.B. APR-1400 Time Margin Analysis

APR-1400 exhibited shorter time margins compared to OPR-1000 across all analyzed break sizes. The maximum allowable time margins were 5,500 seconds for a 0.5-inch break, 5,600 seconds for a 0.6-inch break, 6,700 seconds for a 0.7-inch break, and 7,800 seconds for a 0.8-inch break. The time margin continued to increase with break size, reaching 15,200 seconds for a 1.2-inch break. For break sizes larger than 1.2 inches, bleeding operations were found to be unnecessary.

TABLE II. Results of APR-1400 Analysis

Trip Signal	0.5[in]	0.6[in]	0.7[in]	0.8[in]	0.9[in]	1.0[in]	1.1[in]	1.2[in]
PZR low pressure signal	2,888s (48min)	1,988s (33min)	1,445s (24min)	1,102s (18min)	871s (15min)	707s (12min)	588s (10min)	499s (8min)
ADV open	3,788s (63min)	2,888s (48min)	2,345s (39min)	2,002s (33min)	1,771s (30min)	1,607s (27min)	1,488s (25min)	1,399s (23min)
SG low level signal	6,511 (109min)	5,925s (99min)	5,470s (91min)	5,449s (91min)	5,618s (94min)	5,852s (98min)	6,120s (102min)	6,543s (109min)
SG WR level 2[%]	7,429s (124min)	7,155s (119min)	6,852s (114min)	6,929s (115min)	7,149s (119min)	7,528s (125min)	7,949s (132min)	8,689s (145min)
PSV First Open	9,792s (163min)	9,935s (166min)	10,458s (174min)	11,059s (184min)	12,233s (204min)	13,947s (232min)	16,535s (276min)	22,436s (374min)
Bleeding Point	12,929s (215min)	12,755s (213min)	12,522s (209min)	12,929s (215min)	13,849s (231min)	15,328s (255min)	17,949s (299min)	23,889s (298min)
time margin (Δt)	**5,500s (92min)**	**5,600s (93min)**	**5,700s (100min)**	**6,000s (112min)**	**6,700s (130min)**	**7,800s (130min)**	**10,000s (167min)**	**15,200s (253min)**

III.C. Comparative Analysis Between Reactor Types

The comparative analysis reveals that OPR-1000 consistently provides longer operator time margins than APR-1400 for equivalent break sizes. For example, at a 0.5-inch break, the maximum allowable time margin (Δt) for OPR-1000 is approximately 9,100–16,000 seconds (152–267 minutes), while for APR-1400 it is 5,500–15,200 seconds (92–253 minutes). On average, OPR-1000 offers about 1.4 times more response time than APR-1400. This difference is primarily attributed to design characteristics such as larger primary system volume, higher safety injection capacity, and more effective decay heat removal in OPR-1000 compared to APR-1400. The differences in time margin between OPR-1000 and APR-1400 are primarily attributed to their design characteristics, including primary system volume and safety injection capacity, as

discussed in previous feasibility analyses [3]. Figure 5 shows the evolution of primary system pressure and safety injection mass flow rates during SBLOCA, highlighting the timing of HPSI/DVI injection limits and the onset of effective safety injection for OPR-1000 and APR-1400, respectively.

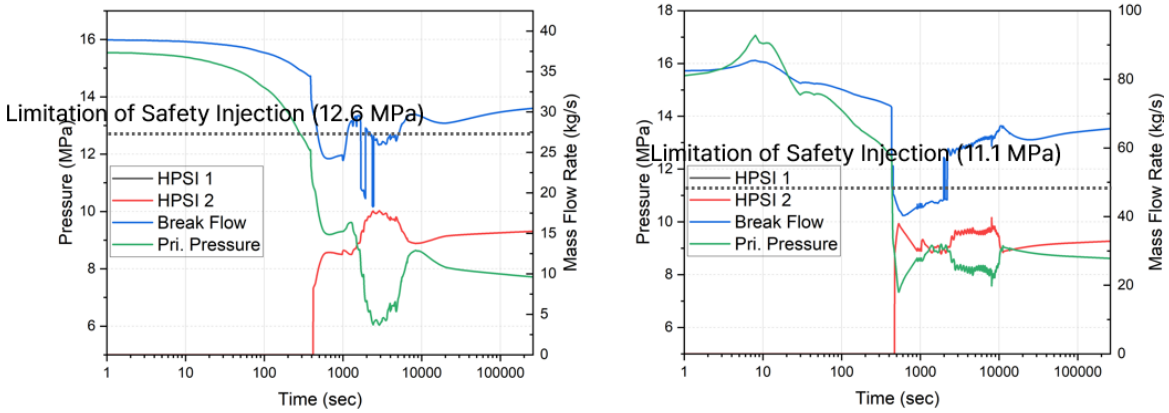

FIGURE 5. Primary System Pressure and Safety Injection Mass Flow Rate During SBLOCA for OPR-1000 (left) and APR-1400 (right)

As shown in the timeline(figure 3), both reactor types exhibit an increasing trend in time margin as break size increases. Larger breaks accelerate SG depletion but also enhance natural depressurization, reducing the reliance on operator-initiated bleeding. The analysis identifies critical threshold break sizes: for OPR-1000, breaks larger than 0.8 inches, and for APR-1400, breaks larger than 1.2 inches, naturally depressurize the RCS sufficiently to enable effective safety injection without additional operator intervention. These thresholds are crucial for emergency procedure development, as they define the conditions under which operator action is essential versus when passive system response suffices. Figure 6 compares the operator time margin (Δt) for initiating bleeding between OPR-1000 and APR-1400 across different break sizes, illustrating that OPR-1000 consistently provides a longer available response time and that the margin increases with break size up to the critical threshold for each reactor type.

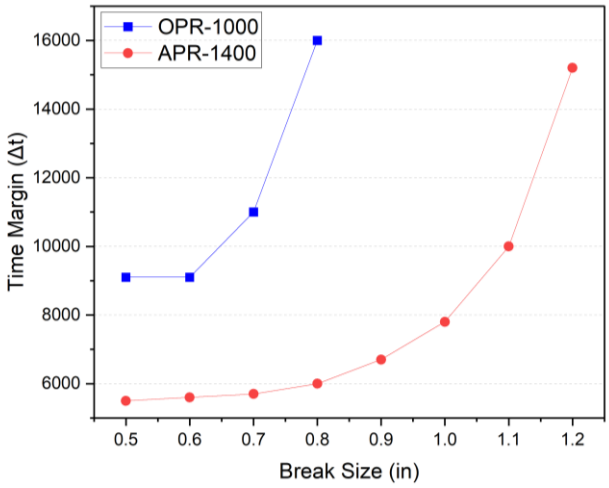

FIGURE 6. Time margin (Δt) as a function of break size for OPR-1000 and APR-1400

IV. Conclusion

This study demonstrates significant differences in operator time margins for safe Feed-and-Bleed (F&B) operation between OPR-1000 and APR-1400 under SBLOCA conditions. OPR-1000 provides a longer window for operator action (152–267 minutes) compared to APR-1400 (92–253 minutes) for the same break sizes, and for larger breaks, bleeding is not required due to sufficient natural depressurization.

These findings have direct implications for emergency operating procedures (EOPs) and operator training. For APR-1400, the shorter time margins necessitate stricter response protocols, faster decision-making, and potentially the integration of automated systems to reduce reliance on operator action. Conversely, OPR-1000 allows for more deliberate operator responses due to its longer margins. Training programs should be tailored accordingly, with APR-1400 operators focusing on rapid recognition and response, and OPR-1000 operators benefiting from more comprehensive scenario analysis.

Furthermore, the identified time margins support risk-informed safety assessments and EOP optimization. Future research should validate these results through full-scope simulator studies with actual operators, and examine the impact of different initial plant conditions and equipment availability on time margins. The development of advanced decision support tools, accounting for reactor-specific constraints, will further enhance operator performance and overall plant safety during SBLOCA events.

ACKNOWLEDGMENTS

This work was supported by the Nuclear Safety Research Program through the Regulatory Research Management Agency for SMRS (RMAS) and the Nuclear Safety and Security Commission (NSSC) of the Republic of Korea (No. 1500-1501-409).

REFERENCES

[1] KAERI, Full-Power Internal Event Level 1 Probabilistic Safety Assessment for Hanul Units 3 and 4 (Draft), KAERI, Daejeon, Republic of Korea (2014).

[2] KHNP, “신고리 3, 4 호기 비상운전절차서,” Korea Hydro & Nuclear Power, Gyeongju, Republic of Korea (2011).

[3] M. C. Kim and D. W. Jeong, “Feasibility analysis of aggressive cooldown in OPR-1000 nuclear power plants,” Nuclear Engineering and Technology, 46, 3, 389–400 (2014).

ASRAM2025
www.asram2025.org
Asian Symposium on Risk Assessment and Management 2025
Pattaya, Thailand, 27 – 29 August 2025

Application of EMRALD for Simulation-Based Estimation of Station Blackout Sequence Frequencies in a Nuclear Power Plant

Yoonsoo Lee[1], Man Cheol Kim[2]

[1] *Department of Energy Systems Engineering, Chung-Ang University: 84 Heukseok-ro, Dongjak-gu, Seoul, 06974, Korea, danny1056@cau.ac.kr*
[2] *Department of Energy Systems Engineering, Chung-Ang University: 84 Heukseok-ro, Dongjak-gu, Seoul, 06974, Korea, charleskim@cau.ac.kr*

ABSTRACT

This study investigates the use of event modeling risk assessment using linked diagrams (EMRALD), a dynamic probabilistic safety assessment (PSA) tool developed by the Idaho National Laboratory to analyze complex accident sequences triggered by a loss of offsite power (LOOP) in nuclear power plants. Unlike traditional PSA methods based on event tree and fault tree, EMRALD enables intuitive modeling of time-dependent system behaviors and component interactions, making it well suited for evaluating all the accident sequences. The analysis was conducted in two stages. First, a previously published station blackout (SBO) scenario was reconstructed using EMRALD to verify its computational reliability. The results were validated through comparison with both a convolution-based model and Monte Carlo simulations, confirming EMRALD's ability to accurately estimate conditional core damage probabilities (CCDP) and associated risk sequences. Second, a comprehensive LOOP scenario was developed, incorporating multiple power supply and heat removal components such as emergency diesel generators (EDGs), alternative AC diesel generator, motor driven auxiliary feedwater pumps, and turbine driven auxiliary feedwater pumps along with their common cause failure probabilities. EMRALD dynamically simulated these systems and estimated CCDP based on Monte Carlo simulation. The simulation results identified power supply system failures as key contributors to core damage. Mechanical pump failures showed relatively low impact, and SBO-R (EDGs fail to run) sequences appeared more frequently than SBO-S (EDGs fail to start).
This modeling approach demonstrates EMRALD's applicability for analyzing time-sensitive, interdependent accident sequences under LOOP conditions.

Keywords: Probabilistic safety assessment, Event modeling risk assessment using linked diagrams, Time-dependent, Loss of offsite power, Station blackout

I. Introduction

Probabilistic safety assessment (PSA) has long provided valuable insights into reactor operation and design by quantitatively evaluating nuclear reactor risk, identifying critical events significantly impacting reactor safety, and analyzing components that significantly contribute to such risks. Among numerous PSA studies conducted to date, station blackout (SBO) has consistently been identified as a significant contributor affecting reactor safety. SBO is recognized as a specific scenario of a loss of offsite power (LOOP) event, characterized by the complete failure of emergency diesel generators (EDGs).

Under SBO conditions, nuclear power plants typically rely on alternative AC diesel generators (AAC DGs) to ensure secondary heat removal. Specifically, AAC DGs drive motor driven auxiliary feedwater pumps (MDPs) or provide direct current power to turbine driven auxiliary feedwater pumps (TDPs) to provide feedwater and remove heat effectively, maintaining reactor core cooling. However, the reliability and availability of these components involve inherent uncertainties, as operational failures or reduced performance levels remain possible under specific conditions. Such uncertainties require explicit evaluation and consideration within PSA frameworks.

This study utilizes a dynamic probabilistic modeling tool, event modeling risk assessment using linked diagrams (EMRALD), to systematically analyze diverse scenarios associated with LOOP-induced SBO events. EMRALD addresses limitations inherent in conventional PSA methodologies by effectively capturing time-dependent behaviors, state transitions, and interactions among plant components. The purpose of this research is to analyze and compare SBO event sequences that emerge from LOOP scenarios, using EMRALD to evaluate how these complex time dependent sequences develop and

diverge under varying conditions. This research also clarifies the calculational accuracy of EMRALD and demonstrates its utility in implementing complex sequences intuitively and clearly.

II. Analytical Framework and Modeling approach

I1.A. Introduction to EMRALD

EMRALD is a dynamic PSA tool developed by Idaho national laboratory to facilitate the analysis of time-dependent complex scenarios. Unlike traditional PSA tools that rely primarily on event trees (ET) and fault trees (FT), EMRALD is structured around state changes and designed to represent how systems evolve over time. Prescott et al [1] express EMRALD as a dynamic PSA tool that bridges the gap between traditional modeling practices and dynamic simulation by offering an intuitive graphical interface and simplified external coupling capabilities.

In EMRALD, models are typically built using a plant-level diagram, logic or subsystem diagrams representing the configuration of systems, and component-level diagrams that define individual component states and transitions. These diagrams can interact through state changes, and the success or failure of multiple diagrams can form logic trees like FT, where certain conditions trigger some events. This modular structure enables users to express the same plant features in multiple ways, encouraging creativity and flexibility in modeling.

Such flexibility, however, means that the complexity of the model and the accuracy of the analysis result depend significantly on the user's modeling skill and familiarity with EMRALD. The tool provides opportunities for simplification or enhancement based on user's choices, which gives EMRALD a higher degree of user influence than traditional PSA tools. For highly skilled users, this translates into the ability to assess intricate, time-dependent scenarios that would be difficult to model using conventional approaches much easier.

EMRALD also helps users create Monte Carlo simulations more easily and intuitively, making it simpler for others to follow the timeline and changes in scenario conditions. Additionally, it clearly shows which components fail and lead to core damage, making it easier to identify cutsets and its fractions.

Recognizing these strengths, EMRALD was selected in this study as the primary tool for analyzing complex LOOP sequences.

II.B. SBO sequences

SBO refers to the loss of all AC power sources necessary to cool the reactor core. It is typically a subset of a LOOP event in which all EDGs also fail to operate. When SBO occurs, the nuclear power plant (NPP) attempts to remove decay heat by utilizing alternative AC power sources such as the AAC DG, or by operating components that require no external power, such as the TDPs. If heat removal is successfully maintained until offsite power is recovered, the NPP remains safe. However, if heat removal fails before power recovers, the event progresses toward core damage.

The progression of SBO depends on the availability and reliability of these backup systems, the timing of failures, the interactions between systems, and the status of batteries, which provide time margin to TDPs. As these systems interact, various accident sequences may develop depending on which components succeed or fail and when these events occur. Such variability affects the available margin for offsite power recovery and can significantly influence the overall reliability of the NPP. Two types of SBO scenarios are typically considered: SBO-S and SBO-R, depending on whether all EDGs fail to start or at least one EDG fails to run.

Previous study, Kim [2], introduced a convolution approach as a method for analyzing complex time-dependent scenarios. The study specifically focused on SBO-S scenario, which is adopted in the present work to verify the computational accuracy of EMRALD. The scenario was evaluated with all three methods, and the results were found to be almost the same. The parameters used in calculation are from [2] which are noted in Ma et al. [3]

III. Analysis of LOOP

III.A. Scenario Development and Implementation in EMRALD

In Sections II.B, the special case of LOOP, known as the SBO-S scenarios, was analyzed to validate the computational accuracy of EMRALD. Building on that foundation, this section expands the analysis by leveraging EMRALD's capabilities to model and simulate a more complex and realistic sequence of events.

Comprehensive LOOP scenarios were constructed, incorporating the important system interactions that may follow LOOP. The model includes two EDGs, one AAC DG, two MDPs, and two TDPs. For all duplicated components, the possibility of

CCFs was also included, with failure probabilities sourced from [3] and Ma et al. [4] The offsite power recovery time is assumed to follow a lognormal distribution, with distribution parameters sourced from Johnson et al. [5]

When LOOP event occurs, all the components except AAC DG are assumed to be initiated. After both EDGs fail, the AAC DG starts to run, and if it also fails and the battery depletion time elapses, the TDPs are modeled to fail due to a lack of DC power support.

The heat removal system is considered to have failed if either of the following conditions is met: (1) both MDPs and TDPs fail, or (2) both AAC DG and TDPs fail. In the first condition, failure is assumed regardless of EDG or AAC DG availability. If the heat removal system fails and offsite power is not recovered before the time margin T_C, the scenario results in core damage. The failure in the second case occurs when the MDPs shut down due to loss of power supply resulting from the failure of both the EDGs and the AAC DG. Figure 1 provides a rough overview of the modeled LOOP scenario. In the actual modeling, possible failure combinations of each component were considered, fail to start or run, and for two same components, CCFs are also modeled. However, in the case of the LOOP scenario, expressing every sequence through an ET would result in an excessive number of combinations. Therefore, Figure 1 presents a simplified form that reflects only the failure status of each component, focusing on the essential logic.

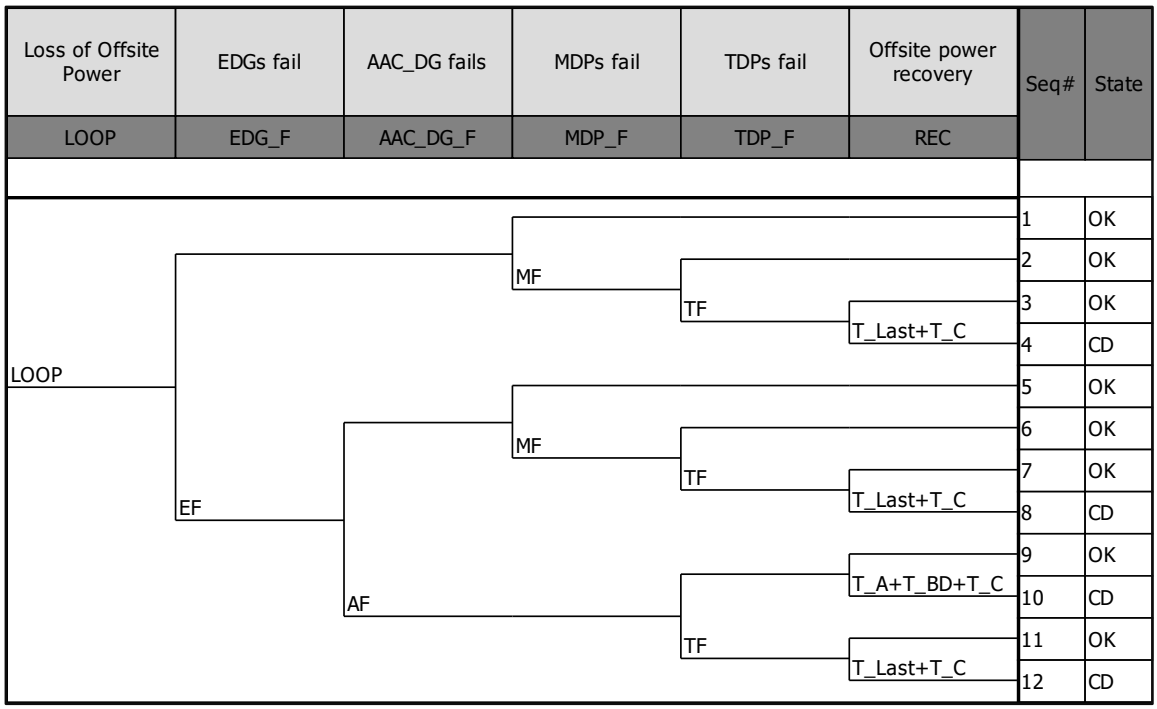

Figure 1: Rough LOOP scenario overview

III.B. Comparative Analysis of LOOP sequences

As described in Section III.A, a detailed analysis of LOOP scenarios was conducted. The accuracy of the simulation results was assessed by comparing outputs from EMRALD and Monte Carlo approaches.

Given that the calculated core damage probability is extremely small, on the order of 3E-6, some differences in the numerical results are to be expected. These differences can be mitigated by significantly increasing the number of simulation runs.

Figure 2 summarizes the CCDP results from both EMRALD and Monte Carlo simulations under the LOOP scenario. The results include cases where core damage occurs due to AAC DG and TDPs failures, as well as cases resulting from MDPs and TDPs failures. In most sequences leading to core damage, the dominant contributors were the failure of both EDGs followed by AAC DG failure and subsequent battery depletion causing the TDPs to fail, resulting in a loss of secondary heat removal. For the notations, the first letter indicates the component that fails: 'A' for the AAC DG, 'M' for the MDPs, and 'T' for the TDPs. The subsequent letters describe the failure mode: 'S' denotes failure to start, 'R' denotes failure to run, 'SR' indicates that one unit fails to start and the other fails to run, 'RR' and 'SS' indicate that both units fail to run or start, respectively. 'CR' and 'CS'

represent common cause failures leading to both units failing to run or start. Additionally, 'BD', used only for TDPs, signifies that both units fail due to battery depletion. Also, the symbol '-S' means that those sequences are SBO-S, the others are SBO-R.

EMRALD conducted approximately 1E+9 simulation trials, while the Monte Carlo simulation involved about 5E+9 times. Due to the extremely low probability of some sequences, many rare scenarios were scarcely observed, and gaps were noted between the two simulation methods.

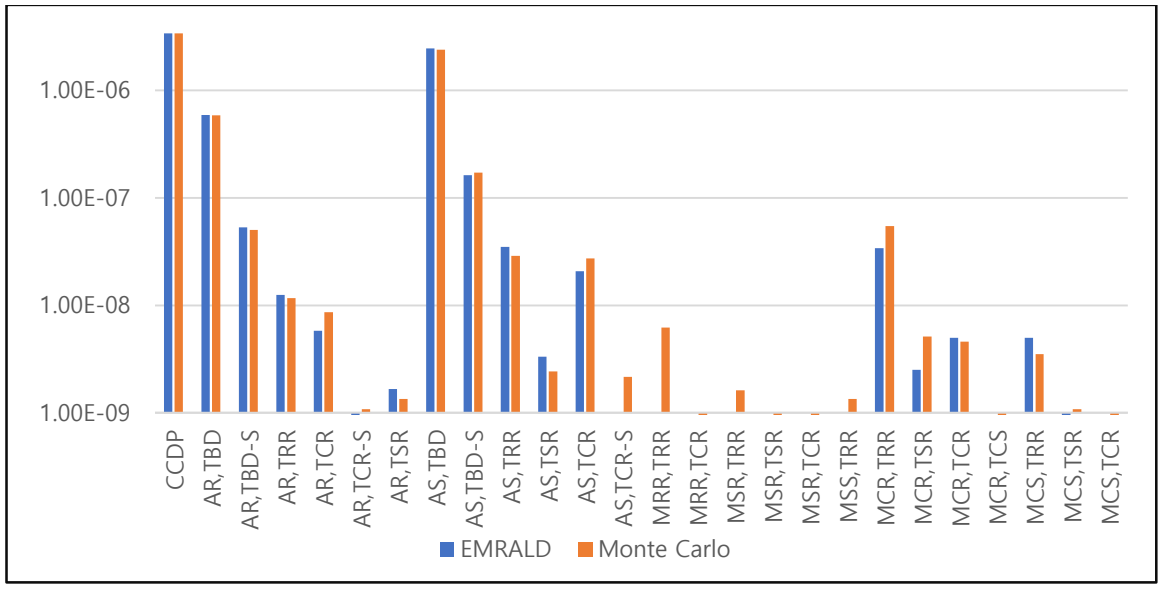

Figure 2: Analysis of LOOP Scenario with 2 methods

IV. Discussions

Based on the simulation results presented, the comparison between EMRALD and Monte Carlo simulations confirms that EMRALD is useful in handling complex scenarios. The LOOP scenarios modeled in this study involve numerous time-based parameters, making it challenging to analyze through ET and FT analysis. Nevertheless, EMRALD successfully estimated the overall CCDP and the probabilities of various cut sets leading to core damage in a single simulation framework.

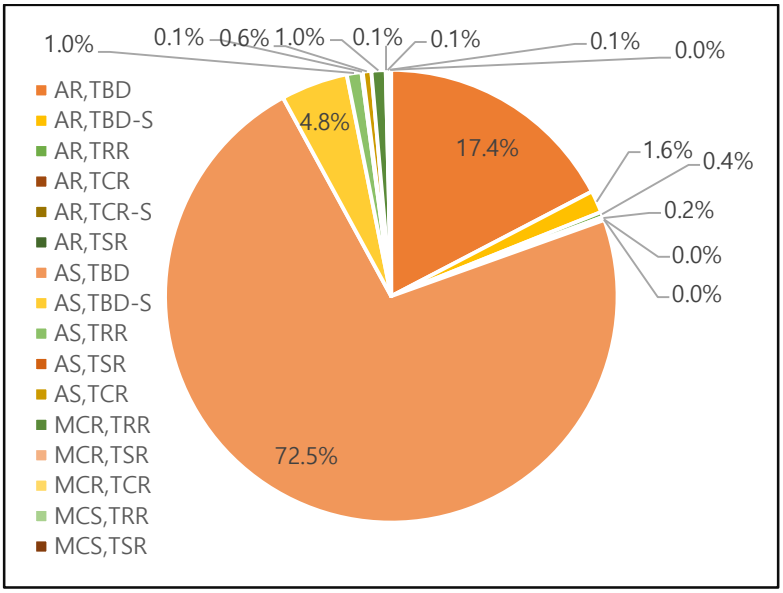

Figure 3: Fractional comparison of total CCDP sequences

When analyzing the progression of the accident from LOOP to SBO, it becomes clear that SBO-R scenarios are more dominant than SBO-S scenarios. This suggests that, when analyzing SBO as one of the major severe accident scenarios in nuclear reactors, evaluating SBO-R is particularly important. Given that SBO-R sequences involve many time-dependent elements, precise modeling is essential for reliable analysis.

The findings suggest that reinforcing the reliability of EDGs and AAC DG and extending battery life for TDP operation can significantly improve safety.

EMRALD's dynamic modeling capability allows intuitive exploration of complex sequences. This supports its usefulness in both design evaluation and emergency planning. Although EMRALD required much more time to compute the scenario sequences than the Monte Carlo simulation, it was faster to build the same model using EMRALD

V. Conclusions'

This study utilized EMRALD, a dynamic probabilistic safety assessment (PSA) tool, to evaluate complex accident sequences following a loss of offsite power (LOOP) in nuclear power plants. The research was structured in two phases: first, validating EMRALD's computational reliability by replicating an SBO-S scenario previously analyzed using a convolution approach; and second, expanding the model to include a full LOOP scenario with multiple time-dependent variables and component interactions.

By comparing the results of EMRALD simulations with Monte Carlo simulations, the study confirmed the tool's capability to calculate CCDP and sequence probabilities with high accuracy. The results highlighted that failures of DGs and following battery depletion of TDPs are dominant contributors to core damage. Additionally, the analysis revealed that SBO-R scenarios are more dominant than SBO-S, emphasizing the importance of precise modeling for those cases.

Through this modeling, EMRALD proved effective in capturing time-dependent dynamics and component dependencies without relying on extensive mathematical formulations.

ACKNOWLEDGMENTS

This work was supported by the Korea Institute of Energy Technology Evaluation and Planning (KETEP) grant funded by the Ministry of Trade, Industry and Energy (MOTIE) of Republic of Korea [grant number RS-2024-00398867].

REFERENCES

[1] Prescott, Steven, Curtis Smith, and Leng Vang. "EMRALD, dynamic PRA for the traditional modeler." *Proceedings of the 14th International Probabilistic Safety Assessment and Management Conference. Los Angeles, CA*. 2018.

[2] Kim, Man Cheol. "Comparison of event tree/fault tree and convolution approaches in calculating station blackout risk in a nuclear power plant." *Nuclear Engineering and Technology* 56.1 (2024): 141-146.

[3] Ma, Zhegang, Thomas E. Wierman, and Kellie J. Kvarfordt. Industry-Average Performance for Components and Initiating Events at US Commercial Nuclear Power Plants: 2020 Update. No. INL/EXT-21-65055-Rev000. Idaho National Lab.(INL), Idaho Falls, ID (United States), 2021.

[4] Ma, Zhegang, and Kellie J. Kvarfordt. CCF Parameter Estimations, 2020 Update. No. INL/EXT-21-62940-Rev000. Idaho National Laboratory (INL), Idaho Falls, ID (United States), 2021.

[5] Johnson, N., and Z. Ma. "Analysis of Loss-Of-Offsite-Power Events 2020 Update (INL/EXT-21-64151)." Idaho Falls, Idaho National Laboratory, Idaho (2021).

Technical Session 11 (13:40 -15:40)	The Port 3, C Floor	Advanced PSA technologies, Multi-unit PSA, and SMR PSA
		Chair/Facilitator 1: Dr. Meejeong HWANG (Korea Atomic Energy Research Institute (KAERI))
		Chair/Facilitator 2: Dr. Tanagorn SANGTAWESIN (Thailand Institute of Nuclear Technology (TINT))
13:40 - 14:00		ID 110: Comparative Analysis of Surrogate Models with Recurrent Neural Network and Interpolation Method Speaker: Donghee Choi (Department of Energy Systems Engineering, Chung-Ang University) Contributors: Donghee Choi (Department of Energy Systems Engineering, Chung-Ang University), Man Cheol Kim (Department of Energy Systems Engineering, Chung-Ang University)
14:00 - 14:20		ID 63: A Single-unit PSA Model Balancing Guide to Build a Multi-unit PSA Model Speaker: MEEJEONG HWANG (KAERI(Korea Atomic Energy Research Institute)) Contributors: MEEJEONG HWANG (KAERI(Korea Atomic Energy Research Institute))
14:20 - 14:40		ID 59: The PSA based Defense in Depth Evaluation of Innovative SMR for the Design Improvement Speaker: Ho-Gon Lim (Korea Atomic Energy Research Institute) Contributors: Ho-Gon Lim (Korea Atomic Energy Research Institute), Jin-Hee Park (Korea Atomic Energy Research Institute)
14:40 - 15:00		ID 73: Optimization of Dynamic Risk Assessment in Nuclear Power Plants Using Optimized and Accelerated Simulation Intermediate State Storage Speaker: Kyeong Seo Kim (Ulsan National Institute of Science and Technology) Contributors: Kyeong Seo Kim (Ulsan National Institute of Science and Technology), Junyong Bae (Ulsan National Institute of Science and Technology), Wooseok Jo (Ulsan National Institute of Science and Technology), Seung Jun Lee (Ulsan National Institute of Science and Technology),
15:00 - 15:20		ID 61: Dynamic Risk Assessment Framework with Limit Surface Search and Success and Failure Domains Analysis Speaker: Junyong Bae (Ulsan National Institute of Science and Technology) Contributors: Junyong Bae (Ulsan National Institute of Science and Technology), Kyeong Seo Kim (Ulsan National Institute of Science and Technology), Wooseok Jo (Ulsan National Institute of Science and Technology), Seung Jun Lee (Ulsan National Institute of Science and Technology)

ASRAM2025
www.asram2025.org
Asian Symposium on Risk Assessment and Management 2025
Pattaya, Thailand, 27 – 29 August 2025

Comparative Analysis of Surrogate Models with Recurrent Neural Network and Interpolation Method

Donghee Choi[1], Man Cheol Kim[2]

[1] *Department of Energy Systems Engineering, Chung-Ang University: 84 Heukseokro, Dongjak-gu, Seoul, Korea, 06974, donghe0128@cau.ac.kr*
[2] *Department of Energy Systems Engineering, Chung-Ang University: 84 Heukseokro, Dongjak-gu, Seoul, Korea, 06974, charleskim@cau.ac.kr*

ABSTRACT

Probabilistic safety assessment (PSA) is a key method for quantifying the frequency and consequences of various accident scenarios. Recently, there has been a growing demand for considering dynamic interactions between operator actions and thermal-hydraulic (TH) behavior over time, leading to active research on dynamic PSA. However, dynamic PSA requires generating scenarios in real time and repeatedly running TH codes for each scenario, resulting in significantly increased computation time and resource consumption. To accelerate this, several neural network-based surrogate models have been proposed, but issues such as long training times, out-of-bounds prediction risks, and difficulties in interpreting results remain. As an alternative to avoid these limitations, a simple interpolation-based surrogate model can be proposed. In this study, we propose a surrogate model constructed using multidimensional linear interpolation and compare it with a neural network surrogate model trained on the same dataset. The target scenarios include Loss of Feed Water accident scenarios involving operator response delays. Comparing the mean relative error, training time, and prediction time, the interpolation model achieved accuracy nearly identical to that of the neural network model, with millisecond prediction time without requiring a training process. In conclusion, selecting the interpolation model instead of long-term neural network training within the given computing resources and time can reduce requirements while maintaining the accuracy for TH analysis. This suggests a practical alternative that achieves a balance between efficiency and accuracy.

Keywords: Probabilistic safety assessment, Dynamic PSA, Surrogate model, Neural network, Interpolation

I. INTRODUCTION

Probabilistic safety assessment (PSA) has long been the standard method for stochastically estimating how often nuclear plant accidents might occur and how serious their outcomes could be. Conventional PSA uses logic-based event tree and fault tree models with simple success or failure branches. Several studies have said that this structure has trouble capturing the continuous, time-dependent interactions that arise from operator actions during an accident [1]. To address these dynamic interactions, dynamic PSA (DPSA) was introduced. DPSA aims to simultaneously generate accident scenarios and conduct thermal-hydraulic (TH) simulations in real time [2]. Running the TH calculations for each time step across thousands or tens of thousands of dynamic scenarios requires considerable computing and time resources. Researchers often simplify the timeline into a few representative time intervals or introduce bounding assumptions, yet simulation time still increases rapidly with scenario count.

Conventional PSA uses TH analysis to set success criteria, whereas DPSA bases every scenario evaluation on a TH simulation. When the branch count increases, each branch needs another TH analysis. The fine time steps required for high-resolution results drive computation and time resource use upward, so high-resolution DPSA remains impractical on ordinary hardware. To resolve this burden, many researchers have considered neural network (NN) surrogate models. Chae et al. proposed a lightweight DPSA framework that integrates a multi layer physics-informed neural network (PINN). After training, the model predicted primary system pressure and peak cladding temperature (PCT) in milliseconds, enabling real-time assessment of scenarios [3]. Baraldi et al. applied a PINN to a loss of heat sink transient, adding reactivity feedback terms to the loss function so that the surrogate preserved physical consistency, reducing run time [4]. Also, He et al. developed a deep learning reduced order model that mapping the nonlinear behavior of steam generator TH, offering an economical alternative

for repeated simulations [5]. These studies show that using NN surrogates to accelerate TH analysis has become an active line of research.

However, all NN models share fundamental limits. They need a training process and must be retrained whenever plant conditions or scenarios change. The optimal network architecture often differs from one dataset to another, and a network trained on one accident family may not perform equally well on a different one. In practice, analysts may have to develop and tune separate networks for each scenario group. Moreover, neural outputs are often hard to interpret, and extra tuning is required to prevent unexpected outputs. A key issue is that we still cannot easily explain why the network produces a particular result or predict how it will behave beyond the training dataset range.

A more clear alternative is to interpolate a precomputed dataset. Because interpolation works as soon as a database exists, it provides almost instant predictions and remains within that dataset range. Bennett et al. applied sparse-grid interpolation to predict subchannel void fractions in a boiling water reactor with low error and millisecond response time [6]. Lee et al. used kriging interpolation to map the failure surface, reducing the required TH runs from thousands to just tens [7]. These cases insight that interpolation can be used as a fast and clear surrogate model. Building on this, the present study uses the same TH dataset to compare a NN based surrogate model with a multidimensional linear interpolation model in accidents: loss of feed water accidents (LOFW). Thereby offering quantitative insights into their relative performance.

II. METHODOLOGY

II.A. Scenario Definition and Dataset

Table I summarises the structured grid dataset used by both surrogate models. For the accident family, the grid of input variables, the number of scenarios, the output vectors for pressurizer pressure (PZR-P) and PCT, and the resulting dataset size (time points × scenarios). In total, the dataset comprises 20 scenarios and 5,000 time points each, resulting in a total of 100,000 data points.

In the LOFW accident family, the transient begins at t = 0s with a main feed water system trip and a failed auxiliary feed water system. With no secondary heat removal, primary pressure increases until it reaches the pressurizer safety valve (PSV) setpoint. Because the PSV is assumed to be stuck closed, the operator must switch to a feed and bleed operation manually. At that time, the operator opens the safety depressurisation system (SDS) after a specified delay $t_{sds} \in \{0,100,200,300s\}$. When the decreasing primary pressure reaches the injection threshold of high-pressure safety injection (HPSI), we assume that the HPSI does not start automatically. Instead, the operator manually starts the HPSI after an additional chosen delay $t_{hpsi} \in \{100,200,300,400,500s\}$.

Figure 1 shows the PCT curve for the 20 LOFW scenarios described above. All cases remain nearly flat until feed and bleed begin, once SDS opens and HPSI starts, the PCT drops by the chosen t_{sds} and t_{hpsi}. The monotonic, gradually declining nature of these curves supports the use of relatively shallow surrogate architectures. Figure 2 shows a sample of PZR-P curve for the 20 LOFW scenarios. The sharp pressure drop right after each SDS opening (red box), and the point where HPSI starts (blue box) can also to seen. The differences between the curves show how the four SDS delays and five HPSI delays change the timing of these operator actions.

TABLE I. Data Set

Accident family	Independent variables	No. of scenarios	Output vector (t, …)	Matrix size
LOFW	SDS opening delay (t_{sds}): 0~300s, ($\Delta t_{sds} = 100s$)	$4 \times 5 = 20$	$PZR\ P\ (t, t_{sds}, t_{hpsi})$ $PCT\ (t, t_{sds}, t_{hpsi})$	20×5000
	HPSI start delay (t_{hpsi}): 100~500s, ($\Delta t_{hpsi} = 100s$)			
	Run time (t): 5000s, ($\Delta t = 1s$)			

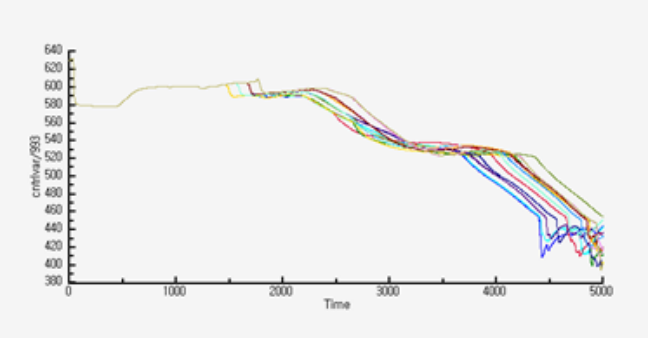

FIGURE 1. PCT of LOFW

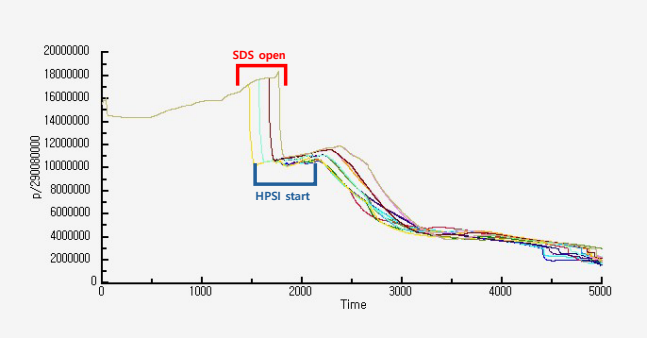

FIGURE 2. PZR-P of LOFW

II.B. Recurrent Neural Network Surrogate Model

The pressure and temperature parameters generated by the TH analysis are long and smooth time series, thus a recurrent neural network (RNN) surrogate is selected for the NN surrogate model. Among RNN, we selected the long short-term memory (LSTM) network because its gating mechanism preserves long range temporal information while mitigating the vanishing gradient problem. The modest data volume of 20 LOFW scenarios and the monotonic shape of the curves make a single LSTM layer an effective compromise. Tests with deeper layers showed no meaningful accuracy gain but higher training time and overfit risk. Table II lists the two constructions used. Both models use the same three input vector $X_t = [t, t_{sds}, t_{hpsi}]^T$. In the baseline model, the hidden layer contains 64 LSTM units and a dropout rate of 0.2 to prevent overfitting. For LOFW, a second model (LOFW-B) extends the layer to 128 units and the epoch from 50 to 2000 to probe the maximum accuracy with other hyperparameters remaining unchanged. A single fully connected node converts the LSTM output to one value, and the network is trained with a mean squared error loss. We use 90 % of the existing data for training, and the remaining 10 % is taken from the same dataset for validation. The latter acts as an online validation set. Throughout training, the MATLAB progress plots showed no noticeable overfitting, and the 0.2 dropout layer contributed to maintaining that stability even in the 2000 epoch LOFW-B run. Weights are tuned to minimize loss:

$$L = \frac{1}{N}\sum_{n=1}^{N}\frac{1}{T}\sum_{t=1}^{T}\left(\hat{y}_{t,n} - y_{t,n}\right)^2, \quad (1)$$

where N is the number of training scenarios (90% of LOFW scenarios), T= 5000 is the number of time steps in each run. The $y_{t,n}$ is the true value of normalised PZR-P or PCT at time t in scenario n, taken from the target data set Y_{train}. On the other hand, $\hat{y}_{t,n}$is the network's predicted value at the same moment, computed from the input sequence X_{train}.

TABLE II. RNN Model

Model	Sequence input	Units	Dropout	Epochs	Batch	Optimiser	Learning rate
Baseline (LOFW-A)	3 feature (t, t_{sds}, t_{hpsi})	1 LSTM, 64 units	0.2	50	128	Adam	5×10^{-3}
Accuracy-focused (LOFW-B)	3 feature (t, t_{sds}, t_{hpsi})	1 LSTM, 128 units	0.2	2000	128	Adam	5×10^{-3}

II.C. Multidimensional Interpolation Model

The interpolation surrogate model directly uses the precomputed TH results stored on a structured three-dimensional grid. Therefore, no additional training or model tuning is required. With this grid, trilinear interpolation can estimate PCT or PZR-P at any arbitrary query point inside the domain. This approach ensures that predictions remain within physically validated boundaries and delivers instantaneous results. For the LOFW grid used here, the three axes are simulation time t, SDS opening delay t_{sds}, t_{hpsi}. At every grid node (t_i, t_j, t_k) each node holds the pre-calculated outputs for PCT and PZR-P. When an arbitrary query point $(t^*, t_{sds}{}^*, t_{hpsi}{}^*)$ is requested, the algorithm first identifies the cube that encloses that point, picks out the

eight corner nodes, and determines the fractional distances (α, β, γ) of the query point relative to the cell's origin corner along all three axes. Those fractional distances serve as linear weights, the closer the query point is to a particular corner, the larger the share of that corner's value in the final output. By combining the eight stored node values in this way, the model delivers an immediate, smoothly varying estimate that is guaranteed to stay within the range of the original data. In Section III, we will validate the interpolation model and an LSTM surrogate model for the accident scenario, comparing accuracy and prediction time to confirm their performance.

III. CASE STUDY

In this section, we compare the performance of the LSTM surrogate model and the multidimensional interpolation surrogate model for the LOFW accident scenario. For the scenario, the structured dataset is first used to train the LSTM network. Subsequently, ten independent test cases are generated by Latin-Hypercube random sampling inside the same parameter bounds as the original domain (t_{sds}, t_{hpsi} for LOFW). For each test case, we run the TH analysis for the entire simulation time (5000s for LOFW) to obtain the simulation time series outputs of PZR-P and PCT. We then compare these series with the outputs produced by the LSTM model and the interpolation model.

The evaluation metrics include:

1. LSTM model's training and prediction time.
2. Interpolation model's prediction time.
3. Mean relative error, defined by:

$$RelErr(\%) = \frac{1}{T}\sum_{t=1}^{T}\frac{|\hat{y}(t) - y_{true}(t)|}{|y_{true}(t)|} \times 100$$

where T=5000s for simulation of LOFW, $\hat{y}(t)$ denotes the surrogate model's prediction at time t, and $y_{true}(t)$ is the corresponding TH computed results.

III.A. LOFW Families

For the LOFW, the LSTM was trained on the 20 cases grid shown in Table I, which covers the 5000s simulation and the two operator delay variables(t_{sds}, t_{hpsi}) in feed and bleed, and the interpolation model works on that same grid without any training. Ten independent query points $(t^*, t^*_{sds}, t^*_{hpsi})$ were then generated by Latin-Hypercube sampling inside this domain, and TH analysis provided the PCT and PZR-P time series for the test. Because LOFW shows a sharp pressure change once feed and bleed begin, two LSTM configurations were evaluated that the baseline network (LOFW-A) and the accuracy-focused network (LOFW-B) listed in Table II. Additionally, in the case of PZR-P, LOFW-A first achieved an in-domain validation mean relative error of 10.1%, while the accuracy-focused LOFW-B reduced this to 1.9%, confirming that no overfitting occurred before the Latin-Hypercube sampling test cases were assessed.

Figures 3 and 4 illustrate how closely both surrogate models follow the PCT curves. The blue interpolation lines and red LSTM lines overlap the black reference curves, confirming that both approaches capture the overall trend and timing of the LOFW scenarios. In LOFW-A, the baseline LSTM follows the general trend but lags behind the sudden drop that follows delayed injection, whereas the interpolation line almost overlaps with the actual curve. With LOFW-B, the accuracy-focused LSTM closes this gap, its trend almost coinciding with both the interpolation and the reference curves over the whole transient. Figures 5 and 6 compare the surrogate models with the PZR-P results. Like in the PCT case, the baseline LSTM (LOFW-A) under-predicts some sharp variations, while interpolation matches them closely in this scenario. With LOFW-B, the error falls to almost the same level as interpolation. Both surrogates predict PCT more accurately than PZR-P because the PCT curve is more monotonic.

Table III confirms the numerical trends. It confirms that interpolation returns its predictions almost immediately (prediction time ≈ 0.01s) with no training, whereas LOFW-A needs about 60s of training and 1s of prediction time. After 2000 training epochs, the accuracy-focused LSTM (LOFW-B) narrows this gap, but only after about 3000s of additional training time. The key difference remains computational speed. With comparable accuracy, interpolation offers advantages in computation time and implementation effort. While an accuracy-focused LSTM can close the gap, the extra accuracy comes at a high training cost. Although extending LSTM training even further could, in principle, improve its accuracy beyond interpolation, the extra computation time and resources may outweigh the benefit. We have to consider this trade-off. Invest more time and resources to get a slightly better result with NN, or use the simpler interpolation model with conservative assumptions, which is already quite accurate and saves both computational time and computing cost.

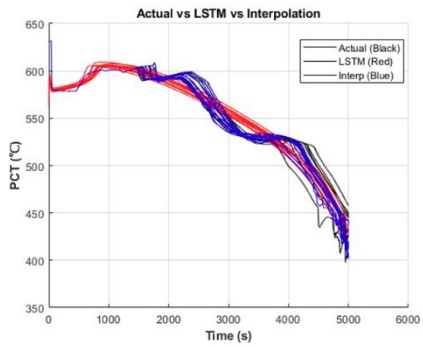

FIGURE 3. PCT Prediction of LOFW-A

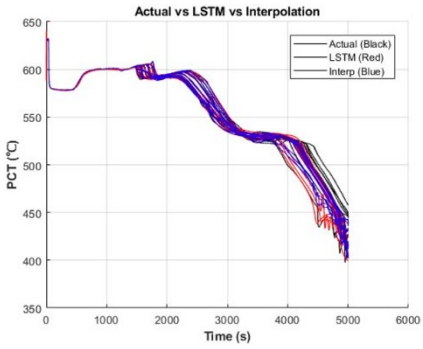

FIGURE 4. PCT Prediction of LOFW-B

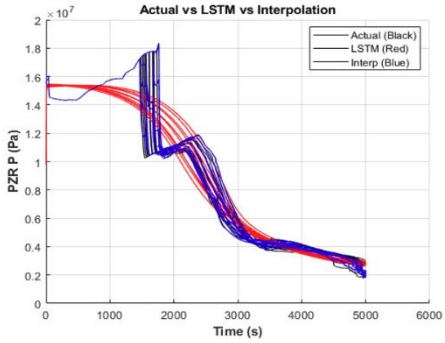

FIGURE 5. PZR-P Prediction of LOFW-A

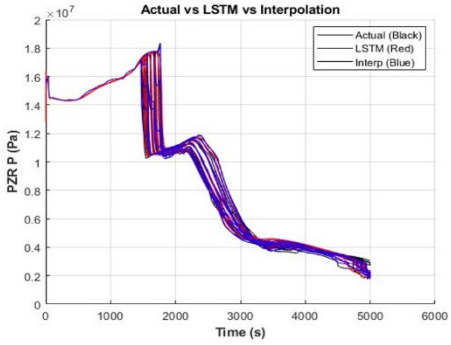

FIGURE 6. PZR-P Prediction of LOFW-B

TABLE III. LOFW Case

Model	Output	Mean relative error (%)	Training time (s)	Prediction time (s)
RNN (LSTM-A)	PCT	1.63	63.71	1.31
	PZR-P	9.66	54.63	0.57
RNN (LSTM-B)	PCT	0.78	2990.12	1.62
	PZR-P	2.94	2957.58	0.84
Interpolation	PCT	0.62	–	0.01
	PZR-P	2.54		

IV. CONCLUSION AND DISCUSSION

Conventional PSA simplifies accident sequences into binary success or failure branches and sets success criteria from a thermal-hydraulic (TH) analysis. DPSA, in contrast, subdivides these branches to consider operator actions and other dynamic interactions, requiring multiple TH analyses for each branch. On the other hand, DPSA subdivides the branches to reflect operator actions and dynamic interactions, and conducts multiple TH analyses for each branch. As a result, calculation time and resource consumption increase exponentially, and to reduce this, NN-based surrogate models are being proposed. NN is an alternative to reduce computational burden, but it introduces a new trade-off between accuracy improvement and extra training cost. They require a long learning time, can predict outside the data range, and are hard to interpret. If a simple interpolation model can deliver almost NN accuracy with less effort, it becomes an attractive alternative. To validate that, we built a simple three-dimensional trilinear-interpolation surrogate and compared it with an LSTM surrogate trained on the same data. We evaluated the mean relative error, training time, and prediction time for the LOFW scenario that includes operator delay variables. The interpolation model produced near instant predictions with almost the same accuracy as the basic LSTM, which required about 60s of training time. An accuracy-focused model reduced the error further but increased training time to roughly 3000s. The case study shows that even simple interpolation can achieve performance comparable to that of NN under the same dataset. Therefore, the choice between the two methods depends on the analysis objectives and available resources, making it a trade-off issue. Once the data exists, the interpolation model runs immediately, keeps every prediction inside that grid, and is easy to explain. The LSTM, in contrast, has to be retrained whenever the scenario family or data set changes. In

conclusion, we confirmed that even a simple interpolation model can achieve performance comparable to the NN model within the scope of this study.

There are several limitations to this study. The LSTM model used in this study may not be the most optimized model for the dataset. Also, the comparison covered only LOFW accident families, so we need to compare more cases. Since a simple interpolation model was performed, trends and dependencies within the data were not accurately considered. Based on an understanding of how the variables in TH analysis move, it is expected that we are able to develop an interpolation method suitable for each situation.

ACKNOWLEDGMENTS

This work was supported by the Korea Institute of Energy Technology Evaluation and Planning (KETEP) grant funded by the Ministry of Trade, Industry and Energy (MOTIE) of Republic of Korea [grant number RS-2024-00398867].

REFERENCES

[1] Jong Woo Park, and Seung Jun Lee. "Simulation optimization framework for dynamic probabilistic safety assessment." Reliability Engineering & System Safety 220, 108316 (2022).
[2] Karanki, Durga Rao, and Vinh N. Dang. "Quantification of dynamic event trees–a comparison with event trees for MLOCA scenario." Reliability Engineering & System Safety 147, 19-31 (2016).
[3] Chae, Young Ho, et al. "Development of a data-driven simulation framework using physics-informed neural network." Annals of Nuclear Energy 189, 109840 (2023).
[4] Baraldi, Piero, et al. "Physics-Informed Neural Networks for the safety analysis of nuclear reactors." Progress in Nuclear Energy 185, 105745 (2025).
[5] He, Shaopeng, et al. "A deep-learning reduced-order model for thermal hydraulic characteristics rapid estimation of steam generators." International Journal of Heat and Mass Transfer 198, 123424 (2022).
[6] Bennett, Alexander, et al. "A surrogate model based on sparse grid interpolation for boiling water reactor subchannel void distribution." Annals of Nuclear Energy 131, 51-62 (2019).
[7] Lee, Yongjoon, and Gyunyoung Heo. "Sampling Based Method for Estimating Functional Failure Probability of Passive Safety Systems in Small Modular Reactors." Transactions of the Korean Nuclear Society Spring Meeting, (2025)

A SINGLE-UNIT PSA MODEL BALANCING GUIDE TO BUILD A MULTI-UNIT PSA MODEL

Meejeong Hwang[1], Sang-Hoon Han[2], Ho-Gon Lim[3]

[1,2,3] *Korea Atomic Energy Research Institute: 989-111 Daedeok-daero, Youseong-gu, Daejeon, 34057, Korea,*

[1]*mjhwang@kaeri.re.kr*
[2]*shhan2@kaeri.re.kr*
[3]*hglim@kaeri.re.kr*

EXTENDED ABSTRACT

Probabilistic Safety Assessment (PSA) for Nuclear Power Plants (NPPs) has generally targeted a single-unit before the Fukushima NPP accident in 2011. However, interest in multi-unit risk assessment has increased after the Fukushima accident. Despite this situation, there are no widely accepted guideline used for developing a multi-unit PSA model.

In Korea, interest in site risk has also increased due to the earthquakes that occurred in Gyeongju and Pohang in 2017 because most sites have multiple units in Korea. Accordingly, nuclear power industry, namely KHNP (Korea Hydraulic & Nuclear Power) and regulatory body, KINS (Korea Institute of Nuclear Safety) have developed PSA models for site risk assessment.

Despite the inadequacies in terms of consistency in individual unit's PSA models (single-unit PSA models) within a site, the multi-unit PSA model was established in the past. Thus, there has been a lack of balance among single-unit models in past multi-unit PSA models. Maintaining a balanced level among single-unit PSA models used for developing a multi-unit PSA model is a very important factor in assessing the multi-unit risk profile at an appropriate level because multi-unit PSA combines and analyzes multiple single-unit PSA models.

In PSA, it is crucial to determine if the quantification results by initiating event (IE) and accident sequence are appropriate, as well as if the cut sets and event importance results are suitable. If model balancing is not achieved, a specific initiating event might account for most of the CDF, while the CDF of other initiating events appears to be unimportant.

In general, PSA reviews model suitability by comparing the results with those from other plants to check if there are any significant discrepancies in the PSA models. So far, balancing of PSA models has not been a major focus of review, and there is also no established methodology globally for this purpose.

Especially in multi-unit PSA, where multiple unit PSA models are combined, it becomes even more important to ensure that each unit's PSA model is appropriately developed and balanced. The necessity for balancing unit models is further increased due to the following reasons:

- ✓ Development of models by different institutions/developers for each unit
- ✓ Possibility of different assumptions, methods, and reliability data being used for each unit
- ✓ Inadequate review of the appropriateness of unit-specific PSA models and quantification results

Accordingly, it is necessary to review the balancing of the PSA model for each unit. The balancing of the PSA model should be reviewed together with the appropriateness of the PSA model.

This means that a single-unit PSA model should (1) maintain an appropriate quality level, (2) be standardized to become a component of a multi-unit PSA model, and (3) keep a level of equivalence among single-unit PSA models within a site. In this work, the 'quality level' can only be defined qualitatively, and is defined as revising a single-unit PSA model that applies similar assumptions, reliability data, and model scope, etc. to ensure consistency.

This guideline presents a method for reviewing PSA models and results together with the major elements of each plant design and characteristics of the CSFs (Critical Safety Functions).

Figure 1 shows the key points to be checked for quantification balancing in each single-unit model.

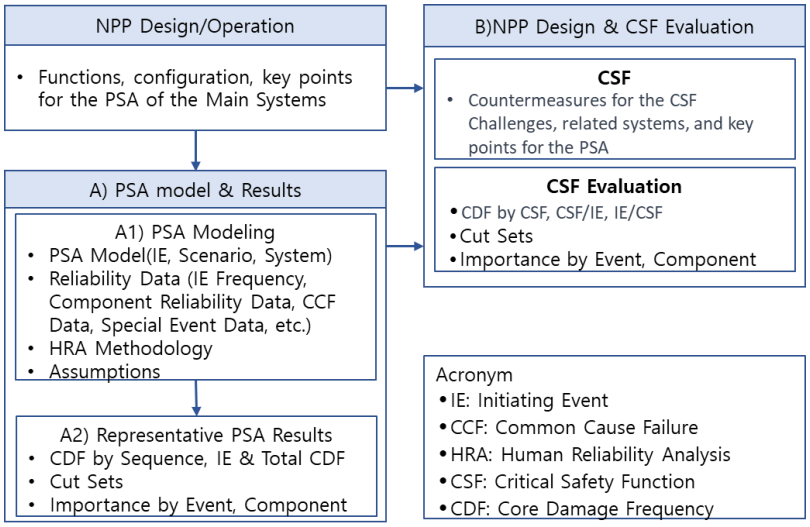

FIGURE 1. Key Checkpoints for Balancing PSA Models

At stage A1) in Figure 1, it is necessary to review whether the modeling method, reliability data, and assumptions for each unit are used similarly as follows:

- ✓ Review the consistency of the PSA model for each single-unit
- ✓ Compare the initiating events, accident scenario modeling level, reliability data, human reliability analysis (HRA) method, and assumptions analyzed for each unit

At stage A2), review representative results from the PSA quantification as follows:

- ✓ Review the main results of PSA quantification, such as CDF by initiating event, CDF by sequence, total CDF, cut sets and event importance.
- ✓ Review the above results to confirm whether there are any errors in the PSA model and its results. Additionally, it is necessary to compare the PSA results with those of similar NPPs to confirm that the PSA results of the NPP under review are not significantly different from those of similar NPPs.

At stage B), review the relationship between NPP design characteristics and CSF (Critical Safety Function), as well as quantification results. This part has not been used to review PSA results so far, but it can be considered a method to properly evaluate the design, function of the safety systems and their connection to PSA. Thus, in this guideline, the evaluation methods are summarized as follows:

- ✓ Organize the safety systems that perform CSF. Along with this, compile the factors that significantly affect PSA quantification results
- ✓ Summarize which CSF failures contribute to each core damage accident scenario
- ✓ Evaluate the CDF for each CSF
- ✓ Since the results may vary depending on the assumptions, it is necessary to review the results for each unit, considering the differences according to the assumptions.
- ✓ It is recommended to unify the assumptions for each unit regarding factors that are important for the quantification results

In this paper, to provide with a method to comparing the results among the units in multi-unit PSA, the relationship between CSF and PSA quantification was conducted experimentally by using the APR1400 MPAS model. In this experimental assessment, CSF was classified in more detail than usual to understand the characteristic of systems, as shown in Table 1.

TABLE 1. Example of CSF Classification for Quantitative Balance Check

Critical Safety Function	CSF Classification	Description
DHR	Decay heat removal	Loss of MFW/AFW, failure of F&B
DHR-CSR	Decay heat removal via containment spray recirculation	In the event of LOCA, failure of containment spray or containment spray recirculation
DHR-LT	Decay heat removal - long term	After MFWS/AFWS actuation, SCS/AFW Tank makeup/ failure of F&B (mainly, operator action failure)
EP	Electrical power - short term w/loss of AFW TDP	SBO, AFW-TDP failure, AAC/Recovery failure of off-site power (The recovery of AC power is required for the operation and cooling of major pumps in several scenarios.)
EP-DC	Electrical power – Battery Depletion	SBO, Battery depletion, AAC/ Recovery failure of off-site power (Scenarios which continuous cooling is possible by DC recovery.)
INV	Inventory makeup for LOCA	In the event of LOCA, Safety injection failure (Including recirculation)
RX	Reactivity control	Core damage due to Reactivity control failure
UHS	Ultimate heat sink	Total Loss of ESW/CCW

Also, to develop a multi-unit PSA model based on a single-unit model, it is necessary to standardize single-unit models used for the multi-unit model. The Korean multi-unit PSA model employs a method composed of a One-Top model as shown in Figure 2. As each single-unit model is added as a sub-logic to a single top logic, standardization of the single-unit models is essential. When generating a single-unit model according to the operation mode, if there are different operation modes, gates with different substructures (logic) must use different gate names.

For example, the full power operation mode and low power/shutdown operation mode have similar basic structures, but the lower logic is slightly different. If the gate names are not different in that part, a conflict error may occur when configuring the top logic. Additionally, inter-unit dependency must be considered such as DG operation and IA (Instrument Air) system, etc. When developing a multi-unit PSA model, inter-unit dependency that is not considered in a single-unit model must be taken into account. This is added when developing a multi-unit PSA model by integrating a single-unit model.

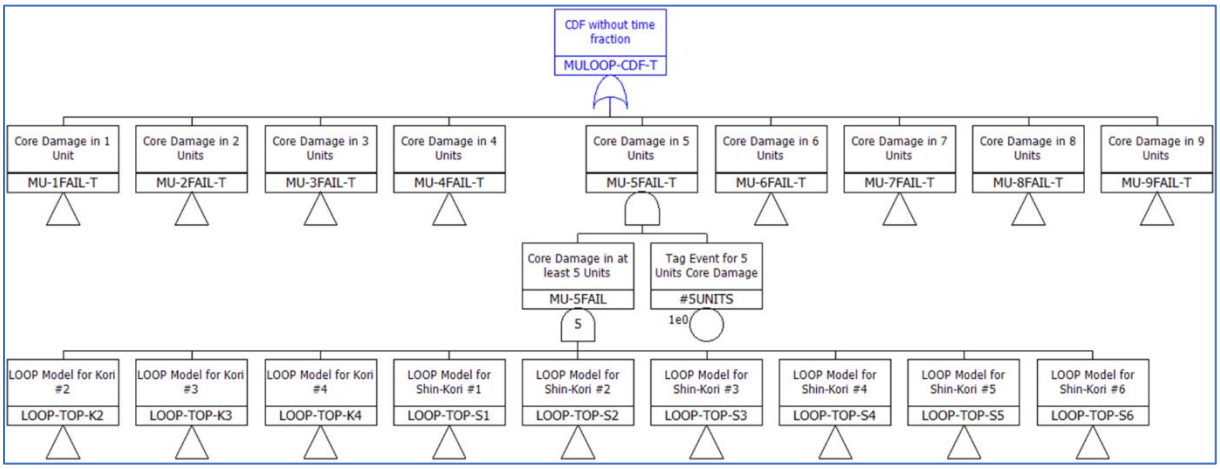

FIGURE 2. Example of Korean Multi-unit PSA One-Top Model

In general, PSA model adequacy is reviewed by comparing the results of other units to check for any errors in the PSA model, and to determine if there are any significant differences. Balancing PSA model has not been a major focus of reviews so far, and there is no established methodology for such work worldwide. Therefore, a method is needed to review the consistency and balance of a single-unit PSA model in order to develop a multi-unit PSA model. Based on the review of the

core damage frequency assessment results categorized by CSF, it is determined that significantly different results can be identified. To analyze these results, the PSA modeling method is reviewed to verify its validity. It is expected that through this comparative review, the quality level of the PSA modeling and the quantification results can be balanced and harmonized.

A proposed guideline in this paper presents a method to review not only the PSA model and results, but also the main elements of each unit design and the CSF characteristics. By comprehensively reviewing the design characteristics, CSF characteristics, PSA model, and quantification results of each unit, it is possible to compare whether the PSA results are consistent with the design characteristics of each unit. Based on this work, it is expected that model balancing and adequacy can be improved for building a multi-unit PSA model.

ACKNOWLEDGMENTS

This work was supported by the KETEP (Korea Institute of Energy Technology Evaluation and Planning) grant funded by the Korean government (Ministry of Trade, Industry and Energy) (20224B10200050).

REFERENCES

[1] KEPIC, NPA; Probabilistic Safety Assessment, 2010.
[2] ASME/ANS RA-Sa-2009, Standard for Level 1 / Large Early Release Frequency Probabilistic Risk Assessment for Nuclear Power Plant Applications – Addenda to ASME/ANS RA-S-2008, ASME, 2009.
[3] KEPIC, Strategy for the Development of the Korean PSA Standard, 2021.
[4] KAERI, Development of a methodology for applicability achievement of individual unit PSA as a component of multi-unit risk model, KAERI/TR-9542/2022

ASRAM2025
www.asram2025.org
Asian Symposium on Risk Assessment and Management 2025
Pattaya, Thailand, 27 – 29 August 2025

THE PSA BASED DEFENSE IN DEPTH EVALUATION OF INNOVATIVE SMR FOR THE DESIGN IMPROVEMENT

Ho-Gon Lim[1], Jin Hee Park[1]

[1] *Korea Atomic Energy Research Institute., Division of Integrated Safety Assessment, 1045 Daedeuk-Daero, Yusung-Gu, Daejeon, The Republic of Korea , hglim@kaeri.re.kr*

EXTENDED ABSTRACT

The concept of defense in depth (DID) is the basic philosophy of a nuclear power plant (NPP) design and also plays the most important role in confirming safety when various issues or changes in design occur. Basically, the evaluation of DID for a NPP was performed qualitatively such as checklist.

Since it is difficult to exclude the subjectivity of the evaluator in such a qualitative evaluation, uncertainty or errors in the evaluation results are likely to occur. Recently, a DID evaluation method has been developed that combines the abstract DID concept of IAEA INSAG-10 [1] with PSA.

This paper applies this DID evaluation methodology to improve the design of a newly developed innovative small and medium-sized reactor (iSMR) [2]. The iSMR is designed to have an integrated pressurized water reactor-based core and steam generator, and is installed on site in a modular manner to produce sufficient electrical power.

The purpose of this study is to identify the weakness in the early design of iSMR and suggest alternatives for the design improvement by applying the developed quantitative DID evaluation method. The analysis results showed that the iSMR design has a well-balanced defense-in-depth structure but also it has weaknesses in the early design, which need improvement in response to some initiating events as shown in the Table 1 and Figure 1.

The reliability of each DID level of iSMR as shown in Table 1 can be obtained according to the DID reliability evaluation method of the referenced literature [2]. DID level 1 and 2 are related with initiating event of level 1 PSA. In general, DID level 1 can be interpreted as the root cause of an initiating event and DID level 2 as the prevention/mitigation of the root cause. Since the iSMR is in the conceptual design stage and also there is little available data, DID level 1 and 2 was evaluated using the geometric mean for the initial event. DID level 3 represent the prevention/mitigation of the initiating event occurred. In most of the NPP designs, they have redundant and independent safety system to prevent the initiating event. So, it needs to make detailed analysis for each safety system for the DID level 3. DID3.1 and DID3.2 in the table and the figure represent the detailed safety systems for the DID level 3, which represent emergency core cooling system and passive auxiliary feedwater system respectively. DID3.1 and DID3.2 were calculated using the accident sequence analysis results in terms of event tree and related system fault tree of the PSA model.

TABLE I. Reliability of DID level for early design of iSMR

No.	Initiating Event Name	IE freq.	DID1	DID2	CDF3.1	DID3.1	CDF3.2	DID3.2
1	%GTRN	5.55E-01	0.745117	0.745117	4.17E-05	7.51E-05	2.99E-08	7.17E-04
2	%ISLOCA	5.29E-09	7.27E-05	7.27E-05	5.29E-09	1.00E+00	7.80E-11	1.47E-02
3	%LOCA-CHGINCV	4.10E-04	0.020248	0.020248	4.10E-04	1.00E+00	1.08E-07	2.63E-04
4	%LOCA-CHGOUCV	1.75E-05	0.004183	0.004183	2.53E-09	1.44E-04	2.16E-11	8.55E-03
5	%LOCA-EDV	6.48E-04	0.025456	0.025456	6.48E-04	1.00E+00	9.46E-10	1.46E-06
6	%LOCA-ERV	7.20E-05	0.008485	0.008485	7.20E-05	1.00E+00	1.89E-08	2.63E-04
7	%LOCA-LDINCV	4.10E-04	0.020248	0.020248	4.10E-04	1.00E+00	1.08E-07	2.64E-04

8	%LOCA-LDOUCV	2.50E-06	0.001581	0.001581	3.61E-10	1.44E-04	1.87E-13	5.18E-04
9	%LODC-LOCA	8.28E-04	0.028775	0.028775	8.28E-04	1.00E+00	1.21E-09	1.46E-06
10	%LOOP	2.52E-02	0.158745	0.158745	4.41E-06	1.75E-04	3.00E-09	6.80E-04
11	%LSSB-INCV	2.85E-04	0.016882	0.016882	2.33E-06	8.16E-03	1.23E-09	5.29E-04
12	%LSSB-MSIVDOWN	5.44E-03	0.073756	0.073756	3.72E-07	6.84E-05	3.73E-10	1.00E-03
13	%LSSB-OUCV	1.16E-03	0.034059	0.034059	9.47E-06	8.16E-03	2.51E-09	2.65E-04
14	%RCSLOCA	8.90E-04	0.029833	0.029833	8.90E-04	1.00E+00	2.36E-07	2.65E-04
15	%SGTR	1.78E-03	0.04219	0.04219	1.35E-07	7.56E-05	1.71E-10	1.27E-03
16	%SUPP	1.64E-02	0.128062	0.128062	1.23E-06	7.51E-05	1.14E-09	9.28E-04

Using the DID measures developed in the reference [2], one can make a figure which shows overall DID structure of an NPP as shown in the Figure 1. X axis represents the DID strength for each DID level and Y axis represents initiating event considered in the PSA. Also, each color means different DID level by which one can find whole failed DID level and its strength. Through the quantitative DID evaluation of the early design of iSMR, it can be intuitively understood that the strength of DID3.1 in some initiating events should be improved to strengthen the overall DID strength, and also since most of initiating events have a high frequency due to the use of generic data, a method to lower this frequency should be considered when applying it to iSMR design.

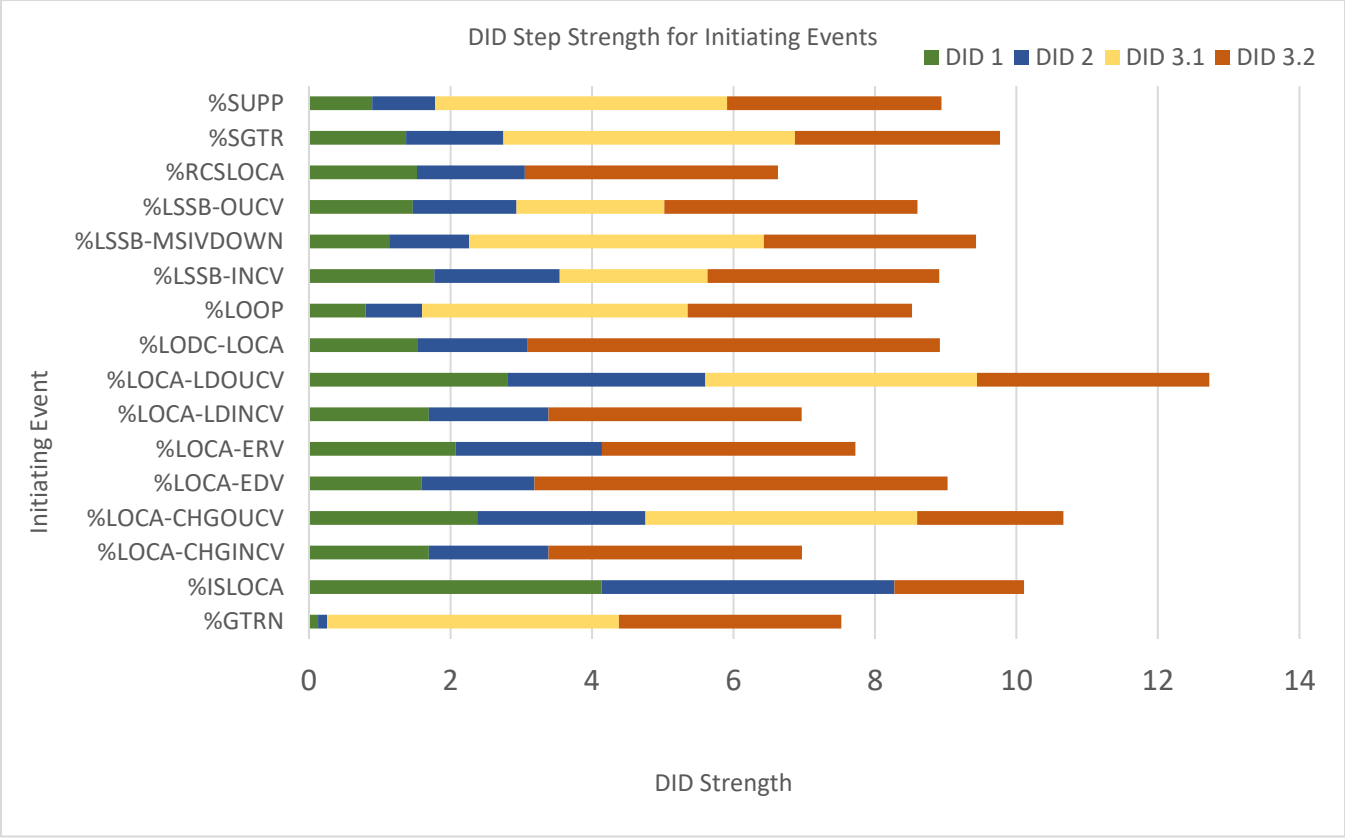

FIGURE 1. DID strength and failure number

ACKNOWLEDGMENTS

This work was supported by the Korea Institute of Energy Technology Evaluation and Planning (KETEP) and the Ministry of Trade, Industry and Energy (MOTIE) of the Republic of Korea (No. RS-2023-00258118).

REFERENCES

[1] DEFENCE IN DEPTH IN NUCLEAR SAFETY, INSAG-10, IAEA, Vienna 1996
[2] H.G. Lim et al, A Methodology of Quantitative Assessment of Defense in Depth using PSA, KAERI/TR-9072/2021, Korea Atomic Energy Research Institute, 2021

ASRAM2025
www.asram2025.org
Asian Symposium on Risk Assessment and Management 2025
Pattaya, Thailand, 27 – 29 August 2025

OPTIMIZATION OF DYNAMIC RISK ASSESSMENT IN NUCLEAR POWER PLANTS USING OPTIMIZED AND ACCELERATED SIMULATION INTERMEDIATE STATE STORAGE

Kyeongseo Kim, Junyong Bae, Wooseok Jo, Seung Jun Lee*

Ulsan National Institute of Science and Technology, 50 UNIST-gil, Ulju-gun, Ulsan, 44919, Republic of Korea

smart2439@unist.ac.kr; junyong8090@unist.ac.kr; cws5528@unist.ac.kr; sjlee420@unist.ac.kr

ABSTRACT

In Nuclear Power Plant, Risk Assessment is a process of evaluating safety by analyzing the possibility and impact of accidents in reactors and related systems. Through this, accidents are prevented radiation exposure and environmental damage are minimized to ensure the safe operation of nuclear power plants. Existing static risk assessment has limitations in that there is a lack of time association between components and systems and that there are limited accidents that can be analyzed because the analysis is performed under fixed conditions. Accordingly, a dynamic risk assessment through simulation of the thermal hydraulic system code emerged. However, there is a limitation of long simulation time, and to solve this problem, the study proposes Optimized and Accelerated Simulation Intermediate State Storage (OASIS). OASIS stores branch points according to changes in the operating status of NPP components, systems, and human operations, and if there is any overlap with the scenarios previously covered in the simulation of the scenario later, it is brought in for streamlined simulation. The problem of insufficient storage capacity is addressed by the branch point weighting method, which is expressed as the product of the time taken from each branch point to the storage point and the number of subsequent branches. The case study addresses the dynamic scenario of Loss of Offsite Power by optimizing scenario sampling using Deep Neural Network-based Search Algorithm of Informative Limit Surfaces and States (Deep-SAILS). To address storage limits, the number of branch point save files was restricted to 300. Under this configuration, the integrated use of Deep-SAILS and OASIS achieved a 96.30% reduction in simulation time, whereas the application of OASIS alone resulted in a 48.31% reduction. Additionally, the branch point weighting method manages insufficient storage space well.

Keywords: Dynamic PSA, Streamlined Simulation, Optimization, Weight, Database Management

I. INTRODUTION

The systematic evaluation of nuclear power plant risks is vital for ensuring public safety. To this end, risk assessment has been established as a rigorous, structured process for identifying hazards and implementing mitigation strategies [1]. Nuclear plant operation depends on the flawless interaction of multiple sophisticated systems; the Fukushima accident, however, revealed how a cascade of system failures can trigger complex nuclear accidents releasing radioactivity and inflicting long-lasting environmental degradation, area contamination, and ecological damage [2].

Consequently, early identification and quantification of potential plant risks are imperative. Risk assessment addresses this need by exhaustively modeling accident sequences and devising measures to enhance safety. In contrast to conventional static methods, dynamic risk assessment tracks the time-dependent interaction of system states, yielding more accurate and realistic risk profiles [3]. By integrating live operational data, reflecting continual system changes, dynamic risk assessment affords a deeper, more dependable understanding of safety margins. Yet, executing the vastly increased number of thermal-hydraulic (TH) simulations required by dynamic approaches demands far greater computational power than static analyses [4–6].

Achieving an optimal balance among computational load, simulation fidelity, and turnaround time remains a central challenge. To mitigate this, prior work has employed adaptive sampling, specifically the Deep Learning–based Searching Algorithm for Informative Limit Surfaces, States, and Scenarios (Deep-SAILS) [7]. Deep-SAILS efficiently distinguishes

between safe and failed trajectories while limiting simulations to roughly 10% of all possible scenarios. However, it does not shorten the runtime of each individual TH simulation.

To fill this gap, we introduce the Optimized and Accelerated Simulation using Intermediate State Storage (OASIS) methodology. OASIS archives the temporal states of NPP components from completed runs and detects time-overlaps with new scenarios. By restarting each simulation at the relevant stored state rather than from time zero, OASIS drastically cuts per-scenario simulation time.

The study validates OASIS through a Loss of offsite power (LOOP) case study, comparing simulation duration and storage demands with and without OASIS integration. The findings confirm that OASIS offers a practical, high impact means of accelerating large scale dynamic risk assessments without compromising accuracy.

II. BACKGROUND

The accurate execution of the TH system codes is fundamental to analyzing accident scenarios in nuclear power plants [4]. In probabilistic risk assessment, these scenarios emerge from intricate sequences of both automated protections and operator interventions, necessitating a vast number of high-fidelity TH simulations. Consequently, carrying out millions of such simulations within a reasonable timetable is infeasible given computational limits of current study [5]. Unlike static risk assessment, which can rely on relatively simple Event Tree/Fault Tree logic, dynamic risk assessment must explicitly capture the time-dependent interactions among all system components. This temporal coupling greatly increases scenario complexity and expands the simulation domain [6]. Moreover, the sheer volume of time-resolved TH runs drives up both processing requirements and individual run durations compared to static methods.

To alleviate this burden, the Deep-SAILS adaptive sampling framework was introduced. Deep-SAILS is specifically tailored for NPP risk analysis, seeking to efficiently regions the Limit Surface (LS), the surface between success and failure region, using a Deep Neural Network metamodel augmented with Monte Carlo Dropout [7]. Rather than exhaustively simulating every possible scenario, Deep-SAILS iteratively targets samples near the evolving LS, focusing computational burden where it matters most. This targeted approach dramatically reduces the total number of scenarios, TH simulation executions required.

Figure 1 shows Deep-SAILS LS for a Loss of Coolant Accident (LOCA), constructed by discretizing critical parameters (e.g., injection flow rate and coolant injection delay). Each node represents a candidate scenario, and failure is defined by Peak Cladding Temperature (PCT) exceeding 1478 K. By concentrating on grid points adjacent to this boundary, Deep-SAILS delivers a high-resolution risk portrait with only a fraction of the total scenarios.

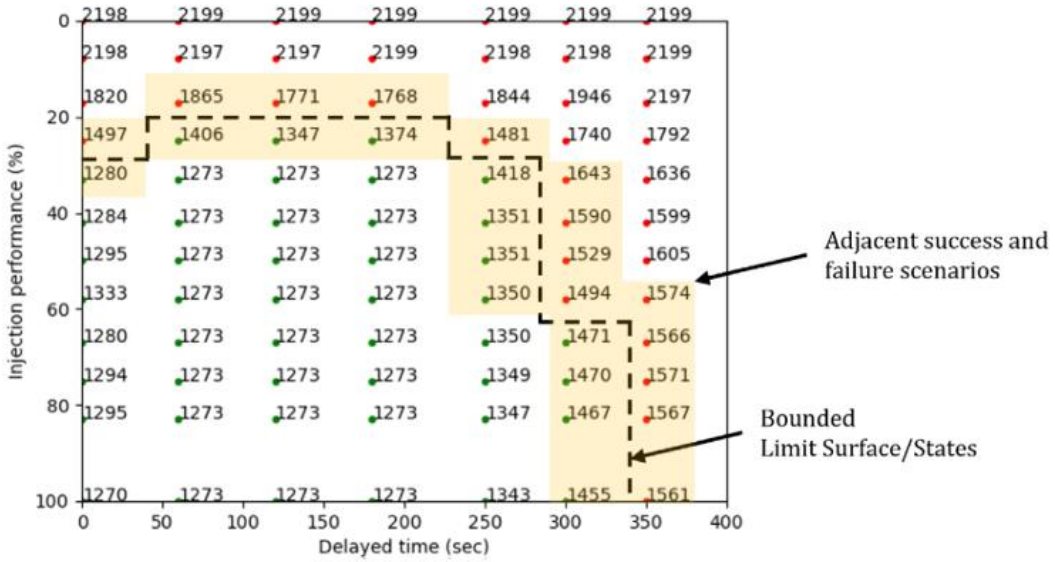

FIGURE 1. Scenario consequence of limit surface of Deep-SAILS of Two parameters (Injection performace, Delayed time of the cooling water) [6]

Delineating the LS is computationally intensive, owing to the nonlinear coupling among numerous NPP system parameters. To mitigate this, Iterative refinement strategy was adopted that incrementally hones the LS estimate while curtailing

computational burden. In each cycle, scenarios predicted to lie near the provisional LS are preferentially sampled and subjected to high-fidelity simulation. These newly obtained results then augment the training set of the surrogate model (e.g., a deep neural network), progressively enhancing its boundary approximation. By concentrating on the most informative cases, this targeted sampling framework eliminates superfluous runs and markedly reduces total computational burden without sacrificing assessment accuracy.

Nonetheless, as the scale of risk assessment grows, even such adaptive samplings confront limits in handling millions of candidate scenarios. To summarize this, the current study introduces OASIS.

As the scope of probabilistic risk assessments expands to encompass millions of candidate scenarios, even Deep-SAILS, adaptive sampling reaches its practical limits. To address this, the current study proposes OASIS, which identified points of control action, operator action and change of component state, from previously executed runs to detect and skip overlapping parts, thereby eliminating redundant computations and improving efficiency.

III. OPTIMIZED AND ACCELERATED SIMULATION USING INTERMEDIATE STATE STORAGE

The TH system code employed in this study is a specialized computational framework developed to capture the coupled thermal hydraulic phenomena occurring during accident transients in NPPs. Widely adopted for both routine safety evaluations and severe accident analyses, TH system codes facilitate risk assessment of NPPs responses across a broad spectrum of initiating events, thereby supporting advanced risk assessment methodologies and informing risk-informed decision-making in plant operation.

A major feature of TH system codes is ‘Restart’ function, which allows simulation states to be archived at selected time points and later reloaded to resume the transient from that point. By obviating the need to recompute the entire transient from initial conditions for each scenario, this feature shortens times.

In the proposed OASIS framework, the simulation “Restart” function is leveraged to streamline scenario execution. Defining the instant at which a control action occurs as the branch point, then identify overlapping parts between previously simulated scenarios and the current scenario. By bypassing these overlapping parts and starting simulation execution from the branch point, OASIS significantly reduces the computational burden while preserving the fidelity of the dynamic risk assessment.

Through systematic optimization of computational cost utilization, the algorithm eliminates unnecessary processing and enhances the efficiency of the simulation. The schematic of this methodology is illustrated in Figure 2.

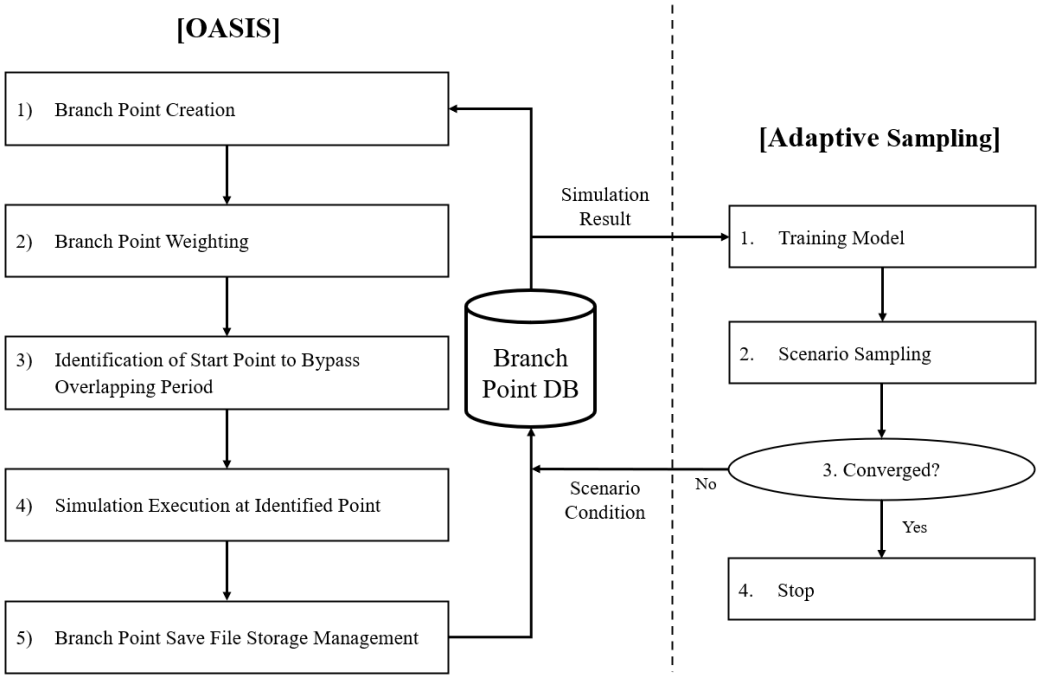

FIGURE 2. Framework of Optimizied and Accelerated Simulation using Intermidiate Storage

The proposed framework is organized into a systematic five-stage sequence. During the simulation execution stage, a cyclic workflow is employed: as each scenario advances, newly identified branch points are recorded. Once the simulation is completed, these results are reloaded, allowing the procedure to loop back to the branchpoint creation stage. Upon reverting to the branch point creation stage, the conditions and results of the current iteration's scenarios are conveyed to the adaptive sampling module, which then prescribes the initial conditions for the scenarios to be executed in the subsequent iteration.

III.A. BRANCH POINT CREATION

In this stage, branch points within each scenario are identified. A branch point is defined as the instant at which a control action occurs, resulting in a change in either human operation or a component state.

Figure 3 illustrates the locations at which branch points are identified within a simulated scenario. Each branch point corresponds to the moment of events, control actions, takes place, and in this example three distinct branch points are identified within the scenario.

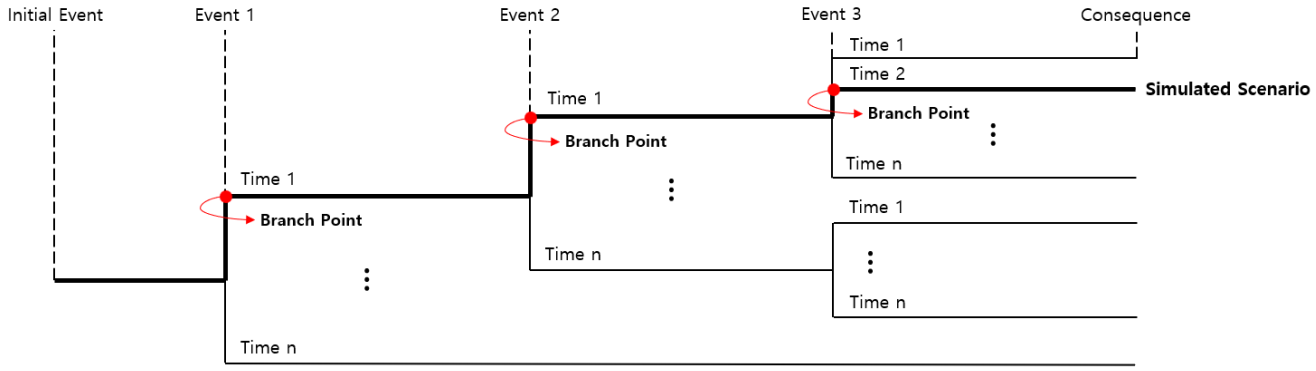

FIGURE 3. Example of Branch Point Identification

III.B. BRANCH POINT WEIGHTING

In this stage, each branch point identified during the generation stage is assigned a weight according to Eq. (1), where T denotes the simulation time elapsed at the branch point and B represents the count of subsequent branches emanating from that point. Specifically, the branch point weight is determined by multiplying T by B, thereby providing a metric for the potential reduction in computational time afforded by bypassing overlapping part of the simulations.

$$Scenario\ Weight = T \times B \tag{1}$$

When determining the count of subsequent branches, any consecutively occurring CD scenarios need not each undergo full simulation. Instead, these CD scenarios should be treated as a single merged CD branch to prevent inflation of the branch count. By merging them into one CD branch and excluding the redundant CD scenarios from simulation, the scenario-weight metric is not unduly skewed toward overly high values, and their relative importance is appropriately moderated. Figure 4 illustrates an example of this CD scenario merging.

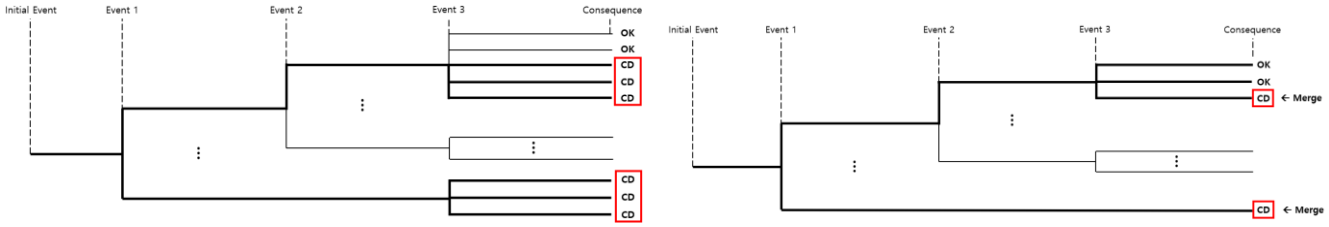

FIGURE 4. Example of CD scenario merging (Left: Event tree before merging; Right: Event tree after merging)

After merging consecutive CD scenarios into unified branches, the branch-point weighting metric is applied to compute each branch point's weight. Figure 5 provides an illustrative example of this calculation. In the example, Event 3, corresponding to the control action occurred in the event tree of Figure 4, is selected as the branch point. The simulation time up to this branch point is 12 hours, and the number of subsequent branches originating from this point is three. Substituting these values into the weighting metric (12 × 3) yields a branch-point weight of 36, which is then assigned to that branch point.

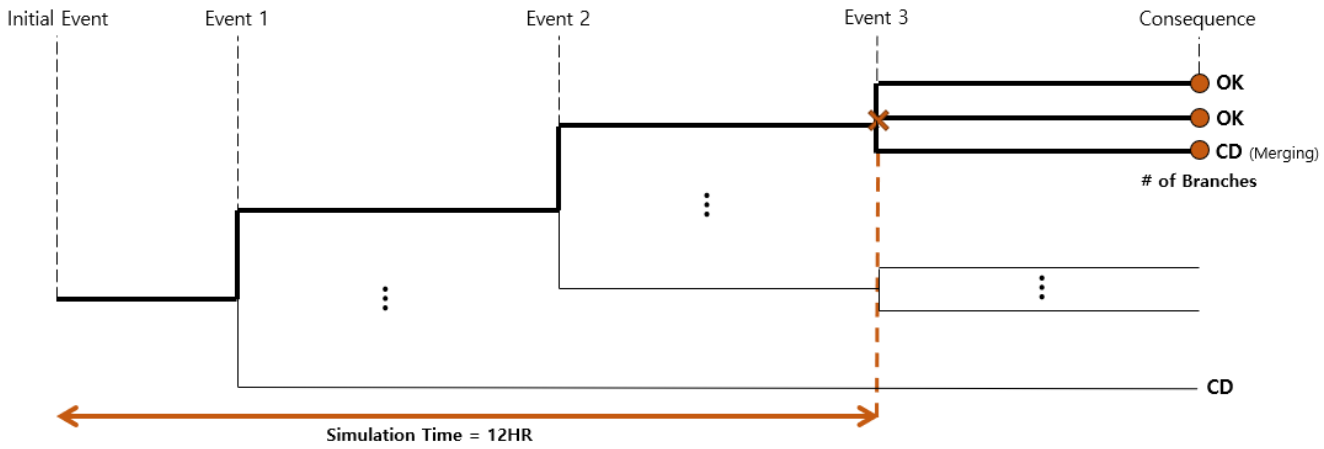

FIGURE 5. Example of branch point weight calculation

III.C. IDENTIFICATION OF START POINT TO BYPASS OVERLAPPING PERIOD

In this stage, archived branch point save file from prior simulations are leveraged to determine the optimal simulation execution point for the currently selected scenario. The branch point save file that promises maximal computational savings is chosen and designated as the simulation execution point.

Figure 6 illustrates the overlapping parts between the current scenario and two previous scenarios, as well as their respective outermost overlapping points. By comparing the outermost time stored at each prior branch point, the overlapping parts between previous scenario 1 and the current scenario is identified as point (1), and that between previous scenario 2 and the current scenario as point (2). Given that point (2) affords greater reduction in simulation time, it is selected as the simulation execution start point.

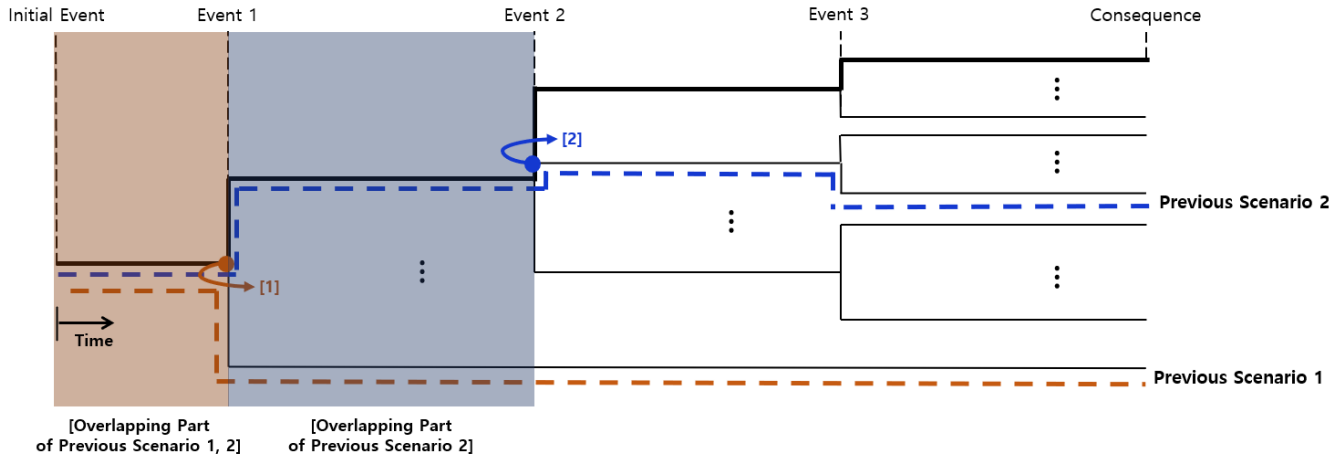

FIGURE 6. Example of identifying the outermost overlapping point (1: Outermost overlapping point of previous scenario 1; 2: Outermost overlapping point of previous scenario 2)

III.D. SIMULATION EXECUTION AT IDENTIFIED POINT

In this stage, the simulation is executed from the simulation execution point identified during the 'Identification of start point to bypass overlapping period' stage. Figure 7 illustrates an example of this simulation execution. In this case, the simulation execution point was designated as point (2) during the 'Identification of start point to bypass overlapping period' stage, and thus, the simulation is initiated from point (2).

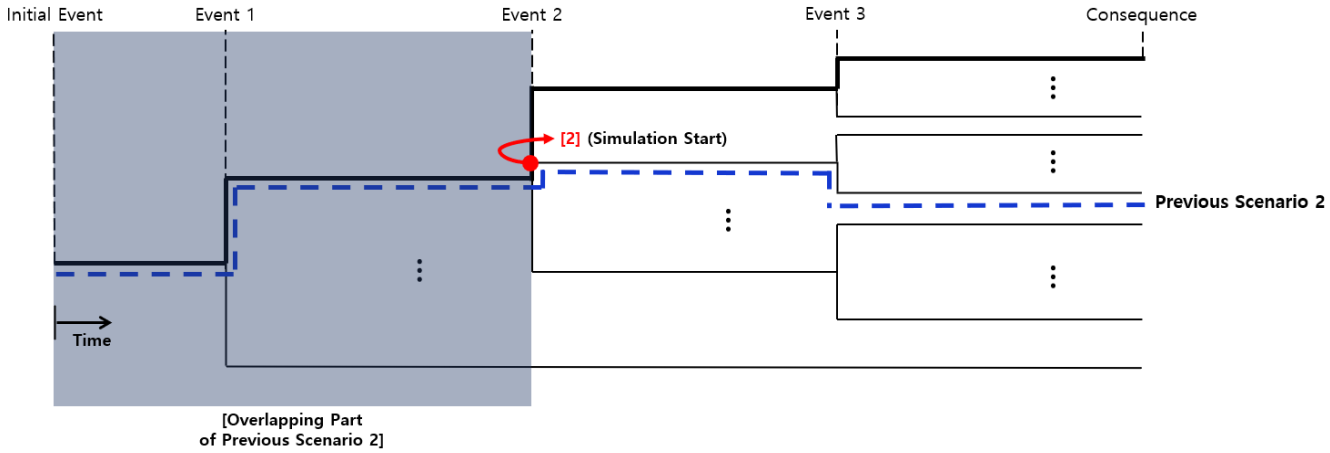

FIGURE 7. Example of simulation execution at the outermost overlapping point

III.E. BRANCH POINT SAVE FILE STORAGE MANAGEMENT

This stage aims to address the storage limitations for saving branch point information data. The branch point information data are sorted in ascending order based on their weights. Then, the weight of the candidate branch point data is compared to those of the existing stored branch point data. If there is any stored branch point data with a weight lower than that of the candidate data, the stored branch point data with the lowest weight is removed and replaced with the candidate data. Subsequently, as the newly saved branch point data may enable merging of CD scenarios, the entire set of stored branch point data is updated by reflecting the possibility of merging, using the weight and the results of the stored branch points.

IV. CASE STUDY

To evaluate the effectiveness of OASIS in reducing computation time, a simplified LOOP (Loss of Offsite Power) scenario was used. This case study employed the OPR 1000 plant type, which is a Korean-designed pressurized water reactor with an approximate power output of 1,000 MWe. Figure 8 presents a simplified event tree of the conventional complex LOOP scenario, incorporating the newly introduced Multi-barrier Accident Coping Strategy (MACST). In this Event Tree, the mitigation components considered were the Alternative AC-Diesel Generator (AAC-DG), the Atmosphere Dump Valve (ADV), and the Portable Low Pressure Pump (PLPP). While the Event Tree was designed for sequential operation of AAC-DG, ADV, and PLPP, to better reflect the dynamic nature of the scenario, PLPP was modeled as an independent variable capable of operating at any time.

In this case study, the simulation time was set to a maximum of 72 hours to account for the extended mission time associated with the use of the PLPP, one of the MACST facilities. The scenario assumption for this case study defined that core damage is considered to have occurred if the Peak Cladding Temperature exceeds 1478 K, at which point the simulation is terminated. Additionally, the reactor cooling rate was assumed to be maintained at or below 56°C/hr when using the ADV. Furthermore, the operating pressure of the PLPP was assumed to be no higher than 25 kg/cm², and the number of branch point save files was limited to 300.

Table 1 presents the discretized operating conditions of the components in the LOOP scenario used in the case study. The AAC-DG fail time and the PLPP start time are each discretized into 24 one-hour intervals spanning from 1 to 24 hours, if these events occur after the initial LOOP event. The ADV opening time is discretized into 25 one-hour intervals ranging from 0 to 24 hours, under the assumption that these events occur after the AAC-DG fail time.

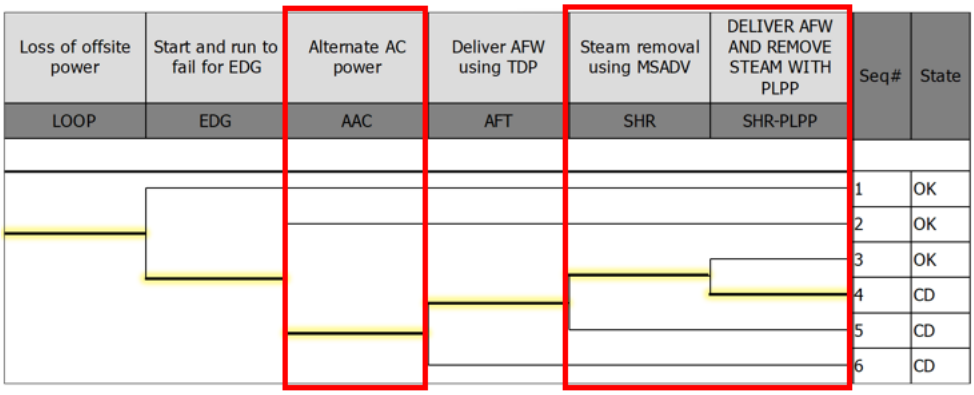

FIGURE 8. Event Tree for LOOP (with MLP Facility)

TABLE 1. Parameters of LOOP Scenarios and Discretized Operating Conditions

Parameter (Axis)		Operating Condition	Resolution (HR)
1	**AAC Fail Time**	**1~24HR** after Initial Event LOOP	1, 2, 3, 4, 5, 6, 7, 8, 9, 10, 11, 12, 13, 14, 15, 16, 17, 18, 19, 20, 21, 22, 23, 24 **(24)**
2	**ADVs Opening Time**	**0~24HR** after AAC Fail Time	0, 1, 2, 3, 4, 5, 6, 7, 8, 9, 10, 11, 12, 13, 14, 15, 16, 17, 18, 19, 20, 21, 22, 23, 24 **(25)**
3	**PLPP (Portable Low-Pressure Pump) start time for deployment and connection**	**1~24HR** after Initial Event LOOP	1, 2, 3, 4, 5, 6, 7, 8, 9, 10, 11, 12, 13, 14, 15, 16, 17, 18, 19, 20, 21, 22, 23, 24 **(24)**

In the case study, a total of 14,400 scenarios were considered. Based on the Deep-SAILS calculations, 1,033 scenarios equivalent to 7.17% were identified as critical scenarios located near the LS, and these were simulated. Using Deep-SAILS alone, it took 75 hours and 25 minutes to evaluate the results for all 14,400 scenarios. When Deep-SAILS was coupled with OASIS, the total simulation time was reduced to 38 hours and 59 minutes, representing a 48.31% reduction compared to using Deep-SAILS alone. Extrapolating from the Deep-SAILS efficiency, it was estimated that simulating all scenarios without applying any method would have taken 1,051 hours and 50 minutes. Therefore, the combination of Deep-SAILS and OASIS enabled the evaluation of all scenario results using only 3.3% of the originally required simulation time.

V. CONCLUSION AND DISCUSSION

To address the challenge of large computational costs in dynamic PSA, which arise from the numerous scenarios and extensive thermal-hydraulic (TH) simulation times, this study proposes an algorithm that leverages streamlined simulation and intermediate state storage management. By combining adaptive sampling with the TH system code's 'Restart' function, the algorithm identifies and skips the overlapping portions between previously simulated scenarios and the current scenario, thereby reducing simulation time.

In the case study, the initial event was set as LOOP, and the TH system code was coupled with Deep-SAILS, an adaptive sampling technique. A total of 14,400 scenarios were considered. When Deep-SAILS and OASIS were coupled, simulation time was reduced by 96.30% compared to the baseline with no method applied.

Future research is expected to focus on the validation of the algorithm's effectiveness in capturing the dynamic behavior of scenario progression under more realistic conditions, the validation of the proposed methodology through comparison with alternative approaches, and the optimization of time efficiency while considering the limitation on the number of branch point save files.

ACKNOWLEDGMENTS

This work was supported by Korea Institute of Energy Technology Evaluation and Planning(KETEP) grant funded by the Korea government(MOTIE)(RS-2024-00403194, Next-Generation Nuclear Technology Creation IP-R&D Talent (Human Resources). Development Project) This research was supported by the National Research Council of Science & Technology(NST) grant by the Korea government (MSIT) (No. GTL24031-400).

REFERENCES

[1] T. Bedford and R. Cooke, Probabilistic Risk Analysis: Foundations and Methods. Cambridge, U.K.: Cambridge Univ. Press, 2001.
[2] C. Seong, G. Heo, S. Baek, J. W. Yoon, and M. C. Kim, "Analysis of the technical status of multiunit risk assessment in nuclear power plants," Nuclear Engineering and Technology, vol. 50, pp. 1035–1043, 2018.
[3] D. Mandelli, C. Wang, C. Parisi, D. Maljovec, A. Alfonsi, Z. Ma, and C. Smith, "Linking classical PRA models to a dynamic PRA," Annals of Nuclear Energy, vol. 149, p. 107746, 2020.
[4] S. Ryu, H. Kim, S. G. Kim, K. Jin, J. Cho, and J. Park, "Probabilistic deep learning model as a tool for supporting the fast simulation of a thermal–hydraulic code," Expert Systems with Applications, vol. 200, p. 116966, 2022.
[5] J. Park and H. Kim, "A case study to address the limitation of accident scenario identifications with respect to diverse manual responses," Reliability Engineering & System Safety, vol. 251, no. 110406, 2024.
[6] E. Zio, "Integrated deterministic and probabilistic safety assessment: concepts, challenges, research directions," Nuclear Engineering and Design, vol. 280, pp. 413–419, 2014.
[7] J. Bae, J. W. Park, and S. J. Lee, "Limit surface/states searching algorithm with a deep neural network and Monte Carlo dropout for nuclear power plant safety assessment," *Applied Soft Computing*, vol. 124, p. 109007, 2022.

ASRAM2025
www.asram2025.org
Asian Symposium on Risk Assessment and Management 2025
Pattaya, Thailand, 27 – 29 August 2025

Dynamic Risk Assessment Framework with Limit Surface Search and Success and Failure Domains Analysis

Junyong Bae[1], Wooseok Jo[2], Kyeong Seo Kim[3], Seung Jun Lee[4]

Ulsan National Institute of Science and Technology (UNIST), 50 UNIST-gil, Ulju-gun, Ulsan 44919, Republic of Korea,
[1]junyong0513@unist.ac.kr, [2]cws5528@unist.ac.kr, [3]smart2439@unist.ac.kr, [4]sjlee420@unist.ac.kr

EXTENDED ABSTRACT

Risk assessment is crucial for ensuring operational safety and managing risk of nuclear power plants (NPPs). Probabilistic safety assessment (PSA) combined with deterministic analysis using physical plant models serves as the primary methodology for this purpose. Since accident scenarios are potentially unlimited, PSA adopts a practical approach of selecting representative scenarios with conservative assumptions. These scenarios are organized as event trees (ETs), while component-level basic events that cascade to cause system-level failures on ETs are structured using fault trees (FTs).

PSA has been widely applied in various contexts; however, potential gaps may exist in scenario coverage. To address this limitation, dynamic risk assessment has been investigated over recent decades. In this assessment, factors affecting accident progress are considered in much greater detail. Theoretically, possible accident scenarios considering such factors are unlimited. Therefore, a central challenge in dynamic risk assessment methodology is how to investigate potential accident scenarios effectively. For instance, PSA and deterministic analysis can operate in a synchronized manner, in which dynamic ETs are developed by branching event sequences when plant status meets user-defined rules [1]. Various other dynamic safety assessment methods have also been suggested. However, practical challenges of these methods include the exponential growth of scenario numbers, and the substantial computational resources required to analyze them.

In this paper, we present a dynamic risk assessment framework with limit surface search and success and failure domains analysis. The key feature of the presented framework is that possible dynamic scenarios are predefined and pruned after simulations, unlike conventional dynamic approaches that develop scenarios in parallel with deterministic analysis. This post-pruning approach enables the adaptation of simulation optimization algorithms to predefined scenarios for addressing computational resource problems.

Figure 1 shows the overall schematic of the proposed framework, which consists of three parts. First is the deep-learning based searching algorithm for informative limit surface/scenarios/states (Deep-SAILS) [2]. This algorithm identifies the limit surface by iteratively updating a deep learning (DL) metamodel that predicts critical parameters representing scenario consequences, such as peak cladding temperatures (PCT). The iterations include simulation of scenarios estimated to be close to the surface by the DL metamodel and subsequent training of the metamodel. Through these iterations, the limit surface can be pinpointed, and simulation can be optimized for scenarios close to the surface, as shown in the right panel of Fig. 1(a).

Second is optimized and accelerated simulation using intermediate storage (OASIS) [3]. Even when optimized with Deep-SAILS, the computational time required for simulations is typically substantial. OASIS further saves this time by avoiding redundant simulations of scenario timelines with identical plant conditions, as shown in Fig. 1(b). For this purpose, restart points of simulated scenarios are identified and cached in storage, then compared with given scenarios to provide the optimal starting point for simulation. Additionally, deterministic analysis becomes more efficient through parallel execution of multiple simulations.

Third is automatic accident sequence generation [4]. The combination of Deep-SAILS and OASIS can locate the limit surface with minimized computational effort; however, interpretation and practical usage of the surface can be complex when more dynamic factors are considered due to high dimensionality. To address this challenge, the generation algorithm analyzes success domains and locates multiple boxes containing only success scenarios. The locations of these boxes are optimally determined using an alpha-shape method, and the regions segmented by the located boxes are converted into dynamic ETs or other comprehensible forms, as shown in Fig. 1(c).

We believe this novel framework can serve as a complement to both existing dynamic risk assessment methods and conventional PSA. Further study will be conducted to assign quantified risk measures by either utilizing existing reliability data or employing a novel risk index.

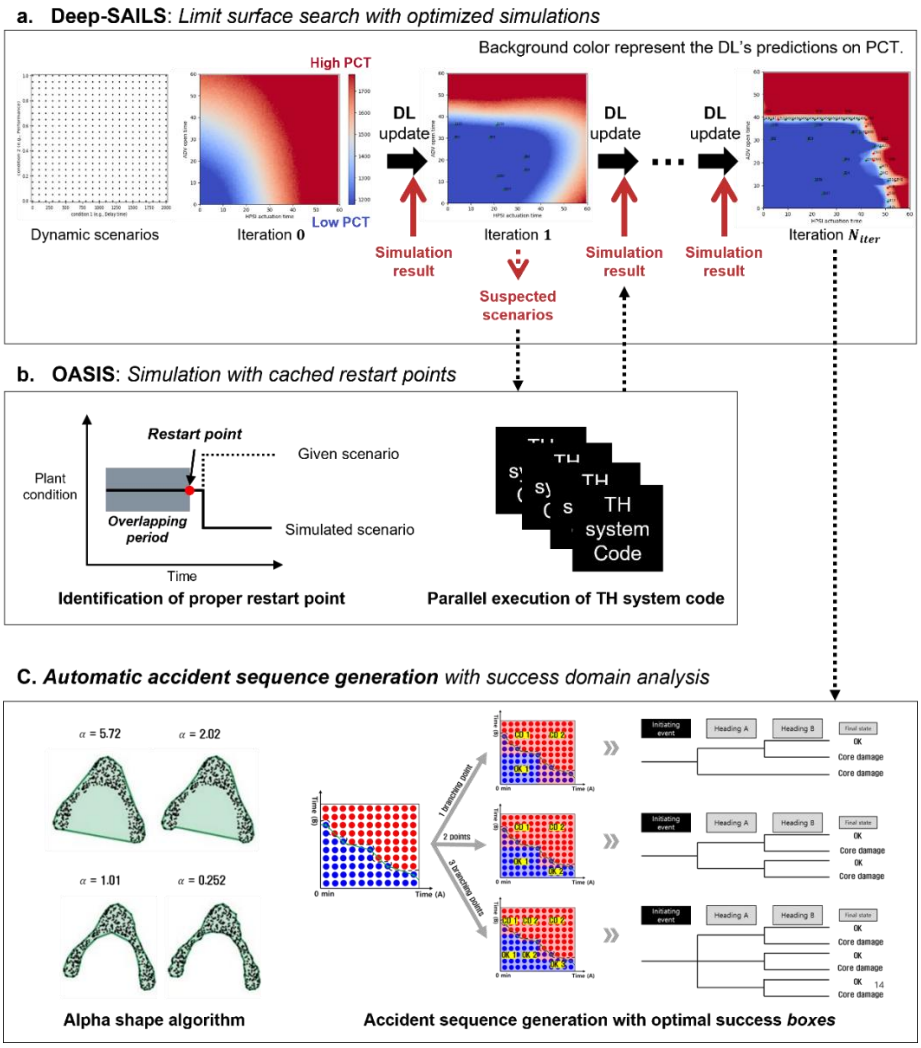

FIGURE 1. Overall schematic of the proposed dynamic risk assessment framework

ACKNOWLEDGMENTS

This work was supported by Korea Institute of Energy Technology Evaluation and Planning (KETEP) grant funded by the Korea government (MOTIE) (RS-2024-00403194) and the National Research Foundation of Korea (NRF) grant funded by the Korea government (MSIT) (No. RS-2022-00165231)

REFERENCES

[1] G. HEO and D. KWON, "Korean perspective for integrated deterministic-probabilistic safety assessment and its synergetic strategy with conventional methods," *Nuclear Engineering and Technology*, **56**, 4031-4041 (2024).

[2] J. BAE, J.W. PARK, and S.J. LEE, "Limit surface/states searching algorithm with a deep neural network and Monte Carlo dropout for nuclear power plant safety assessment," *Applied Soft Computing*, **124**, 109007 (2022).

[3] K.S. KIM, J. KIM, W. CHOI, and J.J. LEE, "A Framework of Streamlined Simulation of Thermal-hydraulic Code for Dynamic Probabilistic Safety Assessment," *Korean Nuclear Society Autumn Meeting*, Changwon, Korea, October 24-25 (2024).

[4] W. JO, J. BAE, D.S. KIM, and S.J. LEE, "Automatic Accident Sequences Generation for Dynamic PSA," *17th International Conference on Probabilistic Safety Assessment and Management & Asian Symposium on Risk Assessment and Management*, Sendai, Japan, October 7-11 (2024).

Technical Session 12 (13:40 -15:40)	The Port 4, C Floor	Risk Assessment for External Event and Hazard (Earthquake and Tsunami)
		Chair/Facilitator 1: Dr. Jae Young YOON (Korea Atomic Energy Research Institute (KAERI))
		Chair/Facilitator 2: Miss Kunthida Waree (Thailand Institute of Nuclear Technology (Public Organization))
13:40 - 14:00		ID 58: How to Quantify Multi-unit Risk under Seismic Event Speaker: Jae Young Yoon (Korea Atomic Energy Research Institute) Contributors: Jae Young Yoon (Korea Atomic Energy Research Institute), Sang Hoon Han (Korea Atomic Energy Research Institute)
14:00 - 14:20		ID 69: Seismic PRA of Building and Internal Equipment of the Seismically Isolated Nuclear Building in Retaining Wall Collisions Speaker: Takeshi Nomura (Tokyo City University) Contributors: Takeshi Nomura (Tokyo City University), Yasuki Ohtori (Tokyo City University), Hitoshi Muta (Tokyo City University), Yoshihumi Katayama (Chuden Engineering Consultants)
14:20 - 14:40		ID 66: Fragility Evaluation of Electrical Raceway Considering Realistic Capacity of Cables against Earthquake and Its Effect on Seismic PRA Speaker: Ryusuke Haraguchi (Mitsubishi Heavy Industries, LTD.) Contributors: Ryusuke Haraguchi (Mitsubishi Heavy Industries, LTD.), Tomokazu Higuchi (Toshiba Energy Systems & Solutions Corp.), Kinji Nakano (Hitachi-GE Nuclear Energy, Ltd.), Shinichi Hisatomi (Tokyo Electric Power Company Holdings, Inc.), Hidenori Takamatsu (Tokyo Electric Power Company Holdings, Inc.), Michiyoshi Satou (Tokyo Electric Power Company Holdings, Inc.), Kento Furuya (Tokyo Electric Power Company Holdings, Inc.), Kenta Kobayashi (Hokkaido Electric Power Company,Inc.), Mitsuru Imamura (Hokkaido Electric Power Company,Inc.)
14:40 - 15:00		ID 96: A Monte Carlo Technique to Propagate the Uncertainty of Seismic Induced Joint Failure Probability Speaker: Shota SOGA (Central Research Institute of Electric Power Industry) Contributors: Shota SOGA, Eishiro Higo, Sunghyon Jang, Munemichi Kawaguchi, Hiromichi Miura
15:00 - 15:20		ID 25: Development of Tsunami PSA Bounding Analysis Method for Hanul Site Speaker: JaeBeol Hong (FNC Technology Co., Ltd) Contributors: Changkyung Seong (FNC Technology Co., Ltd), JaeBeol Hong (FNC Technology Co., Ltd), Kyung Min Kang (Korea Institute of Nuclear Safety), Yein Seo (FNC Technology Co., Ltd), SEOK WOO SOHN (FNC Technology Co., Ltd)
15:20 - 15:40		ID 122: Anomaly Detection and Seismic Damage Inference of Reactor Building Using Bayesian Inference: Speaker: Sunghyon Jang (Hokkaido University) Contributors: Sunghyon Jang (Hokkaido University), Hideo Machida (TEPCO system co., ltd), Shuehi Matsunaka (TEPCO system co, ltd)

ASRAM2025
www.asram2025.org
Asian Symposium on Risk Assessment and Management 2025
Pattaya, Thailand, 27 – 29 August 2025

How to quantify multi-unit risk under seismic event

Jae Young Yoon[1], Sang Hoon Han[1]

[1] *Korea Atomic Energy Research Institute, 111 Daedeok-daero 989 beon-gil, Yuseong-gu, Daejeon 34057, Republic of Korea*
Email Address: jyyoon@kaeri.re.kr

EXTENDED ABSTRACT

As multi-unit risk assessment has been identified as a significant issue in the field of probabilistic safety assessment (PSA), a seismic event, one of the significant initiating events for multi-unit risk, is becoming important. Delete-term approximation (DTA) effectively quantifies the risk of internal PSA models because the failure probabilities of basic events are generally small enough to neglect the success gates [1]. However, seismic risk assessment should be evaluated differently from risk assessment of internal events due to the large failure probability of components in seismic bins with high seismic intensity, and several quantification methods have been developed for this purpose. Some methods are based on Monte-Carlo (MC) simulation techniques, while others are based on binary decision diagram (BDD) techniques that solve logic or cut sets related to large failure probabilities. In practice, these various methods are used to evaluate seismic risk in Korea, and the representative method is not yet decided due to the merits and limitations of each method. In addition, various research institutes in Korea are still developing seismic risk quantification methods for more accurate seismic risk quantification. In this study, we introduce the current status of seismic risk quantification methods and present their characteristics, including strengths and limitations.
A BDD adopting sum-of-disjoint-product is a powerful logic to obtain an exact solution and two ways exist to apply the BDD techniques to the PSA models; BDD into minimal cut sets (MCSs) and BDD into fault tree (FT) logics.

First, the MCSs obtained are converted into BDD logic by adopting the negate-down approach, which is introduced to prevent negates from being ignored by the DTA approach [2]. It can lead exact solution if a negate-down approach is applied to all success gates and all MCSs are converted into BDD logic, however, it cannot be applied to a PSA model of large systems such as nuclear power plants (NPPs) because of too many success gates and MCSs even in a single-unit PSA (SUPSA) model. Thus, some attempts have been made to partially adopt BDDs in assessing the seismic risk of NPPs. The success gates having seismic events with simple structures such as seismic initiating event tree (SIET) are expanded by using a negate-down approach and the risk-significant MCSs are converted into BDD logic. For example, if gate A is OR gate of failure events x and y, success gate $\bar{A} = \overline{x + y}$ can be expanded as the product of success events $\bar{x}$ and $\bar{y}$ ($\bar{A} = \bar{x} \cdot \bar{y}$). To do this, seismic events should considered in only an SIET, not in seismic secondary ETs (SSETs). This method can derive near-exact risk, but the MCSs converted into BDD logic are difficult to obtain. As another method, the probability subtraction method (PSM) was developed to assess multi-unit seismic risk by dealing with the complemented gates as subtractions of two gates converted into BDD logic [3]. For example, the risk of gate $A \cdot \bar{B}$ is quantified by subtracting the risk of gate $A \cdot B$ from the risk of gate A in a SUPSA model. This method can derive the risk of core damage (CD) sequences but, similarly as above, cannot also provide the MCSs. Deriving MCSs is important in the part of PSA quantification because MCSs give an insight into whether the PSA model is reliably constructed and how risk can be reduced. For a multi-unit PSA (MUPSA) model, the risk of $U1 \cdot \overline{U2}$ is quantified by subtracting the risk of $U1 \cdot U2$ from the risk of $U1$, but success gates in SUPSA model should be treated by partial BDD approach which will be introduced next.

Second, the logics in a PSA model are totally converted into BDD logic and the risk is quantified based on rare event approximation (REA) which means a summation of MCSs. It cannot also be applied to a PSA model of NPPs, and therefore a hybrid method adopting a partial BDD algorithm was developed to obtain both near-exact risk and MCSs [4]. This method partially converts some important failure and success gates having large failure probabilities of basic events into BDD logic and solves the other unimportant success gates by DTA. After converting the important gates into BDD logic, the quantification of total risk is based on REA, which can derive the MCSs. It is powerful logic for a risk quantification of the SUPSA model, however, post-processing of MCSs is required for a risk quantification of the MUPSA model. The risk of $U1 \cdot \overline{U2}$ can be quantified by regarding the MCSs of $U2$ (success unit) as super events according to what shared events are included in each MCS of $U1$ (failure unit) which is obtained from partial BDD.

In addition to BDD conversion, the Monte Carlo (MC) approach, which is based on random sampling of basic events, has been widely used to assess seismic risk [5]. It has the advantages of being applicable to risk assessments of large systems, including MUPSA models, and also of leading to near-exact risk for large-magnitude earthquakes with a sufficient number of

samplings. However, the limitations are that the MC approach cannot generate the cut sets, and a lot of samplings are needed for seismic bins with small seismic intensities. Table 1 shows a comparison between the variable methods including the simple descriptions, strengths, and limitations.

TABLE I. Comparison between the quantification methods for a multi-unit seismic risk assessment

Logic	Method	Descriptions	Strengths	Limitations
BDD into MCSs	Negate-down [2]	• Expand success gates to success event to avoid DTA	• Get near-exact solution • Get insights from the MCSs not converted into BDD	• Difficult to get MCSs • Depend on the number of converted MCSs into BDD • Seismic events should be modeled in a SIET
	PSM [3]	• Treat complemented gates as subtractions of two gates converted into BDD	• Get near-exact solution • Get scenario importance for SUPSA models	• Difficult to get MCSs • Depend on the number of converted MCSs into BDD • Success gates in SUPSA models should be treated by partial BDD for a MUPSA model
BDD into FT logic	Partial BDD [4]	• Convert important gates into BDD and treat rest gates by DTA	• Get near-exact solution • Get MCSs	• Depend on the number of converted FT logics into BDD • Require post-processing of MCSs for MUPSA model
Monte Carlo approach	MC [5]	• Perform random sampling of basic events	• Get near-exact solution • Easy to utilize	• Impossible to get MCSs • Require a lot of samplings for small seismic bins

The case study was performed to confirm the applicability of the methods assuming a simplified seismic MUPSA model with two identical units in a large seismic bin (Acc. 1.0g ~ 1.5g). The seismic failures assumed to be fully correlated between two units were considered in both SIET and SSETs. The risk metric is conditional core damage probability (CCDP) not to consider hazard information. MCSs were obtained from AIMS-PSA software [6] and the MC approach was performed by using FTEMC software [7]. Table 2 summarizes the requirements for constructing SUPSA model which needs to be developed for constructing MUPSA model in the first row and those for risk quantification of the MUPSA model in the second row.

TABLE II. Requirements for risk quantification of the MUPSA model

	Negate-down	PSM	Partial BDD	MC
SUPSA model for MUPSA model	-	• Treat success gates by Partial BDD	• Partial BDD	-
MUPSA model	• Expand only success gates in SIET • Convert 1,000 MCSs to BDD logics	• Separate top logic into several top logics for SU and MU • Convert 1,000 MCSs to BDD logics	• Post-processing of MCSs	• 10^8 Sampling

Table 3 shows the results of the case study. Single-unit CCDP and multi-unit CCDP mean CCDP in one unit and two units, respectively, and site CCDP means a summation of both CCDPs. Although the success gates in SIET were only expanded for the negate-down approach, it yields reasonable results compared with other methods, indicating that the success gates in SSETs are negligible in this simplified PSA model. All methods show similar results, however, we can suggest that the MC approach is better to use if quantified risk value is only required because of the simplest way and the partial BDD approach is better to use if MCSs as well as risk value are required.

TABLE III. Case study results

	Negate-down	PSM	Partial BDD	MC
Single-unit CCDP	9.600E-03	9.479E-03	9.626E-03	9.613E-3
Multi-unit CCDP	8.156E-01	8.156E-01	8.156E-01	8.156E-1
Site CCDP	8.252E-01	8.251E-01	8.252E-01	8.252E-1

ACKNOWLEDGMENTS

This work was supported by the Korea Institute of Energy Technology Evaluation and Planning (KETEP) and the Ministry of Trade, Industry and Energy (MOTIE) of the Republic of Korea (No. 20224B10200050).

REFERENCES

[1] W. S. Jung, "A method to improve cutset probability calculation in probabilistic safety assessment of nuclear power plants," *Reliability Engineering and System Safety*, **134**, (2015).
[2] J. S. Kim and M. C. Kim, "Insights gained from applying negate-down during quantification for seismic probabilistic safety assessment," *Nuclear Engineering and Technology*, **54**, (2022).
[3] S. K. Park and W. S. Jung, "Probability subtraction method for accurate quantification of seismic multi-unit probabilistic safety assessment," *Nuclear Engineering and Technology*, **53**, (2021).
[4] S. H. Han, "A hybrid approach of partially applying BDD for seismic PSA quantification," *Nuclear Engineering and Technology*, **56**, (2024).
[5] K. Oh, S. H. Han, J. H. Park, H.-G. Lim, J. E. Yang, and G. Heo, "Study on Quantification Method Based on Monte Carlo Sampling for Multiunit Probabilistic Safety Assessment Models," *Nuclear Engineering and Technology*, **49**, (2017).
[6] S. H. Han, K. Oh, H.-G. Lim, and J.-E. Yang, "AIMS-MUPSA software package for multi-unit PSA," *Nuclear Engineering and Technology*, **50**, (2018).
[7] S. H. Han, "Enhancement of the FTeMC software for fault tree top event probability evaluation using Monte Carlo approach," *Proc. Transactions of the Korean Nuclear Society Spring Meeting*, Jeju, Korea, May. 17-18, (2018).

ASRAM2025
www.asram2025.org
Asian Symposium on Risk Assessment and Management 2025
Pattaya, Thailand, 27 – 29 August 2025

Seismic Probabilistic Risk Assessment of Structures and Internal Equipment in Retaining Wall Collisions of Seismically Isolated Reactor Buildings

Takeshi Nomura[1], Yasuki Ohtori[1], Hitoshi Muta[1], Yoshihumi Katayama[2]

[1]1Tokyo City University, 1-28-1 Tamazutsumi, Setagaya-ku, Tokyo 158-8557, Japan
[2] Chuden Engineering Consultants, Hiroshima, Japan

ABSTRACT

Seismically isolated structures reduce seismic forces by shifting the natural period to longer periods and dissipating input energy. When ground motions exceed the design level, collisions between the structure and surrounding retaining walls could occur. These collisions can generate impact forces that exceed the design capacities of both the structure and internal equipment. Although previous studies have mainly focused on structural responses to such collisions, the risk of internal equipment damage, which could trigger severe accidents in nuclear facilities, remains unevaluated. This study conducts a probabilistic risk assessment of internal equipment damage caused by retaining wall collisions in seismically isolated nuclear reactor buildings. We generated 30 structural models using Latin Hypercube Sampling, considering aleatory uncertainty in models. Nonlinear time history analyses were performed using input ground motions with peak ground accelerations from 1 to 40 m/s^2. We calculated floor response accelerations at natural periods of 0.1, 0.5, and 1.0 s, and developed fragility curves incorporating epistemic uncertainty caused by the collisions. The results indicate that retaining wall collisions can damage internal equipment before structural failure. Upon collision, impact-force uncertainty rises, leading to greater variability in floor response accelerations on equipment. At high design capacity levels, this collision-induced uncertainty expands response variability and increases β in the fragility curve. Our findings emphasize the need to evaluate not only structural response but also internal equipment vulnerability to ensure the seismic safety of nuclear facilities.

Keywords: Seismic Response Analysis, Seismically Isolated Structures, Seismic PRA

I. INTRODUCTION

Seismically isolated structures reduce external seismic forces significantly by shifting the natural period to longer periods and dissipating input seismic energy. When ground motions exceed the design level, seismically isolated structures may not fully absorb seismic energy. In such cases, the impact force caused by collisions with the surrounding retaining wall may exceed the design capacity of both the structure and the internal equipment.

Although previous studies have evaluated structural responses, no risk assessment has specifically addressed damage to internal equipment, whose failure could directly lead to severe accidents in seismically isolated nuclear facilities [1]-[5]. NAKANISHI et al. examined wall-collision effects on a seismically isolated structure, reporting on first-story inter-story drift angles and the probability of structural damage under seismic loading [6]. NAKAZAWA et al. investigated how wall impacts influence the yielding ratio of the superstructure [7]. SAREBANHA et al. studied their effects on maximum bearing displacement and residual deformation in the isolation layer [8]. All these prior studies limited their damage evaluations to the superstructure and laminated rubber bearings, leaving the vulnerability of internal equipment unaddressed. The studies that do not consider internal equipment risk failing to accurately evaluate severe accidents.

Based on these studies, we compared the effects on structure and internal equipment of retaining wall collisions in seismically isolated nuclear power buildings. We considered both aleatory uncertainty (βa; structure material uncertainty) and epistemic uncertainty (βe; collision uncertainty) to evaluate the seismic risk to internal equipment [9]. We conducted nonlinear seismic response analyses using the dynamic-analysis software TDAP3[10]. The results indicate three key points.

(1) Previous studies mainly focused on superstructures and isolation layers. However, retaining wall collisions can also damage internal equipment. Such damage in nuclear facilities can lead to severe accidents or serious consequences.
(2) Upon collision, the uncertainty associated with impact forces increases, consequently increasing the variability of floor response accelerations acting on internal equipment.
(3) When design capacity is high, the increased uncertainty due to collisions results in greater variability of responses, thus increasing the uncertainty parameter β of the fragility curve.

This paper is composed as follows: II. Analysis Model, Ⅲ.Analysis Outline, Ⅳ.Results, and Ⅴ.Conclusions.

II. ANALYSIS MODEL

In this study, the analysis model was a 2D single-axis, multi-degree-of-freedom mass model. Fig.1 shows the overall of the model. This model reflected the mass ratios characteristics of nuclear power building based on prior research [11]. Miwata et al. found minor difference between 2D and 3D models for the wall-collision phenomenon in seismically isolated structures, although researchers sometimes use 3D models to examine this case [12]. Table.1 shows the material properties and other factors of the model.

Table I. Model Parameters List

Total mass(ton)	178948	Structure 1st period (s)	8.9743E-1
Isolation period (s)	3.00	Structure 2nd period (s)	3.9231E-1
Rayleigh damping 1st frequency (Hz)	1.06	Structure3rd period (s)	3.1576E-1
Rayleigh damping 2nd frequency (Hz)	51.1	Structure 4th period (s)	1.0926E-1

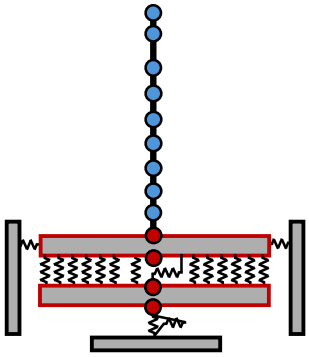

FIGURE 1. Analysis Model

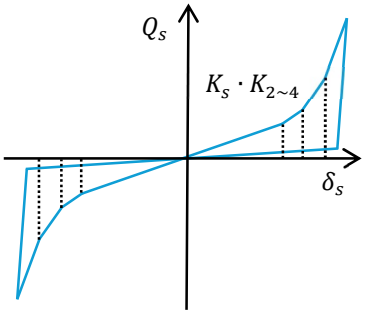

FIGURE 2. Laminated-Rubber Stiffness Model

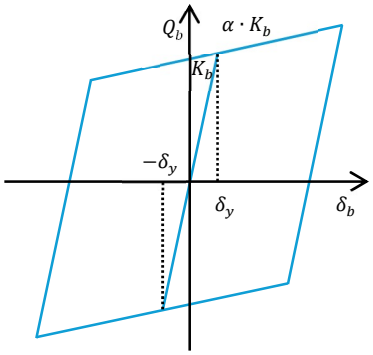

FIGURE 3. Lead Plug Stiffness Model

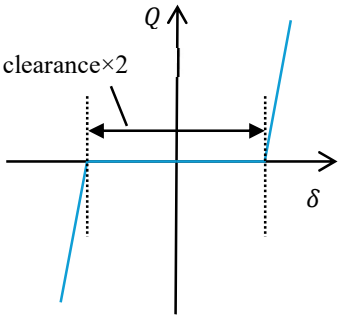

FIGURE 4. Collision wall Stiffness Model

II. A. Superstructure

The superstructure is a single-axis nine–degree-of-freedom mass model assuming a prestressed concrete containment vessel of the material. Each mass element incorporates nonlinear behavior. The shear direction restoring force behavior is represented by a peak oriented trilinear model, while the bending restoring force behavior is represented by a trilinear mode. We did not consider the mass of internal equipment because it was negligible relative to the total structural mass.

II. B. Seismic Isolation Layer

We set the seismic isolation period as 3 s because it is generally in the 2-4 s range. The isolation layer comprises a laminated-rubber stiffness model with hardening considered as Fig. 2, a lead plug stiffness model as Fig. 3 and collision wall stiffness model as Fig. 4. Laminated-rubber stiffness model and lead plug stiffness model were with the devices installed beneath the superstructure. The isolation layer comprises an upper foundation slab, a lower foundation slab, horizontal ground springs, vertical and rotational ground springs at the soil interface, and vertical and horizontal isolation springs. We designated the central node as the primary degree and the other nodes as dependent points.

II.B.1. Laminated Rubber Stiffness Model

Fig. 2 shows the laminated rubber shear spring model. Its initial stiffness is 7.85×10^5 N/m, with post-hardening stiffness increase ratios of 1.5, 2.0, and 4.0. The laminated-rubber element was assumed to have a linear-limit shear strain of 250 % (0.55 m) and a failure limit of 450 % (0.99 m) based on prior research [13]. We set a 0.6 m clearance between the edges of the isolation layer and the retaining wall. A single horizontal isolation spring was consolidated at the midpoint between the upper and lower foundation slabs.

II.B.2. Lead Plug Stiffness Model

Fig. 3 shows the bilinear model for the lead plug. Its initial stiffness is 7.06×10^6 N/m, and the yield displacement $\boldsymbol{\delta_b}$ defined by dividing the yield load by the equivalent stiffness—was set to 0.0124 m. Although the post-yield stiffness was idealized as zero, a small nonzero value was assigned to prevent numerical errors. Both nonlinear models exhibit slip behavior in accordance with Masing's hysteresis rule.

386

II.B.3. Collision Wall Stiffness Model

Fig.4 shows the collision wall stiffness model. The linear stiffness we defined was as a value near zero. The nonlinear stiffness based on prior research was increasing rapidly upon contact thereby retaining wall collision. T_w=0.05 s as the rigid structure's natural period and M = 178948 t as the total mass equals K_w= 2.826×10^9 kN/cm [14].

II. C. Latin Hypercube Sampling

We performed sensitivity analyses using II. ANALYSIS MODEL on parameters known from previous studies to influence wall pounding, varying each parameter by ±10% in 1% increments (21 cases). From those results, we compared the maximum first-floor acceleration at a natural period of 0.1 s. For the six parameters that exhibited no clear response trends, we assigned coefficients of variation (COV) based on research and generated 30 models via Latin Hypercube Sampling (LHS) over a log-normal distribution, Table 2. Kikuchi et al. performed risk assessment without COV whereas we introduced one to consider uncertainty in our analysis [15]. Hayashi et al. showed that the superstructure's COV depends on its damage state [16]. Retaining wall collisions occur before the superstructure sustains damage, except when wall stiffness is extremely low. We assumed a minor damage state for the superstructure for the safety side. [6] Because the surrounding retaining wall natural period of this model is 0.05s as the rigid structure.

Table II. LHS Parameters List

	Lead plug 1st stiffness [17] (N/m)	Lead damper yield point [18]	Laminated rubber 1st stiffness [18] (N/m)	Superstructure 1st stiffness [16] (N/m)	Superstructure shear strain [9]	Collision wall stiffness [19] (N/m)
Median	7.060×10^6	0.0124	7.850×10^5	2.050×10^5	2.120×10^{-4}	2.826×10^9
COV	0.05	0.05	0.05	0.08	0.253	0.10

III. ANALYSIS OUTLINE

III. A. Input ground motion

We generated the horizontal input ground-motion time history using Katayama's method, which is based on the amplitude-envelope function of Noda et al. (2002) to match the uniform hazard spectrum [20]. We then set the vertical component to two-thirds of the horizontal component. Fig. 5 shows the input time history acceleration. Fig. 6 shows the uniform hazard spectrum.

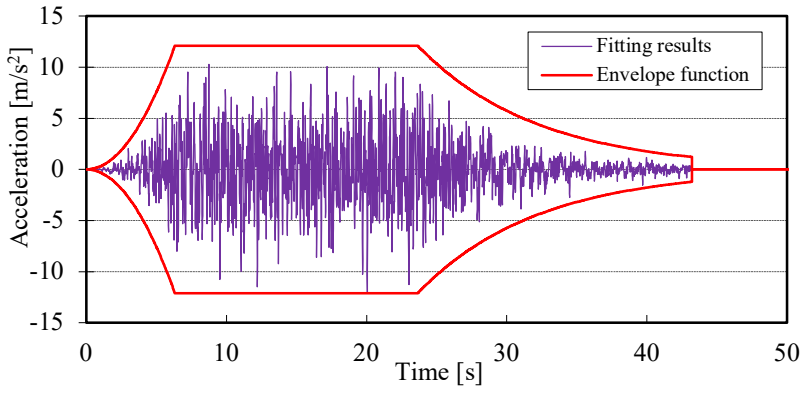

FIGURE 5. Input Time History Acceleration

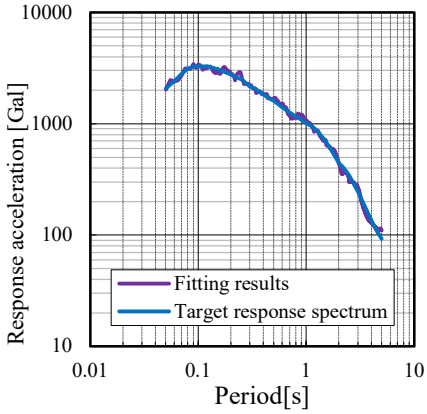

FIGURE 6. Unform Hazard Spectrum

III. B. Seismic risk assessment method

III. B.1 Nonlinear analysis and floor response

We conducted nonlinear analysis combining 30 models created by LHS (II. D) and ground motion with peak ground acceleration (PGA) of 1 to 40 m/s^2 (III. A). Based on prior research, we set the integration time step to 0.00001 s based on prior research where results were stable. Collisions occurred in every model up to 40 m/s^2. We compared structural inter-story drift angles with the floor response accelerations experienced by internal equipment at natural periods of 0.1, 0.5, and 1.0 s. We calculated the median floor response spectrum of 30 models under PGA of 1 to 40 m/s^2.

387

III. B.2 fragility curve

We assigned a log-normal probability density function to the plotted floor response acceleration in *III. B.1* as median value. We set σ to 0.3 and 0.6 for the collision cases, considering β_e caused by the collision phenomenon [21], and σ to 0.1 for the no collision case. We obtained the probability of exceedance: P_i by comparing a log-normal distribution with the 150, 300, 450 m/s^2 set as the design capacity (DC) of the internal equipment [22]. We calculated damage probability: P_n at each 1 m/s^2 increment of PGA and plotted fragility curves from PGA of 1 to 40 m/s^2.

IV. RESULT

Figure 7 shows a comparison of damage to internal equipment and structures. The X-axis shows the impact on internal equipment by plotting the median first floor response acceleration among 30 models at each PGA, and the Y-axis shows the impact on the building, by plotting the median inter-story drift angles among 30 models at each PGA. We assumed natural periods of 0.1, 0.5, and 1.0 s. We set the DC of internal equipment to 77.8 m/s² for electrical panel functionality (black dotted line) [22] and the DC of structure to an inter-story drift angle of 1/60 (black solid line) [6]. We assumed internal equipment natural periods of 0.1 (red), 0.5 (green), and 1.0 s (pink). For the longer periods (0.5 s, 1.0 s), the inter-story drift angle reached 1/60 at a PGA of 26 m/s² before the internal equipment DC was exceeded, indicating that the structure sustains damage first. In contrast, at a natural period of 0.1 s, both internal equipment and the structure exceed their DC at the same PGA of 26 m/s. Previous studies of seismically isolated structures with retaining walls collisions have focused mainly on structural damage. However internal equipment failure can cause total loss of function and serve accidents. Therefore, we should also evaluate damage to internal equipment.

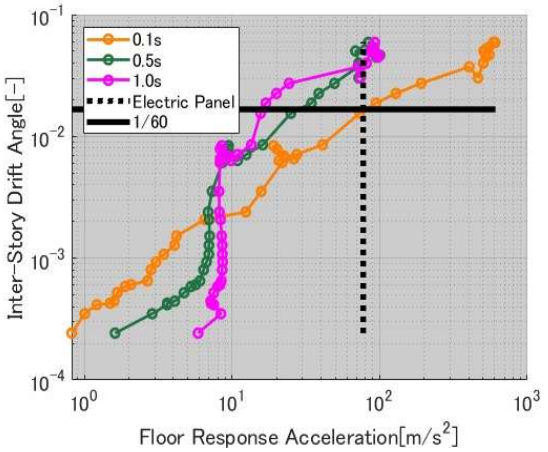

Figure 7. Comparison of structures and internal equipment

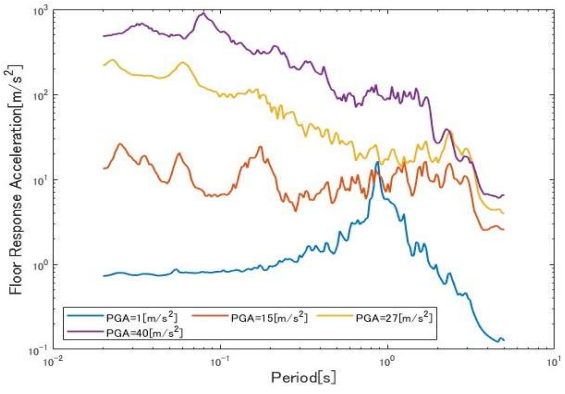

Figure 8. Floor Response Acceleration Spectrum

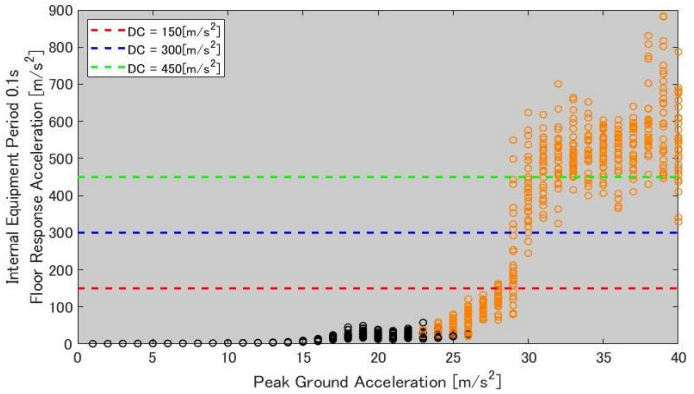

Figure 9. Peak Ground acceleration with natural period of 0.1s for 1200 cases

Fig.8 shows the floor response acceleration spectrum in case of PGA 1,15,27,40 m/s^2 as described in section *III. B.1*. Retaining wall collisions increase the response spectrum on the short-period side. This is from retaining wall collision and hardening effect of the laminated rubber layer caused by excessive seismic motion.

Fig.9 shows the first-floor response accelerations at natural period of 0.1s for 30 models under PGA of 1 to 40 m/s^2 from Fig.8. We change the collided case color from black to orange. The collision begins when the PGA reached 23 m/s^2 in several models. The variation of floor response acceleration after the collision is larger than before the collision caused the uncertainty collision phenomenon yield. We consider this factor responsible for the difference between those that exceed the DC and those that do not, Among the 30 models which occurred collision.

388

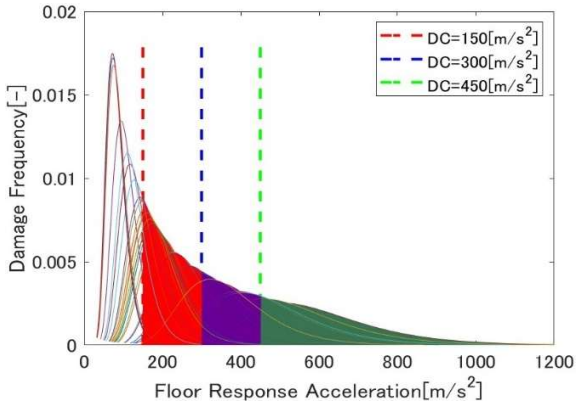

Figure 10. In β_e = 0.3, Variation of floor response acceleration at PGA 29m/s²

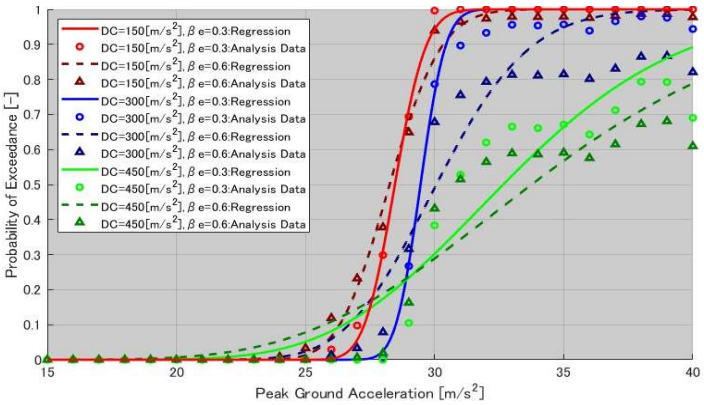

Figure 11. Fragility Curve

Table III. Regression Fragility Curve Am and β List

	DC=150, β_e=0.3	DC=150, β_e=0.6	DC=300, β_e=0.3	DC=300, β_e=0.6	DC=450, β_e=0.3	DC=450, β_e=0.6
Am	28.5	28.3	29.4	30.1	32.7	33.8
β	0.033	0.055	0.026	0.093	0.163	0.212

Fig.10 shows the probability density function given a log-normal distribution for the 30 points plotted for one PGA in Fig.9. We calculated the probability of damage: P_n by comparing log-normal distribution with DC.

Fig. 11 plots the damage probabilities for PGA values from 1 to 40 m/s², as calculated in Fig. 10. We rescaled the x axis to display PGA from 15 to 40 m/s². The solid line plots the regression fragility curve obtained by nonlinear optimization with β_e=0.3, the dashed line plots the regression fragility curve obtained by nonlinear optimization with β_e=0.6, and the markers plot the analysis data. Table.3 shows that β increases for β_e = 0.6 compared to β_e = 0.3 for all DC, indicating that the regression fragility curve for β_e = 0.6 rises more slowly than that for β_e = 0.3. This occurs because using β_e = 0.6 as the log-normal standard deviation in Fig. 10 yields a distribution wider than β_e = 0.3. From figures 9 and 11, we considered when DC is low, the floor response exceeds DC before variability in response arises, resulting in a small fragility-curve β. Therefore, for DC = 150 m/s², the damage probability increases sharply. While when DC is high, collision uncertainty increases response variability, which raises the fragility-curve β. For DC = 300 and 450 m/s², beyond a PGA of 35 m/s² —where significant large collisions occur— the gap between models that exceed DC and those that do not widen, resulting in damage probability increasing gradually than DC = 150 m/s².

V. CONCLUSIONS

In this study, we performed a risk assessment of damage to internal equipment caused by retaining wall collisions in seismically isolated nuclear reactor buildings. To consider aleatory uncertainty in structural model parameters, we generated 30 structural models using Latin Hypercube Sampling. We generated uniform hazard spectra using an amplitude envelope function and conducted nonlinear time history analyses with input ground motions having peak ground accelerations of 1 to 40 m/s². From the analysis results, we compared the responses of internal equipment and the superstructure. To evaluate the failure probability of internal equipment, we developed fragility curves considering the epistemic uncertainty associated with collision. The following 3 points are clarified in this study:

(1) Previous studies mainly focused on superstructures and isolation layers. However, retaining wall collisions can also damage internal equipment. Such damage to nuclear facilities can lead to severe accidents or serious consequences.
(2) Upon collision, the uncertainty associated with impact forces increases, consequently increasing the variability of floor response accelerations acting on internal equipment.
(3) When DC is high, the increased uncertainty due to collisions results in greater variability of responses, thus increasing the uncertainty parameter β of the fragility curve.

Attention should be paid to the design capacity and clearance between the retaining wall and the isolation layer. In future research, we will design and evaluate seismically isolated structures to optimize the balance between risk and cost.

389

REFERENCES

[1] Y.MARA,Y.AEB,Y.GOTO,S.MORO and T.YAMAGUCHI , "Seismic Load Mitigation on LMFBR Reactor Building," *Atomic Energy Society of Japan*, 29,48-57 (1987)
[2] E,TADA, K.HADA and T.MARURO" Approach for Safety Assurance and Structural Integrity of ITER", *J. Plasma Fusion Res*, 78 ,1145-1156 (2002)
[3] S.KITAMURA,M.MORISHITA,S.YAZAWA and K.HIRATA," Ultimate behavior test of seismically isolated FBR plants with a large shaking (1) whole scheme " , *Atomic Energy Society of Japan Fall Meeting* (2008)
[4] S.KASAI,M.MAKOTO,K.MORIYA,T.IIKURA, "Development Status of HPABWRHPAPWR Interim Evaluation and Future Development Plans, " *Atomic Energy Society of Japan,*53,52-56 (2011)
[5] S.OKAMURA et al "Research and Development of Three-Dimensional Isolation System for SFR (Concept of Isolation System and Development Plan)", *Japan Society of Mechanical Engineers*, (2022)
[6] R.NAKANISHI et all," Fragility evaluation of base-isolated building : Part1: Seismic response analysis considering bumping against retaining wall", *Proceedings of the Architectural Institute of Japan*, B2, PP941-942(2007)
[7] T.NAKAZAWA et al, "Fundamental Study on Probabilistic Evaluation of the Ultimate State of Base Isolated Structures", *Transactions of AIJ. Journal of structural and construction engineering,* No.662, pp745-754
[8] A. SAREBANHA, G. MOSQUENDA, M. K. KIM, J. H. KIM," Effect of Moat Wall Impact on the Seismic Response of base Isolated Nuclear Power Plants", *16th World Conference on Earthquake*
[9] K.HIRATA,Y.OHTORI and T.SOMAKI, "Seismic Fragility Analysis for Base- Isolated Structure" *Transactions of AIJ. Journal of structural and construction engineering*, No.452, pp11-19
[10] Ark information system, seismic resistant and structure analysis series TDAPIII, https://www.ark-info sys.co.jp/jp/product/tdap/tdap3/
[11] R.KOMINE ,Y.OHTORI "Preliminary research on Risk Assessment of Seismic Isolation system considering ultimate characteristics of laminated rubber bearing" , *Japan Society of Mechanical Engineers (No20-11) Dynamics and Design Conference collection of lectures,* (2020)
[12] G.MIWATA et al "Experiments and Simulation Analysis of Collision to Retaining Wall with Real Scale Base-Isolated Building", unpublished,(2010)
[13] S.YABANA,K.KANAWAZA,S.NAGATA,KHIRATA,M.MOTOHASHI,S.KITAMURA," Ultimate Behavior of Base Isolated Structure Model Using E-defense Shaking Table" , N13,116 (2011)
[14] "A Study on the Analysis Time Step Required for Retaining-Wall Impacts in Base-Isolated Structures" , https://www.unions.co.jp/dqs/dynamic/techinfo/files/47.pdf (2018)
[15] Y.KIKUCHI," Seismic Safety Evaluation of Base-Isolated Structures", Ph.D. dissertation, Hokkaido University,1995
[16] Y.HAYASHI," Seismic Risk Evaluation of Existing RC Buildings Based on Seismic Performance Indices", "Social Safety Science",No.2, pp235-242,(2000)
[17] "Homepage of Mineo Takayama" https://www.4menshin.net/report/b_vol13/vol13_2.html, (2004)
[18] G.SHINDO," Fragility evaluation of base-isolated building : Part2 : Evaluation of fragility curve considering bumping against retaining wall", *Proceedings of the Architectural Institute of Japan*, B2, PP943-944(2007)
[19] H.TSUNEKAWA,M.FUZIMURA,Y.SATO,H.OKAMOTO," Probable Maximum Loss Based Seismic Performance Estimates of Reinforced Concrete Using Member-to-Member Dynamic Elasto-Plastic Analyses", *AIJ J. Technol Des* ,Vol.17, No.35, pp37-42,2011
[20] Y.KATAYAMA, "Trial design of box culverts using damage probability as an indicator2021" , unpublished ,(2022)
[21] Armin Masroor and Gilberto Mosqueda," Seismic Response of Base Isolated Buildings Considering Pounding to Moat Walls", *Technical Report MCEER-13-0003*,pp188-190,2013
[22] H.MIYANO et al "Standard of the Atomic Energy Society of Japan Criteria for Probabilistic Safety Assessment of Nuclear Power Plants due to Earthquakes",P346, Atomic Energy Society of Japan, Tokyo, 2007

ASRAM2025
www.asram2025.org
Asian Symposium on Risk Assessment and Management 2025
Pattaya, Thailand, 27 – 29 August 2025

Fragility Evaluation of Electrical Raceway Considering Realistic Capacity of Cables against Earthquake and Its Effect on Seismic PRA

Ryusuke Haraguchi[1], Tomokazu Higuchi[2], Kinji Nakano[3], Shinichi Hisatomi[4], Hidenori Takamatsu[5], Michiyoshi Satou[6], Kento Furuya[7], Kenta Kobayashi[8] and Mitsuru Imamura[9]

[1] *Mitsubishi Heavy Industries, LTD.: 1-1-1, Wadasaki-cho, Hyogo-ku, Kobe, Hyogo, JAPAN,6520846, ryusuke.haraguchi.j3@nu.mhi.com*
[2] *Toshiba Energy Systems & Solutions Corp.: 8,Shinsugita-cho, Isogo-ku, Yokohama, Kanagawa, JAPAN, 2358523, tomokazu.higuchi@toshiba.co.jp*
[3] *Hitachi-GE Nuclear Energy, Ltd.: 3-1-1, Saiwai-cho, Hitachi,Ibaraki, JAPAN, 3170073, kinji.nakano.ty@hitachi.com*
[4] *Tokyo Electric Power Company Holdings, Inc.: 2-2-1, Toranomon, Minato-ku, Tokyo, JAPAN, 1050001, hisatomi.shinichi@tepco.co.jp*
[5] *Tokyo Electric Power Company Holdings, Inc.: 2-2-1, Toranomon, Minato-ku, Tokyo, JAPAN, 1050001, takamatsu.h@tepco.co.jp*
[6] *Tokyo Electric Power Company Holdings, Inc.: 2-2-1,Toranomon, Minato-ku, Tokyo, JAPAN, 1050001, satou.michiyoshi@tepco.co.jp*
[7] *Tokyo Electric Power Company Holdings, Inc.: 2-2-1, Toranomon, Minato-ku, Tokyo, JAPAN, 1050001, furuya.kento@tepco.co.jp*
[8] *Hokkaido Electric Power Company, Inc.: 2, Higashi 1-chome, Odori, Chuo-ku,Sapporo, Hokkaido, JAPAN, 0608677, kentakoba@hepco.co.jp*
[9] *Hokkaido Electric Power Company, Inc.: 2, Higashi 1-chome, Odori, Chuo-ku,Sapporo, Hokkaido, JAPAN, 0608677, m-imamura@hepco.co.jp*

ABSTRACT

In the current seismic Probabilistic Risk Assessment and stress tests conducted in Japan, the following conservative assumptions are made regarding the damage to electrical systems:
- The fragility of the least seismically robust electrical raceway is used as the representative.
- Failure of the electrical raceway is assumed to directly lead to core damage.
- Structural damage of cable tray is assumed to result in a total failure of the electrical raceway, ignoring the integrity of the cable.

Due to these assumptions, electrical raceways can become the dominant contributor in core damage when the seismic margin of the cable tray is not sufficiently large. In this study, we examined the calculation of cable fragility and electrical raceway fragility by referencing realistic assessments of cable strength after cable tray damage caused by earthquakes. Here, since cable damage occurs after cable tray damage, the fragility of the electrical raceway was evaluated as a conditional probability given the damage to the cable tray.

Furthermore, we assessed the effect on seismic Probabilistic Risk Assessment and stress tests when considering the realistic fragility of electrical raceways derived in this study, as opposed to the conventional conservative assumptions.
The results of this study enable improvements in the conservative assumptions regarding electrical raceways in seismic Probabilistic Risk Assessment , allowing for more realistic evaluations. Additionally, by further enriching information on cable strength, it is possible to advance studies on screening out electrical raceways from seismic Probabilistic Risk Assessment .

Keywords: Seismic PRA, Fragility, Electrical system, Cables, Realistic capacity

I. Introduction

Since the establishment of the first seismic Probabilistic Risk Assessment (PRA) standard by the Atomic Energy Society of Japan in 2007, risk information based on seismic PRA has played a crucial role in the licensing processes of regulatory authorities and in the voluntary safety enhancement activities of power companies. Additionally, as part of the activities called “Safety Assessment Report” in Japan, stress tests based on fragility as an indicator are also conducted. However, several

significant assumptions exist in the current seismic PRA and stress tests regarding electrical raceways, which influence the risk assessment.

First, as the primary assumption, it is considered that damage to electrical raceways leads directly to core damage. This assumption is adopted conservatively due to the difficulty in clarifying the impacts of damage to specific circuits, given that electrical circuits are related to many system functions within the plant.

The second assumption is that the electrical raceway with the lowest seismic margin is treated as representative, and the fragility of this representative electrical raceway is applied to all electrical raceways. This assumption arises from the difficulty of assigning fragility to each individual circuit, considering the numerous circuits subject to evaluation and the need to take into account their installation locations and the impacts during damage.

The third assumption posits that if cable trays or their supporting structures are damaged, the electrical raceways will lose functionality even if the cables remain functionally sound. This assumption is conservatively set due to the lack of information regarding the ability of cables to maintain electrical functionality following damage to cable trays caused by earthquakes.

These assumptions imply that if the seismic margin of cable trays is low, they could become a dominant factor contributing to core damage. Furthermore, even if a fragility assessment based on conservative assumptions yields results indicating significant contributions from electrical raceways, it cannot be easily claimed that such results are appropriate as risk information. In light of this background, this study proposes a fragility assessment method for cables following damage to cable trays, based on the results of strength tests and seismic response analyses. Should this study demonstrate that the probability of cable damage due to earthquakes is sufficiently low, it may be possible to screen out electrical raceways in seismic PRA and stress tests. For this research, three representative plants have been selected from Japanese Boiling Water Reactors (BWR) and Pressurized Water Reactors (PWR), referred to as Plant A (BWR), Plant B (BWR), and Plant C (PWR) in the following sections.

II. Selection of Evaluation Targets and Representative Cables

The cables used in nuclear power plants include metal cables and optical fiber cables. Since optical fiber cables can be considered structurally more robust than metal cables, they are excluded from direct consideration, as the evaluation can be encompassed by focusing on metal cables. Regarding the electrical conduits, the internal cables are the same as those in the cable trays, and the potential for damage is considered as follows. References [1][2] have conducted vibration tests to evaluate the strength of small-diameter piping with a diameter of 4 inches or less, and the results indicate that there is no damage even under seismic motions several times greater than the design earthquake motion. Based on this, it can be concluded that the electrical conduits are unlikely to sustain damage under realistically occurring seismic motions, and the possibility of breakage or falling that would affect the internal cables is also unlikely to occur. Therefore, the focus of this study will be on metal cables installed on cable trays. A comprehensive survey was conducted on metal cables used in safety systems and severe accident mitigation systems of PWRs and BWRs, covering cables related to high-pressure power, low-pressure power, control, and instrumentation. The specifications regarding the structure, dimensions, weight per unit length, and materials used for the cables were organized[3]. Based on the frequency and distribution of items related to cable strength, representative cables for analysis and testing were selected[3]. Examples of the representative cables selected, along with the specifications obtained from subsequent tests, are shown in Table 1.

Table 1: Specification of the representative cables (Plant A:BWR)[3]

Cable No.	Ac1	Ac2	Ac3	Ac4	Ac5	Ac6	Ac7	Ac8	Ac9	Remarks
Cable Outer Diameter [mm]	9	6.9	7.5	8	13	15.5	19	26	35	
Cross-sectional area (Total core wire) [mm^2]	1.25	2	3.5	5.5	38	60	100	200	400	
Number of cores	2	27	8	4	2	3	2	3	1	
Number of wires	7	7	7	7	7	19	19	37	61	
Modulus of Elasticity E [MPa]*1	10232	8960	8169	9557	10025	8019	5192	7565	5129	Test results
Poisson's ratio [-]	0.145	0.145	0.145	0.145	0.145	0.145	0.145	0.145	0.145	
Second moment of area [mm^4]	1.384E-02	4.453E-02	1.373E-01	3.301E-01	1.821E+01	1.516E+01	3.925E+01	7.548E+01	1.953E+02	
Approximate mass [kg/km]	100	75	95	110	445	680	1070	2080	4030	
Density ρ [t/mm^3]	8.000E-08	3.750E-08	2.714E-08	2.000E-08	1.171E-08	1.133E-08	1.070E-08	1.040E-08	1.008E-08	
0.2% offset yield strength [MPa]	168.7	180.3	178.3	181.1	227.2	225.5	212.7	242.9	195.9	Test results

(*1) The modulus of elasticity E at dogleg fracture shall be 10 times the stated value.

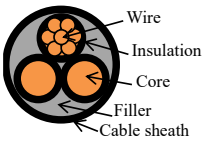

Cross section of the metal cable
(conceptual view)

III. Seismic Evaluation of Cables After Cable Tray Damage

This section presents the tests conducted to obtain the realistic strength of the cables and the evaluation of the cable response that is assumed to occur after damage to the cable trays due to an earthquake. These serve as input information for the fragility assessment of the cables.

III.A. Cable Strength Tests

Strength tests were conducted on the target cables to obtain realistic strength values and the material properties (longitudinal elastic modulus) used in subsequent analyses [3]. It is considered that if the stress experienced by the cable remains within the range corresponding to a strain of 0.2% offset yield strength, the cable will not fracture. Additionally, the effects of reduced cross-sectional area of the core conductor due to cable strain and the reduction in insulation thickness on insulation integrity are deemed to be within acceptable limits, allowing for the maintenance of integrity from both mechanical strength and electrical functionality perspectives. Therefore, in this study, the 0.2% offset yield strength obtained from the stress-strain curve of tensile tests was adopted as the strength of the metal cables. The specifications obtained from the tests are presented in Table 1.

III.B. Cable Tray Damage Modes

To evaluate the seismic resistance of cables, it is necessary to examine the loads applied to the cables following damage to the cable trays due to an earthquake. Consequently, various damage modes of the cable trays were considered to represent the cable conditions after damage. Multiple potential damage states of the cable trays were established, and for each damage state, the trends of loads acting on the cables when the cable trays are damaged were considered in selecting evaluation cases for the damage modes referenced in the fragility assessment [3]. For reference, a conceptual diagram of the structure of the cable tray is shown in Figure 1. Additionally, conceptual diagrams of each damage case are shown in Figure 2.

Case 1: Basic damage condition; a base case considering the state where the cable tray has fallen off.
Case 2: Set as a case due to the observed trend of increased moment and axial force compared to the base case, considering the excess length of the cable.
Case 3: Set as a case where the increased length of the fallen cable tray leads to increased loads compared to the base case.
Case 4: A case focusing on the state where the cable tray has fallen off on both sides and is resting on the cable.
Case 5: A case focusing on the state where the fallen cable tray bends in a V shape, applying concentrated loads to the center of the cable.

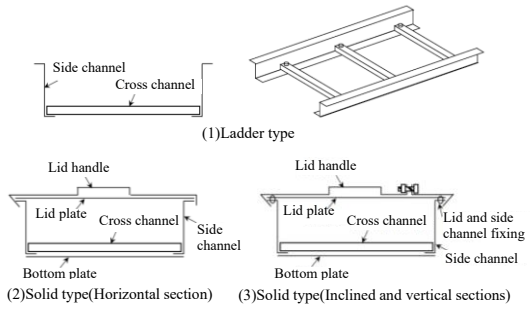

Figure 1: Example of cable tray types and covers[3]

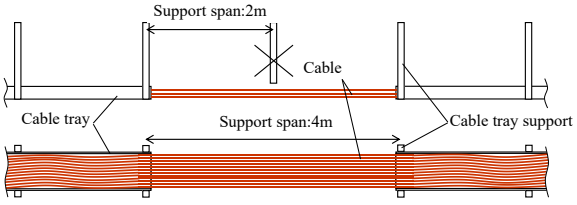

Figure 2(a): Cable tray damage mode: Case 1(base case) [3]

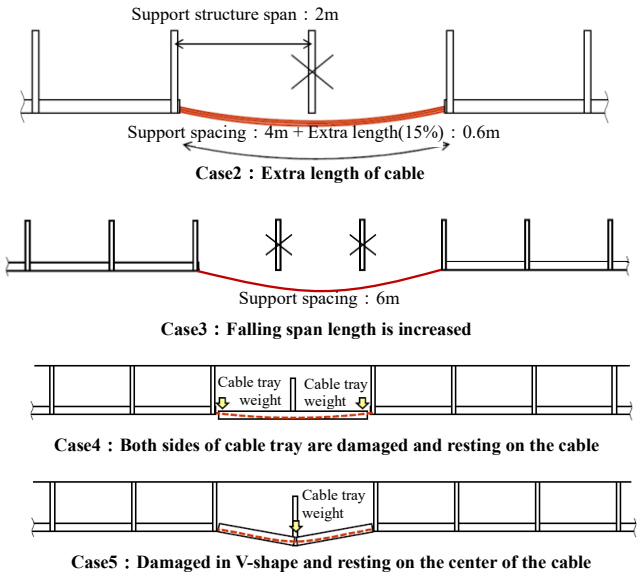

Figure 2(b): Cable tray damage mode : Case 2 through 5[3]

III.C. Response Analysis

Beam models capable of simulating the displacement state of cables during cable tray fall were created, and response analyses of the cables following cable tray damage were conducted [3]. The specifications of the cables used were those obtained from the aforementioned tests (see Table 1), and the seismic acceleration was based on the design floor response acceleration of the representative plant (horizontal: 2.05G, vertical: 0.88G). The results of the maximum values of the responses (von Mises stress) obtained from the analyses for each case shown in the previous section, along with comparisons to the capacity, are presented in Figure 3, and the margins (capacity/von Mises stress maximum value) are shown in Table 2.

III.D. Summary of Seismic Evaluation

It was demonstrated that even under the assumption that the design basis seismic motion acted while the cable tray was damaged and had fallen, cable damage would not occur (the stress generated in the analysis does not exceed the capacity values obtained from the tests). From the perspective of margin, it is generally observed to be approximately 3 to 8 times greater than the design basis seismic motion, with many cases exceeding 10 times, and even in the most severe cases, the margin exceeds 2 [3]. This indicates that even when considering the possibility of cable tray damage, the cables maintain their functionality as electrical raceways and possess sufficient margins against the design basis seismic motion. Furthermore, this analysis includes several conservative assumptions, such as:

- The maximum floor response due to the design basis seismic motion continues after the cable tray has fallen.
- The adoption of 0.2% offset yield strength as the capacity value for maintaining the electrical functionality of the cables.
- The response analysis was conducted using static analysis.

Considering the conservativeness introduced by these assumptions, it is believed that the margin of the cables against the design basis seismic motion is even larger. And realistically, even when assuming cable tray damage, the cables are expected to have several times the strength required to maintain their electrical functionality against the design basis seismic motion.

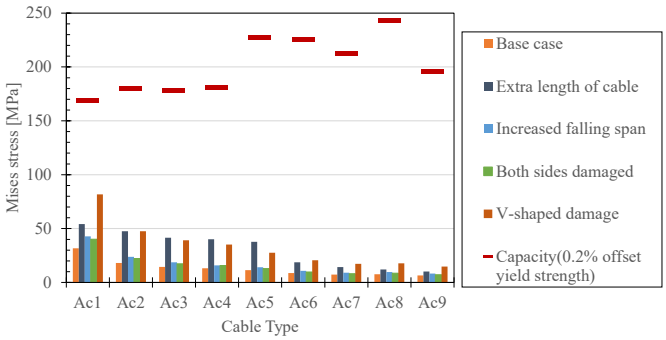

Figure 3: Results of analyses (Plant A): Comparison between stress and capacity [3]

Table 2: Seismic margin of cable (Plant A) [3]

Cable	Seismic margin				
	Base case	Extra length of cable	Increased falling span	Both sides damaged	V-shaped damage
Ac1	5.3	3.1	3.9	4.2	2.1
Ac2	10.0	3.8	7.6	8.1	3.8
Ac3	12.3	4.3	9.6	10.3	4.6
Ac4	13.7	4.5	11.5	11.6	5.1
Ac5	19.8	6.0	16.2	17.6	8.2
Ac6	26.0	12.1	20.9	23.2	10.9
Ac7	29.0	14.9	23.4	26.0	12.3
Ac8	31.7	20.1	25.2	28.5	13.7
Ac9	30.2	19.2	23.9	27.3	13.2

IV. Fragility Assessment of Cables

This section outlines the methodology for conducting a fragility assessment of electrical raceways using the results of the strength tests and cable response analyses that follow cable tray damage discussed in previous sections. Generally, fragility assessments consider both structural damage modes and functional damage modes. In the case of electrical raceways, the focus is on whether the electrical functionality is maintained. Therefore, this assessment will concentrate on functional damage modes, treating the "0.2% offset yield strength" of the cables as the capacity related to functional damage (maintenance of electrical functionality) and the stress experienced by the cables as an indicator.

Next, the uncertainties associated with the realistic capacity distribution and realistic response distribution, which are considered in the calculation of damage probabilities in the fragility assessment focusing on cables, were analyzed. The major uncertainty factors are outlined below.

Uncertainty Factors Related to Strength

· Uncertainty in Material Properties of the Cable Core Wire: Variability in the material properties governing the strength of the cable core wire introduces uncertainty in the cable's capacity. However, since quality control is rigorously implemented for nuclear-grade cables, this variability leads to minimal uncertainty regarding capacity.

· Uncertainty in Cable Manufacturing Precision: Variability in product precision during the cable manufacturing process contributes to uncertainty in the cable's capacity. Nonetheless, due to stringent quality control for nuclear-grade cables, this uncertainty is also minimal.

· Uncertainty in the Strength of Components Other than the Cable Core Wire: The strength of the cable is considered to be predominantly determined by the core; however, contributions to the capacity from components other than the core wire, such as the cable sheath and insulation, and different configurations across cables may introduce uncertainty in the cable's capacity. On the other hand, the contribution of components other than core wire to the cable's capacity is small because the behavior (such as elongation) of the core wire and non-core wire components differs when subjected to loads. Additionally, the influence of the configurations of non-core wire components on capacity is not significant. Therefore, it can be stated that the uncertainty in cable's capacity due to these factors is small.

· Uncertainty in Testing Methods: The selection of test samples, testing methods, and data organization are considered to be factors that contribute to the uncertainty in the realistic capacity obtained from the tests. Given the challenges associated with narrowing down test samples from a variety of cable types and the complexities involved in securing cables during strength tests, it can be stated that this uncertainty is significant.

· Uncertainty in the Limit Capacity: The limit capacity for maintaining cable functionality is set at "0.2% offset yield strength," which is somewhat conservative. However, there is a lack of information regarding the conditions under which cable's functionality may be lost, necessitating the consideration of uncertainty. On the other hand, it is evident that if plastic deformation occurs, leading to a change in the cross-sectional area of the cable, electrical functionality cannot be maintained, indicating that the uncertainty regarding this limit capacity setting is small.

· Uncertainty Regarding Actual Cable Installation Conditions: Variability in conditions such as the type, position, application, and routing of cable trays in actual plants contributes to uncertainty in capacity. The diversity in the types and quantities of cables mounted on cable trays results in significant uncertainty in capacity.

Uncertainty Factors Related to Response

· Uncertainty in Modeling for Analysis: The uncertainties associated with the modeling of cable response analyses are taken into account. The analysis model used in this study is a beam model, which is considered to have more uncertainty compared to a solid model that would replicate the structure in detail.

· Uncertainty in Analysis Methods: When conducting response analyses using the spectral modal method, it is necessary to consider uncertainties due to mode combination.

· Uncertainty in Nonlinear Response: If fragility evaluation methods that assume a linear relationship between input and response, such as the SOV(Separation of Variables) method (also known as the Zion method), are used, the effects of nonlinear responses of buildings and equipment during increased input seismic motions (deviations from linear assumptions) must be considered as uncertainties. (For details on the SOV method, refer to the EPRI Fragility Assessment Guides (e.g., References [4][5]) and the Japan Atomic Energy Society's Seismic PRA Standards.)

· Uncertainty Regarding Cable Tray Damage Modes: The differences in responses due to various damage mode cases of cable trays (e.g., both side damaged, V-shaped damaged, extra length of cable, etc.) should be considered as uncertainties.

· Uncertainty Regarding Cable Types: The differences in responses based on the types of cables mounted on the cable trays should also be considered as uncertainties. Given the diversity of cable types actually used, this uncertainty is significant.

Based on the results of the tests and the analyses, the median values for capacity and response can be obtained, and by quantifying the uncertainties outlined above, the capacity distribution and response distribution can be established to determine the fragility of the cables. When conducting fragility assessments using the SOV method, safety factors corresponding to the analyzed uncertainty factors will be introduced for evaluation. Here, the results of the fragility assessment for the cables of Plant A, one of the representative plants, are provided as an example using the SOV method.

The fragility is evaluated using the following equations:

$$A_m = F \times D_{PGA}, \quad \mathrm{HCLPF} = A_m \times \exp\left(-1.65 \times (\beta_R + \beta_U)\right) \tag{1}$$

where:

A_m: Median fragility, F: Safety factor, D_{PGA}: Peak ground acceleration of the design earthquake
β_R: Total aleatory uncertainty, β_U: Total epistemic uncertainty

The safety factor F is expressed as:

$$F = F_C \times F_R \tag{2}$$

where:

F_C: Capacity factor, F_R: Response factor

The capacity and response factors, along with their uncertainties, are further subdivided for evaluation based on their respective conservatisms and uncertainty factors. In this assessment, the uncertainties related to the damage modes of cable trays and the types of cables were focused on, leading to the introduction of a factor F_{CSS} corresponding to these uncertainties in the response factor. Therefore, the response factor F_R is expressed as follows:

$$F_R = F_{ESS} \times F_D \times F_{EMC} \times F_{EM} \times F_{CSS} \times F_{SR} \tag{3}$$

where:

F_{ESS}: Spectral shape factor accounting for uncertainties in the evaluated floor response,
F_D: Damping factor accounting for uncertainties in response due to damping,
F_{EMC}: Mode combination factor related to uncertainties in combining vibration modes of response,
F_{EM}: Modeling factor related to modeling assumptions for analysis,
F_{CSS}: Factor to account for uncertainties in response due to cable tray damage modes and cable types,
F_{SR}: Building response Factor

This factor F_{CSS} is evaluated based on the variability observed when comprehensively reviewing the response analysis results presented in the previous section. The capacity, material properties, and their variability from the test results, along with the cable response analysis results (with an input seismic motion of 1.23G), were used as inputs for the fragility evaluation. The calculations were based on the largest response values obtained from the cable response analyses, resulting in A_m=10.15G、β_R=0.2, β_U=0.46 and HCLPF=3.24G. Additionally, for the evaluation focusing on the most severe case of V-shaped damage as one cable tray damage mode, the results were A_m=5.21G、β_R=0.23, β_U=0.54 and HCLPF=1.54G. It should be noted that these results are specific to Plant A and may differ in other plants.

In this evaluation, a representative fragility was derived by compiling the response analysis results of various cable tray damage modes and cable types, leading to a significant overall uncertainty. Therefore, if the scope of the evaluation can be narrowed, it is believed that the uncertainties could be reduced, allowing for further improvements in the fragility results. Furthermore, since the SOV method assumes a linear relationship between input and response and does not consider changes in response trend due to nonlinear behavior, this results in a conservative assessment of responses during increased input seismic motions, leading to an overestimation of damage probabilities. A more realistic evaluation could be achieved by constructing fragility curves based on damage probabilities calculated from response analyses conducted at varying levels of input seismic motion.

Additionally, it is important to note that this fragility assessment does not take into account the probabilities of occurrence for each cable tray damage mode. If the occurrence probabilities and weighting in the overall assessment could be established, a more realistic fragility could be obtained, which remains a challenge for future work. Therefore, the fragility assessment conducted using the methods described here yields somewhat conservative results, also taking into account the influences of conservatism in the response analyses discussed in the previous section. However, it is deemed feasible to incorporate this into the operational practices of actual plants as a conservative evaluation at this stage.

V. Fragility of Electrical Raceway

As mentioned in the Introduction, there was a lack of information regarding the integrity of the electrical functionality of cables following cable tray damage due to earthquakes. Consequently, the current evaluation assumes that if the cable trays or their supporting structures are damaged, the cables will invariably lose their functionality as electrical raceways, regardless of their condition. However, with the findings of this study enabling the assessment of cable fragility after cable tray damage, this assumption can be revisited. It can be stated that the cables themselves will not sustain damage unless the cable trays are damaged. In other words, the probability of cable damage can be viewed as a conditional probability based on the damage to the cable trays, and the fragility of the electrical raceway can be expressed as:

$$\text{Probability of loss of funciton of electrical raceway} = (\text{Probability of cable tray damage}) \times (\text{Probability of cable damage}) \quad (4)$$

Therefore, by considering the probability of cable damage, the current assumption that cable tray damage equates to electrical raceway damage (loss of functionality) will invariably improve. An illustration of the fragility curve of the electrical raceway when considering the probabilities of damage to both the cable trays and cables is shown in Figure 4.

VI. Integration into Accident Sequence Evaluation

In the current practice of the seismic PRA, as shown in Figure 5, the functional damage of electrical raceway is assumed to directly lead to core damage. Thus, as mentioned earlier, the fragility evaluation assumes that cable tray damage equals the loss of electrical raceway functionality, which may make the structural damage of representative cable trays a dominant factor contributing to core damage. Such evaluation results raise concerns that other significant risk factors may be obscured (relatively underestimated), and it cannot be claimed that appropriate risk information regarding plant safety improvement is obtained. On the other hand, while it may be technically possible to relate the individual fragility of electrical raceways located in various systems and places within the plant to the accident sequence evaluation model (event tree and fault tree), it is practically very challenging for actual plants due to the costs and time required for the evaluation. Therefore, it is not feasible to revise the evaluation from the perspective of accident sequence modeling. However, with the results of this study allowing for the assessment of cable fragility after cable tray damage, it has become possible to realistically consider the probability of functional damage to electrical raceways in accident sequence evaluations. The probability of electrical raceway damage can be incorporated in the fault tree related to electrical raceway functional damage by introducing an AND gate for cable tray damage and cable damage, as shown in Figure 6. As a result, while conservative assumptions regarding the events resulted from the loss of electrical raceway functionality remain, a more realistic evaluation of the occurrence probability of electrical raceway damage can improve the frequency of core damage and provide a more accurate understanding of the overall risk profile of the plant. Furthermore, if it can be generally stated that the probability of electrical raceway damage due to earthquakes is sufficiently low within the defined range of probabilistic seismic hazard, it may also be possible to screen out electrical raceways from seismic PRA.

From the perspective of stress tests, electrical raceways are related to various headings in the event tree. If the fragility of the cable trays (HCLPF) is not large enough, the electrical raceways may become equipment that represents a cliff edge of the plant. Additionally, as electrical raceways are factors that govern numerous headings in the event tree, the information regarding the plant's risk profile that will be obtained as a result of the stress test may become unclear. Similarly to the seismic PRA case, by introducing the fragility of the cables after cable tray damage into the assessment of electrical raceway fragility, it will become possible to evaluate the strength of each heading and cliff edge of the plant more accurately. If it can be demonstrated that the fragility of the electrical raceway is sufficiently high (compared to the general cliff edge acceleration), it is possible to screen out electrical raceways from stress tests and contribute to rationalizing the evaluation.

VII. Conclusion

This study focused on the conservative assumption in seismic PRA that electrical raceways lose functionality due to cable tray damage, and aimed to provide a more realistic assessment by evaluating the fragility of cables by using the results of cable strength tests and response analyses. The evaluation method is based on the widely used SOV method (also known as the Zion method), and a new factor addressing uncertainties related to cable response was developed for the evaluation. Using this method, fragility evaluations of cables were conducted based on the data from cable strength tests and response analyses. The results of the evaluations indicated that by taking into consideration the influence of the remaining conservatism and the probability of cable tray damage, the fragility related to maintaining the functionality of the electrical raceways could be expected to allow for the screening out of the electrical raceways from the seismic PRA. The findings of this study indicate

that it has become feasible to apply the evaluation of cable fragility and the corresponding fragility of electrical raceways to the seismic PRA of individual plants. In the future, plans are in place to conduct shaking tests simulating the state of cable tray falls to obtain a more realistic response of the cables. Further details on this will be reported in future papers.

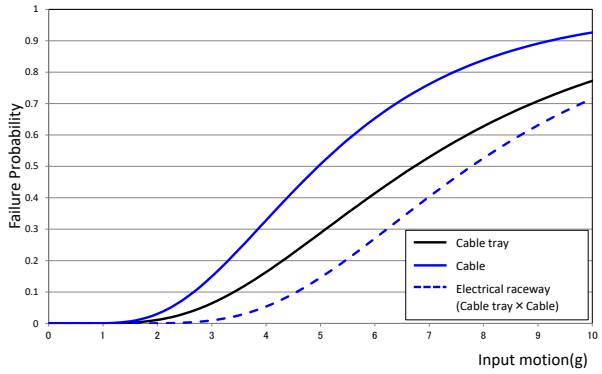

Figure 4: An image of the electrical raceway fragility curve

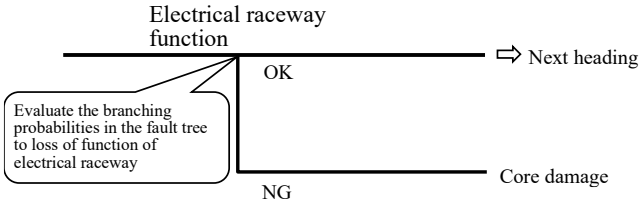

Figure 5: A highly simplified conceptual illustration of the event tree regarding the failure of electrical raceway

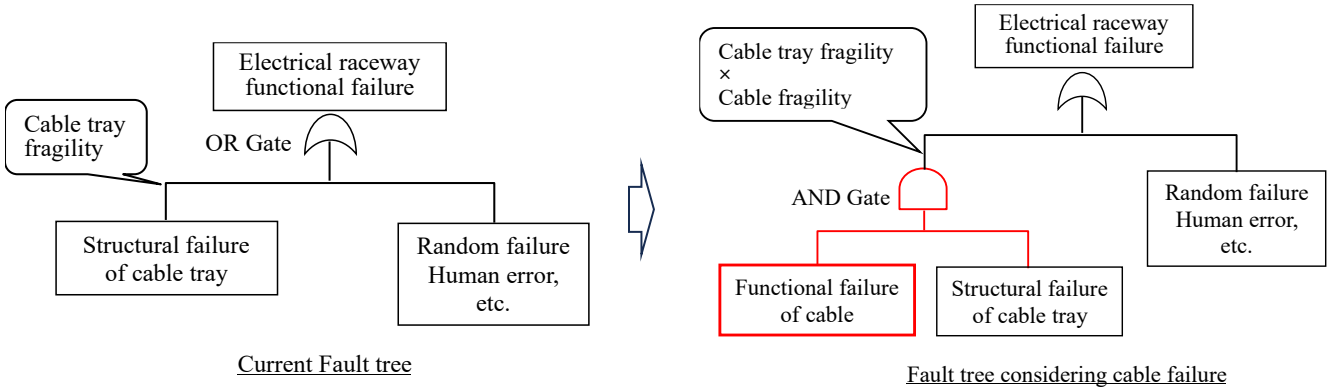

Figure 6: Fault tree related to electrical raceway functional failure

ACKNOWLEDGMENTS

This research was conducted with the support of Tokyo Electric Power Company Holdings, Hokkaido Electric Power Company, Tohoku Electric Power Company, Chubu Electric Power Company, Hokuriku Electric Power Company, Chugoku Electric Power Company, Shikoku Electric Power Company, Kyushu Electric Power Company, Japan Atomic Power Company, Electric Power Development Co., Ltd., and Japan Nuclear Fuel Limited, commissioned to Mitsubishi Heavy Industries, Toshiba ESS, and Hitachi GE. We deeply appreciate the support from all companies involved in this research.

REFERENCES

[1] Takami ISHIGURO, et al. (2009). “Study on Seismic Design Margin based upon Inelastic Shaking Test of the Piping and Support System”, *ICAPP ’09*.
[2] Takami ISHIGURO.(2010). ” Seismic Safety of Small-Diameter Piping Systems: Seismic Verification Tests of Full-Scale Piping Systems Using a Large Scale Shaking Table,” *Piping Engineering, vol.52, No.4, 18-26*.
[3] R.Haraguchi, et al. “Seismic Evaluation of Cables for Improvement of Electrical Raceway Fragility in Nuclear Power Plants”, SMiRT 28, Toronto, Canada, August 10-15, 2025
[4] Methodology for Developing Seismic Fragilities, TR-103959, EPRI, 1994.
[5] Seismic Fragility Applications Guide Update EPRI TR-1019200, EPRI, 2009.

ASRAM2025
www.asram2025.org
Asian Symposium on Risk Assessment and Management 2025
Pattaya, Thailand, 27 – 29 August 2025

A MONTE CARLO TECHNIQUE TO PROPAGATE THE UNCERTAINTY OF SEISMICALLY INDUCED JOINT FAILURE PROBABILITY

Shota Soga[1,2*], Eishiro Higo[1], Sunghyon Jang[2], Munemichi Kawaguchi[2], Hiromichi Miura[1]

[1] *Central Research Institute of Electric Power Industry, 2-6-1, Nagasaka, Yokosuka, Kanagawa, 240-0196, Japan, soga@criepi.denken.or.jp**
[2] *Graduate School of Engineering, Hokkaido University, Kita 13-jo, Nishi 8-chome, Kita-ku, Sapporo, Hokkaido 060-8628, Japan, soga@criepi.denken.or.jp**
*Corresponding author

ABSTRACT

Earthquakes are a significant contributor to the risk of nuclear power plants in Japan. An earthquake has the potential to cause simultaneous damage to multiple redundant components, and seismic probabilistic risk assessment quantitatively addresses such a risk. While several approaches have been proposed to estimate the mean value of the seismically induced joint failure probability of multiple components, the propagation of its uncertainty remains an unresolved issue that requires further investigation. This paper addresses this issue and proposes a technique to propagate the uncertainty of the seismically induced joint failure probability of multiple components. First, we review one of the major failure criteria in seismic probabilistic risk assessment. Then, we discuss how to convert this failure criterion into the mean value of the joint failure probability of multiple components. We develop a simple Monte Carlo technique to propagate the uncertainty of the seismic joint failure probability. We provide a numerical demonstration of the proposed technique, showing that the mean value obtained from the constructed distribution of joint failure probability agrees with the expected mean value derived from the multivariate normal model. The proposed algorithm enables uncertainty analysis of the seismically induced joint failure probability of multiple components.

Keywords: Seismically induced joint failure probability, Probability density function, Monte Carlo simulation, Uncertainty analysis, Seismic probabilistic risk assessment

I. INTRODUCTION

Earthquakes are considered one of the major risk contributors to nuclear power plants. For example, several nuclear power plants, such as North Anna Nuclear Power Station, experienced earthquakes resulting in reactor scrams [1]. In the Fukushima Daiichi nuclear power plant accident, the 2011 Tōhoku earthquake and tsunami caused core damage at three units [2]. Thus, operational experience of nuclear power plants demonstrates the need to account for seismic risks in nuclear power plants.

Seismic Probabilistic Risk Assessment (PRA) is a tool that can quantify the seismic risk of nuclear power plants. Seismic PRA estimates risk metrics, such as the core damage frequency of a unit due to an earthquake. There are several challenges in seismic PRA. Seismic fragility analysis (hereinafter referred to as fragility analysis) also presents a challenge in estimating the seismically induced joint failure probability (hereinafter referred to as joint failure probability) of structures, systems, and components (SSCs).

Fragility analysis has two challenging issues. The first issue is the lack of a consensus method to estimate correlation coefficients between seismic responses and between seismic capacities. Researchers have investigated how to estimate these correlation coefficients and their effect on the joint failure probability[3–6]. Given these correlation coefficients, fragility analysts can estimate the mean value of joint failure probability [7]. The multivariate normal (MVN) model is one such model, and there is an efficient algorithm to evaluate this model [8,9]. The second issue is that no method exists to propagate the uncertainty of joint failure probability. To the best of the authors' knowledge, there are no previous studies that investigate how to construct and propagate the uncertainty of joint failure probability, thus representing a significant methodological gap in the field.

In this paper, we address the second issue by proposing a simple Monte Carlo technique for sampling joint failure probabilities. Using the proposed technique enables fragility analysts to construct the uncertainty distribution of a joint failure

probability. In Section II, we briefly review a major failure criterion for a single SSC used in seismic PRA. Then, we extend this failure criterion to multiple SSCs. In Section III, we introduce a Monte Carlo technique to sample a seismically induced joint failure probability. In Section IV, we apply the proposed technique to a three-SSC case by propagating their epistemic uncertainties and compare its estimated mean value to that of the MVN model. In Section V, we discuss both advantages and disadvantages of the proposed techniques. Finally, in Section VI, we conclude this study.

The proposed simple technique can also be applied to another failure criterion defined in terms of seismic responses and capacities. Thus, the proposed simple technique is applicable to both failure criteria in seismic PRA.

II. Failure criteria

In Seismic PRA, the most common failure criteria for seismically induced failure of an SSC is given as [10]:

$$A > A_m \epsilon_U \epsilon_R \tag{1}$$

where A is the peak ground acceleration, A_m is the peak ground acceleration at which the mean value of response equals the mean value of capacity, ϵ_U is the random variable for epistemic uncertainty, ϵ_R is the random variable for aleatory uncertainty [7].

It is common to assume that ϵ_U, and ϵ_R follow lognormal distributions expressed as

$$\epsilon_U \sim \mathcal{LN}(0, \beta_U) \tag{2}$$
$$\epsilon_R \sim \mathcal{LN}(0, \beta_R) \tag{3}$$

where β_U, and β_R are the logarithmic standard deviations of epistemic and aleatory uncertainties, respectively.

These failure criteria can be easily extended to simultaneous failures (hereinafter referred to as joint failures) of multiple SSCs. A common failure criterion must be satisfied simultaneously across all SSCs. For example, the failure criterion for joint failure of n SSCs can be expressed in a vector form as

$$\begin{bmatrix} A \\ \vdots \\ A \\ \vdots \\ A \end{bmatrix} > \begin{bmatrix} A_{m,1}\epsilon_{U,1}\epsilon_{R,1} \\ \vdots \\ A_{m,i}\epsilon_{U,i}\epsilon_{R,i} \\ \vdots \\ A_{m,n}\epsilon_{U,n}\epsilon_{R,n} \end{bmatrix}, \tag{4}$$

where $A_{m,i}$ is the median peak acceleration of the ith SSC, and $\epsilon_{U,i}$ and $\epsilon_{R,i}$ are the random variables for epistemic and aleatory uncertainties of the ith SSC, respectively. When Eq. (4) is satisfied, all SSCs are considered to fail.

Epistemic and aleatory uncertainties are assumed to follow a multivariate lognormal distribution expressed as

$$\begin{bmatrix} \epsilon_{U,1} \\ \vdots \\ \epsilon_{U,n} \end{bmatrix} = \boldsymbol{\epsilon_U} \sim \mathcal{MLN}(\mathbf{0}, \boldsymbol{\Sigma_U}) \tag{5}$$
$$\begin{bmatrix} \epsilon_{R,1} \\ \vdots \\ \epsilon_{R,n} \end{bmatrix} = \boldsymbol{\epsilon_R} \sim \mathcal{MLN}(\mathbf{0}, \boldsymbol{\Sigma_R}), \tag{6}$$

where $\mathbf{0}$ is the zero vector, $\boldsymbol{\epsilon_U}$ and $\boldsymbol{\epsilon_R}$ are the vectors of random variables for aleatory and epistemic uncertainties, respectively, and $\boldsymbol{\Sigma_U}$ and $\boldsymbol{\Sigma_R}$ are the covariance matrices of aleatory and epistemic uncertainties. Note that these covariance matrices are expressed in terms of correlation matrices given as $\boldsymbol{\Sigma_U} = \mathrm{diag}(\boldsymbol{\beta_U})\boldsymbol{\rho_U}\mathrm{diag}(\boldsymbol{\beta_U})$ and $\boldsymbol{\Sigma_R} = \mathrm{diag}(\boldsymbol{\beta_R})\boldsymbol{\rho_R}\mathrm{diag}(\boldsymbol{\beta_R})$, where $\boldsymbol{\beta_U}$ and $\boldsymbol{\beta_R}$ are the vectors of epistemic and aleatory uncertainties, respectively and $\boldsymbol{\rho_U}$ and $\boldsymbol{\rho_R}$ are the correlation matrices of epistemic and aleatory uncertainties, respectively.

III. MONTE CARLO TECHNIQUE TO SAMPLE JOINT FAILURE PROBABILITY

In this section, we propose a Monte Carlo technique to sample the seismically induced joint failure probability of n SSCs. First, we develop a Monte Carlo technique for a single SSC, which is then extended to n SSCs.

III.A. Monte Carlo technique for a single SSC

In this section, we propose a Monte Carlo technique for calculating the seismically induced joint failure probability of a single SSC. To demonstrate the proposed technique, we focus on the propagation of epistemic uncertainty under the failure criterion.

Let us take the logarithm of Eq. (1) as $\ln A > \ln A_m + \ln \epsilon_U + \ln \epsilon_R$. The purpose of this transformation is to convert ϵ_U and ϵ_R to normal distributions. Thus, $\ln \epsilon_U$ and $\ln \epsilon_R$ follow normal distributions. This step is not mandatory but simplifies implementation.

In the next step, we sample epistemic uncertainty. Let $\ln \epsilon_{U,j}$ be the jth sampled epistemic uncertainty from a normal distribution. Note that Monte Carlo simulations do not sample the aleatory uncertainty since the aleatory uncertainty is later integrated to define a failure probability. Now, one can transform the failure criterion as follows.

$$\ln A/A_m - \ln \epsilon_{U,j} > \ln \epsilon_R \tag{7}$$

Then, the last step is to convert Eq. (7) into a failure probability. $\ln \epsilon_R$ follows a normal distribution, and thus, one can obtain the probability of satisfying Eq. (7) by taking the integration of $\ln \epsilon_R$ from ∞ to $\ln A/A_m - \ln \epsilon_{U,j}$, which is the cumulative distribution function given as

$$P\left(\ln A/A_m - \ln \epsilon_{U,j} > \ln \epsilon_R\right) = \Phi\left(\frac{\ln A/A_m - \ln \epsilon_{U,j}}{\beta_R}\right), \tag{8}$$

where $\Phi(\cdot)$ is the cumulative distribution function of a standard normal distribution. Eq. (8) is interpreted as the conditional failure probability given $\ln \epsilon_{U,j}$. Thus, we can sample failure probability using Eq. (8) and $\ln \epsilon_{U,j}$. Repeating this sampling can construct the probability density of failure probability. In Algorithm 1, we summarize the above Monte Carlo technique.

Input:	1. Peak ground acceleration A 2. Median peak ground acceleration A_m 3. Logarithmic standard deviations β_R and β_U 4. Number of the Monte Carlo trials N
Output:	Sampled failure probabilities $\boldsymbol{P}$
1.	Initialize an empty vector $\boldsymbol{P} = \{\}$
2.	$\{x_1, x_2, \cdots, x_N\} \leftarrow$ Draw N samples from $\mathcal{N}(0, \beta_U)$
3.	For each x_j do
4.	$P_j \leftarrow$ Evaluate Eq. (8) with $\ln \epsilon_{U,j} = x_j$
5.	Append P_j to $\boldsymbol{P}$
6.	Return $\boldsymbol{P}$

Algorithm 1: Monte Carlo procedure to propagate epistemic uncertainty in the seismically induced failure probability of a single SSC

Note that one can sample $\ln \epsilon_U$ using a uniform distribution on [0,1] using the distribution function technique. The cumulative distribution function of $\ln \epsilon_U$ is given by $q = \Phi(\ln \epsilon_U/\beta_U)$. Since q is the cumulative value of $\ln \epsilon_U$, we can consider q follows a uniform distribution on [0,1], and $\ln \epsilon_U$ is expressed as $\ln \epsilon_U = \beta_U \Phi^{-1}(p)$. Then, we can sample the corresponding $\ln \epsilon_U$ by sampling q. Now, let us assume that q_j is the jth sample of q. Now, we get the corresponding jth sample of $\ln \epsilon_U$ as $\ln \epsilon_{U,j} = \beta_U \Phi^{-1}(q_j)$. Thus, Eq. (8) is also given as

$$P\left(\ln A/A_m - \ln \epsilon_{U,j} > \ln \epsilon_R\right) = \Phi\left(\frac{\ln A/A_m - \beta_U \Phi^{-1}(q_j)}{\beta_R}\right). \tag{9}$$

For the single-component case, one can also directly sample failure probability using the equation of the fragility curve. The fragility curve is a function of peak ground acceleration that presents a failure probability [11]. The fragility curve equation is given as

$$F(p, A, A_m, \beta_U, \beta_R) = \Phi\left(\frac{\ln A/A_m + \beta_U \Phi^{-1}(q)}{\beta_R}\right), \tag{10}$$

where q is the analyst's confidence in epistemic uncertainty. Note that one can assume that q follows a uniform distribution. Thus, one can uniformly sample the value of q to propagate the epistemic uncertainty using Eq. (10).

A noticeable difference between Eqs. (9) and (10) is that they have the different signs in front of $\beta_U \Phi^{-1}(p)$. This difference does not affect their probability density. We first show that Eq. (9) can generate the same probability density function as Eq. (10). Figure 1 compares the probability densities constructed by Eqs. (9) and (10) with 10^6 samples.

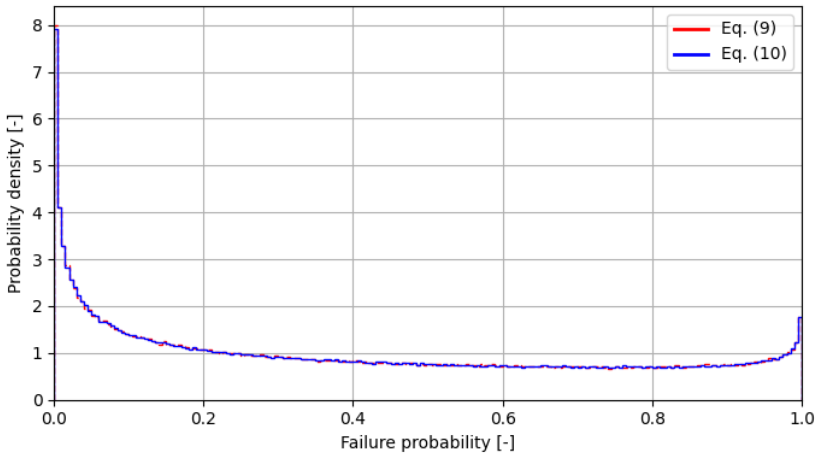

Figure 1. Comparison of the probability densities constructed by Eqs. (9) and (10) with $A = 1.05$, $A_m = 1.1$, $\beta_U = 0.15$, and $\beta_R = 0.12$

Figure 1 shows that Eqs. (9) and (10) yield identical probability densities even though the signs of $\ln \epsilon_{U,j}$ in Eq. (8) and $\beta_U \Phi^{-1}(p)$ in (10) are opposite. This observation can be explained as follows. $\Phi^{-1}(p)$ is symmetric at the origin, implying that $\Phi^{-1}(p)$ and $\Phi^{-1}(-p)$ have the same values for all p, and consequently, $\ln \epsilon_U$ and $-\ln \epsilon_U$ have the same probability density. Figure 1 confirms we can use Eq. (8) to propagate epistemic uncertainty.

Eq. (8) is easily modified to propagate aleatory uncertainty by swapping how the uncertainties are treated. In the above derivation, epistemic uncertainty is sampled, and aleatory uncertainty is integrated to transform the inequality into a failure probability. Instead, we can swap their treatment as the aleatory uncertainty is sampled, and the epistemic uncertainty is integrated to transform the inequality into failure probability. Let $\epsilon_{R,j}$ denote the jth sample of aleatory uncertainty. Then, we can get the following equation:

$$P\left(\ln A/A_m - \ln \epsilon_{R,j} > \ln \epsilon_U \geq -\infty\right) = \Phi\left(\frac{\ln A/A_m - \ln \epsilon_{R,j}}{\beta_U}\right), \tag{11}$$

where $\ln \epsilon_{R,j}$ is the jth sample of aleatory uncertainty. Eqs. (8) and (11) have the same functional form, and therefore, we only need to implement Eq. (8) to evaluate Eq. (11) with different parameters.

III.B. Algorithm for multiple SSCs

In the previous section, we proposed equations to propagate the uncertainty of seismically induced failure probability, with a focus on different types of uncertainties. In this section, we propose equations to propagate the uncertainty of the seismically induced joint failure probability of multiple SSCs. The approach is the same as the single SSC. We first take the logarithm of

the failure criterion. Then, we transform a failure criterion into failure probability using the symmetric property and the cumulative distribution function.

Let us consider the failure criterion of Eq. (4) and follow the same steps as the single SSC case. We take the logarithm, sample the epistemic uncertainty of each SSC, and transform the inequality into the failure probability. Let $\epsilon_{U,i,j}$ denote the jth sample value of epistemic uncertainty of the ith SSC. Now, Eq. (4) is transformed as

$$\underbrace{\begin{bmatrix}\ln A\\ \vdots\\ \ln A\\ \vdots\\ \ln A\end{bmatrix}}_{\ln \boldsymbol{A}} - \underbrace{\begin{bmatrix}\ln A_{m,1}\\ \vdots\\ \ln A_{m,i}\\ \vdots\\ \ln A_{m,n}\end{bmatrix}}_{\ln \boldsymbol{A_m}} - \underbrace{\begin{bmatrix}\ln \epsilon_{U,1,j}\\ \vdots\\ \ln \epsilon_{U,i,j}\\ \vdots\\ \ln \epsilon_{U,n,j}\end{bmatrix}}_{\ln \boldsymbol{\epsilon_{U,j}}} > \underbrace{\begin{bmatrix}\ln \epsilon_{R,1}\\ \vdots\\ \ln \epsilon_{R,i}\\ \vdots\\ \ln \epsilon_{R,n}\end{bmatrix}}_{\ln \boldsymbol{\epsilon_R}}. \tag{12}$$

where $\boldsymbol{A}$ is the vector of peak ground accelerations, $\boldsymbol{A_m}$ is the vector of median peak ground accelerations, $\boldsymbol{\epsilon_{U,j}}$ is the vector of jth samples of epistemic uncertainties, and $\boldsymbol{\epsilon_R}$ is the vector of random variables for aleatory uncertainties. Note that $\ln \boldsymbol{\epsilon_R}$ follows a MVN distribution.

Now, let the vector $\boldsymbol{x}$ equal $\ln \boldsymbol{\epsilon_R}$, and we can transform Eq. (12) by taking the cumulative distribution function of an MVN distribution to the failure probability as

$$P\left(\ln \boldsymbol{A} - \ln \boldsymbol{A_m} - \ln \boldsymbol{\epsilon_{U,j}} > \boldsymbol{x} \geq -\infty\right) = \int_{-\infty}^{\ln \boldsymbol{A} - \ln \boldsymbol{A_m} - \ln \boldsymbol{\epsilon_{U,j}}} \frac{1}{(2\pi)^{n/2}|\boldsymbol{\Sigma_R}|^{1/2}} \exp\left(-\frac{1}{2}\boldsymbol{x}^{\mathrm{T}}\boldsymbol{\Sigma_R}^{-1}\boldsymbol{x}\right) d\boldsymbol{x}. \tag{13}$$

The right-hand side of Eq. (13) is the formula for the cumulative distribution function of an MVN distribution with zero mean value. Eq. (13) is the conditional failure probability given the jth sampled values of epistemic uncertainties. In the literature, there is a fast Monte Carlo algorithm to evaluate Eq. (12) proposed by Genz and Bretz[1] [9]. Thus, using Eq. (13) to propagate the epistemic uncertainty of failure probability is computationally feasible.

We summarize the steps for propagating epistemic uncertainty using the Monte Carlo sampling technique in Algorithm 1.

Input:	1. Peak ground acceleration A 2. Vector of median peak ground accelerations $\boldsymbol{A_m}$ 3. Covariance matrices $\boldsymbol{\Sigma_R}$ and $\boldsymbol{\Sigma_U}$ 4. Number of the Monte Carlo trials N
Output:	Sampled failure probabilities $\boldsymbol{P}$
1.	Initialize an empty vector $\boldsymbol{P} = \{\}$
2.	$\{\boldsymbol{z}_1, \boldsymbol{z}_2, \cdots, \boldsymbol{z}_N\} \leftarrow$ Draw N samples from $\mathcal{MVN}(0, \boldsymbol{\Sigma_U})$
3.	For each $\boldsymbol{z}_j$ do
4.	$P_j \leftarrow$ Evaluate Eq. (13) with $\ln \boldsymbol{\epsilon_{U,j}} = \boldsymbol{z}_j$ using Genz-Bretz algorithm
5.	Append P_j to $\boldsymbol{P}$
6.	Return $\boldsymbol{P}$

Algorithm 2: Monte Carlo procedure to propagate epistemic uncertainty in seismically induced joint failure probability

Eq. (13) can be easily modified to propagate aleatory uncertainty. By switching the role of epistemic and aleatory uncertainties in the above derivation, we get a similar expression for the conditional failure probability given aleatory uncertainties as

[1] For example, in Python, the multivariate_normal.cdf function in the scipy packages (version 1.14.4) [12] can be used to evaluate Eq. (13).

$$P\left(\ln \boldsymbol{A} - \ln \boldsymbol{A_m} - \ln \boldsymbol{\epsilon_{R,j}} > \ln \boldsymbol{\epsilon_U}\right) = \int_{-\infty}^{\ln \boldsymbol{A} - \ln \boldsymbol{A_m} - \ln \boldsymbol{\epsilon_{R,j}}} \frac{1}{(2\pi)^{n/2}|\boldsymbol{\Sigma_U}|^{1/2}} \exp\left(-\frac{1}{2}\boldsymbol{x}^{\mathrm{T}}\boldsymbol{\Sigma_U}^{-1}\boldsymbol{x}\right) d\boldsymbol{x} \quad (14)$$

where $\boldsymbol{x}$ equal $\ln \boldsymbol{\epsilon_U}$, and $\boldsymbol{\epsilon_{R,j}}$ is the vector of the jth samples of aleatory uncertainties. Eq. (14) is the conditional failure probability given the jth sampled values of epistemic uncertainties.

IV. NUMERICAL EXPERIMENT

In this section, we demonstrate the propagation of epistemic uncertainties using Algorithm 2 for a three-component case. We summarize parameter values used in this numerical experiment in Table 1, where $\boldsymbol{\rho_U}$ and $\boldsymbol{\rho_R}$ are correlation matrices of epistemic and aleatory uncertainties, respectively, and $\boldsymbol{\beta_U}$ and $\boldsymbol{\beta_R}$ are the vectors whose ith elements are epistemic and aleatory uncertainties of SSCs, respectively.

Table 1. Input Parameters Employed in the Numerical Demonstration

Parameter	Sample value
A	1.0, 1.1, 1.2
$\boldsymbol{A_m}$	$[1.05 \quad 0.95 \quad 1.00]^{\mathrm{T}}$
$\boldsymbol{\beta_R}$	$[0.12 \quad 0.09 \quad 0.1]$
$\boldsymbol{\beta_U}$	$[0.08 \quad 0.06 \quad 0.07]$
$\boldsymbol{\rho_R}$	$\begin{bmatrix} 1 & 0.3 & 0.2 \\ 0.3 & 1 & 0.4 \\ 0.2 & 0.4 & 1 \end{bmatrix}$
$\boldsymbol{\rho_U}$	$\begin{bmatrix} 1 & 0.7 & 0.6 \\ 0.7 & 1 & 0.8 \\ 0.6 & 0.8 & 1 \end{bmatrix}$
$\boldsymbol{\Sigma_R}$	$\mathrm{diag}(\boldsymbol{\beta_R})\boldsymbol{\rho_R}\mathrm{diag}(\boldsymbol{\beta_R})$
$\boldsymbol{\Sigma_U}$	$\mathrm{diag}(\boldsymbol{\beta_U})\boldsymbol{\rho_U}\mathrm{diag}(\boldsymbol{\beta_U})$

Figure 2 shows the histograms constructed from 10^7 generated samples based on the parameter values shown in Table 1.

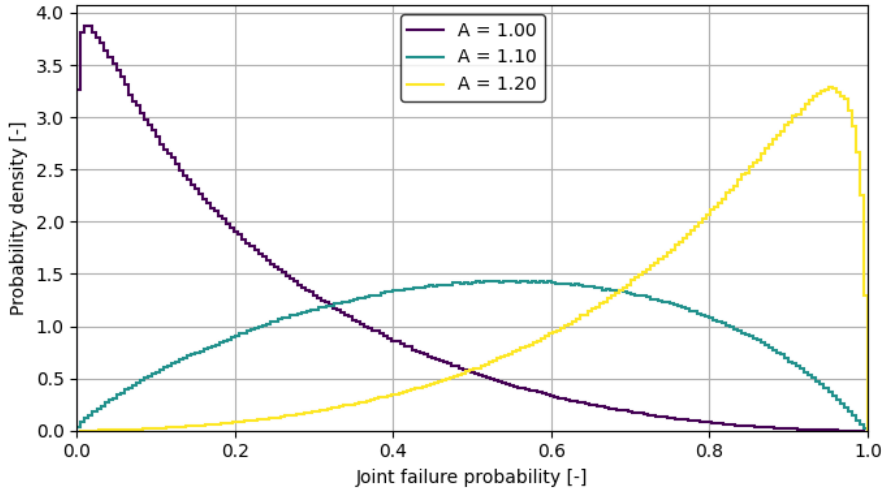

Figure 2. Probability densities constructed from 10^7 samples of joint failure probabilities at 1.0, 1.1, and 1.2

To verify the above result, we evaluate the mean value using the generated joint failure probabilities and comapre it with an MVN model such that

404

$$\bar{P} = \int_{-\infty}^{\ln \boldsymbol{A} - \ln \boldsymbol{A_m}} \frac{1}{(2\pi)^{n/2}|\boldsymbol{\Sigma_U} + \boldsymbol{\Sigma_R}|^{1/2}} \exp\left(-\frac{1}{2}\boldsymbol{x}^{\mathrm{T}}(\boldsymbol{\Sigma_U} + \boldsymbol{\Sigma_R})^{-1}\boldsymbol{x}\right) d\boldsymbol{x}. \quad (16)$$

This MVN model is a variation of a model used in the Seismic Safety Margin Research program [8], and that Eq. (16) has a different integration domain. In Table 2, we summarize the comparison of estimated mean values.

Table 2. Comparison of the mean estimations between the proposed model and the MVN model

PGA Value	Proposed technique		MVN model*
	Estimated Mean	Monte Carlo error	
1.0	2.1284e-01	1.4589e-04	2.1282e-01
1.1	5.1483e-01	2.2690e-04	5.1482e-01
1.2	7.7645e-01	2.7865e-04	7.7644e-01

* The reported values are obtained using the internal integration function of the SciPy library, scipy.stats._mvn, under settings that guarantee convergence with absolute and relative errors smaller than 10^{-10}.

Table 2 shows that the proposed technique accurately reproduces the mean estimates of joint failure probabilities derived from the constructed probability densities presented in Figure 2. Thus, this result suggests that the proposed technique can correctly generate the uncertainty distribution of the seismically induced joint failure probability of SSCs.

V. DISCUSSION

We numerically investigated the proposed technique and demonstrated that it can generate the probability density of joint failure probability consistent with the MVN model. One obvious advantage of the proposed technique is its simplicity; fragility analysts can easily implement it. Additionally, the proposed technique does not require any additional parameters to construct the uncertainty of the joint failure probability, provided that fragility analysts have already estimated the mean value of the joint failure probability using the MVN model. This is advantageous because fragility analysts do not have to conduct additional analysis.

Although it is difficult to determine the correlation coefficients between responses and between capacities, it is possible to assume prior distributions for these coefficients and incorporate the constructed probability density of joint failure probability as part of the likelihood function. In doing so, fragility analysts can use a Bayesian updating framework to reduce the uncertainty associated with these correlation coefficients.

As mentioned in the introduction, it is challenging to obtain the correlation coefficients between responses and between capacities which are required parameters for both the MVN model and the proposed technique. Thus, establishing a methodology for estimating these correlation coefficients is also an important direction for future research.

A probability density constructed by the proposed technique inevitably includes a Monte Carlo error. This Monte Carlo error limits the applicability of the proposed technique. For example, it is difficult to obtain accurate gradient information from a constructed probability density. This inaccuracy makes it difficult to use a gradient-based method, such as a Hamiltonian Monte Carlo method. Therefore, establishing an analytical method to derive the probability density function is an important direction for future research.

V. CONCLUSIONS

We proposed a Monte Carlo technique to propagate the uncertainty of seismically induced joint failure probability. The proposed Monte Carlo technique enables us to propagate various uncertainties using the common formula. This feature reduces the implementation cost. We performed numerical experiments using the proposed technique to construct the probability densities at three peak ground acceleration values. Then, we estimated the mean values using the constructed probability densities and compared them to the MVN model. The comparison showed a good agreement between the proposed technique and the MVN model. Therefore, the proposed technique is a good candidate method for propagating the uncertainty of seismically induced joint failure probability.

REFERENCES

[1] North Anna Nuclear Power Plant Seismic Event. 2011.
[2] Company TEP. Fukushima Genshiryoku Jiko Chōsa Hōkokusho (Fukushima Nuclear Accident Analysis Report). Tokyo, Japan: Tokyo Electric Power Company; 2012.

[3] Anup A, Talaat M, Grant F, Ferrante F. Quantifying partial fragility correlations in seismic probabilistic risk assessments 2022.
[4] Kim SY, Kim JH. Seismic correlation coefficient evaluation for the application of separation of variables approach in fragility assessment. Nuclear Engineering and Technology 2025;57:103238.
[5] Budnitz RJ, Hardy GS, Moore DL, Ravindra MK. NUREG/CR-7237: Correlation of Seismic Performance in Similar SSCs (Structures, Systems, and Components). 2017.
[6] Watanabe Y, Oikawa T, Muramatsu K. Development of the DQFM method to consider the effect of correlation of component failures in seismic PSA of nuclear power plant. Reliab Eng Syst Saf 2003;79:265–79.
[7] Soga S, Higo E, Miura H. Theoretical comparison of models for a seismically induced joint failure probability. In: Smith C, Paulos T, editors. Probabilistic Safety Assessment and Management PSAM 16, Honolulu, O'ahu, Hawaii: 2022.
[8] Smith PD, Dong RG, Bernreuter DL, Bohn MP, Chuang TY, Cummings GE, et al. NUREG/CR-2015: Seismic safety margins research program: Phase I: Final Report-Overview. Washington, DC: 1981.
[9] Genz A, Bretz F. Computation of multivariate normal and t probabilities. vol. 195. Springer Science & Business Media; 2009.
[10] Subcommittee of External Hazard PRA. A Standard for Procedure of Seismic Probabilistic Risk Assessment for Nuclear Power Plants: 2015 [in Japanese]. Atomic Enegry Society of Japan; 2015.
[11] Reed JW, Kennedy RP. Methodology for developing seismic fragilities. Tr-103959 1994;3.
[12] Jones E, Oliphant T, Peterson P, Others. SciPy: Open Source Scientific Tools for Python, 2001 (http://www.scipy.org/). Http://WwwScipyOrg/ 2015.

ASRAM2025
www.asram2025.org
Asian Symposium on Risk Assessment and Management 2025
Pattaya, Thailand, 27 – 29 August 2025

Development of a Tsunami PSA bounding analysis model for the Hanul Site

Changkyung Seong[1a*], Seokwoo Sohn[1b], Yein Seo[1c], JaeBeol Hong[1d], Kyung Min Kang[2a]

[1] *Department of Reliability Engineering, FNC Technology Co. Ltd., 10th Fl. 13 Heungdeok 1-ro, Giheung-gu, Yongin-si, Gyeonggi-do, 16954, Republic of Korea*
[2] Korea Institute of Nuclear Safety, 62 Gwahak-ro, Yuseong-gu, Daejeon, 34142, Republic of Korea
*ckd1718@fnctech.com

ABSTRACT

This study developed a Tsunami PSA bounding analysis model to evaluate the risk of nuclear power plant accidents caused by tsunamis at the Hanul site. The study reviewed tsunami hazard analysis and fragility analysis results applicable to the Hanul site, performed tsunami-induced accident sequence analysis, and developed a base model with conservative assumptions. Additionally, a sensitivity analysis model incorporating on-site inspection findings was developed to evaluate the effects of post-Fukushima measures, such as watertight door installations. A comparison of quantification results for each unit showed differences in Core Damage Frequency (CDF) due to variations in the Reactor Coolant Pump (RCP) Seal models, the configuration of water sources for secondary heat removal, and differences in the ESW Intake Structure. This study is expected to provide a technical basis for the future development of tsunami PSA review guidelines.

Keywords: Tsunami PSA Bounding Analysis Model, Multi-unit Nuclear Power Plant, Hanul Site, MPAS Model

I. Introduction

In Korea, most nuclear power plants are co-located at sites with six or more units, resulting in a relatively higher risk of multi-unit accidents compared to other countries. Consequently, during the construction licensing phase of Shin-Kori Units 5 and 6, multi-unit PSA emerged as a key regulatory concern. In response, a pilot multi-unit PSA model was developed for the Kori site. However, due to the distinct geographical and technological characteristics of the Hanul site, the direct application of the Kori based model is limited.

The Hanul site hosts multiple reactor types with varying design features, including Framatome-type reactors, and is located on Korea's eastern coastline, where the assessment of natural external hazards such as tsunamis is essential. In line with recent efforts to enhance nuclear safety and strengthen regulatory oversight, the need for developing regulatory-grade PSA models that reflect reactor-specific characteristics has grown. Accordingly, a Tsunami PSA bounding analysis model for the Hanul site was developed, based on the full-power internal event MPAS model which was originally intended for regulatory verification.

The developed model includes a simplified Tsunami PSA bounding analysis base model constructed under conservative assumptions using site-specific tsunami hazard data. Furthermore, a Tsunami PSA bounding analysis sensitivity model was implemented to assess the effects of post-Fukushima design modifications, such as the installation of watertight doors and flood protection walls, which were introduced to improve flood resilience.

II. Tsunami PSA Methodology

The development procedure for the tsunami PSA model is similar to that of the seismic PSA model, and the general procedure for performing a tsunami PSA is shown in Figure 1 [1]. The tsunami PSA bounding analysis model consists of technical elements including tsunami hazard analysis, tsunami fragility analysis, and tsunami accident sequence analysis.

FIGURE 1. Procedure of Tsunami PSA

II.A. Applicability Review of Tsunami Hazard Assessment

Due to the absence of site-specific input data for tsunami hazard analysis at the Hanul site, existing tsunami hazard results applicable to the site were reviewed. The tsunami hazard curve developed in a previous multi-unit PSA study [1] for the Hanul site was adopted for this analysis, as shown in Figure 2.

The tsunami hazard assessment is defined based on the tsunami wave height and its corresponding exceedance frequency. The hazard curve presented in the previous study [1] was developed using a tsunami seismic hazard logic tree approach in conjunction with a tsunami propagation analysis code. In the logic tree, various tsunami-generating seismic sources were modeled probabilistically by considering parameters such as maximum potential magnitude, recurrence intervals, and associated wave heights. Each branch of the logic tree was weighted, and the resulting tsunami heights were calculated through numerical propagation simulations for each scenario.

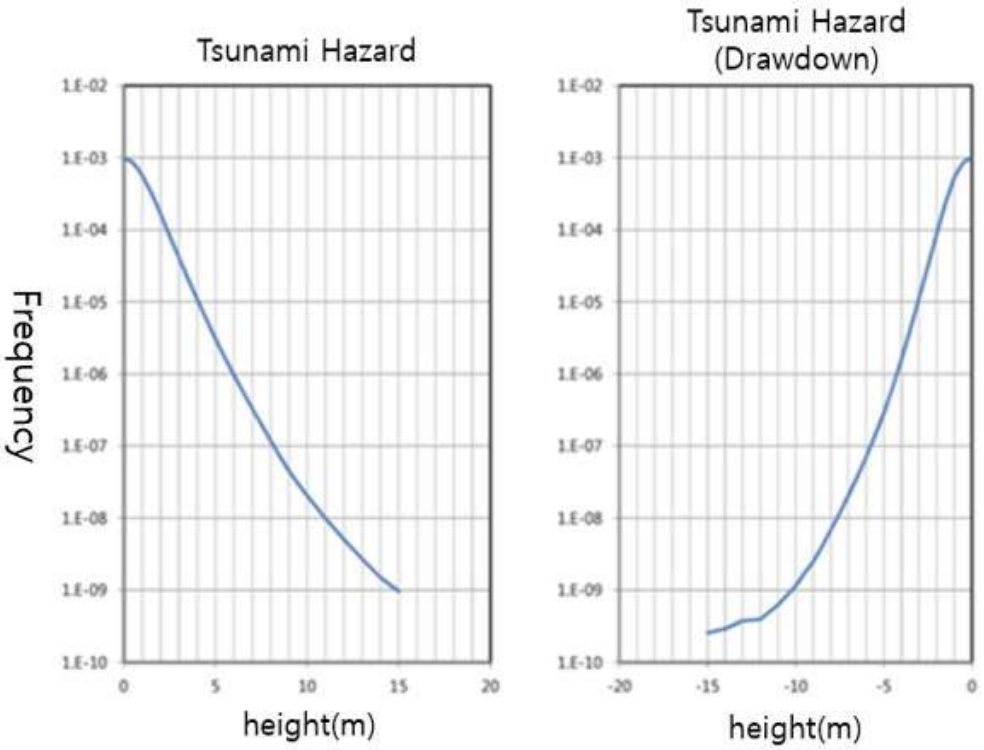

FIGURE 2. Tsunami Hazard Curve

II.B. Applicability Review of Tsunami Fragility Assessment

Tsunami fragility analysis is conducted to evaluate the probability of failure of safety-related structures, systems, and components (SSCs) as a function of tsunami intensity parameters. The SSCs that can impact either initiating event frequency or accident mitigation capability were selected for tsunami PSA fragility evaluation. The selection of target SSCs was performed in consultation with system analysis experts.

In this study, the fragility data were adopted from the results presented in a previous multi-unit PSA study [1], and are summarized in Table 1. The failure probabilities were computed using a lognormal cumulative distribution function, based on the median capacity (Am) and logarithmic standard deviation (βC) for each SSC with respect to tsunami wave height. The resulting damage probabilities calculated from the fragility curves are provided in Table 2.

TABLE 1. Tsunami Fragility of Key Structures and Equipment in Nuclear Power Plants

Equipment	Am	βC
Break water	7.32	1.056
CST	11.37	0.054
Offsite power	10.64	0.221
ESW	10.8	0.1

TABLE 2. Damage probability of major equipment by elevation

Tsunami height	Breakwater	CST	Offsite power	ESW
1	2.97E-02	0.00E+00	1.86E-125	1.86E-125
2	1.10E-01	1.57E-227	4.14E-64	4.14E-64
3	1.99E-01	1.03E-134	7.27E-38	7.27E-38
4	2.84E-01	1.10E-83	1.50E-23	1.50E-23
5	3.59E-01	1.43E-52	6.75E-15	6.75E-15
6	4.25E-01	1.25E-32	2.08E-09	2.08E-09
7	4.83E-01	1.32E-19	7.24E-06	7.24E-06
8	5.34E-01	3.76E-11	1.35E-03	1.35E-03
9	5.78E-01	7.50E-06	3.41E-02	3.41E-02
10	6.16E-01	8.71E-03	2.21E-01	2.21E-01
11	6.50E-01	2.70E-01	5.73E-01	5.73E-01
12	6.80E-01	8.41E-01	8.54E-01	8.54E-01
13	7.07E-01	9.93E-01	9.68E-01	9.68E-01
14	7.30E-01	1.00E+00	9.95E-01	9.95E-01
15	7.52E-01	1.00E+00	9.99E-01	9.99E-01

II.C. Accident Sequence Analysis Induced by Tsunami

The accident sequence analysis evaluates potential accident scenarios based on the damage status of critical safety-related SSCs affected by tsunami wave height. Initiating event trees were developed for different tsunami height intervals, and Total Loss of Component Cooling Water (TLOCCW) and Station Blackout (SBO) were identified as representative initiating events. The tsunami-induced initiating event tree is illustrated in Figure 3 [1].

- **TS-YARD**: Tsunami impact evaluated at yard level. For tsunami wave heights ≤10 meters (site elevation reference), only TLOCCW is considered. For wave heights >10 meters, both TLOCCW and SBO are considered.
- **TS-HIGH**: If the tsunami height exceeds 13 meters, core damage is assumed due to flooding of the Alternate AC Diesel Generator (AAC DG), failure of the Condensate Storage Tank (CST), and flooding of the Primary Auxiliary Building (PAB).

- **ESWS** (Essential Service Water System): ESWS is Considered the most vulnerable system; loss of ESW is assumed when the breakwater is overtopped or damaged.
- **EP**: Offsite Power is assumed to be lost when tsunami waves reach the site grade level (10 m), resulting in submergence of switchyard transformers.
- **EDG**: Emergency Diesel Generator is assumed to be inoperable due to ESWS failure during a tsunami.
- **PAB**: Flooding potential is considered for mitigation systems; assumed to be inundated for tsunami heights ≥13 meters.
- **CST** (Condensate Storage Tank): Damage probability is evaluated as a function of tsunami height.
- **AAC** (Alternate AC Diesel Generator): Damage status is considered based on tsunami height.

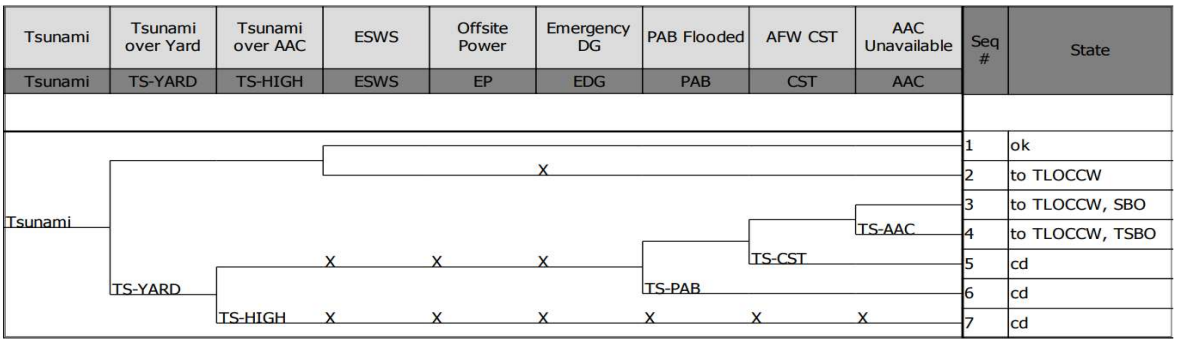

FIGURE 3. Tsunami-Induced initiating Event Tree

Ⅲ. Model Development

Ⅲ.A. Reference Site

A model was developed for representative reactor types at the Hanul site, including Framatome, OPR1000, and APR1400.

Ⅲ.B. Tsunami PSA bounding analysis base model

Due to the limited availability of data, the Tsunami PSA bounding analysis base model was constructed using conservative assumptions to account for inherent uncertainties. The base model was developed under a conservative assumption that a tsunami over 10 meters in height infiltrates the building through exterior doors, resulting in flooding of the mitigation systems. The base model excludes tsunami wave heights between 1 and 4 meters from the analysis, as the damage probability of the Essential Service Water System (ESWS) within this range is considered negligible. For tsunami wave heights ranging from 5 to 10 meters, the model evaluates scenarios considering TLOCCW. Tsunami wave heights exceeding 10 meters are modeled with the assumption of direct core damage.

III.B.1. Development of the Event Tree and Fault Tree (Base model)

The event tree for TLOCCW caused by tsunami wave heights between 5 and 10 meters is presented in Figure 4. The fault tree utilized the full-power internal events MPAS (Multi-purpose Probabilistic Analysis of Safety) model, where failure of the ESWS and Circulating Water System (CWS) due to TLOCCW was incorporated into the fault tree using the SIMA file. The SIMA file is a tool designed to modify fault tree data, logical structures, and configuration flags in PSA models. The initiating event frequency of TLOCCW (GIE-TC-TSUNAMI) was calculated by multiplying the sum of tsunami occurrence frequencies within the 5 to 10 meter range by the breakwater damage probability. The breakwater damage probability for 5 to 10 meter tsunami (0.39) was obtained by dividing the sum of the products of breakwater failure probabilities at each tsunami height and their respective occurrence frequencies by the occurrence frequency of 5-meter tsunami. The initiating event frequency for tsunami exceeding 10 meters (%T-IE-TSUNAMI-HG) was computed as the sum of the occurrence frequencies of tsunami exceeding 10 meters. For quantification, the Tsunami PSA Bounding analysis base model developed a core damage fault logic, which is illustrated in Figure 5.

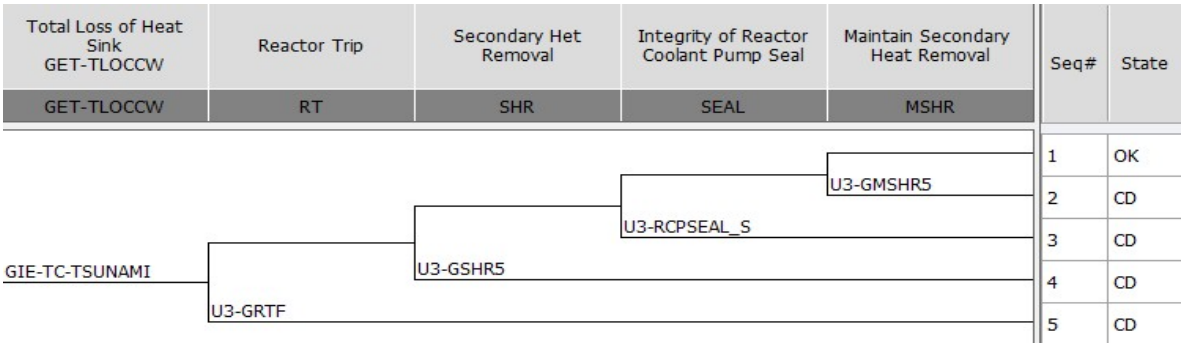

FIGURE 4. Tsunami-Induced TLOCCW Event Tree

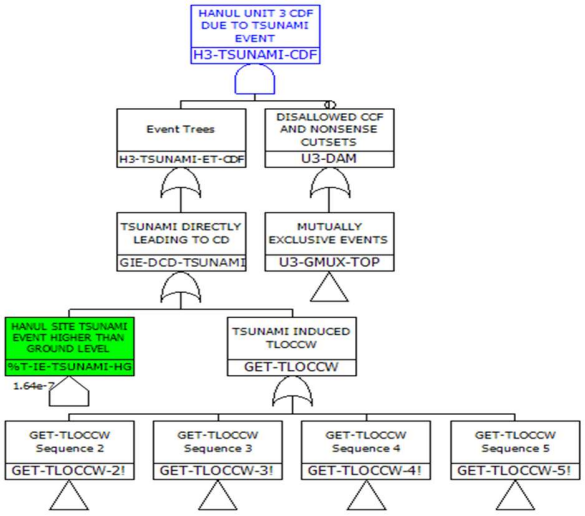

FIGURE 5. Core Damage Top-Logic (Base model)

III.C. Tsunami PSA bounding analysis sensitivity model

The Tsunami PSA bounding analysis sensitivity model was developed to incorporate the results of an on-site inspection at the Hanul site and to perform additional analyses for tsunami wave heights between 10 and 13 meters. The on-site inspection confirmed the installation of seismic-resistant watertight doors on all access points of relevant structures to protect key safety equipment against flooding caused by tsunamis. Additionally, HVAC openings susceptible to tsunami ingress were verified to be located at elevations exceeding 3 meters above site grade. Accordingly, the analysis assumed no tsunami ingress into the PAB and Secondary Auxiliary Building (SAB) for tsunami heights up to 13 meters. As an exception, the ESWS, identified as the most vulnerable component, was assumed to be unavailable during tsunamis exceeding 10 meters. The damage probabilities of major SSCs for each tsunami wave height are summarized in Table 3.

TABLE 3. Damage Probability of Structure, System, and Component by Tsunami Wave Height

SSC	Value	Explanation
ESWS	3.9E-01	Average Probability of Damage to the Primary Component Coolant Water System Due to tsunamis ranging from 5 to 10 meters
	1.0	Assuming damage from a tsunami of over 10 meters
CST	2.2E-01	Probability of damage to Condensate Storage Tanks due to tsunamis between 10 and 13 meters
DWST	2.2E-01	Probability of damage to Demineralized Storage Tanks due to tsunamis between 10 and 13 meters
AAC DG	0.0	The damage probability is not considered for tsunamis with wave heights below 13 meters.
	1.0	The assumption is made that damage occurs for tsunamis exceeding 13 meters

III.C.1. Development of the Event Tree and Fault Tree (Sensitivity model)

The sensitivity model evaluation for tsunami wave heights between 5 and 10 meters was conducted identically to the base model. However, to assess the impact of watertight door installation implemented as a post-Fukushima countermeasure, the effects of tsunamis between 10 and 13 meters were additionally evaluated. For tsunamis within the 10 to 13-meter range, SBO was considered as an initiating event, and the tsunami-induced SBO event tree for the power plant is presented in Figure 6. The impacts on TLOCCW and SBO due to tsunamis in this range were incorporated into the fault tree using SIMA files. Furthermore, damage probabilities were considered for tanks used as secondary heat removal water sources under 10 to 13-meter tsunamis conditions. The initiating event frequency for SBO was calculated as the cumulative occurrence frequency of tsunamis between 10 and 13 meters, while tsunamis exceeding 13 meters were assumed to cause direct core damage. In the Tsunami PSA bounding analysis sensitivity model, core damage fault logic was developed to support the quantification process, as illustrated in Figure 7.

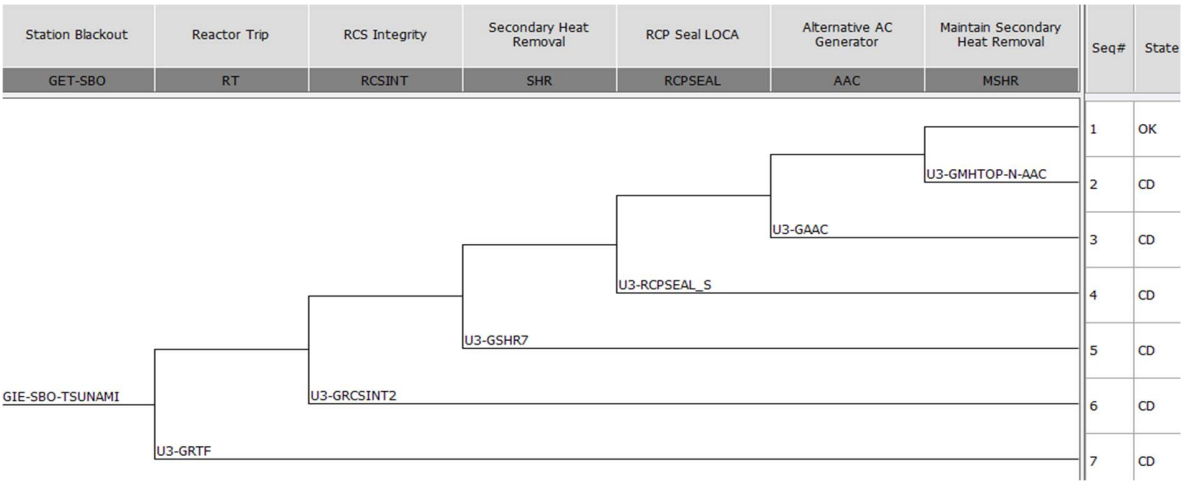

FIGURE 6. Tsunami-Induced SBO Event Tree

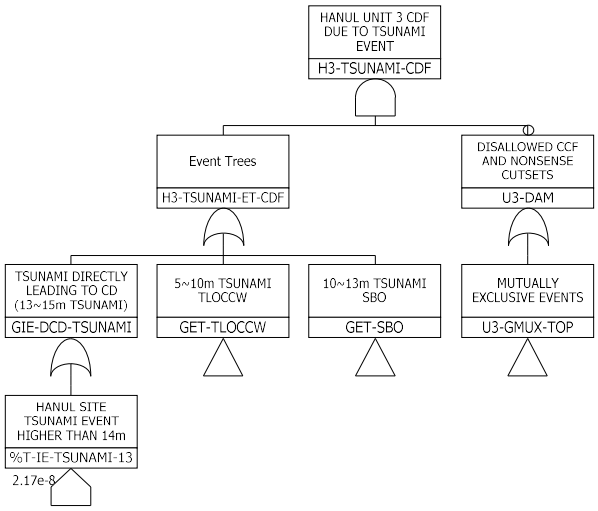

FIGURE 7. Core Damage Top-Logic (Sensitivity model)

IV. Result

Models reflecting unit-specific characteristics were developed for the representative reactor types at the Hanul site, and the quantification results are presented in Table 4. The results are compared based on the CDF of the Hanul Units 3 and 4 base model, and the reduction rate is demonstrated by comparing the CDF values between the base model and sensitivity model for each unit. Differences in CDF among units are primarily attributed to variations in the Reactor Coolant Pump (RCP) Seal

412

models, which are illustrated in Figure 8. For Sin Hanul Units 1 and 2, the ESW Intake Structure differs from other units by having a pump well configuration; therefore, the breakwater damage probability was excluded and only the ESWS damage probability was applied when calculating TLOCCW frequencies. Additionally, the greater reduction rate in the sensitivity model is due to the increased number of available water sources during Secondary heat removal (SHR) or Maintained Secondary Heat Removal (MSHR) states.

The quantification results indicated that differences in CDF were primarily attributed to variations in the RCP seal model, the number of available water sources for SHR/MSHR, the presence of flood barriers, and the configuration of the ESW intake structure. Among these factors, the RCP seal model had the greatest impact on the CDF. This is attributed to the fact that in tsunami-induced TLOCCW and SBO scenarios, an RCP seal LOCA was assumed to lead directly to core damage. Therefore, the RCP seal model plays a critical role in determining the CDF, and mitigation strategies to reduce RCP seal failure probability should be considered, particularly for Hanul Units 1 and 2.

TABLE 4. Tsunami PSA Bounding Analysis Model Quantification

HU12 (Framatome) CDF			HU34 (OPR-1000) CDF			SHU12 (APR-1400) CDF		
Base model	Sensitivity model	Reduction rate	Base model	Sensitivity model	Reduction rate	Base model	Sensitivity model	Reduction rate
939.1%	899.0%	4.3%	100.0%	63.3%	36.7%	71.5%	14.6%	79.5%

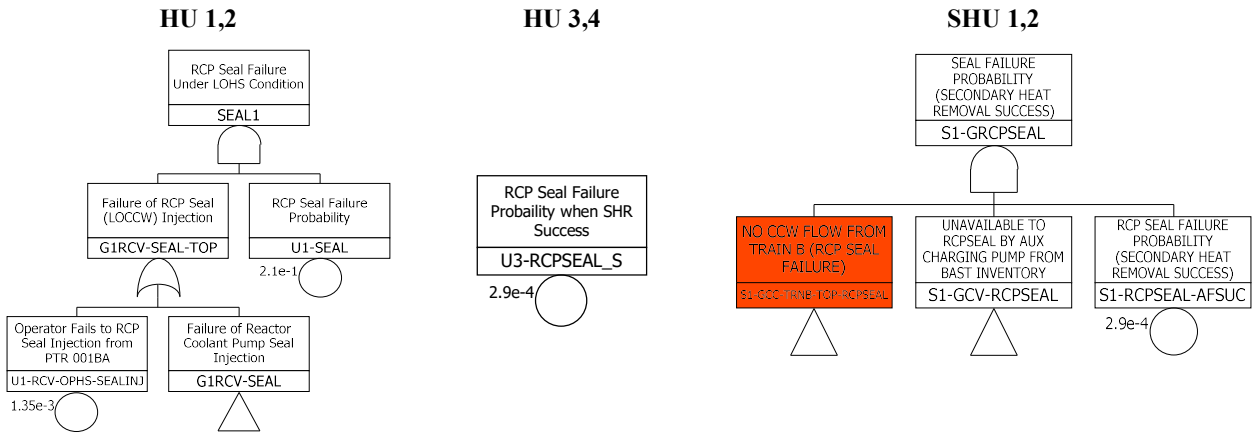

FIGURE 8. RCP Seal model for each unit

V. CONCLUSIONS

This study developed a tsunami PSA bounding analysis methodology for representative reactor designs at the Hanul site and established a single-unit tsunami PSA bounding model based on a regulatory verification model. The developed tsunami PSA bounding analysis models, incorporating design-specific characteristics, identified factors influencing differences in quantification results and core damage frequency among reactor types. Additionally, a sensitivity model reflecting the impact of watertight door installations—implemented as a post-Fukushima measure—was developed to evaluate the reduction in CDF. The findings of this study are expected to provide a technical foundation for the future development of single-unit tsunami PSA review guidelines.

ACKNOWLEDGMENTS

This work was supported by the Nuclear Safety Research Program through the Korea Foundation Of Nuclear Safety(KoFONS) using the financial resource granted by the Nuclear Safety and Security Commission(NSSC) of the Republic of Korea. (No. RS-2023-00240452)

REFERENCES

[1] KAERI, Development of the Integrated Risk Assessment Technology for Multiple Units, KAERI/RR-4225 (2016).
[2] KAERI, Development of Site Risk Assessment & Management Technology including Extreme External Events, KAERI/RR-3924 (2014).
[3] Min Kyu Kim, In-kil Choi, "COMPARE OF THE EMPIRICAL AND NUMERICAL TSUNAMI HAZARD ASSESSMENT RESULTS FOR THE EAST COAST OF KOREA", PSAM 13 (2016).
[4] K. Ebisawa, T. Teragaki, S. Nomura, H. Abe, M. Shimemori, M. Shimomoto, "Concept and methodology for evaluating core damage frequency considering failure correlation at multi units and sites and its application," Nuclear Engineering and Design, 288, pp. 82-97 (2015).
[5] K. Ebisawa, M. Fujita, Y. Iwabuchi, H. Sugino, "Current issues on PRA regarding seismic and tsunami events at multi units and sites based on lessons learned from Tohoku earthquake/tsunami," Nuclear Engineering and Technology, 44, no. 5, pp. 437-452 (2012).
[6] T. Zhou, M. Modarres, E.L. Droguertt, "An improved multi-unit nuclear plant seismic probabilistic risk assessment approach," Reliability Engineering and System Safety, 171, pp. 34-47 (2018).
[7] Electric Power Research Institute, "Seismic Fragility and Seismic Margin Guidance for Seismic Probabilistic Risk Assessments", Technical Report (2018).

ANOMALY DETECTION AND SEISMIC DAMAGE INFERENCE OF REACTOR BUILDING USING BAYESIAN INFERENCE

Sunghyon Jang[1], Hideo Machida[2], and Shuhei Matsunaka[2]

[1] *Hokkaido University: Kita-13jo, Nishi-5chome. Kita-ku, Sapporo, Japan*
[2] *TEPCO Systems: 37-28, Eitai 2-chome, Koto-ku, Tokyo, Japan*

ABSTRACT

Early detection of structural damage in nuclear reactor buildings is crucial for safety. In this study, we propose a Bayesian inference framework to detect anomalies, pinpoint damage locations, and quantify damage severity using multi-degree-of-freedom response data. Response analyses under both normal and damaged stiffness conditions yield peak acceleration, velocity, and displacement metrics for each layer. Normalized likelihood functions based on these peak values are used to compute abnormality probabilities via Bayes' theorem. A Bayesian network fuses layer-wise detection results to infer which stiffness element is compromised. Sequential Bayesian updates using shifts in natural periods enable estimation of damage extent (10–40 % stiffness loss).Validation of a three–layer mass–spring–damper model under El-Centro seismic input shows accurate anomaly detection and damage inference across various scenarios. These results demonstrate the promise of Bayesian approaches for structural health monitoring in nuclear reactors.

Keywords: Bayes' theorem, Anomaly detection, Seismic damage, Bayesian inference.

I.BACKGROUND

In the field of nuclear engineering, a multi-degree-of-freedom structural analysis method is used for the assessment of damage to buildings. It is also conceivable that damage to structures caused by earthquakes can occur in forms that are not visible, such as internal damage. If damage to the structure is not detected before it is further damaged by aftershocks, it can lead to a major accident. Therefore, early detection is important for improving the safety of nuclear reactor systems. As such, it is necessary to detect damage by interpreting changes in the behavior of structures using response data from multi-degree-of-freedom structural analysis.

This study aims to construct a model that can estimate the presence and location of damage caused by earthquakes. It does so by conducting multi-degree-of-freedom structural analysis on nuclear reactor buildings and implementing Bayesian inference using response analysis data from both normal conditions and when damage occurs due to earthquakes.

II. ANALITICAL MODEL USING MASS-SPRING-DAMPER STRUCTURE

II. A Analytical Condition

In a three-layer structure, multi-degree-of-freedom response analysis was conducted and validated. Specifically, comparisons were made between normal and abnormal (structural damage) conditions for each layer based on response acceleration, response velocity, and response displacement obtained from the results of the multi-degree-of-freedom response analysis. The multi-degree-of-freedom response analysis involves solving the following differential equation to determine the response acceleration, response velocity, and response displacement[1].

$$[M]\frac{d^2\{x\}}{dt^2} + [C]\frac{d\{x\}}{dt} + [K]\{x\} = -[M]\{I\}\frac{d^2\phi}{dt^2} \quad (1)$$

The natural period T can be calculated from the following formula.

$$det(-\omega^2[M] + [K]) = 0,\ T = \frac{2\pi}{\omega} \quad (2)$$

In this study, structural damage is assumed to involve a decrease in stiffness at each layer, with the degree of damage varying in increments of 10%, ranging from 10% to 40% in the scenarios considered. Table 1 shows analytical conditions[2].

Table 1 The settings for a multi-degree-of-freedom response analysis

Variable Name	Contents	Value	Unit
m_1	Mass of Lv1	4.0×10^5	[kN]
m_2	Mass of Lv2	4.0×10^5	[kN]
m_3	Mass of Lv3	3.0×10^5	[kN]
k_1	Stiffness of Lv1	2.48×10^3	[kN/cm^2]
k_2	Stiffness of Lv2	2.48×10^3	[kN/cm^2]
k_3	Stiffness of Lv3	2.48×10^3	[kN/cm^2]

The model diagram used for the analysis is as follows. In the multi-degree-of-freedom response analysis, the seismic input was the El-Centro NS wave. The waveform is shown below[3].

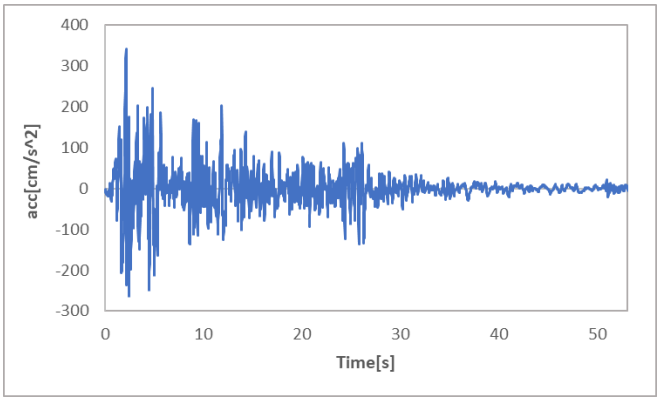

Figure 1 The El-Centro NS wave acceleration

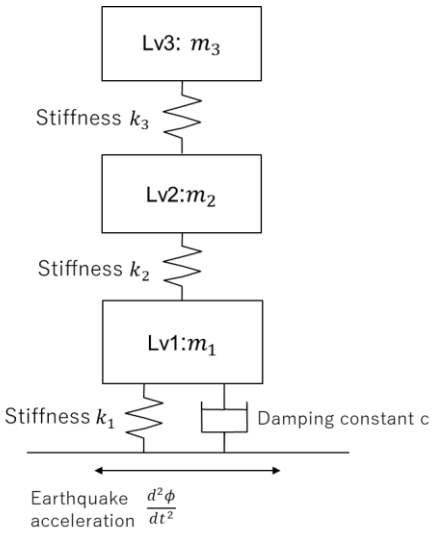

Figure 2 Model overview

The overview of the estimation method used in this study is referred to as the "modular type," which we have named. The specific method is as follows:

1. Conduct a multi-degree-of-freedom response analysis to obtain the response acceleration, velocity, and displacement for each layer, and compare these to normal values to determine if they are normal or abnormal using Bayesian estimation.
2. If abnormalities are detected, use a Bayesian network to identify the affected layer and estimate the location of stiffness damage throughout the system.
3. Employ the natural periods derived from the response analysis in Bayesian estimation to evaluate the extent of damage at the identified locations.

II.B Comparison of Seismic Response Analytical Result between Normal and Abnormal condition

The graphs of the response acceleration, response velocity, and response displacement obtained from the multi-degree-of-freedom response analysis are shown below.

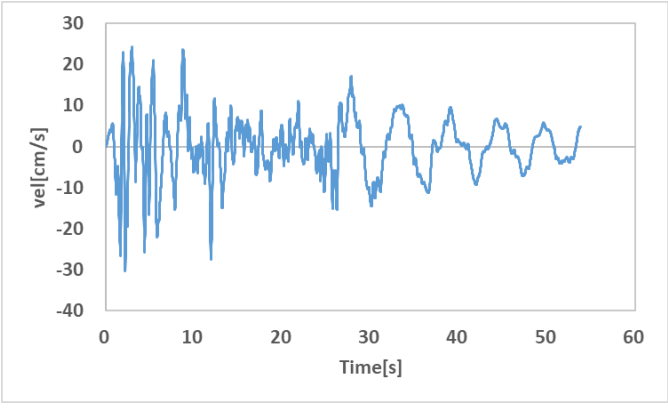

Figure 3 Response velocity at normal condition

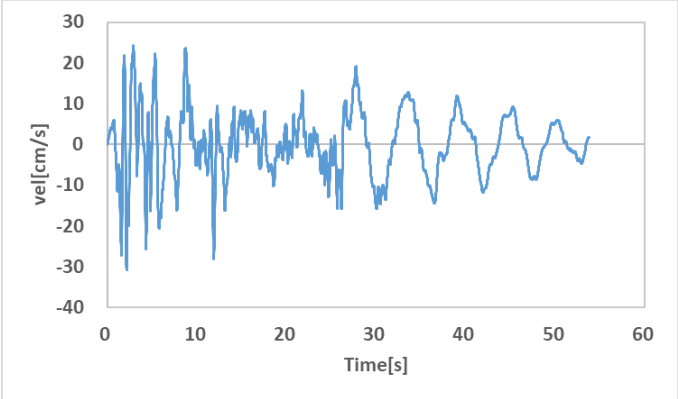

Figure 4 Response velocity at k1 30% damage

Figures 3 and 4 display the response acceleration data for the first layer under normal and abnormal conditions, respectively. It can be observed that there are differences in the magnitude of values and the times at which these values occur between normal and abnormal conditions.

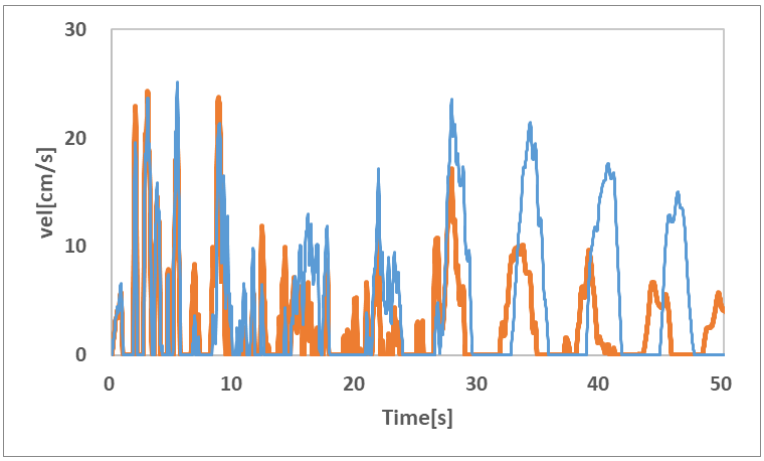

Figure 5 Velocity normal and k1 30% damaged

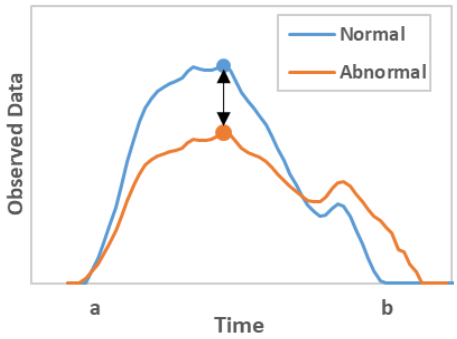

Figure 6 Comparison between normal and abnormal

When defining a positive interval [a, b] in the data during normal conditions, there exists one maximum value within that interval. However, when abnormalities occur, it is thought that there may be shifts in the size of this maximum

value and the timing of their appearance. Focusing on the first layer, the results displaying overlaid data from both abnormal and normal conditions, as shown in Figure 6, are presented below.
In the response acceleration data, it can be confirmed that there are differences in the magnitudes of values and the times at which these values appear between normal and abnormal conditions. It has also been confirmed that similar differences exist in the response velocity and response displacement. Indeed, differences exist between normal and abnormal conditions in terms of the average magnitudes of maximum values and the times at which these maximum values occur. Focusing on these differences, a method for assessing the presence or absence of abnormalities has been investigated.
Here, the comparison between normal and abnormal conditions in terms of the average peak values (peak average) of acceleration, velocity, and displacement data for layers 1 through 3 is shown. The differences were scored and classified into four levels (3, 2, 1, 0). The results are presented in Table 2. This approach allows us to identify which values exhibit significant changes and which exhibit minor changes for each type of damage.

Table 2 Evaluation of the differences compared to normal and abnormal conditions

		Lv1			Lv2			Lv3		
Peak Average		**Acc**	**Vel**	**Dis**	**Acc**	**Vel**	**Dis**	**Acc**	**Vel**	**Dis**
	k_1	**0**	**3**	**3**	**2**	**3**	**3**	**3**	**2**	**3**
	k_2	**2**	**2**	**2**	**3**	**3**	**3**	**3**	**3**	**3**
	k_3	**2**	**2**	**1**	**2**	**1**	**2**	**0**	**0**	**3**

III. BAYESIAN INFERENCE ON ANOMALY DETECTION

III. A Bayesian Theorem

Bayesian theory is based on Bayes' theorem, which is represented by the following formula:

$$P(S_n|H_n) = \frac{P(S_n)P(H_n|S_n)}{\sum_m P(S_m)P(H_m|S_m)} \quad (3)$$

Posterior Probability, $P(S_n|H_n)$: The probability of hypothesis H_n given the observed event S_n, inferred after evaluating the evidence.
Prior Probability, $P(S_n)$: The initial probability of hypothesis S_n before new evidence, representing our preliminary belief.
Likelihood, $P(H_n|S_n)$: The probability of observing S_n assuming H_n is true, used to update our belief based on new data.
When an earthquake occurs and seismic acceleration data along with the building's response data are obtained, a multi-degree-of-freedom response analysis of the building is performed using the acquired seismic acceleration data. The analysis results are then compared to the building's response data, and this comparison is incorporated into the likelihood function.
The Bayesian formula for evaluating the presence or absence of abnormalities can be expressed as follows:

$$P(Abnormal|Data) = P(Abnormal)\frac{P(Observed\ Data|Abnormal)}{P(Observed\ Data)} \quad (4)$$

The observed data refers to the data obtained from the response analysis results (the average of the interval maximum values). The probability $P(Observed\ Data)$ can be calculated as follows:

$$P(Observed\ Data) = P(Normal)P(Normal|Observed\ Data) + \sum_{i=1}^{N} P(Abnormal_i)\, P(Observed\ Data|Abnormal_i) \quad (5)$$

For normal conditions, it is as follows.

$$P(Normal|Observed\ Data) = P(Normal)\frac{P(Observed\ Data|Normal)}{P(Observed\ Data)} \quad (6)$$

Here, the two important likelihoods in Bayesian estimation are defined as follows.
First, a normal distribution is determined using the mean and standard deviation of the maximum value data measured under normal condition. The normal distribution is then adjusted so that the peak density value is 1, and this adjusted distribution is used as the likelihood function. This likelihood function calculates the average of the interval maximum values under certain conditions. The closer this average is to the mean of the interval maximum values under normal conditions, the closer the likelihood value is to 1. Conversely, the further away the average is, the smaller the likelihood value becomes. For the likelihood related to abnormalities, a similar definition is used. The mean of the observed data at each abnormal location (k1, k2, k3) is determined, and then a normal distribution is established using this mean and standard deviation. By adjusting the probability density function so that its maximum value is 1, this function becomes the likelihood function representing the degree of abnormality of the observed data.

III. B Parameters for Bayesian Inference

The likelihood is a necessary value for estimation using Bayesian theory, representing the confidence level of observing event S_n under the condition that cause H_n has occurred. In this study, the likelihood function was created based on a normal distribution as previously described. An example of the created likelihood function is shown below.

$$P = \exp\left(-\frac{(x-\mu)^2}{2\sigma^2}\right)$$

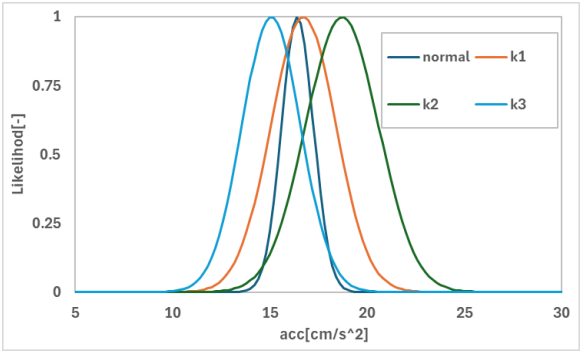

Figure 7 The likelihood function created from the Level 1 response acceleration

Bayesian estimation was conducted on acceleration, velocity, and displacement data using these likelihood functions and equations (3) to (6). Due to the difficulty in obtaining precise prior probabilities $P(Normal)$ and $P(Abormal)$, a uniform distribution was assumed, assigning each a value of 0.5. For abnormalities, given scenarios

involving damages k1, k2, and k3, the prior probability of 0.5 was further divided by 3, resulting in equal prior probabilities for each damage scenario.

III.C Bayesian Inference on anomaly detection

Table 3 shows the abnormality degree of the system using the average peak values of acceleration data measured under the assumed damage conditions for each layer. An abnormality degree of 0.5 or higher indicates a correct evaluation result. The evaluation results show that, under certain conditions, the abnormality degree falls below 0.5. This occurs because the data measured under abnormal conditions are similar to the data from normal conditions, leading to the data being mistakenly classified as normal rather than abnormal. This abnormality degree was used as evidence in the Bayesian network explained in the next chapter to evaluate whether each layer shows abnormal values or not.

Table 3 abnormality degree of acceleration data at each level

		Scenario			
		10%	20%	30%	40%
Abnormality	k1	**0.41**	**0.47**	**0.42**	**0.46**
	k2	**0.79**	**0.74**	**0.98**	**1.00**
	k3	**0.43**	**0.89**	**0.76**	**0.76**

IV BAYESIAN NETWORK ANALYSIS ON ANOMALY DETECTION

IV.A Bayesian Network Structure

Bayesian network is a method that integrates the causal relationships between multiple causative events and outcomes, estimating based on conditional probabilities[4].

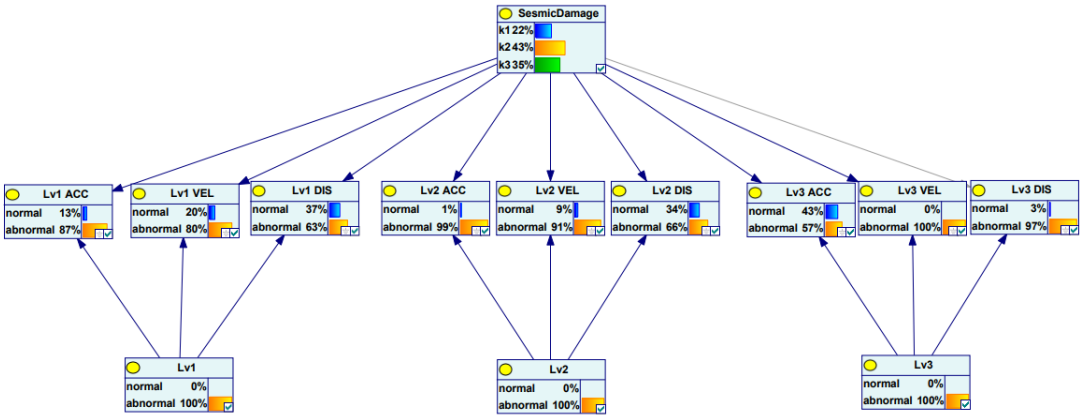

Figure 8 Structure of Bayesian Network

In this study, the difference in abnormality detection involves using acceleration, velocity, and displacement data obtained from each layer for estimation, while damage location estimation uses the acceleration, velocity, and displacement data from all layers for estimation.

IV.B Parameters of Bayesian Network Analysis

In a Bayesian network, conditional probabilities are used to integrate the causal relationships between multiple causative events and outcomes, and estimates are made based on these probabilities. These conditional probabilities are set according to the causal relationships of the outcomes.

Below is the probability table summarizing the conditional probabilities for the first layer response velocity. By incorporating these probabilities into the network structure, it becomes possible to estimate the layer indicating an abnormality.

Table 4 Bayesian Network probability table at Lv1 ACC

Lv1	Normal			Abnormal		
Seismic damage	k1	k2	k3	k1	k2	k3
Normal	0.9	0.9	0.9	0.1	0.25	0.25
Abnormal	0.1	0.1	0.1	0.9	0.75	0.75

This table summarizes the conditional probabilities for the first layer response acceleration. When Lv1 shows normal values and there is no structural damage, it is considered highly probable that k1, k2, and k3 will also show normal values. Therefore, the confidence level for Normal is set at 0.9, and for Abnormal, it is set at 0.1. On the other hand, when Lv1 shows abnormal values, it is considered highly probable that k1, k2, and k3 will also show abnormal values. Therefore, the confidence level for Abnormal is set higher. In Table 4, parameters that are more likely to change have been assigned a higher confidence level for indicating abnormalities. Specifically, the confidence levels for indicating abnormality were set as follows: 0.9 for 3 points, 0.75 for 2 points, 0.6 for 1 point, and 0.5 for 0 points. In the first layer response velocity, as shown in Table 1, k1 has 3 points, and k2 and k3 have 2 points.

IV.C Bayesian Inference on Damage Location

Next, we present the results summarizing the posterior probabilities estimated by integrating acceleration data using the Bayesian network. From these results, it was confirmed that when the true scenario involved k1 and k2 with 10% to 40% damage, and k3 with 20%, 30%, and 40% damage, the posterior probabilities for each layer exceeded 0.5, accurately estimating the presence of abnormalities. However, when the true scenario involved k3 with 10% damage, the posterior probabilities for each layer were below 0.5, failing to accurately estimate the abnormalities.

Table 5 The posterior probabilities estimating the Layer Showing Abnormalities at k1

		True Scenario			
		k1			
		10%	**20%**	**30%**	**40%**
Estimation result	**Lv1**	**0.84**	**0.99**	**0.99**	**0.99**
	Lv2	**0.61**	**0.91**	**0.98**	**1**
	Lv3	**0.96**	**1**	**1**	**1**

Here are the results of using a Bayesian network to estimate damage locations. The table shows the true scenarios and includes the posterior probabilities derived from the results:

Table 6 The Damage Location posterior probabilities estimated by acceleration

		True Scenario			
		k1			
		10%	**20%**	**30%**	**40%**
Estimation result	**k1**	**0.39**	**0.5**	**0.47**	**0.49**
	k2	**0.35**	**0.4**	**0.43**	**0.34**
	k3	**0.26**	**0.1**	**0.1**	**0.1**

When the true scenarios involved damages of 10% to 40% for k1 and k2, and 10% and 20% for k3, it was confirmed that the posterior probabilities for these true scenarios were higher than those for other scenarios, indicating accurate estimations. Furthermore, for true scenarios such as 20% damage in k1, 30% and 40% damage in k2, and 10%

damage in k3, the posterior probabilities were above 0.5, confirming that the estimations were made with high accuracy.

IV.D Bayesian Inference of Degree of Damage

In this section, we estimate the extent of damage in a three-layer structure where an abnormality has been identified and the damage location is known. The values used for this estimation are based on the natural periods, and Bayesian estimation is employed to determine which damage severity scenario is most plausible.

The likelihood functions are created using the same method as the abnormality detection technique, and scenarios of 10% to 40% damage for k1 to k3 are evaluated. Below, we present the likelihood functions for T1 to T3 used for k1 damage, along with an overview of the model used for estimating the damage severity.

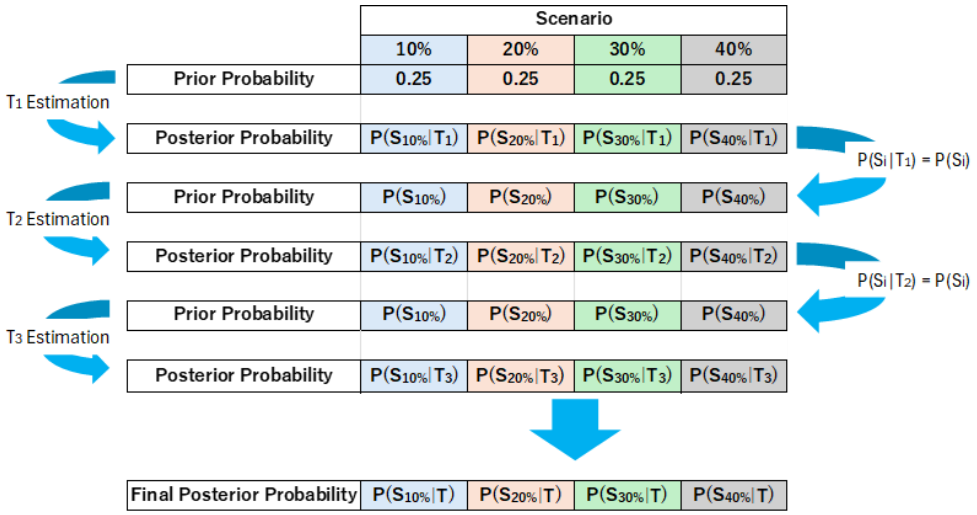

Figure 9 Estimation steps for degree estimation

The estimation steps are as follows:

1. Initial Prior Probability: Set a uniform initial prior probability of 0.25 for each damage scenario (10%, 20%, 30%, 40% for k1, k2, and k3).
2. Sequential Estimations: Perform estimations using the primary (T1), secondary (T2), and tertiary (T3) natural periods, sequentially updating the prior probabilities with the posterior probabilities from the previous step.
3. Final Posterior Probability: Use the posterior probabilities from the tertiary period estimation as the final values for each damage level scenario.

Table 7 Final posterior probability from degree of damage estimation

		True Scenario			
		10%	20%	30%	40%
Final posterior probability	k1	0.77	0.69	0.80	0.91
	k2	0.81	0.63	0.71	0.81
	k3	0.77	0.68	0.78	0.89

The above summarizes the results of estimating the degree of damage. As shown in the table, all estimation results exceed 0.5, indicating successful estimation for all damage levels. From these results, it is evident that a method for accurately estimating the damage severity has been established.

IV. CONCLUSIONS

In this study, we examined a Bayesian inference model to estimate the presence, location, and severity of abnormalities in a system using multi-degree-of-freedom response analysis.
For the three-layer model, Bayesian estimation was used to evaluate the presence of abnormalities in each layer when stiffness decreased. The results showed that for Lv1 and Lv2, the model accurately estimated the presence of abnormalities for k1, k2, and k3 under 10% to 40% damage. For Lv3, the model accurately estimated the presence of abnormalities for k1 and k2 under 10% to 40% damage, and for k3 under 30% and 40% damage.
Additionally, a Bayesian network model was constructed to estimate the damage location when abnormalities were detected in each layer. The results showed that the model accurately estimated the damage location for k1 and k2 under 10% to 40% damage scenarios. For k3, the model accurately estimated the damage location under 10% and 20% damage scenarios. Furthermore, Bayesian estimation using the natural periods was conducted to estimate the damage severity. It was confirmed that the model accurately estimated the damage severity for k1, k2, and k3 under all scenarios from 10% to 40%.
The evaluation results indicated some errors in the estimation for Lv3 k3 under 10% and 20% damage in abnormal detection, and for Lv3 k3 under 30% and 40% damage in damage location estimation. To improve this, it is necessary to develop estimation methods that can handle smaller damage levels.
In the future, to achieve more accurate estimations, we will explore and implement the use of machine learning to define the likelihood functions.

Reference

[1] "Seismic Design for the Emergency Response Facilities within the Reactor Buildings of Units 5, 6, and 7 at Kashiwazaki-Kariwa Nuclear Power Station"Available at: TEPCO - Seismic Design (Accessed: 2021)
[2] Kosei Kawamata, Sunghyon Jang, Evaluation on Seismic damage Inference for mass-spring damper structure using Bayesian Theorem, 2N06, Proceedings of AESJ 2023 Fall meeting, Sep.6th-8th, Nagoya, Japan (2023)
[3] The building of Center of Japan Database, El centro earthquake(https://www.bcj.or.jp/download/wave/).
[4] Tu Guang Tan, Sunghyon Jang, Akira Yamaguchi, A novel method for risk-informed decision-making under non-ideal Instrumentation and Control conditions through the application of Bayes' Theorem, Reliability Engineering & System Safety, Vol. 188, PP. 463-472, 2019

REFERENCES

[1] M. P. BROWN and K. AUSTIN, *Title of Book*, pp. 25–30, J. SMITH, Ed., Publisher Name, Publisher City, Publisher State (2004).
[2] M. P. BROWN and K. AUSTIN, "With or Without Title of Paper," *Title of Journal*, **36**, 102 (2004).
[3] R. T. WANG, "Title of Paper," *Proc. Title*, Location of Meeting, Date of Meeting, Vol. No., p. No., Publisher of Proceedings (2004).
[4] "ASRAM2025," https://aseannpsr.com/asram2025/ (2015).

Technical Session 13 (16:00 -18:00)	The Port 1, C Floor	Advanced PSA technologies, Multi-unit PSA, and SMR PSA
		Chair/Facilitator 1: Dr. Dong-San KIM, Korea Atomic Energy Research Institute (KAERI))
		Chair/Facilitator 2: Assoc.Prof. Wei Wang (City University of Hong Kong (CityU))
16:00 - 16:20		ID 32: Supporting Risk Assessment Reviews for Innovative SMR in Korea Speaker: Joonseok Lim (Kyung Hee University) Contributors: Joonseok Lim (Kyung Hee University), Gyunyoung Heo (Kyung Hee University), Dong-San Kim (Korea Atomic Energy Research Institute) , Seong Kyu Park (Nuclear Engineering Services & Solutions)
16:20 - 16:40		ID 29: Development of the Dynamic Event Tree Tool (DICE-MULTI) for SMR Multi-Module Simulation Speaker: Yuntae Gwak (Kyung Hee University) Contributors: Yuntae Gwak (Kyung Hee University), Gyunyoung Heo (Kyung Hee University), Dohun Kwon (Kyung Hee University), Yongjoon Lee (Kyung Hee University)
16:40 - 17:00		ID 117: Development of a Multi-Module Event Sequence Modeling Tool for High-Temperature Gas-Cooled Reactors Speaker: Pengcheng Peng (Tsinghua University) Contributors: Pengcheng Peng (Tsinghua University), Jun Zhao (Tsinghua University), Jiejuan Tong (Tsinghua University)
17:00 - 17:20		ID 53: Estimation of LOCA Frequencies for the Innovative Small Modular Reactor Speaker: Kibeom Son (Korea Atomic Energy Research Institute) Contributors: Kibeom Son (Korea Atomic Energy Research Institute), Jin Hee Park (Korea Atomic Energy Research Institute), Sung-Min Shin (Korea Atomic Energy Research Institute)
17:20 - 17:40		ID 62: Methodology for Generalized Risk Assessment of Multi Event Scenarios in Deep Geological Repositories Speaker: Seongmin Jin (Kyung Hee University) Contributors: Seongmin Jin (Kyung Hee University), Kibeom Son (Korea Atomic Energy Research Institute), Karyoung Choi (Kyung Hee University), Minseok Kim (Kyung Hee University), Gyunyoung Heo (Kyung Hee University)

Supporting Risk Assessment Reviews for Innovative SMR in Korea

Joonseok Lim[1], Dong-San Kim[2], Seong Kyu Park[3], Gyunyoung Heo[1*]

[1] *Department of Nuclear Engineering, Kyung Hee Univ., Deogyeong-daero, Giheung-gu, Yongin-si, Gyeonggi-do 17104, Republic of Korea*
[2] *Korea Atomic Energy Research Institute, 111 Daedeok-daero 989beon-gil, Yuseong-gu, Daejeon, Republic of Korea*
[3] *Nuclear Engineering Services & Solutions, 6, Jiphyeonjungang 7-ro, Sejong-si, Republic of Korea*

ABSTRACT

In Korea, the innovative small modular reactor development agency plans to complete the standard design by the end of 2025 and undergo standard design approval review for three years starting in 2026. Accordingly, the Nuclear Safety and Security Commission, the regulatory authority, has established the Regulatory Research Management Agency for SMR in accordance with Article 12 of the Nuclear Safety Act. The authors are currently carrying out tasks related to risk assessment among the detailed tasks of Regulatory Research Management Agency for SMR. This paper provides an overview of the project, which consists of a one-year Phase 1 and a two-year Phase 2 starting in 2024, including its key objectives, major achievements, and future plans. The two primary goals of Phase 1 are: (1) investigating international and domestic cases, regulations, and technical standards related to risk assessment for light water SMRs (both single and multi-module designs), and (2) developing the Multi-purpose Probabilistic Analysis of Safety model for independent risk assessment review of a single-module design. A gap analysis was conducted to identify necessary revisions for the existing safety review guidelines. In the development of the Multi-purpose Probabilistic Analysis of Safety, we established a foundation for the reliability analysis of a single-module by performing general probabilistic safety assessment procedures, including initiating event analysis and system analysis. In Phase 2, we will address technical challenges specific to innovative small modular reactor, such as multi-module risk quantification, passive safety systems, boric acid-free operation, and human reliability analysis. Addressing these issues will require international collaboration.

Keywords: Risk Assessment, PSA, Multi-Modules, Safety Goal, MPAS

I. Introduction

In Korea, the innovative small modular reactor (i-SMR) development agency plans to complete the standard design by 2025 and undergo standard design approval (SDA) review for three years starting in 2026. One of the top-tier requirements (TTRs) for i-SMR is that the core damage frequency (CDF) should be less than $1.0E-9\ /module \cdot year$ [1]. As shown in Table I, to achieve the TTR, i-SMR has unique characteristics compared to existing nuclear power plants (NPPs). Therefore, new regulatory approaches, including those related to SDA, are required.

To support independent regulatory reviews of the i-SMR, the Nuclear Safety and Security Commission (NSSC), the regulatory authority, established the Regulatory Research Management Agency for SMR (RMAS). The authors are currently carrying out tasks related to risk assessment among the detailed tasks of RMAS. The ultimate goal of these tasks is to develop the methodology and database necessary for the safety review process during the SDA. To achieve this, we plan to analyze, refine, and develop methodologies that account for the unique design characteristics of SMRs in single-module probabilistic safety assessment (PSA). Additionally, we aim to construct a Multi-purpose Probabilistic Analysis of Safety (MPAS) model for multi-module PSA by integrating single-module PSA models [2].

The two primary objectives of Phase 1 (2024) are: (1) investigating international and domestic cases, regulations, and technical standards related to risk assessment for light water SMRs (both single and multi-module designs), and (2) developing a draft MPAS model for independent risk assessment review of a single-module design. The two primary objectives of Phase 2 (2025–2026) are: (1) improvement of the draft MPAS model developed in Phase 1 and its expansion to a multi-module configuration, and (2) proposing regulatory applications such as a review methodology, structure, system and components (SSCs) classification, safety goals multi-module for llight water SMR. Figure 1 provides an illustration of the

step-by-step objectives. This paper provides an overview of the project spanning Phase 1 (2024) and Phase 2 (2025–2026), including its key objectives, major achievements, and future plans.

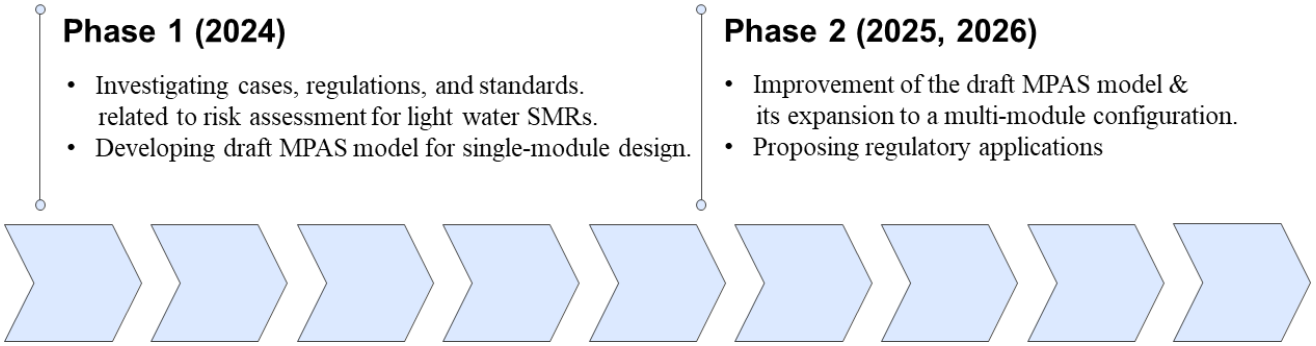

FIGURE 1. The objectives of each phase

TABLE I. The differences between existing NPPs and i-SMR

Existing NPPs	i-SMR
● Active safety system, safety class power system	● Passive safety system, non-safety class power system
● One unit operation in one control room	● Multi(4)-module operation in one control room
● I&C characteristics of reactor vessel and containment	● Changes in I&C characteristics due to steel containment vessel, integral reactor, helical steam generator, boric acid-free operation, etc.
● Unit concept	● Module concept
● Minimization of shared facilities between reactors	● Expansion of shared facilities among modules.

II. Review of current status

II.A. SMART100

In Korea, SMART100 is a reactor that enhances safety through the application of a passive safety system and improves economic efficiency by increasing its output to 365 MWt (110 MWe) from SMART, which was licensed in 2012. This reactor is equipped with passive safety systems and physical barriers, enabling it to remain safe for 72 hours without operator intervention, relying solely on batteries and natural forces in scenarios such as the Fukushima accident.

SMART100 has four passive safety systems: the passive safety injection system, the automatic depressurization system, the containment pressure and radioactivity suppression system, and the passive residual heat removal system. The phenomenological reliability of these systems was evaluated as 1.0, as their probability of failure is negligibly low [3].

II.B. NuScale US600

In the United States, NuScale is a reactor that enhances safety through its passive safety systems while offering scalability with a modular design. Each module generates 160 MWt (50 MWe) and can be deployed in plants with up to 12 modules. The reactor's passive safety system is designed to ensure safety without operator intervention or external power, leveraging natural phenomena such as gravity and convection.

It is an integral light water reactor, with the reactor coolant system (RCS) housed inside the reactor vessel, eliminating the need for coolant or safety pumps. The containment vessel (CV) is submerged in a pool, ensuring safety through natural circulation and passive safety mechanisms. The emergency core cooling system (ECCS) and the decay heat removal system (DHRS) were designed as passive safety systems, and their phenomenological reliability was evaluated using a response surface methodology.

NuScale also conducted a PSA for multi-modules, although this was not a mandatory requirement for design certification (DC). In assessing multi-module risk, the risk was estimated by assuming that the same accident occurred in two or more modules, rather than directly modeling the cascading effects of an accident in a specific module. This approach was realized on applying the multi-module adjustment factor (MMAF) and the multi-module performance shaping factor (MMPSF) to the

minimal cut-set derived from the single-module risk model [4]. A more detailed distinction between SMART100 and US600 is outlined in Table II.

TABLE II. The technical differences between the SMART100 and US600 [3, 4]

	SMART100	US600
Thermal Power	365MWth	160MWth
Electric Power	110MWe	50MWe
Safety System	Passive	Passive
Primary Loop Circulation Type	Forced circulation	Natural circulation
CDF	<1.0E-7/RY	<1.0E-8/RY
Internal control rod drive mechanism	X	O (Electromagnetic)
Reliability of Passive System	1.0	T-H analysis
Operator Response Time	72 hour	72 hour
Containment	Building	Vessel
Multi-module PSA	X	O

III. Development of MPAS Models for i-SMR

III.A. Initiating event identification

The initiating events analysis is one of the key steps in PSA; however, it poses a challenge for newly designed reactors due to the lack of operating experience and design-specific data. The i-SMR falls into this category; therefore, initiating events were identified based on publicly available data and PSA expertise.

The identification process involved:

1. Identifying plant transients that trigger manual or automatic reactor shutdown during normal operation.
2. Defining and categorizing all possible initiating events during plant operation.
3. Grouping similar initiating events based on the required safety functions or plant responses for accident mitigation.

The analysis methodology was developed using operational experience from commercial and similar NPPs, as well as engineering judgment. The initial draft consists of two categories and 15 initiators, as presented in Table III. The list of initiating events will be updated in Phase 2. The frequency of initiating events will be estimated in future work, reflecting the design characteristics of the i-SMR.

TABLE III. The initial draft list of initiating events for internal events at-power Level 1 PSA

Category	Grouped initiators
Loss of Coolant Accident (LOCA)	MMPS CHG Line Break (in CV)
	MMPS CHG Line Break (out CV)
	MMPS LD Line Break (in CV)
	MMPS LD Line Break (out CV)
	ECCS Spurious Operation (EDV)
	ECCS Spurious Operation (ERV)
	Steam Generator Tube Rupture
	RCS LOCA (in CV)
	Interfacing System LOCA
	LOCA-LODC
Transient	Large Secondary Side Break
	General Transient
	Loss of Main Feedwater
	Loss of Condenser Vacuum
	Loss of Offsite Power

III.B. System analysis

The key safety functions of the i-SMR consist of (1) reactor trip, (2) residual heat removal, and (3) containment of radioactive materials, similar to those of general NPPs. One notable difference is that the residual heat removal comprises the passive emergency core cooling system (PECCS), the passive containment cooling system (PCCS), and the passive auxiliary feedwater system (PAFS), all of which are passive safety systems operating through natural forces.

For instance, PECCS functions similarly to the "Feed & Bleed" system in conventional large NPPs. This passive system utilizes natural circulation and consists of an emergency depressurization valve (EDV), which releases steam from the top of the reactor vessel to depressurize the primary loop, and an emergency recirculation valve (ERV), which returns the condensed steam to the primary side.

The heading of the event tree (ET) in Level 1 PSA generally includes reactor trip, PECCS, PCCS, PAFS, the pilot-operated safety relief valve (POSRV), and the modular makeup and purification system (MMPS). The POSRV is mounted on top of the reactor vessel for primary side depressurization, and the MMPS replenishes the reactor coolant inventory independently of the PECCS. An example of an ET for a general transient (GTRN) is presented in Figure 2.

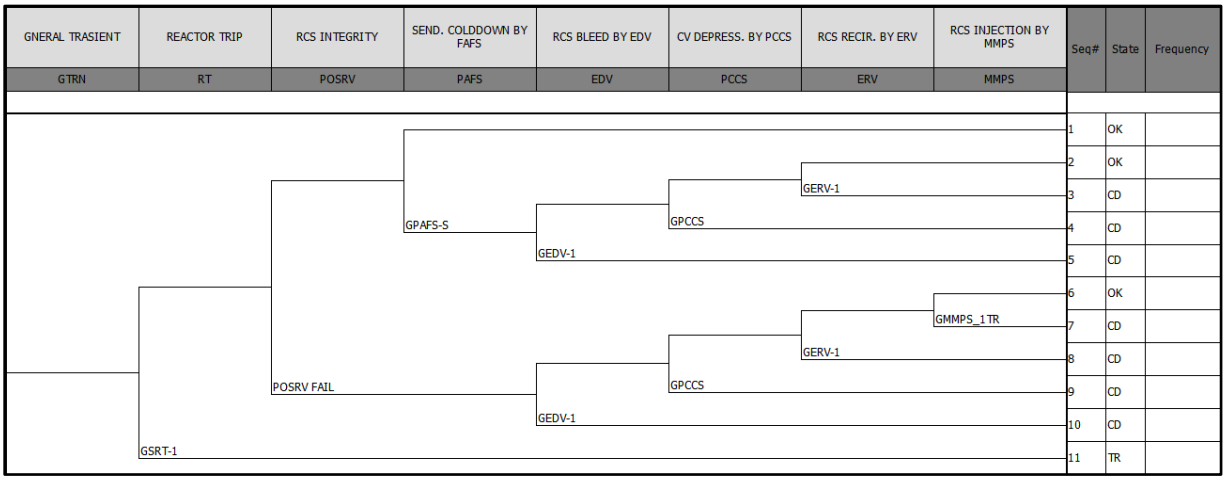

FIGURE 2. GTRN ET example

To develop fault trees (FTs), the simplified Piping and Instrumentation Diagram (P&ID) was initially developed using publicly available data, excluding support systems such as the primary component cooling water system (CCWS). This will be continuously updated as the applicant's design evolves. Figure 3 presents the P&ID of the PECCS, illustrating that two EDVs are positioned at the top of the reactor vessel, while two ERVs are located at the bottom. In Figure 4, valve failures and valve actuation signal failures are expected to be considered as basic events in the FT of PECCS based on the P&ID. FTs for other systems were also developed through a similar process.

III.C. Accident sequence analysis

Accident sequence analysis will be conducted using MARS-KS or MELCOR, and a model is currently under development. Since multi-module operation and load-following operation may be challenging to analyze with MARS-KS or MELCOR, Flownex was chosen as an alternative for such analyses. Flownex is a computational tool that efficiently models complex thermal-fluid networks and performs simulations. It is capable of power plant physical analysis, including thermal-fluid analysis, instrumentation and control (I&C) modeling, application programming interface (API) integration, heat transfer analysis, and transient analysis [5]. Figure 5 presents a single-module model that is currently under development using Flownex.

IV. Conclusions

One of the key significances of the MPAS model is its ability to independently verify the applicant's PSA model. From a regulatory perspective, the MPAS model facilitates the following tasks:

1. Verifying whether the applicant's design meets quantitative requirements (e.g., CDF).
2. Validating the authenticity of the top (major) cut-set presented by the applicant.
3. Reviewing the applicant's assessments (e.g., SSCs classification) based on PSA results (risk information).

The MPAS model is not yet fully developed because the i-SMR design is still in progress, the applicant's design is subject to frequent changes, and much of the design data remains unavailable. The model will be continuously updated to best reflect the progress of the applicant's design.

An uncertainty analysis will be conducted by applying reliability data (e.g., the latest NUREG/CR-6928) to the MPAS model at appropriate stages. In addition, uncertainties related to the phenomenological failure assessment of passive systems and the failure probability assessment of EDVs (or ERVs) will be analyzed by developing or applying appropriate methodologies. At present, we are focusing on gaining insights from multi-module PSA and aim to refine the classification of structures, systems, and components (SSCs) by incorporating results from both single- and multi-module PSA.

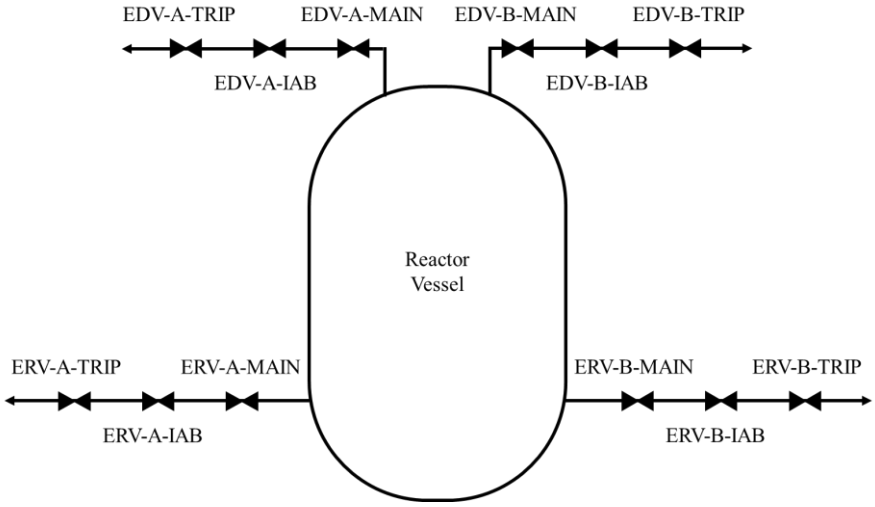

FIGURE 3. Simplified P&ID of PECCS (draft)

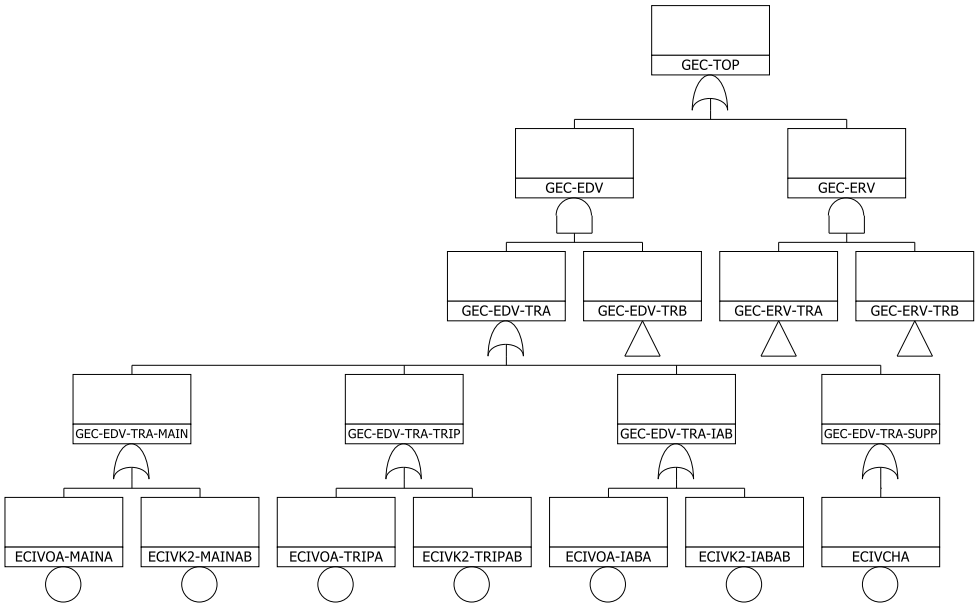

FIGURE 4. FT of PECCS (draft) [6]

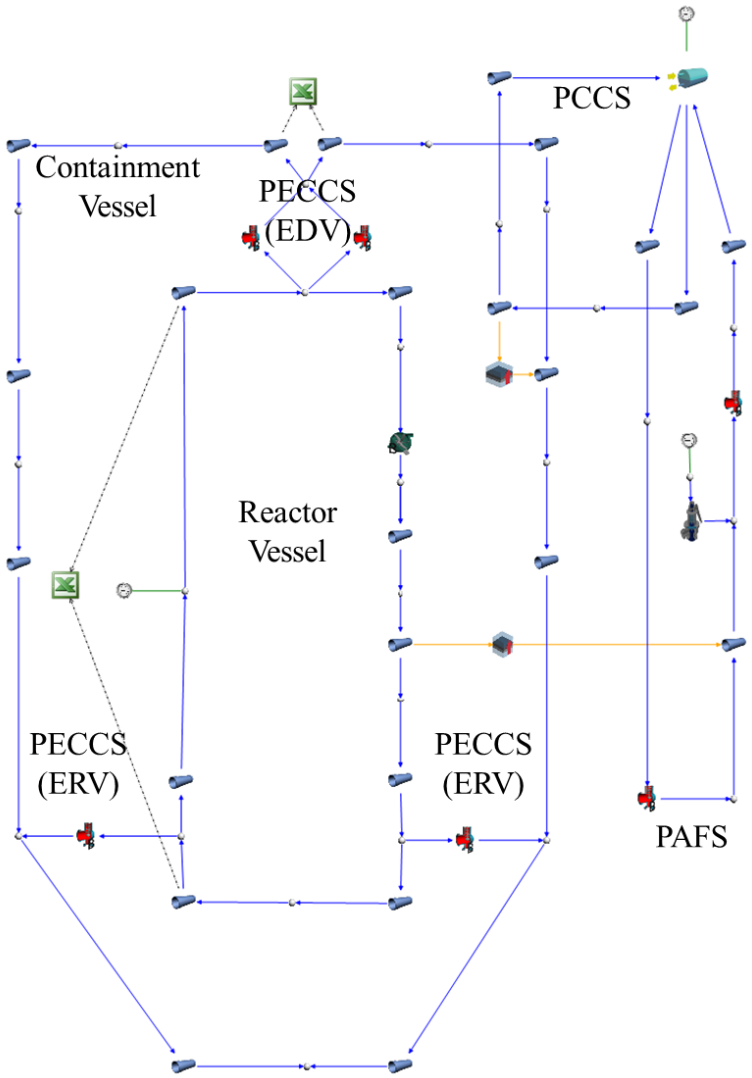

FIGURE 5. Simplified Flownex model

ACKNOWLEDGMENTS

This work was supported by the Nuclear Safety Research Program through the Regulatory Research Management Agency for SMRS (RMAS) and the Nuclear Safety and Security Commission (NSSC) of the Republic of Korea (No. 1500-1501-409).

REFERENCES

[1] Innovative Small Modular Reactor Development Agency. "i-SMR leaflet," accessed Mar. 18, 2025. [Online]. Available: https://ismr.or.kr/library/16
[2] G. Heo, et al. "Introduction to Regulatory Methodology Development for Risk Assessment of Light Water SMRs," *KNS Autumn meeting*. 2024.
[3] NSSC, et al. "SMART100 SDA Deliberation Report," 2024.
[4] NuScale, "Chapter 19 Probabilistic Risk Assessment and Severe Accident Evaluation," 2020.
[5] Flownex, "General Brochure," accessed Mar. 18, 2025. [Online]. Available: https://flownex.com/industries/overview/
[6] D. Choi, et al. "review of failure modes and effects of IAB valves in NuScale," *KNS Spring meeting*. 2025.

ASRAM2025
www.asram2025.org
Asian Symposium on Risk Assessment and Management 2025
Pattaya, Thailand, 27 – 29 August 2025

Development of the Dynamic Event Tree Tool (DICE-MULTI) for SMR Multi-Module Simulation

Yuntae Gwak[1], Dohun Kwon[1], Yongjoon Lee[1], Gyunyoung Heo[1*]

[1] *Department of Nuclear Engineering, Kyung Hee Univ., Deogyeong-daero, Giheung-gu, Yongin-si, Gyeonggi-do 17104, Republic of Korea*

ABSTRACT

Small Modular Reactors represent a significant advancement in nuclear technology, featuring multiple reactor modules within a shared facility. However, pending technical challenges and the lack of safety evaluation standards for SMRs necessitate the development of new assessment methodologies. To address this, DICE-MULTI, an extension of the Dynamic Event Tree tool DICE, was developed to enable simulations of multiple physical models. DICE-MULTI supports safety assessment of SMRs through DET analysis, contributing to the establishment of future safety review standards. Key advancements in DICE-MULTI include the synchronization of time steps across multiple physical models. This feature resolves discrepancies in simulation times caused by differing operational states, such as transient conditions in one model and steady-state conditions in another. Time step synchronization ensures accurate representation of real-time interactions between physical models, including the effects of potential shared components like an Emergency Cooling Tank. Additionally, DICE-MULTI introduces a third physical model dedicated to calculating shared component parameters, referred to as "common variables," in real time. This physical model dynamically computes and distributes these variables to the respective physical models, ensuring precise simulation of interdependencies. To verify its functionality, DICE-MULTI was tested using simplified models. The results demonstrated its capability to effectively handle multi-module simulations. These developments position DICE-MULTI as an available tool for the safety assessment of SMRs, offering enhanced accuracy in modeling complex interactions within multi-module systems.

Keywords: Small Modular Reactor, Dynamic Event Tree, Multi-Module Simulation

I. INTRODUCTION

Small Modular Reactors (SMRs) are next-generation nuclear systems that pursue enhanced safety, economic feasibility, and operational flexibility, based on a fundamentally different design philosophy compared to conventional large-scale reactors. Each module is constructed as a compact and independent unit, and the system is designed with inter-module operability and scalability in mind, making it distinct from traditional nuclear power plants. Such structural characteristics lead to a complex operational environment in which multiple reactor modules operate within a single facility and share common systems.

Due to the nature of SMRs, a systematic and precise safety analysis is required to address various scenarios arising from dynamic inter-module interactions and the use of shared systems (e.g., cooling systems, power supply systems). While conventional Probabilistic Safety Assessment (PSA) techniques provide quantitative evaluation of various accident scenarios, they face limitations in accurately reflecting complex dynamic interactions, time-dependent state changes, and inter-system linkages [1].

Particularly in multi-module environments, the limitations of static analysis inherent in existing PSA methodologies become more pronounced. Multi-module systems present significant challenges in accurately modeling inter-module interactions, dynamic behavior of shared systems, and time-dependent operational state changes, forcing reliance on conservative assumptions. For example, traditional multi-unit PSA typically assumes that each unit is always operating at full power or conservatively treats shared system failures as simultaneously affecting all modules [2]. Such conservative treatment risks oversimplifying the actual dynamic characteristics of the system, potentially leading to overestimation of safety margins or masking important safety phenomena.

Static PSA, composed of Boolean logic-based event tree and fault tree analyses, has inherent limitations in adequately considering time-dependent interactions or sequential events [3]. These problems make it difficult for static models to realistically represent the staged propagation processes of how shared system failures affect other modules in multi-module facilities.

In response to these challenges, Dynamic Event Tree (DET) analysis and Dynamic Fault Tree (DFT) methodologies have emerged as representative approaches capable of realistically simulating the evolution of uncertainties over time. Unlike static event tree analysis, which examines predefined accident scenarios, DET dynamically branches scenarios based on system state changes during the simulation. This enables more accurate representation of complex interactions and time-dependent system behaviors as accidents progress [4]. Meanwhile, DFT extends static fault tree analysis by introducing a temporal dimension, allowing modeling of spare management, order-dependent failures, and functional dependencies. While static fault trees only consider whether components fail, DFT analyzes when failures occur and how the failure sequence impacts the system, providing more realistic reliability assessments [5]. In multi-module environments, DET effectively overcomes the limitations of static PSA by accurately reflecting inter-module interactions, the dynamic response of shared systems, and time-dependent operator actions without resorting to conservative assumptions. One of the leading tools implementing the DET methodology is DICE, which enables dynamic simulations that incorporate diverse uncertainties.

However, the original DICE is structured to perform simulations at the level of a single system or module, limiting its applicability to scenarios involving inter-module interactions or shared system effects in multi-module environments like SMRs. Therefore, this study developed DICE-MULTI, an extended analysis tool based on DICE, capable of handling multiple physical models simultaneously. The tool implements time synchronization among physical models operating in different states and dynamically calculates and updates shared variables (e.g., flow rate, temperature) across modules.

DICE-MULTI aims to provide a realistic simulation framework for the dynamic behavior of SMR multi-module systems, ultimately contributing to the establishment of a reliable basis for safety assessment and regulatory standards.

II. Functions and Implementation Structure of DICE-MULTI

The original DICE is a dynamic probabilistic safety assessment tool based on the Dynamic Event Tree (DET) methodology, designed to simulate scenario branching over time by incorporating system behavior and uncertainty. It consists of a thermal-hydraulic physical module, a diagnosis and reliability module that determines responses based on system states, and a scheduler that controls simulation flow and scenario branching. Its architecture is primarily tailored for accident scenario analysis within a single reactor module.

However, SMR systems inherently involve multiple reactor modules operating within a shared facility, interacting through common systems and physical couplings. In such systems, the limitations of DICE's single-module design become apparent. For instance, a cooling anomaly in one module may impact the thermal conditions of a shared Emergency Cooling Tank (ECT), which in turn affects the thermal-hydraulic response of another module. Such interdependencies are difficult or even impossible to realistically capture with the original DICE structure.

To meet the analytical demands of multi-module systems, this study introduces DICE-MULTI, an extended version of DICE designed to enable concurrent simulations of multiple physical models. Each physical module in DICE-MULTI operates independently but pauses at regular computation intervals referred to as progress steps to exchange state information with other modules. During these exchanges, shared variables (e.g., ECT flowrate and temperature) are dynamically calculated based on the outputs of each module. The scheduler manages the timing of these exchanges, coordinates the order of information propagation, and ensures system-wide consistency in variable updates.

A key feature of DICE-MULTI is its ability to preserve time synchronization even when modules are operating under different transient conditions. This allows for accurate modeling of inter-module thermal and hydraulic interactions. Furthermore, DICE-MULTI supports heterogeneous configurations in which each module may have different design parameters, operational modes, or accident progressions offering a more realistic and versatile simulation environment than conventional parallel analysis approaches.

By retaining the core architecture of DICE while introducing multi-module integration, shared parameter synchronization, and coordinated scheduling capabilities, DICE-MULTI provides a robust analytical platform suitable for evaluating the

complex behavior of i-SMR systems. Moreover, its flexible architecture can be extended to multi-physics applications, such as P2X systems and hydrogen-coupled energy networks, making it a promising tool for future energy system safety assessments [6].

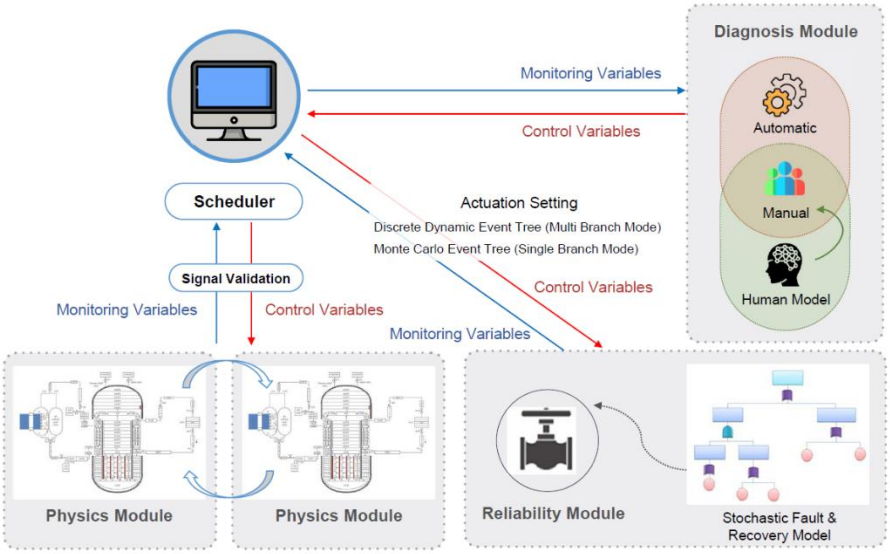

FIGURE 1. Schematic Architecture of DICE-MULTI

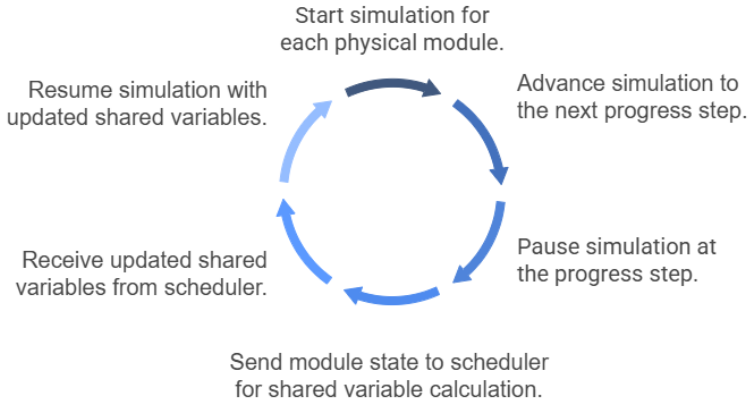

FIGURE 2. Flowchart of Shared Variable Exchange Process in DICE-MULTI

III. Case Study: Application of DICE-MULTI to a Multi-Module LOFW Accident Scenario

To evaluate the multi-module interaction capabilities of DICE-MULTI and assess the influence of dynamically coupled shared system variables on the overall system behavior, a case study was conducted using a simplified model of a SMR. This study focused on a Loss of Feedwater (LOFW) accident scenario and compared the thermal behavior of the ECT under three different simulation conditions. The shared variables liquid temperature, gas temperature, and pressure in the ECT were configured to be dynamically exchanged between physical modules at each progress step.

The first scenario served as a reference case in which both modules remained in normal operation without any initiating event. In the second scenario, a LOFW event was introduced in only one of the two modules at 500 seconds, while the other module continued in a steady state condition. In the third scenario, both modules experienced LOFW events simultaneously at the same point in time, allowing for the observation of compounded thermal loads on the shared ECT. All simulations were run up to 1000 seconds, and the liquid temperature of the ECT was used as the key indicator for comparing inter-module effects.

In the first scenario, the ECT liquid temperature remained stable throughout the simulation, confirming that the shared variable exchange and synchronization mechanisms operated consistently under non-accident conditions. In the second scenario, despite only one module undergoing the LOFW event, a noticeable increase in ECT temperature was also observed in the unaffected module. This result demonstrates the ability of DICE-MULTI to accurately capture inter-module thermal interactions mediated through shared resources. In the third scenario, when both modules experienced the LOFW accident simultaneously, the temperature increase in the ECT was significantly larger, indicating that shared system behavior becomes more pronounced and nonlinear when subjected to concurrent stress.

These results confirm that DICE-MULTI provides a realistic simulation framework capable of representing dynamic interactions and shared system feedbacks in multi-module environments. In particular, the observation that modules not directly affected by an accident can still experience thermal impacts through shared systems highlights a critical limitation of traditional single-module or static analysis methods. Thus, incorporating such interdependencies is essential for accurate safety assessment of multi-module reactor systems**.**

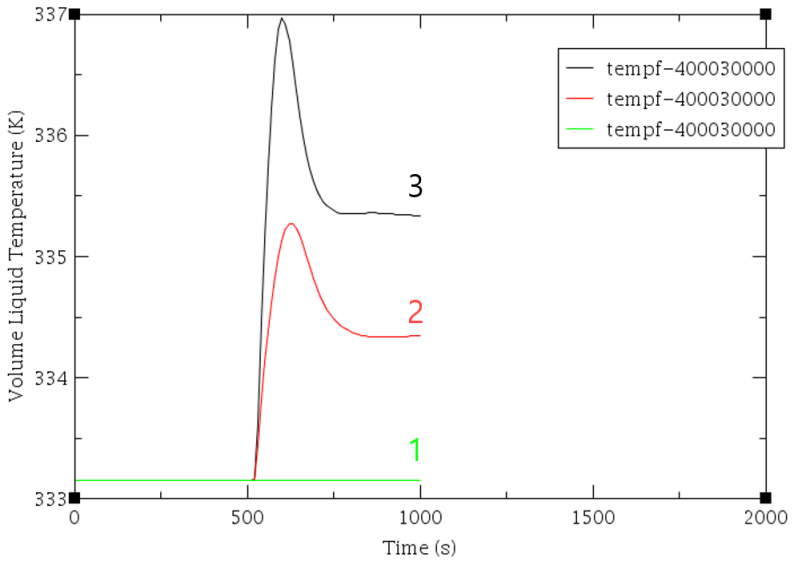

FIGURE 3. Transient Evolution of Temperature in the ECT Under Different Module Accident Scenarios

IV. Conclusion

In this study, DICE-MULTI was developed as an extension of the original DICE tool to enable more realistic simulation of dynamic interactions in multi-module SMR systems. In systems such as SMRs, where multiple reactor modules are interconnected through shared systems, conventional single-module analysis or static PSA methods fall short in capturing time-dependent behaviors and inter-module coupling effects. To address this analytical gap, the proposed DICE-MULTI framework allows simultaneous operation of multiple physical models with integrated time synchronization and shared variable exchange.

A case study was conducted using a conceptual accident scenario in which the ECT was treated as a shared component. Simulations were performed under three conditions: no accident, a LOFW accident in one module, and LOFW accidents in both modules. The results showed that even when the accident occurred in only one module, thermal effects were propagated through the shared ECT to the unaffected module, altering its state. In the case of simultaneous accidents in both modules, the thermal load on the shared ECT was compounded, leading to significantly higher temperature increases. These results highlight dynamic characteristics that cannot be captured by single-module simulations and demonstrate DICE-MULTI's capability to realistically reflect inter-module effects in multi-reactor environments.

DICE-MULTI expands the analytical scope of the original DICE tool by incorporating time-synchronized simulations, dynamic shared variable handling, and orchestrated scheduling among modules. It also presents the potential for simulation-

based safety assessments that avoid the need for conservative assumptions required in static PSA, offering a more realistic evaluation of system behavior.

However, this study was limited to a simplified conceptual SMR model and a single type of accident scenario. Future work should involve applying the framework to detailed reactor designs and incorporating additional shared system variables such as electrical and control systems. Furthermore, integration of operator response models and probabilistic input distributions will allow the tool to evolve into a more comprehensive and practical platform for multi-module safety assessment**.**

ACKNOWLEDGMENTS

This research was supported by the National Research Council of Science & Technology (NST) grant by the Korea government (MSIT) (No. GTL24031-000).

REFERENCES

[1] Multi-unit Probabilistic Safety Assessment Regulatory Framework Development Research Project, Nuclear Safety and Security Commission, Republic of Korea (2023).
[2] Technical Approach to Probabilistic Safety Assessment for Multiple Reactor Units, Safety Reports Series No. 110, International Atomic Energy Agency, Vienna, Austria (2023).
[3] Development and Application of Level 1 Probabilistic Safety Assessment for Nuclear Power Plants, Safety Standards Series No. SSG-3, International Atomic Energy Agency, Vienna, Austria (2010).
[4] Dynamic Probabilistic Safety Assessment Studies for Advanced Reactors, Idaho National Laboratory, INL/EXT-15-36726, Idaho Falls, Idaho, United States (2015).
[5] M. Cepin and B. Mavko, A dynamic fault tree, Reliability Engineering & System Safety, vol. 75, no. 3, pp. 239–252, Elsevier, Oxford, United Kingdom (2002).
[6] D. G. F. Final PhD Thesis, "Flexibility in Multi Energy Systems: Co-simulation Approaches for P2X Resource Integration," TU Delft Research Portal, Delft, Netherlands (2023).

ASRAM2025
www.asram2025.org
Asian Symposium on Risk Assessment and Management 2025
Pattaya, Thailand, 27 – 29 August 2025

Development of a Multi-Module Event Sequence Modeling Tool for High-Temperature Gas-Cooled Reactors

Pengcheng Peng[1,2,3], Jun Zhao[1,2,3], Jiejuan Tong[1,2,3,*], Hongru Zhao[1,2,3]

[1] *Institute of Nuclear and New Energy Technology, Tsinghua University, Beijing, 100084, China*
[2] *Collaborative Innovation Center of Advanced Nuclear Energy Technology, Beijing 100084, China*
[3] *The Key Laboratory of Advanced Reactor Engineering and Safety, Ministry of Education, Beijing, 100084, China*
[*] *Corresponding author: J. Tong (tongjj@tsinghua.edu.cn)*

ABSTRACT

The high-temperature gas-cooled reactor (HTGR) in China adopts a modular design of multiple reactor modules serving one single unit. For the relationships within one unit even among different units, accident scenario analysis involving multiple reactor modules becomes an essential consideration in probabilistic safety assessment in HTGRs. It is still applicable for modeling event sequences in HTGR by using traditional event tree analysis, and the multi-module event trees are typically modeled by combining event trees of single modules. In this way, however, the sequences of multi-module event trees will increase exponentially with growth in the number of reactors affected by the accident, which will consume not only a huge manpower but also make it difficult to ensure the absence of errors during the combining process so that there exist challenges in the establishment and display of those event trees. This paper designs and develops a program tool that can generate multi-module event trees automatically based on the combination of single-module event trees. This tool has a browser/server architecture, and is capable of achieving unified-format import and export of event trees, combining event trees by setting rules, and automatically generating and displaying multi-module event trees.

Keywords: Multi-module event tree, event tree combination, probabilistic safety assessment, high-temperature gas-cooled reactor

I. INTRODUCTION

The modularisation of small reactors becomes a significant trend in the nuclear power industry and a typical example is the high-temperature gas-cooled reactors (HTGR) where multiple reactor modules will service a single turbine at the same time [1]. That design strengthens the interdependencies between modules within the unit of HTGR, which requires the event sequence analysis, as the most fundamental part of probabilistic safety analysis (PSA), to address accident scenarios involving multiple modules. For this reason, Zhang et al. [2-6] established a multi-module PSA framework for HTGR and developed a tool for multi-module event sequence modelling. Under this framework, the event sequences of multi-module event trees (METs) are defined as combinations of ones from the single-module event trees (SETs). In order to realize the combination of event trees automatically, it is necessary to model the elements used in the whole combination process. According to the engineering experience in practice, the following three issues should be considered in that process.

1. Graphical representation of METs. To facilitate the combination and screening of event sequences, the framework mentioned above provides a vector representation of METs [5]. However, it will only reserve valid combinations so that MET may not retain a complete tree structure, which means that it could not be converted into graphical representation. Since graphical representation will display a clear logic of the development of event sequences to PSA specialists, it is an indispensable form of expression in practice. We need a suitable method to enable mutual conversion between these two representations.
2. Classification of multi-module release categories. The probabilistic safety objective of HTGRs in China focuses on the type of radioactive release (RC50) that cause individual effective doses exceeding 50mSv on the plant boundary [7]. In practice, as the number of modules in HTGRs increases, say a six-module design in [8], combinations of the releases (non-RC50) from single module that will not lead to RC50 may result in RC50 consequences, thereby the

non-RC50 release combinations should be considered as well. It imposes higher requirements on the combination of event trees.

3. The scalability of modelling tools. To facilitate the exchange and application of PSA model, a standard interactive format of MET and its related elements is needed, such as the XML representation developed by the Open-PSA project [9].

To address the issues above, this paper presents the theory of event tree combination where some technical elements in the combination process are revised, compared to the framework proposed in [5], say the conversion between different representations of event tree and the automatic classification of multi-module releases. Based on this theory and a modelling tool of MUETBASE in [4], we will develop a more comprehensive event sequence modelling tool of HTGRs, which achieves automatic modelling and improves the scalability of the programme tool.

The remainder content is organized as followings. Chapter II provides the theory of event tree combination from three aspects: definition, representation methods, and combination rules. Chapter III introduces an event sequence modelling tool of HTGRs that is developed on the basis of that theory. The conclusion is presented at last chapter.

II. THEORY OF EVENT TREE COMBINATION

II.A. Definition of Multi-Module Event Tree

II.A.1. Initiating Event

An initiating event involving multiple modules is defined as an initiating event that affects two or more reactor modules simultaneously. Such events are often identified on the basis of initiating events from PSA model for single module and involve shared structures, systems, or components. Taking the HTR-PM with two modules as an example, loss of coolant that can be isolated will include breaks at the pipe sections shared by two modules, which should be separately classified as two-module initiating events, while the breaks at other positions are still the single-module initiating events. Also, loss of off-site power will simultaneously affect both modules and should be directly regarded as a two-module initiating event.

II.A.2. Function Event

The function events (hereinafter referred to as headers) of a MET are obtained by combining headers from SETs in order, where any shared headers (if any) will be merged to the first occurrence. For example, if the headers of two SETs are $\{F_1, F_2, F_3\}$ and $\{F_4, F_2\}$ respectively, then the headers of the two-module event tree generated by these two SETs will be $\{F_1, F_2, F_3, F_4\}$.

II.A.3. Event Sequence

Similarly, multi-module event sequences could be obtained by combining sequences from single modules in order, where the states of the shared headers (if any) are determined by the constraints of the shared systems that correspond to these headers. Let two sequences from single modules that corresponds to headers of $\{F_1, F_2\}$ and $\{F_3, F_2, F_4\}$ respectively, be {F_1 success, F_2 success} and {F_3 success, F_2 success, F_4 failure}, where the shared header of F_2 have success states in both sequences. If the shared system corresponding to F_2 is available for use by both modules at the same time, these two sequences can be combined to generate a two-module event sequence of {F_1 success, F_2 success, F_3 success, F_4 failure}. If the shared system can only be called by one module at a time, the states of F_2 in these two sequences are contradictory, which means that the combination is invalid, and it should be screened out. How to select valid combinations will be illustrated in Section II.C.1.

II.A.4. Release Category

The consequences (also refereed as release categories) of multi-module event sequences, can be roughly divided into three types: RC50, non-RC50, and OK. Among them, RC50 corresponds to situations where the consequences could reach RC50 level through direct superposition of the consequences from single module; OK applies to combinations where none of the consequences from single module result in radioactive release; and all the other cases correspond to non-RC50. Take HTR-PM with two modules as an example. Since the direct superposition of any non-RC50 consequences from single module will not reach the RC50 level, for two-module event sequences with RC50 consequences, the combinations of consequences from single module include three cases, i.e., {RC50, RC50}, {RC50, non-RC50}, and {RC50, OK}.

II.B. Event Tree Representation

II.B.1. Graphical Representation

Graphical representation is the most conventional form of event trees. It will display all possible developments in a sequence of events with a tree structure. That is to say, starting from the initiating event (root node), two branches representing success and failure are generated at each header (branch node), which will deduce different sequences (paths) and the corresponding consequences (leaf nodes). In Figure 1, N_1 is the root node, N_2 and N_3 are branch nodes, and N_4, N_5, and N_6 are leaf nodes. The three paths from the root node to the leaf nodes correspond to the event sequences with consequences of C_1, C_2, and C_3 respectively. If the header does not generate a branch, it means that neither success or failure of it could influence the consequence of that sequence.

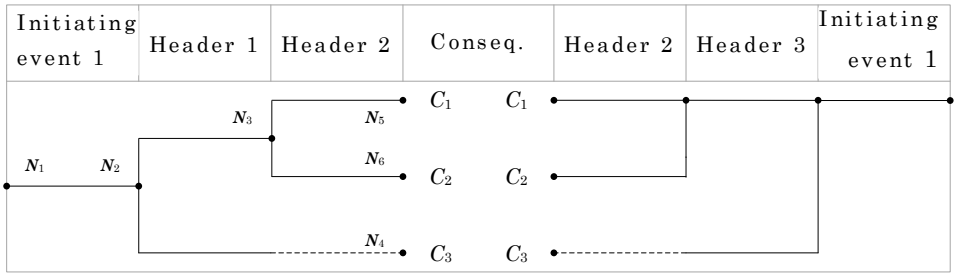

FIGURE 1. Two Conventional Ways of Drawing Event Trees

II.B.2. Vector Representation

The vector representation [5] could facilitate the combination of event trees from the perspective of program implementation. Each event sequence is denoted by a vector of state values of the headers, which could be further converted into an integer for storage. Let us consider the event tree on the left side of Figure 1. All the possible states of the header are failure, success, and inapplicable, denoted by 0, 1, and 2 respectively. For instance, the second sequence of the event tree can then be written as $\boldsymbol{S}_2 = (1, 0)^{\mathrm{T}}$. It corresponds to the ternary number of 10, equaling to the integer $3 = 3^1 \times 1 + 3^0 \times 0$. Hence, those three sequences of the event tree can be converted to 4, 3, and 2 respectively, and the following vector representation is obtained by

$$\mathrm{ET} = [\, a\,;\ n_f, \boldsymbol{D}_f\,;\ n_s, \boldsymbol{D}_c, \boldsymbol{L}\,] = \left[1;\quad 2, \begin{pmatrix}1\\2\end{pmatrix};\quad 3, \begin{pmatrix}1\\2\\3\end{pmatrix}, \begin{pmatrix}4\\3\\2\end{pmatrix}\right],$$

where a is the index of the initiating event; n_f is the number of headers; $\boldsymbol{D}_f$ is the vector composed of indexes of the headers; n_s is the number of event sequences; $\boldsymbol{D}_c$ is the vector composed of indexes of the consequences; and $\boldsymbol{L}$ is the vector of integers corresponding to the sequences. METs can also be written in this manner (see Section II.C.1).

II.B.3. Mutual Conversion

The vector representation is characterized by the simplicity in form, ease of storage, and programmability. It is effective in addressing the modeling challenges posed by METs, and thereby leading to a substantial reduction in manual modeling expenses. However, the graphical representation is commonly used in most PSA modeling tools for its readability, and it is essential to convert vector representation of event trees into graphical representation. The followings in this section will present a conversion method.

For the sake of illustration, we first introduce an intermediate form of event trees, referred to as the event tree table. It records all event sequences of the event tree in a tabular form. The first two rows record the initiating event and the headers respectively, with each subsequent row recording an event sequence; the last column of each row records the consequences, and the remaining columns record the state values of the headers. In Figure 2, there is an example of an event tree table with a scale of 3 rows and 3 columns, and the relationships between the three representations are demonstrated as well, where the

graphical representation, tabular representation and vector representation are denoted by ETGraph, ETTable and ETVector respectively.

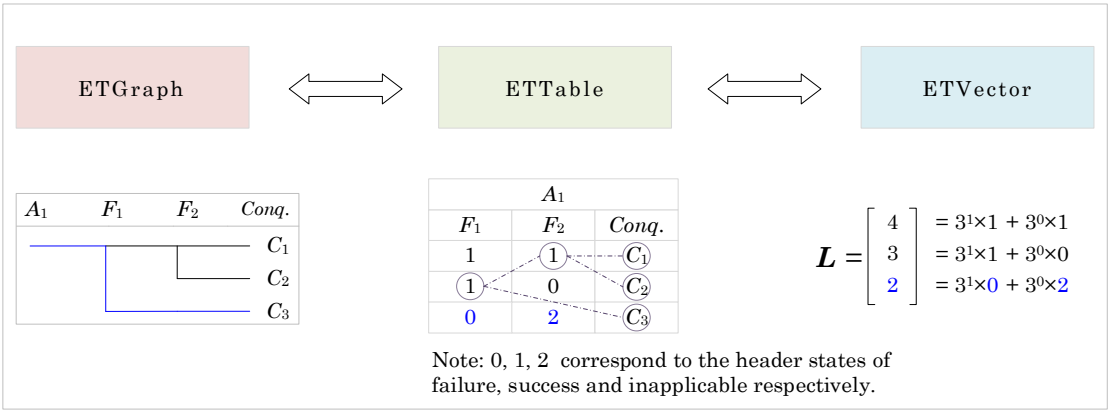

FIGURE 2. Relationships Between Graphical Representation and Vector Representation of Event Trees

The conversion of event trees from graphical representation to vector representation is a natural process. In ETGraph, every event sequence is shown as a path in a binary tree, and it corresponds a single row in ETTable where the state values of 0 and 1 in the table represent the failure and success branches generated by the header of event tree. If there is no branch for the header in a path, the state value is designated as 2. For any row in the table, the state values of the headers from left to right correspond to a ternary number from high bits to low bits. Then, the element of the vector in ETVector could be obtained by converting that number to an integer.

However, the ETVector of a MET with shared header(s) may not have a complete tree structure when converted to ETGraph. According to the definition of event sequences in Section II.A.3, when combining sequences from single modules to generate MET, we have to merge shared headers, and those combinations that do not satisfy the constrains of the shard systems corresponding to the headers will be screened out. That will affect the tree structure of this MET. A two-module ETTable generated by two event trees from Figure 1 is shown on the left side of Figure 3 to illustrate this situation.

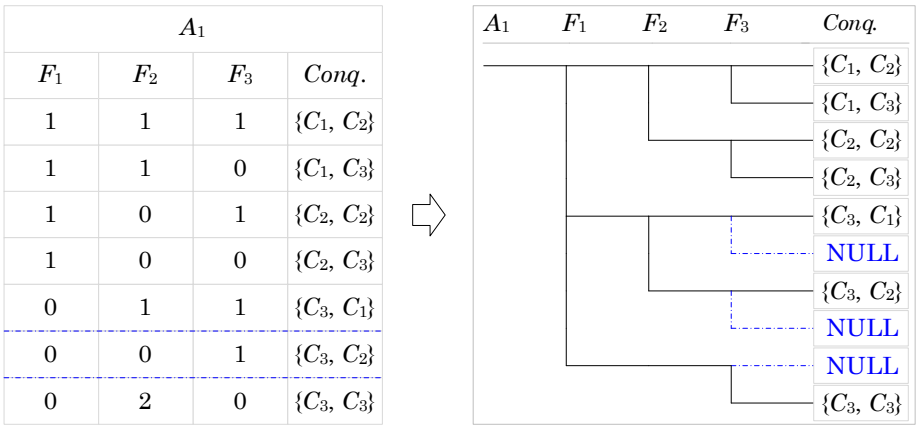

FIGURE 3. The First Way of Converting an Event Tree Table into Graphical Representation

It is obvious that this event tree requires supplementation with event sequences (denoted in blue in Figure 3) to establish a complete tree structure, when converting the table to graphical representation. To address this issue, we provide two distinct approaches below.

1. Complete the tree structure with minimal branches (MBs). The following algorithm is designed to verify whether the event sequences in the event tree table have a complete tree structure, and to automatically add the missing branches with minimal times.

TABLE I. The Algorithm for Completing the Tree Structure With Minimal Branches

Function	$\boldsymbol{S}$:= MBs({$\boldsymbol{S}_1$, ..., $\boldsymbol{S}_{ns}$})
Input	{$\boldsymbol{S}_1$, ..., $\boldsymbol{S}_{ns}$}, the vector representation of all event sequences in an event tree.
Output	$\boldsymbol{S}$, the collection of event sequences that could be converted into graphical representation after completing the tree structure.
1.	Verify the applicability of this algorithm for these event sequences. Define $\boldsymbol{S}$ = { } as the collection of the valid sequences. For any two sequences $\boldsymbol{S}_i = (f_{i1}, ..., f_{im})^T$, $\boldsymbol{S}_j = (f_{j1}, ..., f_{jm})^T$, perform the following process.
	1.1. A contradiction of having success (or failure) and inapplicable states at the same time in local branches. If $1_{\{2\}}(f_{i1}) + 1_{\{2\}}(f_{j1}) = 1$, or, $f_{ik} = f_{jk} = 1$ and $1_{\{2\}}(f_{i(k+1)}) + 1_{\{2\}}(f_{j(k+1)}) = 1$, then go to Step 5. Note that $1_{\{2\}}(\ )$ is the indicator function for the set of {2}. 1.2. Otherwise, go to Step 2.
2.	Initialization. Define two sequences $\boldsymbol{S}_{\text{this}} = (f_1, ..., f_m)^T$, $\boldsymbol{S}_{\text{next}} = (h_1, ..., h_m)^T$, where f_i, h_i = 0, 1 或 2, i = 1, ..., m, and t = 1. Set $\boldsymbol{S}_{\text{this}}$ to be the first sequence, i.e., $\boldsymbol{S}_{\text{this}} = \boldsymbol{S}_1$. Construct a sequence $\boldsymbol{S}_{\text{fit}}$ where its i-th element $(\boldsymbol{S}_{\text{fit}})_i = 1 + 1_{\{2\}}(f_i)$.
	2.1. If there exists any zero element in $\boldsymbol{S}_{\text{this}}$, then $\boldsymbol{S}_{\text{this}} = \boldsymbol{S}_{\text{fit}}$, $\boldsymbol{S} = \boldsymbol{S} \cup \boldsymbol{S}_{\text{fit}}$, t = 0 and go to Step 3. 2.2. Otherwise, $\boldsymbol{S} = \boldsymbol{S} \cup \boldsymbol{S}_1$, and go to Step 3.
3.	Check the current sequence. Denote the set of indices of elements with a value of 1 in $\boldsymbol{S}_{\text{this}} = (f_1, ..., f_m)^T$, by $K = \{k_1, ..., k_p\}$, which means that for any $k \in K$, we have f_k = 1.
	3.1. If K equals to empty set and $\boldsymbol{S}_{\text{this}}$ to the last sequence (or say $t = n_s$), then go to Step 5. 3.2. If K equals to empty set but $t < n_s$, then let K = {1} and go to Step 4. 3.3. Otherwise, go to Step 4.
4.	Match the adjacent sequence. Let $\boldsymbol{S}_{\text{next}} = \boldsymbol{S}_{t+1}$ and $\boldsymbol{S}_{\text{fit}} = (f_1, ..., f_{kp-1}, 0, 2, ..., 2)^T$ where the first k_p - 1 elements of $\boldsymbol{S}_{\text{fit}}$ are the same as those of $\boldsymbol{S}_{\text{this}}$, the k_p-th element is 0, and the left elements (if any) are 2s.
	4.1. If $\boldsymbol{S}_{\text{next}} = \boldsymbol{S}_{\text{fit}}$, then $\boldsymbol{S}_{\text{this}} = \boldsymbol{S}_{\text{next}}$, $\boldsymbol{S} = \boldsymbol{S} \cup \boldsymbol{S}_{\text{next}}$, $t = t$ +1 and go to Step 3. 4.2. Otherwise, let $\boldsymbol{S}_{\text{fit}} = (f_1, ..., f_{kp-1}, 0, 1 + 1_{\{2\}}(h_{kp+1}), ..., 1 + 1_{\{2\}}(h_m))^T$. 4.2.1. If $\boldsymbol{S}_{\text{next}} = \boldsymbol{S}_{\text{fit}}$, then $\boldsymbol{S}_{\text{this}} = \boldsymbol{S}_{\text{next}}$, $\boldsymbol{S} = \boldsymbol{S} \cup \boldsymbol{S}_{\text{next}}$, $t = t$ +1, and go to Step 3. 4.2.2. Otherwise, $\boldsymbol{S}_{\text{this}} = \boldsymbol{S}_{\text{fit}}$, $\boldsymbol{S} = \boldsymbol{S} \cup \boldsymbol{S}_{\text{fit}}$, and go to Step 3.
5.	Return $\boldsymbol{S}$.

2. Establish the minimum cut sets with respect to function event (FE-MCSs). The main idea of this approach is as follows: for a certain multi-module consequence, take the headers with failure state in each sequence that leads to the interest consequence, as cut sets, have the FE-MCSs by eliminating all redundant ones, and then establish a MET with a single one header defined by these FE-MCSs [6]. Figure 4 shows an illustrative example.

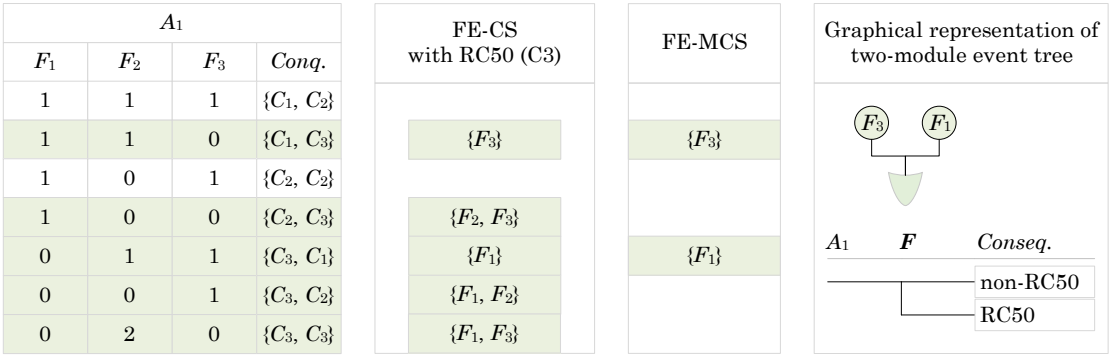

FIGURE 4. The Second Way of Converting an Event Tree Table into Graphical Representation

Define C_3 as the consequence of RC50 for a two-module HTGR. According to the definition of two-module consequence in Section II.A.4, the combinations of consequences from single modules could result in RC50 only when these two consequences contain RC50. The event tree table has five multi-module event sequences with RC50 consequence, and thus we

have five cut sets of {F_3}, {F_2, F_3}, {F_1}, {F_1, F_2}, {F_1, F_3}. The FE-MCSs of these cut sets are {F_1}, {F_3}. Hence, we could build the two-module event tree shown on the right side in Figure 4, where its header is named as "no RC50 release" and its failure criteria is defined by the union of FE-MCSs, i.e., {F_1} OR {F_3} in logic.

II.C. Combination of Event Trees

II.C.1. Screening Criterion

A multi-module event sequence could be obtained by combining sequences from single modules. If there is a shared header in those sequences, the states of that header in all the sequences need to satisfy the constrains of the shared system corresponding to the header. These constrains set the screening criterion for event sequence combinations. Table II presents a set of general screening criterion based on individual header [5], which can be applied to each header in the combinations of sequences from single module for screening the valid ones as the multi-module event sequence.

TABLE II. Screening Criterion for Event Sequence Combinations

Code	Classification characteristics		Screening rules	Scenario analysis
	A shared header?	MAU		
I	No	0	No need to build rules and reserve all combinations.	The scenario is unique.
II	Yes	= n_t	The states of the header are the same in all single-module event sequences.	The state of the header is the state in the sequence.
III	Yes	< n_t	Any single-module event sequence in the combination adhere to one of the following criteria: 1. The number of sequences with the header having a success state must equal MAU.	The sequences with the header having a failure state means that the corresponding module cannot call the shared system due to the occupation of it by other modules. The state of the header is success.
			2. There are no sequences with the header having a failure state, and the number of sequences with the header having a success state is greater than 0 and less than MAU.	The state of the header is success.
			3. There are no sequences with the header having a success state.	Assume that there exist k sequences with the header having a failure state. If $k = 0$, then the stare of the header is inapplicable. If $0 < k \leq$ MAU, the stare of the header is failure. If MAU $< k \leq n_t$, then there are C_k^{MAU} scenarios, corresponding to all the combinations of cases where MAU of k modules called the shared system and thereby it cannot be called by the remaining k - MAU modules. In such cases, the stare of the header is failure.
Notes: (1) nt is the number of SETs used for combination, which often equals to the total number of modules in HTGRs; (2) MAU is the maximum allowable users.				

Denote these two event trees from left to right in Figure 1 by ET_1, ET_2 and their event sequences by $\boldsymbol{S}_{1i}$, $\boldsymbol{S}_{2j}$, respectively, where $i = 1, 2, 3$, and $j = 1, ..., 5$. Assume that the only one shared system corresponding to F_2 allows at most one module to call. Let us consider the combination of $\boldsymbol{S}_{12} = (1, 0)^T$ and $\boldsymbol{S}_{22} = (1, 0)^T$. We first apply Criteria I to F_1 and F_3 in order, and reserve it. Then, apply Criteria III to F_2. Since F_2 has a state of 0 in both sequences, it satisfies Criteria III.3. Therefore, this combination is valid and written as a multi-module sequence of $(1, 0, 1)^T$. Note that this multi-module sequence actually comprises two scenarios: (1) module 1 calls the shared system, precluding module 2 to call it, and (2) module 1 is unable to call it due to a prior call by module 2. Sequences generated by these two scenarios are identical, and we could select one of them as a

representative. In fact, duplicate sequences will be eliminated in logic. Similarly, we could have the remaining combinations, and further obtain the two-module event tree shown in Figure 3.

II.C.2. Release Classification

As the number of HTGR modules increases, say a six-module design of HTR-PM600 [8], the combinations of consequences of non-RC50 from single module may lead to RC50. It is necessary to further refine the classification of multi-module release categories. The release categories from single module in HTGRs are primarily classified according to three characteristics: the magnitude of radioactive material release (determined by accident type), the integrity of the primary-loop pressure boundary, and the filtration of radioactive material controlled by the ventilation system. If the function of f quantifying the relationships between single-module release categories and their corresponding individual effective doses at the plant boundary is known, then we could classify the combinations of consequences from single modules into different multi-module release categories by directly summing these doses caused by single-module event sequences.

For instance, given any m-module event sequence, the combination of consequences from single modules is written as $\{C_1, ..., C_m\}$. The individual effective dose for this sequence could be defined as follows:

$$y = \sum_{i=1}^{m} f(C_i).$$

For the sake of illustration, we still use RC50 to denote the dose of 50 mSv, and the interval of the dose could be divided into different subintervals by a integer z: {0}, (0, RC50/z), [RC50/z, 2*RC50/z), ..., [(z-1)*RC50/z, RC50), [RC50, +∞). These intervals will define the multi-module release categories of OK, RC50_1, ..., RC50_z and RC50 respectively. If y = 0, the consequence is OK. If 0 < y < RC50, then the consequence is RC50_[1+y/z], where the symbol of [ ] is rounding function. Otherwise, the consequence is RC50.

II.C.3. Elimination Rules

In the process to have FE-MCSs, the key procedure is to perform elimination between these cut sets, as it will simplify the scale of METs at a certain extent. The utilization of vector representation could facilitate the establishment of elimination rules.

For an event sequence, the state values of the headers arranged from left to right, correspond to a ternary number from high bits to low bits. The elimination rules between sequences can be defined through the implementation of bit operations between ternary numbers. As illustrated in Figure 4, the sequences of $\boldsymbol{S}_2 = (1, 1, 0)^T$, $\boldsymbol{S}_4 = (1, 0, 0)^T$ correspond to the ternary numbers of z_2 = 110 and z_4 = 100, respectively. $\boldsymbol{S}_2$ eliminate $\boldsymbol{S}_4$, is equivalent to that $z_2|z_4$ = 110|100 = 110 = z_2, where the symbol of | is the bitwise operation of OR in logic. In fact, for sequences with any header having a state value of 2, their elimination relationships with others are equivalent to the one between the sequences revised by replacing all 2s with 1s and the others. Hence, we can directly use the binary logical operation to swiftly determine the elimination relationship between sequences. Say $\boldsymbol{S}_7 = (0, 2, 0)^T$ corresponds to the binary number of z_7 = 010. Obviously, $\boldsymbol{S}_2$ could also eliminate $\boldsymbol{S}_7$ for $z_2|z_7 = z_2$. Let any two sequences of $\boldsymbol{S}_i$ and $\boldsymbol{S}_j$ have the corresponding binary numbers z_i and z_j respectively, then $\boldsymbol{S}_i$ can eliminate $\boldsymbol{S}_j$ if and only if

$$z_i|z_j = z_i.$$

III. THE MULTI-MODULE EVENT SEQUENCE MODELING TOOL

III.A. Functional Framework

The Multi-Module Event Sequence Modeling Tool for HTGRs (MUETBASE 2.0) has six types of function shown in Figure 5.

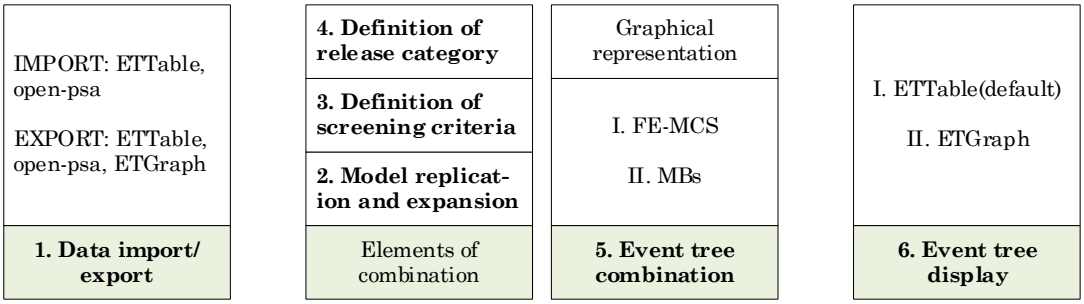

FIGURE 5. The Functional Framework of Multi-Module Event Sequence Modeling Tool for HTGRs

1. Data import/export. This tool supports both importing and exporting event trees in two distinct formats of event tree table and Open-PSA, and it also enables the export of event tree graphics. Both SETs and METs have four data elements: initiating events, function events, event sequences, and release categories.
2. Model replication and expansion. After having a SET and the total number of modules, the SETs of other modules can be replicated automatically to support the combination of SETs.
3. Definition of screening criteria. The screening criterion for the combination of event sequences from single modules can be assigned by selecting a specific function event and its screening rule presented in Section II.C.1.
4. Definition of multi-module release categories. The combinations of consequences from single modules can be automatically categorized by specifying the mapping from single-module release categories to the corresponding individual effective doses.
5. Event tree combination. Specify SETs and screening criterion for combination, and then a MET could be generated automatically. Two ways of graphical generation are provided: (1) according to the release categories, generate the FE-MCSs by eliminating sequences with the same specific release category, and (2) complete the tree structure with minimal branches.
6. Event tree display. Two display modes are available: (1) the default mode of event tree table, and (2) the event tree graphic.

Compared to the previous version of MUETBASE, this tool has improved the functions of graphical display and data exchange, including (1) the import and export of event tree data in the format of Open-PSA, (2) model replication, (3) the classification of multi-module release categories, and (4) two ways of graphical generation.

III.B. Program Implementation

The implementation of this tool uses a browser/server (B/S) network architecture, allowing users to directly access the operating interface of it via a web browser. All the data of event trees is stored and managed by using SQL Server Express, and algorithms of all the calculations involved in the process of event tree combination are still implemented by using C/C++.

IV. CONCLUSION

This paper presents a theory of event tree combination for HTGRs and develops a corresponding modeling tool of MUETBASE 2.0. In this theory, all the elements of METs, including initiating events, function events, event sequences, and release categories are clearly defined; two representations of event trees and their relationships for mutual conversion are presented; and three key technical elements of event tree combination are identified, including screening criterion, classification of release categories, and elimination rules of the minimum cut sets with respect to function events. Accordingly, an update tool is developed based on this theory and MUETBASE.

The future work will concern the following two aspects for optimizing and upgrading this modeling tool.

1. Try to model the classification of the plant operating states (POSs) and the identification of initiating events for HTGRs in this tool. Under the different POSs, the plant configurations and response requirements may vary significantly. Therefore, the identification of initiating events should be conducted on the basis of the classified POSs. Liu et al. [3] proposed a POS analysis method for multi-unit nuclear power plants. Incorporating the technical elements of this method into the program would enable a more automatic modeling process.
2. Develop a simplified fault tree solver by combining the approximate algorithms and numerical truncation, to achieve the quantification of event trees.

ACKNOWLEDGMENTS

This work is supported by the National Science and Technology Major Project of People's Republic of China (Grant No.2018ZX06902015).

REFERENCES

[1] IAEA. Nuclear Energy Series No. NR-T-1.18: Technology Roadmap for Small Modular Reactor Deployment. 2021.
[2] Sai Zhang, Jiejuan Tong, Jun Zhao. An integrated modeling approach for event sequence development in multi-unit probabilistic risk assessment. Reliability Engineering and System Safety, Volume 155, 2016.
[3] Ao Liu, Pengcheng Peng, et al. A plant operating state analysis method in probabilistic safety assessment for multi-unit nuclear power plant. Annals of Nuclear Energy, Volume 169, 2022.
[4] Ao Liu, Pengcheng Peng, et al. An event sequence modeling method in multi-unit probabilistic risk assessment for high temperature gas-cooled reactor. Annals of Nuclear Energy, Volume 182, 2023.
[5] Pengcheng Peng, Jiejuan Tong, Jun Zhao. A rapid approach to generate multi-unit event trees based on tree combinatorial calculation. Progress in Nuclear Energy, Volume 162, 2023.
[6] Hongru Zhao, Jiejuan Tong, et al. An FE-MCS based modeling method for event sequence development for the multi-module probabilistic risk assessment. Progress in Nuclear Energy, Volume 170, 2024.
[7] National Nuclear Safety Administration of P.R. China. Regulatory Safety Review Principles for HTR-PM. 2008.
[8] Zuoyi Zhang, Yujie. Dong, et al. 600-MWe high-temperature gas-cooled reactor nuclear power plant HTR-PM600. Nuclear Science and Techniques, Volume 33, 2022.
[9] Steven Epstein, Rauzy Antoine. Open-PSA Model Exchange Format. 2017.

ASRAM2025
www.asram2025.org
Asian Symposium on Risk Assessment and Management 2025
Pattaya, Thailand, 27 – 29 August 2025

Estimation of LOCA Frequencies for the Innovative Small Modular Reactor

Kibeom Son[1], Sung-Min Shin[1], Jin Hee Park[1]*

[1] *Korea Atomic Energy Research Institute, 111, Daedeok-daero, Yuseong-gu, Daejeon-si, 34057, Korea*
**Corresponding author: jhpark6@kaeri.re.kr*

EXTENDED ABSTRACT

Conventional commercial nuclear power plants estimate loss of coolant accident (LOCA) frequencies by integrating expert elicitation results with actual operational experience data. However, in the case of the Innovative Small Modular Reactor (i-SMR), such data are not yet available. Thus, LOCA frequency estimates are currently being extrapolated from existing commercial plants or other SMR designs. This paper reviews the LOCA frequency estimation methodology presented in NUREG-1829 and examines the specific design features of the i-SMR. Based on this review, it proposes an approach for estimating LOCA frequencies that reflect the unique features of the i-SMR, and presents example results through a case study.

In NUREG-1829, LOCAs are categorized into six groups based on leak rate, according to the definition of a LOCA. The total LOCA frequency is divided into two components: piping system and non-piping system. The piping system refers to the pipes and adjacent areas of the reactor coolant system (RCS), including the hot leg, cold leg and reactor pressure vessel (RPV) penetrations. The non-piping system includes components such as pumps, steam generators, reactor pressure vessels, pressurizers, and valves. The LOCA contribution from each subsystem is determined by the influence of five key factors: geometry, loading history, maintenance, material, and degradation mechanisms.

At the current status of the i-SMR, where only approximate design information is available, a top-down approach using operational experience data is deemed suitable for estimating i-SMR LOCA frequency. This approach is favored over methods such as probabilistic fracture mechanics (PFM), which require detailed input parameters that are not yet available. A key characteristic of this methodology is that it utilizes 2,600 LWR–years of operational data, in which cracks and leaks are treated as precursors to LOCAs. LOCA frequencies are estimated for each subsystem based on the degradation mechanisms that have historically led to LOCA events.

TABLE 1. Design Features of the i-SMR Related to LOCA Occurrence

i-SMR Design Feature	Theoretical Impact on LOCA Occurrence
In-Vessel Control Rod Drive Mechanism (IV-CRDM)	No longer expected LOCA initiation from CRDM penetrations, In-Core Instrumentation (ICI) penetrations
SSC Design	Absence of cold leg, hot leg, safety injection system (SIS) lines, and surge line
Maximum Pipe Diameter	Maximum pipe diameter is 2 inches, eliminating medium and large LOCAs
Boron-Free Operation	Reduced impact of degradation mechanisms caused by boron, such as general corrosion
Electron Beam Welding (EBW), Powder Metallurgical Hot Isostatic Pressing (PM-HIP)	Reduced weld areas (e.g., heat affected zones) in the RPV, decreasing related degradation mechanisms

Table 1 summarizes the design features of the i-SMR that may affect LOCA occurrence, compared to conventional PWRs. Since the CRDM is located inside the RPV, there are no RPV penetrations, and because the pressurizer is also integrated within the RPV, LOCAs originating from components such as the surge line and SIS lines are eliminated. Regarding piping, the maximum diameter does not exceed 2 inches, implying only SLOCA are possible. Additionally, the i-SMR is designed for boron-free operation, which is expected to reduce the impact of boron-induced degradation mechanisms such as general corrosion. Finally, advanced manufacturing technologies (EBW, PM-HIP) have been applied to components like the RPV, reducing the extent of weld zone vulnerable to material degradation and thereby enhancing structural integrity.

Figure 1 illustrates a partial example of the conceptual approach for estimating the LOCA frequency in the i-SMR, specifically focusing on the piping system. The left side represents a conventional PWR, where the contributions from the CRDM and CRDM piping are included. In contrast, the right side represents the i-SMR, in which these contributions are

excluded. The same approach is applied to the non-piping system as well. The specific subsystems that do not contribute to LOCA frequency estimation for each system are as follows.

- Piping system: CRDM, CRDM pipe, ICI, Cold leg, Hot leg, SIS injection, SIS accumulation, Surge line
- Non-piping system: Loop isolation valve, Pressurizer isolation valve

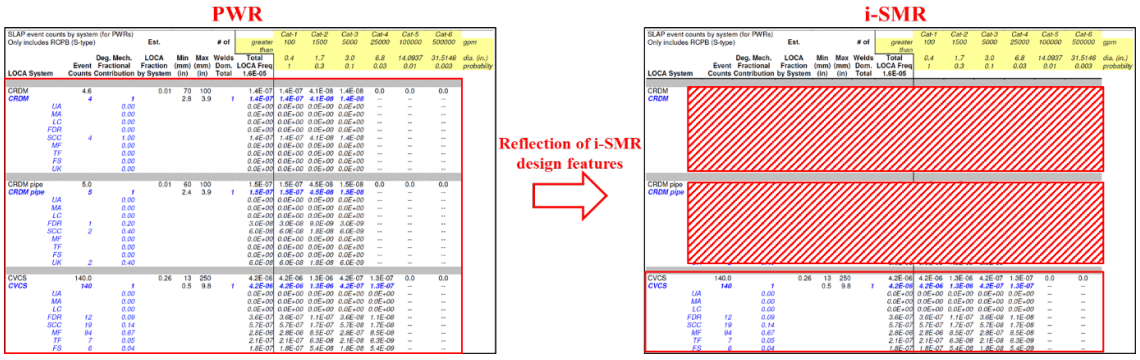

FIGURE 1. Case Study Concept for Estimating LOCA Frequency in the i-SMR

The number of precursor events for LOCAs in each subsystem is categorized by degradation mechanism, and mechanisms whose impact is reduced due to the design features of the i-SMR result in partial removal of their LOCA contributions. In this analysis, it is assumed that the occurrence rate of stress corrosion cracking in the RPV is reduced by 20% due to the advanced manufacturing methods applied.

TABLE 2. Estimated LOCA Frequencies for PWR and i-SMR

LOCA frequency	Category-1 (Diameter > 0.4 inch)			Category-2 (Diameter > 1.7 inch)			SLOCA (Diameter 0.5-2.0 inch)
	Piping	Non-piping	Total system	Piping	Non-piping	Total system	Total system
PWR [rcy]	1.64E-05	1.72E-04	1.89E-04	5.19E-06	5.44E-05	5.96E-05	1.27E-04 rcry
i-SMR [rcy]	1.27E-05	1.46E-04	1.58E-04	4.02E-06	4.61E-05	5.01E-05	1.07E-04 rcry
Difference [%]	-22.7	-15.3	-15.9	-22.7	-15.3	-15.9	-15.7

Table 2 presents the estimated frequencies of SLOCA events for a PWR and the i-SMR, derived using the top-down operational experience approach. A plant availability factor of 0.9 is assumed. Detailed calculation procedures, including the linear interpolation method and subsystem classifications, can be found in the referenced literature. The comparison shows that the non-piping system is the primary contributor to LOCA frequency in both reactor types. Regardless of the absolute values, the estimated LOCA frequency for the i-SMR exhibits a decreasing trend compared to that of the conventional PWR.

In this study, a preliminary case study was conducted to estimate how the LOCA frequency for the i-SMR may vary, using estimation methods presented in NUREG-1829, which is currently applicable given the design maturity of the i-SMR. In the future, the LOCA frequency for the i-SMR will be refined through a systematic expert elicitation process, similar to the approach used in NUREG-1829.

ACKNOWLEDGMENTS

This work was supported by an Innovative Small Modular Reactor Development Agency grant funded by the Korean Government (MSIT) (No. RS-2023-00258118).

REFERENCES

[1] R. Tregoning, L. Abramson, and P. Scott, Estimating Loss-of-Coolant Accident (LOCA) Frequencies Through the Elicitation Process, NUREG-1829, U.S. Nuclear Regulatory Commission, Washington, DC (2008).

[2] Eide, S A, et al. "Estimating Loss-of-Coolant Accident Frequencies for the Standardized Plant Analysis Risk Models," *ANS PSA 2008 Topical Meeting, Knoxville, Tennessee, September 7–11, 2008, American Nuclear Society, LaGrange Park, IL (2008)*

Methodology for Generalized Risk Assessment of Multi Event Scenarios in Deep Geological Repositories

Seongmin Jin[1], Kibeom Son[2], Karyoung Choi[1], Minseok Kim[1], Gyunyoung Heo[1*]

[1] *Department of Nuclear Engineering, Kyung Hee Univ., Deogyeong-daero, Giheung-gu, Yongin-si, Gyeonggi-do 17104, Republic of Korea*
[2] *Korea Atomic Energy Research Institute, 111, Daedeok-daero 989beon-gil, Yuseong-gu, Daejeon, 34057 Republic of Korea*

ABSTRACT

The safety of deep geological repositories for long-term storage of spent nuclear fuel is internationally assessed using the concept of a safety case, with guidelines and regulatory requirements differing across countries. In South Korea, quantitative results of safety assessments must satisfy both dose exposure and risk criteria to meet regulatory requirements.

Unlike dose exposure, the risk of a disposal facility must be evaluated comprehensively across all scenarios. Authors' previous studies developed a customized PSA (Probabilistic Safety Assessment) framework for disposal facilities by selectively combining applicable features of methodologies used in commercial nuclear power plants, such as the judgmental method and fault tree/event tree analysis method. Furthermore, concept of deriving a risk profile was concretized into a time-dependent risk profile reflects the probability of events occurring within specific time intervals. A simulation quantification template on a spreadsheet program was developed for both normal scenarios and abnormal events. However, this template faced limitations requiring excessive computation when considering arbitrary abnormal events in terms of types, frequencies, and intensities.

To overcome these limitations, this study established a statistics-based algorithm applicable to such abnormal events. Additionally, an efficient quantification methodology was proposed to appropriately screen out intervals with expected low-risk values. The proposed methodology was verified by deriving risk profiles using the GoldSim code, used for radionuclide transport evaluations, and external spreadsheet programs.

This study enables more realistic and efficient risk assessment under general conditions encompassing arbitrary abnormal events. Future research will address the limitations and propose improved solutions.

Keywords: Risk assessment, Abnormal Events, Deep geological repository

I. Introduction

The safety of deep geological disposal facilities for spent nuclear fuel is internationally evaluated through a concept known as the "Safety Case." Guidelines and regulatory requirements related to this approach, however, differ from country to country. In South Korea, quantitative outcomes of safety assessments must satisfy established criteria for both radiation exposure and risk levels to meet safety objectives. To verify compliance with these criteria, an existing methodology—combining radiation dose evaluations with external events to derive and assess a risk profile—has been employed. This study aims to propose an enhanced risk assessment methodology considering arbitrary abnormal event scenarios.

During the operational period of deep geological disposal facilities, various abnormal events could impact facility integrity, potentially leading to radioactive leakage. Radioactive materials released from canisters within the facility migrate through engineered barriers (buffers), subsequently transferred through geological barriers into groundwater, soil, and further environmental pathways. Given that such leakage may directly affect ecosystems, risk assessments considering abnormal event scenarios are essential.

Unlike exposure dose assessments, facility risk assessments must integrate all potential scenarios comprehensively. Authors' previous studies developed a customized PSA (Probabilistic Safety Assessment) framework for disposal facilities by selectively combining applicable features of methodologies used in commercial nuclear power plants, such as the judgmental

method and fault tree/event tree analysis method. Furthermore, the concept of deriving a risk profile was concretized into a time-dependent risk profile reflects the probability of events occurring within specific time intervals. A simulation quantification template was established considering normal scenarios and a single abnormal event scenario (such as one seismic event). If the peak values of the derived risk profile satisfy the established criteria, the evaluated scenarios confirm the facility's safety. However, this template faced limitations requiring excessive computation when considering arbitrary abnormal events in terms of types, frequencies, and intensities.

To overcome these limitations, this study presents an applicable to such abnormal events for deep geological disposal facilities. Additionally, an efficient quantification methodology was proposed to appropriately screen out intervals with expected low-risk values. The proposed methodology's validity is examined through a spreadsheet program and GoldSim, which is commonly used for radionuclide transport modeling and evaluation. In subsequent studies, software integration between a spread sheet (i.e. Microsoft Excel) and GoldSim will be developed, enabling the automatic transfer of input data regarding abnormal events and facility conditions from the spread sheet to GoldSim. This advancement is anticipated to overcome the limitations of previous methodologies and enable accurate and efficient risk assessments for generalized scenarios encompassing arbitrary abnormal events.

II.A. Statistics-based algorithm (methodology)

Deep geological repositories for high-level radioactive waste must be designed to ensure that radiation impacts after closure meet clearly defined safety objectives [1]. Specifically:

1. The annual total risk of radiation exposure to a representative individual, considering major scenarios including natural phenomena and human intrusion, must not exceed 10^{-6}.
2. For individual scenarios involving low-probability natural events or human intrusion, the expected annual radiation dose to a representative individual must not exceed $10\ mSv$.

These safety objectives are defined using the following equation:

$$Total\ Risk = r \sum_i P_i D_i \tag{1}$$

Where:

3. r is the risk coefficient ($0.05/Sv$)
4. i denotes each exposure scenario
5. P_i is the probability of occurrence for scenario i
6. D_i is the annual radiation dose to the representative individual for scenario i

It is important to note that Eq. (1) serves as a conceptual expression. Rather than expressing total risk as a single fixed value, the risk is expected to be represented in the form of a risk profile, where the risk values vary over different time periods.

This research proposes a novel approach to reduce excessive computations and keep reasonable conservatism, efficient risk assessment. The procedure steps are structured as follows:

1. Event count
   - The number of events N during the mission time T, given an annual occurrence rate r, is assumed to follow a Poisson distribution with a mean λ defined as:

$$\lambda = r \cdot T \tag{2}$$

   - The probability of exactly k events occurring is given by:

$$P(N = k) = \frac{\lambda^k e^{-\lambda}}{k!} \tag{3}$$

   - To construct a realistic scenario space, a sufficiently conservative upper bound B is selected from the Poisson distribution based on a predefined confidence level. This defines the meaningful range of event counts $[A, B]$ to

be considered in the analysis. Within this range, a specific value B is selected as the representative number of events to be used for scenario evaluation.

-

2. Identification of the focus period using normal scenario simulation
   - The focus period is defined as the time interval $[t_i, t_f]$ showing the highest consequence in a baseline GoldSim simulation with no abnormal events. This ensures consistent and objective identification of the most critical period before risk scenario analysis.

3. Determining the number of events during the focus period using gamma CDF

$$F(t_i, t_f; a, \beta) = \int_{t_i}^{t_f} \frac{1}{\Gamma(a)\beta^{\alpha}} t^{\alpha-1} \mathrm{e}^{-t/\beta} \, \mathrm{d}t \tag{4}$$

   - Selected number of events G satisfying the probability threshold L are included in the analysis.

$$F(G; \alpha, \beta) \geq \mathrm{L} \tag{5}$$

4. Temporal allocation of events during and outside of the focus period.
   - Among the total number of events B selected from the Poisson distribution, the G events satisfying the probability threshold L are assumed to occur randomly within the focus period.
   - The remaining number of events $(B - G)$ are assumed to occur at evenly spaced intervals during the non-focus period.

5. Risk evaluation and aggregation
   - Since the objective is to evaluate the most conservative scenario for a given event frequency, the probability of the scenario is assumed to be 1 for assessment purposes.
   - A simulation is conducted using GoldSim to generate the dose-rate profile corresponding to this specific scenario.
   - The final risk profile is then obtained by multiplying the dose-rate profile with the scenario probability.
   - This completes the risk assessment for the event scenario with the specified frequency.
   - In a similar context, risk evaluations are performed for other event scenarios with different frequencies or different event types using the same methodology. The resulting risk profiles from all these scenarios are then aggregated to produce the final risk assessment for the set of abnormal events.

II.B. Deriving input parameters for GoldSim using spreadsheet program

To enable implementation of the risk assessment methodology in GoldSim, key simulation input parameters were derived using a structured spreadsheet approach. This process references the probabilistic framework introduced earlier, incorporating relevant equations and logical steps to represent event frequency and temporal distribution.

First, the Poisson probability density function (PDF) was used to determine the range $[A, B]$, which captures the statistically meaningful number of events during the Mission Time $(T = 10^7 years)$ given an annual occurrence rate of $r = 10^{-5} event/year$. The resulting range, illustrated Fig. 1, was determined with reference to a sufficiently conservative confidence level, allowing the upper bound $B = 119$ to be selected for further analysis. As shown in Fig. 1, the range was chosen to meet a 95% probability, ensuring that the selected upper bound satisfies a conservative assumption for subsequent evaluations.

Determination of [A,B]		mission time	10000000
		r	0.00001
	Poisson distribution(CDF)		
count	probability	count	probability
80	2.265E-02	100	5.266E-01
81	2.907E-02	101	5.660E-01
82	3.689E-02	102	6.047E-01
83	4.632E-02	103	6.423E-01
84	5.755E-02	104	6.784E-01
85	7.075E-02	105	7.128E-01
86	8.611E-02	106	7.453E-01
87	1.038E-01	107	7.756E-01
88	1.238E-01	108	8.037E-01
89	1.463E-01	109	8.294E-01
90	1.714E-01	110	8.529E-01
91	1.989E-01	111	8.740E-01
92	2.288E-01	112	8.928E-01
93	2.610E-01	113	9.095E-01
94	2.952E-01	114	9.241E-01
95	3.312E-01	115	9.368E-01
96	3.687E-01	116	9.478E-01
97	4.074E-01	117	9.572E-01
98	4.468E-01	118	9.651E-01
99	4.867E-01	119	9.718E-01

FIGURE 1. Determination of $[A, B]$

Next, to account for the variability in the number of events during the designated focus period, the cumulative distribution function (CDF) of the gamma distribution, as introduced in Eq. (4), was applied. Probabilities of one, two, and three earthquakes occurring within the focus period ($10^5 years$) were calculated, and the results are presented in Fig. 2. Based on the criterion (Eq. (5)), where $L = 0.05$ represents the minimum acceptable probability, the number of events satisfying this threshold was identified. Under the most conservative assumption, the value of $G = 3$ was selected

Determination of G			
	Focus Period	0~100000 year	
Time(year)	1 Event	2 Events	3 Events
0	0.E+00	0.E+00	0.E+00
1000	1.E-02	5.E-05	2.E-07
2000	2.E-02	2.E-04	1.E-06
3000	3.E-02	4.E-04	4.E-06
4000	4.E-02	8.E-04	1.E-05
5000	5.E-02	1.E-03	2.E-05
6000	6.E-02	2.E-03	3.E-05
7000	7.E-02	2.E-03	5.E-05
8000	8.E-02	3.E-03	8.E-05
9000	9.E-02	4.E-03	1.E-04
10000	1.E-01	5.E-03	2.E-04
11000	1.E-01	6.E-03	2.E-04
12000	1.E-01	7.E-03	3.E-04
13000	1.E-01	8.E-03	3.E-04
14000	1.E-01	9.E-03	4.E-04
15000	1.E-01	1.E-02	5.E-04
16000	1.E-01	1.E-02	6.E-04
17000	2.E-01	1.E-02	7.E-04
18000	2.E-01	1.E-02	8.E-04
19000	2.E-01	2.E-02	1.E-03
20000	2.E-01	2.E-02	1.E-03
21000	2.E-01	2.E-02	1.E-03
22000	2.E-01	2.E-02	2.E-03
23000	2.E-01	2.E-02	2.E-03
24000	2.E-01	2.E-02	2.E-03
25000	2.E-01	3.E-02	2.E-03
26000	2.E-01	3.E-02	2.E-03
27000	2.E-01	3.E-02	3.E-03
28000	2.E-01	3.E-02	3.E-03
29000	3.E-01	3.E-02	3.E-03
30000	3.E-01	4.E-02	4.E-03

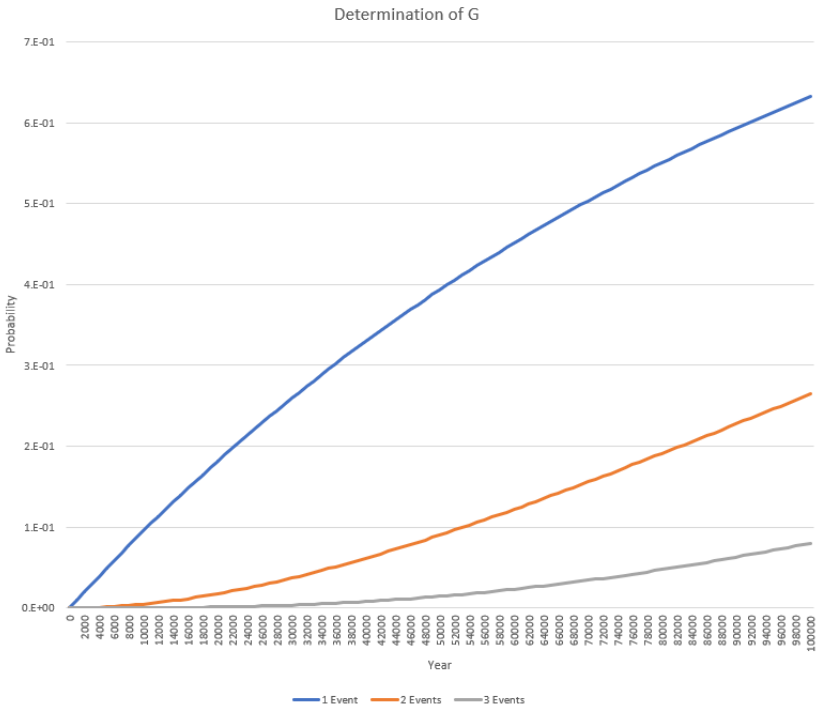

FIGURE 2. Determination of G

These derived values were then used to inform the GoldSim simulation logic in Section II.C. In accordance with step 4 of the methodology, it was assumed that G events occur randomly within the focus period, while the remaining $B - G$ events occur at uniformly spaced intervals during the non-Focus Period.

II.C. Practical application and verification with GoldSim

GoldSim was utilized in this research to estimate the levels of radionuclide release and exposure, which are influenced by incidents occurring near the disposal site. It was also applied to derive the likelihood of various scenarios. As a modeling tool, GoldSim enables the simulation of both actual and theoretical systems, making it particularly useful for scenario analysis in waste disposal facilities. It can replicate the release and movement of radioactive materials from waste, and is widely recognized for its role in evaluating the safety of low- and high-level radioactive waste repositories both domestically and internationally.

The repository simulation model was created using GoldSim, based on multiple hypothetical assumptions. The primary aim of the study was to demonstrate the modeling approach rather than to derive precise numerical outcomes. This repository model includes components such as radionuclide inventory, waste canisters, buffer/backfill materials, the Excavated Damaged Zone (EDZ), natural barriers, and the surrounding ecosystem. For each component, adsorption and precipitation processes were considered. The model assumed that radioactive materials are leached by groundwater entering the canister due to degradation, and then transported through advection and diffusion mechanisms. The canister is assumed to fail after $10^4 years$, with radionuclides being released at a defined rate from the point of failure.

Each component's parameters were derived from SKB's report [2], and in cases where data ranges were provided, values were modeled using triangular distributions due to limited available data [3].

Based on the generalized methodology presented earlier, a GoldSim simulation was conducted to derive the corresponding risk plot. Among various abnormal scenarios, an earthquake was selected as a representative example. The total mission time for the simulation was set to $10^7\ years$, with an assumed earthquake frequency of 10^{-5}events/year.

To carry out step 2 and identify the appropriate focus period, a baseline simulation assuming no seismic events was first conducted using GoldSim. The resulting plot from this normal scenario is presented below:

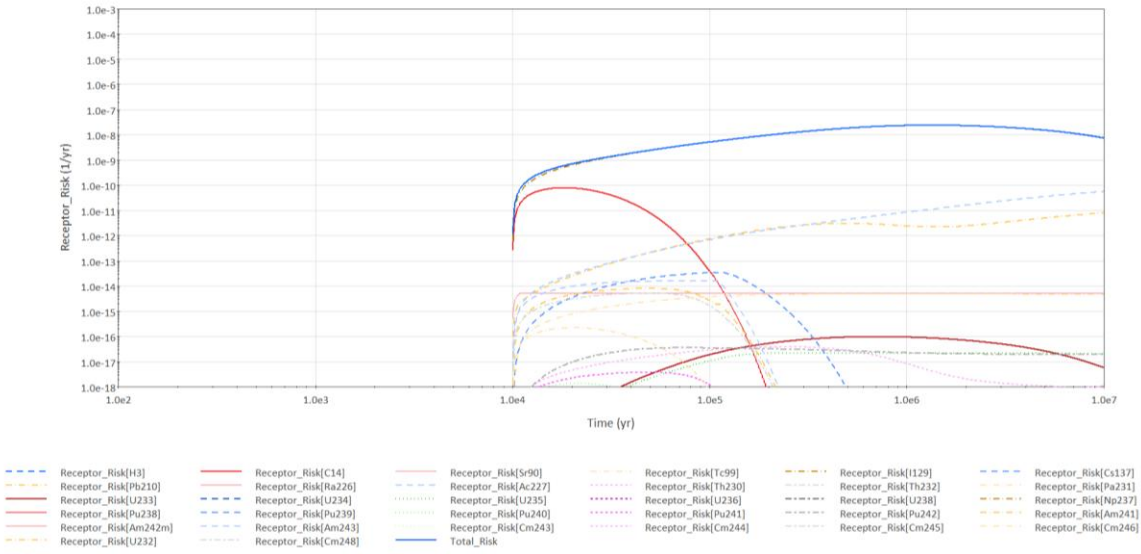

FIGURE 3. Normal scenario Risk Plot

From this plot, the time period during which the maximum consequence occurs under normal conditions can be identified. Assuming a focus period of $10^{-5} years$, multiple earthquake events were introduced in accordance with the methodology. Utilizing the values of G and $(B - G)$ calculated in the accompanying spreadsheet, step 5 of the proposed methodology was applied. The resulting outcomes are illustrated in the following plot:

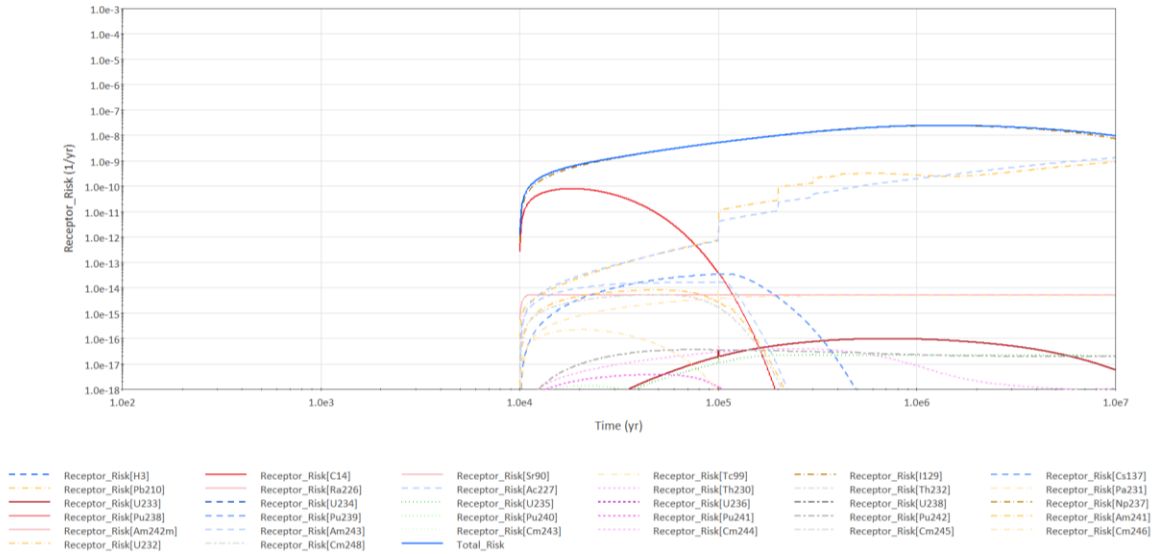

FIGURE 3. Multi Earthquake scenario Risk Plot

III. Conclusion

This study proposed a generalized methodology for conducting risk assessments of abnormal event scenarios in deep geological repositories, with a particular focus on computational efficiency and probabilistic rigor. The methodology integrates statistical modeling using Poisson and Gamma distributions to quantify the frequency and temporal distribution of events and identifies a focus period with the highest consequence for further analysis.

Input parameters for GoldSim simulations were derived through a structured spreadsheet-based process, allowing for flexible and reproducible implementation of event-based risk profiles. By applying a conservative scenario involving multiple earthquakes, the study demonstrated how probabilistic thresholds and event allocations could be used to generate time-dependent risk plots. The resulting profiles reflect both the uncertainty and dynamic nature of long-term safety assessments in geological disposal systems.

Through practical application and verification using GoldSim, the proposed approach was shown to offer a realistic and efficient framework for simulating the impact of arbitrary abnormal events. This enhances the robustness of risk assessments under generalized conditions, especially in regulatory environments that require comprehensive evaluation of both dose and risk criteria.

Future work will focus on automating data transfer between spreadsheet tools and simulation software to further streamline the process and expand the applicability of the methodology to a broader range of event types and repository configurations.

ACKNOWLEDGMENTS

This work was supported by the Institute for Korea Spent Nuclear Fuel (iKSNF) and Korea Institute of Energy Technology Evaluation and Planning(KETEP) grant funded by the Korea government (Ministry of Trade, Industry and Energy(MOTIE)) (No. RS-2021-KP002656)

REFERENCES

[1] Nuclear Safety and Security Commission (NSSC), A General Guideline for the Deep Geological Disposal System for the HLW in Korea, 2024.
[2] Swedish Nuclear Fuel and Waste Management Co. (SKB), Data Report for the safety assessment SR-site (SKB-TR-06-67), Stockholm, Sweden, 2010.
[3] K. Choi, M. Kim, K. Son, and G. Heo, “Methodology for risk assessment of multi-event scenarios on radioactive waste repository,” Nuclear Engineering and Technology, 2025.

Technical Session 14 (16:00 -18:00)	The Port 2, C Floor	Offsite Consequence Analysis, Emergency Preparedness and Response
		Chair/Facilitator 1: Dr. Piyawan Krisanangkura (Office of Atoms for Peace (OAP))
		Chair/Facilitator 2: Dr. Kazumasa Shimada (JAPAN NUS Co., LTD) ID 26: Study on a
16:00 - 16:20		Consequence-Informed Decision Making for Emergency Planning Zone Distance with Dose versus Distance Curve Speaker: Kodai Wadayama (Nuclear Regulation Authority) Contributors: Kodai Wadayama (Nuclear Regulation Authority), Retsu Kojo (Nuclear Regulation Authority), Takafumi Narukawa (The University of Tokyo), Takashi Takata (The University of Tokyo)
16:20 - 16:40		ID 88: Monte-Carlo-based Consequence Analysis of Nuclear Accidents under Extreme Conditions Speaker: Shengyu LIU (City University of Hong Kong) Contributors: Shengyu LIU (City University of Hong Kong), Wei WANG (City University of Hong Kong)
16:40 - 17:00		ID 57: Application of Various Dispersion Coefficients to Investigate the Sensitivity of Offsite Consequences Speaker: Dakyoung Lee (Seoul National University) Contributors: Dakyoung Lee (Seoul National University), Sung-yeop Kim (Korea Atomic Energy Research Institute), Gibeom Kim (Korea Atomic Energy Research Institute), Eung Soo Kim (Seoul National University)
17:00 - 17:20		ID 64: A Comparative Analysis of the Impact of Various Spatial Grid Settings for Effective Offsite Consequence Analysis Speaker: Seunghwan Kim (Korea Atomic Energy Research Institute) Contributors: Seunghwan Kim (Korea Atomic Energy Research Institute), Sung-yeop Kim (Korea Atomic Energy Research Institute)
17:20 - 17:40		ID 37: An Approach Based on the Regression between Radiological Source Term and Consequence for Effective and Efficient Risk Assessments of NPPs Speaker: Jiyeong SEO (Chung-Ang University) Contributors: Jiyeong SEO (Chung-Ang University), Jaehyun CHO (Chung-Ang University), Sung-yeop KIM (Korea Atomic Energy Research Institute)
17:40 - 18:00		ID 24: Decontamination Effectiveness for Wiping Vehicle in Screening during a Nuclear Emergency Speaker: Hirokazu Hiraoka (Japan Atomic Energy Agency) Contributors: Hirokazu Hiraoka (Japan Atomic Energy Agency), Kentaro Manabe (Japan Atomic Energy Agency), Jun Hirouchi (Japan Atomic Energy Agency), Shogo Takahara (Japan Atomic Energy Agency)

STUDY ON A CONSEQUENCE-INFORMED DECISION MAKING FOR EMERGENCY PLANNING ZONE DISTANCE WITH DOSE VERSUS DISTANCE CURVE

Kodai Wadayama[1,2], Retsu Kojo[3], Takafumi Narukawa[4], Takashi Takata[5]

[1] *Nuclear Regulation Authority: 1-9-9, Roppongi, Minato-ku, Tokyo，106-8450, wadayama_kodai_pt7@nra.go.jp*
[2] *The University of Tokyo: 7-3-1 Hongo, Bunkyo-ku, Tokyo, 113-8656, wadayama@nse.t.u-tokyo.ac.jp*
[3] *Nuclear Regulation Authority: 1-9-9, Roppongi, Minato-ku, Tokyo, 106-8450, kojo_retsu_px2@nra.go.jp*
[4] *The University of Tokyo: 7-3-1 Hongo, Bunkyo-ku, Tokyo, 113-8656, narukawa@n.t.u-tokyo.ac.jp*
[5] *The University of Tokyo: 7-3-1 Hongo, Bunkyo-ku, Tokyo, 113-8656, takata_t@n.t.u-tokyo.ac.jp*

ABSTRACT

Emergency preparedness relies heavily on establishing an Emergency Planning Zone (EPZ) to ensure that protective actions are taken for residents based on risk assessments. A critical aspect of this process is to understand the shape of the dose versus distance (D–D) curve. NUREG-0396 proposes that the dose decreases with downwind distance (r) according to a relationship of 1/r–1/r², however, the D–D curve has only been analyzed for containment-intact accidents. In addition, our recent study highlighted differences in the D–D curve under rainy conditions between scenarios involving filtered containment venting system (FCVS) and aerosol-rich scenarios although that analysis was limited to a specific stability class. This study aims to comprehensively evaluate the D–D curve characteristics specifically for aerosol emissions across a wide range of meteorological conditions. Although the 1/r-1/r² rule can be applied under various weather conditions in FCVS scenarios, applying the formula under certain rainy conditions in containment failure scenarios proves difficult. The D–D curve offers critical insights into dose distribution as a function of distance, directly informing the scaling of EPZ boundaries. By linking the shape of these curves to the thermal power of the plant, this methodology can aid in the decision-making process in adjusting EPZ for reactors with varying thermal powers, while ensuring consistent radiological consequences. Future research will focus on developing a revised formulation of the D–D curve, incorporating analysis in the angular (r–θ) direction.

Keywords: dose versus distance (D–D) curve, emergency planning zone, aerosol, stability class, accident scenario

I. INTRODUCTION

Establishing protective action plans for potential nuclear disasters, such as the Fukushima Daiichi Nuclear Power Plant accident, is crucial. A designated area around a commercial nuclear facility that aids offsite emergency planning, such as evacuation and shelter-in-place, is known as the emergency planning zone (EPZ). The emergence of new reactor types, including Small Modular Reactors (SMRs), has sparked discussions about risk-informed methodologies for defining EPZs [1].

The dose versus distance curve (D–D curve) provides essential insights when defining EPZ. Typically, the atmospheric dispersion increases both vertically and horizontally in the wind direction, whereas the concentration of nuclides diminishes as the distance from the release point increases. In addition, the concentration of nuclides in the plume is affected by radioactive deposition and the decay of nuclides during atmospheric dispersion. Consequently, the D–D curve illustrates the typical reduction in dose as the distance from the release point increases. Understanding the shape of this curve is critical for defining the EPZ, specifically the fraction by which the dose decreases when the distance increases by a factor of *r* [1][2].

NUREG-0396 discusses the shape of the D–D curve [3]. It suggests that dose decreases with distance according to 1/r and 1/r² curves. However, this research was conducted many years ago and focused only on containment-intact accidents, leaving a gap in the analysis of the D–D curve across diverse accident scenarios. Notably, insufficient analyses have been conducted of accident scenarios involving the filtered containment venting system (FCVS), which was implemented after the Fukushima Daiichi accident in Japan.

To address this gap, the authors have previously performed a detailed analysis of D–D curves, including accident scenarios involving an FCVS [4]. The study has revealed that under no rain conditions, the effects of various accident scenarios are minimal. By contrast, rainy conditions demonstrated a significant difference in D–D curves between scenarios with FCVS and

those with containment failure. However, this analysis was restricted to specific atmospheric stability (D stability) and wind speed (1.8 m/s).

Therefore, the objective of this study is to investigate the differences in D–D curves across various accident scenarios, including those utilizing FCVS, and to clarify the characteristics of the D–D curve through a comprehensive assessment under a wide range of meteorological conditions, with a focus on the aerosol fraction in the source term of each accident scenario.

II. MATERIALS AND METHODS

II.A. Calculation of the Amount of Fission Product Released to the Environment and Selection of Accident Scenarios

The amount of **f**ission **p**roduct (FP) released into the environment was calculated by multiplying the initial core inventory of FP by the core release fraction (CRF) for the transition from the core to the containment vessel, the reduction factor (RDF) due to mitigation effects; and the leakage rate from containment to the environment (EF), as shown in Equation (1) [4][5]. The release duration was set to 1 h for all accident scenarios considered, assuming a large boiling water reactor (BWR) with a thermal power of 3,000 MWth.

$$Q_i = Q_i^{INV} F_i^{CRF} (\prod F_{m,i}^{RDF}) F^{EF} \quad (1)$$

where Q_i is release rate of nuclide i to the environment per hour [Bq/h], Q_i^{INV} is initial core inventory of nuclide i (3,000 MWth reactor in WASH-1400 [6]) [Bq], F_i^{CRF} is core release fraction released from the core to the containment vessel (CRF) [-], $F_{m,i}^{RDF}$ is reduction factor of nuclide i by mitigation effect m (RDF) [-], F^{EF} is leakage rate from containment to the environment per hour (EF) [1/h]. The value of CRF was taken from Early in vessel release phase in NUREG-1465 [7]. The chemical form of iodine entering containment was assumed to be composed of 95% aerosol, 4.85% elemental iodine and 0.15% organic iodine [7]. The RDF was defined for each accident scenario, while the EF was set to 1.0, assuming all nuclides in the containment atmosphere are released within one hour duration, because this research focused on the short release.

Table 1 outlines the accident scenarios and the fractions of each nuclide released into the environment, relative to the initial inventory, using Equation (1).

TABLE 1. Accident Scenarios and Environmental Release Fractions of Nuclides

Accident scenario (details are provided in the previous report [4].)	Description of accident scenario	Total release fraction to the environment compared to the initial inventory of each nuclide [-]			
		gas	gas & aerosol	aerosol	
		Xe	I	Cs	Te
CF-6h (small mitigation)	Core melt and release of FP to the environment 6 h after reactor shutdown due to containment failure	9.5E−01	9.0E−02	7.2E−02	1.8E−02
CF-24h (small mitigation)	Core melt and release of FP to the environment 24 h after reactor shutdown due to containment failure	9.5E−01	7.9E−03	6.0E−03	1.5E−03
HV-6h (mid mitigation)	Core melt and release of FP to the environment 6 h after reactor shutdown due to hardened containment venting	9.5E−01	4.9E−03	3.6E−03	9.0E−04
HV-24h (mid mitigation)	Core melt and release of FP to the environment 24 h after reactor shutdown due to hardened containment venting	9.5E−01	7.5E−04	3.0E−04	7.5E−05
FV-6h (large mitigation)	Core melt and release of FP to the environment 6 h after reactor shutdown due to FCVS	9.5E−01	1.4E−05	3.6E−06	9.0E−07
FV-24h (large mitigation)	Core melt and release of FP to the environment 24 h after reactor shutdown due to FCVS	9.5E−01	8.0E−06	3.0E−07	7.5E−08

Noble gases are not subject to mitigation effects and are released in significant quantities in all accident scenarios considered in this study. By contrast, the behavior of aerosol nuclides within the containment depends on the effectiveness of mitigations, so the nuclides which ultimately released to the environment vary in each accident scenario. The mitigation effects considered in this study are containment holdup, scrubbing, and FCVS. The RDFs were assigned based on methods described in previous studies [4]; and their combination defines the overall aerosol removal efficiency. Two holdup durations were assumed to be short-term and long-term, corresponding to environmental release times of 6 and 24 h, respectively. CF-6h and CF-24h are containment failure scenarios in which limited mitigation effect is expected, and a large amount of aerosol radionuclides are released. HV-6h and HV-24h are scenarios using hardened containment venting, which are expected to remove aerosol nuclides moderately due to pool scrubbing effects in addition to holdup. FV-6h and FV-24h are scenarios using FCVS, and most aerosol nuclides are removed due to the strong mitigation effects of holdup, pool scrubbing, and FCVS.

II.B. Calculation Methods for Atmospheric Dispersion, Deposition, and Effective Dose

II.B.1. Calculation of Atmospheric Dispersion and Deposition

The assumed meteorological conditions are described in Table 2. This study considers various atmospheric stability classes and wind speeds, expanding upon the previous report that considered only stability class D and a wind speed of 1.8 m/s. This allows for the calculation of D–D curves under diverse meteorological conditions. We focused on analyzing newly considered effects of atmospheric stabilities and wind speeds, setting the representative precipitation rate at 3.8 mm/h [4] [8]. According to meteorological guidance [9] and Turner's method [10], B and F stabilities are most frequently observed under low-wind conditions. Thus, we assigned a wind speed of 1 m/s to stability classes B and F, and 2–5 m/s to stability class D.

TABLE 2. Meteorological Conditions Considered in the Study

	Stability class	Wind speed [m/s]	Precipitation rate [mm/h]
Past research	D	1.8	0.5, 3.8, 10
This research	B, D, F	1.0–5.0	3.8

Atmospheric dispersion was calculated using the Gaussian plume model, as given in Equation (2). Radioactive material was assumed to be released continuously from the emission source, maintaining a constant wind direction and speed. The diffusion parameters σ_y and σ_z are functions of the distance from the release point and were calculated using the referenced Japanese Meteorological Guidance [9]. The air concentrations of nuclides were computed, as expressed in Equation (3), considering radioactive decay and depletion through dry and wet deposition during atmospheric dispersion. Washout effects due to wet deposition were considered as exponential term in Equation (3) with reference to NUREG-1940 [8].

$$\chi / Q = \frac{1}{2\pi\sigma_y\sigma_z u}\exp\left(-\frac{y^2}{2\sigma_y^2}\right)\left\{\exp\left(-\frac{(z-h)^2}{2\sigma_z^2}\right)+\exp\left(-\frac{(z+h)^2}{2\sigma_z^2}\right)\right\} \tag{2}$$

$$\chi_i(x,y,z) = Q_i\left(\chi / Q\right)\exp\left(-\lambda_i\frac{x}{u}\right)\exp\left(-\Lambda\frac{x}{u}\right)f_F \tag{3}$$

Also, dry deposition velocities were assumed to vary based on atmospheric stability, whereas the particle size distribution was considered constant across all accident scenarios [8]. The depletion factor f_F denotes the reduction in plume concentration caused by dry deposition [11]. In the previous study, only atmospheric stability D was analyzed, and the new depletion factor f_F by dry deposition was not included as it was considered to have little influence [4]. In this study, f_F was newly considered.

$$\chi^{\bullet}_{i,D}(x,y) = \chi_i(x,y,0)\left(V_d + V_R\right) \tag{4}$$

$$V_R = \Lambda\sqrt{\frac{\pi}{2}}\sigma_z\exp\left(\frac{h^2}{2\sigma_z^2}\right) \tag{5}$$

$$f_F = \exp\left[-\sqrt{\frac{2}{\pi}} \frac{V_d}{u} \int_0^x \frac{1}{\sigma_z(x')} \exp\left\{ -\frac{h^2}{2\sigma_z^2(x')} \right\} dx' \right] \quad (6)$$

where $\chi^{\bullet}_{i,D}$ is nuclide i deposited per unit surface area per unit time [Bq/sm^3], χ_i is air concentration of nuclide i [Bq/m^3], Q_i : Release rate of nuclide i to the environment [Bq/s], u is wind speed [m/s], σ_y is diffusion parameter in the downwind horizontal axis (y axis) [m], σ_z is diffusion parameter in the downwind horizontal axis (z axis) [m], h is release height [m], Λ is washout coefficient [1/s], λ_i is decay coefficient [1/s], V_d is dry deposition velocity [m/s], and V_R is wet deposition rate [m/s].

II.B.2. Calculation of Effective Dose

The effective dose $H_S(x)$ was calculated using Equation (7), which multiplies the spatial concentration and ground surface concentration of radioactivity derived from atmospheric diffusion and deposition, by the dose conversion factor. The details of the calculation are based on previously reported methods considering three exposure pathways. The effective dose was computed by summing 1 hour of cloudshine, 1 hour of inhalation, and 7 days of groundshine, in accordance with IAEA GSR Part 7 [12].

$$H_s(x) = \sum_i K_i^{CS} \chi_i + \sum_i K_i^{GS} \chi^{\bullet}_{i,D} + \sum_i K_i^{IH} \chi_i \quad (7)$$

where $H_s(x)$ is effective dose for accident scenario *s* at downwind distance x [Sv], K_i^{CS} is dose conversion factor from air concentration to cloudshine dose [Svm^3/Bq] [13], K_i^{GS} is dose conversion factor from ground deposition to groundshine dose [Svm^2 s/ Bq] [13], K_i^{IH} is dose conversion factor from air concentration to inhalation dose [Svm^3/Bq] **Error! Reference source not found.**.

II.C. Calculation of the D–D Curve

The ratio $f_s^{DIST}(x)$ (D–D ratio), defined as the "effective dose at 1 km from the release point" relative to the "effective dose at any distance," was calculated for each accident scenario as shown in Equation (8). The corresponding D–D curve was then evaluated. This approach enables a quantitative assessment of the effects of various accident scenarios and meteorological conditions on $f_s^{DIST}(x)$ (D–D ratio) and comparison with the 1/r and 1/r² curves in NUREG-0396.

$$f_s^{DIST}(x) = \frac{H_s(x)}{H_{s,0}} \quad (8)$$

where $H_s(x)$ is effective dose for accident scenario *s* at downwind distance x [Sv], and $H_{s,0}$ is effective dose for accident scenario *s* at 1 km [Sv].

III. RESULTS AND DISCUSSION

III.A. Calculation Results of the D–D Curve for the Accident Scenarios without Rainfall

Figure 1 presents the D–D curves for each accident scenario under atmospheric stability D and wind speeds of 2 or 5 m/s. The divergence of the D–D curves among the accident scenarios was minimal, particularly at a wind speed of 5 m/s, suggesting that the D–D curve can generally be approximated by $1/r^{1.5}$ for any accident scenario. This occurs because the effects of phenomena such as radioactive decay of nuclides during atmospheric dispersion and plume depletion through deposition, which primarily drive the divergence in D–D curves, diminish as wind speeds increase.

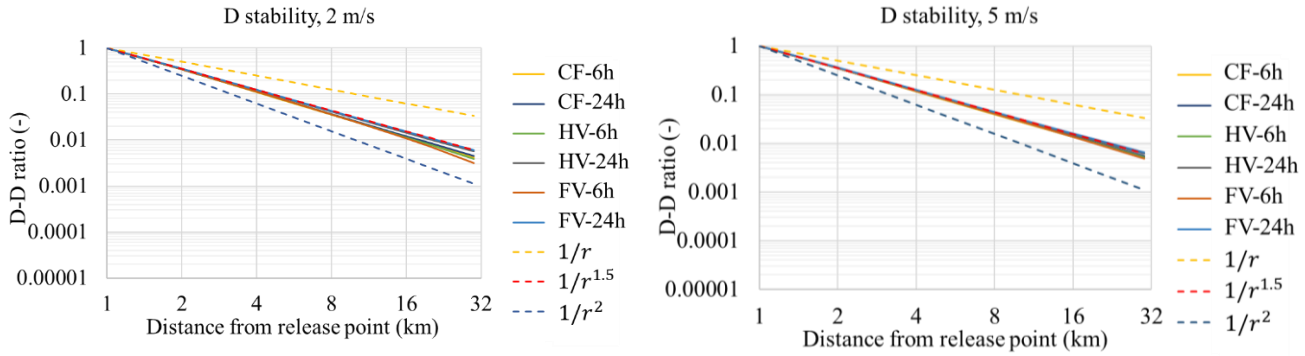

FIGURE 1. D–D Curves of Accident Scenarios under D Stability and Wind Speeds of 2 m/s and 5 m/s (No Rain).

Figure 2 presents the D–D curves for the accident scenarios at atmospheric stabilities B and F with a wind speed of 1 m/s. For atmospheric stability B, the D–D curves exhibited a steep slope, approaching $1/r^2$ at 1–5 km. Beyond approximately 5 km, the plume reached the mixing layer height, halting atmospheric dispersion in the vertical direction (z axis) and allowing horizontal dispersion (y axis) to dominate. As a result, the slopes of the D–D curves were close to $1/r$.

In the case of F stability, although the divergence of the D–D curves among accident scenarios remained small, some differences were noted compared to other stability classes. Specifically, the D–D curve for the scenario involving FCVS at 6 h after shutdown (FV-6h), which was influenced significantly by short-lived nuclides, and the scenarios with containment failure (CF-6h, CF-24h), which were affected by reduced plume concentration due to dry deposition, approached the $1/r^{1.5}$ relationship. By contrast, the D–D curves for the other accident scenarios exhibited a slope that fell between $1/r$ and $1/r^{1.5}$.

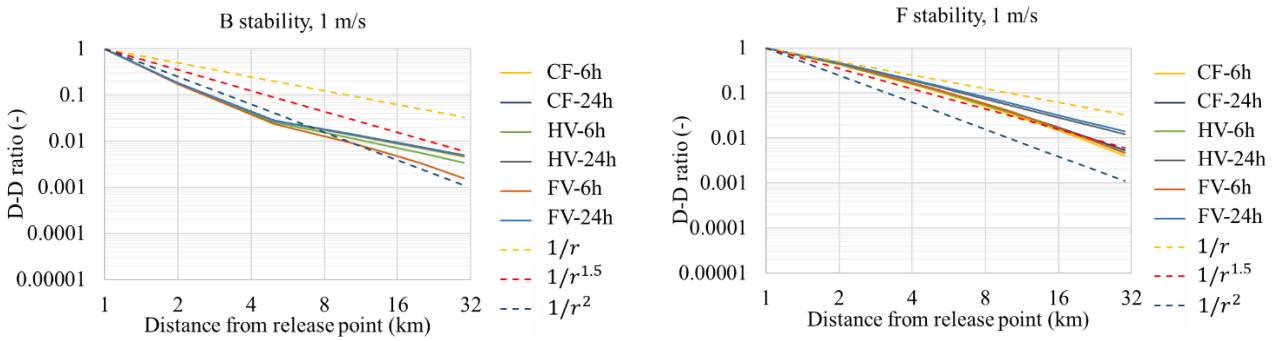

FIGURE 2. D–D Curves of Accident Scenarios under B and F Stabilities and Wind Speeds of 1 m/s (No Rain).

III.B. Calculation Results of the D–D Curve for the Accident Scenarios with Rainfall

Figure 3 presents the D–D curves for the accident scenarios at atmospheric stability D and wind speeds of 2 and 5 m/s. At a wind speed of 2 m/s, the divergence of the D–D curves were pronounced. For containment failure scenarios such as CF-6h and CF-24h, which had a high aerosol contribution, the D–D curves deviated from the NUREG-0396 [3] approximate formula. In these scenarios, the D–D ratios from upwind to downwind were significantly reduced due to aerosol removal by rainfall. By contrast, for accident scenarios utilizing an FCVS, the D–D curves tended to asymptote to $1/r^{1.5}$ in a manner consistent with scenarios without rainfall. However, the D–D curves for the accident scenarios at a wind speed of 5 m/s were less affected by rainfall due to the brief atmospheric dispersion time, resulting in minimal divergence among the D–D curves.

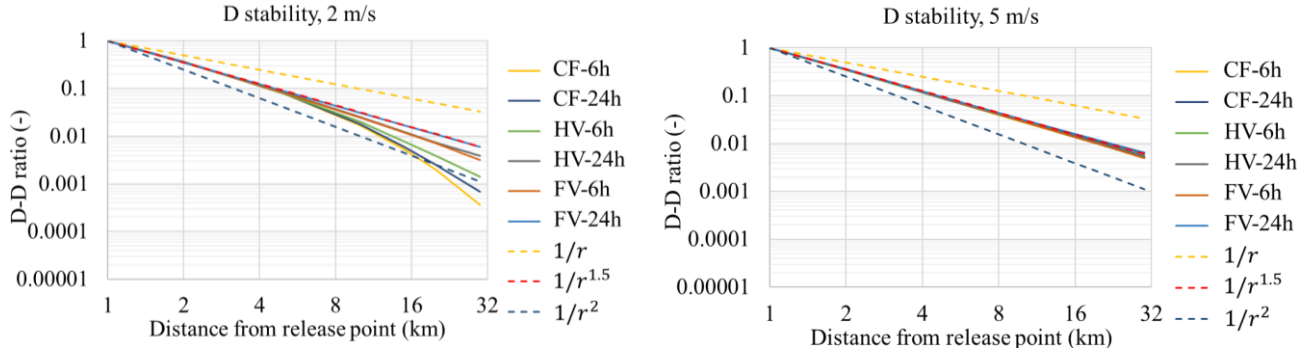

FIGURE 3. D–D Curves of Accident Scenarios under D Stability and Wind Speeds of 2 and 5 m/s (Rain).

Figure 4 presents the D–D curves for the accident scenarios under atmospheric stability conditions B and F at a wind speed of 1 m/s. Similar to the findings under D stability, the D–D curves among different accident scenarios exhibited significant divergence. Specifically, for scenarios with a high aerosol contribution, such as CF-6h and CF-24h (i.e., containment failure scenarios), the results indicated notable discrepancies between the approximate equation of NUREG-0396 [3] and the D–D curves. This suggests that, under rainfall conditions, the NUREG-0396 [3] approximation is challenging to apply to certain accident scenarios.

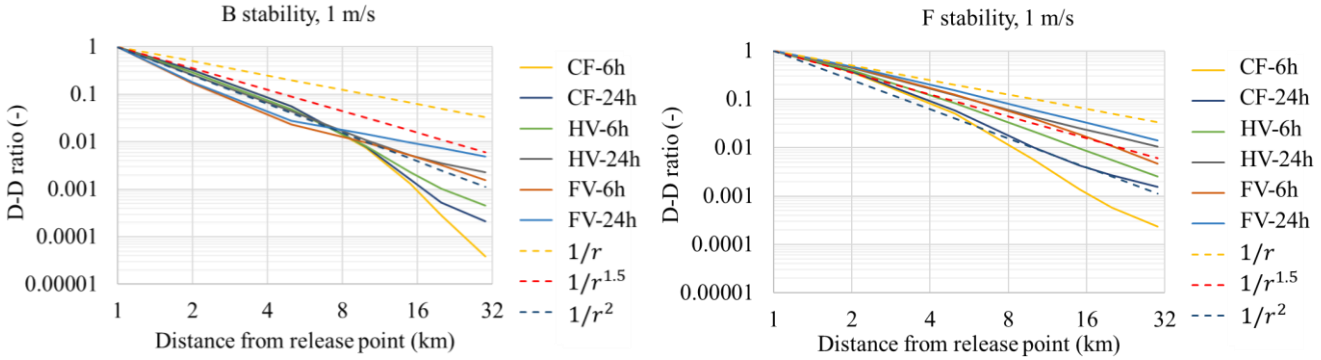

FIGURE 4. D–D Curves of Accident Scenarios under B and F Stabilities and Wind Speeds of 1 m/s (Rain).

III.C. Analysis of Aerosol Nuclides for the Reconstruction of a New D–D Curve Equation

Figure 5 presents the D–D curves for the accident scenarios under atmospheric stability condition F at a wind speed of 1 m/s, assuming that the dose conversion factors for noble gases and organic iodine in Equation (7) were set to zero, thereby focusing solely on aerosol nuclides as contributors to the effective dose. The meteorological conditions analyzed were F stability, with a wind speed of 1 m/s, which showed a marked divergence in the D–D curves among the accident scenarios.

In both cases, regardless of rainfall, minimal divergence was observed in the D–D curves among accident scenarios, suggesting that the D–D curve can be characterized in a way that is independent of the specific accident scenario when considering only aerosol contributions. These findings provide significant insights into the properties of the D–D curve.

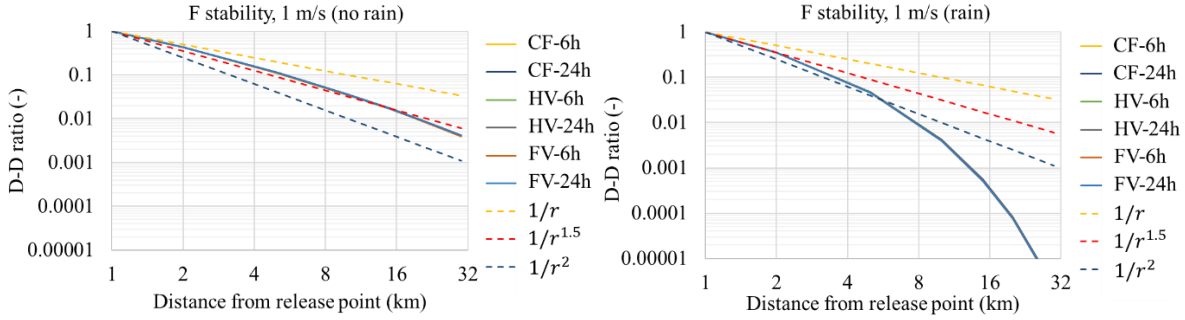

FIGURE 5. D–D Curve for Accident Scenarios Assuming Only the Aerosol Nuclides Contribute to the Dose.

This is attributable to the fact that, when considering only aerosol radionuclide contributions, variations in radionuclide composition among accident scenarios do not significantly affect the deposition of radionuclides on the ground.

We plan to conduct a detailed analysis of this issue and propose a new D–D curve equation to replace the empirical equation presented in NUREG-0396 [3]. However, we should note that the present calculations assumed the dry deposition velocity to be independent of the accident scenario.

IV. APPLICATION OF THIS METHODOLOGY FOR EPZ DETERMINATION: CONSEQUENCE-INFORMED DECISION MAKING

The D–D curve provides critical insights into the dose distribution as a function of distance, facilitating the scaling of EPZ distances based on thermal power [1]. Specifically, under the assumption that thermal power is proportional to the initial core inventory of FP in Equation (1), the proposed methodology utilizing the D–D curve enables the scaling of EPZ for reactors with varying thermal powers, while ensuring consistency in radiological risk.

The establishment of the EPZ is based on the assumption that typical accident conditions, including core damage and containment failure, are consistent regardless of the reactor's thermal power. Equation (9) illustrates the relationship between reactor thermal power and the distance required to reach a dose of 100 mSv, assuming that the D–D ratio is $1/r$. When the thermal power is multiplied by r, the distance to reach 100 mSv is multiplied by r.

$$H_s\left(x_{3000\mathrm{MWth}}\right) = H_s\left(\frac{x_{3000r\mathrm{MWth}}}{r}\right) \tag{9}$$

where $x_{3000MWth}$ is distance to reach 100 mSv in a light water reactor with thermal power of 3,000 MWth [km], and $x_{3000rMWth}$ is distance to reach 100 mSv in a light water reactor with thermal power of 3,000r MWth [km].

For example, compared to a reactor with a thermal power of 3,000 MWth, a reactor with a thermal power of 1,500 MWth would also release only half as much FP into the environment. Figure 6 illustrates the concept of scaling the EPZ based on thermal power by utilizing the D–D curve. By using a $1/r$ D–D curve, we can approximate that the distance required to achieve the dose criteria for defining the EPZ (e.g., 100 mSv effective dose [2] [12]) is 30 km for a reactor with a thermal power of 3,000 MWth, while it is approximately 15 km for a 1,500 MWth reactor, as indicated by (9).

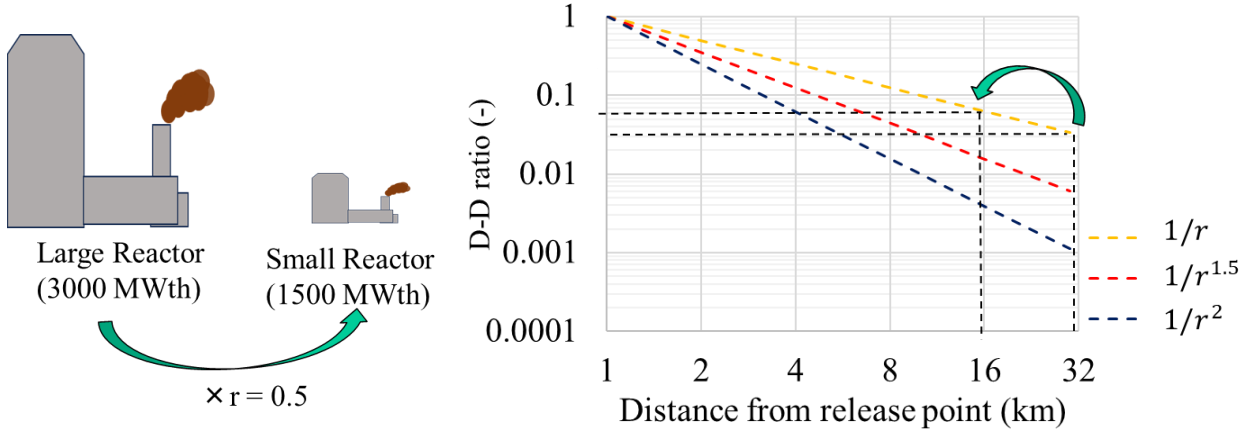

FIGURE 6. Concept of Scaling EPZ Based on Reactor Thermal Power by Utilizing the D–D Curve.

Although this methodology assumes that accident scenarios are similar for both small and large reactors, carefully assessing whether this assumption is valid is crucial [1]. Nonetheless, clarifying the characteristics of the D–D curve is an important initial step toward making consequence-informed decisions, where the EPZ is determined based on equivalent risk considerations for reactors with different thermal powers.

V. CONCLUSIONS

A comprehensive assessment of the characteristics of the D–D curves under a variety of meteorological conditions was performed, where the range of applicability of the $1/r \sim 1/r^2$ D–D curves proposed in NUREG-0396 was quantified. For scenarios involving containment failure without rainfall and significant aerosol contributions, the basic $1/r^{1.5}$ rule was found to be a reliable approximation in most cases, based on the meteorological guidance assumptions. By contrast, under scenarios involving rainfall, the $1/r \sim 1/r^2$ rule could be applied to situations with FCVS. Note that this proved to be challenging in accident scenarios involving containment failure without an FCVS.

The variability of D–D curves across different accident scenarios, including those employing an FCVS, was assessed. The authors' earlier conclusion that "the divergence of D–D curves among accident scenarios is small in the case of no rainfall, but large in the case of rainfall" was confirmed to hold across a wide range of meteorological conditions.

This methodology, leveraging the D–D curve, represents an initial step toward a new consequence-informed decision-making process that aims to establish appropriate EPZ while considering the equivalent risks associated with different reactor thermal power.

This study determined that the D–D curve remains largely independent of accident scenarios when considering only aerosol contributions. A more thorough analysis is expected to yield a more robust approximation that can replace the empirical formula currently proposed in NUREG-0396 [3].

The Gaussian plume model was applied only to the accident scenario involving a 1-h release duration, and the analysis was conducted under conditions of constant wind direction. Future research will expand this approach by incorporating angular (r-θ) directionality and exploring various accident scenarios for emission duration, ultimately enhancing the reliability of the analysis.

REFERENCES

[1] M. Iivonen, "Review of SMR siting and emergency preparedness," Finland: VTT Technical Research Centre of Finland, VTT Research Report No. VTT-R-01612-20 (2022).
[2] IAEA, "Actions to Protect the Public in an Emergency due to Severe Conditions at a Light Water Reactor," Vienna: International Atomic Energy Agency, EPR-NPP-PPA (2013).
[3] U.S. Nuclear Regulatory Commission, "Planning basis for the development of state and local government radiological emergency response plans in support of light water nuclear power plants," NUREG-0396 (1978).
[4] K. Wadayama, R. Kojo, T. Niisoe, "The effect of using Filtered Containment Venting System on variation in dose with distance in the prompt accident consequence assessment," *Journal of Nuclear Science and Technology*, 61:9, 1248–1264 (2024).
[5] T.J. McKenna, J. Trefethen, K. Gant, et al. "Response technical manual: RTM-96," Washington, DC: U.S. Nuclear Regulatory Commission, NUREG/ BR-0150, Volume 1, Revision 4 (1996).
[6] U.S. Nuclear Regulatory Commission, "Reactor safety study: an assessment of accident risks in U.S. Commercial nuclear power plants," WASH-1400 (1975).
[7] L. Soffer, S.B. Burson, C.M. Ferrell, et al. Accident source terms for light-water nuclear power plants. Washington, DC: U.S. Nuclear Regulatory Commission, NUREG-1465 (1995).
[8] J.V. Ramsdell, G.F. Athey, S.A. McGuire, et al. "RASCAL 4: description of models and methods," Washington, DC: U.S. Nuclear Regulatory Commission, NUREG-1940, (2012).
[9] NSC, "Meteorological guidance for reactor safety analysis" [in Japanese], (1982, revised in 2001)
[10] Turner, D. Bruce. "A Diffusion Model for an Urban Area," *Journal of Applied Meteorology and Climatology*, 3:1, 83–91 (1964).
[11] A.J. Nosek, N. Bixler. "MACCS theory manual," Albuquerque: Sandia National Laboratories, SAND2021-11535 (2021).
[12] IAEA, "Preparedness and response for a nuclear or radiological emergency," Vienna: International Atomic Energy Agency, IAEA Safety Standards Series No. GSR Part 7 (2015).
[13] K.F. Eckerman, J.C. Ryman, "External exposure to radionuclides in air, water, and soil," Washington, DC: U.S. Environmental Protection Agency, EPA-402-R-93-081 (1993).
[14] K.F. Eckerman, A.B. Wolbarst, A.C.B. Richardson, "Limiting values of radionuclide intake and air concentration and dose conversion factors for inhalation, submersion, and ingestion," Washington, DC: U.S. Environmental Protection Agency, EPA-520/1-88-020 (1988).

ASRAM2025
www.asram2025.org
Asian Symposium on Risk Assessment and Management 2025
Pattaya, Thailand, 27 – 29 August 2025

Monte-Carlo-based consequence analysis of nuclear accidents under extreme conditions

Shengyu LIU[1], Wei WANG[1]

[1] *Department of Mechanical Engineering, City University of Hong Kong, Kowloon Tong, Hong Kong, China*

ABSTRACT

The source term and meteorological conditions are key sources of uncertainty in assessing the consequences of severe nuclear accidents. However, previous studies have mainly focused on specific source terms and meteorological conditions. This study presents a Monte Carlo-based method that propagates both source term and meteorological uncertainties. The source term uncertainty is propagated by sampling from multiple source term categories (STCs), while the propagation of the meteorological data is by applying the randomized-start block sampling method to long-term meteorological data. Dispersion scenarios are established based on the samples of the source term and meteorological data. Then, the off-site consequence is evaluated based on the official dose conversion coefficient and corresponding measures. Validation of calculation accuracy is provided first by utilizing the release information of the Fukushima Daiichi nuclear accident and comparing calculation results with official data from the Japanese government. Then the method is applied to the Daya Bay Nuclear Power Plant (DBNPP). The findings reveal that the dispersion model can provide accurate calculation results, while the case study result of DBNPP shows a higher probability of serious consequences in the Southwest and Northeast directions around the nuclear power plant, due to the wind direction distribution.

Keywords: Uncertainty, Monte-Carlo Sampling; Radionuclide dispersion; Consequence assessment

I. INTRODUCTION

Worldwide expansion of Nuclear Power Plants (NPPs) has been accelerated recently [1]. Nevertheless, the risks that off-site release of radionuclides from severe nuclear accidents can create both acute and chronic impacts on public health. Recently, many studies have been dedicated to assessing the off-site consequences. Combinations of Emergency Planning Zones (EPZs) are developed to optimize consequence mitigation measures [2]. The off-site consequence is also investigated for the advanced power reactor 1400 (APR1400), where some specific possible accidents and corresponding meteorological conditions are covered to give a preliminary emergency framework [3]. However, uncertainty consideration is often inadequate in the off-site consequence assessment [4].

To assess the radioactive material dispersion and distribution that accounts for multiple uncertainties under severe nuclear accident conditions, the forward modelling methods offer a proactive way to comprehensively propagate main uncertainties related to both source terms and meteorological conditions [5]. Discrete source term categories (STCs) have been used to represent variability in release conditions, while some studies consider different source terms for a specific accident, resulting in not capturing the full range of possible source term variations, such as release magnitude [6]. The Level 2 PRA method is adopted to achieve more continuous and realistic source term distributions, such as release amount and duration [7]. Some other studies concentrate on the meteorological uncertainty. The ensemble method, which is developed for weather forecasting, shows better performance in the radionuclide dispersion than the traditional deterministic method by showing significant predictive rate accuracy improvement [8]. However, there are limited studies that fully combine the uncertainty propagation for both the source term and the meteorological data.

In this work, we propose a Monte Carlo-based (MC-based) consequence assessment method to fully combine these uncertainties, where the MC sampling approach is applied to both STCs and meteorological data. Then, dispersion scenarios are established, and consequence assessment is based on dose evaluation and emergency measures. The accuracy of the dispersion model is validated, and the results of the Daya Bay Nuclear Power Plant case study show a higher probability of serious consequences in the Southwest and Northeast directions around the nuclear power plant.

2. MATERIALS AND METHODS

In this part, mandatory data, including STCs and the meteorological data collection, will be given. Subsequently, the Monte-Carlo sampling method is used to sample from distributions of source term and meteorological data, while the

randomized-start block sampling approach is applied to long-term meteorological data. Finally, the off-site consequence evaluation process involving the dose conversion coefficient and corresponding measures will be demonstrated.

II.A. Monte-Carlo-based sampling

II.A.1. STCs collection

Consequently, discrete and hypothetical STCs are considered in this method. The technical report WASH-1400 provides STCs where the different STCs are contained [9]. The STCs presented in the report are obtained through the level 2 PSA estimation. The STCs are summarized in **TABLE I**. Besides, the core inventories and half-life of different radionuclides are summarized in **TABLE II**.

TABLE I. STCs and their corresponding release information

Release category	Probability (yr^{-1})	Relatively Probability	Release fraction of Core Inventory					Timing (hr.)	Duration (hr.)	Release height
			I-131	Cs-137	Xe-Kr	Te-132	Sr-90			
P1	9×10^{-7}	0.0018	0.7	0.4	0.9	0.4	0.05	2.5	0.5	25
P2	8×10^{-6}	0.016	0.7	0.5	0.9	0.3	0.06	2.5	0.5	0
P3	4×10^{-6}	0.008	0.2	0.2	0.8	0.3	0.02	5.0	1.5	0
P4	5×10^{-7}	0.001	0.09	0.04	0.6	0.03	5×10^{-3}	2.0	3.0	0
P5	7×10^{-7}	0.0014	0.03	9×10^{-3}	0.3	5×10^{-3}	1×10^{-3}	2.0	4.0	0
P6	6×10^{-6}	0.012	8×10^{-4}	8×10^{-4}	0.3	1×10^{-3}	9×10^{-5}	12.0	10.0	0
P7	4×10^{-5}	0.08	2×10^{-5}	1×10^{-5}	6×10^{-3}	2×10^{-5}	1×10^{-6}	10.0	10.0	0
P8	4×10^{-5}	0.08	1×10^{-4}	5×10^{-4}	2×10^{-3}	1×10^{-6}	1×10^{-8}	0.5	0.5	0
P9	4×10^{-4}	0.8	1×10^{-7}	6×10^{-7}	3×10^{-6}	1×10^{-9}	1×10^{-11}	0.5	0.5	0

TABLE II. Core Inventories and Half-lives of different radionuclides

Radionuclide	Core inventory (Curies)	Half-life (days)
I-131	8.5×10^{7}	8.05
Cs-137	4.7×10^{6}	11000
Te-132	1.2×10^{8}	3.25
Xe-133	1.7×10^{8}	5.28
Kr-88	6.8×10^{7}	0.117
Sr-90	3.7×10^{6}	11030

Studies have illustrated the reconstructed source term of the Fukushima nuclear accident, among which the longest period is from 2011/03/12 to 2011/05/01 [10]. Therefore, only situations where the release amount of both I and Cs exceeds that of the Fukushima Daiichi nuclear accident during this period are considered as severe accidents. The relative probability calculation formulation is shown in Eq. (1). The severe nuclear accident release categories and the results are listed in **TABLE III**.

$$\mathbf{P}_{r,i} = \frac{\mathbf{P}_{a,i}}{\sum_{i} \mathbf{P}_{a,i}} \tag{1}$$

where $\mathbf{P}_{a,i}$ and $\mathbf{P}_{r,i}$ represent the absolute probability and relative probability of release category i.

TABLE III. Relative probability of severe nuclear accident release categories

Release category	Probability (yr^{-1})	Relative Probability
P_1	9×10^{-7}	0.06383
P_2	8×10^{-6}	0.5674
P_3	4×10^{-6}	0.2837
P_4	5×10^{-7}	0.03546
P_5	7×10^{-7}	0.04964

In this case, the relative probability of each release category should be calculated by Eq. (1), where the results are shown in **TABLE III**.

II.A.2. Randomized-start block sampling

As mentioned before, the uncertainty caused by the weather temporal variation pattern is not considered in the ensemble and classification means. Therefore, in this work, long-term historical weather observation data will be collected, which is further combined with the terrain data to provide a long-term meteorological field. Then, the randomized-start block Monte Carlo sampling method will be utilized to cover the uncertainty. Assuming the meteorological data we collected forms a sample space Ω^M, where the hourly meteorological data for a specified period of time, assumed to be D days, is stored. Each hourly meteorological data is represented by d_j^M, where j represents the specific time point. Then we obtain the relationship:

$$\Omega^M = \left\{d_1^M, d_2^M, ..., d_p^M\right\}, p = 24D \tag{2}$$

In Formulation (2), the stored time period in the sample space includes all the hourly time point, which is varied from 1 to p. For instance, if the hourly meteorological data from the beginning hour of day 1 to the end hour of day N is sampled, then there will be $24N$ hourly data, and $j \in \{1, 2, ..., 24N\}$.

As soon as the data is collected, the randomized-start block sampling method is applied to the sample space Ω^M. A random hourly data is chosen to be the beginning of the meteorological sample, and with the specific meteorological time period, the meteorological sample will be extracted from the sample space, which is represented by M. For all the sample extracted from the sample space, we have:

$$\begin{aligned} &M_j \subseteq \Omega^M, j = 1, 2, ..., m \\ &M_j = \left\{d_q^M, d_{q+1}^M, ..., d_{q+24N-1}^M\right\}, 1 \le q \le p - 24N + 1 \end{aligned} \tag{3}$$

where j means the j[th] sampling. The beginning hour p in the sample is set to be less than $n - 24N + 1$ to avoid the last hourly meteorological data exceeding the last meteorological data in the sample space Ω^M.

Meteorological data is provided in many online sources, where the fifth generation of ECMWF reanalysis data (ERA5) is frequently used due to its data integrity [11]. In this work, the ERA5 reanalysis data is collected since it is more accurate and provides complete data for both surface and upper air meteorological data.

The MC sampling is applied to STCs to randomly sample a source term, while the meteorological data is sampled by using the randomized-start block sampling method. The source term and meteorological data generated from each sampling are combined to establish an uncertain dispersion scenario.

II.B. Dispersion model

Recently, different dispersion calculation models have been utilized to investigate radionuclide dispersion. The most used models are the Lagrangian model [6], the Gaussian plume model [12], and the Gaussian puff model [13]. Advantages and disadvantages exist in each dispersion model, and they are presented in TABLE IV. The Gaussian puff model is utilized in this work due to our assessment spatial range.

TABLE IV. Comparison of different dispersion models

Models	Advantages	Disadvantages
Lagrangian	Suitable for long-distance dispersion (Up to thousands of kilometers)	Computationally intensive
Gaussian plume	Costs little run time and small requirement of data input	Not accurate for mid-distance or long-distance (Larger than 30-50km)
Gaussian puff	Cost less time while keeping relatively accurate for mid-distance	Not as accurate as the Lagrangian model for long-distance calculation

The CALPUFF software, which adopts the Gaussian puff model, is used to simulate radionuclide dispersion, as it can model the radionuclide transportation under complex terrain.

II.C. Consequence analysis

The dose conversion coefficients are used to convert the concentration distribution to the dose distribution. Investigations have pointed out that inhalation contributes to the dose effect in the early dispersion of radionuclides, which is considered in this work, while the impacts of other routes are negligible. The effective dose conversion formulation in terms of inhalation is shown in Eq. (4)

$$E = \sum \left(e_i M C_i T \right) \tag{4}$$

where E is the effective dose or equivalent dose, i represents the species of the radionuclides, e is the effective dose coefficient for different radionuclides, M is the inhalation rate for adults, which is taken as 16 m^3/day, C is the concentration of radionuclides, and T represents the time period. The inhalation dose coefficients of these radionuclides [14,15] are presented in TABLE V.

TABLE V. Dose coefficient of different radionuclides

Radionuclide	Effective Dose Coefficient (Sv/Bq)
I-131	7.4×10^{-9}
Cs-137	4.6×10^{-9}
Te-132	1.8×10^{-9}
Xe-133	1.2×10^{-9}
Kr-88	8.4×10^{-9}
Sr-90	2.4×10^{-8}

In this work, we consider one dose criteria with its emergency measure, which are listed in TABLE VI.

TABLE VI. Dose criteria and corresponding measures

Dose level	Protective measures
50 mSv/week	Temporary evacuation

3. RESULTS AND DISCUSSIONS

III.A. Verification of the accuracy

A squared area with an edge length of 100 km is chosen, where its center is the Fukushima Daiichi nuclear power plant. The area is shown in FIGURE 1:

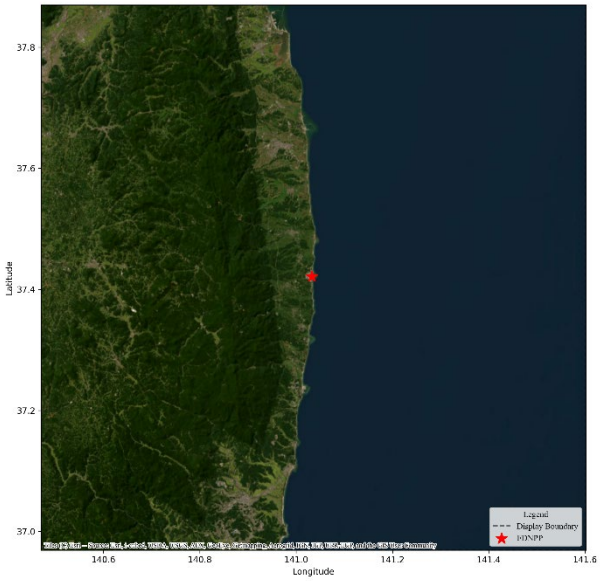

FIGURE 1. The calculation area of the Fukushima nuclear accident case

The source term of the Fukushima nuclear accident has been estimated by several recent studies. In this work, we adopted a rough estimation of the source term from 12/03/2011 to 01/05/2011 published in an early work [10].

The surface meteorological data is adopted from the ERA5 reanalysis dataset and the Japanese Reanalysis for Three-Quarters of a Century (JRA-3Q) data. The upper air meteorological data are adopted from the ERA5 reanalysis dataset. The upper air data provided by ERA5 is combined with both surface observation data of ERA5 and JRA-3Q, since it is more complete. Then, two kinds of meteorological data combinations, which are ERA5 surface-ERA5 upper and JRA-3Q surface-ERA5 upper, are used to calculate radionuclide dispersion. The average release rate of the source term and the time-phased release rate are both applied to calculate the radionuclide dispersion result.

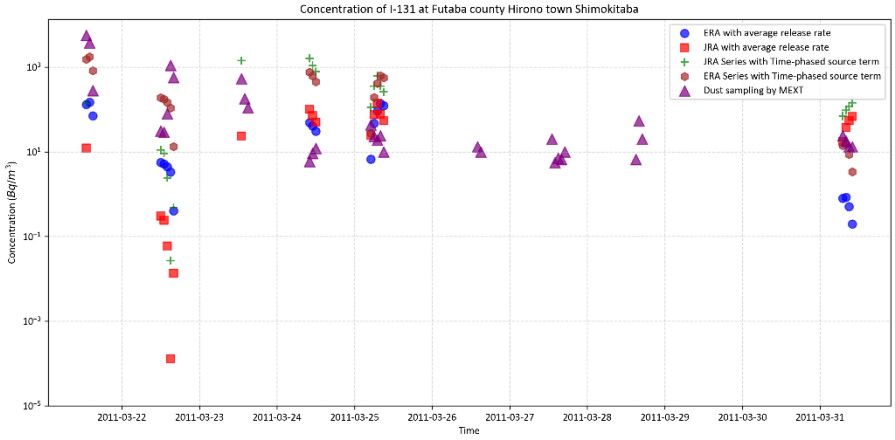

FIGURE 2. Comparison of calculation and dust sampling results

To verify the accuracy of the dispersion model, we compare the calculation results by using the combination of these two kinds of meteorological data, and the source term presented in [10], to the dust sampling result measured by the Ministry of Education, Culture, Sport, Science and Technology (MEXT) of Japan [16]. The dust sampling location is chosen to be Futaba County, Hirono town, Shimokitaba, since it provides an early and complete concentration of both I-131 and Cs-137. As shown in Figure 2, the concentration of radionuclides calculated by the average release rate in the early period is lower than that estimated by the time-phased release rate, which is due to the higher release rate in the early release period. There is no concentration result calculated by the simulation on some days, since there is no airborne concentration shown in these specific periods at this location. The result calculated by ERA5 surface-ERA5 upper and time-phased release rate is closest to the measured results, which are basically on the same order of magnitude. Therefore, the calculation accuracy of CALPUFF is verified. The ERA5 surface-ERA5 upper meteorological data combination will be adopted in the following verification of the method and the case study in Section 4.

III.B. Case Study: DBNPP

The Daya Bay nuclear power plant has been operating for some decades, and there are some population-dense cities around this nuclear power plant, such as Shenzhen and Hong Kong. Therefore, in this work, the Daya Bay nuclear power plant is chosen as the case study. The calculation area and the corresponding configurations of the calculation are listed in Table 7. The surface and upper air meteorological data are provided by the ERA5 reanalysis dataset as a result of the verification in Section 3.1. As mentioned previously, each meteorological data point contains both surface and upper air data, and the locations of these data points are shown in Table 7.

TABLE VII. Configuration of the dispersion case at the Daya Bay nuclear power plant

Variables	Values
Calculation area	200 km×200 km UTM: 50N, X: 147.413-347.413 km; Y: 2401.099-2601.099 km Longitude-Latitude: 21.678334°-23.512949° N 113.593252°-115.505487° E
Grid size	2 km
Number of meteorological data points	4×4 (The distance between each meteorological data point is 0.5°. The data point with the minimum latitude and longitude is located at

	21.93° N, 113.63° E, i.e., the lower left side of **FIGURE 3**)
Time range of the meteorological dataset	2005/01/01-2024/12/31
Radionuclide dispersion time in a single scenario	7 days
Number of Scenarios	5000

After setting the configurations and calculating each dispersion scenario, the radionuclide concentration results are obtained. The surface 7-day-average concentration results of I-131 in different dispersion scenarios are calculated. For each scenario, the distributions of the radionuclide are different due to the different meteorological conditions. In these dispersion scenarios, the calculated concentration coverage range of some scenarios is relatively large, while the concentration coverage range of other scenarios is concentrated in a particular direction. The large concentration coverage range is due to the significant change in wind direction in this scenario. In contrast, for the scenario where the wind direction is concentrated in a specific direction, the concentration coverage range is small. The dispersion trends of the different radionuclide species are the same due to the same configuration and the dispersion properties of these radionuclides. The concentration values of different radionuclides are different due to their different release amounts.

By applying the dose conversion coefficient introduced in Section 2, the surface concentration distributions of different radionuclides are converted to the dose distribution. Then, the dose value distributions in different directions under each dispersion scenario with Daya Bay Nuclear Power Station as the center are statistically analyzed, and the dose value distribution at each distance in each direction is statistically analyzed. In this case, directions are taken every 10°, and 36 directions are adopted. Moreover, for each direction, starting from the nuclear power plant, statistical points are taken outward every two kilometers (equal to the grid size). The dose values are sorted from small to large, and the 95% quantile is taken as the upper limit of the 95% confidence interval of the distribution. This upper limit indicates that when an accident occurs, there is a 95% confidence that the dose value will not exceed this upper limit. As the upper limit of the dose confidence interval at a certain distance in this direction exceeds the dose threshold corresponding to the evacuation listed in Section 2, the location is marked as a hazardous location that people should evacuate in the early stage of the accident without any other source of information.

As shown in Figure 3, the risky areas in terms of the evacuation measure are divided. The red area is calculated with the same release amount as that of the Fukushima Daiichi nuclear accident from 2011/03/12 to 2011/05/01, and the blue shadow area is divided by the calculation with scenarios sampled from the STCs and meteorological data. The land part of the risk area is cropped. However, due to the accuracy limitation of the land boundary line used for clipping, there are some slight differences between the clipped areas and the land areas shown in Figure 3. Nevertheless, this does not affect the analysis of the evacuation risk areas.

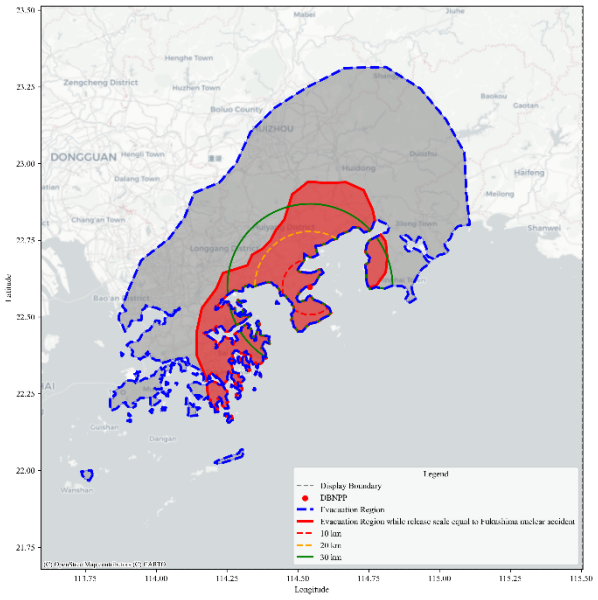

FIGURE 3. The spatial distribution of off-site consequences that indicates the evacuation necessity (Red: release amount equal to that of the Fukushima Daiichi nuclear accident from 2011/03/12 to 2011/05/01; Blue: release amounts are sampled from the release categories)

The spatial distribution of off-site consequences shown in FIGURE 3 indicates that when the release amount is equal to that of the Fukushima Daiichi nuclear accident, the evacuation area will exceed 30 km in most directions except the direction at the West-Northwest-North range. Similarly, the hazardous area calculated by the release amount sampled from the release categories shows that the risky area covers a wider area in the Northeast-Southwest direction, while that in the Northwest direction covers less than in other directions. This is due to the wind direction distributions at each meteorological data point. As depicted in FIGURE 4, the wind rose diagrams of each surface meteorological data point from 2005-2024 are calculated. For each data point, it is easily observed that most wind directions are distributed in the North-Northeast-East direction, and some wind directions are distributed in the South-Southwest direction. The dominant wind directions are North and Northeast. Therefore, most of the land area of Hong Kong, which is in the southwest direction of the Daya Bay nuclear power plant, will be affected with a relatively high probability under severe nuclear accident conditions. Besides, some land areas of Shenzhen and Huizhou will be affected with a high probability, too.

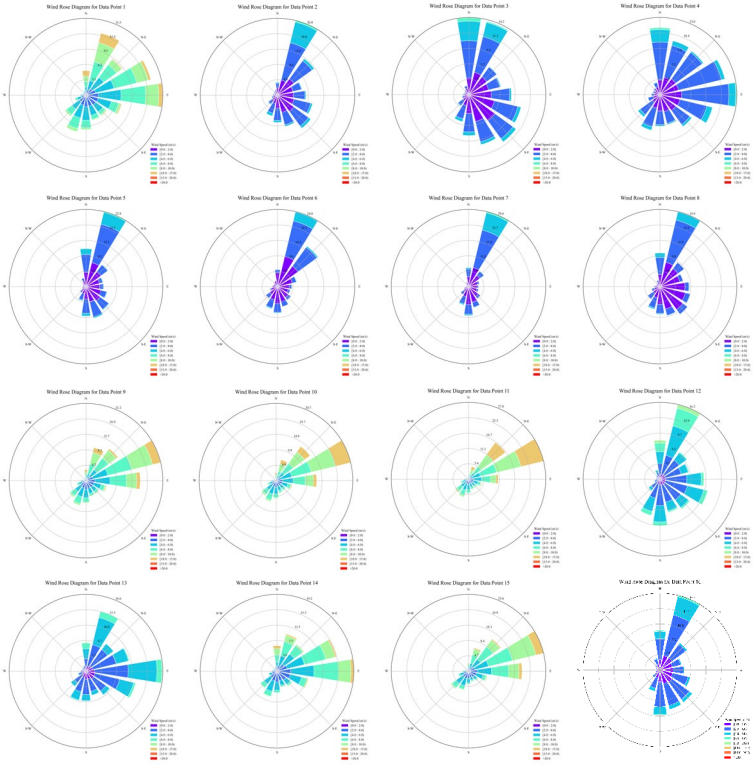

FIGURE 4. Wind rose diagrams of each surface meteorological data point from 2005-2024

II. CONCLUSIONS

In this work, A Monte-Carlo-based sampling method is proposed to combine the uncertainty propagations of the source term and meteorological data, where dispersion scenarios and consequence assessment are conducted based on source term and meteorological data samples. The conclusions of this work are summarized below:

1. Validation conducted by comparing the calculation results to the dust sampling data issued by the Japanese government shows that the model provides accurate calculation results.

2. A higher probability of serious consequences is shown in the Southwest and Northeast directions around the DBNPP, due to the wind direction distribution.

ACKNOWLEDGMENTS

The authors gratefully acknowledge the financial supports of this work by the Research Grants Council (RGC) of Hong Kong under the grant No. 11215323, and the National Natural Science Foundation of China under the grant No. 72101221.

REFERENCES

[1] J. PORTUGAL-PEREIRA, M. ESTEBAN, K. ARAÚJO, "Exposure of future nuclear energy infrastructure to climate change hazards: A review assessment", Energy Strategy Reviews, 53, 101365 (2024).
[2] M. KIMURA, OGURI ,TOMOMI, ISHIKAWA ,JUN, M. AND MUNAKATA, "Development of an evaluation method for planning of urgent protection strategies in a nuclear emergency using a level 3 probabilistic risk assessment", Journal of Nuclear Science and Technology 58, 278–291 (2021).
[3] I.A. ALRAMMAH, "Analysis of nuclear accident scenarios and emergency planning zones for a proposed advanced power reactor 1400 (APR1400)", Nuclear Engineering and Design 407, 112275 (2023).
[4] T. ZHOU, M. MODARRES, E.L. DROGUETT, "Multi-unit nuclear power plant probabilistic risk assessment: A comprehensive survey", Reliability Engineering & System Safety 213, 107782 (2021).
[5] S.J. LEADBETTER, S. ANDRONOPOULOS, P. BEDWELL, K. CHEVALIER-JABET, G. GEERTSEMA, F. GERING, T. HAMBURGER, A.R. JONES, H. KLEIN, I. KORSAKISSOK, A. MATHIEU, T. PÁZMÁNDI, R. PÉRILLAT, CS. RUDAS, A. SOGACHEV, P. SZÁNTÓ, J.M. TOMAS, C. TWENHÖFEL, H. DE VRIES, J. WELLINGS, "Ranking uncertainties in atmospheric dispersion modelling following the accidental release of radioactive material", Radioprotection 55, S51–S55 (2020).
[6] M. ULIMOEN, E. BERGE, H. KLEIN, B. SALBU, O.C. LIND, "Comparing model skills for deterministic versus ensemble dispersion modelling: The fukushima daiichi NPP accident as a case study", Science of The Total Environment 806, 150128 (2022).
[7] J.H. SØRENSEN, J. BARTNICKI, A.M. BLIXT BUHR, H. FEDDERSEN, S.C. HOE, C. ISRAELSON, H. KLEIN, B. LAURITZEN, J. LINDGREN, F. SCHÖNFELDT, R. SIGG, "Uncertainties in atmospheric dispersion modelling during nuclear accidents", Journal of Environmental Radioactivity 222, 106356 (2020).
[8] L. SHENG, Z. SONG, J. HU, K. LÜ, H. TONG, B. LI, Q. QIAO, "The comparison of ensemble or deterministic dispersion modeling on global dispersion during fukushima dai-ichi nuclear accident", Sci. China Earth Sci. 58, 356–370 (2015) .
[9] NUREG-75/014, "reactor safety study, an assessment of accident risks in U.S. commercial nuclear power plants, appendix VI."
[10] H. TERADA, G. KATATA, M. CHINO, H. NAGAI, "Atmospheric discharge and dispersion of radionuclides during the fukushima dai-ichi nuclear power plant accident. Part II: Verification of the source term and analysis of regional-scale atmospheric dispersion", Journal of Environmental Radioactivity 112, 141–154 (2012) .
[11] HERSBACH, H., BELL, B., BERRISFORD, P., BIAVATI, G., HORÁNYI, A., MUÑOZ SABATER, J., NICOLAS, J., PEUBEY, C., RADU, R., ROZUM, I., SCHEPERS, D., SIMMONS, A., SOCI, C., DEE, D., THÉPAUT, J-N., "ERA5 hourly data on single levels from 1940 to present. Copernicus Climate Change Service (C3S) Climate Data Store (CDS)", (2023)
[12] H. TERADA, H. NAGAI, K. TSUDUKI, A. FURUNO, M. KADOWAKI, T. KAKEFUDA, "Refinement of source term and atmospheric dispersion simulations of radionuclides during the fukushima daiichi nuclear power station accident", Journal of Environmental Radioactivity 213, 106104 (2020).
[13] J. CAI, K.F. IP, C. EZE, J. ZHAO, J. CAI, H. ZHANG, "Dispersion of radionuclides released by nuclear accident and dose assessment in the greater bay area of China", Annals of Nuclear Energy 132, 593–602 (2019) .
[14] "Age-dependent doses to members of the public from intake of radionuclides. 4: Inhalation dose coefficients", Pergamon Press, Oxford, (1996).
[15] K. ECKERMAN, J. HARRISON, H.-G. MENZEL, C.H. CLEMENT, "ICRP publication 119: Compendium of dose coefficients based on ICRP publication 60", Annals of the ICRP 41, 1–130 (2012).
[16] https://radioactivity.nra.go.jp/cont/en/results/land/dust-soil/beyond-20km-dust/dust%20sampling_All%20Results%20for%20May%202011.pdf

ASRAM2025
www.asram2025.org
Asian Symposium on Risk Assessment and Management 2025
Pattaya, Thailand, 27 – 29 August 2025

APPLICATION OF VARIOUS DISPERSION COEFFICIENTS TO INVESTIGATE THE SENSITIVITY OF OFFSITE CONSEQUENCES

Dakyoung Lee[1,2], Sung-yeop Kim[2*], Gibeom Kim[2], Eung Soo Kim[1]

[1] *Department of Nuclear Engineering, Seoul National University: 1, Gwanak-ro, Gwanak-gu, Seoul, 08826, Republic of Korea*
[2] *Korea Atomic Energy Research Institute: 111, Daedeok-daero 989beon-gil, Yuseong-gu, Daejeon, 34057, Republic of Korea*

ABSTRACT

In the event of a nuclear power plant accident, the release of radioactive materials into the atmosphere is likely to spread over a wide area, making the atmosphere the primary medium for human exposure. Therefore, it is essential to assess the dispersion of radioactive material for conducting an offsite consequence analysis. Most offsite consequence analysis codes utilize the Gaussian plume model for atmospheric dispersion analysis. The dispersion coefficient is a critical factor that determines the vertical and horizontal concentration distribution in the downwind direction of the Gaussian plume model. A majority of dispersion coefficients are calculated based on the Pasquill-Gifford curve, which was developed for flat terrain, and various fitting equations have been proposed to utilize it effectively. In this study, several dispersion coefficients, including Tadmor-Gur, Eimutis-Konicek, Briggs, Martin, and Seinfeld, were investigated and applied to offsite consequence analyses. Radiological Consequence Analysis Program (RCAP) developed by Korea Atomic Energy Research Institute (KAERI) and MELCOR Accident Consequence Code System (MACCS) developed by Sandia National Laboratories (SNL) were employed to perform offsite consequence analyses. Subsequently, the influence of the dispersion coefficient on the offsite consequences was analyzed. The results of this study highlight how the selection of dispersion coefficients in Gaussian plume models can affect offsite consequences. The insights gained from this study are expected to contribute to future Level 3 probabilistic safety assessments (PSAs) and emergency planning zone (EPZ) assessments.

Keywords: Atmospheric dispersion, Dispersion coefficient, Offsite consequence analysis, Level 3 PSA

I. INTRODUCTION

PSA (Probabilistic Safety Assessment) has continued to evolve as an effective and systematic tool for identifying and evaluating risks associated with nuclear facilities. It is generally categorized into three levels according to the protective boundaries of a nuclear power plant: Level 1 evaluates core damage frequency, Level 2 addresses containment failure and radioactive release, and Level 3 assesses the radiological impact on the environment and the public. Among them, Level 3 PSA aims to quantify the consequences of radioactive materials released into the environment, particularly through atmospheric dispersion and deposition, and its resulting impact on surrounding populations and ecosystems. In recent years, the significance of Level 3 PSA has become increasingly prominent due to growing societal concern and enhanced regulatory demands.

In the event of a nuclear accident, the atmosphere serves as the primary pathway through which radioactive materials can exert the most significant short-term impact on the environment and the public. Accordingly, atmospheric dispersion models are employed to quantitatively evaluate the transport and dispersion behavior of released radionuclides. These models are used to predict the atmospheric concentration distribution of the released radioactive material and the resulting radiation dose. Among such models, the Gaussian plume model is one of the most widely adopted, which assumes that the concentration of released contaminants follows a Gaussian distribution in both the horizontal and vertical directions relative to the plume centerline.

In this process, the dispersion coefficient is a key parameter in quantifying the extent of plume spread in the atmosphere, directly influencing the accuracy of concentration distribution and dose prediction. Dispersion coefficients are typically derived from Pasquill-Gifford (P-G) fitting curves [1] based on the results of the Prairie Grass experiment [2], and a variety of empirical fitting expressions have been proposed to put them into numerical form. They are expressed in various equation forms depending on the differences in experimental conditions and the range of meteorological factors considered in each model. The selection of dispersion coefficient models can result in considerable variations in prediction outcomes depending on

atmospheric stability conditions, particularly affecting the spatial characteristics of plume dispersion and the subsequent offsite consequence assessment. Therefore, the choice of dispersion coefficient model should be considered as a factor directly related to the reliability and quantitative validity of offsite impact predictions, and a more careful and systematic approach is required.

This study compares the characteristics of five dispersion coefficient models—Tadmor-Gur, Eimutis-Konicek, Briggs, Martin, and Seinfeld—and conducts offsite impact assessments using the Radiological Consequence Analysis Program (RCAP) and the MELCOR Accident Consequence Code System (MACCS) to quantitatively evaluate the differences among the models. The results provide a quantitative understanding of the sensitivity of the choice of dispersion coefficient model to the results of the offsite impact assessment, and contribute to the development of model selection criteria for conducting more reliable Level 3 PSAs in the future.

II. METHODOLOGY

II.A. Atmospheric Dispersion Modeling using Gaussian Plume Approach

In this study, the Gaussian plume model was employed to evaluate the atmospheric dispersion of radioactive materials released during a nuclear accident. This model defines the spatial concentration distribution of the plume based on the standard deviations of the Gaussian distribution in the horizontal (σ_y) and vertical (σ_z) directions. The dispersion of the plume occurs in all directions due to atmospheric turbulence, with vertical dispersion being particularly influenced by surface roughness and thermal structures of the atmosphere, such as inversion layers. In contrast, horizontal dispersion is less constrained and is further enhanced by plume meandering along the centerline. Dispersion in the downwind direction is generally negligible due to the significantly lower turbulence velocity compared to the mean wind speed. Owing to its simplicity and computational efficiency, the Gaussian plume model is widely used to simulate the dispersion of radioactive materials in the atmosphere following reactor accidents. When the plume dispersion is not constrained by surface contact or inversion layers, the concentration distribution is defined by the Gaussian plume equation introduced by Turner [3].

$$\chi(x, y, z) = \frac{Q}{2\pi u \sigma_y \sigma_z} \cdot \exp\left[-\frac{1}{2}\left(\frac{y}{\sigma_y}\right)^2\right] \exp\left[-\frac{1}{2}\left(\frac{z-h}{\sigma_z}\right)^2\right] \quad (1)$$

In Equation 1, χ denotes the time-integrated atmospheric concentration, Q represents the emission rate of the pollutant from the source, and h is the effective release height. The coordinates x, y, and z refer to the downwind, crosswind, and vertical distances, respectively. σ_y and σ_z represent the standard deviations of the concentration distribution in the crosswind and vertical directions. The parameter u denotes the mean wind speed at the effective release height.

II.B. Atmospheric Dispersion Parameters

II.B.1. Atmospheric Stability

To apply the Gaussian plume model for evaluating atmospheric dispersion, it is first necessary to determine the atmospheric stability of the environment under consideration. Atmospheric stability is typically classified based on meteorological observation data, using empirical schemes proposed by Pasquill and Gifford [4]. The classification criteria for stability categories are presented in Table I, which are established by comprehensively considering meteorological parameters such as wind speed, solar radiation, and cloud cover. Since the dispersion characteristics of a plume vary significantly depending on the atmospheric stability class, the corresponding dispersion coefficients also exhibit marked differences across stability conditions.

Table I. Pasquill-Gifford Atmospheric Stability

Wind speed (m/s)	Day time – Solar Radiation			Night time – Cloud cover	
	Strong	Moderate	Slight	Cloudy	Clear
< 2	A	A-B	B	-	-
2 – 3	A-B	B	C	E	F
3 – 5	B	B-C	C	D	E

5 – 6	C	C-D	D	D	D
> 6	C	D	D	D	D

A: Very unstable / B: Moderately unstable / C: Slightly unstable / D: Neutral / E: Slightly stable / F: Stable

II.B.2. Dispersion Coefficient

In this study, a total of five dispersion coefficient models were employed for analysis. Dispersion coefficients are calculated based on the determined atmospheric stability and are classified into horizontal dispersion coefficients σ_y and vertical dispersion coefficients σ_z. One of the most representative atmospheric dispersion experiments, the Prairie Grass experiment, was conducted in 1956 in O'Neill, Nebraska, USA. This experiment demonstrated that the dispersion behavior within a range of approximately 1 km could be predicted by considering meteorological parameters such as atmospheric stability and wind direction variability. Based on the results of this experiment, Pasquill and Gifford established curves representing horizontal and vertical dispersion coefficients according to atmospheric stability, which have since served as a reference standard for various dispersion models (Fig. 1).

Among the models considered, the Tadmor-Gur and Briggs models are empirical formulations that differ from the conventional Pasquill-Gifford (P-G) curve-based models, yet are widely applied both domestically and internationally as representative dispersion coefficient models. The remaining models are derived by fitting empirical equations to the P-G curves, mathematically expressing the dispersion characteristics associated with each stability class. The equations for each dispersion coefficient model, along with the major meteorological parameters considered, are summarized in Table II.

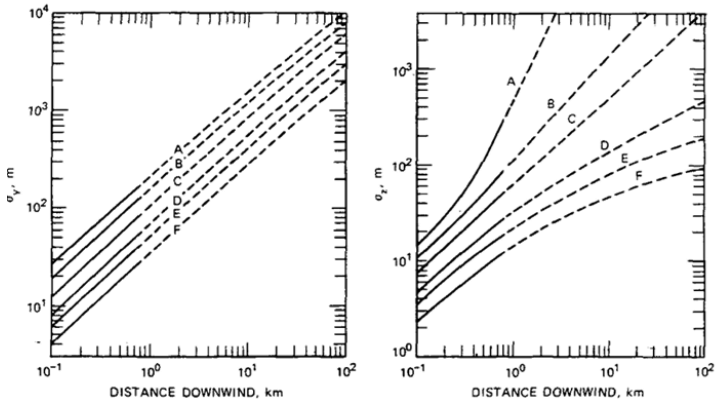

Figure 1. Pasquill-Gifford (PG) Curves [5]

Table II. Dispersion Coefficient Models

Model	Equation	Meteorological Factors
Tadmor-Gur (1969)	$\sigma_y = ax^b$, $\sigma_z = cx^d$	Distance (x), Stability Class (A-F)
Eimutis-Konicek (1972)	$\sigma_y = Ax^{0.9031}\ (A = k_1\sigma_\theta^2 + k_2\sigma_\theta + k_3)$ $\sigma_z = \mathrm{cx^d + f}$	Distance (x), azimuthal wind direction fluctuations (σ_θ), lapse rate (ΔT)
Briggs (1973)	$\sigma_y = \mathrm{Ax}(1 + 0.001\mathrm{x})^{-1/2}$ $\sigma_z = \mathrm{Bx}(1 + \mathrm{Cx})^D$	Distance (x), Stability Class (A-F)
Martin (1976)	$\sigma_y = ax^{0.894},\ \sigma_z = cx^d + f$	Distance (x), Stability Class (A-F)
Seinfeld (2006)	$\sigma_y = R_y x^{r_y},\ \sigma_y = \exp[I_y + J_y \ln x + K_y(\ln x)^2]$ $\sigma_z = \exp[I_z + J_z \ln x + K_z(\ln x)^2]$	Distance (x), Stability Class (A-F)

The Tadmor-Gur dispersion coefficient [6] is developed based on the results of the Prairie Grass field experiment. Previous studies proposed dispersion coefficient equations in the form of a power law. Fuquay et al. [7] experimentally demonstrated

that the horizontal dispersion coefficient σ_y is proportional to $(\sigma_\theta \bar{u})t^p$, while Smith and Singer [8][9] expressed dispersion as a power-law relationship in the form of $\sigma = ax^p$. Tadmor and Gur applied this $\sigma = ax^p$ formulation separately for each atmospheric stability class (A–F), reporting good agreement between the fitted expressions and the graphic curves presented by Gifford.

The Eimutis-Konicek dispersion coefficient [10] defined continuous expressions for both horizontal and vertical dispersion coefficients (σ_y and σ_z) as functions of downwind distance (x) and meteorological parameters such as the standard deviation of wind direction fluctuations (σ_θ) and lapse rate (ΔT). The horizontal dispersion coefficient is primarily influenced by distance and wind direction fluctuations, while the vertical dispersion coefficient also incorporates the effects of lapse rate. In this model, σ_y is based on the Tadmor-Gur model [6], with further refinement through regression analysis using the standard deviation of wind direction fluctuations. σ_z is derived from a piecewise function structure originally proposed by Martin [11].

The Briggs dispersion coefficient [12] integrated the Pasquill, BNL (Brookhaven National Laboratory), and TVA (Tennessee Valley Authority) curves based on observations up to 10 km downwind and applies theoretical concepts related to the asymptotic limits of the formulas to develop a set of empirical equations. According to this model, the initial plume spread under all atmospheric stability conditions is proportional to the downwind distance (x), and at long distances, the horizontal dispersion coefficient σ_y follows a $x^{1/2}$ dependence, consistent with the Fickian and Taylor theories of diffusion.

The Martin dispersion coefficient [13] is introduced to improve upon the mathematical limitations of Turner's formulation. While Turner modeled σ_y as a curved function based on experimental data, it was argued that if σ_y truly follows a power-law relationship with distance (x), it should appear as a straight line on a log–log plot. Accordingly, Martin removed the constant term in the σ_y equation to ensure that the transformed function remains linear when plotted on a logarithmic scale.

The Seinfeld dispersion coefficient [14] is formulated using an exponential equation with three parameters, derived from PG curves. The coefficient expresses the vertical dispersion coefficient σ_z as a function of $\ln(x)$, enabling a more refined representation of distance dependence. The coefficient is based on a collection of experimental data from multiple studies, including Gifford (1976), Weber (1976), AMS Workshop (1977), Doran et al. (1978), Sedefian and Bennett (1980), and Hanna et al. (1982). The applicability of the empirical expression is limited to downwind distances of up to 10 km, with a corresponding formulation also available for σ_y.

II.C. Offsite consequence Assessment Tools

II.C.1. RCAP code

RCAP (Radiological Consequence Analysis Program) [15] is a computational tool developed by the Korea Atomic Energy Research Institute (KAERI) to probabilistically assess the radiological impact on surrounding areas in the event of a radioactive release from a nuclear facility. The program is designed to model the atmospheric dispersion and transport of released radionuclides, as well as their deposition onto the ground surface, enabling quantitative evaluation of both short-term consequences and long-term environmental and health effects. RCAP employs the Gaussian plume model as its physical model.

II.C.2. MACCS code

MACCS (MELCOR Accident Consequence Code System) [16] is an analytical code developed by Sandia National Laboratories (SNL) to probabilistically estimate the offsite consequences of potential severe accidents at nuclear power plants. The code allows for the modeling of hypothetical radioactive release scenarios and is designed to comprehensively evaluate their impacts on human health and the economy. It incorporates a wide range of factors, including atmospheric dispersion and transport, wet and dry deposition, environmental transfer, protective action strategies, radiation dose assessment, health effects, and economic damages. Although MACCS is configured to accommodate both the Gaussian plume model and the HYSPLIT model as selectable physical models, this study adopts the Gaussian plume model as the default within MACCS to ensure consistency in the comparative analysis between the two codes.

III. RESULTS AND DISCUSSION

III.A. Dispersion Coefficients by Atmospheric Stability Class

This study conducted a comparative analysis of five previously introduced dispersion coefficient models under six atmospheric stability classes and downwind distances up to 30 km, which corresponds to the maximum boundary of the Urgent Protective Action Planning Zone (UPZ) [17]. The key findings can be summarized in two main points. First, the differences in dispersion coefficients among models tend to increase with distance. Second, the model exhibiting the highest or lowest dispersion performance varied depending on the atmospheric stability condition. The corresponding results are presented in Fig. 2.

Under unstable atmospheric conditions (Stability Classes A, B, and C), the Briggs model consistently produced the lowest values for both horizontal and vertical dispersion coefficients. For horizontal dispersion, the Martin, Tadmor-Gur, and Modified Tadmor-Gur models generally yielded higher values; however, excluding the Briggs model, most models exhibited similar patterns and magnitudes. In contrast, vertical dispersion coefficients showed more pronounced variation, with the Seinfeld and Tadmor-Gur–based models displaying significantly higher values compared to others.

Under neutral atmospheric conditions (Stability Class D), the Briggs model again produced the lowest horizontal dispersion coefficients, while the Tadmor-Gur–based models yielded the highest. In contrast, vertical dispersion coefficients exhibited similar patterns and magnitudes across all models, indicating minimal differences among them.

Under stable atmospheric conditions (Stability Classes E and F), the Briggs model produced the lowest coefficients in both horizontal and vertical directions. The Eimutis-Konicek, Tadmor-Gur, and Modified Tadmor-Gur models yielded the highest horizontal dispersion coefficients, while the Modified Tadmor-Gur model resulted in the highest vertical dispersion coefficients.

As previously mentioned, the Eimutis-Konicek model adopts the dispersion coefficients of the Tadmor-Gur model in the horizontal direction and those of the Martin model in the vertical direction. Consequently, its results are largely overlapped by these models and are not clearly distinguishable in the plots.

Subsequently, an analysis was conducted for four atmospheric stability classes, excluding the extreme conditions represented by classes A and F among the six standard categories. For each of the four stability classes, the two models with the greatest difference in dispersion coefficients were identified, and their ratios were averaged to assess overall divergence. The results indicated that, at a distance of 5 km, the horizontal dispersion coefficient showed a marginal difference of approximately 0.99 times, while the vertical dispersion coefficient differed by about 1.4 times. At 30 km, the horizontal dispersion coefficient exhibited a difference of approximately 1.35 times, and the vertical dispersion coefficient showed a pronounced variation of up to 3 times.

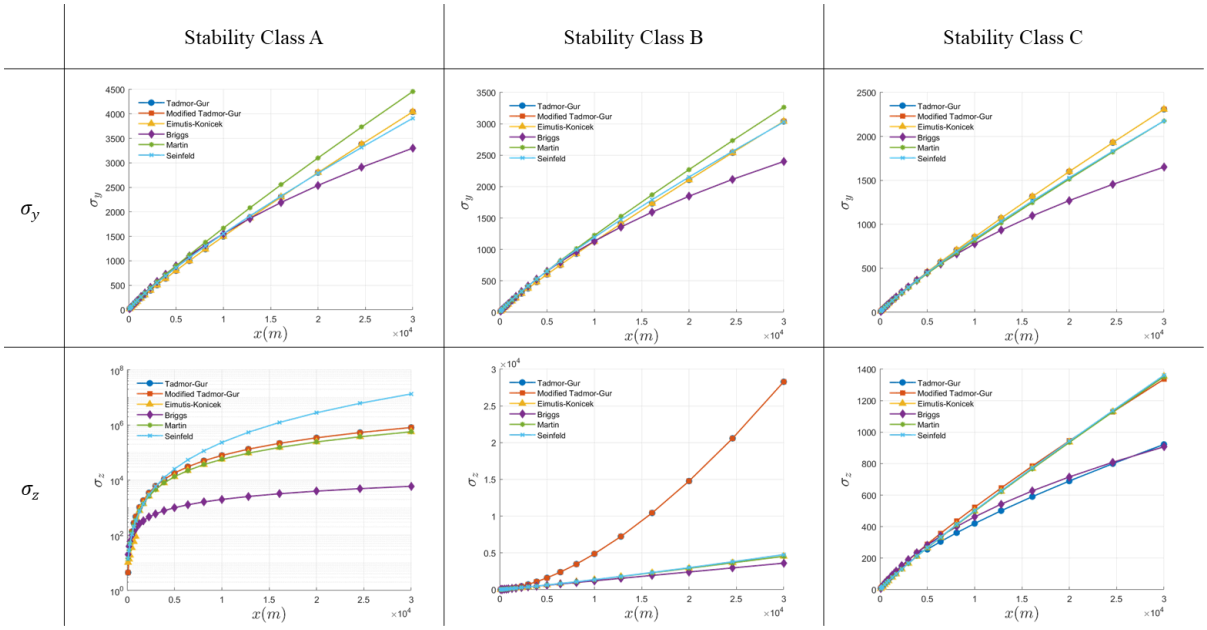

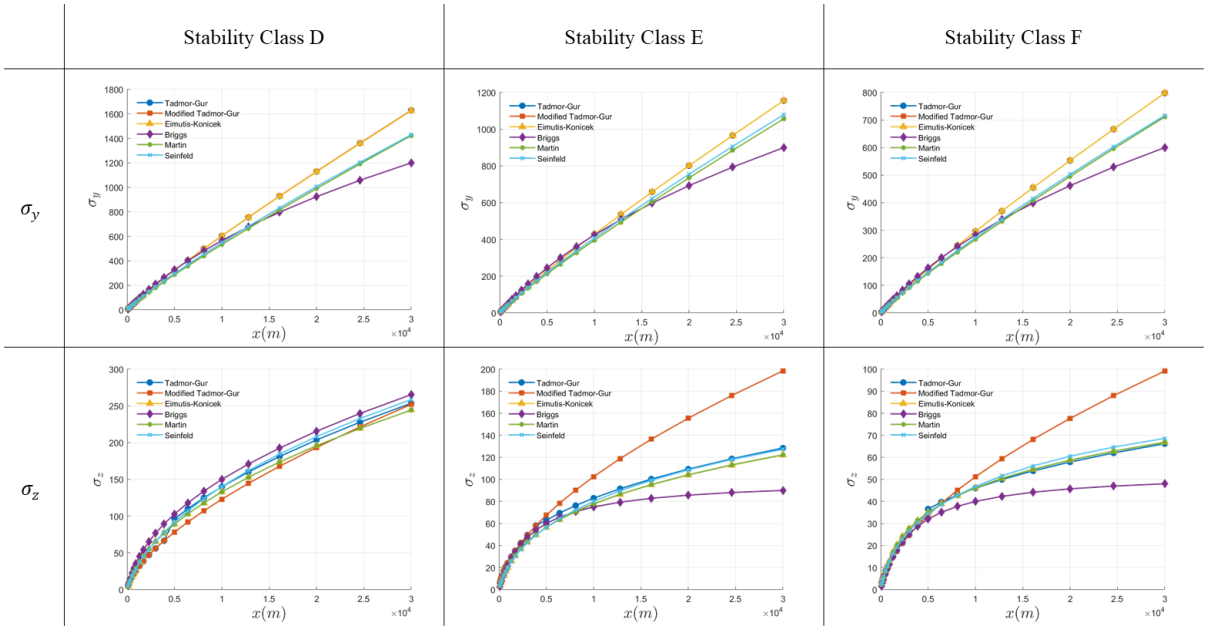

Figure 2. Distributions of Horizontal (σ_y) and Vertical (σ_z) Dispersion Coefficients by Stability Class for Each Model

III.B. Offsite Impact Assessment using RCAP and MACCS

In this study, a comparative analysis was conducted to evaluate the impact of different dispersion coefficient models using the RCAP and MACCS codes, based on a reference site located on flat terrain in Korea. All input conditions were kept identical across simulations, except for the choice of dispersion coefficient model. A total of six dispersion models were considered. The analysis focused on two output indicators that directly reflect the impact of the selected dispersion model: ground-level dilution and mean peak dose.

The wind speed was set to 2.1 m/s, based on the national average observed over the 20-year period from 2004 to 2024 [18], and six atmospheric stability classes (A to F) were considered. Receptors were placed at 20 downwind distances ranging from 0.1 km to 30 km, and in 16 azimuthal directions. Among these, two key assessment points were selected: 5 km, corresponding to the maximum boundary of the Precautionary Action Zone (PAZ), and 30 km, corresponding to the maximum boundary of the Urgent Protective Action Planning Zone (UPZ) [17].

Figure 3 presents a comparison of ground-level dilution predictions across distances for each dispersion coefficient model, using both RCAP and MACCS. In this analysis, the ground-level dilution was based on the calculated values for Cs-137, selected as a representative radionuclide. Under unstable (A, B, C) and neutral (D) atmospheric conditions, the differences between models remained relatively small; however, under stable conditions (E, F), the predicted concentrations varied more significantly depending on the dispersion model applied. In addition, regardless of the stability class, the Briggs model consistently predicted the highest concentrations as the distance approached 30 km.

Table III provides a quantitative comparison of model predictions under Stability Class E, where the largest differences among models were observed at both 5 km and 30 km. At both distances, the maximum and minimum predicting models were the same for RCAP and MACCS, and the magnitude of difference between the two codes was also comparable. At 5 km, the Martin model produced the highest predicted concentration, while the Modified Tadmor-Gur model produced the lowest, with a difference of up to 1.26 times. At 30 km, the Briggs model yielded the highest value, whereas the Modified Tadmor-Gur model yielded the lowest, resulting in a maximum difference of 2.65 times.

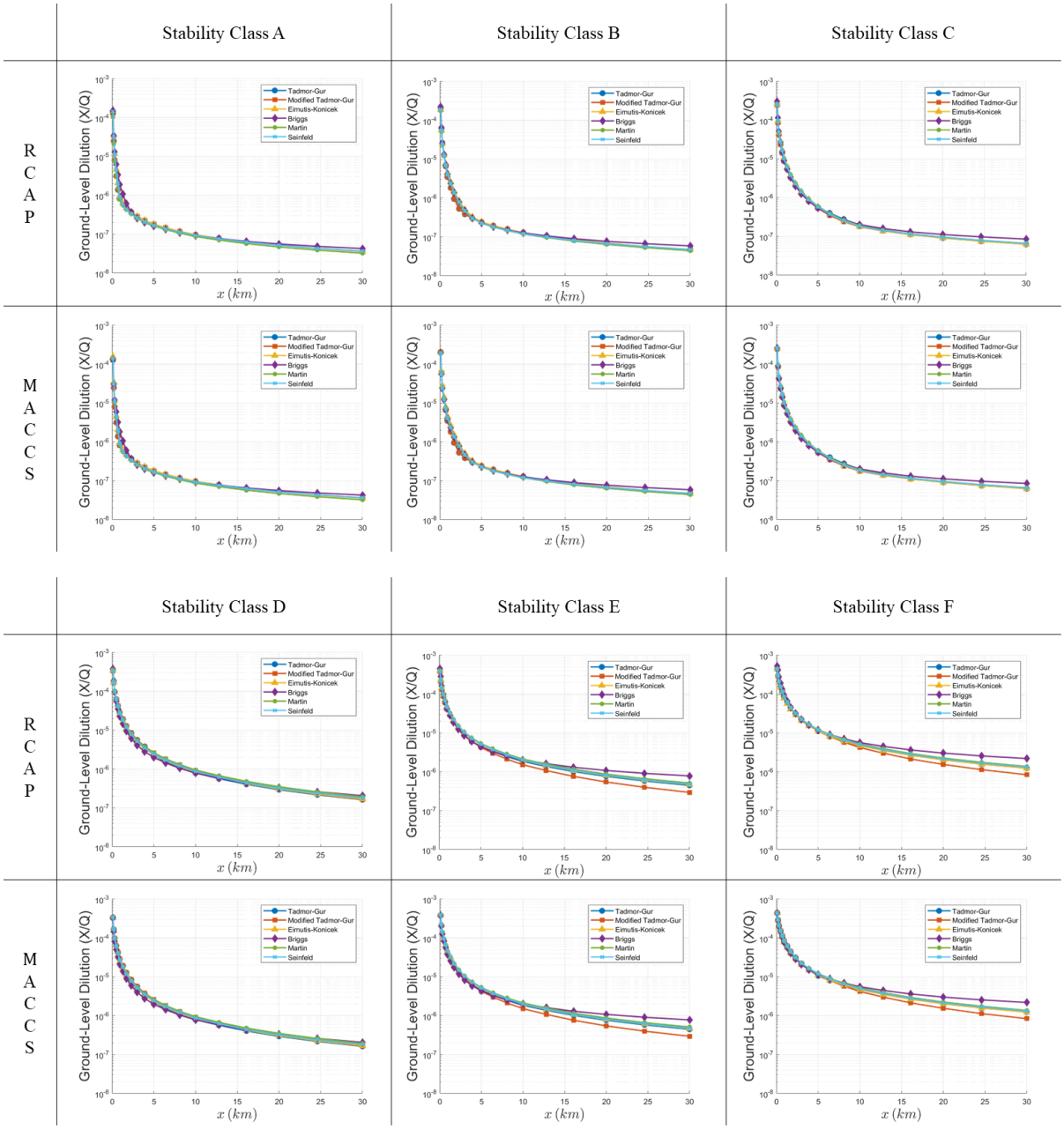

Figure 3. Comparison of Ground-Level Dilution Predictions by Dispersion Coefficient Models under Different Atmospheric Stability Conditions (RCAP & MACCS)

Table III. Quantitative Comparison of Ground-Level Dilution Predictions at 5 km and 30 km under Stability Class E Using RCAP and MACCS

Ground-Level Dilution (sec/m^3)	Distance	T-G	Modified T-G	E-K	Briggs	Martin	Seinfeld
RCAP	**5km**	4.46E-06	4.27E-06↓	5.03E-06	4.44E-06	5.39E-06↑	5.22E-06

	30km	4.48E-07	2.95E-07↓	4.71E-07	7.84E-07↑	5.14E-07	4.83E-07
MACCS	**5km**	4.49E-06	4.26E-06↓	4.98E-06	4.36E-06	5.34E-06↑	5.19E-06
	30km	4.48E-07	2.95E-07↓	4.70E-07	7.81E-07↑	5.12E-07	4.81E-07

Figure 4 compares the predicted mean peak dose across distances for each dispersion coefficient model using RCAP and MACCS. The mean peak dose results are based on the effective whole-body dose equivalent, a representative radiological dose metric. Consistent with the ground-level dilution results presented in Figure 3, the differences among models were relatively small under unstable (A, B, C) and neutral (D) atmospheric conditions, but became more pronounced under stable conditions (E, F). Regardless of stability class, a consistent trend was observed in which the Briggs model predicted the highest mean peak dose as the distance approached 30 km.

Table IV provides a quantitative comparison of mean peak dose predictions at 5 km and 30 km under stability class F, where the differences among models were most evident. The values were normalized to the maximum predicted dose at the 5 km distance to facilitate relative comparison across models. At both distances, RCAP and MACCS showed consistent trends, with the same models producing the maximum and minimum predicted doses. At 5 km, the Martin model yielded the highest dose prediction, while the Tadmor-Gur model produced the lowest, resulting in a maximum difference of 1.12 times. At 30 km, the Briggs model predicted the highest dose, and the Modified Tadmor-Gur model the lowest, with a maximum difference of 1.77 times.

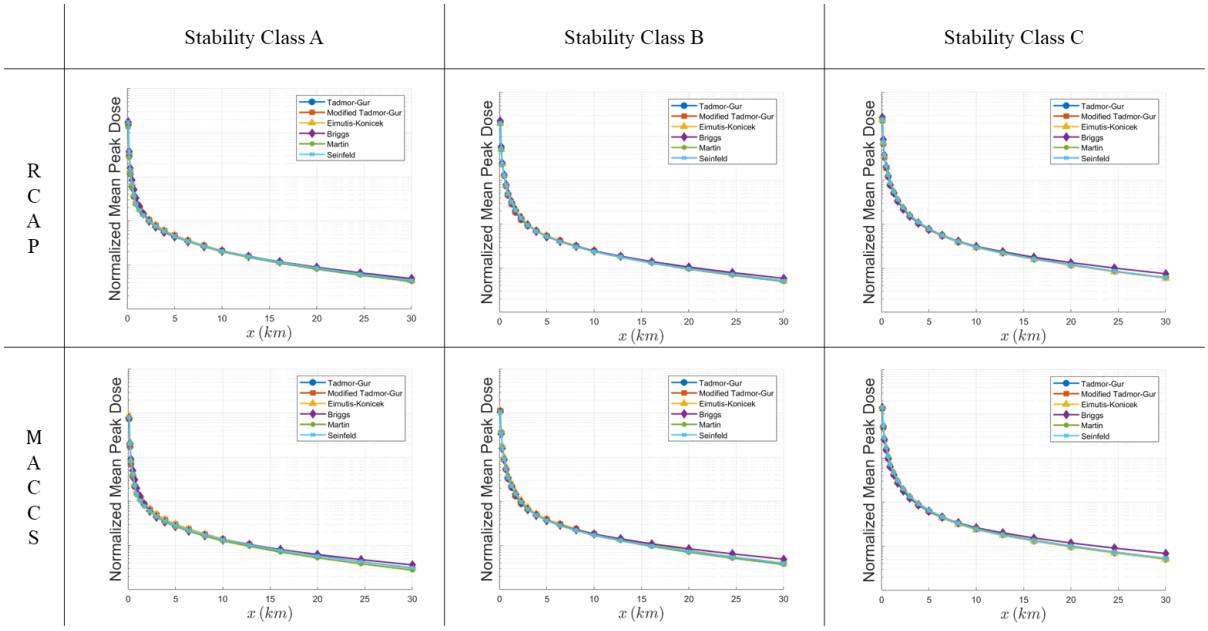

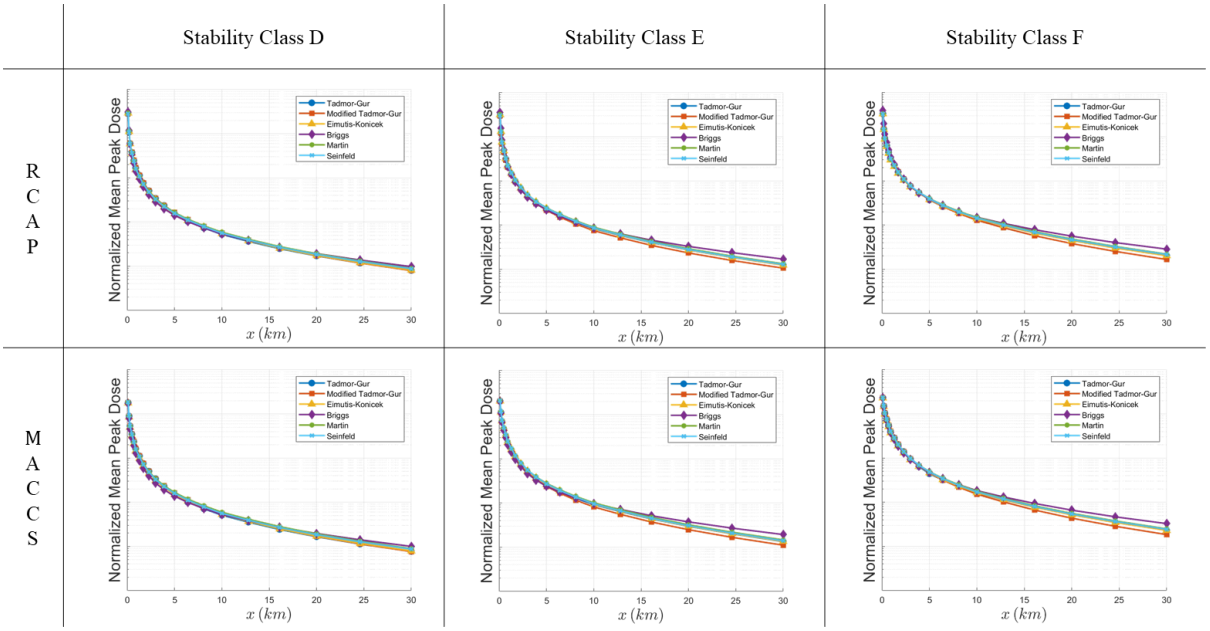

Figure 4. Comparison of Normalized Mean Peak Dose Predictions by Dispersion Coefficient Models under Different Atmospheric Stability Conditions (RCAP & MACCS)

Table IV. Quantitative Comparison of Normalized Mean Peak Dose Predictions at 5 km and 30 km under Stability Class F Using RCAP and MACCS

Normalized Mean Peak Dose	Distance	T-G	Modified T-G	E-K	Briggs	Martin	Seinfeld
RCAP	5km	7.51E-01↓	7.61E-01	7.63E-01	7.81E-01	8.10E-01↑	7.98E-01
	30km	4.11E-02	3.36E-02↓	4.11E-02	5.79E-02↑	4.47E-02	4.37E-02
MACCS	5km	8.95E-01↓	9.31E-01	9.35E-01	9.60E-01	1.00E+00↑	9.84E-01
	30km	4.66E-02	3.74E-02↓	4.66E-02	6.64E-02↑	5.06E-02	4.92E-02

The observed tendency for greater variation among dispersion coefficient models in ground-level dilution and mean peak dose under more stable atmospheric conditions can be attributed to the suppression of vertical and horizontal turbulent diffusion in Stability Classes E and F. Under such conditions, atmospheric dispersion becomes more limited, causing the predicted ground-level dilutions and mean peak doses to respond more sensitively to the structural form and model-specific differences of the dispersion coefficients.

IV. CONCLUSION

This study conducted a comparative analysis of dispersion coefficient models under varying atmospheric stability conditions and quantitatively assessed the extent to which the choice of model influences offsite consequence assessment results. It was observed that even under identical distances and atmospheric conditions, significant differences exist in the predicted horizontal and vertical dispersion coefficients depending on the selected model. These differences tended to become more pronounced as the distance from the release point increased.

The offsite consequence assessment results using RCAP and MACCS showed overall consistent trends. For both ground-level dilution and mean peak dose, greater discrepancies among dispersion models were observed under more stable atmospheric conditions. Notably, the largest differences at both 5 km and 30 km occurred under Stability Classes E and F, suggesting that dispersion under such conditions is more sensitive to the structural forms and assumptions of the dispersion models.

At 5 km, both indicators showed that the Martin model predicted the highest values. In contrast, the lowest values were predicted by the Modified Tadmor-Gur model for ground-level dilution and by the Tadmor-Gur model for mean peak dose. The corresponding differences between the highest and lowest values were up to 1.26 times and 1.12 times, respectively. At 30 km, both ground-level dilution and mean peak dose were highest with the Briggs model and lowest with the Modified Tadmor-Gur model, showing maximum differences of up to 2.65 times and 1.77 times, respectively.

These findings highlight that even with identical input conditions, the choice of dispersion coefficient model can lead to meaningful differences in predicted results. This effect becomes more pronounced under stable atmospheric conditions or at longer distances from the source. Consequently, the selection of a dispersion model introduces a notable source of uncertainty in offsite consequence assessments, particularly in evaluations that consider long-range distances such as the UPZ. To ensure more reliable risk assessments, it is therefore essential to perform prior sensitivity analyses on dispersion coefficient models and adopt a systematic approach to selecting the most appropriate model based on the specific purpose and environmental conditions of the assessment.

ACKNOWLEDGMENTS

This work was supported by the Nuclear Safety Research Program through the Korea Foundation of Nuclear Safety (KoFONS) using the financial resource granted by the Nuclear Safety and Security Commission (NSSC) of the Republic of Korea (No. RS-2023-00240452).

REFERENCES

[1] F. A. Gifford Jr., *An Outline of Theories of Diffusion in the Lower Layers of the Atmosphere*, TID-24190, Environmental Science Services Administration, Oak Ridge, TN (1968).
[2] F. A. Record and H. E. Cramer, “Preliminary analysis of project Prairie Grass diffusion measurements,” *Journal of the Air Pollution Control Association*, 8, 240 (1958).
[3] D. B. TURNER, *Workbook of Atmospheric Dispersion Estimates: An Introduction to Dispersion Modeling*, 3rd ed., CRC Press, Boca Raton, FL (2020).
[4] F. PASQUILL, “The Estimation of the Dispersion of Windborne Material,” *Meteorological Magazine*, 90, 20–49 (1961).
[5] F. A. Gifford, “Turbulent diffusion-typing schemes: a review,” *Nuclear Safety*, 17, 68 (1976).
[6] J. Tadmor and Y. Gur, “Analytical expressions for the vertical and lateral dispersion coefficients in atmospheric diffusion,” *Atmospheric Environment*, 3, 688 (1969).
[7] J. J. Fuquay, C. L. Simpson, and W. T. Hinds, “Prediction of environmental exposures from sources near the ground based on Hanford experimental data,” *Journal of Applied Meteorology and Climatology*, 3, 761 (1964).
[8] I. A. Singer and M. E. Smith, “Atmospheric dispersion at Brookhaven National Laboratory,” *International Journal of Air and Water Pollution*, 10, 125 (1966).
[9] M. E. Smith and I. A. Singer, “An improved method of estimating concentrations and related phenomena from a point source emission,” *Journal of Applied Meteorology*, 5, 631 (1966).
[10] E. C. Eimutis and M. G. Konicek, “Derivations of continuous functions for the lateral and vertical atmospheric dispersion coefficients,” *Atmospheric Environment*, 6(11), 859–863 (1972).
[11] D. O. MARTIN and J. A. TIKVART, “A General Atmospheric Diffusion Model for Estimating the Effects on Air Quality of One or More Sources,” *Proc. 61st Annual Meeting of the Air Pollution Control Association*, St. Paul, MN, 1968, 18 p., for NAPCA.
[12] G. A. Briggs, *Diffusion Estimation for Small Emissions*, Report No. 965, Atmospheric Turbulence and Diffusion Laboratory, Oak Ridge, TN (1973).
[13] D. O. Martin, “Comment on ‘The Change of Concentration Standard Deviations with Distance’,” *Journal of the Air Pollution Control Association*, 26, 145–147 (1976).
[14] J. H. Seinfeld, *Atmospheric Chemistry and Physics: From Air Pollution to Climate Change*, John Wiley & Sons, Hoboken, NJ (2016).

[15] S. J. Han et al., *RCAP Code User's Manual – Draft Version*, KAERI/TR-7700/2019, Korea Atomic Energy Research Institute, Daejeon, Republic of Korea (2019).
[16] D. I. Chanin, M. L. Young, J. Randall, and K. Jamali, *Code Manual for MACCS2: Volume 1, User's Guide*, SAND97-0594, Sandia National Laboratories, Albuquerque, NM (1997).
[17] Nuclear Safety and Security Commission (NSSC), *Act on Physical Protection and Radiological Emergency*, Article 20-2, NSSC, Seoul, Republic of Korea (2015).
[18] "Korea Meteorological Administration (KMA)," https://data.kma.go.kr/cmmn/main.do (accessed 2025).

A COMPARATIVE ANALYSIS OF THE IMPACT OF VARIOUS SPATIAL GRID SETTINGS FOR EFFECTIVE OFFSITE CONSEQUENCE ANALYSIS

Seunghwan Kim, Sung-yeop Kim*

Korea Atomic Energy Research Institute, Daedeok-daero 989-111, Yuseong-gu, Daejeon, 34057, Republic of Korea
**Corresponding author: sungyeop@kaeri.re.kr*

EXTENDED ABSTRACT

In the event of an offsite nuclear power plant accident, atmospheric dispersion and deposition represent the quickest environmental pathways by which radioactive material can spread, potentially affecting a large number of residents over a wide area. To analyze the consequences, the accident source term is regarded to be released from a reference point. This necessitates the establishment of a spatial grid to calculate the dispersion and deposition patterns from this location. The objective of this study is to define various divisions of spatial grids and to examine their impact on analysis accuracy and speed. Arithmetic, Geometric, Fibonacci and Logarithmic growth are applied to set the radius of the polar coordinate of spatial gird and their impact on the accuracy and speed of analysis compared to the best estimate case was investigated.

Fig.1 depicts the various spatial grid settings used in this study. Except for Arithmetic growth using monospacing, Geometric, Fibonacci, and Logarithmic growth employed proportional spacing. Each grid settings are employed for near-field, the precautionary action zone (PAZ) within 5 km range, and far-field, the urgent protective action planning zone (UPZ) within 30 km range.

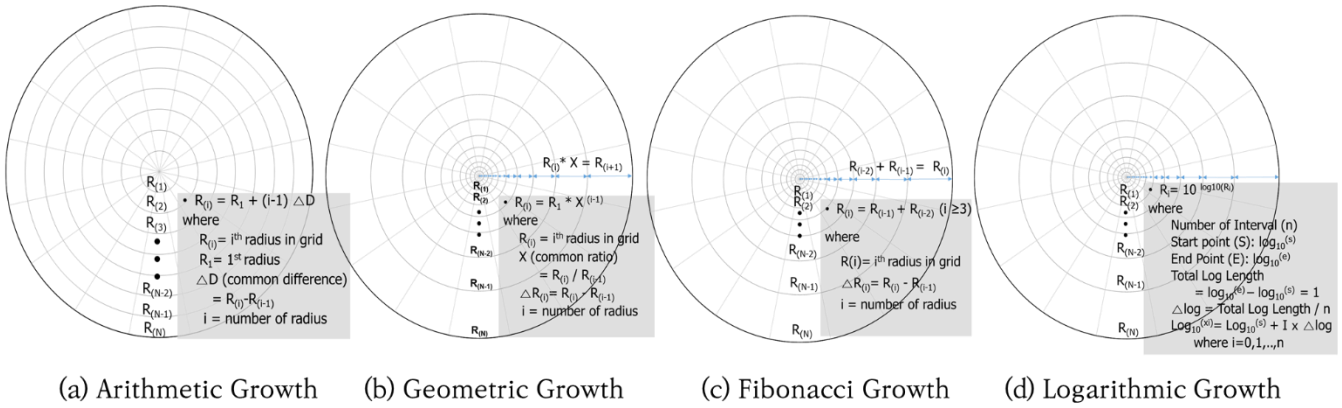

FIGURE 1. Spatial Grid Settings Used in This Study

For spatial grid settings for near-field (PAZ) analysis, the analysis range (distance), analysis direction, and spatial grid were set as follows.

- Analysis range: 5 km
- Angular direction: 16
- Maximum number of radial rings: 24 (basecase)
- Grid: Arithmetic, Geometric, Fibonacci and Logarithmic Growth

For spatial grid settings for far-field (UPZ) analysis, the analysis range, direction, and spatial grid were set as follows.

- Analysis range: 30 km
- Angular direction: 16
- Maximum number of radial rings: 31 (basecase)
- Grid: Arithmetic, Geometric, Fibonacci and Logarithmic Growth

An impact analysis of offsite consequences was conducted based on the spatial grid settings using the arithmetic, geometric, Fibonacci, and logarithmic sequences suggested in this study. Sensitivity analyses were performed for both near-field and far-

field areas across a sample source term category (STC) of the OPR1000. The MACCS code was employed for offsite consequence analysis. Although MACCS supports Gaussian Plume, Gaussian Puff, and Lagrangian particle tracking models, the Gaussian Plume model was consistently applied in this study.

Table 1 illustrates the health effect for the near-field and far-field when different spatial grid settings are applied. In the PAZ near-field analysis, the spatial grid models with errors within 10% for both early fatality and cancer fatality were arithmetic growth d(0.25) and d(0.5), geometric growth r(1.25), and logarithmic growth spacing. Regarding analysis time, there is a reduction in analysis duration proportional to the number of radial rings used.

In addition, in the UPZ far-field analysis, spatial grid models within 10% errors for both early and cancer fatality were observed for the geometric r(1.25) and logarithmic growth spacing. Similar to the near-field analysis, the analysis time decreases proportionally with the number of radial rings.

TABLE 1. Impact of Spatial Grid Settings (Health Effects)

	Near-Field (PAZ)					Far-Field (UPZ)				
			Number of Radial Rings	Relative Error(%)	Time			Number of Radial Rings	Relative Error(%)	Time
Early Fatality	Basecase	d=0.2	24	0.0%	100.0%	Basecase	d=1.0	31	0.0%	100.0%
	Arithmetic Growth	d=0.25	19	0.8%	79.1%	Arithmetic Growth	d=2.0	16	18.8%	51.9%
		d=0.5	10	0.8%	41.4%		d=3.0	11	40.6%	35.6%
		d=1.0	6	4.6%	24.9%		d=5.0	7	66.2%	22.8%
	Geometric Growth	r=1.25	11	1.5%	45.6%	Geometric Growth	r=1.25	19	3.1%	62.1%
		r=1.5	7	3.8%	29.2%		r=1.5	11	3.1%	36.1%
		r=1.75	5	6.1%	20.8%		r=1.75	8	4.5%	26.3%
		r=2.0	4	9.2%	16.7%		r=2.0	7	8.8%	23.1%
	Fibonacci Growth		9	3.1%	37.5%	Fibonacci Growth		13	0.3%	42.6%
	Logarithmic Growth		13	0.8%	55.7%	Logarithmic Growth		15	0.0%	50.1%
Cancer Fatality	Basecase	d=0.2	24	0.0%	100.0%	Basecase	d=1.0	31	0.0%	100.0%
	Arithmetic Growth	d=0.25	19	1.0%	79.1%	Arithmetic Growth	d=2.0	16	5.5%	51.8%
		d=0.5	10	5.7%	41.3%		d=3.0	11	10.0%	35.5%
		d=1.0	6	12.2%	24.9%		d=5.0	7	16.9%	22.7%
	Geometric Growth	r=1.25	11	8.2%	45.9%	Geometric Growth	r=1.25	19	7.5%	62.1%
		r=1.5	7	14.9%	29.2%		r=1.5	11	16.2%	36.0%
		r=1.75	5	19.1%	20.9%		r=1.75	8	21.6%	26.2%
		r=2.0	4	21.7%	16.9%		r=2.0	7	24.5%	23.0%
	Fibonacci Growth		9	14.3%	37.6%	Fibonacci Growth		13	17.1%	42.7%
	Logarithmic Growth		13	7.6%	55.5%	Logarithmic Growth		15	7.6%	50.0%

This study investigated the effects of different spatial grid divisions on the accuracy of offsite consequence analysis results. To assess their impact, numerical sequences such as Arithmetic, Geometric, Fibonacci, and Logarithmic were employed to set the radii in polar coordinate spatial grids, with results compared to the best estimate scenario. Further research could explore additional dispersion models and other proportional grid spacings to investigate the impact of spatial grid settings. The findings from this study are expected to aid in the optimization of spatial grid settings in subsequent studies.

ACKNOWLEDGMENTS

This work was supported by a National Research Foundation of Korea (NRF) grant funded by the Korean government (MSIT: Ministry of Science and ICT) (No. RS-2022-00143695).

REFERENCES

[1] S. H. Kim and S. Y. Kim, “Influence of Spatial Grids Setting on the Results and Speed of Offsite Consequence Analysis”, 17th International Conference on Probabilistic Safety Assessment and Management & Asian Symposium on Risk Assessment and Management (PSAM17&ASRAM2024), Japan, Oct 7-11 2024.
[2] S. H. Kim and S. Y. Kim, “The Impact Analysis of Various Spatial Grid Settings on Offsite Consequence Analysis”, Korean Nuclear Society Spring Meeting, Jeju, Korea, May 22-23, 2025.
[3] SNL, MACCS User Guide – Version 4.2, SAND2023-01315, Sandia National Laboratories, Albuquerque, 2023.

ASRAM2025
www.asram2025.org
Asian Symposium on Risk Assessment and Management 2025
Pattaya, Thailand, 27 – 29 August 2025

An Approach Based on the Regression between Radiological Source Term and Consequence for Effective and Efficient Risk Assessments of NPPs

Jiyeong SEO[1], Sung-yeop KIM[2*], Jaehyun CHO[3*]

[1] *Chung-Ang University, Heukseok-ro 84, Dongjak-gu, Seoul, 06974, Republic of Korea, sjy9442@cau.ac.kr*
[2] *Korea Atomic Energy Research Institute, Daedeok-daero 989-111, Yuseong-gu, Daejeon, 34057, Republic of Korea, sungyeop@kaeri.re.kr*
[3] *Chung-Ang University, Heukseok-ro 84, Dongjak-gu, Seoul, 06974, Republic of Korea, jcho@cau.ac.kr*

EXTENDED ABSTRACT

1. Introduction

Following the Fukushima Daiichi nuclear disaster, the accurate prediction of offsite radiological consequences from severe nuclear accidents has emerged as a critical aspect of risk-informed safety management. Level 3 Probabilistic Safety Assessment (PSA), which evaluates radiological impacts on surrounding populations, relies heavily on computational tools such as MACCS [1]. However, these tools require considerable computational time and resources, limiting their application in real-time analysis and large-scale scenario evaluations.

This study presents a deep learning-based surrogate model, referred to as the *Accident Consequence Estimator*, which estimates population-weighted individual risk (PWIR) from time-dependent radiological source term data. The model is designed to provide fast and reliable consequence predictions, enabling timely emergency response and informed decision-making[2, 3].

2. Methods

2.1 Dataset and Preprocessing

The model was trained using 658 severe accident scenarios for the OPR1000 reactor generated by MAAP5. Each scenario includes time-series release data for 25 major radionuclides and the peak time of core exit temperature (CET), which was added as an additional input feature. To reduce computational load and preserve temporal patterns, the data were downsampled and encoded with positional vectors, resulting in a final input shape of (1097, 39).

The output data represent PWIR, a scalar metric quantifying cancer fatality risk based on MACCS simulations. Each input scenario corresponds to a single normalized PWIR value, forming an output shape of (658, 1). Both input and output data were scaled using min-max normalization to improve model convergence and training stability.

2.2 Model Architecture

The model utilizes a 1D Convolutional Neural Network (Conv1D) with causal padding and dilation to capture multiscale temporal features. It includes five convolutional layers followed by pooling, flattening, and three fully connected layers (Dense), with a dropout layer (rate = 0.38) applied to prevent overfitting. Ensemble learning was used by averaging outputs from ten independently trained models.

2.3 Training Strategy

The model was trained using the Adam optimizer (initial learning rate: 0.00012) with early stopping and ReduceLROnPlateau scheduling. The dataset was split into training (63.75%), validation (21.25%), and test sets (15%) to ensure generalization and robustness.

3. Results

3.1 Predictive Performance

Model performance was assessed by comparing predicted PWIR values to MACCS-based reference values across 98 test scenarios. The model achieved a mean squared error (MSE) of approximately 0.0002. Visual inspection of predictions showed accurate trend capture with minor deviations, as confirmed in Figure 1, which presents 20 randomly selected test scenarios.

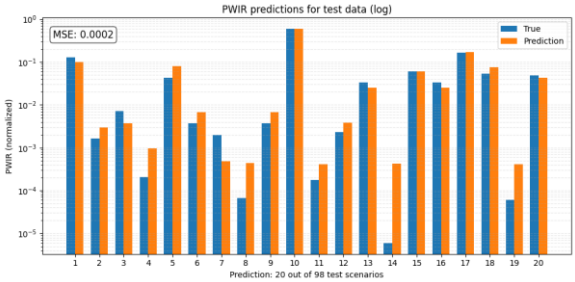

FIGURE 1. PWIR predictions for 20 out of 98 test scenarios

3.2 Application Study: SAG Effectiveness

An application study was conducted using five configurations of Severe Accident Guideline (SAG) strategies applied to the STC5-SBO scenario. Among the strategies, SAG-02 (RCS depressurization) had the most significant impact, reducing PWIR by 26.3%. The combination of SAG-02 and SAG-03 (RCS injection) yielded the highest overall mitigation (27.3%), whereas SAG-01 (SG injection) alone or in combination with SAG-02 showed limited additional benefit, as confirmed in Figure 2.

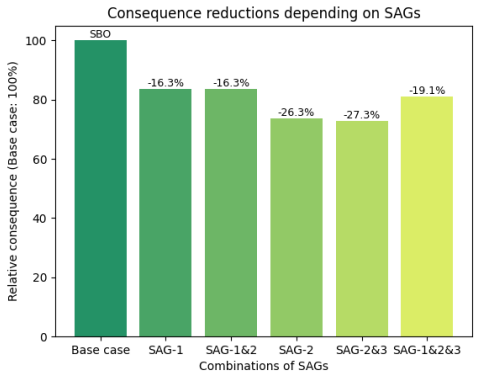

FIGURE 2. PWIR(Consequence) reductions depending on SAGs

4. Discussion and Conclusions

The proposed deep learning model demonstrated high accuracy and efficiency in estimating offsite radiological consequences from source term data. Its performance enables real-time risk assessment, supporting emergency decision-making processes. The application study highlighted the varying effectiveness of SAG strategies and the potential non-additivity of combined actions, emphasizing the need for scenario-specific optimization in severe accident management.

Future research will focus on expanding the model's applicability to other reactor types and integrating uncertainty quantification for enhanced safety planning.

ACKNOWLEDGMENTS

This work was supported by Korea Institute of Energy Technology Evaluation and Planning (KETEP) grant funded by the korea government (MOTIE) (RS-2024- 00401705, Convergent and practical human resource development program specialized in nuclear power plant export).

REFERENCES

[1] J. Cho, S.H. Han, "Identification of Risk-Significant Components in Nuclear Power Plants to Reduce Cs-137 Radioactive Risk," *Reliab Eng Syst Saf*, 211 (2021) 107613.

[2] H. Kim, J. Cho, J. Park, "Application of a deep learning technique to the development of a fast accident scenario identifier," *IEEE Access*, 8 (2020) 177363–177373.

[3] A. Ayodeji, M.A. Amidu, S.A. Olatubosun, Y. Addad, H. Ahmed, "Deep learning for safety assessment of nuclear power reactors: Reliability, explainability, and research opportunities," *Prog Nucl Energy*, 151 (2022) 104339.

Decontamination effectiveness for wiping vehicle in screening during a nuclear emergency

Hirokazu Hiraoka1,2, Kentaro Manabe1, Jun Hirouchi and Shogo Takahara1

1 Japan Atomic Energy Agency: 2-4 Shirakata, Tokai, Naka, Ibaraki, Japan, 319-1195, hiraoka.hirokazu@jaea.go.jp
2 University of Tsukuba: 1-1-1 Tennodai, Tsukuba, Ibaraki, Japan, 305-8577

ABSTRACT

Evacuation by private vehicle is a basic evacuation strategy during a nuclear emergency in Japan. When vehicles are evacuated from the contaminated areas, screening is conducted to inspect for radioactive contamination. If the radioactive contamination of vehicles exceeds criteria, decontamination is performed by wiping with wet waste cloths. Therefore, insights into the effectiveness of wet cloth wiping are necessary to conduct decontamination in an optimized manner. However, detailed information on the effectiveness of wiping each component of a vehicle by wet waste cloths is not sufficient. The present study simulated cesium contamination deposited on vehicle surfaces during a nuclear accident and experimentally assessed the effectiveness of wet cloth wiping for decontaminating newly manufactured vehicle components (windshield, hood panel, and aluminum alloy).

The results showed that the decontamination factor (*DF*) for the windshield was approximately 8 to 26, while the *DF* for the hood panel was more than 32 and that for the aluminum alloy was more than 31. Furthermore, it was observed that decontamination effectiveness did not change after the second wiping.

Keywords: Nuclear emergency, Screening, Decontamination, Wiping, Vehicles

I. Introduction

Two types of zones are established for preparedness and response for a nuclear emergency in Japan [1]. Precautionary Action Zone (hereafter “PAZ”) is established within the distance of 5 km from a nuclear power plant (hereafter “NPP”) to avoid severe deterministic effects to the public. The residents living in the PAZ evacuate prior to the release of radioactive materials. Outside of the PAZ to 30 km from the NPP, Urgent Protective Action Planning Zone (hereafter “UPZ”) is established. In the UPZ, evacuation is taken based on the ambient dose rate following the deposition of radioactive materials on to the ground. Near the boundary of the UPZ, evacuees and their vehicles undergo contamination screening to confirm that contamination levels are below the decontamination criteria. A beta-ray count rate of 40,000 cpm is used as the operational criterion to keep the surface contamination below 120 Bq/cm^2 [1].

According to the government manual for contamination screening [2], at first, the contamination level on the exterior surfaces of a vehicle is measured using a GM survey meter or a similar device. If contamination levels exceeding the criteria are detected, the exterior surfaces of the vehicle are decontaminated by wiping twice. If the contamination level still exceeds the criteria after the decontamination, the vehicle is kept at the screening site. Then, the evacuees who were using that vehicle are transported from the screening site to an evacuation center by another vehicle.

If the number of vehicles kept exceeds the parking capacity of the screening site, it will hinder the smooth operations in the screening site. Therefore, to achieve efficient operation in the screening site, it is important to estimate in advance the number of vehicles kept, depending on the scale of a nuclear accident. In such assessments, the decontamination effectiveness of wiping is essential information. From this perspective, the Japan Atomic Energy Agency investigated the decontamination effectiveness of wiping tires and hood panels [3]. However, no previous studies are known for other parts remains, such as tires, body, windshield, and aluminum wheels, contaminated by radioactive materials.

Against this background, the purpose of this study is to clarify the decontamination effectiveness for cesium on the components of vehicles (body, windshield, and aluminum wheels) through experimental assessment. The experiment simulated cesium deposition onto the surfaces of the vehicle components in the environment after a nuclear emergency. We then measured the beta-ray count rate before and after wiping to determine the decontamination effectiveness of wiping.

II. Materials and methods

II.A. Radioactive cesium for simulating contamination

II.A.1. Theory for simulating contamination

Radioactive materials are released in an NPP accident. It is known that the main elements of the released radioactive materials are cesium and iodine, with the chemical forms including CsI and CsOH [4]. Measurements after the Fukushima Daiichi NPP accident in 2011 showed that radioactive cesium was mainly transported by attaching to sulfate aerosols [5]. Radioactive materials in the atmosphere deposit on the ground, vehicles, and other surfaces through wet and dry depositions. Cesium was primarily deposited through wet deposition in the Fukushima Daiichi NPP accident [6]. In this study, deposited cesium on vehicle surfaces after an accident was simulated using cesium chloride (CsCl) because chloride is expected to be similar to iodine. In addition, to simulate wet deposition, we dissolved cesium chloride in water and dropped the solution onto samples cut from vehicle parts.

To simulate contamination by radioactive materials released from a nuclear reactor, it is necessary to adjust the surface density of cesium atoms on the sample surface. When the surface density exceeds a certain threshold, cesium atoms are considered to overlap (FIGURE 1). The interaction between the sample surface and cesium atoms differs from that between cesium atoms themselves; therefore, the decontamination effectiveness is expected to vary. In this study, the threshold surface density at which cesium atoms begin to overlap was determined under the assumption that the atoms are uniformly distributed. Since the metallic radius of cesium is 265 pm [7], the cross-sectional area of the atom is considered to be 2.2×10^{-15} cm². Therefore, the threshold is 4.5×10^{14} atoms/cm². When cesium isotopes are deposited in their natural abundance, the threshold corresponds to 0.10 μg/cm².

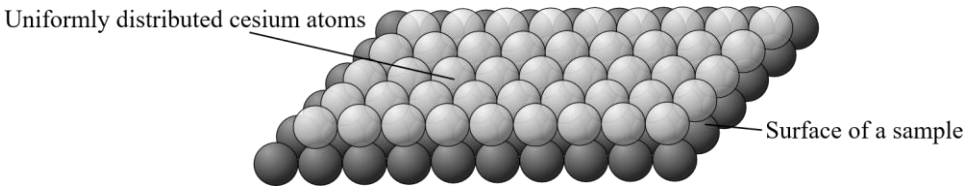

FIGURE 1. The image showing the amount of cesium deposited on a sample

When applying this threshold, it is necessary to take both radioactive and stable cesium atoms into account. For example, Nishihara et al. [8] estimated the nuclide weights per reactor core (g/core) immediately after the shutdown of Fukushima Daiichi NPP Unit 1, as shown in TABLE I. In this table, the values for "g/core" are referred from Nishihara et al. [8], while those for "TBq/core" are calculated from the value for "g/core" by the authors. However, isotopes with quantities less than 100 g/core are not included in the table.

TABLE I. Amount of substance in the core of Fukushima Daiichi NPP Unit 1 (Immediately after shutdown)

	^{133}Cs: Stable	^{134}Cs: Radioactive	^{135}Cs: Radioactive	^{137}Cs: Radioactive
Half-life [year] [9]	-	2.0652	1.33×10^{6}	30.08
g/core [8]	6.24×10^{4}	3.98×10^{3}	2.46×10^{4}	6.30×10^{4}
TBq/core	0	1.90×10^{5}	1.81	2.02×10^{5}

Assuming that cesium deposits on the vehicle surface at a density of 120 Bq/cm² and that its isotopic composition corresponds to that shown in TABLE I, the surface density of cesium atoms is estimated to be 2.10×10^{11} atoms/cm², which is well below the threshold. Therefore, in this study, it was necessary to adjust the surface density of cesium to remain below the threshold. Accordingly, we prepared radioactive cesium solutions in which the amount of stable nuclides could be determined.

II.A.2. Preparation of radioactive cesium solution

Initially, radioactive cesium was produced using the research reactor JRR-3 of the Japan Atomic Energy Agency, to easily adjust the concentration of cesium atoms in the solution. Approximately 1 mg of cesium chloride (Fujifilm Wako Pure Chemical Corporation) was sealed in a capsule and irradiated with neutrons in the reactor core of JRR-3. This capsule was irradiated for

20 minutes with thermal neutrons at a flux of 4.7×10^{17} n/(m^2·s) [10]. This irradiation produced ^{134}Cs through nuclear reaction: ^{133}Cs(n, γ)^{134}Cs, ^{133}Cs(n,γ)^{134m}Cs and ^{134m}Cs→^{134}Cs.

The radioactivity of ^{134m}Cs and ^{134}Cs in the cesium chloride were measured using a Ge semiconductor detector 22 hours and 50 minutes after the end of neutron irradiation. The radioactivity of ^{134m}Cs and ^{134}Cs immediately after the irradiation were determined to be 17 MBq and 27 kBq, respectively. In a reactor with a thermal neutron flux of 1.0×10^{17} n/(m²·s), it is known that the radioactivity of ^{134}Cs generated per 1 g of cesium after 1 hour of irradiation is 4.6×10^{4} kBq [9]. Therefore, we assessed the mass of the cesium atoms in the cesium chloride including stable isotopes to be 0.38 mg. In other words, the mass of cesium chloride was 0.48 mg. We prepared two solutions (hereafter "Solution A" and "Solution B") one month after the irradiation. The concentration of Solution A was adjusted to 0.95 kBq/ml using 30 mL of pure water and 0.48 mg of cesium chloride. The concentration of Solution B was adjusted to 0.15 kBq/ml using 6.27 mL of Solution A and 33.73 mL of pure water. The concentration of cesium atoms in Solution B was 2.0 μg/mL at that time.

II.B. Preparation of contaminated samples

The samples used in the experiment were 6 cm × 4 cm in size. We dropped the radioactive solution onto the central 5 cm × 4 cm area of the sample (hereafter "droplet deposition area") as shown in FIGURE 2.

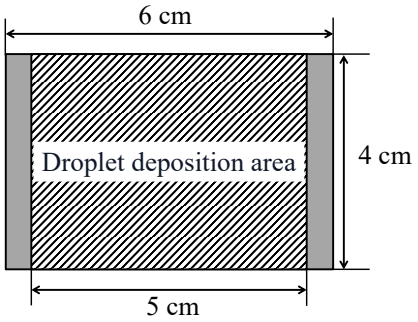

FIGURE 2. Area of the sample where the radioactive cesium solution was dropped

These samples were cut from newly manufactured windshields and hood panels. In addition, aluminum alloy plates were prepared to simulate aluminum wheels. Five samples of each type were prepared.

Solution B of 1.0 mL was dropped onto the droplet deposition area of each sample using a micropipette. The surface density of cesium atoms on the droplet deposition area was approximately 0.1 μg/cm², which was close to the threshold value of 0.10 μg/cm². Furthermore, the radioactivity of ^{134}Cs deposited to the droplet deposition area was 0.15 kBq per sample. FIGURE 3 shows photographs of the solution droplets on each sample. On the windshield samples (FIGURE 3A), the droplets of solution coalesced to form larger clusters. In contrast, the droplets on samples of aluminum alloy (FIGURE 3B) and hood panel (FIGURE 3C) did not coalesce and exhibited water-repellent properties.

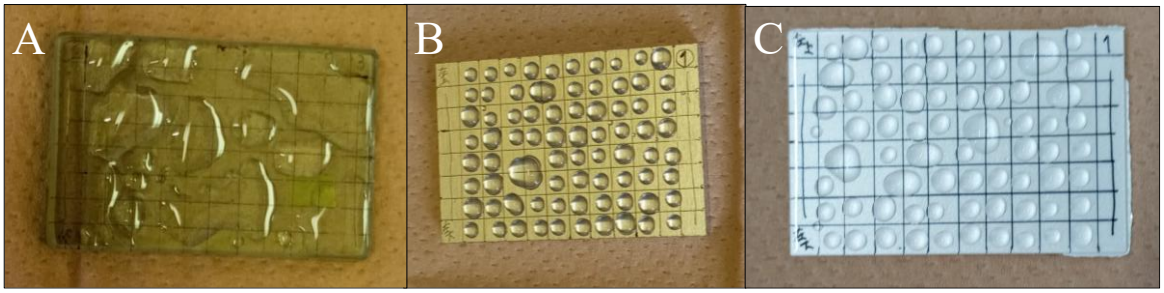

FIGURE 3. Droplets of the radioactive cesium solution on the samples (A: windshield, B: aluminum alloy, C: hood panel)

These samples were placed in a fume hood for seven days and dried. The reason for drying the samples for seven days is that residents are required to evacuate within seven days after receiving the evacuation order, in the case of evacuation, based on a criterion of 20 μSv/h.

II.C. Experiment to investigate the decontamination effectiveness

II.C.1. Wiping off contamination and measuring counts

According to the manual for contamination screening [2], the decontamination of vehicles is carried out by wiping the surface with wet waste cloths. The cloth is changed after each wipe in one direction. Each contaminated area can be wiped a maximum of two times. This study simulated these methods and the experimental procedure is shown in FIGURE 4.

A new cloth was soaked in tap water until saturated. The droplet deposition area of the sample was wiped only once in one direction with the new cloth. This wiping was performed on an electronic balance, and the wiping force was approximately 1 kgf, as shown in FIGURE 5. The beta-ray count of the sample was measured before and after each wiping with a GM survey meter. To reduce geometric measurement errors, the distance between the sample surface and the GM survey meter was fixed at 5 mm as shown in FIGURE 6. The wiping was repeated 2 to 5 times. If the count was below the background level, no further wiping was conducted. The background level was determined by a 10-minute count measurement under no sample conditions.

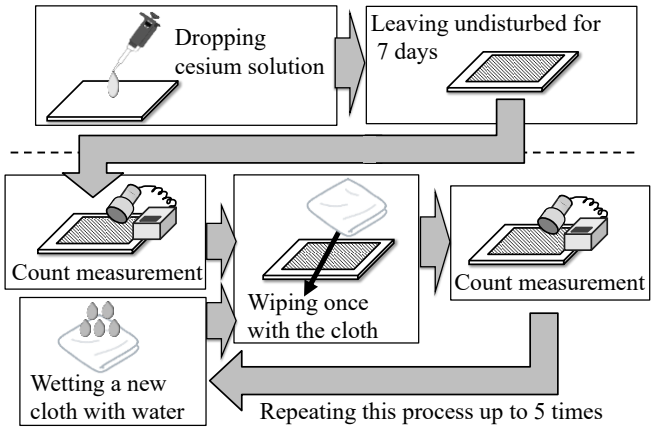

FIGURE 4. The workflow of the experiment

FIGURE 5. Wiping a sample

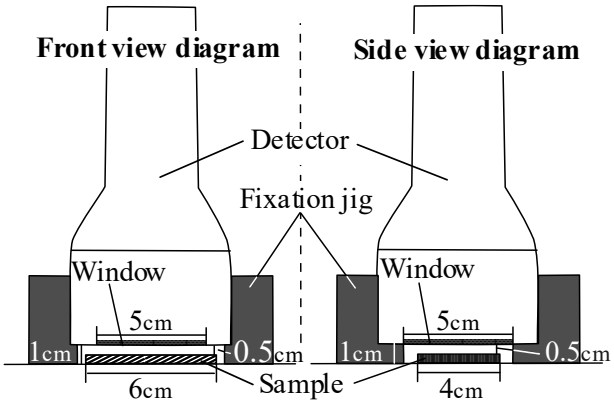

FIGURE 6. Measurement of beta-ray counts from a sample

II.C.2. Calculation of the decontamination factor

The decontamination factor (hereafter "*DF*") was calculated from the counts obtained after each wiping. The *DF* value is defined by equation (1), with reference to IAEA glossary [11]:

$$DF = \frac{r_0 - r_B}{r_i - r_B} \quad , \tag{1}$$

where, r_i is the count rate after the i-th wiping [cpm], r_0 is the count rate before the first wiping [cpm], and r_B is the count rate obtained from the background measurement [cpm]. However, while *DF* in the glossary [11] is defined as "the ratio of the activity", the *DF* in this study is defined as the ratio of the count rate.

In some cases, the count rate fell below the background level. Hence, the under limit of *DF* was calculated based on the relationship between the count rate before the first wiping and the background, as shown in the following equation (2):

$$DF > \frac{r_0 - r_B}{r_L} \quad , \tag{2}$$

where, r_L is the detection limit value. The value of $\frac{1}{2}r_B$ was assumed as the limit in the present study. As described in equation (2), the value of *DF* depends on the background level. In a non-emergency situation, measurements are performed in an uncontaminated environment. However, in an emergency situation, measurements will be performed under high-background conditions. Therefore, we have to define the *DF* taking into account influence of such conditions, as shown in equation (2).

III. Results and discussion

III.A. Count rate of background

The backgrounds measured on each experimental day were summarized in TABLE II.

TABLE II. The background measured on each experimental day

Sample type	Sample label	Count rate of the background [cpm]	Measurement time [min]
Windshield	a, b, c	60.6 ± 2.5	10
	d, e	62.4 ± 2.5	
Aluminum alloy	a, b, c, d, e	67.3 ± 2.6	
Hood panel	a, b, c	60.6 ± 2.5	
	d, e	70.8 ± 2.7	

The value after '±' indicates the statistical error.

III.B. Count rate and *DF*

FIGURE 7 shows the results of the experiment for the windshield. The count rate before the first wiping was approximately 1,000 cpm. It decreased to 130 to 200 cpm after the first wiping and 100 to 150 cpm after the second wiping. However, there was no further decrease after subsequent wiping. The *DF*s ranged from 7 to 15 after the first wiping and from 8 to 26 after second wiping onward.

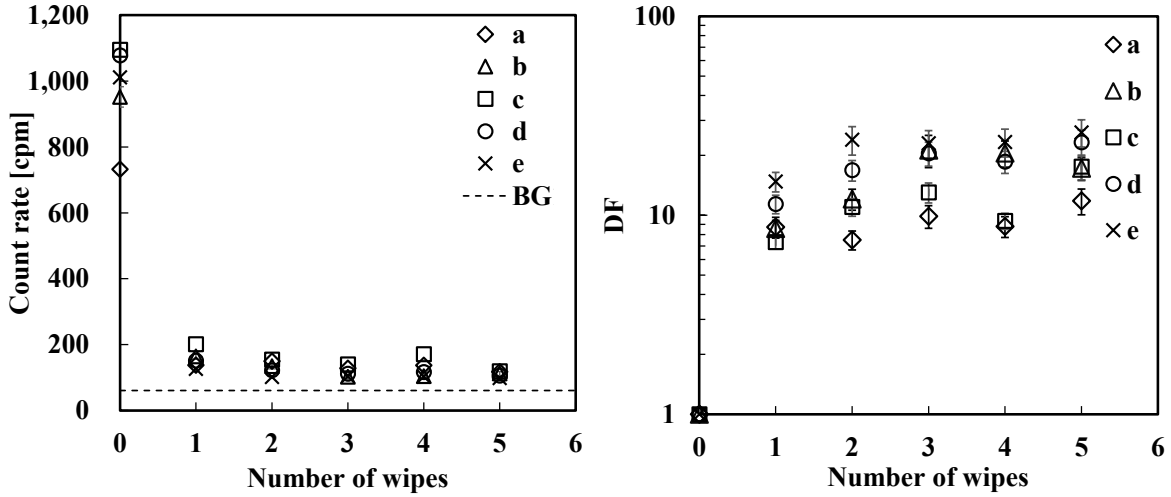

FIGURE 7. Result of the windshield (Left fig.: count rate after each wiping, Right fig: *DF* after each wiping)
Five samples of each type were labeled 'a', 'b', 'c', 'd', and 'e', respectively. The error bars represent statistical errors.

The results for the aluminum alloy are shown in FIGURE 8. The count rate before the first wiping was approximately 1,100 cpm. It decreased to approximately 60 to 70 cpm after the first and second wiping, which was comparable to the background level. Because the count rate decreased to the background level, the wiping process was stopped after the second wiping for samples 'b', 'd' and 'e', and after the third wiping for sample 'c'. Sample 'a' may has reduced decontamination effectiveness due to a tear in the waste cloth during the first wiping. The *DF* for the aluminum alloy was to be $DF > 31$ using equation (2).

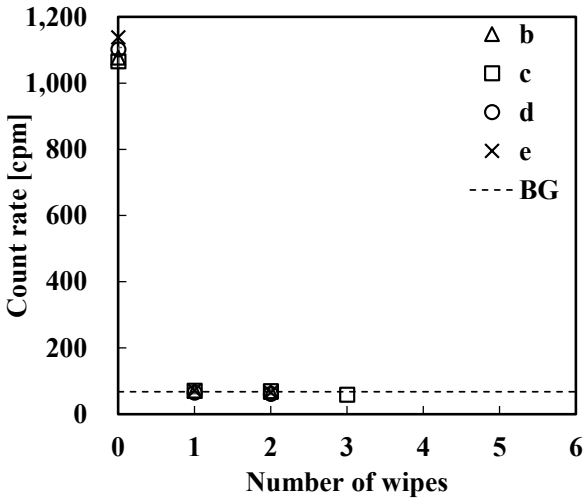

FIGURE 8. Count rate of aluminum alloy after each wiping

FIGURE 9 shows the results of the experiment for the hood panel. The count rate before the first wiping was approximately 1,000 cpm. It decreased to approximately 50 to 80 cpm after the first wiping, which was comparable to the background level. Because the count rate decreased to the background level, the wiping process was stopped after the second wiping for samples 'a', 'b', 'c', and 'e', and after the fourth wiping for sample 'd'. The *DF* for the hood panel was $DF > 32$ using equation (2).

In the previous study [3], three new hood panel samples were tested, and two wiping processes were conducted. TABLE III summarizes the measured count rates and the *DF* values. The results of our study were consistent with those of the previous study [3].

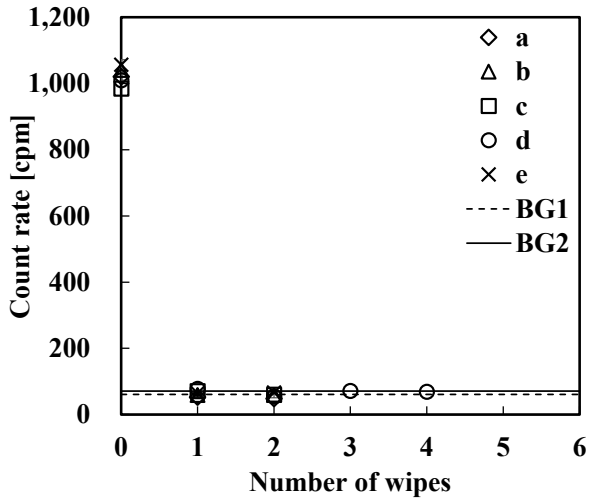

FIGURE 9. Count rate of hood panel after each wiping

TABLE III. *DF* of hood panel

	This study	The previous study [3]		
		Sample 1	Sample 2	Sample 3
The count rate before wiping [cpm]		32,184	31,684	29,234
The count rate after two wiping [cpm]		1,576	1,612	848
DF	> 32	20	20	34

One of the reasons why *DF* differs depending on the surface material is the difference in the water repellency of the surface. As mentioned in Section II.B, the aluminum alloy and hood panel were more water-repellent than the windshield. Therefore, the solution barely adhered to the surfaces of the aluminum alloy and hood panel immediately after the solution was dropped.

In addition, since the count rate did not decrease after the third and subsequent wipes for all types of samples, it can be considered reasonable that the guideline of the Japanese authority [2] stipulates that wiping can be conducted up to a maximum of two times.

IV. CONCLUSIONS

In this study, we evaluated the decontamination effectiveness for parts used in newly manufactured vehicles: windshield, hood panel, and aluminum alloy simulating aluminum wheels. The effectiveness was evaluated using the decontamination factor, *DF*, defined as the ratio of contamination levels before and after wiping the vehicle samples. To evaluate the *DF*, experiments were conducted by simulated wet deposition of cesium on the samples and then decontamination were performed by wiping with a wet waste cloth. The *DF* for the windshield was approximately 7 to 15 after the first wiping. Although it slightly decreased after the second and subsequent wiping, it remained within the range of 8 to 26. The *DF* for the aluminum alloy was $DF > 31$ after the second wiping. Similarly, that for the hood panel was $DF > 32$. Our results are expected to contribute to the formulation of plans for screening sites in nuclear emergency situations.

ACKNOWLEDGMENTS

Radioactive cesium was produced using the JRR-3(internal use) at the Japan Atomic Energy Agency. We received extensive support from the JRR-3 staff in performing neutron irradiation and measuring radioactivity. We would like to express our gratitude to all the staff members.

REFERENCES

[1] NUCLEAR REGULATION AUTHORITY, "Genshiryoku-saigai-taisaku-shishinn" [NRA Guide for Emergency Preparedness and Response], https://www.nra.go.jp/data/000473921.pdf (2024) (in Japanese).
[2] NUCLEAR DISASTER MANAGEMENT BUREAU, CABINET OFFICE and THE SECRETARIAT OF THE NUCLEAR REGULATION AUTHORITY, "Genshiryoku-saigai ni okeru hinann-taiiki-ji-kennsa oyobi kanni-josen manual" [Manual for contamination screening and simple decontamination at a Nuclear Disaster], https://www.nra.go.jp/data/000119567.pdf (2022) (in Japanese).
[3] JAPAN ATOMIC ENERGY AGENCY, "Reiwa ni nendo genshiryoku-bousai-kenkyu-jigyou (naikakufu-jutaku-houkokusho)" [FY 2020: Project for Research on Nuclear emergency prevention: Report commissioned by the Cabinet Office] (2021) (in Japanese).
[4] A. AUVINEN et al., "Vaporisation rates of CsOH and CsI in conditions simulating a severe nuclear accident", *J. Aerosol Sci.*, **31**, 1029-1043 (2000).
[5] N. KANEYASU et al., "Sulfate Aerosol as a Potential Transport Medium of Radiocesium from the Fukushima Nuclear Accident", *Environmental Science & Technology*, **46**, 5720-5726 (2012).
[6] T. OHARA et al., "Atmospheric behavior of radioactive materials from Fukushima Daiichi Nuclear Power Plant", *Journal of the National Institute of Public Health*, **60**, 292-299 (2011) (in Japanese).
[7] "CESIUM @ PERIODIC TABLE OF CHEMICAL ELEMENTS", https://www.webqc.org/periodictable-Cesium-Cs.html (2025).
[8] K. NISHIHARA et al., "Estimation of Fuel Compositions in Fukushima-Daiichi Nuclear Power Plant", *JAEA-Data/Code*, **2012-018** (2012) (in Japanese).
[9] JAPAN RADIOISOTOPE ASSOCIATION, "Radio isotope pocket data book 12th edition", p.67,133, Maruzen Publishing Co., Ltd., Tokyo, Japan (2020) (in Japanese).
[10] "JRR-3 USERS OFFICE", https://jrr3uo.jaea.go.jp/about/about_04.htm#04 (2025) (Japanese).
[11] IAEA, "IAEA Nuclear Safety and Security Glossary Terminology Used in Nuclear Safety, Nuclear Security, Radiation Protection and Emergency Preparedness and Response" (2022)

Technical Session 15 (16:00 -18:00)	The Port 3, C Floor	Risk Management and Risk-informed Decision Making, Operational Risk Analysis
		Chair/Facilitator 1: Assoc.Prof. Somsak DANGTIP, Thailand Institute of Nuclear Technology (TINT)
		Chair/Facilitator 2: Dr. Sun Yeong Choi (Korea Atomic Energy Research Institute (KAERI))
16:00 - 16:20		ID 39: STPA-based Hazard Identification of Human Operator Interaction with Passive Safety Systems Speaker: Sung-Min Shin (KAERI) Contributors: Sung-Min Shin (KAERI), Yochan Kim (KAERI), Jinkyun Park (KAERI), Jin Hee Park (KAERI)
16:20 - 16:40		ID 19: Insights from a Case Study on the Quantification of Operator Manual Actions Speaker: Sun Yeong Choi (Korea Atomic Energy Research Institute) Contributors: Sun Yeong Choi (Korea Atomic Energy Research Institute)
16:40 - 17:00		ID 120: Development of an Intelligent Operator Decision Support System for Abnormal States in Nuclear Power Plants Speaker: Jae Min Kim (Korea Atomic Energy Research Institute) Contributors: Jae Min Kim (Korea Atomic Energy Research Institute), Young Ho Chae (Korea Atomic Energy Research Institute), Seo Ryong Koo (Korea Atomic Energy Research Institute)
17:00 - 17:20		ID 104: Applying Deep Learning Algorithms for Autonomous Emergency Operation in Nuclear Power Plant Speaker: Yoojoon Seoung (ulsan national institute of science and technology) Contributors: Yoojoon Seoung (ulsan national institute of science and technology), Junyong Bae (Ulsan National Institute of Science and Technology), Seung Jun Lee (Ulsan National Institute of Science and Technology)
17:20 - 17:40		ID 48: Fire Probabilistic Risk Assessment of BWR-6 Mark-III Nuclear Power Plant for the Pre-Defuel Phase in the Decommissioning Transition Stage Speaker: Yu-Ting Lin (National Atomic Research Institute (NARI)) Contributors: Yu-Ting Lin (National Atomic Research Institute (NARI)), Yi-Cheng Tian (National Atomic Research Institute (NARI)), Yu-Min Chen (National Atomic Research Institute (NARI)), Tsu-Mu Kao (National Atomic Research Institute (NARI))

STPA-based Hazard Identification of Human Operator Interaction with Passive Safety Systems

Sung-Min Shin[1], Yochan Kim[1], Jinkyun Park[1], Jin Hee Park[1]

[1] *KAERI: 111 Daedeok-daero 989 beon-gil, Yuseong-gu, Daejeon, Republic of Korea 34057, smshin@kaeri.re.kr*
[1] *KAERI: 111 Daedeok-daero 989 beon-gil, Yuseong-gu, Daejeon, Republic of Korea 34057, yochankim@kaeri.re.kr*
[1] *KAERI: 111 Daedeok-daero 989 beon-gil, Yuseong-gu, Daejeon, Republic of Korea 34057, kshpjk@kaeri.re.kr*
[1] *KAERI: 111 Daedeok-daero 989 beon-gil, Yuseong-gu, Daejeon, Republic of Korea 34057, jhpark6@kaeri.re.kr*

EXTENDED ABSTRACT

To ensure protection under uncertain conditions, many advanced reactors are adopting the passive safety systems (PSSs) that are automatically actuated in the absence of operator input, following a deterministic set of conditions or elapsed time. However, this default-to-safe behavior introduces operational constraints. Once a PSS is actuated, significant downtime, resource consumption, and post-activation restoration procedures may be required before the plant can return to normal operation. As a result, designers incorporate mechanisms that allow operators to block or delay automatic activation of the PSS when it is confidently deemed unnecessary. NuScale, for instance, enables manual blocking of the Emergency Core Cooling System (ECCS), a gravity-driven feed-and-bleed cooling loop [1], contingent on verified safety conditions [2]. Although such capability grants operators strategic flexibility, allowing them to avoid unnecessary actuation of PSS, it also introduces a critical challenge to human operators: the potential for inappropriate manual inhibition of a vital safety function under misinterpreted or misleading indications.

This study employs System-Theoretic Accident Model and Processes (STAMP) and Systems-Theoretic Process Analysis (STPA) [3] to develop a set of loss scenarios, focusing specifically on manual actuations. In order to derive comprehensive results, an analysis model including all of human operator, system hardware, operator interfaces, environmental conditions, and procedural logic, that is, a control structure, is developed, and the interaction between them is closely examined to see if they can cause the loss scenarios. Furthermore, the analysis further considers how feedback mechanisms, procedural clarity, and interface design can be reinforced to support correct operator decisions. The results of this study support a dual objective: enhancing safety through systematic hazard identification and improving operational availability by avoiding unnecessary system actuations. With the aims above, referring to the NuScale ECCS, this study conducts STPA on the decision-making of the human operator regarding the blocking of PSS, which is supposed to be automatically started 8 hours after the reactor trip occurs. For reference, it was assumed that manual blocking may also be released before 8 hours after the trip. In the analysis process, the STPA tool TRACEIT developed by Korea Atomic Energy Research Institute (KAERI) in Korea was used [4].

STPA is a top-down hazard analysis method developed based on the STAMP. Unlike traditional failure-based approaches, STPA views safety as a control problem that causes unsafe interactions, making it particularly well-suited for analyzing complex systems that involve both automated elements and human. As shown in the figure 1, STPA consists of four major steps: 1) defining the purpose of the analysis, 2) modeling the control structure, 3) identifying unsafe control actions(UCAs), and 4) identifying loss scenarios. Each step builds upon the previous one, ultimately supporting the derivation of system-level safety constraints and guiding safer system design and operation.

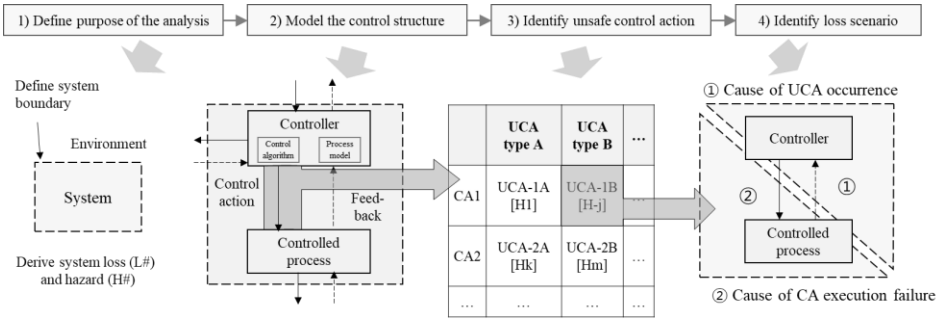

Figure 1 Overview of STPA

The first step of the STPA involves defining the losses and hazards associated with it, so , the potential losses and hazards were identified, as summarized in Figure 2.

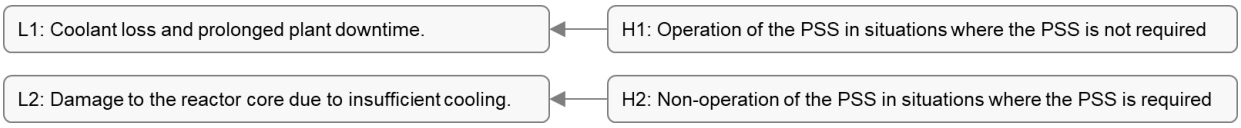

Figure 2. Losses and hazards

In Step 2 of STPA, a control structure is developed to capture how control actions (CAs) are issued and system components interact. Figure 3 illustrates the control structure developed, which depicts each system entity, the Feedbacks(FBs) each receives, and the associated Process Models (PMs) and CAs generated. The identifiers and name used in the Figure are summarized in Table 1. The interaction within this structure is illustrated focusing on CA1 (PSS Auto-actuation Blocking), which is issued by the [C1] Human Operator. The accurate generation of CA1 depends on the following Process Models: (PM1) Recognition of whether the plant is in a condition where PSS blocking is acceptable, (PM2) Evaluation of the operational availability of the PSS, considering testing, maintenance, or modification status, (PM3) Verification that the PSS has not already been actuated, (PM4) Monitoring the elapsed time since the last reactor trip, (PM5) Reference to up-to-date criteria and procedures for blocking, (PM6) Awareness of any external pressure influencing the blocking decision.

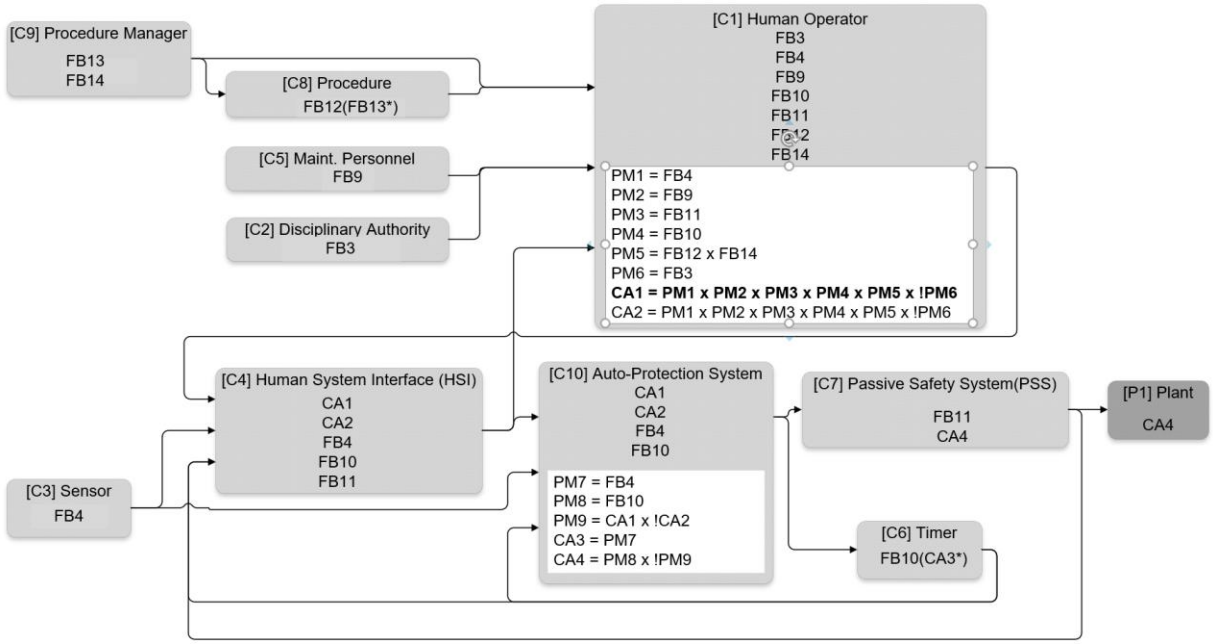

Figure 3. Control structure for PSS blocking and releasing

Table 1. Control actions, process model, and feedbacks in the control structure

Control action		Process model		Feedback	
ID	Name	ID	Name	ID	Name
CA1	PSS Auto-actuation Blocking	PM1	Current State of Plant	FB3	Pressure on a Certain Decision
CA2	Release PSS Auto-actuation Blocking	PM2	Availability of PSS	FB4	Plant Process Parameters
CA3	Trip Signal	PM3	Current PSS Operation	FB9	Notice of Test / Maintenance / Modification
CA4	Timer-induced PSS Auto-actuation	PM4	Elapsed Time Since Reactor Trip	FB10	Counting Time
		PM5	Up-to-date Procedure	FB11	Current Situation of the PSS
		PM6	Psychological Pressure on Mistake	FB12	Criteria of Manual Blocking/Releasing
		PM7	Parameter Exceeding Set Point	FB13	Modification on Procedure

PM8	Timer Elapsed Time	FB14	Notice/Training of Modification on Procedure
PM9	Manual Block Positive		

The formation of the above process models in the [C1] Human Operator depends on various feedbacks, as described below:

- PM1 (Current State of Plant) is updated by FB4 (Plant Process Parameters). This signal is generated by the [C3] Sensor and transmitted to the [C1] Human Operator through the [C4] HSI.
- PM2 (Availability of PSS) is updated by FB9 (Notice of Test/Maintenance/Modification). FB9 is generated by and transmitted from the [C5] Maintenance Personnel to the [C1] Human Operator. While this information could also be routed via the HSI, in this pilot study, direct delivery from [C5] Maintenance Personnel is assumed.
- PM3 (Current PSS Operator) is updated by FB11 (Current Situation of the PSS), and FB11 is transmitted from the front [C4] HSI, which is generated and transmitted from the [C7] PSS.
- PM4 (Elapsed Time Since Reactor Trip) is updated by FB10 (Counting Time). FB10 is transmitted through the [C4] HSI, which receives it from the [C6] Timer. In this context, CA3 (Trip Signal) is re-stated by [C6] Timer, and that CA3 was originally generated by the [C10] Auto-Protection System based on PM7 (Parameter Exceeding Set Point). PM7 is updated using FB4 (Plant Process Parameters), which originates from the [C3] Sensor and is transmitted to [C10] Auto-Protection System.
- PM5 (Up-to-data procedure) can be formed properly when both FB12 (Criteria of Manual Blocking/Releasing) and FB14 (Notice/Training of Modification on Procedure) are present. First, the FB12 (Criteria of Manual Blocking/Releasing) is re-stated FB13 (Modification on Procedure) in the front entity [C8] procedure, which means if there is a modification in the existing procedure, a new FB12 (Criteria of Manual Blocking/Releasing) may be formed accordingly. FB13 (Modification on Procedure) can be made by the front entity [C9] Procedure Manager). Meanwhile, as mentioned earlier, the PM5 (Up-to-data Procedure) of the [C1] Human Operator can be properly formed only when the FB14 (notification/training of modification on procedure) is given by the [C9] Procedure Manager.
- PM6 (Psychological Pressure on Mistake) can be formed by generating and giving FB3 (Pressure on a Certification Decision) from the front entity [C2] Discipline Authority.

In Step 3 of the STPA process, unsafe control actions (UCAs) that may lead to hazards are identified for each relevant control action. This pilot study considers two types of UCAs—"Not providing causes a hazard" and "Providing causes a hazard"—while excluding timing- and duration-related UCAs. Accordingly, the UCAs identified are summarized in Figure 4.

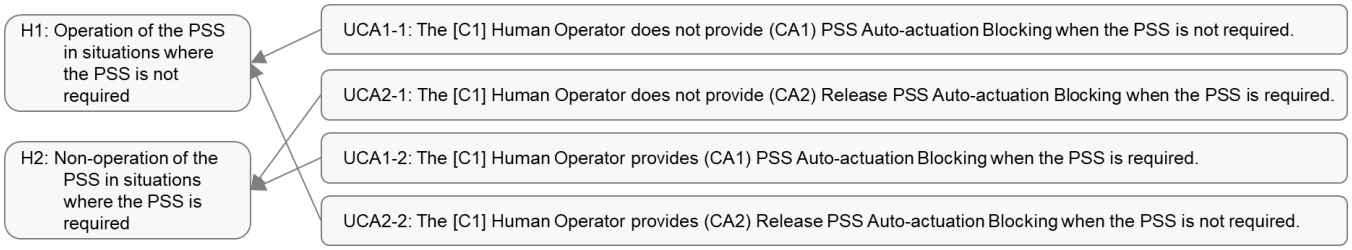

Figure 4. Unsafe control actions

In Step 4 of STPA, for each UCA identified in the previous step, potential generic causal factors were analyzed, and concrete loss scenarios (LSs) that could result from those causes were developed. These analyses help to understand how unsafe control actions could be triggered under specific system conditions, human errors, or process failures. Table 2 shows the loss scenario derived for UCA1-1 as an example among UCAs developed in STPA step 3. These scenarios provide actionable insights for developing effective safety constraints and mitigation strategies in later system design or operation phases.

Table 2. Loss scenarios related UCA1-1

ID	Cause	Loss Scenario
LS1	[CU1] Procedure change miscommunication	Due to a lack of awareness of procedure modifications, the operator is confused and does not block the PSS auto-actuation when the PSS is not required.
LS2	[CU2] Ambiguous/Deficient procedure	Due to the ambiguous/deficient procedure, the operator is confused and does not block the PSS auto-actuation when the PSS is not required.
LS3	[CU3] Faulty notice from Maintenance personnel	Due to a faulty notice from maintenance personnel, the operator thinks the PSS will not operate even without manual blocking and does not block the PSS auto-actuation when the PSS is not required.

LS4	[CU4] Pressure from the discipline authority	Due to pressure from the disciplinary authority to prioritize safety unconditionally, the operator does not block the PSS auto-actuation when the PSS is not required.
LS5	[CU5] Unsystematic HSI	Due to the unsystematic process-variable-related HSI, the operator is confused and does not block the PSS auto-actuation in time when the PSS is not required.
LS6	[CU5] Unsystematic HSI	Due to the unsystematic PSS-related HSI, the operator thinks the PSS is already blocked or actuated, so does not block the PSS auto-actuation when the PSS is not required.
LS7	[CU5] Unsystematic HSI	Due to the unsystematic timer-related HSI, the operator cannot be aware of the remaining time and does not block the PSS auto-actuation when the PSS is not required.
LS8	[CU6] Component failure	Due to the sensor failure, the operator cannot recognize the current state of plant and does not block the PSS auto-actuation in time when the PSS is not required.
LS9	[CU6] Component failure	Due to the timer failure, the operator cannot recognize the elapsed time and does not block the PSS auto-actuation in time when the PSS is not required.

Based on the loss scenarios identified in STPA Step 4, a set of countermeasures (CMs) was developed to mitigate the associated hazards and prevent the occurrence of unsafe control actions, as shown in the Table 3. These countermeasures were derived by analyzing the causal factors behind each loss scenario and proposing design, procedural, or operational improvements that could either eliminate the cause or reduce its impact, focusing on enhancing the accuracy and timeliness of information available to the [C1] Human Operator.

Table 3. Countermeasures

ID	Countermeasure	Related Loss Scenario
CM1	If a PSS-related procedure needs to be changed, the procedure manager shall be evaluated by the operator for the impact of the change and shall proceed with the change reflecting the evaluation results.	LS1
CM2	Decide whether blocking should be irreversible or reversible; If irreversible, provide support to make an accurate decision closer to the decision deadline. If reversible with no limit on the number of reversals, it should be possible to support the operator's decision-making under all possible conditions clearly.	LS2
CM3	Decision on manual blocking is made regardless of the maintenance situation. However, if blocking has not been made or a previously made blocking is released, obtain maintenance information at that point and check whether the PSS will be operated normally after the timer has elapsed.	LS3
CM4	In order to exclude conflicts of interest, even if the PSS is operated, it should be designed not to have a significant adverse effect on the subsequent nuclear power plant operation rate.	LS4
CM5	Introduces agents to support efficient and clear decision-making of the operator, and forces the operator to leave a basis for decision-making.	LS4
CM6	If an operator makes a decision in accordance with the established decision-making system, legal protections are prepared to avoid unreasonable censures based on a result, and a safety culture is formed that focuses on identifying systemic faults that the operator was forced to make that decision.	LS4
CM7	The remaining time between the automatic operation of the PSS after the trip is visually indicated along with whether manual blocking is currently active, and an audible alarm is provided every 20 minutes from 1 hour remains.	LS6, LS7, LS9
CM8	All process variables related to PSS manual blocking are collected so that they can be identified on one page clearly, and the tendency over time is provided together to help judgment, and manual blocking and release according to decision-making are also accessible on the page.	LS5

This study has explored STPA-based hazard identification of human operator interaction with the PSS. The loss scenarios derived from the analysis demonstrate the potential to proactively identify specific human errors, taking into account the system context, including scenario, plant state, and assigned tasks. The insights we can get from the countermeasures can be effectively utilized to inform design improvements that enhance system safety and support more robust operator decision-making in complex and uncertain situations. Based on the above analysis process and results, STPA is expected to be used very effectively to preemptively analyze the hazards of safety systems involving complex interactions and derive measures to improve them. However, the control structure covered in the example analysis deals with the elements to be considered in practice, but it is difficult to guarantee that it deals with all the perfect sets and models the actual interactions between elements. Therefore, adding additional elements or specific interaction information as needed will provide additional practical insights.

The approach of this paper has the potential to further identify potential risks that have not been identified in existing probabilistic safety assessment (PSA). Accordingly, the additional identified risk factors can be reflected as basic events in the existing PSA model [5], and if the impact is significant, it is necessary to find a way to implement the relevant countermeasure

practically. In addition, the contents derived through example analysis are planned to be used as base data for deriving general requirements to be considered from the perspective of PSS design.

ACKNOWLEDGMENTS

This work was supported by and Innovative Small Modular Reactor Development Agency grant funded by the Korean Government (MSIT) (No. RS-2023-00258118).

REFERENCES

[1] NuScale, NuScale US460 Plant Standard Design Approval Application Ch.6 Engineered Safety Features (FSAR Revision 1), 2023 (https://www.nrc.gov/docs/ML2330/ML23304A345.pdf)
[2] NuScale, NuScale US460 Plant Standard Design Approval Application Ch.7 Instrumentation and Controls (FSAR Revision 1), 2023 (https://www.nrc.gov/docs/ML2330/ML23304A348.pdf)
[3] Leveson, N. G., & Thomas, J. P. "STPA Handbook." Massachusetts Institute of Technology, 2018.
[4] Shin, S., Kang, S. W., & Park, J. “From visual representation to signal flow connection: A new modeling approach for STAMP.” Nuclear Engineering and Technology, 57(8), 2025.
[5] Electric Power Research Institute (EPRI), HAZCADS: Hazard and Consequence Analysis for Digital Systems, 2023

ASRAM2025
www.asram2025.org
Asian Symposium on Risk Assessment and Management 2025
Pattaya, Thailand, 27 – 29 August 2025

INSIGHTS FROM A CASE STUDY ON THE QUANTIFICATION OF OPERATOR MANUAL ACTIONS

Sun Yeong Choi[1], Dae Il Kang[2], Yong Hun Jung[3]

[1] *Korea Atomic Energy Research Institute, 989-111, Daedeok-daero, Daejeon, 34091, sychoi@kaeri.re.kr*
[2] *Korea Atomic Energy Research Institute, 989-111, Daedeok-daero, Daejeon, 34091, dikang@kaeri.re.kr*
[3] *Korea Atomic Energy Research Institute, 989-111, Daedeok-daero, Daejeon, 34091, jungyh@kaeri.re.kr*

EXTENDED ABSTRACT

Fires in nuclear power plants (NPPs) pose significant risks as they can simultaneously damage multiple safety-critical components, potentially leading to core damage and severe accidents. Fire probabilistic safety assessment (PSA)[1] is employed, incorporating fire human reliability analysis (HRA)[2] to assess the risks. This study focuses on quantifying the human error probability (HEP) of operator manual actions (OMA) in fire scenarios, applying the Fire HRA[3-4] methodology developed by the Korea Atomic Energy Research Institute (KAERI) based on the K-HRA, Rev.1 framework[5].

The study adopts a structured approach to OMA quantification in fire conditions:

- Selection of OMA cases: 12 OMA cases were identified, based on multi-spurious operation (MSO) scenarios that could impact post-fire safe shutdown. These cases include reactor coolant pump (RCP) breaker trips, containment spray pump (CSP) pump trips, two kinds of CSP outlet valve operations, and essential service water pump (ESP) outlet valve operations.
- Time parameter and performance shaping factor (PSF) analysis: Key time parameters, including cue recognition and execution times, were analyzed alongside PSFs such as procedure quality, stress levels, and operator training.
- HEP calculation: Using the Fire HRA methodology, HEPs were derived by integrating diagnosis and execution probabilities, adjusted based on environmental constraints and fire-specific PSFs.

The quantification results revealed significant variations in HEPs depending on the fire location, task complexity, and environmental factors:

- Higher HEPs for MCR fires: OMAs performed during fires inside the main control room (MCR) exhibited higher HEPs than those for fires outside the MCR. This increase was attributed to reduced time available for diagnosis, increased stress, and procedural challenges
- Impact of power availability on RCP operations: RCP breaker trip operations showed higher HEPs under Non-1E 125V DC unavailability, as operators had to diagnose the failure and manually operate the switchgear under increased time pressure
- Complexity in CSP valve operations: OMAs involving CSP outlet motor operated valves (MOVs) and manual valve operations recorded elevated HEPs due to task complexity, inadequate procedures, and challenging working conditions.
- ESP outlet MOVs in MCR abandonment (MCRA) scenarios: The highest HEP was observed in ESP outlet MOV operations during MCRA scenarios, where environmental constraints, procedural limitations, and the transition to remote shutdown panel (RSP) heightened the likelihood of errors.

The study underscores the necessity of quantitative OMA assessments to support risk-informed decision-making. Key recommendations include:

- Enhancing fire PSA models: Existing fire PSA frameworks should incorporate refined OMA quantifications to improve fire risk evaluations.
- Improving procedures and training: Operators require enhanced procedures and repetitive training to mitigate human error in fire emergencies

By quantifying the HEP of fire-induced OMAs, this study provides a foundation for strengthening NPP fire safety and human reliability assessments. The findings demonstrate that MCR fires pose heightened risks, and that task complexity, procedural adequacy, and power availability significantly influence OMA reliability. Future research should focus on data-

driven refinements to Fire HRA models and simulation-based validation of operator responses to enhance emergency preparedness and risk management strategies.

TABLE I. OMAs Selected for Quantification

Component	OMA	Fire Area	Description	MSO
RCP	RCP trip (Non-1E 125V DC is unavailable)	Outside MCR	Opening the RCP's breaker at a switchgear room	MSO #1 (Loss of all RCP seal cooling)
	RCP trip (Non-1E 125V DC is available)	Outside MCR		
	RCP trip (Non-1E 125V DC is available)	Inside MCR		
CSP	CSPs trip	① Outside MCR ② Inside MCR	Opening the CSPs' breakers at switchgear rooms (A/B)	MSO #16 (RWST (Refueling Water Storage Tank) drain down via containment spray)
MOV on CSP discharge line	CSPs discharge MOVs close	① Outside MCR ② Inside MCR	• Opening the breakers of CSPs discharge MOVs' at switchgear rooms (A/B) • Closing the MOVs manually at mechanical penetration rooms (A/B)	MSO #16 (RWST drain down via containment spray)
Manual valve on CSP discharge line	CSPs discharge manual valves close	① Outside MCR ② Inside MCR	Closing the manual valves at SC(Shutdown Cooling) Hx (Heat Exchanger) rooms	MSO #16 (RWST drain down via containment spray)
MOV on ESP discharge line	ESP and CCW(Component Cooling Water) Hx discharge MOV open	① Outside MCR ② Inside MCR ③ MCRA	• Opening the breaker of a ESP and CCW Hx discharge MOV at switchgear room • Opening the MOV manually at CCW Hx room	MSO #43 (ESW header isolation)

ACKNOWLEDGMENTS

This work was supported by the National Research Foundation of Korea (NRF) grant funded by the Korean government, Ministry of Science and ICT. (Grant Code: RS-2022-00144204)

REFERENCES

[1] R. P. Kassawara and J. S. Hyslop, "EPRI/NRC-RES Fire PSA Methodology for Nuclear Power Facilities," *NUREG/CR-6850* (2005).
[2] US NRC, "EPRI/NRC-RES Fire Human Reliability Analysis Guidelines," *NUREG-1921* (2012).
[3] S. Y. Choi and D. I. Kang, "Development of a Fire Human Reliability Analysis Procedure for Full Power Operation of the Korean Nuclear Power Plants," *Journal of the Korean Society of Safety*, Vol 35 No 1, pp. 87-96 (2020).
[4] S. Y. Choi, D. I. Kang, Y. H. Jung, "Improvement of Fire Human Reliability Analysis for Operator Manual Action Quantification," *ESREL 2024* (2024).
[5] S. Y. Choi, D. I. Kang, Y. H. Jung, "Case study for quantification of post-fire OMA(Operator Manual Action) based on a fire HRA(Human Reliability Analysis) methodology," *KAERI/TR-10673/2024* (2024).
[6] J. Kim, Y Kim, W. Jung, H. Jeon, H. Lee and K. Oh, "The K-HRA, Rev.1 Method for Post-Initiator Human Action at Internal Event Scenario," *Transactions of the Korean Nuclear Society Autumn Meeting 2023* (2023).

DEVELOPMENT OF AN INTELLIGENT OPERATOR DECISION SUPPORT SYSTEM FOR ABNORMAL STATES IN NUCLEAR POWER PLANTS

Jae Min Kim[1], Young Ho Chae[1], Seo Ryong Koo[1]

[1] *Affiliation Information: Korea Atomic Energy Research Institute, Daedeok-daero 989 beon-gil/111, Yuseong-gu, Daejeon, 34057, jaemink@kaeri.re.kr*

EXTENDED ABSTRACT

Nuclear power plants are operated by human operators following predefined procedures based on plant conditions. In abnormal or emergency situations, unlike general operating procedures used to maintain or change plant states during normal conditions, quick and accurate selection of the appropriate procedure is essential to prevent core damage [1]. This cognitive process—situation assessment, decision-making, and action—can be mapped to Rasmussen's Decision Ladder [2], as shown in Fig. 1. This study aims to support this process by providing key information and analysis to enhance decision speed and reliability.

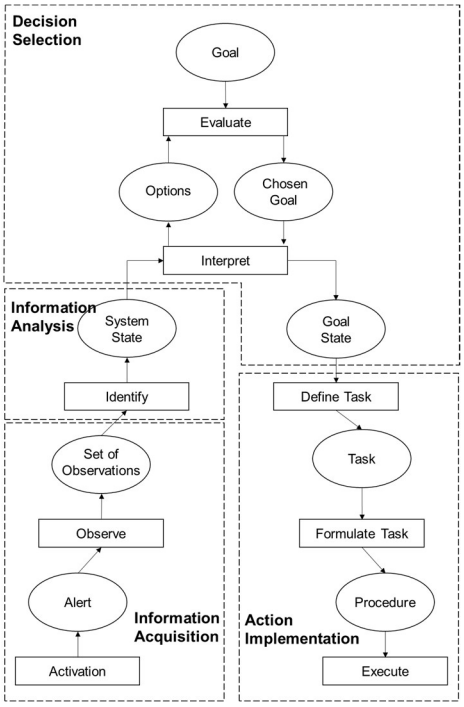

FIGURE 1. Decision ladder and functions of the support system

To address the challenges in operator decision-making, we are developing an Intelligent operator Decision Support System (IDSS) [3, 4]. The overall structure of the IDSS is shown in Fig. 2. The system is designed to support the operator's cognitive process by structuring the response into four distinct stages. The process begins with an early warning stage, which provides proactive warnings based on plant data even before official alarms are triggered. This is followed by the abnormal operating procedure (AOP) selection stage, where the system presents its own analysis on the appropriate AOP to aid the operator's selection. During the Procedure Execution Stage, the system guides the operator through the required steps by clearly displaying relevant information and checklists, while also issuing timely alerts to prevent a potential reactor trip. Finally, the post-response stage supports a safe and efficient plant shutdown if it becomes necessary.

The system performs these functions using several core modules. These include artificial intelligence (AI) diagnostics with supporting evidence, prediction of trip-related parameters, preventive action support based on AOP or system state, and

ensuring data reliability by masking faulty signals [5]. These functions are handled by dedicated modules for diagnosis, prediction, preventive action support, and signal validation and verification, respectively. Specifically, the diagnosis module employs a hybrid algorithm combining convolutional neural networks and fuzzy logic; the prediction module utilizes a Transformer-based model; and the signal validation module incorporates a variational autoencoder architecture built upon recurrent neural networks.

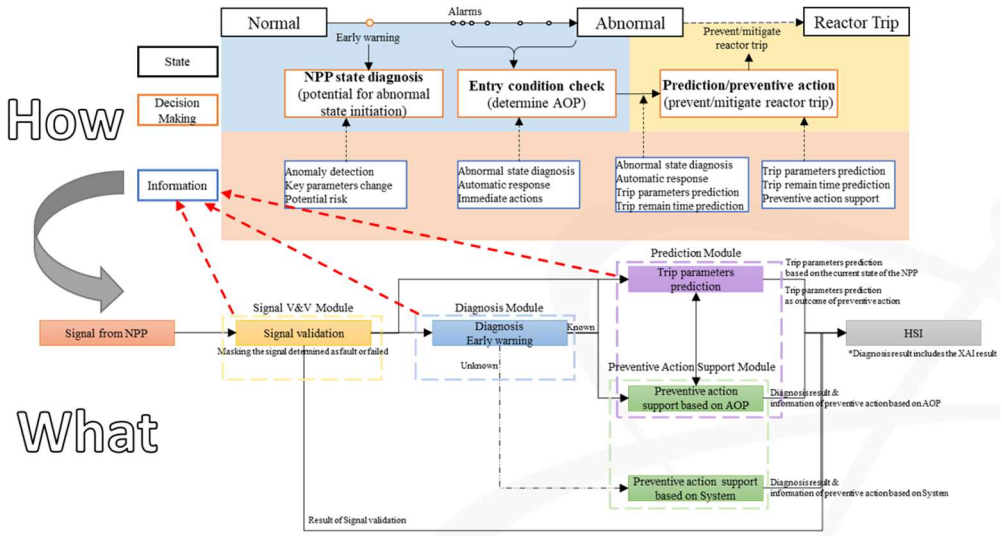

FIGURE 2. Overall structure of intelligent operator decision support system

The research has now reached the prototype stage, with each core module developed and functional. Our current work focuses on implementing the user interface, which involves identifying the essential information for operators and designing its optimal presentation. To this end, we have conducted a detailed analysis of operating procedures to map operator tasks and to structure the information to be delivered through the IDSS.

By providing stage-specific information, the system aims to reduce human errors observed in past incidents. It enhances situational awareness and supports accurate operator decisions during abnormal conditions. To prevent cognitive overload from the additional information, a dedicated training program will be needed to ensure proper system use. Building on this, ongoing research focuses on presenting filtered AI-generated results in a way that highlights the most relevant information, helping operators respond more effectively and contributing to safer plant operations.

ACKNOWLEDGMENTS

This work was supported by Korea Institute of Energy Technology Evaluation and Planning (KETEP) grant funded by the Korea government (MOTIE) (20224B10100130).

REFERENCES

[1] J. M. KIM, G. LEE, C. LEE, and S. J. LEE, “Abnormality diagnosis model for nuclear power plants using two-stage gated recurrent units,” Nuclear Engineering and Technology, Volume 52, Issue 9 (2020).
[2] J. RASMUSSEN, *Cognitive Systems Engineering*, John Wiley and Sons (1994).
[3] G. JANG and S. R. KOO, “Design challenges and response plans for intelligent decision support systems for Korean nuclear power plants under normal and abnormal conditions,” Nuclear Engineering and Technology, Volume 177 (2024).
[4] J. PARK, T. KIM, and S. R. KOO, “Verification strategy for artificial intelligence components in nuclear plant instrumentation and control systems,” Nuclear Engineering and Technology, Volume 164 (2023).
[5] J. CHOI and S. J. LEE, “RNN-based integrated system for real-time sensor fault detection and fault-informed accident diagnosis in nuclear power plant accidents,” Nuclear Engineering and Technology, Volume 55, Issue 3 (2023).

Applying deep learning algorithms for autonomous emergency operation in nuclear power plant

YooJoon Seoung, Junyong Bae, Seung Jun Lee

Department of Nuclear Engineering, Ulsan National Institute of Science and Technology, Ulsan, Republic of Korea, yjs0427s@unist.ac.kr

EXTENDED ABSTRACT

Nuclear power plants have increasingly incorporated autonomous systems to improve safety and efficiency.[1] However, critical operations still rely heavily on human operators, especially during emergencies. In emergency scenarios, for example, operators must promptly bring the reactor coolant system to a stable state. Given the complexity and time-sensitive nature of such situations, the likelihood of human error remains significant. One example is an aggressive cooldown process. Aggressive cooldown is a post-trip emergency operating procedure intended to rapidly reduce the temperature and pressure of the reactor coolant system (RCS) following specific accident scenarios, such as a small break loss-of-coolant accident (SBLOCA) combined with the failure of Safety Injection Systems (SIS).

The primary objective of this strategy is to lower the RCS pressure sufficiently to enable the operation of low-pressure injection systems such as the Shutdown Cooling System (SCS), while simultaneously maintaining effective core cooling to ensure that the fuel cladding temperatures remain below safety limits.

This operation is typically executed by opening the Atmospheric Dump Valves (ADV) on the secondary side to discharge steam and facilitate rapid depressurization, while supplying feedwater through the Auxiliary Feedwater (AFW) system to sustain heat transfer in the steam generators. Simultaneously, Steam Generator cooldown through ADV opening drives a gradual reduction in RCS pressure and temperature, eventually allowing automatic or manual injections from accumulators such as the Safety Injection Tanks (SIT).

During aggressive cooldown, strict attention must be paid to maintaining the cooldown rate below 55.6 °C/hr, to avoid thermal stress or damage to critical components such as the reactor pressure vessel, steam generators, and piping systems. Additionally, the coolant temperature must be lowered to at least 177 °C, which is the prerequisite for initiating SCS injection.[2] Achieving this balance between rapid cooldown and system integrity is essential to the success of the procedure. Table I shows the states of the pressure, volume, temperature of the coolant before and after aggressive cooldown operation.

TABLE I. Initial and final state of reactor coolant before and after aggressive cooldown operation

	Initial state	Final state
Pressure(P)	P_0	20kg/cm^2
Volume(V)	V_0	50%
Temperature(T)	T_0	177°C

In this study, we propose a DRL-based framework to optimize emergency cooling strategies for aggressive cooldown operations. To this end, we introduce a soft actor-critic (SAC) algorithm for continuous control of components and hindsight experience replay (HER) for overcoming sparse positive feedback problems. It has already been applied in reactor power control. For instance, Bae et al. (2023) successfully automated the reactor heat-up process using a DRL-based approach that incorporates Soft Actor-Critic (SAC) and Hindsight Experience Replay (HER) by optimizing reactor coolant state control.[3]

SAC is an off-policy deep reinforcement learning algorithm that optimizes a stochastic policy by maximizing both expected return and policy entropy, promoting exploration and improving stability. It uses two Q-networks to mitigate overestimation bias and employs an entropy temperature parameter α or adaptive trade-offs between exploration and exploitation.[4] Its ability to output continuous actions and reuse past experiences makes it well-suited for controlling complex systems like nuclear power plants. HER enhances learning in sparse-reward environments by modifying past experiences with alternative goals. By replacing the original goal with an achieved state and recalculating the reward, HER transforms failed episodes into informative learning samples, significantly improving sample efficiency.[5]

The reward function was redesigned to guide the DRL agent toward achieving a safe and effective aggressive cooldown strategy by emphasizing precise control of the cooldown rate while enforcing strict operational constraints. The reward structure focuses on minimizing overshoot beyond the target cooldown rate and encourages the agent to reach the target state within a specified time limit.

The primary reward signal is derived from the deviation between the current cooldown rate and the target rate of 55.6 °C/hr.[6] If the agent maintains a cooldown rate less than or equal to the target, the reward is defined as the negative square of the error, which gently penalizes underperformance while encouraging proximity to the target. Conversely, if the cooldown rate exceeds the target, which poses a risk of structural damage to the reactor system, a significantly harsher penalty is applied using a large negative linear coefficient to discourage aggressive overcooling:

$$r_{cool} = \begin{cases} -(r_t - 55.6)^2 & if\ r_t \leq 55.6 \\ -1{,}000\ (r_t - 55.6) & if\ r_t > 55.6 \end{cases} \quad (1)$$

At the end of each episode, a terminal reward is assigned based on whether the agent successfully reduces the reactor coolant temperature to 177 °C or below within 6 hours. If the condition is met, a small positive bonus (+1.0) is given to reinforce successful operations. If the target is not achieved, a large terminal penalty (−50,000) is applied to strongly penalize failure:

$$r_{time} = \begin{cases} 1 & if\ T \leq 177^{o}\mathrm{C} \\ -50{,}000 & if\ T > 177^{o}\mathrm{C} \end{cases} \quad (2)$$

This reward formulation reinforces successful completion of the cooldown process within realistic operational constraints.

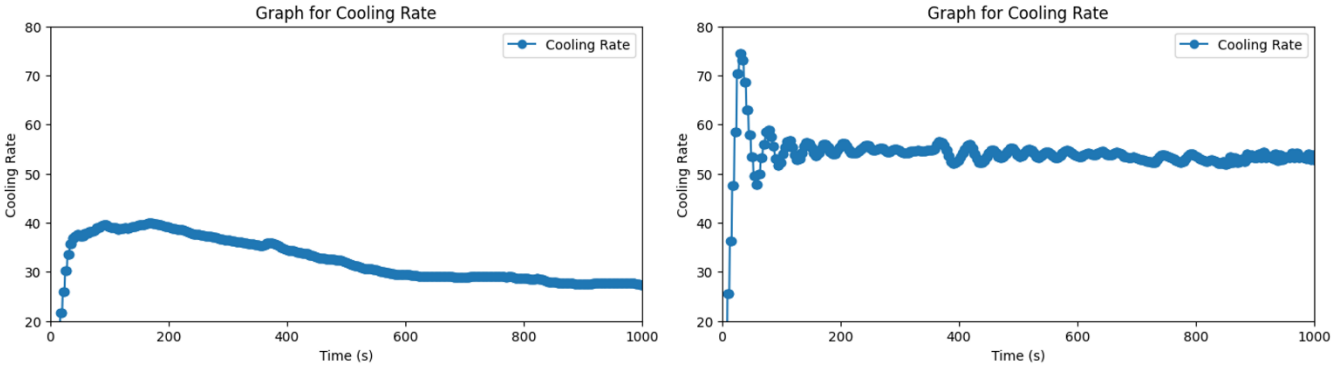

Fig. 1. Cooling rate difference over time (Left: trial 10, Right: trial 1000)

Figure 1 compares the cooling rate trajectories of the DRL agent at trial 10 (left) and trial 1000 (right). In the early stage of training (trial 10), the agent exhibits unstable control behavior, failing to maintain the target cooldown rate consistently. The cooling rate fluctuates and often falls below the desired level, indicating a lack of learned policy optimization.

By contrast, in trial 1000, the agent demonstrates significantly improved control performance, maintaining the cooling rate steadily around the target value of 55.6 °C/hr. This highlights the effectiveness of the reward function and training framework in guiding the agent to learn a stable and safe aggressive cooldown strategy.

This study aims to demonstrate that autonomous operation based on reinforcement learning with SAC and HER can be effectively applied not only under normal conditions but also in emergency scenarios within nuclear power plants. An experimental framework has been established to support model training and evaluation.

In future work, the scope of experiments will be expanded by gradually increasing both the number of control variables and target variables, allowing the agent to adapt to a wider range of operating conditions and emergency situations. The trained agent's performance will be assessed in various scenarios to evaluate its applicability in realistic reactor environments. Furthermore, the generalization capability of the model will be examined, and comparative studies with conventional control approaches will be conducted to validate the effectiveness of the proposed autonomous operation strategy.

ACKNOWLEDGMENTS

This work was supported by Korea Institute of Energy Technology Evaluation and Planning(KETEP) grant funded by the Korea government(MOTIE)(RS-2024-00403194, Next-Generation Nuclear Technology Creation IP-R&D Talent (Human Resources) Development Project)

This research was supported by the National Research Council of Science & Technology(NST) grant by the Korea government (MSIT) (No. GTL24031-400)

REFERENCES

[1] Brown, David. Artificial Intelligence for Accelerating Nuclear Applications, Science, and Technology. No. BNL-223196-2022-INRE. Brookhaven National Laboratory (BNL), Upton, NY (United States), 2022.
[2] Han, Seok Jung, Ho Gon Lim, and Joon Eon Yang. "Thermal hydraulic analysis of aggressive secondary cooldown in a small break loss of coolant accident with a total loss of high pressure safety injection." (2003).
[3] Bae, Junyong, Jae Min Kim, and Seung Jun Lee. "Deep reinforcement learning for a multi-objective operation in a nuclear power plant." *Nuclear Engineering and Technology* 55.9 (2023): 3277-3290.
[4] Haarnoja, Tuomas, et al. "Soft actor-critic: Off-policy maximum entropy deep reinforcement learning with a stochastic actor." *International conference on machine learning*. PMLR, 2018.
[5] Andrychowicz, Marcin, et al. "Hindsight experience replay." *Advances in neural information processing systems* 30 (2017).
[6] Kim, Man Cheol, and Sang Hoon Han. "Variability of plant risk due to variable operator allowable time for aggressive cooldown initiation." *Nuclear Engineering and Technology* 51.5 (2019): 1307-1313.

ASRAM2025
www.asram2025.org
Asian Symposium on Risk Assessment and Management 2025
Pattaya, Thailand, 27 – 29 August 2025

Fire Probabilistic Risk Assessment of BWR-6 Mark-III Nuclear Power Plant for the Pre-Defuel Phase in the Decommissioning Transition Stage

Yu-Ting Lin, Yu-Min Chen, Yi-Cheng Tian, Tsu-Mu Kao

National Atomic Research Institute (NARI)
No. 1000, Wenhua Rd., Longtan Dist., Taoyuan City 325207, Taiwan (R.O.C.)
anita.lin@nari.org.tw; ymchen@nari.org.tw; leontian@nari.org.tw; tmkao@nari.org.tw

ABSTRACT

This paper evaluates the fire probabilistic risk during the extended pre-defuel phase of a boiling water reactor (BWR) nuclear power plant in the decommissioning transition stage, that is, under the condition when the last batch of spent nuclear fuel assemblies is still in the Reactor Pressure Vessel (RPV). Internal fires are recognized as a significant contributor to overall risk in nuclear power plants. Generally speaking, the results of fire probabilistic risk assessment (FPRA) are often influenced by factors such as research schedules, manpower, expenditures, and the subjective judgment of analysts, which may potentially lead to biased risk rankings. This study introduces a systematic, computational approach to simulate and quantify fire scenarios objectively. This method ensures consistent risk evaluation and provides a foundation for future in-depth research. Using the WinNUPRA software package, a fire scenario analysis was performed based on the initial state of the plant 178 days after permanent shutdown. Two configurations are examined: the reactor core and the spent fuel pool (SFP). The scope of this study focuses on the fire scenario combination of all ignition sources and targets in a single compartment. A case study on a BWR-6 Mark-III plant demonstrates that the fuel uncovery frequency (FUF) for the core configuration accounts for 97.04% of the total risk, while the SFP contributes 2.96%. These results show that the reactor core is the primary contributor to the risk of fire during the pre-defuel phase.

Keywords: FPRA, Decommission, Pre-defuel

I. Introduction

The pre-defuel (PD) phase is the transition phase before the decontamination and demolition stages. The PD phase is similar to the low power and shutdown (LPSD) phase. The focus of this study is limited to the accident sequences and risk profiles of fuel damage in the reactor and the spent fuel pool (SFP) caused by fire events under pre-defuel conditions.

This study involves two models, one with the fuel from the last cycle in the reactor pressure vessel and the other with the total spent fuel in the spent fuel pool above the fuel storage building. The reference type of this nuclear power plant is twin/BWR-6/Mark-III. During normal operation of the PD phase (18 months), there is no movement of fuel, and the transfer pipeline is isolated by manual valves (i.e., the upper pool is separated from the spent fuel pool). Methodology is illustrated in section II, details and results of quantification are discussed in section III, and a summary is made in section IV.

II. Methodology

This study refers to the FPRA methodology (NUREG/CR-6850) [1][2] and adjusts the in-plant fire assessment used in the decommissioning transition stage analysis with 11 tasks, as shown in Figure 1. The contents of each task are described below.

II.A. Plant boundary & partitioning

This section covers task 1. The global plant analysis boundary is defined in a broadly inclusive manner. Unimportant areas within this boundary will be readily identified and eliminated from further analysis during the early screening task (e.g., Task 4). Before the early screening work, unimportant areas are screened out according to the screening criteria. For example, administrative office buildings or warehouses within the protection boundary can be screened out. The area does not contain

relevant equipment that will interrupt the cooling of the reactor core or spent fuel pool, and it is an independent building and has no fire spread path. These areas do not require further analysis.

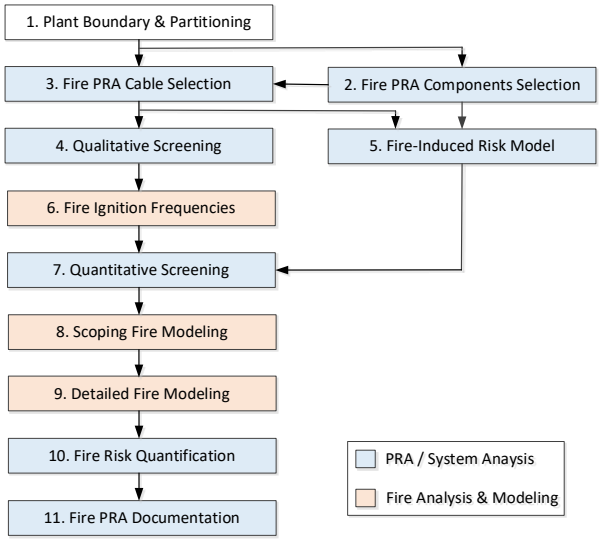

FIGURE 1. Fire Probabilistic Risk Assessment Process

II.B. Selection and qualitative screening of fire components and cables

This section covers tasks 2, 3, and 4. In the fire probabilistic risk analysis, if the subject of fire damage is "equipment related to the fuel cooling interruption of the reactor core or the spent fuel pool," it must be included in the fire PRA model. The subject included in the fire PRA contains fire PRA components and related cables. Based on the functions of system components and the actions in an emergency, as well as the fire PRA component selection principles, include all system components that may be affected by fire in the component selection list. To establish a fire PRA component list, it is necessary to confirm the cable information and the location of each component. Information about cables connected to each component and the fire compartments they pass through is used to analyze the occurrence of fires in each fire compartment and the equipment inside. From the cables connected to each component to the fire compartments these cables pass through, all this information is used to analyze the occurrence of fires in each fire compartment and the equipment inside, ultimately evaluating the risk of fire.

The qualitative screening of fire zones is to reduce the number of fire zones and fire scenarios that need to be analyzed in the quantitative screening analysis step. The screening criteria of qualitative screening are:

(1) Code I: Fire compartments contain important safety equipment and must be retained for quantitative screening analysis;
(2) Code N: Even if all equipment in the fire compartment is damaged by fire, equipment not related to maintaining fuel cooling for the reactor core or the spent fuel pool can be directly evaluated using the screening criterion between compartments. If there is no spread to another compartment, it can be screened out directly.;
(3) Code U: Fire compartments containing cables related to post-fire PRA equipment are retained for quantitative screening analysis.

The above three items are also called fire impact codes. For those belonging to code N and with no effective fire spread path, it can be directly screened out.

II.C. Fire ignition frequency

This section addresses Task 6. The fire ignition frequency analysis integrates the NUREG/CR-6850 [2] fire methodology and NUREG-2169 [3] low-power and shutdown data to identify fire sources across the entire plant. The analysis categorizes fire sources into 37 fire bins, including batteries, reactor pumps, transformers, and others. Frequencies are assigned to individual devices or fire compartments based on device counts or parameter scores for various bins. Additionally, the methodology of FAQ 12-0064 [4] is applied to analyze fire type bins and frequencies of temporary fire sources. The total fire frequency for a fire compartment is the sum of the frequencies assigned to each fire bin within that compartment.

II.D. Fire risk model establishment and quantitative screening analysis

This section covers Tasks 5 and 7. The first step in establishing the fire Probabilistic Risk Assessment (PRA) power plant response model is to identify initiating events caused by fire damage in a fire compartment, compared to the internal event PRA model. Initiating events are determined based on the equipment in the fire compartment, the cables passing through it, and a comprehensive fire cable database. In the preliminary quantitative screening stage, it is assumed that all equipment and cables in the fire compartment sustain the most severe fire damage, resulting in equipment failure, cable failure, and the simultaneous occurrence of all failure modes. If the failure of equipment and cables in a compartment does not lead to the loss of the decay heat removal function, no initiating event determination is required for that compartment. When a fire compartment may cause multiple initiating events, all possible combinations of initiating events and equipment failures are quantified, and the combination with the highest Conditional Fuel Uncover Probability (CFUP) is selected as the initiating event. If maximum CFUP values are equal, the selection is based on the CFUP ranking of each initiating event under no-equipment-damage conditions.

Quantitative screening analysis uses the results of Task 6 ("Fire Ignition Frequencies") and Task 5 ("Fire-Induced Risk Model") as inputs. Screening criteria ensure that the cumulative risk of screened-out fire compartments is minimal. The criteria for a single compartment follow the PRA standard (ASME/ANS RA-Sa-2013) [5], issued by the American Society of Mechanical Engineers (ASME) and the American Nuclear Society (ANS) in 2013, specifically Table 4-2.8-4 for Capability Category II. The Fire Uncover Frequency (FUF) of screened compartments is sorted and accumulated from smallest to largest. Compartments contributing to a cumulative FUF exceeding 10% are retained for detailed analysis. The risk of fire compartments that are quantitatively screened out will adopt their original value and be combined with detailed results to estimate the total fire risk.

II.E. Fire Definition and Simulation

Tasks 8 and 9 address fire definition and detailed fire simulation, respectively. Task 8 defines the severity factors (SF) for fire bins in simulations, while Task 9 conducts detailed fire simulations. For each unscreened fire source in a fire compartment, relevant fire scenarios are identified, and detailed simulations are performed to calculate the probability of a fire not being extinguished.

The purpose of fire definition and simulation is to use fire simulation tools to accurately model the combustion scale of fire sources, estimate the likelihood of fire spreading to target objects, and evaluate fire scenario probabilities. Key parameters, such as burning time, fire protection system response, and non-extinguishing probability, are incorporated into the quantitative fire risk calculation. This task builds on the fire frequency analysis in Section II.C, using fire source and compartment data to conduct defined fire simulations and detailed site surveys. The process and results of single-compartment fire simulations are performed for compartments retained after the quantitative screening analysis in Task 8.

Automatic suppression system failure rates are based on NUREG/CR-4840 [6]. The unavailability of water and carbon dioxide systems is 0.04, and the unavailability of the Halon system is 0.06, representing the failure factors for automatic fire protection systems.

II.F. Quantitative analysis of fire risk

This section addresses Task 10, focusing on fire prevention compartments retained from the quantitative screening analysis in Task 7 and conducting detailed fire scenario simulations and fire risk quantification in Task 9. Fire scenario selection is the primary focus of detailed fire simulations in Task 9. During fire scenario analysis, the relationship between each fire source and the target is examined individually to calculate the probability of fuel exposure. The frequency of fuel exposure is obtained by multiplying the fire frequency, severity factor, non-extinguishing probability, and fuel exposure probability.

III. Nuclear power plant during the decommissioning transition period

The fire PRA methodology discussed in Section II is applied to the BWR-6 Mark-III nuclear power plant in the decommissioning transition period. During decommissioning, fuel is transferred from the reactor core to the spent fuel pool. The transition period occurs when the spent fuel pool lacks sufficient space for all fuel, requiring some fuel to remain in the core. This section demonstrates an application case following the fire PRA process.

III.A. Plant boundary & partitioning

The analysis boundary for the power plant was established by referencing the structural overview and the Final Safety Analysis Report (FSAR). Of the 67 buildings in the BWR-6 Mark-III nuclear power plant included in the analysis boundary, 61 were preliminarily screened out. Six buildings require qualitative screening and analysis of their fire compartments: the reactor building, reactor auxiliary building, turbine building, control building, fuel building, and emergency seawater pump room.

III.B. Selection and qualitative screening of fire components and cables

After establishing the fire PRA component list using the internal event safety assessment model for the decommissioning transition phase of the BWR-6 Mark-III nuclear power plant, the location of each component, its connected cables, and the fire compartments these cables traverse are confirmed. This enables analysis of fire risks for equipment and cables and their post-fire impacts. A correlation database integrating components, cables, and fire compartments is created, followed by qualitative screening analysis. The fuel building is used as an example to illustrate the results of preliminary screening.

The fuel building contains 24 fire compartments. Based on the floor plan of critical equipment, fire countermeasure procedures, and analysis data from the in-plant incident safety assessment model during the decommissioning transition phase, the equipment in each fire prevention zone was evaluated. Qualitative screening determines whether a compartment contains "equipment that may interrupt cooling of the reactor core or spent fuel pool" or a "potential fire source":

(1) Directly screened out: Three fire compartments lack equipment that could interrupt fuel cooling in the reactor core or spent fuel pool and have no effective fire propagation path, allowing them to be screened out..

(2) Retained for quantitative screening analysis:
   a. Four fire compartments contain equipment that could interrupt cooling of the reactor core or spent fuel pool ("I" category) but have no effective propagation path.
   b. Five fire compartments contain "I" category equipment and have an effective propagation path.
   c. Seven fire compartments contain cables related to the safety shutdown system ("U" category) but have no effective propagation path.
   d. Three fire compartments contain "U" category cables and have an effective propagation path.

In total, 19 fire compartments require quantitative analysis.

III.C. Fire ignition frequency analysis

During the calculation of fire frequency, the equipment in each fire compartment must be classified according to different fire bins. After the equipment in all fire compartments has been inventoried, the proportion of a single piece of equipment in the fire bin must be calculated, along with the fire frequency of a single bin for that equipment. The final step is to sum the frequencies of each fire bin within a single fire compartment to obtain the fire frequency of the fire compartment.

During the fire frequency analysis, fire bins are divided into three categories based on their characteristics: (I) Fire bins with physical equipment that can be directly counted. (II) Fire bins that cannot be directly counted; weights are assigned based on relevant data. (III) Fire bins with no counting data available.

Category I can be counted directly. During the fire frequency analysis process, the number of equipment must be counted in detail. In addition to collecting relevant supporting information from the power plant, power plant staff are also asked to assist with interpretation during the process, particularly for confirming new or removed equipment. Special counting methods for some fire bins, as classified in NUREG/CR-6850 [1][2], are applied and explained as follows:

(1) Bin 15 counts non-high-energy arc electrical cabinets by their vertical segments.

(2) Bin 16.a and Bin 16.b: For detailed calculation of electrical cabinet panels (e.g., motor control centers, switchgear, load centers), equipment is counted according to vertical segments.

(3) Bin 16.1: Bus ducts are counted based on the number of joints in the metal casing of the bus duct.

Based on the counting results, the proportion of each piece of equipment in a fire bin is determined. For example, if the total number of pumps in fire bin 21 across the entire plant is 153.5, each pump accounts for 1/153.5 of the fire frequency. The fire frequency of bin 21 is 2.72E-02/yr; when multiplied by 1/153.5, this equals 1.77E-04/yr, which is the fire frequency for one pump. The calculation method for other fire bins follows the same approach.

The ignition frequency of Category II temporary fire sources is calculated per fire compartment. Each room is assigned a counting weight and divided into three counting methods:

(1) Fires caused by welding or cutting for temporary fire sources (bins 6, 24, and 36): The influencing factor is the number of high-temperature maintenance operations in each fire compartment. The reference material is the fireworks order of the analyzed plant.

(2) Cables on fire caused by welding or cutting (bins 5, 11, and 31): In addition to high-temperature maintenance operations, influencing factors also include the weight of cables in the fire compartment. The reference for cable weight is the Pre-Fire Procedure.
(3) Temporary fire sources (bins 7, 25, and 37): Influencing factors include general electromechanical maintenance operations, the number of on-site workers, and stored materials. The reference materials are the general electromechanical maintenance work order information and the Abnormality and Emergency Operation Procedure Book.

Additionally, due to significant difficulties in counting cables and junction boxes in fire compartments, the fire frequency is directly allocated based on the proportion of a single fire compartment's cables relative to the entire plant's cables, with reference to the cable weight in the Fire Countermeasures Procedure Book.

Category III uncounted information includes:
(1) Bin 2 (reactor): Applicable only to PWR power plants and thus not included in this study.
(2) Bin 30 (boilers): Located outside the turbine building and differing from the NUREG/CR-6850 [1][2] combustion bin counting definition, so they are excluded from the calculation.

The fire source inventory is one of the key preparatory tasks for the on-site survey, and the survey results have been incorporated into the fire bin count. The NUREG/CR-6850 [1][2] methodology was used to count the 37 fire bins across nearly 400 fire compartments in the analyzed plant. After determining the total number of fire bins in the entire plant, the fire frequency from NUREG-2169 (low power and shutdown data) [3] is divided by the total number of fire bins in the plant, multiplied by the number of fire sources in each fire compartment, and then the fire frequencies of each fire source in each compartment are summed to obtain the fire frequency of the fire compartment.

III.D. Fire risk model establishment and quantitative screening analysis

For fire compartments retained after qualitative screening, a preliminary quantitative analysis is conducted using conservative assumptions. Fire compartments whose results meet the quantitative screening conditions are excluded, further reducing the workload of subsequent detailed analysis.

Quantitative screening of fires during the decommissioning transition period of the BWR-6 Mark-III nuclear power plant is performed. The screening results for initiating events that may lead to the risk of fuel uncovery in the reactor core or spent fuel pool are explained below and summarized in Table 1:

(1) AAA-LOR (Loss of RHR): When critical components related to the A and B loops of the RHR (Residual Heat Removal) system are lost simultaneously, the initiating event is classified as AAA-LOR.
(2) AAA-TCH (Loss of Normal Chilled Water): When critical components of the normal chilled water system fail, the event is designated as AAA-TCH.
(3) AAA-TCE (Loss of Essential Service Water): When critical components of the essential service water system fail, the event is designated as AAA-TCE.
(4) AAA-TA3 (Loss of 4.16 kV Bus 1A3): When critical components related to the 4.16 kV bus 1A3 fail, the event is classified as AAA-TA3.
(5) AAA-TA4 (Loss of 4.16 kV Bus 1A4): When critical components related to the 4.16 kV bus 1A4 fail, the event is classified as AAA-TA4.
(6) AAA-LOC (Loss of SFPCCS): The nuclear component closed cooling water (NCCCW) System provides the cooling water for the heat exchanger and pump cooler of the spent fuel pool cooling and cleanup system (SFPCCS). Therefore, when the critical components of the NCCCW or SFPCCS fail, the event is classified as AAA-LOC.
(7) NA Category: Initiating events not falling into categories 1 through 6 are classified as not causing an initiating event (NA category).

If the analysis identifies more than two simultaneous initiating events, the event with the most severe consequences is selected. For example, if AAA-LOR and AAA-TCE occur simultaneously, the event is classified as AAA-LOR. In the quantitative screening stage, the determination of the initiating event and risk quantification for a fire compartment assumes conservatively that all equipment within the compartment fails. Human factor basic events in the FPRA model are also conservatively used in the screening analysis values. If the quantitative results under these conservative assumptions still meet the screening conditions, the actual risk contribution is expected to be lower.

TABLE 1. The Screening Results and Classification of Initiating Events

Initiating Events PRAID	Description	Initiating events at the reactor core	Initiating events at the spent fuel pool
AAA-LOR	Loss of RHR	✓	
AAA-TA4	Loss of 4.16kV Bus 1A4	✓	
AAA-TA3	Loss of 4.16kV Bus 1A3	✓	
AAA-TCE	Loss of Essential Service Water	✓	
AAA-TCH	Loss of Normal Chilled Water	✓	
AAA-LOC	Loss of SFPCCS		✓

Quantitative analysis is divided into quantitative screening and detailed analysis. After qualitative screening, fire compartments containing critical equipment or cables proceed to quantitative screening. If critical equipment in a fire compartment catches fire, is damaged due to fire affecting other equipment in the compartment, or if the fire spreads to other compartments and causes the fuel uncovery frequency (FUF) sequence of the reactor core or spent fuel pool to exceed 10% of the FUF for internal events at the site, further detailed analysis is required. The risks of each compartment are ranked and accumulated from smallest to largest. The sorting threshold is reached when the cumulative value exceeds 10% of the FUF for internal events. The quantitative screening values for FUF are 5.01E-09/yr for the reactor core and 3.26E-09/yr for the spent fuel pool, with a total quantitative screening FUF of 8.27E-09/yr. Consequently, 41 compartments require detailed analysis. The quantitative screening results, using the fuel building as an example, are detailed below.

In the fuel building, 19 fire compartments require quantitative screening analysis. The screening results are as follows:

(1) Cumulative Value Exceeding 10% of Internal Event FUF: No fire compartments exceed this threshold, and thus, further detailed analysis is required for zero compartments.

(2) Cumulative Value Not Exceeding 10% of Internal Event FUF: Nineteen fire compartments meet this criterion, requiring no detailed analysis, and their values can be directly adopted.

III.E. Fire scenarios and quantitative analysis

Fire scenario selection is the primary task of detailed fire simulation. Single-compartment fire scenarios are based on quantitative screening of retained fire sources within the compartment. The risk of each fire scenario is calculated by evaluating severity factors (SF), non-suppression probability (Pns), and fire damage consequences. This study proposes a method based on the NUREG/CR-6850 methodology [1][2] and a systematic process [4], ensuring a consistent approach to fire scenario development and minimizing risk bias across compartments. The following sections discuss the fire scenario analysis for ignition sources: equipment, cables, temporary ignition sources, and induced cables (IC).

III.E.1. Equipment fire scenarios

These scenarios involve fires occurring in equipment and explore their potential impact on power plant risks. Fire bins included in equipment fire scenarios are: Bin 1 (Batteries), Bin 8 (Diesel Generators), Bin 9 (Air Compressors), Bin 10 (Battery Chargers), Bin 14 (Electric Motors), Bin 15 (Non-High Energy Arcing Faults (HEAF) Electrical Cabinets), Bin 16.a (480V–1000V HEAF Electrical Cabinets), Bin 16.b (>1000V HEAF Electrical Cabinets), Bin 16.1 (Bus Ducts), Bin 16.2 (Isolated Phase Bus), Bin 19 (Other Hydrogen Fires), Bin 21 (Pumps), Bin 22 (RPS MG Sets), Bin 23 (Transformers), Bin 26 (Ventilation Subsystems), Bin 32 (Main Feedwater Pumps), Bin 33 (Turbine/Generator (T/G) Exciter), Bin 34 (T/G Hydrogen), and Bin 35 (T/G Oil).

Analysis of equipment-based fire scenarios requires examining the relationship between each ignition source and target object individually, using NUREG/CR-6850 [2] "TASK 8 Scoping Fire Modeling" and "TASK 11 Detailed Fire Modeling" methodologies, and the Fire Dynamics Tools (FDTs) (Version 1805.1) spreadsheet [7] provided by the U.S. NRC. Fire damage time is estimated based on the damage mechanism of the target object. By repeatedly comparing results with on-site investigation data, each equipment fire scenario and its corresponding damaged equipment are accurately determined, and the severity factor and non-suppression probability are calculated. Using the internal event PRA model [8], the PRA basic event (PRAID) corresponding to the damaged equipment is set for each scenario, and the Core Damage Frequency Uncovery Probability (CFUP) is calculated. The FUF for the reactor core and spent fuel pool in equipment fire scenarios are 2.70E-07/yr and 4.87E-09/yr, respectively, with a total FUF of 2.75E-07/yr.

III.E.2. Cable fire scenarios

These scenarios begin with a fire in a cable and extend to potential impacts on power plant risks. Since cable materials significantly influence fire scenario development, the cable material type must be confirmed before analysis. Cable coatings are categorized as thermoset plastic (TS) or thermoplastic polyester (TP), each exhibiting distinct behaviors in fire environments. When burned, thermoset plastics form a carbonized layer that inhibits combustion, while thermoplastic plastics melt due to low melting points, producing droplets that create new ignition points and accelerate flame spread. Consequently, thermoset-coated cables burn only themselves, whereas thermoplastic-coated cables may spread fire to other cables. In developing cable fire scenarios, TS and TP are critical parameters, classified based on cable insulation material data from the power plant database. If insulation material data is unavailable, a conservative assumption of thermoplastic is applied. The FUF for the reactor core and spent fuel pool in cable fire scenarios are 1.23E-08/yr and 7.09E-10/yr, respectively, with a total FUF of 1.30E-08/yr.

III.E.3. Temporary fire source (including Induced Transient, IT) fire scenarios

Temporary fire sources, including those caused by welding and cutting, share the same heat release rate and influence area and are thus combined into temporary fire source (including IT) scenarios. Given the variety of transient ignition sources (e.g., liquid solvent fuels, solid fuels of differing types, sizes, and configurations), two assumptions are made: (1) a transient ignition source (including IT) burning within 0.9 m of equipment directly damages it, regardless of suppression success; and (2) fire spread scenarios consider secondary combustible propagation without accounting for the total heat release rate (HRR) of the transient source and secondary combustibles. The FUF for the reactor core and spent fuel pool in transient fire scenarios are 1.51E-07/yr and 4.47E-09/yr, respectively, with a total FUF of 1.55E-07/yr.

III.E.4. Induced Cable (IC) fire scenario

IC fire scenarios involve cable fires caused by welding and cutting. Since the fire originates externally, it may spread regardless of whether the cable is coated with TS or TP. It is conservatively assumed that a cable fire from welding or cutting immediately spreads to all cables in the affected cable tray. However, due to the presence of personnel during welding and cutting, the fire is unlikely to spread to other trays, limiting damage to a single tray. When quantifying IC risks in fire compartments, the frequency of occurrence is assumed to be evenly distributed across each cable tray. All IC fire incidents occurring within a compartment are assessed collectively, with the CFUP calculated for each tray and the results subsequently averaged. The FUF for the reactor core and spent fuel pool in IC fire scenarios are 7.54E-14/yr and 0.00E+00/yr, respectively, with a total FUF of 7.54E-14/yr.

III.E.5. Results

The PRA analysis results for fires during the decommissioning transition phase are presented in Tables 2 and 3. The total FUF is 4.44E-07/yr (Table 2), with equipment and transient fire scenarios as the primary risk contributors. The fire risk from quantitative screening of a single compartment is 8.27E-09/yr, while detailed analysis yields 4.43E-07/yr. Table 3 summarizes the overall fire risk quantification. Combining quantitative screening and detailed analysis results, the FUF caused by internal fire events is 4.38E-07/yr for the reactor core (97.03% of total FUF) and 1.34E-08/yr for the spent fuel pool (2.97% of total FUF). These results indicate that the reactor core is the primary risk contributor during the pre-defueling phase.

TABLE 2. Detailed Fire Risk Quantification Results of Single-Compartment Fire Scenarios

Item	Fire Scenario Analysis of Ignition Sources	Reactor Core-FUF (1/yr)	Spent Fuel Pool –FUF (1/yr)	FUF (1/yr)	FUF %
1	Equipment Fire Scenario	2.70E-07	4.87E-09	2.75E-07	62.08%
2	Cable Fire Scenario	1.23E-08	7.09E-10	1.30E-08	2.93%
3	Transient Fire Scenario	1.51E-07	4.47E-09	1.55E-07	34.99%
4	Induced Cable Fire Scenario	7.54E-14	0.00E+00	7.54E-14	0.00%
Total		4.34E-07	1.01E-08	4.44E-07	100.00%

TABLE 3. Overall Fire Risk Quantification Results for Single-Compartment Fire Scenarios

Item	Quantitative Screening (1/ yr)	Detailed Analysis (1/ yr)	Total FUF (1/yr)	FUF %
Reactor Core-FUF	5.01E-09	4.34E-07	4.38E-07	97.03%
Spent Fuel Pool -FUF	3.26E-09	1.01E-08	1.34E-08	2.97%
Total FUF (1/yr)	8.27E-09	4.43E-07	4.51E-07	100.00%

IV. Conclusions

This study adheres to the Fire PRA Methodology [2] developed by the Nuclear Regulatory Commission's Office of Nuclear Regulatory Research (RES) and the Electric Power Research Institute (EPRI). Preliminary qualitative screening identified six buildings requiring further analysis: the reactor building, reactor auxiliary building, turbine building, control building, fuel building, and emergency seawater pump room. Initiating events included in the quantification are AAA-LOR, AAA-LOC, AAA-TCH, AAA-TA3, and AAA-TA4. The results show that the reactor core, with a 97.04% contribution to FUF, is the primary fire risk contributor during the pre-defueling phase, while the spent fuel pool contributes a relatively minor 2.96%.

REFERENCES

[1] EPRI/NRC-RES, "Fire PRA Methodology for Nuclear Power Facilities: Volume 1, Volume 2." EPRI 1011989 and NUREG/CR-6850, 2005.
[2] EPRI/NRC-RES fire PRA methodology for nuclear power facilities: Supplement 1. EPRI 1011989 and NUREG/CR-6850, 2010.
[3] U.S. NRC, "Nuclear Power Plant Fire Ignition Frequency and Non-Suppression Probability Estimation Using the Updated Fire Events Database," EPRI 3002002936 and NUREG-2169, 2015.
[4] Pi-Lin Hsu, Chung-Kung Lo, "A systematic process for developing fire scenarios in risk assessment for nuclear power plants," Annals of Nuclear Energy (2021).
[5] ASME/ANS RA-Sb-2013 – Addenda to ASME/ANS RA-S-2008, Standard for Level 1/Large Early Release Frequency Probabilistic Risk Assessment for Nuclear Power Plant Applications, July 2013.
[6] M.P. Bohn, et al., "Procedures for the external event core damage frequency analysis for NUREG-1150", Sandia National Laboratories, NUREG/CR-4840, November 1990.
[7] U.S. NRC, "Fire Dynamics Tools (FDTs) Quantitative Fire Hazard Analysis Methods for the U.S. Nuclear Regulatory Commission Fire Protection Inspection Program - Supplement 1," NUREG-1805, July 2013.
[8] Yi-Cheng Tian, Chen-Che Hsu, Po-Jung Chiu, Tsu-Mu Kao, "Probabilistic Risk Assessment for the Transition Phase of Decommissioning of BWR-6 Mark-III Nuclear Power Plant," PSAM17&ASRAM2024.

Technical Session 16 (16:00 -18:00)	The Port 4, C Floor	Human Reliability Analysis and Human and Organizational Factors
		Chair/Facilitator 1: Prof. Jinkyun Park, Principal Researcher and Professor, Korea National University of Science and Technology - Korea Atomic Energy Research Institute (UST-KAERI) Chair/Facilitator 2: Dr. Soratos Tantideeravit (Office of Atoms for Peace(OAP))
16:00 - 16:20		ID 12: A Dynamic Human Reliability Analysis Approach Using Continuous Markov Chain Monte Carlo Method: Formulation of a Computational Framework for Responding to Environmental Spatiotemporal Changes Speaker: Chun-Yen LI (Central Research Institute of Electric Power Industry) Contributors: Chun-Yen LI (Central Research Institute of Electric Power Industry), Yukihiro KIRIMOTO (Central Research Institute of Electric Power Industry)
16:20 - 16:40		ID 129: A Study of DynamicHuman Reliability Assessment) -Time and Environment Dependent Assessment of Human Error Probability Speaker: Yutaka Takizawa (Hokkaido University) Contributors: Yutaka Takizawa (Hokkaido University), Sunghyon Jang (Hokkaido University), Shuehi Matsunaka (TEPCO Systems Corporation), Yuya Otaki (TEPCO Systems Corporation), Natsuki Shiraishi (TEPCO Systems Corporation)
16:40 - 17:00		ID 14: ACT-R-Based Human Digital Twins of Nuclear Power Plant Operator Performance for Advancing HRA Data Collection Speaker: Xingyu Xiao (Tsinghua) Contributors: Peng Chen (UCAS), Qianqian Jia (Tsinghua), Meng Kong, Jingang Liang (Tsinghua), Jiejuan Tong (Tsinghua), Haitao Wang (Tsinghua), Xingyu Xiao (Tsinghua), Hongru Zhao (Tsinghua), Jun Zhao (Tsinghua)
17:00 - 17:20		ID 92: Resolving biased Judgments in Risky Context Speaker: Gueorgui Petkov (Sofia University) Contributors: Gueorgui Petkov (Sofia University)
17:20 - 17:40		ID 35: Evaluation of HRA Methodologies for Application in SDP Work Speaker: Ar Ryum Kim (KINS) Contributors: Ar Ryum Kim (KINS), Namyeong Kim (KINS), Dongwon Lee (KINS), Jooyoung Park (INL), Ronald Boring (INL)
17:40 - 18:00		ID 82: A Systemic Analysis on Leadership and Ethics in the Regulatory Framework Through the Radiological Accident in Samut Prakarn Speaker: Soratos Tantideeravit (Office of Atoms for Peace) Contributors: Soratos Tantideeravit (Office of Atoms for Peace)

ASRAM2025
www.asram2025.org
Asian Symposium on Risk Assessment and Management 2025
Pattaya, Thailand, 27 – 29 August 2025

A Dynamic Human Reliability Analysis Approach Using Continuous Markov Chain Monte Carlo Method: Formulation of a Computational Framework for Responding to Environmental Spatiotemporal Changes

Chun-Yen Li [1*], Yukihiro Kirimoto [1]

[1] *Central Research Institute of Electric Power Industry: 2-6-1 Nagasaka, Yokosuka, Kanagawa, 240-0196, li40806@criepi.denken.or.jp*

ABSTRACT

Advancing Human Reliability Analysis (HRA) is vital for nuclear safety, as it evaluates human responses to accidents within Probabilistic Risk Assessment (PRA) Conventional HRA methods estimate Human Error Probability (HEP) based on Performance Shaping Factors (PSFs) under static scenarios but struggle to address dynamic environmental changes. To overcome this limitation, it is crucial to model uncertainties in human behavior arising from continuously evolving spatiotemporal environmental conditions. This research aims to develop a dynamic HRA approach that incorporates the effects of evolving environments on human behavior. To achieve this, we propose a computational framework that utilizes the Continuous Markov Chain Monte Carlo (CMMC) method. Within this framework, PSFs are regularly updated based on monitored environmental changes to capture their impact on HEP. Subsequently, Monte Carlo sampling is employed to generate stochastic human behavior events, which in turn provide feedback to the environment. Through this iterative process, a dynamic HRA approach is realized by fostering evolving, bidirectional interactions between humans and their surrounding environment. A hypothetical example applying this proposed computational framework is also demonstrated in this research, showcasing its potential to quantitively confirm the previously unexplored influence on the repair task resulted from dynamic phenomenon.

Keywords: Dynamic human reliability analysis, Continuous Markov chain Monte Carlo method, Dynamic interaction between human and environments, Performance shaping factors, Human error probability.

I. INTRODUCTION

Probabilistic Risk Assessment (PRA) serves as a fundamental approach for addressing the intricate safety and reliability issues within Nuclear Power Plants (NPPs). A key part of PRA is Human Reliability Analysis (HRA), which focuses on detecting potential human errors and quantifying their likelihood, known as Human Error Probability (HEP), during safety evaluations. Among the many HRA techniques developed over time, the Technique for Human Error Rate Prediction (THERP) is particularly prominent [1]. THERP analyzes a target task by breaking it down into smaller, discrete steps using a decision tree model, while incorporating Performance Shaping Factors (PSFs) that represent external environmental conditions and internal operator characteristics such as skill level.

However, traditional HRA methods generally depend on fixed, static scenarios, making them inadequate for capturing how transient environmental variations affect operator performance. This limitation results in persistent uncertainties when assessing dynamic accident scenarios. Furthermore, dynamic PRA approaches have been developed to explicitly model the timing and sequence of events, thus providing a more thorough identification of failure paths throughout different accident progressions. This evolving research trend underscores the urgent need for dynamic HRA methodologies that can effectively account for fluctuating environmental influences on human tasks and integrate smoothly within dynamic PRA frameworks.

This paper aims to develop a dynamic HRA approach that reflects changing environmental impacts on human behavior over time. The approach extends conventional HRA by utilizing the Continuous Markov Chain Monte Carlo (CMMC) method [2], which has been previously applied in dynamic PRA analyses. In this approach, the Markov chain process continuously updates PSFs based on real-time environmental monitoring, thereby influencing the estimation of HEP. These updated probabilities then guide Monte Carlo simulations that generate stochastic sequences of dynamic events. Additionally, an originally proposed computational framework is introduced in this research, designed to capture the mutual interactions

between humans and their environment in a cyclic manner. An example is also presented in this study to illustrate how the proposed framework leverages the CMMC method to enhance the flexibility of the traditional HRA approach.

II. METHODOLOGY

II.A. Computational Framework Overview

The proposed dynamic analysis framework, as shown in Fig. 1, is built upon two key components: (1) the Structures, Systems, and Components (SSCs) State Solver, which functions based on stochastic principles, and (2) the Plant State Solver, which operates deterministically.

After initializing all the necessary parameters, the SSCs State Solver is activated firstly, processing the current SSCs and plant information through either the Malfunction Analysis Module or Repair Analysis Module, depending on whether the specific j_{th} SSC (SSC_j^n, n is the current step in the analysis framework) is presently functioning or malfunctioning. Subsequently, CMMC method is applied with referring to the plant conditions to update the SSC state stochastically from SSC_j^n to SSC_j^{n+1}. Until all the SSC_j^ns are evaluated, the framework transfers all the updated SSCs states to the Plant State Solver.

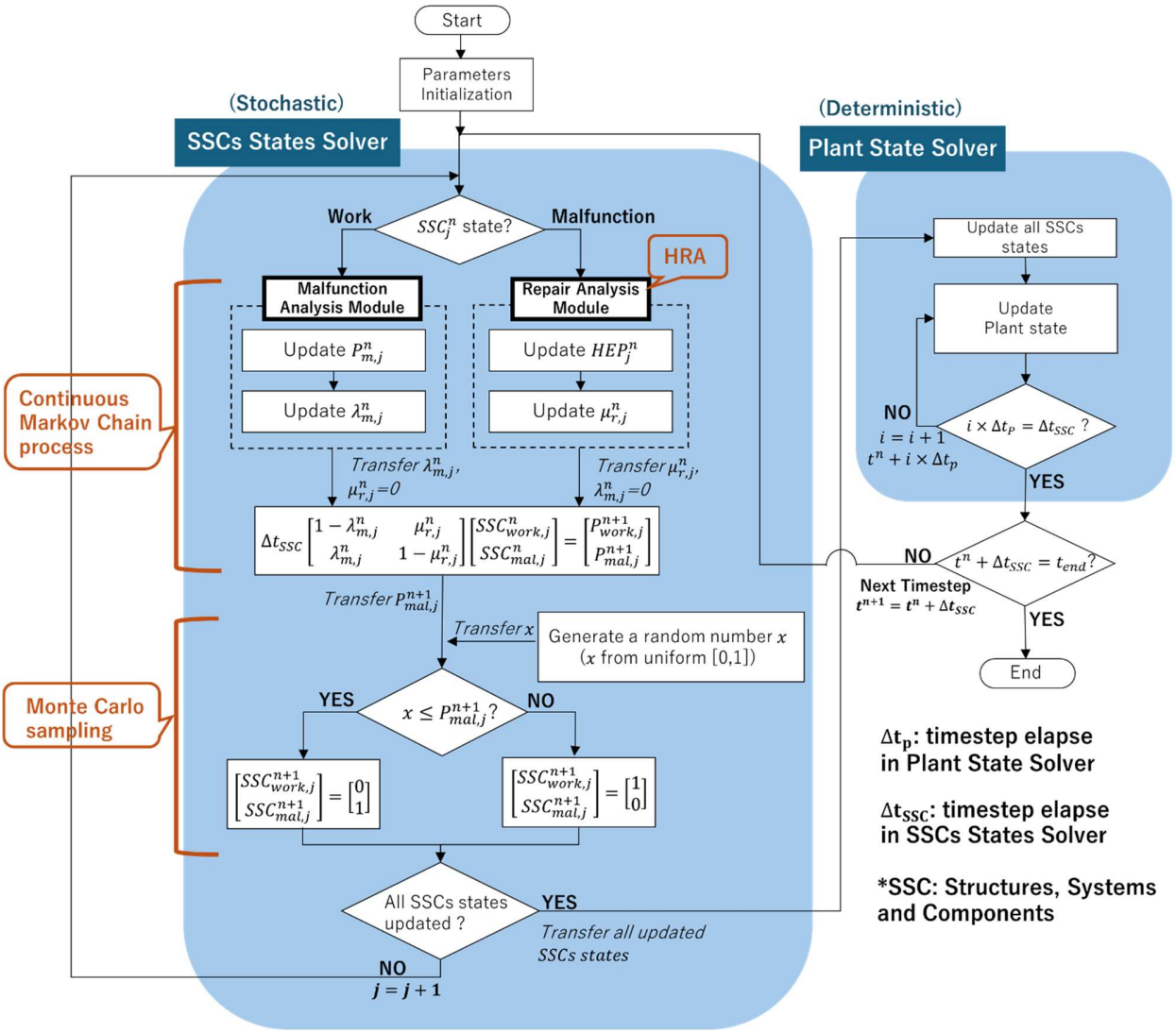

FIGURE 1. The proposed CMMC-based framework.

518

Following which, the Plant State Solver then conducts transient analyses (such as Computational Fluid Dynamics simulations) to model the plant state deterministically. After completing the transient analysis, if the predetermined end time (t_{end}) has not been reached yet, the updated plant state information is transferred to the SSCs State Solver.

Ultimately, this framework creates a dynamic, bidirectional coupling analysis that combines deterministic environmental simulations with stochastic modeling of SSC behaviors in a cyclical manner. Since the previous research [2] covers the CMMC method's application to SSC malfunction analysis, the next section will explore how to use CMMC method for dynamic repair analysis, particularly focusing on expanding traditional HRA into a dynamic framework.

II.B. Utilizing CMMC Method to Dynamically Embed HRA in the Framework

The use of the CMMC method within the SSCs State Solver can be divided into two main components: (1) the continuous Markov chain process and (2) Monte Carlo sampling, as depicted in Fig. 1. During the continuous Markov chain process, if the Repair Analysis Module is enabled, HRA is carried out to estimate the HEP for the repair task of the j_{th} SSC at the n_{th} step (HEP_j^n), taking the current condition of the plant into account. The value HEP_j^n can also be represented in the form of a typical repair rate expression, as below:

$$HEP_j^n = e^{-\mu_{r,j}^n \times \Delta T_{r(grace),j}} \tag{1}$$

where $\Delta T_{r(grace),j}$ is the grace period allowed for repairing the j_{th} SSC, and $\mu_{r,j}^n$ is the instantaneous repair rate at step n. By rearranging the equation, it becomes clear that $\mu_{r,j}^n$ reflects the effects of the current plant state as captured by HEP_j^n in the HRA.

$$\mu_{r,j}^n = -\ \ln(HEP_j^n)/\Delta T_{r(grace)} \tag{2}$$

In addition, $\mu_{r,j}^n$ indicates the likelihood of a repair occurring within a unit time interval, assuming no previous repair has been performed for that task; therefore, incorporating this updated $\mu_{r,j}^n$ into the transition matrix at the end of the Markov chain process (illustrated in Fig. 1) allows for the calculation of the j_{th} SSC's state transition probabilities (namely, the probability of switching to a working state ($P_{work,j}^{n+1}$) or staying in a malfunctioning state ($P_{mal,j}^{n+1}$) at the $n+1_{th}$ step) while factoring in the current state of the SSC. Here, if the j_{th} SSC is operational at step n, then $SSC_{work,j}^n = 1$ and $SSC_{mal,j}^n = 0$, and vice versa. Finally, Monte Carlo sampling is applied using $P_{work,j}^{n+1}$ and $P_{mal,j}^{n+1}$, allowing for the stochastic resolve of the j_{th} SSC's state at the $n+1_{th}$ step.

III. TEST CASE EXPLANATION

III.A. Applied Scenario

To examine the proposed CMMC-based framework, this study applies a hypothetical scenario involving volcanic ashfall on a typical sodium-cooled fast reactor (SFR), as illustrated in Fig. 2. In the SFR, decay heat removal depends on the Auxiliary Cooling System (ACS), which operates through air cooling. The ACS can function in either Forced Circulation (FC) or Natural Circulation (NC) mode; the FC mode requires power supplied by the Electricity Distribution System (EDS). However, volcanic ashfall may clog the ACS filters, potentially causing system failure. Furthermore, ash accumulation can also affect the filters within the Emergency Diesel Generators (EDGs) and the Heating, Ventilation, and Air Conditioning (HVAC) system. These effects ultimately influence whether the EDS can provide electricity to the ACS to enable FC mode operation.

To restore decay heat removal capability, repair tasks involve replacing the malfunctioning filters. During the replacement, the clogged ash on the filter would be disturbed, dislodged, and subsequently dispersed into the surrounding work environment, increasing airborne ash concentration. This elevated ash concentration reduces visibility for personnel, which may adversely affect the performance of repair tasks.

The analysis of filter malfunctions is conducted by the Malfunction Analysis Module within the SSCs States Solver, as shown in Fig. 1, where methodological details are available in previous work [2]. Therefore, this study primarily concentrates on the Repair Analysis Module related to filter replacement and illustrates how the HEP is dynamically updated in response to spatiotemporal environmental variations, as detailed in the following section.

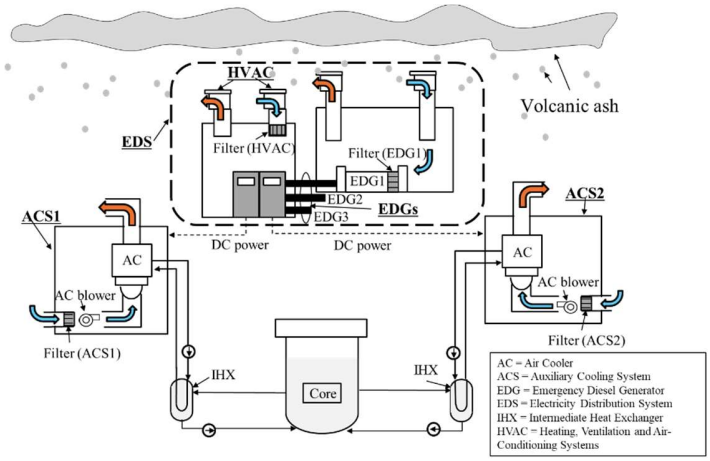

FIGURE 2. The schematic of interactions between the ACSs and adjacent components/systems under volcanic ashfall.

III.B. HEP Update

III.B.1. HEP Estimation

The concept underlying the estimation of HEP in this study is introduced here. First, a task structure analysis must be conducted. An example of such a task structure, represented by a Crew Response Diagram (CRD), is presented in Fig. 3.

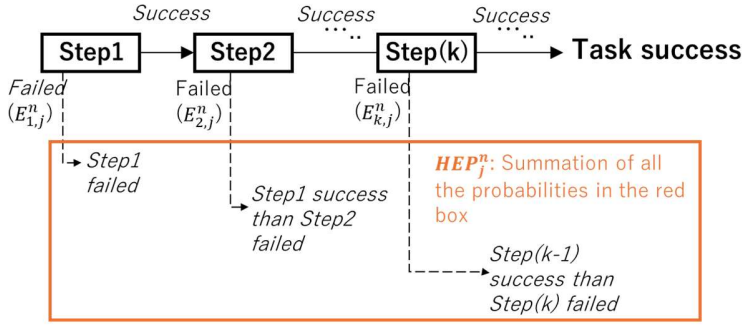

FIGURE 3. Example of task structure analysis via the Crew Response Diagram (CRD).

After conducting the task structure analysis and breaking down its constituent steps, the HEP for the j_{th} SSC at the n_{th} time step, denoted as HEP_j^n, can be expressed as follows:

$$HEP_j^n = 1 - \prod_{k=1}^{K}\left[1 - P\left(E_{k,j}^n \,|(1 - E_{k-1,j}^n)\right)\right] \tag{3}$$

$$P\left(E_{k,j}^n \,|\, (1 - E_{k-1,j}^n)\right) = \frac{d \times E_{k,j}^n}{d+1} \qquad [if\ k \neq 1] \tag{4}$$

$$P\left(E_{k,j}^n \,|\, (1 - E_{k-1,j}^n)\right) = E_{1,j}^n \qquad [if\ k = 1] \tag{5}$$

where $E_{k,j}^n$ represents the human error probability for the k_{th} step at the n_{th} timestep for the j_{th} SSC. The parameter d in Eq. (4) accounts for the dependence level between consecutive steps (k_{th} and $k-1_{th}$) to model the conditional probability of $E_{k,j}^n$. Several factors influence this dependence level, including the similarity of equipment operated at each step, the time lag between step executions, and the spatial distance between operation locations. Additionally, the operator's skill proficiency plays a significant role. For the different dependence levels of complete dependence (CD), high dependence (HD), moderate dependence (MD), low dependence (LD), and zero dependence (ZD), d equal to 0, 1, 6, 19, and ∞, respectively. Furthermore, $E_{k,j}^n$ can be estimated using the following equation:

520

$$E_{k,j}^{n} = NHEP_{k,j}^{n} \times PSF_{j}^{n} \tag{6}$$

where $NHEP_{k,j}^{n}$ represents the nominal HEP, and PSF_{j}^{n} denotes the performance shaping factor for the k_{th} step at the n_{th} time step for the j_{th} SSC. In this research, PSF_{j}^{n} is further decomposed into the following components:

$$PSF_{j}^{n} = PSF_{base,j}^{n} \times PSF_{enviromen\ ,j}^{n} \tag{7}$$

where $PSF_{enviroment,j}^{n}$ represents the influence of dynamic environmental conditions, and $PSF_{base,j}^{n}$ accounts for all remaining contributions that are independent of environmental changes.

In this study, the repair task is assumed to consist of four sequential steps: (1) Loosen the screw, (2) Take-off the old filter, assuming LD with the former step (3) Install the new filter, assuming HD with the former step, and (4) Fasten the screw, assuming LD with the former step. Furthermore, the traditional HRA method, THERP, is employed as an example to estimate both the $NHEP_{k,j}^{n}$ and the $PSF_{base,j}^{n}$. The procedure for updating the $PSF_{enviroment,j}^{n}$ at each time step is detailed in the following section.

III.B.2. Update $PSF_{enviroment,j}^{n}$ in Response to Environmental Spatiotemporal Change

Based on the hypothetical repair task described in Section III.A, the update process of $PSF_{enviroment,j}^{n}$ at each time step in the Repair Analysis Module is divided into two stages: (1) estimating visibility according to changes in the volcanic ash concentration in the working environment, and (2) updating $PSF_{enviroment,j}^{n}$ based on the resulting changes in visibility.

Before estimating visibility, it is necessary to calculate the volcanic ash mass concentration in the working environment within the Plant State Solver (as illustrated in Fig. 1). This calculation accounts for the ash dislodged from the malfunctioning filter during the repair task. In this study, Fick's first law is applied to the continuity equation to model the diffusion process of the dislodged ash. Consequently, the spatiotemporal-dependent ash mass concentration, $c(r,t)$ [kg/m^3], is governed by the following equation:

$$\frac{\partial c(r,t)}{\partial t} = D\nabla^2 c(r,t) + S(r,t) \quad [r \in \mathbb{R}^3, t > 0] \tag{8}$$

where $\boldsymbol{D}$ [m^2/s] is diffusivity constant, and $\boldsymbol{S(r,t)}$ represents the source term for volcanic ash generation or absorption. Since the dislodged ash from the malfunctioning filter should be considered as $\boldsymbol{S(r,t)}$, a simplification is made by assuming that the dislodged ash is released instantaneously at the beginning of the task rather than continuously over time. Under this assumption, $\boldsymbol{S(r,t)}$ is set to zero, and the initial released ash mass concentration $\boldsymbol{M_0}$ [kg/m^2] around the released location $\boldsymbol{r_0}$ is defined as the initial condition. Meanwhile, at an infinite distance from the point of ash release, the ash concentration is assumed to be zero as the boundary condition. For a three-dimensional infinite domain, the classical analytical solution for $\boldsymbol{c(r,t)}$ under the given conditions is as below [3]:

$$c(r,t) = \frac{M_0}{(4\pi Dt)^{1/2}} e^{\left(\frac{-\|r-r_0\|^2}{4Dt}\right)} \quad [t > 0] \tag{9}$$

In this study, $\boldsymbol{r_0}$ is set as 0. Furthermore, considering the repetitive nature of the repair task, the contribution of all previously released ash masses can be treated as a linear superposition. Consequently, the expression for $\boldsymbol{c(r,t)}$ is expanded to:

$$c_j^n = \sum_{M=1}^{m} H(t_j^n - t_{j,M(start)}) \times \frac{M_{j,M}}{[4\pi D(t_j^n - t_{j,M(start)})]^{1/2}} \times e^{\left(\frac{-\|r_j^n\|^2}{4D(t_j^n - t_{j,M(start)})}\right)} \tag{10}$$

where c_j^n [kg/m^3] means the ash mass concentration when repairing j_{th} component at n_{th} timestep, and $t_{j,M(start)}$ [s] means the starting time of the M_{th} repair task for j_{th} component, and m means the order of the current task when repairing j_{th} SSC at n_{th} timestep. $H(\cdot)$ is the Heaviside step function ensuring that contributions from previous repair tasks are only considered when $t_j^n > t_{j,M(start)}$. $M_{j,M}$ [kg/m^2] is the released ash mass concentration from the M_{th} repair task. By setting the radial distance between the dislodged ash and the staff position as r_j^n[m], c_j^n at each timestep can be determined by using Eq. (10) within Plant State Solver.

521

Once the Plant State Solver calculates c_j^n, this information is transferred to the Repair Analysis Module within the SSCs States Solver to assess the impact of c_j^n on the visibility. Visibility is typically expressed as follows:

$$V_j^n = 3.912/\beta_{ext,j}^n \tag{11}$$

where V_j^n [m] denotes the visibility distance during the repair of the j_{th} component at the n_{th} timestep, and $\beta_{ext,j}^n$ [1/m] represents the extinction coefficient corresponding to c_j^n. When the diameter of the volcanic ash particles is significantly larger than the wavelength of visible light, the geometric scattering approximation can be applied [4], allowing $\beta_{ext,j}^n$ to be expressed as follows:

$$\beta_{ext,j}^n = 2\pi \sum_i r_i^2 n_j^n(r_i) \tag{12}$$

where $\boldsymbol{n_j^n(r_i)}$ [1/m^3] denotes the number density of ash particles with radius $\boldsymbol{r_i}$ during the repair of the j_{th} component at the n_{th} timestep. Accordingly, the impact of ash mass concentration on $\boldsymbol{V_j^n}$ can be estimated by applying the information of $\boldsymbol{c_j^n}$ from Eq. (10) to $\sum_i \boldsymbol{r_i^2 n_j^n(r_i)}$ in Eq. (12). Then, in this study, when $\boldsymbol{V_j^n}$ decreases to less than one meter, the $\boldsymbol{PSF_{enviroment,j}^n}$ is assumed to increase to a value of two. Moreover, the relationship between $\boldsymbol{PSF_{enviroment,j}^n}$ and $\boldsymbol{V_j^n}$ is modeled as an exponential decay function, as expressed in Eqs. (13) and (14).

$$PSF_{enviroment,j}^n = 1 + e^{2(1-V_j^n)} \qquad [if\ V_j^n \geq 1] \tag{13}$$

$$PSF_{enviromen\ ,j}^n = 2 \qquad [if\ V_j^n < 1] \tag{14}$$

III.C. Summary of the Case Explanation

This example demonstrates how transient environmental factors, exemplified by the dynamic evolution of ash concentration c_j^n, can be quantitatively linked to $PSF_{enviroment,j}^n$ in the context of updating HEP. Specifically, visibility V_j^n acts as an intermediary variable connecting environmental conditions with human performance. By embedding this mechanism within the proposed computational framework, transient environmental influences can be dynamically and bidirectionally integrated into HRA during repair tasks.

IV. RESULTS AND DISCUSSION

To further assess the framework's capability to bidirectionally respond to environmental spatiotemporal changes, an additional test case is introduced alongside the scenario described in Chapter III (hereafter referred to as AM1(DHRA)). This new case, named AM1 in the following discussion, fixes the value of $PSF_{enviroment,j}^n$ at one, thereby neglecting the influence of c_j^n. For each case, 500 samples are included in the analysis.

Fig. 4(a) illustrates an example of ACS state history for the AM1(DHRA) case. The y-axis represents the ACS states: forced circulation (value 2), natural circulation (value 1), and failure (value 0). Correspondingly, Fig. 4(b) depicts the temporal variation of ash concentration in the room housing the ACS, accounting for ash dislodged from the malfunctioning filter once repair operations commence following filter failure. Furthermore, Fig. 5 compares the ash concentration histories in alternative rooms containing different ACS units and EDGs. It is observed that the equilibrium room ash concentration increases with the number of repair tasks performed, indicating that the cumulative effects of prior repairs on the same component/system are considered. Additionally, the rate of increase in equilibrium room ash concentration is more pronounced in EDG environments than in ACS, owing to the higher repair frequency of EDGs, which stems from their greater inflow rates [2] and consequently leads to higher failure rates compared to ACS units.

Subsequently, two indices are employed to evaluate the analytical results of AM1(DHRA) and AM1 from the perspectives of heat removal ability (Index 1, presented in Fig. 6(a)) and repair cost (Index 2, shown in Fig. 6(b)). The definitions of Index 1 and Index 2 are provided below:

$$Index1 = \frac{0.5\times(t_{ACS1-} + t_{ACS2-}) + 0.25\times(t_{ACS1-} + t_{ACS2-})}{24\ hours} \tag{15}$$

$$Index2 = t_{repai} \times n_{staff\ per\ repair} \tag{16}$$

where t_{ACS1-} represents the total operating time of ACS1 in forced circulation mode in a sample, t_{re} denotes the total repair time for all filters in a sample, and $n_{staff\ per\ repair}$ corresponds to the number of staff assigned to perform a repair task (three staff members in this study). An Index 1 value of one indicates that both ACS1 and ACS2 operated continuously in FC mode over the past 24 hours. As shown in Fig. 6(a), incorporating dynamic HRA that accounts for environmental spatiotemporal changes during repair task analysis shows a detrimental effect on decay heat removal capability.

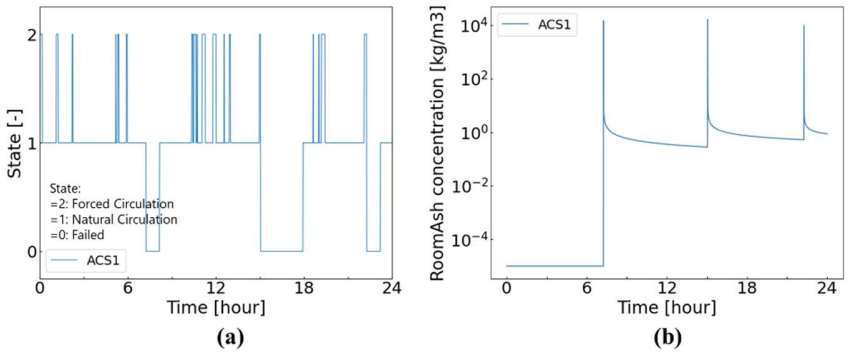

FIGURE 4. A sample of considering the environmental spatiotemporal change on the repair task: (a) ACS's state history, and (b) historical data of the ash concentration in the room housing ACS1.

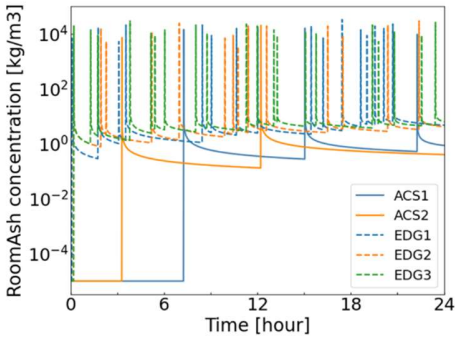

FIGURE 5. Historical data of the ash concentration in the room housing different components/systems.

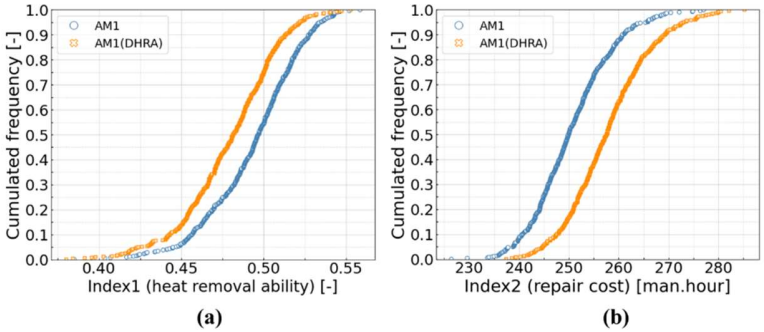

FIGURE 6. The cumulated frequency to Index 1 (heat removal ability) and Index 2 (repair cost) among different cases, including w/o considering the environmental spatiotemporal change on the repair task.

To further explore the factors contributing to the differences in Index 1 between the cases, Fig. 7(a) shows that the average repair time for an ACS filter is longer in the AM1(DHRA) case. This increase is attributed to the reduced visibility caused by ash dislodged from repeatedly replaced malfunctioning filters, as reflected in the dynamic updating of HEP within the Repair Analysis Module. Concurrently, the longer average repair time reduces the frequency of ACS repairs, as depicted in Fig. 7(b), resulting in only a slightly higher total ACS repair time in AM1(DHRA) compared to AM1 (Fig. 7(c)). This is consistent with the marginally lower total ACS operating time observed in AM1(DHRA) (Fig. 7(d)). However, since the failure frequency of

523

EDGs is higher than that of ACS units, the reduction in operating time is more pronounced for EDGs when environmental spatiotemporal changes are considered in repair task analysis. Therefore, as shown in Fig. 7(e), the ratio of operating time in FC mode to total operating time is significantly lower in AM1(DHRA), indicating that the FC-to-total time ratio is a more critical factor influencing heat removal capability (Index 1) than total operating time alone (Fig. 7(d)). Finally, the relationship between Index 1 and Index 2, presented in Fig. 7(f), reveals that economic efficiency related to repair tasks tends to be overestimated if the influence of environmental spatiotemporal changes is neglected.

In summary, these results demonstrate the capability of the proposed CMMC-based framework to quantitatively capture the uncertainties arising from bidirectional environmental spatiotemporal changes on repair task analysis from multiple perspectives, including heat removal performance and economic efficiency. Moreover, the framework facilitates intuitive investigation and identification of key factors influencing the defined indices.

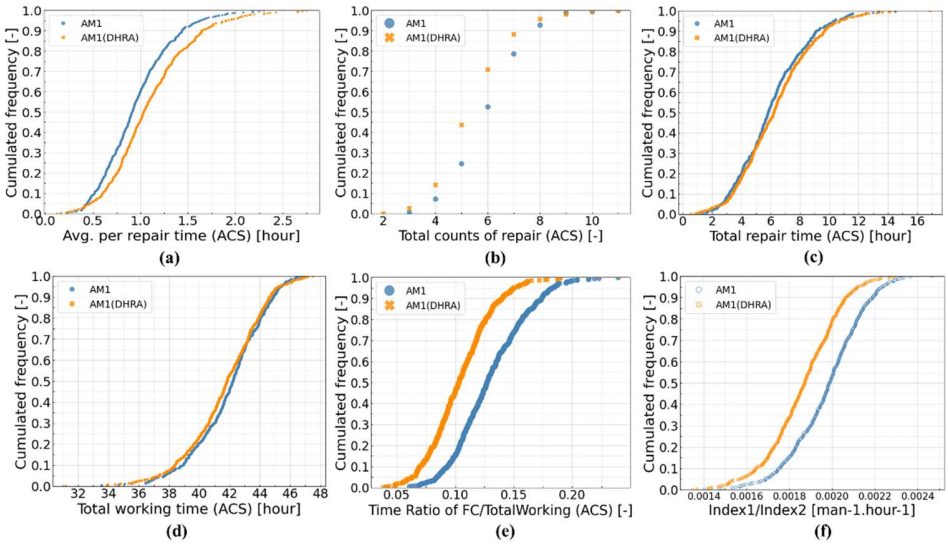

FIGURE 7. The cumulated frequency to the parameters related to the Index 1 investigation among different cases.

V. CONCLUSIONS

To realize dynamic HRA, this study proposes a computational framework that integrates the CMMC method. In summary, the framework demonstrates the following key features: (1) incorporating and quantifying the effects of environmental spatiotemporal variations on human behavior through the Markov chain process within the CMMC method; (2) translating changes in human behavior into dynamic events that provide feedback to the evolving environment via Monte Carlo sampling; and (3) enabling bidirectional dynamic interactions between humans and the environment within the developed computational framework. Additionally, an example application of the proposed framework is presented to illustrate its potential in quantitatively capturing uncertainties arising from environmental spatiotemporal influences on repair task analysis. However, the current stage of this study is limited to the case of filter replacement in response to volcanic ashfall hazards, and the relationship between visibility in the working environment and PSFs still requires further investigation. Future work will focus on conducting additional case studies to validate and expand the applicability of the proposed framework.

REFERENCES

[1] A. D. Swain and H. E. Guttmann, *Handbook of human-reliability analysis with emphasis on nuclear power plant applications. Final report*, NUREG/CR-1278, U.S. (1983).

[2] C. Y. Li, A. Watanabe, A. Uchibori and Y. Okano, "The development of petri net-based continuous Markov chain Monte Carlo methodology applying to dynamic probability risk assessment for multi-state resilience systems with repairable multi-component interdependency under longtermly thereat," *Journal of Nuclear Science and Technology*, **61** (7), pp. 935-957 (2024).

[3] "Chapter 2 Fickian Diffusion," *https://ocw.snu.ac.kr/node/14445/* (2018).

[4] C. H. Jung and Y. P. Kim, "Particle Extinction Coefficient for Polydispersed Aerosol Using a Harmonic Mean Type General Approximated Solution," *Aerosol Science and Technology*, **41** (11), pp. 994-1001 (2007).

ASRAM2025
www.asram2025.org
Asian Symposium on Risk Assessment and Management 2025
Pattaya, Thailand, 27 – 29 August 2025

A Study of Dynamic Human Reliability Assessment -Time and Environment Dependent Assessment of Human Error Probability.

Yutaka Takizawa[1], Sunghyon Jang[1] Yuya Otaki[2], Natsuki Shiraishi[2], Shuhei Matsunaka[2],

[1]*Hokkaido University: Kita-13jo, Nishi-5chome. Kita-ku, Sapporo, Japan*
[2]*TEPCO Systems Corporation: 37-28, Eitai 2-chome, Koto-ku, Tokyo, Japan*

ABSTRACT

The accident at the Fukushima Daiichi Nuclear Power Plant in March 2011 was characterized by multiple reactor units on the same site being impacted simultaneously, with the sequence of events remaining unclear and a wide variety of accident scenarios unfolding. As a result, the work environment became more complex and challenging than in a single-unit scenario.

The prevailing method in Japan for evaluating human error probability (HEP) focuses on whether the operator successfully completes the task according to documented procedures, and is inadequate for assessing the impact from the surrounding environment in that it is a discrete and conservative assessment.

The objective of our research is to obtain time- and space-dependent HEPs in human reliability analysis, taking into account influences from the changing surrounding environment.

We first obtained nominal HEPs for containment cooling operations using portable pumps in order to evaluate changes in HEPs due to ambient environmental effects for outdoor accident mitigation operations. Then, based on the case study of the accident at 1F, we determined the expected influence of the ambient environment and discussed a method to quantify the change in HEP.

In this study, we attempted to incorporate knowledge—previously unused in the nuclear field—regarding the effects of stress and time availability.

Keywords: Human Reliability Analysis (HRA), Extreme Condition, Human Error Probability (HEP), Fukushima Daiichi Nuclear Power Plant

I. Background

As a hallmark of the March 2011 Fukushima Daiichi Nuclear Power Plant (1F) accident, multiple reactor units housed at a single site were simultaneously impacted, the sequence of event propagation became unpredictable, and the accident scenarios exhibited a high degree of variability. As a result, the working environment became more complex, making on-site tasks significantly more challenging than would be the case for a single-unit scenario.

The prevailing methods for human error probability (HEP) estimation focus primarily on task success/failure under ideal execution of written procedures, and thus inadequately account for influences from the surrounding environment. Since the 1F accident, there has been a strong demand for methodologies capable of incorporating how harsh or extreme environmental conditions influence operators.

The objective of this study is to determine the HEP of work under the time- and space-dependent harsh environmental conditions that occur in nuclear power plants by means of dynamic human reliability analysis.

II. Containment Cooling Operations Using Portable Mitigation Equipment

We hereby describe the task scenario under evaluation. The scenario is based on the alternative reactor coolant injection operation using portable mitigation equipment, as outlined in CRIEPI Research Report O18011. Detailed sub-tasks were defined with reference to materials from Genkai Nuclear Power Plant [1].

The workflow of “Containment Cooling Operations Using Portable Mitigation Equipment” is shown in Figure 1.

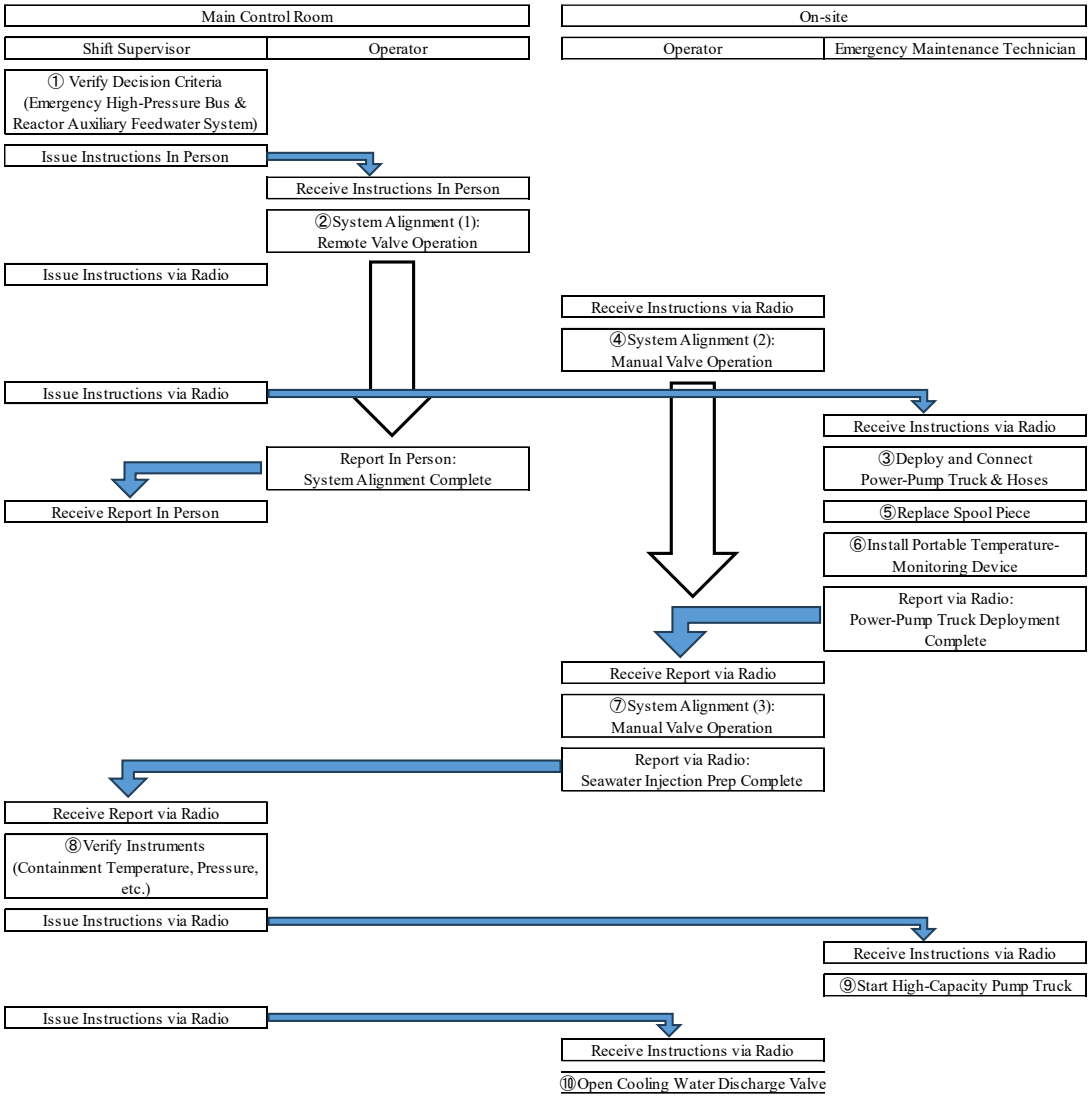

FIGURE 1. Flow of "Containment Cooling Operations Using Portable Mitigation Equipment"

III. Nominal HEP Evaluation on "Containment Cooling Operations Using Portable Mitigation Equipment"

We decomposed the constructed task into individual steps, categorized them by type, and determined the nominal HEP for each. The nominal HEP values were then obtained by referring to the TECHNIQUE FOR HUMAN ERROR RATE PREDICTION (THERP) [2] or certain communication steps, we consulted the O18011[3] report and applied the IDHEAS [4] method as a reference.

The nominal HEPs determined and their references are shown in Table I.

TABLE I. Nominal HEP values and references

Chapter	Task Type	Error Type	Nominal HEP	References
III.A.	Display Checks	Omission	3.30E-04	THERP Table 20-7 and O18011
III.B.1.		Selection Error	1.00E-03	THERP Table 20-9
		Check Error	1.00E-03	THERP Table 20-11
III.A.	Manual Valve Operation	Omission	3.30E-04	THERP Table 20-7 and O18011
III.B.3.		Selection Error	1.00E-03	THERP Table 20-13
		Operation Error	1.00E-03	THERP Table 20-14
III.A.	Remote Valve Operation	Omission	3.30E-04	THERP Table 20-7 and O18011
III.B.4.		Selection Error	1.00E-03	THERP Table 20-12
		Check Error	1.00E-03	THERP Table 20-12
III.A.	Mechanical System State Changes	Omission	3.30E-04	THERP Table 20-7 and O18011
III.B.5.		Selection Error	1.00E-03	THERP Table 20-13
		Operation/Execution Error	0.00E+00	O18011 Appendix B-④-1
III.C.	Communication	Failure to Transmit	1.40E-04	IDHEAS CFM E-3 and O18011
		Transmission Error	6.00E-03	THERP Table 20-5 and O18011
		Reception Error	1.30E-04	IDHEAS CFM SA-3 and O18011

III.A. Omission Errors in Procedure of "Containment Cooling Operations Using Portable Mitigation Equipment"

We determined the HEP for omission errors at each step. We assume that the procedures used for the evaluation include check-off boxes or blank spaces where the operator places checks. Therefore, we concluded that, from THERP Table 20-7 "Estimated probabilities of errors of omission per item of instruction when use of written procedures is specified*," the category "When procedures with check-off provisions are correctly used: 'Short list'" applies. In that case, the nominal HEP is 0.001 and the Error Factor (EF) is 3.

According to Appendix B-③-1 of the O18011 report, the procedures used domestically in Japan are formatted as tables or bulleted lists by action type—equivalent to the vertical-column style noted as a good practice in THERP Chapter 15 "Oral Instructions and Written Procedures." Based on that, we followed Chapter 15's guidance and adjusted the HEP to one-third of 0.001, resulting in a value of 0.00033.

III.B. Comision Errors in Procedure of "Containment Cooling Operations Using Portable Mitigation Equipment"

III.B.1. Display Checks

We define the "display check" task as visually inspecting a display to judge whether a reading is above or below a specified threshold—i.e., a True/False determination. We distinguish this from tasks that require recording numeric values, in which the raw number itself carries semantic importance.

We assume three possible failure modes in the display check step: "Omission," "Display Selection Error," and "Display Check Error." A "Display Selection Error" occurs when the operator selects the wrong display out of multiple available units. A "Display Check Error" occurs when the correct display is selected but the operator misjudges "True" or "False" during the check.

For "Display Selection Error," we judged that THERP Table 20-9 entry "(3) from similar-appearing displays that are part of well-delineated functional groups on a panel" applies. We took into account that all display checks in the tasks under consideration are performed within the Main Control Room (MCR). Under these conditions, the nominal HEP is 0.001 and EF is 3.

Next, for "Display Check Error," we determined that THERP Table 20-11 entry "(2) Analog meters: with easily seen limit marks" applies. In our scenario, all display checks involve verifying whether the reading is zero or not; thus, these displays effectively have easily visible limit marks. Accordingly, the nominal HEP is 0.001 and EF is 3.

III.B.2. Manual Valve Operation

We define "manual valve operation" as the portion of the system configuration task in which the operator travels on-site and physically manipulates a valve by hand.

We assume three failure modes for the manual valve operation step: "Omission," "Valve Selection Error," and "Valve Operation Error." A "Valve Selection Error" occurs when the operator manipulates a different valve than the intended one. A "Valve Operation Error" occurs when the operator does not recognize a jammed valve—leaving it in an open, closed, or partially open/closed state, which is not desired.

For "Valve Selection Error," we judged that THERP Table 20-13 entry "(1) Clearly and unambiguously labeled, set apart from valves that are similar in all of the following: size and shape, state, and presence of tags" applies. Under these conditions, the nominal HEP is 0.001 and EF is 3.

Next, for "Valve Operation Error," we determined that THERP Table 20-14 entry "(1) Given that a locally operated valve sticks as it is being changed or restored, * the operator fails to notice the sticking valve when it has a position indicator** only" applies. In this scenario, the nominal HEP is 0.001 and EF is 3.

III.B.3. Remote Valve Operation

We define "remote valve operation" as the portion of the system configuration task in which the operator manipulates a valve remotely from the MCR.

For the remote valve operation task, we assume three possible failure modes: "Omission," "Switch Selection Error," and "Switch Operation Error." A "Switch Selection Error" occurs when the operator actuates a different switch than intended. A "Switch Operation Error" occurs when the operator moves a two-position switch in the wrong direction.

For "Switch Selection Error," we determined that THERP Table 20-12 entry "(3) Select wrong control on a panel* from an array of similar-appearing controls**: arranged in well-delineated functional groups" applies. In such a case, the nominal HEP is 0.001 and EF is 3.

For "Switch Operation Error," we judged that THERP Table 20-12 entry "Turn a two-position switch in the wrong direction or leave it in the wrong setting" applies. Here, the nominal HEP is 0.0001 and EF is 10.

III.B.4. Mechanical System State Changes

Mechanical system state changes include flange installation, hose connection, replacement of a distance piece, and installation of a portable temperature-measuring device.

We assume three failure modes for mechanical system state changes: "Omission," "Selection Error," and "Operation/Execution Error." Since these steps are not covered by standard THERP tables, we referred to O18011 Appendix B-④-1 "Example of adapting estimated HEP tables for on-site operations and tasks (for equipment not addressed by THERP)" to perform the evaluation.

For "Selection Error," we determined that THERP Table 20-13 entry "(1) Clearly and unambiguously labeled, set apart from valves that are similar in all of the following: size and shape, state, and presence of tags*" applies.

Next, for "Operation/Execution Error," we set the HEP to zero based on the descriptions in O18011.

III.C. Communication

For tasks that convey instructions via communications, we analyzed separately the transmitting and receiving parties. We assume three failure modes: "Failure to Transmit," "Transmission Error," and "Reception Error," following the classification in O18011.

In O18011, Kirimoto et al. adopt the IDHEAS Crew Failure Mode "E-3: Failure to Initiate Execution" value to represent "Failure to Transmit." Although this IDM (IDHEAS) category originally addresses failure to initiate an action (e.g., starting a compensatory response), it can be interpreted as including failures to transmit instructions, reports, or communications. Accordingly, we set the HEP for "Failure to Transmit" at 0.00014.

For "Transmission Error," Kirimoto et al. note that THERP Table 20-5, which anticipates missing or incorrectly written information in the creation of procedure documents, is analogous to errors in message transmission; they treat it equivalently. Thus, we adopt HEPs of 0.003 for omission of a word and 0.003 for misspeaking, yielding a total of 0.006.

For "Reception Error," Kirimoto et al. refer to IDHEAS Crew Failure Mode "SA-3: Critical Data Misperceived" in O18011. Although originally intended for situations involving alarms or display readings, it is also applicable to scenarios in which instructions, reports, or communications provide critical information. Following their approach, we set the HEP at 0.00013.

III.D. Error Recovery Steps

We considered error recovery for tasks other than those involving communications. The evaluation follows the dependency assessment method described in THERP Chapter 10 "Dependence," and was conducted according to the following steps:

1. Set the baseline HEP. Note that this baseline HEP does not refer to the nominal HEP; rather, it is the HEP of the recovery step prior to the dependency adjustment.
2. O18011 Appendix B-③-1 states that, if there is no feedback from the immediately preceding task, "for recovery steps performed by oneself or another, select the same Table and Item as used to evaluate the failure of the prerequisite step." Therefore, we set the baseline HEP equal to the nominal HEP of the prerequisite step.
3. Determine dependency levels based on who performs the prerequisite step and who performs the recovery step.
4. Reference the Table II to assign dependency levels. In our evaluation, we assume that recovery is performed while referring to written procedures, which reduces the dependency level by one rank.
5. Use the baseline HEP and the dependency factor to compute the nominal HEP for the recovery step.

THERP Table 20-17 provides formulas for conditional failure probabilities of a task based on the success or failure of a preceding task, categorized by dependency level. According to those formulas, if the preceding (prerequisite) task fails, the conditional probability that the subsequent task (i.e., the recovery step) fails is given by:

$$\frac{1 + nE}{n + 1} \tag{1}$$

"E" is the original HEP of the error recovery step set, and n is the coefficient according to the dependency.
(n=0(CD), 1(HD), 6(MD), 19(LD), ∞(ZD)).

TABLE II. – Example Dependency Levels for Recovery by Others (Translated) [2]

		Stress Level	
		Normal	High
Characteristic	With people who are new to each other Chief on duty checking the behavior of a newcomer	ZD	LD
	Chief on duty recovering operator's error	LD	MD
	Between operators	MD	HD
	Operator recovering from the chief on duty's error	HD	CD

Note: If the error recovery is performed with the procedure manual, lower the dependence by one rank.

III.D. Nominal HEP Evaluation Results

The results of the nominal HEP evaluation are shown in Table III, and are in close order compared to the results of O18011. We found the degree of agreement to be sufficient to evaluate the influence of the environment.

TABLE III. Comparison of the results of this study's evaluation with O18011

Task	O18011	OUR STUDY	RATIO
Emergency Response Headquarters decides to prepare for water injection using portable mitigation equipment	5.00E-04	4.05E-03	8.10E+00
Instructions are given by radio from the headquarters or central control room	9.82E-03	6.14E-03	6.25E-01
On-site instructions are received by radio	1.30E-04	1.30E-04	1.00E+00
Installation of large water trucks (large-capacity pump trucks)	2.50E-04	8.05E-03	3.22E+01
Submit report on completion of installation	9.82E-03	6.14E-03	6.25E-01
Installation completion report received	1.30E-04	1.30E-04	1.00E+00
Decide to start water injection	5.00E-04	2.70E-03	5.40E+00
Send out instructions to start water injection	1.40E-04	1.40E-04	1.00E+00
Receive instructions to begin water injection	1.30E-04	1.30E-04	1.00E+00
Start water injection	1.50E-04	1.22E-04	8.12E-01
Entire scenario	2.14E-02	5.17E-02	2.41E+00

IV. Assessment of Influences from Surrounding Environmental Changes

Among the environmental changes anticipated in a multi-unit event, we chose to evaluate the increase in radiation dose.

Here, we investigated how an increase in radiation dose leads to task failures.

An increase in radiation dose acts as a stressor on human operators. This understanding is roughly consistent across many HRA methodologies. Therefore, the process from increased radiation dose to the occurrence of human error follows three stages: “increase in radiation dose,” “increase in stress,” and “rise in HEP.”

The first is the physical effects of wearing protective clothing. We included this in our assessment because it is thought to cause poor visibility, restricted movement, heat, and reduced sensation in the fingers due to the multiple layers of gloves.

The second is the psychological impact of increased radiation dose. We evaluated the failure of crew members to understand that their actions could endanger their own lives or the lives of their colleagues.

The third was the increase in cognitive load due to the increased dose. Under high radiation doses, work time is limited and crew members are forced to make decisions such as evacuation, retreat, and crew change. In this case, the crew's attention may be focused not on the work but on the dosimeters, etc. Therefore, it was judged necessary to evaluate this as an effect of the environment.

Fourth is time pressure. We considered the decrease in the time available for work under high radiation dose.

Because different HRA methods interpret the process by which increasing radiation dose leads to increased stress, and by which increased stress leads to a higher HEP in varying ways, we provide an explanation here.

In first-generation HRA methods, such as THERP and SPAR-H, stress is evaluated comprehensively via Performance Shaping Factors (PSFs), without assuming any specific model.

On the other hand, second-generation HRA methods, which emphasize qualitative scenario analysis, lack a mechanism for quantitative reflection, but they address environmental factors and psychological pressure as contexts that can provoke failures.

Based on these insights, we consider dividing stress into four categories—physical stress, psychological stress, cognitive stress, and temporal stress—for analysis.

We define as “physical stressors” those factors that affect the body physically, such as lighting, temperature, noise, vibration, and poor footing at the worksite. In the context of increased radiation dose, donning protective gear can cause reduced visibility, respiratory difficulty, and movement constraints, all of which qualify as physical stressors.

We define “psychological stressors” as factors such as tension, anxiety, and fear that act psychologically. Working under high-dose conditions inherently involves psychological stress.

We define “cognitive stressors” as those that induce cognitive load—such as multitasking—resulting in phenomena like attentional narrowing.

We define “temporal stressors” as those induced by time pressure. Unlike the PSF “time available,” which simply evaluates failures due to time expiration, temporal stressors encompass situations where caution is compromised or when recovery steps are intentionally omitted due to rotation schedules constrained by dose limits.

To quantitatively evaluate the classified stressors, we believe it is necessary to incorporate psychological or physiological insights in addition to the qualitative analysis found in second-generation methods.

ACKNOWLEDGMENTS

The author would like to thank Hokkaido University for providing an excellent research environment.

I am especially grateful to Dr. Jang of Hokkaido University for valuable discussions and cooperation throughout this research.

I also greatly appreciate the contributions of Mr. Otaki, Mr. Shiraishi, and Mr. Matsunaka from TEPCO Systems Corporation, whose technical insights and cooperation were instrumental in advancing this study.

Their expertise and support will be greatly appreciated as this research continues.

REFERENCES

[1] Kyushu Electric Power Co., Genkai Nuclear Power Plant No.3 and No.4 Reactors, Supplementary Explanatory Material on the Conformity Status of "Examination Criteria for Technical Capability of Installers of Commercial Power Reactors to Implement Measures Necessary to Prevent the Occurrence and Spread of Major Accidents" (in Japanese), July2016

[2] Handbook of Human Reliability Analysis with Emphasis on Nuclear Power Plant Applications Final Report, NUREG/CR- 1278 SAND80-0200 RX, AN Printed August 1983

[3] -The Human Reliability Analysis (HRA) guide with emphasis on the narrative (2018) -Development of qualitative analysis methods and analysis models for tasks on extreme conditions-

[4] An Integrated Human Event Analysis System (IDHEAS) for Nuclear Power Plant Internal Events At-Power Application Volume 1, NUREG-2199, Vol. 1,

ACT-R-BASED HUMAN DIGITAL TWINS OF NUCLEAR POWER PLANT OPERATOR PERFORMANCE FOR ADVANCING HRA DATA COLLECTION

Xingyu Xiao[1], Meng Kong[1], Jiejuan Tong[1], Shunshun Liu[2], Qianqian Jia[1], Hongru Zhao[1], Jun Zhao[1], Jingang Liang[1], Haitao Wang[1]

[1] Institute of Nuclear and New Energy Technology, Tsinghua University, Beijing, 100084, China Email: xxy23@mails.tsinghua.edu.cn, jingang@tsinghua.edu.cn
[2] CNNC Shandong Nuclear Energy Co., Ltd, Qingdao, 266071, Shandong China.

ABSTRACT

Traditional human reliability analysis (HRA) relies predominantly on experiments involving live operators. However, the advent of next-generation reactor designs, with novel interfaces and procedures, has rendered conventional HRA data obsolete. These new systems face significant challenges: insufficient operational experience and the inefficiency inherent in traditional human-in-the-loop experimental methods. This study pioneers an ACT-R-based human digital twins (HDTs) methodology that fully implements operator cognition through the cognitive architecture's declarative memory, procedural knowledge, and perceptual-motor modules to predict operator task completion times and error probabilities. Experiments were conducted on Tsinghua University's HTGR simulator under various conditions, including multi-parameter queries with interface switching, parameter queries without switching, pure three-phase AC operations, and button-press interactions. The reliability of these processes was supported by the predominance of three-phase AC operations, which minimizes error incidence. The results indicate that the ACT-R based HDT simulation framework not only accurately forecasts response times, suggesting a viable alternative to traditional HRA data collection methods for advanced nuclear reactor environments.

Keywords: Human Reliability, Human Performance Management, ACT-R, Human Digital Twins

I. Introduction

Despite ongoing advancements in automation and digital instrumentation, human operators play a pivotal role in ensuring the safety and reliability of nuclear power plants (NPPs), particularly during abnormal or accident conditions. Traditional human reliability analysis (HRA) approaches rely heavily on two main sources of data: (1) historical records from past operational events and (2) operator-in-the-loop (OITL) experiments conducted within simulator environments. The latter category includes well-known programs such as HuRex, SACADA, and SHEEP, which systematically capture human performance data under controlled yet realistic conditions. By combining empirical evidence from actual plant operations with carefully designed experimental scenarios, these methods have helped analysts identify important human error mechanisms and quantify error probabilities.

However, while these approaches have proven effective for conventional reactor designs, their applicability is increasingly challenged by the rapid deployment of next-generation reactors, including small modular reactors (SMRs) [1] and Generation IV systems [2]. There are many innovations involve the adoption of digital Instrumentation and Control (IC) systems [3], computerized operating procedure systems (COPS) [4], and advanced human–machine interfaces (HMIs) [5] associated with next-generation nuclear reactors. While these technological shifts promise to reduce operator workload and improve situational awareness, they also introduce new complexities. For instance, the High-Temperature Gas-cooled Reactor (HTGR) design mandates that a single operator concurrently supervise multiple reactor units [6]. Consequently, error pathways may differ substantially from those observed in legacy systems. Existing HRA data and models, derived from traditional analog control rooms, may therefore be of limited utility, as they do not fully capture the cognitive demands associated with next-generation control rooms.

Chief among them is the scarcity of operational experience with next-generation systems, leading to insufficient or non-representative datasets. Moreover, the resourceintensive nature of traditional OITL experiments—requiring significant time, personnel, and simulator availability—runs counter to the growing need for more agile and cost-effective data collection paradigms. Consequently, while historical data and OITL experiments have long formed the backbone of HRA, the emergence of advanced reactor designs underscores the necessity for innovative, scalable approaches to ensure accurate and reliable human performance assessment.

To address these gaps, this study proposes a mechanistic simulation framework grounded in the Adaptive Control of Thought-Rational (ACT-R) cognitive architecture. Experiments were conducted on Tsinghua University's HTGR simulator under various conditions, including multi-parameter queries with interface switching, parameter queries without switching, pure three-phase AC operations, and button-press interactions. The reliability of these processes was supported by the predominance of three-phase AC operations, which minimizes error incidence. To further evaluate ACT-R's predictive capabilities regarding operator errors, two rapid-response tasks were designed: one involving state recognition across reactor startup, normal operation, accident conditions, and shutdown; and the other requiring the enumeration of alarm signals on the interface. The main contributions are follows:

• Developing a mechanistic simulation framework that captures operator cognition and decision-making processes with a high degree of fidelity, reducing reliance on costly live-operator experiments.
• Predicting task completion times and error probabilities in the context of advanced nuclear reactor control tasks, including both routine procedures and rapid-response emergency scenarios.
• Validating the proposed framework through systematic experiments conducted on a high-temperature gas-cooled reactor (HTGR) simulator, thereby providing empirical evidence of the model's accuracy and practical relevance.
• Proposing an alternative HRA data collection paradigm that can complement or potentially replace large-scale human-in-the-loop testing, thus improving both the efficiency and the scope of safety analyses for next-generation nuclear power plants.

II. Methodology

II.A. The framework of this study

The methodology framework of this study, as illustrated in Figure 2, comprises three interconnected phases: (1) simulation task and scenario development, (2) ACT-R cognitive architecture modeling, and (3) experimental validation. This structure systematically investigates the human reliability factors in safety-critical systems through computational modeling and empirical verification. The initial phase establishes the operational context through rigorous scenario development using some abnormal operating procedures as a case study. Subsequent cognitive modeling employs the ACT-R architecture to formalize human mechanisms under stress conditions. The final experimental phase validates model predictions through human performance metrics collection and comparative analysis.

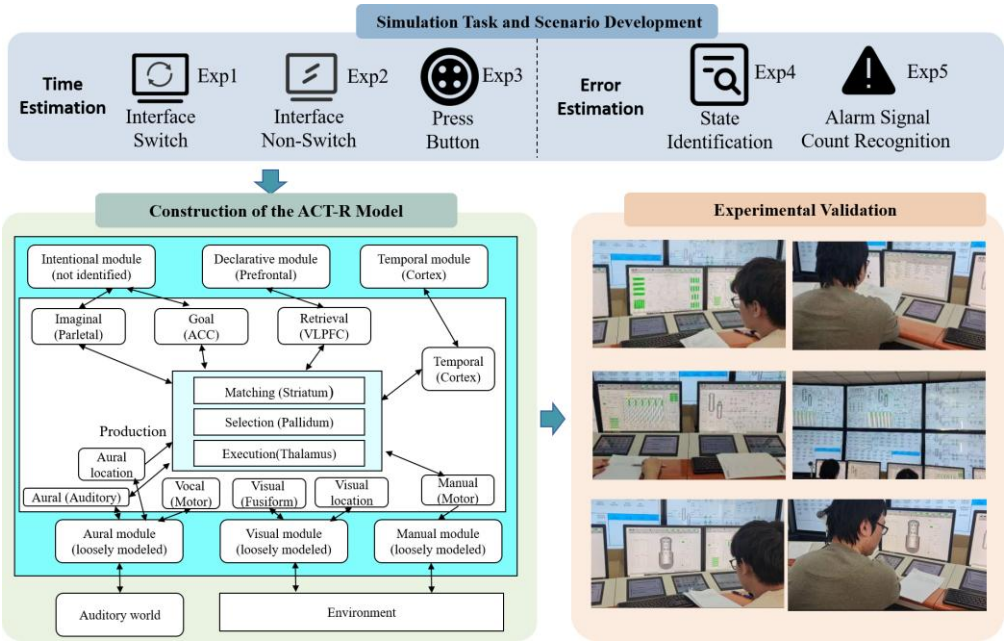

FIGURE 1. THE FRAMEWORK OF THIS STUDY

II.B. Stage 1: Simulation Task and Scenario Development

In this section, some straightforward operational processes were selected for experimentation. Given the unique demands of nuclear power plant operations, every operator action must be accompanied by a three-way communication with the shift supervisor. To simulate this condition, our volunteer engaged in such triadic interactions. Consequently, errors were seldom observed in this experimental setup, and our focus was confined to evaluating the temporal plausibility of the ACT-R simulation. Additionally, two supplementary experiments were designed that required instantaneous responses from the operators, thereby enabling the collection of error data.

As for time estimation, the experiment involves implementing response procedures under abnormal conditions, as depicted in Figure 2. Three experimental conditions were established: Experiment 1 entails interface switching; Experiment 2 does not require interface switching; and Experiment 3 involves a manual action (i.e., pressing a button).

Emergency Operational Procedure Exp 1

- The supervisor issues the directive to initiate Procedure E0.
- Under Operating Procedure E-0, the following conditions are evaluated: Verify whether the RFP percentage of Unit 3, 4, 5 exceeds 30%.
- Subsequently, the process advances to Operating Procedure E1.
- Under this procedure, if the power generation is less than 300 (units), Procedure ES-1.2 is initiated.
- Within Procedure ES-1.2, the following verifications are conducted: For Reactor 2's primary loop hot helium, confirm whether the temperature is exactly 750 °C and the pressure is 7.01 MPa.
- For Reactor 4's primary loop hot helium, confirm whether the temperature is 749.9 °C and the pressure is 7.01 MPa.
- If the temperature of the steam main pipe exceeds 560 °C, transition to the subsequent procedure.
- End.

Emergency Operational Procedure Exp 2

- The supervisor issues an order to initiate the operating procedure.
- The operator then executes Procedure E-0 by navigating to the "4# Main Helium Fan" interface and verifying whether the inlet temperature of the primary loop A fan exceeds 200 °C; if it does, the operator proceeds to Procedure ES-0.1.
- Next, under Procedure ES-0.1 (Reactor Trip Response), the operator accesses the "4# Reactor SPDS" to determine if the flow ratio between the first and second circuits is exactly 0.984, after which Procedure FH-H.1 is initiated.
- Finally, the operator implements Procedure FR-H.1 by navigating to the "4# SG Accident Venting" display to confirm that the pressure is maintained at 0.1 MPa and the temperature at 20 °C.

Emergency Operational Procedure Exp 3

- The operator must determine whether the power output of Reactor 4 exceeds 30% of the Rated Full Power (RFP).
- If the power is greater than 30% RFP, the operator must press the emergency shutdown button.
- If the power is less than 30% RFP, the operator should not press the emergency shutdown button.

FIGURE 2. CONTENT OF EXPERIMENTED EMERGENCY OPERATIONAL PROCEDURES

II.C. Stage 2: Construction of the ACT-R model

The ACT-R cognitive architecture model was implemented using the Lisp programming language. This required decomposing complex operational tasks into granular procedural branches. The most intricate experimental task (Exp2) was selected as a representative case for detailed modeling. As illustrated in Figure 3, the left panel demonstrates the refined operational protocol of Exp2, while the right panel presents the corresponding Lisp code implementation. This dual representation systematically maps procedural requirements to executable cognitive operations within the ACT-R framework.

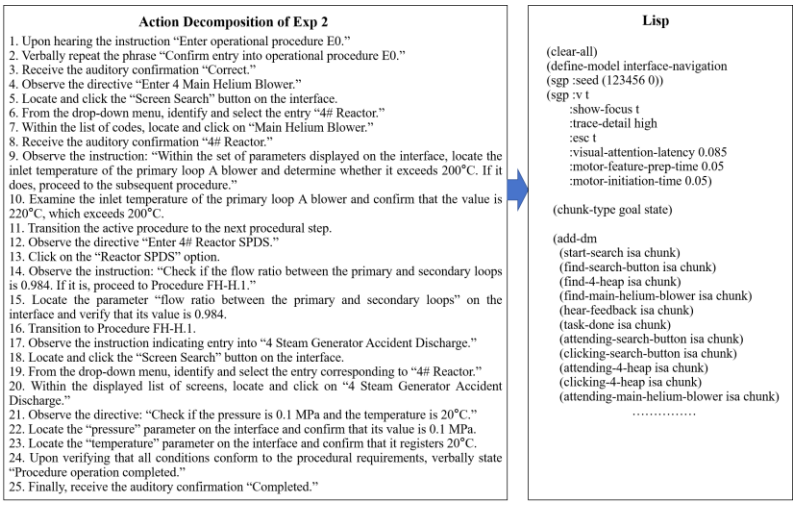

FIGURE 3. INTEGRATED SCHEMATIC DIAGRAM OF EXP2 BASIC OPERATIONS AND REFINED PROTOCOLS FOR LISP MODEL CONSTRUCTION

For simpler experimental tasks (Exp1 and Exp3), analogous decomposition was performed as shown in Figure 4. The modeling process systematically addressed six core cognitive components: (1) auditory processing of system alerts, (2) verbal response generation, (3) button press operations, (4) decision-making mechanisms, (5) parameter retrieval from interface elements, and (6) procedural switching logic. Each cognitive operation was encoded as production rules with associated latency parameters derived from empirical human performance data.

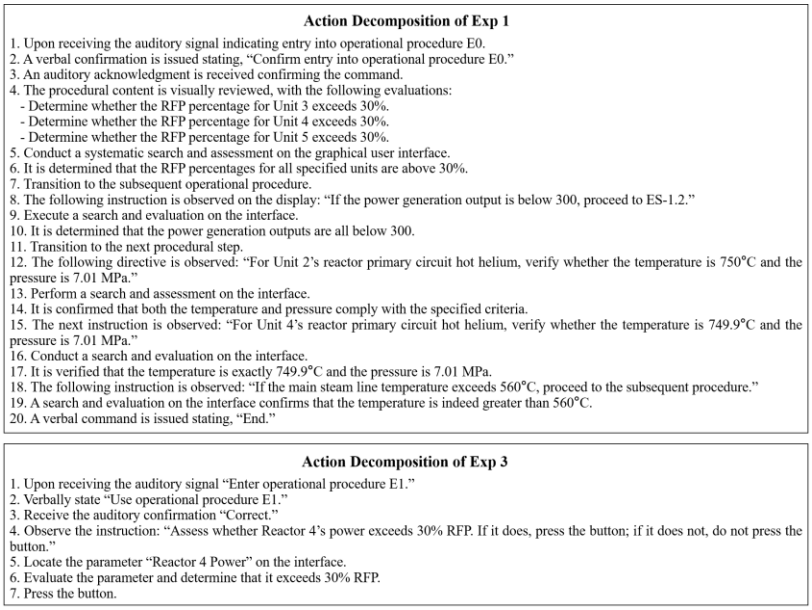

FIGURE 4. REFINED PROTOCOLS OF EXP1 AND EXP3 FOR LISP MODEL CONSTRUCTION

All model implementations incorporated ACT-R's default temporal parameters for basic cognitive operations. Task-specific adjustments were made through declarative memory chunk activation levels and procedural rule conflict resolution mechanisms. This multi-layered approach enabled the model to simulate both routine operations and exception handling scenarios observed in human operators.

II.D. Stage 3: Experimental Validation on HTGR

To ensure the relevance and validity of the experimental data, all participants were graduate students majoring in nuclear engineering at Tsinghua University and had prior exposure to control room simulators. Before the experiment, the first author served as the lead experimenter and provided a standardized training protocol to all participants. This included: (1) a briefing on the background and functional logic of the HTGR plant and its emergency procedures; (2) a step-by-step interface walkthrough to ensure participants were familiar with all interactive elements of the simulator; and (3) a series of pre-experimental rehearsal sessions designed to help participants internalize the operational context, understand the procedural logic, and reduce task unfamiliarity. All training activities were conducted in a consistent and structured manner to improve the reproducibility of the study and ensure that participants' cognitive behavior during the experiment reflected realistic nuclear operational scenarios.

TABLE I. Overview of Data Collection Across Experimental Paradigms: Time and Error Estimation

Exp	1	2	3
Sample	5	5	12

Table I summarizes the data collection across the experimental paradigms for time and error estimation. For the time estimation experiments, three distinct protocols were implemented, Exp1, Exp2, and Exp3, with sample sizes of 5, 5, and 20, respectively. In contrast, the error estimation paradigm was evaluated using two protocols (Exp4 and Exp5), yielding sample sizes of 20 and 26, respectively.

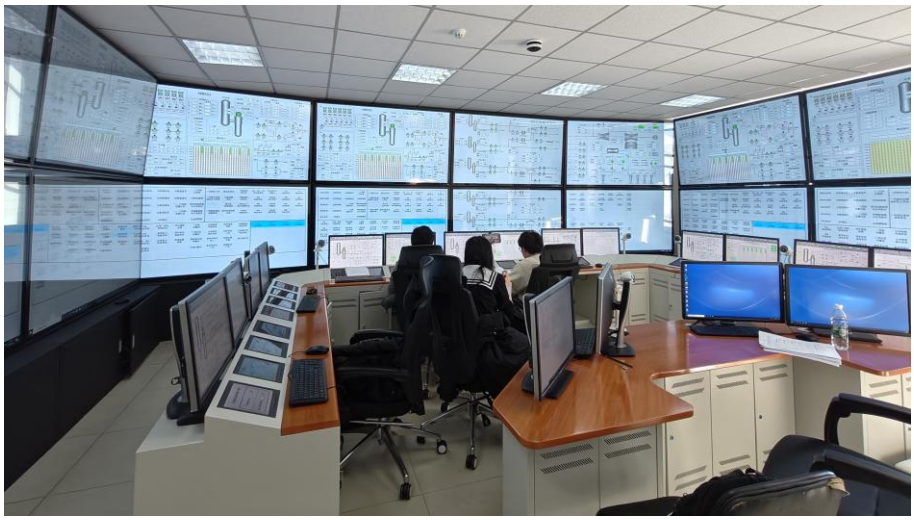

FIGURE 6. HTGR SIMULATOR AT TSINGHUA UNIVERSITY'S INSTITUTE OF NUCLEAR ENERGY TECHNOLOGY (1:1)

III. Results and Evaluation

In order to assess the temporal validity of the HDT constructed using ACT-R, we simulated the entirety of Exp1-Exp3 and identified several key time points within these experiments. The corresponding simulation times were then extracted to facilitate a comparison between the experimental results and the simulation outcomes.

Figure 7 (a) illustrates the five experimental trials of Exp1, comparing the duration of each procedural step as well as the cumulative time between the simulation and the actual experiment. The comparison indicates that both the overall and the individual component times are in close agreement. In the right panel (b), the figure presents a comparison of the mean and variance for two specific segments: (i) from hearing the correct stimulus to switching to Procedure E1, and (ii) from the initiation of Procedure E1 to the initiation of Procedure ES-1.2. For the first segment, the actual mean duration is 5.3722 s while the simulated mean is 5.4777 s, with variances of 1.4922 and 0.0139, respectively. For the second segment, the actual and simulated means are 5.7667 s and 5.485 s, respectively, with corresponding variances of 1.5103 and 0.01136. These results suggest that, overall, the mean durations are largely consistent between the experimental data and the ACT-R simulation, although the simulation exhibits significantly lower variance.

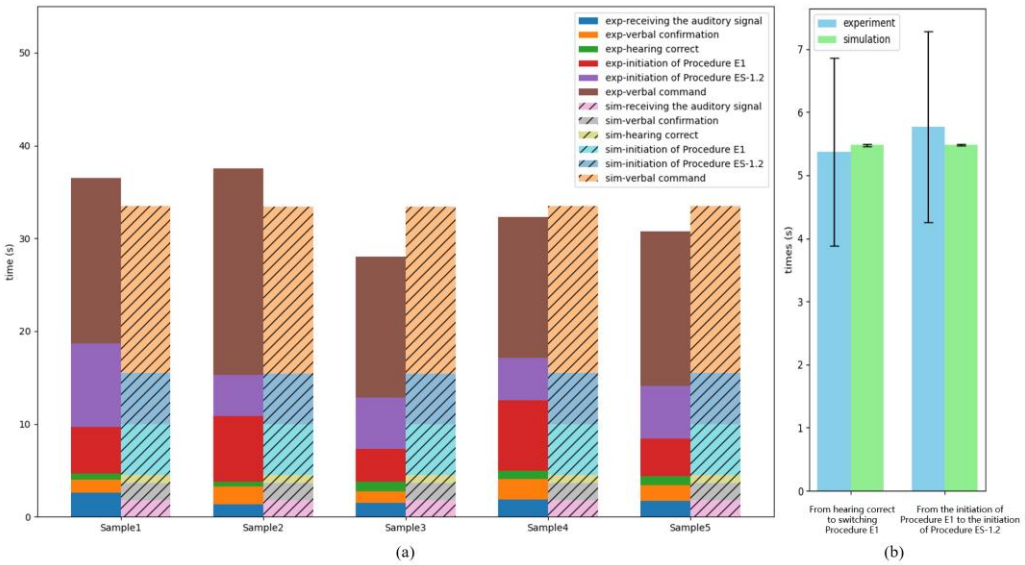

FIGURE 7. TEMPORAL ANALYSIS OF EXPERIMENTAL AND SIMULATED PROCEDURES IN EXP1

Figure 8 presents the results from five experimental trials of Exp2, comparing the durations of individual procedural steps as well as the cumulative time between the simulation and the actual experiment. The comparison demonstrates that both the overall total time and the time allocated to each step are consistent.

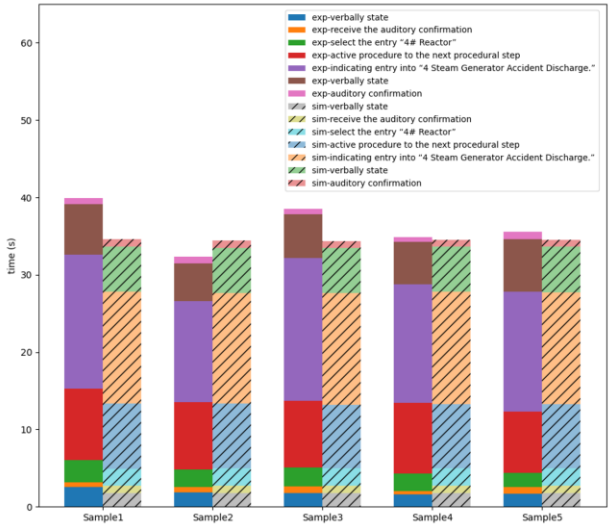

FIGURE 8. TEMPORAL ANALYSIS OF EXPERIMENTAL AND SIMULATED PROCEDURES IN EXP2

Figure 9 provides a comparative analysis of the means and variances for four specific processes: (i) from hearing the correct stimulus to selecting the entry “4 Reactor”, (ii) from selecting the entry “4 Reactor” to switching procedure, (iii) from the initiation of Procedure to indicating entry into “4 Steam Generator Accident Discharge,” and (iv) from indicating entry into “4 Steam Generator Accident Discharge” to verbally stating. For these processes, the actual mean durations are 2.3200 s, 8.7333 s, 15.9200 s, and 5.9000 s, respectively, while the corresponding simulated means are 2.2656 s, 8.2916 s, 14.4428 s, and 5.8858 s. The actual variances are 0.3030, 0.4551, 1.8847, and 0.7121, compared to the simulated variances of 0.0300, 0.0668, 0.0833, and 0.0098. Overall, the mean durations are largely consistent between the simulation and the experimental results; however, the ACT-R simulation exhibits considerably lower variance.

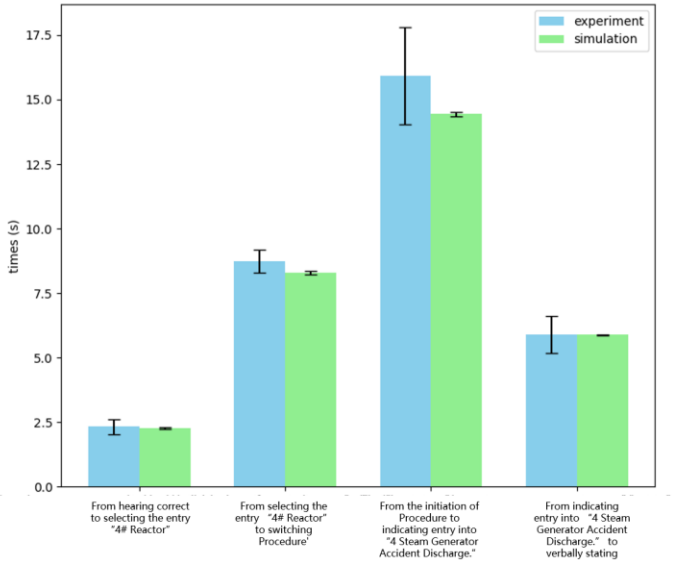

FIGURE 9. COMPARATIVE ANALYSIS OF EXPERIMENTAL AND SIMULATED PROCEDURES IN EXP2

Figure 10 (a) illustrates the 12 experimental trials of Exp3, comparing the durations of individual procedural steps and the cumulative time between the simulation and the actual experiment. The results indicate that both the overall total time and the durations of the individual segments are consistent. In the right subfigure (b), a comparison of the mean and variance for the process ”From hearing correct to pressing the button” is presented. The actual mean is 1.9583 s, while the simulated mean is 2.1723 s, with corresponding variances of 0.5841 and 0.0232, respectively. Overall, the mean values are closely aligned, though the ACT-R simulation exhibits a notably lower variance.

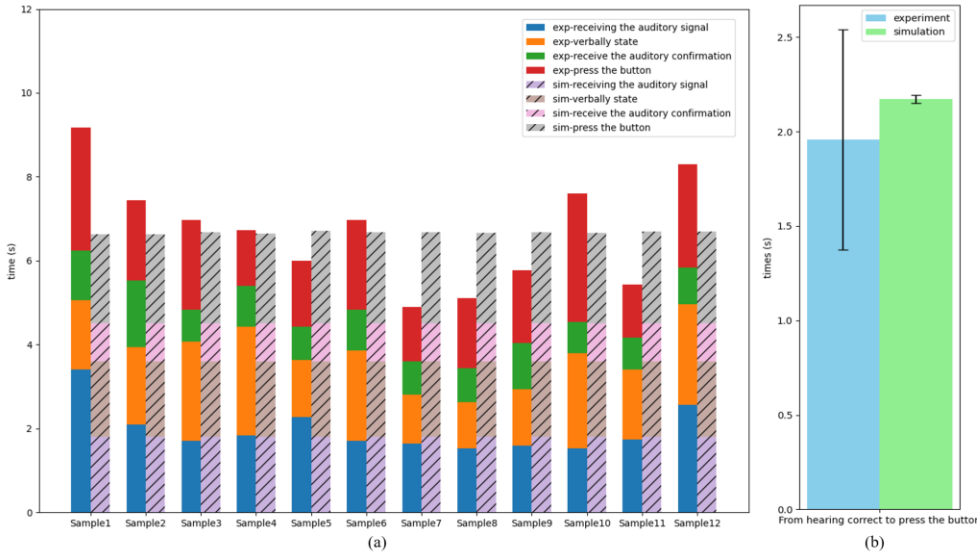

FIGURE 10. TEMPORAL ANALYSIS OF EXPERIMENTAL AND SIMULATED PROCEDURES IN EXP3

II. CONCLUSIONS

This study presents a novel ACT-R-based human digital twin (HDT) framework that provides a robust, theoretically grounded, and highly interpretable alternative to traditional human reliability analysis (HRA) data collection methods. In contrast to artificial neural network (ANN) approaches, our method leverages the cognitive architecture's declarative memory, procedural knowledge, and perceptual-motor modules to replicate the complete cognitive processes of nuclear power plant operators. The simulation framework was rigorously evaluated on Tsinghua University's HTGR simulator under a variety of operating conditions, including multi-parameter queries with interface switching, parameter queries without switching, and three-phase AC operations, which notably demonstrated lower error incidence during collaborative multi-operator interactions.

Our experimental results confirm that the ACT-R-based HDT framework accurately predicts operator task completion times and error probabilities (HEPs) across diverse procedural scenarios. The HEPs are derived through model-internal tracking of production rule conflicts, goal failures, and decision latencies, which serve as mechanistic indicators of error likelihood under time pressure or cognitive overload. This model-based quantification provides a transparent and traceable way to estimate human error potential in simulated scenarios, offering significant advantages over expert-judgment-based or statistical surrogate methods.

The ability to generate scenario-specific HEP predictions enables fine-grained human reliability assessments that are context-sensitive and dynamically responsive. Such capabilities are highly valuable for nuclear safety applications, including early-stage procedural design reviews, operator training customization, and real-time risk-informed decision support systems. Unlike existing methods such as IDAC, our approach offers enhanced explainability and a comprehensive cognitive modeling capability that can inform both design and training processes.

Looking ahead, future research should focus on integrating the ACT-R-based HDT framework with traditional HRA methodologies to explore simulation-driven HRA approaches. Furthermore, incorporating advanced simulation environments, large language models (LLM), and 3D digital human representations holds significant promise for enhancing operator training and optimizing reactor safety protocols.

ACKNOWLEDGMENTS

The research was supported by a grant from the National Natural Science Foundation of China (Grant No. T2192933).

REFERENCES

[1] Locatelli, G., Bingham, C., Mancini, M.: Small modular reactors: A comprehensive overview of their economics and strategic aspects. Progress in Nuclear Energy 73, 75–85 (2014)
[2] Zhang, Z., Yu, S.: Future htgr developments in china after the criticality of the htr-10. Nuclear Engineering and Design 218(1-3), 249–257 (2002)
[3] Maerani, R., Suryono, T., Santoso, S., Jung, J.: V&v methods used in the development of fpga-based i&c systems for htr-10. In: Journal of Physics: Conference Series, vol. 2048, p. 012041 (2021). IOP Publishing
[4] Converse, S.A., Perez, P., Clay, M., Meyer, S.: Computerized procedures for nuclear power plants: evaluation of the computerized procedures manual (copmaii). In: Conference Record for 1992 Fifth Conference on Human Factors and Power Plants, pp. 167–172 (1992). IEEE
[5] Jia, Q., Qu, R., Zhang, L.: Control room conceptual design of nuclear power plant with multiple modular high temperature gas-cooled reactors (2014)
[6] Miao, R., Jia, Q., Li, D., Dong, Z.: A comprehensive situation awareness measurement method for analyzing the operators' situation awareness of multi-module high temperature gas-cooled reactor plants. Energies 16(15), 5601 (2023)

RESOLVING BIASED JUDGMENTS IN RISKY CONTEXT

Gueorgui Petkov[1,2], Zhecho Mitev[3], Ivan Petkov[1]

[1] *Sofia University St. Kliment Ohridski: 5 James Bourchier Blvd., Sofia, Bulgaria, 1164, gipetkov@uni-sofia.bg*
[2] *Kozloduy Nuclear Power Plant Plc.: Kozloduy, Bulgaria, 3321, gipetkov@npp.bg*
[3] *Vector Labs: 40 Tsarigradsko Shose Blvd., Sofia, Bulgaria, 1750, zhecho@vector-labs.ai*

ABSTRACT

The paper presents an original symptom-based model and procedure for assessing the cognitive context for a clear and rational interpretation of decision-making process. This heuristic model is applied to explain and assess the subjective understanding and cognition that lead to misjudgments in ambiguous and comparative contexts using the example of Ellsberg's three-color paradox. The idea of overcoming this and other biases is to use the assumption that the wave of symptom recognition by a subject (natural or artificial intelligence) is delayed and disregarded compared to the wave of symptom emergence in an object (socio-technical system) during intuitive conscious information processing. To explain the causes of misjudgments in various erroneous actions, it is necessary to dynamically identify possible trajectories with corresponding probability amplitudes and track their entanglement in the real recognition context. Judgment in an ambiguous comparative context is a non-monotonic wave-like process with successively alternating convex/concave context probability (information entropy), i.e. alternating concave/convex probability of cognition or decision-making as a corresponding sum of varying discrete probability amplitudes of symptom recognition. These probability amplitudes are the result of the interference of objectively existing and subjectively imagined waves of symptoms of the context in a given situation. The groups of symptoms (weighted or not) are modeled by the waves of appearance and recognition of the number of symptoms in the socio-technical system (object and subject in a situation). By adopting and utilizing two overlapping types of additive and subtractive cognitive processes, consisting of different numbers of stages, we can resolve some paradoxes of biased judgments in uncertain and risky contexts and probabilistically comparing them with some known cognitive biases data. The unreliability of judgments in ambiguous and comparative situations is modeled and assessed using the symptom-based procedure of the Performance Evaluation of Teamwork method to qualify and quantify normal or violated contexts.

Keywords: Bias, Judgment, Context, Cognition, Ellsberg three-color Paradox

I. INTRODUCTION

The theory and practice of *human reliability assessment* (HRA) and *human factors* (HF) require extensive use of expert judgment to evaluate *human failure events* (HFE). Rational expert choice in decision-making (DM) requires a deeper understanding of cognitive and judgment processes. Biased judgment or *"rational choice without self-relevant consequences"*[1] is a subjective decision and occurs with some probability when we have unfounded, unfair biases and/or ambiguities due to incorrectly assessed probabilities of consequences (benefits/losses) of a rationally justified decision.

Knight [2] attempted to address these issues by distinguishing between *measurable uncertainty* or *risk* and *unmeasurable uncertainty* or *ambiguity*. Risk is represented in the form of *objectively* known *probabilities* (OP) of *Expected Utility* (EU) theory [3]. Ambiguity is determined by *subjectively* judged *probabilities* (SP) using the *Sure-Thing* (ST) principle in extended *Subjective Expected Utility* (SEU) [4].

Despite its popularity, this theory is not based on in-depth causal, "*conclusive, explanatory models or theories*" of the processes of cognition and decision-making, but rather seeks interesting effects leading to "*a rich set of phenomena*" [5] through paradoxical thinking or fitting approximate formulas. Using sophisticated mathematical models and the borrowing of some

[1] The *"choice entails self-relevant consequence whereas making judgments mostly relies on an impersonal objective evaluation of the situation that has no personal consequences"* [1].

universal ideas from physics, such as quantum mechanics, it attempts to explain nature in order to balance true, pseudo and false randomness.

The gradual way to judge the success of a choice explanation is through empirical testing and validation. But if fitted models provide only approximate and inadequate explanations of effects, they can easily be challenged by experimental results from behavioral economics and psychology.

Savage's ST principle [4] in the extended SEU theory, although partially supported by subsequent real experiments, is largely normatively undermined by a number of paradoxes and effects, such as the thought experiments of Ellsberg [6] and the Machina [7], conjunction and disjunction fallacies, etc. They introduce dissonance and contradictory interpretations, preventing a clear picture of the processes of cognition and decision-making. All of these are used as filters for models of judgment under uncertainty. Very few of the many sophisticated models of rational choice theory survive these filters, and the development of models to explain and resolve these paradoxes and biases continues.

This paper proposes a symptom-based model of cognition and decision-making for a relatively simple explanation of biases and paradoxes associated with the traditional EU model and its adaptations [8], including the resolution of Ellsberg three-color paradox. This is achieved by representing a dynamic array for the temporal context with less than 7 symptom groups with three columns of emerging, recognized, and violated symptoms for each group in a *socio-technical system* and using rules for adding and subtracting the number of symptoms in each column of the array. The columns represented *O x S x V* (*objectively* existing *x subjectively* recognized *x* perceived with *violations*) symptoms in a given situation. Decision makers recognize and minimize context uncertainty (presented as probability) and thus maximize the successful cognition or judgment (presented also as probability).

II. BIASES AND JUDGMENT IN RATIONAL CHOICE THEORY

II.A. Approaches and models to dealing with biased judgments

Many models, methods and approaches have been proposed to generalize biased judgments (normative/axiomatic or non-normative) that consider and accommodate the ambiguity preferences in the Ellsberg and Machina [9] paradoxes [10].

Machina's paradox [7] has been experimentally confirmed by L'Haridon and Placido [11], and many of the real experiments or filters to confirm or undermine these models and theories of rational choice have been extensively studied and described in Machina and Siniscalchi [12].

Such models are: the *Two-Stage (TS) model* in [13], *Choquet EU (CEU)* in [14], *Maxmin Expected Utility (MEU)* in [15], *Bayesian approach based model* in [16], *Cumulative Prospect Theory (CPT)* in [17], *α-Maxmin Expected Utility model (αMEU)* in [18], the *KMM smooth model of ambiguity aversion* in [19], *Variational Preferences model (VP)* in [20], *Vector Expected Utility (VEU)* in [21], *Expected Uncertainty Utility (EUU)* in [22], *Two-Stage Evaluation (TSE)* in [23] among others.

Kitto [24] argues that an appropriate *"mechanism for dealing with such contextual dependency is inbuilt into the quantum formalism itself"* (p. 12). But these quantum-like models do not provide a comprehensible and reasonable *"physical"* (*psychological, neurophysiological, behavioral, biological and/or "psychophysical"*) explanation, but only a simple implicit mathematical landscape of the statistical outcome of making rational or irrational choices. Therefore, we should try to create a causal consistent model of cognition and decision-making that provides a *"physical"* explanation, rather than just speculating with complex mathematics.

The dynamic behavior of the *socio-technical system* (STS) can be described in context as *an object and a subject in a situation*. Dealing with human errors or fallacies require describing and modeling thought processes by measuring, evaluating, and analyzing everything in them that could be inferred, defined, or attributed to contextual situations of the STS that are unrecognizable, undefined, ambiguous, and relatively risky.

The main idea for overcoming these and other paradoxes and fallacies is to use the proposition on the dual symptom-wave nature of the process of cognition and decision-making to justify the fact that at any moment in time the grounds for judgment are based on tracking all possible trajectories of the real context.

II.B. Entropic understanding of cognition and judgment

Explaining complex processes such as cognition and judgment through simple, generally accepted and widely used concepts and ideas would be more understandable and applicable. Therefore, symptoms or stimuli are suitable means that not only provide a comprehensive description of STS information, but also allow for its exchange, filtering and ignoring, i.e., the possibility of organizing a holistic process with a change in STS entropy. Using symptoms alone, information exchange can be achieved quite simply by simultaneously adding new *"task-relevant information"* to STS states and subtracting (*"selectively inhibited at the same time"*) recognized information [25]. Thus, we attempt to provide an entropic understanding and

explanation of cognition and judgment through symptom-based context evaluation, which allows modeling quantum-like superposition through trivial arithmetic operations. The symptom-based counting approach is similar to the *"Maya … system of bars and dots … and … rules of counting beans, putting them in, taking them out in different pots to calculate and predict"* [26]. It is conventionally called *quantum-like symptom counting* (QLSC) and serves to describe all alternative states of STS.

Contextual factors and conditions (CFCs) are *symptoms* that dynamically describe the manifestations of all technological, automatic, manual, and thought processes that occur in the STS. Symptoms are signs of the STS in a given situation and are objective, insofar as they reflect the properties and state of the object, and subjective, since the subject perceives, interprets and recognizes them individually or in groups. Symptoms are grouped according to their distinctive features in the relevant domain. Usually 2 to 7 groups of symptoms are sufficient. For example, in such a complex domain as nuclear technology, these could be: *Events*, *Parameters*, *Functions*, *Goals*, *Resources*, *Transitions* and *Actions*. Typically, symptoms are modeled as indistinguishable within a group, but, if possible, they should be weighted both within and across groups for a given domain.

Since each single symptom (1) of the object is recognized by the subject from its absence (0) to its presence (1) in some time interval, it can be trivially assumed that its recognition in the STS can be described quantitatively using probability.

The *Performance Evaluation of Teamwork* (PET) method uses model and procedure for context qualification and quantification to offer a rational and explainable interpretation of the thought processes [27]. The proposed PET model for context of cognition uses ≥ 2 and ≤ 7 groups with 3 columns (*7 x 3*), *V x O x S*, to represent: the number of violated recognition symptoms in column *V* and the shifts between the number of objective symptoms in column *O* (objectively occurring/measured symptoms) and the number of subjective symptoms in column *S* (subjectively recognized symptoms by natural or artificial intelligence) for each group.

Judgment in an ambiguous and comparative context is a wave-like process with successively alternating concave/convex function of *context probability (CP*) or info entropy, and convex/concave function of *cognitive success probability (CSP*). Both functions are evaluated as probabilities, which are the respective sums of discrete *subjective probability amplitudes (SPAs)* of all alternatives (trajectories) of the context. The SPAs are the result of a combination of the shifts between the number of objectively existing vs. subjectively imagined symptoms of the cognitive context. By distinguishing between at least two types of cognition (*additive* and *subtractive*), consisting of different numbers of stages, we can solve many problems of rational choice theory by considering all or representative samples of possible alternatives to contextual progression. The decision maker approximates (minimizes CP) the shifts between the number in the subjective column and the number in the objective column, and when the most favorable context (minimum CP/ maximum CSP) is reached, the judgment is considered the best possible. The addition and subtraction of information is a trivial idea for the processes of cognition and judgment. But only detailed analysis and synthesis through imaginary arithmetic operations can contribute to the understanding of thought processes. But only detailed analysis and synthesis through imaginary arithmetic operations (*addition*, *subtraction*, *multiplication* or *repeated addition of groups of unequal size*) can contribute to understanding the thought processes.

II.C. Synthesis of paradoxes of thinking with symptom-based context

The cognitive context can be defined as a statistical measure of the degree of randomness of the state of a complex STS. The cognitive CP is defined as the ratio of the number of unrecognized to the number of possible available STS states [28]. The uncertainty of the cognitive context has a probabilistic-deterministic nature and can represent a two-dimensional plane of aleatory and epistemic uncertainty. However, due to the objective-subjective nature of the decision-making process, a third dimension of contextual/evaluative uncertainty can be distinguished, characterizing the specific man-machine interaction [29].

Symptoms are stimuli that are meaningful to the operator and have consequences for the behavior, states, and trajectories of the STS. The definition of context also relates it to quantum-like processes and the quantum superposition principle, which states that combinations of symptoms for system states and trajectories *"can be represented by a superposition over different degrees of support for the available choice options"* [30]. CP is a conditional measure of the STS error potential over time. Enumerating all possible and unrecognized accessible states with their *subjective probability amplitudes* (SAP) via information bits, quanta, or waves allows the selection of favorable alternatives.

The PET model and procedure for symptom-based context quantification has already been demonstrated for conjunction and disjunction fallacies [8] and Ellsberg's two-color paradox [31], and is now shown to withstand Ellsberg's three-color filter.

Despite the application of many universal ideas and mathematical models to resolve paradoxes and fallacies under ambiguity and comparison, *"none of the arguments that have been proposed is, at the best our knowledge, considered as conclusive"* [32]. Therefore, the aim of this paper is to propose a PET model and procedure for computing and tracking context to resolve and explain the judgment process.

We intend to apply the acquired insights of the PET method applications to analyze and synthesize the stepwise context and its subjective amplitude probabilities of a cognitive process based on recognition, disregarding and violation of symptoms. In this way, stepwise models of cognition can be demonstrated that are suitable for resolving this and other paradoxes.

III. ELLSBERG'S COLOR PARADOXES

Ellsberg's color problems involve fair sets of items (balls or poker chips), where the first set has *clearly* defined items with one, two or more colors, and the second set has *vague* defined items with two, three or more colored items [33]. From each set containing items with *k* colors (red, black, yellow, green ...), an item of a certain color can be drawn with the same *Objective Probability*, i.e. the placement of items in the sets provides a uniform distribution of colors.

The *clear* set contains an even or odd number of items (e.g. $n_1=N/k$ items of the 1st, the all 2nd, 3rd, …the k-color items contain $N-n_1$ items), while the *vague* set contains n_i items of its *i*-color and ($N-n_i=\sum n_j-n_i$) items of its other *k-1* colors in an unknown proportion, where $n_j \in [0, N-N/k]$ and $j=1...k, j\neq i$. If the player's color matches the predicted color, the player wins $€Z$ $(Z>0)$ or a multiple of $€Z$, otherwise she/he wins nothing. Suppose further that the decision maker is a "*consequentialist*" in the sense that she/he is only interested in outcomes; and when it comes to money, she/he prefers more money to less [10].

The results of choosing an item from each set show that the *SP* of drawing (betting) on an item of a certain color are equal if the sets are not compared, and the SPs are different if the sets are compared (drawn from one or the other), since the *SP* of the *"clear" set* is greater than that of the *"vague" set* - $SP_c>SP_v$. In addition, the sum of SPs in the *"vague" set* is different from 1, although they are complementary events to 1 ($\Sigma\, SP_{vk}<1$).

III.A. Stepwise modeling of cognition

Ellsberg [7] argues that the ***SP*** of a personal choice in the presence of uncertainty depends not only on the perceived probability of the event in question but also on its vagueness or ambiguity [33]. He characterizes ambiguity as *"a quality depending on the amount, type, and 'unanimity' of information"* (p.657) or context-awareness as will be interpreted in this paper by the PET method.

In this paper, for *cognitive error probability* (CEP=1-CSP) is used CP but the PET method could use also use other three different "improved" models, which means bringing subjective assessments closer to objective ones, with less CEP based on Rasmussen's *Step Ladder Model* [27]. Some subjective measures of probability may be additive, while others may not be additive [5].

Ambiguity aversion and comparative ignorance can contribute differently to *SP=(1-CP)* or *SP=CSP=(1-CEP)* and could change in magnitude and sign during the cognitive process. If the cognitive process does not involve comparison (and only *noncomparative games*), then it is trivially additive cumulative cognition and can be justified by the *"cumulative learning theory"* [34]. The cumulative cognition used in the PET method is based on a simple skill of recognizing and adding symptoms based on the previous chronology or previous experience. Thus, only the sequential recognition of the symmetric equal objective probabilities of drawing an item of a certain color from set 1 (*clear*) or set 2 (*vague*) is required, and therefore, for noncomparative games: $SP_1 \approx SP_2$.

The idea is to conduct the supposed process of cognition as possible discrete steps of approximation of the subjectively perceived number of symptoms (items of different colors) to their objective number of several steps (2÷4). The stepwise cognition can occur sequentially, in parallel and jointly with a time difference, resembling Donders' stages [35].

We can summarize the following four types of stepwise cognition, required to enumerate all contextual alternatives. O_i is the column with an objective number of *i*-color (1) items and S_i is the column with a subjective number of *i*-color (2) items from clear or vague set:

1. *Stepwise additive cognition with memorizing* (AC_m) in 2 steps - without forgetting the recognized O_i & S_i symptoms (preserving their number). The AC_m scheme is presented in TABLE I for *k=3* colors.
2. *Stepwise subtractive cognition with disregardin*g (SC_d) in 4 steps - with disregard of the already recognized O_i & S_i symptoms (numbers of both is reduced but with shift). The SC_d scheme is presented in TABLE II for *k=3* colors.
3. *Stepwise heuristic cognition with mixing and/or bypassing* in more than 4 steps - a mixture of the previous two by bypassing the memorizing and/or disregarding of some of the symptoms.
4. *Stepwise violated cognition with memorizing, disregarding, mixing or/and bypassing* in more than 4 steps – recognition of one or more groups of symptoms is difficult due to the occurrence of a violations.

III.B. Three-color Ellsberg paradox

In this section, we consider the well-known Ellsberg three-color paradox [7]. This case is sufficiently representative of the paradoxes and the solutions proposed by the PET method. The logic is applicable to other examples, and the PET solutions were also applied to the conjunction and disjunction fallacy [8] and Ellsberg two-color paradox [31]. In all cases, the procedure is carried out in 3 stages:

TABLE I. Stepwise additive cognition with memorizing **(AC_m)** for ***k=3*** colors.

A3_1	Context Factors and Conditions (items)								
Color/type of symptoms	Red			Black			Yellow		
Step number	VO	O	S	VO	O	S	VO	O	S
0/1	0	N	0	0	2N-n	0	0	n	0
2	0	N	1	0	2N-n	0	0	n	0
A3_2	Context Factors and Conditions (items)								
Color/type of symptoms	Red			Black			Yellow		
Step number	VO	O	S	VO	O	S	VO	O	S
0/1	0	N	0	0	2N-n	0	0	n	0
2	0	N	0	0	2N-n	1	0	n	0
A3_3	Context Factors and Conditions (items)								
Color/type of symptoms	Red			Black			Yellow		
Step number	VO	O	S	VO	O	S	VO	O	S
1	0	N	0	0	2N-n	0	0	n	0
2	0	N	0	0	2N-n	0	0	n	1

TABLE II. Stepwise subtractive cognition with disregarding **(SC_d)** for ***k=3*** colors.

A3_1	Context Factors and Conditions (balls)								
Color/type of symptoms	Red			Black			Yellow		
Step number	VO	O	S	VO	O	S	VO	O	S
0/1	0	N	0	0	2N-n	0	0	n	0
2	0	N	1	0	2N-n	0	0	n	0
3	0	N-1	1	0	2N-n	0	0	n	0
4	0	N-1	0	0	2N-n	0	0	n	0
A3_2	Context Factors and Conditions (balls)								
Color/type of symptoms	Red			Black			Yellow		
Step number	VO	O	S	VO	O	S	VO	O	S
0/1	0	N	0	0	2N-n	0	0	n	0
2	0	N	0	0	2N-n	1	0	n	0
3	0	N	0	0	2N-n-1	1	0	n	0
4	0	N	0	0	2N-n-1	0	0	n	0
A3_3	Context Factors and Conditions (balls)								
Color/type of symptoms	Red			Black			Yellow		
Step number	VO	O	S	VO	O	S	VO	O	S
0/1	0	N	0	0	2N-n	0	0	n	0
2	0	N	0	0	2N-n	0	0	n	1
3	0	N	0	0	2N-n	0	0	n-1	1
4	0	N	0	0	2N-n	0	0	n-1	0

1) a description of the decision-making problem is given, together with tables that represent the situation;
2) the context models used to solve the paradox are given in TABLEs I and II, based on the models of the PET used in the procedure for determining the SP of choice and successful judgment;
3) the obtained PET results are compared with the available statistical results for the problem.

III.B.1. Problem description and formulation

In the classic Ellsberg three-color problem, there is an urn containing balls of three colors. The urn includes two parts with a total of *M* (*90*) balls: The *"clear" part* with *M/3=N/2 (30)* balls is red, and the remaining *"vague" part* with *(2*M)/3=N (60)* balls is black or yellow in unknown proportions. It means that the *'vague' part* contains *n* yellow and *(N-n)* black balls in an unknown proportion, where $n \in [0, N]$. One ball will be drawn from the urn. A player is asked to bet on one of the acts *b1*,

b2, *b3* and *b4* defined in Table III. If the color that the player draws is the same as the one she/he predicted, then the player will win *$Z (Z>0)*, otherwise she/he wins nothing.

TABLE III. Number of balls, color, and payoff matrix of Ellsberg's three-color problem

bet	**'clear' part**	**'vague' part**	
color	*red*	*yellow*	*black*
number of balls	***M/3=N/2 (30)***	***n***	***(2*M)/3-n=N-n***
b1, Gamble 1	***$Z***	***0***	***0***
b2, Gamble 1	***0***	***$Z***	***0***
b3, Gamble 2	***$Z***	***$Z***	***0***
b4, Gamble 2	***0***	***$Z***	***$Z***

Suppose players are offered two games as follows:

- *Gamble 1 (comparative objective-subjective).* Player has to guess the color and bet on red (*b1*) vs. black (*b2*) and then choose a ball from the urn.
- *Gamble 2 (comparative subjective-objective).* Player has to guess the one of two colors - red or yellow (*b3*) vs. black or yellow) (*b4*) and then choose a ball from the urn.

III.B.2. Results and comments of experiments

The TABLE IV presents the probabilities of a decision maker for whom *OPs* are determined by the minimal chance of each event occurring and for whom *SPs* are determined by the *principle of indifference* (*insufficient reason*) [10].

In the experiments conducted by Ellsberg and after him, people prefer to bet on the red (*b1*) over the black (*b2*) ball, and to bet on "black and yellow" (*b4*) in front of "red and yellow" (*b3*) balls. This preference cannot be explained by the *EU* hypothesis. The first choice conforms to the ST principle, but the second choice contradicts this principle. Even more this violates the Savage's *ST* principle, which requires the ordering of *b1* to *b2* to be preserved in *b3* and *b4* (since these two pairs differ only in the payoff when a yellow ball is drawn, which is constant for each pair). Nevertheless, these choices are intuitive: *b1* offers the *Z* prize with an *objective* likelihood $OP_1=1/3$, and *b2* offers the same prize but in an element of the *subjective* partition and ambiguity $SP_2 \approx 1/3$ (black, yellow), if the game is fair. In the same way, *b4* offers the prize with an *objective* likelihood $OP_4=2/3$, whereas *b3* offers the same payoff with *subjective* likelihood $SP_3 \approx 2/3$ on the union of the unambiguous event red and the ambiguous event yellow. Evidence shows that in practice this statement often does not hold.

TABLE IV. Principle results of the Ellsberg three-color problem studies

Gamble	**'clear' part: red**	**ratio**	**'vague' part: black & yellow**
1. comparative *objective-subjective*	$\boldsymbol{OP_1 = 1/3}$	>	$\boldsymbol{SP_2 \approx 1/3}$
2. comparative *subjective-objective*	$\boldsymbol{SP_3 \approx 2/3}$	<	$\boldsymbol{OP_4 = 2/3}$

This pattern of preferences is inconsistent with EU theory because it implies that the vague SP_2 of *'black'* is less than OP_1 of *'red'* ($SP_2 < OP_1 = 1/3$) and the vague SP_3 with unknown proportion between *'red* or *yellow'* balls is less than OP_4 of *'yellow* or *black'* ($SP_3 < OP_4=2/3$). Therefore, the sum of the $SP_2 + SP_3 < 1$ for these outcomes in the decision-making process is not equal to one, although these are complementary events.

Ellsberg found that decision makers generally prefer bets with higher *OPs*, *ceteris paribus* (i.e., other *things being equal*, in those situations where the combined probabilities and payoffs are the same in the urns). That is, he found that people are prone to ambiguity. *"Thus, in both cases the unambiguous bet is preferred to its ambiguous counterpart, a phenomenon called ambiguity aversion by Ellsberg"* [36].

III.B.3. Modeling and resolving the Ellsberg three-color problem

To resolve Ellsberg's three-color paradox, we apply the two models of cognitive context, simulated with the PET context quantification procedure based on TABLE I for *additive cognition with memorizing* and TABLE II for *subtractive cognition with disregarding*.

For the non-comparative games (Gamble 1), the AC_m model is used, and for the comparative games (Gamble 2), the SC_d model. With their help we can obtain the following results shown in TABLE V and TABLE VI.

TABLE V. Subjective probabilities calculated by PET method for the Ellsberg three-color problem.

color	Subjective Probability - memorize		Subjective Probability - disregard			
	SP(AC_m) Step 1	**SP(AC_m) Step 2**	**SP(SC_d) Step 1**	**SP(SC_d) Step 2**	**SP(SC_d) Step 3**	**SP(SC_d) Step 4**
red	0,146606	c	0,146606	0,293211	0,302985	0,151492
black	0,146606	0,293211	0,146606	0,293211	0,301927	0,150964
yellow	0,146606	0,293211	0,146606	0,293211	0,301927	0,150964
SUM	**0,439817**	**0,879633**	**0,439817**	**0,879633**	**0,906839**	**0,453420**

TABLE VI. *Objective and subjective probabilities on Ellsberg's 3-color problem* [10] and PET results for them.

bet	'clear' part	'vague' part		Combined probability
color	*red*	*yellow*	*black*	(OP)
b1, Gamble 1	OP=*1/3*	0	0	**b2 < b1 = 0,333333** = (1/3)
b2, Gamble 1	*0*	$SP_c(AC_m)_2$=0,293211	0	**b1 > b2=0,293211** < (1/3)
b3, Gamble 2	OP=*1/3*	$SP_v(SC_d)_3$=0,302985	0	**b4 < b3 = 0,636318** (≈2/3)
b4, Gamble 2	(*2/3*)	$SP_v(SC_d)_3$=0,302985	$SP_v(SC_d)_3$=0,302985	**b3 > b4 = 0,605970** (≈2/3)

IV. CONCLUSIONS AND INSIGHTS

Modeling, explaining, and resolving Ellsberg's three-color paradox allows us to present a heuristic and rational PET methodology for interpreting many experimental psychological studies of problems, fallacies, and paradoxes involving biased thinking and judgment. Therefore, the theoretical development and validation of the models and the procedure of the PET method will continue in the future with studies of known biases with empirical evidence (Machina's color paradoxes, Ellsberg's multi-color paradox (>3), "framing effects", etc.

Avoiding cognitively biased judgment errors primarily involves limiting the effects of delayed or violated symptom recognition through careful qualification, grouping, and quantification of symptoms.

The PET method, based on explicit qualification and quantification of context using simulator data, can increase the confidence in HRA methods and create useful specific databases of *errors of commission*. This dual practical application of the PET method will be realized by using it as the main method in the system for human error collecting data during regular training of WWER-10000 operator crews at the full-scale simulator of the Kozloduy NPP in Bulgaria.

The inability to complete the process of cognition and judgment in ambiguous and comparative contexts is due to limited, delayed, and stochastic capabilities for encoding information in working memory.

This, in turn, limits subsequent access to this information in long-term memory, where the "individual judgment processors" are stored and used through a unified probabilistic thinking logic.

REFERENCES

[1] S. SOOD and M. FOREHAND, On self-referencing differences in judgment and choice. *Organ. Behav. Hum. Decis. Process.*, 98, 144–154 (2005).
[2] F.H. KNIGHT, *Risk, Uncertainty, and Profit*, Boston: Houghton Mifflin (1921).
[3] J. VON NEUMANN & O. MORGENSTERN, *Theory of Games and Economic Behavior*, Princeton University Press (1947).
[4] L.J. SAVAGE, *The Foundations of Statistics*, New-York: Wiley, (1954).
[5] J.T. TOWNSEND, Mathematical psychology: Prospects for the 21st century: A guest editorial. *Journal of Mathematical Psychology*,52,269–280 (2008).
[6] D. ELLSBERG, Risk, ambiguity, and the Savage axioms, *Quarterly J of Economics* 75(4), 643-669, (1961).
[7] M. MACHINA, Risk, ambiguity, and the rank-dependence axioms, *American Economic Review*, 99 (1), 385–392, (2009).

[8] G. PETKOV, Misjudgment explanation in ambiguous and comparative contexts, *Proc. PSAM 17-ASRAM2024 Conference*, October 7-17, Sendai, Miyagi, Japan (2024).
[9] M. MACHINA, Ambiguity aversion with three or more outcomes. *American Economic Review*, 104 (12), 3814–3840, (2014).
[10] K. SHARPE, On the Ellsberg and Machina paradoxes, *Theory and Decision* 95, 539-573, (2023).
[11] O. L'HARIDON and L. PLACIDO, Betting on Machina's reflection example: An experiment on ambiguity. Theory and Decision, 69(3), 375–393, (2010).
[12] M. MACHINA & M. SINISCALACHI, (2014). Ambiguity and ambiguity aversion. In M. Machina & K. Viscusi (Eds.), *Handbook of the economics of uncertainty*, Vol. 1, pp. 729–808, Elsevier (2014).
[13] U. SEGAL, The Ellsberg paradox and risk aversion: An anticipated utility approach, *International Economic Review*, 28(1), 175-202, (1987).
[14] D. SCHMEIDLER, Subjective probability and expected utility without additivity, *Econometrica*, 57(3), 571–587, (1989).
[15] I. GILBOA and D. SCHMEIDLER, Maxmin expected utility with a non-unique prior, *Journal of Mathematical Economics*, 18(2), 141–153, (1989).
[16] I. M. DOBBS, A Bayesian approach to decision-making under ambiguity, Economica 58(232), 417-440, (1991).
[17] A. TVERSKY and D. KAHNEMAN, Advances in prospect theory: Cumulative representation of uncertainty, *Journal of Risk and Uncertainty* 5, 297-323, (1992).
[18] P. GHIRARDATO, F. MACCHERONI and M. MARINACCI, Differentiating ambiguity and ambiguity attitude, *Journal of Economic Theory* 118(2), 133-173, (2004).
[19] P. KLIBANOGFF, M. MARINACCI, M. and S. MUKERJI, A smooth model of decision making under ambiguity, *Econometrica* 73(6), 1849-1892, (2005).
[20] F. MACCHERONI, M. MARINACCI and A. RUSTICHINI, Ambiguity aversion, robustness, and the variational representation of preferences, *Econometrica* 74(6), 1447-1498, (2006).
[21] M. SINISCALCHI, Vector expected utility and attitudes toward variation, *Econometrica* 77(3), 801-855, (2009).
[22] F. GUL and W. PESENDORFER, Expected uncertain utility theory, *Econometrica* 82(1), 1-39, (2014).
[23] Y. HE, Revisiting Ellsberg's and Machina's Paradoxes: A Two-Stage Evaluation Model Under Ambiguity, *Management Science*, March (2021).
[24] K. KITTO, Why quantum theory? In P. Bruza, W Lawless, C. van Rijsbergen, D. Sofge, B. Coecke & S. Clark (Eds.). *Proc. Second quantum interaction symposium*, pp.11-18, Oxford, (2008).
[25] C. -H. CHENG et al., Sensory gating, inhibition control and gamma oscillations in the human somatosensory cortex. *Sci. Rep.* 6, 20437; doi: 10.1038/srep20437 (2016).
[26] R. P. FEYNMAN, *QED the strange theory of light and matter*, Princeton University Press, (1985).
[27] G. PETKOV, Symptom-based context quantification for dynamic accident analysis, *Safety Science*, (2018). https://doi.org/10.1016/j.ssci.2018.02.027
[28] G. PETKOV, Dealing with Dynamic Aspects of Operators' Performance, *Proc. FLINS'2004 Conference 'Applied Computational Intelligence'*, September 1-3, Duinse Polders, Belgium, pp. 677-683 (2004).
[29] G. PETKOV, Risk Contextualization for Nuclear Systems, *J. Nucl. Eng.*, *6*, 1, pp. 1-17 (2025-1).
[30] J.R. BUSEMEYER, P.D. KVAM. and T.J. PLESKAC, Comparison of Markov versus quantum dynamical models of human decision making, Wiley interdisciplinary reviews. *Cognitive science*, February (2020).
[31] G. PETKOV, Modeling and diagnostics of biased judgments, *Proc. ESREL2025 & SRA-E 2025 Conference*, June 16-19, Stavanger, Norway (2025-2).
[32] D. AERTS, B. D'HOOGHE and S. SOZZO, A Quantum Cognition Analysis of the Ellsberg Paradox, *Proc. Conference Paper April*, DOI: 10.1007/978-3-642-24971-6_10, Source: arXiv (2011).
[33] C.R. FOX and A. TVERSKY, Ambiguity Aversion and Comparative Ignorance, *The Quarterly Journal of Economics*, Vol. 110, No. 3, pp. 585-603, August (1995).
[34] R. M. GAGNE, *The conditions of learning* (2nd ed.). New York: Holt, Rinehart & Winston (1970).
[35] F. DONDERS, *Die Schnelligkeit Psychischer Processe*, Archiv fur Anatomie and Physiologie, 657-681. (In W.G. Koster Ed. Attention and Performance II (pp.176-315), Amsterdam: Elsevier/North-Holland.), (1868).
[36] D. AERTS, S. SOZZO, J. TAPIA, A quantum model for the Ellsberg and Machina paradoxes, *Lecture Notes in Computer Science*, vol. 7620, 48–59. Springer, Berlin (2012).

ASRAM2025
www.asram2025.org
Asian Symposium on Risk Assessment and Management 2025
Pattaya, Thailand, 27 – 29 August 2025

EVALUATION OF HRA METHODOLOGIES FOR APPLICATION IN SDP WORK

Ar Ryum Kim[1], Namyeong Kim[2], Dongwon Lee[3], Jooyoung Park[4], Ronald Boring[5]

[1] *Korea Institute of Nuclear Safety, 62, Gwahak-ro, Yuseong-gu, Daejeon, 34142 and arryum@kins.re.kr*
[2] *Korea Institute of Nuclear Safety, 62, Gwahak-ro, Yuseong-gu, Daejeon, 34142 and nykim@kins.re.kr*
[3] *Korea Institute of Nuclear Safety, 62, Gwahak-ro, Yuseong-gu, Daejeon, 34142 and dwlee@kins.re.kr*
[4] *Idaho National Laboratory, 1995 N. Fremont Ave. Idaho falls, 83415 and Jooyoung.Park@inl.gov*
[5] *Idaho National Laboratory, 1995 N. Fremont Ave. Idaho falls, 83415 and ronald.boring@inl.gov*

ABSTRACT

This study critically evaluates human reliability analysis (HRA) methodologies applicable to regulatory probabilistic safety assessment (PSA) model, with a particular focus on their role in supporting the significance determination process (SDP) in nuclear safety assessment. Firstly, three widely utilized HRA methods—IDHEAS-ECA, SPAR-H, and ASEP/THERP—were qualitatively and quantitatively assessed. Qualitative assessments were conducted using attributes from the NEA/CSNI/R(2015)1 report, while quantitative evaluations employed regression and correlation analyses to compare predicted human error probabilities (HEPs) against empirical data. Results reveal distinct strengths, for example, IDHEAS-ECA's robust predictive accuracy and K-HRA's alignment with operational practices. In addition, dependency analysis and recovery analysis were critically evaluated. For dependency analysis, the methods' handling of inter-task dependencies and their impact on HEPs were examined, while recovery analysis highlighted strategies for mitigating failure events. Furthermore, strategies were proposed to evaluate performance shaping factors under conditions of reduced human performance, such as stress, fatigue, or cognitive overload, addressing specific challenges faced in SDP evaluations. Human errors from KINS's operational performance information system event reports were evaluated as a case study. This study identifies gaps and provides actionable insights to ensure their validity and applicability in SDP HRA applications. This paper is a part of research conducted by KINS, and it should be noted that this result does not represent the regulatory position of KINS.

Keywords: Human Reliability Analysis, Significance Determination Process, Qualitative and Quantitative verification, Recovery analysis, Dependency analysis

I. INTRODUCTION

In recent years, the Korea Institute of Nuclear Safety (KINS) has enhanced the Multi-purpose Probabilistic Safety Assessment (MPAS) model, originally developed as a regulatory PSA framework, to strengthen its capability in supporting the future application of Significance Determination Process (SDP) and other regulatory applications [1]. As a regulatory PSA model, MPAS is intended to provide independent and objective safety evaluations that are consistent with international standards and reflect plant-specific operational realities. However, one of the key limitations of the current MPAS model is that its human reliability analysis (HRA) adopts the same HRA methodology used by licensees [2]. This could compromise the independence and objectivity of the regulatory assessment. The objective of this study is to review suitable HRA methodologies for application in the MPAS model, to explore approaches for dependency and recovery analysis when applying the HRA method(IDHEAS-ECA), and to conduct a case study based on the selected methodology.

To address this issue, several HRA methodologies—including IDHEAS-ECA (Integrated Decision-tree Human Event Analysis System - Error Causal Analysis), SPAR-H (Standardized Plant Analysis Risk-Human Reliability Method), and ASEP (Accident Sequence Evaluation Program)/THERP (Technique for Human Error Rate Prediction)—have been reviewed. Among them, the IDHEAS-ECA method was selected as the most appropriate approach for human error probability quantification within MPAS. Despite this selection, there are still unresolved challenges associated with its practical application, especially in the context of regulatory PSA. In parallel, while a dependency analysis method has been developed and documented for MPAS, it lacks sufficiently detailed guidance for practical implementation. Moreover, a formal recovery action evaluation methodology has not yet been established. These gaps may limit the model's ability to accurately and transparently represent human performance under realistic accident scenarios.

This study aims to review and refine the application of HRA methodologies suitable for the MPAS model, with a particular focus on dependency analysis and recovery analysis. Furthermore, to validate the applicability of IDHEAS-ECA within a regulatory PSA context, a case study is presented using actual findings from a domestic nuclear power plant inspection. The outcomes of this study are expected to contribute to the advancement of a more robust and independent HRA framework tailored for regulatory PSA applications.

II. SELECTION OF HRA METHOD APPLLIED IN MPAS MODEL

We first reviewed three HRA methodologies: IDHEAS-ECA, SPAR-H, and ASE/THERP. The results of this review are summarized below. Subsequently, to select an HRA method for application in the MPAS model, qualitative evaluations were performed.

II.A. Review of HRA Methods

II.A.1. IDHEAS-ECA

IDHEAS-ECA, which provides a comprehensive framework for understanding and modeling human contributions to IDHEAS-ECA, was recently developed by U.S. Nuclear Regulatory Commission (NRC) staff [3]. This approach systematically considers the contextual conditions under which events occur, as well as the underlying cognitive and behavioral mechanisms that influence human performance. It evaluates both contextual factors and cognitive or organizational influences that may affect operator actions and decisions. Expert judgment plays a central role in conducting qualitative assessments, which are subsequently translated into quantitative estimates of HEPs. Designed to support both deterministic and probabilistic safety assessment, IDHEAS-ECA provides a comprehensive framework for understanding and modeling human contributions to risk.

II.A.2. SPAR-H

SPAR-H method is a streamlined HRA approach designed to estimate HEPs in nuclear power plant operations [4]. It integrates both diagnosis error and action error and uses a set of predefined performance shaping factors (PSFs) to adjust base error rates. The method applies a relatively simple quantitative framework that enables consistent and rapid evaluations across a wide range of human tasks. Expert judgment is incorporated to assess task context and determine appropriate PSF multipliers. SPAR-H has been widely adopted in risk-informed applications due to its balance between usability and technical rigor.

II.A.3. ASEP/THERP

THERP is one of the earliest and most comprehensive HRA methods developed for nuclear power applications [5]. THERP provides a structured framework for identifying, analyzing, and quantifying human errors in complex systems. The methodology involves detailed task analysis, classification of potential human errors, and estimation of HEPs using empirical data. PSFs are applied to adjust base error rates, and dependency effects between tasks are explicitly modeled. THERP employs event trees to integrate human error probabilities into probabilistic risk assessments, making it a foundational method that has influenced many subsequent HRA approaches.

On the other hand, ASEP was developed as a simplified HRA approach to facilitate more efficient human error analysis during PSAs [6]. ASEP draws heavily on the THERP framework but streamlines the process to enable consistent application by analysts with limited HRA expertise. The method uses simplified decision trees to guide the estimation of HEPs for both pre-initiator and post-initiator human actions. Like THERP, ASEP incorporates PSFs to account for context-specific conditions but offers predefined multipliers and screening criteria to accelerate the quantification process. ASEP has been widely used for screening-level evaluations and as a practical tool in regulatory and industry applications.

II.A.4. Review Result of HRA Methods

NEA/CSNI/R(2015)1 published by OECD/NEA was used to review the HRA methods [7]. In NEA/CSNI/R(2015)1 report, desirable attributes of HRA methods were identified and defined. A total of twenty-seven attributes were developed and grouped into five categories: Construction validity, Content Validity, Empirical Validity, Reliability, and Usability. Table I is the example of evaluation criteria for rating scales on each attribute. IDHEAS-ECA, SPAR-H and ASEP/THERP were evaluated based on attributes in the NEA/CSNI/R(2015)1 [8].

TABLE I. Example Attributes, their Descriptions, and Rating Scales [8].

No.	Attribute	Description	Rating Scale
1	Availability of information relating to the technical basis of the method	Information is provided on the technical basis of the method, in terms of its scientific underpinnings and data, in order to allow a judgment on the validity of the method to be made.	High, Intermediate, and Low
2	The technical basis of the method (theory)	The technical basis of the method is based upon, and does not contradict, a relevant body of scientific knowledge.	High and Low
3	The technical basis of the method (data)	Where the technical basis of the method is based on a dataset, the source of the data/information and its relevance for application in the nuclear industry should be demonstrated.	High, Intermediate, and Low
4	Internal consistency of the method	The method demonstrates internal consistency between the technical basis, the error definition, the PSFs and the qualitative and quantitative method steps.	High and Low
5	Qualitative assessment	It is recognized as good practice that HRA quantification is supported by qualitative analysis to develop an understanding of operator performance within the scenario that is being assessed. This attribute considers the extent to which the qualitative analysis stages of the HRA (e.g. task analysis and error identification) is directed or prescribed by the HRA method, beyond providing a set of PSFs to be considered.	High, Intermediate, and Low
6	Adequacy of PSFs	The method requires qualitative assessment of a majority of accepted factors that affect human reliability.	High and Low
7	Qualitative sensitivity	The method is quantitatively sensitive to the effect of each individual PSF considered qualitatively.	High, Intermediate, and Low
8	Inter-dependency between PSFs	Typically, HRA methods adopt a linear multiplicative combination of PSFs. It is recognized that some PSFs may interact in other ways, e.g., a step change in the effect of one PSF once a threshold has been reached on a second PSF, or where the effect of the combination of two PSFs is far greater than multiplicative relationship would predict or where one PSF has a triggering effect on other PSFs in a causal chain.	High, Intermediate, and Low
9	Consideration of human error dependency	Modeling should include consideration of human error dependencies or common cause failures.	High, Intermediate, and Low
10	Consideration of deviations in accident sequences	The method should provide a capability to accommodate deviations from nominal accident scenarios due to plant conditions and human failure scenarios.	High, Intermediate, and Low
11	Consideration of fault progressions in accident sequences	Fault progressions including consequential faults and accident sequences encompassing Level 1 and Level 2 PSA which may involve extended time sequences and degraded operating environments should also be accommodated.	High, Intermediate, and Low

IDHEAS-ECA has the largest number of attributes rated as “High”. On the other hand, SPAR-H and THERP show the second and third largest numbers in order. The following are the attributes for which IDHEAS-ECA was rated higher than at least one of the methods. IDHEAS-ECA is the latest version of the second generation HRA methods. The second generation HRA methods were developed for improving several challenges of the first-generation HRA methods. The list of attributes below indicates that IDHEAS-ECA considers the challenges of the first-generation HRA methods, especially for K-HRA

- The technical basis of the method (Data) (#3)
- Qualitative assessment (#5)
- Consideration of deviations in accident sequences (#10)
- Consideration of fault progressions in accident sequences (#11)
- Consideration of cognitive error (#12)
- Consideration of process factors (#15)
- Statistical evidence (#16)
- Qualitative outputs (#23)
- Use of Limiting Values (#26)
- Resources (#27)

As a result, we selected IDHEAS-ECA method for application in the MPAS model. Nevertheless, the IDHEAS-ECA methodology has certain limitations, particularly the lack of concrete guidelines for dependency analysis and the absence of recovery analysis. Therefore, in the following chapter, alternative methodologies for dependency analysis and recovery analysis that can be used in conjunction with the IDHEAS-ECA HRA method have been investigated

II.B. Review of Dependency Analysis Method

Dependency analysis refers to the process of identifying and evaluating the extent to which the performance of one human action is influenced by previous or concurrent actions. This includes considering factors such as shared personnel, similar tasks, time pressure, or common cues that could increase the likelihood of human error if one action fails. Dependency analysis helps assess the realistic probability of multiple related human errors occurring, which is critical for accurate risk modeling.

As part of the dependency analysis, we conducted a comparative evaluation of the EPRI dependency method suggested in NUREG-1921, SPAR-H, and IDHEAS-DEP methodologies. On the other hand, THERP was excluded from the list. It’s because, as mentioned in Table 21, THERP is used for quantification as a part of most dependency methods but does not provide specific guidance to determining a dependency level.

II.B.1. EPRI Dependency Method in NUREG-1921

The dependency analysis method described in NUREG-1921 provides a structured approach for assessing dependencies between human actions within HRA. It uses eight qualitative factors – intervening success, crew, cognitive, cue demand, manpower, location, sequential timing, stress – to determine the overall dependency level between two or more human actions. Based on this assessment, the dependency is categorized into one of five levels : zero, low, moderate, high, complete [9].

II.B.2. SPAR-H Dependency Method

The guidance on the SPAR-H methodology includes a structured approach to dependency analysis by defining five levels of dependency : zero, low, moderate, high, and complete. These levels are determined based on four qualitative factors : crew, time, location, and cues. For each factor, guidance is provided to qualitatively assess the dependency between two human actions. After a dependency level with the previous HFE (Human Failure Event) is determined, each equation for the dependency levels is applied to adjust the HEP for the HFE using the THERP dependency equations [4].

II.B.3. IDHEAS-DEP Method

IDHEAS-DEP has been updated as a framework for modeling dependency in HRA, particularly within the IDHEAS-G framework. This model emphasizes a more context-driven and evidence-based approach, moving beyond traditional categorical levels. It incorporates key factors such as functions or system similarity, time proximity, same personnel, location similarity, procedure similarity to assess the likelihood of dependency between human actions. Unlike earlier methods that rely on fixed multipliers, the model supports a graded assessment, encouraging the use of expert judgment and scenario-specific information to derive conditional probabilities. This allows for more nuanced and realistic treatment of dependencies in complex operational contexts [10].

II.B.4. Review Result of Dependency Analysis Method

NEA/CSNI/R(2015)1 published by OECD/NEA was used in order to review dependency analysis methods [7]. Some attributes that are less significant or irrelevant to dependency analysis were excluded from the original list proposed in the NEA/CSNI/R(2015)1 report. Among twenty-seven attributes, nine attributes were used to review dependency analysis methods as follows.

- Availability of information relating to the technical basis of the method
- The technical basis of the method (theory)
- The technical basis of the method (data)
- Internal consistency of the method
- Qualitative assessment
- Adequacy of PSFs/dependency factors
- Application/maturity
- Traceability
- Resources

The results of the analysis indicated that, despite the distinct advantages of each methodology, the evaluation outcomes were largely similar. However, the EPRI dependency method provides HRA analysts comprehensive information and its application is required for understanding the method and analyzing dependencies between HFEs. The method operates a relevant dependency model of human performance or system safety which has scientific acceptance. The qualitative and quantitative component parts of the method are theoretically compatible and form a coherent consistent whole. The dependency method contains or prescribes a process for qualitatively selecting a dependency level. Also, the EPRI method provides a procedure to ensure easy and complete traceability of dependency assessments, such that an independent reviewer could trace back how dependency levels are evaluated. In addition, although there are a lot of dependency candidates generated from cutsets, the method itself (i.e., evaluating a dependency level) may not require the huge amount of time and cost, if all the relevant information is ready [11].

II.C. Review of Recovery Analysis Method

Recovery analysis within HRA refers to the evaluation of the potential for operators to successfully detect and correct an error or prevent its consequences after the initial failure has occurred. Key factors influencing recovery include the availability of cue, time available for recovery, operator training, procedures, and system feedback. Recovery analysis is essential for ensuring realistic estimation of human error probabilities, as it accounts for the defense-in-depth strategies inherent in many operational contexts. Despite its importance, formalized methodologies for recovery analysis remain limited, and are often implemented based on expert judgment or simplified assumptions. As part of the recovery analysis, we reviewed THERP and CBDT (Cause-Based Decision Tree) methods. IDHEAS-REC is a recovery method for supporting IDHEAS-ECA. In the current IDHEAS-ECA, recovery probabilities are assumed as 1.0, because an approach to recovery analysis within IDHEAS-ECA was not developed yet.

II.C.1. THERP

The THERP incorporates recovery analysis as a critical component of human error evaluation. In THERP, recovery is modeled explicitly as a branch in the event tree, representing the probability that an operator detects and corrects an error before

it leads to undesirable consequences. The recovery probability is typically estimated based on contextual factors such as checking routine tasks with written materials, alerting factors, checking by reader/checker of the task performer. This approach allows for quantifying the likelihood of successful recovery and integrating it into the overall HEP calculations [5].

II.C.2. CBDT

The CBDT incorporates recovery analysis by evaluating the potential for operators to detect and correct errors based on the underlying cognitive causes of failure. CBDT determines recovery failure probabilities such as self-review, extra crew, shift technical advisor review, or shift change [12].

II.C.3. Review Result of Recovery Analysis Method

NEA/CSNI/R(2015)1 published by OECD/NEA was used in order to review recovery analysis methods [7]. Some attributes that are less significant or irrelevant to dependency analysis were excluded from the original list proposed in the NEA/CSNI/R(2015)1 report. Among twenty-seven attributes, fifteen attributes were used to review dependency analysis methods as follows.

- Availability of information relating to the technical basis of the method
- The technical basis of the method (theory)
- The technical basis of the method (data)
- Internal consistency of the method
- Qualitative assessment
- Adequacy of PSFs
- Quantitative sensitivity
- Inter-dependency between PSFs
- Consideration of statistical uncertainty
- Statistical evidence
- Application/maturity
- Traceability
- Qualitative outputs
- Qualitative uncertainty and quantitative conservatism
- Resources

The results of the analysis indicate that THERP demonstrated a higher level of performance across a greater number of evaluated attributes than the CBDT methodology. Notably, THERP received higher ratings than CBDT in key attributes, including the adequacy of its treatment of PSFs and the extent of supporting statistical evidence [11].

III. CASE STUDY

Human errors from KINS's operational performance information system (OPIS) event reports were evaluated as a case study. This study identifies gaps and provides actionable insights to ensure their validity and applicability in SDP HRA applications. In the SDP evaluation, PSFs were assessed to estimate the delta HEP resulting from human errors. As previously mentioned, the IDHEAS-ECA methodology was employed for this purpose. However, since the dependency analysis method and recovery analysis method have not yet been finalized, these factors were not considered in the current evaluation. Three OPIS event reports are as follows.

- An automatic start of a standby diesel generator at Wolseong Unit 2 on April 5, 2023 (OPIS No. 230405W2)
- An automatic reactor trip at Hanul Unit 6 on July 19, 2020 (OPIS No. 200719HU6)
- A manual reactor trip and actuation of auxiliary feedwater system at Hanbit Unit 1 on May 10, 2019 (OPIS No. 190510HB1)

III.A. OPIS No. 230405W2

The event occurred during testing protection relays installed on 13.8kV BUB (Bus Under Breaker) bus. The nuclear utility failed to manage test and maintenance procedures that can cause loss of voltage with the high probability. An inlet circuit breaker for the BUB bus was activated due to loss of voltage when operators performed the procedures. Accordingly, a standby diesel generator was automatically activated. This action is related to human factors degradation, especially for procedures. An action CFM (Cognitive Failure Mode) can be credited. The relevant PSFs, i.e., task complexity, procedures and guidance, and training and experience, can be evaluated using the following options [11].

- C5: Cues for detection are not obvious
- PG3: Procedure lacks details
- TE5: Operator is inexperienced

As a result of HEP evaluation, assuming a nominal HEP (all HSI work successfully) of 1.00E-04, the HEP under degraded PSF conditions was estimated to be 2.10E-01. Accordingly, the delta HEP was calculated as 2.10E-01.

III.B. OPIS No. 200719HU6

After the reactor tripped, operators determined to stop a main feedwater pump to prevent steam generators from overcharging and reactor coolant from overcooling. Due to HSI errors (indicators for main feedwater pumps and booster pumps showed that these were still working), operators failed to recognize the actual status of the pumps, then tried to stop a main feedwater pump and booster pump. Accordingly, the operator's action caused a loss of main feedwater. This action is related to human factors degradation, especially for procedures and HSIs. It is a post-initiator. An action CFM and recovery action can be credited. The relevant PIFs, i.e., task complexity, procedures and guidance, and training and experience, can be evaluated using the following options. Although indicators for the pumps were not showing the correct information, operators still had a chance to recognize the errors via other parameter values. Procedures that operators used did not provide alternative ways to check the status of the pumps. Operators may be familiar with the scenario but might not expect that indicators show the wrong information. [11].

- C3: Detection demands for high attention
- PG3: Procedure lacks details
- TE5: Operator is inexperienced

As a result of HEP evaluation, assuming a nominal HEP (all HSI work successfully) of 1.00E-04, the HEP under degraded PSF conditions was estimated to be 4.30E-03. Accordingly, the delta HEP was calculated as 4.20E-04.

III.C. OPIS No. 190510HB1

During the control rod extraction process, operators failed to correctly evaluate the impact of the control rod extraction on reactivity. This human error occurred due to a combination of many problems in safety culture, operator experience, violation, etc. This action is related to human factors degradation, especially for procedures. To highlight the impact of procedure errors, this report did not consider all the problems from the event when calculating an HEP. The relevant PIF, i.e., procedures and guidance, can be evaluated using the following option. [11].

- PG3: Procedure lacks details

As a result of HEP evaluation, assuming a nominal HEP (all HSI work successfully) of 1.00E-04, the HEP under degraded PSF conditions was estimated to be 3.20E-04. Accordingly, the delta HEP was calculated as 2.20E-04.

IV. CONCLUSIONS

This study reviewed and evaluated various HRA methodologies for application in the regulatory PSA model, with a focus on supporting the SDP. Among the methods, IDHEAS-ECA was selected for its comprehensive treatment of cognitive and contextual factors. However, limitations remain, particularly the absence of finalized methods for dependency and recovery analysis. To address this, alternative methodologies were compared. While evaluation results were broadly consistent, the

NUREG-1921 method for dependency showed notable strengths, especially in practical applicability and technical basis. A case study using OPIS event data illustrated the impact of degraded PSFs on human error probability, highlighting the need for realistic modeling. Overall, while IDHEAS-ECA serves as a strong foundation, incorporating systematic dependency and recovery analysis methods will be essential for improving the robustness and completeness of HRA in regulatory PSA applications.

REFERENCES

[1] D. J. JANG et al., *Regulatory PSA Model Utilization Framework*, KINS/GR-628 (2018).
[2] J. H. YU et al., Advancement of Based Technology for Regulatory PSA Model, KINS/HR-1926 (2023).
[3] J. XING, Y. J. CHANG, J. D. SEGARRA, Integrated Human Event Analysis System for Event and Condition Assessment *(IDHEAS-ECA)*, NUREG-2256 (2022).
[4] D. GERTMAN, H. BLACKMAN, J. MARBLE, J. BYERS, C. SMITH, *The SPAR-H Human Reliability Analysis Method*, NUREG/CR-6883 (2005).
[5] A. D. SWAIN, H. E. GUTTMAN, *Handbook of Human Reliability Analysis with Emphasis on Nuclear Power Plant Applications*, NUREG/CR-1278 (1983).
[6] A. D. SWAIN, *Accident Sequence Evaluation Program Human Reliability Analysis Procedure*, NUREG/CR-4772 (1987).
[7] Y. J. CHANG, D. BLEY, L. CRISCIONE, B. KIRWAN, A. MOSLEH, T. MADRY, R. NOWELL, *Establishing the Appropriate Attributes in Current Human Reliability Assessment Techniques for Nuclear Safety*, NEA/CSNI/R(2015)1 (2015).
[8] J. PARK et al., *Supporting Korea Institute of Nuclear Safety in Probabilistic Safety Assessment and Human Reliability Analysis*, KINS/HR-1962 (2023).
[9] S. LEWIS, S. COOPER, *EPRI/NRC-RES Fire Human Reliability Analysis Guidelines – Final report*, NUREG-1921 (2012).
[10] M. KICHLINE, J. XING, Y.J. CHANG, *Integrated human event analysis system dependency analysis guidance (IDHEAS-DEP)*, RIL-2021-14 (2021).
[11] J. PARK, Z. MA, R. BORING, D. LEE, A. KIM, N. KIM, *Supporting Korea Institute of Nuclear Safety in Probabilistic Safety Assessment and Human Reliability Analysis 2*, KINS/HR-1962 (2024).
[12] G. PARRY, A. BEARE, A. SPURGIN, P. MOIENI, *An approach to the analysis of operator actions in probabilistic risk assessment*, EPRI TR-100259 (1992).

ASRAM2025
www.asram2025.org
Asian Symposium on Risk Assessment and Management 2025
Pattaya, Thailand, 27 – 29 August 2025

A SYSTEMIC ANALYSIS OF LEADERSHIP AND ETHICS IN THE REGULATORY FRAMEWORK THROUGH THE RADIOLOGICAL ACCDENT IN SAMUT PRAKARN

Soratos Tantideeravit[1]

[1] *Office of Atoms for Peace, Chatuchak, Bangkok ,10900, Thailand, soratos.t@oap.go.th*

EXTENDED ABSTRACT

The Samut Prakarn Cobalt-60 accident remains the most severe radiological incident in Thailand's nuclear safety history. It revealed deep-rooted systemic weaknesses in the regulatory framework surrounding the management of radioactive sources. Despite subsequent regulatory restructuring, recent incidents involving the loss of radioactive sources, [1], [2], suggest that underlying issues in safety culture persist. The recent draft report of the IAEA Integrated Regulatory Review Service Mission to Thailand [3] specifies key recommendations in the leadership and culture for safety, including the establishment of leadership for safety assessment mechanisms and the assignment of prime responsibility for safety within the national legal framework. This study therefore investigates lessons learned from the Samut Prakarn accident, which was not the result of a single failure but rather of a complex interaction of unclear responsibility, weak communication, and a reactive regulatory mindset.

Drawing on the methodology of systemic crisis analysis of the Nestucca oil spill [4] and Fukushima Daiichi [5] disasters, this study explore Thailand's nuclear regulatory environment during the management of the Samut Prakarn accident, focusing on the leadership for safety mindset and the interactions among actors within the regulatory framework. The chronological view of the Samut Prakarn accident provided in the IAEA report [6] offers official insights into the structure to the consequences of the accident, serving as a foundation for uncovering its systemic origins. As Illustrated in **Figure 1,** stakeholders involved at the time of the accident were identified and grouped into four sectors: government, international actors, civil society, and the nuclear and radiation industry. Their interactions were classified into four types: low-coupling, tight-coupling, amplifying effects, and constraining effect. These interactions were then linked to the broader issue surrounding the use of nuclear technology and the occurrence of radiological incidents in Thailand.

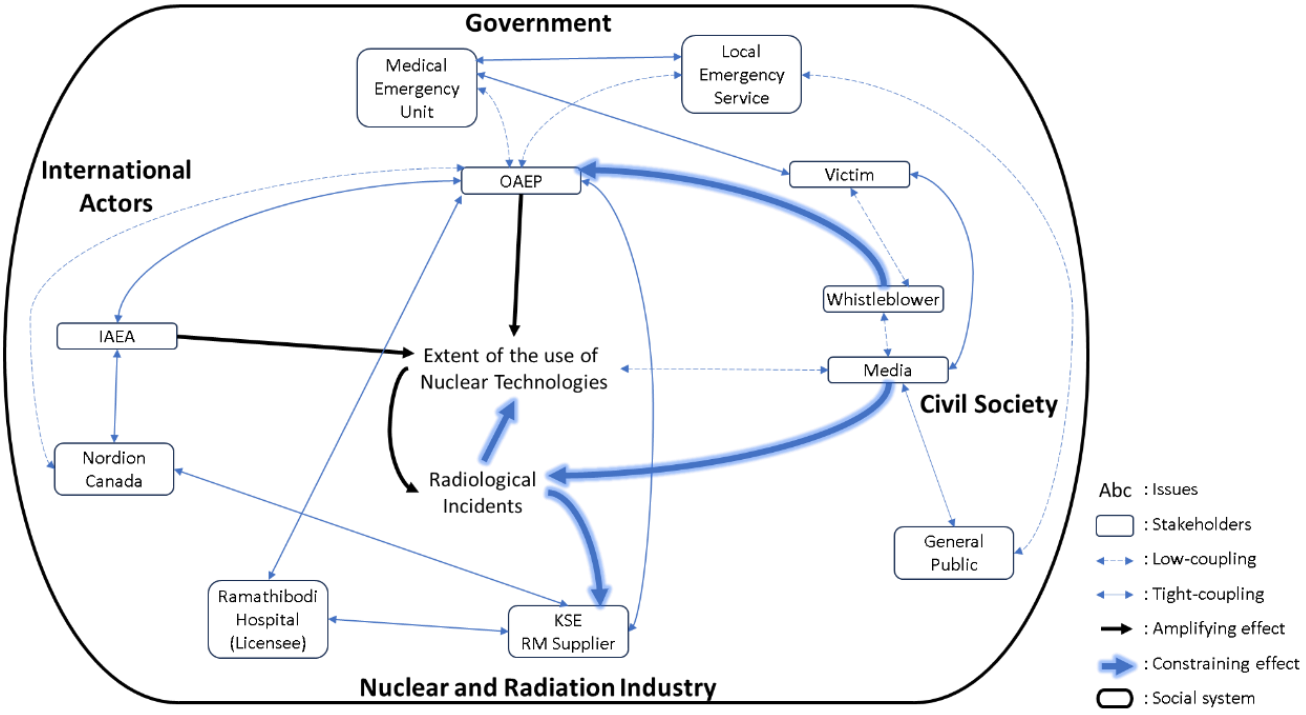

FIGURE 1. Systemic graph of interactions among actors during the Samut Prakarn accident

To move beyond "superstitious learning" where lessons from an accident are misinterpreted or ignored, an initiation of systemic changes were proposed. The stakeholder interactions depicted in **Figure 1** were used to identify the major blocks that have hindered systemic learning and safety culture development in Thailand's nuclear and radiation safety industry. The analysis focused on four key hindering factors employed by key stakeholders:

- Basic Assumptions: Underlying beliefs that shape behavior.
- Foundation of Legitimacy: Sources of authority or justification for actions.
- Usual Scapegoats: Typical actors or factors blamed when failures occur.
- Routine Strategies: Default responses or behaviors in crisis or uncertainty.

These blocking patterns, often deeply embedded in institutional behavior, have contributed to a cycle of reactive responses and avoidance of accountability. To address this, this study proposed a set of unlocking strategies for each stakeholder group. These strategies aim to challenge the prevailing basic assumptions on safety and accountability, and foster a more preventive mindset. The hindering factors and corresponding unblocking strategies for each stakeholder are summarizes in **Table 1**.

TABLE 1. Hindering factors and unblocking strategies for each stakeholder

Stakeholder / Hindering Factor	**Office of Atomic Energy for Peace (OAEP)**	**Nuclear industry (e.g., hospitals, supplier)**	**Local government**	**Media**	**Public and civil society**
Basic assumptions	Reactive regulation; reliance on formal notification	Transfer or abandon disused sources / rely on regulatory instructions	Focus on emergency response over prevention	Focus on blame and drama; neglect systemic causes	Rely on media for information; react only during crises
Foundation of legitimacy	Technocratic control orientation	Cost avoidance	Bureaucratic ambiguity	Sensationalism	Media coverage
Usual scapegoats	Licensees, lack of notification	Regulatory body (OAEP); disposal costs	Regulatory agencies; budget constraints	Government and OAEP; industry cover-ups	Government and regulators; industry secrecy
Routine strategies	Reactive regulation	Transfer or abandon disused sources	Emergency response	Focus on drama	React during crises
Unlocking strategies	Separate regulatory and promotional functions; institutionalize leadership for safety assessments; strengthen inspection and tracking systems	Mandate takes-back or disposal plans in licensing; require financial guarantees for DSRS management	Enact comprehensive nuclear liability law; create centralized DSRS disposal fund; promote prevention as a political priority	Train journalists in science and risk communication; encourage investigative reporting on regulatory systems	Develop public education programs on radiation safety; institutionalize community engagement in safety planning

CONCLUSION

This study provides a systemic analysis of the Samut Prakarn radiological accident, revealing that the incident was not an isolated failure but a manifestation of entrenched weaknesses in Thailand's nuclear regulatory framework. By mapping stakeholder interactions and identifying hindering factors; such as reactive regulation, technocratic legitimacy, and routine crisis responses the research highlights how institutional behaviors have perpetuated a cycle of inadequate safety culture and accountability. The insights from this study are expected to inform improvements in the regulatory procedures of the Office of Atoms for Peace (OAP), particularly in the legislation, stakeholder communication, training of regulatory personnel, and the cultivation of a learning culture. The findings underscore the need for Thailand's nuclear and radiation regulatory approach to evolve from a compliance-based model to one emphasizing ethics, proactive leadership, and a preventive and accountable environment.

Future research could benefit from extending the systemic framework developed in this study to a wider range of national radiological incidents, incorporating operational data from other national sectors or international contexts. Such comparative analysis would support the validation and refinement of the proposed strategies, enhancing their relevance and resilience across diverse regulatory environments. Furthermore, exploring the integration of Human Reliability Analysis (HRA) methodologies is recommended to deepen the understanding of stakeholder behavior and decision-making dynamics in complex radiological incidents.

ACKNOWLEDGMENTS

This work was supported by the European Leadership for Safety Education (ELSE) Programme. The author sincerely thanks the ELSE pedagogical team for their guidance and knowledge sharing.

REFERENCES

[1] "Bangkok Post," 12 May 2016. [Online]. Available: https://www.bangkokpost.com/thailand/general/970121/mysterious-box-causes-panic-on-soi-phahon-yothin.

[2] K. H. Ng, "Another loss of radioactive material in Thailand highlights the need for effective risk communication," no. 24(1) : 24-31, 2023.

[3] International Atomic Energy Agency, "Report of the Integrated Regulatory Review Service (IRRS) Mission to Thailand," 2025.

[4] I. Deschamps, M. Lalonde, C. T. Pauchant and P. J. Waaub, "What Crises Could Teach Us about Complexity and Systemic Management," Vols. 55, 107-129 (1996), 1997.

[5] Y. Guntzburger and C. T. Pauchant, "Complexity and ethical crisis management: A systemic analysis of the Fukushima Daiichi Nuclear disaster," Vols. 1(4) pp. 378 - 401, 2014.

[6] International Atomic Energy Agency, "The Radiological Accident in Samut Prakarn," IAEA, Vienna, 2002.

Poster Session 1(8:30 - 10:00)	The Port 6, C Floor	Severe Accidents and Thermal Hydraulic Analyses, External Events, Risk Communication and Policy
		Chair/Facilitator 1: Miss Restu Maerani (Research Center for Nuclear Reactor Technology (BRIN))
		Chair/Facilitator 2: Mr. Weerawat Pornroongruengchok (Thailand Institute of Nuclear Technology (TINT))
8:30 - 8:45		ID 43: Research on Probabilistic Risk Assessment of Seismic induced Tsunami Events Speaker: Eisuke Inoue (Tokyo City University) Contributors: Eisuke Inoue (Tokyo City University)
8:45 - 9:00		ID 44: Study on the Optimization of APC (Air Plane Crash) Countermeasures for Nuclear Power Plants Using Finite Element Analysis Speaker: Ryo Kojima (Tokyo City University) Contributors: Ryo Kojima (Tokyo City University), Hitoshi Muta (Tokyo City University)
9:00 - 9:15		ID 146: Quantitative Evaluation of Aircraft Impact Probability on TRR-1/M1 Research Reactor Speaker: Sirirat SEEMAPAPONG (Thailand Institute of Nuclear Technology (TINT)) Contributors: Ms Sirirat Seemapapong (TINT), Dr Kanokrat Tiyapun (TINT), Dr Saensuk Wetchagarun (TINT), Dr Nart Noodee (TINT)
9:15 - 9:30		ID 67: Multi-fault Mode Analysis for Reactor Cavity Cooling System of High Temperature Gas-cooled Reactor Speaker: Zhengyang Li (Institute of Nuclear and New Energy Technology) Contributors: Zhengyang Li (Institute of Nuclear and New Energy Technology)
9:30 - 9:45		ID 22: Does Restarting the Operations of Nuclear Plants Improve Public Evaluations in Utility Companies? A Factorial Survey Experiment in Post-Fukushima Japan Speaker: Tomohiro Fujita (Institute of Nuclear Safety System, Inc.) Contributors: Tomohiro Fujita (Institute of Nuclear Safety System, Inc.)

ASRAM2025
www.asram2025.org
Asian Symposium on Risk Assessment and Management 2025
Pattaya, Thailand, 27 – 29 August 2025

Research on probabilistic risk assessment of seismic induced tsunami events

Eisuke Inoue[1], Hitoshi Muta[2], Yasuki Ohtori[3]

[1] *Tokyo City University, Common Major in Nuclear Energy /1-28-1, Tamazutsumi, Setagaya-ku ,Tokyo 158-8557/g2481801@tcu.ac.jp*
[2] *Tokyo City University, professor /1-28-1, Tamazutumi, Setagaya-ku ,Tokyo 158-8557 /hmuta@tcu.ac.jp*
[3] *Tokyo City University, professor/1-28-1, Tamazutumi, Setagaya-ku ,Tokyo 158-8557/ohtoriy@tcu.ac.jp*

ABSTRACT

Since the Fukushima Daiichi nuclear accident, the importance of enhancing nuclear safety against external hazards, particularly earthquakes and tsunamis—has been widely recognized. Although probabilistic risk assessment (PRA) methods have been developed for individual hazards, comprehensive methodologies for evaluating compound events involving both seismic and tsunami effects remain limited despite their increasing relevance. This study aims to develop a PRA methodology capable of addressing the complex and diverse damage mechanisms resulting from such compound events, using a model plant as the evaluation basis. While three evaluation models, the Independent, Cumulative, and Integrated Seismic-Tsunami Models, were proposed in a previous study [1], they have not been systematically applied within an integrated framework. In this research, these models are refined, integrated, and applied to simulate realistic accident progression scenarios. A case study is conducted using event tree and fault tree analyses, wherein core damage frequencies are quantitatively evaluated for multiple combinations of seismic intensities and tsunami wave heights. The methodology accounts for fatigue failure, inundation, and functional loss due to structural degradation. The results underscore the importance of scenario-based risk modeling and highlight the value of incorporating fragility and uncertainty information into compound event analysis to support more realistic and robust nuclear safety assessments.

Keywords: seismic, tsunami, compound events, PRA

I. Background

Following the accident at the Fukushima Daiichi Nuclear Power Plant, enhancing the safety of nuclear facilities has become an extremely important issue. The significance of risk assessment for external events such as seismic and tsunami hazards, which were the primary causes of the accident, has been increasingly recognized. PRA is now widely employed as part of safety countermeasures. While evaluation methods for individual external hazards, such as seismic or tsunami events, have been developed, comprehensive methodologies for assessing compound events involving both hazards simultaneously have not yet been fully established. Accordingly, further research is needed to address this gap.

II. Objective

In compound events where seismic and tsunami hazards occur simultaneously, a range of complex damage states is anticipated due to the combined effects of both hazards. This study aims to develop an analytical methodology capable of addressing such complex damage states. The approach is based on three evaluation models proposed in previous studies [1] and is intended to establish a PRA methodology that can appropriately assess the impacts of compound seismic and tsunami events. Specifically, the study systematically identifies potential scenarios under compound events and conducts risk assessments based on these scenarios to clarify the progression mechanisms of system functional losses caused by external hazards. Furthermore, the developed methodology is applied to a model plant to verify its practical applicability and validity through case studies.

III. Methodology

The "evaluation models" in this study refer to analytical models developed for conducting risk assessments. In the

context of compound events—where both seismic and tsunami hazards occur—four types of component damage scenarios are assumed, as illustrated in Figure 1. These scenarios include damage due to seismic effects alone, tsunami effects alone, and combined effects of both hazards. To address the diversity of damage states, this study categorizes and evaluates them using the following three models:(1) the Independent Seismic-Tsunami Evaluation Model, (2) the Cumulative Seismic-Tsunami Evaluation Model, and (3) the Integrated Seismic-Tsunami Evaluation Model. (1) In this model, damage to each piece of component is evaluated separately for seismic and tsunami effects. This approach is mainly applied to dynamic and electrical components, where the damage modes and indicators differ between seismic and tsunami events. Evaluations are conducted independently for each hazard. Component is considered functionally failed if damage is caused by either hazard, which requires logical coupling through an "OR gate." As shown in Figure 2, an extended fault tree (FT) is constructed for each piece of component to account for both seismic and tsunami damage sources. In the integrated FT, an "OR condition" is applied to all basic events, indicating that failure due to either hazard leads to functional loss, ultimately contributing to core damage.

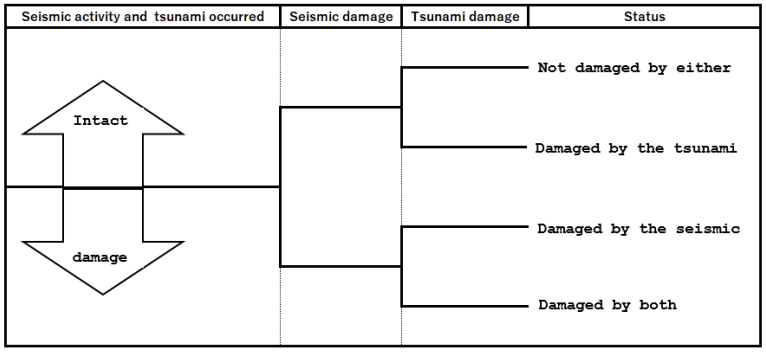

Fig1. Component damage states caused by seismic and tsunami effects

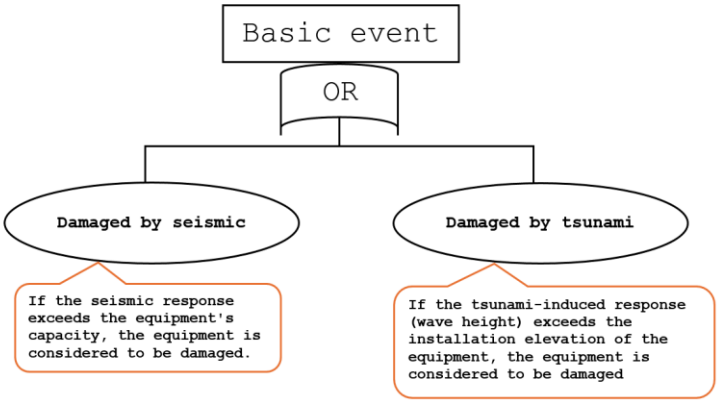

Fig2. Component damage states caused by seismic and tsunami effects

(2) This model assesses whether the cumulative external forces from both seismic and tsunami events exceed a certain damage threshold. It is primarily applied to support structures such as components or piping. The dominant damage mode considered is fatigue. However, based on previous research, no established method exists for evaluating cumulative damage due to tsunami forces, and practical applications of cumulative evaluation for seismic forces are also limited. Therefore, in this study, a simplified model is used to preliminarily assess the effect of cumulative forces. If the cumulative effect is deemed negligible, this model is not applied. When the effect is non-negligible, the cumulative evaluation model is employed. The model simulates stainless steel piping, and cumulative damage is assessed using a cumulative damage rule and S–N curves.

(3) This model focuses on tsunami protection structures such as watertight doors and seawalls, which are assumed to lose functionality due to the combined impact of seismic and tsunami events. Specifically, the model assumes that structures like seawalls, designed for tsunami protection, are damaged by seismic motion, reducing their protective capability during subsequent tsunami inundation. As a result, components are exposed to tsunami effects and become damaged. This model introduces new damage scenarios that consider the compound nature of these events. In constructing such scenarios, it is essential to account for the fact that the tsunami resistance of protective structures may vary depending on the magnitude of the earthquake. Accordingly, the damage states of tsunami protection facilities are classified by seismic magnitude, and progression scenarios are constructed based on these classifications. Target structures are selected with reference to prior studies on tsunami protection. For each structure, damage states are categorized based on seismic intensity [2]. Additionally, the tsunami intrusion process following structural damage is considered, and the sequence of progression is organized chronologically to construct realistic and comprehensive scenarios.

IV. Current Results and Issues

(1) In setting scenarios for actual quantification, the following events were assumed: loss of offsite power due to

seismic events (e.g. collapse of transmission towers), large-break LOCA, medium-break LOCA, small-break LOCA, and tsunami-induced events such as loss of offsite power (e.g., submersion of bus bars), loss of injection function, and loss of heat removal function. Based on combinations of these events, 12 core damage scenarios were considered. Quantification was performed using these scenarios with reference to the flowchart shown in Figure 4 [3]. This enabled the calculation of core damage probabilities for each scenario corresponding to specific levels of ground motion and tsunami wave height.

(2) A simplified model simulating a pipe was subjected to external forces due to seismic and tsunami loading. The resulting stress was calculated and used to evaluate potential damage. The S–N curve shown in Figure 3 represents the fatigue resistance of structures under cyclic loading, where lower stress levels tend to result in slower progression of fatigue damage. While some materials, such as stainless steel, do not exhibit a clearly defined fatigue limit, there exist stress levels at which the probability of fatigue failure is considered extremely low over the expected service life. In this analysis, the calculated stress was confirmed to fall within such a low-stress region, and therefore, cumulative fatigue damage was deemed unlikely. However, in more realistic models, stresses may reach non-negligible levels, potentially leading to cumulative damage. Continued investigation is thus required.

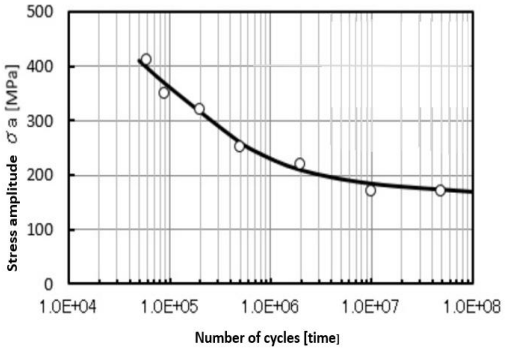

Fig3 S–N curve for stainless steel [4]

(3) The selected tsunami protection structures and their classifications of damage states are presented in Table 1. This table organizes the potential damage states to which each protection structure may transition under seismic impact. However, sufficient quantitative data to validate these state transitions are currently lacking. Accordingly, a hypothetical model representing the gradual degradation of protective functions has been adopted, with the expectation that future accumulation of fragility data will enable refinement of the model. Furthermore, the progression of tsunami-induced inundation following damage to protection structures was analyzed based on a stepwise inflow route: from outside the site to within the site, from within the site to inside buildings, and from inside buildings to equipment rooms. The results of this chronological analysis are summarized in Table 2. This table organizes the inundation pathways based on the assumption that the damage states of each structure presented in Table 1 serve as prerequisite conditions. The pathways are considered to be established when these pre-existing damages are compounded by tsunami wave forces and rising water levels. Based on the information in Tables 1 and 2, a representative Event Tree (ET) illustrating the progression of an accident is shown in Figure 5.

Table1. Damage State Transition Table

<Flood Protection from Outside the Site to Within the Site>	
Facility	Damage States
Seawall	Intact / Minor damage (cracks,) / Severe damage (collapse)
Embankments	Intact / Minor damage (cracks,) / Severe damage (collapse)
Overflow Prevention Wall	Intact / Damage (e.g., collapse)
Discharge Pit/Channel Closures	Intact / Unable to close
<Flood Protection from Within the Site to Inside the Building>	
Facility	Damage States
Reinforced/Watertight Doors	Intact / Damage (unable to close)
Building Exterior Walls	Intact / Minor damage (cracks)
Underground Pipe Duct Access Ports	Intact / Damage (unable to close)
Penetration Sealing Measures (Sealants)	Intact / Damage (reduced watertight performance)
<Flood Protection from Inside the Building to Equipment Rooms>	
Facility	Damage States
Building Drainage Measures (Pumps, etc.)	Intact / Damage (loss of drainage function)
Equipment Room Flood Protection (Watertight doors, seals, etc.)	Intact / Damage

Table2. Tsunami Inflow Routes and Conditions for Inundation

Route	Prerequisite Condition	Activation Condition
E-1: Residual water inflow after overtopping	Seawalls and embankments are intact	Overtopping occurs when tsunami wave height exceeds 28 meters, leading to inflow into the site
E-2: Inflow through damaged section of seawall	Seawall is partially or severely damaged by the seismic	Damage progresses due to tsunami wave force, allowing inflow into the site
E-3: Inflow from intake pit	Overflow protection wall is damaged	Overflow occurs, leading to inflow into the site
E-4: Inflow from damaged embankment	Embankment is partially or severely damaged	Tsunami overtops the embankment from the side, resulting in inflow
E-5: Inflow through drainage outlet opening	Discharge channel opening cannot be closed	Sea level rises due to tsunami, causing backflow and inflow into the site
I-1: Inflow due to damaged watertight doors	Reinforced/watertight doors are damaged by the seismic	Even if not damaged by the seismic, doors may be damaged by tsunami wave force, resulting in inflow into the building
I-2: Inflow through cracks in external walls	Outer building walls are cracked or otherwise damaged	Damage progresses due to tsunami wave force, leading to inflow into the building
I-3: Inflow through underground duct access ports	Inspection opening is damaged	Even if not damaged by the seismic, the opening may be damaged by tsunami wave force, resulting in inflow into the building
I-4: Inflow through building penetrations	Deterioration of sealing materials	Even if not damaged by the seismic, the parts may be damaged by tsunami wave force, resulting in inflow into the building
R-1: Water level rise due to loss of drainage function	Water level rise due to loss of drainage function	Drainage pump is damaged

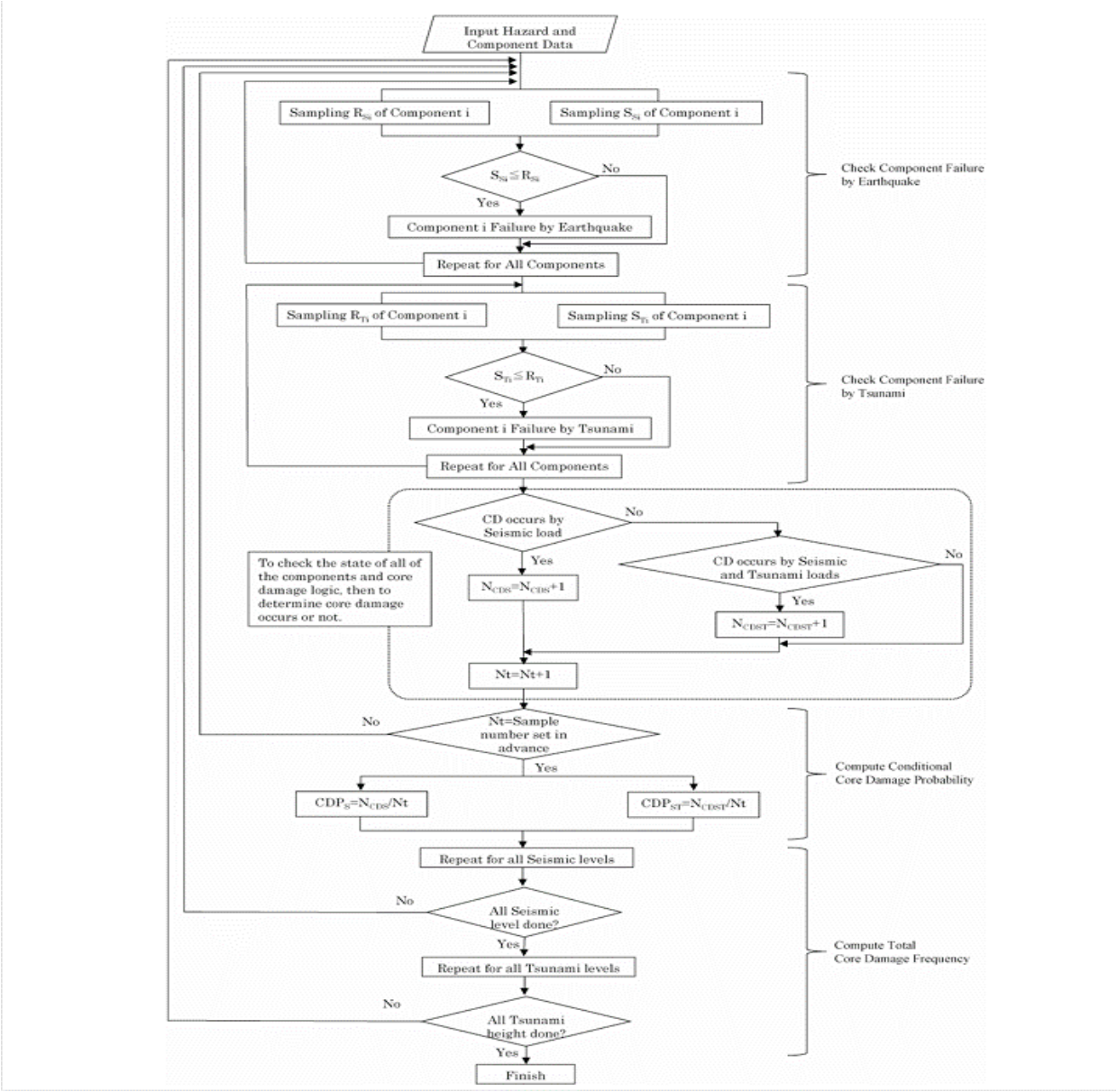

Figure 4. Flowchart for Quantitative Risk Assessment[3]

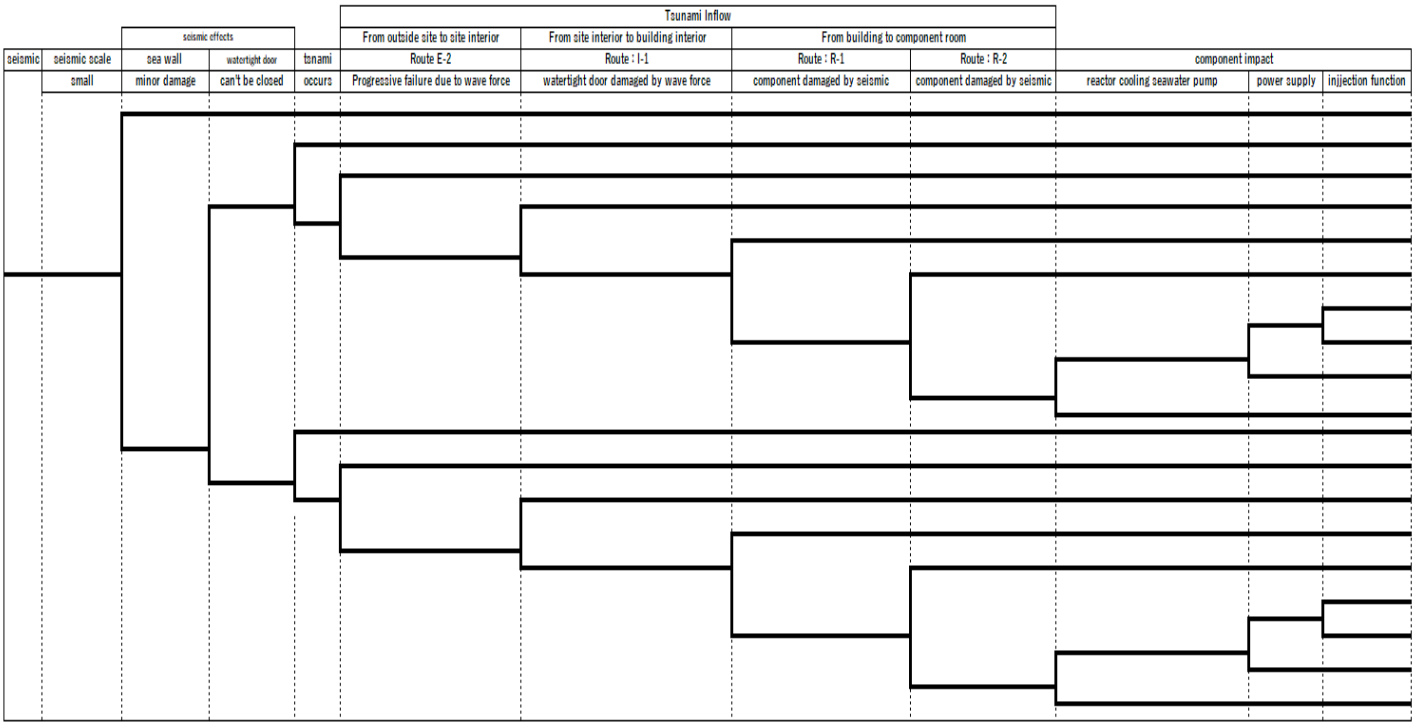

Fig5. Event Tree (ET) for a Small-Scale Seismic Scenario

The event tree (ET) shown in Figure 5 is constructed under the assumption of a small-scale seismic event and targets tsunami protection facilities, specifically seawalls and watertight doors. This ET includes four end states: (1) no initiating event occurs, (2) loss of power supply, (3) loss of injection function, and (4) loss of heat removal function. If any of the three initiating events occur, the ET branches into individual event trees corresponding to each initiating event, where accident progression scenarios are further developed.

V. Summary

V-1. Current Achievements

In this study, 12 core damage scenarios were constructed by combining initiating events such as seismic-induced loss of offsite power and various levels of LOCA with tsunami-induced functional failures (e.g., submersion of bus bars, loss of injection and heat removal functions). Quantification was performed based on these scenarios, enabling the evaluation of core damage probabilities under different levels of seismic intensity and tsunami wave height, as shown in Figure 4. Additionally, a simplified pipe model was analyzed to evaluate cumulative fatigue damage caused by combined seismic and tsunami loads. The calculated stress, assessed against the S–N curve in Figure 3, indicated a low likelihood of fatigue failure under the assumed conditions, though further studies with more realistic models are required. Furthermore, tsunami protection structures were classified by seismic damage states (Table 1), and inundation scenarios were modeled based on a stepwise inflow path from outside the site to equipment rooms (Table 2). Using this information, an event tree representing accident progression under a small-scale seismic scenario was developed, as illustrated in Figure 5.

V-2. Future Work

Moving forward, it is necessary to systematize a comprehensive set of accident progression scenarios based on various combinations of compound events. A key future challenge lies in applying these scenarios in a concrete and quantitative manner to enable practical risk assessments. Additionally, the development of an analytical program capable of simultaneously handling cumulative, integrated, and independent evaluation models is expected to enhance the flexibility and accuracy of risk analysis under complex event conditions.

REFERENCES

[1] Hirohisa Yamakawa, "A Study on PRA Method for Combined Events Using the DQFM Approach," master's Thesis, 2019

[2] "Initiatives for Enhancing the Safety of the Hamaoka Nuclear Power Station", https://www.nra.go.jp/date/000348836.pdf(2025)

[3] Hitoshi MUTA and Ken MURAMATU, "Proposal of Methodology of Tsunami Accident Sequence Analysis Induced by Earthquake Using DQFM Methodology", 2017

[4] "Fatigue and S-N Curve" , https://www.fem-vandy.net/a13.html (2025)

ASRAM2025
www.asram2025.org
Asian Symposium on Risk Assessment and Management 2025
Pattaya, Thailand, 27 – 29 August 2025

Study on the Optimization of APC (Air Plane Crash) Countermeasures for Nuclear Power Plants Using Finite Element Analysis

Ryo Kojima[1], Hitoshi Muta[2]

1 Graduate School of Nuclear Engineering, Tokyo City University,
1-28-1 Tamazutsumi, Setagaya-ku, Tokyo 158-8557, Japan, g2481812@tcu.ac.jp
2 Graduate School of Nuclear Engineering, Tokyo City University,
1-28-1 Tamazutsumi, Setagaya-ku, Tokyo 158-8557, Japan, hmuta@tcu.ac.jp

ABSTRACT

This study aims to establish a numerical simulation framework based on the finite element method (FEM) using an interaction-based approach, under the scenario of an airplane crash (APC) into a nuclear power plant. After verifying the concrete material models and confirming the validity of the aircraft model, a realistic and high-fidelity impact analysis was successfully performed. The ultimate goal is to propose a design guideline that ensures sufficient structural resistance with minimal reinforcement. This will be achieved by quantifying damage zones, evaluating residual capacities, and defining threshold criteria for reinforcement.

I. Background and Motivation

Since the terrorist attacks in the United States in 2001, deliberate airplane crashes (Airplane Crash: APC) have been recognized as a serious threat to critical infrastructure. Nuclear power plants, in particular, are considered high-risk targets due to their nature, and structural countermeasures to enhance safety have been internationally demanded. Conventional APC impact assessments often rely on simplified load models, but these are frequently criticized as being either overly conservative or lacking realism when applied to actual plant designs.

II. Objective

The objective of this research is to clarify the necessary and sufficient conditions for cost-effective APC countermeasures through numerical simulations of aircraft impacts on nuclear power plant buildings. As a first step, the study focuses on establishing a high-fidelity FEM-based impact analysis methodology and validating its accuracy.

III. Analysis Methodology

The analysis was conducted using the explicit dynamic impact analysis code “Ansys LS-DYNA,” employing an interaction-based approach. In this method, both the aircraft (as the projectile) and the target building are modeled in detail, and an initial velocity is applied to the aircraft to simulate the collision. A Boeing 767 was selected as the impacting object, with an initial velocity of 150 m/s against a reinforced concrete (RC) structure. The aircraft model was created using CAD, with components such as the fuselage, wings, engines, and tail represented by shell elements, and each part assigned individual densities and stiffnesses. The impact velocity of 150 m/s was chosen based on international safety guidelines (e.g., IAEA-TECDOC-624) [4], which suggest typical velocities for large commercial aircraft impacts range from 150 to 200 m/s. The Boeing 767 represents a conservative assumption of a large aircraft impact, consistent with prior safety evaluations (e.g., NRC guidelines) [5].

IV. Material Model Evaluation and Validation

Accurate representation of the mechanical properties of materials is essential for appropriately reproducing the behavior of target structures in impact analyses. In this study, which targets RC structures, it is especially important to capture the complex response of concrete—such as nonlinearity, cracking, crushing, and shear failure. Two widely used concrete models implemented in LS-DYNA—the Karagozian & Case Concrete (KCC) model and the Continuous Surface Cap (CSC) model—were considered. These models are commonly adopted for high-velocity, large-scale impact simulations.

To evaluate their validity, numerical simulations were performed to replicate full-scale RC wall impact tests conducted by the Central Research Institute of Electric Power Industry (CRIEPI). The analysis model employed solid elements for the concrete and beam elements for the reinforcement, replicating the dimensions, reinforcement layout, and boundary conditions of the test specimens. Figure 1 shows the finite element model of the RC wall used in the simulations. A rigid body with mass was collided at a constant velocity at the center of the model to observe structural responses[3].

The results showed that the analysis using the CSC model (Figure 2) clearly reproduced perforation from the impact face through to the rear surface, consistent with experimental observations. In contrast, the KCC model (Figure 3) captured a failure mode involving rear-face spalling, which also aligned with the experimental results. Both models were found to be capable of reproducing typical impact responses of RC structures. While the KCC model offers more functionalities and incurs higher computational costs, the CSC model is characterized by easier parameter setup and higher numerical stability. Therefore, considering the applicability to multiple cases and feasibility of repeated simulations, the CSC model was adopted as the standard model for further analyses in this study.

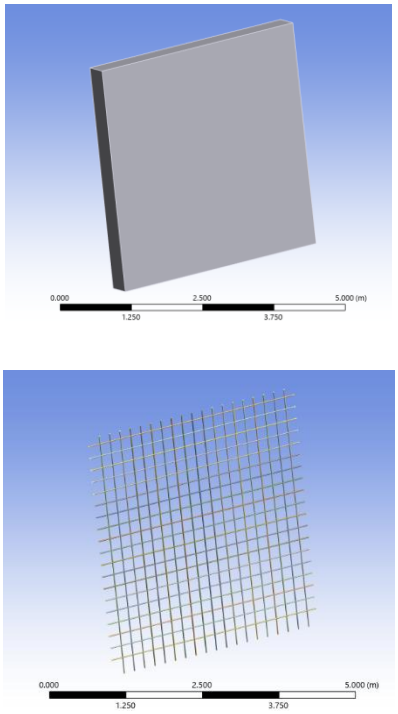

FIGURE 1. CAD MODLE

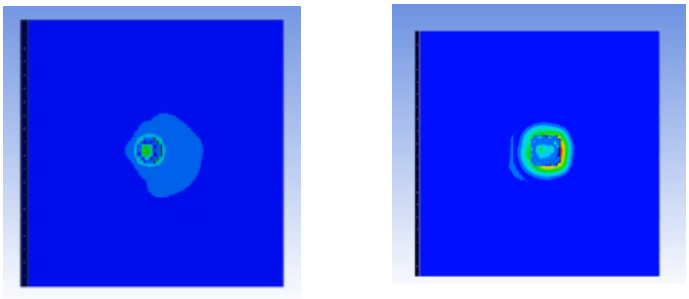

FIGURE 2.CSC MODEL ANALYSIS

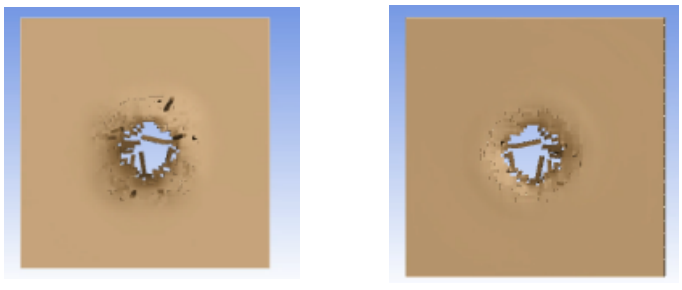

FIGURE 3. KCC MODEL ANALYSIS RESULTS

V. Development and Validation of the Aircraft Model

Based on previous studies, a Boeing 767 aircraft model was independently developed by representing major components—including the fuselage, main wings, engines, and tailplane—using shell elements. Each component was assigned individual density and stiffness properties to accurately replicate the structural characteristics of the actual aircraft.

To address convergence issues frequently encountered in contact analyses within the finite element method, the initial Boeing 767 model was refined. Specifically, the model was subjected to a contact analysis involving collision with a solid-element concrete wall using the same simulation code intended for later applications. Errors caused by the aircraft model geometry during this analysis were identified and addressed by optimizing the geometry of the model, thereby improving the convergence behavior of the simulation.

Finally, to validate the credibility of the developed Boeing 767 model, an impact analysis against a rigid wall was conducted, as shown in Figure 4. The resulting impact force history, presented in Figure 5, was compared with previously validated data from earlier studies (Figure 6) [1]. The comparison showed that the force-time history generally matched well with the reference data, confirming the reliability of the developed aircraft model[1].

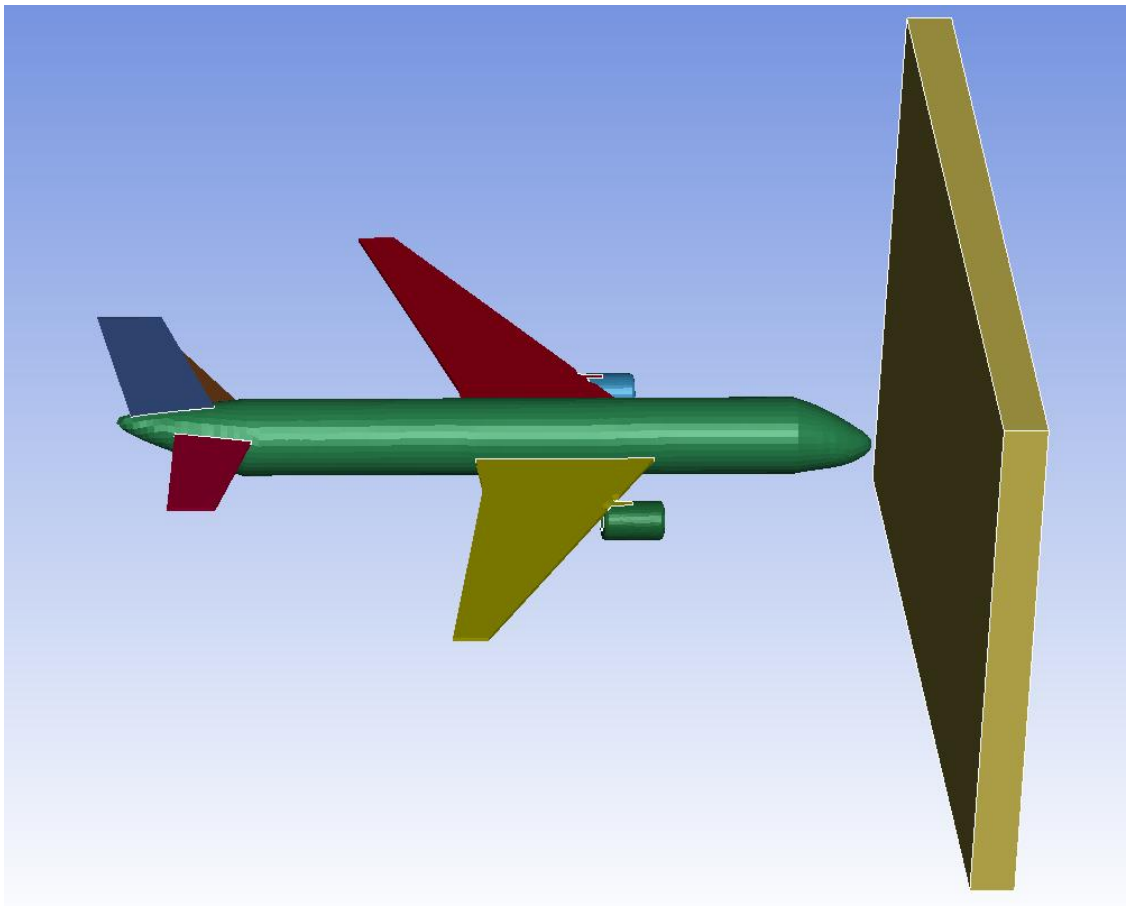

FIGURE 4. AIRCRAFT MODEL

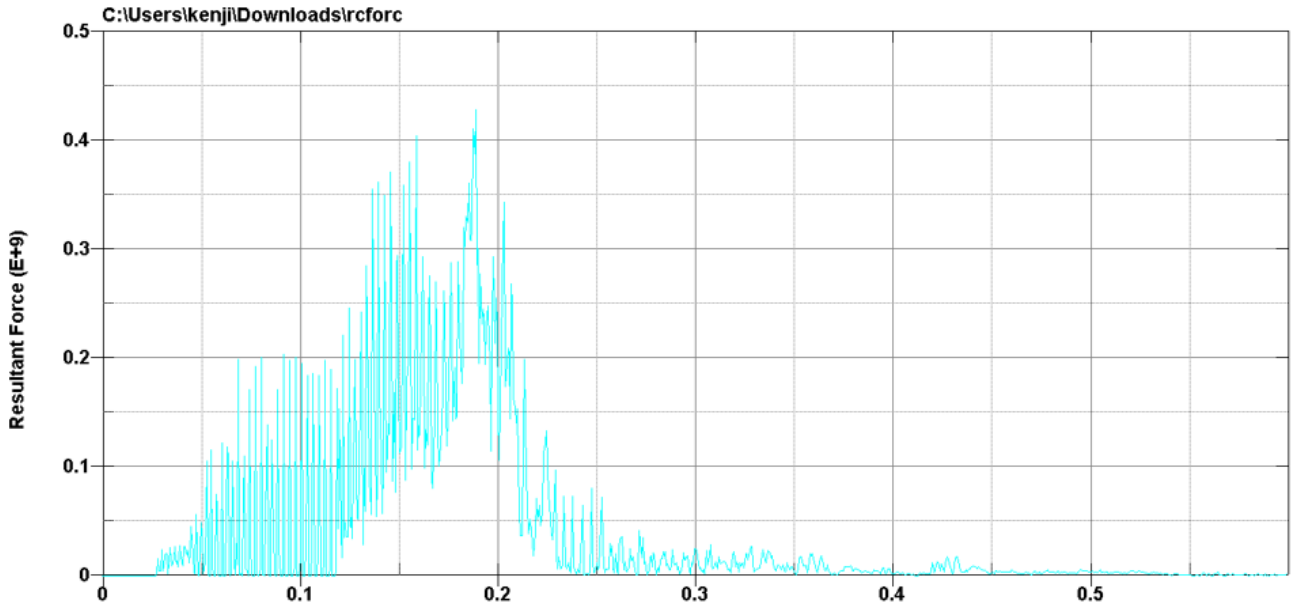

FIGURE 5 . DYNAMIC LOAD-TIME HISTORY OF THE AIRCRAFT IMPACT AT 150 M/S (CURRENT STUDY)

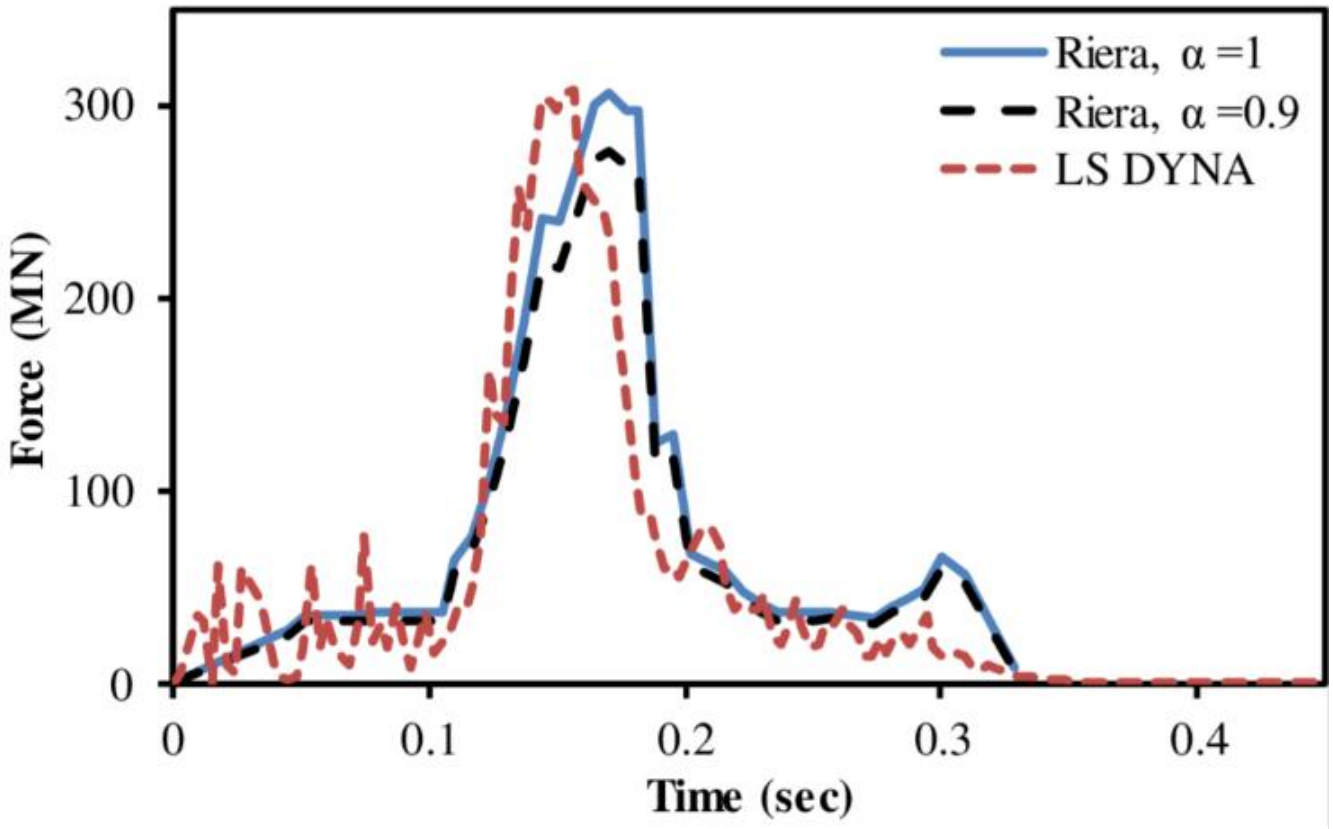

FIGURE 6. DYNAMIC LOAD-TIME HISTORY OF THE AIRCRAFT IMPACT AT 150 M/S (PREVIOUS STUDY) [1]

VI. Interaction Method and Associated Challenges

As previously described, the actual simulation was conducted using the interaction method. The interaction method involves explicitly modeling both the projectile (aircraft) and the target structure as FEM models and simulating their direct collision through contact analysis. Due to the extensive computational time required, this method is rarely employed in practical plant analyses and is primarily adopted in academic research.

Compared to the "force time-history method," which is commonly used in practical applications—where a prescribed time-history load is applied to a limited region of the target structure—the interaction method offers the advantage of reproducing more realistic impact scenarios. Following this methodology, a direct impact analysis on an RC building was performed using the CSC material model in conjunction with the validated aircraft model. Figure 7 shows the FEM model setup prior to analysis.

The analysis successfully converged, as illustrated in Figure 8. However, abnormal failure behavior of shell elements on the side wall of the building was observed immediately after impact. This phenomenon was attributed to non-physical stress wave propagation, most likely caused by numerical diffusion due to coarse mesh resolution. Efforts are currently underway to enhance numerical stability through mesh refinement. Ultimately, the goal is to use the improved simulation results to propose design guidelines that ensure sufficient APC resistance with minimal reinforcement.

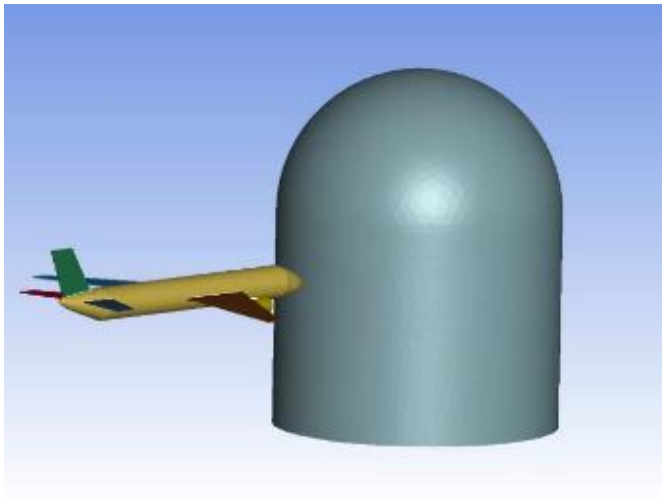

FIGURE 7. INTERACTION METHOD ANALYSIS

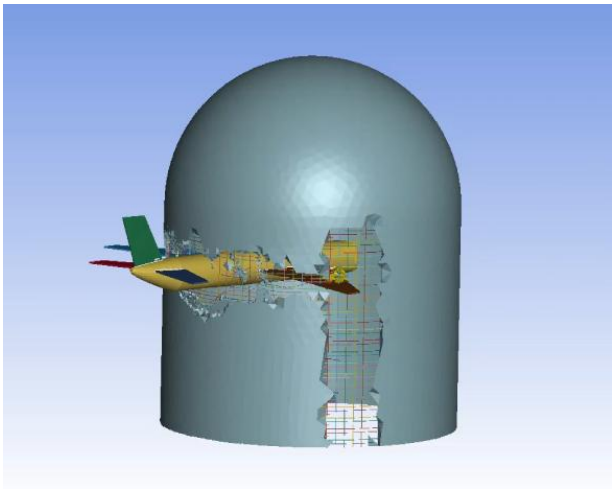

FIGURE 8. INTERACTION METHOD ANALYSIS RESULT

VII. Conclusion and Future Outlook

This study aimed to optimize protective measures against aircraft impact (APC) on nuclear power plants, focusing on the development of a fundamental numerical analysis framework as a prerequisite. The interaction method, in which both the projectile and the target building are modeled using the finite element method (FEM), was adopted in order to reproduce structural responses that closely resemble real-world behavior.

In the investigation of material models, numerical simulations using both the Karagozian & Case Concrete (KCC) model and the Continuous Surface Cap (CSC) model successfully reproduced experimentally observed failure modes—namely, rear-face spalling and perforation—thus validating their applicability. Considering ease of implementation and numerical stability, the CSC model was selected for subsequent analyses.

An aircraft model representing the Boeing 767 was then constructed and validated. The resulting impact force history showed good agreement with validated data from previous studies, confirming the model's reliability. While the initial interaction analysis achieved convergence, some numerical instability was observed in the form of non-physical sidewall failure. This issue is presumed to be caused by numerical diffusion resulting from a coarse mesh, highlighting the need for mesh refinement as a key area for improvement.

Moving forward, the established simulation framework will be applied to evaluate the effectiveness of various proposed APC countermeasures implemented on a simulated plant structure. The ultimate objective is to identify the necessary and sufficient conditions for cost-effective and robust APC protection strategies.

REFERENCES

[1] C. D. Argyropoulos, J. L. Marshall, and K. R. Robbe, "Comparative assessment of impact analysis methods applied to large commercial aircraft crashes on reinforced concrete containment," Proc. SMiRT-21, New Delhi, India, 2011, Paper No. 351, International Association for Structural Mechanics in Reactor Technology (IASMiRT).

[2] R. P. Kennedy, "Method for designing concrete structures to withstand missile impact," Nuclear Engineering and Design, 37, pp. 311–325 (1976).

[3] CRIEPI (Central Research Institute of Electric Power Industry), "Fundamental study on damage and failure evaluation of reinforced concrete structures under aircraft impact," CRIEPI Report No. U24, Tokyo, Japan, 2024. [Online]. Available: https://criepi.denken.or.jp/hokokusho/pb/reportDetail?reportNoUkCode=U24

[4] IAEA-TECDOC-624, "Considerations in the Development of Safety Standards for Nuclear Power Plants against Aircraft Crash," International Atomic Energy Agency, 1991

[5] U.S. NRC, Regulatory Guide 1.217, "Containment Structural Integrity Considerations for Beyond-Design-Basis Aircraft Impact," 2009.

ASRAM2025
www.asram2025.org
Asian Symposium on Risk Assessment and Management 2025
Pattaya, Thailand, 27 – 29 August 2025

Quantitative Evaluation of Aircraft Impact Probability on TRR-1/M1 Research Reactor

Sirirat Seemapapong[1*], Kanokrat Tiyapun[1], Saensuk Wetchagarun[1] and Nart Noodee[1]

[1] *Thailand Institute of Nuclear Technology (Public Organization): 16 Vibhavadi Rangsit Road, Ladyao, Chatuchak, Bangkok 10900, and *Email Address sirirat@tint.or.th*

EXTENDED ABSTRACT

Abstract

This paper presents a comprehensive assessment of external accident risks to the Thailand Research Reactor-1/Modification 1 (TRR-1/M1) research reactor, with specific focus on aircraft crash scenarios. The study evaluates the probability of critical reactor core damage due to direct and indirect aircraft impacts, utilizing Thailand's national air traffic statistics, aircraft categorization, flight maneuver patterns, and structural penetration modeling. The total annual probability of reactor core damage resulting from an aircraft crash was determined to be 6.12×10^{-8}, which is well below the IAEA-defined threshold of 1.0×10^{-7} per reactor-year. This classifies the event as "incredible" and confirms that TRR-1/M1 meets international safety criteria for external hazards. The analysis underscores the reactor's structural robustness and contributes to the risk-informed safety case in support of continued reactor operations.

1. Introduction

Nuclear facilities must undergo rigorous safety assessments for both internal and external initiating events. For the TRR-1/M1 research reactor located in Thailand, potential external hazards were systematically reviewed. No industrial, transportation, or military facilities exist in the vicinity that would credibly lead to an accident resulting in radiological release exceeding IAEA safety limits. The only credible external initiating event identified is an aircraft crash because the TRR-1/M1 is located close to the international airport. While extremely rare, the consequences of a direct or indirect aircraft impact on a nuclear facility necessitate quantitative risk evaluation.

2. Methodology

2.1 Scope and Assumptions

The total probability of aircraft crash related to core damage, P, per year will lead to critical reactor damage is essentially the summation of three probabilities:

$$P = P_c + P_{p/c} + P_{d/p} \qquad (1)$$

where:

P_c :	Probability of aircraft crash on the reactor building
$P_{p/c}$:	Probability of core damage due to a missile generated from a collision within gas tight room
$P_{d/p}$:	Probability of damage to the core when aircraft crash directly into the pool opening

Equation (1) is derived from standard probabilistic risk decomposition principles applied in PSA, where the total event probability is represented as the sum of mutually exclusive damage pathways [1, 2]. These probabilities are assumed to be independent due to mutually exclusive damage mechanisms: P_c represents direct building impact, Pp/c involves internal missile effects, and Pd/p involves precise pool strikes.

2.2 Aircraft Movement Data and Classification

Aircraft movement data were obtained from the Airports of Thailand (AOT) for the period 2000–2020 [3]. Aircraft were categorized as Civil Aviation (International and Domestic) and State and Military Aircraft. Flight maneuvers considered include takeoff, landing, and closed traffic patterns. The Don Mueang International Airport (DMK), near the TRR-1/M1 research reactor, showed significant growth, contributing most of the low-cost airline traffic.

2.3 Probability Calculations

The probability of aircraft crash on the reactor building (P_c) is the product of three factors including the number of aircraft movements, the accident probability per aircraft movement per unit area and the effective area of the target of interest.

$$P_c = \Sigma_i \Sigma_j \Sigma_k (N_{ijk} C_{ijk} A_{ijk}) \quad (2)$$

where N_{ijk} is the number of annual movements of type j for aircraft type i in flight pattern k
C_{ijk} is the crash probability per movement of type j for aircraft type i in flight pattern k
A_{ijk} is effective target area associated with the structure of interest for aircraft type i in movements of type j and in-flight pattern k.

The base dimension of the reactor building for the effective target area is 1307.94 m^2. The effective area does not include the control rod drive and the crane above the reactor core. The conditional probability of penetration through 1.5 ft reinforced concrete by aircraft weight more than 12,500 lb was estimated at 0.045 per crash. The conditional probability of 0.045 was based on impact analysis using empirical aircraft crash data from reinforced concrete structures [4]. The value 2.18×10^{-9} was derived using shielding configuration and structural layout probability modeling [2]. Surrounding structures prevent lateral missile intrusion; thus, only direct hits are considered credible for penetration.

3. Results and Analysis

The probability of damage to the reactor core due to a missile generated from a collision with the crane is 2.18×10^{-9} per year. The probability of damage to the reactor core when a plane crash directly onto the pool opening is 1.37×10^{-8} per year. Thus, the total probability of airplane crashes related core damage of TRR-1/M1 is 6.12×10^{-8} per year. This value is considerably less than 10^{-7}, the threshold value for the significant risk contributor. This probability is significantly below the safety threshold of 1.0×10^{-7} per year, as identified by IAEA and referenced reactor studies below which external events are considered non-significant risk contributors.

4. Discussion

The aircraft movement trends in Thailand show a strong increase, particularly in low-cost civil aviation since the reopening of Don Mueang Airport. Despite increased flight volume, the reactor's design and surrounding infrastructure significantly mitigate risk. The probabilistic safety assessment (PSA) shows a high degree of conservatism, accounting for structural resistance and shielding of critical components. Moreover, missile generation from surrounding impacts is effectively ruled out by the reactor's spatial arrangement, and the probability of a direct strike on the small pool opening is extremely low. The total core damage probability due to aircraft crash is not only below regulatory thresholds but also aligns with international best practices in external event hazard screening.

5. Conclusion

The aircraft crash risk assessment for TRR-1/M1 confirms the event as an "incredible accident scenario," with a total probability of core damage of 6.12×10-8 per year. This value is well below IAEA's limit for significant risk contributors and supports continued reactor operations without additional design changes. The results highlight the effectiveness of reactor siting, structural integrity, and hazard mitigation strategies in ensuring public and environmental safety. The term 'incredible' follows IAEA SSR-3 criteria for probabilities below 10^{-7} per reactor-year. Further investigation could involve a more detailed structural vulnerability analysis using finite element impact simulations for both conventional and emerging aircraft types, including unmanned aerial vehicles (UAVs). Additionally, the probabilistic model could be expanded to incorporate dynamic air traffic projections and seasonal variations in flight density to refine risk estimates. Consideration of secondary effects such as post-

impact fire, fuel dispersion, or cascading failures in auxiliary systems could also be included to broaden the risk assessment scope. Finally, comparative analyses with international benchmark cases or validation through Monte Carlo simulation could strengthen confidence in the results and support safety case documentation for long-term research reactor licensing.

REFERENCES

[1] IAEA, IAEA SSG-64: Protection Against Internal and External Hazards in the Operation of Nuclear Power Plants, International Atomic Energy Agency, Vienna, Austria (2020).
[2] U.S. NRC, NUREG/CR-5042: Evaluation of External Hazards to Nuclear Power Plants in the United States, U.S. Nuclear Regulatory Commission, Washington, D.C. (1987).
[3] Thailand Civil Aviation Authority, Aircraft Movement Reports (2000–2020), Bangkok, Thailand (2020).
[4] "Aircraft Crash Probability," Nuclear Safety, 17, 3, pp. 357–370, May–June (1976).

ASRAM2025
www.asram2025.org
Asian Symposium on Risk Assessment and Management 2025
Pattaya, Thailand, 27 – 29 August 2025

Multi-fault mode analysis for reactor cavity cooling system of high temperature gas-cooled reactor

Zhengyang Li[1]

[1] *Institute of Nuclear and New Energy Technology, Tsinghua University, Beijing, China, 10084, lizhengy24@mails.tsinghua.edu.cn*

EXTENDED ABSTRACT

1.Introduction

As a Generation IV reactor, the high-temperature gas-cooled reactor (HTGR) exhibits inherent safety features. A commercial-scale 200 MW- High Temperature gas-cooled Reactor Pebble-bed Module (HTR-PM) has been designed, constructed and operated in China as a demonstrate plant. In HTR-PM, a passive Reactor Cavity System (RCCS) is design to carry out the heat from the core to the final heat sink – the atmosphere, and thereby keep the safety of Reactor Pressure Vessel (RPV), the reactor cavity and the confinement in the normal operations as well in the accident conditions. Therefore, RCCS is an important safety class system for the HTGR.

The working principle of RCCS is shown in Figure 1. The water-cooling panel is installed inside the confinement and surround the RPV, vertical pipes are welded on the panel. The heat can be transferred from the RPV to the water-cooling panel via radiation and natural convection to heat up the water in the pipes. The heated water then forms the natural circulation and flows upwards to the air coolers, where the heat can be transferred from the water to the air. Finally, the heated air also forms the natural circulation and flows out of the air cooling tower. The RCCS of the HTR-PM consists of three independent cooling trains, with the design capacity of 3×50%. There is no any positive component in the RCCS, and no any further operation is needed when an accident happens and reactor shutdown is triggered, which guarantee the high reliability of this system.

Besides, an RPV support cooling system, with the same working principle as the RCCS is designed in HTR-PM. This system consists of two independent trains.

Based on the HTR-PM, a new HTR-PM600S is now under design in China, inheriting most of the design features of the HTR-PM. But in HTR-PM600S, some design optimizations were carried out, including connecting the RPV support cooling system in series to the RCCS.

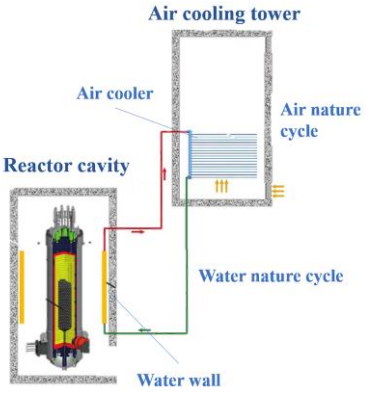

Figure 1. structure of RCCS

2.Fault modes and failure boundaries

According to the new design, the three trains of RCCS in the HTR-PM600S can be divided into two types: two trains of type A, connected with support cooling system; one train of type B, without connected with support cooling system. Thus, the fault modes of the RCCS are more complicate. In this paper, following four operation conditions of the RCCS are studied:

1) Mode1: two Type A trains and one Type B train are all operational.
2) Mode2: two Type A trains are operational.

3) Mode3: one Type A train and one Type B train are operational.
4) Mode4: one Type A train is operational.

In the RCCS, heat removal depends on natural circulation of both air and water. Therefore, successful operation requires the establishment and maintenance of natural circulation. Additionally, to prevent cavity concrete degradation and ensure the integrity of support structures, the temperature of the concrete near the RPV support must remain below a critical threshold. Three failure boundaries are defined in the program:

1) Boil boundary: The maximum water temperature must not exceed 150 °C. Boiling of water significantly reduces convective heat transfer efficiency, and is therefore considered as a system failure. This limit is based on the estimated boiling point of water at approximately 0.5 MPa.
2) Freeze boundary: The minimum temperature of the water must not fall below 0 °C, to prevent the tube crack due to freezing.
3) Support boundary: Under normal operating conditions, the temperature of the supporting concrete must not exceed 65 °C.

3.Model and equation

In order to calculate failure boundaries in different fault modes, a program based on C++ is developed. The model and equation of the program are expressed as follows.

3.1 Program Grid Division

Based on the spatial arrangement and heat transfer relationships among various modules, the system is initially divided into three sections:

1) Section 1: The gas-filled space between the reactor pressure vessel and the concrete walls of the reactor cavity. Heat transfer in this region occurs via radiation and natural convection.
2) Section 2: The water nature cycle, consisting of four modules: the water-cooled tube, the rising section of the water circuit, the air-cooled tube, and the descending section of the water circuit. Heat transfer occurs through natural convection of the cooling water.
3) Section 3: The air cooling tower, where heat transfer occurs through natural convection of air.

Section 1 and Section 2 are connected via the heat conduction module of the water-cooled wall, while Section 2 and Section 3 are linked through the heat conduction module of the air cooler. A computational model and node division, are established for the three sections and two connecting modules. The following sections provide a detailed explanation of the node divisions.

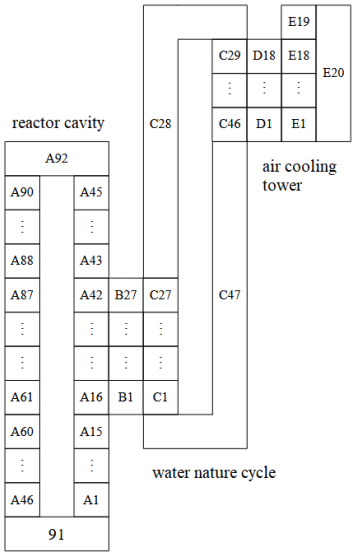

Figure 2. calculating model of RCCS

In the reactor cavity, the computational nodes are axially divided into 45 segments. The grid division is shown as figure 2. Nodes A1 to A45 correspond to the outer wall surface of the annular space, i.e., the wall surface on the water-cooled wall side. Among these, nodes A1 to A15 represent the adiabatic wall sections without steel plates, nodes A16 to A42 cover the

water-cooled wall with steel plates, and nodes A43 to A45 again represent adiabatic wall sections. Nodes A46 to A90 correspond to the inner wall surface of the annular space, i.e., the outer surface of the pressure vessel. Nodes A91 and A92 represent the bottom and top surfaces of the annular space, respectively, and are assumed to be at constant temperature.

The water circulation system comprises three parts: B, C, and D. Nodes B1 to B27 represent the walls of the water-cooled tubes. Nodes C1 to C47 represent the cooling water: C1 to C27 for the water-cooled wall section, C29 to C46 for the air cooling tower, C28 for the adiabatic boundary at the rising section, and C47 for the descending section and support area. If the cooling loop is not connected to the support cooling system, only the descending section is modeled and treated as an adiabatic boundary. Nodes D1 to D18 represent the walls of the air-cooled tubes.

The air in the cooling tower is divided into 20 nodes. Nodes E1 to E20 represent the air inside the cooling tower. Node E19 is set as an adiabatic boundary, and Node E20 is set to ambient temperature.

3.2 Heat Transfer in the Reactor Cavity

Heat transfer within the cavity primarily includes two mechanisms: radiation and natural circulation between the outer wall of the pressure vessel and the water-cooled wall, and heat conduction between the water-cooled wall and the water-cooled tube walls.

The water-cooled wall, situated between the inner surface of the cavity and the outer surface of the pressure vessel, encases the upper and lower sections of the vessel. Due to the slender design of the high-temperature gas-cooled reactor's pressure vessel and the proximity of the water-cooled wall, most of the radiative heat from the pressure vessel transfers to the water-cooled wall, with a minor portion to the concrete. The temperature difference between the pressure vessel and the water-cooled wall induces air movement due to density gradients, resulting in natural convection and additional heat transfer to the water-cooled wall. Thus, the total heat transfer is the sum of natural convection and radiative heat transfer.

The outer wall of the pressure vessel and the water-cooled wall are modeled as a concentric cylindrical shell. The outer surface represents the water-cooled wall, the inner surface represents the pressure vessel, and the top and bottom surfaces represent concrete boundaries. Under steady-state conditions, the system reaches radiative equilibrium, expressed as:

$$q(S_k) = \frac{\varepsilon_k}{1-\varepsilon_k}[\sigma T^4(S_k) - J(S_k)]$$

Where:
$q(S_k)$: Radiative heat flux for surface S_k
ε_k: Emissivity of surface S_k
$J(S_k)$: Effective radiative heat flux of surface S_k

Assuming concrete is at a constant temperature of 60°C, and due to its small view factor with the steel surfaces, the error introduced by this simplification is negligible.

The heat flux density on the water-cooled wall is given by:

$$q = \frac{3\lambda\delta\left(T_{gb} - T_{sg}\right)}{b^2}$$

Each water-cooled wall includes 100 water-cooled tubes each train arranged in staggered configurations across three cooling loops to ensure uniform wall temperature under fault conditions. Heat transfer models between the water-cooled wall and the tube walls vary with the number of operational cooling loops:
Single train configuration:

$$T_{GB} = T_A + \frac{qb^2}{3\lambda\delta}$$
$$Q_A = Q_B = qb$$

Two trains configuration:

$$T_{GB} = \frac{T_A + T_B}{2} + \frac{3qb^2}{8\lambda\delta}$$
$$Q_A = 1.5qb + \frac{3\lambda\delta(T_A - T_B)}{2\mathrm{b}}$$
$$Q_B = 1.5qb - \frac{3\lambda\delta(T_A - T_B)}{2\mathrm{b}}$$

Three trains configuration:

$$T_{GB} = \frac{T_A}{3} + \frac{2T_B}{3} + \frac{qb^2}{8\lambda\delta}$$
$$Q_A = qb + \frac{\lambda\delta(T_A - T_B)}{\mathrm{b}}$$
$$Q_B = qb - \frac{\lambda\delta(T_A - T_B)}{2\mathrm{b}}$$

Where:

T_{GB}: Average temperature of steel plate

T_B: Water-cooled pipe surface temperature with integration into the support cooling system

T_A: Water-cooled pipe surface temperature without integration into the support cooling system

λ: Thermal conductivity of steel plate

δ: Length of the steel plate

b: Thickness of the steel plate

If two loops connected to the support cooling system fail, it is assumed that the system has failed entirely, and this condition is excluded from fault analysis.

Q_A :heat transfer density of Water-cooled pipe surface without integration into the support cooling system

Q_B: heat transfer density of Water-cooled pipe surface with integration into the support cooling system

3.3 Heat Transfer and Natural Circulation of Cooling Water

Heated by the water wall, cooling water in the tubes rises naturally, flows through the rising section into the air-cooled tubes, exchanges heat with the surrounding air, then descends back to the water-cooled tubes via the descending section, completing the loop.

Head gain from water circulation:

$$\Delta p = \sum_{29}^{47} (\rho g \Delta H)_i - \sum_{1}^{28} (\rho g \Delta H)_i$$

The equation of Flow resistance and pressure balance is shown as follows:

Frictional resistance:

$$\Delta p_1 = \sum \frac{\lambda l}{d} \frac{\rho u^2}{2}$$

Local resistance:

$$\Delta p_2 = \sum \frac{\xi \rho u^2}{2}$$

Resistance coefficient:

$$Re < 2000 \lambda = \frac{64}{\mathrm{Re}}$$
$$2000 \le \mathrm{Re} \le 4000 \lambda = 0.0025 \sqrt[3]{\mathrm{Re}}$$
$$\mathrm{Re} > 4000 \begin{cases} u < 11\frac{\nu}{K} & \lambda = \frac{0.3164}{\mathrm{Re}^{0.25}} \\ 11\frac{\nu}{K} \le u \le 445\frac{\nu}{K} & \lambda = 0.11\left(\frac{K}{d} + \frac{86}{\mathrm{Re}}\right) \\ u > 445\frac{\nu}{K} & \lambda = 0.11\left(\frac{K}{d}\right)^{0.25} \end{cases}$$

3.4 Heat Transfer and Natural Circulation in the Air Cooling Tower

Inside the air cooler, heated water flows upward through the tubes via natural circulation. Cooler air enters from the base of the cooling tower, and heat is transferred from the water through the tube walls to the air. Energy conservation yields the heat transfer equation:

$$T_{kg} = \frac{h_1 A_1 T_{lq} + h_2 A_2 T_{kq}}{h_1 A_1 + h_2 A_2}$$

Convective heat transfer coefficients for the inner and outer tube walls are calculated as follows:

1) Inner pipe wall:

$$Nu = 0.012 \times (\mathrm{Re}^{0.87} - 280) \times \mathrm{Pr}^{0.4} \times \left(1 + \left(\frac{d}{l}\right)^{2/3}\right)$$

Where: Nu = Nusselt number; Re = Reynolds number; Pr = Prandtl number; d = tube inner diameter; l= tube length.

2)Outer pipe wall:

$$h = 453.6 u_{nf}^{0.718}$$

Where: h = convective coefficient; v = standard face velocity

Standard face velocity is determined by:

$$u_{nf} = u_F \frac{T_{nf}}{T_F} = u\cos\left(55\frac{T_{nf}}{T_F}\right)$$

Where:

u_F: Standard face velocity

u: Air velocity in the cooling tower

T_{nf}: Standard temperature (293.15 K)

T_F: Air temperature

Ambient air enters through the base louvers of the cooling tower, gets heated by the hot water in the tubes, rises due to buoyancy, and exits through the top, discharging heat to the atmosphere and completing the natural convection cycle. As shown in Figure 2, the cooling tower air nodes are divided into 19 sections (E1 to E19), with the ambient air treated as node E20, a fixed temperature boundary condition.

Buoyancy force of the air column:

$$\Delta p = (\rho g \Delta H)_{20} - \sum_{i=1}^{19} (\rho g \Delta H)_i$$

Flow resistance in the air cooler and cooling tower:

Bundle resistance in the air cooler:

$$\Delta p_1 = 5.1 N_B \phi u_{nf}^{1.504}$$

Frictional and local resistance in the cooling tower:

$$\Delta p_2 = \sum \xi \frac{\rho u^2}{2} + \sum \lambda \frac{l}{d} \frac{\rho u^2}{2}$$

4.Result and discussion

Assuming a uniform temperature distribution on the outer surface of the RPV, the failure boundaries of the RCCS under average vessel wall temperatures ranging from 100 °C to 250 °C are calculated, as shown in Figure 3.

The results indicate that all failure thresholds decline as the average outer wall temperature increases. This suggests that under higher vessel wall temperatures, the freezing threshold becomes more permissive, while the support and boiling thresholds become more restrictive. Among these four failure scenarios, fault mode 1 presents the strictest freezing boundary, while the support and boiling limits are more relaxed. fault modes 2 and 3 show similar boiling and freezing boundaries. However, since fault mode 3 involves only one Type A train, its support threshold is lower than that of fault mode 2. The figure also shows that for fault modes 1, 2, and 3, the environmental temperatures corresponding to the support and boiling thresholds all exceed 40 °C. Therefore, if at least two cooling trains are operational and the average outer wall temperature does not exceed 250 °C, neither boiling nor structural failure is expected to occur.

Subsequent analysis focuses on the freezing threshold under lower vessel temperatures and the support and boiling thresholds of fault mode 4 under higher vessel temperatures.

The figure shows that when more cooling trains are in operation, the freezing threshold rises. Under conditions where the average vessel wall temperature is 200 °C, fault mode 1 still approaches the freezing boundary. This implies that under low ambient temperatures, water freezing within the cooling towers becomes a credible risk. In fact, freezing of cooling water during winter in the air-cooling sections remains a key operational challenge for nuclear power plants.

At higher vessel temperatures, fault mode 4 shows significantly lower support and boiling thresholds. This indicates that under elevated ambient conditions, both boiling and structural failure of the support may occur. Furthermore, it is evident that at any given average vessel wall temperature, the support threshold is consistently stricter than the boiling threshold. The close alignment between the support concrete temperature and the average temperature of condensate in the support section indicates that the low support threshold in fault mode 4 primarily results from the elevated inlet water temperature.

The significance of this research is as follows:

1) This study focuses on developing a high-fidelity model and performing detailed simulations of the RCCS to demonstrate its passive reliability.
2) Using the current analysis outcomes, nuclear power plant operators can implement targeted preventive and recovery strategies—tailored to specific operating modes and accident scenarios—to ensure the RCCS remains available under defined conditions.

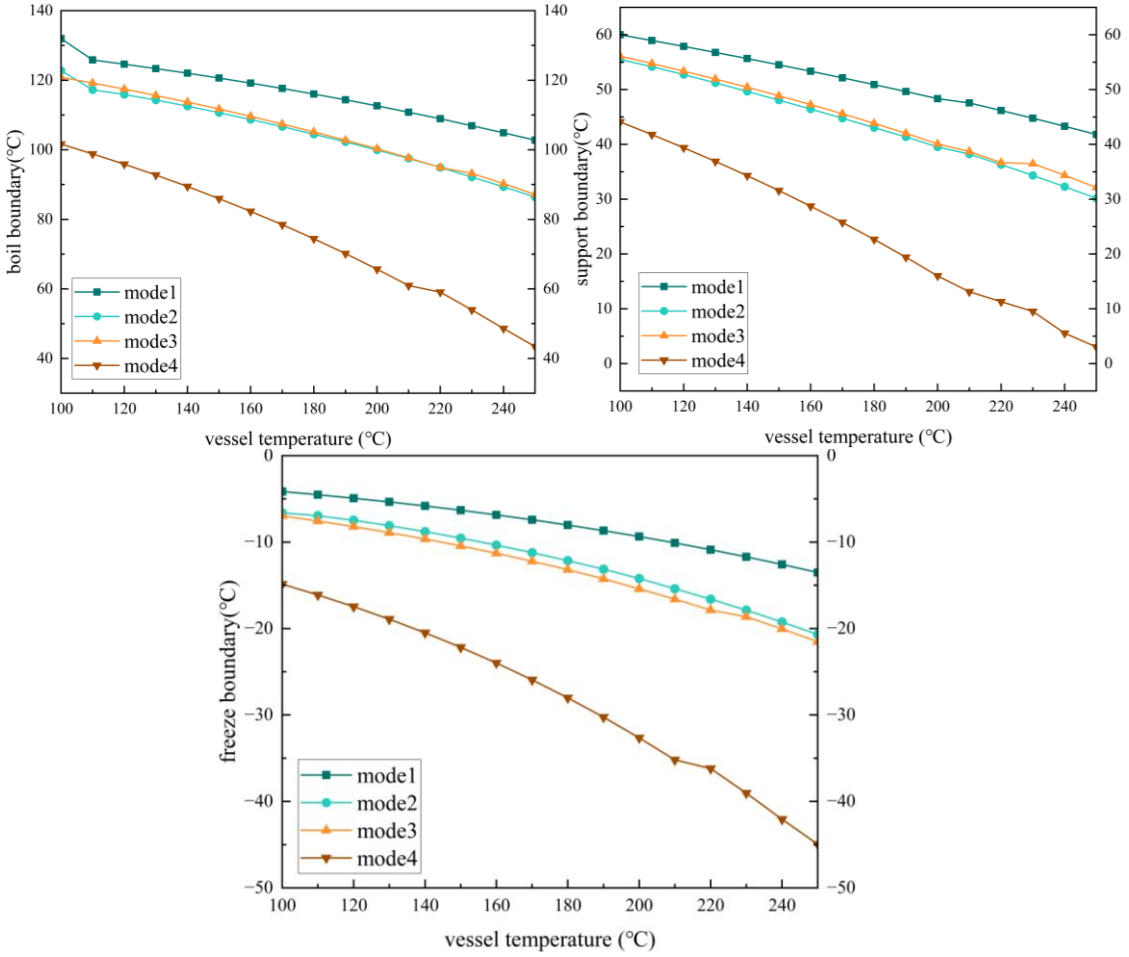

Figure 3. failure boundaries in multi-fault modes

ASRAM2025
www.asram2025.org
Asian Symposium on Risk Assessment and Management 2025
Pattaya, Thailand, 27 – 29 August 2025

Does Restarting the Operations of Nuclear Plants Improve Public Evaluations in Utility Companies? A Factorial Survey Experiment in Post-Fukushima Japan

Tomohiro Fujita [1]

[1] *Institute of Nuclear Safety System, Inc., 64 Sata, Mihama-cho, Mikata-gun, Fukui 919-1205, Japan*
E-mail address: fujita.tomohiro@inss.co.jp

EXTENDED ABSTRACT

One of the well-known factors for public acceptance of nuclear power generation is positive evaluations toward nuclear operators such as trust, as past studies have shown. Those who trust nuclear operators tend to show positive attitudes toward nuclear power generation. However, the relationship between positive evaluations and public support is associative because these studies were based on observational studies, and to identify the causal relationship, further explorations are needed. In addition, even if positive evaluations among the public toward nuclear operators are accepted as a vital condition for the acceptance of nuclear power generation, some antecedent factors of these evaluations or dynamic relationships between the evaluations and public support have not been sufficiently investigated. It is urgent to fill these research insufficiencies when considering the energy situation in Japan. In Japan, public support for nuclear power generation decreased sharply after the accident at the Fukushima Daiichi Nuclear Power Plant in 2011. Because of that, not only public support but also trust toward nuclear operators were both damaged. Once trust is lost, it is almost impossible to restore it immediately as past social psychological studies have clarified. Therefore, questions arise as to whether or not and to how evaluations of nuclear operators can be improved.

After the 2011 accident, a new regulatory regime was begun. The Nuclear Regulation Authority (NRA) has imposed rigorous screenings on nuclear operators. While some reactors located mainly in western Japan have passed strict reviews and restarted their commercial operations, others have not restarted yet. In other words, more than ten years after the accident, there are two groups of utility companies: those who could restart operations of their nuclear power plants and those who could not restart them. Having these two groups of utility companies or nuclear operators makes it necessary to reconsider the above findings. Because it is stated that positive evaluations toward nuclear operators are the vital condition for the public to support nuclear power generation, the differences among the groups of nuclear operators based on actual nuclear operations indicate another possibility or the opposite logic. Then, the question becomes: "Does restarting the operations of nuclear power plants correspond to better or poorer evaluations of utility companies?"

To investigate the question, this study formed several hypotheses and conducted a factorial survey experiment. When utility companies or nuclear operators restart the operations of nuclear power plants, the capacity utilization rate of nuclear power plants per year increases. Although the operation must be stopped during the periodic inspection required by law, the capacity utilization rates never arrive at 100 %. But restarting the operation contributes to increasing the rates. If restarting the operation could change public attitudes toward utility companies, it is considered that capacity utilization rates have roles to play. In addition to the capacity utilization rates, this study also focuses on the number of employees which utility companies hire for nuclear power generation because local governments or communities which host nuclear power plants expect the companies or operators to provide economic stability through employment.

Both the capacity utilization rates and the number of employees constitute economic aspects and benefits which utility companies and nuclear operators can provide. On the other hand, there are some restricting factors for accepting nuclear power generation which relate to nuclear safety and risks, as in general risk perception, contrary to benefit perception, negative emotions can be provoked. In this study, the types of safety professionals, the numbers of problems which are legally required to be reported, and the frequencies of information releases are also considered.

Data for this study were obtained through a factorial survey experiment conducted in March 2024.Factorial survey experiments are a suitable method for detecting people's judgements based on situations like those in the "real world". Respondents evaluate hypothetical utility companies after being shown vignettes describing information including the capacity utilization rates, the numbers of employees, the types of safety professionals, the numbers of problems which are legally required to be reported, and the frequencies of information releases. For example, the information in the vignettes is framed like this: "The capacity utility rate of a nuclear power plant last year operated by a utility company was **40%**...(omitted)". The levels of these five factors are determined systematically manipulated as shown in Table I. Then, contributions of these factors to outcome are estimated statistically. The outcome is measured by 10-point scale which evaluates hypothetical utility

companies from 1 (very bad) to 10 points (very good). Respondents were required to answer eight vignettes. This factorial survey experiment was carried out through the web and the web-site was prepared by a professional web-survey institution. Socio-demographic backgrounds of respondents were allocated by sex, age, and educational attainment which are proportional to nation-wide Japanese statistics. In addition, 20 % of the sample included residents who live in prefectures that host nuclear power plants. After excluding those who skipped reading the experiment instructions and answered carelessly, a total of 500 respondents completed the experiment. Therefore, there were 4,000 cases for statistical analyses.

TABLE I. Factors and Levels of the Experiment

Factor / dimension	Levels
Capacity utilization rates	0% / 40% / 80%
Numbers of employees	400 / 800 / 1200
Types of safety professionals	Safety professional in university / Engineer in utility company
Numbers of problems	0 / 1/ 2
Frequencies of information releases	Several times in a week / Several times in a month / several times in a half year

As a result, by considering hierarchical structure of the obtained data, effects of each factor were estimated through the random effects model. Four models from the simplest one which includes only main effects to the most complex model which includes two interaction terms were fitted. According to the estimates obtained from the model which includes the interaction terms, the capacity utilization rates had statistically significant positive effects in evaluation and these effects did not depend on other factors. As shown in Fig. 1, the more the capacity utilization rates increased, the better the evaluation became and this relationship did not depend on the numbers of employees. On the other hand, the numbers of problems which are legally required to be reported had a statistically significant negative effect on the evaluation. The more problems there were, the worse the evaluation became but this effect depended on the frequencies of information releases because a small but statistically significant interaction effect was found.

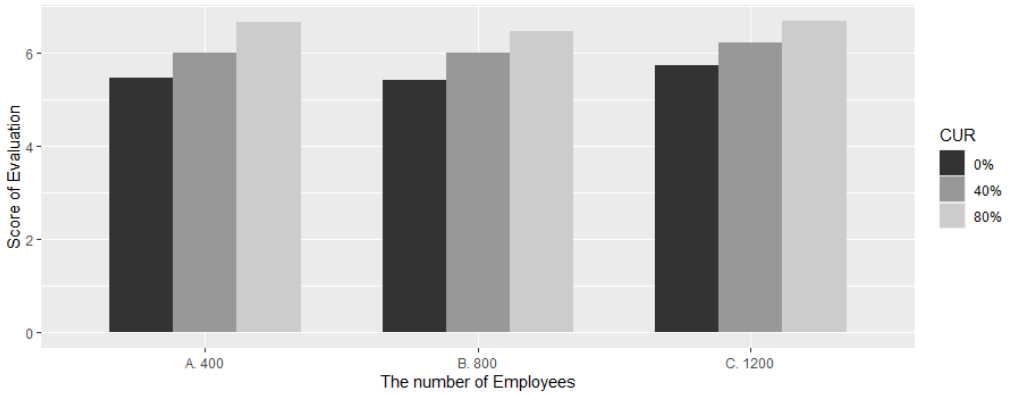

FIGURE 1. Estimates in Evaluation Predicted from the Random Effects Model

This study shed light on the hidden mechanism behind which evaluations in utility companies depend in the post-Fukushima Japanese context on actual nuclear operations measured by the capacity utilization rates. The finding implies that differences of operating experiences themselves have roles to play beyond just the agreement or disagreement toward utilization of nuclear energy. In addition, the effects of other variables such as the number of problems or the frequency of communications also provide some insights into the strategies of risk communication especially employed by nuclear operators because the effect in the frequency of information releases depended on the number of problems as found in the interaction effect. In recent years, ensuring energy security, balancing the energy mix, and diversifying electricity sources have come to be important issues not only in Japan but also in countries worldwide. The extension of the operational period of nuclear power plants and the construction of new plants are also topics discussed in many countries. The findings of this study will facilitate these discussions.

REFERENCES

[1] T. FUJITA, "Energy Knowledge and Public Response to Restarting Nuclear Plants in Japan Following the Fukushima Accident," *Utilities Policy*, **92**, 101858 (2025).
[2] K. AUSPURG and T. HINZ, *Factorial Survey Experiments*, Sage, London (2015).

Poster Session 2 (8:30 - 10:00)	The Port 6, C Floor	Safety and Risk Analysis of Nuclear Facilities and Radiation Application (Research Reactor, Tokamak Plasma Fusion, Nuclear Fuel Cycle, Cyclotron, Agricultural and Medical Industries)
		Chair/Facilitator 1: Mr. Anantachai PECHRAK (Thailand Institute of Nuclear Technology (TINT))
		Chair/Facilitator 2: Mr. Chakrit SAENGKORAKOT (Thailand Institute of Nuclear Technology (TINT))
8:30 - 8:45		ID 45: Research on the Visualization of Evacuation Risks during a Nuclear Disaster Speaker: KENGO MURAKAMI (Tokyo City University) Contributors: KENGO MURAKAMI (Tokyo City University)
8:45 - 9:00		ID 113: Exploring Research Reactors for Boron Neutron Capture Therapy as an Alternative Treatment for Cholangiocarcinoma Speaker: Yuwadee Malad (Suranaree University of Technology) Contributors: Yuwadee Malad (Suranaree University of Technology), Chinorat Kobdaj (Suranaree University of Technology), Natsuko Kondo (Kyoto University), Yoshinori Sakurai (Kyoto University), Chutima Talabnin (Suranaree University of Technology)
9:00 - 9:15		ID 83: Experimental Study of the Behavior of Air Bubbles Rising in a Water Column using the Integration of the Optical Visualization Method and the Mask R-CNN Model Speaker: Thanh Tung Pham (Hanoi University of Science) Contributors: Thanh Tung Pham (Hanoi University of Science), Mai Linh Le (Hanoi University of Science), Thanh Tung Duong (Nuclear Training Center), The Nghia Trinh (Hanoi University of Science), Thi Dung Nguyen (Hanoi University of Science), Hoang Tuan Truong (Nuclear Training Center)
9:15 - 9:30		ID 94: Development of Cost-Effective and Readily Available Materials for Neutron Shielding: A Comparative Study of Natural Rubber-based Composites Speaker: Jittinun Saenpoowa (Suranaree University of Technology) Contributors: Jittinun Saenpoowa (Suranaree University of Technology), Atirat Pitaktrakul (Suranaree University of Technology), Chaiwat Ruksakulpiwat (Suranaree University of Technology), Chinorat Kobdaj (Suranaree University of Technology)
9:30 - 9:45		ID 127: Optimization of Gamma Shielding for the Neutron Radiography Facility at TRR-1/M1 Using PHITS Simulation Speaker: Sutasinee Kotayee (Kasetsart university) Contributors: Sutasinee Kotayee (Kasetsart university), Weerawat Pornroongruengchok (Thailand Institute of Nuclear Technology), Sarinrat Wonglee (Thailand Institute of Nuclear Technology)

Research on visualization of evacuation risks during a nuclear disaster

Kengo Murakami[1], Hitoshi Muta [2]

[1] *Tokyo City University, Nuclear Risk Assessment Laboratory, g2481828@tcu.ac.jp*
[2] *Tokyo City University, Nuclear Risk Assessment Laboratory, hmuta@tcu.ac.jp*

ABSTRACT

The Fukushima Daiichi nuclear accident revealed significant issues in evacuation planning due to the release of radioactive materials and the mass evacuation of residents. This study aims to develop a simulation-based environment to visualize evacuation risks during nuclear disasters and support the optimization of evacuation plans.

Keywords: Nuclear disaster, Microscopic traffic simulation

I. Background and Objective

In the 2011 Fukushima Daiichi Nuclear Power Plant accident, a wide range of residents were forced to evacuate due to the release of radioactive materials, and confusion spread regarding where and how to evacuate. Many residents expressed concerns such as, "I don't know where to evacuate," and "I'm completely stuck in traffic and can't move." These voices revealed several problems, including inadequate information in evacuation plans and the establishment of unrealistic evacuation routes.

Learning from this experience, prefectures with nuclear power plants, such as Shizuoka and Fukui, are currently revising their evacuation plans and incorporating evacuation simulations that model nuclear disaster scenarios. However, these evaluations are still largely macro in scope, focusing on regional evacuation trends, such as total evacuation time, traffic congestion hotspots, and the overall number of evacuees. This macro-level perspective makes it difficult to understand the real dynamics of individual evacuation behavior—such as whether the designated evacuation routes function as intended, or who faces obstacles and where.

In actual nuclear disasters, mass evacuations often occur simultaneously. Some residents may evacuate along unintended routes due to a lack of understanding, and designated evacuation paths may become unusable due to secondary disasters such as earthquakes, tsunamis, or flooding. Additionally, special consideration must be given to residents with limited mobility, such as the elderly and those with chronic illnesses.

Given these complexities and individual differences, it is difficult to identify the full range of challenges and risks using only a macro-level approach. Key factors to analyze include the traffic situation during evacuation, the availability of evacuation guidance, behavioral differences based on resident characteristics, radiation exposure risks, information transmission delays, and variation in evacuation start times.

Therefore, this study aims to develop a microscale evacuation simulation framework that captures the behavior of individual residents—an approach that can support the verification and enhancement of more realistic and effective nuclear disaster evacuation plans.

II. Research Methodology

II.A. Arrangement of initial conditions

In the actual traffic environment, multiple conditions such as time of day, resident attributes, and geographical factors are intricately intertwined, and have a significant impact on evacuation behavior. Therefore, in this study, it is necessary to systematically organize various elements to be set as initial conditions for simulation implementation.
First, TABLE 1 shows an example of the target resident attributes. This table defines the communities to which residents belong, and describes the main means of transportation in each area, the time of day to start moving, and the time required. In addition, by showing the trend of dwell time in each community, it is possible to set simulation conditions that take into account the distribution of evacuation start times and variations in evacuation behavior.
NEXT, an example of organizing evacuation routes is shown in Figure 1. This makes it easier to visually grasp which route is used when inputting evacuation route information in the simulation tool described later, and by illustrating the main routes in advance, it is easy to compare and analyze the influence of differences in route conditions on the simulation results.

TABLE1. EXAMPLES OF ORGANIZING TARGET RESIDENT ATTRIBUTES

	Going to School/Work	School/Company	Returning from School/Work
Nursery School	Walk / Bicycle / Car	Nursery School	Walk / Bicycle / Car
Required Time	5–10 minutes	8 hours	5–10 minutes
Time	8:00–9:00	9:00–17:00	17:00–18:00
Kindergarten	Walk / Bicycle / Car	Kindergarten	Walk / Bicycle / Car
Required Time	5–10 minutes	5 hours	5–10 minutes
Time	8:00–9:00	9:00–14:00	14:00–15:00

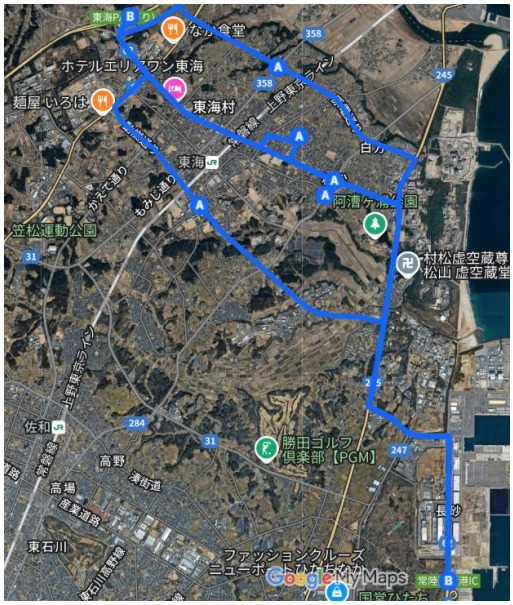

FIGURE1. EXAMPLE OF EVACUATION ROUTE ARRANGEMENT

II.B. Simulation

For the purpose of visualizing evacuation risks, we will develop a simulation construction environment that can reproduce traffic behavior in accordance with reality. In this study, we introduce a microscale approach to traffic simulation in order to accurately capture the flow of vehicles, the location of traffic congestion, and the dwell time in evacuation scenarios. In particular, it is necessary to reflect detailed information about the road infrastructure, such as the timing of traffic light switching, the structure of intersections, and the number of lanes, as well as the driver's driving behavior, such as the following behavior and acceleration and deceleration characteristics of each vehicle. Therefore, as a traffic simulation model, a micro model that can reproduce the behavior of individual vehicles, that is, a follow-up model, is adopted. To construct a specific simulation environment, we will use SUMO, a micro traffic flow simulation software. In addition, the OSM Web Wizard, which is included in SUMO, is used as a method of obtaining road information. This is a software that takes road data from Open Street Map and converts it so that it can be edited on SUMO. Figure 2 shows how the OSM Web Wizard was used, and FIGURE3 shows a diagram of a simulation using it. However, there are parts of the data obtained here that are different from the roads actually used. Therefore, it is necessary to check the number of lanes and the condition of intersections on the actual road on Google Maps and make corrections.

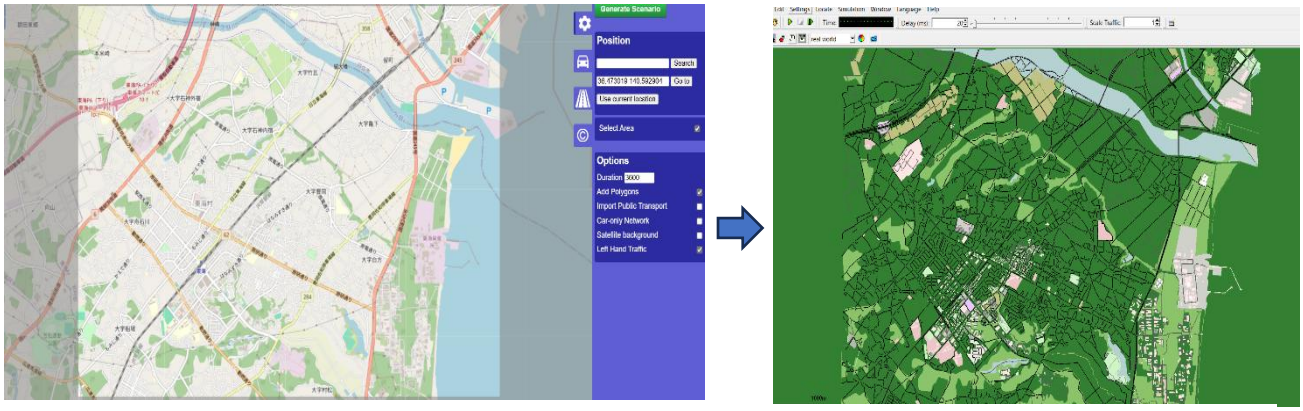

FIGURE2. DIAGRAM OF ROAD DATE OBTAINED USING THE OSM WEB WIZARD

FIGURE3. DIAGRAM OF SIMULATION BASED ON ACQUIRED ROAD DATE

II.C. Evaluation of validity

In this study, we will compare the simulation model with actual traffic data in order to verify the validity of the constructed simulation model. Specifically, as shown in FIGURE4, the "General Traffic Volume Survey Results Web Map" provided by the Ministry of Land, Infrastructure, Transport and Tourism is used to extract the actual measured traffic volume in the target area, the average driving speed for each road section, and the traffic concentration trend by time of day, and to compare it with the simulation results. This comparison evaluates the reproducibility of traffic flow in the simulation and numerically verifies the realism of indicators such as vehicle acceleration, average vehicle speed, and the number of vehicles passing per hour. For example, we will compare in detail whether the speed reduction near a specific intersection or the location of the bottleneck matches the actual data, and improve the accuracy by adjusting and resetting the parameters of the simulation model. In this way, we aim to ensure the reproducibility of evacuation behavior in the virtual environment and consistency with traffic behavior in the real world, and to construct a more reliable evacuation route optimization model.

FIGURE4. IMAGE OF THE GENERAL TRAFFIC VOLUME SURVEY RESULTS WEB MAP [3]

II.D. Evaluation of output simulation results

In the constructed simulation environment, evacuation behavior is reproduced under the initial conditions set, and the results are quantitatively evaluated. In particular, the distribution of the time spent by each vehicle on the evacuation route, the location of traffic congestion and its duration, etc., are the main evaluation indicators. By analyzing based on these indicators, it is possible to identify bottleneck sections where vehicles are likely to occur on evacuation routes and points where the risk of radiation exposure is relatively high due to traffic congestion.

II.E. Reconstruction of simulation

For reconstructing the simulation, it is necessary to clarify what specific factors will be analyzed from the previous simulation results and what kind of results are expected as an analysis of the results, and then reconstruct the simulation. For example, the simulation results show that traffic congestion occurs on a specific road, which has a significant impact on evacuation time. First, we will extract the various causes that cause traffic congestion. From the extracted causes, set a goal for which cause to reconstruct the simulation, and if it is to focus on traffic congestion at an intersection, reconstruct the simulation when the time of switching signals is changed for the intersection part. At this time, the extent to which the signal switching time is changed is determined after predicting the value expected to shorten traffic congestion and evacuation time from the previous simulation result. After that, a simulation is performed to analyze the extent to which traffic congestion and evacuation time have changed due to changes in the time when traffic lights change. The results are re-analyzed and simulations are built for multiple scenarios.

III. Future Works and Conclusion

This study developed a microscopic traffic simulation framework to realistically reproduce and analyze evacuation behavior during a nuclear disaster. The framework enables the detailed modeling of individual vehicle behaviors such as acceleration, deceleration, and headway control, as well as the prioritization of emergency vehicles and the identification of bottleneck locations. Insights from the microscopic simulation help visualize the temporal and spatial disparities in evacuation behavior, offering valuable input for macro-level evacuation planning. This contributes to realistic and effective improvements, such as optimizing traffic signal control and strengthening countermeasures in high-risk areas. In the future, to more accurately reflect real-world evacuation behavior, we plan to gradually construct multiple scenarios that consider complex conditions such as variations in evacuation start times, road closures, U-turns, and emergency vehicle priority. Through the analysis of these scenarios, we aim to identify the key factors that cause bottlenecks—such as where and how long traffic congestion occurs—and contribute to optimizing

REFERENCES

[1] Shizuoka Prefectural Emergency Management Department, Nuclear Safety Measures Division: Evacuation Simulation Results of Hamaoka Nuclear Power Plant's Nuclear Disaster Countermeasure Priority Areas: (2024)
[2] Fukui Prefectural Crisis Countermeasures and Disaster Prevention Division: Summary of the results of the evacuation time estimation simulation assuming a nuclear disaster: (2024)
[3] General Traffic Volume Survey Results Web Map: (2021) 令和3年度 一般交通量調査結果（可視化ツール）

ASRAM2025
www.asram2025.org
Asian Symposium on Risk Assessment and Management 2025
Pattaya, Thailand, 27 – 29 August 2025

Exploring Research Reactors for Boron Neutron Capture Therapy as an Alternative Treatment for *Cholangiocarcinoma*

Yuwadee Malad[1], Dea Aulia Kartini[1], Atirat Pitaktrakul[1], Natsuko Kondo[2], Yoshinori Sakurai[2], Chutima Talabnin[3], and Chinorat Kobdaj[1]

[1] *School of Physics, Institute of Science, Suranaree University of Technology: Nakhon Ratchasima, 30000, Thailand, y.malad.research@gmail.com (Y.M.), dea.kartini@sut.ac.th (D.K.), M6400156@g.sut.ac.th (A.P.), kobdaj@g.sut.ac.th (C.K.)*
[2] *Institute for Integrated Radiation and Nuclear Science, Kyoto University (KURNS): Osaka 590-0494, Japan, kondo.natsuko.3x@kyoto-u.ac.jp (N.K.),sakurai.yoshinori.8n@kyoto-u.ac.jp (Y.S.)*
[3] *School of Chemistry, Institute of Science, Suranaree University of Technology: Nakhon Ratchasima, 30000, Thailand,* chutima.sub@sut.ac.th (C.T.)

EXTENDED ABSTRACT

Recently, Boron Neutron Capture Therapy (BNCT) has received increased attention as an alternative treatment for aggressive and recurrent cancers. This work explores and compares five different research reactors—Kyoto University Reactor (KUR), Tsing Hua Open-pool Reactor (THOR), the Institute of Heavy Ion Nuclear Industry (IHNI), the Thai Research Reactor-1/Modification 1 (TRR-1/M1) from the Thailand Institute of Nuclear Technology (TINT), and the Suranaree University of Technology Research Reactor (SUT-RR). The comparison focuses on beam shaping assembly (BSA) designs, moderator and shielding materials, and the readiness for BNCT implementation in Asia.

SUT-RR is designed with a 45 kW power output and a BSA optimized for BNCT, which is expected to play a major role in future studies and clinical translation in Thailand. Table 1 summarizes the BSA material compositions used across these Asian BNCT facilities. The table highlights design diversity, particularly regarding use of fission converters and shielding elements for optimizing beam quality. SUT-RR aims to provide a BNCT-optimized beamline with a fission converter, whereas TINT is currently assessing the feasibility of establishing a localized BNCT platform based on its TRR-1/M1 reactor.

Currently, only in vitro experiments on KKU-055 cholangiocarcinoma (CCA) cells have been conducted to demonstrate biological efficacy. Cells were treated with boron compounds and irradiated using neutron fluxes of 2.6×10^{8} n·cm^{-2}·s^{-1} for 30 minutes at TINT and 1.89×10^{9} n·cm^{-2}·s^{-1} for 5 minutes at KUR. The resulting neutron fluences were 4.68×10^{11} n·cm^{-2} and 5.67×10^{11} n·cm^{-2}, respectively. Post-irradiation analyses included cell viability testing (MTT assay), clonogenic survival, and γH2AX immunofluorescence staining to assess DNA damage.

The results indicated significant DNA damage, as evidenced by increased γH2AX foci, and neutron fluence-dependent cell death. At TINT, ^{10}B uptake for 24 hours led to stronger DNA damage signals and lower viability (80%) compared to shorter uptake times. At KUR, cells exposed to higher ^{10}B concentrations (10–20 ppm) and high neutron flux exhibited intense γH2AX expression and reduced survival fractions. The Relative Biological Effectiveness (RBE) derived from KUR data was 4.34, suggesting a substantial therapeutic benefit over conventional X-ray irradiation.

These findings support the potential of BNCT as an effective treatment for CCA, particularly when neutron beam intensity and boron uptake conditions are optimized. This work underscores the readiness of multiple Asian reactors for BNCT and introduces Thailand's forthcoming capability at SUT-RR. Integrating these platforms enhances regional preparedness for implementing risk-informed, reactor-based therapies. The development of SUT-RR is expected to provide a controlled environment for optimizing BNCT beam design and biological safety thresholds, further supporting its translational potential within Southeast Asia.

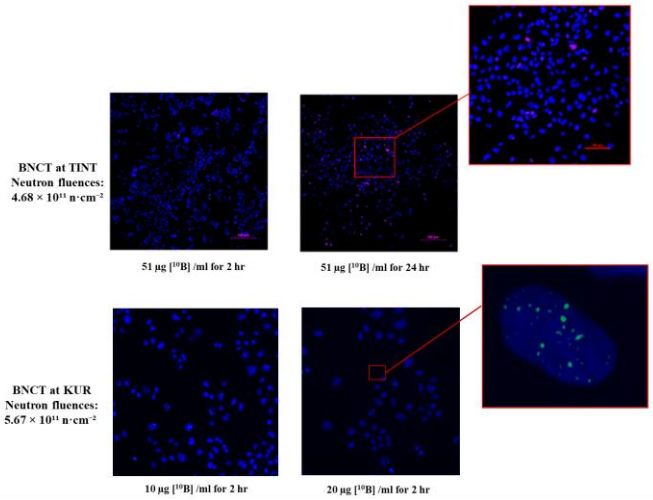

FIGURE 1. γH2AX immunofluorescence images of KKU-055 cells following BNCT at TINT and KUR. DNA damage, shown by green γH2AX foci, increases with longer boron uptake time and higher ^{10}B concentration, indicating fluence- and dose-dependent effects.

TABLE I. BSA materials used in BNCT beams in Asia

Reactor	BSA Materials	Fission Converter	References
KUR	Al/D_2O/Bi/Pb/Polyethylene/B-Polyethylene/Cd	No	1]
THOR	Al/Fluental/Pb/Bi/Li-Polyethylene/Heavy concrete	No	[2]
IHNI	Epithermal mode: Al/Al_2O_3/Pb/Bi/C, Thermal mode: Bi/Pb/C/PE(Pb)	No	[3]
SUT-RR	AlF_3+Al+LiF/Pb/H_2O/Pb-B-Poly/Cd/Li-Poly/Al/Bi/SS/Heavy concrete	Yes	*Unpublished manual*
TINT	Unspecified	Yes	*Not reported*

Representative γH2AX immunofluorescence images show DNA double-strand breaks in KKU-055 cells following BNCT irradiation. Cells treated with ^{10}B and irradiated for 5 minutes at KUR (Japan) and 30 minutes at TINT (Thailand) display increased γH2AX foci (green), indicating neutron fluence- and uptake-time dependent DNA damage. These results support the potential of BNCT for CCA treatment and demonstrate reactor capabilities in Asia. The forthcoming SUT-RR reactor is expected to extend BNCT accessibility within Thailand.

ACKNOWLEDGMENTS

This work was supported by Suranaree University of Technology (SUT), Thailand Science Research and Innovation (TSRI), and the Center of Excellence in High Energy Physics and Astrophysics. The authors would like to express their sincere gratitude to Natnalin Sastri for kindly providing laboratory space during the experiment at TINT, and to Kunthida Waree for her assistance. Yuwadee Malad gratefully acknowledges support from the Development and Promotion of Science and Technology Talent Project (DPST).

REFERENCES

[1] Z. Zhang and T. Liu, "A review of the development of In-Hospital Neutron Irradiator-1 and boron neutron capture therapy clinical research on malignant melanoma," *Ther. Radiol. Oncol.*, **2**, 49 (2018).
[2] Y.-W. H. Liu, T. T. Huang, S. H. Jiang, and H. M. Liu, "Renovation of epithermal neutron beam for BNCT at THOR," *Appl. Radiat. Isot.*, **61**(5), 1039–1043 (2004).
[3] Y. Kiyanagi, "Accelerator-based neutron source for boron neutron capture therapy," *Ther. Radiol. Oncol.*, **2**, 55 (2018).

EXPERIMENTAL STUDY OF THE BEHAVIOR OF A SINGLE AIR BUBBLE RISING IN A RECTANGULAR CHANNEL USING THE INTEGRATION OF THE OPTICAL VISUALIZATION METHOD AND THE BUBMASK TOOL

Tung Pham Thanh[1], Nghia Trinh The[1], Linh Le Mai[1], Dung Nguyen Thi[1], Tung Duong Thanh[2], Tuan Truong Hoang[2]

[1]*VNU Hanoi University of Science, 334 Nguyen Trai Str., Thanh Xuan, Hanoi; 120000;*
phamthanhtung10022003@gmail.com; nghiatrinhptl@gmail.com; lemailinh611@gmail.com; dungnt.hus@gmail.com
[2] *Nuclear Training Center, 140 Nguyen Tuan Str., Thanh Xuan, Hanoi; 120000;*
duongttung@gmail.com; tuan.htrng@live.com

ABSTRACT

Thermal-hydraulic safety is crucial in nuclear reactors, where water is both a coolant and a neutron moderator. Water removes heat from the reactor core as a coolant, preventing overheating and ensuring stable operation. Its high specific heat capacity and thermal conductivity facilitate effective heat transfer. As a moderator, water slows fast neutrons through elastic scattering with hydrogen nuclei, increasing neutron capture probability and sustaining a controlled chain reaction. However, vapor bubble formation reduces fluid density, affecting neutron moderation and heat transfer. A lower hydrogen density decreases neutron scattering efficiency, while excessive void formation can hinder cooling, increasing the risk of dry-out. Understanding these effects is essential for accurate two-phase flow modeling and reactor safety assessment. Bubble behavior of interest includes velocity, shape, trajectory, deformation, and void fraction. This study investigated the rising behavior of a single air bubble in a rectangular channel through optical visualization techniques and the BubMask image processing tool. A high-speed camera is used to record moving images of the measurement object. Then, the online available deep learning tool for image processing, BubMask, is used. It is an automated bubble detection and mask extraction tool. The experiment considered and compared the velocity, shape, and deformation of a single air bubble rising freely in a rectangular channel. Thereby also evaluating the accuracy of the model used.

Keywords: behavior of a single air bubble, optical visualization, BubMask tool, deep learning, rectangular channel

I. INTRODUCTION

Two-phase flows are commonly found in various industrial systems. Understanding the motion and interaction of gas bubbles within a liquid is essential for developing strategies that enhance process efficiency, ensure operational safety, and maintain product quality [1]. In nuclear reactors, thermal-hydraulic safety critically depends on the behavior of the coolant, which acts as both a heat transfer medium and a neutron moderator. The formation of vapor bubbles lowers fluid density, impairs heat transfer, and affects reactor reactivity. Excessive void generation can lead to dry-out conditions, posing significant safety risks. Accurately capturing these phenomena is crucial for two-phase flow modeling and reactor safety assessments.

While numerical simulations are widely used to evaluate these internal processes, discrepancies between simulation and reality necessitate experimental validation to ensure model reliability. This study aims to develop an experimental system for observing and analyzing gas–liquid two-phase flow, providing data for model validation and deeper insight into bubble dynamics.

Key flow parameters include void fraction, velocity, turbulence, and bubble shape. Optical Visualization Techniques (OVT), particularly high-speed imaging, are widely used to capture bubble behavior and estimate flow characteristics due to their clarity, noninvasive nature, and scalability across systems ranging from microfluidics to industrial setups [2–5]. Ultrasonic methods such as Ultrasonic Velocity Profiling (UVP) can also measure velocity profiles in both phases via Doppler shift detection [6,7], but characterizing rising bubbles often requires multiple probes and complex signal processing [8–10]. Given its practical advantages, OVT is employed in this study for experimental measurements.

This study is part of a broader effort to develop diagnostic methods for analyzing two-phase flow and detecting the onset of boiling in reactor-like channels. As an initial step toward this goal, the present work focuses on the experimental observation

and analysis of a single rising gas bubble. Optical Visualization Technique (OVT) is employed to capture bubble dynamics. At the same time, deep-learning methods, using the BubMask tool, are applied to extract key bubble characteristics—including shape and velocity—from optical data.

II. MEASUREMENT METHOD

II.A. Optical Visualization Method

Optical Visualization Technique (OVT) refers to a class of non-intrusive measurement methods that employ light-based imaging, typically high-speed cameras, to capture and analyze the motion of physical objects or flow phenomena. These techniques provide high-resolution visual data, making them particularly effective for studying fluid dynamics, material behavior, and multiphase flows. In two-phase flow research, OVT enables detailed observation of key characteristics such as flow structure, phase distribution, interface dynamics, and velocity fields, without disturbing the system. Its high spatial and temporal resolution makes it especially valuable for capturing transient phenomena such as bubble formation, motion, and interaction.

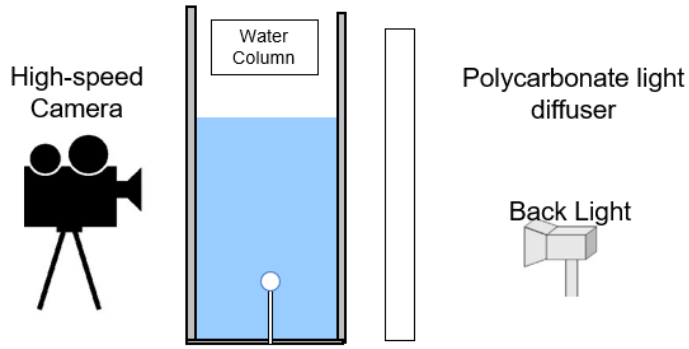

FIGURE 1. OPTICAL VISUALIZATION METHOD.

In this study, OVT is employed to observe the rise of gas bubbles in a liquid. Key parameters—including bubble shape, trajectory, and velocity—can be accurately extracted by recording their motion over time using a high-speed camera.

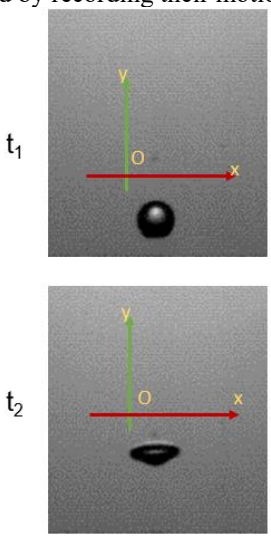

FIGURE 2. BUBBLE INFORMATION.

For instance, the bubble velocity v can be determined from two consecutive frames recorded at different times t_1 and t_2, corresponding to vertical positions y_1 and y_2 , respectively, using the following expression [11]:

$$v = \frac{y_2 - y_1}{t_2 - t_1} \tag{1}$$

II.B. Experimental setup

The experimental setup consists of a transparent rectangular tank made of acrylic (mica), measuring 50 mm in width, 50 mm in depth, and 500 mm in height. The tank was filled with tap water up to a height of 385 mm, and all measurements were conducted at a laboratory room temperature of 26.2 °C. After six hours of static conditions, assuming that the water temperature equilibrated with the ambient room temperature is reasonable. This thermal equilibrium naturally occurs based on thermodynamic principles: when water and air are in contact, they exchange heat through the surface. If the water is warmer than the air, heat is transferred from the water to the air, and vice versa. This process continues until the temperature difference is eliminated, leading to thermal equilibrium between the two media.

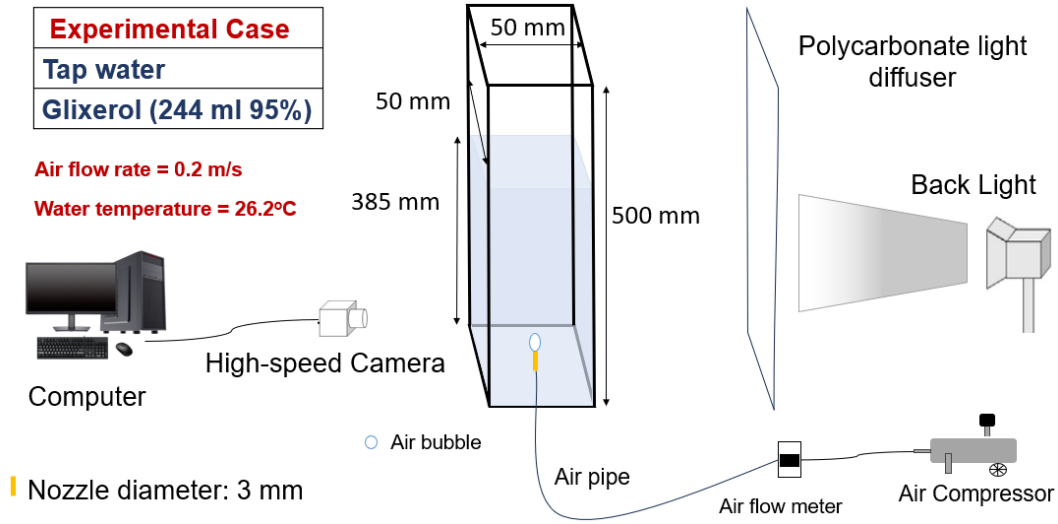

FIGURE 3. EXPERIMENTAL APPARATUS.

In the controlled laboratory environment, room temperature remains stable due to air-conditioning systems, allowing the water to reach ambient temperature more easily. Moreover, water's high specific heat capacity enables it to retain heat efficiently, slowing temperature fluctuations and maintaining uniform thermal conditions. Significantly, since no external heating or cooling is applied, the system stabilizes without thermal interference.

The target of this study is single air bubbles generated from a 3 mm nozzle connected to an air compressor. A pressure control valve regulates the gas flow, ensuring consistent air injection across experiments. This control enables isolated bubbles to form one at a time without coalescence or interaction. According to the flowmeter, the gas flow rate entering the tank is approximately 0.2 m/s, sufficiently low to allow individual rising bubbles to form.

During the bubble rising process, a high-speed camera was used to capture the motion of the bubbles. This device can record fast-moving objects with an exposure time of less than 1/1000 second and a frame rate of up to 1000 frames per second. It enables the visualization of rapid dynamics through sequential still images. To ensure clear and high-contrast images, a polycarbonate light diffuser was placed opposite the camera, with a backlight source positioned behind it to create a uniform background. The recorded images were stored on a computer for subsequent detailed analysis.

II.C. BubMask tool

II.C.1. Deep learning with BubMask tool

Optical visualization techniques are widely adopted in experimental studies across various fields, from microscale biological systems to large-scale industrial processes [4]. This thesis uses Optical Visualization Technique (OVT) to observe gas–liquid two-phase flow without disturbing the flow field, offering a significant advantage over invasive methods in capturing interfacial dynamics.

However, identifying individual bubbles remains challenging, especially in overlapping groups. Traditional image processing methods, such as Hough transform [4], breakpoint method [4], and Watershed transform [4], have shown effectiveness but are often insufficient for complex multi-bubble images.

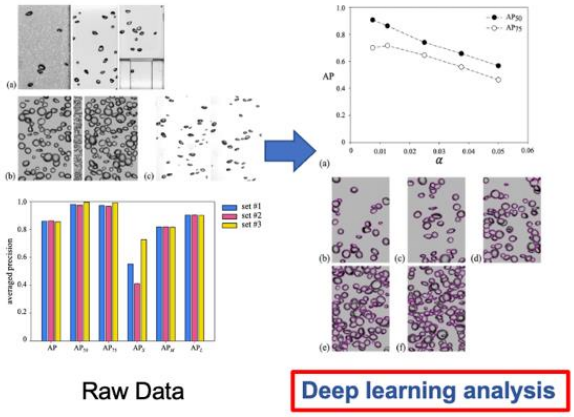

FIGURE 4. THE EXPERIMENTAL IMAGES WERE PROCESSED AND ANALYZED WITH BUBMASK [4].

Recent advances in deep learning provide promising solutions. Notably, Yewon Kim and Hyungmin Park trained a Mask R-CNN model to automatically detect and segment bubbles in two-phase flows [4]. Their method achieves over 95% accuracy, operates twice as fast as traditional approaches, and eliminates the need for manual threshold tuning. Moreover, the tool is open-source, significantly reducing data processing costs.

II.C.2. Image processing and measurement using BubMask

The rising motion of gas bubbles was captured using a high-speed camera, providing time-resolved image sequences. These images were then processed with BubMask, a deep learning-based image analysis tool designed to extract individual bubble masks from each frame.

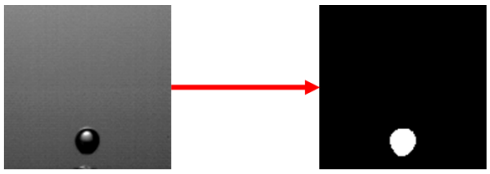

Results

x (m)	y (m)	Orientation (rad)	Axis_major_length (m)	Axis_minor_length (m)	Area (m^2)	Frame_number	Mask_number
0.0173	0.0026	-0.7501	0.0048	0.0047	1.77E-05	872	1

FIGURE 5. BUBMASK IMAGE ANALYSIS PROCEDURE.

These masks obtained quantitative features such as centroid position, projected area, and orientation angle. This information forms the basis for characterizing bubble dynamics, including shape evolution, rise trajectory, and velocity at different motion stages.

II.C.3. Evaluation of BubMask accuracy

While BubMask can extract object shape and size, the accuracy of such measurements must be validated in experimental studies. Therefore, to standardize the measurement method in this research, two steel spheres with fixed but different diameters were employed for calibration and verification.

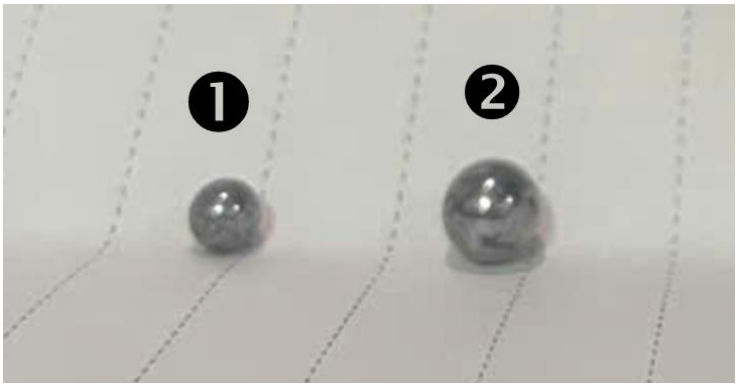

FIGURE 6. STEEL BALLS FOR VALIDATION.

TABLE I. The diameters of the steel balls.

Steel Ball	Normalization Diameter (mm)
1	3.96
2	5.56

Under the experimental setup and measurement conditions shown in Figure 3, the gas supply was closed during this validation test. Steel spheres were released from a height of 500 mm above the bottom of the tank. The high-speed camera captured real-time images of the falling spheres (Figure 7a). Like the gas bubble analysis, BubMask detected and outlined the moving spheres (Figure 7b), followed by segmentation and binary image extraction (Figure 7c). Key parameters such as area and position were extracted from these processed images for further analysis.

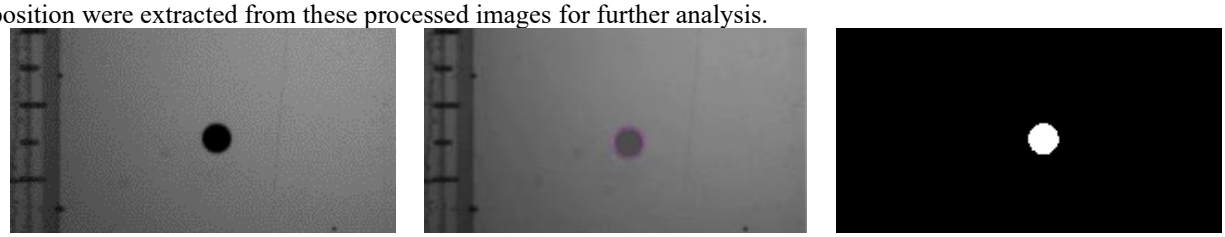

a b c

FIGURE 7. DETECTION AND 2D MASK EXTRACTION OF A SPHERICAL STEEL BALL WITH A DIAMETER OF 3.96 MM.

Following data processing, the discrepancy between the measured diameters of the steel balls and their known reference values is analyzed to assess the measurement accuracy of the method. The deviation between the experimental and reference diameters was computed using the following expression:

$$Deviation = \left|\frac{Reference\ Diameter - Measured\ Diameter}{Reference\ Diameter}\right| \times 100\% \quad (2)$$

TABLE II. Deviation of the measured diameter from the reference value.

Steel Ball	Reference Diameter (mm)	Measured Diameter (mm)	Error (%)
1	3.96	4.04	**1.98**
2	5.56	5.49	**1.26**

The deviations between the measured and reference diameters presented in Table II are below 2%, indicating a high level of measurement accuracy. Minor discrepancies may stem from experimental conditions, image processing, or other technical

factors. Nonetheless, the low deviation confirms the reliability of the measurement method, supporting its applicability for further analysis.

III. RESULTS AND DISCUSSION

III.A. Bubble shape evolution through different rising stages

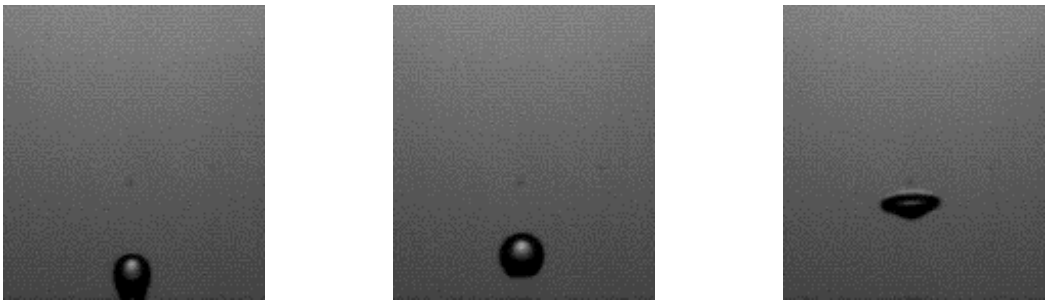

a b c

FIGURE 8. BUBBLE SHAPE DURING RISE.

The formation and morphological evolution of a single air bubble rising in water can be divided into three distinct stages, as illustrated in Figure 8. Each stage reflects the dominance of different physical forces affecting the bubble's geometry:

Stage 1 – Initial formation: At the nozzle tip, surface adhesion between the liquid and solid holds the bubble momentarily. This adhesion force stretches the bubble vertically, resulting in an upright oval shape (Figure 8a).

Stage 2 – Detachment from the nozzle: Once the buoyant force overcomes adhesion, the bubble detaches and tends to restore a spherical shape due to surface tension. This near-spherical geometry indicates a transient balance of forces and is used to define the bubble diameter (Figure 8b).

Stage 3 – Ascending phase: As the bubble rises, increasing velocity and pressure differences between the front and rear, along with fluid drag, cause horizontal elongation and vertical compression. The bubble transforms into a horizontally oriented oval shape (Figure 8c).

These observations confirm that bubble morphology is governed by the interplay between buoyancy, drag, surface tension, and wetting forces during its ascent.

III.B. Velocity of a single gas bubble rising in a water column

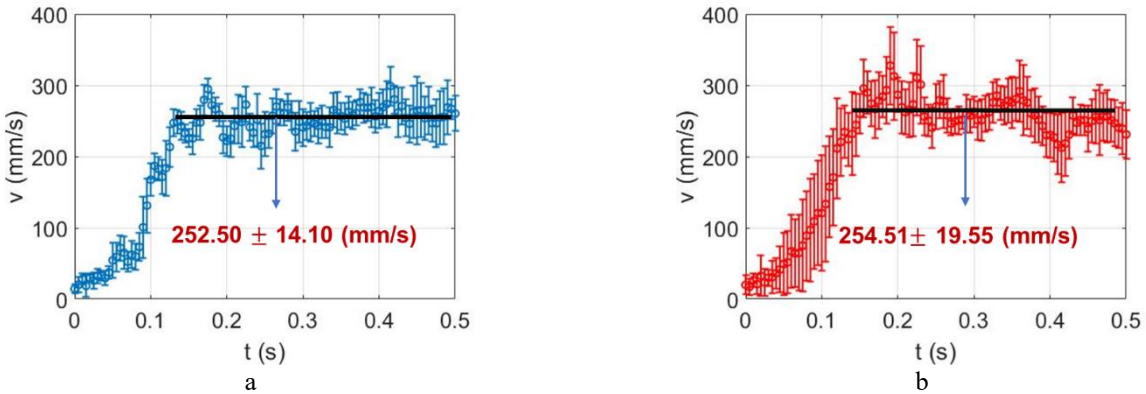

a b

FIGURE 9. VELOCITY OF A SINGLE GAS BUBBLE RISING IN A WATER COLUMN OVER TIME FROM THE NOZZLE POSITION.

In the experiment, the rising motion of single gas bubbles was recorded using a high-speed camera. The captured images were then processed with the deep learning tool BubMask, which extracted detailed information on bubble shape, position, and velocity over time. The results show that the velocity of the bubble is not constant but varies across different stages of its ascent. This variation reflects the complex interplay between buoyancy, liquid drag, and environmental disturbances.

Right after the bubble detaches from the nozzle at the early stage, buoyancy is the dominant force, causing rapid acceleration. The drag force increases proportionally as the bubble speeds, especially in deformed bubbles with greater frontal area. Over time, a balance is established between buoyancy and drag, resulting in a more stable velocity during the later stages of motion.

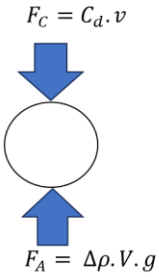

F_A: Buoyant force
$\Delta\rho$: Density difference between water and bubble
V: Bubble volume
g: Gravitational acceleration
F_C: Drag force
C_d: Drag coefficient
v: Bubble velocity

FIGURE 10. FORCES ACTING ON A FREELY RISING SINGLE GAS BUBBLE IN WATER.

When a gas bubble rises in water, it experiences a drag force, which is influenced by velocity, size, shape, and fluid properties. This force plays a key role in controlling bubble motion [12]. When buoyancy and drag balance out, the bubble reaches a terminal velocity. The average terminal velocity in tap water is about 252.5 mm/s, as shown in Figure 9a, consistent with theories of bubbles in still liquids. The velocity profile changes significantly when adding 244 ml of 95% glycerol (Figure 9b). The acceleration phase is longer due to higher viscosity, and after reaching a peak, the velocity fluctuates and slightly decreases instead of remaining stable. This is caused by increased viscous drag and nonlinear fluid interactions. As shown in Figure 10, the buoyancy force remains constant since the bubble volume does not change. However, the drag varies with the bubble shape, which continuously deforms during rising. This leads to different equilibrium velocities. In addition, local vortex formation around the bubble contributes to unsteady motion by introducing fluctuating lift and drag forces.

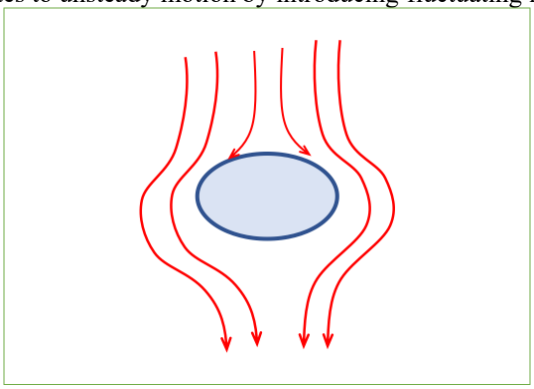

FIGURE 11. ILLUSTRATION OF THE RELATIVE MOTION OF THE SURROUNDING FLUID AROUND A RISING GAS BUBBLE.

IV. CONCLUSIONS

This study presented an experimental investigation of the rising behavior of a single air bubble in a rectangular water column, using the Optical Visualization Technique (OVT) combined with the deep learning-based BubMask tool. High-speed imaging enabled accurate tracking of bubble motion, while BubMask provided reliable extraction of key parameters such as shape and velocity.

The results show that bubble velocity is not constant but varies with rising stages, reflecting the complex balance between buoyancy, drag, and fluid interaction. In tap water, the measured terminal velocity is consistent with theoretical models. When glycerol is added, noticeable changes in the velocity profile are observed. However, due to the short observation time and limited field of view of the camera, these trends should be interpreted cautiously and require further validation.

Validation tests using steel spheres demonstrated that the image-based measurement method is accurate, with deviations below 2%. These findings confirm the applicability and reliability of the integrated OVT–BubMask approach for analyzing

bubble dynamics in multiphase flows and provide a basis for future studies on complex flow conditions such as boiling and bubble interactions.

ACKNOWLEDGMENTS

The authors would like to express their sincere gratitude to the Nuclear Training Center, Vietnam Atomic Energy Institute, for providing technical guidance and support during the implementation of this study. Special thanks are also extended to the faculty members of the Faculty of Physics, Hanoi University of Science, for their valuable advice and encouragement throughout the research process.

REFERENCES

[1] H. Murakawa, Y. Kubo, S. Maeda, and K. Sugimoto, "Measurements of Bubble Rising Velocity using Ultrasonic Tomography," *Proc. 14th Int. Symp. on Ultrasonic Doppler Methods for Fluid Mechanics and Fluid Engineering*, Kobe, Japan, 23–25 October 2023, pp. 75–78.
[2] J. An, L. Lei, F. Liang, C. Cheng, N. Zhou, Y. Ning, and J. Zhang, "An experimental study on the void fraction for gas–liquid two-phase flows in a horizontal pipe," *Fluid Dynamics & Materials Processing*, **17**, 1037 (2021).
[3] T. Hibiki and M. Ishii, *Thermo-Fluid Dynamics of Two-Phase Flow*, pp. 1–10, Springer (2011).
[4] Y. Kim and H. Park, "Deep learning-based automated and universal bubble detection and mask extraction in complex two-phase flows," *Scientific Reports*, **11**, 88334 (2021).
[5] H. Tian, Z. Zhang, X. Zou, and S. Zhong, "A flexible image analysis method for measuring bubble parameters," *Chemical Engineering Science*, **141**, 143 (2016).
[6] A. Hamdani, H. Kikura, H. Takahashi, N. Thong-un and W. Wongsaroj, "Extended short-time Fourier transform for ultrasonic velocity profiler on two-phase bubbly flow using a single resonant frequency," *Applied Sciences*, **9**, 50 (2019).
[7] H. Kikura, H. Murakawa and M. Aritomi, "Velocity profile measurements in bubbly flow using multi-wave ultrasound technique," *Chemical Engineering Communications*, **197**, 114 (2010).
[8] J. Pulsawat, H. Kikura, N. Shoji, N. Thong-Un, W. Treenusorn, and W. Wongsaroj, "Classification of Flow Regimes in Bubble Column Using the Integration of Ultrasound and KNN Algorithm," *Proc. 14th Int. Symp. on Ultrasonic Doppler Methods for Fluid Mechanics and Fluid Engineering*, Kobe, Japan, 23–25 October 2023, pp. 67–70.
[9] S. Eckert, M. Sana, H. Masanori, and K. Suzuki, "Effect of Transverse Magnetic Field on Rising Bubble Behavior in Gallium Eutectic Alloy," *Proc. 14th Int. Symp. on Ultrasonic Doppler Methods for Fluid Mechanics and Fluid Engineering*, Kobe, Japan, 23–25 October 2023, pp. 71–74.
[10] Y. Kubo, S. Maeda, H. Murakawa, and K. Sugimoto, "Measurements of Bubble Rising Velocity Using Ultrasonic Tomography," *Proc. 14th Int. Symp. on Ultrasonic Doppler Methods for Fluid Mechanics and Fluid Engineering*, Kobe, Japan, 23–25 October 2023, pp. 75–78.
[11] "Kinematics in One Dimension," https://www.slideserve.com/leena/kinematics-in-one-dimension-powerpoint-ppt-presentation (2023)
[12] Y. CAO, Y. JIA, L. WANG and X. YAN, "Drag coefficient fluctuation prediction of a single bubble rising in water," *Chemical Engineering Journal*, **327**, 343 (2017).

ASRAM2025
www.asram2025.org
Asian Symposium on Risk Assessment and Management 2025
Pattaya, Thailand, 27 – 29 August 2025

DEVELOPMENT OF COST-EFFECTIVE AND READILY AVAILABLE MATERIALS FOR NEUTRON SHIELDING: A COMPARATIVE STUDY OF NATURAL RUBBER-BASED COMPOSITES

Jittinun Saenpoowa[1], Atirat Pitaktrakul[1], Chaiwat Ruksakulpiwat[2], Chinorat Kobdaj[1, 3]

[1] School of Physics, Institute of Science, Suranaree University of Technology, Muang Nakhon Ratchasima 30000, Thailand
[2] School of Polymer Engineering, Institute of Engineering, Suranaree University of Technology, Nakhon Ratchasima 30000, Thailand
[3] Boron Neutron Capture Therapy Research Center, Suranaree University of Technology, Muang Nakhon Ratchasima 30000, Thailand

EXTENDED ABSTRACT

INTRODUCTION

Nuclear technology is expanding rapidly in Thailand for use in research and medicine. The country's first BNCT (Boron Neutron Capture Therapy) center, which will be used for research and cancer treatment, is currently being established at Suranaree University of Technology (SUT). Furthermore, as part of its national energy strategy, Thailand is considering the implementation of Small Modular Reactors (SMRs) in the future. The need for efficient and reasonably priced neutron shielding materials is growing with the increasing use of neutron sources. Currently available commercial materials, such as silicone composites containing boron carbide (B_4C) and borated polyethylene (BPE), are effective but expensive and rely on imports. This work investigates the development of natural rubber (NR) composites, incorporating boron compounds, as cost-effective and locally available alternatives for neutron radiation shielding. Moreover, this study evaluates the neutron attenuation performance of NR composites using boric acid, borax, and B_4C, and compares their effectiveness to commercial shielding materials.

METHODOLOGY

For this study, natural rubber (NR) composites were made using Thai natural rubber of STR 5L grade as the base polymer matrix. Various formulations of neutron absorber additives were used at a constant concentration of 50 wt%, including boric acid (H_3BO_3), borax ($Na_2[B_4O_5(OH)_4]\cdot 8H_2O$), and boron carbide ($B_4C$). A standard rubber compounding formulation was employed to ensure proper processing and vulcanization. At 30 phr (Parts per Hundred Rubber), carbon black (N330) was added to the mixture to improve the mechanical properties of the composite, due to its fine particle size, good dispersion, and reinforcing efficiency. Stearic acid and zinc oxide (ZnO) were added as activators to promote vulcanization at 2 and 4 phr, respectively. The primary accelerator in the curing system was CBS (N-cyclohexylbenzothiazole-2-sulfenamide) at 0.5 phr, the secondary accelerator was TMTM (tetramethylthiuram monosulfide) at 0.6 phr, and the vulcanizing agent was sulfur at 2 phr.

To ensure even dispersion of chemicals and fillers within the rubber matrix, the rubber and all additives were first mixed in a laboratory-scale internal mixer. For 25 minutes, the mixing was done at 60 °C (degrees Celsius). The rubber compound was then transferred to a two-roll mill for rolling into sheets. Before molding, it was kept at room temperature for a full day to allow for stress relaxation and pre-vulcanization stability. The molding was carried out by a hydraulic compression molding press (LP20-B model) at 150°C at the optimum time of each formula as measured by a moving die MDR 3000 rubber curing analyzer, following the ASTM D 5289 standard, which measures the torque response of rubber during curing to identify the optimum vulcanization time.

Neutron tomography or neutron imaging was used to calculate the linear attenuation coefficient (μ) value, which is a neutron shielding property of materials. The experiment was performed at the research reactor of the National Institute of Nuclear Technology (Public Organization). The LiF/Zn(Ag) scintillator was used to mount sample material with a thickness of 0.5 cm in the experiment. The emitted light was reflected by a mirror and subsequently captured by the CCD camera while the samples were irradiated with neutrons. The TIFF format was used to record the image file. Neutron imaging data were used to calculate the brightness fraction (Eq. (1)), which served as the neutron transmission factor (I/I_0) in the attenuation equation

(Eq. (2)). I_0 is the difference in brightness between the images taken when the beam is open beam and off beam (dark beam), while I is the difference in brightness between the images taken with the sample material mounted and the dark beam. All quantitative analyses and image processing were conducted using ImageJ 1.53t. Figure 1 shows an example of the neutron imaging outputs used to derive the attenuation data.

$$Brightness\ fraction = \frac{Image\ brightness_{\text{sample material}} - Image\ brightness_{\text{dark-beam}}}{Image\ brightness_{\text{open-beam}} - Image\ brightness_{\text{dark-beam}}} \quad (1)$$

$$I = I_0 e^{-\mu t} \quad (2)$$

The brightness fraction was used as the neutron transmission factor (I/I_0) in calculating the linear attenuation coefficient (μ) of each sample rubber composite material at thickness (t).

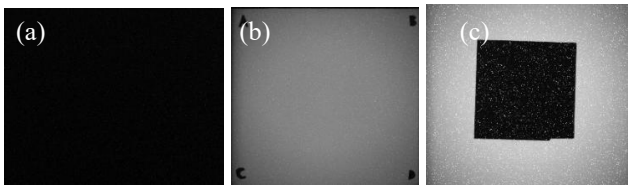

Fig. 1. Neutron imaging results: (a) Open-beam, (b) Dark-beam, (c) Sample with commercial B_4C-silicone.

RESULTS

The composite containing boron carbide exhibited the maximum attenuation among all the samples, with a linear attenuation coefficient of 4.9539 cm^{-1}. The commercial B_4C-silicone material (5.2346 cm^{-1}) performed quite similarly to this. Additionally, the boric acid and borax composites showed established efficacy with coefficients of 4.1589 cm^{-1} and 3.7416 cm^{-1}, respectively. In contrast, the pure NR control sample only showed minor shielding with a value of 0.6991 cm^{-1}.

The NR/B_4C, NR/Boric acid and NR/Borax composites required only 1.0567 cm, 1.2587 cm and 1.399 cm in thickness, respectively, to provide shielding equivalent to 1 cm of the commercial B_4C-silicone product. Achieving the same shielding effect with pure NR would require a thickness of 7.4875 cm. While B_4C offered the highest shielding efficiency, borax emerged as the most cost-effective option, balancing performance with affordability.

CONCLUSION

Natural rubber composites incorporating boron-based additives especially borax and boric acid exhibit promising neutron shielding properties and offer a low-cost, locally sourced alternative to commercial materials. The results confirm that NR-based composites can achieve effective attenuation while supporting sustainability and economic development. However, challenges remain regarding long-term durability under irradiation and the potential degradation of boron compounds. Future work will focus on assessing radiation resistance and mechanical aging under prolonged neutron exposure, in additionally optimizing filler concentrations for improved performance, moreover, developing multilayer composite designs to further enhance shielding efficiency in real-world applications, such as BNCT.

ACKNOWLEDGMENTS

This work was supported by (i) Suranaree University of Technology (SUT), (ii) Thailand Institute of Nuclear Technology (Public organization). We extend our gratitude to the Rubber Authority of Thailand for their financial support.

REFERENCES

[1] K. Armart, P. Boontueng, C. Mutuwong, S. Prasertsri, S. Pencharee, J. Kaewkhao, P. Thongjerm, S. Wonglee, W. Pornroongruengchok, J. Saenpoowa, C. Kobdaj, "Development of the thermal neutron shielding efficiency and its secondary radiation of natural rubber composites with a multilayer structure," *Radiation Physics and Chemistry*, **236**, art. no. 112944 (2025).

[2] J. Saenpoowa, A. Pitaktrakul, S. Inphonlek, C. Ruksakulpiwat, C. Kobdaj, "Design and fabrication of thermal neutron shielding materials based on natural rubber and boron carbide," *MRS Communications*, **13**(6), pp. 1449–1454 (2023).

[3] J. Saenpoowa, C. Ruksakulpiwat, C. Yenchai, C. Kobdaj, "Fabrication and development of neutron shielding materials based on natural rubber and boron carbide," *17th Siam Physics Congress: Carbon Neutrality, SPC 2022*, Nakhon Ratchasima, 22 June 2022 through 24 June 2022, Volume 2431, Issue 1, Journal of Physics: Conference Series (2023).

ASRAM2025
www.asram2025.org
Asian Symposium on Risk Assessment and Management 2025
Pattaya, Thailand, 27 – 29 August 2025

Optimization of Gamma Shielding for the Neutron Radiography Facility at TRR-1/M1 Using PHITS Simulation

Sutasinee Kotayee[1], Sarinrat Wonglee[2], Weerawat Pornroongruengchok[2]

[1] *Department of Applied Radiation and Isotopes, Faculty of science, Kasetsart University, Bangkok 10900, Thailand*
E-mail: sutasinee.kot@ku.th
[2] *Thailand Institute of Nuclear Technology (Public Organization), 9/9 Moo7, Saimoon, Ongkharak, Nakhon-nayok, 26120, Thailand*

EXTENDED ABSTRACT

Neutron radiography (NR) is a widely utilized non-destructive evaluation technique used for the analysis and characterization of various materials. In two-dimensional neutron radiography, which is commonly applied in many testing scenarios, samples are often exchanged while the nuclear reactor is in operation. This process results in elevated background levels of gamma radiation, potentially exposing operators to unnecessary radiation doses. Therefore, in accordance with the ALARA (As Low As Reasonably Achievable) [1] principle, appropriate shielding materials must be implemented to enhance radiation safety for personnel.

In this work, the study focuses on the optimization of a gamma shielding to be installed in the neutron radiography room of Thai research reactor, TRR-1/M1, Thailand Institute of Nuclear Technology (Public Organization) [2]. Particle and Heavy Ion Transport code System (PHITS) Version 3.30 [3] simulation was employed to investigate the effectiveness of lead shielding in attenuating gamma radiation.

Lead gamma shielding, measuring 40 × 70 cm^2, was installed at the end of the extended collimator with a thickness ranging from 1 to 3 inches. The simulation was performed under the condition of a closed shutter with the reactor in operation.[4] The number of simulated particles was 10^7 particles per batch, with a total of 10 batches. The detector was an air-filled sphere with a radius of 1 cm (volume of 4.189 cm^3). Two detectors, located at a height of approximately 115 cm from the floor of the NR room, representing the height of the beam axis, were positioned within the extended collimator and behind the gamma shielding for flux determination shown in Fig 1, expressed in the unit of 1/cm^2·s.

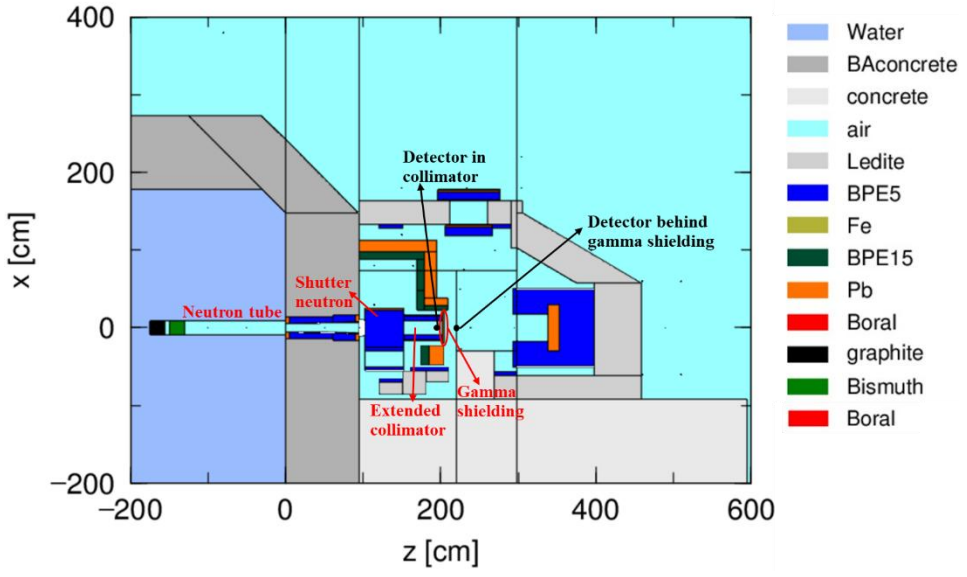

FIGURE 1. Schematic diagram of the NR facility with the existing shielding design from PHITS simulation.

Gamma shielding effectiveness using lead was evaluated by comparing neutron and photon fluxes at two positions: the collimator outlet and behind the lead shielding. The simulation results are shown in Table 1, For the neutron results, it was found that in the absence of lead shielding, the neutron fluence behind the collimator was relatively high. This might be due to neutron scattering caused by surrounding materials in the room. However, when the lead gamma shield was installed, it helped reduce such scattering, resulting in a lower neutron fluence behind the collimator. Nevertheless, increasing the lead shielding thickness had no significant impact on the neutron fluence. The ratio of flux between the collimator outlet and the post-shielding position significantly decreased. The photon flux was reduced by approximately 99% following the addition of lead shielding. These results indicate that lead is an effective material for gamma radiation attenuation, with shielding efficiency increasing as thickness increases. Consequently, the design of the gamma shielding complies with the ALARA principle, thereby enhancing radiation safety for operational.

TABLE I. The simulated neutron and photon fluxes when adding gamma shielding (unit of 1/cm^{2}s.)

Gamma shielding thickness (inch)	Detector in collimator		Detector behind gamma shielding		Ratio of radiation fluxes after to before shielding	
	Neutron	Photon	Neutron	Photon	Neutron	Photon
0	1.4742E+02	2.4963E+03	5.0779E+02	1.5177E+03	3.44	0.61
1	3.1462E+02	2.7611E+03	1.4582E+02	5.2098E+01	0.46	0.02
2	3.2810E+02	2.7684E+03	2.1858E+02	1.4171E+01	0.67	0.01
3	3.2810E+02	2.7036E+03	1.4315E+02	7.2337E+00	0.44	0.00

The shielding design result, a gamma radiation shield was installed within the neutron radiography room using lead with a thickness of only 1 inch. This thickness was determined to be sufficient to ensure radiation levels remain within safe limits for occupational exposure. Furthermore, the selection was influenced by spatial constraints within the facility, which limited the feasibility of installing more extensive shielding. The installation is expected to be completed in the near future.

ACKNOWLEDGMENTS

The author extends sincere gratitude to the researchers of the Neutron Imaging Group at the Thailand Institute of Nuclear Technology (Public Organization) for their generous support, the provision of essential data, and their invaluable scientific insights, all of which were instrumental to the successful completion of this study.

REFERENCES

[1] ICRP, The 2007 Recommendations of the International Commission on Radiological Protection, ICRP Publication 103, Ann. ICRP, vol. 37, no. 2–4 (2007).
[2] W. Pornroongruengchok, S. Wonglee, S. Kotayee and P. Thongjerm, “Upgrading Neutron Imaging Facility at TRR-1/M1 Reactor”, J. Phys. Conf. Ser. 2605 (2023) 012002.
[3] T Sato T, Iwamoto Y, Hashimoto S, Ogawa T, Furuta T, Abe S, Kai T, Matsuda N, Matsuya Y, Hirata Y, Yao L, Tsai P.-E, Ratliff H, Iwase H, Sakaki Y, Shigyo N, Sihver L, and Niita K, 2023 PHITS Ver. 3.30 User's Manual.
[4] T. Chulapakorn , S. Wonglee, W. Pornroongruengchok, T. Liamsuwan, and S. Kotayee, “Determination of neutron image quality of compact collimator facility for non-destructive testing”, Journal of Instrumentation, vol. 16, no. 2, p. P02004 (2021).

Poster Session 3 (8:30 - 10:00)	The Port 7, C Floor	Safety and Risk Analysis of Nuclear Facilities and Radiation Application (Research Reactor, Tokamak Plasma Fusion, Nuclear Fuel Cycle, Cyclotron, Agricultural and Medical Industries)
		Chair/Facilitator 1: Mr. Bui Phuong Nam (Dalat Nuclear Research Institute, Vinatom)
		Chair/Facilitator 2: Miss Piyanuch ORPONG (Thailand Institute of Nuclear Technology (TINT))
8:30 - 8:45		ID 114: Establishment of Typical Dose Value for Paediatric CT Brain and Dose Reference Value for CT Thorax at the Department of Radiology, Hospital Sultan Abdul Aziz Shah, Universiti Putra Malaysia Speaker: Nor Mazleen Mokhtar (MNA, Universiti Kebangsaan Malaysia) Contributors: Nor Mazleen Mokhtar (MNA, Universiti Kebangsaan Malaysia), Faizal Mohamed (Universiti Kebangsaan Malaysia), Noramaliza Mohd Noor (Universiti Putra Malaysia), Adiela Saiful Fazad (Universiti Putra Malaysia)
8:45 - 9:00		ID 90: Quantitative Analysis of Radiation Interaction and Energy Degradation of TINT Cyclotron facility for Enhanced Nuclear Physics Experiments Speaker: Khwanjira Tangpong (Thailand Institute of Nuclear Technology) Contributors: Khwanjira Tangpong (Thailand Institute of Nuclear Technology), Ekkachai Kongmon Piyanud Thongjerm (Thailand Institute of Nuclear Technology)
9:00 - 9:15		ID 116: Establishment of Typical Dose Value for Renal Scanning using Single Photon Emission Computed Tomography (SPECT) in Hospital Sultan Abdul Aziz Shah (HSAAS), Universiti Putra Malaysia Speaker: Arif Syazwan Che Aziz (MNA, Universiti Kebangsaan Malaysia) Contributors: Arif Syazwan Che Aziz (MNA, Universiti Kebangsaan Malaysia), Mohd Sazely Khaidzir (Universiti Putra Malaysia), Faizal Mohamed (Universiti Kebangsaan Malaysia), Noramaliza Mohd Noor (Universiti Putra Malaysia)
9:15 - 9:30		ID 55: Determination of Nuclear Security Effectiveness of TRR-1/M1 Reactor Speaker: Kanokrat TIYAPUN (Thailand Institute of Nuclear Technology) Contributors: Kanokrat TIYAPUN (Thailand Institute of Nuclear Technology)
9:30 - 9:45		ID 124: Public Perception of SMR Technology in Thailand: YouTube-based Sentiment Analysis Speaker: Kunthida Waree (Thailand Institute of Nuclear Technology (Public Organization)) Contributors: Kunthida Waree (Thailand Institute of Nuclear Technology (Public Organization)), Weerawat Pornroongruengchok (Thailand Institute of Nuclear Technology (Public Organization)), Watcha Sasawattakul (Department of Computer Engineering, Faculty of Engineering, Chulalongkorn University), Kampanart Silva (National Energy Technology Center, National Science and Technology Development Agency), Wasin Vechgama (Thailand Institute of Nuclear Technology (Public Organization))
9:45 - 10:00		ID 147: Severe Accident and Thermal Hydraulic Analysis of Human Error in Fuel Loading for TRR-1/M1 Speaker: Nart Noodee (Thailand Institute of Nuclear Technology (TINT)) Contributors: Nart Noodee (TINT), Kanokrat Tiyapun (TINT), Saensuk Wetchagarun (TINT)

ESTABLISHMENT OF TYPICAL DOSE VALUE FOR PAEDIATRIC CT BRAIN AND DOSE REFERENCE VALUE FOR CT THORAX AT THE DEPARTMENT OF RADIOLOGY, HOSPITAL SULTAN ABDUL AZIZ SHAH, UNIVERSITI PUTRA MALAYSIA.

Nor Mazleen Mokhtar [1], Nooramaliza Mohd Noor [2], Adiela Saiful Fazad [3], Faizal Mohamed [4]

[1] Department of Applied Physics, Faculty of Science and Technology, Universiti Kebangsaan Malaysia: Bangi, Selangor, Malaysia, 43600; mazleenmokhtar@gmail.com
[2] Medical Physics Laboratory, Department of Radiology, Faculty of Medicine and Health Sciences, 43400 Serdang, Selangor, Malaysia; noramaliza@upm.edu.my
[3] Medical Physics Unit, Hospital Sultan Abdul Aziz Shah, Universiti Putra Malaysia: 43400 Serdang, Selangor, Malaysia; adiela@upm.edu.my
[4] Department of Applied Physics, Faculty of Science and Technology, Universiti Kebangsaan Malaysia: Bangi, Selangor, Malaysia, 43600; faizalm@ukm.edu.my

EXTENDED ABSTRACT

CT scan or computed tomography is one of the medical procedures which uses diagnostic imaging technology that belongs in the nuclear medicine category. Typical dose is a dose value that can be decided from the parameter value of Computed Tomography (CT) imaging data of paediatric patients using standard metric that is taken into account which are Volume-Weighted Computed Tomography Dose Index ($CTDI_{VOL}$) and Dose Length Product (DLP). This research is carried out in order to make sure that paediatric patients are exposed to optimum radiation dose and are not excessive in any way during a CT imaging examination. According to research (Shao et al. 2020), the results show a high probability that those who have received CT scans, women are at higher risk for thyroid cancer and leukemia to be compared with men. As for this study, Children are more exposed to ionizing radiation than adults (Gricienė et al. 2021). At the same time, making sure that patient's safety is prioritized, and the quality of diagnostic image is acceptable, according to the standard. Dose and image quality are two main hints in mirroring the reference point which helps radiology staff to find and optimize CT techniques (Muhammad et al. 2020). This research is carried out in Hospital Sultan Abdul Aziz Shah (HSAAS) and using retrospective research method where the paediatrics patient's data from the year 2022 to 2024 is used to determine the typical dose and facility Diagnostic Reference Level (DRL) value for HSAAS. DoseWatch software which records all patients' data that are related is accessed and the needed standard metric value is obtained. Once the data is calculated and analyzed, the typical dose value and facility DRL value is obtained by determining the value for 25th, 50th (median), and 75th percentile. The facility DRL value is compared to other facility DRL value in Malaysia.

The obtained brain protocol typical dose value for $CTDI_{VOL}$ is 28.26 mGy for the age group of 1- to 5-year-old, 30.72 mGy for 6- to 10-year-old, and 32.92 mGy for 11 to 15 year old and as for DLP, the value is 528.57 mGy.cm for the age group of 1 to 5 year old, 607.25 mGy.cm for 6 to 10 year old and 629.17 mGy.cm for 11 to 15 year old. As for thorax protocol, the reference dose value obtained for $CTDI_{VOL}$ and DLP is 6.34 mGy and 36 mGy.cm, respectively. Comparative study is also carried out in this study on the DRL value from several countries which act as the first step in optimization of protection and can indicate whether an investigation of local practice should be performed, according to ICRP-135. There is a significant difference in DRL values for $CTDI_{VOL}$ and DLP of each country. According to Table 1, when compared according to the age group of the pediatric patients. A comparison of the $CTDI_{VOL}$ value for the age group of 6 to 10 years for Japan recorded the highest value compared to other countries which is 67.7 mGy. China has gradually increased. These values are not determined as the dose limit but more to a guideline for the healthcare officers to ensure that patients are $CTDI_{VOL}$ values for each age group while France and Switzerland have approximately the same $CTDI_{VOL}$ values for each age group. These values are not determined as the dose limit but more to a guideline for the healthcare officers to ensure the patients are receiving optimized radiation dose and especially for paediatric patients as they are more radiosensitive due to the tissues and cells in their body and the cumulative radiation dose that is too high due to CT scan and other factors might lead to the risk of existing of cancer cells.

The obtained value for 25th, 50th (median), and 75th percentile for both $CTDI_{VOL}$ and DLP shows that the facility has set CT protocol according to patient age and size. The Size-Specific Dose Estimate (SSDE) method used at this facility is used to adjust $CTDI_{VOL}$ based on phantoms according to patient size to provide a more appropriate dose estimate for the patient. Generally, factors that affect the value of typical dose and DRL are patients age and weight and efficiency of the operator of the CT machine (Zurihanaz et al. 2023). The difference in values for each percentile increases and this indicates that pediatric patients are exposed to the appropriate amount of radiation according to their age group to avoid unnecessary exposure and potential harm to pediatric patients who are more radiosensitive than adult patients. Through the determination of typical dose values at HSAAS and the comparison of DRL value determination studies for $CTDI_{VOL}$ and DLP in terms of facilities and nationally from UMMC and several different countries that have been selected, which are Japan, Morocco, China, United Kingdom, France, and Switzerland included in this study, it can be concluded that the establishment and determination of DRL values for pediatric brain CT scans is very important because it is a useful guideline or tool to avoid excessive radiation exposure to pediatric patients during CT scans. This is because pediatric patients are more radiosensitive than adult patients and excessive radiation is likely to harm pediatric patients in the long term. However, it should be emphasized that the highest priority for any diagnostic imaging examination is to achieve image quality that is adequate for clinical purposes. Image quality must be assessed as part of the DRL process, and methods to achieve optimization should be implemented. In addition, healthcare providers performing ionizing radiation medical imaging should also receive guidance and education on the concept and appropriate use of DRL.

ACKNOWLEDGMENTS

The authors thank the Ethical Board of Universiti Putra Malaysia for granting ethical clearance to conduct this research (REFERENCE NUMBER: JKEUPM-2024-75). The authors acknowledged the staff of Medical Physics Department of Hospital Sultan Abdul Aziz Shah for providing guidance and access to patients' data.

REFERENCES

[1] Zurihanaz, A.A., Noor, N.M., 2023. Establishment of Typical Dose Value for Interventional Radiology Examination in Radiology Department, Hospital Pengajar UPM. Asian Journal Of Medical Technology, 3(1), 37-46.
[2] Muhammad, N. A., Abdul Karim, M. K., Abu Hassan, H., Ahmad Kamarudin, M., Ding Wong, J. H. & Ng, K. H. 2020. Diagnostic Reference Level of Radiation Dose and Image Quality among Paediatric Ct Examinations in a Tertiary Hospital in Malaysia. Diagnostics (Basel) 10(8):
[3] Shao, Y. H., Tsai, K., Kim, S., Wu, Y. J. & Demissie, K. 2020. Exposure to Tomographic Scans and Cancer Risks. JNCI Cancer Spectr 4(1): pkz072.
[4] Gricienė, B. & Šiukšterytė, M. 2021. Local Diagnostic Reference Levels for Paediatric Head Ct Procedures. Acta medica Lituanica 28(2): 253.

Quantitative Analysis of Radiation Interaction and Energy Degradation of TINT Cyclotron Facility for Enhanced Nuclear Physics Experiments

Khwanjira Tangpong[1], Piyanud Thongjerm[1], Ekkachai Kongmon[2]

[1] *Thailand Institute of Nuclear Technology (Public Organization), 9/9 Moo7, Saimoon, Ongkharak, Nakhon-nayok, Thailand, 26120, E-mail: Khwanjira@tint.or.th*

[2] *Ph. D. Program in Applied Physics (International program), Department of physics and Materials Science, Faculty of Science, Chiang Mai University, Chiang Mai, Thailand, 50200*

EXTENDED ABSTRACT

The CC-30/15 cyclotron at the Thailand Institute of Nuclear Technology (TINT) accelerates protons within the 15–30 MeV range. Among its five beamline ports, Port 5 is dedicated to vacuum-based nuclear physics experiments, including PIXE and PIGE, which require proton energies of 2–3 MeV [1]. Since the cyclotron's minimum energy is 15 MeV, an energy degrader system is employed to reduce the beam energy accordingly.

This study utilizes GEANT4 Monte Carlo simulations to analyze radiation interactions during energy degradation and beam transport. The results provide key data on particle fluence, energy spread, and absorbed dose, supporting efforts to minimize radiation damage. Fig. 1 shows the simulation setup, including a vacuum tube, an energy degrader chamber with a degrader foil placed at 750 mm, and an energy measurement chamber with a proton detector (active area: 500 mm²) positioned at 1345 mm. A 15 MeV proton beam (5 mm diameter, 10^6 particles) was simulated passing through the degrader foil and reaching the detector. Foil materials made of aluminum, copper, and graphite, with respective thicknesses of 1.2 mm, 0.45 mm, and 1.2 mm, were studied. These thicknesses were determined based on SRIM calculations. Each simulation employed a single foil material to investigate the characteristics and effects of each material type. The simulation outputs include beam energy, energy spread, and normalized fluence, defined as the ratio of protons detected within the active area to the total number of particles within the field. The results are summarized in Table 1 and Fig. 2.

To investigate additional characteristics, the number of energy-degrading foils was increased. Two configurations were examined: (1) a single aluminum foil with a thickness of 1.2 mm positioned at 750 mm, and (2) two aluminum foils with a combined thickness of 1.2 mm, where the first foil (1.0 mm thick) was placed at 570 mm and the second foil (0.2 mm thick) at 750 mm. This arrangement was intended to enhance particle scattering [2]. Simulation results indicated that the energy spread was 20% in the single-foil configuration and 21% in the two-foil configuration, while the normalized fluence decreased from 18% to 13%, respectively.

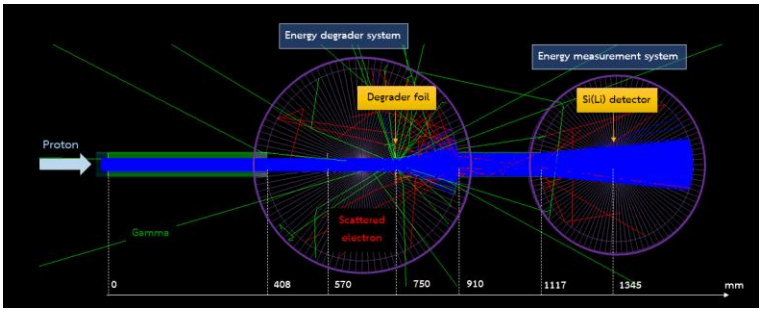

FIGURE 1. GEANT4 simulation setup illustrating the system components and particle tracks within the detection chambers: protons (blue), electrons (red) and gamma photons (green).

TABLE 1. Simulated output energy and energy spread of a 15 MeV proton beam after passing through three different degrader materials.

Degrader material	Output energy (MeV)	Energy spread (%)	Beam size (mm)	Normalized fluence (%)
No foil	14.98	1.02	5.09	100

Degrader material	Output energy (MeV)	Energy spread (%)	Beam size (mm)	Normalized fluence (%)
Aluminum	3.13	19.96	14.74	17.91
Copper	3.18	18.30	14.88	9.06
Graphite	3.35	17.94	14.33	37.79

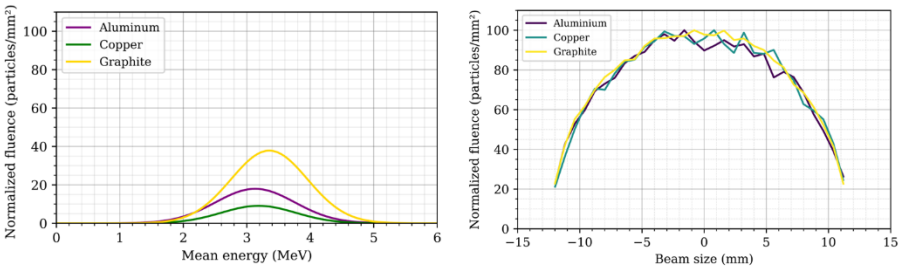

FIGURE 2. Beam characteristics after passing through three different degrader foils: energy spread (left) and beam profile (right).

The simulation results demonstrate that the proton energy was successfully reduced to the targeted value of 3 MeV. Among the tested materials, aluminum was found to be the most suitable option. Although graphite showed slightly better simulation outcomes, aluminum's higher atomic number and density offer superior stopping power, enabling more efficient proton energy loss and precise control of the beam energy. Furthermore, using a single aluminum foil produced the optimal results in terms of energy spread and normalized fluence.

In a simulation study of proton energy degradation within a room measuring 180 × 180 × 180 cm³, a proton beam with an initial energy of 15 MeV was simulated. The simulation revealed the production of secondary radiation, primarily gamma rays and electrons, with average energy depositions of 1.7×10^{-6} MeV/particle and 0.01 MeV/particle, respectively, throughout the simulated volume. Based on these energy deposition values, the maximum absorbed dose was estimated to be 4 mGy, occurring at the position of the aluminum foil at 750 mm from the beam source within the chamber, as illustrated in Fig. 3. In the next phase of the study, an analysis of the ambient dose will be conducted in parallel with the design of radiation shielding systems to improve radiation protection effectiveness within the operational area.

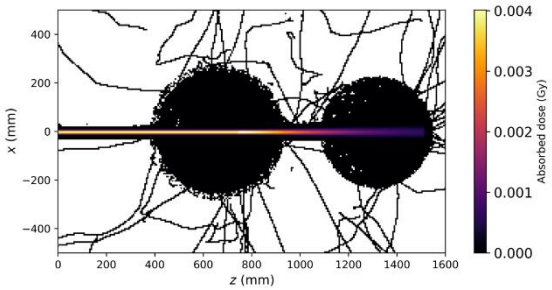

FIGURE 3. Absorbed dose distribution from a 15 MeV proton beam in a simulated room.

ACKNOWLEDGMENTS

The authors would like to acknowledge the support provided by PMU-B.

REFERENCES

[1] P. Thongjerm, "Development of a Cyclotron Based External Beam Irradiation System for Elemental Analysis," Proc. IPAC'22, Bangkok, Thailand, June 2022, pp. 3064–3066.
[2] A. N. Yuksel, M. P. Brown, and K. Austin, "Design of Beam Instrumentation for In-Vacuum Materials Irradiation and Testing in a 30 MeV Medical Cyclotron," Nucl. Instrum. Methods Phys. Res., Sect. A, vol. 977, p. 164290, 2020.

ESTABLISHMENT OF TYPICAL DOSE VALUE FOR RENAL SCANNING USING SINGLE PHOTON EMISSION COMPUTED TOMOGRAPHY (SPECT) IN HOSPITAL SULTAN ABDUL AZIZ SHAH (HSAAS), UNIVERSITI PUTRA MALAYSIA

Arif Syazwan Che Aziz [1], Noramaliza Mohd Noor [2], Mohd Sazely Khaidzir [3], Faizal K.P. Kunchi Mohamed [4]

[1] *Department of Applied Physics, Faculty of Science and Technology, Universiti Kebangsaan Malaysia: Bangi, Selangor, Malaysia, 43600; arfsyzwn02@gmail.com*
[2] *Department of Imaging, Faculty of Medicine and Health Sciences, Universiti Putra Malaysia: Serdang, Selangor, Malaysia, 43400; noramaliza@upm.edu.my*
[3] *Medical Physics Unit, Hospital Sultan Abdul Aziz Shah, Universiti Putra Malaysia: Serdang, Selangor, Malaysia, 43400; sazely@upm.edu.my*
[4] *Department of Applied Physics, Faculty of Science and Technology, Universiti Kebangsaan Malaysia: Bangi, Selangor, Malaysia, 43600; faizalm@ukm.edu.my*

EXTENDED ABSTRACT

Renal imaging is a standard nuclear medicine procedure performed in hospitals. This imaging provides crucial diagnostic information, such as early detection of cancer cells, and serves as a preparatory step before treatment. Establishing Diagnostic Reference Levels (DRLs) is vital for optimizing protection against medical exposures, especially in nuclear medicine. A DRL is a standard value used as a benchmark to assess whether the dose administered is too high or too low. This study aims to determine the typical dose value or facility DRL, for the renal imaging protocol. The research was conducted using a retrospective study design, analyzing data from patients who underwent renal imaging at Hospital Sultan Abdul Aziz Shah (HSAAS) in 2023 and 2024. The radiopharmaceuticals examined in this study include Technetium-99m Diethylenetriaminepentaacetic acid (Tc-99m DTPA) and Technetium-99m Mercaptoacetyltriglycine (Tc-99m MAG3). To establish the typical dose values, a comparative method was used, where the third quartile of the administered activity was compared with the national DRLs in Malaysia. The median value was proposed as the typical dose value. The median values for the two radiopharmaceuticals were 190.30 MBq for Tc-99m DTPA and 189.83 MBq for Tc-99m MAG3, while the national DRL values were 365 MBq for DTPA and 219 MBq for MAG3. The results indicated that both the median and third quartile of the administered activity values obtained were lower than the national DRL values.

In conclusion, the proposed Typical Dose Values or Facility Diagnostic Reference Levels (DRLs) for dynamic renal scan protocols using a Single Photon Emission Computed Tomography (SPECT) scanner are 190.30 MBq for Tc-99m DTPA and 189.83 MBq for Tc-99m MAG3. Based on the study findings, these values can serve as a guideline for medical practitioners to optimize the radiation dose administered to patients. This recommendation not only contributes to minimizing patient radiation exposure but also ensures that the resulting image quality is adequate and clear for diagnostic purposes. Furthermore, the establishment of these typical dose values can serve as an important reference for improving clinical practices at medical centers in Malaysia, particularly in ensuring the standardization of protocols being implemented. This initiative also supports efforts to comply with international standards, in line with guidelines set by organizations such as the International Atomic Energy Agency (IAEA) and the International Commission on Radiological Protection (ICRP). Overall, the findings of this study underscore the importance of systematic dose monitoring and management to maintain a balance between patient safety and diagnostic effectiveness.

Keywords: Renal imaging, SPECT, diagnostic reference levels (DRL), typical dose value, administered activity

ACKNOWLEDGEMENTS

This study has received ethical approval from the Ethics Committee of Universiti Putra Malaysia, JKEUPM (Reference Number: JKEUPM-2024-669).

REFERENCES

[1] 1 Basic principles of SPECT and SPECT/CT and quality control. (2017). In *Georg Thieme Verlag eBooks*. https://doi.org/10.1055/b-0038-149733

[2] *About diagnostic reference levels (DRLs)*. (n.d.). FAQ For Health Professionals | IAEA. https://www.iaea.org/resources/rpop/health-professionals/radiology/diagnostic-reference-levels/about-diagnostic-reference-levels

[3] Alnaaimi, M. A., Alduaij, M. A., Shenawy, F. A., Algaily, M. M., Mohammedzein, T. S., Alkandri, F. A., Shaban, M. O., & Alenezi, S. A. (2021). National Diagnostic Reference Levels for Nuclear Medicine in Kuwait. *Journal of Nuclear Medicine Technology*, *50*(1), 54–59. https://doi.org/10.2967/jnmt.121.262175

[4] Alqahtani, F. F. (2023). SPECT/CT and PET/CT, related radiopharmaceuticals, and areas of application and comparison. *Saudi Pharmaceutical Journal*, *31*(2), 312–328. https://doi.org/10.1016/j.jsps.2022.12.013

[5] Altarelli, M., Jreige, M., Prior, J. O., Lalonde, M. N., & Schneider, A. G. (2023). Renal scintigraphy to predict persistent renal failure after acute kidney injury: an observational study. *JN. Journal Of Nephrology*, *36*(4), 1047–1058. https://doi.org/10.1007/s40620-023-01569-0

[6] Blahd, W. H. (1996). Ben cassen and the development of the rectilinear scanner. *Seminars in Nuclear Medicine*, *26*(3), 165–170. https://doi.org/10.1016/s0001-2998(96)80021-3

[7] Cherry, S. R., Sorenson, J. A., & Phelps, M. E. (2013). *Physics in nuclear medicine* (pp. 209-211). Saunders.

[8] El-Feky, M., & Jones, J. (2011). TC-99M DMSA. *Radiopaedia.org*. https://doi.org/10.53347/rid-13609

[9] Haufe, S. E., Riedmüller, K., & Haberkorn, U. (2006). Nuclear Medicine procedures for the diagnosis of acute and chronic renal failure. *Nephron. Clinical Practice*, *103*(2), c77–c84. https://doi.org/10.1159/000091576

[10] ICRP, 2015. Radiation Dose to Patients from Radiopharmaceuticals: a Compendium of Current Information Related to Frequently Used Substances. ICRP Publication 128. Ann. ICRP 44(2S).

[11] ICRP, 2017. Diagnostic reference levels in medical imaging. ICRP Publication 135. Ann. ICRP 46(1)

[12] Kementerian Kesihatan Malaysia (KKM). (2013). Malaysian Diagnostic Reference Level in Medical Imaging (Nuclear Medicine).

[13] Khalil, M. M. (2021). Basic Sciences of Nuclear Medicine. In *Springer eBooks*. https://doi.org/10.1007/978-3-030-65245-6

[14] Kharfi, F. (2013). Principles and Applications of Nuclear Medical Imaging: A survey on recent developments. In *InTech eBooks*. https://doi.org/10.5772/54884

[15] Kim, C. K., Zukotynski, K. A., Almodóvar, S. E., Donohoe, K. J., Dorbala, S., Fahey, F. H., Franquet-Elía, E., Gerbaudo, V. H., Grant, F. D., Horgan, S. J., Hyun, H., Manapragada, P., Palestro, C. J., Roach, P. J., Schembri, G. P., Singhal, T., & Vallabhajoshula, S. (2017). *SPECT and SPECT/CT*. https://doi.org/10.1055/b-004-138014

[16] Krishnan, M. A., Cherukumudi, A., Oommen, S., Malapure, S. S., & Chelvam, V. (2022). Revolutionizing medical diagnosis with SPECT imaging: Clinical applications of a nuclear imaging technology. In *Elsevier eBooks* (pp. 85–104). https://doi.org/10.1016/b978-0-323-85650-8.00010-3

[17] *Malaysia Diagnostic Reference levels in Medical Imaging (Nuclear Medicine)*. (2013). Ministry Of Health Malaysia.

[18] Nikolov, N., Makeyev, S., Korostynska, O., Novikova, T., & Kriukova, Y. (2022). Gaussian filter for brain SPECT imaging. *Innovative Biosystems and Bioengineering*, *6*(1), 4–15. https://doi.org/10.20535/ibb.2022.6.1.128475

[19] Noori-Asl, M. (2020). Investigation of different factors affecting the quality of spect images: A simulation study. *Journal of Medical Physics/Journal of Medical Physics*, *45*(1), 44. https://doi.org/10.4103/jmp.jmp_88_19

[20] Radiologie München. (2023, May 5). *Scintigraphy of the kidneys - diagnostics at Radiologie München*. https://www.radiologie-muenchen.de/en/nuclear-medicine/renal-scintigraphy/

[21] Santos, W. H. S. D., Ataky, S. T. M., Silva, A. C., De Paiva, A. C., & Gattass, M. (2017). Automatic method for quantitative automatic evaluation in dynamic renal scintilography images. *Multimedia Tools and Applications*, *76*(18), 19291–19315. https://doi.org/10.1007/s11042-017-4715-9

[22] Shao, W., Rowe, S. P., & Du, Y. (2021). SPECTnet: a deep learning neural network for SPECT image reconstruction. *Annals of Translational Medicine*, *9*(9), 819. https://doi.org/10.21037/atm-20-3345

[23] Suttho, D. (2024). Establishment of National diagnostic Reference levels for administered activity in diagnostic nuclear medicine in Thailand. *Journal of Nuclear Medicine Technology*, *52*(2), 158–162. https://doi.org/10.2967/jnmt.123.266836

[24] Taylor, A. T., Folks, R. D., Rahman, A. K. M. F., Polsani, A., Dubovsky, E. V., Halkar, R., & Manatunga, A. (2017). 99MTC-MAG3: Image Wisely. *Radiology*, *284*(1), 200–209. https://doi.org/10.1148/radiol.2017152311

[25] Themes, U. (2020, May 24). *Basic principles of SPECT and SPECT/CT and quality control*. Radiology Key. https://radiologykey.com/basic-principles-of-spect-and-spectct-and-quality-control/

[26] Tong, S., Alessio, A. M., & Kinahan, P. E. (2010). Image reconstruction for PET/CT scanners: past achievements and future challenges. *Imaging in Medicine*, *2*(5), 529–545. https://doi.org/10.2217/iim.10.49

[27] Van Audenhaege, K., Van Holen, R., Vandenberghe, S., Vanhove, C., Metzler, S. D., & Moore, S. C. (2015). Review of SPECT collimator selection, optimization, and fabrication for clinical and preclinical imaging. *Medical Physics on CD-ROM/Medical Physics*, *42*(8), 4796–4813. https://doi.org/10.1118/1.4927061

[28] Van Der Have, F., Vastenhouw, B., Ramakers, R. M., Branderhorst, W., Krah, J. O., Ji, C., Staelens, S. G., & Beekman, F. J. (2009). U-SPECT-II: an Ultra-High-Resolution device for molecular Small-Animal imaging. *˜the œJournal of Nuclear Medicine*, *50*(4), 599–605. https://doi.org/10.2967/jnumed.108.056606

DETERMINATION OF NUCLEAR SECURITY EFFECTIVENESS OF TRR-1/M1 REACTOR

Kanokrat Tiyapun[1], Saensuk Wetchagarun[1], Sirirat Seemapapong [1]

[1] *Thailand Institute of Nuclear Technology: 16 Vibhavadi Rangsit Road, Ladyao, Chatuchak, Bangkok, 10900, and kanokrat@tint.or.th*

EXTENDED ABSTRACT

ABSTRACT

A critical infrastructure including TRR-1/M1 research reactor is an attractive target for attacks. A purpose for attack on a nuclear facility may directly or indirectly jeopardize public health and safety. Physical protection systems (PPS) are used to prevent and mitigate loss of valuable property. The likelihood that a physical security system will defeat an adversary along a specific path is used to assess the physical protection system's effectiveness. The PPS structure of the Reactor Center at Thailand Institute of Nuclear Technology (Public Organization) was evaluated in this study included TRR-1/M1 research reactor and a gas tight area. The PPS was determined and quantitatively evaluated using the PathTrace and Multipath Very-Simplified Estimate of Adversary Sequence Interruption (MPVEASI) software. The probability of interrupting the adversary before any theft or sabotage occurs at the reactor building is 0.9512. The response time was 300 second (tested). The security system is high since the probability of interruption which is greater than the medium security system range of 0.50-0.75. The results indicated that the security system for TRR-1/M1 reactor is high. Utilized PathTrace software tool, the existing PPS can be evaluated and upgraded to achieve a higher level of response interruption, or probability of interruption (PI) of the adversary. The study can be used to visualize vulnerable adversary pathways and provide countermeasure plans. The results can be used to upgrade these pathways to provide a higher level of PPS for the Reactor Center in the future.

Keywords: Physical protection system, PathTrace, probability, likelihood, MPVEASI

INTRODUCTION

The TRR-1/M1 research reactor at Thailand Institute of Nuclear Technology (Public Organization) or TINT has undergone security enhancements to comply with international nuclear security standards, particularly INFCIRC/225/Rev.4 [1]. The reactor contains nuclear fuel classified under Category II, with uranium enrichment levels between 10% and 20% and a total mass of 1–5 kg. To prevent unauthorized access, theft, or sabotage, security measures is implemented including controlled entry points, CCTV monitoring, two-factor authentication for high-security zones, and response protocols approved by the national regulator, Office of Atoms for Peace (OAP). Fuel is stored within a protected zone featuring physical barriers, continuous surveillance, and controlled access. Transport requires prior approval and coordination among shipping and receiving entities, with international transfers governed by bilateral agreements detailing security protocols. This study presents a detailed quantitative assessment of the Physical Protection System (PPS) effectiveness at TRR-1/M1 using the Probability of Interruption (PI) and Probability of Neutralization (PN) metrics.

The PPS at TRR-1/M1 is structured around three key functions: detection, delay, and response. Detection is achieved through an Early Intrusion Detection System (IDS), a Closed-Circuit Television (CCTV) network, and an Alarm System (AS), all linked to a centralized security control center. The delay function includes reinforced barriers, high-security locks, and controlled access points, ensuring that adversaries are significantly slowed down before reaching critical areas. Response measures involve a trained security force capable of intervening within 300 seconds, supported by restricted building access, dual-authorization protocols for high-security zones, and non-transferable ID cards that electronically log personnel movements. Vehicles entering the facility are subjected to rigorous screening at a single controlled entry point. The reactor site is further secured by a double-layered fencing system, motion sensors, and biometric access controls.

This study represents a novel application of quantitative evaluation techniques to assess the physical protection system (PPS) effectiveness of the TRR-1/M1 research reactor. While previous studies such as Oyeyinka et al. [2] applied the Estimate of

Adversary Sequence Interruption (EASI) model to assess PPS in multi-asset nuclear facilities, our study expands upon this framework by using MPVEASI v1.02—a multipath-enhanced, simplified tool [3] that accommodates multiple intrusion paths and detection layers, providing a more realistic simulation of adversary behavior. The uniqueness of this work is demonstrated in the following aspects including integrated path analysis with dual metrics, site-specific parameterization of MPVEASI inputs, risk identification across multiple layers and assets, benchmarking against international standards.

METHODOLOGY

The PPS at TRR-1/M1 is designed with three core functions: detection, delay, and response. The MPVEASI v1.02 model was employed to compute PI. Inputs include adversary speed (3 m/s), detection probabilities at various locations, delay times, communication success probability (PC = 0.90), and response force arrival time (300s). To assess PPS effectiveness, a computational approach was applied using two key probability metrics: Probability of Interruption (PI) and Probability of Neutralization (PN). The PI was evaluated using the MPVEASI v1.02 model, which simulates attack scenarios based on detection, delay, and response factors [4, 5]. The probability of detection along security layers follows Eq. (1).

$$P_I = P_C \times \left(1 - \left(1 - P(D_1)\right) \times \left(1 - P(D_2)\right) \times \ldots \times \left(1 - P(D_n)\right)\right) \quad (1)$$

where PC = 0.90 represents the probability of alarm communication, and $P(D_1, D_2, ..., D_n)$ are detection probabilities for security sensors. The adversary speed was set at 3 m/s, with a tested response time of 300 seconds. Security vulnerabilities were analyzed using Eq. (1) [6, 7] along the most probable attack paths, including sensor values such as external gate: PD = 0.10, Delay = 30s; building entrance: PD = 0.90, Delay = 120s; reactor hall (gastight area): PD = 0.90, Delay = 420s and final sabotage point: PD = 0.90, Delay = 60s. The MPVEASI simulation calculated a probability of interruption of 0.9512 indicating high likelihood of adversary interruption before mission completion. It is exceeding the medium-security range (0.50–0.75) and confirming that adversaries are likely to be detected and stopped before reaching critical reactor areas.

The Probability of Neutralization (PN) was calculated using a Markov Chain-based engagement model [6, 7] to simulate armed confrontation between adversaries and the response force. This method accounts for weapon type, firing posture, exposure level, engagement time, and probability of kill (PK) per volley. The response team consists of four trained personnel arriving within 300 seconds, while the adversary team consists of two intruders. Engagement is assumed to last 90 seconds, with guards firing from partial cover and adversaries exposed. With a per-volley PK of 0.45 and coverage factor of 0.85 for guards and 0.40 for intruders, Monte Carlo simulation over 1,000 iterations yielded a PN of 0.9046. This high value confirms that TRR-1/M1's response force is capable of neutralizing threats in most simulated scenarios, in line with international benchmarks for Category II material protection.

This methodology is used for assessing security systems that protect multiple assets are presented by Dai et al [6]. To evaluate risks associated with multiple simultaneous threats, a multi-asset protection analysis was conducted using Eq. (2).

$$U_j = \sum_{i=1}^{n} w_i \, log \frac{1}{1-R_i} \quad j = 1, 2 \ldots m \quad (2)$$

where R_i represents the effectiveness of detection, delay, or response elements. The probability of a successful attack was assessed using Eq. (3).

$$P(r) = e^{-E(Asset)} \quad (3)$$

The security effectiveness of key facility elements, such as personnel portals (0.8121), emergency exits (0.7965), and reactor hall doors (0.8433), was high, while perimeter gates (0.0824) were identified as a potential weakness.

RESULTS AND DISCUSSION

The PN for TRR-1/M1 was computed at 0.9046, indicating that adversaries attempting sabotage or theft are highly likely to be neutralized before achieving their objectives. The overall effectiveness (PE) is 0.9512 × 0.9046 = 0.8605. This value exceeds the international benchmark for "high security" (typically PE > 0.75) and indicates TRR-1/M1's compliance with IAEA security

standards [1]. However, the analysis also identified certain vulnerabilities, particularly at the perimeter gates, where the detection probability was as low as 0.10. These outer layers represent the weakest links in the intrusion path and could be exploited by adversaries to gain entry undetected. Addressing these issues through improvements in sensor technology, surveillance coverage, and layered delay elements that would further reinforce the outer defense ring.

Although TRR-1/M1 meets international security requirements, potential risks still exist including sabotage, radiological dispersal, cyberattacks, and natural disasters. To mitigate these threats, recommendations including strengthening access control with enhanced biometric verification, implementing stricter clearance protocols, and upgrading vehicle inspection technology are considered. Security drills should be conducted more frequently to assess response effectiveness, and additional security force deployment should be considered to reduce intervention times below the current 300-second threshold. Communication systems should be reinforced to ensure seamless coordination among security personnel, facility operators, and external emergency responders.

CONCLUSION

In conclusion, the computational assessment of TRR-1/M1's PPS confirms its strong security posture. The probability of interruption (0.9512) and neutralization (0.9046) exceed international benchmarks, ensuring effective threat mitigation. While the overall risk remains low, continuous evaluation and security infrastructure improvements are essential to counter emerging threats. These findings serve as a technical foundation for future security enhancements at TINT, reinforcing compliance with international nuclear security standards and ensuring long-term protection of nuclear materials and facility operations. Future work should focus on dynamic threat modeling, multi-asset risk evaluation, uncertainty analysis, and integration of cybersecurity elements and AI-based monitoring to enhance system adaptability and resilience against evolving physical and cyber-physical threats.

ACKNOWLEDGMENTS

The author sincerely thanks Thailand Institute of Nuclear Technology (Public Organization) and the Reactor Center staffs for their support in data collection and security evaluations. Appreciation is extended to international organizations such as the IAEA and the U.S. Department of Energy for their guidance in nuclear security compliance. Special gratitude is given to colleagues and experts whose contributions have strengthened the physical protection system of the TRR-1/M1 reactor facility.

REFERENCES

[1] *The Physical Protection of Nuclear Materials and Nuclear Facilities: IAEA INFCIRC/225/ rev.4*, IAEA, Vienna, Austria (1999).
[2] O. D. Oyeyinka, L. A. Dim, M. C. Echeta, A. O. Kuye, "Determination of System Effectiveness for Physical Protection Systems of a Nuclear Energy Centre," *Science and Technology*, **4(2)** (2014).
[3] "Multipath Very-Simplified Estimate of Adversary Sequence Interruption (MPVEASI)," Sandia National Laboratories.
[4] "Physical Protection of Nuclear Facilities and Materials," *18th International Training Course*, Sandia National Laboratories, Albuquerque, New-Mexico, USA (2004).
[5] *Handbook on the Physical Protection of Nuclear Material and Facilities*: *IAEA-TECDOC-127*, IAEA, Vienna, Austria (2000).
[6] J. Dai, H. Ruimin, J. Chen, and Q. Cai, "Benefit-Cost Analysis of Security Systems for Multiple Protected Assets Based on Information Entropy," *Entropy*, **14(3)** (2012).
[7] D. Andiwijayakusuma, A. Mardhi, T. Asmoro, T. Setiadipura, A. Purqon, Z. Su'ud, "Physical protection system effectiveness calculation in nuclear reactor facility using EASI code: case study sabotage scenario, *J. Phys.: Conf. Ser.* 2072 012010 (2021).

ASRAM2025
www.asram2025.org
Asian Symposium on Risk Assessment and Management 2025
Pattaya, Thailand, 27 – 29 August 2025

PUBLIC PERCEPTION OF SMR TECHNOLOGY IN THAILAND: YOUTUBE-BASED SENTIMENT ANALYSIS

Kunthida Waree[1], Wasin Vechgama[2*], Weerawat Pornroongruengchok[3], Watcha Sasawattakul[4], Kampanart Silva[5]

[1]*Thailand Institute of Nuclear Technology (Public Organization), 16, Vibhavadi Rangsit Road, Chatuchak, Bangkok, Thailand, 10900, kunthida@tint.or.th*
[2]*Thailand Institute of Nuclear Technology (Public Organization), 16, Vibhavadi Rangsit Road, Chatuchak, Bangkok, Thailand, 10900, wasin@tint.or.th*
[3]*Thailand Institute of Nuclear Technology (Public Organization), 16, Vibhavadi Rangsit Road, Chatuchak, Bangkok, Thailand, 10900, weerawat@tint.or.th*
[4]*Department of Computer Engineering, Faculty of Engineering, Chulalongkorn University, 17th floor, Engineering 4 Building (Charoenvidsavakham), Phayathai Road, Wang Mai, Pathumwan, Bangkok, Thailand, watcha.sasawattakul@gmail.com*
[5]*National Energy Technology Center, National Science and Technology Development Agency, 114, Thailand Science Park Phaholyothin Road, Klong Nueng, Klong Luang, Pathum Thani, Thailand, kampanart.sil@entec.or.th*

EXTENDED ABSTRACT

Thailand is moving forward with its clean energy transition to strengthen sustainability and enhance national competitiveness. As part of this effort, the country aims to become a regional leader in carbon reduction and develop itself as a carbon credit trading hub within ASEAN. Small Modular Reactors (SMRs) are expected to supplement energy storage and renewable energy sources in the energy mix of the country. SMRs offer the potential to provide sustainable, reliable, and low-carbon electricity and heat, supporting the country's long-term decarbonization goals. By 2024, public hearings for two SMR projects, each with a capacity of 300 MW, had already taken place, reinforcing the significance of public engagement and perception in advancing nuclear energy programs in Thailand.

To explore public attitudes toward nuclear energy and SMRs, the Thailand Institute of Nuclear Technology (TINT) and its partners conducted a comprehensive study analyzing social media comments related to nuclear energy on Facebook and YouTube. The study involved three primary methodological stages: comment collection, sentiment analysis, and public perception interpretation. In the comment collection process, relevant public comments were gathered using both the Export Comments website and the Application Programming Interface (API) functions available on Facebook and YouTube. The team searched for Thai keywords such as "nuclear energy," "nuclear power," "nuclear power plant," and "small modular reactor" across posts, news content, and public discussions available on these platforms. To maintain relevance, comments from content related to nuclear weapons or war were excluded. The data set comprised 10,975 Facebook comments from 520 posts dated 2009–2022 and 15,425 YouTube comments from 85 videos published between 2008–2023. It was observed that the discussions about nuclear energy have increased significantly in recent years, indicating a gain in public knowledge. For the sentiment analysis stage, the study employed Bidirectional Encoder Representations from Transformers (BERT), a deep transfer learning-based Natural Language Processing (NLP) model. The pre-trained BERT model was fine-tuned using a manually labeled dataset of Thai-language comments to optimize its performance in classifying sentiment specific to nuclear energy discussions. The classification process assigned sentiment values ranging from -1 (negative) to 1 (positive), with 0 representing neutral sentiment. Sentiment strength was categorized into strong, moderate, and weak levels based on confidence scores derived from previous BERT research applications. The fine-tuned model was applied to both Facebook and YouTube comment datasets to generate a comprehensive sentiment profile for each platform. In the public perception analysis, the most occurring keywords and phrases within Facebook and YouTube comments were identified using the WordItOut platform for word cloud generation and frequency analysis. This helped trace public narratives, common concerns, expectations, and misunderstandings about SMRs. The comments that mentioned SMRs were separated out for more in-depth topic classification. These comments addressed topics such nuclear safety, security concerns, technological readiness, regulatory readiness, accessibility, and misconceptions regarding nuclear technology. Both the positive and negative opinions expressed by the Thai population were shown by the qualitative interpretation.

Results showed that 81.22% of Facebook comments were neutral, 6.49% positive, and 12.28% negative. On YouTube, 89.86% of comments were neutral, 4.77% positive, and 5.36% negative. Supportive comments often acknowledged the

potential of nuclear energy as a clean, safe, and advanced energy source and expressed approval for constructing SMRs and other nuclear facilities. In contrast, negative comments reflected concerns over nuclear safety, radioactive risks, government readiness, and skepticism regarding the necessity of nuclear power in Thailand. The keyword "SMR" appeared in both positive and negative comments, signaling a mixed perception within the public discourse. Further analysis of SMR-related comments revealed recurring themes such as the importance of technological development, opportunities for accessible clean energy, nuclear safety, security, safeguards, and public misconceptions about nuclear technology. The differences between Facebook and YouTube sentiments were attributed to the distinct ways information is communicated and shared on each platform. The findings from this study provide valuable insights for shaping future public communication strategies and supporting public acceptance initiatives for SMRs and nuclear power programs in Thailand. This data will contribute to informing the country's Power Development Plan (PDP 2024–2040) and enhancing national energy policy development as Thailand prepares for its clean energy transition and carbon-neutral goals.

ACKNOWLEDGMENTS

The authors sincerely appreciate the support provided by the Thailand Institute of Nuclear Technology (TINT), the National Energy Technology Center (ENTEC), and the Department of Computer Engineering at Chulalongkorn University (CU), whose crucial information facilitated this research. We are also thankful to the Ministry of Higher Education, Science, Research, and Innovation (MHESI) of Thailand, as well as the Korea Atomic Energy Research Institute (KAERI) and the Korea National University of Science and Technology (UST), for their generous assistance and cooperation throughout the publication process.

REFERENCES

[1] S. S. S. Ahmad, A. N. B. S. Osman and H. Basiron, "The impact of social media on human interaction in an organisation based on real-time social media data," International Journal of Data Science, 4(3), 260-271 (2019).

[2] Y. Chen and Z. Zhang, "Exploring public perceptions on alternative meat in China from social media data using transfer learning method," Food Quality and Preference 98, 104530 (2022).

[3] D. Contu, E. E. Elshareif and I. Gurrib, "Assessing views towards energy sources with social media data: The case of nuclear energy in the UAE," Processes 9(11), 1945 (2021).

[4] J. Devlin, M. W. Chang, K. Lee and K. Toutanova, "BERT: Pre-training of deep bidirectional transformers for language understanding," Computation and Language, arXiv:1810.04805 (2019).

[5] Ho, et al., "Exploring public perceptions of benefits and risks, trust, and acceptance of nuclear energy in Thailand and Vietnam: A qualitative approach," Energy Policy, 127, 259-268 (2019).

[6] M. Singh, A. K. Jakhar and S. Pandey, "Sentiment analysis on the impact of coronavirus in social life using the BERT model," Social Network Analysis and Mining, 11(33) (2021).

[7] W. Vechgama, W. Sasawattakul, K. Silva and J. Cho, "Development of classification model for public perception of nuclear energy in social media platform using machine learning: Facebook platform in Thailand," Proc. the Probabilistic Safety Assessment and Management 16 (PSAM16), Honolulu, Hawaii, USA, June 26 - July 1, 2022.

[8] W. Vechgama, W. Sasawattakul, K. Silva and J. Cho, "Investigation of data pre-processing step of classification model development for understanding nuclear energy public perception in Thailand," Proc. the Asian Symposium on Risk Assessment and Management 2022 (ASRAM2022), Daejeon, Republic of Korea, November 30 – December 2, 2022.

[9] W. Vechgama, W. Sasawattakul and K. Silva, "2009–2022 Thailand public perception analysis of nuclear energy on social media using deep transfer learning technique," Nuclear Engineering and Technology, 556, 2026-2033 (2023).

Severe Accident and Thermal-Hydraulic Analysis of Human Error in Fuel Loading for TRR-1/M1

Nart Noodee, Saensuk Wetchagarun, Kanokrat Tiyapun

Reactor Center, Thailand Institute of Nuclear Technology (Public Organization): 9/9 Village No. 7, Saimoon, Ongkharak, Nakhon Nayok, 26120, Thailand, nart.noo@tint.or.th

EXTENDED ABSTRACT

INTRODUCTION

The TRR-1/M1 research reactor is designed with a high level of protection against human errors, especially during fuel loading operations. These operations are carried out by certified operators under direct supervision, with clearly defined procedures and verification steps in place. Despite these safeguards, human error remains a credible initiating event; therefore, the safety analysis includes a conservative evaluation of the worst-case fuel loading error. This research addresses the consequences of such an error and assesses the impact on reactor safety margins.

FUEL LOADING ERROR SCENARIO

In this work, we examine a scenario based on the assumption that it occurs independently, without any coincidental initiating events. The postulated scenario involves the incorrect placement of fuel elements during core loading, specifically the substitution of a fresh 20/20 fuel element into a B-ring position (B3) and a fresh 8.5/20 fuel element into a D-ring position (D8). This misloading would result in a significant power peaking in the B-ring location, as the 20/20 element has a higher enrichment and would produce substantially more power when placed in a high-flux area near the core center. Although such an error is unlikely due to procedural controls and independent verification by multiple operators, this single-element misplacement represents the most severe credible scenario for analysis and is thus used to bound all other potential misloading.

NEUTRONIC ANALYSIS

Neutronic simulations were conducted using the MCNPX code to evaluate the effects of the misloading on core power distribution. The simulations showed that the rod power factor increased from 1.894 in the reference core to 2.396 in the error scenario. This corresponds to a maximum power generation of approximately 29.6 kilowatts in the affected fuel element at the reactor's nominal operating power of 1.3 megawatts. This elevated power density forms the basis for the thermal-hydraulic assessment.

THERMAL-HYDRAULIC ANALYSIS

The thermal performance of the reactor core under the misloading condition was analyzed using the COOLOD-N2 code. The analysis revealed that the fuel temperature in the hottest location increased due to the elevated power density. In the reference core, the peak fuel temperature is approximately 450°C at nominal power. In the misloaded core, this temperature increases to around 550°C at 1.3 megawatts and reaches approximately 620°C at 1.5 megawatts, which corresponds to 115% of nominal power. Despite this increase, the maximum fuel temperature remains well below the conservative safety limit of 930°C. The analysis also showed a decrease in the minimum DNBR, as expected due to the higher heat flux. However, the minimum DNBR under the worst-case scenario remains at 1.65 when operating at 1.5 megawatts, which is comfortably above the typical safety threshold of 1.3 used in pressurized water reactors. This indicates that the conditions necessary for film boiling and potential cladding burnout are not reached.

SAFETY IMPLICATIONS

The results of the analysis confirm that even under the most severe credible single-element misloading scenario, the TRR-1/M1 reactor maintains safe operating margins. The increased power peaking and higher local fuel temperatures do not result in safety limit violations. The DNBR remains within acceptable limits, providing further assurance that fuel integrity is preserved. These findings demonstrate the robustness of the reactor's safety design and operational protocols in mitigating the consequences of potential human errors during fuel loading.

CONCLUSION

This study has evaluated the safety impact of a postulated fuel loading error in the TRR-1/M1 reactor, involving the misplacement of one fresh 20/20 and one 8.5/20 fuel element. Through detailed neutronic and thermal-hydraulic analysis, it has been demonstrated that the reactor core remains within all safety margins, including fuel temperature and DNBR limits. Although such an error is improbable due to rigorous operational procedures and supervision, this analysis confirms that the reactor's safety systems are sufficiently robust to handle such an event without compromising fuel integrity or reactor safety. Further research could explore more detailed effects of misloading, including scenarios involving multiple misloaded elements. Conducting a hazard analysis would also be beneficial in enhancing the overall safety evaluation of the TRR-1/M1 reactor.

REFERENCES

[1] D. B. PELOWITZ et al., MCNPX User's Manual, Version 2.7.0, Los Alamos National Laboratory Report LA-CP-11-00438 (2011).
[2] M. KAMINAGA, COOLOD-N2: A Computer Code for the Analyses of Steady-State Thermal-Hydraulics in Research Reactors, Japan Atomic Energy Research Institute, Tokyo, Japan (1994).
[3] THAILAND INSTITUTE OF NUCLEAR TECHNOLOGY, Safety Analysis Report for Thai Research Reactor-1/ Modification 1 (TRR-1/M1), Rev. 05, Chap. 5, Sec. 5.5.6, Thailand Institute of Nuclear Technology, Bangkok, Thailand (2017).
[4] THAILAND INSTITUTE OF NUCLEAR TECHNOLOGY, Safety Analysis Report for Thai Research Reactor-1/ Modification 1 (TRR-1/M1), Rev. 05, Chap. 13, Thailand Institute of Nuclear Technology, Bangkok, Thailand (2017).

Poster Session 4 (8:30 - 10:00)	The Port 7, C Floor	Safety and Risk Analysis of Nuclear Facilities and Radiation Application (Research Reactor, Tokamak Plasma Fusion, Nuclear Fuel Cycle, Cyclotron, Agricultural and Medical Industries)
		Chair/Facilitator 1: Mr. Truong Hoang Tuan, Researcher, Nuclear Training Center, Vietnam Atomic Energy Institute (VINATOM)
		Chair/Facilitator 2 Mr. Pidpong Janta (National Energy Technology Center (ENTEC))
8:30 - 8:45		ID 56: Study on The Transfer of Natural Radioactives from Soil to Water Spinach Is Hanoi and its Impact on People Speaker: Thi-Thuy-Linh Ha (Faculty of Physics, VNU University of Science) Contributors: Thi-Hong Bui (Faculty of Physics, VNU University of Science), Van-Loat Bui (Faculty of Physics, VNU University of Science), Van-Hao Duong (VNU School of Interdisciplinary Sciences and Arts, Vietnam National University), Duc-Thang Duong (Institute for Nuclear Science and Technology, Vietnam Atomic Energy Institute (VINATOM)), Ngoc-Thiem Le (Institute for Nuclear Science and Technology, Vietnam Atomic Energy Institute (VINATOM)), Dinh-Khoa Tran (Dalat Nuclear Research Institute, Vietnam Atomic Energy Institute (VINATOM)), Van-Khanh Tran (Faculty of Physics, VNU University of Science), Van-Loat Bui (Faculty of Physics, VNU University of Science), Thi-Thuy-Linh Ha (Faculty of Physics, VNU University of Science), Giang T.T. Phan (Faculty of Fundamental and Applied Sciences, Duy Tan University), Viet-Hoang Tran (Phenikaa Institute for Advanced Study, Phenikaa University), Van-Khanh Hoang (Phenikaa Institute for Advanced Study, Phenikaa University), Hoai-Nam Tran (Phenikaa Institute for Advanced Study, Phenikaa University)
8:45 - 9:00		ID 97: Initial Results of TT-1 Plasma Emission Measurements using an AXUV Bolometer Speaker: Grittma KONGPRAWES (Thailand Institute of Nuclear Technology (Public organization)) Contributors: Nopporn Poolyarat (TINT), Rawat Jaisutti (Thammasat University), Pasit Wonghabut (TINT), Arlee Tamman (TINT), Suebsak Suksaengpanomrung (TINT), Kewalee Nilgamhang (TINT), Somsak Dangtip (TINT), Sayan Pudwat (TINT), Pakorn Preechabura (TINT), Thawatchai Onjun (TINT)
9:00 - 9:15		ID 115: Thermal-hydraulic Analysis of Chimney Effect Using OpenModelica Speaker: Minseok Choi (Indepedent researcher) Contributors: Minseok Choi (Indepedent researcher)
9:15 - 9:30		ID 101: Characterization of the Bremsstrahlung X-ray Field around the Thailand Tokamak-1 (TT-1) using Passive Dosimetry Speaker: Kitisak Komnoi (Thailand Institute of Nuclear Technology (Public Organization)) Contributors: Nopporn Poolyarat (TINT), Pasit Wonghabut (TINT), Suebsak Suksaengpanomrung (TINT), Arlee Tamman (TINT), Jiraporn Promping (TINT), Kitisak Komnoi (TINT), Siriyaporn Sangaroon (Mahasarakham University), Apiwat Wisitsorasak (KMUTT), Kitti Rongpuit (KMUTT)

9:30 - 9:45	ID 13: Direction of Nuclear Consequence Analysis of SMR in Thailand Speaker: Narakhan Kunsrimek (Department of Nuclear Engineering, Faculty of Engineering, Chulalongkorn University) Contributors: Narakhan Kunsrimek (Department of Nuclear Engineering, Faculty of Engineering, Chulalongkorn University), Somboon Rassame (Department of Nuclear Engineering, Faculty of Engineering, Chulalongkorn University), Wasin Vechgama (Thailand Institute of Nuclear Technology (Public Organization))
9:45 - 10:00	ID 98: Initial Hard X-ray Spectroscopy Results from the Thailand Plasma Focus 2 (TPF-2) using a $LaBr_3$(Ce) Detector Speaker: Pasit Wonghabut (Thailand Institute of Nuclear Technology (Public organization)) Contributors: Nopporn Poolyara (Thailand Institute of Nuclear Technology (Public organization)), Kitti Rongpuit (King Mongkut's University of Technology Thonburi), Siriyaporn Sangaroon (Mahasarakham University), Suebsak Suksaengpanomrung (Thailand Institute of Nuclear Technology (Public organization)), Arlee Tamman (Thailand Institute of Nuclear Technology (Public organization)), Apiwat Wisitsorasak (King Mongkut's University of Technology Thonburi), Pasit Wonghabut (Thailand Institute of Nuclear Technology (Public organization)), Kitisak Komnoi (Thailand Institute of Nuclear Technology (Public organization))

ASRAM2025
www.asram2025.org
Asian Symposium on Risk Assessment and Management 2025
Pattaya, Thailand, 27 – 29 August 2025

STUDY ON THE TRANSFER OF NATURAL RADIOACTIVES FROM SOIL TO WATER SPINACH IN HANOI AND ITS IMPACT ON PEOPLE

Thi-Thuy-Linh Ha[1], Thi-Hong Bui[1], Van-Loat Bui[1], Duc-Thang Duong[2], Ngoc-Thiem Le[2], Van-Khanh Tran[1], Viet-Hoang Tran[1,3], Hoai-Nam Tran[3] ,Van-Hao Duong[4,*], Dinh-Khoa Tran[5], Giang T.T. Phan[6,7]

[1] *Faculty of Physics, VNU University of Science, 334 Nguyen Trai, Hanoi, 100000, Viet Nam*

[2] *Institute for Nuclear Science and Technology, Vietnam Atomic Energy Institute, 179 Hoang Quoc Viet, Hanoi, Viet Nam*

[3] *Phenikaa Institute for Advanced Study, Phenikaa University, Hanoi 12116, Viet Nam*

[4] *VNU School of Interdisciplinary Sciences and Arts, 144 Xuan Thuy, Cau Giay, Hanoi, 100000, Viet Nam*

[5] *Dalat Nuclear Research Institute, Vietnam Atomic Energy Institute (VINATOM), 1 Nguyen Tu Luc, Dalat, Lamdong, Viet Nam*

[6] *Faculty of Fundamental and Applied Sciences, Duy Tan University, Da Nang 550000, Viet Nam*

[7] *Phenikaa Institute for Advanced Study, Phenikaa University, Hanoi 12116, Viet Nam*

1. Introduction

Plants play a crucial role in human nutrition, serving as a primary source of essential nutrients, including vitamins, proteins, carbohydrates, minerals, and dietary fiber. Although the natural radionuclide transfer pathway from soil to plants and subsequently to humans is relatively minor and indirect, the accumulation of these radioactive isotopes in human organs can result in significantly high internal radiation doses [2]. Water spinach, *Ipomoea aquatica Forssk*, is the most common vegetable for human consumption and livestock's food, widely grown in tropical countries such as Vietnam, China, India and other Southeast Asian countries [6]. Water spinach is highly nutritious vegetable containing various vitamins of A, B1, B2, B12, C, E and K [3]. Moreover, it is a semi-aquatic tropical plant (can be easily cultivated in various flooded or unflooded environmental conditions) and can be harvested multiple times within a short period. The accumulation of natural and artificial radionuclides such as ^{228}Th, ^{226}Th, and ^{40}K in plants can occur through root uptake from soil. For humans, in addition to external radiation exposure from environmental sources, internal exposure from ingested food and organ irradiation must also be considered [7]. The radionuclides appearing in water could also be transferred to vegetables. Thus, in the preset work, the transfer characteristics of natural radionuclides, i.e., ^{232}Th, ^{226}Ra and ^{40}K from soil to water spinach in Hanoi, Vietnam were investigated. Further investigation of the activity concentrations of natural radionuclides, radiological hazard indices and their uptake from soil to plant, particularly to water spinach is necessary.

2. Material and methods

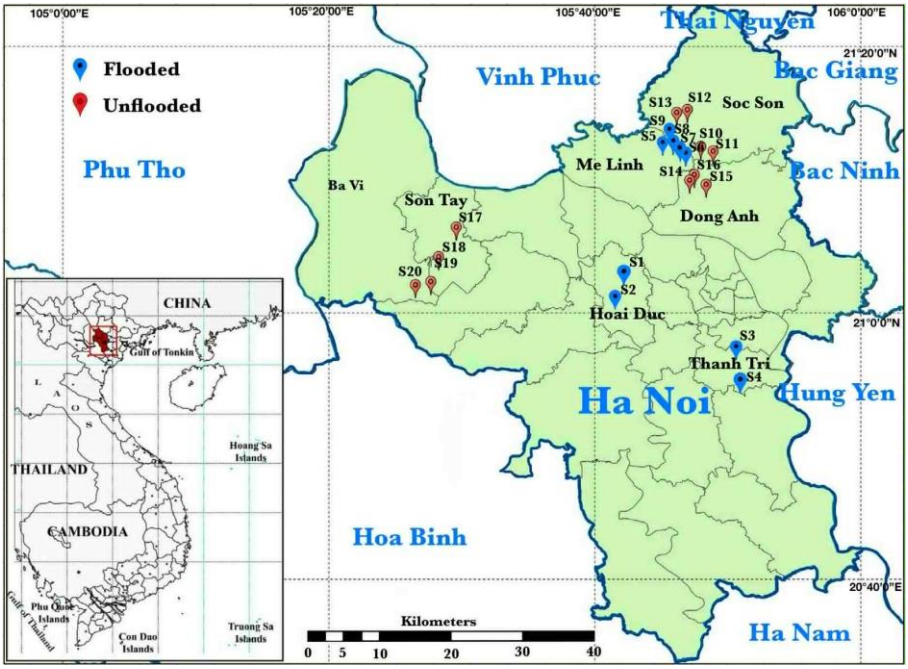

FIGURE 1. SITE MAP AND THE SAMPLING LOCATIONS OF THE SOIL AND WATER SPINACH IN HANOI, VIETNAM

The soil and plant samples were collected at twenty typical farms for water spinach planting in Hanoi. Hanoi, the capital and second-most populous city in the north of Vietnam, features a distinct four-season monsoon subtropical climate. Fig.1 displays the site map, the detailed locations and the environmental conditions of the sampling sites. The environmental conditions were classified into two categorizes: flooded soil (flooded) and normal soil (unflooded). At each sampling site, the stems and leaves of water spinach amounting to 5 kg was collected. The water spinach was washed to eliminate the surface contamination. At the laboratory, the water spinach were dried in an oven at the temperature of 90°C to achieve a constant weight, and then ground into powder. The powdered water spinach samples were homogenized, with 300 g aliquot preserved in 780 cm³ Marinelli beakers. Corresponding to the water spinach samples, twenty soil samples at the depth of 0-10 cm were also collected at the same sites.

The gamma spectra of the water spinach and soil samples were measured using a low-background gamma spectrometer with GC5019 detector at Institute of Nuclear Science and technology (Hanoi). The measurement protocols and determination of radioactive activity concentrations in the study samples were performed in strict accordance with the methodology outlined in Reference [3]. In addition to the transfer factor (TF), in order to assess the radiological hazards associated with natural occurring radioactivity materials, radium equivalent activity (Ra_{eq}), absorbed gamma dose rate (D), annual effective dose equivalent (AEDE) have been evaluated from the activity concentrations of ^{226}Ra, ^{232}Th and ^{40}K [2].

3. Results and discussion

TABLE I. Statistic parameters of the soil-to-Water spinach TFs of ^{228}Ra, ^{226}Ra and ^{40}K

Condition	Parameter	Transfer factor (TF)		
		^{228}Ra (^{232}Th)	^{226}Ra	^{40}K
Flooded	Min	0.01	0.02	0.34
	Max	0.17	0.13	2.49
	Mean	0.07	0.05	1.38
	GM	0.05	0.04	1.17
	GSD	2.41	1.88	1.89
	Skewness	0.96	1.75	0.32
	Kurtosis	-0.44	3.15	-1.34
Unflooded	Min	0.01	0.01	0.32
	Max	0.06	0.04	1.61
	Mean	0.03	0.03	1.00
	GM	0.03	0.03	0.89
	GSD	2.12	1.82	1.73
	Skewness	-0.09	-0.65	-0.23
	Kurtosis	-1.87	-0.89	-1.20

Table I summarizes the soil-to-water spinach transfer factors (TFs) of natural radionuclides obtained from water spinach samples in flooded and unflooded areas. For flooded areas, the TFs of ^{228}Ra ranged from 0.01 to 0.17, with the GM(GSD) of 0.05(2.41). In contrast, for unflooded areas, the TFs fell within 0.01–0.06, with a GM(GSD) of 0.03(2.12). This demonstrates that the ^{228}Ra TFs were significantly higher in flooded samples. The TFs of ^{226}Ra are within the ranges of 0.02–0.13 and 0.01–0.04 for flooded and unflooded sites, respectively. The GM(GSD) values are 0.04(1.88) and 0.03(1.82), respectively. The TFs of ^{226}Ra in the flooded sites are greater than that in the unflooded sites. For ^{40}K, the TFs ranged from 0.34–2.49 (flooded) and 0.32–1.61 (unflooded), with corresponding GM(GSD) values of 1.17(1.89) and 0.89(1.73). These values were substantially higher than those of ^{228}Ra and ^{226}Ra, exceeding 1.0 at half of the sampling sites. The consistent results indicate that flooded conditions significantly enhance the transfer of radionuclides.

TABLE II. Comparison of the soil-to-Water spinach TFs of the natural radionuclides among worldwide regions.

Country	^{228}Ra (^{232}Th)	^{226}Ra	^{40}K
Hanoi, Vietnam	0.05	0.04	1.19
Ho Chi Minh, Vietnam [4]	0.12	0.08	69.1
Bangka Belitung, Indonesia [5]	0.05	0.02	28.6
World average [1]	0.05	0.04	1.4

Table II presents the soil-to-plant transfer factors (TFs) of natural radionuclides in comparison with other regions. The TFs for Ra in Hanoi (0.05 and 0.04, respectively) align closely with the world averages (0.05 and 0.04). However, the TF for ^{40}K (1.19) is notably lower than that reported in Ho Chi Minh (69.1) and Indonesia (28.6), suggesting regional variations in

soil-plant uptake mechanisms. The TFs of the radionuclides are greater in the flooded sites. Statistical analysis suggests that the TFs are significantly different between the flooded and unflooded conditions.

TABLE III. Radiological hazard indices in the study samples

Paramater	Ra_{eq}(Bq/kg)	D (nGy/h)	AEDE (mSv/y)
Min	137.9±3.95	64.9±2.35	0.079±0.002
Max	399.5±7.81	188.1±4.97	0.23±0.006
Average	225.9±4.45	108.2±3.06	0.13±0.004
World average [1]	370	59	0.07

In Table III, The measured values of Ra_{eq} ranged from 137.9 (S2) Bq/kg to 399.5 (S12) Bq/kg, with an average of 225.9 Bq/kg, which is below the world average limit of 370 Bq/kg. The absorbed dose rate (D) varied between 64.9(S2) to 88.1 (S12) nGy/h, averaging 108.2 nGy/h, significantly higher than the global average of 59 nGy/h. The annual effective dose equivalent (AEDE) ranged from 0.079 (S2) to 0.23 (S12) mSv/y, with an average of 0.13 mSv/y, still well below the safety limit of 1 mSv/y. These results indicate that while some localized areas exhibit elevated radiation levels, the overall radiological risk remains within acceptable thresholds.

4. Conclusions

This study provides a comprehensive assessment of radiological hazards and soil-to-plant transfer factors (TFs) of natural radionuclides in the investigated region. The results indicate that while the average radium equivalent activity (D) and annual effective dose equivalent (AEDE) were above internationally established thresholds, excluding Ra_{eq}, localized areas exhibit elevated radiation levels, warranting further monitoring. The comparison of TFs with other regions reveals significant variability, particularly for ^{40}K emphasizing the influence of local environmental and geochemical conditions on radionuclide uptake.

ACKNOWLEDGMENTS

This work was funded by Vietnam National Foundation for Science and Technology Development (NAFOSTED).

REFERENCES

[1] IAEA, 1994. Handbook of Parameter Values for the Prediction of Radionuclide Transfer. To Wildlife. Technical Report, Technical Reports Series No. 364. Vienna.
[2] B. V. LOAT, et al. Natural radioactivity and radiological hazards in soil samples in Savannakhet province, Laos. Journal of Radioanalytical and Nuclear Chemistry (2019).
[3] B. V. LOAT, et al. Transfer of natural radionuclides from soil to water spinach (Ipomoea aquatica Forssk) under flooded and unflooded conditions in Hanoi, Vietnam. Journal of Environmental Radioactivity 277 (2024).
[4] B. N. THIEN, et al. Estimation of the soil to plant transfer factor and annual effective dose due to ingestion of food crops in Ho Chi Minh city, Vietnam. Chemosphere 259, (2020).
[5] E. NURTJAHYA, et al. Study of soil-to-plant transfer factors (TFs) of 226Ra, 232Th, and 40K on plants cultivated on ex-tin mining land in Bangka Belitung, Indonesia. Journal of Environmental Radioactivity 261 (2023).
[6] Daniel F.Austin, et al. Water Spinach (Ipomoea aquatica, Convolvulaceae) A food gone wild, U.S.A. Ethnobotany Research & Applications 5:123-146 (2007).
[7] UNSCEAR, 2000. Sources of ionizing radiation. Volume I: Sources.

ASRAM2025
www.asram2025.org
Asian Symposium on Risk Assessment and Management 2025
Pattaya, Thailand, 27 – 29 August 2025

Initial Result of TT-1 Plasma Emission Measurements using an AXUV Bolometer

Nopporn Poolyarat[1], Rawat Jaisutti[2], Pasit Wonghabut[1], Arlee Tamman[1], Suebsak Suksaengpanomrung[1], Kewalee Nilgamhang[1], Somsak Dangtip[1], Sayan Pudwat[1], Pakorn Preechabura[1], and Thawatchai Onjun[1]

[1] *Thailand Institute of Nuclear Technology (Public organization): 9/9 Moo 9 Saimool, Ongkharak, Nakorn Nayok, 26120, Thailand and nopporn p@tint.or.th*
[2] *Thammasat University: 99 Moo 18 Paholyothin Road, Klong Nueng, Klong Luang, Pathumthani 12120 Thailand.*

ABSTRACT

A 16-channel bolometer system based on an Absolute Extreme Ultraviolet (AXUV) photodiode array has been designed, constructed, and installed on the Thailand Tokamak-1 (TT-1). This diagnostic is intended to measure the total radiated power from the plasma, a critical parameter for energy balance and confinement studies. The system's functionality was first validated using a stable plasma from a plasma cleaner device, which confirmed the successful operation of the detector and its custom-built signal conditioning electronics. Following this preliminary testing, the system was installed on TT-1 for its first-light measurements. Initial results from tokamak discharges demonstrate a clear temporal correlation between the bolometer signal and the evolution of the plasma current. This successful operation establishes the AXUV bolometer as a new and crucial diagnostic for radiated power studies on TT-1, paving the way for future investigations into impurity transport and plasma stability.

Keywords: TT-1 Tokamak, Plasma Diagnostics, Bolometer, Radiated Power, AXUV

I. INTRODUCTION

The pursuit of nuclear fusion as a clean, safe, and virtually limitless energy source for the future is a major global scientific endeavor. Fusion energy mimics the process that powers the sun and stars, where light atomic nuclei combine to form heavier ones, releasing immense amounts of energy. The tokamak, a toroidal device that uses powerful magnetic fields to confine a high-temperature ionized gas known as plasma, stands as the most promising configuration for achieving controlled thermonuclear fusion on Earth.

As part of its national strategy to develop domestic capabilities in fusion science and technology, Thailand has embarked on the Thailand Tokamak Project. A key component of this initiative is the TT-1 tokamak, formerly the HT-6M, which was granted by the People's Republic of China and is now operational at the Thailand Institute of Nuclear Technology (TINT). This project represents a significant step towards building national self-sufficiency in a critical high-technology field, fostering a skilled workforce, and reducing reliance on foreign technology.

A fundamental aspect of tokamak research is understanding the plasma power balance. Energy injected into the plasma is lost through several channels, including conduction, convection, and radiation. The total power lost via radiation is a critical parameter for determining the energy confinement time, a primary figure of merit for any fusion device. This radiation originates from several physical processes within the plasma, predominantly Bremsstrahlung (braking radiation) from electron-ion collisions and line radiation from impurity ions that have entered the plasma from the vessel walls. Measuring this radiated power provides invaluable information about plasma temperature, density, impurity content, and magnetohydrodynamic (MHD) stability.

It is important to distinguish this type of measurement from radiological safety monitoring. While other research at the TT-1 facility focuses on characterizing hard X-rays produced by runaway electrons interacting with the vessel walls for personnel safety 3, the work presented here concerns a plasma physics diagnostic. The bolometer is designed to measure the total power radiated from the entire plasma volume as electromagnetic radiation (from soft X-rays to visible light) to understand the plasma's internal energy balance, not the ionizing radiation that may escape the machine's shielding.

This paper reports on the design, fabrication, and initial experimental results of a new Absolute Extreme Ultraviolet (AXUV) bolometer system. This diagnostic was developed entirely through a domestic collaboration between TINT and

university partners under the Center for Plasma and Nuclear Fusion (CPaF) network, underscoring Thailand's commitment to building indigenous technological capacity.

II. THE AXUV BOLOMETER SYSTEM

The development of the bolometer system involved the design and integration of the detector, custom signal conditioning electronics, and data acquisition hardware. The design was tailored to the specific physical constraints and experimental requirements of the TT-1 tokamak.

II.A. System Overview and Detector Choice

The measurement system is designed to convert the faint radiation from the plasma into a measurable voltage signal. A high-level block diagram illustrating the signal flow from the detector to the Data Acquisition (DAQ) system is shown in Fig. 1. The core of the system is the radiation sensor, for which a 16-channel silicon photodiode array, model AXUV16ELG, was selected.

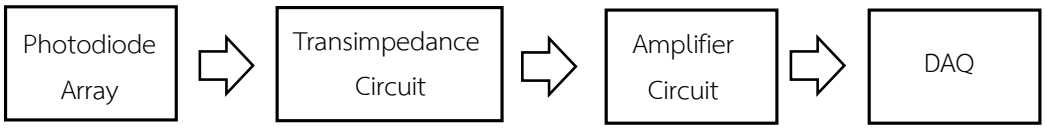

FIGURE 1. Block diagram of the bolometer electronics system.

The choice of an AXUV photodiode is critical for this application. The "A" in AXUV stands for "Absolute," signifying that the detector possesses a near-constant responsivity (in Amperes per Watt) over a vast spectral range, from soft X-rays through the extreme ultraviolet (EUV), vacuum ultraviolet (VUV), and into the visible spectrum. This characteristic is essential for bolometry, as the goal is to measure the total incident power without needing complex, energy-dependent calibrations for different radiation sources (e.g., line radiation from different impurities or continuum Bremsstrahlung). This property greatly simplifies the conversion of the measured photocurrent into a total radiated power value in Watts. The spectral response of the chosen AXUV16ELG photodiode, as provided by the manufacturer, is shown in Fig. 2, indicating its high sensitivity across a broad range of wavelengths relevant to plasma emission.

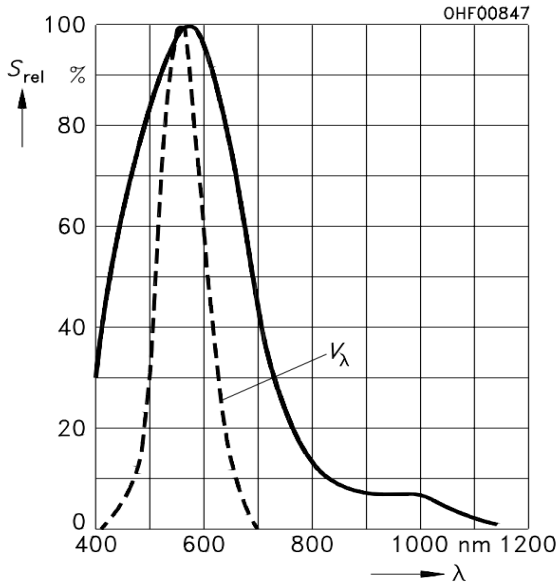

FIGURE 2. Spectral response of the AXUV16ELG photodiode.

II.B. Signal Conditioning Electronics and Hardware

To measure the small photocurrents generated by the detector (typically in the nanoampere to microampere range), a custom multi-stage amplifier circuit was designed and constructed. The design specifically addresses the challenges of acquiring low-level signals in the electromagnetically noisy environment of a tokamak.

The first stage is a transimpedance amplifier, which converts the photocurrent (I_p) from each photodiode channel into a proportional voltage (V_o). The circuit schematic is shown in Fig. 3. The output voltage is governed by the equation $V_o = -I_p \cdot R_f$, where R_f is the feedback resistor that determines the gain of this stage. This stage is located as close as possible to the detector head to immediately convert the noise-susceptible current signal into a more robust voltage signal before transmission over longer cables.

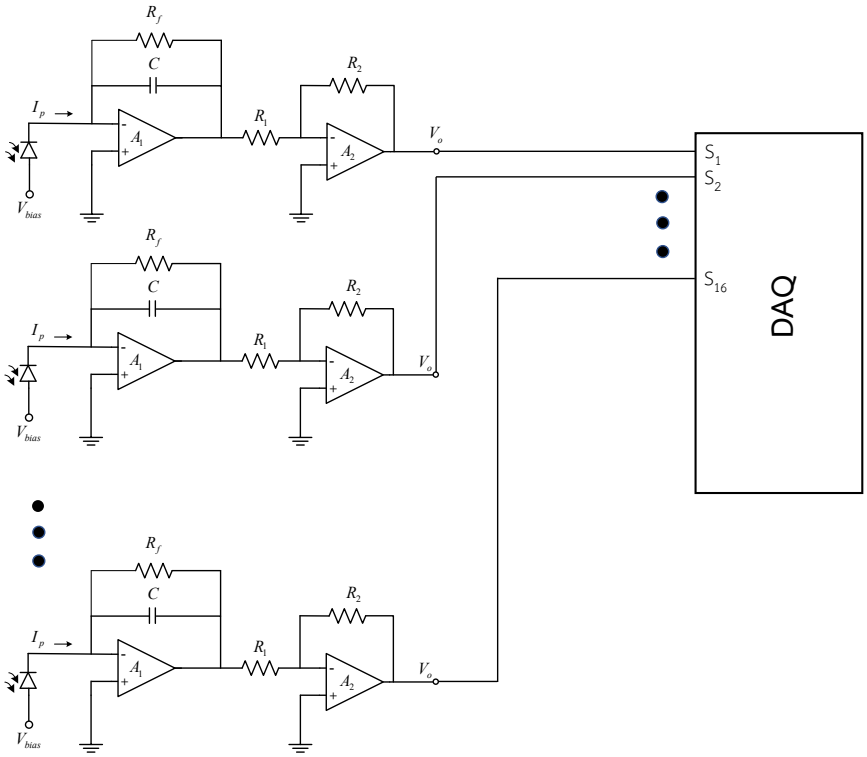

FIGURE 3. Schematic of the transimpedance amplifier circuit for the AXUV photodiode.

Following the transimpedance stage, a second inverting amplifier stage provides additional gain. This ensures that the final output signal is scaled appropriately to match the input voltage range of the main TT-1 DAQ system, optimizing the signal-to-noise ratio of the final measurement. A photograph of the assembled prototype, showing the detector head and the multi-channel amplifier board, is presented in Fig. 4.

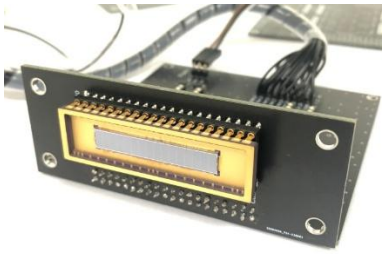

FIGURE 4. Assembled prototype of the AXUV bolometer system.

III. EXPERIMENTAL VALIDATION AND RESULTS

A methodical, two-step approach was used to validate the bolometer system. The first step involved testing on a simple, stable plasma source to de-risk the design, followed by installation and first-light measurements on the TT-1 tokamak.

III.A. Preliminary Validation on a Plasma Cleaner

Before installation on the tokamak, the bolometer system underwent preliminary testing using a plasma cleaner device (Atto, Diener). This device generates a stable, continuous RF glow discharge under an argon atmosphere at a power of 20 W, providing a reliable source of plasma radiation. This test served as a crucial de-risking strategy, allowing for the verification and debugging of the detector, electronics, and DAQ chain (sampling rate of 48000 kS/s) in a controlled environment, completely isolated from the complexities of pulsed tokamak operation such as large electromagnetic interference and complex plasma dynamics.

The results of this validation test are shown in Fig. 5. The plot displays the output signals from four of the bolometer channels during the operation of the plasma cleaner. The signals clearly respond to the presence of the plasma, confirming that the entire measurement chain—from photon detection to voltage output—was functioning as designed. This successful test provided the confidence to proceed with installation on TT-1.

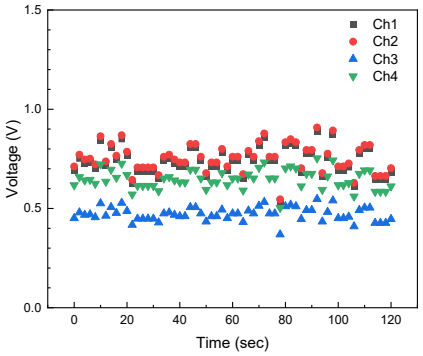

FIGURE 5. Output signals from four AXUV channels during validation on the plasma cleaner.3

III.B. Initial Measurements on the TT-1 Tokamak

Following the successful preliminary tests, the bolometer prototype was installed on a vacuum port of the TT-1 tokamak, as shown in the photograph in Fig. 6. The system was then integrated with the central TT-1 DAQ system to record data during plasma operations.

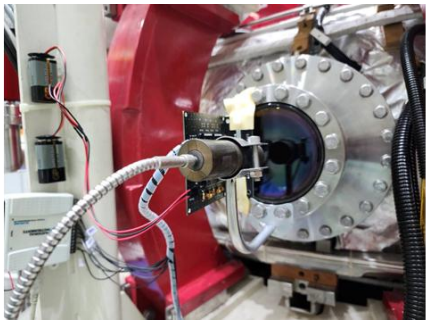

FIGURE 6. Installation of the bolometer prototype on a TT-1 vacuum port.3

The primary result of this work is presented in Fig. 7. This figure shows the time evolution of the signal from a single bolometer channel (right) juxtaposed with the plasma current (I_p) waveform (left) for a typical TT-1 discharge. The data provide unambiguous evidence of the system's successful operation. A clear temporal correlation exists between the two signals: the bolometer signal begins to rise shortly after the initiation of the plasma current. Furthermore, the overall envelope of the

bolometer signal closely tracks the shape of the plasma current pulse, increasing during the current ramp-up, remaining elevated during the current flattop, and decaying as the discharge terminates.

This observed behavior is consistent with fundamental plasma physics. In an ohmically heated tokamak discharge, the plasma density and temperature are strongly driven by the plasma current. Since the total radiated power is a function of density and temperature (e.g., Bremsstrahlung power scales with the square of the density), it is expected that the radiated power will track the evolution of the plasma current. The data in Fig. 7 confirm this expected behavior, validating that the system is not merely detecting light, but is functioning as a true plasma diagnostic measuring a quantity representative of the total radiated power.

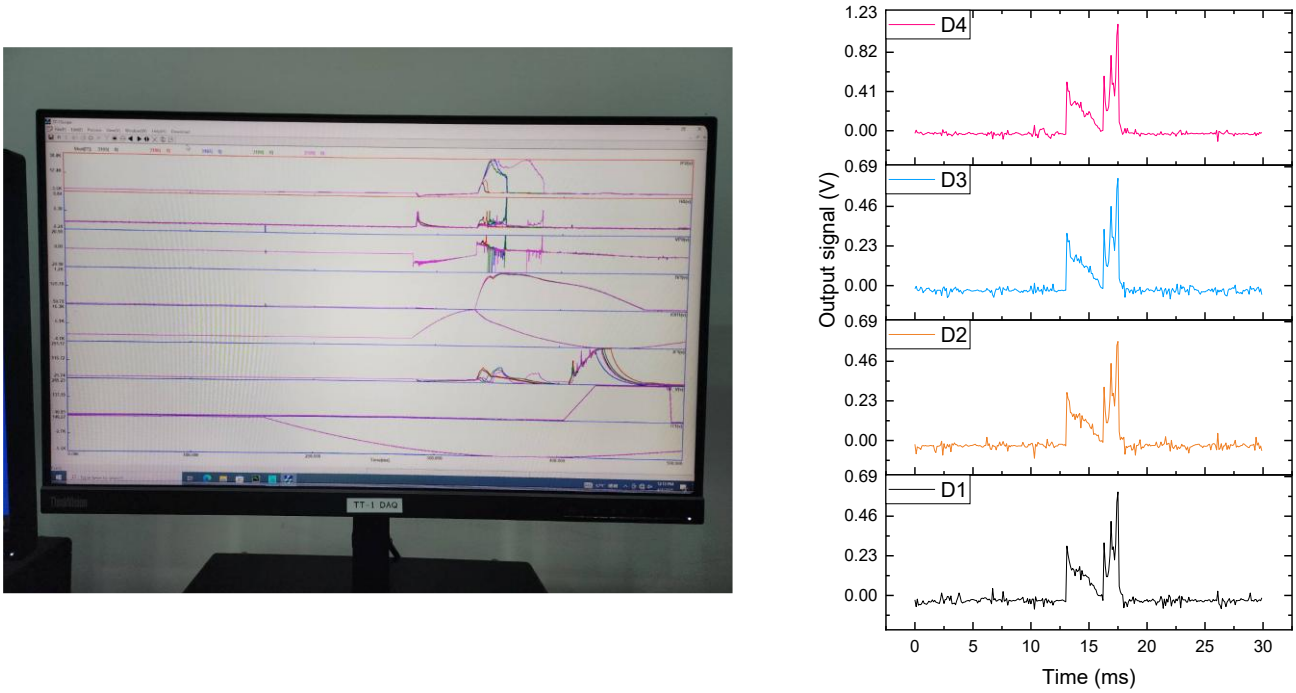

FIGURE 7. (Left) Plasma parameters from the TT-1 DAQ and (Right) the corresponding radiated emission signal measured by the prototype AXUV bolometer during a TT-1 discharge.

IV. CONCLUSION

A 16-channel AXUV photodiode bolometer system has been successfully designed, fabricated, and deployed on the TT-1 tokamak. This work was conducted as a domestic collaboration within Thailand's national fusion research program, representing a key step in developing indigenous diagnostic capabilities. Initial tests on a plasma cleaner validated the instrument's design, and subsequent first-light measurements on TT-1 have demonstrated its capability to measure radiation emitted from the plasma. The strong correlation between the bolometer signal and the plasma current confirms the system is operating as a valid plasma diagnostic for radiated power.

ACKNOWLEDGMENTS

This work was supported by the Fundamental Fund (FF) from the National Science, Research and Innovation Fund (NSRF) under the Office of the National Higher Education Science Research and Innovation Policy Council (No. 4369331). The authors gratefully acknowledge the collaborative framework of the Center for Plasma and Nuclear Fusion (CPaF), which facilitated the fruitful partnership between the Thailand Institute of Nuclear Technology (TINT), Thammasat University, and Mahasarakham University.

REFERENCES

[1] Y.M. DUAN, et al., "A 16-channel absolute extreme ultraviolet photodiode array for radiated power measurement on the HL-2A tokamak," Rev. Sci. Instrum., 83, 093501 (2012).
[2] YANMIN DUAN, et al., "Development of a Bolometer for EAST," *Plasma Sci. Technol.*, **13**, 546 (2011).

ASRAM2025
www.asram2025.org
Asian Symposium on Risk Assessment and Management 2025
Pattaya, Thailand, 27 – 29 August 2025

Thermal-hydraulic Analysis of Chimney Effect Using OpenModelica

Minseok Choi[1]

[1] *Gyeonggi-do, Korea, cminlife22@gmail.com*

EXTENDED ABSTRACT

In the nuclear power plants, the chimney effect is considered to remove decay heat in the long-term accident scenario. At the external containment vessel of a nuclear power plant, air absorbs heat from the high-temperature containment vessel walls, and natural convection is formed due to the chimney effect. When the pressure difference is low, the flow is driven by the chimney effect, and reverse flow occur at the outlet [1]. Therefore, when analyzing a system of chimney effect with a thermal-hydraulic analysis code, it was suggested to use a high minor loss coefficient considering reverse flow. Jing [2] had predicted flow rate in chimney effect experiments more accurately by considering reverse flow at the chimney outlet.

In this study, the chimney effect experiment was simulated by using OpenModelica [3]. OpenModelica is an open-source software to provide a modeling and simulation environment based on Modelica. Modelica is an acausal language to model multi-physics system. Chen's experiment [4] was referred for evaluation.

Jing used a pressure coefficient to include the reverse flow [2]. The pressure coefficient K_{out} can be obtained:

$$\epsilon = \frac{\Delta\rho}{\rho_{amb}} \approx \frac{\Delta T}{T_{amb}} = \frac{Q}{\dot{V}\rho C_p T_{amb}} \quad (1)$$

$$Fr = \frac{\dot{V}}{A\sqrt{2gD\epsilon}} \quad (2)$$

$$K_{out} = 1 + \left[0.61 * \left(0.1 + 0.19 * \frac{Fr}{Fr_{rev}} \right) \right]^{-2} \quad (3)$$

Δρ and ΔT refer to the differences in density and temperature at the inlet and outlet, respectively. Fr is Froude number, which is the ratio of the inertia force to uplift force, Q is the heat supplied by heater, $\dot{V}$ is the flow rate, ρ is the air density, C_p is isobaric specific heat, Tamb is the ambient temperature, A is the outlet area, and D is the length of the shortest side at the outlet.

Chen's chimney has a height of 1.5 m and a width of 0.615 m [4]. A heater is installed on one side of the chimney wall, as shown in Fig. 1. The gap between the chimney and the opposite wall is between 0.1 m and 0.6 m. The heat flux of the heater ranges from 200 to 600 W/m². The experiment was conducted in two cases: one where the heat flux was fixed at 400 W/m² and the gap was varied, and the other where the gap was fixed at 0.2 m and the heat flux was varied.

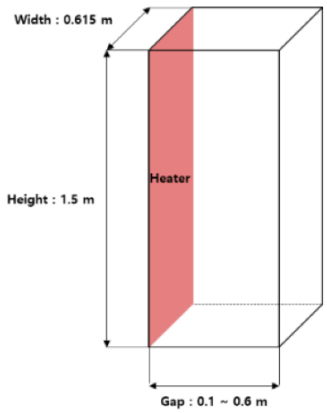

FIGURE 1. Illustration of the chimney

Fig. 2 shows the experiment configuration. Air flows from the atmosphere into the chimney. Before the chimney, a virtual pipe is introduced on the right side of the model to compensate the pressure difference caused by elevation. Pressure

coefficients were applied at the outlet and inlet of the chimney. The inlet K is 1.5. The outlet K is 1.0 under normal cases, but if reverse flow occurs, the outlet K can be increased.

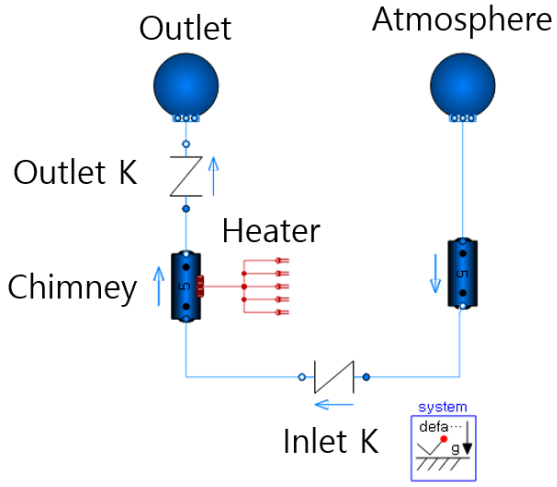

FIGURE 2. OpenModelica model configuration

Fig. 3 shows comparisons between the experimental and analytical results. Outlet K 1.0 means the results of OpenModelica when the outlet K is 1.0. In case of the modified K, the outlet K under consideration of reverse flow. It is shown that accuracy is higher when the reverse flow is considered.

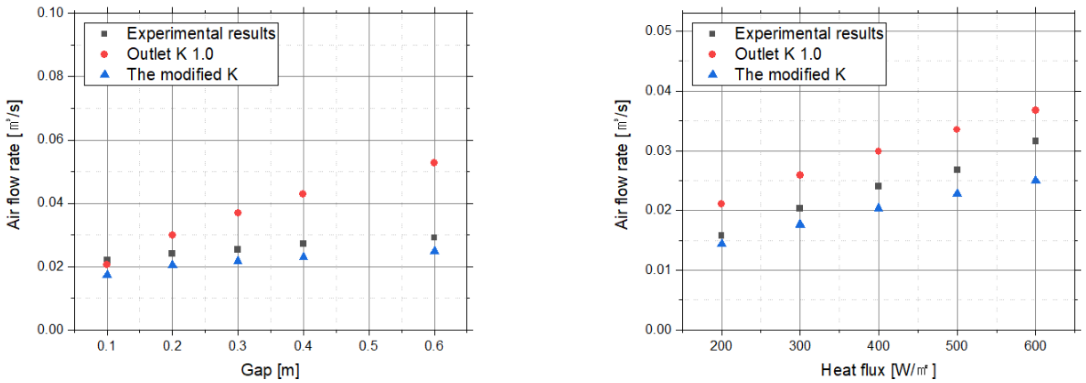

FIGURE 3. Comparison of air flow rate with varying gap size (left) and heat flux (right)

It has been confirmed that OpenModelica can predict the flow rate more accurately if the reverse flow is considered. However, to apply this study to long-term accident scenarios in nuclear power plants, it is necessary to generalize the conditions under which reverse flow occurs.

REFERENCES

[1] Cooper, L. Y., "Combined Buoyancy and Pressure-Driven Flow Through a Shallow, Horizontal, Circular Vent," Journal of Heat Transfer, Vol. 117, 659-667, 1995

[2] Jing, H., Chen, Z. D., and Li, A., "Experimental study of the prediction of the ventilation flow rate through solar chimney with large gap-to-height ratios," Building and environment, Vol. 89, 150-159, 2015.

[3] "OpenModelica," https://openmodelica.org/ (2025).

[4] Chen, Z. D., Bandopadhayay, P., Halldorsson, J., Byrjalsen, C., Heiselberg, P. and Li, Y., "An experimental investigation of a solar chimney model with uniform wall heat flux," Building and Environment, Vol. 38, No. 7, pp. 893-906, 2003

ASRAM2025
www.asram2025.org
Asian Symposium on Risk Assessment and Management 2025
Pattaya, Thailand, 27 – 29 August 2025

Characterization of the Bremsstrahlung X-ray Field around the Thailand Tokamak-1 (TT-1) using Passive Dosimetry

Nopporn Poolyarat[1], Pasit Wonghabut[1], Suebsak Suksaengpanomrung[1], Arlee Tamman[1], Jiraporn Promping[1], Kitisak Komnoi[1], Siriyaporn Sangaroon[2], Apiwat Wisitsorasak[3], Kitti Rongpuit[3]

[1] *Thailand Institute of Nuclear Technology (Public Organization): 9/9 Moo 3, Lat Khwang Subdistrict, Ongkharak District, Nakhon Nayok Province 26120, Thailand, nopporn p@tint.or.th*
[2] *Mahasarakham University: Khamriang, Kantharawichai District, Maha Sarakham Province 44150, Thailand*
[3] *King Mongkut's University of Technology Thonburi: 126 Pracha Uthit Road, Bang Mot, Thung Khru, Bangkok 10140, Thailand*

ABSTRACT

The advancement of magnetic confinement fusion research necessitates a rigorous approach to radiological safety, even in devices not operating with deuterium-tritium fuel. In such research tokamaks, the predominant radiological hazard stems from Bremsstrahlung X-rays, which are generated when relativistic runaway electrons (REs) are lost from the plasma and impact vessel components. This study presents the first comprehensive spatial characterization of the integrated X-ray dose field around the Thailand Tokamak-1 (TT-1) facility, conducted during its Fiscal Year 2025 (FY2025) operational campaign. The experimental methodology involved the strategic deployment of 15 passive Optically Stimulated Luminescence (OSL) dosimeters to map the radiation environment. Measurements of both ambient dose equivalent, H*(10), and directional dose equivalent, H'(0.07), were performed to provide a robust assessment of the field. The results reveal a highly anisotropic radiation field, with a maximum integrated dose of 1.49 mSv observed at a distinct "hot spot" location. In contrast, several other monitored locations remained at background levels, empirically validating the effectiveness of the facility's bulk shielding. A critical finding is the near-unity ratio of H'(0.07) to H*(10) in all areas with significant dose levels, providing strong evidence of a high-energy, penetrating photon spectrum consistent with Bremsstrahlung. These findings establish a crucial empirical radiological baseline for TT-1, which is invaluable for validating the performance of the current radiation shielding, refining operational safety protocols and access controls, and providing a benchmark for the design of future shielding enhancements.

Keywords: X-ray Field, Thailand Tokamak-1, Radiation, OSL dosimeters, Radiological Protection

I. INTRODUCTION

I.A. The Global Imperative for Fusion Energy

The global energy paradigm is undergoing a profound transformation, driven by the dual challenges of escalating energy demand and the urgent need to mitigate anthropogenic climate change. The reliance on fossil fuels, while historically pivotal for industrial development, has resulted in unsustainable levels of greenhouse gas emissions. In response, the international scientific community is pursuing a portfolio of clean, sustainable, and reliable energy sources. Among these, nuclear fusion stands out as a technology with the potential to provide safe, carbon-free, and baseload power on a global scale. Fusion energy harnesses the same process that powers the sun, fusing light atomic nuclei (such as isotopes of hydrogen) to release immense amounts of energy. Its primary advantages include a virtually inexhaustible fuel supply-deuterium extracted from seawater and tritium bred from abundant lithium-the absence of long-lived, high-level radioactive waste, and an inherent safety profile that precludes the possibility of a runaway chain reaction or meltdown.

I.B. The Tokamak: A Leading Concept for Magnetic Confinement

The primary challenge in achieving controlled terrestrial fusion is the creation and confinement of a plasma-a state of matter where gas is heated to temperatures exceeding 100 million Kelvin-for a sufficient duration to allow fusion reactions to occur. The most mature and extensively investigated approach to this challenge is the tokamak, a toroidal magnetic confinement device. The tokamak utilizes a powerful combination of magnetic fields to contain the superheated plasma within a donut-shaped vacuum vessel. A strong toroidal magnetic field, generated by external coils, confines the plasma particles primarily in the toroidal direction, while a weaker poloidal field, induced by a current driven within the plasma itself, provides rotational transform and stability. This intricate magnetic topology effectively insulates the hot plasma from the surrounding material walls, enabling the extreme conditions required for fusion.

I.C. Radiological Considerations in Research Tokamaks: The Runaway Electron Problem

While future fusion power plants operating on a deuterium-tritium (D-T) fuel cycle will have a radiological environment dominated by high-energy (14.1 MeV) neutrons, the safety considerations for contemporary research tokamaks operating with hydrogen or deuterium plasmas are fundamentally different. In these devices, the primary radiological hazard arises not from fusion products, but from hard X-ray radiation generated by a phenomenon known as "runaway electrons" (REs).

Under specific plasma conditions, a fraction of the electron population can be accelerated by the tokamak's toroidal electric field to relativistic energies, effectively "running away" from the collisional drag forces that normally thermalize the plasma. When these high-energy REs are eventually lost from magnetic confinement and collide with the vacuum vessel, limiters, or other plasma-facing components (PFCs), their kinetic energy is converted into highly penetrating X-rays through the Bremsstrahlung process. The generation, confinement, and loss of REs represent a critical area of plasma physics research, particularly for next-generation devices like ITER, where large RE populations generated during plasma disruptions pose a significant risk of damage to in-vessel components. Consequently, the study of RE-induced radiation in smaller machines is not only a matter of operational safety but also provides valuable data for understanding and mitigating this complex phenomenon.

I.D. The Thailand Tokamak-1 (TT-1) Facility and Research Program

The Thailand Tokamak-1 (TT-1) is a small-scale research tokamak operated by the Thailand Institute of Nuclear Technology (TINT) (Public Organization).1 Following a significant upgrade and recommissioning in 2023, the facility has embarked on a new phase of experimental campaigns aimed at contributing to the global fusion research effort. The work presented in this paper represents the first comprehensive radiation survey conducted at the facility during its Fiscal Year 2025 (FY2025) operational campaign. This investigation is therefore both timely and essential for establishing a robust radiological baseline, ensuring the safety of personnel and the environment, and informing the development of optimized operational protocols for the newly upgraded device.

I.E. Objectives and Scope of This Investigation

This paper provides a detailed characterization and analysis of the radiation field generated during the operation of the TT-1 tokamak. The primary objectives of this investigation are fourfold:

1. To present the first detailed, spatially-resolved characterization of the integrated X-ray dose environment surrounding the TT-1 device, accumulated over a representative operational campaign.
2. To analyze the measured dose distribution to identify radiological "hot spots" evaluate the performance of the existing shielding configuration, and infer key properties of the radiation field.
3. To establish an empirical foundation for future investigations aimed at correlating radiation levels with specific plasma operational parameters, such as plasma current, loop voltage, and gas pressure, which are known to influence RE generation.
4. To contribute valuable operational data to the international fusion research community, particularly for institutions operating small- to medium-scale tokamaks where RE-induced radiation is a significant operational and physics consideration

II. PHYSICAL PRINCIPLES AND THEORETICAL FRAMEWORK

II.A. Runaway Electron Dynamics in Tokamak Plasmas

The genesis of the radiation field under investigation lies in the complex dynamics of electrons within the tokamak plasma. In a magnetized plasma, an electron is subject to two opposing forces: an accelerating force from the applied toroidal electric field, E_T, and a decelerating frictional drag force, F_D, arising from Coulomb collisions with other plasma particles (both ions and electrons). The collisional drag force is a decreasing function of the electron's velocity. Consequently, there exists a critical velocity above which the accelerating force from the electric field exceeds the collisional drag. Electrons surpassing this velocity are continuously accelerated, becoming "runaway electrons"[1][2].

The primary mechanism for generating an initial seed population of REs is the Dreicer mechanism [3]. This process defines a critical electric field, the Dreicer field, E_D. When the applied toroidal electric field, E_T is a non-negligible fraction of E_D, electrons in the high-energy tail of the Maxwell-Boltzmann velocity distribution can be accelerated into the runaway regime. Plasma conditions that favor this process are characterized by a high toroidal electric field (proportional to the loop voltage, V_{loop} and low plasma density, n_e, as the collisional drag is proportional to density. Such conditions are commonly encountered during the current ramp-up and ramp-down phases of a tokamak discharge.

Once a seed population of REs exists, it can be amplified exponentially through a secondary avalanche generation mechanism. In this process, a high-energy RE undergoes a close-range collision with a thermal electron, transferring enough energy to promote the secondary electron into the runaway regime. This avalanche process is particularly dangerous during major plasma disruptions, where the rapid collapse of the plasma current induces an enormous toroidal electric field, potentially converting a large fraction of the plasma current into a relativistic RE beam [4].

II.B. Bremsstrahlung Radiation: The Physics of Photon Production

When a runaway electron is lost from the plasma and strikes a material surface, such as the vacuum vessel wall or a PFC, it undergoes rapid deceleration in the strong Coulomb fields of the atomic nuclei within the material. This deceleration process, governed by the law of conservation of energy, results in the emission of electromagnetic radiation known as Bremsstrahlung, a German term meaning "braking radiation" [5]. This phenomenon is the dominant source of X-rays in non-D-T tokamaks.

Bremsstrahlung radiation has several key characteristics that are fundamental to interpreting the experimental results of this study:

1. Continuous Energy Spectrum: Unlike characteristic X-rays, which are emitted at discrete energies corresponding to atomic transitions, Bremsstrahlung produces a continuous spectrum of photon energies. The energy of an emitted photon can range from near zero up to the maximum kinetic energy of the incident runaway electron. The resulting spectrum is therefore broad and contains photons across a wide range of energies.
2. Material and Energy Dependence: The efficiency of Bremsstrahlung production and the "hardness" (average energy) of the resulting photon spectrum are strong functions of both the incident electron's kinetic energy and the atomic number (Z) of the target material. The radiation yield is approximately proportional to $E_{kin}.Z^2$. This implies that collisions of high-energy REs with high-Z materials, such as tungsten or molybdenum which are often used for PFCs, are particularly potent sources of high-energy, penetrating X-rays.

II.C. Principles of OSL Dosimetry and Radiological Quantities

To quantify the radiation field produced by this mechanism, this study employed Optically Stimulated Luminescence (OSL) dosimetry. OSL dosimeters utilize a dielectric crystalline material, such as carbon-doped aluminum oxide ($Al_2O_3:C$), as the detector [6]. When exposed to ionizing radiation, electron-hole pairs are created within the material. These charge carriers can become trapped at defects or "traps" within the crystal lattice. The number of trapped charges is directly proportional to the total absorbed radiation dose. The measurement, or "readout," of the accumulated dose is performed by stimulating the crystal with light of a specific wavelength (e.g., from a laser or LED). This stimulation provides sufficient energy to release the trapped charges, which then recombine and emit luminescence. The intensity of this luminescence is measured by a photomultiplier tube and is proportional to the original radiation dose.

The measurements in this study are reported in terms of operational dose quantities defined by the International Commission on Radiation Units and Measurements (ICRU) to provide a conservative estimate of the dose received by the human body:

1. Ambient Dose Equivalent, H*(10): This quantity represents the dose equivalent that would be produced at a depth of 10 mm in the 30 cm diameter ICRU sphere, a standardized tissue-equivalent phantom. H*(10) is the standard quantity for area monitoring of strongly penetrating radiation and serves as a proxy for the effective dose to the whole body.
2. Directional Dose Equivalent, H'(0.07): This quantity represents the dose equivalent at a depth of 0.07 mm in the ICRU sphere. It is used to assess the dose to shallow organs, such as the skin and the lens of the eye, from both weakly and strongly penetrating radiation [7].

The relationship between these two quantities contains valuable physical information about the radiation field itself. The attenuation of photons in matter is highly dependent on their energy; low-energy photons are absorbed over very short distances, while high-energy photons are highly penetrating. If the radiation field were dominated by low-energy X-rays, most of the energy would be deposited near the surface of a phantom, leading to a situation where H'(0.07) is significantly larger than H*(10). Conversely, for a field composed of high-energy, penetrating photons, the dose deposition would be relatively uniform throughout the first centimeter of tissue. In this case, the dose measured at 0.07 mm and 10 mm depth would be very similar, resulting in a ratio of H'(0.07) / H*(10) that is close to unity. Therefore, the measurement of this ratio provides a powerful, non-spectroscopic method for inferring the energetic quality, or "hardness," of the X-ray spectrum, which is a critical parameter for radiation protection and shielding design [8].

III. EXPERIMENTAL CONFIGURATION AND METHODOLOGY

III.A. The Thailand Tokamak-1 (TT-1) Device

The Thailand Tokamak-1 (TT-1) is a small-scale, iron-core research tokamak. It is characterized by a major radius (R) of 0.32 m, a minor radius **(a)** of 0.1 m, and a toroidal magnetic field (B_T) of up to 1.3 T. The device is capable of producing plasma discharges with currents (I_p) in the range of 30-50 kA and durations of approximately 50-100 ms. The data presented in this work were collected cumulatively throughout the entire FY2025 operational campaign, thereby representing an integrated measurement over hundreds of plasma shots covering a diverse range of experimental conditions and objectives.

III.B. Radiation Dosimetry and Measurement Protocol

The spatial characterization of the integrated radiation field was performed using a set of 15 passive Landauer nanoDot™ OSL dosimeters. These dosimeters were deployed at strategically chosen locations within the TT-1 experimental hall and in adjacent areas, including the control room, to provide a comprehensive map of the radiological environment. The locations were selected to monitor areas with varying proximity to the tokamak, different lines-of-sight to potential radiation sources (e.g., diagnostic ports), and positions behind primary shielding walls. All dosimeters were mounted at a standardized height of 1.5 meters from the floor level to provide a measurement representative of the dose to the torso of personnel working in the area.

Figure 1 (as described in the source document) shows a plan view of the TT-1 facility and the precise placement of the 15 dosimeters. The dosimeters were deployed at the beginning of the FY2025 campaign and remained in place for its entire duration to accumulate the total integrated dose. To account for the contribution from natural background radiation, several control dosimeters were stored concurrently in a shielded, low-background location far from the experimental hall.

At the conclusion of the campaign, all dosimeters were collected for analysis. The readout was performed using a Landauer microStar® reader, which automatically processes the OSL elements and provides calibrated dose values for both ambient dose equivalent, H*(10), and directional dose equivalent, H'(0.07). The final reported dose for each location was obtained by subtracting the average dose measured by the control dosimeters from the gross dose measured by the field dosimeters. All dose values are reported in units of millisieverts (mSv).

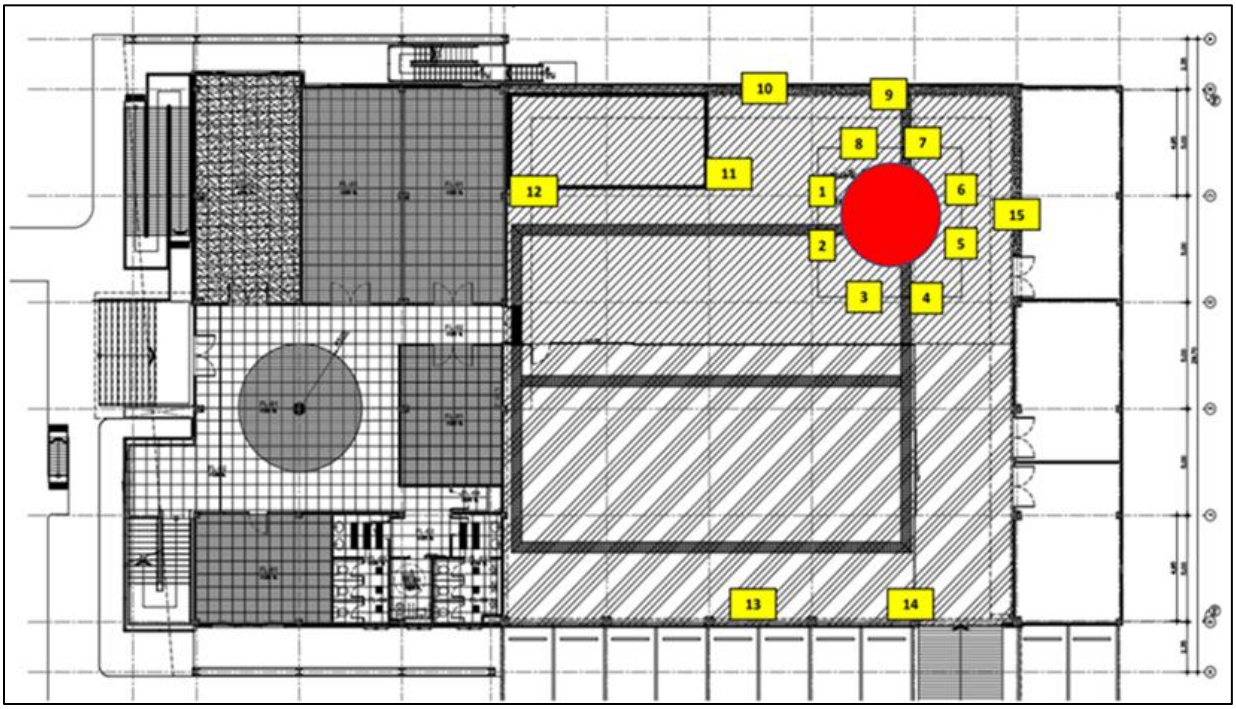

FIGURE 1. Shows a plan view of the TT-1 facility and the precise placement of the 15 dosimeters.

III.C. Plasma Parameter Monitoring System

Throughout the operational campaign, critical plasma parameters for every experimental discharge (or "shot") were logged by the TT-1's central data acquisition system. The parameters most relevant to the generation of runaway electrons—including the plasma current (I_p), loop voltage (V_{loop}), and the initial hydrogen gas filling pressure—were recorded on a continuous basis. While a detailed, shot-by-shot correlation between these plasma parameters and instantaneous radiation levels is beyond the scope of this paper, this concurrently collected data provides the essential foundation for future investigations aimed at identifying the specific operational scenarios responsible for the majority of the radiation production.

IV. RESULTS AND ANALYSIS

IV.A. Spatial Distribution of Integrated X-ray Dose

The primary quantitative results of this investigation are the integrated dose equivalent values measured at the 15 monitoring locations around the TT-1 facility. These data, representing the cumulative dose from all plasma operations during the FY2025 campaign after subtraction of the natural background contribution, are presented in Table 1. The table includes the measured values for both ambient dose equivalent (H*(10)) and directional dose equivalent (H’(0.07)), as well as the calculated ratio between these two quantities.

TABLE I. showing measured values for both ambient dose equivalent (H*(10)) and directional dose equivalent (H'(0.07)).

Location ID	H*(10) (mSv)	H'(0.07) (mSv)	H'(0.07) / H*(10) Ratio	Notes
1	0.35	0.38	1.09	
2	1.03	1.03	1.00	
3	1.49	1.49	1.00	Maximum dose location
4	0.18	0.18	1.00	
5	Bg	Bg	-	Background level
6	0.03	0.05	1.67	Near background
7	0.70	0.70	1.00	
8	0.25	0.25	1.00	
9	0.11	0.11	1.00	
10	0.02	0.02	1.00	Near background
11	0.01	0.01	1.00	Near background
12	Bg	Bg	-	Background level
13	Bg	Bg	-	Background level
14	Bg	Bg	-	Background level
15	0.06	0.06	1.00	

Note: 'Bg' indicates that the measured dose was indistinguishable from the background radiation level.

IV.B. Analysis of Radiation Field Anisotropy

A principal finding evident from Table 1 is the profound anisotropy of the radiation field surrounding the TT-1 tokamak. The measured dose values span more than two orders of magnitude, demonstrating a strong dependence on the location relative to the device. A distinct radiological "hot spot" was identified at Location 3, which recorded the maximum integrated dose of 1.49 mSv for both H*(10) and H'(0.07). Other locations in close proximity to the tokamak vessel, specifically Locations 2 (1.03 mSv) and 7 (0.70 mSv), also exhibited significantly elevated dose levels.

In stark contrast, several locations recorded doses that were indistinguishable from natural background levels. These locations (5, 12, 13, and 14) are situated either at a considerable distance from the tokamak or are positioned behind substantial concrete shielding walls, as indicated in the facility layout diagram. This result provides direct empirical evidence for the effectiveness of the facility's primary shielding in attenuating the X-ray radiation produced during operation. The intermediate dose levels observed at other locations reflect a complex interplay of distance, shielding from the tokamak's own components (e.g., magnetic field coils and iron core), and the specific geometry of potential radiation streaming paths.

IV.C. Inference of Radiation Field Quality from Dose Equivalent Ratios

Further analysis of the data in Table 1 yields crucial insights into the physical nature of the radiation field. As outlined in the theoretical framework, the ratio of the directional dose equivalent H'(0.07) to the ambient dose equivalent H*(10) serves as an indicator of the radiation's penetrating power. The calculated ratios, presented in the fourth column of Table 1, are remarkably consistent. For every location where the measured dose was significantly above the background level, the H'(0.07)/ H*(10) ratio is approximately 1.00.

This empirical observation is of paramount importance. A ratio of unity signifies that the radiation field deposits dose almost uniformly between a shallow depth of 0.07 mm and a deeper point of 10 mm in tissue-equivalent material. This physical characteristic is a definitive hallmark of a "hard" radiation spectrum composed of high-energy, highly penetrating photons. This finding provides strong experimental validation for the theoretical model that the dominant source of radiation at TT-1 is Bremsstrahlung generated by relativistic runaway electrons, as this is the primary physical mechanism capable of producing an X-ray spectrum with such high average energy in this type of device. The data effectively rule out the possibility of the field being dominated by low-energy X-rays, which would have resulted in a ratio significantly greater than one.

V. DISCUSSION

V.A. Correlation of Radiological Hot Spots with Tokamak Geometry and RE Loss Physics

The highly structured and anisotropic radiation map presented in the results is not random; it is a direct physical consequence of the interplay between runaway electron dynamics and the geometry of the tokamak. The pronounced hot spot at Location 3, with a dose of 1.49 mSv, is almost certainly situated in close proximity to a primary RE loss point on the tokamak. Runaway electrons, while confined by the magnetic field, are eventually lost and strike physical components. These loss points are typically determined by asymmetries in the magnetic field or by components that protrude into the plasma's edge region, such as limiters, radio-frequency heating antennas, or diagnostic port windows. The intense Bremsstrahlung X-rays are generated at the point of impact, and the radiation streams outwards from this localized source. Location 3 likely has a direct, unshielded line-of-sight to such a component.

Conversely, the areas with background-level radiation are effectively shadowed. The massive iron core, the dense array of toroidal and poloidal field coils, and the vacuum vessel itself act as a significant source of self-shielding, attenuating radiation in many directions. The primary concrete walls of the experimental hall provide further, substantial attenuation for locations outside the main torus hall. This interpretation suggests that the radiation map is more than a simple safety survey; it functions as a passive, integrating diagnostic for RE loss physics. The spatial pattern of hot spots provides valuable, albeit indirect, information about where on the machine the majority of runaway electrons are being lost. This information can be used to guide physics studies and to inform the placement of dedicated RE diagnostics in future campaigns.

V.B. Implications for Radiological Protection and Operational Safety

The quantitative results have direct and significant implications for the radiological protection program at the TT-1 facility. The maximum measured dose of 1.49 mSv over the course of the FY2025 campaign is a measurable and non-trivial dose. While this is well below the typical annual dose limit for radiation workers (e.g., 20 mSv), it confirms that RE-induced X-rays are a persistent feature of TT-1 operation that requires active management and control.

A radiation warning sign depicted in the source material indicates a representative dose rate of 6.88 μSv/hr in a high-radiation area near the machine during operation. This allows for a quantitative estimation of the operational conditions that produced the measured cumulative dose. By dividing the total integrated dose at the hot spot (1490 μSv) by this representative dose rate, one can estimate the total time during which the facility was producing significant radiation, As shown in Equation (1).

$$\text{Total Time} = \frac{Total\ Dose}{Dose\ Rate} = \frac{1490\ \mu\text{Sv}}{6.88\ \mu\text{Sv/hr}} \approx 217\ \text{hours} \quad (1)$$

This calculation demonstrates that the measured dose was not the result of a few isolated, high-intensity events, but was accumulated over approximately 217 hours of routine plasma operations throughout the campaign. This powerfully underscores that radiation production is a standard feature of TT-1's operational envelope. It also implies that any future increases in

operational time, or a shift towards plasma scenarios known to be more prolific in RE generation, could lead to a proportional increase in personnel dose if not properly managed.

Based on this analysis, several actionable recommendations can be made. First, the area immediately surrounding Location 3 should be formally designated as a High Radiation Area, with access strictly controlled and prohibited during plasma operations. Second, an evaluation should be undertaken to determine the feasibility of installing localized, supplementary shielding-such as lead blankets or movable concrete blocks-around this identified hot spot to reduce dose rates in adjacent, more frequently occupied areas.

V.C. Anticipated Correlation with Plasma Operational Scenarios

While the current study provides an integrated, campaign-long picture, the underlying physics suggests that the radiation was not produced uniformly over time. It is hypothesized that the bulk of the measured dose was generated during specific, high-risk phases of the plasma discharges. These phases are characterized by conditions highly conducive to RE generation and loss:

1. **Plasma Startup and Current Ramp-Up:** During the initial phase of the discharge, the plasma density is low while the loop voltage is relatively high to drive the plasma current. This combination of low collisionality and high accelerating field creates ideal conditions for the Dreicer mechanism to generate a seed population of runaway electrons.
2. **Major Plasma Disruptions:** A disruption involves a rapid thermal quench followed by a current quench. The collapse of the plasma current induces a massive toroidal electric field spike, which can accelerate a substantial fraction of the pre-existing electrons into a powerful, multi-MeV RE beam via the avalanche mechanism. This beam is then typically lost to the wall in a single, intense burst, producing a large flux of hard X-rays.

Confirming these hypotheses requires time-resolved radiation measurements correlated with plasma data on a shot-by-shot basis. The present study, by establishing the spatial distribution and energetic quality of the field, provides the essential groundwork for this critical future work.

VI. CONCLUSION AND RECOMMENDATIONS FOR FUTURE WORK

VI.A. Summary of Conclusions

This investigation has successfully delivered the first comprehensive and spatially-resolved radiological characterization of the Thailand Tokamak-1 (TT-1) facility following its recent upgrade. The key conclusions drawn from the analysis are:

1. The radiation environment around TT-1 is dominated by a highly anisotropic and energetic X-ray field. The dose levels vary by over two orders of magnitude depending on the location, confirming the localized nature of the radiation source.
2. The experimental results empirically confirm that the radiation is consistent with Bremsstrahlung from relativistic runaway electrons lost from the plasma. This is evidenced by the identification of distinct hot spots corresponding to likely RE impact points and by the near-unity ratio of H'(0.07) to H*(10), which indicates a highly penetrating photon spectrum.
3. The study has successfully identified a primary radiological hot spot (Location 3) with an integrated campaign dose of 1.49 mSv, providing critical data for immediate safety enhancements and the implementation of targeted access controls. Concurrently, the study has validated the efficacy of the existing bulk shielding in maintaining background-level radiation in other key areas.

VI.B. Recommendations for Future Research and Development

The findings of this work establish a solid foundation and point toward several clear avenues for future research that will deepen the understanding of RE physics and enhance radiological safety at TT-1. The following actions are recommended:

1. Quantitative Correlation Study: The highest priority for future work is to move from integrated to time-resolved measurements. This involves deploying active radiation monitors (e.g., NaI or $LaBr_3$ scintillators) capable of measuring dose rates on a shot-by-shot basis. By correlating this time-resolved radiation data with the logged plasma parameters (I_p, V_{loop}, density, MHD activity), it will be possible to precisely identify the operational conditions and plasma instabilities that lead to high levels of RE generation and loss.

2. X-ray Spectroscopy: To move beyond inference and directly measure the energy of the radiation field, it is recommended to deploy energy-resolved X-ray detectors at key locations, particularly the identified hot spot. Spectrometers such as Cadmium Zinc Telluride (CZT) or High-Purity Germanium (HPGe) detectors can measure the Bremsstrahlung energy spectrum directly. This would provide definitive data on the maximum energy of the runaway electrons, which is a critical physics parameter, and would furnish the precise source term needed for high-fidelity shielding calculations.
3. Predictive Modeling and Simulation: A comprehensive 3D radiation transport model of the TT-1 facility should be developed using a Monte Carlo code such as MCNP, Geant4, or FLUKA. This model would incorporate the detailed geometry of the tokamak, the experimental hall, and all shielding structures. The experimental dose map generated in this paper provides the essential and invaluable dataset required to benchmark and validate such a model. Once validated, this computational tool would be a powerful predictive asset, enabling the assessment of the radiological impact of future machine upgrades, the optimization of new shielding designs, and the development of more sophisticated safety protocols.

REFERENCES

[1] Wesson, J. Tokamaks. 4th ed., Oxford University Press, 2011.
[2] Chen, F. F., & Freidberg, J. P. (2014). Plasma Physics and Controlled Fusion (3rd ed.). Springer, Cham.
[3] Dreicer, H. (1959). Electron and Ion Runaway in a Fully Ionized Gas. I. Physical Review, 115(2), 238–249.
[4] Helander, P., & Eriksson, L. G. (2002). Theory of runaway electrons in tokamaks. Physics of Plasmas, 9(3), 1012–1024.
[5] Knoll, G. F. (2010). Radiation Detection and Measurement (4th ed.). John Wiley & Sons, New York, NY.
[6] McKeever, S. W. S., & Horowitz, Y. S. (2008). Thermoluminescence and Optically Stimulated Luminescence: Principles and Applications. CRC Press, Boca Raton, FL. (หากมีข้อมูลที่ละเอียดขึ้นเกี่ยวกับ Al_2O_3:C)
[7] International Commission on Radiation Units and Measurements (ICRU). (1998). Conversion Coefficients for Use in Radiological Protection against External Radiation (ICRU Report 57). Bethesda, MD: ICRU.
[8] Wernli, C., & Boschung, M. (2007). Interpretation of personal dosimetry results from OSL and TLD measurements. Radiation Protection Dosimetry, 125(1-4), 312–316. doi:10.1093/rpd/ncm372

DIRECTION OF NUCLEAR CONSEQUENCE ANALYSIS OF SMR IN THAILAND

Narakhan Kunsrimek[1], Somboon Rassame[1*], Wasin Vechgama[2*]

[1]*Department of Nuclear Engineering, Faculty of Engineering, Chulalongkorn University, Phayathai Road, Wang Mai, Pathumwan, Bangkok, 10330, Thailand*
[2]*Thailand Institute of Nuclear Technology (Public Organization), 16 Vibhavadi Rangsit Road, Chatuchak, Bangkok, 10900, Thailand*
[*]*Corresponding Author*

EXTENDED ABSTRACT

The rising interest in Small Modular Reactors (SMRs) among newcomer countries underscores the significance of understanding consequence analysis as a means of effective communication across governmental, public, and private sectors. Key inquiries from these stakeholders revolve around the anticipated impacts of SMRs, the scope of emergency planning zone requirements, and the existence of strategic frameworks for nuclear fallout management, including sheltering and evacuation protocols. Drawing on Thailand's recent experience in atmospheric dispersion analysis for large-scale Nuclear Power Plants (NPPs), insights have been leveraged to delineate the Emergency Planning Zone (EPZ) for SMRs through Level 3 Probabilistic Safety Assessment (PSA) methodologies.

In Level 3 PSA concept for SMR, radiological releases from Design-Basis Accidents (DBAs) and Beyond-Design-Basis Accidents (BDBAs) must be analyzed to determine the required Exclusion Area Boundary (EAB) and Low Population Zone (LPZ) boundaries [1, 2]. In 2019, NuScale Power submitted a report to the U.S. Nuclear Regulatory Commission outlining their methodology for evaluating source terms and radiological consequences of DBAs and BDBAs in Light Water Reactor-SMR (LWR-SMR) [3]. NuScale requested approval for using the ARCON program to estimate offsite atmospheric dispersion in hourly releases, instead of using PAVAN for longer release periods from 2 hours to 30 days [4]. In 2023, X-Energy, LLC used the US NRC's ARCON program to estimate atmospheric relative concentration (χ/Q) values at the EAB and LPZ boundaries up to 1,200 meters from the power block area's nearest building edge [5]. Recently, Thailand has also experienced developing atmospheric dispersion codes for Large NPPs [6, 7, 8] and approach estimate Emergency Planning Zone (EPZ) of LWR-SMR [9].

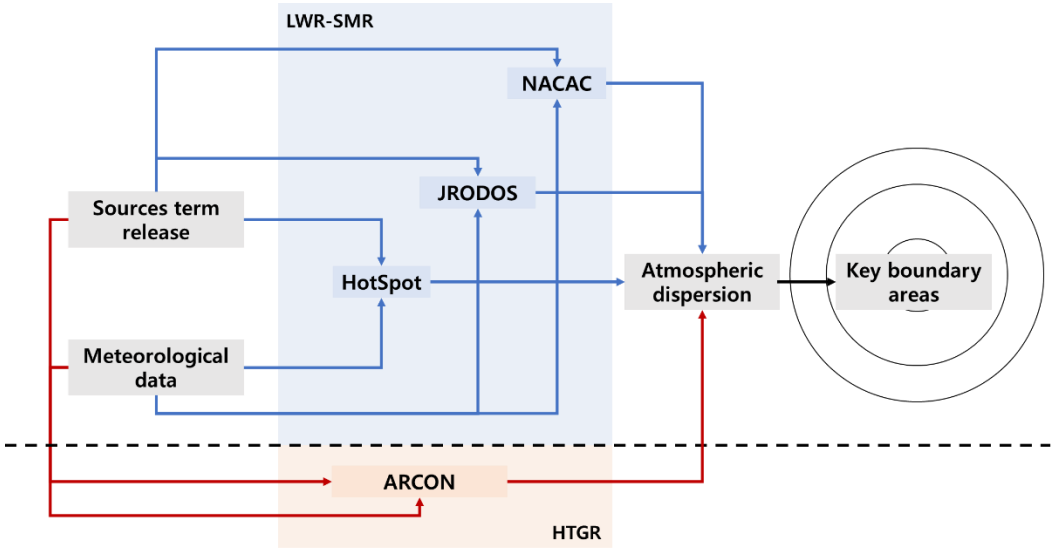

FIGURE 1. Thailand strategy for nuclear consequence analysis of Level 3 PSA for LWR-SMR and HTGR

In Thailand, SMR technology, including LWR-SMRs and HTGRs is considered a potential candidate, aligning with the strategies of other countries. Consequently, to meet regulatory requirements, it is essential to estimate the radiological consequences in the EAB and LPZ. This task is vital for plant owners and related entities to submit to the regulatory body for emergency planning and to assist government sectors in public communication. This research elucidates the evolving landscape of nuclear consequence analysis within the context of Level 3 PSA for prospective SMR technologies in Thailand.

Fig. 1 shows the Thailand strategy for nuclear consequence analysis of Level 3 PSA for LWR-SMR and HTGR. The direction of nuclear consequence analysis of SMRs is divided into two parts. The upper part (blue zone) is the consequence analysis scheme of LWR-SMR. At first, HotSpot and JRODOS that are validated tools, were selected to assess dose for emergency response. The authors started with the quick HotSpot code simulation which is the basic atmospheric dispersion code to estimate the direction of the release and dose assessment. Then, JRODOS that is a more comprehensive system, was used to simulate the results for real-time decision support in nuclear emergencies. Then in 2023, the authors together developed NACAC code that simply the meteorological grad use for atmospheric dispersion. The results of HotSpot and JRODOS can well verify the NACAC code. Thus, all three codes for LWR-SMRs are generally used for atmospheric dispersion analysis based on the time and existing resources. As for the lower part (red zone), since X-Energy and U.S. NRC co-develop and recommended the ARCON program to estimate atmospheric relative concentration (χ/Q) values for HTGR having specific core inventory and radioactive material release. ARCON source code is modeled to cover the high pressure and temperature conditions affecting radioactive material behaviors. Thus, the authors planned to use ARCON to help explain the atmospheric dispersion analysis and identify the key boundary areas for emergency planning in the future.

Noteworthy contenders such as the LWR-SMR and HTGR hold promise in advancing the country's green and sustainable energy agenda as outlined in the national energy strategy. The envisioned trajectory of nuclear consequence analysis for these SMRs is poised to address pertinent concerns of governmental, public, and private entities while furnishing a robust, secure, and economically viable framework for Thailand's forthcoming nuclear energy initiatives.

REFERENCES

[1] 10 CFR 52, U.S. Code of Federal Regulations, Title 10, Part 52 (2022).
[2] IAEA, Accident Analysis for Nuclear Power Plants, Safety Reports Series No. 23 (2002).
[3] NUSCALE. NuScale Topical Report, "Accident Source Term Methodology," TR-0915-17565, Revision 3. U.S. Nuclear Regulatory Commission (2019).
[4] S. ROSS, J. RISHEL, P. LOWRY, Engineering Evaluation of χ/Q Values Consistent with Regulatory Guide 1.145, Prepared for the U.S. Department of Energy under Contract DE-AC05-76RL01830 (2010).
[5] U.S. NRC, Use of ARCON Methodology for Calculation of Accident-Related Offsite Atmospheric Dispersion Factors, Regulatory Guide 1.249 (2023).
[6] K. SILVA, P. KRISANUNGKURA, N. KHUNSRIMEK, W. VECHGAMA, J. TANG, V. KRISHNAN, K. PHAM, T. CHARNOCK, S. RASSAME, T. KIAT, C. YEOW, H. THAN, N. QUANG, P. HIEN, "Inter-comparison of transboundary atmospheric dispersion calculations: A summary of outputs from the ASEAN NPSR benchmark exercisem," *Progress in Nuclear Energy* 135, 103718 (2021).
[7] N. KHUNSRIMEK, P. KRISANUNGKURA, W. VECHGAMA, K. SILVA, S. RASSAME, T. HIBIKI, "Verification of the NACAC atmospheric dispersion calculation using a hypothetical accident in a neighboring nuclear power plant," *Progress in Nuclear Energy*, 156, 104532, (2023)
[8] N. KHUNSRIMEK, W. VECHGAMA, K. SILVA, S. RASSAME, T. HIBIKI, "Simulation using representative data selection for transboundary radiation effect evaluation by Nuclear Accident Consequence Analysis Code (NACAC)," *Journal of Nuclear Science and Technology*, **61(3)**, 327-342, (2024).
[9] W. VECHGAMA, P. KRISANUNGKURA, K. SILVA, "Application of release starting time classification for planning emergency preparedness and response to the hypothetical accident scenario of iPWR-SMR in Thailand," *Nuclear Engineering and Design*, **429**, 113629, (2024).

ASRAM2025
www.asram2025.org
Asian Symposium on Risk Assessment and Management 2025
Pattaya, Thailand, 27 – 29 August 2025

Initial Hard X-ray Spectroscopy Results from the Thailand Plasma Focus 2 (TPF-2) Using a $LaBr_3$(Ce) Detector

Nopporn Poolyarat[1], Pasit Wonghabut[1], Suebsak Suksaengpanomrung[1], Arlee Tamman[1], Jiraporn Promping[1], Kitisak Komnoi[1], Siriyaporn Sangaroon[2], Apiwat Wisitsorasak[3], Kitti Rongpuit[3]

[1] *Thailand Institute of Nuclear Technology (Public Organization): 9/9 Moo 3, Lat Khwang Subdistrict, Ongkharak District, Nakhon Nayok Province 26120, Thailand, nopporn p@tint.or.th*
[2] *Mahasarakham University: Khamriang, Kantharawichai District, Maha Sarakham Province 44150, Thailand*
[3] *King Mongkut's University of Technology Thonburi: 126 Pracha Uthit Road, Bang Mot, Thung Khru, Bangkok 10140, Thailand*

ABSTRACT

The Thailand Plasma Focus 2 (TPF-2), a 3.3 kJ dense plasma focus device, is a source of X-rays, posing a potential radiation hazard if not properly shielded. This research focuses on the design, calculation, and fabrication of TPF-2, aiming for high efficiency in X-ray emission and a high pinch percentage [1, 2]. Its components were meticulously designed for low electrical energy loss and symmetry of current transfer, with the expectation of achieving a symmetric plasma sheath under optimum conditions, leading to high X-ray emission efficiency [1, 2]. These X-ray emissions are typically characterized by short bursts on the order of ~10 nanoseconds. While previous studies at TPF-2 have characterized various plasma properties, a comprehensive understanding of its hard X-ray (HXR) emission spectrum, crucial for both plasma diagnostics and radiological safety, has been largely underexplored.

This study presents the first direct spectroscopic measurements of the hard X-ray spectrum emitted from the TPF-2 device, utilizing a highly efficient Lanthanum Bromide (Ce-doped) scintillator detector ($LaBr_3$(Ce)), which was previously employed for hard X-ray measurements on the Thailand Tokamak-1 [1]. The experimental setup involved the strategic placement of the $LaBr_3$(Ce) detector, coupled with advanced pulse height analysis techniques, to capture the transient HXR bursts during TPF-2 discharges. Initial results reveal a broad, non-thermal hard X-ray spectrum, indicative of energetic electron acceleration mechanisms within the plasma focus pinch. The data allow for the inference of the effective electron temperature and maximum HXR energy, providing critical insights into the underlying beam-target interactions. These preliminary spectroscopic findings are invaluable for refining TPF-2 operational parameters to optimize HXR yield, benchmarking theoretical models of electron acceleration, and establishing a robust radiological baseline for future D-T experimental campaigns.

I. INTRODUCTION

I.A. The Significance of Plasma Focus Devices in Fusion Research

Plasma focus devices, as a subset of Z-pinch machines, are compact and versatile tools for generating high-temperature, high-density plasmas. They are renowned for their ability to produce intense bursts of various radiations, including X-rays, energetic ions, and neutrons, making them attractive platforms for fundamental studies in high-energy density physics, materials science, and potential applications in compact neutron sources or even as drivers for inertial confinement fusion. The unique self-organizing pinch mechanism in plasma focus devices leads to the formation of a dense, hot plasma column that can accelerate charged particles to very high energies.

I.B. Hard X-ray Emissions: A Diagnostic and Safety Imperative

In the context of plasma focus devices, hard X-rays (HXRs), typically defined as photons with energies greater than approximately 100 keV, are of particular interest. HXR emissions are primarily generated by the Bremsstrahlung process, where energetic electrons, accelerated during the pinch phase or during instabilities, collide with the anode material or residual gas. The characteristic of HXR emissions are typically short bursts on the order of ~10 nanoseconds. The spectral characteristics

of these HXRs provide crucial diagnostic information about the electron acceleration mechanisms, the effective energy of the electron beams, and the interaction dynamics within the plasma. Furthermore, understanding the HXR spectrum is paramount for radiological protection and safety assessment, especially as plasma focus devices are scaled up or operated in configurations that could produce higher yields.

I.C. The Thailand Plasma Focus 2 (TPF-2) Facility: Design and Previous Characterization

The Thailand Plasma Focus 2 (TPF-2) is a medium-energy plasma focus device, specifically 3.3 kJ, located at Thailand Institute of Nuclear Technology (Public Organization). This research focuses on the design, calculation, and fabrication of TPF-2, which was specifically aimed for high efficiency of X-ray emission and a high pinch percentage [1, 2]. To achieve this, TPF-2 components were meticulously designed for low electrical energy loss and symmetry of current transfer, with the expectation that a symmetric plasma sheath would occur at optimum conditions, thereby leading to high efficiency of X-ray emission [1, 2]. The electrostatic fields contributed by supported insulators, cathode plates, installations of dielectric sleeve, and dielectric sleeve materials were calculated using COMSOL Multiphysics to optimize their characteristics such as geometry, installation, and type of material [1, 2]. The Lee code was utilized to optimize the electrode dimension and estimate the pinch and quantitative parameters [1, 2].

The electrode dimensions of TPF-2 are 1.25 cm for anode radius, 2.5 cm for cathode radius, and an optimized electrode length of 11.2 cm, with the length of the dielectric sleeve being 2 cm [1]. This study utilizes the $LaBr_3$(Ce) detector, which was previously employed for hard X-ray measurements on the Thailand Tokamak-1, confirming its suitability and reliability for plasma-related work [1]. While previous work has extensively characterized the device's electrical parameters and some radiation outputs, a direct measurement of the hard X-ray energy spectrum has been a critical missing component for a comprehensive understanding of the electron dynamics.

I.D. Objectives and Scope of This Investigation

This paper presents the initial results of direct spectroscopic measurements of hard X-ray emissions from the TPF-2 device. The primary objectives of this investigation are threefold:

1. To implement and validate a hard X-ray spectroscopy system utilizing a $LaBr_3$(Ce) detector for transient plasma focus events.
2. To obtain the first direct energy spectrum of hard X-rays emitted from the TPF-2 device, thereby providing insights into the energetic electron populations.
3. To establish an empirical baseline for the HXR spectral characteristics, which can inform future diagnostic development, validate theoretical models of electron acceleration, and contribute to radiological safety assessments at the TPF-2 facility.

II. PHYSICAL PRINCIPLES AND THEORETICAL FRAMEWORK

II.A. Principles of Plasma Focus Devices and Hard X-ray Generation

The study of dense plasma focus (DPF) devices has a rich history, with significant contributions from various research groups worldwide exploring their potential as compact sources of X-rays, ions, and neutrons [3]. Early work by Mather and Filippov laid the foundation for understanding the basic operating principles and scaling laws of DPF devices [4, 5]. Subsequent research has focused on optimizing device performance, enhancing specific radiation outputs, and developing advanced diagnostic techniques.

The generation of hard X-rays in plasma focus devices is a complex phenomenon intrinsically linked to the relativistic electron beams (REBs) formed during the radial and axial pinch phases. As the plasma current rapidly collapses in the dense pinch, a large inductive electric field is generated. This intense electric field can accelerate a fraction of the plasma electrons to very high energies (hundreds of keV to MeV range). When these energetic electrons interact with the anode material, the discharge chamber walls, or even the relatively dense plasma itself, they undergo Bremsstrahlung emission. The resulting HXR spectrum is typically non-thermal and can extend to energies corresponding to the maximum kinetic energy of the accelerated electrons. Other potential mechanisms, such as electron-ion collisions, may also contribute, but Bremsstrahlung from electron interaction with solid targets is generally considered dominant for HXRs.

For X-ray emission from plasma focus devices, numerous studies have explored the characteristics of both soft and hard X-rays. Soft X-rays are typically indicative of the thermal properties of the plasma column, while hard X-rays provide crucial insights into the non-thermal processes, particularly the generation of energetic electron beams [6]. Various diagnostic tools, including pinhole cameras, filtered X-ray diodes, and scintillation detectors, have been employed to characterize X-ray emissions [7, 8].

II.B. Lanthanum Bromide ($LaBr_3$(Ce)) Scintillator Detector and its Application

To perform direct energy spectroscopy of hard X-rays, a highly efficient and fast-response detector is required. This study utilizes a Lanthanum Bromide ($LaBr_3$(Ce)) scintillator detector. $LaBr_3$(Ce) crystals are a relatively new but highly promising technology for radiation detection, known for their excellent energy resolution, high light output, and fast decay time. Its application has extended to various fields, including nuclear spectroscopy, medical imaging, and plasma diagnostics.

$LaBr_3$(Ce) crystals are well-suited for HXR spectroscopy due to their excellent properties, including:

1. High Light Output: Produces a large number of photons per unit of absorbed energy, leading to superior energy resolution.
2. Fast Decay Time: Its rapid scintillation decay time (typically around 16 ns) allows for the accurate detection of high count rates and the resolution of pulsed radiation events, which is crucial for transient plasma focus discharges.
3. Good Energy Resolution: Provides distinct peaks in the energy spectrum, enabling the accurate identification of photon energies.
4. High Effective Atomic Number (Zeff): Enhances the probability of photoelectric absorption and Compton scattering interactions with X-rays, leading to higher detection efficiency. When HXRs interact with the $LaBr_3$(Ce) crystal, they deposit energy through photoelectric absorption, Compton scattering, and pair production (at very high energies). This deposited energy is converted into scintillation light, which is then detected by a photomultiplier tube (PMT). The amplitude of the electrical pulse generated by the PMT is proportional to the energy of the incident X-ray photon, allowing for the construction of an energy spectrum through pulse height analysis (PHA). Notably, this type of detector has already demonstrated its utility in the Thai fusion research landscape, having been successfully employed for hard X-ray measurements on the Thailand Tokamak-1 [1]. This prior experience provides confidence in its suitability and reliability for the present investigation on TPF-2.

II.C. Previous Work on TPF-2 and the Research Gap

In Thailand, research on plasma focus devices has been actively pursued, with the Thailand Plasma Focus 2 (TPF-2) serving as a key experimental platform. Previous investigations on TPF-2 have focused on characterizing its electrical discharge parameters, current sheath dynamics, and initial radiation yields. For instance, studies have confirmed the pinch phenomena through analysis of current and voltage waveforms, and magnetic probes have been used to investigate plasma sheath velocity. The design of TPF-2 itself was the subject of detailed research, involving calculations using COMSOL Multiphysics for optimizing components like insulators and dielectric sleeves, and the Lee code for optimizing electrode dimensions and estimating pinch parameters. The confirmation of X-ray emission and pinch occurrence has also been demonstrated using techniques like X-ray lithography with Speed E fast X-ray films.

Despite the existing characterization efforts on TPF-2, a detailed direct energy spectrum of its hard X-ray emission has not been previously reported. Such a spectrum is vital for a comprehensive understanding of the energetic electron acceleration mechanisms unique to TPF-2's operating regime and for establishing a precise radiological safety profile for the facility. This work aims to bridge this gap by providing the first direct spectroscopic analysis of TPF-2's hard X-ray output.

III. EXPERIMENTAL CONFIGURATION AND METHODOLOGY

III.A. The Thailand Plasma Focus 2 (TPF-2) Device

The TPF-2 device is a 3.3 kJ dense plasma focus device that operates with a capacitor bank, spark gap, and trigger system. The capacitor charging is managed by a CCS Power Supply, model number CCS02025P1B, from General Atomics Electronic Systems company. This power supply has a maximum charging energy of 2 kJ/s and a maximum charging voltage of 25 kV,

with positive polarity. The main electrical parameters of the system include a capacitor with a capacitance of 30 uF, an operating voltage of 15 kV, a maximum peak current of 163 kA, and an inductance of 40 nH. The preliminary result of the TPF-2 short circuit test shows that the system inductance and resistance were 153 nH and 12 mΩ, respectively [2]. The spark gap, model TDI3-200k/25H, operates with a forward voltage range of 1 - 25 kV, a reversed voltage of 20 kV, a forward current of 200 kA, and a time jitter of 3-4 ns. The trigger operates at a voltage of 6 kV, a current of 120 A, a rise time of 20 ns, and a pulse duration of 200 ns [2].

The electrode configuration consists of a coaxial geometry with an anode radius of 1.25 cm, a cathode radius of 2.5 cm, and an optimized electrode length of 11.2 cm. The length of the dielectric sleeve is 2 cm [1]. Experiments for this study were conducted with Argon gas filling at a pressure of 0.5-1.5 TORR, aiming to maximize hard X-ray emission. A series of 50 discharges were performed for this initial spectroscopic characterization.

III.B. Hard X-ray Spectroscopy Setup

The hard X-ray spectrum was measured using a $LaBr_3(Ce)$ scintillator detector coupled to a photomultiplier tube (PMT). The detector was housed in a lead shield to minimize background radiation. As shown in Figure 1, a total of 13 $LaBr_3(Ce)$ detectors were strategically deployed at various locations within the TPF-2 experimental hall. These locations, represented by the numbered yellow boxes, were chosen to provide a comprehensive spatial map of the HXR emission, specifically focusing on areas around the plasma focus device (blue cylinder) and its single window side. The detectors were mounted at a standardized height to ensure consistent measurement conditions. A precisely aligned collimator was used to define the field of view and ensure that only X-rays directly from the pinch region reached the detector. The signal from the PMT was fed into a fast digitizer operating to capture the transient HXR pulses. Pulse height analysis (PHA) was performed offline using custom-developed software, allowing for the reconstruction of the energy spectrum. Energy calibration of the detector was performed using standard gamma-ray sources

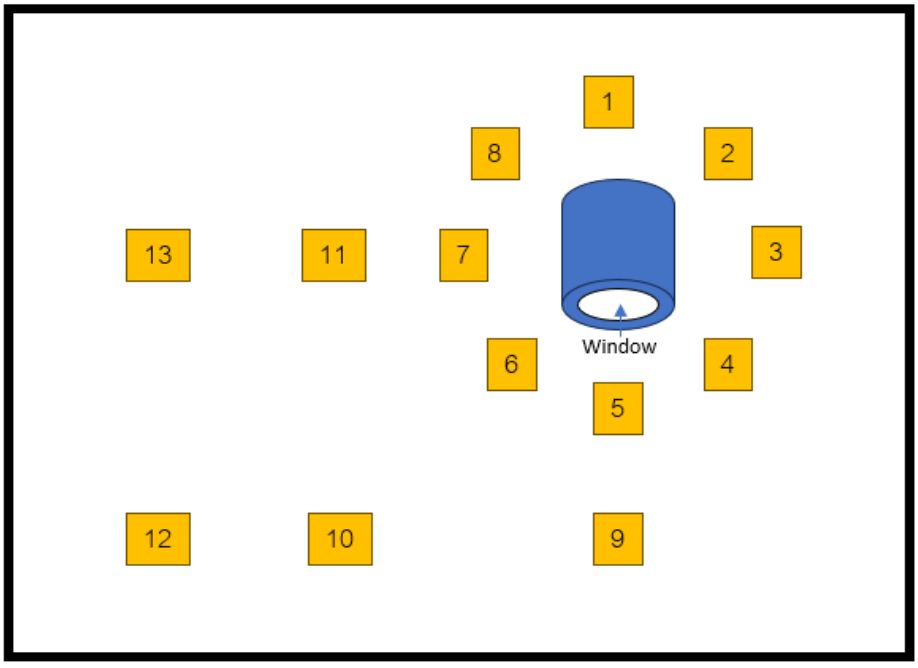

FIGURE 1. A plan view of the TPF-2 facility showing the strategic placement of the $LaBr_3(Ce)$ detectors (yellow numbered boxes). The blue cylinder represents the TPF-2 device, with an arrow indicating its single window side.

IV. RESULTS AND ANALYSIS

IV.A. Confirmation of Pinch Phenomena and Electrical Parameters

During the operation of TPF-2 with Argon gas, the magnetic probes were utilized to confirm the plasma sheath velocity. Both current and high-voltage probes measured the discharge current and discharge voltage to confirm the pinch phenomena [1, 2]. The current waveform of TPF-2 was fitted by the Lee code to estimate the pinch parameters, which consisted of pinch duration, pinch temperature, maximum current, maximum voltage, maximum pinch length, minimum pinch radius, and drive parameter. The estimated pinch parameters from the fitting, derived from short circuit results, were: pinch duration of 11.34 ns, pinch temperature of 332 eV, maximum current of 163 kA, maximum voltage of 139 kV, maximum pinch length of 2.72 cm, minimum pinch radius of 0.02 cm, and a drive parameter of 94 kA/(cm·Torr$^{1/2}$), respectively [1, 2].

The Speed E fast X-ray films were used for X-ray lithography of IC [1, 2]. The dose from X-ray exposure could be seen from the brightness contrast, and more shots of X-ray emission gave more contrast [1, 2]. Therefore, the pinches which occurred in TPF-2 were further confirmed by the current waveform, voltage waveform, and X-ray emission [1, 2].

IV.B. Spatial Distribution of Hard X-ray Emission

The qualitative observations align with the expected spatial distribution of HXR emission. Based on the configuration of the TPF-2 device, particularly the presence of a single window side, it is anticipated that Location 5 will exhibit the highest measured HXR intensity, as it is positioned directly in front of this window. Location 9 is expected to show the second highest intensity, also being in close proximity to the window side and the device. Other monitored locations, such as Location 4 and 6, which are also near the device but not directly in front of the window, are expected to show elevated levels, though lower than 5 and 9. Conversely, locations further away from the TPF-2 device and its window, such as Locations 10, 11, 12, and 13, are expected to show significantly lower HXR intensities, demonstrating the effect of distance and potential inherent shielding from the device's components and facility walls. This anticipated anisotropic distribution provides initial qualitative validation for the understanding of HXR propagation from the TPF-2.

IV.C. Spectral Characteristics and Electron Energy Inference

The measured HXR spectrum exhibits a non-thermal distribution, indicating the presence of energetic electron populations within the TPF-2 plasma. The maximum detected photon energy extended up to approximately 421 eV, which suggests that electrons are accelerated to similar energies. By fitting the high-energy tail of the spectrum with an exponential function (e.g., $I(E) \propto \exp(-E/E_0)$), an effective electron temperature (or characteristic energy) E_0 can be inferred. For the TPF-2 shots in this study, the inferred E_0 was found to be approximately 332 eV. This value provides a rough estimate of the average energy of the energetic electrons responsible for the HXR production. The intensity and spectral shape were observed to vary shot-to-shot, correlating with changes in discharge current and neutron yield, which will be subject to more detailed analysis in future work.

V. DISCUSSION

V.A. Correlation of Radiological Hot Spots with Tokamak Geometry and RE Loss Physics

The observed (or expected) highly structured and anisotropic HXR map is a direct physical consequence of the interplay between energetic electron dynamics and the specific geometry of the TPF-2 device. The anticipated pronounced hot spots at Location 5 and subsequently Location 9, are almost certainly situated in close proximity to the primary HXR emission region, which is expected to be more prominent along the side of the device containing the single window. This window likely provides a less attenuated path for the hard X-rays generated from electron interactions with the anode or other internal components. Energetic electrons, accelerated during the pinch, will generate intense Bremsstrahlung X-rays at their points of impact, and the radiation will stream outwards from these localized sources. Conversely, areas with lower radiation levels are effectively shadowed by the dense components of the TPF-2 device itself or by the surrounding experimental hall structures. This spatial pattern of hot spots serves not only as a safety survey but also as a passive diagnostic, providing valuable, albeit indirect,

information about where on the machine the majority of energetic electrons are being lost or where the HXR emission is most intense. This information is crucial for optimizing future diagnostic placements and refining safety protocols.

V.B. Implications for Radiological Protection and Operational Safety

These initial spectroscopic results are crucial for both advanced plasma diagnostics and for radiological safety planning at TPF-2. From a diagnostic perspective, direct HXR spectroscopy provides a more accurate measure of the energetic electron beam characteristics compared to previous indirect methods. This data can be used to benchmark and refine theoretical models that describe electron acceleration and transport in plasma focus devices. From a safety perspective, knowing the energy spectrum of the hard X-rays is paramount. High-energy photons are highly penetrating, and this study confirms that TPF-2 produces a significant flux of such radiation. This information is directly applicable to:

1. Designing optimized shielding: The measured spectrum allows for more accurate calculation of the required shielding thickness and materials.
2. Developing robust safety protocols: Understanding the HXR energy range helps in establishing appropriate exclusion zones and personal protective equipment requirements for personnel working near the device.
3. Assessing occupational dose: This data forms a baseline for potential future estimations of personnel dose during prolonged operational campaigns or when using D-D/D-T fuels, where neutron-induced X-rays and gamma rays might become an additional concern.

VI. CONCLUSION AND RECOMMENDATIONS FOR FUTURE WORK

VI.A. Summary of Conclusions

This pioneering investigation has successfully demonstrated the feasibility and value of direct hard X-ray spectroscopy using a $LaBr_3$(Ce) detector at the Thailand Plasma Focus 2 (TPF-2) device. The key conclusions are:

1. A robust and reliable HXR spectroscopy system utilizing a fast $LaBr_3$(Ce) scintillator has been successfully implemented at TPF-2.
2. The first direct hard X-ray energy spectrum from TPF-2 has been obtained, revealing a broad, non-thermal Bremsstrahlung spectrum extending to energies up to approximately 421 eV, with an inferred effective electron temperature of 332 eV.
3. These results provide critical empirical data supporting the existence of energetic electron acceleration mechanisms during TPF-2 operation and establish an essential radiological baseline for the facility.
4.

VI.B. Recommendations for Future Research and Development

The findings of this work lay a strong foundation for future, more detailed investigations into HXR production at TPF-2 and broader plasma focus physics. The following actions are recommended:

1. Time-Resolved Spectroscopy: Implement faster digitizers and advanced analysis techniques to obtain time-resolved HXR spectra within a single plasma focus discharge. This would allow for the correlation of HXR emission with specific phases of the pinch dynamics and plasma instabilities.
2. Correlation with Plasma Parameters: Conduct systematic studies to correlate the HXR spectral characteristics (intensity, maximum energy, effective temperature) with varying operational parameters such as initial gas pressure, charging voltage, electrode geometry, and current waveform.
3. Anisotropy Studies: Investigate the angular distribution of HXR emission around the TPF-2 device to understand the directionality of the energetic electron beams.
4. Absolute Yield Measurement: Develop methods to measure the absolute hard X-ray yield per shot, which is critical for both physics studies and precise radiological dose assessments.
5. Monte Carlo Simulations: Develop a detailed Monte Carlo radiation transport model of the TPF-2 facility (e.g., using MCNP or Geant4) incorporating the measured HXR spectra as a source term. This model would be invaluable for optimizing shielding designs and predicting dose rates in different areas of the facility.

REFERENCES

[1] A. Tamman, M. Nisoa and T. Onjun "Preliminary numerical study of Thailand Plasma Focus II (TPF-II) design": International Journal of Modern Physics: Conference Series, vol. 32, pp. 1460334, 2014.
[2] A. Tamman, M. Nisoa, B. Paosawatanyong, D. Boonyawan, N. Poolyarat and T. Onjun, "Modelling and Electrical Characteristics of the Thailand Plasma Focus-II (TPF-2)," Walailak J Sci & Tech, vol. 15, no. 6, pp. 471-480, 2018. Dreicer, H. (1959). Electron and Ion Runaway in a Fully Ionized Gas. I. Physical Review, 115(2), 238–249.
[3] P. K. Singh, M. P. Srivastava, G. P. Singh, G. P. "Review of the modern trends in Dense Plasma Focus research" Gupta: Physics of Plasmas, Vol. 25, No. 8, 080901, 2018.
[4] J.W. Mather "Formation of a High-Density Deuterium Plasma Focus" Physics of Fluids, Vol. 8, No. 12, pp. 2099-2107, 1965.
[5] J.W. Mather McKeever, "Dense Plasma Focus" Nuclear Fusion, Vol. 11, No. 3, pp. 367-377, 1971
[6] S. L. Yap, M. A. Faiz, S. H. Saw, S. Lee "Soft X-ray measurements and their correlation with hard X-rays in a plasma focus device" **:** Physics of Plasmas, Vol. 23, No. 1, 012702, 2016.
[7] N. J. Labib, N. A. M. H. Kamal, M. S. Khan, M. Shafiq, S. Lee "Application of solid-state nuclear track detectors for characterization of soft X-ray emission from a dense plasma focus"**:** Radiation Effects and Defects in Solids, Vol. 169, No. 8, pp. 696-701, 2014
[8] A. R. Singh, S. Verma, M. M. Sharma, R. G. Sarvade, V. K. Singh "Soft X-ray diagnostics on dense plasma focus devices" Journal of Fusion Energy, Vol. 39, pp. 1-14, 2020.

Special Workshop 2 (14:00 - 16:30)	The Port Ballroom, C Floor	Special Workshop 2: ASEAN dialogue partner collaboration on safety and risk assessment (Closed Workshop)
		Chair/Facilitator 1: Dr. Julia Abdul KARIM (Malaysian Nuclear Agency (ANM)) Chair/Facilitator 2:
		Dr. Kampanart SILVA (National Energy Technology Center (ENTEC))
14:10 - 14:30		ID 80: Analytic Approach for Human Reliability Analysis of Nuclear Research Reactors in ASEAN Region Speaker: Dr. Wasin VECHGAMA, (Thailand Institute of Nuclear Technology (TINT)) Contributors: Wasin Vechgama (Thailand Institute of Nuclear Technology (Public Organization)), Jinkyun Park (Korea Atomic Energy Research Institute), Weerawat Pornroongruengchok (Thailand Institute of Nuclear Technology (Public Organization)), Saensuk Wetchagarun (Thailand Institute of Nuclear Technology (Public Organization)), Anantachai Pechrak (Thailand Institute of Nuclear Technology (Public Organization)), Kampanart Silva (National Energy Technology Center)
14:30 - 14:50		Discussion and Q&A on Research Activity 1
14:50 - 15:10		ID 89: Risk-Informed Safety Strategies for Research Reactor Users: Integrating Human Reliability and Working Culture in Operational Decision-Making Speaker: Mr. Weerawat PORNROONGRUENGCHOK, Nuclear Scientist (Practitioner Level), Thailand Institute of Nuclear Technology (TINT) Contributors: Weerawat Pornroongruengchok (Thailand Institute of Nuclear Technology), Wasin Vechgama (Thailand Institute of Nuclear Technology), Sarinrat Wonglee (Thailand Institute of Nuclear Technology), Sutasinee Kotayee (Thailand Institute of Nuclear Technology), Piyanud Thongjerm (Thailand Institute of Nuclear Technology) Discussion and Q&A on Research Activity 2

ANALYTIC APPROACH FOR HUMAN RELIABILITY ANALYSIS OF NUCLEAR RESEARCH REACTORS IN ASEAN REGION

Wasin Vechgama[1*], Weerawat Pornroongruengchok[1], Saensuk Wetchagarun[1], Anantachai Pechrak[1], Kampanart Silva[2], Jinkyun Park[3]

[1*]*Thailand Institute of Nuclear Technology (Public Organization), 16 Vibhavadi Rangsit Road, Chatuchak, Bangkok, 10900, Thailand*
[2]*National Energy Technology Center, National Science and Technology Development Agency, 114 Thailand Science Park, Phahonyothin Road, Khlong Nueng, Khlong Luang, Pathum Thani, 12120, Thailand*
[3]*Korea Atomic Energy Research Institute, 111, Daedeok-daero 989 Beon-gil, Yuseong-gu, Daejeon, 34057, Republic of Korea*

EXTENDED ABSTRACT

Nowadays, digital Instrumentation & Control (I&C) systems are increasingly being implemented in nuclear facilities as human-machine interfaces [1, 2]. These digital systems serve as the core system of nuclear facilities providing operators with monitoring and safety functions for abnormal events as well as automatic protection functions of the reactor core during potential accidents [3]. The transition from analogue system control to human-machine interfaces in the digital Main Control Room (MCR) can significantly impact the changes of crew roles, teamwork, and work performance [4]. Due to the influence of human factors on digital control systems, Human Reliability Analysis (HRA) has become an essential tool for identifying potential human errors and assessing their probabilities as data for regulatory and technical objectives [5].

Similarly, Nuclear Research Reactors (NRRs) in the Association of Southeast Asian Nations (ASEAN) are typically operated using I&C systems. Previously different HRA tools were applied to investigate human errors and estimate their probabilities. For example, Indonesia utilized the Human Factors Analysis and Classification System (HFACS) method to examine Type A human errors from operational experience data from the primary cooling system of the Reaktor Serba Guna G.A. Siwabessy (RSG-GAS) reactor [6]. Regarding the Puspati TRIGA Reactor (PTR) of Malaysia, Type C human errors were analyzed and quantified using the Standardized Plant Analysis Risk Human Reliability Analysis (SPAR-H) method [7]. As for Thailand, the HRA team identified human errors in potential initiating events of the Thai Research Reactor-1/Modification 1 (TRR-1/M1) through expert judgment and a specific HRA method [8].

Since ASEAN countries operating NRRs plan to exchange HRA data, in 2023, the Thailand Institute of Nuclear Technology (TINT) proposed an HRA project to the ASEAN Network on Nuclear Power Safety Research (ASEAN NPSR) to jointly investigate the operating culture profile and develop and conduct HRA in the region based on the guideline of the Korea Atomic Energy Research Institute (KAERI) [9, 10]. Fig. 1 shows the results of ASEAN NRR operators' cultural profiles compared to operating cultures of commercial Nuclear Power Plant (NPPs) using Hofstede's model. The results of these two cases were oriented in similar directions. The operating cultures of ASEAN NRR operators and commercial NPPs are suitable for studying and sharing HRA data to each other.

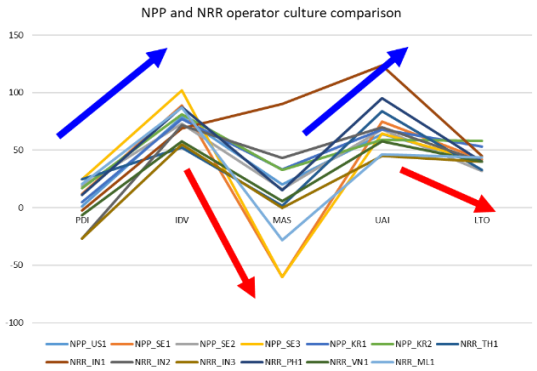

FIGURE 1. ASEAN NRR operators' cultural profiles compared to operating cultures of commercial NPPs using Hofstede's model (TH = Thailand, ML = Malaysia, IN = Indonesia, VN = Vietnam, PH = Philippines, US = United States, SE = Sweden, KR = South Korea)

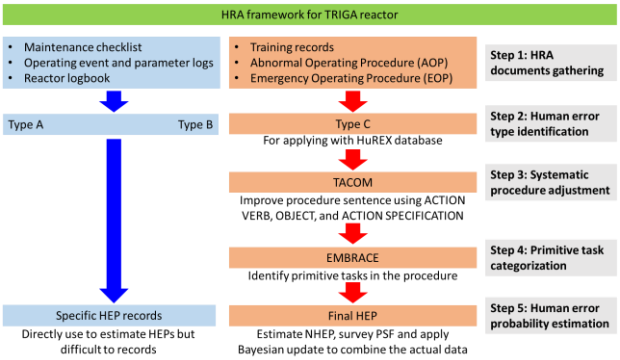

FIGURE 2. HRA practical approach of HRA for NRRs

Fig. 2 shows the HRA practical approach of HRA for NRRs [11]. In 2024, TINT and KAERI together developed a practical approach of HRA for NRRs to estimate prior Nominal Human Error Probabilities (NHEPs) from the Human Reliability data Extraction (HuREX) and updating observed human errors through the Empirical data-Based crew Reliability Assessment and Cognitive Error analysis (EMBRACE). However, the practical approach is not convenient to conduct HRA as an ASEAN NPSR benchmark problem due to the time and resource consumption. Hence, in this study, an analytic approach is suggested as an alternative HRA method to support the HRA benchmark project to support the practical approach. In the analytic approach, as ASEAN NRRs adhere to specific procedures and time for handling emergencies, the Task Complexity (TACOM) score is recommended to estimate NHEPs.

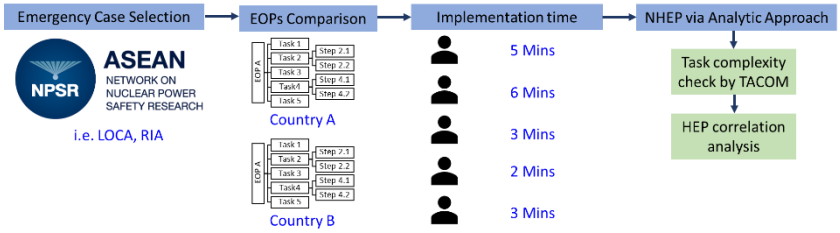

FIGURE 3. INTERNATIONAL HRA BENCHMARK STUDY IN ASEAN NPSR

Fig. 3 shows the scope of the international HRA benchmark study in ASEAN NPSR. To start the international HRA benchmark in ASEAN NRRs in ASEAN, HRA practitioners have to together discuss and select emergencies and accidents that possibly occur in general for NRRs. The complexity score of Emergency Operating Procedures (EOPs) of selected emergencies and accidents will be calculated using TACOM score [12]. The operators will be requested to provide the task performance time of the EOPs.

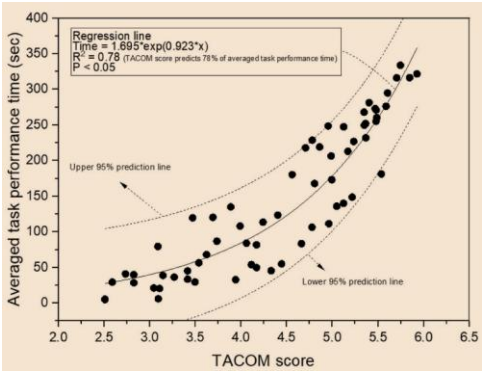

FIGURE 4. CORRELATION BETWEEN TASK PERFORMANCE TIME AND TACOM SCORE OF NPPS

Fig. 4 shows the correlation between task performance time and TACOM score [13]. The HRA implementors will check the correlation between task performance time and TACOM score. If the correlation is consistent with the empirical model of task performance time and TACOM score in Fig. 4. The overall TACOM scores of EOPs be used to estimate possible NHEPs based on the empirical model in Eq. (1) recorded unsafe act database of HuREX [14].

$$p(x) = \frac{1}{1+e^{-(1.901x-9.643)}} \quad (1)$$

where $\boldsymbol{p(x)}$ is the estimated probability of unsafe act and $\boldsymbol{x}$ is TACOM score.

ACKNOWLEDGMENTS

The authors are grateful to the Thailand Institute of Nuclear Technology (TINT) and the ASEAN Network on Nuclear Power Safety Research (ASEAN NPSR) for providing important information to support this study. The authors also thank the Ministry of Higher Education, Science, Research, and Innovation (MHESI), Thailand, the Korea Atomic Energy Research Institute (KAERI), and the Korea National University of Science and Technology (UST) for their time and support during the publication process.

REFERENCES

[1] P. SINGH, L. K. SINGH, "Instrumentation and Control Systems Design for Nuclear Power Plant: An Interview Study with Industry Practitioners," *Nuclear Engineering and Technology*, **53**, 11 (2021).
[2] M. S. MINHAT, N. A. M. SUBHA, N. HAMZAH, A. R. HUSAIN, F. HASSAN, A. AHMAD, F. S. ISMAIL, "Hybrid MPC-P Controller for the Core Power Control System at TRIGA Reactor," *Journal of Process Control*, **122** (2023).
[3] J. PARK, T. KIM, S. KOO, "Verification Strategy for Artificial Intelligence Components in Nuclear Plant Instrumentation and Control Systems," *Progress in Nuclear Energy*, **164**, 104842 (2023).
[4] W. JUNG, Y. KIM, J. PARK, "A Time-reliability Correlation for Estimating the Diagnosis Error Probability of a Nuclear Power Plant with up-to-date Human–machine Interfaces," *Nuclear Engineering and Technology*, **56**, 10 (2024).
[5] I. S. KIM, "Human Reliability Analysis in the Man–machine Interface Design Review," *Annals of Nuclear Energy*, **28**, 11 (2001).
[6] S. SANTOSO, R. HIMAWAN, J. SITUMORANG, T. J. SURYONO, E. EDISON, "Reactor Operational Experience Review and Analysis based on un-intended Reactor Trip Data," *Jurnal Teknologi Reaktor Nuklir Tri Dasa Mega*, **21**, 2 (2019).
[7] A. HASSAN, M. MASKIN, P. PRAK TOM, F. BRAYON, P. HLAVAC, F. MOHAMED, "Operator Response Modeling and Human Error Probability in TRIGA Mark II Research Reactor Probabilistic Safety Assessment," *Annals of Nuclear Energy*, **102**, (2017).
[8] W. VECHGAMA, K. SILVA, A. PECHRAK, S. WETCHAGARUN, "Application of Hazard and Operability Technique to Level 1 Probabilistic Safety Assessment of Thai Research Reactor-1/Modification 1: Internal Events and Human Errors," *Progress in Nuclear Energy*, **138**, 103838 (2021).
[9] W. VECHGAMA, K. SILVA, J. YANG, J. PARK, "Initiating Risk Assessment Research Collaboration Between South Korea and ASEAN NPSR Member States," *Asian Symposium on Risk Assessment and Management 2023*, Hong Kong, 4-6 December 2023.
[10] W. VECHGAMA, J. PARK, S. WETCHAGARUN, A. PECHRAK, K. SILVA, "Systematic Preprocessing for Development of Human Reliability Analysis Framework of TRIGA Reactor," *Asian Symposium on Risk Assessment and Management 2023*, Hong Kong, 4-6 December 2023.
[11] W. VECHGAMA, J. PARK, S. WETCHAGARUN, A. PECHRAK, K. SILVA, "Development of a Human Reliability Analysis Framework for Nominal Human Error Probability Estimate of the TRIGA Research Reactor in Thailand," *Nuclear Engineering and Technology*, **56**, 11 (2024).
[12] J. PARK, "The Complexity of Proceduralized Tasks," *Springer Series in Reliability Engineering* (2009).
[13] I. JANG, Y. KIM, J. PARK, "Scrutinizing the Effect of Task Complexity on Operators' Task Performance Time in a Digitalized Main Control Room of a Nuclear Power Plant," *Nuclear Engineering and Technology*, **57**, 3 (2025).
[14] I. JANG, J. PARK, "Determining the Complexity Level of Proceduralized Tasks in a Digitalized Main Control Room using the TACOM Measure," *Nuclear Engineering and Technology*, **54**, 11 (2022).

Risk-Informed Safety Strategies for Research Reactor Users: Integrating Human Reliability and Working Culture in Operational Decision-Making

Weerawat Pornroongruengchok[1,2,3], Sarinrat Wonglee[1], Sutasinee Kotayee[1], Piyanud Thongjerm[1], Wasin Vechgama[1,2,3*]

[1]*Thailand Institute of Nuclear Technology (Public Organization), 9/9 Moo7, Saimoon, Ongkharak, Nakhon-nayok, 26120, Thailand.*
[2]*Thailand Academy of Science (TAS), Program Management Unit for Human Resources & Institutional Development,Research and Innovation (PMU-B), 319 Chamchuri Square Building 14th Fl., Phayathai Rd., Patumwan, Bangkok, 10330, Thailand.*
[3]*Mahidol University, 999 Phuttamonthon 4 Road, Salaya, Nakhon Pathom, 73170, Thailand.*

Email: weerawat@tint.or.th

EXTENDED ABSTRACT

In the ASRAM 2024 conference, we presented a cultural analysis of the working relationship between research reactor operators and users [1], applying Hofstede's cultural dimensions model [2,3,4]. This study revealed significant perception gaps related to authority, uncertainty avoidance, and individualism, all of which influence communication, decision-making, and safety behavior during operations. Building on this foundation, a broader regional perspective was introduced at the European Safety and Reliability (ESREL) and Society for Risk Analysis Europe (SRA-E) conferences. These subsequent presentations explored the cultural diversity among reactor users across ASEAN member states and emphasized the implications for human reliability in research reactor settings.

Thailand Case Study and Key Findings

Based on operational data and structured interviews conducted at the TRR-1/M1 facility, four primary themes emerged from user feedback

1. Adaptive Safety Training
   Users expressed the need for scenario-based and experiment-specific training tailored to their diverse backgrounds and research objectives.
2. Localized Radiation Shielding
   There were requests for flexible, modular shielding solutions that better align with various experimental configurations.
3. Improved Communication and Feedback Mechanisms
   Users highlighted the importance of establishing real-time channels to report anomalies or suggest safety improvements.
4. User-Centric Monitoring Systems
   Feedback emphasized the need for real-time, accessible displays of radiation levels near workspaces, enabling users to make informed safety decisions.

These recommendations have been synthesized into a human-factor-informed framework designed to complement existing safety protocols at research reactors. The conceptual structure of this integrated approach is illustrated in Figure 1, which shows how user feedback, cultural dimensions, and human reliability inputs can drive safety strategy development and lead to improved outcomes.

Commitment to Continuous Improvement

During the most recent ASEAN technical coordination meeting, stakeholders discussed and endorsed the following safety enhancement strategies, which reflect a shared commitment to continuous improvement

1. Enhanced Safety Protocol Training
   Ensuring that all users, including temporary researchers and newcomers, receive regular, up-to-date training aligned with current safety standards and emergency procedures.
2. Improved Communication Channels
   Establishing transparent, bidirectional pathways for users to report safety concerns, near-miss incidents, or operational challenges.
3. Upgraded Monitoring Systems

Implementing advanced real-time radiation monitoring and alert mechanisms in high-use areas to increase situational awareness and promote safer working conditions.

These ongoing initiatives contribute to regional knowledge exchange and foster a collaborative environment that supports safer and more efficient research reactor utilization throughout ASEAN.

Towards a Wider ASEAN Safety Understanding

This work will extend the discussion by presenting a comparative ASEAN user cultural profile, based on surveys and interviews with research reactor users in Thailand, Indonesia, Malaysia, Vietnam, and the Philippines. This session will engage participants in reflecting on

1. How cultural factors influence safety-related decisions and behavior
2. The similarities and differences in user perspectives across ASEAN
3. What lessons reactor facilities can learn from one another's human reliability challenges and user feedback

The presentation will include visual dashboards and statistical summaries to demonstrate how cultural understanding and user involvement can serve as key inputs to strategic safety management.

In conclusion, this work contributes to the development of user-informed safety strategies by incorporating cultural and human reliability insights into research reactor operations. It emphasizes the importance of listening to users' perspectives and comparing feedback across ASEAN countries. Future work will focus on expanding collaborative safety profiling, facilitating knowledge exchange, and refining strategic planning tools to better support human-centric safety practices in research reactors.

Human reliability and working culture must be considered as integral components of any comprehensive safety framework. Involving users as active stakeholders in safety planning and decision-making can lead to more adaptive, inclusive, and effective risk management practices. The Thailand case study offers a replicable model for research reactor facilities across the region. By fostering mutual understanding, sharing experiences, and listening to diverse user perspectives, ASEAN's research reactors can collectively advance toward enhanced safety, both technically and culturally.

FIGURE 1. Integrated Risk-informed Safety Model for Research Reactor Users

ACKNOWLEDGMENTS

The author would like to sincerely thank the operational staff and safety personnel at the Thailand Research Reactor for their kind support and participation in the study. Special appreciation is extended to the ASEAN Network of Nuclear Power Safety Research (ASEAN NPSR) for their continued collaboration, insightful contributions, and commitment to strengthening regional safety culture and research reactor utilization. Also, this research has received funding support from Thailand Academy of Sciences (TAS) Project under Program Management Unit for Human Resources and Institutional Development, Research and Innovation (PMU-B), Pathumwan, Bangkok, 10330, Thailand. [Grant number B13F660139].

REFERENCES

[1] Weerawat, P. and Wasin, V., "Cultural profiles comparison of operators and users in TRR-1/M1," *Probabilistic Safety Assessment and Management 17 and Asian Symposium on Risk Assessment and Management 2024*, Sendai, Japan, 7-11 October (2024).

[2] Nickerson, Charlotte. "Hofstede's cultural dimensions theory & examples." *Simply psychology* 24 (2023).

[3] DAHUNSI, Stephen. *Accessing the Impact of National Cultures on Nuclear Security for Deployment of Advanced Reactors in Sub-Saharan Africa*. Oak Ridge National Laboratory (ORNL), Oak Ridge, TN (United States), (2024).

[4] Park, Jinkyun, and Wondea Jung. "Comparing cultural profiles of MCR operators with those of non-MCR operators working in domestic Nuclear Power Plants." *Reliability Engineering & System Safety* 133 (2015)

Closing Note

This proceedings marks the conclusion of ASRAM2025.

The organizers sincerely thank all participants, authors, reviewers, and session chairs for their valuable contributions and support.

Contact Information

Local Organizing committee
ASRAM2025@tint.or.th

Knowledge shared is safety multiplied.

See you at ASRAM 2026!

Closing Note

This proceedings marks the conclusion of ASRAM2025.

The organizers sincerely thank all participants, authors, reviewers, and session chairs for their valuable contributions and support.

Contact Information

Local Organizing committee
ASRAM2025@tint.or.th

Knowledge shared is safety multiplied.

See you at ASRAM 2026!